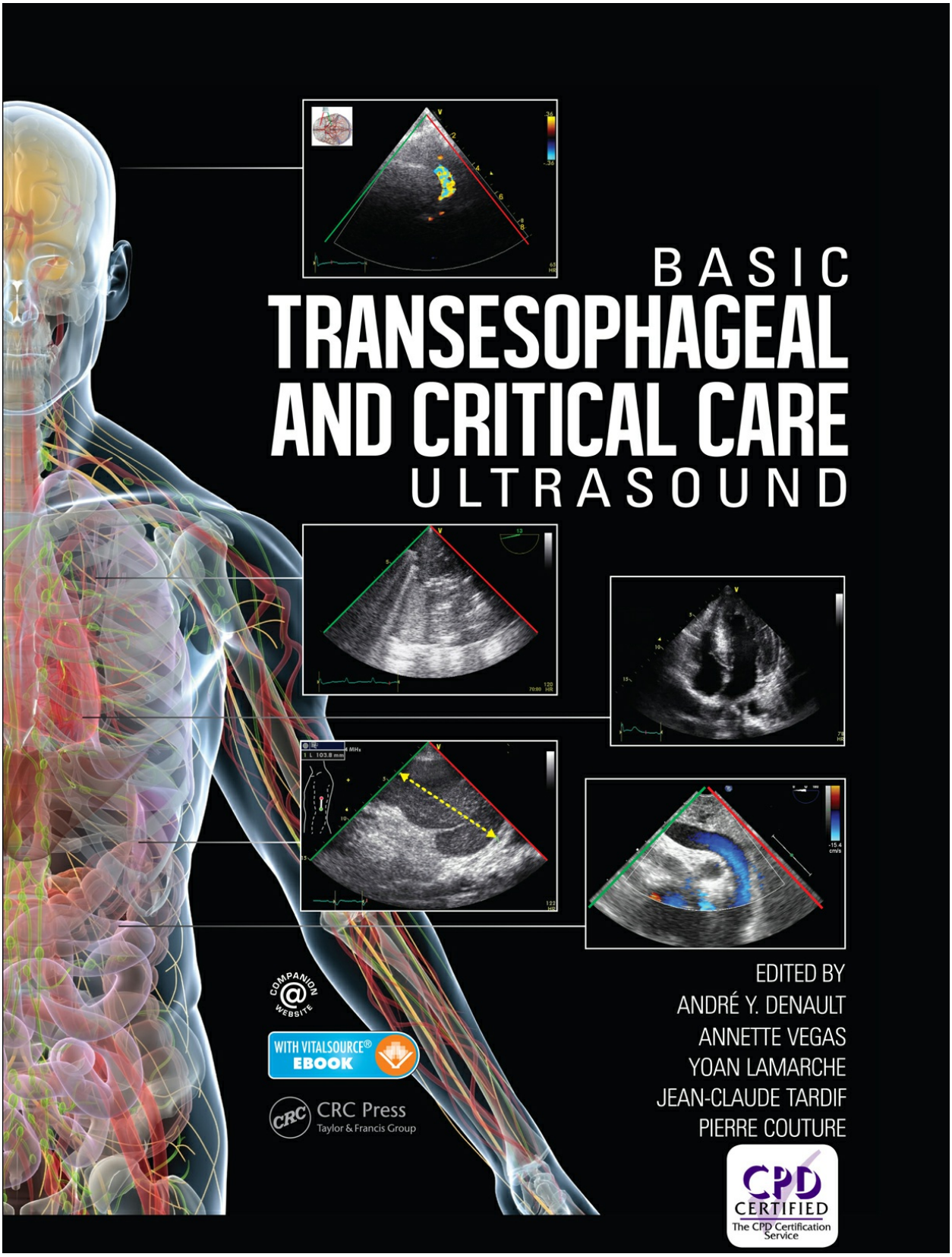
BASIC
TRANSESOPHAGEAL
AND CRITICAL CARE
ULTRASOUND
COMPANION @ WEBSITE
WITH VITALSOURCE® EBOOK
CRC Press
Taylor & Francis Group
EDITED BY
ANDRÉ Y. DENAULT
ANNETTE VEGAS
YOAN LAMARCHE
JEAN-CLAUDE TARDIF
PIERRE COUTURE
CPD CERTIFIED
The CPD Certification Service

BASIC TRANSESOPHAGEAL AND CRITICAL CARE ULTRASOUND

BASIC TRANSESOPHAGEAL AND CRITICAL CARE ULTRASOUND

EDITED BY

ANDRÉ Y. DENAULT
Institut de Cardiologie de Montréal, Québec, Canada

ANNETTE VEGAS
Toronto General Hospital Ontario, Canada

YOAN LAMARCHE
Institut de Cardiologie de Montréal and Hôpital du Sacré-Coeur de Montréal, Québec, Canada

JEAN-CLAUDE TARDIF
Research Center at the Montreal Heart Institute, Québec, Canada

PIERRE COUTURE
Institut de Cardiologie de Montréal, Québec, Canada

CRC Press
Taylor & Francis Group
Boca Raton London New York

CRC Press is an imprint of the
Taylor & Francis Group, an informa business

CRC Press
Taylor & Francis Group
6000 Broken Sound Parkway NW, Suite 300
Boca Raton, FL 33487-2742

CRC Press is an imprint of Taylor & Francis Group, an Informa business

No claim to original U.S. Government works

Printed on acid-free paper

International Standard Book Number-13: 978-1-4822-3712-2 (Pack – Book + eBook)

Visit the Taylor & Francis Web site at
http://www.taylorandfrancis.com

and the CRC Press Web site at
http://www.crcpress.com

Visit Companion Website: www.crcpress.com/cw/denault

Dedication

This book is dedicated to:

My wife Denise Fréchette and my children Jean-Simon, Gabrielle, and Julien who have supported me with love and patience (André Y Denault)

My parents, Patrick and Lena, and my brother Derek, who have always been supportive (Annette Vegas)

Maude and Julien for their support and inspiration (Yoan Lamarche)

Michèle, Jean-Daniel and Pier-Luc (Jean-Claude Tardif)

Frédéric and Noémie (Pierre Couture)

And above all, our patients for whom we believe that knowledge in the use of bedside ultrasound will improve their care.

The editors would like to thank sincerely Dora and Avrum Morrow and the Richard I Kaufman Endowment Fund in Anesthesia and Critical Care.

Avrum Morrow

Richard I Kaufman

List of contributors

Martin Albert, MD, FRCPC Associate Professor of Medicine, Internist and Intensivist, Department of Medicine and Critical Care, Hôpital du Sacré-Coeur de Montréal Research Center and Intensivist, Department of Surgery, Institut de Cardiologie de Montréal, Université de Montréal, Montréal, Québec, Canada

Christian Ayoub, MD, B.Pharm, FRCPC Clinical Assistant Professor, Department of Cardiac Anesthesiology, Institut de Cardiologie de Montréal, Department of Anesthesiology, Maisonneuve-Rosemont Hospital, Université de Montréal, Montréal, Québec, Canada

Mustapha Belaidi, MD Department of Cardiac Anesthesiology, Centre Hospitalier Universitaire (CHU) de Nantes, Nantes, France

François M. Carrier, MD, FRCPC Clinical Assistant Professor, Department of Anesthesiology and Division of Critical Care, Department of Medicine, Centre Hospitalier de l'Université de Montréal (CHUM), Université de Montréal, Montréal, Québec, Canada

D. Catalina Casas Lopez, MD Department of Anesthesia and Perioperative Medicine, London Health Sciences and St. Joseph's Health Care, University of Western Ontario, London, Ontario, Canada

Yiorgos Alexandros Cavayas, MD, FRCPC Critical Care Fellow, Université de Montréal, Montréal, Québec, Canada

David-Olivier Chagnon, MD, FRCPC Department of Radiology, Hôpital Pierre-Boucher, Longueuil, Québec, Canada

Carl Chartrand-Lefebvre, MD, FRCPC Clinical Professor, Department of Radiology, Centre Hospitalier de l'Université de Montréal (CHUM), Université de Montréal, Montréal, Québec, Canada

Robert Chen, MD, FRCPC Assistant Professor of Anesthesia, Cardiac Anesthesia and Intensive Care, University of Ottawa Heart Institute, University of Ottawa, Ottawa, Ontario, Canada

Anne S. Chin, MD, FRCPC Assistant Professor, Department of Radiology, Cardiothoracic Section, Centre Hospitalier de l'Université de Montréal (CHUM), Université de Montréal, Montréal, Québec, Canada

Jennifer Cogan, MD, M.Epid, FRCPC Associate Professor, Department of Anesthesiology, Institut de Cardiologie de Montréal, Université de Montréal, Montréal, Québec, Canada

Geneviève Côté, MD, MSc, FRCPC Assistant Professor, Pediatric Cardiac Anesthesiologist, Department of Pediatric Anesthesia, Centre Hospitalier Universitaire (CHU) Mère-Enfant Sainte-Justine, Université de Montréal, Montréal, Québec, Canada

Pierre Couture, MD, FRCPC Clinical Associate Professor,Cardiac Anesthesiology Department, Institut de Cardiologie de Montréal, Department of Anesthesiology, Université de Montréal, Montréal, Québec, Canada

André Y. Denault, MD, PhD, FRCPC, FASE, ABIM-CCM, FCCS Professor, Critical Care Ultrasound Training Program Director, Department of Cardiac Anesthesiology and Division of Critical Care of the Department of Cardiac Surgery, Institut de Cardiologie de Montréal and Division of Critical

Care of the Department of Medicine, Centre Hospitalier de l'Université de Montréal (CHUM), Université de Montréal, Montréal, Québec, Canada

Georges Desjardins, MD, FRCPC, FASE Associate Professor of Anesthesiology, Director of Perioperative Echocardiography, Department of Anesthesiology, Institut de Cardiologie de Montréal,Université de Montréal, Montréal, Québec, Canada

Vinay K. Dhingra, MD, FRCPC Clinical Associate Professor of Medicine, Medical Director Quality Critical Care Vancouver Acute Clinical Lead, Department of Medicine, Division of Critical Care, Vancouver General Hospital, University of British Columbia, Vancouver, British Columbia, Canada

Jean-Nicolas Dubé, MD, MA, FRCPC Clinicial Instructor, Department of Internal Medicine, Division of Critical Care, Centre intégré universitaire de santé et de services sociaux de la Mauricie-et-du-Centre-du-Québec, Université de Montréal, Trois- Rivières, Québec, Canada

Ashraf Fayad, MD, MSc, FRCPC, FCARCSI, FACC, FASE Associate Professor, Director of Perioperative Hemodynamic Echocardiography, Department of Anesthesiology, University of Ottawa, Ottawa, Ontario, Canada

Gordon N. Finlayson, BSc, MD, FRCPC (Anesth and CCM) Clinical Assistant Professor, Division of Critical Care, Department of Anesthesiology and Perioperative Care, Vancouver General Hospital, University of British Columbia, Vancouver, British Columbia, Canada

Annie Giard, MD, FRCPC Emergency Room Physician, Responsible for Echography Training in Emergency Medicine and Family Medicine, Université de Montréal, ARDMS, Local Manager for the Training of Independent Practitioner of CEUS, Department of Emergency Medicine, CIUSS du Nordde-l'Île-de-Montréal, Installation Hôpital du Sacré-Coeur de Montréal, Montréal, Québec, Canada

Martin Girard, MD, FRCPC Clinical Associate Professor, Department of Anesthesiology, Division of Critical Care of the Department of Medicine, Centre Hospitalier de l'Université de Montréal (CHUM), Université de Montréal, Montréal, Québec, Canada

Donald E.G. Griesdale, MD, MPH, FRCPC Assistant Professor, Department of Anesthesiology, Pharmacology and Therapeutics, Department of Medicine, Division of Critical Care Medicine, Chair, Vancouver Medical Advisory Council, Vancouver General Hospital, University of British Columbia, Vancouver, British Columbia, Canada

Han Kim, MD, FRCPC Assistant Professor, Department of Anesthesia, St. Michael's Hospital, University of Toronto, Toronto, Ontario, Canada

Manoj M. Lalu, MD, PhD, FRCPC Clinical Scholar, Department of Anesthesiology, The Ottawa Hospital, Regenerative Medicine Program, The Ottawa Hospital Research Institute, Ottawa, Ontario, Canada

Yoan Lamarche, MD, MSc, FRCSC Assistant Professor of Surgery, Cardiac Surgeon and Intensivist, Department of Cardiac Surgery, Institut de Cardiologie de Montréal and Hôpital du Sacré-Coeur de Montréal, Université de Montréal, Montréal, Québec, Canada

Moishe Liberman, MD, PhD Associate Professor of Surgery, Director, CHUM Endoscopic in Tracheobronchial and Oesophageal Center (C.E.T.O.C.), Marcel and Rolande Gosselin Chair in Thoracic Surgical Oncology, Scientist, Research Center, Centre Hospitalier de l'Université de Montréal (CHUM), Université de Montréal, Montréal, Québec, Canada

Feroze Mahmood, MD, FASE Associate Professor of Anesthesia, Harvard Medical School, Director Vascular Anesthesia and Perioperative Echocardiography, Beth Israel Deaconess Medical Center, Boston, U.S.A.

Ramamani Mariappan, DA, MD, Dip.NB Professor, Christian Medical College, Vellore, India

Serge McNicoll, MD, CSPQ Cardiologist, Chief of Cardiology Department of the Department of Medicine, Hôpital Régional de St-Jérôme, Université de Montréal, Montréal, Québec, Canada

Massimiliano Meineri, MD Associate Professor of Anesthesia, Staff Anesthesiologist, Director Perioperative Echocardiography, Toronto General Hospital, University of Toronto, Toronto, Ontario, Canada

Scott J. Millington, MD, FRCPC Assistant Professor, Department of Critical Care Medicine, The Ottawa Hospital, University of Ottawa, Ottawa, Ontario, Canada

Blandine Mondésert, MD Assistant Professor, Cardiologist, Division of Cardiac Electrophysiology, Department of Medicine, Adult Congenital Heart Disease Center, Institut de Cardiologie de Montréal, Université de Montréal, Montréal, Québec, Canada

Céline Odier, MD, FRCPC Assistant Clinical Professor, Department of Neurosciences, Centre Hospitalier de l'Université de Montréal (CHUM), Université de Montréal, Montréal, Québec, Canada

Sarto C. Paquin, MD, FRCPC Assistant Professor, Department of Medicine, Division of Gastroenterology, Centre Hospitalier de l'Université de Montréal (CHUM), Université de Montréal, Montréal, Québec, Canada

Eric Piette, MD, MSc, FRCPC Clinical Assistant Professor, Emergency Room Physician, Department of Family Medicine and Emergency Medicine, Hôpital du Sacré-Coeur de Montréal, CIUSS Nord de l'Île de Montréal, Université de Montréal, Montréal, Québec, Canada

Wilfredo Puentes, MD Assistant Professor, Department of Anesthesia and Perioperative Medicine, London Health Sciences and St. Joseph's Health Care, University of Western Ontario, London, Ontario, Canada

Andrea Rigamonti, MD Assistant Professor, Director,Trauma-Neuro Anesthesia and Critical Care Fellowship Program, Departments of Anesthesia and Critical Care, St. Michael's Hospital, Department of Anesthesia and Interdepartmental Division of Critical Care Medicine, University of Toronto, Toronto, Ontario, Canada

Antoine G. Rochon, MD, FRCPC Assistant Professor, Department of Anesthesiology, Cardiac Anesthesiology Fellowship Program Director, Perioperative Transesophageal Echocardiography Training Program Director, Institut de Cardiologie de Montréal, Université de Montréal, Montréal, Québec, Canada

Andrew Roscoe, MB ChB, FRCA Consultant in Anaesthesia and Intensive Care Medicine, Papworth Hospital, Cambridge, U.K.

Karim Serri, MD, FRCPC Associate Professor, Department of Medicine, Critical Care Division, Hôpital du Sacré-Coeur de Montréal, Université de Montréal, Montréal, Québec, Canada

Ying Tung Sia, MD, MSc, FRCPC Clinicial Assistant Professor, Department of Medicine, Division of Cardiology, Centre Hospitalier Régional de Trois-Rivières and Division of Critical Care, Institut de Cardiologie de Montréal, Université de Montréal, Montréal, Québec, Canada

Jean-Claude Tardif, CM, MD, FRCPC, FACC, FAHA, FESC, FCAHS Professor, Director of the Research Center, Department of Medicine, Division of Cardiology, Institut de Cardiologie de Montréal, Université de Montréal, Montréal, Québec, Canada

Annette Vegas, MD, FRCPC, FASE Associate Professor, Staff Anesthesiologist, Department of Anesthesiology, Toronto General Hospital, University of Toronto, Toronto, Ontario, Canada

Claudia H. Viens, MD, FRCPC Assistant Professor, Department of Anesthesiology, Institut de Cardiologie de Montréal, Université de Montréal, Montréal, Québec, Canada

Kim-Nhien Vu, MD Diagnostic Radiology Resident, Department of Radiology, Centre Hospitalier de l'Université de Montréal (CHUM), Université de Montréal, Montréal, Québec, Canada

Contents

Part II

Foreword

Since I first trained in Critical Care Medicine (CCM) in the mid-1980s at the University of Pittsburgh, where Andre Denault then followed, the intensive care unit (ICU) has changed dramatically with regards to the acuity, severity and complexity of the patient population. As clinicians at the bedside, the questions we ask are increasingly complex and the answers we seek are more precise. Non-invasive monitoring is more refined and ultrasound (US) technology has become the modern clinician's stethoscope. US monitoring has gone from echocardiography being performed by a cardiologist in the occasional ICU patient two decades ago, to the intensivist obtaining either a focused or comprehensive echocardiogram and performing US examination of the thoracic and abdominal contents, as well as guiding vascular access and monitoring neurological status. Since all the organs of interest to the CCM physician are accessible by US imaging, the scope of practice is rapidly growing in popularity. This is matched only by the challenge we face in mastering the technology, recognizing the limits, interpreting the results and teaching ultrasound to our students, residents, fellows and colleagues.

It is with these objectives in mind that this textbook on US imaging was wonderfully conceived by the team of experts that Andre has put together. The chapters proceed in more or less the same fashion as US imaging has progressed through the last decades. From basic principles and image acquisition, the reader evolves to transesophageal echocardiography (TEE) and assessing intra-cardiac and extra-cardiac structures and function, as well as all other organs accessible to the TEE platform. The reader then proceeds to transthoracic echocardiography and focused US imaging of the pulmonary and abdominal contents, with a welcome addition regarding brain monitoring. Perioperative and ICU assessments are well dealt with, as are ICU procedures and vascular access in the critically ill patient. Each chapter is rigorously structured and very well referenced with diagrams, intra-operative photographs, illustrations and videos to optimize interactive learning for both the novice, as well as the experienced clinician. Tables and figures abound throughout the text in pragmatic support and as a reminder of concepts, classifications and equations. Last but not least are the chapters dedicated to

simulation training and examination, which are of the utmost importance to those involved in structuring US teaching programs and in abiding by society guidelines and recommendations.

Dr Denault and his team are to be complimented for this comprehensive and rigorous effort in mastering US imaging whether in the operating room or the ICU. It is a reflection of where US imaging has come from and where it is going. However, for US imaging to evolve, we must make certain it is well performed, interpreted and leads to appropriate decision making. This book strives to achieve these goals.

Our CCM training program at the University of Montreal believes US imaging is now an obligatory skill to be mastered during fellowship training. Our fellows go through a 3-month structured US training program in order to become proficient in basic US imaging of the heart and other organs through TEE, TTE and focused US examination. This book recreates how our fellows are being trained and as such, is our textbook of reference. Years of clinical observation and correlation with US imaging by clinicians have gone into this book and I am extremely proud of what it has become and what it will achieve.

Jean-Gilles Guimond MD, FRCPC, FCCP
Program Director, Critical Care Medicine
Université de Montréal, Quebec, Canada

Preface

In 2005, we published our first Transesophageal Echocardiography Multimedia Manual, [1] which was followed in 2011 by a second edition. [2] These manuals were written to help prepare practising anesthesiologists and trainees in cardiothoracic anesthesia and critical care for the National Board of Echocardiography (NBE) Examination of Special Competence in Advanced Perioperative Transesophageal Echocardiography (TEE). In the second edition, several chapters were dedicated to the role of TEE in non-cardiac surgical applications and in the intensive care unit (ICU). The field of TEE has matured significantly over the last decade. In addition, with the widespread availability of ultrasound, there is a growing interest for the applications of bedside ultrasound in the ICU, non-cardiac operating room, and emergency medicine. Furthermore, training guidelines in basic TEE [3] and in critical care ultrasound were published. [4] , [5] Certification in both modalities through the NBE and the American College of Chest Physicians (ACCP) have also became available.

The goal of this manual also remains simple: to prepare anesthesiologists, critical care physicians, fellows, and residents for the NBE Basic Perioperative TEE examination and ACCP critical care ultrasonography certification. This book, whose editors and the majority of its authors are from Canadian universities, also covers the Canadian recommendations for critical care ultrasound training and competency. [6] It is the opinion of the editors that all critical care physicians and general anesthesiologists will eventually become trained in both basic TEE and critical care ultrasound. At the Universite de Montreal in 2013, the Critical Care Program Director, Dr Jean-Gilles Guimond asked me to initiate comprehensive ultrasound training for all our fellows. This is the manual that we will be using.

The manual is divided in two parts. Part I consisting of Chapters 1 to 12 is dedicated to basic TEE. Part II relates to focused bedside ultrasound and includes Chapters 13 to 19. In Chapter 20, two mock exams inspired by the NBE Basic TEE and the ACCP exam are presented, and additional materials are available from the CRC website: https://www.crcpress.com/product/isbn/9781482237122 In Part I, we introduce for the first time a

chapter on extra-cardiac TEE. In addition, in Part II, there is a chapter on ultrasound of the brain. These unconventional areas will become more important in the future as clinicians evaluate not only the etiology of hemodynamic instability, but also the impact on multiple organs such as the kidney, liver, splanchnic perfusion, and brain. This manual is unique because the editors and authors represent several different fields of clinical practice in anesthesia, internal medicine, emergency medicine, and surgery. General anesthesiologists, cardiothoracic anesthesiologists and neuro-anesthesiologists have shared their unique expertise alongside critical care physicians, cardiologists, gastroenterologists, neurologists, emergency medicine specialists, abdominal and thoracic radiologists, and cardiac and thoracic surgeons. I sincerely thank all the authors who have taken the time to contribute to this work.

Such a manual would not have been possible without the support of my four editors. I am very grateful for their contributions. Dr Annette Vegas is a cardiothoracic anesthesiologist with a critical care appointment at the Toronto General Hospital. Annette has been an editor since 2009 and has continuously raised the quality and pertinence of our educational material. She has already published several books in TEE that are carried by ultrasound trainees worldwide. She has contributed to an outstanding free educational website in ultrasound translated into several languages (https://pie.med.utoronto.ca). Her dedication to this manual has been unsurpassed and is remarkable, as it was for the second edition of the TEE manual. Dr Yoan Lamarche is a cardiac surgeon, additionally certified in critical care medicine and TEE, working at both the Montreal Heart Institute (MHI) and Hopital du Sacre-Coeur. He is the director of the MHI Cardiac Surgical ICU. Yoan’s natural leadership, educational skills, common sense, and surgical experience gave this manual clarity and a unique perspective. Dr Jean-Claude Tardif is a cardiologist and the director of the MHI Research Center. Since the perioperative anesthesia TEE program started in 1999 at the MHI, Jean-Claude has strongly supported the Anesthesiology Department in TEE development and expertise. Dr Tardif has played an important role participating in developing our manuals and has also made available the MHI research environment in order to improve the care of our patients in the operating room and the ICU. I met Dr Pierre Couture in 1993 when he returned from Paris after completing his cardiac anesthesia fellowship. We shared a common passion for ultrasound applications and have been working

and publishing together ever since. Pierre was our former Chief of Cardiac Anesthesia at the MHI. He has been helping me in all aspects of the manual, completely rewriting some chapters in order to offer the best to our students and readers. His generosity, kindness, amazing TEE knowledge, and teaching skills are well appreciated in our institution.

Several individuals have played a significant role in the creation of this manual. Mr Denis Babin is the webmaster of the Department of Anesthesiology of the Universitè de Montrèal and my research assistant since 1998. I am fortunate to have such an amazing assistant. His diverse talents in computer science, graphic design, database management, and communication provide the key elements that have made all our manuals so appealing. There is not a single figure or video that Denis has not touched, improved or converted ... I often say, “Denis, would you mind ‘babinising’ this?” Special thanks for the support and advice of my current Chief of Cardiac Anesthesia at the MHI must go to Dr Alain Deschamps. I also thank all my colleagues, anesthesiologists, critical care physicians, cardiac surgeons, and cardiologists at the MHI who have supported and alerted me to interesting cases. Likewise, I thank my critical care colleagues in the ICU of the Centre Hospitalier de l’Universite de Montreal.

This work would not have been possible without financial support. I would like to thank especially Dora and Avrum Morrow. Meeting Mr Avrum Morrow in Old Montreal and seeing the Avmor Collection was an unforgettable moment in my life. In 2014, I had the privilege of being chosen for the Richard I Kaufman Endowment Fund in Anesthesia and Critical Care. This support will allow us to continue our educational and research activities for the coming years. My gratitude to the Kaufman family is beyond words. All this support has been completely dependent on the MHI Foundation and its director Mèlanie LaCouture. The MHI Foundation has been supporting me every year since 1999 and played a key role in contacting those who are supporting this manual and our future development. Special thanks to Josèe Darche from the MHI Foundation. In addition, my appreciation goes to MHI director Dr Denis Roy and to Dr Annie Dore who is responsible for all MHI educational activities, as both have also believed in our initiatives. I am also indebted to the Fondation de l’Association des Anesthèsiologistes du Quebec and president Dr Gilles Plourde and Mr Joseph Bestravos from Sonosite/Fuji for their generous support. Credit must also be given to Mr Fainman for his generous donation that allowed us to buy the first X-Porte ultrasound system

from Sonosite/ Fuji in Canada. Several figures in this book came from this equipment.

Dr Robert Amyot, staff cardiologist at the Hopital du Sacre-Coeur has been an author in our two previous TEE manuals. In 2014 Robert became the president of CAE Healthcare. We acknowledge his support in allowing us to enhance many figures in this manual by extensively using the Vimedix simulator (CAE, Healthcare Canada) to obtain anatomic illustrations and videos. In addition, physicians in Canada have free institutional access to Anatomy.tv powered by Primal Picture (info@primalpictures.com) through Wolters Kluwer Health. This educational site allows clinicians to learn and teach anatomy from a 3D atlas. We are so grateful to both of these companies for allowing us to use their interface throughout the manual.

Finally, many colleagues, residents, and fellows at the MHI have graciously reviewed chapters of this manual, making suggestions and pointing out corrections. I would like to thank all of them which are listed just below.

I hope that you will enjoy reading the 1st Edition of the Basic Transesophageal and Critical Care Ultrasound textbook.

André Denault MD, PhD, FRCPC, FASE, ABIM-CCM, FCCS

Dr William Beaubien-Souligny
Dr Alexandros Cavayos
Dr David Claveau
Dr Joseph Dahine
Dr Andrè Dubè
Dr Roberto Eljaiek
Dr Jessica Forcillo
Dr Caroline Gebhard
Dr Brian Grondin-Beaudoin
Dr Jean-Gilles Guimond
Dr Vincent Lecluyse
Dr Gabrielle Migner-Laurin
Dr Alex Moore
Mrs Antoinette Paolitto
Dr Daniel Parent
Dr Élise Rodrigue
Dr Catalina Sokolof

Dr Francis Toupin
Dr Claudia Viens
Dr Han Ting Wang

REFERENCES

1. DenaultA.Y., CoutureP., TardifJ.C., BuithieuJ.*Transesophageal Echocardiography Multimedia Manual: A Perioperative Transdisciplinary Approach*. New York, NY: Marcel Dekker, 2005.
2. DenaultA.Y., CoutureP., VegasA., BuithieuJ., TardifJ.C.. *Transesophageal Echocardiography Multimedia Manual, Second Edition: A Perioperative Transdisciplinary Approach*. New York, NY: Informa Healthcare, 2011.
3. ReevesS.T., FinleyA.C., SkubasN.J., SwaminathanM., WhitleyW.S., GlasK.E., HahnR.T., ShanewiseJ.S., AdamsM.S., ShernanS.K.. Basic perioperative transesophageal echocardiography. examination: a consensus statement of the American Society of Echocardiography and the Society of Cardiovascular Anesthesiologists. *J Am Soc Echocardiogr*. 2013; *26*: 443–56.
4. MayoP.H., BeaulieuY., DoelkenP., Feller-KopmanD., HarrodC., KaplanA., et al. American College of Chest Physicians/La Sociètè de Rèanimation de Langue Frangaise statement on competence in critical care ultrasonography. *Chest*. 2009; *135*: 1050–60.
5. ViaG., HussainA., WellsM., ReardonR., ElbarbaryM., NobleV.E., et al. International evidence-based recommendations for focused cardiac ultrasound. *J Am Soc Echocardiogr*. 2014; *27*: 683.
6. ArntfieldR., MillingtonS., AinsworthC., AroraR., BoydJ., FinlaysonG., et al. Canadian recommendations for critical care ultrasound training and competency. *Can RespirJ*. 2014; *21*: 341–45.

Abbreviations

2C	two-chamber
2D	two-dimensional
4C	four-chamber
5C	five-chamber
A	amplitude
A	peak late diastolic TMF or TTF velocity
A	atrial contraction
a'	peak late diastolic mitral or tricuspid annular velocity
A dur	duration of TMF A-wave
A4C	apical four-chamber
AA	apical anterior
AA	axillary artery
AAA	abdominal aortic aneurysm
AAL	anterior axillary line
AC	attenuation coefficient
ACA	anterior cerebral artery
ACC	American College of Cardiology
ACCP	American College of Chest Physicians
ACES	Abdominal Cardiac Evaluation with Sonography in Shock
ACGME	Accreditation Council for Graduate Medical Education
ACLS	advanced cardiac life support
ACoA	anterior communicating artery
Adr	adrenal
Adre	adrenaline
AHA	American Heart Association
AIN	apical inferior
AJV	anterior jugular vein

AL	apical lateral / anterolateral
AL	area-length method
Am	peak late diastolic MAV
AMVL	anterior mitral valve leaflet
Ant	anterior
Ao	aorta
AoV	aortic valve
AP	anterior-posterior
AR	atrial reversal
AR	aortic regurgitation
AR dur	atrial reversal pulmonary venous flow velocity duration
ARDS	acute respiratory distress syndrome
AS	apical septal / anteroseptal
ASA	American Society of Anesthesiologists
aSAH	aneurysmal subarachnoid hemorrhage
Asc Ao	ascending aorta
ASD	atrial septal defect
ASE	American Society of Echocardiography
Asr	late diastolic strain rate
At	peak late diastolic tricuspid annular velocity
AV	axillary vein / aortic valve
AVA	aortic valve area
AVC	aortic valve closure
AVM	arteriovenous malformation
AW	anterior window
BA	basal anterior
BA	basilar artery
BAL	basal anterolateral
BART	Blue Away Red Towards (common color map)
BAS	basal anteroseptal
BHI	breath holding index

BIN	basal inferior
BIL	basal inferolateral
BIS	basal inferoseptal
BSA	body surface area
C	carotid segments
C	propagation speed
CA	carotid artery
CAD	coronary artery disease
CAE	Canadian Aviation Electronics
CAS	carotid angioplasty and stenting
CBF	cerebral blood flow
CBFV	cerebral blood flow velocity
CCA	cerebral circulatory arrest
CCCS	Canadian Critical Care Society
CCE	critical care echocardiography
CCS	Canadian Cardiovascular Society
CCTA	coronary computed tomography angiography
CEA	carotid endarterectomy
CFD	color flow Doppler
CFS	cerebrospinal fluid
CHD	congenital heart disease
cm	centimeter
CME	continuing medical education
CMR	cardiovascular magnetic resonance
CO	cardiac output
$^{CO}2$	carbon dioxide
CPB	cardiopulmonary bypass
CPP	cerebral perfusion pressure
CPR	cardiopulmonary resuscitation
CS	coronary sinus
CSA	cross-sectional area

CSE	Canadian Society of Echocardiography
CT	celiac trunk
CT	computed tomography
CTA	computed tomography angiogram
CTP	computed tomography perfusion
CVC	central venous catheters
CVP	central venous pressure
CW	continuous wave
CWD	continuous wave Doppler
CXR	chest radiography
d	diameter
D	diastolic PVF or HVF velocity
D	diastolic
D1	first diagonal
D2	second diagonal
DAP	diastolic arterial pressure
db	decibel
DBP	diastolic blood pressure
DCI	delayed cerebral ischemia
DE-CMR	delayed enhanced cardiovascular magnetic resonance
Des Ao	descending aorta
DF	duty factor
DT	deceleration time
DVT	deep venous thrombosis
E	early diastolic TMF or TTF velocity
E	early filling
e'	peak early diastolic mitral or tricuspid annual velocity
ECA	external carotid artery
ECG	electrocardiogram or electrocardiographic
ECMO	extracorporeal membrane oxygenation
EDA	end-diastolic area

EDV	end-diastolic velocity
EF	ejection fraction
eFAST	extended FAST
EI	eccentricity index
EIV	external iliac vein
Em	early diastolic MAV
ER	emergency room
ERO	effective regurgitant orifice
ESA	end-systolic area
ESLD	end-stage liver disease
Esr	early diastolic strain rate
ET	ejection time
Et	peak early diastolic tricuspid annular velocity
$etco_2$	end-tidal carbon dioxide
ETT	endotracheal tube
EUS	endoscopic ultrasound scanning
EV	eustachian valve
EVAR	endovascular repair of aortic aneurysm
f	frequency (Hz)
FA	femoral artery
FAC	fractional area change
FAST	Focused Assessment with Sonography in Trauma
Fd	Doppler frequency shift
FL	false lumen
FO	foramen ovale or fossa ovalis
FP	foramen primum
FS	foramen secundum
FV	femoral vein
FVd	end-diastolic flow velocity
FVm	mean flow velocity
FVR	flow velocity ratio

FVs	systolic flow velocity
FW	frontal window
g	gram
GCCUS	General Critical Care Ultrasound
GE	gastroesophageal
GI	gastrointestinal
GLS	global longitudinal strain
H	horizontal
HAF	hepatic artery flow
HAV	hemiazygos vein
HCM	hypertrophic cardiomyopathy
HITS	hyperintensity thromboembolic signal
HR	heart rate
HU	Hounsfield unit
HV	hepatic vein
HVF	hepatic venous flow
HVLT	half value layer thickness
IN	inferior
IAS	interatrial septum
IA	innominate artery
IABP	intra-aortic balloon pump
ICA	internal carotid artery
ICCU	Imaging Curriculum in Critical Care Ultrasound
ICM	intercostal muscle
ICP	intracranial pressure
ICU	intensive care unit
IJV	internal jugular vein
IL	inferolateral
IMA	internal mammary arteries
IN	inferior
In-Out	inflow-outflow
IOA	Iindex of autoregulation

IRC	intensity reflection coefficient
IS	inferoseptal
IVC	inferior vena cava
IVCT	isovolumic contraction time
IVRT	isovolumic relaxation time
IVS	interventricular septum
IVUS	intravascular ultrasound
J	joules
L	lateral
LA	left atrium
LAA	left atrial appendage
LACA	left anterior cerebral artery
LAD	left anterior descending
LAFB	left atrio-femoral bypass
LAP	left atrial pressure
LAX	long-axis
LCC	left coronary cusp
LCCA	left common carotid artery
LCX	left circumflex artery
LGC	lateral gain control
LGE	late-gadolinium-enhancement
LH	left heart
LHV	left hepatic vein
LIJV	left internal jugular vein
LK	left kidney
LLL	left lower lobe
LM	left main
LMCA	left middle cerebral artery
LPV	left portal vein
LSCA	left subclavian artery
LSVC	left-sided superior vena cava

LT	liver transplantation
LTICA	left terminal internal carotid artery
L-to-R	left-to-right
LUL	left upper lobe
LUPV	left upper pulmonary vein
LV	left ventricle or left ventricular
LVD	left ventricular minor-axis diameter
LVEDA	left ventricle end-diastolic area
LVEDD	left ventricle end-diastolic diameter
LVEDP	left ventricular end-diastolic pressure
LVEDV	left ventricle end-diastolic volume
LVEF	left ventricular ejection fraction
LVESA	left ventricular end-systolic area
LVESP	left ventricular end systolic pressure
LVIDd	left ventricular internal diameter at end-diastole
LVOT	left ventricular outflow tract
LVOTO	left ventricular outflow tract obstruction
m	meter
MA	mid-anterior
MAL	mid-anterolateral
MAS	mid-anteroseptal
MAV	mitral annular velocity
Max	maximal
MCA	middle cerebral artery
ME	mid-esophageal
MFV	mean flow velocity
MHV	middle hepatic vein
MI	mechanical index
Mid	middle
MIL	mid-inferolateral
MIN	mid-inferior

MIS	mid-inferoseptal
MLS	midline shift
mm	millimeter
mmHg	millimeter of mercury
M-mode	motion mode
Mn	mean
MOC	maintenance of competence
MOD	method of disk
MPA	main pulmonary artery
MPI	myocardial performance index
MR	mitral regurgitation
MRI	magnetic resonance imaging
ms	millisecond
MS	mitral stenosis
MV	mitral valve
MVA	mitral valve area
MVO	mitral valve opening
MW	middle window
NBE	National Board of Echocardiography
NCC	non-coronary cusp
NL	nipple line
Norad	noradrenaline
NS	not specified
OA	ophthalmic artery
ONSD	optic nerve sheath diameter
OR	operating room
P	power
P	pressure
P1	posterior leaflet
PA	pulmonary artery
PAC	pulmonary artery catheter

$PaCO_2$	arterial carbon dioxide tension
PAEDP	pulmonary artery end-diastolic pressure
PAL	posterior axillary line
Pan	pancreas
PaO_2	arterial oxygen tension
Par	systolic radial blood pressure
PASP	pulmonary artery systolic pressure
PC	pericardial cyst
PCA	posterior cerebral artery
PCoA	posterior communicating artery
PCWP	pulmonary capillary wedge pressure
PD	pulse duration
PE	pericardial effusion
PE	pulmonary embolism
PEA	pulseless electrical activity
PecM	pectoralis muscle
PEEP	positive end-expiratory pressure
PFO	patent foramen ovale
PG	pressure gradient
PHT	pressure half-time
PI	pulsatility index
PICC	peripherally inserted central catheter
PISA	proximal isovelocity surface area
PM	papillary muscle
PMD	power mode Doppler
Pms	mean systemic venous pressure
PMV	prosthetic mitral valve
POCUS	point-of-care ultrasound
Post	posterior
PoVF	portal venous flow
Ppa	pulmonary artery pressure

Ppl	pleural pressure
PR	pulmonary regurgitation
Pra	right atrial pressure
PREDV	pulmonary regurgitation end-diastolic velocity
PRF	pulse repetition frequency
PRI	pulmonary regurgitation index
PRP	pulse repetition period
^{P}RV	right ventricular pressure
PSL	parasternal line
PT	pulmonary trunk
PTE	Perioperative Transesophageal Echocardiography
PV	pulmonic valve
PV	pressure-volume
PVAC	pulmonic valve anterior cusp
PVF	pulmonary venous flow
PVLC	pulmonic valve left cusp
PVR	pulmonary vascular resistance
PW	pulsed-wave
PWD	pulsed-wave Doppler
PWT	posterior wall thickness
PWTd	posterior wall thickness diameter
Py	pylorus
Qp	pulmonary flow
Qs	systemic flow
R	radius
RA	right atrium or right atrial
RAA	right atrial appendage
RACA	right anterior cerebral artery
RAP	right atrial pressure
RCA	right carotid artery
RCA	right coronary artery

RCC	right coronary cusp
RH	right heart
RHV	right hepatic vein
RI	resistance index
RIJV	right internal jugular vein
RLPV	right lower pulmonary vein
RMCA	right middle cerebral artery
RML	right middle lobe
ROSC	return of spontaneous circulation
RPA	right pulmonary artery
RPV	right portal vein
R-to-L	right-to-left
RUL	right upper lobe
RUPV	right upper pulmonary vein
RUSH	Rapid Ultrasound for Shock and Hypotension
RV	right ventricle or right ventricular
RVD	right ventricular diameter
RVEF	right ventricular ejection fraction
RVOT	right ventricular outflow tract
RVOTO	right ventricular outflow tract obstruction
Rvr	resistance to venous return
RVSP	right ventricular systolic pressure
RWMA	regional wall motion abnormalities
RWT	relative wall thickness
S	septal
S	systolic
S	systolic pulmonic or hepatic venous flow velocity
s'	systolic tricuspid annular velocity
S wave	inflow during systole
SAM	systolic anterior motion
SaO_2	oxygen saturation

SAP	systolic arterial pressure
SAX	short-axis
SBP	systolic blood pressure
SC	subcostal
SCA	Society of Cardiovascular Anesthesiologists
SCA	subclavian artery
SCA	Society of Cardiovascular Anesthesiologists
SCD	sickle cell disease
ScO_2	brain saturation
SCT	subcutaneous tissue
SCV	subclavian vein
SD	standard deviation
sec	second
SEC	spontaneous echo contrast
SIRS	systemic inflammatory response syndrome
SL	strain longitudinal
SMA	superior mesenteric artery
SP	septum primum
SPECT	single photon emission computer tomography
SPL	spatial pulse length
SPTA	spatial peak temporal average
SR	strain rate
SS	septum secundum
Ssr	peak systolic strain rate
STJ	sinotubular junction
SV	stroke volume
SVC	superior vena cava
SVF	splenic venous flow
SWT	septal wall thickness
SWTd	septal wall thickness in diastole
SX	sub xyphoid

T	period
TAAA	thoraco-abdominal aortic aneurysm
TAMV	time-averaged mean velocity
TAPSE	tricuspid annular plane systolic excursion
TAV	tricuspid annular velocity
TCCS	transcranial color-coded duplex sonography
TCD	transcranial Doppler
TD	thermodilution
TDI	tissue Doppler imaging
TEE	transesophageal echocardiography
TEVAR	thoracic endovascular aortic repair
TG	transgastric
TGC	time gain compensation
Th	wall thickness
TICA	terminal internal carotid artery
TL	true lumen
TMF	transmitral flow
TPR	total peripheral resistance
TR	tricuspid regurgitation
TS	tricuspid stenosis
TTE	transthoracic echocardiography
TTF	transtricuspid flow
TV	tricuspid valve
TVA	tricuspid valve area
TVAL	tricuspid valve anterior leaflet
TVPL	tricuspid valve posterior leaflet
UE	upper esophageal
US	ultrasound
V	vertical
VA	vertebral arteries
Vaso	vasopressin

VC	vena contracta
Vel	velocity
VIRTUAL	Visual Interactive Resource for Teaching, Understanding and Learning
Vmax	maximum jet velocity
Vmv	mitral valve regurgitant velocity
Vp	flow propagation velocity
Vpeak	peak velocity
VR	venous return
VSD	ventricular septal defect
$^{Vt}1/2$	velocity at the pressure half-time point
VTI	velocity time integral
V_{TR}	peak tricuspid regurgitant velocity
W	watts
WMA	wall motion abnormalities
WMSI	regional wall motion score index
Z	impedance
σ	stress
λ	wavelength

How to Use

Sketch and 3D icon correlation and superposition

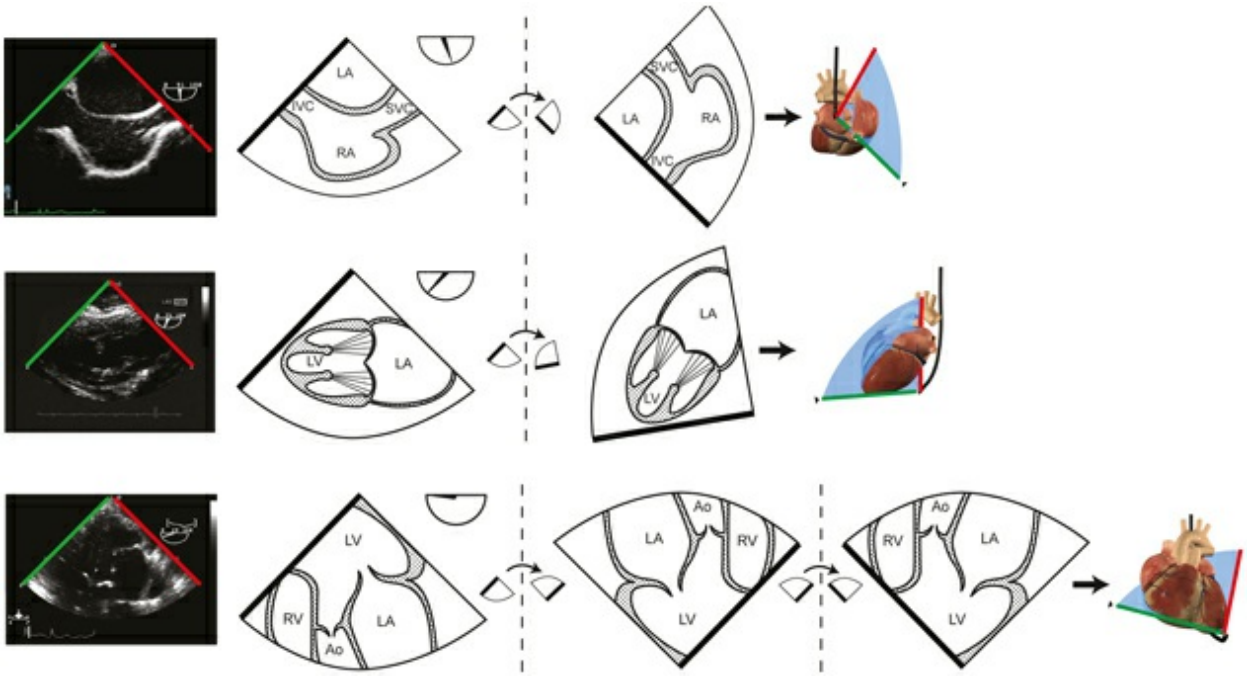

This symbol used in the legend indicates the presence of additional video in relation to the figure available on the Web.(missing video symbol)

The human body icon indicates how the patient was positioned when images or videos were obtained.

http://goo.gl/bba15t

In order to see the video related to the figure, use an application to scan the QR code or with the mouse, click on short URL to view video. The letter(s) before URL address is in relation to which part of the figure, the video is associated.

List of Videos

Video title and figure number

Chapter 2

Chapter 3

Chapter 4

Pulmonary regions ***4.1a & b***
Pulmonary references points ***4.2***
Left lung examination ***4.5a***
Left lung examination ***4.5e***
Left lung examination ***4.5i***
Right lung examination ***4.6a***
Right lung examination ***4.6e***
Right lung examination ***4.6i***
Complex pleural effusion ***4.7a***
Complex pleural effusion ***4.7d***
Hemothorax ***4.8***
Pleural hematoma ***4.9b***
Pleural hematoma ***4.9c***
Pleural hematoma ***4.9d***
Atelectasis ***4.10d***
Pneumonia after lobectomy ***4.11a***
Pneumonia after lobectomy ***4.11b***
Pneumonia after lobectomy ***4.11c***
Pneumonia after lobectomy ***4.11d***
Subcarinal lymph node ***4.14a***
Azygos and hemiazygos venous system ***4.16***
Azygos vein ***4.17a***
Azygos vein ***4.17c***
Examination of the stomach ***4.20d***
Examination of the stomach ***4.20e***
Examination of the stomach ***4.20f***
Gastric abnormalities ***4.21a***
Gastric abnormalities ***4.21b***
Gastric abnormalities ***4.21c***
Spleen anatomy and position ***4.23***
Spleen ***4.24a***
Spleen ***4.24b***
Spleen ***4.24c***
Spleen ***4.24d***
Left kidney ***4.25d***
Left kidney ***4.26a***
Left kidney ***4.26b***
Liver ***4.28***
Hepatic veins ***4.29a***
Hepatic veins ***4.29c***
Hepatic veins ***4.29e***
Portal vein ***4.30a***
Hepatic artery ***4.31a***
Hepatic artery ***4.31b***
Hepatic pathologies ***4.32a***
Hepatic pathologies ***4.32b***
Hepatic pathologies ***4.32c***
Hepatic pathologies ***4.32d***
Portal hypertension ***4.34d***
Whale tail sign ***4.35c***

Whale tail sign ***4.35d***
Splenic Doppler flow ***4.38a***
Splenic Doppler flow ***4.38d***
Abnormal splenic venous flow ***4.39b***
Abnormal splenic venous flow ***4.39e***

Chapter 5

Preload ***5.5a & b***
Preload ***5.6a & d***
Respiratory variation of the SVC ***5.7a***
Respiratory variation of the SVC ***5.7c***
Fractional area change ***5.9a & c***
Eccentricity index ***5.12c-d***
Eccentricity index ***5.12e-f***

TAPSE *5.13*

Pulmonary vein Doppler ***5.15a***
Pulmonary vein Doppler ***5.15d***
Pericardial effusion ***5.18a***
Cardiac tamponade ***5.19b & e***
Pleural and pericardial effusions ***5.20a***
Hypertrophic cardiomyopathy ***5.23a***
Dilated cardiomyopathy ***5.24a***
Takotsubo ***5.26a***
Takotsubo ***5.26b***
Takotsubo ***5.26c***
Takotsubo ***5.26d***
Takotsubo ***5.26e***
Takotsubo ***5.26f***

Chapter 6

LV function ***6.2a, b, & e***
LV function ***6.3a, b, & e***
Left coronary artery ***6.4a***
Left coronary artery ***6.4c***
Right coronary artery ***6.5a***
Right coronary artery ***6.5c***
Right coronary artery ***6.5e***
ECMO ***6.6a***
ECMO ***6.6b***
Radial strain ***6.11a***
LV function ***6.13a***
LV function ***6.13b***
Apical thrombus ***6.14a***
Apical thrombus ***6.14d***
Ruptured papillary muscle ***6.15a***
Inferior LV aneurysm ***6.16a***
Apical ischemic VSD ***6.18c***

Chapter 7

Chapter 8

Chapter 9

Capnography and ventilator flow-time waveforms ***9.10b***
V wave ***9.11a***
V wave ***9.11a***
V wave ***9.11b***
V wave ***9.11c***
V wave ***9.11c***
Systolic blood pressure ***9.12***
lVoT obstruction ***9.13a***
LVOT obstruction ***9.13d***
RVOT obstruction ***9.14a***
RVOT obstruction ***9.14e***
RVOT obstruction ***9.14f***
Acute pulmonary emboli ***9.15a***
Acute pulmonary emboli 9.15b
Cardiac tamponade ***9.16a***
Cardiac tamponade ***9.16c***
Left-sided pneumothorax ***9.17b***
Compression of the RA ***9.18a***
IVC occlusion during Fontan procedure ***9.19a***
Endocarditis with Ao root abscess ***9.20a***
Endocarditis with Ao root abscess ***9.20a***
Endocarditis with Ao root abscess ***9.20c***
Pneumonia ***9.21a***
Peritoneal bleed ***9.22a***

Chapter 11

Patent foramen ovale (PFO) ***11.2a & b***
ASD secundum ***11.5a***
ASD secundum ***11.5d***
Patent Foramen Ovale (PFO) ***11.6c***
Muscular VSD ***11.8a***
Muscular VSD ***11.8c***

Chapter 12

TDI for RV function ***12.3c***
Air emboli *1* ***2.7a***
LUPV stenosis ***12.8a***
Transverse Ao ***12.11a & c***
Left atrio-femoral bypass ***12.13a***
Guidewire position ***12.15a***
Ao arch vessels ***12.16a***
Pleural effusion ***12.19b***
Pleural effusion ***12.19c***
LVOTO and hypoxemia ***12.21a***
LVOTO and hypoxemia ***12.21c***
LVOTO and hypoxemia ***12.21d***
IVC stenosis ***12.22a***
IVC stenosis ***12.22b***
IVC stenosis ***12.22c***

Chapter 13

Chapter 14

Lung point in M-mode ***14.28***
Pleural effusion ***14.29***
Empyema ***14.31***
Percutaneous tracheostomy ***14.34c***

Chapter 15

FOCUS exam ***15.2a***
FOCUS exam ***15.2c***
FOCUS exam ***15.2e***
FOCUS exam ***15.2h***
Asc Ao aneurysm.4a
Asc Ao aneurysm ***15.4b***
Asc Ao aneurysm ***15.4c***
RV Dysfunction ***15.5a***
RV Dysfunction ***15.5g***
RV Dysfunction ***15.5e***
Pleural Effusion ***15.6a***
Pleural Effusion ***15.6c***
RV Dysfunction ***15.10a***
RV Dysfunction ***15.10c***
RV Dysfunction ***15.10e***
RV dysfunction and pulmonary hypertension ***15.12a***
IVC Diameter ***15.13a***
IVC Diameter ***15.13b***
Respiratory variation of the SVC ***15.14a***
Cardiac tamponade ***15.15a***
Pleural Effusion ***15.16a***
Pleural Effusion ***15.16c***
Pleural Effusion ***15.16d***
Thrombus ***15.17a***
Thrombus ***15.17b***
Ventricular Septal Defect ***15.18a***
Ventricular Septal Defect ***15.18b***
Myxoma ***15.19a***
Myxoma ***15.19b***
Pulmonary Embolism ***15.20a***
Pulmonary Embolism ***15.20b***
Ao Dissection ***15.21a***
Ao Dissection ***15.21b***
Takotsubo syndrome ***15.22a***
Takotsubo syndrome ***15.22b***
Outflow Tract Obstruction ***15.23a***
Outflow Tract Obstruction ***15.23c***
Outflow Tract Obstruction ***15.23e***
LVOT obstruction ***15.24a***
LVOT obstruction ***15.24a***

Chapter 16

Abdominal wall varices ***16.2a***

Abdominal wall varices ***16.2b***
Normal liver anatomy ***16.6***
Right posterior axillary coronal upper and mid abdominal US views ***16.7bdf***
Right posterior axillary coronal upper and mid abdominal US views ***16.7h***
Gallbladder ***16.8d***
Gallbladder ***16.8b***
Gallbladder ***16.8c***
Kidney ***16.9a***
Kidney ***16.9b***
Spleen ***16.10a***
Spleen ***16.10b***
Spleen ***16.10b***
Abdominal aorta ***16.12b***
Abdominal aorta ***16.12c***
Abdominal aorta ***16.12d***
Abdominal aorta branches ***16.14ace***
Abdominal aorta branches ***16.14bdf***
IVC ***16.15b***
IVC ***16.15c***
IVC ***16.15d***
HVF ***16.16a***
HVF ***16.16b***
PVF ***16.17b***
Bladder ***16.18a***
Stomach ***16.20a***
Stomach ***16.20a***
Free fluid ***16.21a***
Free fluid ***16.21c***
Subdiaphragmatic abscess ***16.22a***
Rectosigmoid free fluid ***16.23a***
Retroperitoneal hemorrhage ***16.24a***
Abnormal kidneys ***16.25c***
Ileus ***16.26a***
Full stomach ***16.27a***
Full stomach ***16.27b***
Full stomach ***16.27d***
Air in the liver ***16.28a***
Air in the liver ***16.28c***
Abdominal Ao aneurysm ***16.29a***
Abdominal Ao aneurysm ***16.29d***
Ao dissection ***16.30a***
Ao dissection ***16.30b***
IVC ***16.31a***
IVC ***16.31b***
IVC ***16.31c***
IVC ***16.31c***
IVC ***16.31e***
IVC ***16.31f***
Abnormal portal vein vel ***16.32a***
Gallstone complications ***16.33a***

Abnormal gallbladder ***16.34c***
Hydronephosis ***16.35e***
Foley catheter ***16.36a***
Foley catheter ***16.36b***
Foley catheter ***16.36c***
Acute colitis ***16.37a***
Acute colitis ***16.37b***
Abnormal liver ***16.38c***
Abnormal spleen ***16.39a***
Abnormal spleen ***16.39c***

Chapter 17

Internal Mammary Artery ***17.1a***
Internal Mammary Artery ***17.1b***
Effusions ***17.3d***
Pericardiocentesis ***17.5a***
Pericardiocentesis ***17.5b***
Pericardiocentesis ***17.5c***
Pericardiocentesis ***17.6a***
Pericardiocentesis ***17.6b***
Pericardiocentesis ***17.6c***
Pericardiocentesis ***17.6c***
Pleurocentesis ***17.1***
Pleurocentesis ***17.11a***
Pleurocentesis ***17.11b***
Pneumothorax ***17.12b***
Pneumothorax ***17.13a***
Pneumothorax ***17.13c***
Pneumothorax ***17.13c***
Pneumothorax ***17.13b***
Pneumothorax ***17.13d***
Pneumothorax ***17.13d***
Pneumothorax ***17.14***
Paracentesis ***17.16a***
Paracentesis ***17.16b***
Paracentesis ***17.16c***
Paracentesis 17.17

Chapter 18

Central line kit ***18.3***
Internal jugular vein ***18.4***
Internal jugular vein ***18.9a***
Internal jugular vein ***18.9b***
Internal jugular vein ***18.9b***
Internal jugular vein ***18.9c***
Internal jugular vein ***18.9d***
Internal jugular vein ***18.10a***
Internal jugular vein ***18.10b***
Internal jugular vein ***18.10c***

Appendix

Mid-Esophageal Left Atrial Appendage ***A5***
Mid-Esophageal Right Ventricular Outflow Tract ***A6***
Mid-Esophageal Right Ventricular Outflow Tract ***A6***
Mid-Esophageal Bicaval ***A7***
Mid-Esophageal Aortic Valve Short-Axis ***A8***
Mid-Esophageal Aortic Valve Short-Axis ***A8***
Mid-Esophageal Aortic Valve Long-Axis ***A9***
Mid-Esophageal Ascending Aortic Short-Axis ***A10***
Mid-Esophageal Ascending Aortic Long-Axis ***A11***
Transgastric Mid-Papillary Short-Axis ***B1***
Transgastric Basal Short-Axis ***B2***
Transgastric Basal Short-Axis ***B2***
Transgastric Two-Chamber ***B3***
Transgastric Long-Axis ***B4***
Transgastric Right Ventricle ***B5***
Transgastric Inferior Vena Cava Long-Axis ***B6***
Transgastric Inferior Vena Cava Long-Axis ***B6***
Deep Transgastric ***C1***
Descending Aortic Short-Axis ***D1***
Descending Aortic Long-Axis ***D2***
Upper Esophageal Aortic Long-Axis ***E1***
Upper Esophageal Aortic Short-Axis ***E2***

PART I

Chapter 1

Ultrasound Imaging: Acquisition and Optimization

Wilfredo Puentes and Annette Vegas

INTRODUCTION

This chapter presents a brief description of the basic physical principles of ultrasound (US), as well as the steps involved in producing an ultrasound image. Common US probes and key controls on the US machine for acquiring and optimizing the different imaging modes (two-dimensional (2D) and Doppler) are outlined.

BASIC PRINCIPLES OF ULTRASOUND

Sonography comes from the Latin sonus (meaning “sound”) and the Greek word graphien (meaning “to write”). Medical ultrasonography uses high frequency sound waves to create images. To appreciate how this process occurs, it is important to understand some of the concepts related to sound.

Sound Waves

Sound is mechanical energy transmitted as longitudinal pressure waves formed by molecular interaction in a medium, and hence cannot occur in a vacuum. As sound waves travel through a medium, each molecule hits another and returns to its original position, creating more dense (compression) and less dense (rarefaction) regions in the medium. Different properties of the sound wave can be described including: cycle, frequency,

period, wavelength, amplitude, power, intensity, and propagation speed (**Figure 1.1**).

A cycle comprises one rarefaction and one compression of the sound wave. Frequency (f) is the number of cycles in a given time, 1 cycle/second = 1 Hertz (Hz). Period (T) is the time it takes for one complete cycle to pass a point or for a wave to travel a distance of one wavelength. Wavelength (λ) represents the horizontal distance between any two successive equivalent points on the wave or the length of one cycle of the wave. Frequency and period are inversely proportional (f = 1/T), thus a higher frequency has a shorter wavelength and period. For instance, a higher frequency probe, such as a transesophageal echocardiography (TEE) probe, is superior to a transthoracic echocardiography (TTE) probe in detecting endocarditis because small vegetations can be missed with TTE. The TTE probe has a lower frequency and consequently a larger and less precise wavelength.

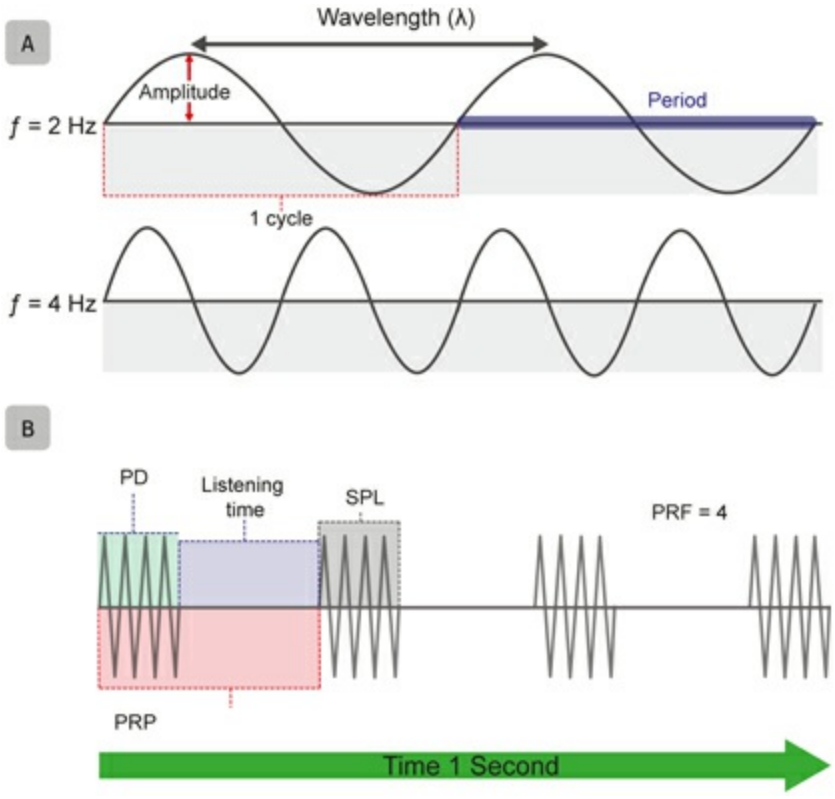

Fig. 1.1 Properties of sound waves and pulses. (A) Sound wave cycle descriptors include period (T), wavelength (x), amplitude and frequency (f) as shown for waves of 2 Hz and 4 Hz frequencies. (B) A pulse is a collection of sound wave cycles with characteristics of pulse duration (PD), pulse repetition period (PRP), spatial pulse length (SPL) and pulse repetition frequency (PRF).

Amplitude (A), power (P) and intensity are strength measurements of the sound wave. All share similar properties as these measurements are: (1) determined by the source, (2) changed by adjusting power on the US machine, and (3) decrease in value from attenuation as US propagates in the body. Amplitude is the difference in maximum and mean values of wave height as measured in decibels (dB). The P refers to the rate of energy transfer, as measured in watts (W) or Joules (J). Intensity (Intensity = P/area) is the concentration of energy in a sound beam or the amount of power per unit of area, as measured in W/cm^2. Intensity establishes the mechanical and thermal bioeffects of US on tissue. Spatial peak temporal average (SPTA) intensity relates to tissue heating and should be <720 mW/cm^2 with clinical imaging to avoid damaging tissues.

Propagation speed is the distance the sound wave travels through a medium per second (distance per time). It is how fast the disturbance is passed from molecule to molecule. Speed depends solely on the medium's properties of stiffness and density. It is slowest through gases, faster through liquids, and fastest through solids. In soft tissue, the propagation speed is equal to 1540 m/s (1.54 mm/μsec). Propagation speed (c) is the product of frequency and wavelength ($c = f \lambda$).

Sound Pulses

Ultrasound systems produce short bursts of sound, called "pulses". A pulse is a collection of sound cycles that travel together. Analogous to the properties of sound waves there are several terms that describe pulsed waves (**Figure 1.1**): pulse duration (PD), spatial pulse length (SPL), pulse repetition frequency (PRF), pulse repetition period (PRP), and duty factor (DF).

The PD is the amount of time to complete a single pulse. Pulse repetition period is the amount of time from the beginning of one pulse to the beginning of the next pulse; it includes the pulse duration and listening time. Pulse repetition frequency is the number of pulses per second; this is reciprocal to pulse repetition period (PRF = 1/PRP). Pulse repetition frequency is important as it affects temporal resolution and also determines the Nyquist limit in Doppler US. In clinical US, the duty factor (DF % = PD/PRP) is the ratio of time that the transducer produces a pulse or is switched on. On average, the transducer is listening 99% of the time, and emitting the US signal for less than 1%, so the normal DF is 0.1–1%. Listening time depends on the distance that the sound wave needs to travel to find the object of

interest, longer distances or greater depth means a longer time listening.

By definition, US has a frequency greater than 20,000 cycles per second (20,000 Hz or 20 KHz). The human audible range is between 20 and 20,000 Hz. For medical diagnosis, US frequency is measured in millions of cycles per second (MHz). Most medical imaging transducers have a frequency range of 2–15 MHz, although some special intravascular US (IVUS) and US biomicroscopy of the eye uses frequencies as high as 60 MHz.

BEHAVIOR OF SOUND IN THE BODY

Understanding how sound waves behave in the body is important for optimizing and interpreting US images. An ultrasound probe generates a sound beam that is meant to travel through the body in a straight line. Most of the initial US beam is lost (attenuation), some continues further on (transmitted) and some returns back to the transducer (reflected). Differences at the tissue interfaces (type, size, and shape) and the angle of beam incidence determines the behavior of sound in the body.

Attenuation refers to loss of US beam energy (-dB) as it travels through tissue (**Figure 1.2 A**). Absorption (**Figure 1.2 B**) is the primary cause of attenuation (80%) as sound is converted to another energy form, such as heat. Reflection, refraction (**Figure 1.2 C**), and scattering (**Figure 1.2 D**) also contribute to attenuation. Attenuation exponentially increases with depth and linearly increases with the US frequency. Higher frequency sound has greater absorption and scattering, and thus poorer penetration. The attenuation coefficient (AC) correlates attenuation with frequency (AC = 0.5 x f or f/2) where f is measured in MHz.

Half power distance or half value layer thickness (HVLT) expresses the amount of attenuation of US in tissues. It is equal to the distance that US travels in particular tissues before the energy or amplitude decreases to half its original value. It is expressed by HVLT = 3/AC. The normal range in clinical practice is 0.25–1.0 cm (**Table 1.1**).

Acoustic impedance is the resistance of different tissues to the passage of sound that is a characteristic of only the tissue. It cannot be measured but is calculated as: impedance in Rayls (Z) = density (kg/m^3) x propagation speed (m/s). Impedance increases when density increases and/ or propagation speed increases, thus it is highest for bone and lowest for air (**Table 1.1**). Air is

almost impermeable to US and this makes it difficult to image air-filled structures, like the lungs, trachea, bronchus and bowel. Most of the US energy is reflected and the rest is absorbed, impeding visualization of the structures localized behind the air. The transducer-skin interface illustrates important principles of acoustic impedance and sound transmission. The transducer surface is constructed with material of similar impedance to skin (matching layer) and the use of gel improves the surface contact by eliminating air, to permit better sound transmission.

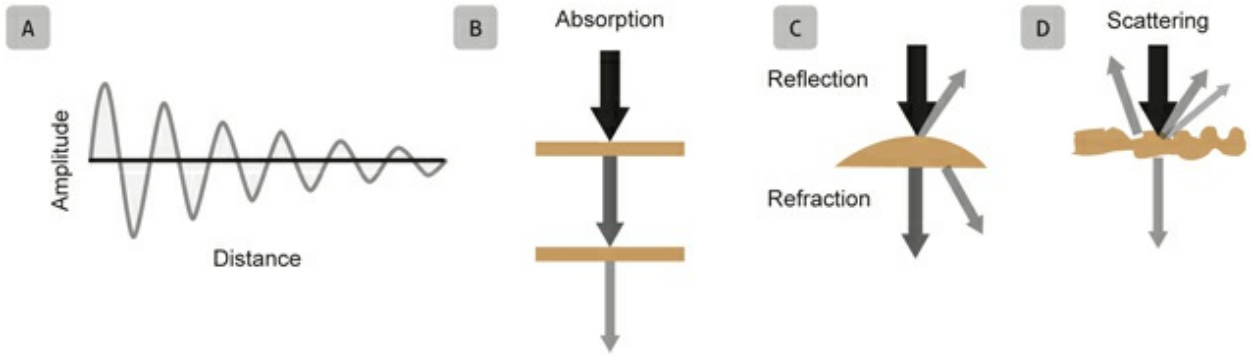

Fig. 1.2 Attenuation. (A) There is a decrease in amplitude (-dB) as a sound wave travels. (B–D) Attenuation may be from absorption, complete or partial reflection, refraction, and scattering of the initial sound signal.

At an interface between two tissues, the differences in acoustic impedance of each tissue determines the percentage of the incident US beam that is reflected back. The greater the acoustic mismatch, the greater the amount of sound that is reflected. The amount reflected is expressed using the Intensity Reflection Coefficient (IRC) or Reflection Coefficient, as calculated from the known impedances (Z_1 and Z_2) between interfaces (**Figure 1.3**). No reflection will occur if the two tissues have identical impedance, allowing the whole sound wave to be transmitted. The relatively small differences in acoustic impedance in soft tissue allow the US beam to travel further and image deeper structures (**Table 1.1**).

In addition, the angle of incidence and the size and shape of tissue at the interface influences sound wave behavior. Complete reflection occurs when the angle of incidence is 90° (normal incidence) and results in optimal 2D imaging (**Figure 1.2c**). At other angles of incidence, only partial return of the sound beam occurs, the remainder is transmitted, but often with a slight deflection in angle (refraction) (**Figure 1.2c**). Thus imaging structures at oblique angles may result in suboptimal images from an incomplete return of

the US signal and can cause artifacts from refraction.

Scattering is redirection of sound in multiple directions that is caused by irregularities of the tissue interface (**Figure 1.2 D**). This occurs when sound interacts with structures much smaller than the transmitted wavelength, resulting in the absorption of US followed by its re-emission in all directions. Scattered echoes originate from the boundary between small, weakly reflective, irregular-shaped objects and these are less angle dependent and less intense. These echoes produce the smaller amplitude, homogeneous pattern of the tissues of many internal structures (liver, muscle).

STEPS IN PRODUCING AN ULTRASOUND IMAGE

Creating an ultrasound image requires equipment that will emit, transmit and process returning sound waves into information on a display. Central to this process is the US transducer, which must convert electrical signals into US, emit the sound beam for brief periods (microseconds), receive returning sound signals and convert these back into electrical signals for display. Processing of returning sound determines how it will be displayed. Manipulation of US machine knobs allows for optimization of the image display.

Table 1.1 Attenuation for Different Tissue Interfaces (for a frequency of 2 MHz).

Medium	Half power distances (cm)	Attenuation	Impedance (Rayls)
Water	380	Extremely low	1.48
Blood, urine	15	Low	1.65
Soft tissues (not muscle)	1–5	Low	1.63
Muscle	0.6–1.0	High	1.71
Bone	0.0–0.7	Higher than muscle	7.8
Air	0.08	Extremely high	0.0004

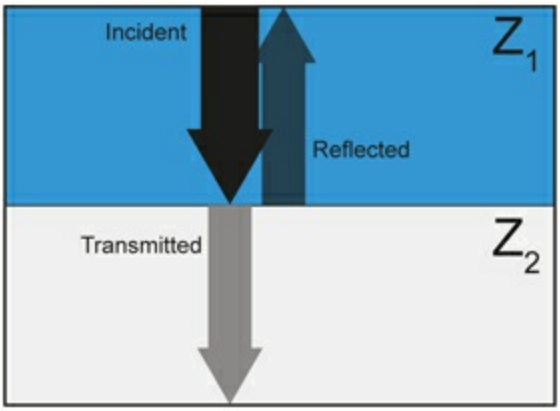

$$IRC\ (\%) = \left(\frac{Z_1 - Z_2}{Z_1 + Z_2} \right) \times 100$$

Fig. 1.3 Reflection. With normal angle (90°) of incidence, reflection depends on the difference in impedances (Z_1 and Z_2) between the mediums. A small reflection will occur if there is a slight difference in impedance. A large reflection will occur if the impedances are substantially different as determined by the intensity reflection coefficient (IRC).

Transducers

A transducer is any device able to convert one form of energy into another. Ultrasound transducers convert electrical energy into acoustic energy and vice versa. The piezoelectric effect describes the ability of certain materials (quartz, ceramics, lithium sulfate, and others) to create voltages with mechanical deformation. When a voltage is applied to a piezoelectric material (reverse piezoelectric effect), it expands and contracts, changing shape to generate mechanical impulses (compressions and refractions) in the form of sound waves (**Figure 1.4**). Piezoelectric material or the ceramic (barium titanate, lead zirconate titanate) is a primary component of US transducers.

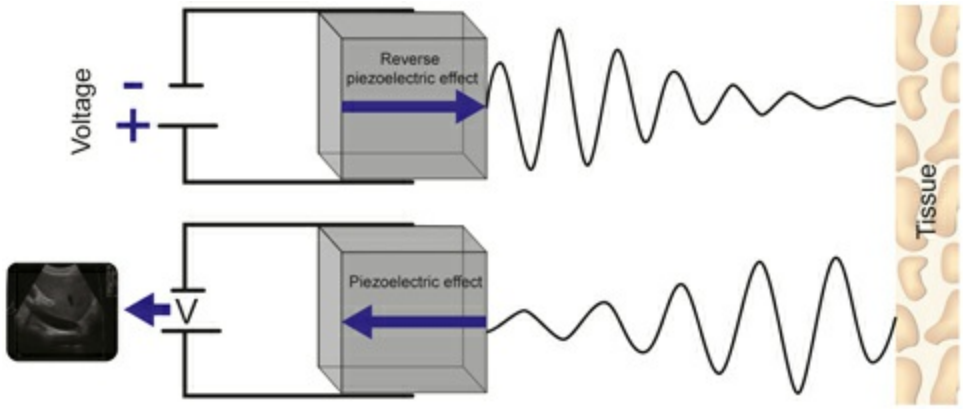

Fig. 1.4 Piezoelectric effect. An electrical voltage is applied to the crystals in the ultrasound probe, causing them to vibrate, creating sound pulses that are emitted by the probe (reverse piezoelectric effect). Returning sound pulses (echoes) reflect back causing the crystals to vibrate again (piezoelectric

effect), now creating an electrical voltage (V) difference, which is processed to the final image displayed on the screen.

Ultrasound Probe

A medical US probe is comprised of several common components that are arranged differently depending on the type of probe (**Figure 1.5**).

1. Piezoelectric element or ceramic generates acoustic pulses and electrical signals when submitted to electrical or mechanical stimulation. The collection and arrangement of active elements (crystals) in a single transducer is the array.
2. Electrodes transmit the electric current to and from the piezoelectric element and records the voltage generated by the returning echoes.
3. Damping or backing material composed of tungsten and rubber reduces the time that the ceramic vibrates following excitation. This shortens the spatial pulse length and improves axial resolution.
4. The matching layer reduces the acoustic impedance mismatch between the patient and the transducer, improving sound transmission.
5. The acoustic insulation prevents the transmission of vibration to the transducer housing.
6. The face plate improves the contact of the probe with the patient.
7. The housing case provides protection for all the probe components.

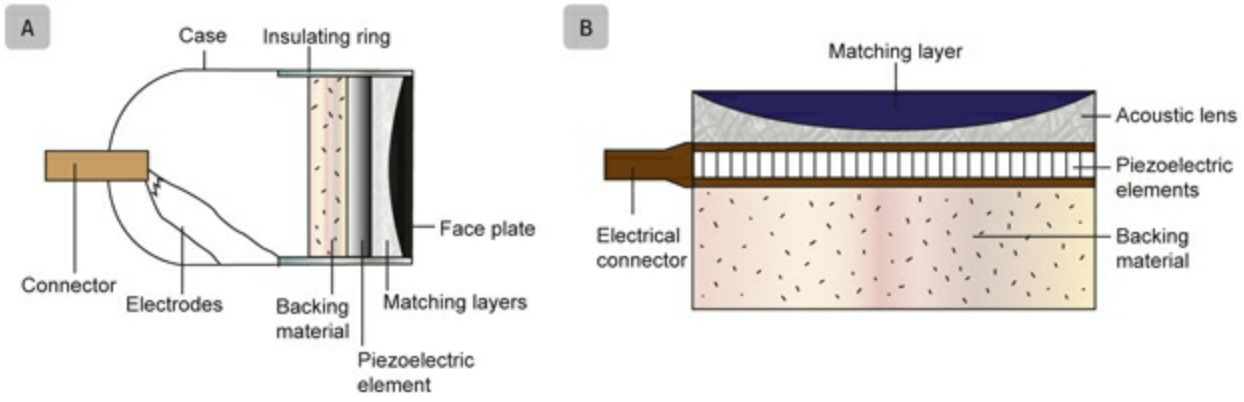

Fig. 1.5 Ultrasound (US) transducers. Schematic representations of US transducers and their principal elements are shown for (A) transthoracic echocardiography (TTE) and (B) transesophageal echocardiography (TEE). (Reproduced with permission from Denault *et al*. [1]).

Ultrasound probes have different scan head designs, frequencies, and

resolution that can be used to obtain images of a target structure with sufficient quality for clinical interpretation (**Figure 1.6**). When performing point of care US, the examiner will need to choose the US probe according to the type of investigation, acoustic window available, and the imaging depth of the tissue to be examined. Each US probe contains a transducer composed of multiple elements (crystals) arranged in a line, curvilinear, or rectangle array. Active elements are fired sequentially (one at a time) or simultaneously (phased) to create a single US beam. All commonly used US probes support imaging modes of 2D, M-mode, spectral and color Doppler. The frequency of the probe will determine the depth of penetration and image quality. A high frequency probe will give better resolution but less penetration; on the other hand, a low frequency probe will allow the interrogation of deeper structures but with lower resolution.

The phased-array US probe has a wide range of frequencies (2–10 MHz) and clinical applications. This transducer allows proper interrogation of the heart, general interrogation of the abdomen, thorax (lung, pleura), and great vessels, and can be used for transcranial Doppler interrogation. Its design with a small footprint makes this probe easy to operate and hold for interrogation through confined regions, such as the intercostal space. It produces images with a wide far-field view and a rapid frame rate suitable for cardiac assessment. Transesophageal echocardiography probes (3.7–7.0 MHz) are phased array probes with a higher frequency than TTE probes (2.5–3.5 MHz).

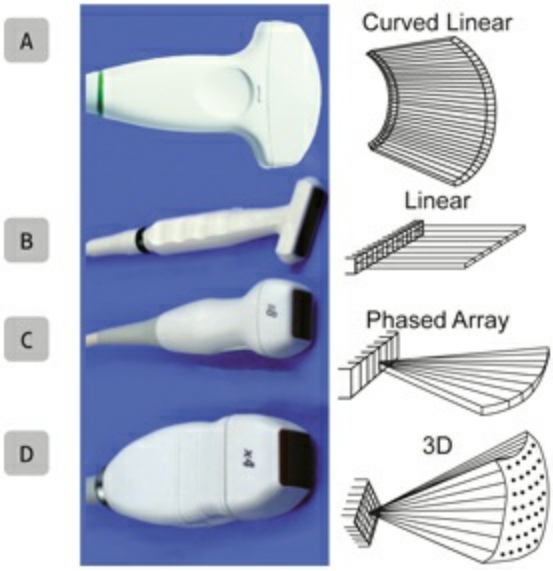

Fig. 1.6 Ultrasound (US) probes. Point of care US mainly uses three types of probes: (A) curved linear array, (B) linear array, and (C) phased array probe. (D) Compare these probes, which give a sector plane image, to the volume scan produced by a three-dimensional (3D) transthoracic probe. (Reproduced with permission from Denault *et al.* [1]).

The linear-array US probe is specially designed for near field imaging. It is a high frequency (7–14 MHz) US probe comprised of elements that are fired sequentially to create a rectangular display. Because of its high resolution, this is an excellent probe to interrogate superficial structures like vessels (diagnosis and procedures), nerves (diagnosis and procedures of regional anesthesia), thyroid, muscle, and testicles.

The curved linear-array US probe is a low frequency transducer (2–5 MHz) designed for interrogation of deeper structures. It is comprised of elements arranged in a curve that are fired in sequence to create a trapezoid-shaped display. It has a wider footprint in comparison to the phased-array probe, giving a broad near, and far-field of view, which is useful for abdominal, obstetric and gynecological examinations. It also allows good imaging of the chest and lung tissue when there is consolidation, masses, or atelectasis. However, thoracic interrogation creates many rib shadowing artifacts due to the large footprint. Its frame rate is too low to accurately interrogate moving structures like the heart.

Imaging Modes and Display

How retuning sound is processed and displayed determines the imaging mode. Current imaging modes include 2D, M-mode, color Doppler, and spectral Doppler.

Although it is no longer used in the clinical setting, amplitude mode (A-mode) made reference to the returning signal strength, measured as amplitude. The higher the reflection, the greater the amplitude displayed (**Figure 1.7 A**). Brightness mode (B-mode) is the translation of A-mode into brightness, representing echoes of high amplitude as bright dots on the screen and vice versa, forming a single scan line (**Figure 1.7 B**). M-mode is essentially B-mode vs time, where time is on the x-axis of the image. M-mode has an outstanding temporal resolution (**Figure 1.7 C**).

The 2D image is generated from data obtained by mechanically or electronically “steering” the US beam through a predetermined pathway, while the data are collected (scan lines) and added up over time to form a composite picture. Each line of the image is a result of a single US pulse

corresponding to a B-mode (**Figure 1.8**). A rapid B-mode scan is also called a real-time scan or 2D echo. The image is shown in gray scale, with high reflectivity (bone) as white, low reflectivity (muscle) as gray, and no reflection (blood) as black.

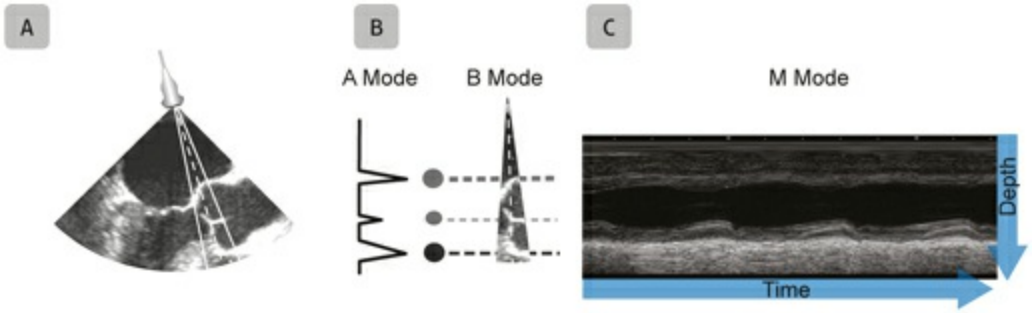

Fig. 1.7 Imaging modes. Returning ultrasound waves can be displayed as amplitude (A-mode), brightness (B-mode), and M-mode. (Reproduced with permission from Denault *et al.* [1]).

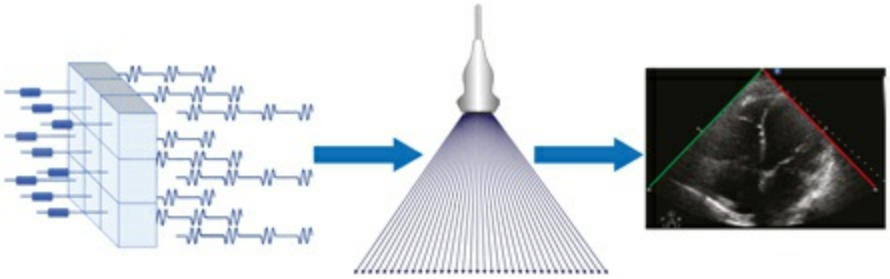

Fig. 1.8 2D Two-dimensional (2D) ultrasound (US). The 2D image is generated from data obtained by mechanically or electronically "steering" the US beam through a predetermined pathway. The goal is to provide pictures or frames as rapidly as possible to faithfully image moving structures. Each line of the image is a result of a single US pulse.

Focus and Resolution

The US beam is a three-dimensional signal. As it propagates, it remains parallel and then quickly converges towards the focal point where it starts to diverge (**Figure 1.9**). The zone between the probe and the focal point is the near-field zone (Fresnel) with a converging profile; and after the focal point, it is the far-field zone (Fraunhofer) that has a divergent profile. The amplitude or intensity of the beam is greater in the center with decreasing intensity towards the edges of the beam. The best imaging quality is generated when the structure being interrogated is localized at the focal zone of the US beam. The focal point can be adjusted on US machines.

Resolution is the ability to image structures on the US display that are in

close proximity to each other as separate structures (spatial), as well as correlated with time (temporal). The better the resolution, the more precise and accurate the image will be. Optimizing temporal and spatial resolutions involves simple adjustments, such as choosing a small region of interest, narrowing the scan sector, decreasing the imaging depth and adjusting the focus point.

Spatial resolution is the ability to distinguish two separate structures in their correct location as unique and distinct structures. Spatial resolution is divided into axial, lateral, and elevational resolution (**Figure 1.9**). Small values mean better resolution. Axial (longitudinal, range, radial, depth) resolution is the ability to recognize two distinct structures one behind the other parallel to the beam axes. Good axial resolution depends on a shorter wavelength and SPL, which comes from using high frequency transducers. Numerically, axial resolution is half the SPL. Lateral (angular, transverse, and azimuthal) resolution identifies two distinct structures, perpendicular to the beam axis. It depends on the beam width. Elevational resolution distinguishes two separate structures along the z-axis or elevational plane. It is determined by US beam height (or thickness), which widens over distance; a thinner beam has better elevational resolution.

Temporal resolution is the ability to correctly determine the position of a structure at a particular instance in time. Good temporal resolution has a high frame rate (images per second) as determined by the number of pulses per scan line, imaging depth, sector width, and line density (number of scan lines per image). Adjusting factors that will decrease the time taken to display an image will increase frame rate and temporal resolution.

Image Optimization and Knobology

Ultrasound machines come with different layouts of controls and buttons that may give the appearance of a very complex system (**Figure 1.10**). This is analogous to a television remote control for which every brand has its own control with a unique distribution of buttons or knobs. In either case even if you are manipulating a control for the first time, the main functions are very intuitive and easy to recognize. Each mode, 2D, M-mode, color Doppler, pulsed wave Doppler (PWD) and continuous wave Doppler (CWD) is activated in a specific way. Basic controls that optimize the image include: gain, depth, focus, and zoom. Measurement tools, such as freeze, caliper, trace, and packages for specific calculations, vary between US machines.

Gain controls the intensity of the echoes as they are received (**Figure 1.11**). It is a post-processing function and does not increase the power transmitted to the patient. Increasing gain amplifies the returning signals making them larger for processing. Every signal is treated identically, affecting the entire brightness of the image. Suboptimal gain adjustment compromises image clarity and quality.

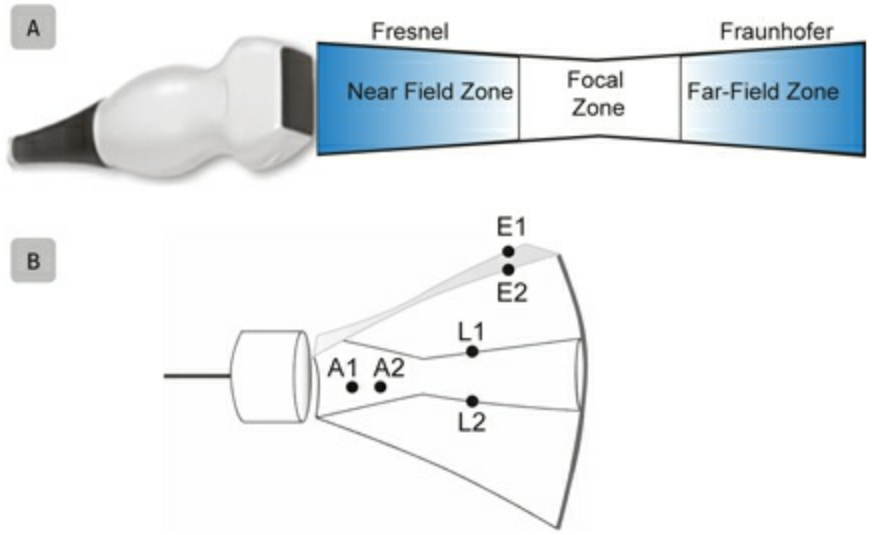

Fig. 1.9 Focus and resolution. (A) The ultrasound beam diameter starts as the same size as the transducer, converges at the focus, and then diverges away from the focus. The best image quality is obtained at the focal zone. (B) Spatial resolution involves the three axes of the ultrasound beam: axial (A1, A2), longitudinal (L1, L2), and elevational (E1, E2). (Adapted with permission from Denault *et al.* [1]).

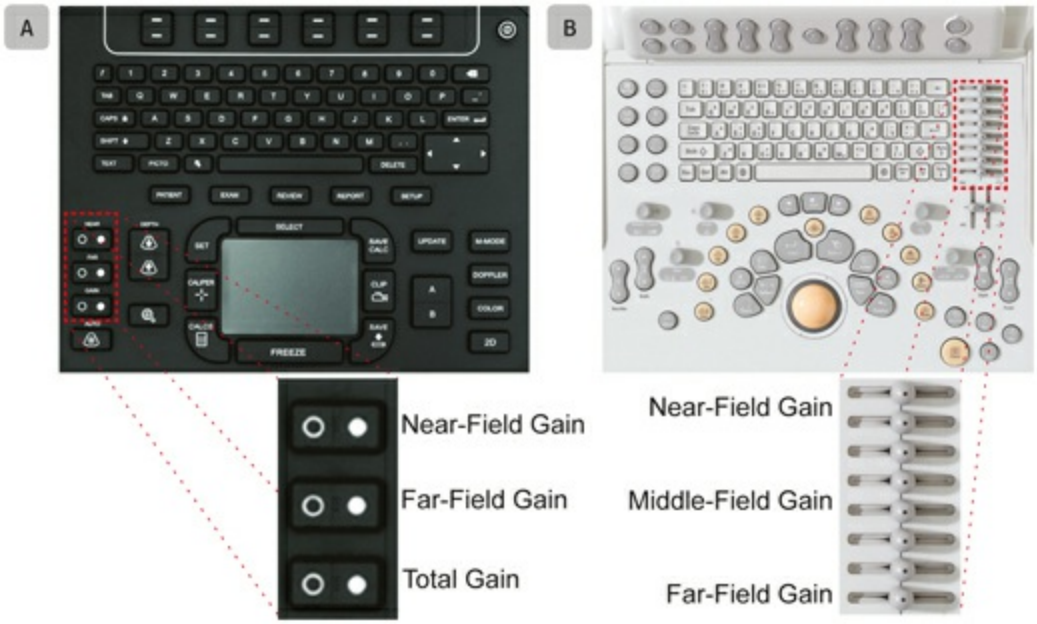

Fig. 1.10 Ultrasound machine. These are examples of the consoles from different ultrasound machines: (A) SonoSite (Bothell, WA, USA) and (B) Philips Healthcare (Andover, MA, USA). The name on each button describes its function.

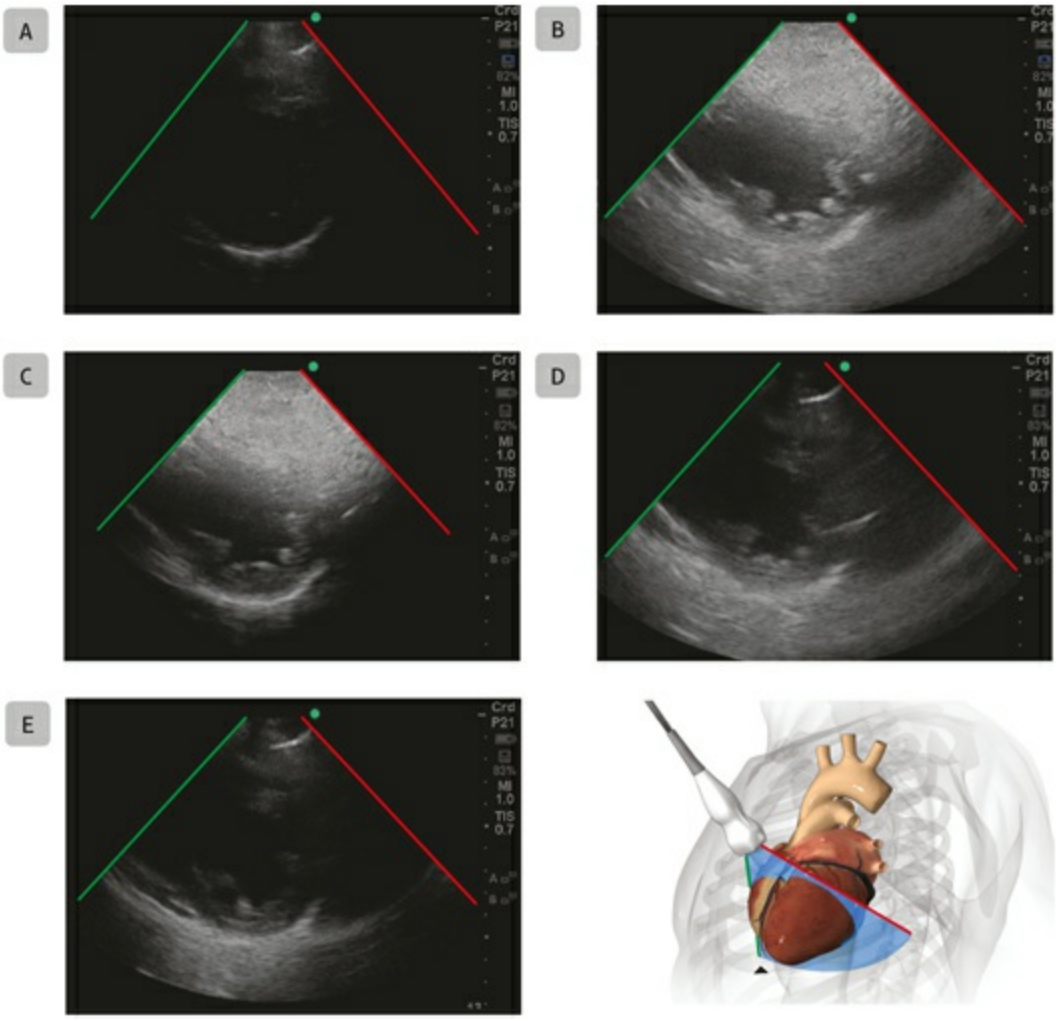

Fig. 1.11 Gain. Adjusting gain alters the ultrasound images on the display from (A) low overall gain, (B) increased overall gain, (C) increased near-field gain, (D) increased far-field gain, and (E) normal gain. All images correspond to transthoracic parasternal short-axis views obtained from the same patient.

The recommended gain adjustment for an optimal imaging acquisition is between 40 and 80%. Time gain compensation (TGC) treats echoes differently, depending on their depth; suppressing near-field and enhancing weaker far-field echoes. Adjusting individual TGC sliders makes all echoes from similar reflectors appear identical regardless of their depth, creating an image of uniform brightness.

Depth is another basic control (knob or button) on the US machine.

Structures in the body are located at different depths. For example, nerves and vessels are located superficially, whereas abdominal or thoracic structures are located more deeply. The proper adjustment of depth will result in adequate resolution and image quality. Changes in depth alter the size of the structures on the screen, as well as image resolution (**Figure 1.12**). It is recommended to start with a deeper visualization to prevent missing additional pathologies (for example, pleural or pericardial effusion when performing cardiac US) and then adjusting the point of interest to the middle of the screen. Information about depth appears on the display as a number. It can also be estimated from the line graduated at 1 cm intervals located on either side of the image.

Focus adjusts the focal zone of the transmitted signal to improve resolution. Activating a button or knob moves a caret (arrowhead) alongside the depth markers on the lateral border of the image sector to a position adjacent to the region of interest. Zoom enables magnification of a selected region of the 2D image by positioning an adjustable sector box. There is enhanced resolution (number of scanned lines, sweep rate, and smoothing) of the structures within the box.

DOPPLER ULTRASOUND

Doppler US can identify not only the presence of moving structures and blood flow, but also the velocity and direction. Doppler US is based on the Doppler effect which states that the frequency of a sound wave reflected by a moving object is different from the emitted frequency. The frequency of sound increases (wavelength decreases) as the moving source approaches an observer and decreases (wavelength increases) as the sound source moves away. If both the sound source and observer are stationary, the frequency and wavelength do not change (**Figure 1.13**).

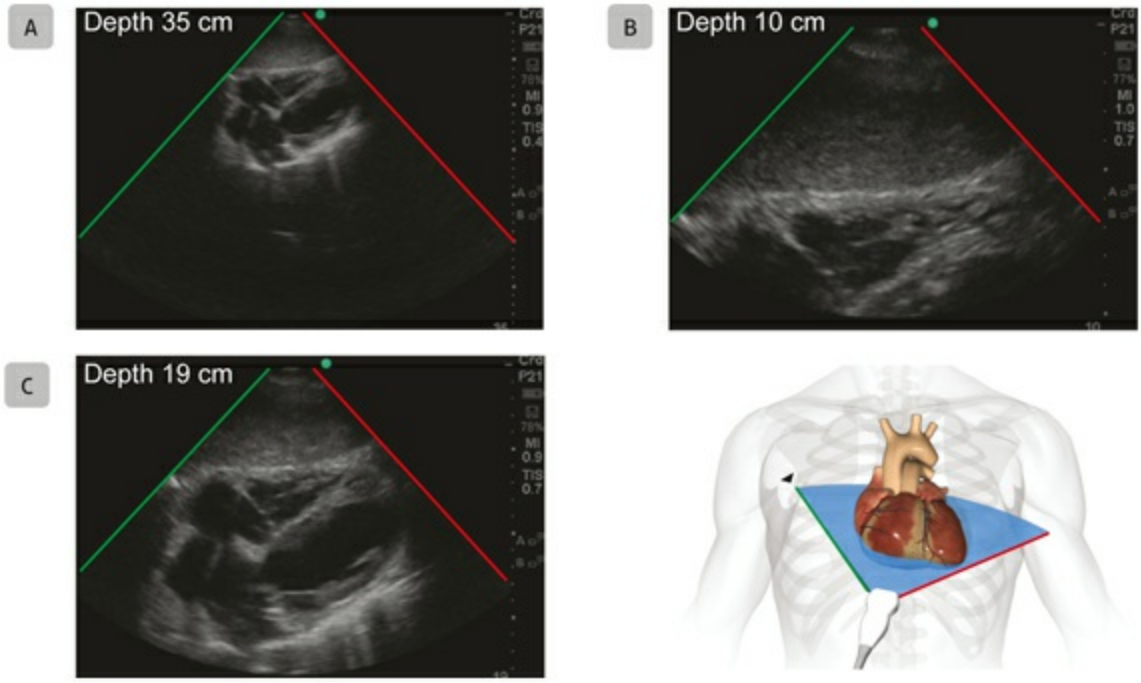

Fig. 1.12 Depth. These transthoracic subcostal or subxyphoid longitudinal views of the heart at different depths were obtained on the same patient within a few seconds. (A) The image acquired at 35 cm depth shows a very small heart and wastes space on the display. (B) The image acquired at 10 cm depth shows only the right ventricle but not the rest of the heart. (C) Adjustment of the depth to 19 cm optimizes the view allowing the entire heart to be properly visualized. Notice that there is a graduated line on the right of each image that corresponds to depth information.

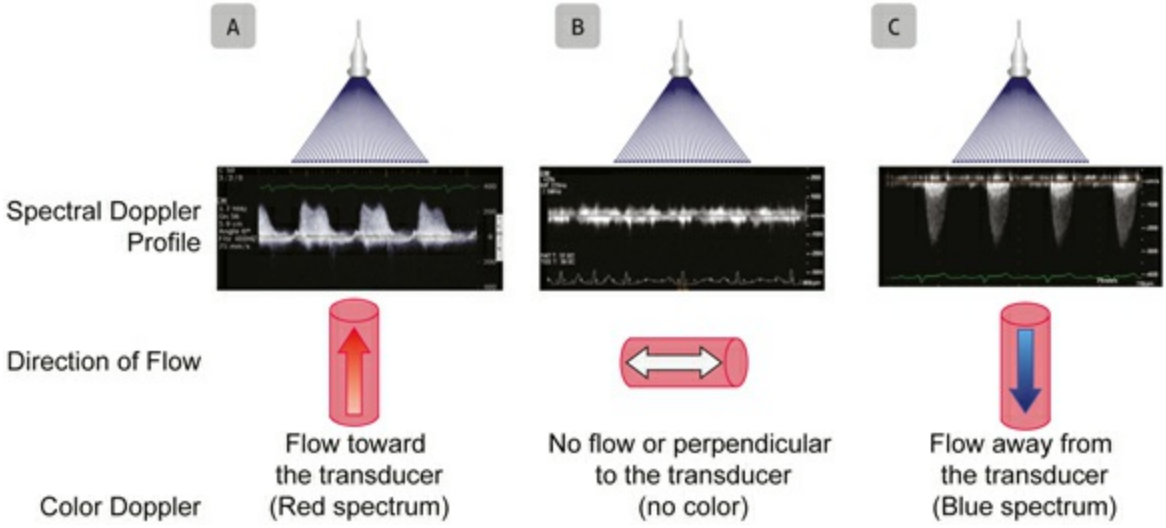

Fig. 1.13 Doppler. Application of the Doppler principle is used to measure blood flow velocity and direction. (A) When flow is directed towards the probe, it will generate a positive Doppler spectral profile and red color when interrogating with color flow Doppler. (B) If there is no movement or if movement is perpendicular to the transducer, no spectral profile will appear and the region will be black in color Doppler. (C) If the flow moves away, the spectral profile will be negative and color flow

will be blue (BART: Blue Away, Red Towards the transducer).

Doppler shift (F_d) is the difference between the transmitted frequency (f_t) and received frequency (f_r) as ($f_r - f_t = f_d$). The Doppler equation describes the relationship between Doppler shift (F_d) and blood flow velocity (v). This equation represents the measurement of velocity ($v = c (f_r - f_t)/2(f_t \cos \theta)$), where c corresponds to the velocity of sound (soft tissue 1.54 mm/ psec) and θ is the angle of incidence. Accurately measuring the true velocity will depend on the angle of incidence of the beam and the direction of motion of the object. If the angle of incidence is perpendicular to flow (θ = 90°), the velocities or direction of flow cannot be measured (**Figure 1.14**).

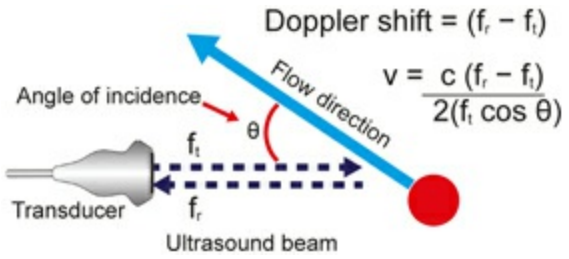

Fig. 1.14 Doppler equation. When the angle of incidence is not parallel to flow, the measure of flow velocity (v) is inaccurate. The ultrasound beam should be aligned parallel to flow as much as possible, to avoid underestimating the velocity. f_r, received frequency; f_t, transducer frequency; c, speed of sound.

Pulse Wave Doppler

Pulse wave Doppler uses only one crystal at a time that must send and receive the sound signal. A small sample box or volume is positioned at the region of interest in a 2D image. The US beam is sent and then the transducer needs to wait until the echo from that depth returns to be presented on a spectral display (**Figure 1.15 A**). The delay between pulse transmission and reception of the returning signal is proportional to the depth of the target. Therefore, the sampling depth determines the rate of US burst transmission, or PRF. The main advantage of PWD is the ability to measure velocity and flow direction at an exact location of interest. This advantage is called “range resolution” or “range specificity” or freedom from range ambiguity artifact. The main disadvantage of PWD is an inaccurate measurement of high velocity signals. These high velocities are displayed as travelling in the opposite direction, a phenomenon called aliasing (**Figure 1.16 A**). Aliasing occurs when the frequency of the Doppler shift of the returning echo exceeds

the maximal frequency that the US system can properly assess. This frequency limit is known as the Nyquist limit and is equal to one-half of the PRF. A deeper positioned sample volume has a lower Nyquist limit and a shallower sample volume, a higher Nyquist limit. Using a lower transmitted frequency will decrease the frequency shift and thus decrease aliasing. Adjustment of the velocity scale and shifting the baseline permits accurate measurement of velocities as long as the Nyquist limit is not exceeded.

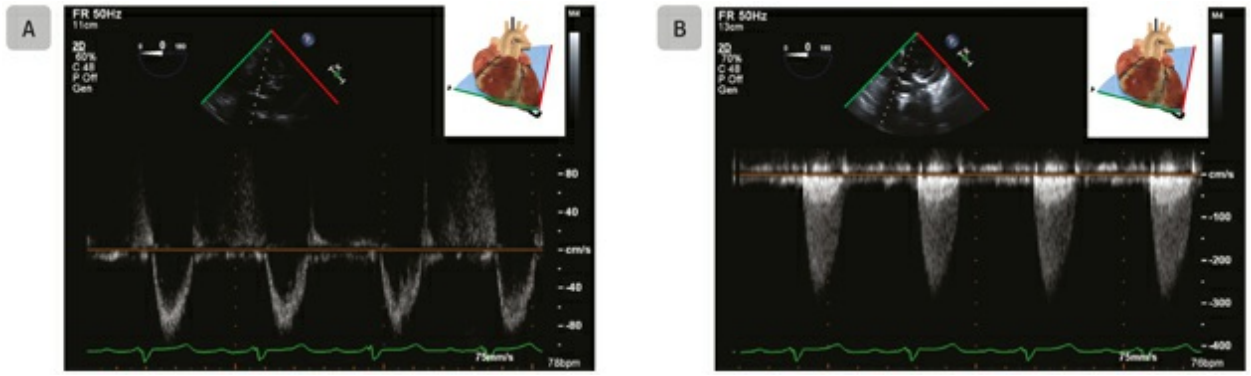

Fig. 1.15 Spectral Doppler. Deep transgastric views with transesophageal echocardiography showing (A) a pulse wave Doppler (PWD) at the left ventricular outflow tract (LVOT) level and (B) a continuous wave Doppler (CWD) spectral trace across a stenotic aortic valve. High velocity is recorded with CWD and low velocity on PWD with the advantage to inform this velocity at one specific point, in this case the LVOT.

Continuous Wave Doppler

Continuous wave Doppler uses two crystals functioning at the same time; one is perpetually sending a signal and the other is listening or receiving the signal. Continuous wave Doppler has an infinite PRF with no Nyquist limit and a duty factor of 100% (**Figure 1.15 B**). Velocities are measured all along the sample line, so the exact location of the peak velocity is unknown. This limitation is called “range ambiguity”. The main advantage of CWD is the ability to measure and display very high velocities without aliasing on a spectral display.

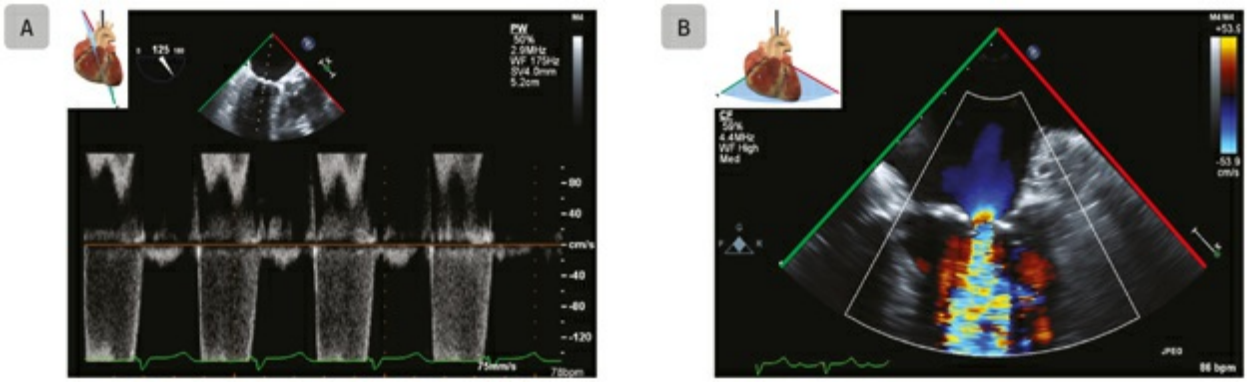

Fig. 1.16 Aliasing. Pulse wave Doppler (PWD) is subject to aliasing artifacts. Mid-esophageal images obtained by transesophageal echocardiography in a patient with mitral stenosis are shown. (A) The spectral trace shows aliasing of flow through a stenotic mitral valve. The Nyquist limit (PRF/2) establishes the maximum velocity that could be measured; after this velocity is exceeded, aliasing will occur. (B) Color Doppler is also subject to aliasing as shown with flow acceleration of color flow above a stenotic mitral valve.

Color Flow Doppler

Color flow Doppler is a form of pulsed Doppler in which velocity and flow direction of blood is presented in real time as color encoded over the gray-scale 2D image. Color flow Doppler presents presents average or mean velocities whereas PWD and CWD present instantaneous peak velocities. Color flow Doppler is subject to range resolution and aliasing. In color Doppler mode, flow velocity, exceeding the maximal value of the color scale, is displayed by an abrupt change in color to the opposite end of the color-coded scale (aliasing), wrongly suggesting a change in flow direction (**Figure 1.16 B**).

The color flow Doppler uses a “map” to convert velocities into colors. This color map with its adjustable velocity scale is located beside the image. Three factors (velocity, amplitude, and variance) are encoded onto the screen using a particular color scheme. A common color map (BART) uses **b**lue to indicate flow **a**way from the probe and **r**ed for flow **t**owards the probe (**Figure 1.17 A**). If there is no flow or if the angle of incidence is 90° (perpendicular to flow), then no color is shown on the screen (**Figure 1.13 B**). An enhanced velocity map shows a brighter color the greater the speed. Variance color map includes additional information about whether the flow is laminar or turbulent (green color). In variance mode, color changes from side to side (green or yellow), as well as up and down **(Figure** 1.17 **B).** When using CFD, the size of the color box will affect temporal resolution. For

instance, small sample boxes will yield a higher frame rate.

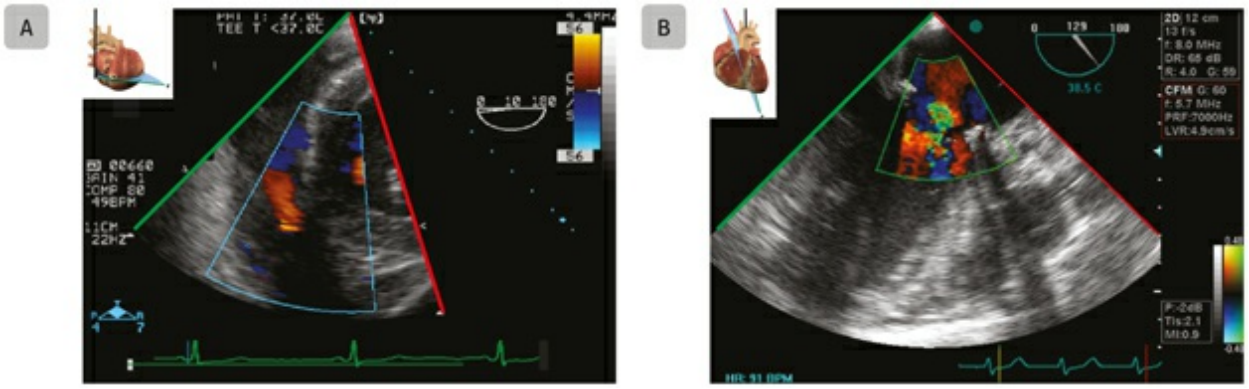

Fig. 1.17 Color flow Doppler. (A) An enhanced velocity map consists of brighter shades of blue and red. (B) A variance color map adds green to the enhanced velocity map to indicate greater variations in flow.

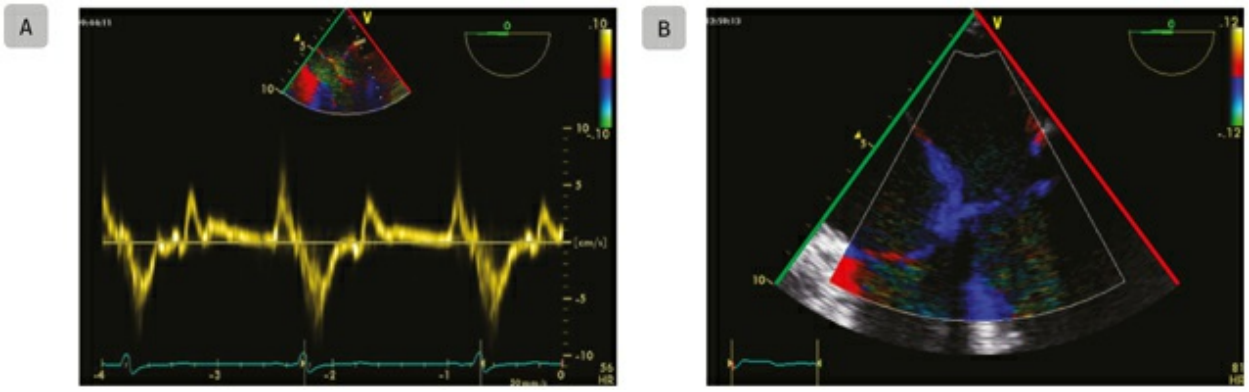

Fig. 1.18 Tissue Doppler imaging (TDI). TDI is shown as (A) a spectral trace of pulsed wave Doppler (PWD-TDI) and (B) as a color-encoded 2D image (2D color-TDI).

Power Doppler

Power Doppler is a Doppler mode that only identifies the presence of flow, but cannot tell information about direction or velocity. It is used to detect the presence of flow in small vessels and veins. Power Doppler is unaffected by the angle of incidence (unless exactly 90°) and is not subject to aliasing as velocities are ignored.

Tissue Doppler Imaging

Tissue Doppler imaging (TDI) is a Doppler mode that filters all high velocity signals and displays only the low Doppler shift from the heart wall. It

measures lower velocities and higher amplitudes. It can be displayed as a spectral trace of peak velocities measured at a specific point (PWD-TDI) (0 1.18 **A**) or as color encoding of mean velocities on a 2D image (2D-TDI) (**Figure 1.18 B**). It is particularly useful in the classification of diastolic function (see Chapter 5, Assessment of Global Ventricular Function, Pericardium, and Cardiomyopathy).

REFERENCE

1. DenaultA.Y., CoutureP., VegasA., BuithieuJ., TardifJ.C.. *Transesophageal Echocardiography Multimedia Manual, Second Edition: A Perioperative Transdisciplinary Approach*. New York: Informa Healthcare, 2011.

Chapter 2

Patient Safety and Imaging Artifacts

Geneviève Côté, André Y Denault and Georges Desjardins

INTRODUCTION

Transesophageal echocardiography (TEE) was first introduced in 1976 as a mean to improve cardiac monitoring by providing “an airless pathway to the heart”. [1] Advancement in transducer technology and the probe’s proximity to the heart inside the esophagus has combined to produce a low risk diagnostic examination. This makes real-time TEE cardiac monitoring very useful in the perioperative period, intensive care unit (ICU) and in the emergency department. Transesophageal echocardiography bypasses variable thicknesses of soft tissue (i.e. in obese patients), bones, and lung parenchyma that may interfere with adequate transthoracic echocardiographic imaging (TTE). Transesophageal echocardiography availability is sometimes limited by the level of expertise necessary for image acquisition and interpretation, as well as the expense of the technology. This chapter will review patient evaluation, contraindications, complications, and imaging artifacts associated with TEE.

CONTRAINDICATIONS

Before proceeding to the TEE examination, it is mandatory to obtain informed consent from the patient. The aims, technique, and risks of the procedure are reviewed (**Figure 2.1**). Patient evaluation and preparation are summarized in **Table 2.1**. Transesophageal echocardiography is a semi-

invasive procedure that is not without risk to the patient. Potential contraindications should be anticipated. In an urgent situation, the benefit of information obtained from the use of TEE as a diagnostic and monitoring tool must be carefully weighed in the overall patient management. [2] Patients should be fasted for at least 6 hours before elective awake examination.

Absolute contraindications to TEE examination are rare, but relative contraindications are numerous (**Table 2.2** and **Figure 2.2**). Patients with a history of gastrointestinal (GI) disease, surgery and/or radiotherapy can undergo TEE examination as long as the disease is inactive or a thorough GI evaluation has been completed. These precautions should be considered when a patient presents with dysphagia, esophageal or gastric pathology: obtain a GI consultation, use a smaller probe (i.e. pediatric), avoid unnecessary probe manipulation, limit the examination, consider other imaging modalities, and request that the most experienced operator performs the examination. [3] , [4] Probe insertion may require neck manipulation. Suspicion of an unstable neck injury, craniofacial trauma, basilar skull fracture or the consequences of cervical spine abnormalities congenital (Trisomy 21, Morquio syndrome) or acquired (rheumatoid arthritis) may make probe insertion difficult, and TEE probe manipulation hazardous. Intrinsic or acquired coagulopathy and thrombocytopenia are relative contraindications.

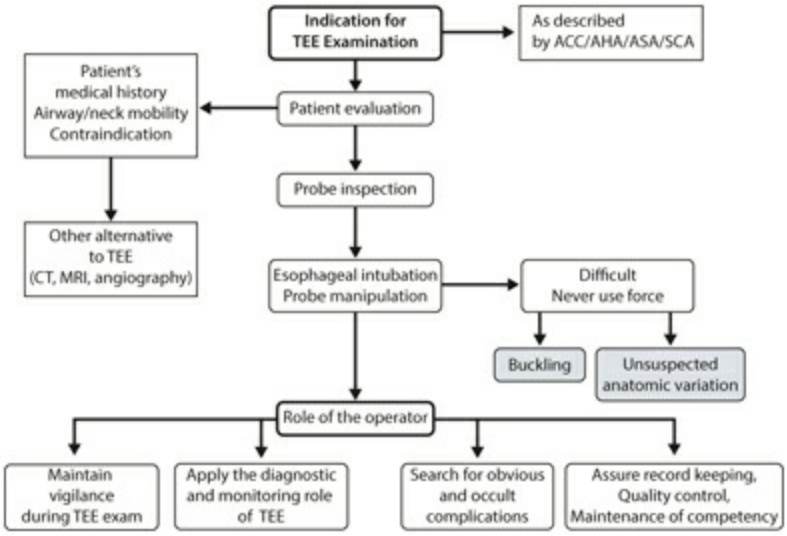

Fig. 2.1 Use of transesophageal echocardiography (TEE). A general approach to the use of TEE is presented. ACC, American College of Cardiology; AHA, American Heart Association; ASA, American Society of Anesthesiologists; CT, computed tomography; MRI, magnetic resonance imaging; SCA, Society of Cardiovascular Anesthesiologists. (Reproduced with permission from Denault *et al.* [5]).

Table 2.1 Patient Evaluation and Preparation for TEE Examination.

Informed consent from patient	
Careful medical history	Absolute and relative contraindications (see **Table 2.2**)
	Medication use
	Drug allergy
Fasting status	Absence of recent food ingestion within 6 hr and no fluid ingestion within 4 hr
Examination	Teeth, oral/dental hygiene, throat or neck deviation, and mobility
	Airway evaluation as for endotracheal intubation
Availability of adequate patient's safety monitoring	Blood pressure, ECG, and saturation monitoring devices
Emergency resuscitation and suctioning equipment	
Trained personnel	

Note: ECG, electrocardiogram; TEE, transesophageal echocardiography.

Table 2.2 Contraindications to TEE.

Absolute contraindications	Relative contraindications
• Lack of informed consent • Unwilling and uncooperative patient • Lack of expertise in intubation of TEE • Esophagectomy • Esophageal obstruction (cancer, stricture) • Gastric volvulus • Active upper gastrointestinal bleeding • Perforated viscus (known or suspected) • Full stomach • Suspected neck injury • Respiratory distress in unintubated patient	• Known esophageal pathology • Esophageal varices without bleeding • Esophageal diverticulum • Esophageal fistula • Esophagitis/inflammatory process • Gastric herniation • Scleroderma • Carcinoma • Penetrating or blunt thoracic trauma • History of previous esophageal surgery • Fundoplication gastric surgery • Cervical abnormalities • Severe cervical osteoarthritis/ osteophytes/ spondylosis • Neck surgery • Radiation therapy to the cervical area • Severe oropharyngeal distortion • Previous radiation therapy to the mediastinum • Bleeding diathesis

Note: TEE, transesophageal echocardiography.

Anatomic variations and conditions can alter TEE imaging. Scoliosis may disrupt the normal relationship between the esophagus, heart, and aorta; preventing the probe alignment in normal classic views used to determine velocity. Head and neck surgery limits free access to the head hindering probe mobilization and image acquisition. Proven hiatus hernia can make probe manipulation and image acquisition difficult (see **Figure 4.22**).

COMPLICATIONS ASSOCIATED WITH TEE EXAMINATION

Gastrointestinal Complications

Intubation and Manipulation

The incidence of failure to intubate the esophagus with the TEE probe ranges from 0 to 1.9%. [2] During awake TEE examination, retching is common (39% incidence), [6] although better analgesia and sedation improve patient tolerance of the procedure. Forceful Valsalva maneuver may cause severe hemodynamic effects, while forceful vomiting may result in Mallory-Weiss syndrome. [7] Occult GI lesions and anatomic variations are risk factors for complications associated with TEE probe insertion, including diverticula, Schatzki's ring, cervical spine arthritis, [8] hiatal hernia, neoplasms, and inflammatory mucosal changes. [2]

An early study of TEE examinations performed on intubated patients in an ICU showed: 5 (13%) required removal of the nasogastric tube, 3 (8%) endotracheal tube cuff deflation, and 1 (3%) direct laryngoscopic assistance. [9] Recommendations to reduce the risk of injury to the oropharynx and esophagus during TEE probe insertion include nasogastric tube removal, temporary endotracheal cuff deflation, and a forward mandibular displacement. [10] Cuff deflation facilitates insertion when double lumen tubes are used in minimally invasive cardiac or thoracic surgery. Compared to blind probe insertion, direct laryngoscopy reduces the incidence of oropharyngeal mucosal injury, odynophagia and the number of attempts. [11]

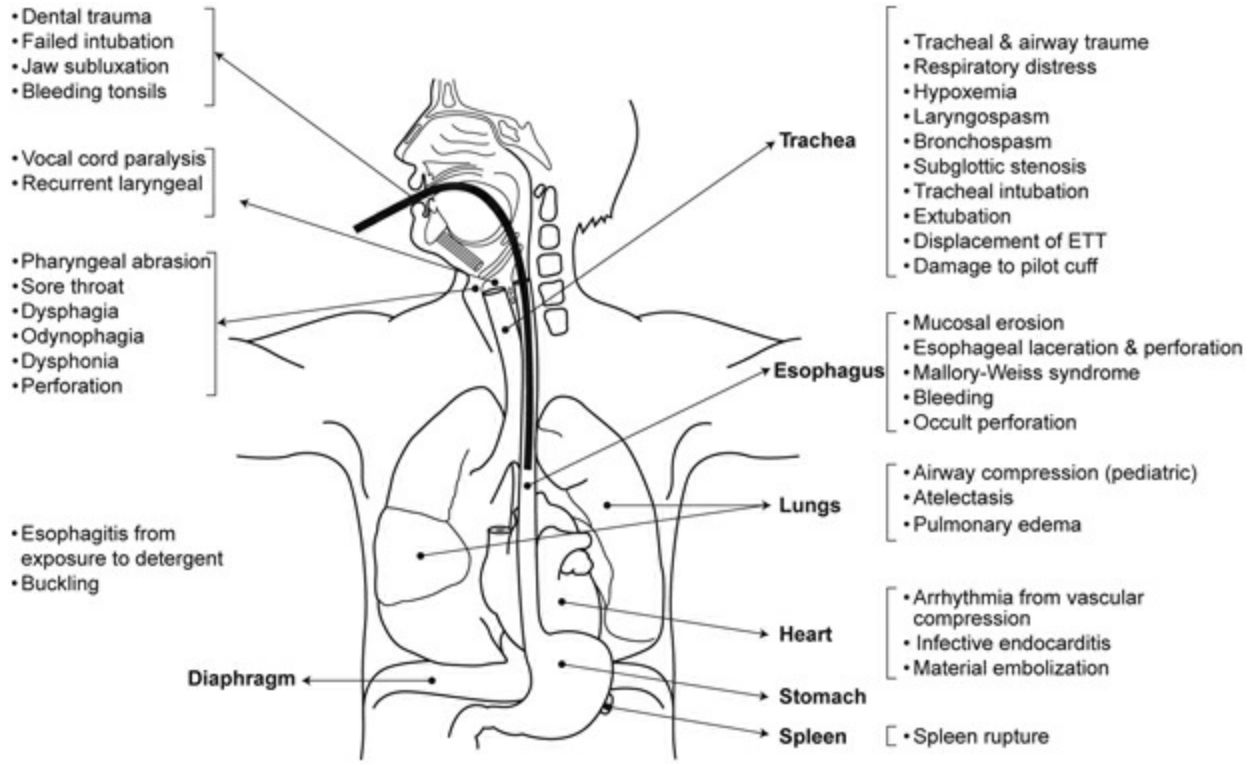

Fig. 2.2 Transesophageal echocardiography (TEE) complications. Summary of transesophageal echocardiography-related complications is shown. ETT, endotracheal tube. (Reproduced with permission from Denault *et al.* [5]*).*

Probe insertion should never meet undue resistance and always occur with monitoring of the ultrasound (US) image. [2] Forceful esophageal intubation can traumatize the vocal cords, and/or the esophageal and GI tract. Probe mobilization in the upper GI tract should not be performed when the probe is in the locked position or the probe tip is flexed. Proper probe inspection before insertion will prevent probe tip buckling. Probe buckling is suspected when imaging is difficult, inappropriate resistance is felt during probe advancement, removal or mobilization and the control knobs are fixed (**Figure 2.3**). [12] , [13] In the event of probe buckling, the probe is advanced into the stomach where it can recover to a neutral position prior to withdrawal (**Figure 2.4**). [13]

GI Trauma and Perforation

Dental trauma, tongue injuries, jaw luxation, tonsillar bleeding, erosion, and submucosal hematoma of the pharyngeal area are injuries related to TEE probe insertion. [2] Patients with fresh thermal burns to the mouth and/or pharynx are at high risk of developing upper airway edema [14] that could impede intubation and increase mucosal friability.

Impingement of bone spurs from the cervical vertebrae on the posterior pharynx may ulcerate the mucosa during probe manipulation. Perioperative TEE is an independent risk factor for dysphagia in adults and children. [15] – [19] Splenic lacerations were described after TEE monitoring during cardiac surgery. [20] , [21] Other foreign bodies inserted in the oesophagus, such as temperature probes, were inadvertently dislodged and even retrieved from the stomach after TEE examination. [22] – [24] .

Upper GI perforations after TEE rarely occur in both pediatric and adult surgical patients with an incidence of 0.01–0.04%, [25] which is a similar rate (0.08–0.13%) for patients undergoing gastroduodenoscopy. [26] When esophageal perforation occurs it may be located in the abdominal (57.3%), intrathoracic (33.3%), or cervical (9.3%) portions of the esophagus. [27] Esophageal injury after TEE examination can arise during probe manipulation, within 24 hours or for up to 8 days thereafter. [28] In the critically ill intubated patient, a high index of suspicion should prevail (**Figure 2.5**). Patients are conscious and sedated for TEE. Perforation is evident from signs

of subcutaneous emphysema, dyspnea, and pain.

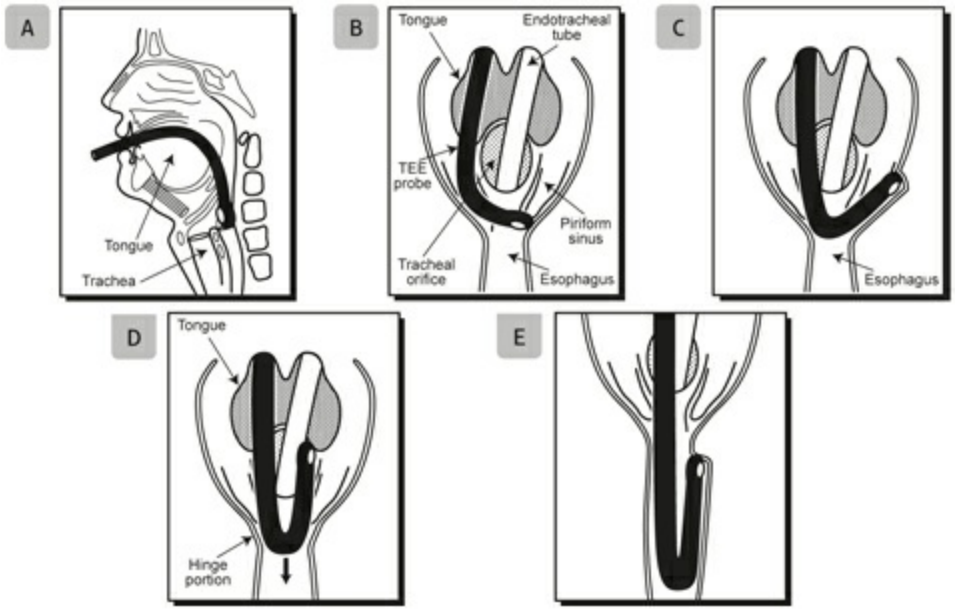

Fig. 2.3 Buckling during transesophageal echocardiography (TEE) probe insertion. (A) Sagittal view of a correctly inserted TEE probe and its relationship with anatomic landmarks. (B-E) Coronal view of the oropharyngeal and upper esophageal area is shown. (B, C) Difficult insertion of the TEE probe often results from a lateral deviation as opposed to the midline probe path of the probe tip. (D) If excessive force is used, the probe tip could become flexed resulting in (E) TEE probe buckling. (Reproduced with permission from Denault *et al.* [5]*).*

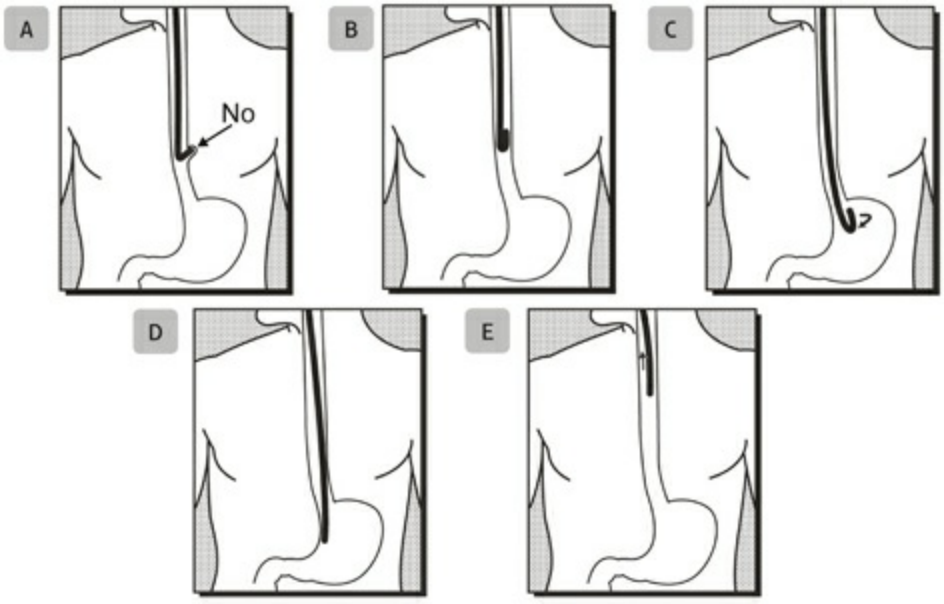

Fig. 2.4 Buckling of transesophageal echocardiography (TEE) probe. (A-C) Buckling of the inserted TEE probe can result in the inability to extract it from the esophagus. (D,E) If this condition is suspected, advancing the probe with retroflexion of the probe tip back to a straight position will lead to

successful removal. (Reproduced with permission from Denault *et al*. [5]).

Bleeding of the GI Tract

Minor mucosal trauma during TEE can cause hematemesis or blood-tinged sputum, although major bleeding complications are rare (0.02–0.1%). [17] , [29] , [30] Direct trauma to the mucosa, a tumor, or esophageal varices can be sources of GI bleeding during TEE probe manipulation. Anticoagulation alone does not appear to greatly increase the risk of TEE-associated bleeding.

Cardiovascular Complications

Cardiovascular complications during TEE rarely occur (0.8%) and manifest as arrhythmia, such as non-sustained ventricular tachyarrhythmia, transient atrial fibrillation, and/or as third degree block. [26] A combination of sedation, endogenous catecholamines, and hypoxemia in patients with reduced systolic function may precipitate heart failure, [31] or fatal ventricular arrhythmia [32] during the TEE procedure. Large variations in intrathoracic pressure and hemodynamic changes from retching have embolized a right atrial mass, mitral valve vegetation, left intracardiac thrombus, and myxoma, as well as caused progressive aortic dissection [33] and cardiac tamponade. [2] Pediatric patients may be more vulnerable during TEE from significant compression by the esophageal probe of vascular structures such as a normally positioned or aberrant right subclavian artery, [34] descending aorta, innominate artery, and pulmonary venous confluence with total anomalous pulmonary venous return. [2]

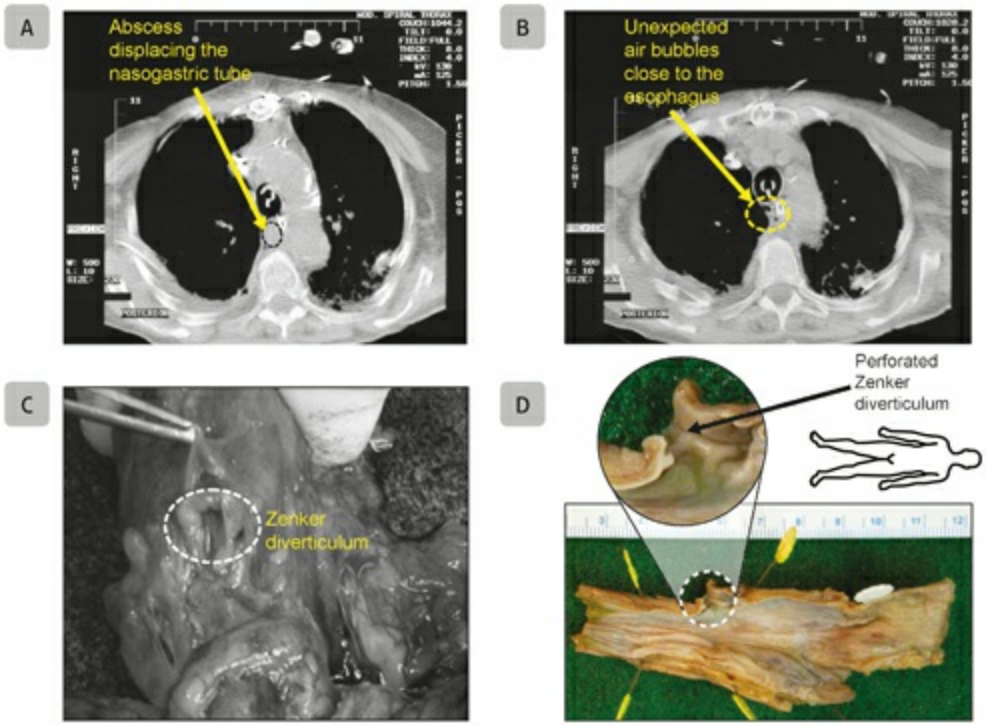

Fig. 2.5 Proximal esophageal perforation. An 82-year-old female died from septic shock after cardiac surgery. Computed tomography scans show an abscess displacing the nasogastric tube and air bubbles close to the esophagus. (C) The autopsy demonstrated the presence of an unexpected perforated Zenker diverticulum. (D) A longitudinal view of the internal esophagus shows the perforated Zenker diverticulum. It was presumably perforated by the TEE probe either intraoperatively or postoperatively. (Reproduced with permission from Denault *et al.* [5]*).*

Respiratory Complications

In the ambulatory setting, respiratory compromise may include aspiration, hypoxia, accidental tracheal intubation, bronchospasm, and laryngospasm. [2] In intubated candidates, airway compression is common in small infants, but also occurs in adults, [35] along with endobronchial tube displacement and accidental extubation. Local anesthetics are often used to topicalize the oropharyngeal area and cases of hypoxemia associated with methemoglobinemia have been reported. [2] Respiratory complications can be diagnosed with TEE to some extent (see Chapter 4, Extra-cardiac Transesophageal Ultrasonography).

Complications Associated with TEE Probe and Probe Maintenance

Biological Effects

There have been no confirmed biological effects from exposure to diagnostic US reported in humans. Thermal effect is the most important bioeffect attributed to diagnostic US. Increase in the temperature of tissue depends on characteristics of the acoustic source, tissue properties, and exposure time. Temperature elevation is offset by heat loss due to blood flow through tissue and heat diffusion. No thermal effects are expected at temperatures less than 38°C, regardless of the duration of exposure. The TEE probe contains a safety feature that automatically disables the probe from imaging in the event of overheating (**Figure 2.6**).

Electrical Safety

Loss of the electrical integrity of the system increases the risks of thermal injury. When defibrillation is necessary, the TEE probe does not have to be unplugged (<50 J). There have been reports of esophageal burns [36] and atrioesophageal fistula with TEE imaging during radiofrequency ablation for atrial fibrillation. [37] , [38]

Maintenance and Cleaning

Maintenance and strict cleaning protocols, [39] including visual inspection and a pressure test, have to be implemented to ensure the probe's integrity and innocuity between patients. Disruption of the protective sheath can create a lumen between the probe's external sheath and internal core. Improper cleaning protocol can cause an accidental chemical burn from residual Cidex® (orthphtaldehyde), [40] , [41] contamination from radionucleotides, [42] latex aerosol- ization, [43] and even a nosocomial outbreak of *Legionella pneumophilia.* [44]

Infection and Prophylaxis

Infectious complications associated with TEE are extremely rare. The American College of Cardiology and the American Heart Association no longer mandate antibioprophylaxis for nondental procedures, such as TEE, gastroscopy, and colonoscopy in the absence of active infection. [45]

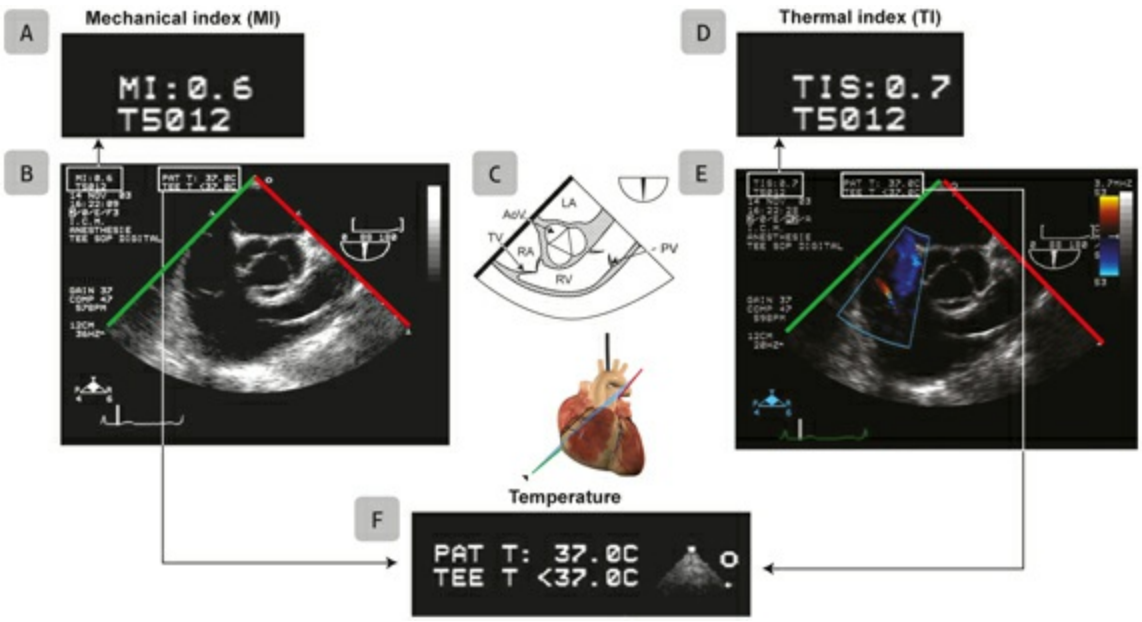

Fig. 2.6 Mechanical and thermal indices. Mid-esophageal right ventricular inflow/outflow tract views in a 64-year-old male scheduled for revascularization. (A—C) The mechanical index (MI) and (D,E) soft tissue thermal index (TIS) and (F) temperature (T) are indicated at the top of the display screen. AoV, aortic valve; LA, left atrium; PAT, patient; PV, pulmonic valve; RA, right atrium; RV, right ventricle; TEE, transesophageal echocardiography; TV, tricuspid valve. (Reproduced with permission from Denault *et al.* [5]*).*

B: https://youtu.be/mx9PS3SU4b0

E: https://youtu.be/9CkOfGhK7uY

ARTIFACTS

A potential complication of TEE is the misinterpretation of artifacts that appear in all US modalities. A thorough understanding of the types and mechanisms of artifacts helps to distinguish these from real structures and avoid diagnostic errors. Imaging artifacts result from violations in the

principles of sound. First, sound travels in a straight line at a constant speed directly to the reflector and back. Second, the imaging beam is thin and reflections occur only along the main beam and are related to tissue characteristics.

Imaging artifacts can be categorized according to the violation of sound as: [46], [47]

1. Propagation path (reverberation, refraction, multipath, grating lobe, range ambiguity).
2. Attenuation (acoustic shadowing, enhancement, focal enhancement).
3. Resolution (axial, lateral, beam thickness, dropout, speckle/noise, near-field clutter).

Artifacts appear in the US image as:

1. Structures that look different from reality (degraded images).
2. Structures that appear to be there when in fact they are not (falsely perceived images).
3. Structures that do not appear to be there when in fact they are (missing images).
4. Structures that appear to be in the wrong location (misregistered locations).

Identifying an artifact requires a high index of suspicion and relies on several criteria that may, or may not, coexist: (1) indistinct boundaries, (2) non-plausible anatomy, (3) extension across normal surrounding structures, (4) disappearance with changes in sector depth setting, imaging planes, and transducer position, (5) absence of independent motion, and (6) absence of influence on blood flow by color Doppler, showing flow crossing the artifact without turbulence or changes in direction or velocity. [48] This section will review common 2D imaging artifacts.

Propagation Path Artifacts

Reverberation

A reverberation is an acoustic phenomenon where sound waves bounce back and forth between two strong reflectors (big structures, small structures, or air) forming multiple reflections of the US beam. Strongly reflective tissue-

air and tissue-fluid interfaces with large impedance discontinuity, such as the aorta-lung interface, anterior wall of the left atrium (LA), diaphragm, and pericardium, are often involved in these artifacts. Moreover, the surface of the US transducer itself may act as a reflector and throw back part of the incoming signal. A reverberation artifact appears on the display at a greater depth (or multiples of the depth) than the actual object location as nonspecific lines, bright areas, or a duplication of a whole structure.

A mirror image artifact is a type of reverberation artifact that results from returning sound bouncing back off a large strong reflector (aortic wall, diaphragm) and then returning towards the transducer. This produces a second less intense duplicate image of the same structure deeper on the screen at twice the distance (**Figure 2.7**). Any 3D, spectral, and color Doppler information of the actual target is also reflected and will be displayed in the artifactual structure. In the presence of a curved, or irregular, reflective surface, the mirror image may be distorted, rendering its recognition more challenging.

A comet tail artifact is another type of reverberation artifact that results from a small reflector (aortic atheroma, mechanical valve) repeatedly reflecting returning sound in line with the US beam (**Figure 2.8**). This creates a single strong linear echo that extends deeper than the reflector. In lungs, comet tails that reach all the way down through the lung are renamed B-lines (see **Figures 14.8–14.12**). The artifact appears as thin closely spaced discrete echoes (clean shadows) of decreasing amplitude and width (tapered triangle). The A-lines on lung US are examples of a reverberation artifact (see **Figure 14.7**).

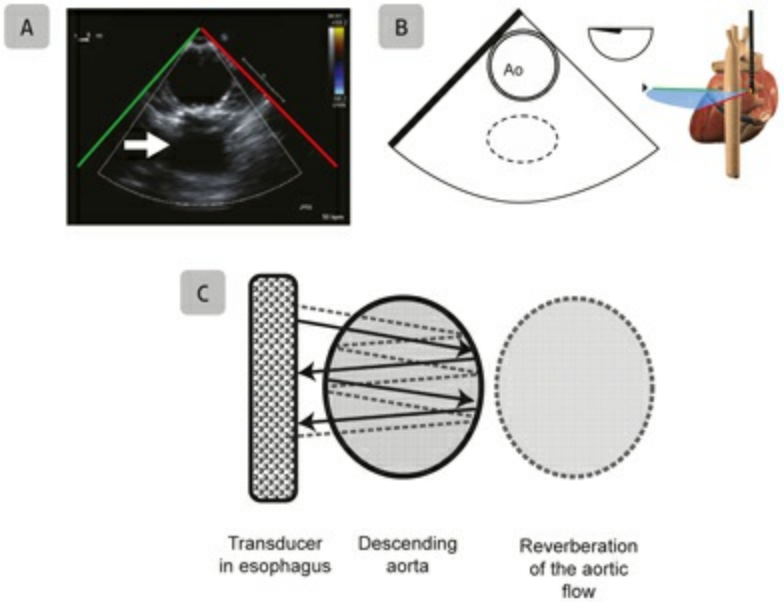

Fig. 2.7 Reverberation. (A,B) A midesophageal short-axis view of the aorta (Ao) at 0° with a reverberation artifact is shown. (C) When a strong reflector is close to the transducer, the returning high-energy echo beam giving the image is reflected on the front part of the transducer and then rerouted toward the reflector for a second time. It gives a second image interpreted by the computer as being at double the distance of the first target. This will also be apparent for color Doppler. (Reproduced with permission from Denault *et al.* [5]).

https://youtu.be/n9VvRh7PLXo

https://youtu.be/Kx7J377256E

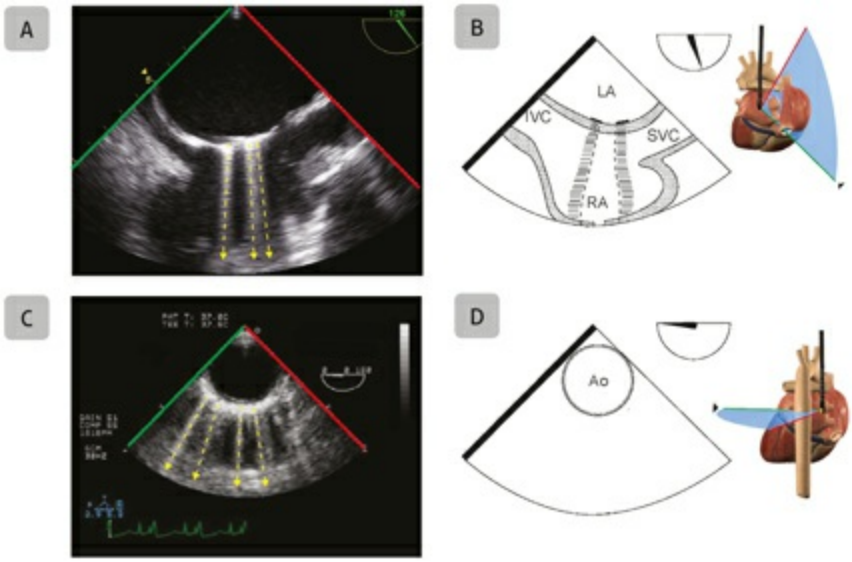

Fig. 2.8 Comet tail and ring-down artifacts. (A,B) Mid-esophageal bicaval view shows residual air in the left atrium (LA). Ring-down artifact is specific to gas bubbles and can be seen when there is residual air in the heart following cardiotomy. (C,D) Descending aorta (Ao) short-axis view shows multiple comet tail artifacts from the lung adjacent to the aortic wall. IVC, inferior vena cava; RA, right atrium; SVC, superior vena cava. (Panels (C) and (D) reproduced with permission from Denault *et al.* [5]).

A: https://youtu.be/NlW0k2IvNtU

A ringdown artifact is often confused with a comet tail artifact or a reverberation artifact. This artifact is a result of fluid trapped by air bubbles that resonate continuously to produce multiple reflections. This appears as a streak posterior to a gas collection composed of numerous thin closely spaced reflections that are less discrete (dirty shadows) than that of a comet tail artifact (**Figure 2.8**).

Refraction

Refraction is the bending of transmitted and reflected waves (**Figure 2.9**). Sound changes direction when (1) it strikes a boundary obliquely and/or (2) the media have different propagation speeds. The degree of directional change is governed by Snell's law according to the incident angle of the US beam and the difference in velocity between the two media. Examples of

refraction artifacts include ghosting, speed error, and edge shadowing, and may result in duplication, enlargement, or even contraction of imaged structures.

Ghosting represents a refraction-type artifact from sound striking a curved boundary obliquely. A structure that is anatomically located lateral to the path of the returning beam is interpreted by the machine as being located in the path of the returning beam. This creates extra echoes as a second copy of the true reflector appears side-by-side of the true anatomic structure. Lateral resolution is degraded as the edges appear blurred.

Edge shadowing (or defocus) artifact is considered a type of refraction artifact that is not a result of acoustic shadowing. The sound beam may bend at the edge of curved structures (aorta, cysts) and lose intensity, producing a shadow. This creates small dark areas (anechoic) under the edges of a circular structure as seen around the aorta in a mid-esophageal (ME) ascending aorta view (**Figure 2.10**).

Grating Lobe

Grating/side lobe artifacts are reflections from highly reflective structures that appear as hyperechoic objects within an anechoic or hypoechoic structure. Every transducer transmits a main beam parallel to the long axis of the transducer. Low amplitude beams also project radially at different angles from this main beam. In a linear-array transducer, these are referred to as side lobes, in a phased-array transducer these are grating lobes. A strong reflector located in a weakly transmitted side lobe may return a signal with enough intensity to be detected. The transducer considers any detected beam as originating from the main axis. Side lobe echoes are not detected when they are superimposed on properly imaged highly echogenic structures. However, side lobe artifacts become obvious when they project over a relatively echo-free region of the heart (**Figure 2.11**). Typically, these appear as “arc-shaped” images originating from a strong reflector (atheroma, catheters) and fading as they move away from that strong reflector.

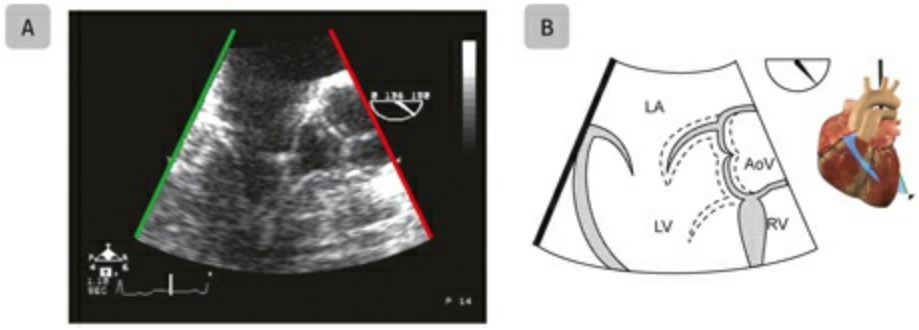

Fig. 2.9 Refraction. (A,B) Mid-esophageal aortic valve (AoV) long-axis view shows distortion and duplication through refraction of part of the ultrasound beam. LA, left atrium; LV, left ventricle; RV, right ventricle. (Reproduced with permission from Denault *et al.* [11]).

A: https://youtu.be/TM5bZ7uqAqU

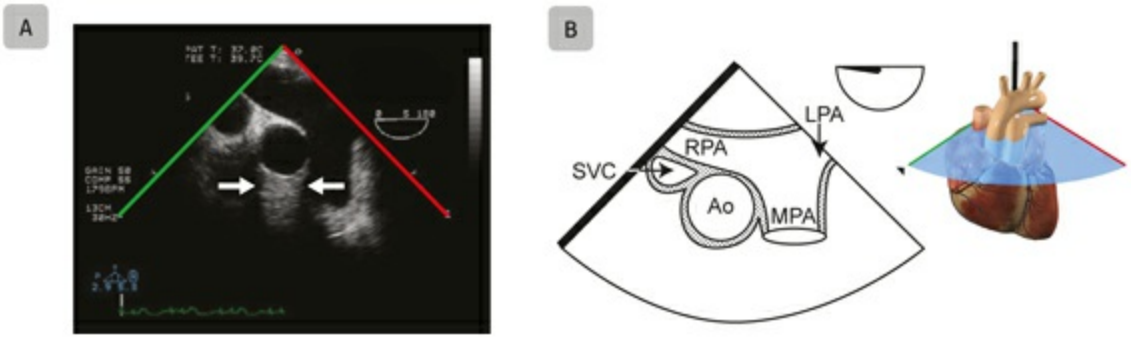

Fig. 2.10 Edge shadowing. (A,B) Mid-esophageal ascending aorta (Ao) short-axis view shows anechoic areas from bending of the US beam at the edge of the ascending aorta. LPA, left pulmonary artery; MPA, main pulmonary artery; RPA, right pulmonary artery; SVC, superior vena cava.(video symbol missing globally).

A: https://youtu.be/TEFer76AjKA

Range Ambiguity

A range ambiguity artifact is a type of propagation path error. In this artifact, echoes from deeper structures appear closer than their actual location

resulting in an unexpected intra-cardiac echo (**Figure 2.12**). The US system assumes that all received echoes are formed from the most recent transmitted pulse. A short US pulse is sent out and returning echoes during the sampling period are assigned a depth. Echoes from deep structures interrogated by the first pulse may arrive at the transducer after the second pulse has been transmitted. These echoes are interpreted as having originated from the most recent transmitted pulse and are incorrectly placed near the transducer in the image.

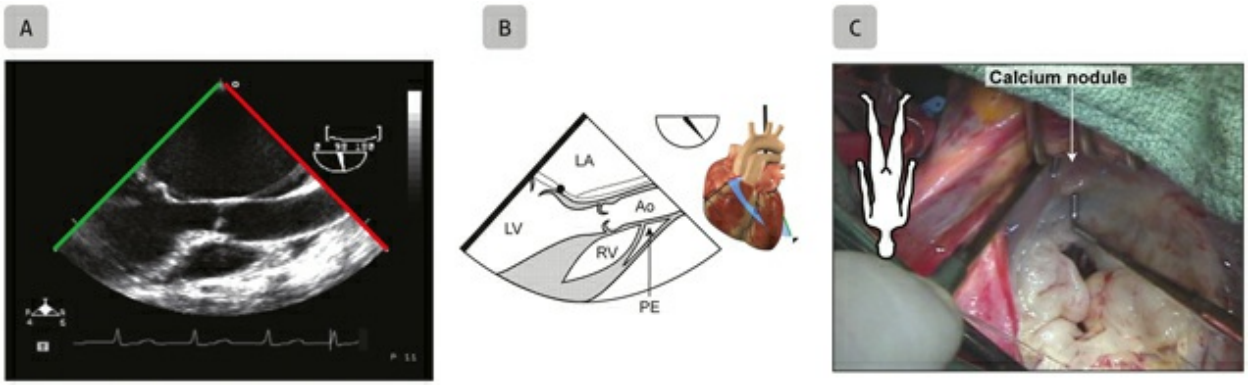

Fig. 2.11 Side lobe artifact. (A,B) Mid-esophageal long-axis view of a 53-year-old female before mitral valve repair shows a side lobe artifact extending along the posterior aspect of the aorta (Ao). (C) Intraoperative view of calcium nodule responsible for the side lobe artifact. LA, left atrium; LV, left ventricle; PE, pericardial effusion; RV, right ventricle. Source: Photo C courtesy of Dr Michel Pellerin. (Reproduced with permission from Denault *et al.* [5]).

A: https://youtu.be/XqsZ2Rl1CUA

C: https://youtu.be/nvpvmJuSrV8

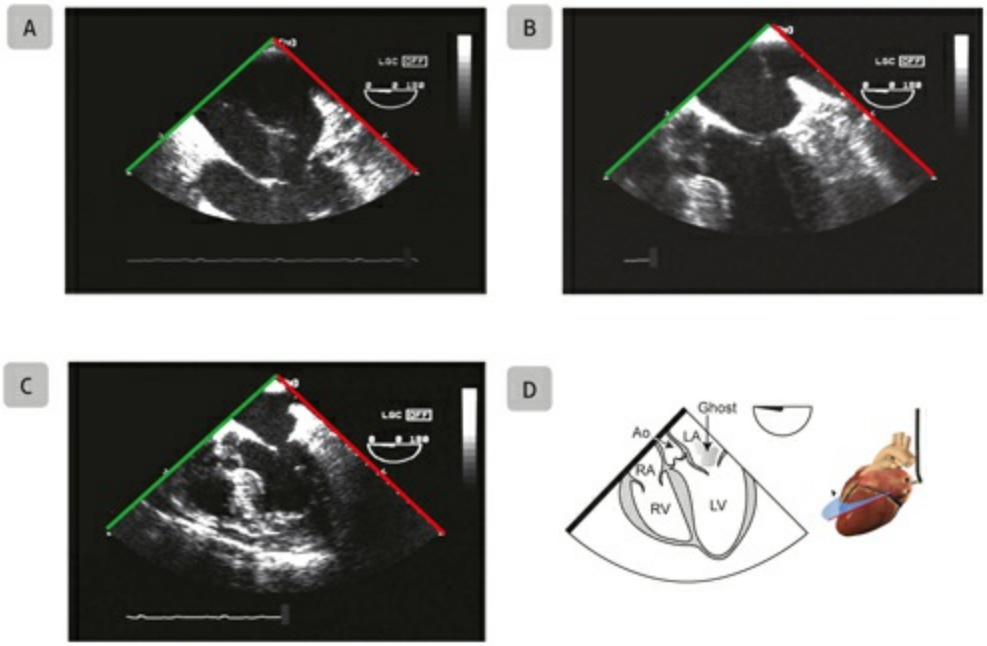

Fig. 2.12 Range ambiguity. (A-D) This mid-esophageal five-chamber view shows an ill-defined artifact located in the left atrium (LA) of a 57-year-old male undergoing coronary revascularization. As the sector depth is increased from (A) 8 cm to (B) 10 cm to (C) 16 cm, there is progressive disappearance of the artifact. Ao, aorta; LGC, lateral gain control; LV, left ventricle; RA, right atrium; RV, right ventricle. (Reproduced with permission from Denault *et al).*

A: https://youtu.be/lPSiR-iCtsM

Attenuation Artifacts

Acoustic Shadowing

Acoustic shadowing is an attenuation-type artifact that results from loss of US beam transmission from high reflection or absorption involving high density structures (calcium, prosthetic valves) (**Figure 2.13**). The distal structures are not seen (anechoic). The shape of the shadow follows the US path, such that a small structure close to the transducer casts a long shadow. While shadowing often confirms the high density of a target, it prevents proper imaging distal to this interposed acoustic obstacle.

Enhancement

An enhancement artifact is a type of attenuation artifact that is the opposite of shadowing. As sound passes through solid tissues, it is gradually attenuated. Fluid-containing structures attenuate sound much less than solid structures, increasing the strength of the transmitted sound pulse. This produces stronger reflections that appear brighter, a hyperechoic distal region under tissue of low attenuation which itself is darker (hypoechoic). An example of this is the transgastric (TG) mid short-axis (SAX) view, where the anterior wall appears brighter than the inferior wall despite its position in the far field of the display (**Figure 2.14**).

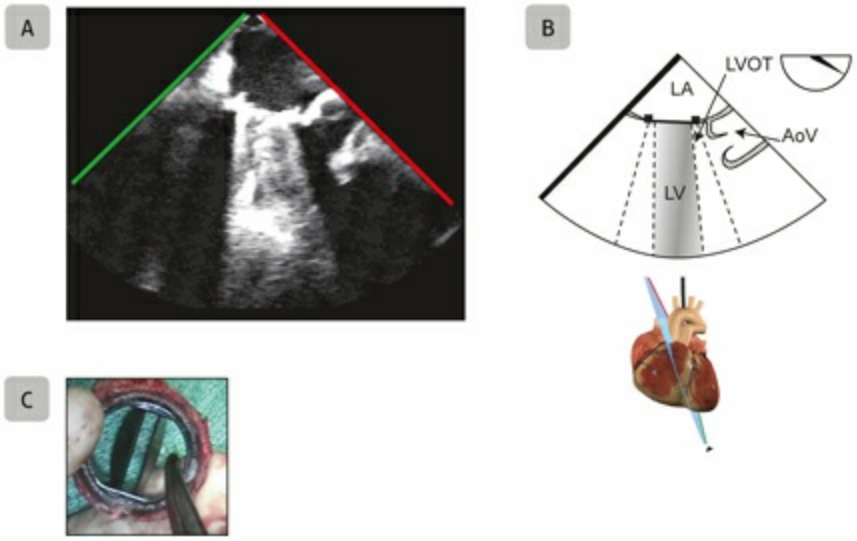

Fig. 2.13 Acoustic shadowing. (A,B) A dense succession of linear echoes extends to the far field from a mechanical bileaflet valve in the mitral position as seen in this mid-esophageal long-axis view. The prosthetic ring acts as an acoustic obstacle and the reverberation artifact is bordered by blind regions (shadowing) preventing visualization of the ventricular cavity and part of the basal ventricular septum. (C) Mechanical bileaflet prosthesis is examined after surgical removal. AoV, aortic valve; LA, left atrium; LV, left ventricle; LVOT, left ventricular outflow tract. Source: Photo C courtesy of Dr Michel Pellerin. (Reproduced with IB1; permission from Denault *et al.* [5]).

C: https://youtu.be/mC0DJrqmzQ0

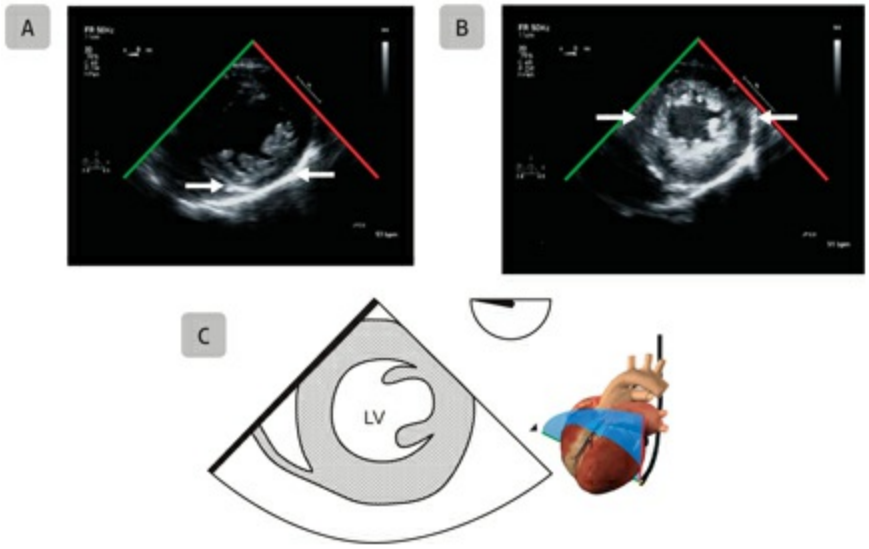

Fig. 2.14 Enhancement and dropout artifacts. Transgastric mid short-axis view shows brightness from enhancement artifact in the far field around the anterior left ventricular (LV) wall as compared with the inferior wall. (A) Note also that the septal lateral walls are poorly visualized due to dropout artifact from the ultrasound beam imaging parallel to the anatomic structure. Transgastric mid short-axis view (B, C) shows brightness from focal enhancement artifact in the middle of the ventricle from repositioning of the focus to this portion of image.

A: https://youtu.be/7QYHIedWK3c

Focal Enhancement

Focal enhancement is a type of attenuation artifact that occurs around the focal zone. There is too much band brightness compared to other depths, which shows as increased side-by-side intensity. This is the same appearance as may occur with incorrect total gain control settings (**Figure 2.14**).

Resolution Artifacts

The US beam has a complex 3D form comprised of x, y, and z axes. Spatial resolution is the ability to distinguish structures in their correct location and relies on the size and shape of the US beam. Resolution is best at the focal zone where the beam is smallest.

Dropout

A dropout artifact is a type of resolution artifact in which structures are not seen. It may result from signal attenuation due to inadequate brightness or power or the use of a high frequency transducer. The artifact may also be the result of the imaging beam positioned parallel to the structure. Optimal 2D imaging occurs when the US beam is perpendicular to the structure. Some structures such as the heart have properties (termed “anistrophy”) that afford a different display depending on the angle of insonation. This is seen in the TG mid-SAX view as the poorly imaged lateral and septal walls that are due to the return of fewer echoes resulting in hypoechoic regions (**Figure 2.14**).

Speckle/Noise

Electrocautery produces a characteristic, fan-shaped interference pattern artifact precluding proper 2D and color Doppler imaging. It is easily identified as this artifact appears only during electrocautery use and disappears when it stops. The screen is then covered by a geometric, regular display bearing no relation or resemblance to any anatomic structure.

Near-Field Clutter

Near-field clutter is a type of resolution artifact that results from high amplitude oscillations of piezoelectric elements. This creates extra echoes in the near field which makes it difficult to differentiate near-field structures. This is commonly seen when using an epi-aortic probe to image the aorta and may be reduced by using a stand-off with a saline-filled glove (**Figure 2.15**). Another example is imaging the descending aorta with TEE. Adjusting gain controls, use of the focal point, and introduction of multifrequency probes, with the highest frequencies dedicated to the near field, improve visualization close to the transducer, and decrease near-field noise.

In summary, careful attention should be provided to both the safe use of TEE and the interpretation of the US images by understanding artifact generation.

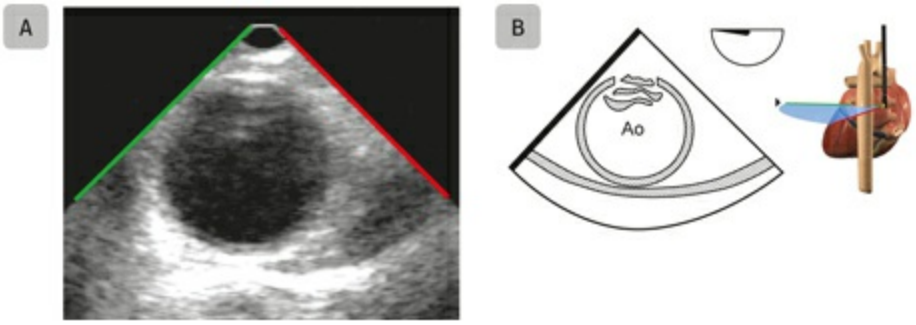

Fig. 2.15 Near-field clutter. (A,B) Linear echoes and poor image definition in the near field prevent optimal visualization of the descending aortic wall close to the transducer in this descending aorta (Ao) short- axis view. (Reproduced with permission from Denault *et al.* [5]).

A: https://youtu.be/usUeAB4qLAw

REFERENCES

1. FosterE., SchillerN.B.. Introduction to transesophageal echocardiography (TEE) with a historical perspective. *Cardiol Clin*2000; *18*: 675–9.
2. CoteG., DenaultA.. Transesophageal echocardiography-related complications. *Can J Anesth*2008; *55*: 622–47.
3. Practice guidelines for perioperative transesophageal echocardiography. An updated report by the American Society of Anesthesiologists and the Society of Cardiovascular Anesthesiologists Task Force on Transesophageal Echocardiography. *Anesthesiology*2010; *112*: 1084–96.
4. HahnR.T., AbrahamT., AdamsM.S., BruceC.J., GlasK.E., LangR.M., *et al*. Guidelines for performing a comprehensive transesophageal echocardiographic examination: recommendations from the American Society of Echocardiography and the Society of Cardiovascular Anesthesiologists. *J Am Soc Echocardiogr*2013; *26*: 921–64.
5. DenaultA.Y., CoutureP., VegasA., BuithieuJ., TardifJ.C.. *Transesophageal Echocardiography Multimedia Manual, Second Edition: A Perioperative Transdisciplinary Approach*. New York: Informa Healthcare, 2011.
6. AeschbacherB.C., PortnerM., FluriM., MeierB., LuscherT.F.. Midazolam premedication improves tolerance of transesophageal echocardiography. *Am J Cardiol*1998; *81*: 1022–6.
7. BadaouiR., ChoufaneS., RiboulotM., BacheletY.. Ossart M. [Esophageal perforation after transesophageal echocardiography]. *Ann Fr Anesth Reanim*1994; *13*: 850–2.
8. TamJ.W., BurwashI.G., AscahK.J., BairdM.G., ChanK.L.. Feasibility and complications of single-plane and biplane versus multiplane transesophageal imaging: a review of 2947 consecutive studies. *Can J Cardiol*1997; *13*: 81–4.
9. KhouryA.F., AfridiI., QuinonesM.A., ZoghbiW.A.. Transesophageal echocardiography in critically ill patients: feasibility, safety, and impact on management. *Am Heart J*1994; *127*: 1363–

71.
10. GunasegaranK., YaoJ., De CastroS., NesserH.J., PandianN.G.. Three-dimensional transesophageal echocardiography (TEE) and other future directions. *Cardiol Clin*2000; *18*: 893–910.
11. NaS., KimC.S., KimJ.Y., ChoJ.S., KimK.J.. Rigid laryngoscope- assisted insertion of transesophageal echocardiography probe reduces oropharyngeal mucosal injury in anesthetized patients. *Anesthesiology*2009; *110*: 38–40.
12. KronzonI., CzinerD.G., KatzE.S., GargiuloA., TunickP.A., FreedbergR.S., *et al*. Buckling of the tip of the transesophageal echocardiography probe: a potentially dangerous technical malfunction. *J Am Soc Echocardiogr*1992; *5*: 176–7.
13. WoodlandR.V., DenneyJ.D., MooreD.W., GreggM.G.. Inability to remove a transesophageal echocardiography probe. *J Cardiothorac Vasc Anesth*1994; *8*: 477–9.
14. MaybauerM.O., AsmussenS., PlattsD.G., FraserJ.F., SanfilippoF., MaybauerD.M.. Transesophageal echocardiography in the management of burn patients. *Burns*2014; *40*: 805–12.
15. HogueC.W.Jr, LappasG.D., CreswellL.L., FergusonT.B.Jr, SampleM., PughD., *et al*. Swallowing dysfunction after cardiac operations. Associated adverse outcomes and risk factors including intraoperative transesophageal echocardiography. *J Thorac Cardiovasc Surg*1995; *110*: 517–22.
16. KohrL.M., DarganM., HagueA., NelsonS.P., DuffyE., BackerC.L., *et al*. The incidence of dysphagia in pediatric patients after open heart procedures with transesophageal echocardiography. *Ann Thorac Surg*2003; *76*: 1450–6.
17. LennonM.J., GibbsN.M., WeightmanW.M., LeberJ., EeH.C., YusoffI.F.. Transesophageal echocardiography-related gastrointestinal complications in cardiac surgical patients. *J Cardiothorac Vasc Anesth*2005; *19*: 141–5.
18. OwallA., StahlL., SettergrenG.. Incidence of sore throat and patient complaints after intraoperative transesophageal echocardiography during cardiac surgery. *J Cardiothorac Vasc Anesth*1992; *6*: 15–16.
19. RousouJ.A., TigheD.A., GarbJ.L., KrasnerH., EngelmanR.M., FlackJ.E.3rd, et al. Risk of dysphagia after transesophageal echocardiography during cardiac operations. *Ann Thorac Surg*2000; *69*: 486–9.
20. ChowM.S., TaylorM.A., HansonC.W.. Splenic laceration associated with transesophageal echocardiography. *J Cardiothorac Vasc Anesth*1998; *12*: 314–16.
21. OlenchockS.A.Jr, LukaszczykJ.J., ReedJ.3rd, ThemanT.E.. Splenic injury after intraoperative transesophageal echocardiography. *Ann Thorac Surg*2001; *72*: 2141–3.
22. BenedictP.E., FoleyK.. Transesophageal echocardiography not without pitfalls. *J Cardiothorac Vasc Anesth*1997; *11*: 123.
23. BrookM., ChardP.S., Brock-UtneJ.G.. Gastric foreign body: a potential risk when using transesophageal echo. *Anesth Analg*1997; *84*: 1389.
24. YasickA., SamraS.K.. An unusual complication of transesophageal echocardiography. *Anesth Analg*1995; *81*: 657–8.
25. HilberathJ.N., OakesD.A., ShernanS.K., BulwerB.E., D'AmbraM.N., EltzschigH.K.. Safety of transesophageal echocardiography. *J Am Soc Echocardiogr*2010; *23*: 220–1.
26. DanielW.G., ErbelR., KasperW., VisserC.A., EngberdingR., SutherlandG.R., *et al*. Safety of transesophageal echocardiography. A multicenter survey of 10,419 examinations. *Circulation*1991; *83*: 817–21.
27. FernandezF.F., RichterA., FreudenbergS., WendlK., ManegoldB.C.. Treatment of endoscopic esophageal perforation. *Surg Endosc*1999; *13*: 962–6.
28. MahmoodF., ChristieA., MatyalR.. Transesophageal echocardiography and noncardiac surgery. *Semin Cardiothorac Vasc Anesth*2008; *12*: 265–89.
29. KallmeyerI.J., CollardC.D., FoxJ.A., BodyS.C., ShernanS.K.. The safety of intraoperative

transesophageal echocardiography: a case series of 7200 cardiac surgical patients. *Anesth Analg*2001; *92*: 1126–30.
30. LawrenceD.R., MoxonR.E., FountainS.W., OhriS.K., TownsendE.R.. Iatrogenic oesophageal perforations: a clinical review. *Ann Roy Coll Surg Engl*1998; *80*: 115–18.
31. KhandheriaB.K., SewardJ.B., TajikA.J.. Transesophageal echocardiography. *Mayo Clinic Proc*1994; *69*: 856–63.
32. Al MoussarihA., DouardH., LafitteS., BroustetJ.P., RoudautR.. Acute myocardial infarction during transesophageal echocardiography. *Echocardiography*1999; *16*: 579–80.
33. Dalby KristensenS., Ramlov IvarsenH., EgebladH.. Rupture of aortic dissection during attempted transesophageal echocardiography. *Echocardiography*1996; *13*: 405–6.
34. GargV., JoshiR.. Compression of undiagnosed aberrant right subclavian artery during transesophageal echocardiography probe insertion. *Ann Cardiac Anesth*2012; *15*: 233–5.
35. NakaoS., EguchiT., IkedaS., NagataA., NishizawaN., ShinguK.. Airway obstruction by a transesophageal echocardiography probe in an adult patient with a dissecting aneurysm of the ascending aorta and arch. *J Cardiothorac Vasc Anesth*2000; *14*: 186–7.
36. DollN., BorgerM.A., FabriciusA., StephanS., GummertJ., MohrF.W., *et al*. Esophageal perforation during left atrial radiofrequency ablation: Is the risk too high?*J Thorac Cardiovasc Surg*2003; *125*: 834–42.
37. MohrF.W., FabriciusA.M., FalkV., AutschbachR., DollN., Von OppellU., *et al*. Curative treatment of atrial fibrillation with intraoperative radiofrequency ablation: short-term and midterm results. *J Thorac Cardiovasc Surg*2002; *123*: 919–27.
38. SonmezB., DemirsoyE., YaganN., UnalM., ArbatliH., SenerD., *et al*. A fatal complication due to radiofrequency ablation for atrial fibrillation: atrio-esophageal fistula. *Ann Thorac Surg*2003; *76*: 281–3.
39. KanagalaP., BradleyC., HoffmanP., SteedsR.P.. Guidelines for transoesophageal echocardiographic probe cleaning and disinfection from the British Society of Echocardiography. *Eur J Echocardiogr*2011; *12*: i17–i23.
40. RaffertyT., LaMantiaK.R., DavisE., PhillipsD., HarrisS., CarterJ., *et al*. Quality assurance for intraoperative transesophageal echocardiography monitoring: a report of 846 procedures. *Anesth Analg*1993; *76*: 228–32.
41. VenticinqueS.G., KashyapV.S., O'ConnellR.J.. Chemical burn injury secondary to intraoperative transesophageal echocardiography. *Anesth Analg*2003; *97*: 1260–1.
42. DunkerD.H., StoddardM.F., PrinceC.R., WilliamsT.E.. Potential for contamination of transesophageal echocardiographic scopes by radionuclides from patients undergoing nuclear imaging studies. *Am Heart J*1995; *130*: 397–8.
43. MullerB.A., SteelmanV.J.. Case report of latex aerosolization from a transesophageal echocardiogram machine. *Allergy Asthma Proc*2004; *25*: 191–4.
44. LevyP.Y., TeysseireN., EtienneJ., RaoultD.. A nosocomial outbreak of *Legionella pneumophila* caused by contaminated transesophageal echocardiography probes. *Infect Contr Hosp Epidemiol*2003; *24*: 619–622.
45. NishimuraR.A., CarabelloB.A., FaxonD.P., FreedM.D., LytleB.W., O'GaraP.T., *et al*. ACC/AHA 2008 Guideline update on valvular heart disease: focused update on infective endocarditis: a report of the American College of Cardiology/American Heart Association Task Force on Practice Guidelines endorsed by the Society of Cardiovascular Anesthesiologists, Society for Cardiovascular Angiography and Interventions, and Society of Thoracic Surgeons. *J Am Coll Cardiol*2008; *52*: 676–85.
46. FaletraF.F., RamamurthiA., DequartiM.C., LeoL.A., MoccettiT., PandianN.. Artifacts in three-dimensional transesophageal echocardiography. *J Am Soc Echocardiogr*2014; *27*: 453–62.

47. KremkauF.W., TaylorK.J.. Artifacts in ultrasound imaging. *J Ultrasound Med*1986; *5*: 227–37.
48. VignonP., SpencerK.T., RambaudG., PreuxP.M., KraussD., BalasiaB., *et al*. Differential transesophageal echocardiographic diagnosis between linear artifacts and intraluminal flap of aortic dissection or disruption. *Chest*2001; *119*: 1778–90.

Chapter 3

Normal Cardiac Anatomy and TEE Imaging Planes

Scott Millington and Annette Vegas

INTRODUCTION

In order to improve efficiency, the sonographer should determine the approximate sequence of ultrasound images that will be acquired during the transesophageal echocardiography (TEE) study prior to inserting the probe. In effect, this decision can be simplified by establishing whether this will be a comprehensive or goal-directed study. This chapter will review the recommended TEE views to complete a basic TEE study, as well as describe options for TEE probe manipulation.

IMAGE SEQUENCE

During a comprehensive study, the entire recommended set of ultrasound images is acquired in a convenient anatomic sequence that minimizes back-and-forth probe movements. This is analogous to the approach used for transthoracic echocardiography (TTE) imaging in stable patients, where image acquisition typically follows a standard sequence for all patients regardless of underlying pathology. A goal-directed study, on the other hand, requires that the image sequence be tailored to answer a specific question or set of questions relevant to the care of the individual patient undergoing the examination. A goal-directed TEE study for a severely hypotensive patient would differ from one performed for a patient who was very hypoxemic, for example.

In the critical care environment, a goal-directed approach to TEE is generally recommended as this more expeditiously yields the information required to answer the question at hand. In most cases, this will also shorten the overall length of the study, an important factor if the patient is unstable or poorly tolerant of sedative medications. A comprehensive approach may be appropriate in a very stable patient, particularly when the study is being compared to a previous study (or will be compared to a future study), or when a trainee is performing the study under supervision. Sometimes, a hybrid approach is best: a goal-directed study can be initiated, and once the clinical question has been answered the remaining views can be obtained to finish the comprehensive examination provided the patient is stable enough to proceed.

NUMBER OF VIEWS

The American Society of Echocardiography (ASE) and the Society of Cardiovascular Anesthesiologists (SCA) endorse two main protocols when performing a comprehensive examination. The basic protocol recommends an 11-view sequence (**Figure 3.1**), [1] while the advanced protocol involves acquisition of a 28-view sequence. [2] In the critical care setting and emergency settings, the 11-view study is sufficient to provide the required information in the majority of patients, and is thus recommended (**Table 3.1**). In unusual circumstances where additional specific information is required (for example, related to pulmonary vein anatomy), it would be reasonable for the TEE provider with a basic skill set to seek help from a more experienced colleague who regularly performs 28-view studies.

TEE PROBE MOVEMENTS

Once the TEE probe has been inserted into the esophagus, it can be manipulated to acquire images as follows (**Figure 3.2**):

- Advancement/withdrawal involves pushing the probe in or pulling it out to view structures that are more caudal or cranial, respectively.
- Rotating or turning is moving the entire probe shaft clockwise to view rightward structures and counterclockwise to view leftward

structures.

- Anteflexion and retroflexion involves turning the larger wheel on the probe handle, moving the probe tip forwards or backwards to view structures at the heart base or towards the apex, respectively.
- Leftward and rightward flexion involves turning the smaller wheel on the probe handle to move the probe tip to the left or right.
- Image plane rotation (**Figure 3.3**) changes the transducer angle to rotate the imaging plane from 0° to 180°, where 0° represents the transverse plane and 90° the longitudinal plane.

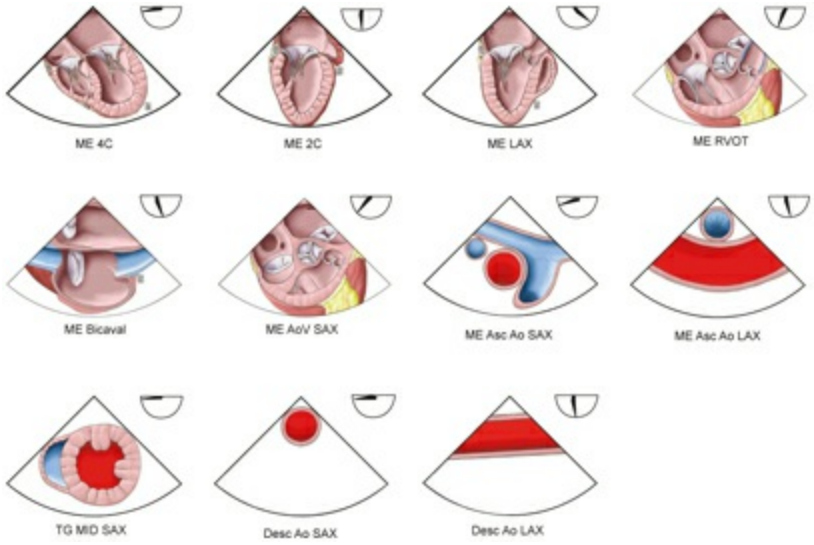

Fig. 3.1 Transesophageal echocardiography (TEE) views. Diagrams of the 11 basic TEE views are shown. Ao, aorta; AoV, aortic valve; Asc, ascending; Desc, descending; LAX, long-axis; ME, midesophageal; RVOT, right ventricular outflow tract; SAX, short-axis; TG, transgastric; 2C, two-chamber; 4C, four- chamber. (Adapted with permission from Denault *et al.* [3]).

Table 3.1 Outline of the 11-View TEE Study.

	Angle	Structures	Diagnosis
ME 4C	0°	RA, RV, LA, LV, TV, MV	Chamber dilatation, systolic dysfunction, pericardial effusion
ME 2C	90°	LA, LV, LAA	LV function, LAA thrombus
ME LAX	120°	LA, LV, AoV, Ao	LV function, AoV disease, LVOT obstruction
ME RVOT	60°	LA, RA, AoV, TV, PV, PA	TV, RVOT obstruction
ME Bicaval	90°	LA, RA, IVC, SVC	PFO
ME AoV SAX	30°	LA, RA, AoV, TV, PV, PA	AoV pathology
ME Asc Ao LAX	100°	RPA, Ao	Ao pathology
ME Asc Ao SAX	10°	PA, Ao	Pulmonary embolism
TG MID SAX	0°	LV, RV	LV function
Desc Ao SAX	0°	Ao	Dissection, aneurysm
Desc Ao LAX	90°	Ao	Dissection, aneurysm

2C, two-chamber; 4C, four-chamber; Ao, aorta; AoV, aortic valve; Asc, ascending; Desc, descending; IVC, inferior vena cava; LA, left atrium; LAA; left atrial appendage; LAX, long-axis; LV, left ventricle; LVOT, left ventricular outflow tract; ME, mid-esophageal; MV, mitral valve; PA, pulmonary artery; PFO, patent foramen ovale; PV, pulmonary vein; RA, right atrium; RPA, right pulmonary artery; RV, right ventricle; RVOT, right ventricular outflow tract; SAX, short-axis; SVC, superior vena cava; TG, transgastric; TV, tricuspid valve.

PROBE DEPTH

Selection of an appropriate probe depth is essential both to orient the sonographer and to enable the acquisition of the required views. Three main depths are measured from the incisors to the tip of the probe:

- Upper-esophageal (UE) Level ~20–30 cm probe depth
- Mid-esophageal (ME) Level ~30–40 cm probe depth
- Transgastric (TG) Level ~40–45 cm probe depth.

Most TEE studies begin at the ME level where the majority of views are obtained. The probe is advanced to obtain at least one image at the TG level, and then withdrawn to the UE level to image the aorta at the end of the study. This approach has the advantage of minimizing movement as the probe is advanced and withdrawn to change levels, avoiding irritation of the esophagus and potential patient discomfort. In urgent situations starting at the

TG level is sometimes preferred, as discussed below.

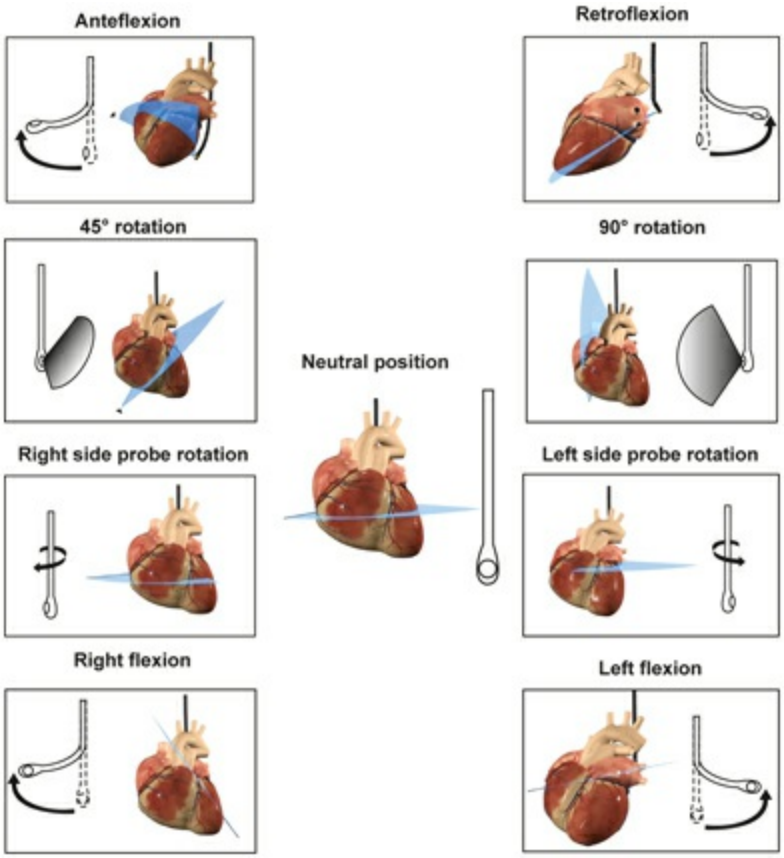

Fig. 3.2 Transesophageal echocardiography (TEE) probe manipulation. Graphic display of TEE probe manipulation and plane orientation is shown. (Adapted with permission from Denault *et al.* [3] *;* video courtesy of Philips).

https://youtu.be/LPhddlvP0VA

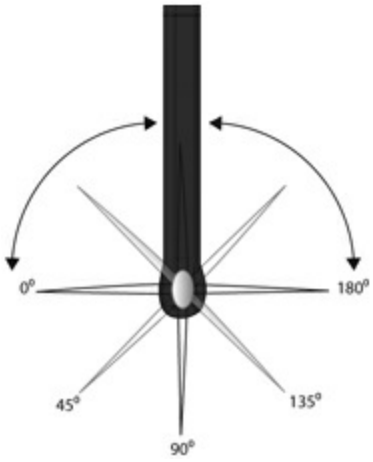

Fig. 3.3 Transesophageal echocardiography (TEE) imaging planes. Diagram of TEE probe image plane rotation from 0° to 180° and 180° to 0°, where 0° represents a transverse plane, perpendicular to the length of the probe.

RECOMMENDED VIEWS FOR A COMPREHENSIVE BASIC EXAMINATION

Mid-esophageal Level

There are eight distinct views to be captured at the ME level: [1]

1. ME Four-Chamber (ME 4C) View. This is often the initial view obtained as the probe is inserted into the patient's esophagus. It functions as a "home base" for novices who can reacquire this familiar view should they become disorientated during the study. The required steps to achieve most other views begin from this view, further emphasizing its importance.

   To acquire the ME 4C view, the probe is gently advanced from the oropharynx in a neutral position with the transducer angle at 0° to the ME level behind the left atrium (LA). As long as the ultrasound beam is pointed anteriorly, the heart appears at approximately 30 cm probe depth for average-sized patients. Several small probe adjustments are usually required to optimize the image (**Figure 3.4**). The probe may be rotated left or right as needed to center the heart in the display. Slight retroflexion may be required to align the imaging plane so that both atria and both ventricles are visible.

Finally, if the left ventricular outflow tract (LVOT) is visible, slightly advancing the probe or rotating the transducer angle to 10° or 20° eliminates this structure from view. Display depth should be adjusted such that the apex of the left ventricle (LV) is seen in the lower portion of the screen, without wasted space below. However, sufficient depth should be obtained in order to exclude conditions such as a pericardial effusion.

Structures identified in the ME 4C view include the LA, right atrium (RA), LV, right ventricle (RV), inter-atrial and inter-ventricular septa, mitral valve (MV), and tricuspid valve (TV); a considerable amount of clinical information is available. Importantly, the size of the four cardiac chambers can be evaluated and directly compared. An assessment of LV systolic function can be made, although only the lateral and septal LV walls are visible. Similarly, while an estimate of RV systolic function can be arrived at, it is important to note that the entire RV free wall cannot be seen. The ME 4C view is an ideal starting point for evaluation of both mitral and tricuspid valves using two-dimensional (2D) imaging, and has good alignment for spectral and color Doppler interrogation. Finally, the presence of a pericardial effusion can be detected when present (see **Figure 5.18**).

2. ME Two-Chamber (ME 2C) View. From the ME 4C view, the transducer angle is rotated to approximately 90°, at which point the right-sided chambers disappear completely leaving only the LA, LV, and MV (**Figure 3.5**). The useful clinical information obtained from this view mainly involves assessment of LV function; here the anterior and inferior walls are easily visualized, with a good opportunity to estimate global LV function.

   The LA is well seen and assessment of the left atrial appendage (LAA) can be attempted when clinically indicated. The LAA can usually be found with the transducer angle at 90°–110°, with clockwise rotation of the probe and anteflexion of the probe tip (**Figure 3.6**). The anatomy of the LAA is complex, and a thorough evaluation requires viewing it from multiple imaging planes. In the ME 2C view, the structure and function of the MV can be assessed

by both 2D and Doppler imaging. A small pericardial effusion under the LAA can be detected, when present.

3. ME Long-Axis (ME LAX) View. Rotating the transducer angle a further 30°–50° from the ME 2C view will bring the LVOT, aortic valve (AoV), and proximal ascending aorta into view at the 2 o'clock position (**Figure 3.7**). Again, this view is most useful for LV assessment; here the anteroseptal and inferolateral walls can be seen. In this view, the structure and function of the AoV can be examined using 2D imaging and color Doppler. However, the AoV/LVOT axis is often horizontal and thus nearly perpendicular to the plane of Doppler interrogation, making spectral Doppler evaluation suboptimal in this view. Additional TG views or a TTE examination are required to obtain proper spectral Doppler alignment. The presence of turbulent systolic flow in the region of the AoV with color Doppler suggests elevated flow velocities and aortic stenosis should be suspected. This can be confirmed by 2D assessment of the valve combined with continuous wave (CW) spectral Doppler measurements of transvalvular velocity. Color Doppler can be used to screen for diastolic regurgitant flow, identifying the presence of aortic regurgitation (see **Figure 7.13**). Though large regurgitant jets are suggestive of severe regurgitation, accurate quantification depends on complex 2D and Doppler assessment from multiple angles of interrogation.

   The ME LAX view is ideal for observing the path of the anterior leaflet of the MV. Of particular interest to point- of-care providers is identifying dynamic obstruction of the LVOT by systolic anterior motion (SAM) of the anterior leaflet; color Doppler can show turbulent flow in the LVOT and associated mitral regurgitation (**Figure 3.8**).
4. ME Ascending Aorta Long-Axis (ME Asc Ao LAX) View. From the ME LAX view the probe is slowly withdrawn until the ascending aorta comes into view in long axis, oriented horizontally on the display (**Figure 3.9**). Frequently, the transducer angle must be reduced towards 90° to achieve an optimal LAX view. The right pulmonary artery (PA) will be visible in SAX at the top of the screen. The key clinical application of this view in urgent situations

is to screen for a type A aortic dissection or other proximal acute aortic syndrome. It should be remembered that there is a blind spot created by the air-filled trachea, which may cause a localized aortic dissection to be overlooked.

5. ME Ascending Aorta Short-Axis (ME Asc Ao SAX) View. A SAX view of the ascending aorta is attained by reducing the transducer angle by exactly 90°, usually to an angle of 0°–20°, from the point where an optimal LAX view was obtained. Centering the PA at the top of the display in the ME Asc Ao LAX view before changing the transducer angle will facilitate the right PA appearing in LAX in the center of the display (**Figure 3.10**).

   If a proximal aortic dissection is suspected, the dissection flap is sometimes better appreciated in SAX where it is frequently easier to distinguish a true flap from an artifact (see **Figure 12.23**). This view is often used to look for a very proximal pulmonary embolism (PE) located in the main PA (see **Figure 12.6**), the saddle position, or the very proximal right or left PA (see **Figure 10.14**). As such, TEE is much more specific than sensitive; whereas visualising an embolus is very rare but obviously very helpful, the absence of a visualized embolus does not exclude a PE. Furthermore, hyperechoic structures in the PA are often artifactual, and great care must be exercised to confirm that a suspected PE is in fact real before establishing this diagnosis and exposing the patient to the risks of anticoagulation, thrombolysis, or embolectomy.
6. ME Aortic Valve Short-Axis (ME AoV SAX) View. To move from a SAX view of the ascending aorta to a SAX view of the AoV usually requires only that the probe be advanced a few centimeters. Once the AoV is seen, it is necessary to slightly adjust the image plane (usually to between 20° and 50°) to acquire an optimal SAX view where all valvular cusps appear symmetric (**Figure 3.11**).

   This view can assess the AoV in detail, although this is not necessary for most point-of-care examinations. In aortic stenosis, a heavily calcified valve will be seen, with greatly diminished cusp motion and reduced effective orifice area (see **Figure 7.4**). A bicuspid (or unicuspid) valve may, on rare occasions, be an

incidental finding.

7. ME Right Ventricular Inflow-Outflow (ME RV In-Out) View. The RV inflow-outflow view (alternately called the ME right ventricular outflow tract (RVOT) view in some publications) lies very close to the previously described ME AoV SAX view. The transducer angle is rotated to approximately 60°, and it may be necessary to advance the probe slightly until both the TV and pulmonic valve (PV) appear (**Figure 3.12**).

   This view provides valuable information about the RV, as the outflow tract is usually clearly seen in the lower portion of the display. When a pericardial effusion or any mechanical or dynamic obstruction of the RVOT is identified, this view can assess its impact on the RV in terms of impediment of flow from collapse (see **Figure 9.14**). The TV can be assessed for the presence of regurgitation, and the systolic PA pressure can be estimated in cases where the regurgitant jet is well aligned. In very rare clinical situations where PV pathology is suspected, an assessment of this structure is possible (see **Figure 7.33**).
8. ME Bicaval View. With clockwise rotation of the probe shaft and the transducer angle at approximately 90°, the ME bicaval view can be found. This view shows the LA and the RA with both the inferior vena cava (IVC) and superior vena cava (SVC) draining into the RA (**Figure 3.13**).

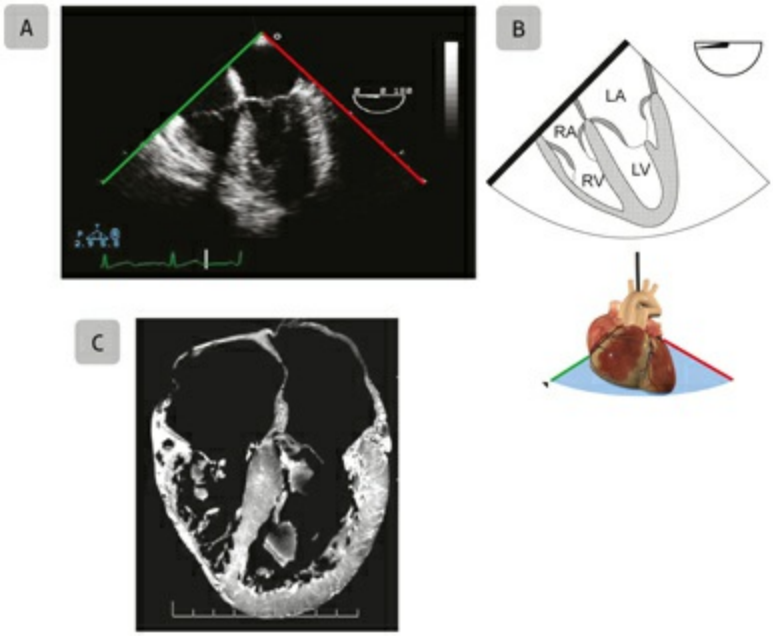

Fig. 3.4 Mid-esophageal four-chamber view. (A,B) This transesophageal echocardiography view at 0° shows all four cardiac chambers compared with (C) a magnetic resonance image. LA, left atrium; LV, left ventricle; RA, right atrium; RV, right ventricle. (Reproduced with permission from Denault *et al.* [3]).

A: https://youtu.be/tr2cPYNJ9uY

C: https://youtu.be/u6Gbqjn5VhM

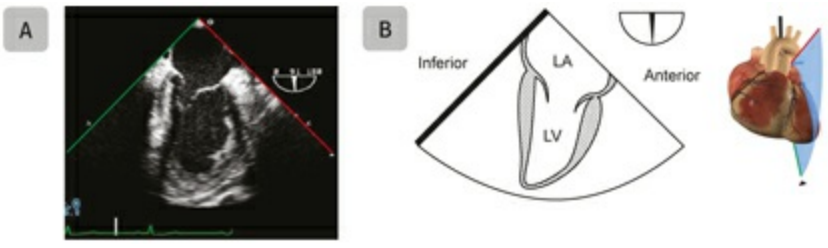

Fig. 3.5 Mid-esophageal two-chamber view. (A,B) This transesophageal echocardiography view obtained at 90° shows only two chambers, the left atrium (LA) and left ventricle (LV). The probe should be manipulated to elongate the LV cavity and avoid foreshortening the LV apex. (Reproduced

with permission from Denault *et al.* [3].

A: https://youtu.be/Fij2TPTqHTo

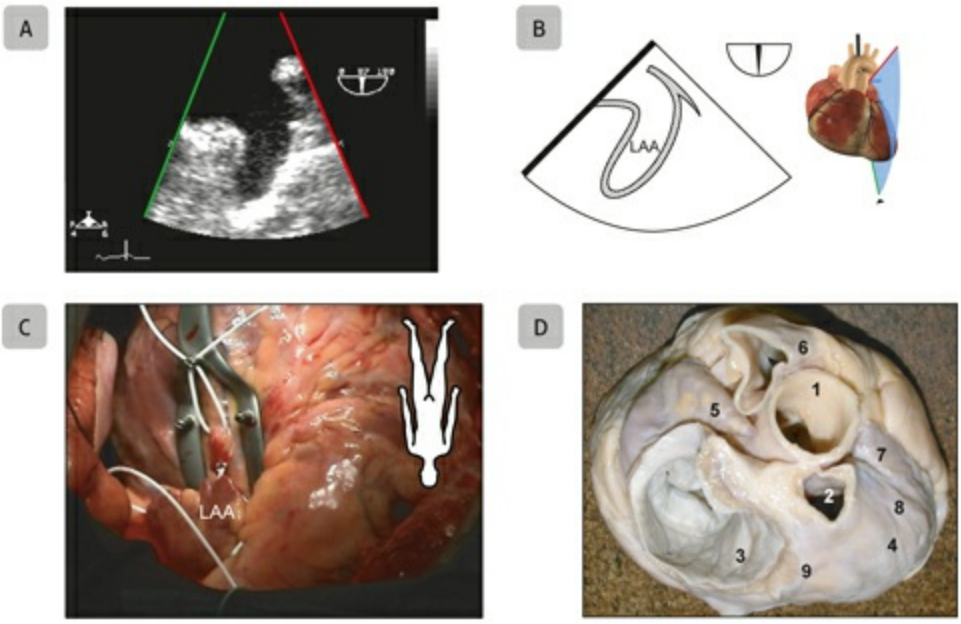

Fig. 3.6 Mid-esophageal (ME) left atrial appendage (LAA) view. (A,B) ME view of the LAA as obtained at 90° is shown. (C) Intraoperative view of the LAA during off-pump bypass surgery. (D) The LAA is anterolateral to the left atrium and close to the left upper pulmonary vein as shown in this anatomic specimen. Source: Panel (C) courtesy of Dr Raymond Cartier. (Reproduced with permission from Denault *et al.* [3]).

A: https://youtu.be/yjFXg6OwgZI

C: https://youtu.be/2iQDIOPZrRk

E: https://youtu.be/-nojWl9Pxgw

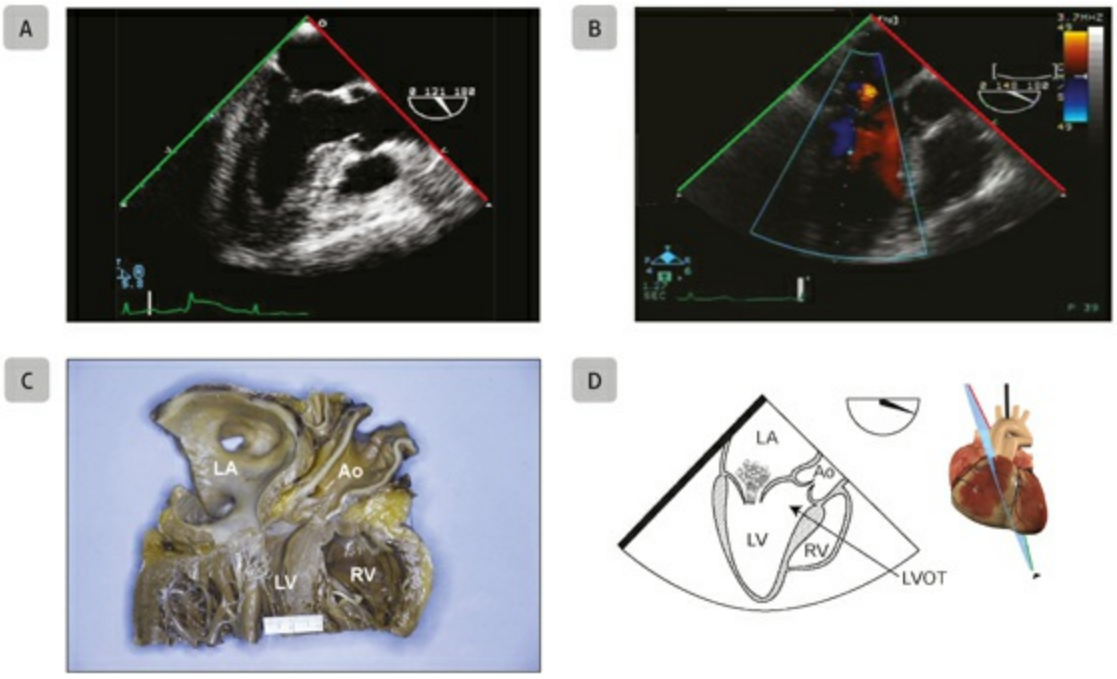

Fig. 3.7 Mid-esophageal long-axis view. Views obtained at 121° and 146° of the LV (A) without and (B, D) with color Doppler in the LVOT compared with (C) an anatomic specimen. Ao, aorta; LA, left atrium; LV, left ventricle; LVOT, left ventricular outflow tract; RV, right ventricle. (Reproduced with permission from Denault *et al.* [3]).

A: https://youtu.be/p2EMyfog86E

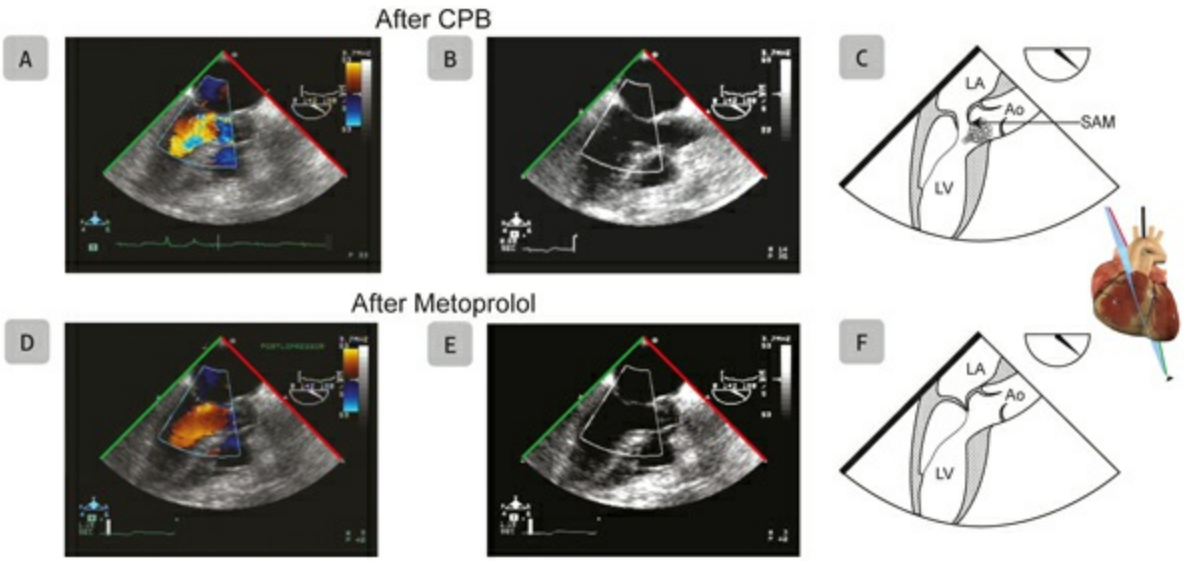

Fig. 3.8 Left ventricular outflow tract (LVOT) obstruction. A 63-year-old female becomes hemodynamically unstable following separation from cardiopulmonary bypass (CPB) after coronary revascularization. (A—C) Mid-esophageal long axis views with and without color Doppler show systolic anterior motion (SAM) of the anterior mitral valve leaflet with flow acceleration in the left ventricular outflow tract (LVOT). (D-F) Following administration of an intravenous bolus of metoprolol, the SAM improves and the patient is clinically more stable. Ao, aorta; LA, left atrium; LV, left ventricle. (Reproduced with permission from Denault *et al.* [3]).

A&D: https://youtu.be/IabeMQX3XSk

B&E: https://youtu.be/AzQjPNumIpc

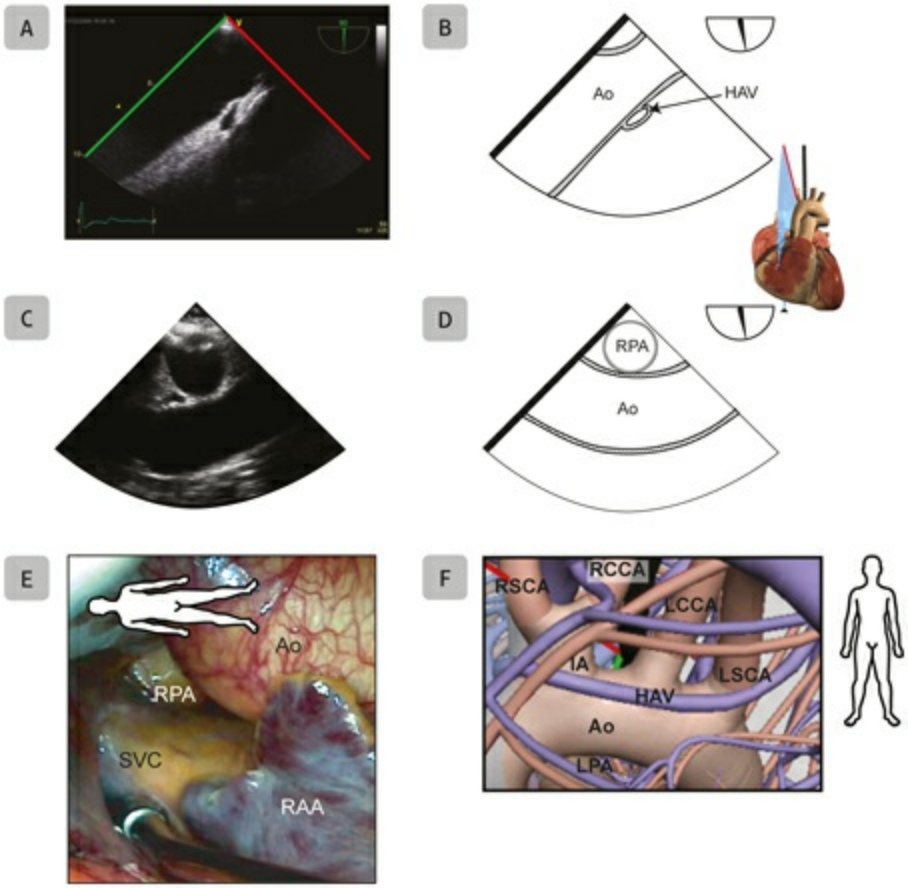

Fig. 3.9 Ascending aorta (Ao) views. (A,B) An upper esophageal view of the proximal ascending Ao and hemiazygos vein (HAV) at 90° is shown. (C,D) Mid-esophageal ascending Ao long-axis view at 100° compared with an intraoperative view of the Ao. Diagram of the relationship of the HAV to the Ao is shown. IA, innominate artery, LCCA, left common carotid artery; LPA, left pulmonary artery; LSCA, left subclavian artery; RAA, right atrial appendage; RCCA, right common carotid artery; RPA, right pulmonary artery; RSCA, right subclavian artery; SVC, superior vena cava. Source: Photo (E) courtesy of Dr Michel Pellerin (Reproduced with permission from Denault *et al.* [3]).

C: https://youtu.be/iEzzV9GD2As

A: https://youtu.be/UDgweQkQmok

E: https://youtu.be/DTgWKhmspzQ

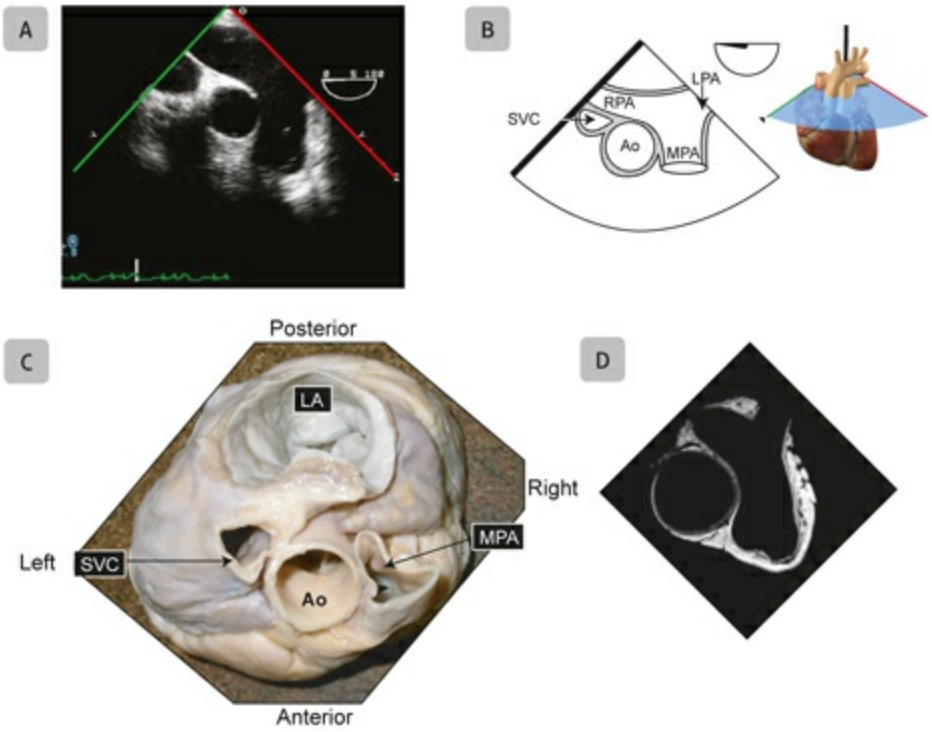

Fig. 3.10 Mid-esophageal (ME) ascending aorta short-axis view. (A,B) ME view at 0° of the great vessels compared with (C) anatomic correlation and (D) magnetic resonance imaging. LA, left atrium; LPA, left pulmonary artery; MPA, main pulmonary artery; RPA, right pulmonary artery; SVC, superior vena cava. (Reproduced with permission from Denault *et al.* [3]).

A: https://youtu.be/weQGfRoOMzo

D: https://youtu.be/RC0RBYIePxU

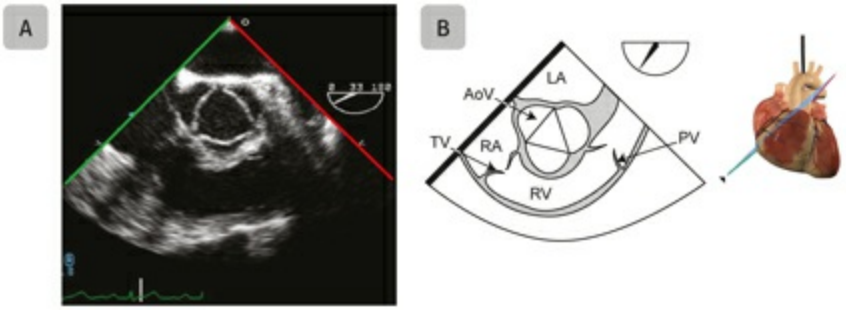

Fig. 3.11 Mid-esophageal aortic valve (AoV) short-axis view. (A,B) This view at 33° of the aortic valve shows all three cusps open during systole. LA, left atrium; PV, pulmonic valve; RA, right atrium; RV, right ventricle; TV, tricuspid valve. (Reproduced with permission from Denault *et al.* [3]).

A: https://youtu.be/EOShcjvD2ME

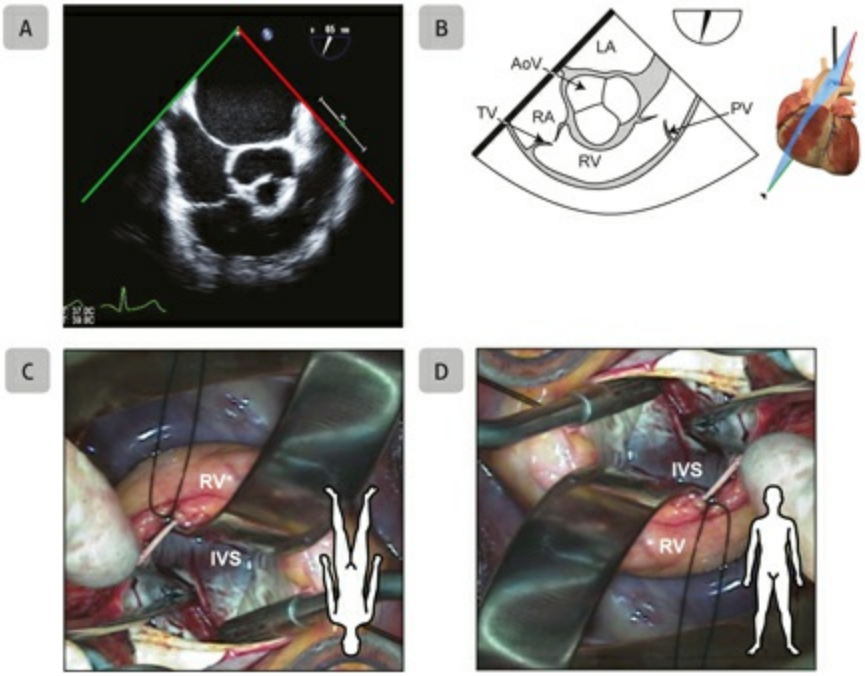

Fig. 3.12 Mid-esophageal right ventricular inflow/outflow view. (A,B) This view obtained at 65° shows the aortic valve (AoV) in the center, the tricuspid valve (TV) on the left, and the pulmonic valve (PV) on the right. (C) The surgical view is repositioned to correlate better with (D) the echocardiographic window. IVS, interventricular septum; LA, left atrium; RA, right atrium; RV, right ventricle. Source: Photo (C) courtesy of Dr Nancy Poirier. (Reproduced with permission from Denault *et al.* [3]).

A: https://youtu.be/M_NWbvD2oZM

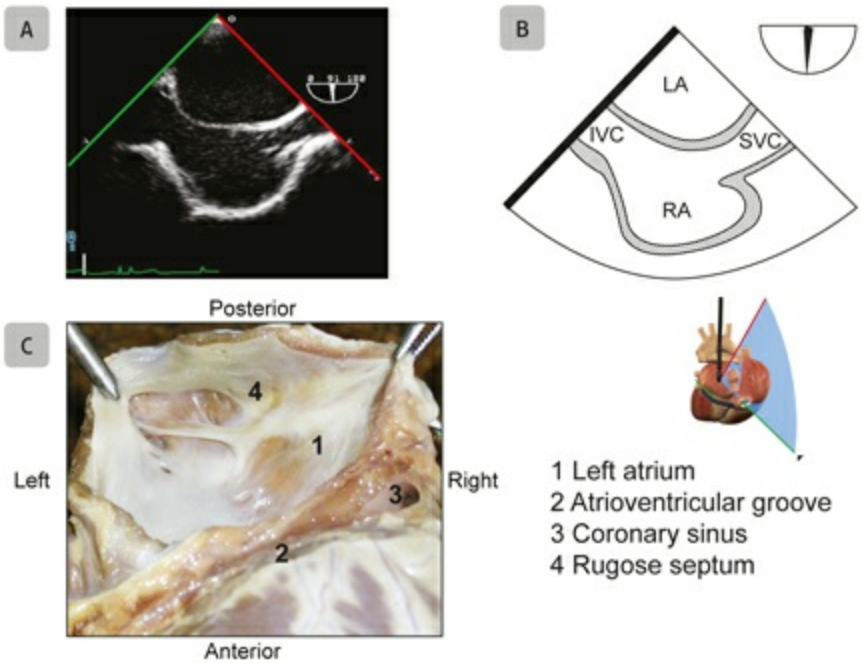

Fig. 3.13 Mid-esophageal bicaval view. (A,B) This view obtained at 91° shows the inferior vena cava (IVC) and superior vena cava (SVC) entering the right atrium (RA). (C) Anatomic features of the interatrial septum are shown for comparison as viewed from the left atrium (LA). (Reproduced with permission from Denault *et al.* [3]*).*

A: https://youtu.be/4QTcklfsJ4M

This view is primarily useful in urgent cases to measure the diameter and degree of respiratory variation of both vena cava to help determine intravascular volume status and volume responsiveness (see **Figure 15.14**). It may be used in the context of procedural guidance. When placing a central venous catheter, detecting the guidewire in the RA confirms venous position prior to vessel dilatation (see **Figure 18.12**). Transvenous pacemakers can likewise be guided into the RA and away from the IVC.

Transgastric Level

There are many potential views that can be obtained from the TG position, with nine distinct views listed in the ASE comprehensive guidelines. [2] From the perspective of a basic TEE examination performed on an acutely ill patient, most of the information required can be achieved by adding a single TG view to the ME views described earlier in this chapter:

Transgastric Mid-Papillary Short-Axis (TG mid SAX) View. This view is usually straightforward to obtain. From the ME 4C view, the unflexed probe is advanced with the transducer angle at 0° into the stomach. As the gastro-esophageal junction is crossed, sufficient anteflexion is added to keep the transducer in contact with the gastric mucosa to prevent air from degrading the image quality. Subtle transducer tip movements may be required to achieve an optimal SAX view at the mid-papillary level where the LV appears round and the papillary muscles are symmetric (**Figure 3.14**).

The TG mid SAX view is primarily useful for assessing LV function. At the ME level, there is no single view where all LV walls can be seen together; instead they must be viewed in pairs from three different views as described earlier. The TG SAX view offers a good representation of global LV function albeit only at the mid-papillary muscle level as the base and apex are not seen in this view. It is also a helpful view to look for regional wall motion abnormalities by direct comparison of the different LV wall segments (see **Figure 6.3**).

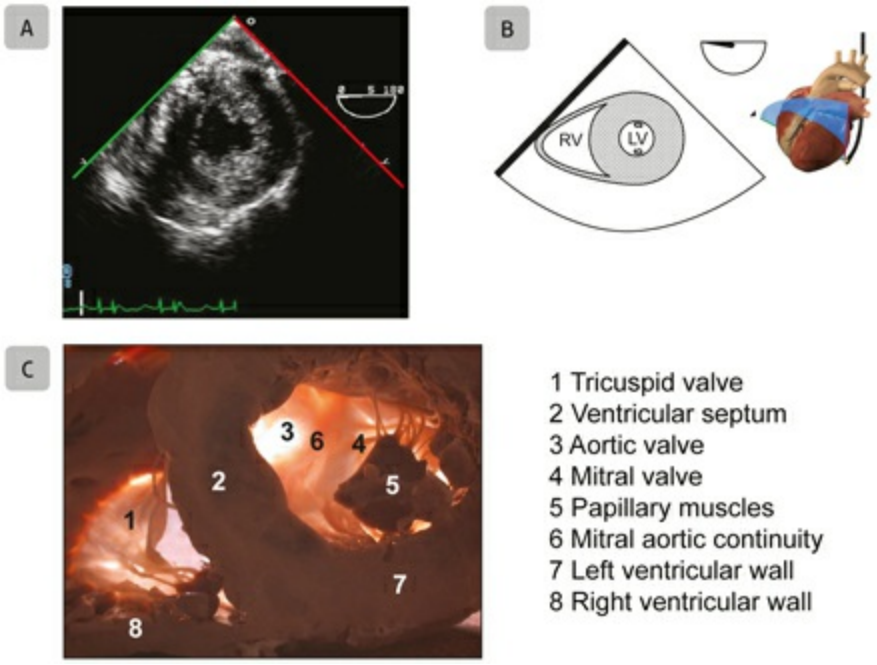

Fig. 3.14 Transgastric mid short- axis view. (A,B) This view obtained at 0° of the left ventricle (LV) at the mid-papillary level with anatomic correlation (C) is shown. RV, right ventricle. (Reproduced with permission from Denault *et al.* [3]).

A: https://youtu.be/V8-y4BgvnKQ

Although the RV free wall may not be seen clearly, important information related to RV size and function can be obtained by examining the interventricular septum (IVS), which is visible in this view. A pressure overloaded RV will cause the IVS to be displaced to the left, resulting in a "D"-shaped LV cavity (see **Figure 5.12**). This can be of great value when acute cor pulmonale is suspected as a cause of shock (perhaps due to a PE), or where the effect of positive pressure ventilation on the RV may be deleterious.

Upper Esophageal Level

Imaging of the descending aorta is less useful in the care of acutely ill patients. However, in some cases where a more distal acute aortic syndrome is suspected or where the source of a thromboembolism is sought, it can be

helpful.

1. Descending Aortic SAX View. To find this view, begin at the ME 4C view and turn the entire probe until the ultrasound transducer is pointed towards the patient's back, and the aorta, in SAX, comes into view at the top of the screen. At this point, the display depth should be decreased until the aorta takes up the majority of the screen. It can be interrogated along its length by advancing the probe towards the stomach and withdrawing it to the upper esophagus (**Figure 3.15 A**).
2. Descending Aortic LAX View. From the position described above, simply increasing the transducer angle to 90° changes the SAX view of the aorta into a LAX view (**Figure 3.15 C**). The same information is available, specifically with respect to aortic diameter, presence of atherosclerotic disease, and presence of an acute aortic syndrome, such as a more distal aortic dissection (see **Figure 12.10**).

RECOMMENDED VIEWS FOR A GOAL-DIRECTED EXAMINATION

As described above, a goal-directed exam is usually more appropriate when imaging patients in urgent situations whether in the intensive care unit, emergency department, or operating room. Pathological states that can cause severe acute illness and can be identified using a goal-directed TEE study have been agreed upon by international consensus. [4] These include pathologies that are common, such as:

1. LV dysfunction
2. RV dysfunction
3. Intravascular hypovolemia or reduced mean systemic venous pressure (see Chapter 9, Basic Hemodynamic Assessment).

Also, pathologies that are less common, but which require a specific change in management should be considered:

1. Pericardial tamponade
2. Acute pulmonary embolism

3. Major valvulopathy (including dynamic obstruction of the LVOT and RVOT)
4. Extra-cardiac conditions resulting in resistance to venous return (pneumothorax, abdominal compartment syndrome, IVC occlusion, etc.) (see Chapters 4 and 9).

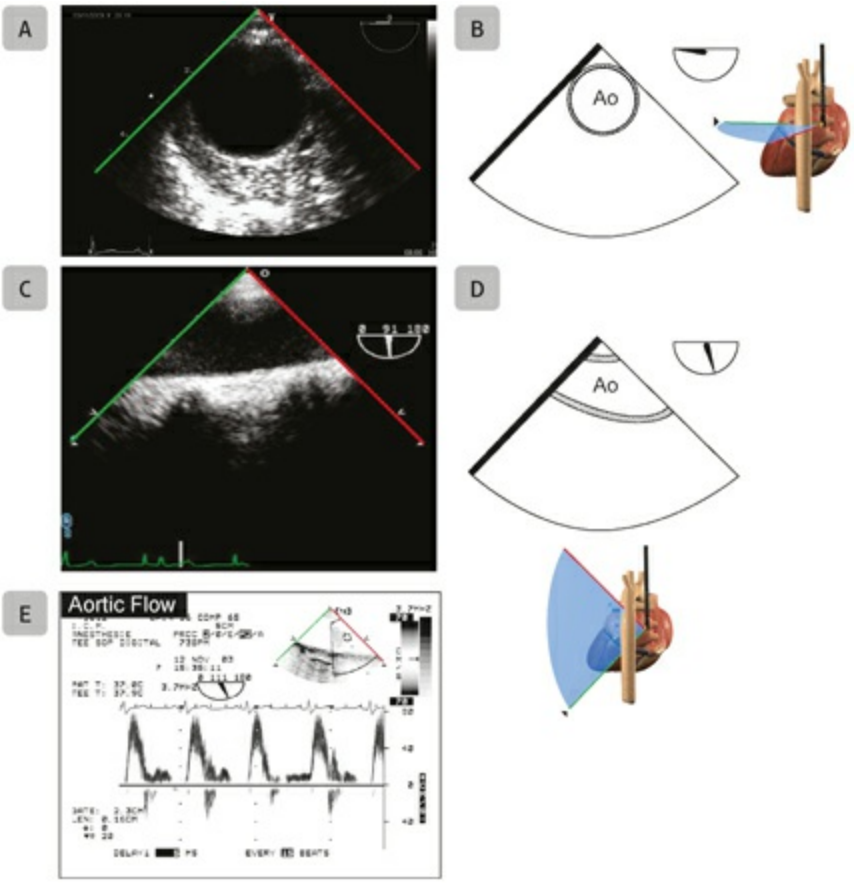

Fig. 3.15 Descending thoracic aorta (Ao) views. The descending Ao is imaged in (A,B) short-axis at 0° and (C,D) long-axis at 90°. (E) A pulsed wave Doppler signal of aortic flow is obtained by placing the sample volume in the proximal portion of the descending Ao. (Reproduced with permission from Denault *et al.* [3]).

A: https://youtu.be/VGF_eT8HQ1k

C: https://youtu.be/v9Z5IGso_fw

Standard Goal-directed Exam: Patients with Shock/ Hypotension

A patient presenting with shock or unexplained severe hypotension is the most common clinical scenario that prompts a goal-directed echocardiographic study, whether TTE or TEE. In this scenario, investigating the seven pathologies described above will identify the etiology of shock in the majority of cases. [5] A suggested approach involves the following TEE views:

1. TG Mid-Papillary Short-Axis (TG mid SAX) View. This is the best single view to investigate the etiology of shock, and fortunately it is easy to acquire in most cases. LV systolic function can be estimated and the position of the IVS interrogated. In cases where RV failure or acute PE are suspected, a dilated or pressure overloaded RV can be diagnosed by looking at the shape of the IVS. Pericardial effusions, especially when circumferential, can be detected. When severe hypovolemia is present, a hyperdynamic LV with a relatively empty cavity in both systole and diastole is expected.
2. ME Four-Chamber (ME 4C) View. Transitioning to this view is simple as the unflexed probe need only be withdrawn to the ME level. This view, as previously described, provides further information related to LV and RV size and function, as well as allowing investigation for pericardial effusion and valvular (MV, TV) dysfunction.
3. ME Long-Axis (ME LAX) View. Moving to this next view is again usually straightforward, requiring only a change in image plane from 0° to approximately 120°. This view reveals the AoV and LVOT, allowing aortic stenosis, aortic insufficiency, or dynamic obstruction of the LVOT to be suspected, if not confirmed (**Figure 3.8**). The MV can be interrogated from another plane, as can the LV. A proximal aortic dissection may be detected if the ascending aorta is seen to be dilated or if an overt dissection flap is visualized.

4. ME Bicaval View. This final recommended view can be slightly more difficult to obtain, but is nonetheless achievable in almost every patient. Evaluation of SVC diameter and respiratory variation provides useful information regarding volume responsiveness, particularly in patients who are mechanically ventilated and not making spontaneous respiratory efforts. [6]
5. ME Right Ventricular Inflow-Outflow (ME RV In-Out) View. This view will be useful in order to exclude RVOT obstruction [7] , which can be associated with reduced preload or secondary to external compression such as a pneumothorax (see **Figure 9.17**). [8] In addition, evaluation for RV failure can be performed using that view and diagnosis such as PE can be obtained if, for instance, a clot is present.

Additional Goal-directed Views: Patients with Dyspnea/Hypoxemia

In many cases where patients are dyspneic or hypoxemic, the possibility of an acute PE or intracardiac shunt is raised. Some of the views described above (particularly the TG midSAX view) will help with respect to the former, but it is recommended that the following views be analyzed carefully:

1. ME Ascending Aorta SAX (ME Asc Ao SAX) View. If there is a very proximal PE, it may be detected here.
2. Modified ME Right Ventricular Inflow-Outflow (ME RV In-Out) View. In addition to providing a look at the RV outflow tract, a slightly modified version of this view shows the inter-atrial septum (IAS) at the 11 o'clock position. Color Doppler can be used to screen the IAS for the presence of a patent foramen ovale, which may be contributing to hypoxemia in the patient.

SUMMARY

There is an unlimited assortment of potential TEE protocols, and indeed the exact image sequence can be modified for a specific patient, even in the context of a goal-directed exam. The image sequences described above can function as templates that will serve novice transesophageal echo-

cardiographers well as they begin to accrue experience. The study can always be expanded to the comprehensive 11- or 28-view exams should time and patient stability permit. Finally, in the presence of hemodynamic instability or hypoxemia with a normal or abnormal cardiac examination, TEE can be used to detect isolated or associated extra-cardiac pathologies in the lung or in the abdominal cavity. This will be discussed in Chapter 4, Extra-Cardiac Transesophageal Ultrasonography.

REFERENCES

1. ReevesS.T., FinleyA.C., SkubasN.J., SwaminathanM., WhitleyW.S., GlasK.E., et al. Basic perioperative transesophageal echocardiography examination: a consensus statement of the American Society of Echocardiography and the Society of Cardiovascular Anesthesiologists. *J Am Soc Echocardiogr*2013;*26*:443–56.
2. HahnR.T., AbrahamT., AdamsM.S., BruceC.J., GlasK.E., LangR.M., et al. Guidelines for performing a comprehensive transesophageal echocardiographic examination: recommendations from the American Society of Echocardiography and the Society of Cardiovascular Anesthesiologists. *J Am Soc Echocardiogr*2013;*26*:921–64.
3. DenaultA.Y., CoutureP., VegasA., BuithieuJ., TardifJ.C.. *Transesophageal Echocardiography Multimedia Manual, Second Edition: A Perioperative Transdisciplinary Approach,* New York: Informa Healthcare, 2011.
4. MayoP.H., BeaulieuY., DoelkenP., Feller-KopmanD., HarrodC., KaplanA., et al. American College of Chest Physicians/La Société de Réanimation de Langue Française statement on competence in critical care ultrasonography. *Chest*2009;*135*:1050–60.
5. JonesA.E., TayalV.S., SullivanD.M., KlineJ.A.. Randomized, controlled trial of immediate versus delayed goal-directed ultrasound to identify the cause of nontraumatic hypotension in emergency department patients. *Crit Care Med*2004;*32*:1703–8.
6. Vieillard-BaronA., CherguiK., RabillerA., PeyrousetO., PageB., BeauchetA., et al. Superior vena caval collapsibility as a gauge of volume status in ventilated septic patients. *Intensive Care Med*2004;*30*:1734–9.
7. DenaultA.Y., ChaputM., CoutureP., HebertY., HaddadF., TardifJ.C.. Dynamic right ventricular outflow tract obstruction in cardiac surgery. *J Thorac Cardiovasc Surg*2006;*132*:43–9.
8. VegasA., DenaultA.Y., RoyseC.. A bedside clinical and ultrasound-based approach to hemodynamic instability. Part II. Bedside ultrasound in shock state. *Can J Anesth*2014;*61*:843–64.

Chapter 4

Extra-Cardiac Transesophageal Ultrasonography

André Y Denault, Sarto C Paquin and Moishe Liberman

INTRODUCTION

The use of the esophagus as an acoustic window to the heart was described by Frazin in 1976. [1] Most of the literature, until recently, has been oriented toward the examination of the cardiovascular system. However, the use of ultrasound in the diagnosis of pulmonary diseases is now well established. [2] Moreover, transesophageal ultrasonography combined with endoscopy (endoscopic ultrasound scanning) has been routinely used by gastroenterologists, pulmonologists, and thoracic surgeons to diagnose and stage pulmonary and gastrointestinal pathologies for the past two decades. [3]

Thoracic and upper abdominal structures can be identified and monitored during either cardiac or extra-cardiac procedures. This chapter will review the basic extra-cardiac examination.

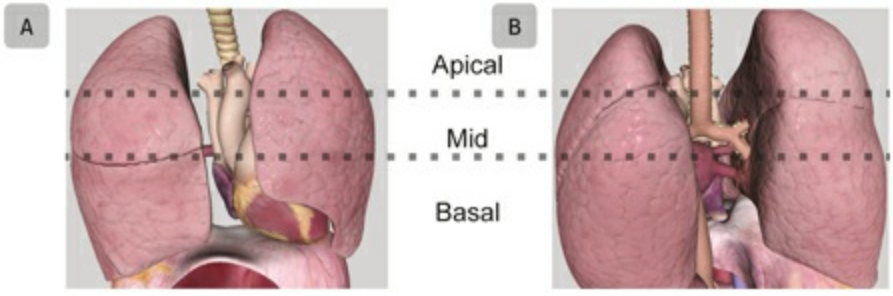

Fig. 4.1 Pulmonary regions. Division of the lung into apical, mid and basal regions is shown from the (A) anterior and (B) posterior perspectives using the Vimedix simulator.

A&B: https://youtu.be/aVsUBWEaiJE

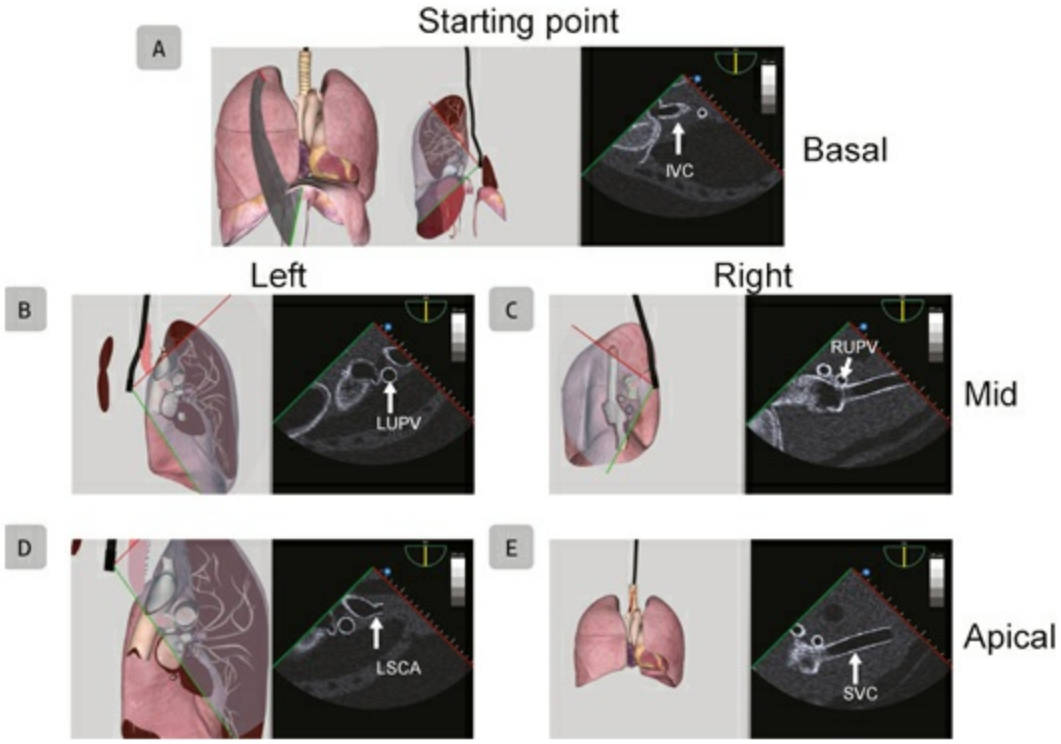

Fig. 4.2 Pulmonary reference points. The entrance of the (A) inferior vena cava (IVC), (B,C) left and right upper pulmonary vein (LUPV and RUPV), (D, E) the origin of the left subclavian artery (LSCA), and the middle portion of the superior vena cava (SVC) are the anatomic landmarks used to divide the lung into basal, mid and apical regions using the Vimedix simulator.

https://youtu.be/QoNOlRzb11Y

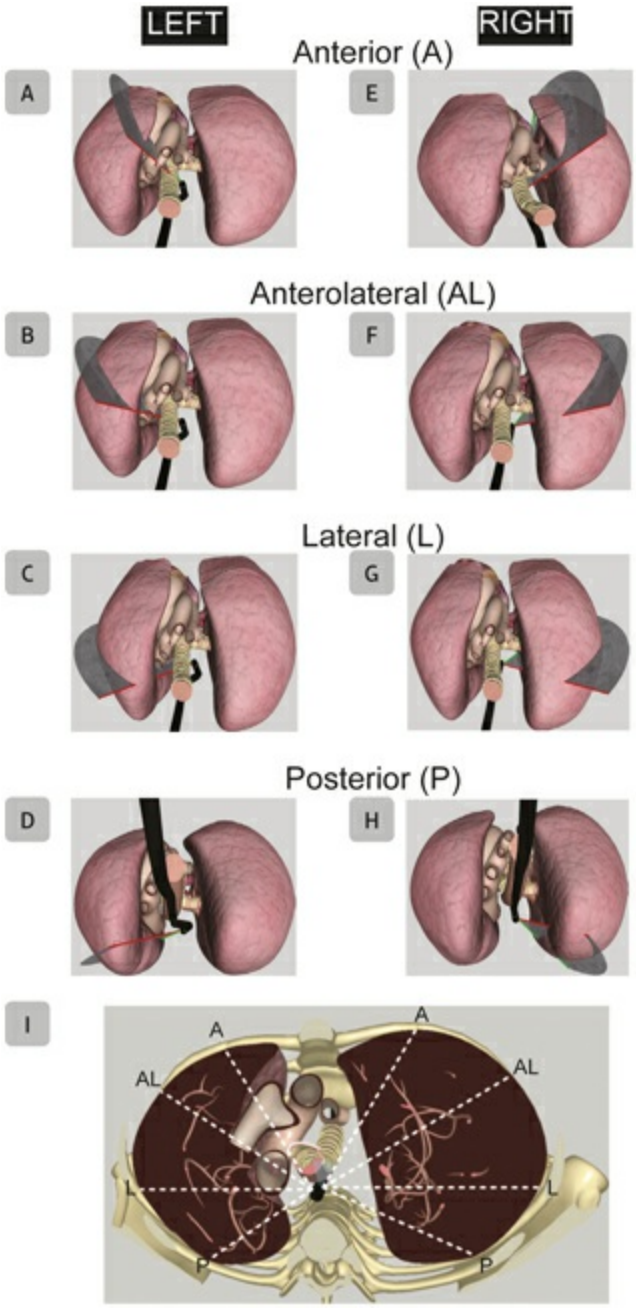

Fig. 4.3 Lung examination. Scan planes for the (A-D) left lung and (E-H) right lung are shown with the Vimedix simulator using a 90° scan plane with transesophageal echocardiography (TEE). (I) Rotating the TEE probe through 360° allows quick examination of both lungs.

RESPIRATORY SYSTEM

Normal lung is difficult to assess using transesophageal echocardiography

(TEE). However, TEE can more easily evaluate abnormal lung [4] and detect pleural effusion and hemothorax. [5] – [7] The CAE Vimedix simulator can demonstrate how to use TEE for the examination of the lung. [8] A key principle of lung evaluation is to obtain simple reference points from which known lung segments can be localized and identified if abnormal. Both the left and right lungs are divided into basal, mid and apical portions (**Figure 4.1**). The intrathoracic part of the inferior vena cava (IVC), right upper pulmonary vein (RUPV), left upper pulmonary vein (LUPV), superior vena cava (SVC) and left subclavian artery (LSCA) are the landmarks used to separate basal from mid and mid from apical portions (**Figure 4.2**). Lower esophageal (LE), mid-esophageal (ME) and upper esophageal (UE) views at 90° can evaluate the respiratory system using TEE (**Figure 4.3**). Alternatively the position of the TEE probe in relation to a clock can localize the ultrasound beam position (**Figure 4.4**). Consequently using TEE, left lung regions can be divided into left anterior (11–12 o'clock), anterolateral (10 o'clock), lateral (9 o'clock), and posterior (8 o'clock) (**Figure 4.3**). The right lung is divided into right anterior (12–1 o'clock), anterolateral (2 o'clock), lateral (3 o'clock), and posterior (4 o'clock) (**Figure 4.3**). Each of these lung sections are further subdivided into basal, mid, and apical levels (**Figures 4.5 and** 4.6). Using this approach, abnormal pulmonary segments or pleural pathologies adjacent to the esophagus can be identified and monitored. Precise intraoperative localization of pulmonary pathologies permits close monitoring and helps determine the effect of therapy such as lung recruitment. **Table 4.1** summarizes the steps used to perform the TEE exam of the respiratory system.

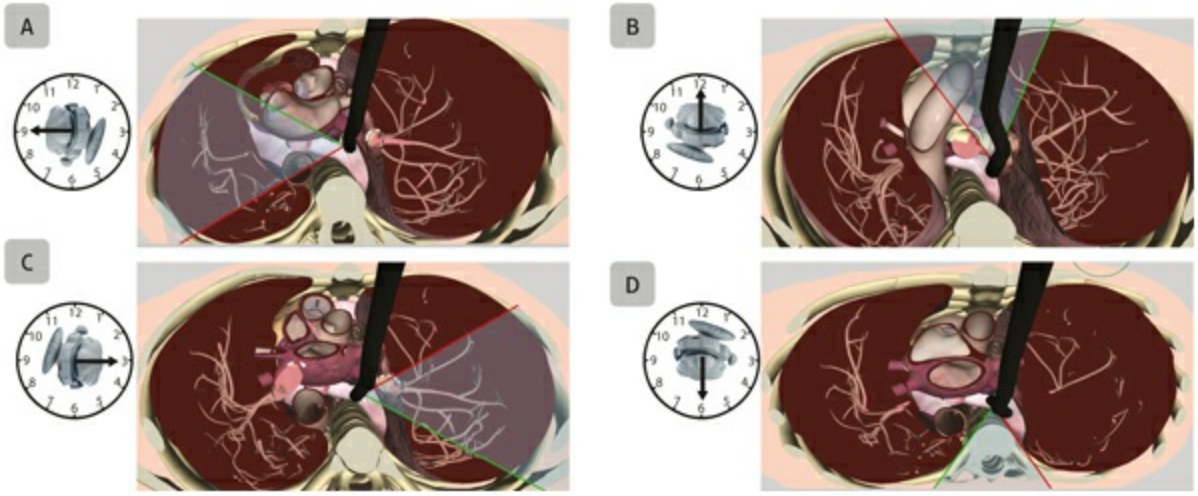

Fig. 4.4 Transesophageal echocardiography (TEE) probe position. The TEE probe handle knob position can be described in relation to a clock face to determine the orientation of the ultrasound scan plane. Scan planes for the lung shown with the Vimedix simulator are: (A) 9 o'clock, left lateral; (B) 12 o'clock, anterior; (C) 3 o'clock, right lateral; and (D) 6 o'clock, posterior.

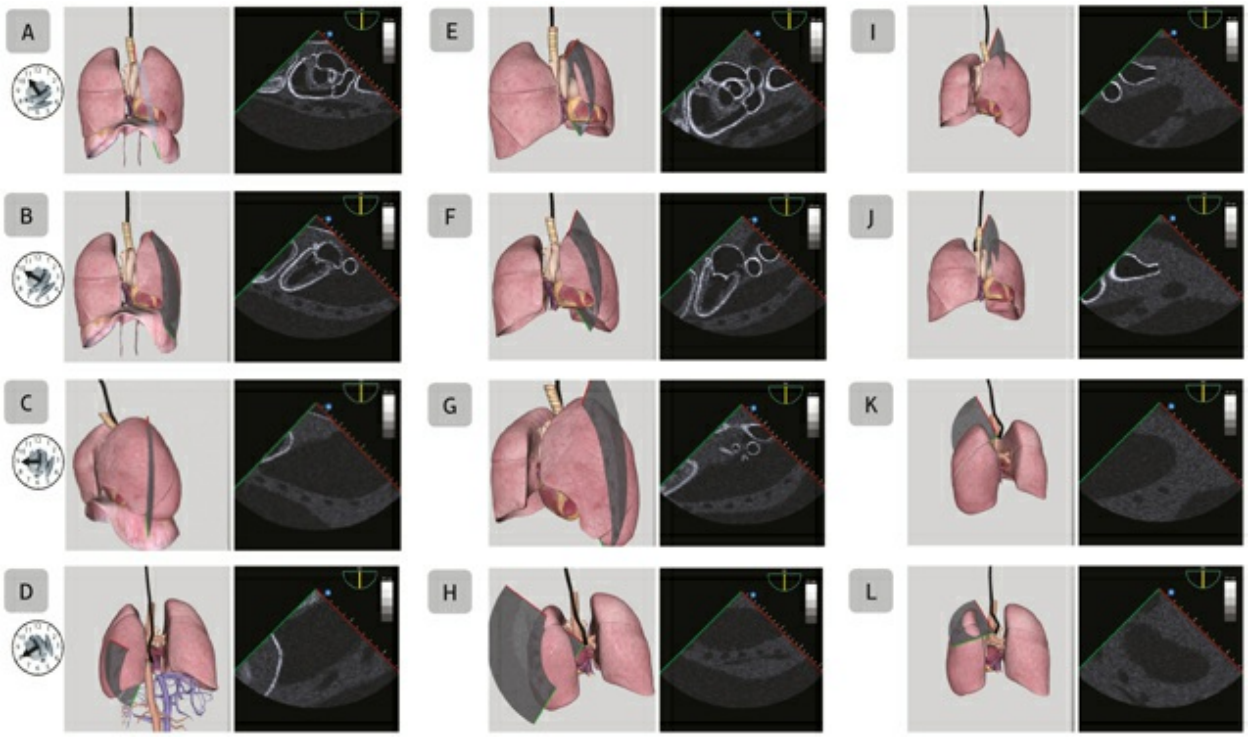

Fig. 4.5 Left lung examination. The left lung is examined by slowly rotating the transesophageal echocardiography probe with a 90° transducer angle between 8 and 11 o'clock to identify the (A—D) basal, (E—H) mid, and (I—L) apical regions of the lung using the Vimedix simulator. Note that the diaphragm is only seen in the basal region.

A-D: https://youtu.be/-NrNLVCtwkA

E-H: https://youtu.be/NPtfHd-hvDA

I-L: https://youtu.be/dWFrlrhpYyc

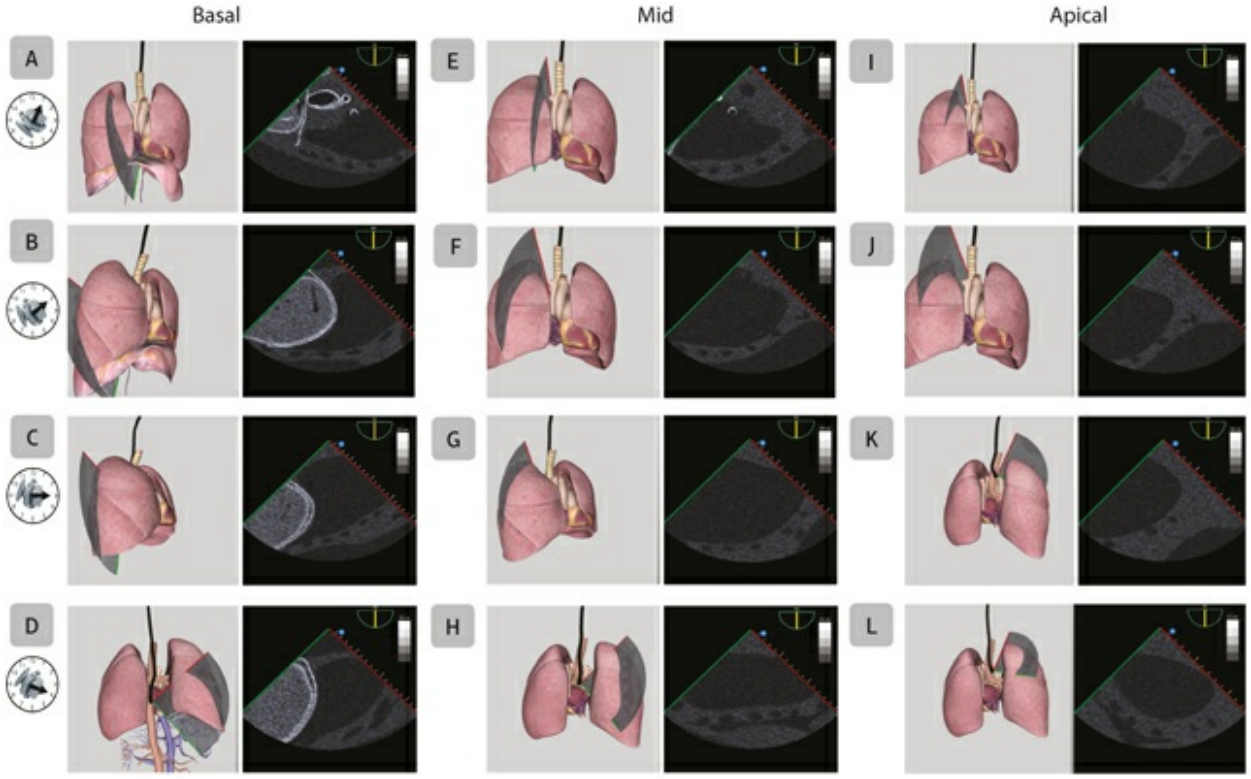

Fig. 4.6 Right lung examination. The right lung is examined by slowly rotating the transesophageal echocardiography probe with a 90° transducer angle between 1 and 4 o'clock to identify the (A—D) basal, (E—H) mid, and (I—L) apical regions of the lung using the Vimedix simulator. Note that the diaphragm is only seen in the basal region.

A-D: https://youtu.be/KV65MHlgbBE

E-H: https://youtu.be/pL-N8UZegN0

I-L: https://youtu.be/u5tYbVwoltE

PULMONARY PATHOLOGY

Pulmonary pathologies encountered with TEE are identical to those described in Chapter 14, Critical Care Examination of the Respiratory System. The major advantage of TEE is that a larger portion of the respiratory system can be examined more rapidly due to the easier acoustic windows provided through the esophagus. TEE also allows a more detailed examination of the dependent lung regions without moving the patient. Finally, in the operating room, when there is no ultrasound access to the chest, TEE can expedite rapid diagnosis associated with hemodynamic instability or hypoxemia. Although more invasive and associated with more complications (see Chapter 1, Ultrasound Imaging: Acquisition and Optimization), we recommend that pulmonary TEE be used only when the information cannot be obtained with surface ultrasound. In addition, small pneumothoraces are difficult to diagnose with TEE as they initially involve the anterior chest cavity. In the presence of a tension pneumothorax, there is phasic compression of the most anterior portion of the heart, which is the right ventricular outflow tract (RVOT) from the left side (see **Figure 9.17**) and compression of the right atrium from the right side (see **Figure 9.18**).

Pleural effusion is a common pulmonary pathology that begins with fluid accumulating in the paravertebral region. It is important to differentiate a pleural effusion from pericardial or peritoneal effusion. A pericardial effusion accumulates anterior to the aorta (see **Figures 5.18 and 17.3**). Peritoneal effusion is subdiaphragmatic and never collects posterior to the IVC (see **Figure 9.22**). [9] Different types of pleural effusion can be observed: some are simple and are purely anechoic and others are complex. In a febrile patient, complex pleural effusion should be considered suspicious for empyema (**Figure 4.7** and see **Figure 14.31**). Hemothorax is typically associated with numerous cellular elements (**Figure 4.8**). The hemothorax will eventually become solid and the term hematoma will be used. Severe hematoma may be difficult to differentiate from consolidation or atelectasis. The presence of color Doppler flow in the abnormal IVC, inferior vena cava; LAA, left atrial appendage; LLL, left lower lobe; LSCA, left subclavian artery; LUL, left upper lobe; LUPV, left upper pulmonary vein; ME, mid-esophageal; RLL, right lower lobe; RML, right middle lobe; RUL, right upper lobe; RVOT, right ventricular outflow tract; RUPV, right upper pulmonary vein; SVC, superior vena cava; TEE, transesophageal echocardiography; US, ultrasound.

Table 4.1 Steps in Performing TEE Examination of the Respiratory System.

1. Use the lowest US probe frequency	
2. Maximize beam width	
3. Start with the basal portion of the lung	a. Identify and center the US beam on the IVC (**Figure 4.2A**)
	b. Keep the diaphragm in the acoustic window
	c. Rotate left (**Figure 4.5A–D**): ME RVOT (lingula), ME 2 chamber (lingula), no heart (end of lingula), aorta (LLL), until no images are seen (vertebral column).
	d. Go back to IVC and rotate right (**Figure 4.6A–D**): RML up to 6 o'clock (RLL), until no images are seen (vertebral column)
4. Mid portion: the diaphragm should not be seen in these views	a. Rotate left and center the US beam to the LAA or LUPV (**Figure 4.2B**)
	b. Rotate left (**Figure 4.5E–H**): ME RVOT (lingula), ME 2 chamber (lingula and LUL), no heart (end of LUL), aorta (LLL), until no images are seen (vertebral column)
	c. Move to the right side and center the US beam on the RUPV (**Figure 4.2C**)
	d. Rotate right (**Figure 4.6E–H**): RML up to 6 o'clock (RLL) until no images are seen (vertebral column)
5. Apical portion	a. Rotate left and center the US beam to the LSCA (**Figure 4.2D**)
	b. Rotate left (**Figure 4.5I–L**): LUL up to 6 o'clock until no images are seen (vertebral column)
	c. Move to the right side and center the US beam on the middle portion of the SVC (**Figure 4.2E**)
	d. Rotate right (**Figure 4.6I–L**): RUL up to 6 o'clock until no images are seen (vertebral column)

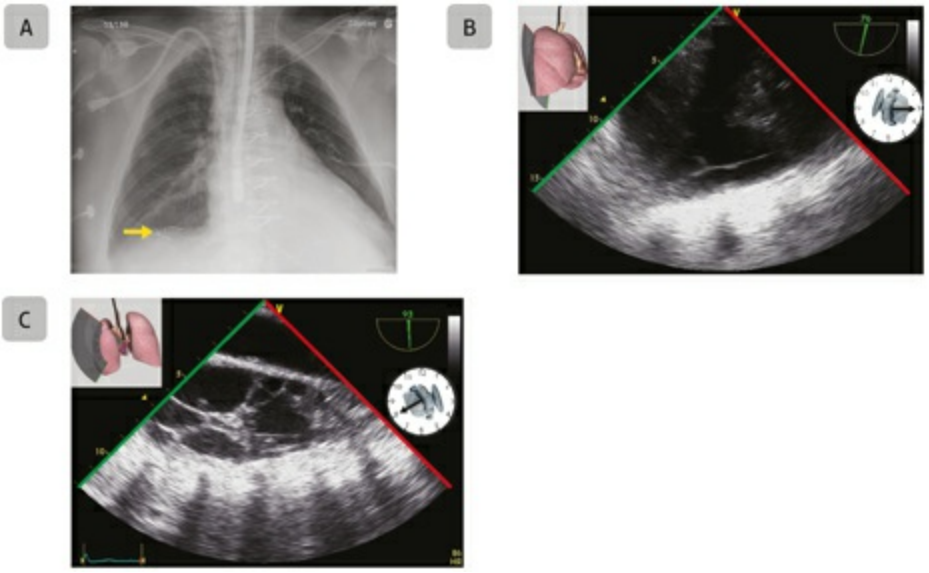

Fig. 4.7 Complex pleural effusion. (A) Chest radiograph and (B) corresponding right basal lateral ultrasound view obtained using transesophageal echocardiography (TEE) of a complex pleural effusion (yellow arrow) in a patient shortly after cardiac arrest. (C) A different patient with a left-sided complex

pleural effusion imaged with TEE is shown.

B: https://youtu.be/fSHf4iGJFiY

C: https://youtu.be/6wGEWI-ySTM

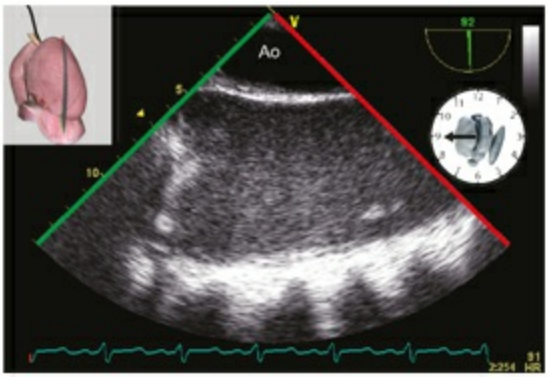

Fig. 4.8 Hemothorax. New onset hemothorax adjacent to the aorta (Ao) in an unstable patient is shown in this left basal lateral ultrasound view obtained using transesophageal echocardiography. Note the cellular elements are typical of blood.

https://youtu.be/W20p9MfgTqM

tissue excludes a hematoma **(Figure** 4.9 **).** Pleural effusion, lung atelectasis and B-lines will commonly co-exist in the same patient **(Figures** 4.10 **and** 4.11 **).** For more details on the ultrasound aspect of several pleural and lung pathologies, the reader is referred to the Chest Sonography [10] and the University of Melbourne online courses. [11]

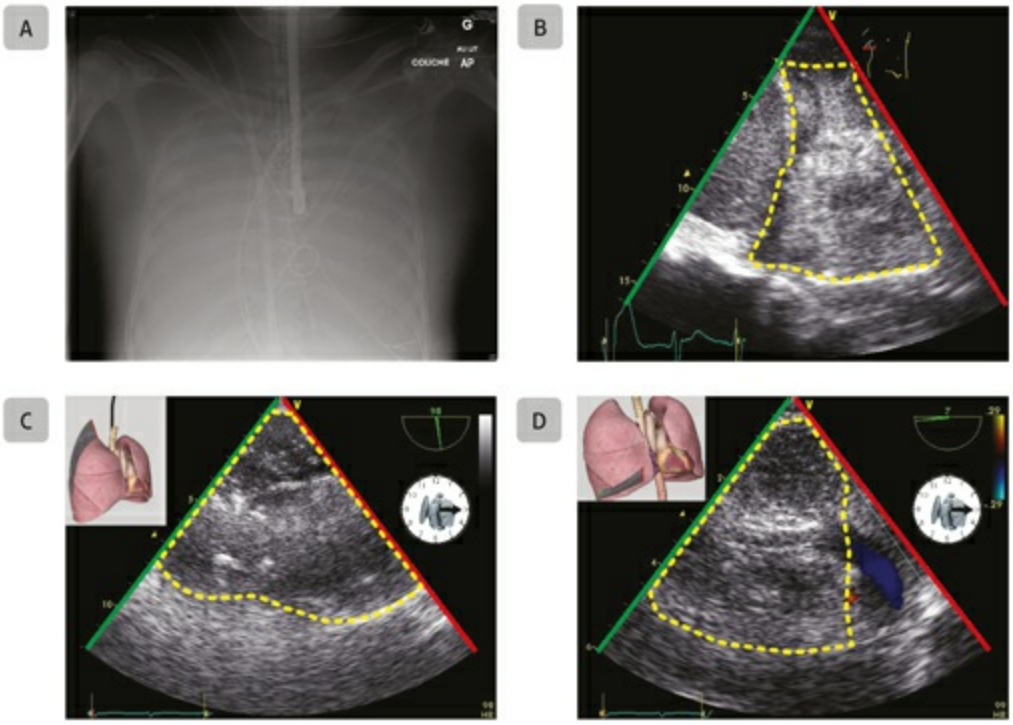

Fig. 4.9 Pleural hematoma. (A) A supine chest radiograph of a 37-year-old male with severe acute respiratory distress syndrome shows whiteouts of both lungs. (B) Transthoracic and (C) transesophageal examinations of the right basal lateral view demonstrate a massive hematoma in the right chest. (D) The absence of color Doppler signal confirms that the abnormal (dotted) area does not correspond to atelectasis or pneumonia. A total of 4 liters of clotted blood was drained intraoperatively.

B: https://youtu.be/rbWljPNn9WM

C: https://youtu.be/STtmH87kvDc

D: https://youtu.be/g8_PTZk2874

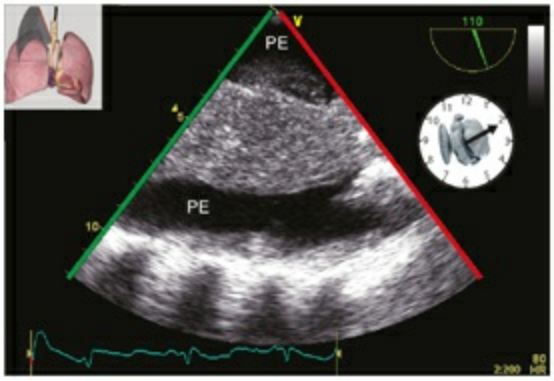

Fig. 4.10 Atelectasis. Right upper lobe anterolateral lung compression resulting in atelectasis and associated with simple pleural effusion (PE) is shown in this ultrasound image obtained using transesophageal echocardiography.

https://youtu.be/RRSIsYbS8kk

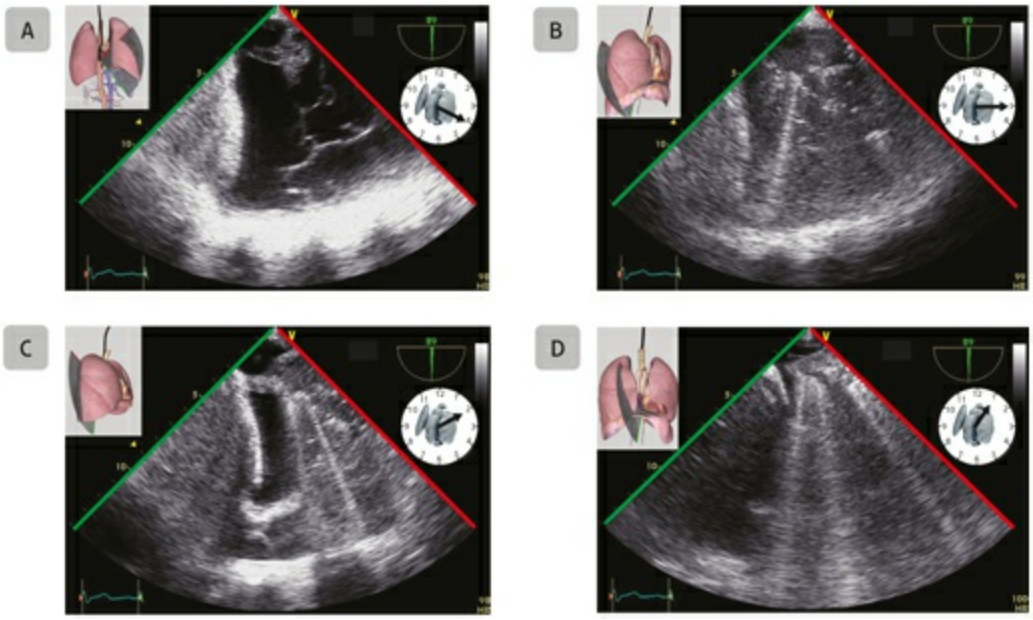

Fig. 4.11 Pneumonia after lobectomy. Ultrasound images of the right lung after a lobectomy are shown using transesophageal echocardiography. (A) A right posterior complex pleural effusion is shown associated with lung consolidation as the ultrasound beam is moved clockwise to the (B) lateral and (C,D) anterolateral positions. In the anterior position, only B-lines are seen.

A: https://youtu.be/5dvyO8ftyVI

C: https://youtu.be/yBgw98YFHH0

B: https://youtu.be/U4Yz4vr0qAg

D: https://youtu.be/-M1kH-45oEo

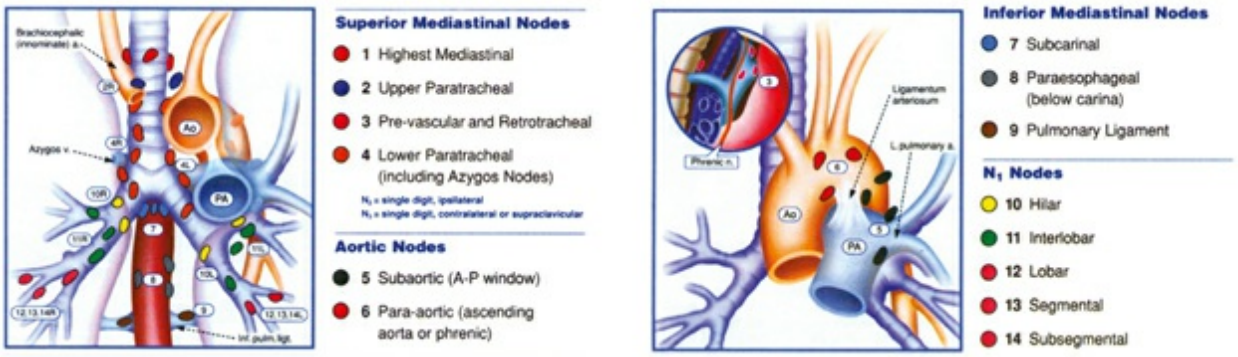

Fig. 4.12 Regional lymph node stations for lung cancer staging. Ao, aorta; A-P, anterior-posterior; PA, pulmonary artery. (Reproduced with permission from Mountain *et al.* [12])

MEDIASTINUM

Staging of lung cancer is performed through identification of different lymph node stations in the mediastinum (**Figure 4.12**). [12] Hilar and mediastinal lymph nodes are some of the most common sites of metastasis in both small and non-small cell lung carcinoma (**Figure 4.13**). [13] In addition, some non-

malignant pathologies, such as sarcoidosis, can present with enlarged mediastinal lymph nodes (**Figure 4.14**). Infectious process, neoplasia, such as lymphomas and germ cell tumors, and other pathologies, such as bronchogenic and foregut duplication cysts, can present as mediastinal masses (**Figure 4.15**). The diagnosis of mediastinal nodes are beyond the scope of the basic examination, but guidelines have been published for those who are interested. [14]

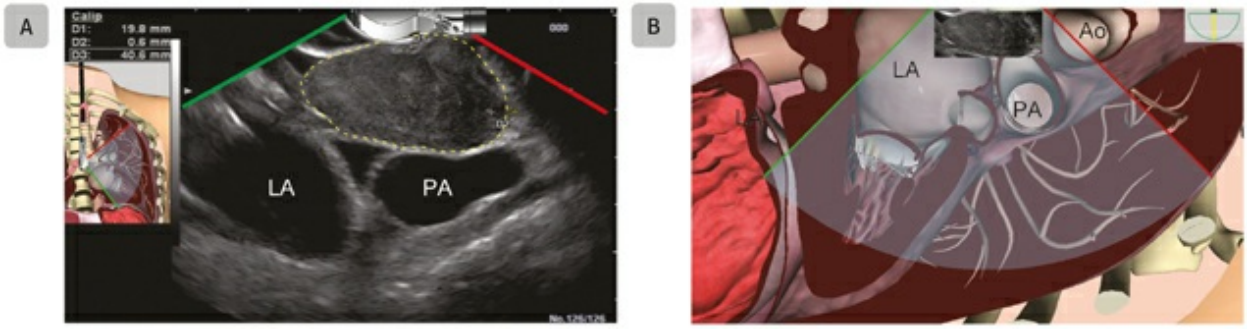

Fig. 4.13 Subcarinal lymph node. (A) Endo ultrasound image of a malignant 4 x 2 cm subcarinal lymph node (Station 7) in a patient with small-cell lung carcinoma. (B) Corresponding anatomic plane using the Vimedix simulator is shown. Ao, aorta; LA, left atrium; PA, pulmonary artery.

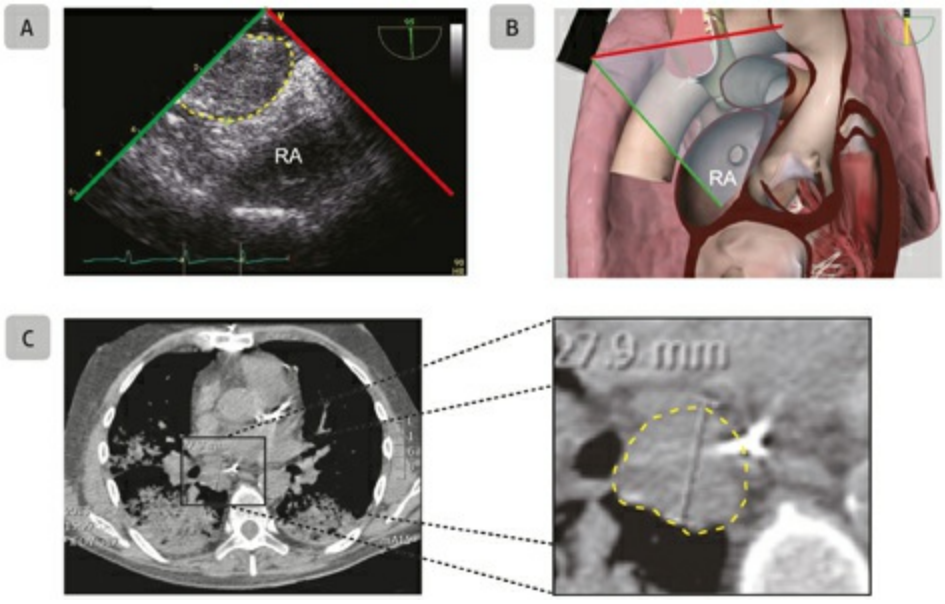

Fig. 4.14 . Subcarinal lymph node. (A) Mid-esophageal bicaval view with medial rotation showing a 19 mm abnormal structure consistent with a subcarinal lymph node (Station 7) close to the right atrium (RA). (B) The anatomic plane, with superimposed pathology, using the Vimedix simulator is shown. (C) The corresponding computed tomographic scan of the patient shows the lymph node. (Reproduced with permission from the University of Melbourne Ultrasound Education Group. [11])

A: https://youtu.be/VlIyrtSmvOo

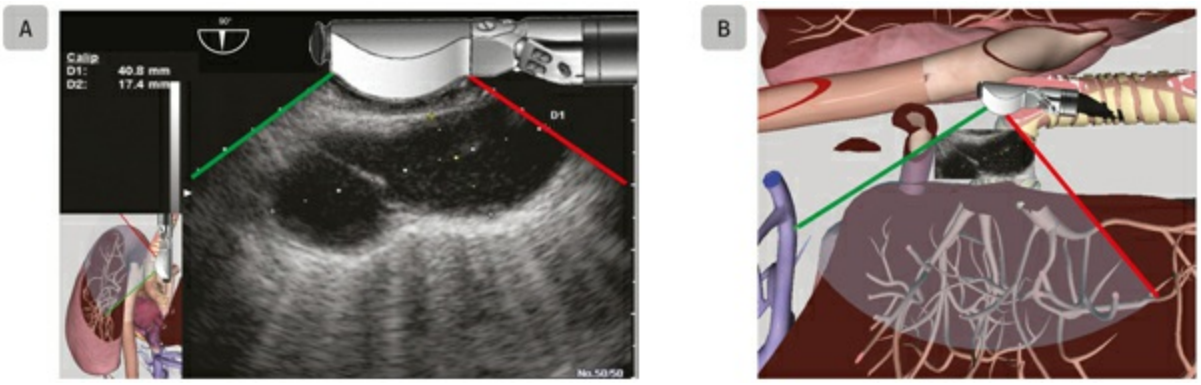

Fig. 4.15 . Bronchogenic cyst. (A) Endo ultrasound image displays an anechoic, septated cystic lesion located between the esophageal wall and the left pleura. (B) Corresponding anatomic plane, with superimposed pathology, using the Vimedix simulator is shown.

AZYGOS VEIN

The azygos vein is commonly seen during examination of the chest. The azygos vein empties into the SVC above the right pulmonary artery from a posterior position (5–6 o'clock). It is located in the right paravertebral region and has numerous collaterals in the thorax and abdomen. The hemiazygos vein connects to the SVC in its left anterolateral and superior portion. It follows the aortic arch anteriorly (see **Figure 3.9**), and lies in the left paravertebral space (**Figure 4.16**). Anatomic variations can occur. To image the azygos vein by TEE, the SVC is identified in a bicaval view (90°) and the probe is withdrawn to above the right pulmonary artery. Right-sided probe rotation using color Doppler (velocity scale <30 cm/s) identifies the azygos vein emptying in the SVC at 0° (**Figure 4.17 A**). The hemiazygos vein is less commonly seen (**Figure 4.17 C**). Lung cancer may invade the azygos vein, leading to focal thrombosis (**Figure 4.18**). Cannulation of the SVC from the cervical or axillary vessels during cardiac surgery or extracorporal membrane oxygenation can be accidently positioned in the azygos vein. If unrecognized, this can cause SVC syndrome. [15]

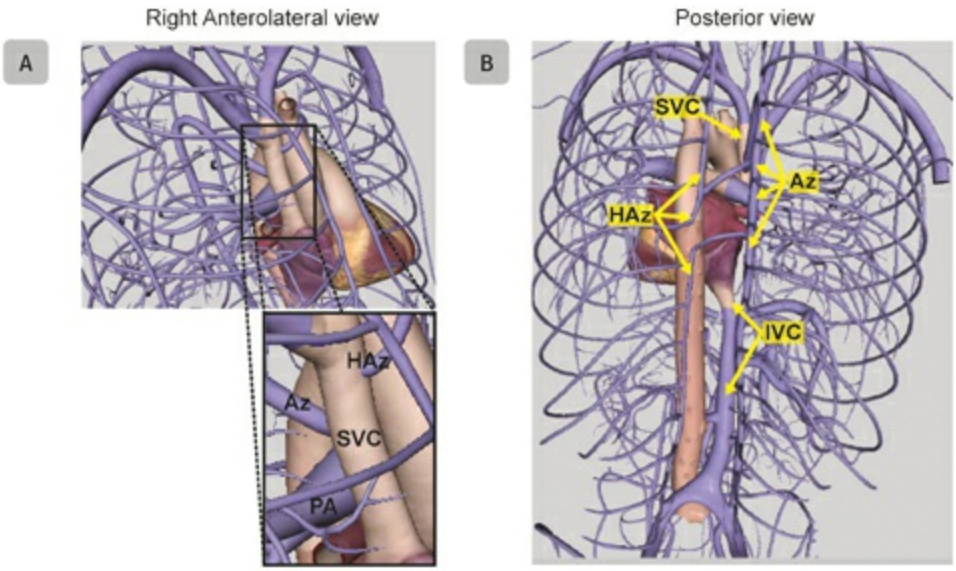

Fig. 4.16 Azygos (Az) and hemiazygos (HAz) venous system. (A,B) Right anterolateral and posterior views of the Az and HAz venous system are shown using the Vimedix simulator. The inset is a zoomed view of the Az vein as it attaches to the posterior portion of the superior vena cava (SVC) above the right pulmonary artery (PA). (B) Posterior view of the aorta and venous system. Note that the HAz vein lies in the left paravertebral space and joins the SVC in a more superior and anterior position. I VC, inferior vena cava.

https://youtu.be/_zbtxS-H7qI

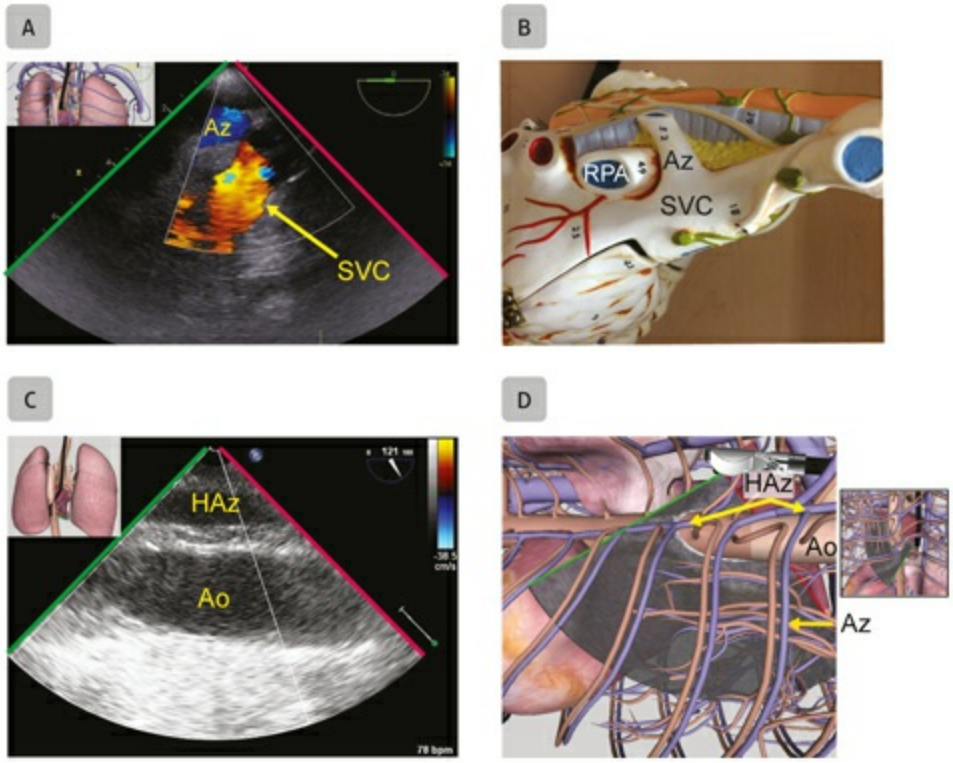

Fig. 4.17 . Azygos (Az) vein. (A) Upper esophageal view at 0° with color Doppler (Nyquist 16 cm/s) of the superior vena cava (SVC) and the Az vein just above the right pulmonary artery (RPA) is obtained using transesophageal echocardiography (TEE). (B) Correlation with an anatomic model is shown. (C) A TEE view of the thoracic aorta (Ao) and posteriorly positioned large hemiazygos (HAz) vein are both shown in long axis with the (D) corresponding anatomic plane using the Vimedix simulator.

A: https://youtu.be/5_3rI4Pveo8

C: https://youtu.be/2kt0v3AHarY

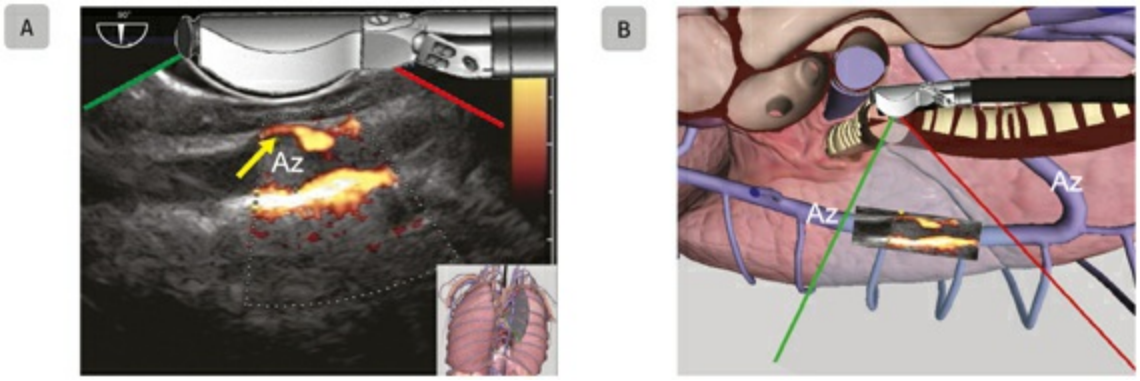

Fig. 4.18 Azygos (Az) vein thrombosis. (A) Endoscopic ultrasound image of a focal thrombus (arrow) in the Az vein in a patient with right-sided lung carcinoma. (B) Corresponding anatomic plane, with superimposed pathology, using the Vimedix simulator is shown.

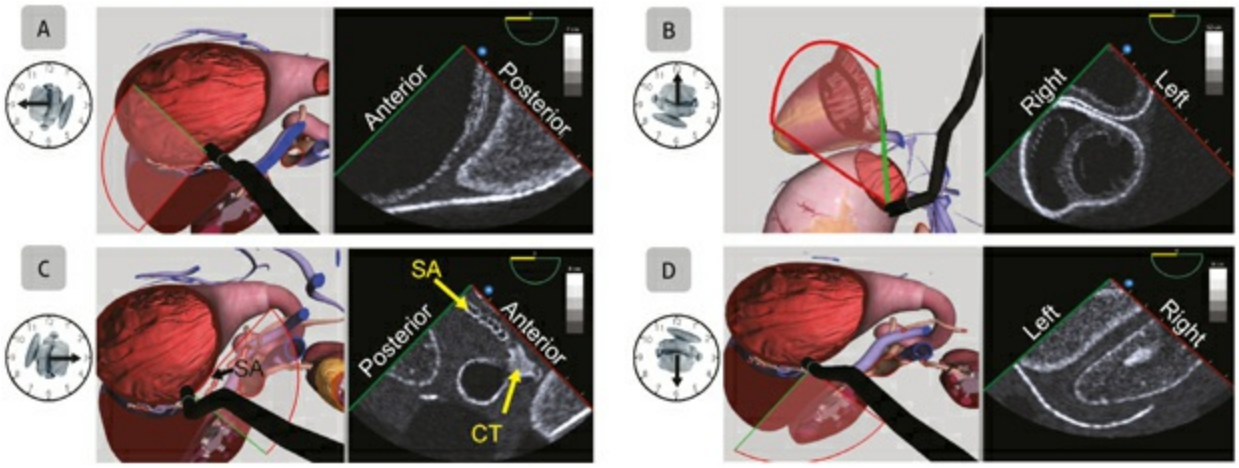

Fig. 4.19 Transesophageal echocardiography (TEE) of the abdomen. The orientation of the TEE probe at 0° in the abdomen is shown using the Vimedix simulator. (A) Beam rotation at 9 o'clock shows the spleen (posterior) on the right side of the image and the fundus of the stomach (anterior) on the left side of the screen. (B) Beam rotation at 12 o'clock shows the transgastric short-axis view with the right side of the screen corresponding to the left heart and the left side of the screen to the right heart. (C) Beam rotation at 3 o'clock shows the celiac trunk (CT) (anterior) on the right side of the screen and the kidney (posterior) on the left side. Note the splenic artery (SA) is directed toward the TEE probe. (D) Beam rotation at 6 o'clock shows the left kidney, on the right side of the display. On the left side of the screen, the spleen is seen. Note the splenic artery (SA) is directed toward the TEE probe.

ABDOMINAL CONTENT

Before examining the abdomen with TEE, it is important to understand the orientation of the image. For the purpose of this chapter, we used the cardiology convention. Therefore, when imaging the heart at 0°, the left side of the ultrasound screen corresponds to right-sided structures and the right

side to the left-sided structures (Figure 4.19b). However, when the probe is rotated in order to visualize posterior structures, then the left and right portions of the screen correspond to the left- and right-sided structures (Figure 4.19d). When the probe is rotated laterally, the right side of the ultrasound display shows posterior structures at 9 o'clock (Figure 4.19a) and anterior structures at 3 o'clock (Figure 4.19c).

However, a long-axis (LAX) view at 90° is often used for visualizing abdominal contents, where the cephalad region is to the right of the screen. This type of LAX view is emerging as the most common mode of scanning the gastrointestinal system during endoscopic ultrasound because of the ability to permit diagnostic biopsy and therapy.

STOMACH

The stomach is the window to the abdomen for TEE. Anatomically, the stomach is divided into the fundus, cardia, body, antrum, and pylorus. For non-gastroenterologists, the TEE probe remains in the gastric body when obtaining a transgastric view (**Figure 4.20 A**). Moving the probe to 90° is the next step in examining the stomach (**Figure 4.20 B**) and the other organs. As the ultrasound plane is turned to the right, the left portion of the liver and the esophagogastric junction will appear close to the junction between the right atrium and IVC (**Figure 4.20 C**). The most common gastric abnormality seen with TEE is a full stomach, for which a nasogastric tube may drain the content after the TEE examination (**Figure 4.21 A**). Gastric wall thickening can occur in patients with severe right-sided heart failure (**Figure 4.21 B**) and in some patients blood clots (**Figure 4.21 C**) or a nasogastric tubing (**Figure 4.21 D**) can be seen. Hiatal hernias may impair probe progression past the esophagogastric junction and may be seen as a redundant pouch underneath the probe (**Figure 4.22**). In that situation, it is important not to force the probe progression.

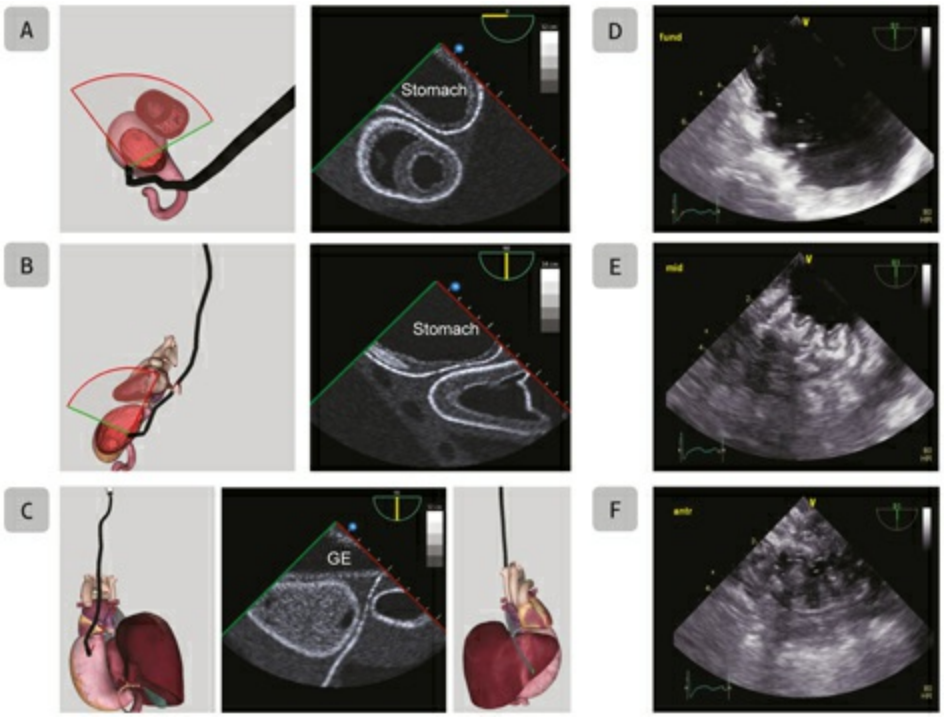

Fig. 4.20 Examination of the stomach. Transesophageal echocardiography (TEE) transgastric views and corresponding Vimedix views of the stomach are shown. (A) At 0° the anterior antrum of the stomach is shown. (B) Advancing the TEE probe transducer angle to 90° examines the more caudal aspect of the stomach. (C) Turning the TEE probe to the right at a 90° transducer angle images the gastroesophageal (GE) junction above the liver. Corresponding TEE images of the fundus (D), mid-portion (E), and antrum (F).

D: https://youtu.be/ccgPnmziHUk

E: https://youtu.be/XP0kxvVzpp4

F: https://youtu.be/0MMu8sJS7cA

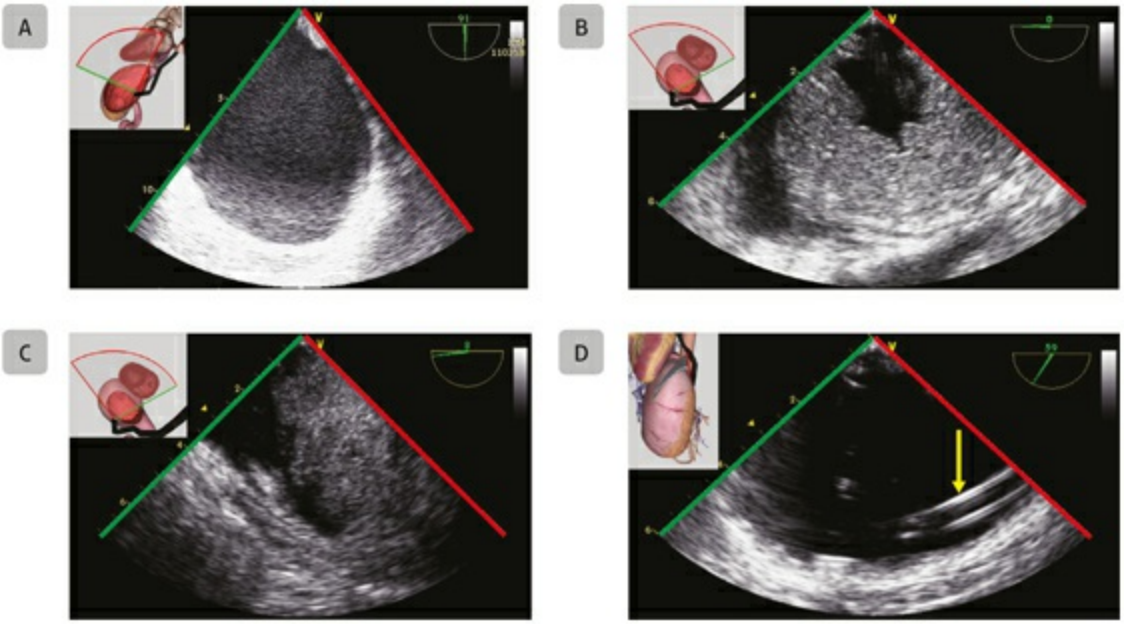

Fig. 4.21 Gastric abnormalities. Transesophageal echocardiography images of the stomach at various transducer angles show (A) full stomach, (B) severe gastric edema in a patient with severe right heart failure, (C) blood clot, and (D) a nasogastric tube (arrow)

A: https://youtu.be/fybd8bgPWjI

B: https://youtu.be/i9s8EDFxgmY

C: https://youtu.be/UkakqVF_680

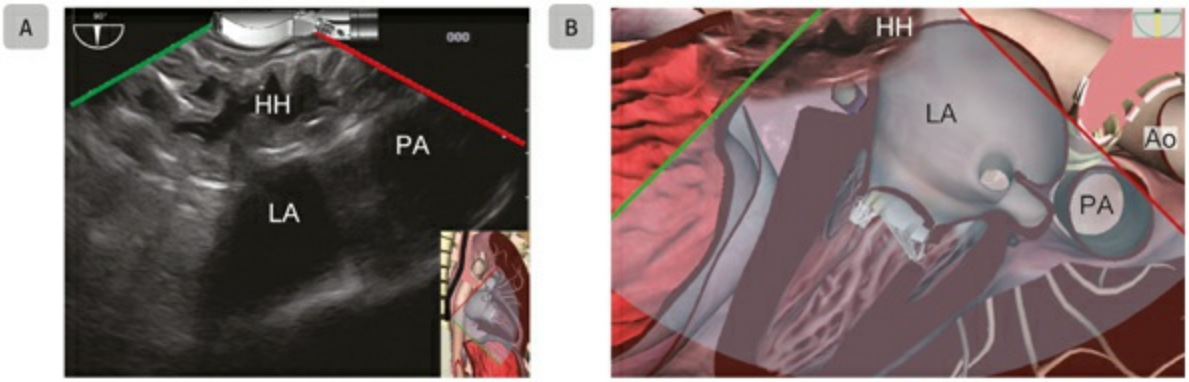

Fig. 4.22 Hiatal hernia (HH). (A) Endoscopic ultrasound view of a HH located between the ultrasound probe and the subcarinal space is shown with (B) a corresponding anatomic plane using the Vimedix simulator. Ao, aorta; LA, left atrium; PA, pulmonary artery.

SPLEEN

The spleen is located beside the stomach on the left side. The upper pole is under the diaphragm, the lower pole is adjacent to the junction of the transverse and descending colon. The left kidney is posterior and lower in relation to the spleen. The tail of the pancreas ends in the splenic hilum (**Figure 4.23**). Identification of the diaphragm is important to distinguish if fluid collections are within the abdomen or pleural space. Recognition of the spleen is useful in order to evaluate arterial and venous Doppler signals to detect surrounding structures or fluid and exclude splenomegaly (**Figure 4.24**). Splenomegaly is suspected when the spleen extends beyond the left kidney with dimensions that exceed normal longitudinal (12–14 cm) and transverse (<5 cm) dimensions. Splenic rupture can be diagnosed in trauma patients using this view.

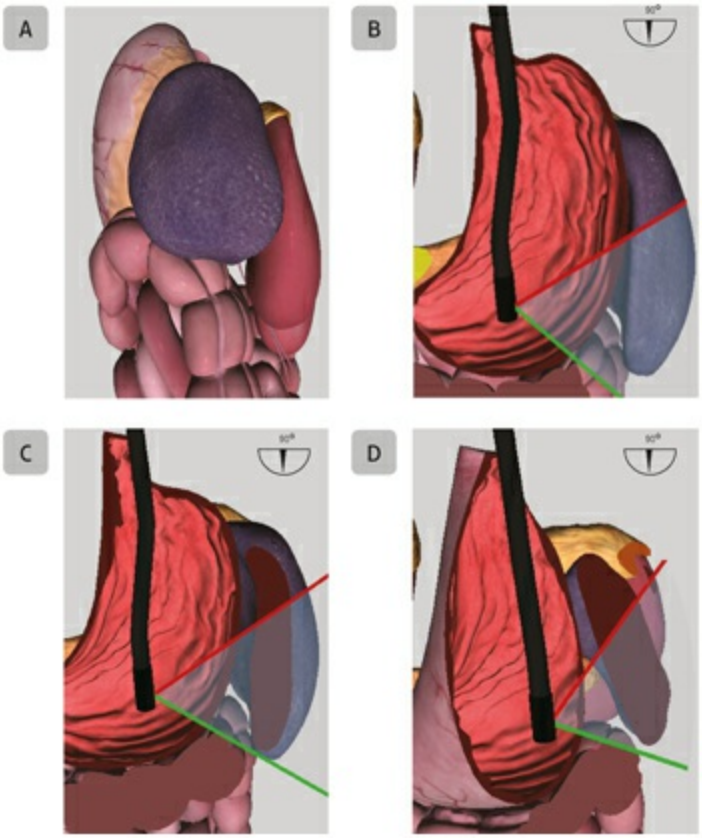

Fig. 4.23 Spleen anatomy and position. The probe position and transesophageal echocardiography (TEE) imaging of the spleen from the stomach is shown using the Vimedix simulator. (A) The spleen is positioned lateral to the stomach, anterior to the kidney and superior to the splenic flexure of the colon. (B-D) Using TEE with a 90° beam orientation, the upper pole of the spleen can be imaged by sweeping the TEE probe counterclockwise from left to right. The lower pole of the spleen is examined by advancing and sweeping the TEE probe back to the left.

https://youtu.be/L3Cu7S5SiVc

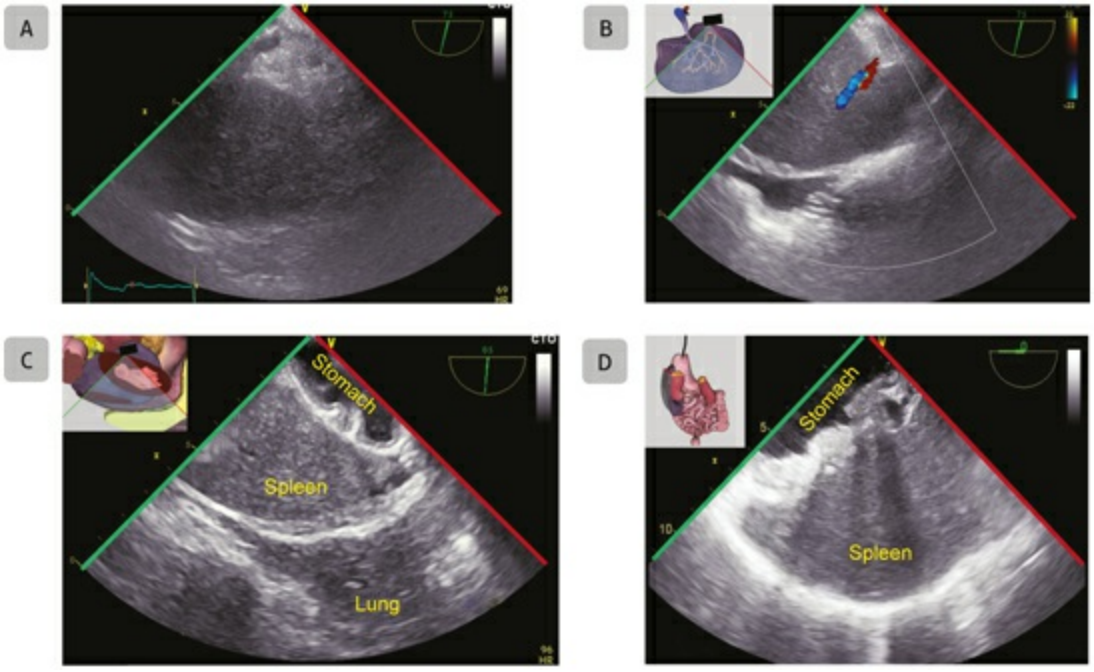

Fig. 4.24 Spleen. Transesophageal echocardiography (TEE) transgastric views of a normal spleen at 75° (A) without and (B) with color Doppler (Nyquist 22 cm/s) are shown. (C) Left basal pulmonary atelectasis seen from a TEE transgastric view at 85° through the spleen. (D) A transgastric TEE view at 0° shows splenomegaly in a 43-year-old male with congenital heart disease. Note that the transverse diameter of the spleen is more than 6 cm (normal <5 cm).

A: https://youtu.be/2qiUDEDbJBk

B: https://youtu.be/YQCRceIcA64

C: https://youtu.be/MLMjSk0aJWI

D: https://youtu.be/Gtbv3SUaFfY

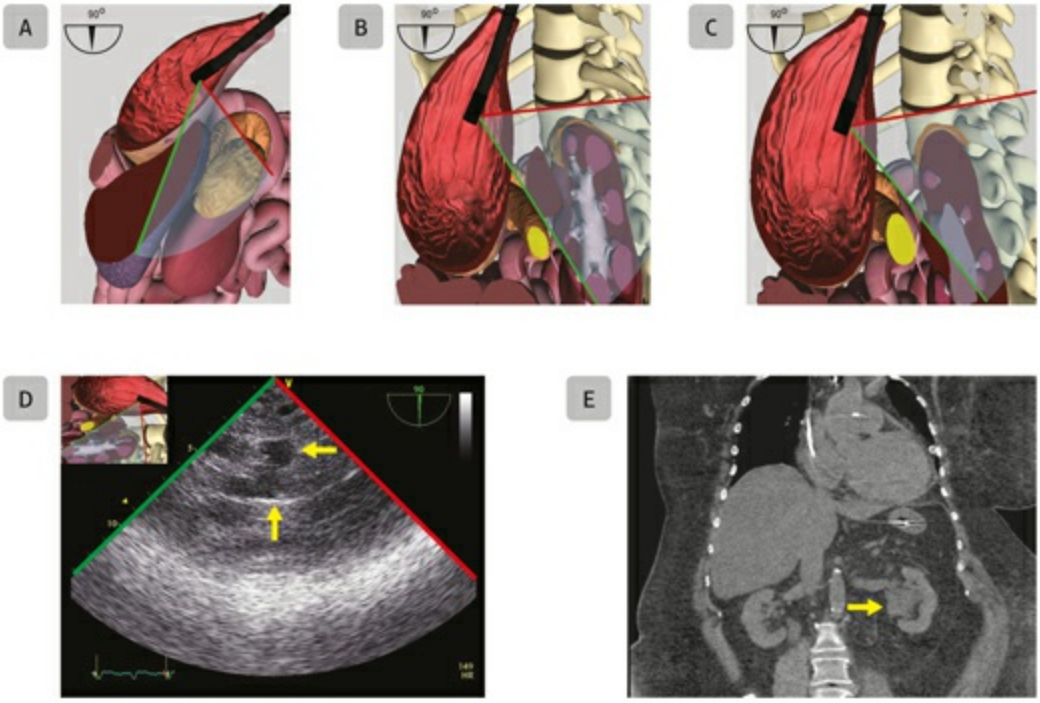

Fig. 4.25 Left kidney. The probe position and transesophageal echocardiography imaging of the left kidney from the stomach, using the spleen as an acoustic window, is shown with the Vimedix simulator. (A—C) Examination of the kidney using a longitudinal view through the stomach with progressive counterclockwise rotation. (D) Numerous left kidney hilar cysts (arrows) with ultrasound and (E) computed tomography correlation in a morbidly obese 54-year-old female in shock are shown.

D: https://youtu.be/6oehzWfLU3A

KIDNEY

The left kidney is an organ frequently seen when performing TEE, but the right kidney is rarely seen. [16] , [17] Once the spleen is identified, rotating the probe using a longitudinal axis (90°) to the left shows the left kidney (**Figure 4.25**). The normal aspect of the kidney with corticomedullary differentiation can be appreciated (**Figure 4.26**). Arterial and venous Doppler can monitor renal perfusion and has diagnostic values in certain conditions. [18] The left adrenal is situated slightly superior to the left kidney. A practical way of

locating the left adrenal is to identify the celiac artery trunk in a longitudinal axis, and then slightly rotate the probe clockwise (**Figure 4.27**).

LIVER

The liver is the largest abdominal organ. The left and right liver lobes are separated anteriorly by the falciform ligament. Transgastric ultrasound by TEE can only visualize the left liver lobe. The Couinaud classification divides the liver into eight independent segments, each of which has its own vascular inflow, outflow, and biliary drainage (see **Figure 16.6**). Identification of these segments is beyond the scope of the basic examination. The liver is examined like the spleen using longitudinal views from left to right for the more apical area and from the right to the left for the caudal area of the liver (**Figure 4.28**). Hepatic veins (**Figure 4.29**), portal vein (**Figure 4.30**), and the hepatic artery (**Figure 4.31**) can be identified with 2D and color Doppler. Commonly encountered pathologies include ascites with or without cirrhosis, liver cysts, abscesses (**Figure 4.32**), intrahepatic biliary ductal dilation, and neoplastic conditions (**Figure 4.33**).

PORTAL HYPERTENSION

Portal hypertension may be encountered in certain pathologies, such as cirrhosis, or various conditions leading to portal vein thrombosis, such as hypercoagulable states, neoplasias directly invading the vessel, acute pancreatitis, and schistosomiasis. Portal hypertension may cause esophageal or gastric varices, with potentially catastrophic consequences if these varices rupture. Transesophageal echocardiography is relatively contraindicated in the presence of known esophageal or subcardial varices (see Chapter 1, Ultrasound Imaging: Acquisition and Optimization). However, some patients undergoing TEE may have unsuspected portal hypertension. Therefore, recognition of esophageal or gastric varices during TEE is important. Portal hypertension can be detected when numerous venous collaterals are visualized in the peri-esophageal or peri-gastric area (**4.34 A,B). When a collateral vein penetrates the esophageal or gastric wall, varices are formed. Varices present as anechoic tubular structures within the gut wall. Esophageal varices may be difficult to identify given that the**

esophageal wall is relatively thin. Gastric varices are most commonly located in the subcardial space or in the fundic area (Figure Figure 4.34 C,D).

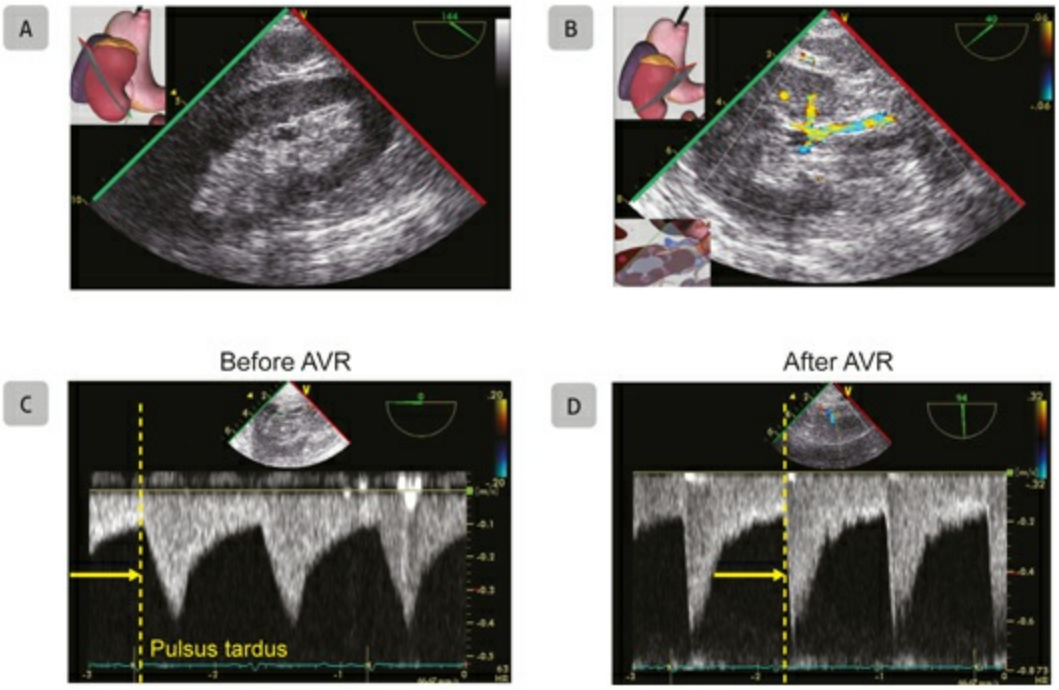

Fig. 4.26 Left kidney. Transesophageal echocardiography images of the left kidney from the stomach are shown. (A) Normal left kidney parenchyma is shown in this 144° view. In some patients, the major axis of the kidney might be slightly oblique. (B) Color Doppler (Nyquist 6 cm/s) of the renal artery at 44° is shown. (C—D) Pulsed wave spectral Doppler of the splenic artery shows the abolition of the pulsus tardus or delayed peak Doppler signal (arrow) in the arterial Doppler signal after aortic valve replacement (AVR) for correction of aortic stenosis.

A: https://youtu.be/Qtv10FEldMg

B: https://youtu.be/q5Q4ul4Qgfo

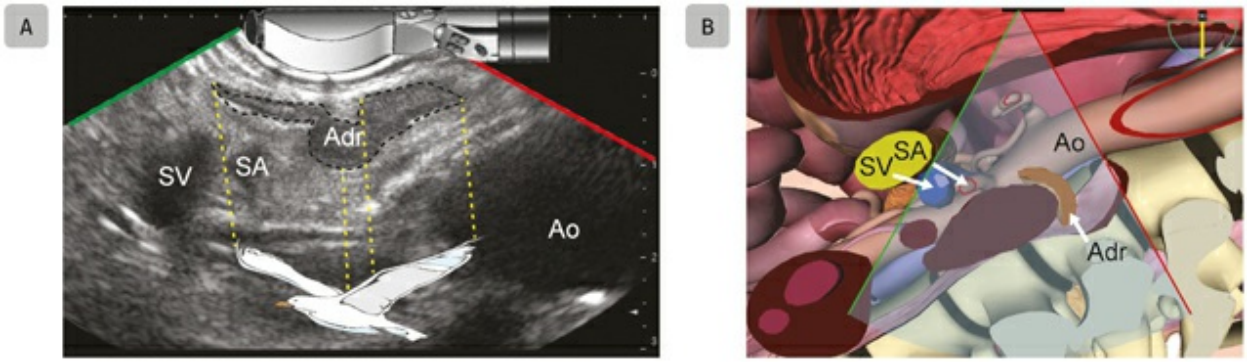

Fig. 4.27 Left adrenal (Adr). (A) Endoscopic ultrasound image of the left Adr, which typically resembles a flying bird ("seagull sign") (B) with corresponding anatomic plane using the Vimedix simulator. Ao, aorta; SA, splenic artery; SV, splenic vein.

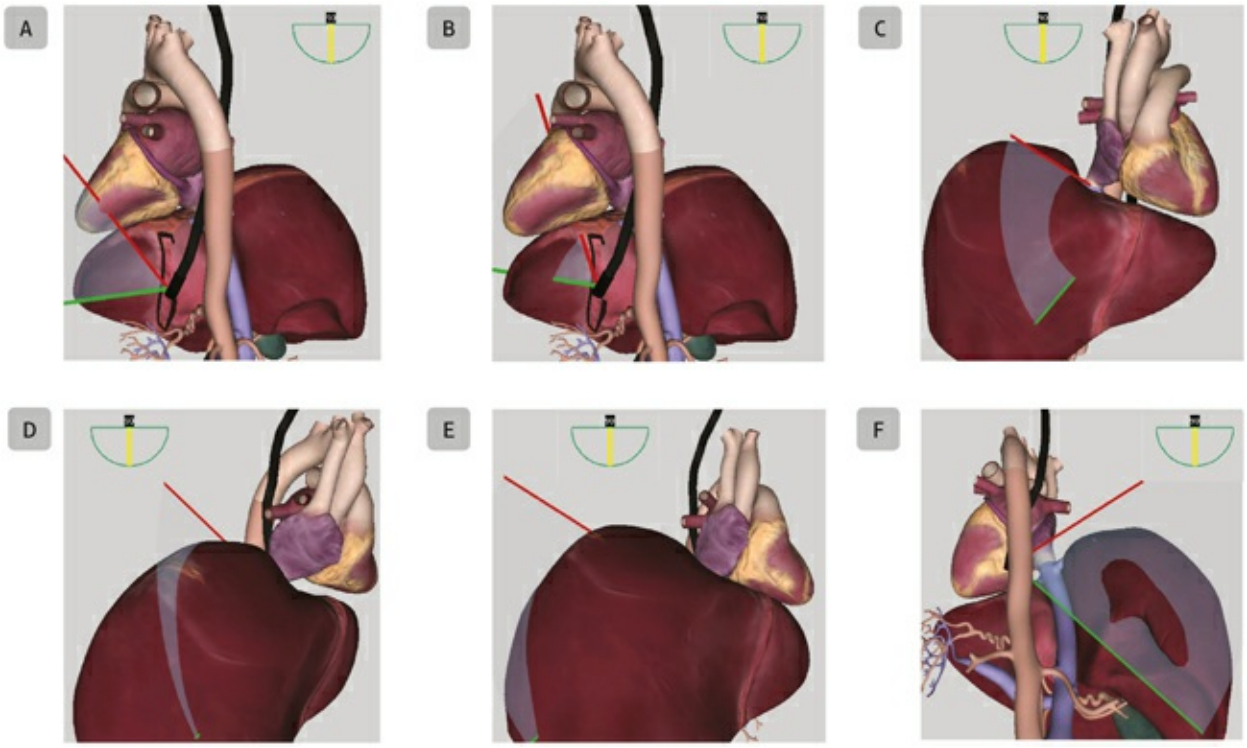

Fig. 4.28 Liver. Scanning sequence of the liver by transesophageal echocardiography is shown using the Vimedix simulator. (A—F) A transgastric view at 90° is obtained. (A—C) The upper portion of the liver is scanned as the ultrasound beam moves from left to right. (D—F) The lower or caudal portion of the liver is scanned by advancing the probe slightly and moving the probe from right to left.

https://youtu.be/9jiB-TzNb2s

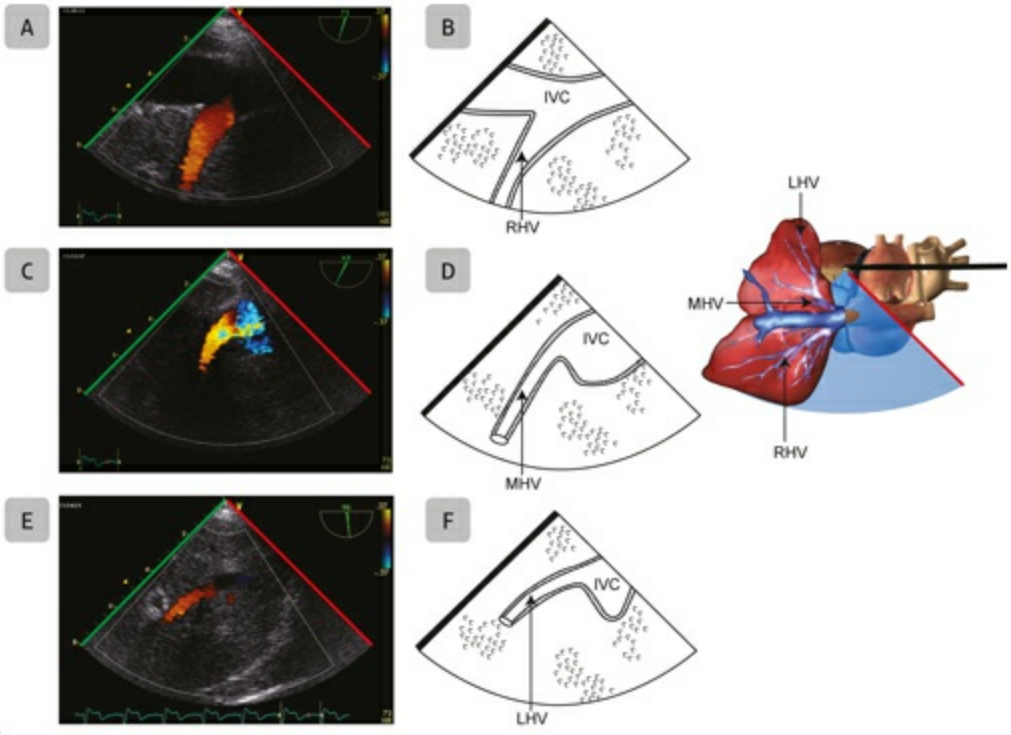

Fig. 4.29 Hepatic veins. Transesophageal echocardiography transgastric views of the liver between 60° to 90° with color Doppler (Nyquist 37 cm/s) display the right (A,B), middle (C,D), and left (E,F) hepatic veins in the majority of patients. IVC, inferior vena cava; LHV, left hepatic vein; MHV, middle hepatic vein; RHV, right hepatic vein. (Reproduced with permission from Denault *et al.* [7])

A: https://youtu.be/k_CdckMKj8w

C: https://youtu.be/FWDjxkqcTg8 E: https://youtu.be/Ys3iFXOkhzo

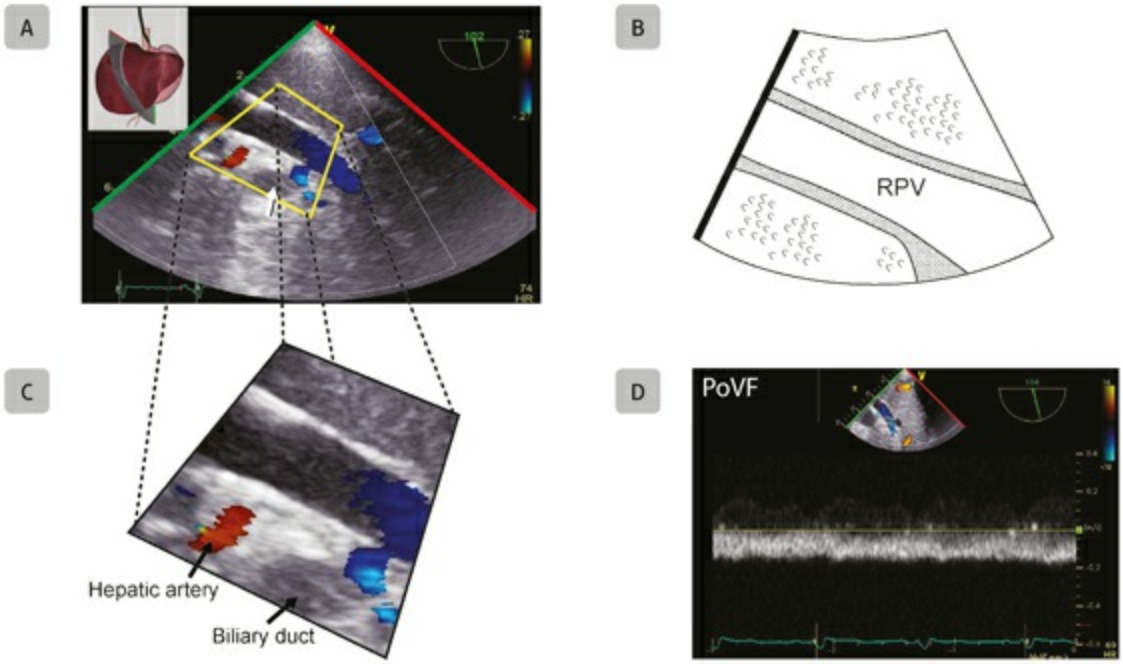

Fig. 4.30 Portal vein. (A—C) Transesophageal echocardiography transgastric views with right-sided rotation shows the main branch of the right portal vein (RPV). Note the portal vein has an hyperechoic sheath around the vein as opposed to the inferior vena cava or the hepatic vein whose wall is barely seen. The hyperechoic sheath results from the proximity of the biliary duct and the hepatic artery, which forms the portal triad. (D) Pulsed wave Doppler of portal vein shows low resistance continuous, monophasic low velocity portal venous flow (PoVF). (Reproduced with permission from Denault *et al.* [7])

A: https://youtu.be/gxhH_a9Hbeo

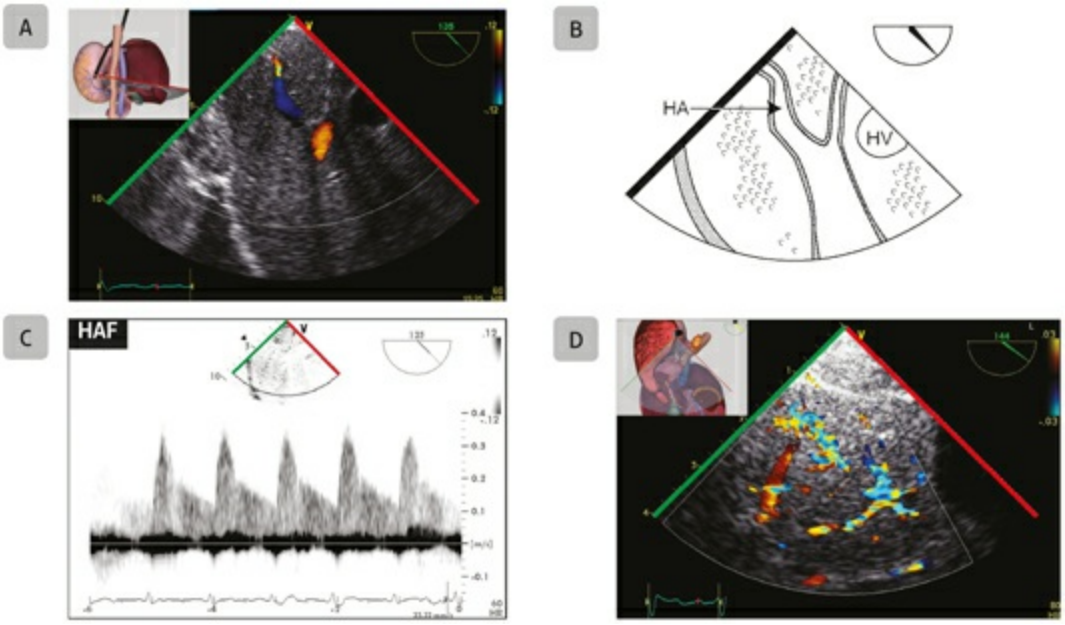

Fig. 4.31 Hepatic artery (HA). (A,B) Transesophageal echocardiography (TEE) transgastric view with rightwards rotation at 135° using color Doppler (Nyquist 12 cm/s) shows the HA. (C) Continuous wave Doppler confirms normal pulsatile hepatic artery flow (HAF). (D) TEE view of the liver with color Doppler at a low Nyquist (30 cm/s) shows the highly vascular structure of the liver. HV, hepatic vein. (Reproduced with permission from Denault *et al.* [7])

A: https://youtu.be/4ht_VAR0L6U

D: https://youtu.be/WfXqfjGtDtw

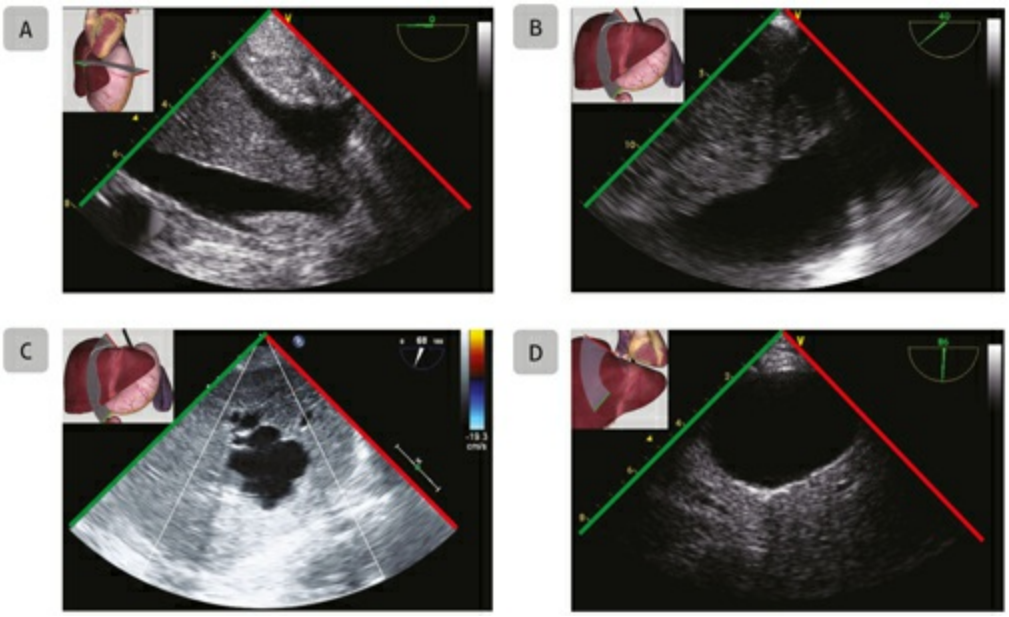

Fig. 4.32 Hepatic pathologies. Transesophageal echo-cardiography images of the liver at various transducer angles show (A) non-complex ascites, (B) irregular liver edge and ascites in a patient with cirrhosis, (C) multiple liver cysts, and (D) a single large liver cyst. The absence of color Doppler flow in (C) confirms the non-vascular nature of anechoic areas suggesting a cyst.

A: https://youtu.be/YNbNYoHTk5w

B: https://youtu.be/BucxjphSyfs

C: https://youtu.be/Q4OdlkO-Mv4

D: https://youtu.be/BCxC6IJTDAg

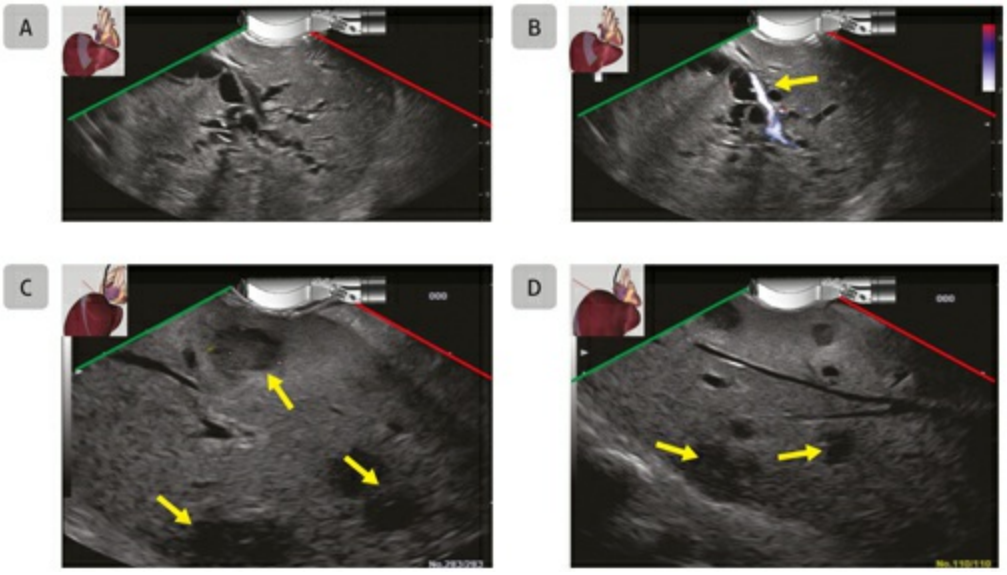

Fig. 4.33 Biliary dilatation and liver metastasis. (A,B) Endoscopic ultrasound views (A) without and (B) with Doppler can help differentiate intrahepatic vessels from the biliary duct. The power Doppler signal (arrow) indicates portal vessels and those areas without a signal are dilated biliary ducts. (C,D) Liver metastasis (arrows) show various heterogeneous aspects and dimensions.

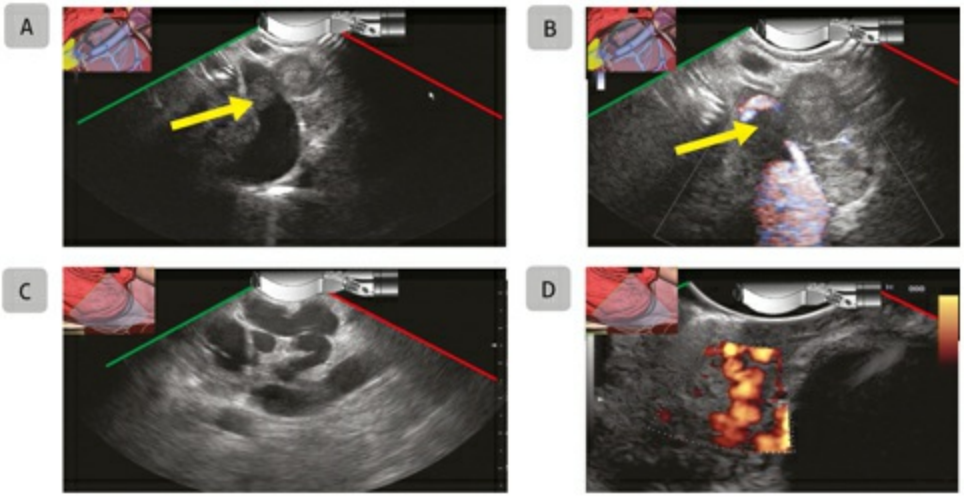

Fig. 4.34 Portal hypertension. (A,B) Endoscopic ultrasound images of the liver show thrombus (arrow) in the extrahepatic portal vein which is confirmed with color Doppler. (C,D) Endoscopic ultrasound image of gastric varices in the stomach fundus, which are confirmed with power color Doppler.

D: https://youtu.be/6vK7gY07mYo

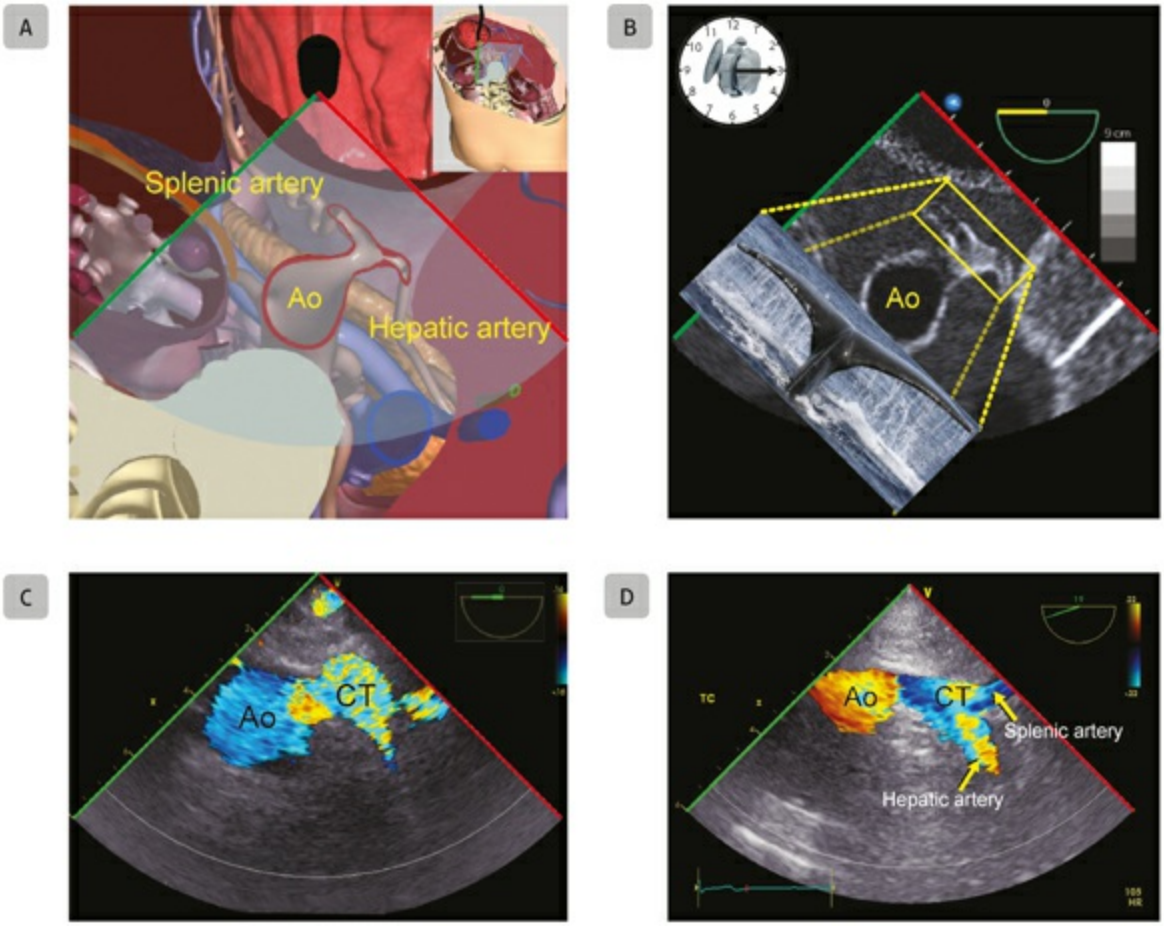

Fig. 4.35 Whale tail sign. (A,B) A mid-gastric view at 6 o'clock using the Vimedix simulator shows the division of the celiac trunk into the hepatic artery (to the right) and the splenic artery (to the left). (C,D) Transesophageal echocardiography transgastric views at 0° with color Doppler (Nyquist 16–22 cm/s) shows the celiac trunk (CT) in relation to the aorta (Ao). Note that the position of the CT in relation to the Ao can vary.

C: https://youtu.be/1cCmTe8TyUE

D: https://youtu.be/OPr3JYbzO3Y

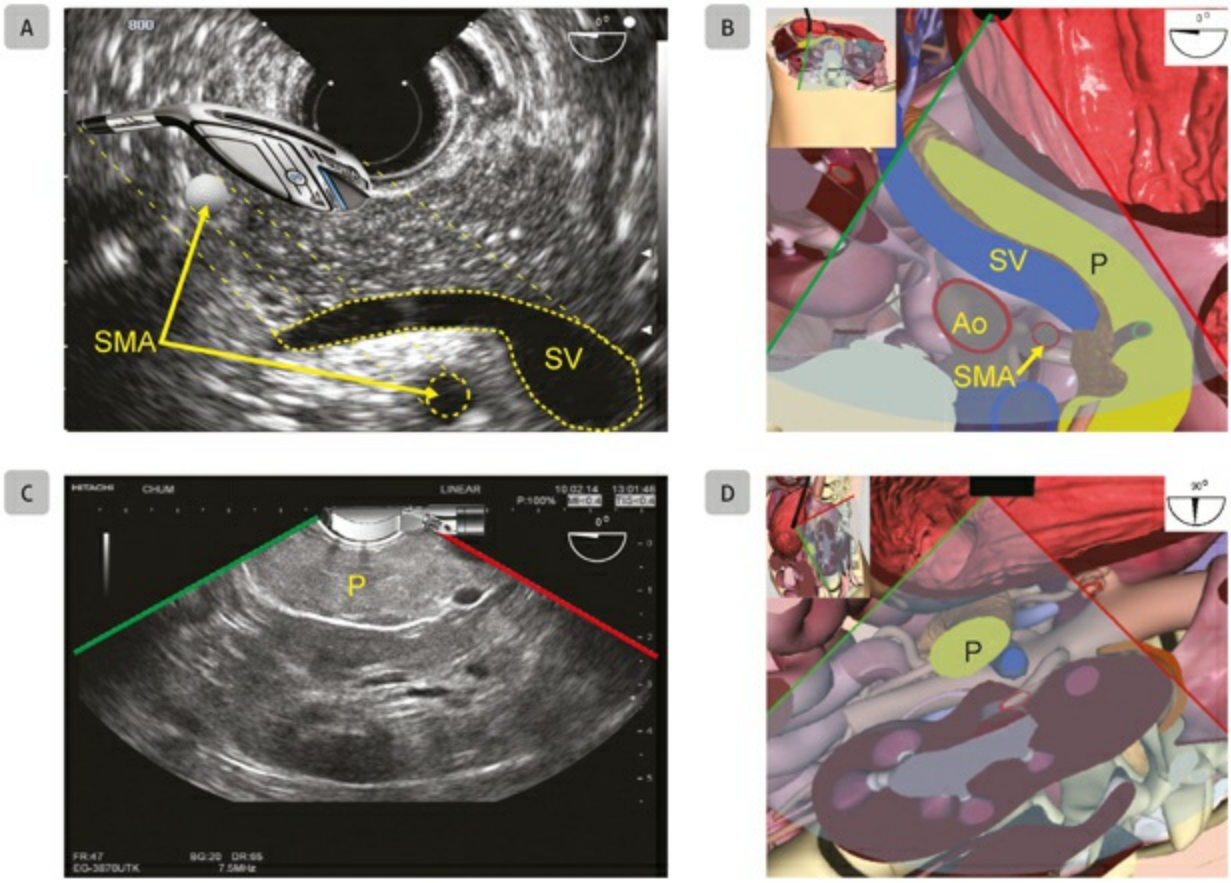

Fig. 4.36 Pancreas. (A, B) Mid-gastric transverse radial endoscopic ultrasound scan shows the golf club and ball sign. The golf club corresponds to the splenic and portal vein confluence. The ball represents the superior mesenteric artery (SMA). Note that the splenic vein (SV) is typically at the lower border of the pancreas. (C) Endoscopic ultrasound longitudinal image shows the body of the pancreas (P). (D) The tail of the pancreas is closely related to the left kidney as shown using the Vimedix simulator. Ao, aorta.

PANCREAS

The pancreas is located behind the stomach. The body is anterior to the aorta, the head is surrounded by duodenum, while the tail ends in the splenic and left kidney hilum. The splenic artery and vein travel along the pancreas, so recognition of those vessels helps to localize the pancreas. The celiac artery trunk is localized at 0° and the two branches, the hepatic artery and splenic artery (whale tail sign) are then identified (**Figure 4.35**). The tortuous splenic artery is then followed, with slight advancement of the probe, until the splenic vein is identified adjacent to it (**Figure 4.36**). The structure between the TEE probe and the splenic vein is the pancreas. Normal pancreatic texture

is isoechoic with dimensions of head (3 cm), body (2–3 cm), and tail (1–2 cm). Once this image is obtained, then the axis of the probe is rotated to 90° and the pancreas is scanned toward the tail (left) and head (right) (**Figure 4.37**). Several Doppler measurements of the celiac trunk, hepatic and splenic artery velocities can be made at this level. Normal splenic vein velocities are monophasic (**Figure 4.38**), but become pulsatile in the presence of right ventricular failure, severe tricuspid regurgitation, and fluid overload (**Figure 4.39**). [19] – [21] **Table 4.2** summarizes the steps used to perform the basic abdominal examination with TEE. There are other abdominal structures, such as small and large bowel, retroperito-neal collections, and gallbladder, that can be visualized in some patients. However, these are less commonly seen and require more experience.

In summary, TEE can be used to easily identify several extracardiac structures. In the following chapters, more examples will be given of this potential new role of extra-cardiac TEE in anesthesia and critical care.

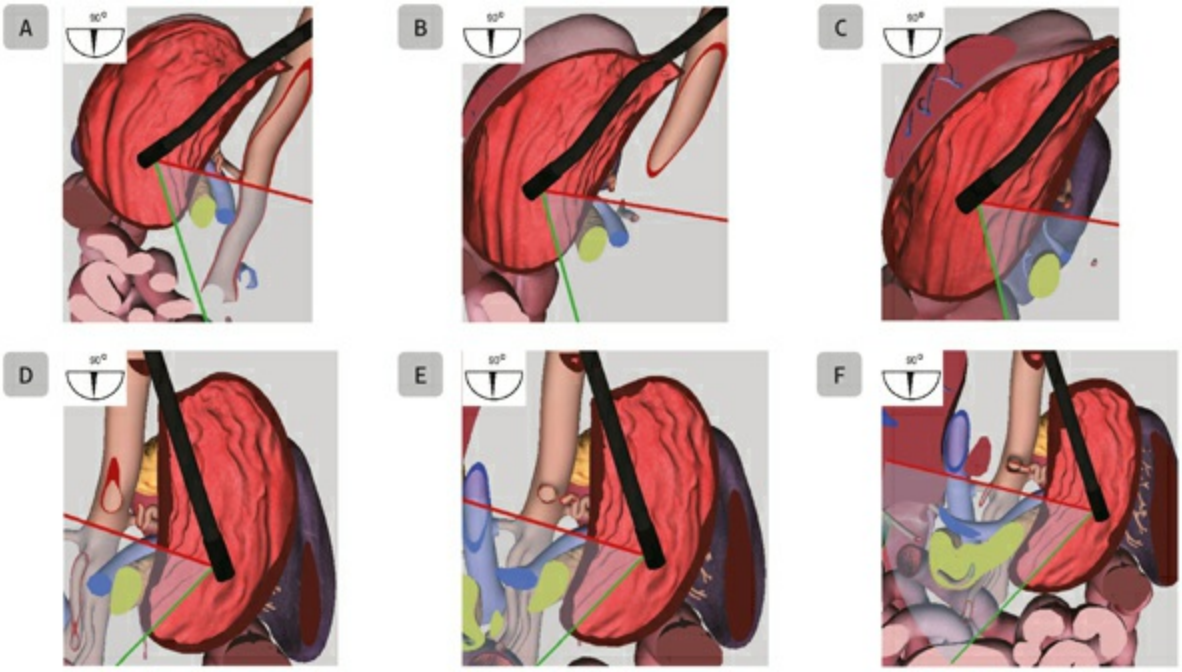

Fig. 4.37 Pancreas examination. Scanning sequence of the pancreas by transesophageal echocardiography is shown using the Vimedix simulator. (A—F) A mid-transgastric view at 90° shows a longitudinal view of the pancreas. (A—C) By scanning in a counterclockwise rotation the body and the tail of the pancreas will be shown. (D—F) In order to see the head of the pancreas, a clockwise rotation is performed.

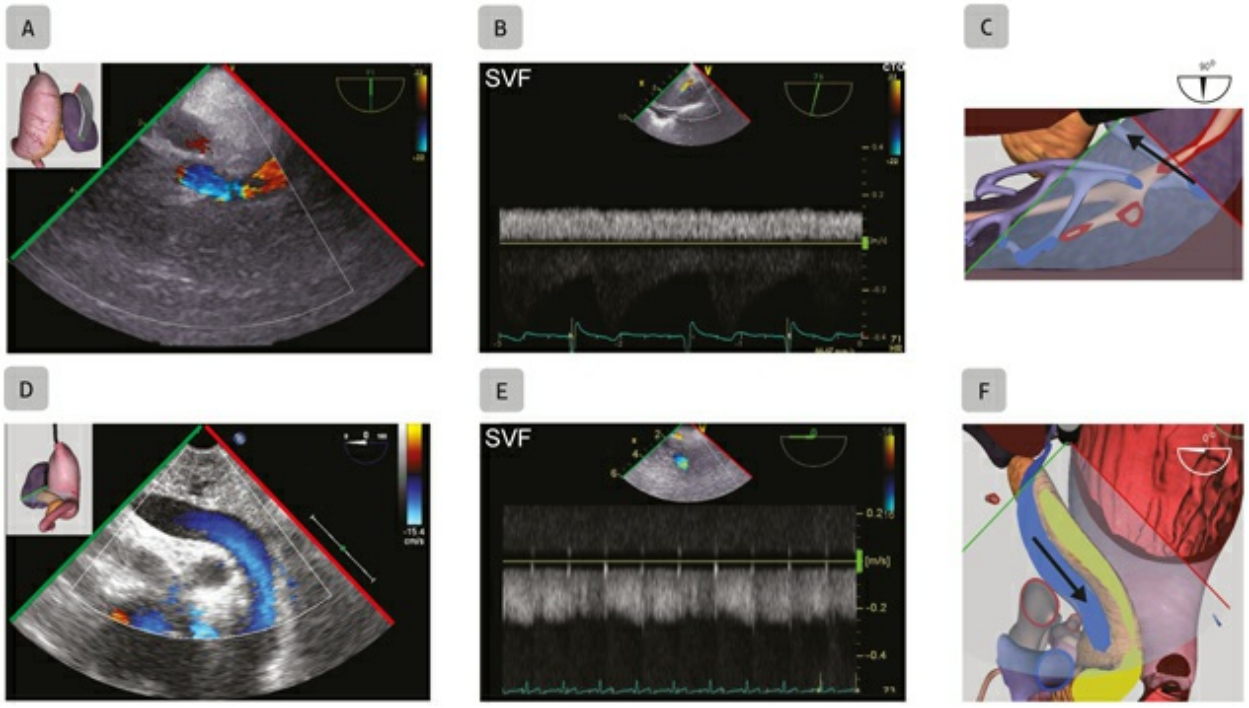

Fig. 4.38 Splenic Doppler flow. (A) Transesophageal echocardiography (TEE) transgastric view at 90° of the spleen with color Doppler (Nyquist 22 cm/s) shows flow in the splenic vessels. (B,C) In this view, a monophasic splenic venous flow (SVF) velocity using pulsed wave spectral Doppler will be seen. Note that the Doppler signal from the splenic hilum is toward the transducer. (D) TEE transgastric view at 0° with color Doppler (Nyquist 15 cm/s) shows flow in the splenic vessels. (E, F) Note that from this transducer position, the Doppler signal is away from the transducer.

A: https://youtu.be/5Nla-NdYe-s

D: https://youtu.be/bgPUDiBb5mU

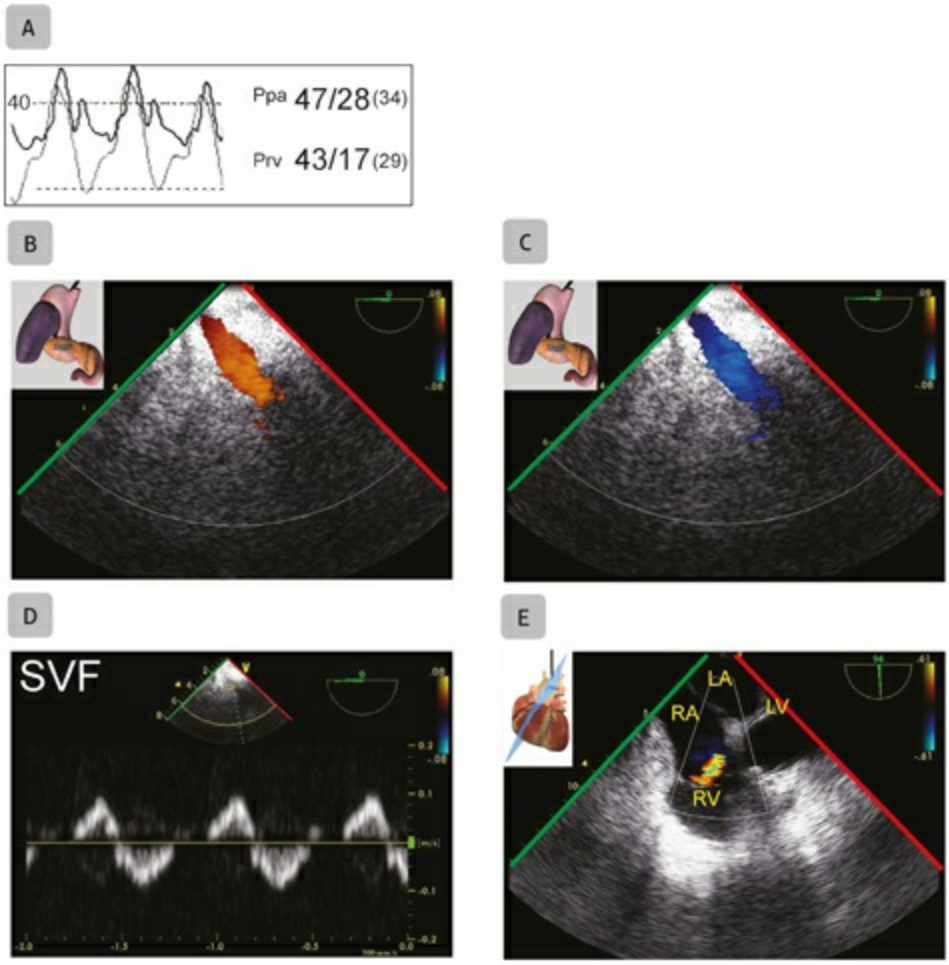

Fig. 4.39 Abnormal splenic venous flow. (A) Right ventricular pressure waveform with a square root sign is indicative of severe right ventricular failure following closure of a ventricular septal defect. (B,C) Transesophageal echocardiography midtransgastric view at 0° with color Doppler (Nyquist 8 cm/s) of the splenic vein shows alternative to and fro splenic venous flow (SVF) which is (D) confirmed in the pulsed-wave signal. (E) This abnormality was associated with only mild tricuspid regurgitation as seen from a mid-esophageal modified right ventricular inflow view. LA, left atrium; LV, left ventricle; RA, right atrium; RV, right ventricle. Ppa, pulmonary artery pressure; Prv, right ventricular pressure.

B: https://youtu.be/kFCuByWTNBo

E: https://youtu.be/q-agdmHP93k

Table 4.2 Steps in Performing TEE Examination of the Abdominal Region.

1.	Use the lowest US probe frequency for distal structures and higher US probe frequency for close structures
2.	Maximize beam width
3.	Start in a TG mid-papillary view (**Figure 4.20A**) at 0° and increase the transducer angle to 90° (**Figure 4.20B**)
4.	Turn the TEE probe to the left until the gastric fundus disappears. The upper pole of the spleen will be seen (**Figure 4.25A**) close to the diaphragm (**Figure 4.24C**) and the kidney will appear (**Figure 4.25B**) as the left-sided rotation continues. Then advance and turn the probe back to the left to complete the examination of the lower portion of the kidney and the lower pole of the spleen. Consider renal (**Figure 4.26**) and splenic Doppler interrogation (**Figure 4.38A–C**)
5.	As the probe is turned to the right, the left lobe of the liver is seen at initially (**Figure 4.20C**). Further beam rotation to the right will expose the subdiaphragmatic portion of the liver (**Figure 4.28**). Advancing the probe with rotation back to the left lobe of the liver will allow examination of a more caudal portion of the liver
6.	Find the thoracic aorta at a transducer angle of 0°. Advance the TEE probe until the celiac truck, hepatic artery, and splenic artery are identified (**Figure 4.35**). Follow the splenic artery back to the left and advance the probe further until the splenic vein is identified (**Figure 4.36**). Consider Doppler interrogation of the splenic vein (**Figure 4.38D–F**)
7.	The pancreas is then localized (**Figure 4.36**) and with a transducer angle at 90° analyzed toward the tail by left-sided probe rotation and toward the head by right-sided probe rotation (**Figure 4.37**)

TEE, transesophageal echocardiography; TG, transgastric; US, ultrasound.

REFERENCES

1. FrazinL., TalanoJ.V., StephanidesL., LoebH.S., KopelL., GunnarR.M.. 1976. Esophageal echocardiography. *Circulation*. *54*:1028.
2. VolpicelliG., ElbarbaryM., BlaivasM., LichtensteinD.A., MathisG., KirkpatrickA.W., et al. 2012. International evidence-based recommendations for point-of-care lung ultrasound. *Intensive Care Med*. *38*:577–91.
3. HawesR.H., FockensP., VaradarajuluS.. 2015. *Endosonography*. 3rd ed. Philadelphia, PA: Saunders/Elsevier.
4. VerhaeghenD., PoelaertJ., AmaR., RoosensC., TempeD.K., ChaneyM.A.. 2005. Case 2–2005: evaluation of the lungs via transesophageal echocardiography. *J Cardiothorac Vasc Anesth*. *19*:242–9.
5. DenaultA.Y., LamarcheY., RochonA., DeschampsA.. 2014. Innovative approaches in the perioperative care of the cardiac surgical patient in the operating room and the intensive care unit. *Can J Cardiol*. *30*:S459–77.
6. DenaultA.Y., CoutureP., TardifJ.C., BuithieuJ.. 2005. *Transesophageal Echocardiography Multimedia Manual: A Perioperative Transdisciplinary Approach*. New York, NY: Marcel Dekker.
7. DenaultA.Y., CoutureP., VegasA., BuithieuJ., TardifJ.C.. 2011. *Transesophageal Echocardiography Multimedia Manual, Second Edition: A Perioperative Transdisciplinary Approach*. New York, NY: Informa Healthcare.
8. BoseR.R., MatyalR., WarraichH.J., SummersJ., SubramaniamB., MitchellJ., et al. 2011. Utility of a transesophageal echocardiographic simulator as a teaching tool. *J Cardiothorac Vasc Anesth*. *25*:212–5.

9. LichtensteinD.. 2002. *General Ultrasound in the Critically Ill*. Heidelberg: Springer-Verlag.
10. MathisG.. 2011. *Chest Sonography*. 3rd ed. Heidelberg: Springer- Verlag.
11. DelageDenault A., Chartrand-LefebvreK., BussierèsJ.2013. *Transoesophageal Echocardiography and the Respiratory System*. Melbourne: University of Melbourne Ultrasound Education Group.
12. MountainC.F., DreslerC.M.. 1997. Regional lymph node classification for lung cancer staging. *Chest*. *111*:1718–23.
13. DetterbeckF.C., PostmusP.E., TanoueL.T.. 2013. The Stage Classification of Lung Cancer: Diagnosis and Management of Lung Cancer, 3rd edn: American College of Chest Physicians evidence-based clinical practice guidelines. *Chest*. *143*:e191S–210S.
14. JakobH., LorenzJ., ClementT., BornerN., SchwedenF., ErbelR., et al. 1990. Mediastinal lymph node staging with transesophageal echography in cancer of the lung. *Eur J Cardiothorac Surg*. *4*:355–8.
15. DenaultA., DeschampsA., MurkinJ.M.. 2007. A proposed algorithm for the intraoperative use of cerebral near-infrared spectroscopy. *Semin Cardiothorac Vasc Anesth*. *11*:274–81.
16. BandyopadhyayS., KumarD.R., PaulA., SundarB.K., RoyD.. 2013. A transesophageal echocardiography technique to locate the kidney and monitor renal perfusion. *Anesth Analg*. *116*:549–54.
17. RoyseC.F., BirdH., RoyseA.G.. 2009. Routine assessment of coeliac axis and renal artery flow is not feasible with transoesophageal echocardiography. *Anaesthesia*. *64*:103–4.
18. ZabalaL., UllahS., PierceC.D., GautamN.K., SchmitzM.L., SachdevaR., et al. 2012. Transesophageal Doppler measurement of renal arterial blood flow velocities and indices in children. *Anesth Analg*. *114*:1277–84.
19. CatalanoD., CarusoG., DiFazzioS., CarpinteriG., ScalisiN., TrovatoG.M.. 1998. Portal vein pulsatility ratio and heart failure. *J Clin Ultrasound*. *26*:27–31.
20. RengoC., BrevettiG., SorrentinoG., D'AmatoT., ImparatoM., VitaleD.F., et al. 1998. Portal vein pulsatility ratio provides a measure of right heart function in chronic heart failure. *Ultrasound Med Biol*. *24*:327–32.
21. HaddadF., Elmi-SarabiM., FadelE., MercierO., DenaultA.Y.. 2016. Pearls and pitfalls in managing right heart failure in cardiac surgery. *Curr Opin Anaesthesiol*. *29*:68–79.

Chapter 5

Assessment of Global Ventricular Function, Pericardium, and Cardiomyopathy

Gordon Finlayson and Vinay Dhingra

INTRODUCTION

Hemodynamic instability in the intensive care unit (ICU) may result from several etiologies, including major cardiac dysfunction. Acute ventricular dysfunction may be seen in a variety of acute critical care settings, such as myocardial ischemia, sepsis, trauma, subarachnoid hemorrhage, post-operative, and both hypothermia, and burn injury. [1] – [4] Transesophageal echocardiography (TEE) provides valuable insight into left ventricular (LV) and right ventricular (RV) dysfunction, myocardial infarction, significant pericardial and valvular heart disease (see Chapter 7, Basic Valve Diseases). Transesophageal echocardiography is generally considered superior to transthoracic echocardiography (TTE) in the ICU for interrogating ventricular function because of the improved quality of the image. This chapter will focus on the evaluation of global ventricular function, pericardial disorders, and cardiomyopathies, including their specific imaging pitfalls.

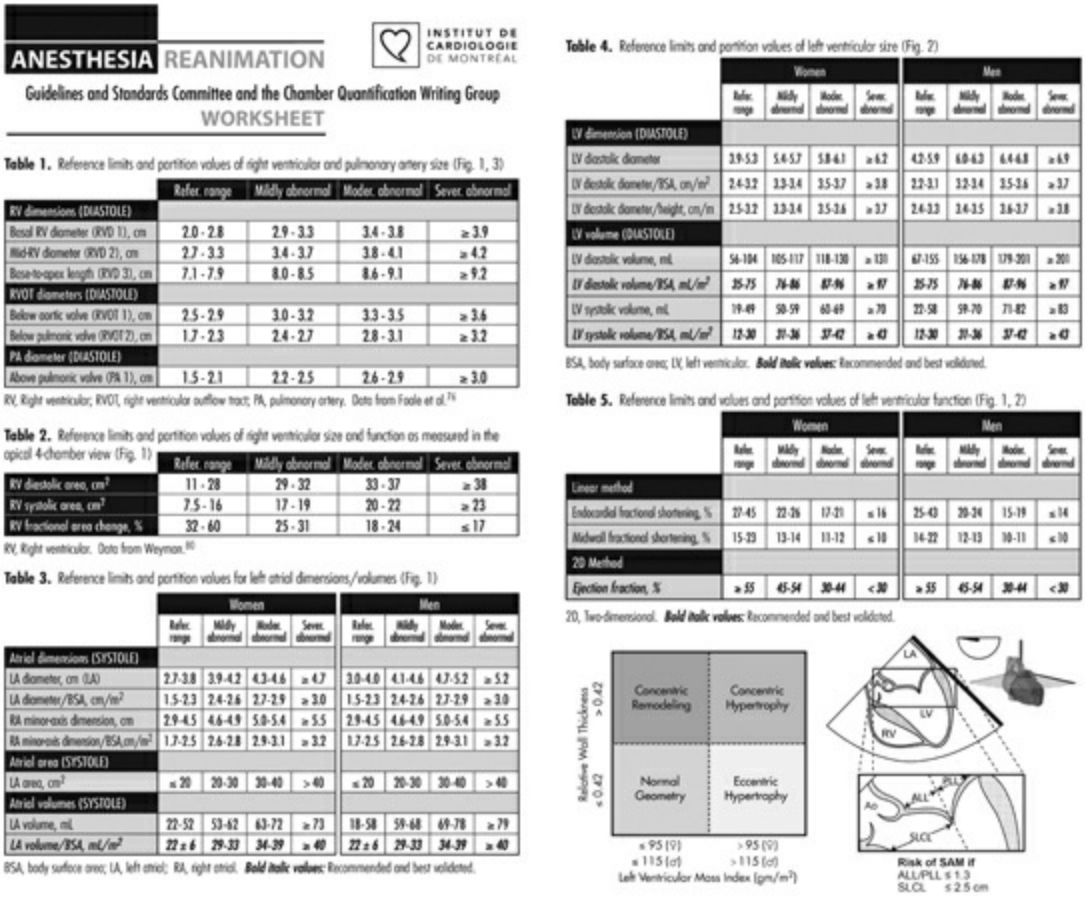

Fig. 5.1 Pocket cards. At the Montreal Heart Institute, handy pocket cards for chamber quantification, ventricular mass, and risk of systolic anterior motion of the anterior mitral valve leaflet have been developed. (Adapted from Lang *et al*. [5]).

LEFT AND RIGHT VENTRICULAR DIMENSIONS

The first step when evaluating ventricular function is to determine if the cardiac cavity dimensions are within the normal range. Guidelines for the quantification of LV and RV size and function have been published. [5] – [7] Pocket cards (**Figure 5.1**) and web-based applications (asecho.org) can be helpful reminders during the evaluation of these measurements. Ideally, measurements should be indexed to body surface area (BSA) (**Figure 5.2**). The key TEE measurements are summarized in **Figure 5.3**. Important measurements are LV dimension, which can be obtained in mid-esophageal (ME) two- and four-chamber views or transgastric (TG) two-chamber view at

90° (**Figure 5.3 A**), LV wall thickness (**Figure 5.3 B**), RV dimensions (**Figure 5.3 C**), RV outflow tract dimensions (**Figure 5.3 D**), and atrial dimensions (**Figure 5.3 E**). Measurement of LV dimension and thickness allows calculation of LV mass, which more precisely determines the presence of LV hypertrophy (**Figure 5.4**). Details for other measurements can be found in recent guidelines by Lang *et al.* [5] and specialized textbooks. [8] Volume measurements are much more precise than 2D measurements, but these require either specialized equipment such as 3D echocardiography or mathematical estimations that are beyond the basic TEE evaluation.

LEFT VENTRICLE SYSTOLIC FUNCTION

Global ventricular function is fundamental for the generation of cardiac output (CO) and can be systematically studied with TEE utilizing 2D, M-mode, and Doppler techniques. The systolic pumping of the LV involves the coordinated contraction of helically arranged muscle fibers of the myocardium, which displace blood and generate the stroke volume (SV). The heart contracts in systole using three movements: (1) base to apex longitudinal shortening of the subendocardium; (2) radial thickening inwards around the long axis of the subepicardium; and (3) circumferential torsion of the base clockwise and the apex counterclockwise. The contractile state of the heart is best described by the end-systolic pressure-volume relationship, which is a relatively load-independent measure of LV contractility (see **Figure 9.4)**. However this relationship is difficult to use in clinical practice and consequently, the assessment of global ventricular function must rely on the evaluation of its determinants, which are preload, contractility, and afterload.

Preload

Preload is the force that stretches the myocardium and is not directly measured but estimated using LV end-diastolic diameter (LVEDD) or volume (LVEDV). Preload affects the initial fiber length and therefore the LV systolic performance via the Frank-Starling mechanism. Echocardiographic correlates of reduced preload include a decrease in LV end-diastolic area (LVEDA), the so-called end systolic cavitary obliteration (**Figure 5.5**). Other signs of reduced preload include the change in diameter

of both the inferior vena cava (IVC) (**Figure 5.6**) and superior vena cava (SVC) (**Figure 5.7)** during respiration (**Table 5.1**). [9] − [11] Preload can also be estimated by the behavior of the atrial septal motion during positive pressure ventilation. The presence of expiratory mid-systolic reversal is associated with a pulmonary capillary wedge pressure (PCWP) <15 mmHg, while when present during all respiratory phases the PCWP is <10 mmHg. [12] A recent study showed that the best predictor of raised PCWP is a fixed curve pattern of the atrial septum. [13]

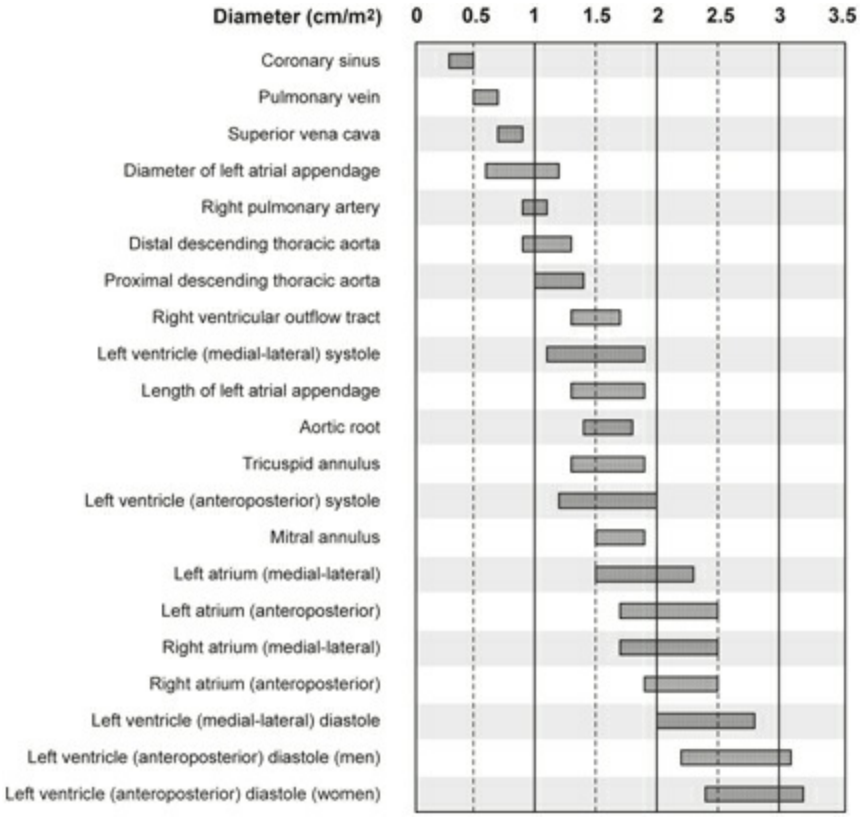

Fig. 5.2 Transesophageal echocardiography (TEE) reference values. The dimensions of cardiac structures indexed to body surface area as measured using TEE are shown. (Reproduced with permission from Denault *et al.* [8] *).*

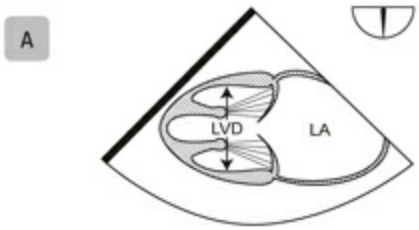

Normal value for 2D LV chamber size

LV internal dimension	Men		Women	
	Mean ± SD	2-SD range	Mean ± SD	2-SD range
Diastolic dimension (mm)	52.2 ± 4.1	42.2 ± 58.4	45.0 ± 3.6	37.8 ± 52.2
Systolic dimension (mm)	32.4 ± 3.7	25.0 ± 39.8	28.2 ± 3.3	21.6 ± 34.8

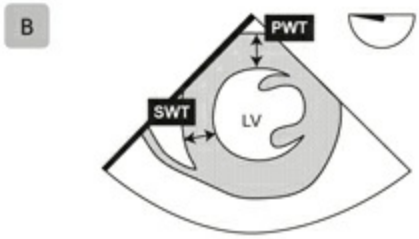

Normal range for LV mass indices

Linear method	Women	Men
Septal wall thickness (cm)	0.6 - 0.9	0.6 - 1.0
Posterior wall thickness (cm)	0.6 - 0.9	0.6 - 1.0

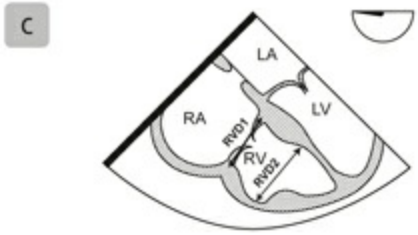

Normal value for 2D RV chamber size

Parameter	Mean ± SD	Normal range
RVD1 (mm)	33 ± 4	25 - 41
RVD2 (mm)	27 ± 4	19 - 35
RV wall thickness (mm)	3 ± 1	1 - 5

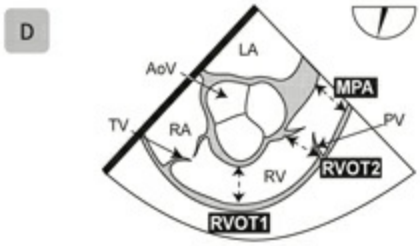

Normal value for 2D RV chamber size

Parameter	Mean ± SD	Normal range
RVOT1 (mm)	28 ± 3.5	21 - 35
RVOT2 (mm)	22 ± 2.5	17 - 27
MPA (mm)	21 ± 3	11 - 31

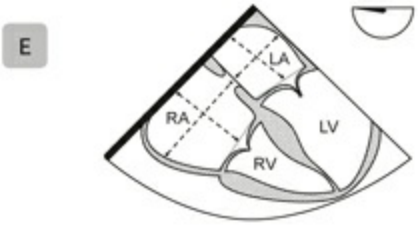

Normal value for RA and LA size

RA size	Women	Men
RA minor axis dimension (cm/m²)	1.9 ± 0.3	1.9 ± 0.3
RA major axis dimension (cm/m²)	2.5 ± 0.3	2.4 ± 0.3
2D echocardiographic RA volume (mL/m²)	21 ± 6	2.4 ± 7
LA size		
AP dimension (cm)	2.7 - 3.8	3.0 - 4.0
AP dimension index (cm/m²)	1.5 - 2.3	1.5 - 2.3
4C area index (cm²/m²)	9.3 ± 1.7	8.9 ± 1.5
2C area index (cm²/m²)	9.6 ± 1.4	9.3 ± 1.6
4C volume index MOD (mL/m²)	25.1 ± 7.2	24.5 ± 6.4
4C volume index AL (mL/m²)	27.3 ± 7.9	27.0 ± 7.0
2C volume index MOD (mL/m²)	26.1 ± 6.7	27.1 ± 7.9
2C volume index AL (mL/m²)	28.0 ± 7.3	28.9 ± 8.5

Fig. 5.3 Basic transesophageal echocardiography (TEE) measurements. (A) Left ventricular minor-axis diameter (LVD) at end diastole is obtained from a transgastric (TG) two-chamber (2C) view of the left ventricle (LV) at 90°-110° with corresponding normal dimensions. (B) Wall thickness of the LV is obtained using septal wall thickness (SWT) and posterior wall thickness (PWT) from a TG mid short-axis view at 0° at end diastole. Table of normal and abnormal values (in cm) for wall thickness is shown. (C) TEE measurements, at end diastole, of various right ventricular diameters (RVD) obtained from a mid-esophageal four-chamber (4C) view optimized to the maximum right ventricular (RV) size by varying angles 0°-20°. The table shows normal and abnormal values for RVD1, RVD2. (D) TEE

measurements, at ventricular end-systole, of the right atrium (RA) and left atrium (LA) from the mid-esophageal 4C view optimally positioned to visualize both chambers. Table of normal and abnormal values for atrial dimensions and volumes as absolute values and indexed to body surface area (BSA). (E) TEE measurements, during end diastole, of the RVOT at two levels (RVOT1, RVOT2) and the MPA from the mid-esophageal right ventricular inflow/outflow view. The normal and abnormal absolute values (in cm) are presented. AL, area-length method; AoV, aortic valve; AP, anteroposterior; MOD, modified Simpson's rule; MPA, main pulmonary artery; PV, pulmonic valve; RVOT, right ventricular outflow tract; SD, standard deviation; TV, tricuspid valve. (Adapted from Lang *et al.* [5] , [6] *;* reproduced with permission from Denault *et al.* [8]).

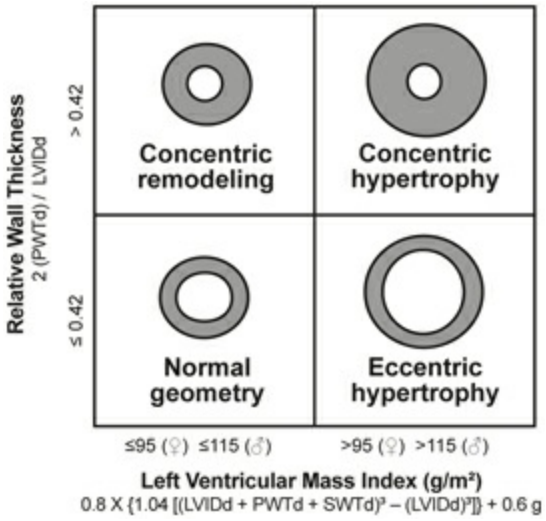

Fig. 5.4 Left ventricle (LV) hypertrophy. Classification of LV hypertrophy is based on the relative wall thickness (RWT) and LV mass. Patients with normal LV mass can have either concentric remodelling (increased RWT >0.42) or normal geometry (RWT <0.42). Patients with increased LV mass can have either concentric (RWT >0.42) or eccentric (RWT <0.42) hypertrophy. These LV mass measurements are based on linear measurements made at end-diastole. g, gram; LVIDd, left ventricular internal diameter in diastole; m, meter; PWTd, posterior wall thickness in diastole; SWTd, septal wall thickness in diastole. (Reproduced with permission from Denault *et al.* [8] *).*

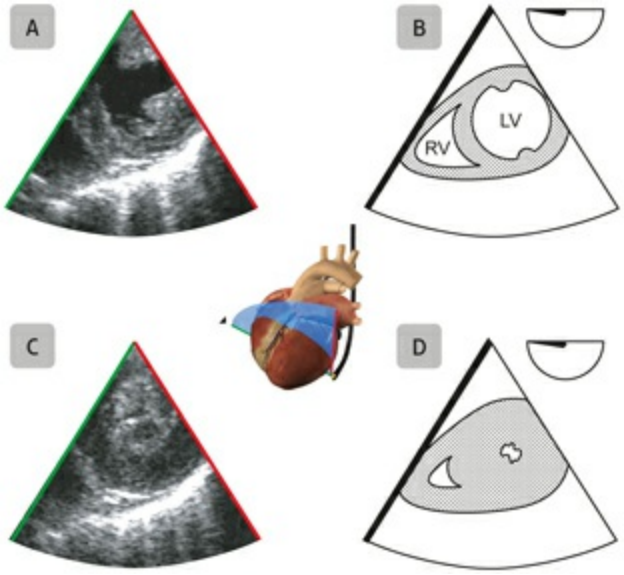

Fig. 5.5 Preload. Left ventricular end systolic cavitary obliteration in an hypovolemic patient with reduced preload on the transgastric mid short- axis views during (A,B) diastole and (C,D) systole. LV, left ventricle; RV, right ventricle. (Reproduced with permission from Denault *et al*. [8]).

A&C: https://youtu.be/DGhxHKrILMQ

Contractility

Contractility represents the inherent strength of the heart muscle in generating pressure independently of the loading conditions. In critically ill patients, LV dysfunction may be due to poor loading conditions, reduction in contractility, or both. Since there are no easily available, completely load-independent indices of basal contractile states, serial assessment of LV function during hemodynamic interventions in the critically ill may be helpful. [4] , [8 – 10] , [14] The LV systolic function is best assessed visually using TEE from the ME four-chmber, two-chamber, and long-axis (LAX) views and the TG two-chamber, basal, and mid short-axis (SAX) views. Contractile function is frequently assessed using the left ventricular ejection fraction (LVEF), LV or RV fractional area change (FAC), and CO measurements. Other less commonly used techniques include fractional shortening, mitral annular motion, myocardial performance index, and pressure volume curves [6] , [8] , [15] , [16] .

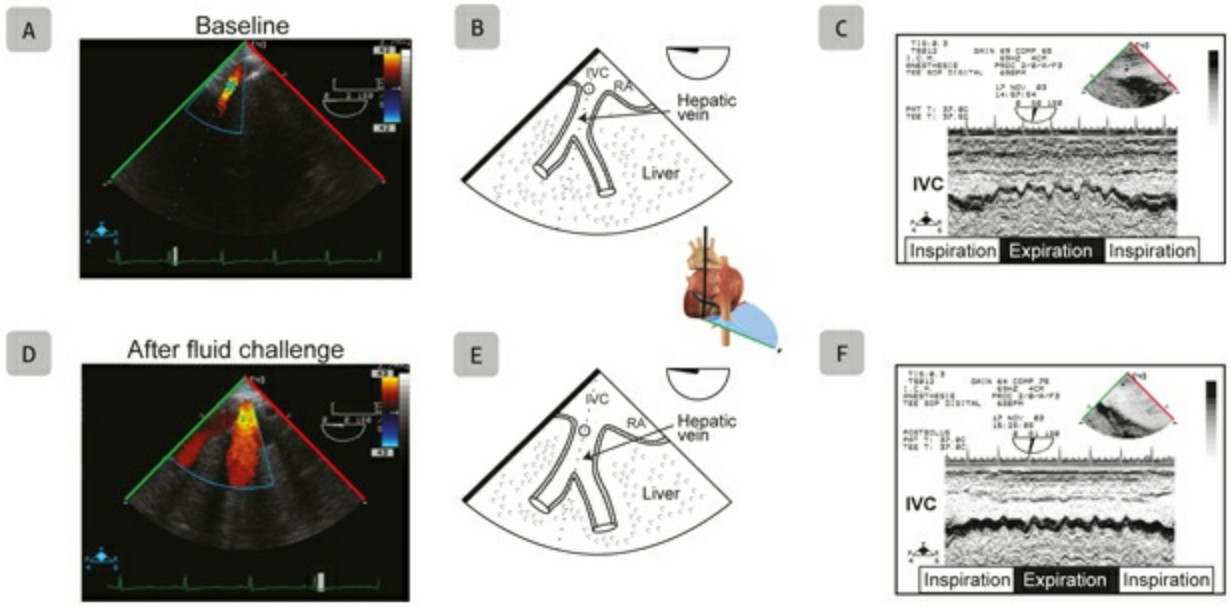

Fig. 5.6 Preload. Reduced preload from hypovolemia as evidenced by both (A,B) a reduced size in the inferior vena cava (IVC) and hepatic veins, as well as (C) collapse with expiration during mechanical ventilation using M-mode. Following a fluid challenge (D, E) both the size of the IVC and hepatic veins enlarge and there is (F) a decrease in IVC collapsibility on M-mode. RA, right atrium. (Reproduced with permission from Denault *et al.* [8]).

A&D: https://youtu.be/YAf-drYfR_4

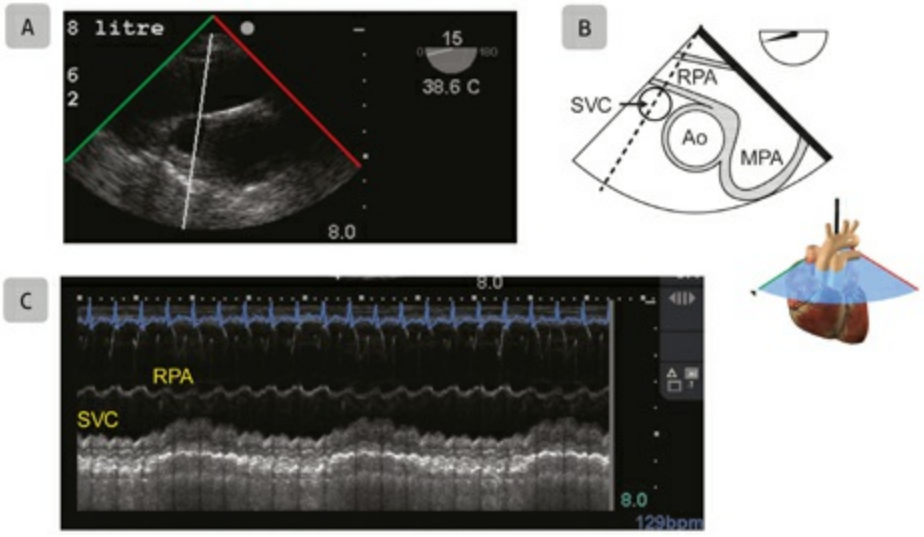

Fig. 5.7 Respiratory variation of the superior vena cava (SVC). (A,B) Mid-esophageal ascending Ao short-axis view in a 76-year-old male in the intensive care unit after removal of 1.8 liters with dialysis is shown. (C) Using M-mode, significant respiratory variation of the diameter of the SVC was present. Ao, aorta; MPA, main pulmonary artery; RPA, right pulmonary artery. (Reproduced with permission from Denault *et al.* [8]).

A: https://youtu.be/KHhd3Rst2Rw

C: https://youtu.be/7oh-bCwhKGE

Table 5.1 Echocardiographic Estimation of RAP or CVP.

Size of IVC (cm)	Collapse with sniffing (%)	Suggested RAP (mmHg)
≤2.1	>50	0–5
≤2.1	<50	5–10
>2.1	>50	5–10
>2.1	<50	>15
Other indices RAP >15	Restrictive TTF filling Tricuspid E/e' >6 HVF S/D <1	

CVP, central venous pressure; D, diastolic HVF velocity; E, early filling; é, peak early diastolic mitral; HVF, hepatic venous flow; IVC, inferior vena cava; RAP, right atrial pressure; S, systolic HVF velocity; TTF, transtricuspid flow. Adapted from Rudski *et al.* [7].

Ejection Fraction

The LVEF is the most widely used measure of systolic function. It is often assumed to purely reflect ventricular contractility, but it remains load dependent. The normal LVEF is between 63% and 69% using 2D echocardiography. [6], [17] Abnormal values between 40% and 50% are usually

of little clinical significance unless combined with significant mitral regurgitation (MR) or increased oxygen delivery needs. The ejection fraction (EF) is defined as the SV divided by the LVEDV.

EF = EDV - ESV EDV

The LVEF is obtained using systolic and diastolic ventricular volumes from the ME four- and two-chamber views using one of several formulae, such as the Simpson's biplane method of discs (**Figure 5.8**).

Stroke volume is determined by obtaining the volume of a cylinder of blood (cm^3) passing through the area of interest. The area is assumed to be circular and is calculated by obtaining the diameter (D) of the LVOT (at the level of aortic annulus) in the ME aortic valve LAX view. In some patients, the LVOT might not be circular but oval in shape and the use of perpendicular views might give more accurate measurements. The MPA area at the ME ascending aorta SAX view can also be used. The VTI is obtained using pulsed-wave (PW) Doppler sample volume placed at the LVOT in either the deep TG or TG LAX views or at the MPA in the ME ascending aorta SAX view, respectively (**Figure 5.10**). [6] , [15 – 18]

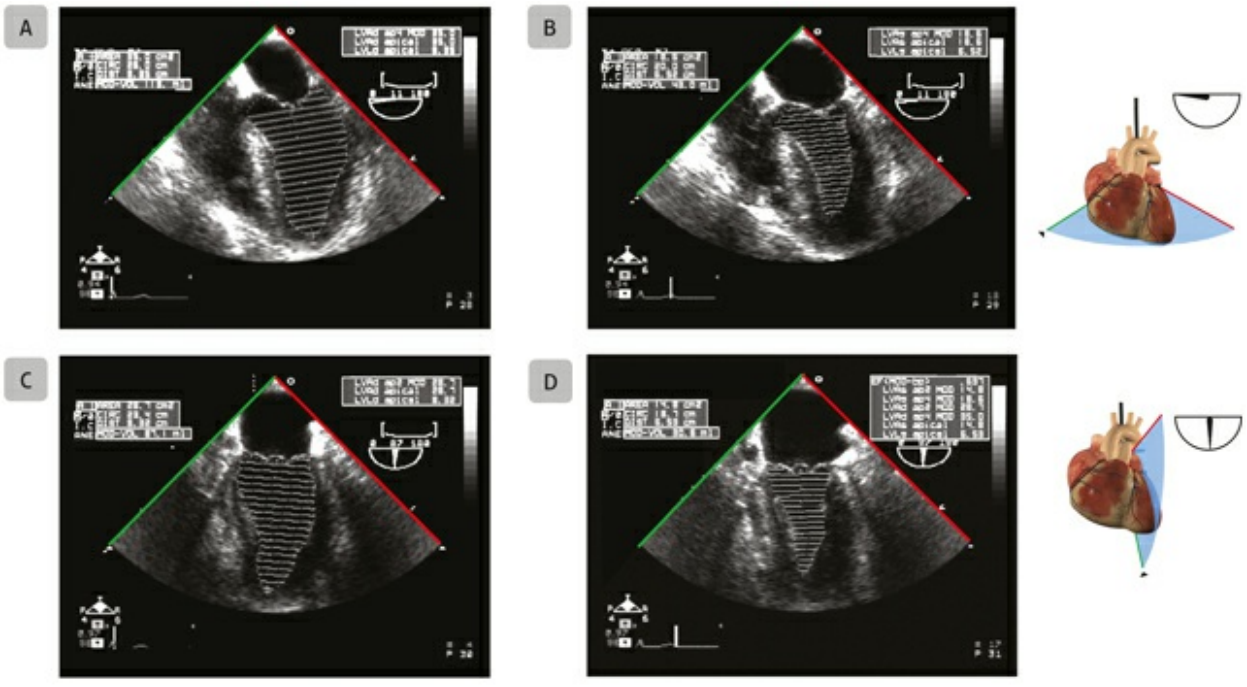

E

Normal ranges and severity partition cutoff values for 2D derived LVEF

Parameter		Normal range	Mildly abnormal	Moderately abnormal	Severely abnormal
LVEF (%)	Male	52 - 72	41 - 51	30 - 40	< 30
	Female	54 - 74	41 - 53	30 - 40	< 30

Fig. 5.8 Ejection fraction. (A—D) Simpson's biplane method for calculating volumetric ejection fraction using end diastolic and systolic area and volume changes in the mid-esophageal two- and four-chamber views on transesophageal echocardiography. (E) Normal values for left ventricular ejection fraction (LVEF) are shown. [6] 2D, 2-dimensional. (Reproduced with permission from Denault *et al.* [8] *).*

The FAC is the percentage change in the end-diastolic area (EDA). It is expressed as:

FAC = (EDA - ESA) / EDA × 100

Fractional area change is measured by tracing the endocardium, excluding the papillary muscles, by either manual or automated border detection methods in the TG SAX view (**Figure 5.9**). The normal values are 40% at the base, 50% at the mid-papillary and 60% at the apical levels. Fractional area change can have good correlation with the LVEF, although regional wall motion abnormalities impair this correlation.

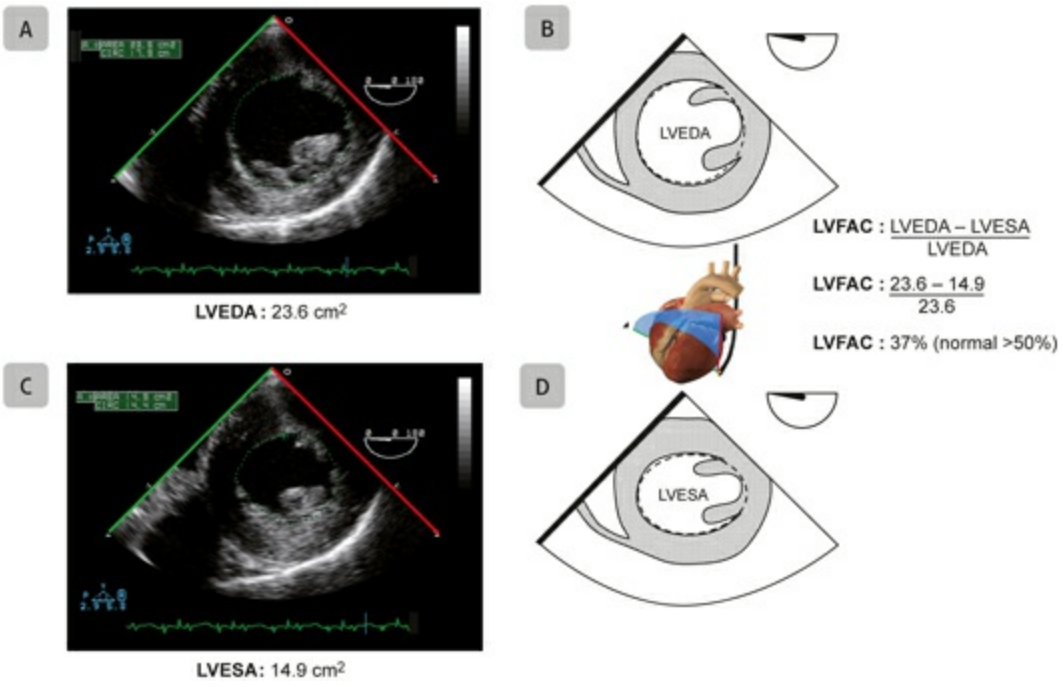

Fig. 5.9 Fractional area change. A 75-year-old male with unstable angina is undergoing emergency revascularization. Transgastric mid short-axis views of the left ventricle in (A,B) diastole and (C,D) in systole provide the measurements to calculate the fractional area change, which was 37%. Note exclusion of the papillary muscles during tracing of the areas. LVEDA, left ventricle end-diastolic area; LVESA, left ventricle end- systolic area; LVFAC, left ventricle fractional area change. (Reproduced with permission from Denault *et al.* [8]).

A&C: https://youtu.be/EcgoeiNoPW8

Cardiac output can be obtained with 2D or more often with Doppler techniques using the velocity time integral (VTI) as blood exits the heart. Generally measured references on the left side are the left ventricular outflow tract (LVOT) and on the right side the main pulmonary artery (MPA) (**Figure 5.10**). The CO is calculated as the product of SV and heart rate (HR).

$$CO = SV \times HR$$

$$SV = \pi D 2 2 \times VTI$$

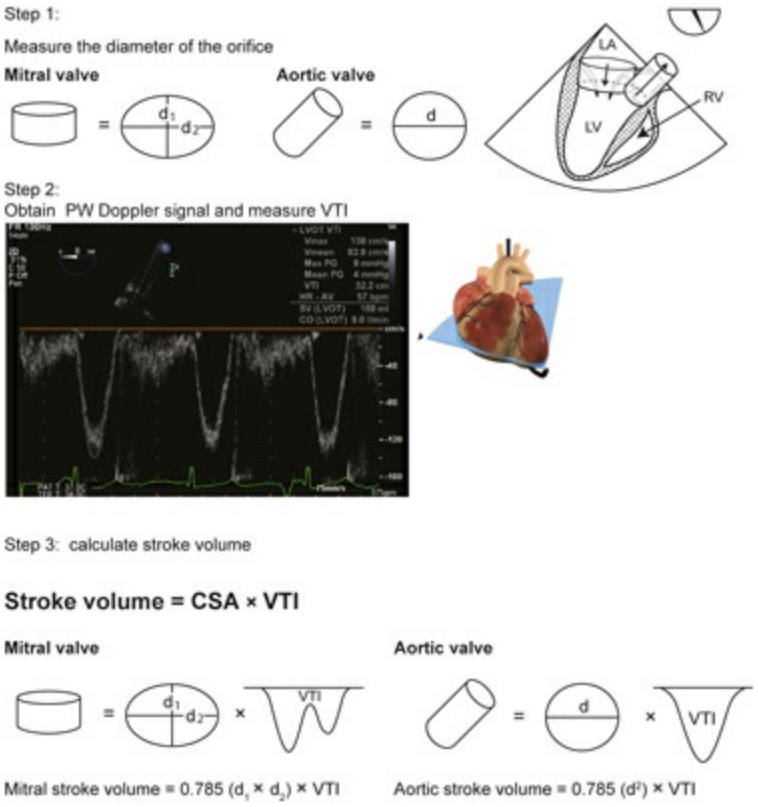

Fig. 5.10 Cardiac output. Steps are shown for the measurement of cardiac output using pulsed-wave (PW) Doppler through the mitral or aortic valves. CSA, crosssectional area; d, diameter; LA, left atrium; LV, left ventricle; RV, right ventricle; VTI, velocity time integral. (Adapted with permission from Denault *et al.* [8]*).*

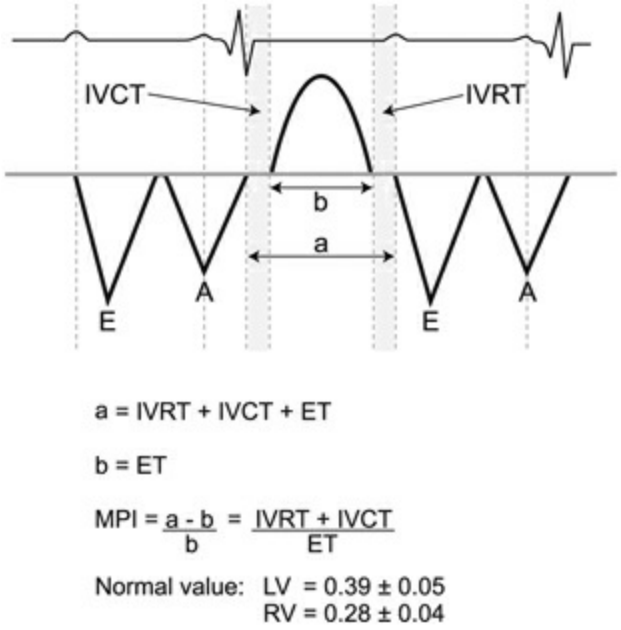

Fig. 5.11 Myocardial performance index (MPI). To calculate the MPI or Tei index of the left ventricle (LV), the transmitral flow (TMF) is used for measurement of the duration "a" from the end of atrial contraction (A-wave) to the beginning of LV filling (E-wave). The ejection time (ET) or "b" is measured from a deep transgastric long-axis view Doppler interrogation of the LV outflow tract. The MPI of the right ventricle (RV) is similarly obtained using the transtricuspid flow and the mid-esophageal ascending aorta short-axis view for the RV outflow tract. A, peak late diastolic TMF velocity; E, peak early diastolic TMF velocity; IVCT, isovolumic contraction time; IVRT, isovolumic relaxation time. (Reproduced with permission from Denault *et al.* [8]*).*

Other Methods

Mitral annulus motion is another method used to assess LV systolic function. This primarily reflects shortening along the major axis of the heart and is measured in the four-chamber view with the ultrasound beam parallel to the mitral annulus. A value of 12 ± 2 mm is considered normal and a motion of <8 mm correlates to an EF <50%. The myocardial performance index or Tei index is another modality that can evaluate both global systolic and diastolic ventricular function. It requires PW Doppler with systolic and diastolic time interval measurements (**Figure 5.11**). [6] , [8] , [15] , [19]

Wall Stress

Left ventricular wall stress is an important mechanical property. In a spherical model of the LV using the law of Laplace, wall stress (σ) is directly proportional to the transmural pressure (P) and the chamber radius (R) and inversely proportional to two times the wall thickness (Th).

$\sigma = PR / 2\ Th$

Multiple methods exist for using non-invasive techniques to ascertain Left ventricular systolic pressure but the simplest is to use the peak systolic arterial blood pressure. Left ventricular afterload is approximated by the end-systolic wall stress calculated using systolic blood pressure and end-systolic dimensions, but this index is rarely used in everyday practice.[20–22]

RIGHT VENTRICULAR SYSTOLIC FUNCTION

Dysfunction of the RV can be primarily ischemic or secondarily from pulmonary disease or LV dysfunction. The triangular shape of the RV makes global function difficult to quantitate with TEE.[7,8,23] Quantitative measurements of RV size and mass remain unreliable with high interobserver variability. Qualitative RV assessment of size uses the ME four-chamber and TG SAX views. The RV should be less than two-thirds of the LV size and should not share the apex in the ME four-chamber view. In the TG SAX view, the RV appears crescentic in shape, smaller in size than the LV, and with the interventricular septum bowing into the RV, such that the LV has circular geometry throughout the cardiac cycle (**Figure 5.12**).[7] The RV systolic function can be estimated using the tricuspid annular plane systolic excursion (TAPSE).[7,24–26] This is a measurement of the movement of the lateral tricuspid valve annulus toward the apex. Alignment is best in an apical four-chamber with TTE, although anatomical M-mode can be used with TEE in a ME four-chamber view (**Figure 5.13**). Tricuspid annular plane systolic excursion correlates to the RVEF as assessed by radionuclide angiography (**Table 5.2**) and has been validated against biplane Simpson's RVEF.[7,24,25] In general, a TAPSE <17 mm has a high specificity but low sensitivity for RV dysfunction. The main advantage is that TAPSE is a simple rapid test but underestimates the complexities of RV structure and is a load-dependent measurement.[7] Doppler assessment of the myocardial performance index or Tei index (**Figure 5.11**) or tissue Doppler (may also be employed to assess RV systolic function.

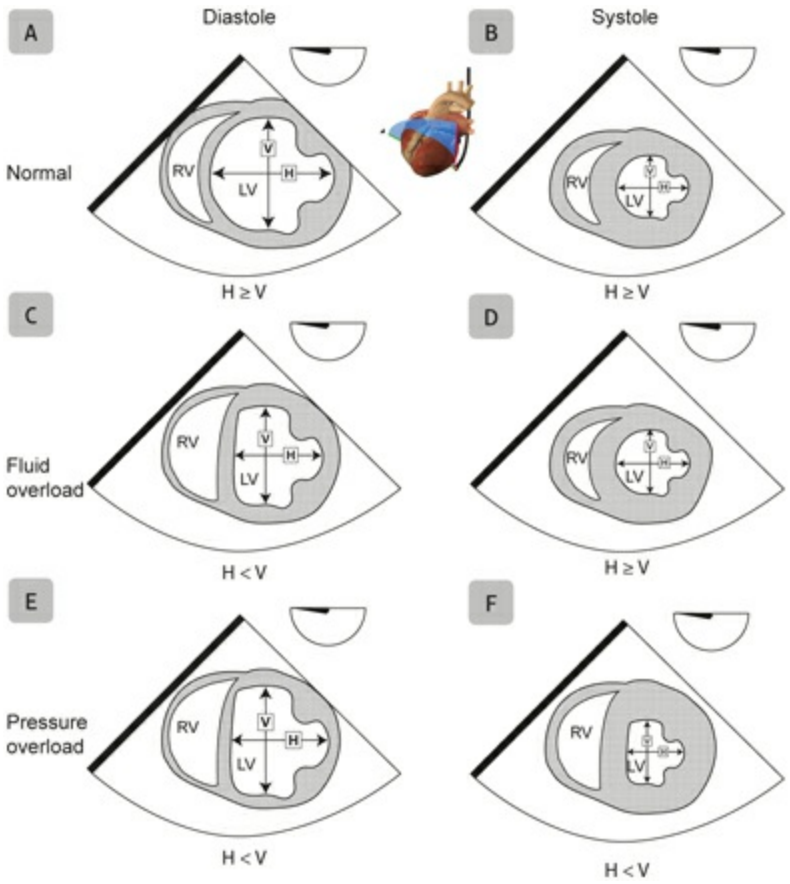

Fig. 5.12 Eccentricity index (EI). (A,B) Using the transgastric mid short- axis view, the EI corresponds to the ratio of the vertical (V)/horizontal (H) diameter of the left ventricle (LV). (C,D) In fluid overload, the H dimension is smaller than V dimension only during systole but (E, F) in pressure overload, it remains smaller in both systole and diastole. RV, right ventricle. (Adapted with permission from Denault *et al.* [8]).

C-D: https://youtu.be/V5VuNftv1e4

E-F: https://youtu.be/AzVii3Fb4Ss

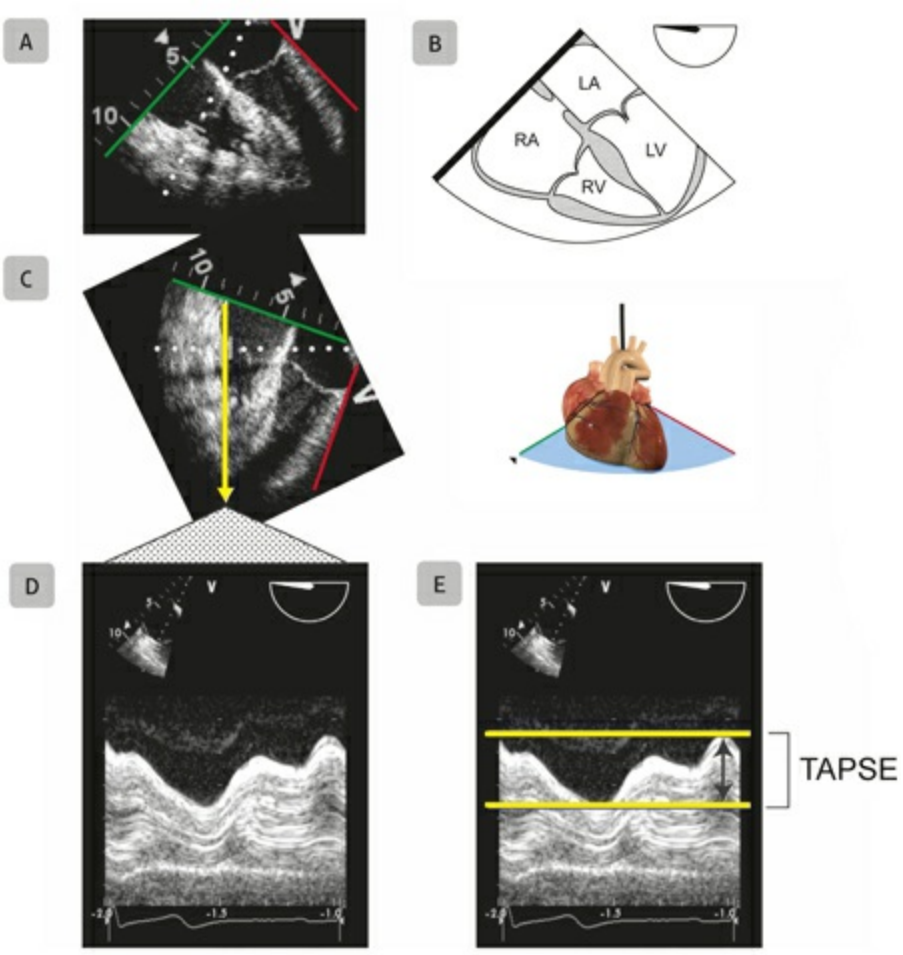

F

Normal values for TAPSE

Parameter	Mean ± SD	Abnormality threshold
TAPSE (mm)	24 ± 3.5	<17

Fig. 5.13 Tricuspid annular plane systolic excursion (TAPSE). (A—E) Steps in the measurement of the TAPSE using anatomic M-mode are shown. (A,B) First, a mid-esophageal four-chamber view is acquired and (C) the M-mode cursor is positioned along the plane of the TAPSE motion to obtain the M-mode image of this displacement (D). The lower point corresponds to the maximal systolic excursion and the upper point is the atrial contraction. (E) The TAPSE is equal to the total systolic displacement of the tricuspid annulus, which is normally 24 ± 3.5 mm. (F) Normal values from Lang *et al.* [6] LA, left atrium; LV, left ventricle; RA, right atrium; RV, right ventricle. (Reproduced with permission from Denault *et al.* [8]).

https://youtu.be/rG3dJ6_J-rc

Table 5.2 Relationship between Tricuspid Annular Plane Systolic Excursion (TAPSE) and Right Ventricular Ejection Fraction (RVEF) [24] , [25] .

TAPSE (mm)	RVEF (%)
5	20
10	30
15	40
20	50

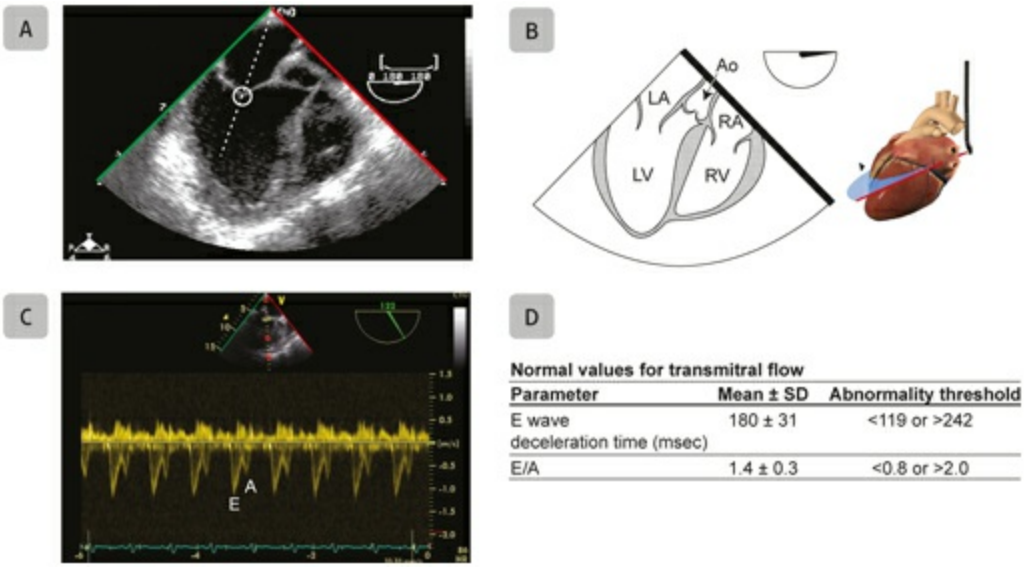

Normal values for transmitral flow

Parameter	Mean ± SD	Abnormality threshold
E wave deceleration time (msec)	180 ± 31	<119 or >242
E/A	1.4 ± 0.3	<0.8 or >2.0

Fig. 5.14 Transmitral flow (TMF). (A-C) Midesophageal long-axis view of the TMF was obtained by positioning the pulse wave Doppler sample volume at the leaflet tips. The spectral tracing shows early (E) and late (A) TMF diastolic velocities. (D) Normal values from Lang *et al.* [6] Ao, aorta; LA, left atrium; LV, left ventricle; RA, right atrium; RV, right ventricle. (Reproduced with permission from Denault *et al.* [8]).

LEFT VENTRICULAR DIASTOLIC FUNCTION

Diastole or LV filling is both a passive and an active process involving the elastic recoil of the LV. This process causes the LV pressure to fall producing a gradient between the left atrium (LA) and LV extending down to the LV apex creating early diastolic filling as demonstrated on Doppler transmitral flow (TMF) as the E wave (**Figure 5.14**). The LV suction created by relaxation is sensitive to myocardial dysfunction. Shortly after the early filling, the pressure gradient decreases. This leads to flow deceleration that is modified by LV chamber stiffness. During the mid-portion of diastole

(diastasis), the pressure equilibrates and TMF essentially ceases. Atrial contraction at the end of diastole produces a second pressure gradient propelling blood from the LA into the LV, producing the A wave on the TMF. Left atrial relaxation following atrial systole results in a decrease in atrial pressure and the start of mitral valve closure. Pulmonary venous flow (PVF) interrogated with PW Doppler demonstrates inflow during systole (S wave) and diastole (D wave) with flow going away from the heart during atrial contraction or atrial reversal (AR) velocity (**Figure 5.15**). Diastolic dysfunction is primarily described by echocardiography through changes in TMF and PVF. Tissue Doppler of the mitral annulus or color M-mode of mitral inflow may also interrogate diastolic dysfunction. Diastolic dysfunction is classified as mild (abnormal relaxation), moderate (pseudonormal), severe (restrictive), which is reversible, or fixed (**Figure 5.16**). [27]

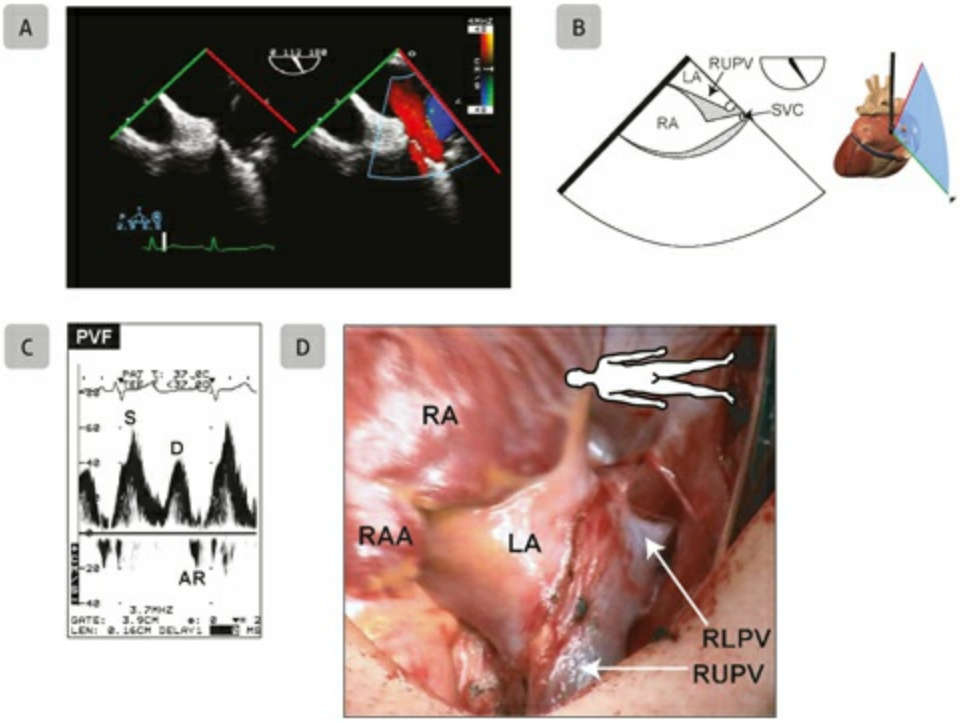

Fig. 5.15 Pulmonary vein Doppler. (A,B) Mid-esophageal color Doppler (Nyquist 48 cm/s) compare view at 118° of the right upper pulmonary vein (RUPV) positioned behind the right atrium (RA) and close to the superior vena cava (SVC) as seen on the intraoperative view (D). (C) Pulsed wave Doppler interrogation of pulmonary venous flow (PVF) shows a normal pattern of systolic (S), diastolic (D), and atrial reversal (AR) PVF velocity. LA, left atrium; RAA, right atrial appendage; RLPV, right lower pulmonary vein. (Reproduced with permission from Denault *et al.* [8] Photo D courtesy of Dr Nancy Poirier.).

A: https://youtu.be/k9mCiLBshnU

D: https://youtu.be/5f-ulY_peBs

In mild diastolic dysfunction, early filling is impaired leading to a decrease in early TMF (F E), and increased reliance on atrial contraction, resulting in a E/A ratio of <0.75. Other findings include a decrease in mitral annular velocity (↓é) by tissue Doppler. As diastolic dysfunction progresses to the moderate range, the LA pressure increases restoring the E wave to the normal range E/A ratio between 0.75 and 1.5 (pseudonormal), but the PVF S decreases below the D wave (S < D); the mitral annular velocity é becomes more delayed and smaller. Deceleration time (DT) also decreases as the LV is pushed to the steeper portion of the pressure volume curve. In severe diastolic dysfunction, the very high LA pressure results in an even larger E and the TMF ratio of E/A is now >1.5; there is even further reduction in the PVF S wave, which is now significantly less than the D wave, DT is very short and there is further reduction and a delay in the mitral annular velocity *é*. A reduction in propagation velocities by color M-mode is seen in all stages of diastolic dysfunction and is quantitatively <45 ms. [27]

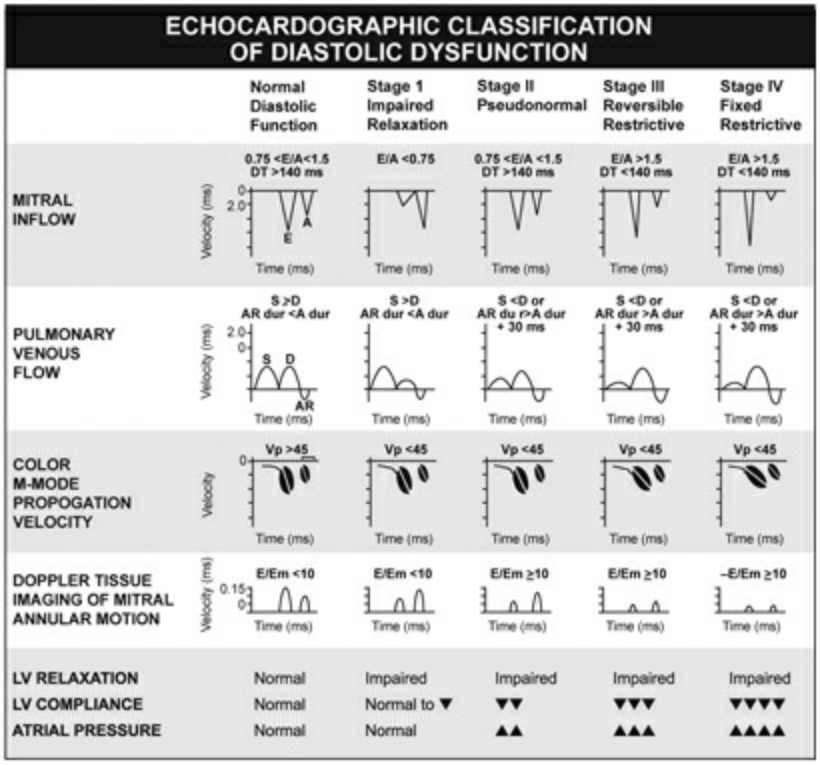

Fig. 5.16 Diastolic dysfunction. Echocardiographic classification of diastolic dysfunction adapted for transesophageal echocardiography is shown. A, peak late diastolic TMF velocity; A dur, duration of TMF A-wave; AR dur, atrial reversal pulmonary venous flow velocity duration; D, diastolic pulmonary venous flow velocity; DT, deceleration time; E, peak early diastolic TMF velocity; Em, early diastolic MAV; LV, left ventricle; MAV, mitral annular velocity; S, systolic pulmonary venous flow velocity; TMF, transmitral; Vp, flow propagation velocity. (Reproduced with permission from Denault *et al.* [8]*).*

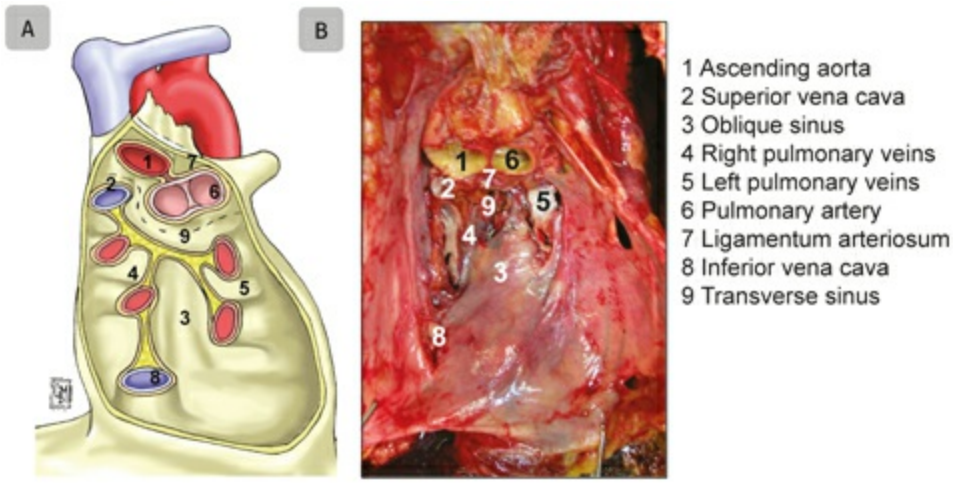

Fig. 5.17 Pericardium. The pericardial sac is shown with the heart removed in (A) an anatomical drawing and (B) autopsy specimen. The oblique pericardial sinus is posterior to the left atrium and left ventricle. The transverse sinus is bounded by the great vessels. Panel A courtesy of Gian-Marco Busato and Photo B courtesy of Dr Nicolas Durrleman. (Reproduced with permission from Denault *et al.* [8]).

Right Ventricular Diastolic Function

Right ventricular diastolic dysfunction is not as widely assessed as LV diastolic dysfunction. However, it may have a particularly important role as an early sign of RV failure [28] , [29] and possibly venous congestion (see **Figure 4.39**). A classification of RV diastolic function has been proposed. [7] , [8] , [30]

PERICARDIUM

Anatomy and Physiology of the Pericardium

The pericardium is comprised of an inner visceral layer covering the epicardium and a fibrous, outer parietal layer. Reflections of these layers converge around the great vessels and posterior to the left atrium, forming the transverse and oblique sinuses (**Figure 5.17**). [31] Although incompletely understood, the primary role of the pericardium is to restrict excessive motion of the heart within the chest. Stability is facilitated in part by ligamentous attachments to the sternum and diaphragm. The pericardial space between the visceral and parietal layers normally contains a small amount of fluid (up to 50 mL). Physiologic intrapericardial pressure ranges are between -5 to 5 cmH_2O and reflect the pleural pressures generated during ventilation. [32] Critical illness may contribute to a pathological accumulation of fluid or debris (hematoma) within the pericardial space that ultimately elevates intrapericardial pressure and restricts CO (**Figure 5.18**).

Quantification of Pericardial Effusions

Accumulation of pericardial fluid typically appears as an echo-free space separating the visceral and parietal pericardium (**Figure 5.18**). Complex pericardial collections may result in regional compression of the underlying heart (**Figure 5.19**). Accurately quantifying the volume of irregularly distributed pericardial effusions (PEs) may be challenging (**Table 5.3**). More uniform effusions are measured by determining the diastolic separation of the pericardial layers and quantified as small (<100 mL and <10 mm separation) moderate (100-500 mL and 10-20 mm separation) and large (>500 mL and >20 mm separation). [32] Misidentifying large left pleural effusions as pericardial in origin may occasionally occur. A distinguishing feature of PE is the presence of fluid juxtaposed between the descending thoracic aorta and

the posterior LV (**Figure 5.20** and see **Figure 17.3**). Misinterpretation of epicardial fat as an effusion is another common pitfall that demands consideration. Epicardial fat is mildly echogenic and typically only distributed anterior to the heart.

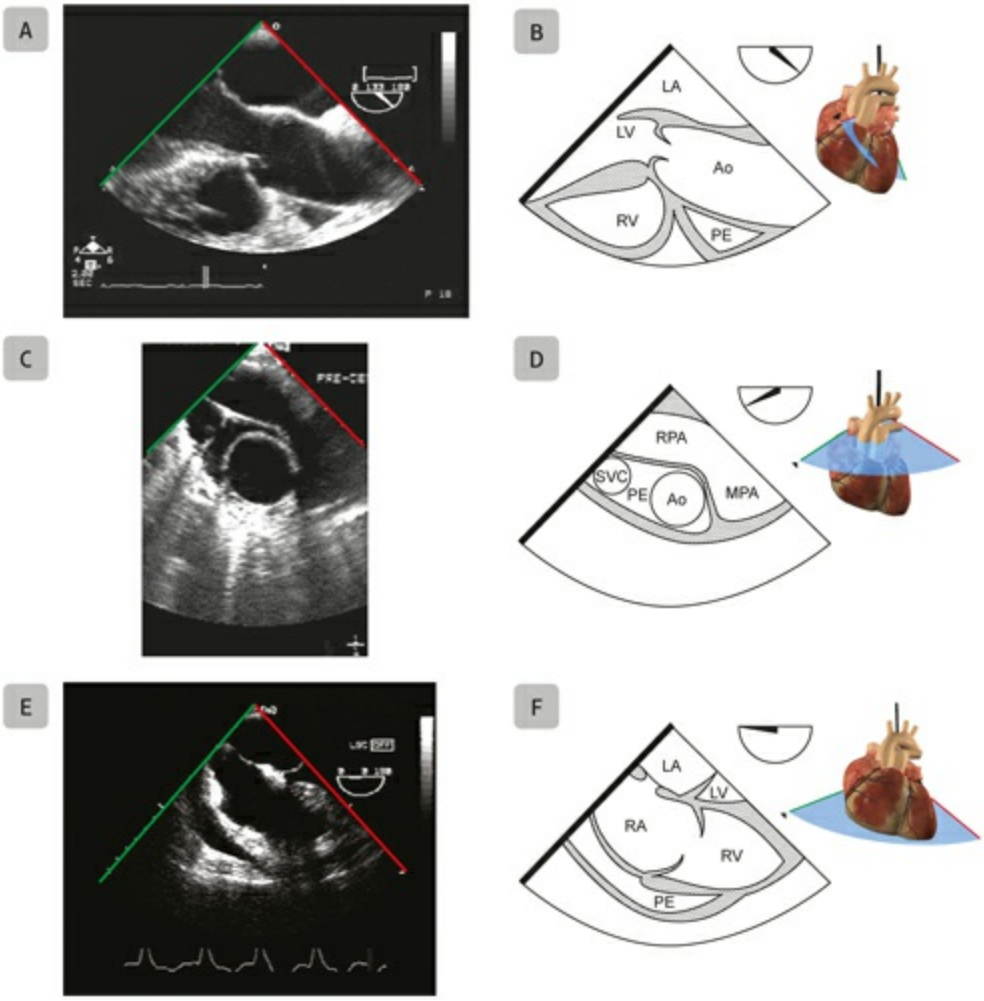

Fig. 5.18 Pericardial effusion (PE).(A,B) In this mid esophageal (ME) aortic valve long-axis view, the PE is anterior to the ascending aorta (Ao) and communicates with the transverse sinus. (C,D) ME ascending Ao short-axis view shows the PE present between the Ao and the superior vena cava (SVC). (E, F) In the ME four- chamber view, the PE is seen anterior to the right ventricle (RV) and right atrium (RA). LA, left atrium; LV, left ventricle; MPA, main pulmonary artery; RPA, right pulmonary artery. (Reproduced with permission from Denault *et al.* [8]).

A: https://youtu.be/x8z3J3ugBo4

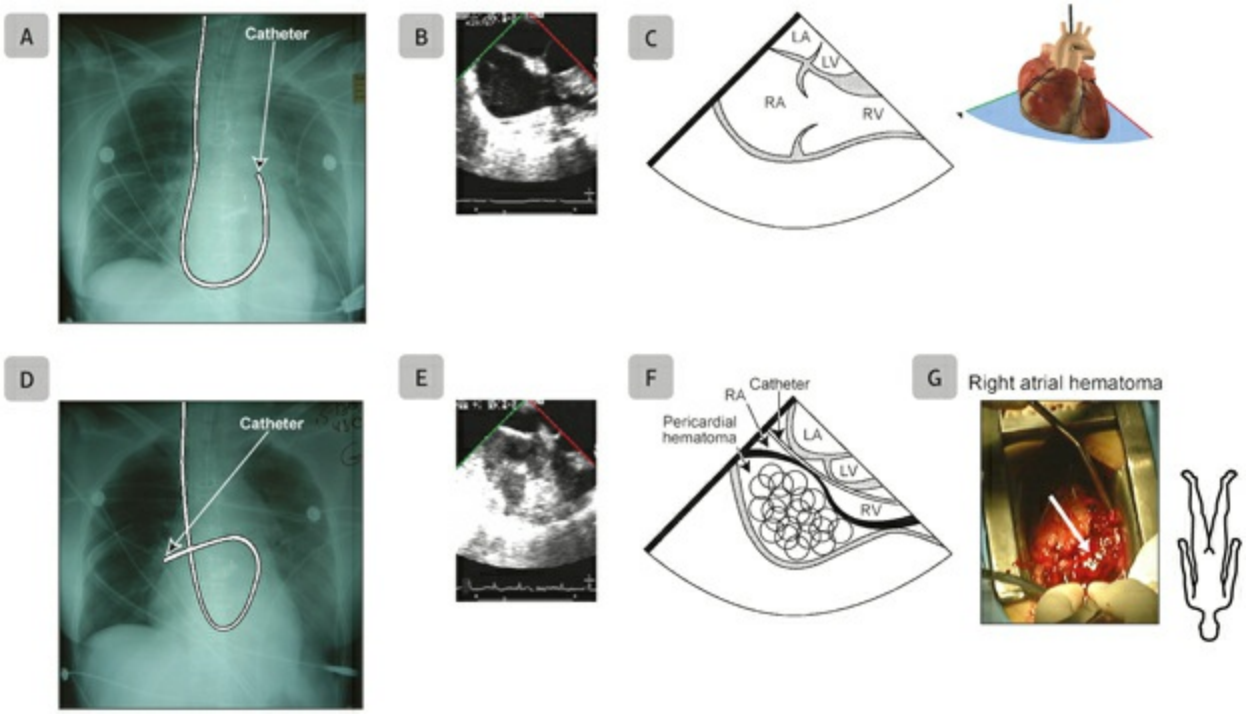

Fig. 5.19 Cardiac tamponade. A 29-year-old female became hemodynamically unstable after aortic valve surgery. (A—D) Cardiac tamponade was suspected from serial chest X-rays as the pulmonary artery catheter tip had moved from its initial medial position (A) to a more distal position (D) from displacement of the right-sided cardiac chambers by the suspected pericardial process. (E, F) Diagnosis by transesophageal echocardiography shows a new pericardial hematoma compressing the right heart chambers, compared with the intraoperative mid-esophageal four- chamber view (B, C). (G) The diagnosis was confirmed at surgical re-exploration. LA, left atrium; LV, left ventricle; RA, right atrium; RV, right ventricle. (Reproduced with permission from Denault *et al.* [8]).

B&E: https://youtu.be/XI80L3hOKb8

Table 5.3 Echo-Free Space between Pericardium and Myocardium to Determine Pericardial Effusion (PE) Grade.

PE grade	Loculated PE (mm)	Circumferential PE (mm)
0	–	–
1 (minimal)	0–9	–
2 (moderate)	10–14	1–9
3 (medium)	15–19	10–14
4 (large)	≥20	≥15

Adapted from Meurin *et al.* [33].

Cardiac Tamponade

In critically ill patients, identification of a PE may contribute important diagnostic or prognostic information. Once identified, the more pressing question is establishing the hemodynamic consequence and whether pericardiocentesis or surgical drainage is required. The pressure-volume relationship of the pericardium is non-linear and is dependent upon the rate of fluid accumulation. Echocardiography is central to estimating the hemodynamic significance of PEs and revealing evidence of cardiac tamponade. Two-dimensional and Doppler patterns focus upon revealing compression of cardiac structures, restriction of venous return, and abnormal flow patterns attributable to exaggerated heart-lung interactions. With circumferential effusions, the right heart is most susceptible to compression owing to its lower intracavitary pressures. Regionalized tamponade, as commonly occurs in the post-surgical setting, may restrict filling of any chamber and demands examination in multiple echocardiographic windows (**Figure 5.19**). [34] Identification of tamponade following cardiotomy may be challenging and remains a clinical diagnosis supported by echocardiography particularly in patients with higher filling pressures and vasoactive support, in which the classical signs will be absent. Hence the term “compensated tamponade” can be used. Pericardial drainage resulting in vasopressor withdrawal is diagnostic of this condition.

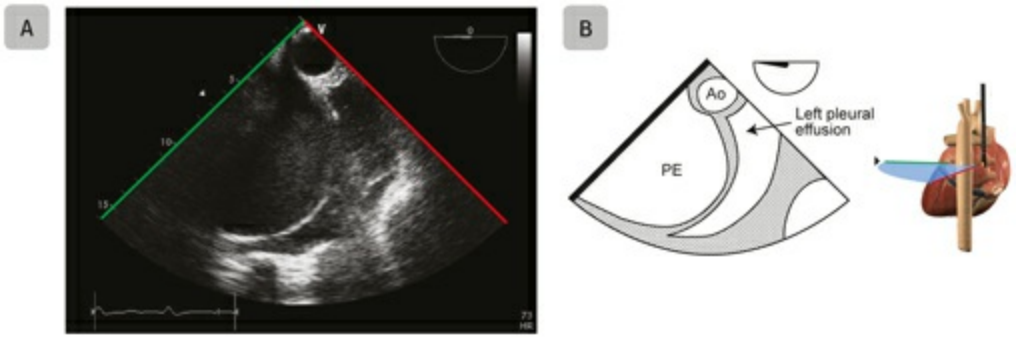

Fig. 5.20 Pleural and pericardial effusions. (A,B) Descending aorta (Ao) short-axis view in a 77-year-old male diagnosed with tamponade shows both pericardial effusion (PE) and pleural effusion. Note that the left pleural effusion is posterior to the descending Ao. (Reproduced with permission from Denault *et al.* [8]).

A: https://youtu.be/UEi4_aFN_gg

Late diastolic invagination of the RA is an early sign of tamponade. Although highly sensitive, the specificity of this finding is low but improves as the duration of compression prolongs beyond a third of the duration of the cardiac cycle. M-mode may assist in quantifying the duration of collapse. Early diastolic compression of the RV-free wall (particularly at the outflow tract) is another specific 2D finding of tamponade. [35] Clinicians need to appreciate that pulmonary hypertension and RV hypertrophy may defend against the development of these two important echocardiographic signs. [36]

Engorgement or plethora of the IVC coupled with reduced variability during ventilation is another echocardio- graphic finding associated with tamponade. A dilated IVC with limited respiratory variability may also be present in pulmonary hypertension, RV dysfunction, severe tricuspid regurgitation, constrictive pericarditis, as well as elevated intrathoracic pressure from dynamic hyperinflation or excessive positive end-expiratory pressure (PEEP). [35] As such, IVC plethora lacks specificity for diagnosing cardiac tamponade in isolation.

During ventilation, variable blood flow velocity across the cardiac valves develops because of phasic changes in intrathoracic pressure. As a result of ventricular interdependence and pericardial constraint, these transvalvular flow velocity changes are reciprocal between the left and right heart.

Institution of mechanical ventilation reverses the timing of flow velocity changes when compared to spontaneous (negative pressure) ventilation. Cardiac tamponade exaggerates this physiologic occurrence and is responsible for the generation of a pulsus paradoxus on clinical examination. Generally speaking, maximal respiratory variability of E wave Doppler velocity of 25%, 50%, and 30% respectively across the mitral, tricuspid, and pulmonic valves suggests the presence of tamponade. [32] As with IVC plethora, this exaggerated respiratory variability may also be found with air trapping. During tamponade, the maximal E wave velocities are generated at the first beat of inspiration or expiration, whereas the onset of maximal velocity change is gradual when attributed to high intrathoracic pressures.

Constrictive Pericarditis

Constrictive pericarditis is rarely encountered in the general ICUs. Congestive symptoms develop as a result of inflammation, fusion, and fibrosis of the visceral and parietal pericardium. Occasionally, the inflammatory process involves the underlying myocardium. Historically, tuberculosis was a common etiology, though contemporary cases are often attributed to remote cardiac surgery or mediastinal radiation. Pathophysiologic features of constrictive pericarditis reflect restricted diastolic filling, exaggerated ventricular interdependence, and intracardiac pressure changes that are divorced from changes in pleural pressure. With constrictive pericarditis, there is a pressure gradient reduction between the pulmonary veins and LA during inspiration with spontaneous (negative pressure) breathing. This limits LV filling and stroke volume. Simultaneously, there is augmented venous return on the right side such that the ventricular septum is abruptly displaced towards the left. The reverse occurs during expiration causing a septal “bounce” - a characteristic feature of constriction. The effects of ventilation on pulmonary and systemic venous blood flow generate unique echocardiographic patterns in patients with constrictive pericarditis. With spontaneous inspiration, reduced pulmonary venous blood flow diminishes early mitral inflow velocities (by more than 25%). Again, the reverse pattern develops on the right side, such that tricuspid inflow velocity is augmented (>25%) compared with expiration. Positive pressure ventilation results in a reciprocal pattern. Respiratory variation of the pulmonary venous diastolic wave is especially pronounced (accelerated during spontaneous inspiration) with constriction. The hepatic

vein flow also demonstrates diastolic flow reversal that is prominent during spontaneous expiration (**Figure 5.21**). Transesophageal echocardiography is superior to TTE at identifying increased pericardial thickness (>3 mm) and can complement other imaging modalities including computed tomography and magnetic resonance imaging. [37]

CARDIOMYOPATHY

Cardiomyopathies are a group of diseases characterized by intrinsic disorders of the myocardium. In 1995, the World Health Organization published a classification scheme for cardiomyopathies, separating them into dilated, hypertrophic, restrictive, arrythmogenic RV dysplasia, and unclassified. The American Heart Association subsequently developed an organization system in 2006 [38] that categorized cardiomyopathies as either primary (predominantly isolated to the heart) or secondary (associated with other organ involvement). Primary etiologies are then subdivided into genetic, mixed, or acquired. While these constructs are useful for scientific study into the complexities of these disorders, they represent an impractical framework for clinicians. Practically speaking, when managing patients with cardiomyopathies in the ICU, the primary focus involves the hemodynamic implications and identifying reversible etiologies that may be amenable to specific medical, surgical, or interventional treatments.

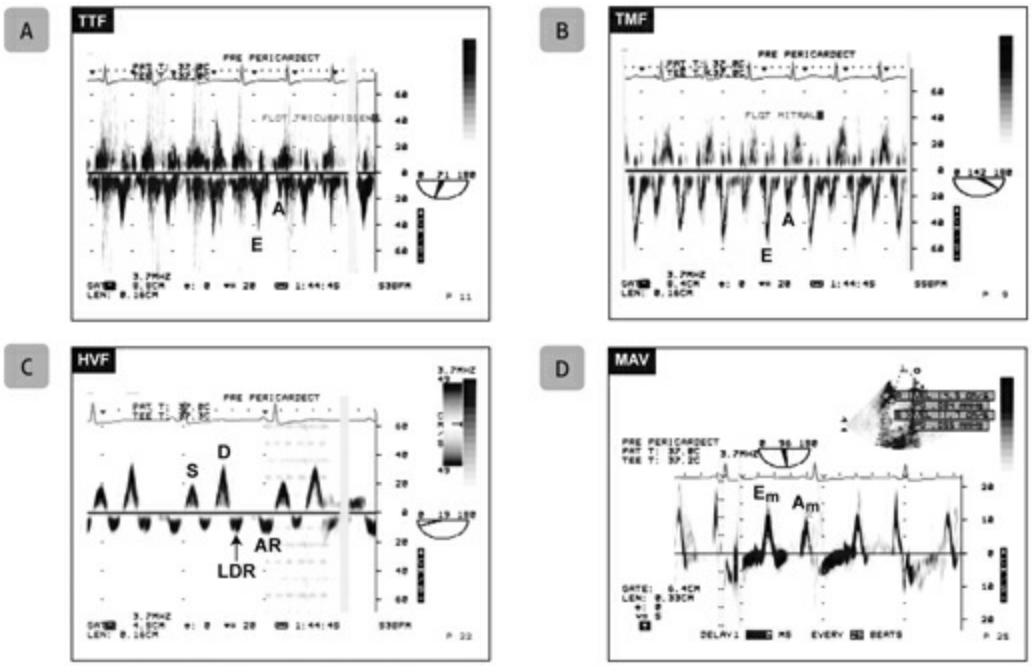

Fig. 5.21 Constrictive pericarditis. A mechanically ventilated 68-year-old male with constrictive pericarditis is scheduled for pericardiectomy. Both the Doppler (A) transtricuspid flow (TTF) and (B) transmitral flow (TMF) demonstrate predominance of the early E diastolic velocity with respiratory variation. (C) Hepatic vein flow (HVF) Doppler tracing shows abnormal systolic (S) blunting with diastolic (D) flow predominance and even late diastolic reversal (LDR). (D) Mitral annular velocity (MAV) shows normal Em velocity which argues against the presence of restrictive cardiomyopathy. A, peak late diastolic TMF or TTF velocity; Am, peak late diastolic MAV; AR, atrial reversal HVF velocity; E, early diastolic TMF or TTF velocity; Em, peak early diastolic MAV. (Reproduced with permission from Denault *et al.* [8]*).*

Hypertrophic Cardiomyopathy

Hypertrophic cardiomyopathy (HCM) is diagnosed on the basis of LV hypertrophy in the absence of hypertension or valvular disease. [39] Its incidence is approximately 1/500 and frequently attributable to mutations in genes encoding sarcomeric proteins. Patterns of hypertrophy are often asymmetric and may include any segment but typically involves the anterior septum. Classically, HCM is identified by septal thickness >15 mm and a septal:posterior wall thickness ratio >1.3 (or 1.5 in the presence of hypertension). [40] Athletic heart and systemic conditions, such as mitochondrial diseases, Fabry's, Freidrich's ataxia, glycogen storage diseases, and amyloidosis, may demonstrate patterns mistaken as HCM. In the ICU, patients with HCM classically present with progressive hemodynamic instability when hypovolemic, following the institution of mechanical ventilation and administration of inotropes. These conditions

precipitate a dynamic left ventricular outflow tract obstruction (LVOTO) (see **Figures 9.11 and 9.13**). [40] Echocardiographic evaluation of patients with HCM should focus on the LVOTO, systolic anterior motion (SAM) of the mitral valve (MV), distribution and severity of hypertrophy, identifying systolic and diastolic dysfunction, and LA size.

Dynamic LVOTO requires consideration as the cause of unexplained hypotension in the critically ill. While HCM can be responsible for this physiology, other predisposing anatomic substrates include MV repair, aortic valve replacement, sigmoid septum, myocardial infarction, and Takotsubo cardiomyopathy. [41] In HCM, LVOTO arises when the hypertrophied septum reduces the LVOT diameter and there is anterior displacement of the mitral apparatus. The systolic excursion of the anterior mitral leaflet towards the ventricular septum is a consequence of the Venturi effect. Critical illness often intensifies the LVOTO because of unfavorable loading conditions, such as reduced preload and afterload, tachycardia, hyperdynamic state, and positive pressure ventilation. [42] Quantification of the gradient can be estimated by performing continuous wave (CW) Doppler across the LVOT. The morphology of the CW envelope appears dagger-shaped in HCM (**Figure 5.22**). Precise localization of the obstruction may be obtained using a combination of color Doppler and serial pulsed wave Doppler measurements. The presence of a resting gradient >30 mmHg is predictive of sudden cardiac death and heart failure.

Systolic anterior motion (SAM) of the MV leaflet provokes a LVOTO and malcoaptation of the mitral leaflets with resultant posteriorly directed MR (**Figure 5.23**). Abnormal morphology of the MV can provoke severe MR in HCM. The duration of leaflet/chordal contact with the septum determines the severity of SAM with <10% of systolic contact being mild and >30% severe. [43] Anterior or central MR demands attention of other causes contributing to MR beyond SAM. Persistent MR in HCM predisposes patients to LA enlargement. Ventricular systolic function in HCM is preserved or hyperdynamic in all but a minority of patients (10-15%). Those with impaired function are characterized as end-stage or “burnt-out” HCM and portend a poor prognosis. Diastolic dysfunction, as impaired relaxation, commonly results from increased LV mass and myocardial fibrosis. Conventional assessment of diastolic dysfunction using mitral inflow velocities in HCM is unreliable.

Dilated Cardiomyopathy

Left ventricular chamber dilation results from a variety of distinct pathologies. Although frequently idiopathic, the dilated cardiomyopathy phenotype may be attributable to infectious, toxic, autoimmune, and systemic disorders. In the context of providing care for the critically ill, it is paramount to identify cases that are acute and reversible. Specifically, structural causes such as advanced valvular lesions or coronary disease may benefit from surgical or percutaneous intervention. Findings of regional wall motion abnormalities (RWMA) and bright areas of myocardial thinning are clues suggestive of myocardial ischemia. [44] Functional preservation of the basal posterolateral segment often occurs in non-ischemic dilated cardiomyopathy. Differentiating primary valvular lesions demands careful interrogation of valve morphology (see Chapter 7, Basic Valve Diseases).

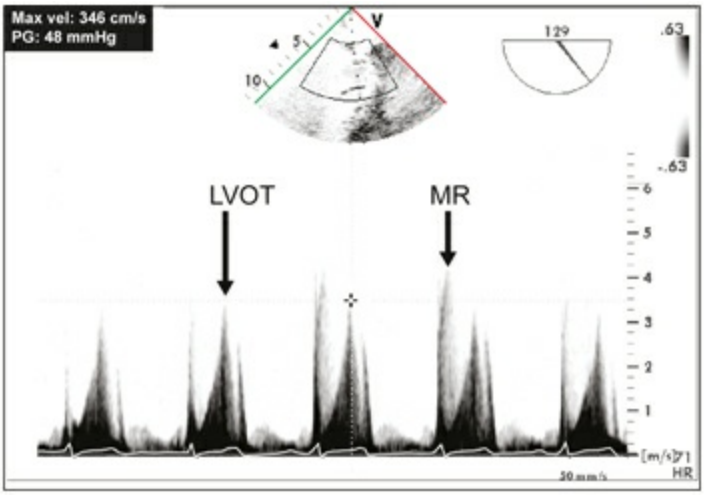

Fig. 5.22 Dagger shape CW Doppler signal. A 60-year- old male with aortic stenosis and septal hypertrophy after aortic valve replacement demonstrates acquired left ventricular outflow tract (LVOT) obstruction. Continuous wave (CW) Doppler of the LVOT obtained in a mid-esophageal long-axis view has a dagger shape, which begins simultaneously or after the QRS, with a 48 mmHg pressure gradient (PG). Also present in the CW Doppler signal is mitral regurgitation (MR). The MR occurs before isovolumic contraction and, in the CW signal, it begins before the QRS of the electrocardiogram. HR, heart rate; Max vel, maximal velocity. (Reproduced with permission from Denault *et al.* [8]).

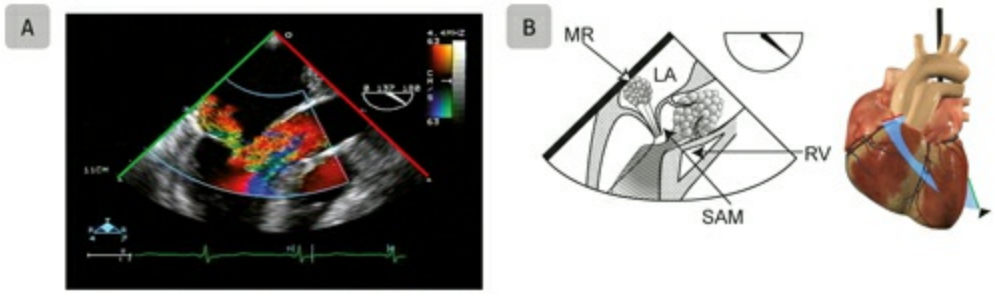

Fig. 5.23 Hypertrophic cardiomyopathy. The preoperative transesophageal echocardiographic exam of a 26-year-old male with hypertrophic cardiomyopathy and refractory symptoms despite optimal medical therapy is shown. (A,B) Mid-esophageal long-axis view with color Doppler (Nyquist 63 cm/s) shows flow acceleration in the subaortic region and posterior directed mitral regurgitation (MR). LA, left atrium; RV, right ventricle; SAM, systolic anterior motion. (Reproduced with permission from Denault *et al.* [8]).

A: https://youtu.be/-pVUpxV3Uck

Dilated cardiomyopathy is a primary myocardial disease resulting in LV dilation and dysfunction (**Figure 5.24**). Key echocardiographic features include ventricular dysfunction (EF <45%), reduced fractional shortening (<25%) and LV end, diastolic chamber dimension (>112%) predicted for age and BSA. [45] The LV geometry becomes spherical in advanced disease. Quantification of this deformation by the sphericity index (the ratio of the long axis from the mitral annulus to apex in the four-chamber view to the mid cavity short axis) predicts functional capacity. The RV is variably affected, and again, involvement correlates with prognosis. Similarly, advanced diastolic dysfunction is predictive of worsening symptomatology and outcome. The presence of spontaneous echo contrast should stimulate an exploration for ventricular or atrial thrombi. While the left atrial appendage is ideally positioned for imaging with TEE, the LV apex is usually best visualized with TTE and aided with contrast. Echocardiography is also useful for directing cardiac resynchronization therapy for patients with dilated cardiomyopathy, although the details are beyond the scope of this text.

Restrictive Cardiomyopathy

Restrictive cardiomyopathy is characterized by increased myocardial stiffness

with reduced ventricular compliance. [46] The classic anatomic features include reduced LV volume with marked atrial dilation and preserved systolic function in the absence of pericardial disease. [47] Ventricular diastolic filling is early and rapid. Physiologic restriction often results from systemic diseases including amyloidosis (**Figure 5.25**), sarcoidosis, hemochromatosis, or hypereosinophilic syndrome. Differentiation between restrictive cardiomyopathy and constrictive pericarditis is paramount owing to the therapeutic implications. In restrictive cardiomyopathy, with increased ventricular stiffness, early diastolic flow is rapid and short in duration. This results in an elevated E wave (E/A ratio is >2) with reduced deceleration time and isovolemic relaxation time. In patients with restrictive cardiomyopathy, there is limited variability in inflow velocities with respiration. This contrasts to the dynamic changes in inflow velocities present in constrictive pericarditis described above. The abnormal septal motion in constrictive pericarditis is absent in restrictive cardiomyopathy. Lateral and septal tissue Doppler diastolic velocities are reduced in restrictive cardiomyopathy, with é <8 cm/s. [46]

Septic Cardiomyopathy

Myocardial dysfunction commonly develops in patients with septic shock, and has been widely recognized following early ventriculography studies. [48] Prior to bedside echocardiography, the prevalence was underestimated in the era of the pulmonary artery catheter. Within the first 48-72 hours of septic shock, LV dysfunction typically manifests as global ventricular dilation, without elevation of filling pressures and preservation of stroke volume. Interestingly, early studies revealed that hyperdynamic ventricular performance portended a reduced survival. Contemporary echocardiographic series fail to confirm this finding - potentially reflecting the influence of varied loading conditions on LVEF and practice changes in the hemodynamic management of septic shock. The pathophysiology of the observed cardiac dysfunction is incompletely understood, though it involves inflammatory cytokines, nitric oxide, endothelin-1, and endotoxins. Although coronary artery disease may exaggerate myocardial dysfunction in sepsis, ischemia does not appear to contribute to impaired cardiac performance. [49 – 52]

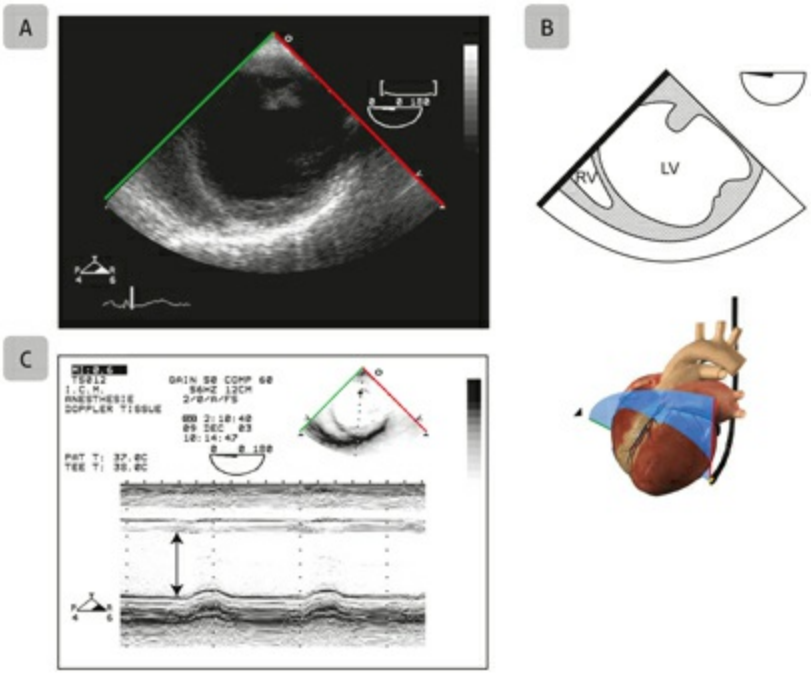

Fig. 5.24 Dilated cardiomyopathy. (A,B) Transgastric mid short-axis view in a 56-year-old female with dilated ischemic cardiomyopathy. (C) M-mode shows akinesis of the inferior wall and hypokinesis of the anterior wall. The left ventricle (LV) end- diastolic diameter (arrow) is dilated at 7.1 cm (normal 5.5 cm). RV, right ventricle. (Reproduced with permission from Denault *et al.* [8]).

A: https://youtu.be/BZnAvJzmWQ8

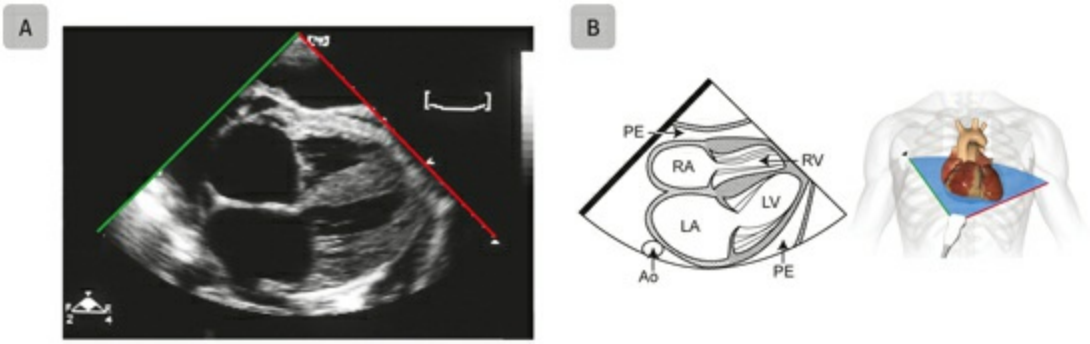

Fig. 5.25 Amyloidosis. (A,B) Transthoracic subcostal view in a patient with amyloidosis shows bi-atrial enlargement, increased ventricular wall thickness with characteristic sparkling appearance and a small circumferential pericardial effusion (PE). Ao, aorta; LA, left atrium; LV, left ventricle; RA, right atrium; RV, right ventricle. (Reproduced with permission from Denault *et al.* [8]).

Stress Cardiomyopathy/Takotsubo Cardiomyopathy

Originally described in Japanese patients, Takotsubo or stress cardiomyopathy is increasingly recognized in critical care. The moniker is derived from the Japanese term for an "octopus trap," describing the typical LV morphology in afflicted patients. [53] Classically, Takotsubo cardiomyopathy occurs following an emotionally stressful event in the life of a post-menopausal female. An increasing number of precipitants are responsible for triggering the acute LV dysfunction in Takotsubo cardiomyopathy, including neurologic disease (**Figure 5.26**), major surgery, respiratory distress, critical illness, acute exacerbations of asthma, or chronic obstructive lung disease. Although the presentation is varied, patients may exhibit evidence of acute LV failure complicated by electrocardiographic (ECG) abnormalities (ST changes/Qt prolongation), arrhythmias, shock, and pulmonary edema. The Mayo diagnostic criteria are transient LV RWMA involving the apical and/or mid-ventricular myocardial segments with RWMA extending beyond a single epicardial coronary artery distribution; absence of obstructive coronary artery disease that could be responsible for the observed RWMA; ECG abnormalities such as transient ST-segment elevation and/or diffuse T Wave inversion associated with a slight troponin elevation; lack of proven pheochromocytoma; and myocarditis. [54]

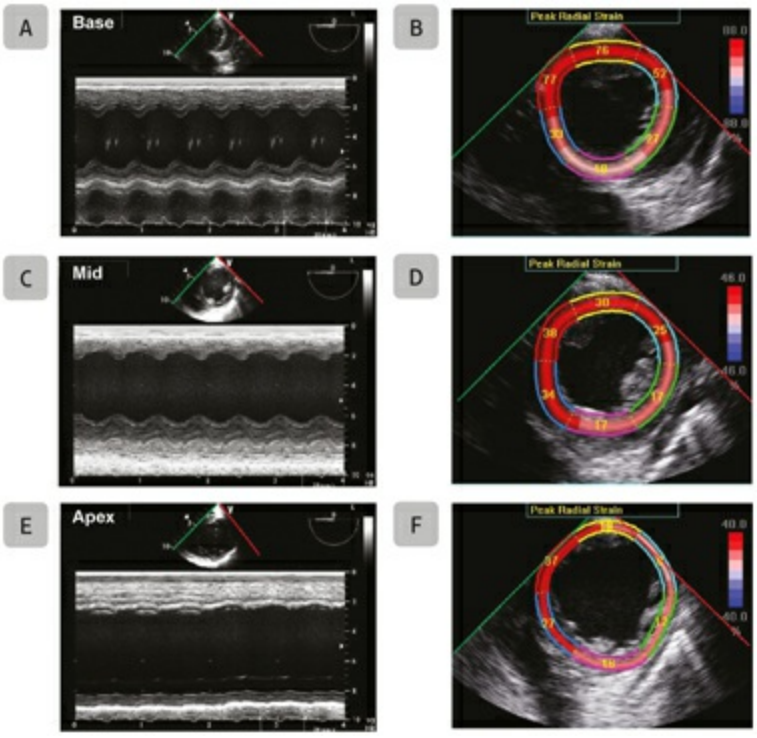

Fig. 5.26 Stress cardiomyopathy (Takotsubo or apical ballooning syndrome). A 70-year- old female after acute perforation of the duodenum is hemodynamically unstable. The transgastric views using M-mode and 2D speckle strain show the typically preserved (A,B) basal function with progressive reduction in wall motion and strain at the (C,D) mid-papillary level and (E, F) apex. The wall motion abnormalities completely resolved the following week. (Reproduced with permission from Denault *et al.* [8]).

A: https://youtu.be/YPrNsH0cqMA

B: https://youtu.be/3tHbAoIiuCc

C: https://youtu.be/-t-fZxIAWic

D: https://youtu.be/iG_BTF9YM_Y

E: https://youtu.be/QijiFA4jPKY

F: https://youtu.be/DKzpbSaoiv4

There are four patterns of LV dysfunction reported with Takotsubo cardiomyopathy. Classically, there is dyskinetic ballooning of the entire LV

apex and mid-anterior wall with compensatory hyperkinesis of the basal segments (**Figure 5.26**). Other observed patterns include a mid-ventricular variant, as well as basal and focal types. [55] Up to 25% of patients may demonstrate a hemodynamically significant LVOTO complicated by SAM. Central MR with distortion of the papillary muscle geometry also occurs. In 2-5% of patients, an apical thrombus may appear demanding anticoagulation. Right ventricular dysfunction occurs infrequently, but would amplify the hemodynamic disturbance.

The pathophysiology of Takotsubo cardiomyopathy is poorly understood, although associated with elevated circulating catecholamines, increased coronary vascular resistance, and impaired microcirculatory coronary flow. [56] Management is supportive and predicated on excluding obstructive coronary lesions, identifying and tailoring resuscitation for those with a LVOTO, and eventually initiating an angiotensin converting enzyme (ACE) inhibitor/B-blocker upon shock resolution. [57] Improvement in LV function occurs within days and complete recovery generally occurs within 8 weeks. Fortunately, mortality for this condition is low (~2%), although episodes of LV dysfunction may recur (~11%).

PITFALLS AND PROBLEMS

There are several limitations when evaluating ventricular function either from an ischemic or non-ischemic origin. The most common issue is that all interpretation is dependent upon image quality. Despite improvement with the use of TEE, up to 10% of patients still have poor image quality. [15] , [58] Foreshortening may overestimate the LVEF. [11] The assessment of LVEF requires geometric assumptions; inter- and intra-observer variability remains high and findings may correlate poorly with clinical status. Doppler examination of the heart requires parallel alignment of the ultrasound beam. Use of Doppler to assess systolic pulmonary artery pressure may be limited by the absence of tricuspid regurgitation. Stroke volume measurement from the LVOT is overestimated with significant aortic regurgitation or if the LVOT diameter is inaccurately measured. Finally, Doppler assessment for diastolic dysfunction is limited by heart rate and rhythm and interpretation must also take into account loading con- ditions. [15] , [58] – [60] Other important issues, such as fluid status and the role of transthoracic echocardiography

during cardiac arrest, will be discussed in more detail in Chapter 15, Critical Care Examination of the Cardiovascular System.

REFERENCES

1. LeeV.H., ConnollyH.M., FulghamJ.R., MannoE.M., BrownR.D.Jr, WijdicksE.F.. Tako-tsubo cardiomyopathy in aneurysmal subarachnoid hemorrhage: an underappreciated ventricular dysfunction. *J Neurosurg*2006;*105*:264–70.
2. ReynoldsE.M., RyanD.P., SheridanR.L., DoodyD.P.. Left ventricular failure complicating severe pediatric burn injuries. *J Pediatr Surg*1995;*30*:264–9.
3. RudigerA., SingerM.. Mechanisms of sepsis-induced cardiac dysfunction. *Crit Care Med*2007;*35*:1599–608.
4. SubramaniamB., TalmorD.. Echocardiography for management of hypotension in the intensive care unit. *Crit Care Med*2007;*35*:S401–7.
5. LangR.M., BadanoL.P., Mor-AviV., AfilaloJ., ArmstrongA., ErnandeL., et al. Recommendations for cardiac chamber quantification by echocardiography in adults: an update from the American Society of Echocardiography and the European Association of Cardiovascular Imaging. *J Am Soc Echocardiogr*2015;*28*:1–39.
6. LangR.M., BierigM., DevereuxR.B., FlachskampfF.A., FosterE., PellikkaP.A., et al. Recommendations for chamber quantification: a report from the American Society of Echocardiography's Guidelines and Standards Committee and the Chamber Quantification Writing Group, developed in conjunction with the European Association of Echocardiography, a branch of the European Society of Cardiology. *J Am Soc Echocardiogr*2005;*18*:1440–63.
7. RudskiL.G., LaiW.W., AfilaloJ., HuaL., HandschumacherM.D., ChandrasekaranK., et al. Guidelines for the Echocardiographic Assessment of the Right Heart in Adults: A Report from the American Society of Echocardiography Endorsed by the European Association of Echocardiography, a registered branch of the European Society of Cardiology, and the Canadian Society of Echocardiography. *J Am Soc Echocardiogr*2010;*23*:685–713.
8. DenaultA.Y., CoutureP., VegasA., BuithieuJ., TardifJ.C.. *Transesophageal Echocardiography Multimedia Manual, Second Edition: A Perioperative Transdisciplinary Approach*, New York: Informa Healthcare, 2011.
9. NarasimhanM., KoenigS.J., MayoP.H.. Advanced echocardiography for the critical care physician: part 1. *Chest*2014;*145*:129–34.
10. NarasimhanM., KoenigS.J., MayoP.H.. Advanced echocardiography for the critical care physician: part 2. *Chest*2014;*145*:135–42.
11. SalemR., ValleeF., RuscaM., MebazaaA.. Hemodynamic monitoring by echocardiography in the ICU: the role of the new echo techniques. *Curr Opin Crit Care*2008;*14*:561–8.
12. KusumotoF.M., MuhiudeenI.A., KuechererH.F., CahalanM.K., SchillerN.B.. Response of the interatrial septum to transatrial pressure gradients and its potential for predicting pulmonary capillary wedge pressure: an intraoperative study using transesophageal echocardiography in patients during mechanical ventilation. *J Am Coll Cardiol*1993;*21*:721–8.
13. HajiD.L., AliM.M., RoyseA., CantyD.J., ClarkeS., RoyseC.F.. Interatrial septum motion but not Doppler assessment predicts elevated pulmonary capillary wedge pressure in patients undergoing cardiac surgery. *Anesthesiology*2014;*121*:719–29.
14. FerradaP., EvansD., WolfeL., AnandR.J., VanguriP., MayglothlingJ., et al. Findings of a randomized controlled trial using limited transthoracic echocardiogram (LTTE) as a hemodynamic

monitoring tool in the trauma bay. *J Trauma Acute Care Surg*2014;*76*:31–7.
15. HahnR.T., AbrahamT., AdamsM.S., BruceC.J., GlasK.E., LangR.M., et al. Guidelines for performing a comprehensive transesophageal echocardiographic examination: recommendations from the American Society of Echocardiography and the Society of Cardiovascular Anesthesiologists. *J Am Soc Echocardiogr*2013;*26*:921–64.
16. KirkpatrickJ.N., VannanM.A., NarulaJ., LangR.M.. Echocardiography in heart failure: applications, utility, and new horizons. *J Am Coll Cardiol*2007;*50*:381–96.
17. SteedsR.P.. Echocardiography: frontier imaging in cardiology. *Br J Radiol*2011;*84*Spec No 3: S237–45.
18. GlassbergH., KirkpatrickJ., FerrariV.A.. Imaging studies in patients with heart failure: current and evolving technologies. *Crit Care Med*2008;*36*:S28–39.
19. Mor-AviV., LangR.M., BadanoL.P., BelohlavekM., CardimN.M., DerumeauxG., et al. Current and evolving echocardiographic techniques for the quantitative evaluation of cardiac mechanics: ASE/EAE consensus statement on methodology and indications endorsed by the Japanese Society of Echocardiography. *J Am Soc Echocardiogr*2011;*24*:277–313.
20. GaaschW.H., BattleW.E., ObolerA.A., BanasJ.S.Jr, LevineH.J.. Left ventricular stress and compliance in man. With special reference to normalized ventricular function curves. *Circulation*1972;*45*:746–62.
21. MahlerF., RossJ.Jr, O'RourkeR.A., CovellJ.W.. Effects of changes in preload, afterload and inotropic state on ejection and isovolumic phase measures of contractility in the conscious dog. *Am J Cardiol*1975;*35*:626–34.
22. ReichekN., WilsonJ., St JohnS.M., PlappertT.A., GoldbergS., HirshfeldJ.W.. Noninvasive determination of left ventricular end-systolic stress: validation of the method and initial application. *Circulation*1982;*65*:99–108.
23. HoS.Y., NihoyannopoulosP.. Anatomy, echocardiography, and normal right ventricular dimensions. *Heart*2006;*92*(Suppl. 1):i2–13.
24. BleekerG.B., SteendijkP., HolmanE.R., YuC.M., BreithardtO.A., KaandorpT.A., et al. Assessing right ventricular function: the role of echocardiography and complementary technologies. *Heart*2006;*92*(Suppl 1):i19–26.
25. KaulS., TeiC., HopkinsJ.M., ShahP.M.. Assessment of right ventricular function using two-dimensional echocardiography. *Am Heart J*1984;*107*:526–31.
26. SatoT., TsujinoI., Oyama-ManabeN., OhiraH., ItoY.M., SugimoriH., et al. Simple prediction of right ventricular ejection fraction using tricuspid annular plane systolic excursion in pulmonary hypertension. *Int J Cardiovasc Imaging*2013;*29*:1799–805.
27. NaguehS.F., AppletonC.P., GillebertT.C., MarinoP.N., OhJ.K., SmisethO.A., et al. Recommendations for the evaluation of left ventricular diastolic function by echocardiography. *J Am Soc Echocardiogr*2009;*22*:107–33.
28. DenaultA.Y., CoutureP.. Practical diastology. *World J Anesthesiology*2014;*3*:96–104.
29. DenaultA.Y., HaddadF., JacobsohnE., DeschampsA.. Perioperative right ventricular dysfunction. *Curr Opin Anaesthesiol*2013;*26*:71–81.
30. DenaultA.Y., CoutureP., BuithieuJ., HaddadF., CarrierM., BabinD., et al. Left and right ventricular diastolic dysfunction as predictors of difficult separation from cardiopulmonary bypass. *Can J Anesth*2006;*53*:1020–9.
31. BraunwaldE.. *Braunwald's Heart Disease : A Textbook of Cardiovascular Medicine,* Philadelphia: Saunders, 2012.
32. SchairerJ.R., BiswasS., KeteyianS.J., AnanthasubramaniamK.. A systematic approach to evaluation of pericardial effusion and cardiac tamponade. *Cardiol Rev*2011;*19*:233–8.
33. MeurinP., TabetJ.Y., ThabutG., CristofiniP., FarrokhiT., FischbachM., et al. Nonsteroidal anti-

inflammatory drug treatment for postoperative pericardial effusion: a multicenter randomized, double-blind trial. *Ann Intern Med*2010;*152*:137–43.
34. DurandM., LamarcheY., DenaultA.. Pericardial tamponade. *Can J Anesth*2009;*56*:443–8.
35. PepiM., MuratoriM.. Echocardiography in the diagnosis and management of pericardial disease. *J Cardiovasc Med (Hagerstown)*2006;*7*:533–44.
36. PlotnickG.D., RubinD.C., FelicianoZ., ZiskindA.A.. Pulmonary hypertension decreases the predictive accuracy of echocardiographic clues for cardiac tamponade. *Chest*1995;*107*:919–24.
37. Dal-BiancoJ.P., SenguptaP.P., MookadamF., ChandrasekaranK., TajikA.J., KhandheriaB.K.. Role of echocardiography in the diagnosis of constrictive pericarditis. *J Am Soc Echocardiogr*2009;*22*:24–33.
38. MaronB.J., TowbinJ.A., ThieneG., AntzelevitchC., CorradoD., ArnettD., et al. Contemporary definitions and classification of the cardiomyopathies: an American Heart Association Scientific Statement from the Council on Clinical Cardiology, Heart Failure and Transplantation Committee; Quality of Care and Outcomes Research and Functional Genomics and Translational Biology Interdisciplinary Working Groups; and Council on Epidemiology and Prevention. *Circulation*2006;*113*:1807–16.
39. LosiM.A., NistriS., GalderisiM., BetocchiS., CecchiF., OlivottoI., et al. Echocardiography in patients with hypertrophic cardiomyopathy: usefulness of old and new techniques in the diagnosis and pathophysiological assessment. *Cardiovasc Ultrasound*2010;*8*:7.
40. ChockalingamA., DorairajanS., BhallaM., DellspergerK.C.. Unexplained hypotension: the spectrum of dynamic left ventricular outflow tract obstruction in critical care settings. *Crit Care Med*2009;*37*:729–34.
41. AfonsoL.C., BernalJ., BaxJ.J., AbrahamT.P.. Echocardiography in hypertrophic cardiomyopathy: the role of conventional and emerging technologies. *JACC Cardiovasc Imaging*2008;*1*:787–800.
42. CaselliS., MartinoA., GenuiniI., SantiniD., CarboneI., AgatiL., et al. Pathophysiology of dynamic left ventricular outflow tract obstruction in a critically ill patient. *Echocardiography*2010;*27*:E122–4.
43. WilliamsL.K., FrenneauxM.P., SteedsR.P.. Echocardiography in hypertrophic cardiomyopathy diagnosis, prognosis, and role in management. *EurJ Echocardiogr*2009;*10*:iii9–14.
44. WoodM.J., PicardM.H.. Utility of echocardiography in the evaluation of individuals with cardiomyopathy. *Heart*2004;*90*:707–12.
45. ThomasD.E., WheelerR., YousefZ.R., MasaniN.D.. The role of echocardiography in guiding management in dilated cardiomyopathy. *Eur J Echocardiogr*2009;*10*:iii15–21.
46. ZwasD.R., GotsmanI., AdmonD., KerenA.. Advances in the differentiation of constrictive pericarditis and restrictive cardiomyopathy. *Herz*2012;*37*:664–73.
47. NihoyannopoulosP., DawsonD.. Restrictive cardiomyopathies. *Eur J Echocardiogr*2009;*10*:iii23–33.
48. ChockalingamA., MehraA., DorairajanS., DellspergerK.C.. Acute left ventricular dysfunction in the critically ill. *Chest*2010;*138*:198–207.
49. HunterJ.D., DoddiM.. Sepsis and the heart. *Br J Anaesth*2010;*104*:3–11.
50. MerxM.W., WeberC.. Sepsis and the heart. *Circulation*2007;*116*:793–802.
51. Romero-BermejoF.J., Ruiz-BailenM., Gil-CebrianJ., Huertos-RanchalM.J.. Sepsis-induced cardiomyopathy. *Curr Cardiol Rev*2011;*7*:163–83.
52. Vieillard-BaronA.. *Septic cardiomyopathy*. *Ann Intensive Care*2011;*1*:6.
53. ChockalingamA., XieG.Y., DellspergerK.C.. Echocardiography in stress cardiomyopathy and acute LVOT obstruction. *Int J Cardiovasc Imaging*2010;*26*:527–35.
54. RichardC.. *Stress-related cardiomyopathies. Ann Intensive Care*2011;*1*:39.
55. GhadriJ.R., RuschitzkaF., LuscherT.F., TemplinC.. Takotsubo cardiomyopathy: still much more to

learn. *Heart*2014;*100*:1804–12.
56. BybeeK.A., PrasadA.. Stress-related cardiomyopathy syndromes. *Circulation*2008;*118*:397–409.
57. KapoorD., BybeeK.A.. Stress cardiomyopathy syndrome: a contemporary review. *Curr Heart Fail Rep*2009;*6*:265–71.
58. PearsonA.C., CastelloR., LabovitzA.J.. Safety and utility of transesophageal echocardiography in the critically ill patient. *Am Heart J*1990;*119*:1083–9.
59. DanielW.G., MuggeA.. Transesophageal echocardiography. *N Engl J Med*1995;*332*:1268–79.
60. SewardJ.B., KhandheriaB.K., OhJ.K., FreemanW.K., TajikA.J.. Critical appraisal of transesophageal echocardiography: limitations, pitfalls, and complications. *J Am Soc Echocardiogr*1992;*5*:288–305.

Chapter 6

Basic Regional Ventricular Systolic Function

Claudia H Viens, Pierre Couture and Antoine G Rochon

INTRODUCTION

Transesophageal echocardiography (TEE) has become a powerful diagnostic tool in the perioperative period and in the intensive care unit (ICU). The presence of segmental wall motion abnormalities (WMA) may be indicative of myocardial ischemia. Detection of regional left ventricular (LV) dysfunction is one of the most common indications for a basic TEE examination. This chapter will focus on the use of TEE in the evaluation of myocardial ischemia and complications of coronary artery disease.

SEGMENTAL MODEL

The American Heart Association (AHA) recommends defining the LV using a 17-segment model (**Figure 6.1**).[1] In the 17-segment model, the LV structure is divided from the base to apex into four levels: basal, mid-papillary, apical and apex, corresponding to the proximal, middle, and apical territories of the coronary arteries. The basal and mid-papillary levels each have six segments (anteroseptal, anterior, anterolateral, inferoseptal, inferior, and inferolateral), whereas there are four apical segments (septal, anterior, lateral, and inferior). The apex is the 17 th segment. Starting with the basal anterior segment, each segment is numbered in a clockwise fashion. From different TEE views, all of the LV segments can be identified and if WMA are observed these can be correlated with the stenotic coronary artery (Figure

6.1). Although visualization of LV segments from the transgastric (TG) mid-papillary short axis (SAX) view has prognostic importance, physicians trained in basic TEE should perform a more comprehensive evaluation of regional LV function. [3]

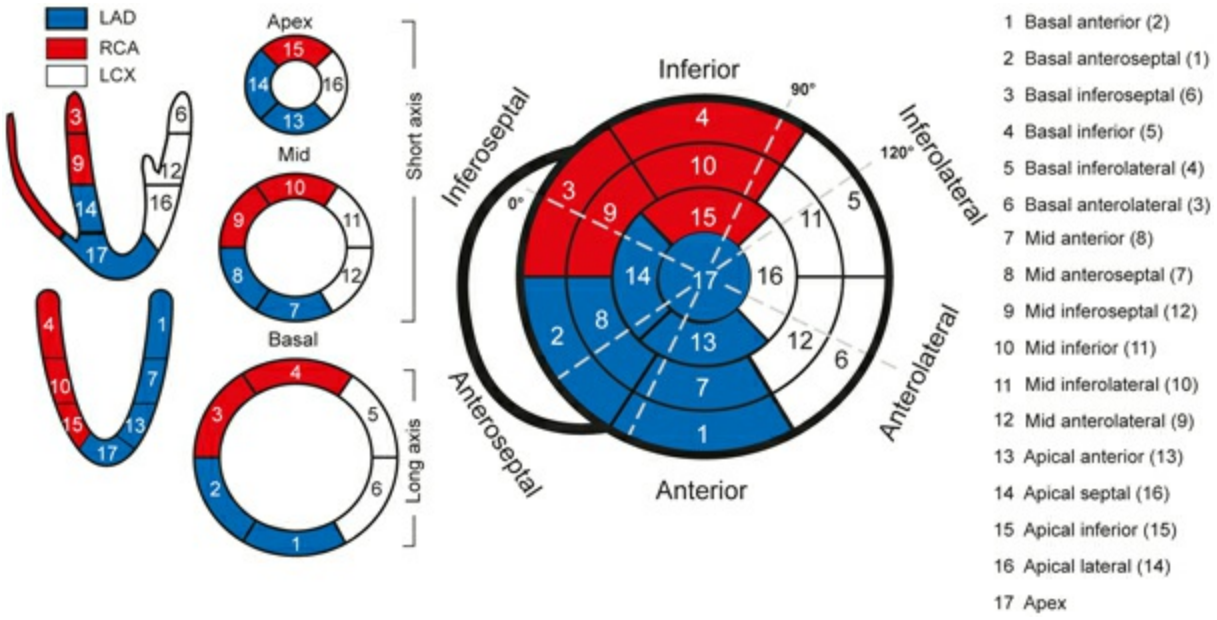

Fig. 6.1 Segmental model of the left ventricle. Transesophageal echocardiographic correlation of coronary artery distribution and the American Heart Association 17-segment model is shown. The corresponding segment numbers from the American Society of Echocardiography are in parentheses. LAD, left anterior descending; LCX, left circumflex artery; RCA, right coronary artery. (Adapted with permission from Denault *et al*. [2])

TEE Views

The mid-esophageal (ME) four-chamber view allows simultaneous visualization of the left and right ventricle (RV) (**Figure 6.2 A,B**). Foreshortening of the left and right ventricular cavities can occur in this view, but can be corrected by retroflexion of the probe tip, although this may degrade the image quality. This view assesses segmental function of the mid-inferior septum and septal apex as perfused by the left anterior descending (LAD) coronary artery, the basal inferior septum by the right coronary artery (RCA) and the basal and mid-anterolateral walls supplied by the circumflex artery. Rotation of the transducer angle to approximately 45° depicts the inferior septum to the left of the screen and the anterolateral wall to the right. With the transducer angle at 90°, the ME two-chamber view (**Figure 6.2 C,D**) shows the inferior wall supplied by the RCA, anterior wall perfused by

the LAD artery, and adjacent portions of the apex that often has dual coronary artery support. Further transducer angle rotation to 120°–150° results in a ME long-axis (LAX) view (**Figure 6.2 E,F**), with the anterior septum and inferolateral wall on the right and left of the screen, respectively.

Using the transgastric (TG) approach (**Figure 6.3**), a series of SAX views can be obtained at 0°–20° by modifying probe depth and probe tip anteflexion. For example, maximal anteflexion generally images the basal LV segments and the mitral valve (**Figure 6.3 A,B**). A lesser degree of anteflexion or slight probe advancement will result in SAX views at the high and low papillary muscle levels (**Figure 6.3 C,D**). In these SAX views, the inferior wall (segments 4, 10, 15 are supplied by the RCA) (**Figure 6.1**) is seen at the top of the display, the anterior wall at the bottom, the inferolateral and anterolateral walls to the right, the anterior and inferior septum to the display lower left and upper left. Further probe advancement will result in a SAX view of the LV apical segments (**Figure 6.3 E,F**).

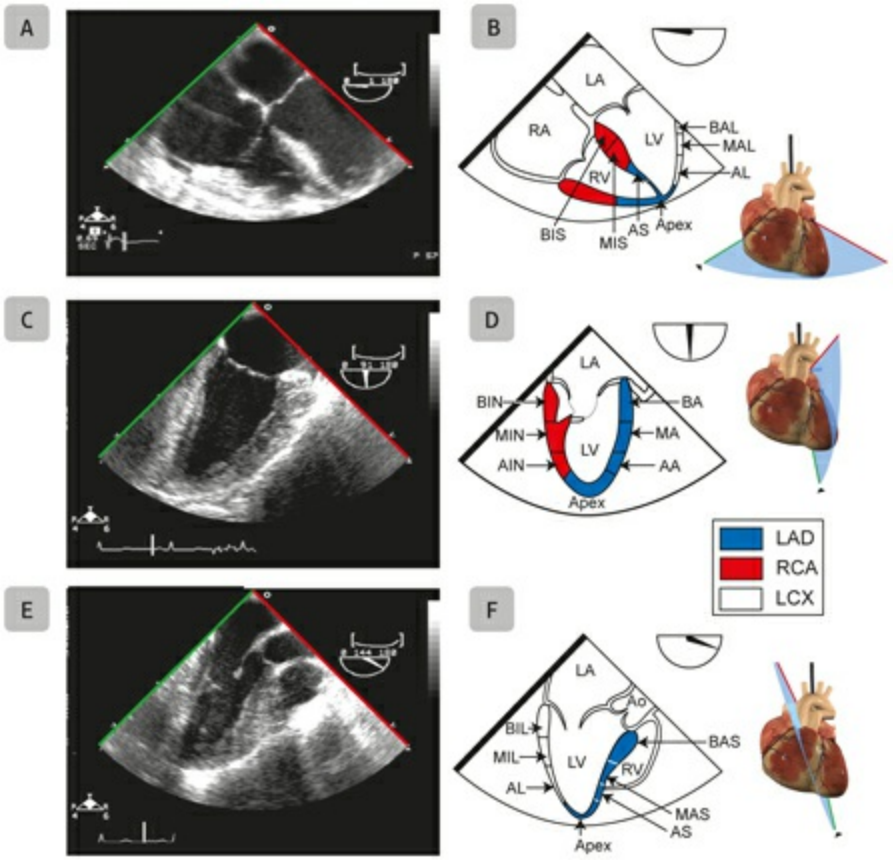

Fig. 6.2 Left ventricle (LV) function. Mid-esophageal views to evaluate right ventricle (RV) and LV function include the (A, B) four-chamber, (C,D) two-chamber, and (E,F) long- axis views. AA, apical

anterior; AIN, apical inferior; AL, apical lateral; Ao, aorta; AS, apical septal; BA, basal anterior; BAL, basal anterolateral; BAS, basal anteroseptal; BIL, basal inferolateral; BIN, basal inferior; BIS, basal inferoseptal; LA, left atrium; LAD, left anterior descending; LCX, left circumflex artery; MA, midanterior; MAL, mid-anterolateral; MAS, mid-anteroseptal; MIL, midinferolateral; MIN, mid-inferior; MIS, mid-inferoseptal; RA, right atrium; RCA, right coronary artery. (Reproduced with permission from Denault *et al.*[2])

A,C&E: https://youtu.be/jGmxgYj5zHc

Transducer angle rotation to 90° yields a transgastric two-chamber view, with the inferior (segments 4, 10, 15 are supplied by the RCA) and anterior (segments 1, 7, 13, 17 are supplied by the LAD artery) (**Figure 6.1**) walls at the display top and bottom, respectively. It is usually possible to visualize the non-truncated, true left ventricular apex (segment 17) on the left of the display in this view and to identify a wall motion abnormality, aneurysm, or thrombus. Further angle rotation to 120°–150° will result in a LAX view, with the inferolateral wall to the left and the anterior septum on the right of the display.

CORONARY ANATOMY AND MYOCARDIAL FUNCTION

The coronary arteries originate from the sinuses of Valsalva and provide blood flow to the myocardium. The left main coronary artery from the left sinus of Valsalva gives rise to the LAD and circumflex coronary arteries (**Figure 6.4 A**). The LAD descends in the anterior ventricular groove to the LV apex and gives off diagonal and septal branches. The circumflex coronary artery courses laterally in the left atrioventricular groove, dividing into obtuse marginal branches. The RCA originates from the right sinus of Valsalva and descends medially in the right atrioventricular groove (**Figure 6.5**). The left main coronary and the RCA can sometimes be seen at their origin in the sinuses of Valsalva in the ME aortic valve LAX and SAX views.

Studies correlating coronary angiography and echocardiography have described the specific coronary perfusion of each LV segments. [1] The LAD

gives blood supply to the anterior segments of the interventricular septum (IVS), to the anterior LV free wall, and to the septal and anterior segments of the apex. The circumflex artery provides blood supply to the inferolateral and the anterolateral LV segments, and to the lateral apex. The RCA provides blood supply to the RV, the LV inferior free wall, the inferior half of the septum, and the inferior apex. Given the coronary distribution, ischemic lesions will translate into regional WMA that can identify the culprit coronary artery (**Figure 6.5**).

Right ventricular anatomy is complex and its function should be examined carefully in multiple views including the ME four chamber, ME RV inflow-outflow, and TG RV inflow views. The RV free wall is perfused by the RCA and due to its thinner structure receives blood flow in both systole and diastole. Importantly, the RV free wall and the septum both contribute equally to RV function. [4] The LAD supplies the anterior two-thirds of the septum. The inferoposterior third of the septum is supplied by the posterior descending artery, a branch of the RCA in 70% of patients.

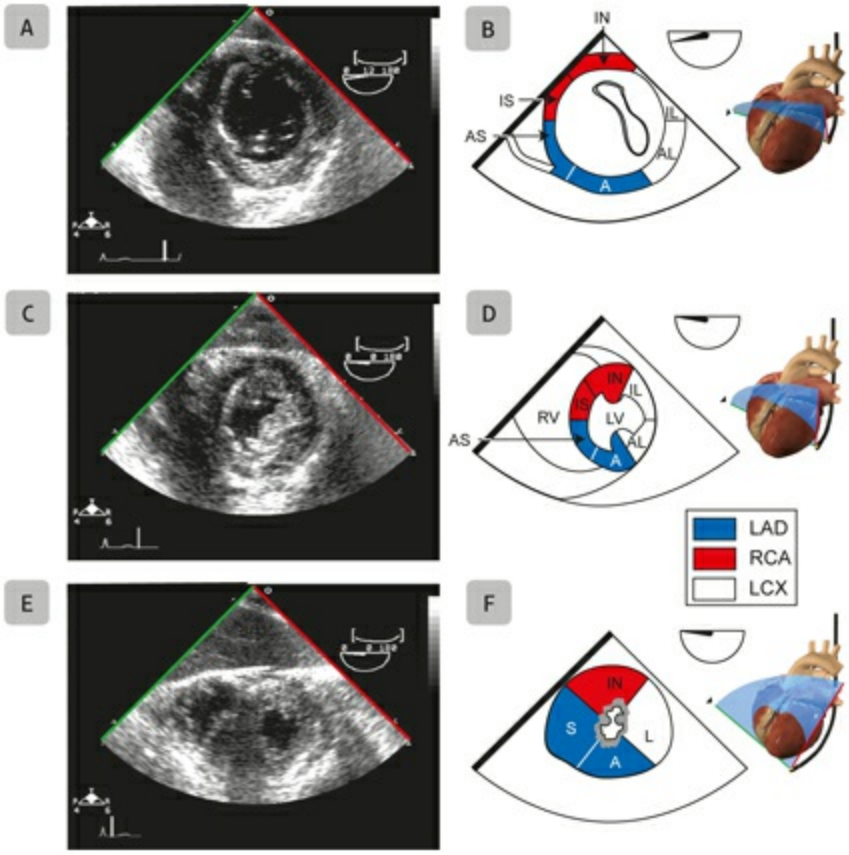

Fig. 6.3 Left ventricle (LV) function. (A, B) Basal, (C,D) mid and (E,F) apical transgastric short-axis

views in a 49-year-old female are shown. A, anterior; AL, anterolateral; AS, anteroseptal; IL, inferolateral; IN, inferior; IS, inferoseptal; L, lateral; LAD, left anterior descending; LCX, left circumflex artery; RCA, right coronary artery; RV, right ventricle; S, septal. (Reproduced with permission from Denault *et al.*[2])

A,C&E: https://youtu.be/VjXTDb8Y8kw

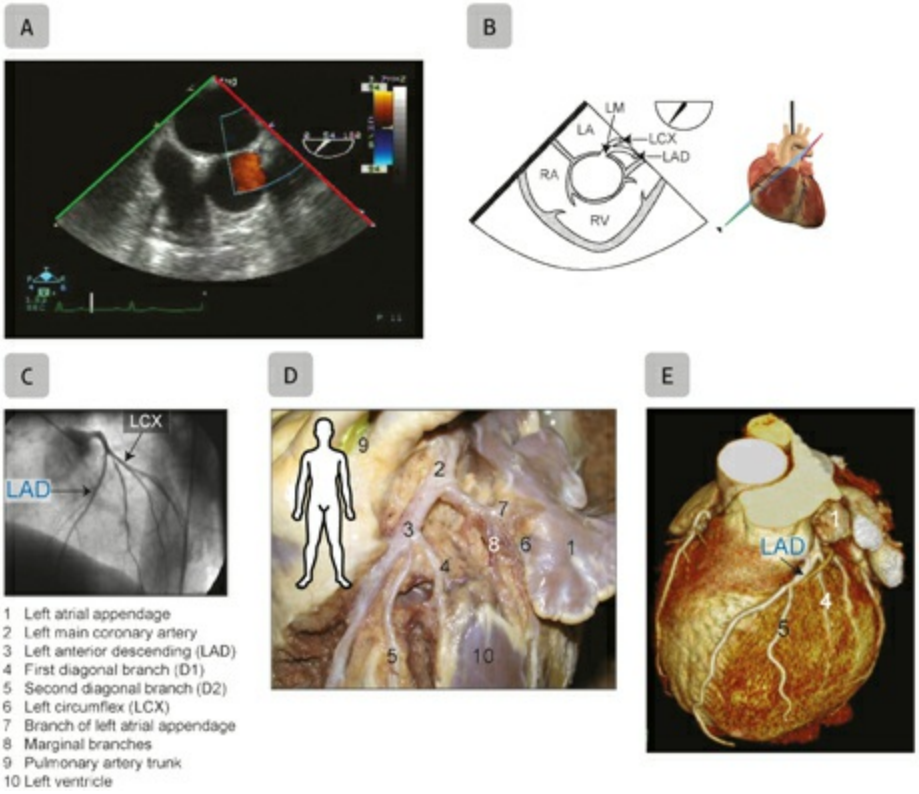

Fig. 6.4 Left coronary artery. (A, B) Mid-esophageal aortic valve short-axis with color Doppler, over the origin of the left main coronary artery is compared to (C) angiography, (D) an anatomic specimen, and (E) 256-slice ECG-gated computed tomography views of the left coronary artery. LA, left atrium; LM, left main coronary artery; RA, right atrium; RV, right ventricle. Photos C-E courtesy of Drs Philippe L L'Allier, Nicolas Durrleman, and Carl Chartrand- Lefebvre. (Reproduced with permission from Denault *et al.*[2])

A: https://youtu.be/VNh2QWrNtig

C: https://youtu.be/Cto1mrGu1U0

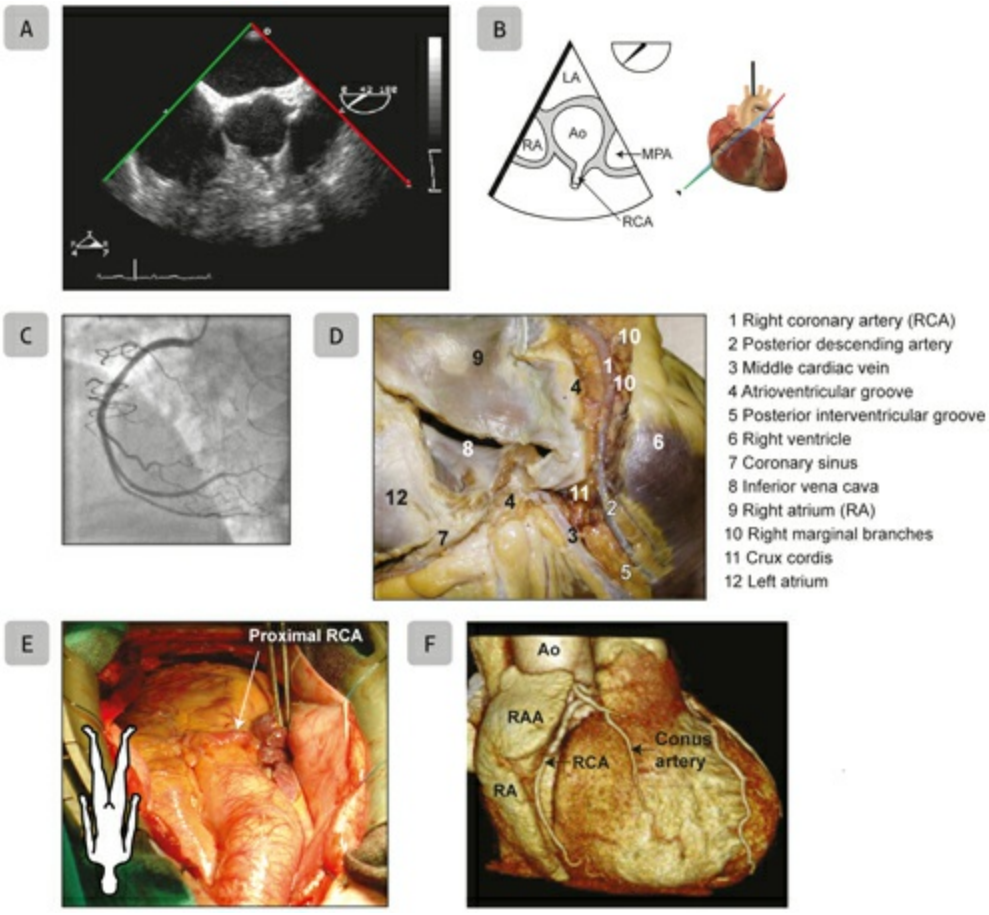

Fig. 6.5 Right coronary artery. (A, B) Mid-esophageal aortic valve short-axis showing the origin of the right coronary artery is compared to (C) angiography, (D) an anatomic specimen, (E) an intraoperative view, and (F) 256-slice ECG-gated computed tomography views of the right coronary artery. Ao, aorta; LA, left atrium; MPA, main pulmonary artery; RAA, right atrial appendage; Photos C-F courtesy of Drs Philippe L L'Allier, Nicolas Durrleman and Carl Chartrand-Lefebvre. (Reproduced with permission from Denault *et al*.[2])

A: https://youtu.be/Pix5-UGzKuQ

C: https://youtu.be/gHJshMjmVzU

E: https://youtu.be/xoW69z93KRc

SEGMENTAL WALL MOTION ANALYSIS

As the LV contracts, its endocardial border will move towards the center of the ventricular cavity (endocardial excursion or radial shortening) resulting in LV myocardial thickening and reduced LV cavity area. Normal LV radial shortening and myocardial thickening is greater than 30%. [5] Segmental WMAs take place in the myocardium within seconds after interruption of myocardial blood flow to the affected segment, many minutes before electrocardiographic (ECG) changes and angina occur. The WMA are classified as hypokinesis when ventricular contraction is reduced in magnitude, akinesis when it is absent, and dyskinesis when there is paradoxical systolic motion (**Table 6.1**). The observation of new WMAs is more sensitive to detect acute ischemia than multi-lead ECG or invasive hemodynamic monitoring. The appearance of new WMAs has been found to predict adverse outcomes after cardiac surgery. [5–7] Decreased myocardial thickening is in fact more specific for diagnosing ischemia. [8]

The regional wall motion score index (WMSI) provides a subjective yet effective means to assess LV function and detect and quantify acute myocardial ischemia (**Table 6.1**). Each of the 17 segments is scored on a scale of 1 to 5. A score of 1 is given to a normally contracting or hyperkinetic segment, 2 for an hypokinetic segment, 3 for an akinetic segment, 4 in the presence of a dyskinetic segment, and 5 for an aneurysmal (diastolic deformation) segment. [9] The WMSI is equal to the sum of the regional scores divided by the number of evaluable segments. It ranges from 1.0 in the normal heart to 3.9 in severe systolic dysfunction. The WMSI has prognostic value in several clinical studies. [10–13]

LIMITATION OF SEGMENTAL WALL ANALYSIS

The observation of WMA has many limitations, despite there being important regional differences in myocardial con- traction. [14] Heterogeneity of normal segmental wall motion, left bundle branch block, RV volume overload, constrictive pericarditis, pacemaker rhythm, and post-cardiac surgery time frame must all be taken into account as these can alter interventricular septal wall motion. Regional WMA detection may also be related to sudden changes in loading conditions.

Furthermore, movements of the ventricular segments are affected by the rotation and the translation of the heart. Tethering of the adjacent myocardium can overestimate the ischemic area. The TG mid-papillary SAX view is often used to detect ischemia, although only six LV segments are evaluated. Other TEE views are needed to analyze all 17 segments. Intraoperative regional WMA are diagnosed with real-time TEE (on-line), and some ischemic episodes may be missed. [15] Finally, new regional WMA in non-cardiac surgery are not always associated with postoperative cardiac complications. [16] The distinction between stunned or hibernating myocardium from infarcted or ischemic myocardium is another limitation of the observation of WMAs. Stunned myocardium suffers from prolonged post-ischemic contractile dysfunction and has been observed clinically in stress-induced angina, unstable angina, post-thrombolysis, after percutaneous transluminal angioplasty and after surgical revascularization. It may take up to several weeks for the stunned myocardium to recover normal function (**Figure 6.6**).

Table 6.1 Wall Motion Scoring Index

Movement	Radial displacement (%)	Thickening
Normal or hyperkinesis = 1	>30	Normal
Hypokinesis = 2	0–30	Decreased
Akinesis = 3	0	Negligible
Dyskinesis = 4	Systolic lengthening	Paradoxical systolic motion
Aneurysmal = 5	Paradoxical displacement	Diastolic deformation

Note: Adapted from Lang et al. [9]

NEW IMAGING MODALITIES

There is still very few data for the routine use and application of these methods; however, they have the potential to improve myocardial function quantification and help detect subclinical myocardial dysfunction.

Tissue Doppler Imaging

Tissue Doppler imaging (TDI) filters out the high velocity signals from blood to isolate the low velocity, high amplitude signals of myocardial tissue movement. Combined with pulsed wave (PW) Doppler, the analysis of direction and velocity of an individual segment of myocardium can quantify regional wall motion (**Figure 6.7**). [17] Maximum velocities below 7.5 cm/s and mean values of 5.5 cm/s are indicative of myocardial dysfunction. Reduction in regional myocardial velocities during ischemia have been observed in clinical studies. [18–20]

However, the simultaneous analysis of multiple segments using PW Doppler is only possible off-line in the majority of ultrasound platforms. Furthermore, being based on the Doppler equation, measured velocities will be inaccurate if the Doppler beam is not parallel to the movement of the interrogated segment. Finally, akinetic segments tethered by adjacent contracting myocardium will have near-normal velocities and the poor spatial resolution does not differentiate between the sub-endocardium and sub-epicardium

Color Tissue Doppler Imaging

Color TDI superimposes color-coded tissue velocity onto a real-time live 2D image that can also be displayed as a curved M-mode (**Figure 6.8**). Color TDI evaluates mean velocities from each pixel so the velocity is lower than that of PW spectral TDI, which measures peak velocities at the sample volume. Color TDI compared with pulsed TDI has superior spatial resolution making it possible to evaluate multiple segments at the same time.

Strain and Strain Rate

In systole, the myocardium shortens in length while it elongates during diastole. Strain measures this deformation during the cardiac cycle. It is defined as the change in myocardial length in relation to myocardial initial length divided by the initial length (**Figure 6.9**).

$$\varepsilon L = L - L\ 0\ L\ 0$$

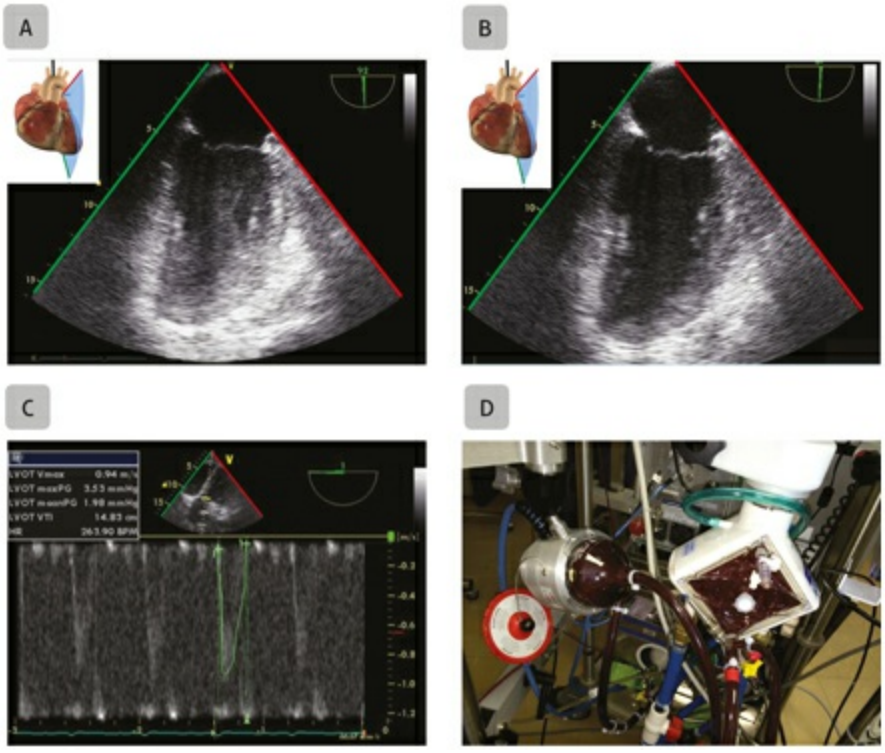

Fig. 6.6 Extracorporeal membrane oxygenation (ECMO). A 37-year-old male has an acute myocardial infarction complicated by cardiogenic shock and is supported by ECMO. (A) Mid-esophageal two-

chamber view shows spontaneous contrast in the left ventricular cavity on ECMO day 2. (B) On ECMO day 4, he completely recovered and was switched to veno-venous ECMO because of severe aspiration pneumonia. (C) At that time, the velocity time integral through the left ventricular outflow tract was below 15 cm. (D) Note the darker venous color of blood in both the inflow and outflow cannula.

A: https://youtu.be/xPvIuc_QeEc

B: https://youtu.be/KkqZZT36gK0

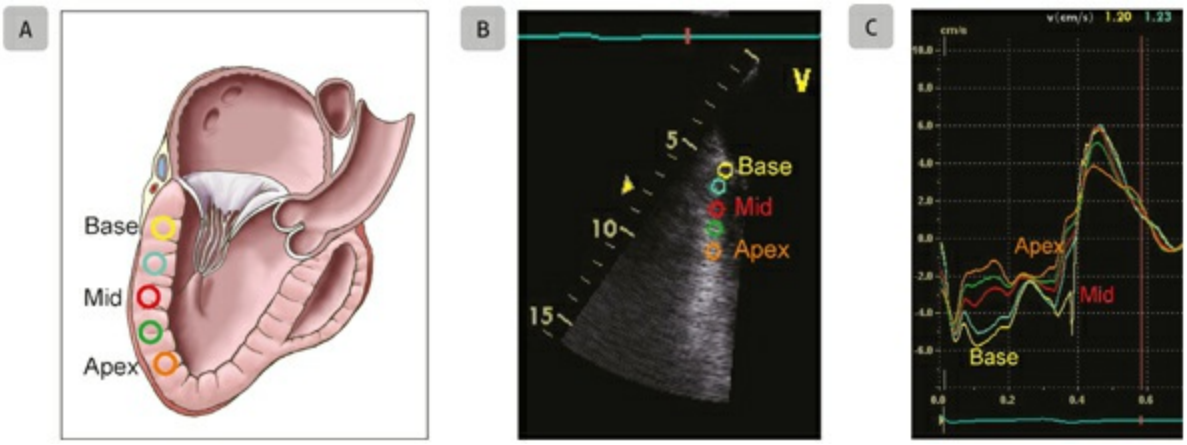

Fig. 6.7 Tissue Doppler imaging (TDI). (A-C) TDI of the mid-esophageal long-axis view of the left ventricle (LV) inferolateral wall in a 56-year-old male is shown. (B) Sample volumes are positioned in the basal (yellow), mid (red), and apical (orange) myocardial segments in this narrowed sector of the inferolateral LV wall. (C) A spectral display over one cardiac cycle shows the individual segment myocardial velocities (cm/s) after off-line post-processing of TDI. Normally the basal segments have higher velocities than the apical segments. Part A courtesy of Gian-Marco Busato. (Reproduced with permission from Denault *et al.*[2])

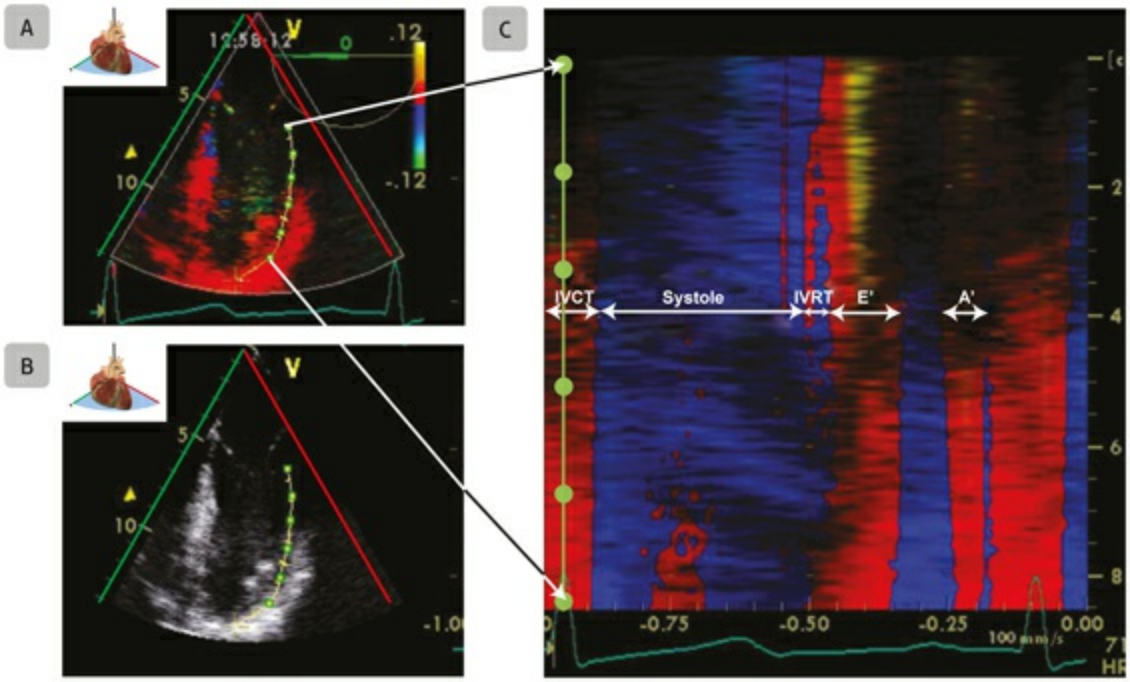

Fig. 6.8 Color tissue Doppler imaging (TDI) curved M-mode. (A) Stored color TDI of a mid-esophageal four-chamber view is shown. (B) The same image with the color overlay turned off: allows visualization of the precise location of the sample points on the anterolateral wall of the left ventricle (LV). (C) Corresponding curved M-mode of the anterolateral wall is displayed for a single cardiac cycle. The duration of each period of the cardiac cycle can be precisely measured in this normal tracing. *A'*, late diastolic velocity; E', early diastolic velocity; HR, heart rate; IVCT, isovolumic contraction time; IVRT, isovolumic relaxation time. (Reproduced with permission from Denault *et al.*[2])

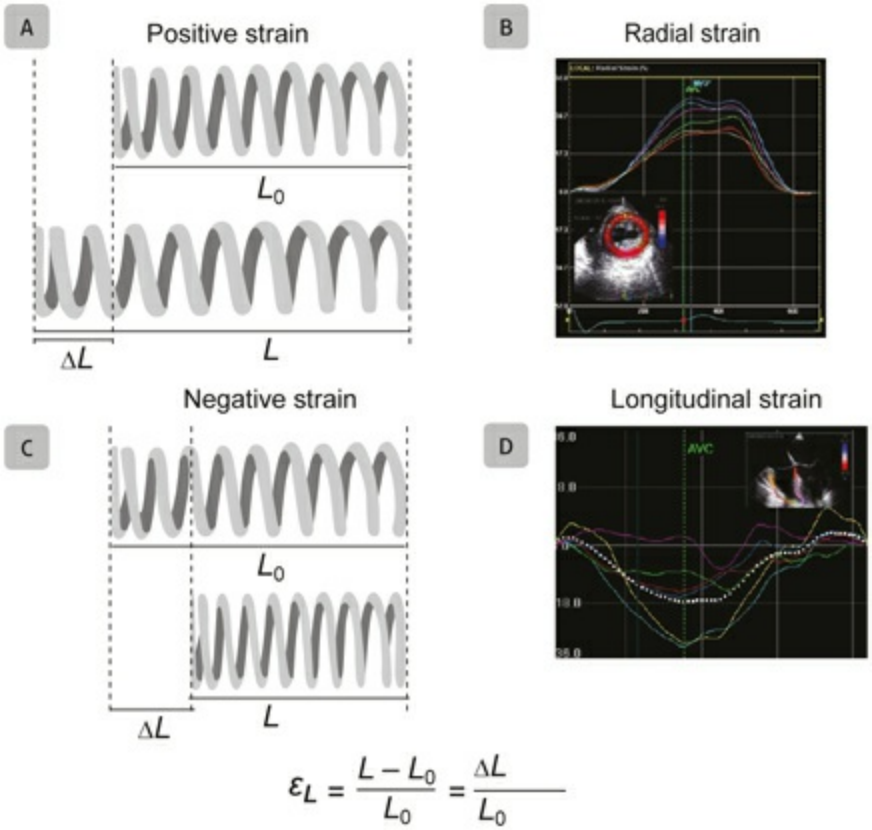

Fig. 6.9 Strain. (A, B) When strain (e) is positive, the initial length value (L_0) is smaller than the final length (L). For instance, in the transgastric mid short-axis view, the myocardial thickness increases during radial shortening. The radial strain obtained from this view will be positive (thickening). (C,D) The opposite applies for a negative strain. Typically, the longitudinal contraction of the left ventricle obtained from a midesophageal four-chamber view has a negative systolic strain. (Reproduced with permission from Denault *et al.*[2])

SR= V 1 − V 2 L

Myocardial ischemia translates into decreased deformation with reductions in systolic strain and SR. By convention, myocardial shortening has a negative SR while myocardial lengthening is positive strain. Radial strain is measured in the TG mid-papillary SAX view and is positive during systole (**Figure 6.9 B**). Longitudinal strain is measured in ME views and is negative during systole (**Figure 6.9 D**). **Fig.** 6.10 Strain rate (SR). (A) Septal velocity-based SR measurement from a mid-esophageal four-chamber view is illustrated. The SR (1/s) represents the difference in velocity (V1 and V2) at two points separated by a distance (L, the offset distance) corresponding to the difference from the transducer to points L1 and L2 (L = L1 - L2). (B) Velocity tracing at two specific points (L1 and L2) are shown. The SR tracing

corresponds to the velocity difference at these two points divided by the length that separates them (L1 - L2). A, atrial contraction; E, early filling; S, systolic. Illustration courtesy of Gian-Marco Busato. (Reproduced with permission from Denault *et al.* [2])

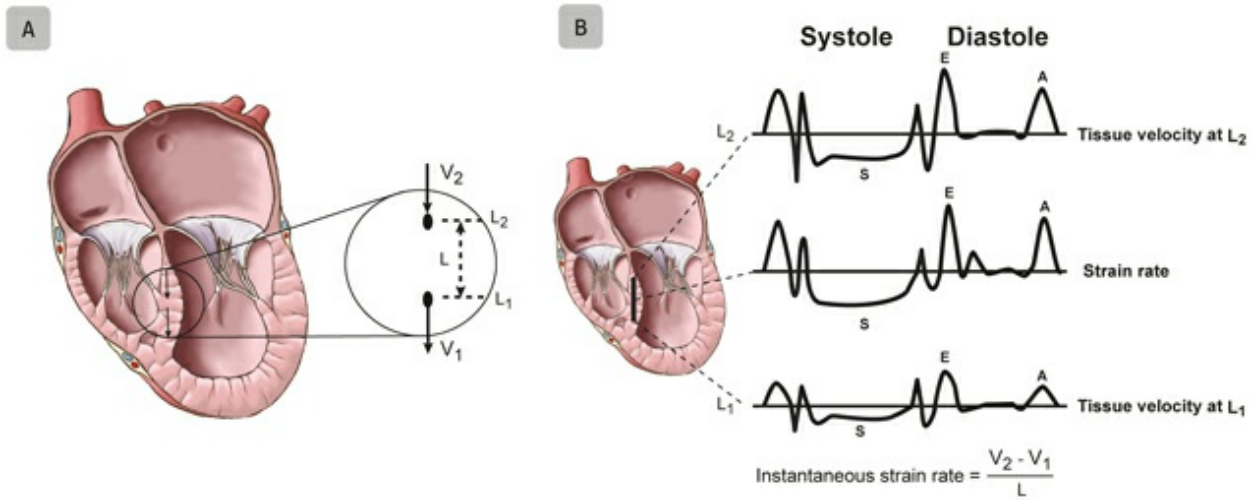

Fig. 6.10 Strain rate (SR). (A) Septal velocity-based SR measurement from a mid-esophageal four-chamber view is illustrated. The SR (1/s) represents the difference in velocity (V1 and V2) at two points separated by a distance (L, the offset distance) corresponding to the difference from the transducer to points L1 and L2 (L = L1 - L2). (B) Velocity tracing at two specific points (L1 and L2) are shown. The SR tracing corresponds to the velocity difference at these two points divided by the length that separates them (L1 - L2). A, atrial contraction; E, early filling; S, systolic. Illustration courtesy of Gian-Marco Busato. (Reproduced with permission from Denault *et al.*[2])

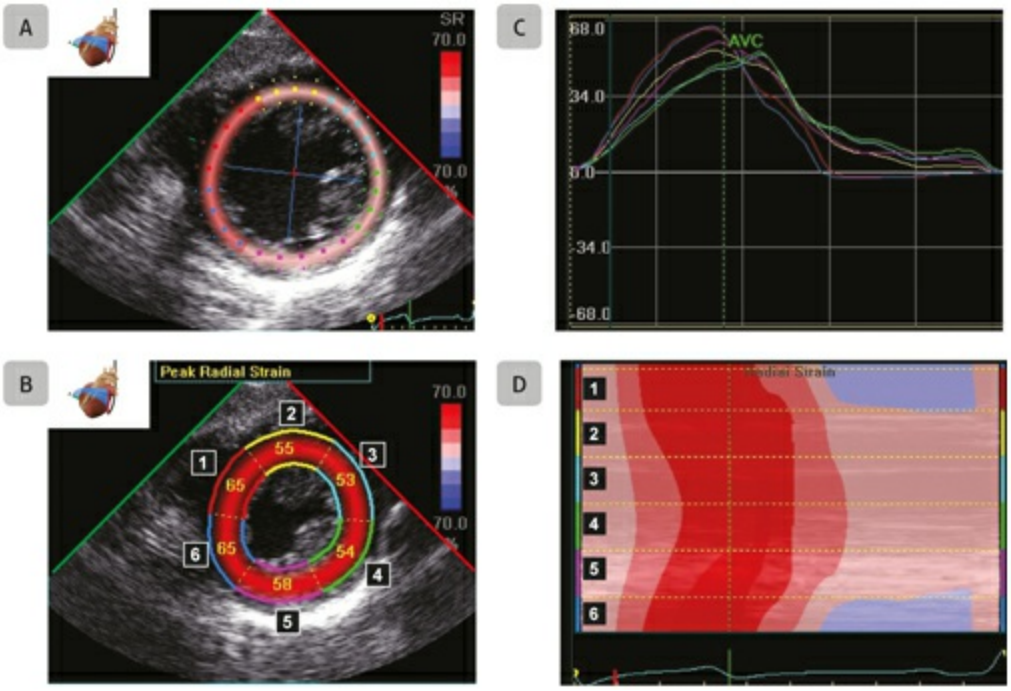

Fig. 6.11 Radial strain. (A, B) Transgastric mid short- axis view with radial strain by 2D speckle tracking in a normal patient is shown. The peak radial strain has a positive value for all left ventricular (LV) segments because of myocardial thickening during systole. (C,D) The change in peak radial strain of each LV segment can be displayed as (C) individual tracings over time or (D) as a curved M-mode map over time. (Reproduced with permission from Denault *et al.*[2])

A: https://youtu.be/Vg_tG4h63q0

Strain was an off-line measure which is now becoming available on-line in a growing number of ultrasound platforms. Strain is obtained from saved TDI loops or by using 2D speckle tracking technology (**Figure 6.11**). Speckle tracking is a technique based on the tracking of interference patterns and natural acoustic reflections created by B-mode imaging. [21] These reflections are “speckles” that have unique patterns for each myocardial segment. Strain and SR can be displayed as a function of time or as curved anatomic M-mode images. Radial and segmental strain and SR will have different values according to the interrogated myocardial segment (**Table 6.2**). Strain will be reduced in the ischemic myocardium and absent in the infarcted heart muscle. Determination of global longitudinal strain (GLS) is

now recommended in the new guidelines for the evaluation of LV function. [22] The normal value is -20%, but may vary slightly according to specific vendors' equipment and software (**Figure 6.12**). 22]

Table 6.2 Strain Rate of Individual Myocardial Segmen

	Septum	Lateral	Inferior	Anterior
Peak systolic wave (Ssr)				
Basal	0.99 ± 0.49	1.5 ± 0.74	0.88 ± 0.39	1.64 ± 0.9
Mid	1.25 ± 0.73	1.29 ± 0.58	0.95 ± 0.54	0.98 ± 0.68
Apical	1.15 ± 0.5	1.09 ± 0.59	1.38 ± 0.45	1.05 ± 0.63
Early diastolic wave (Esr)				
Basal	1.95 ± 0.89	1.92 ± 1.11	1.85 ± 0.89	2.03 ± 0.99
Mid	1.94 ± 0.97	1.71 ± 0.66	1.92 ± 1.2	1.7 ± 0.82
Apical	1.91 ± 0.66	1.81 ± 0.87	2.29 ± 0.88	1.76 ± 0.98
Late diastolic wave (Asr)				
Basal	1.54 ± 0.93	0.93 ± 0.59	1.18 ± 0.78	1.49 ± 0.96
Mid	1.29 ± 0.86	1.48 ± 0.77	0.78 ± 0.62	1.04 ± 0.57
Apical	0.95 ± 0.54	1.07 ± 0.68	1.68 ± 0.76	0.68 ± 0.65

Peak systolic (Ssr), early (Esr), and late (Asr) diastolic strain rates shown in 1/sec. Note that these values were obtained using transthoracic echocardiography. Source: From Sun et al. [23]

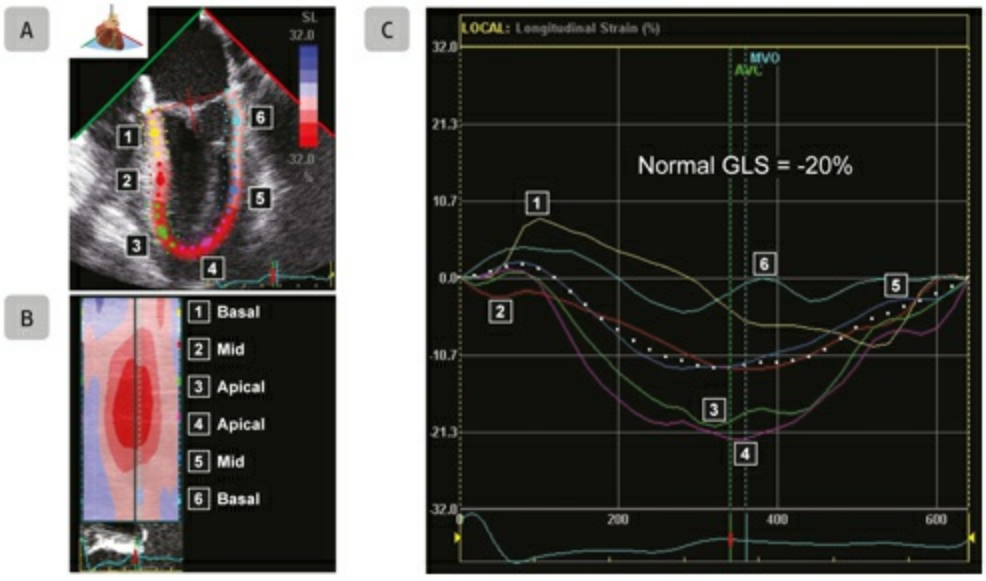

Fig. 6.12 Global longitudinal strain. (A—C) Midesophageal four- chamber view with peak global

longitudinal strain (GLS) by 2D speckle tracking is shown. Both the (B) curved M-mode mapping and(C) individual sampling curves show that the basal regions (1,6) have lower strain value compared to the apical regions (3,4). Normal GLS is -20%.[22] AVC, aortic valve closure; MVO, mitral valve opening; SL, strain longitudinal. (Reproduced with permission from Denault *et al*.[2])

Limitations of TDI to assess strain and SR are poor dataset from reverberations, side lobes or dropout, and poor Doppler alignment. Speckle tracking is less influenced by these artifacts, although reverberations and dropout remain problematic. An advantage of speckle tracking is that the myocardial velocities are independent of the Doppler angle, which permits simultaneous 2D radial and longitudinal assessments.

3D TEE

Three-dimensional TEE is a promising new analytic modality that correlates well with cardiac computed tomography and magnetic resonance imaging analysis of LV morphology and function. [24] However, poor 2D TEE images will result in a poor quality full-volume 3D dataset emphasizing the importance of acquiring high quality 2D images. Software analysis of a full-volume dataset using semi-automated endocardial border detection creates a dynamic cast of the LV endocardial cavity that allows calculation of end-diastolic and end-systolic volumes, stroke volume, and ejection fraction. The endocardial cast is automatically divided into 17 wedges mimicking the ASE 17 segments model (**Figure 6.13**). The regional wall motion analysis is based on volumetric changes over time and allows rapid detection of dyskinetic segments with high sensitivity and specificity. [25] Further studies to assess the use of 3D TEE in the ischemic heart are warranted.

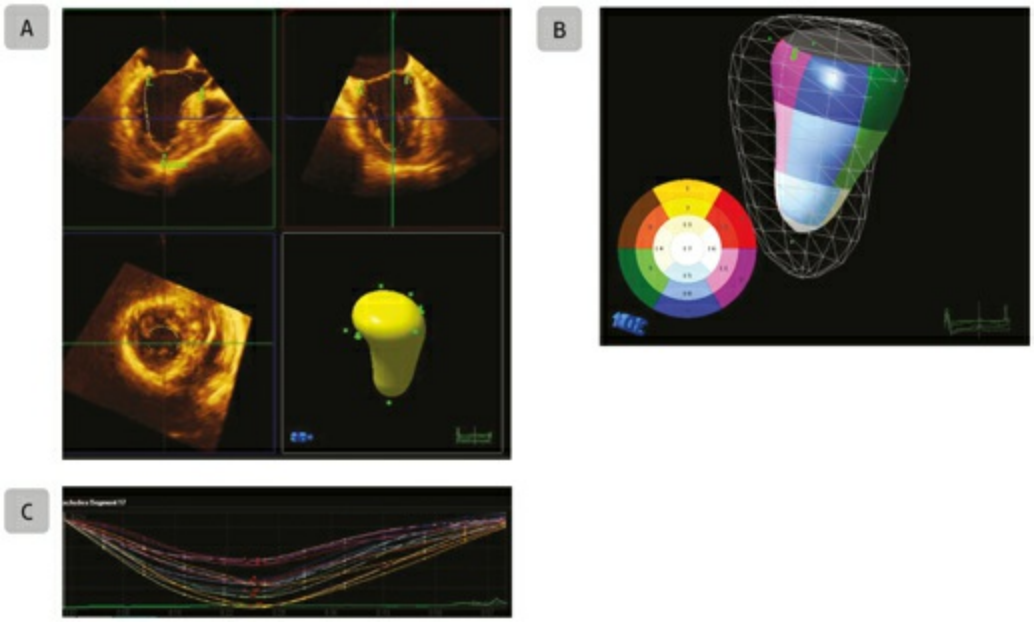

Fig. 6.13 Left ventricular (LV) function. (A) The 3D full volume dataset of the LV can be processed with special analytical software to create (B) a dynamic 17-segment 3D endocardial cast. (C) The change in volume of each of the 17 segments is plotted over time and displayed in the lower diagram. (Reproduced with permission from Denault *et al.*[2])

A: https://youtu.be/At8Q5EStCaU

B: https://youtu.be/NeH9gjxTwMA

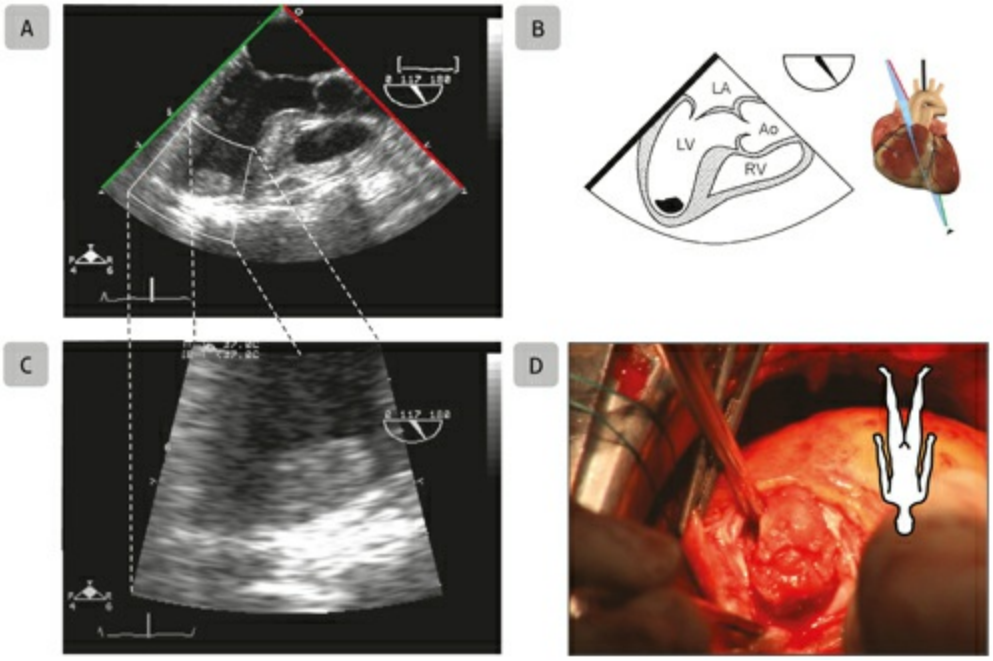

Fig. 6.14 Apical thrombus. (A, B) Left ventricle (LV) apical ball thrombus is seen in a mid-esophageal long-axis view in a 68-year-old female before thrombectomy.Zooming is useful to confirm the observation. Intraoperative findings are shown. Ao, aorta; LA, left atrium; RV, right ventricle. Photo D courtesy of Dr Michel Carrier. (Reproduced with permission from Denault *et al.*[2])

A: https://youtu.be/8CYXpdNfPOY

D: https://youtu.be/f8YQGHA0BgA

ISCHEMIC COMPLICATIONS AND ASSOCIATED FINDINGS

Although the goal of a basic TEE examination is focused on monitoring, those performing basic TEE must be able to recognize specific diagnoses that may require confirmation from an individual with advanced skills.

Left Ventricular Thrombus

Large anterior wall infarction puts the patient at particular risk for thrombus formation, especially in the presence of a ventricular aneurysm (**Figure 6.14**). Transesophageal echocardiography is inferior to TTE for the detection of LV thrombi because of the difficulty in visualizing the LV apex from the esophagus. [26] The deep transgastric or transgastric two-chamber views are the most useful for its detection.

Ischemic Mitral Regurgitation

Although rare (<1% of myocardial infarction) acute mitral regurgitation (MR) caused by partial or complete rupture of a papillary muscle may lead to severe MR and heart failure that requires emergent surgical intervention (**Figure 6.15**). Ischemic MR is more common, less severe, and results from segmental WMA. Assessment of cardiac valve abnormalities is described in Chapter 7, Basic Valve Diseases.

Ventricular Dilatation and Aneurysm

Within 48 hours of myocardial infarction, there can be stretching and thinning of the infarcted zone leading to augmentation of LV end-diastolic volume resulting in LV dilation, aneurysm formation, and myocardial wall rupture. Remodeling of the entire LV cavity involving non-ischemic segments can be observed later. Left ventricular aneurysm is a common complication among survivors of non-reperfused, transmural myocardial infarctions. Aneurysms occur four times more often at the apex and at the anterior wall than the inferobasal wall. True aneurysms result from expansion of the infarcted area and myocardial thinning of all three layers of the ventricular wall. On TEE, the aneurysmal segments are dyskinetic or akinetic distorting the LV shape. They appear as an outpouching of ventricular myocardium with well-defined borders and a wide neck persisting in diastole (**Figure 6.16**). Rupture of the ventricular free wall with a localized hemopericardium contained by the parietal pericardium defines a pseudo-aneurysm and is a rare complication of myo-cardial infarction. On TEE, it will appear as an outpouching connected to the LV cavity by a narrow neck with an abrupt rupture of the myocardial wall. In systole, expansion of the LV pseudo-aneurysm contrasts with the LV cavity getting smaller (**Figure 6.17**).

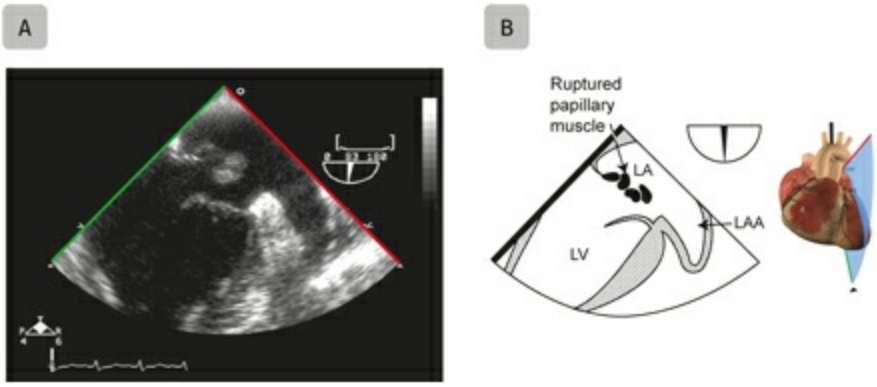

Fig. 6.15 Ruptured papillary muscle. (A, B) Mid-esophageal two-chamber view shows a flail posterior mitral leaflet with acute postero-medial papillary muscle rupture following an inferior myocardial infarction. LA, left atrium; LAA, left atrial appendage; LV, left ventricle. (Reproduced with permission from Denault *et al.*[2])

A: https://youtu.be/GjWv638IKHI

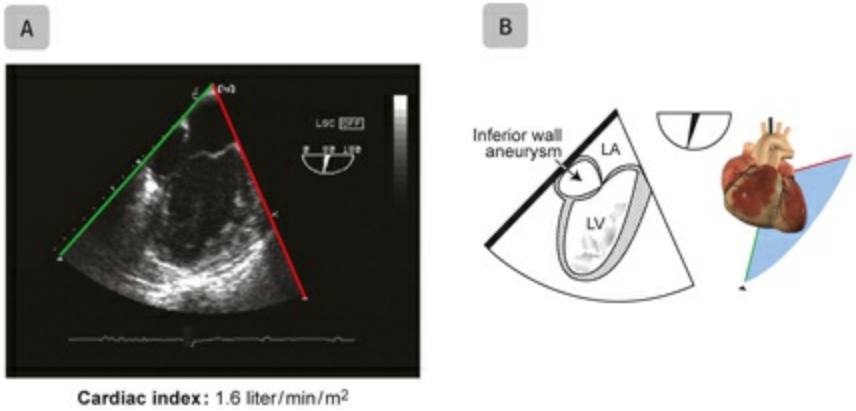

Fig. 6.16 Inferior left ventricle (LV) aneurysm. (A, B) Mid-esophageal two-chamber view shows the presence of spontaneous contrast in the LV with a large inferior basal aneurysm in a 57-year-old male. LA, left atrium. (Reproduced with permission from Denault *et al.*[2])

A: https://youtu.be/Xi33g6TMq8Q

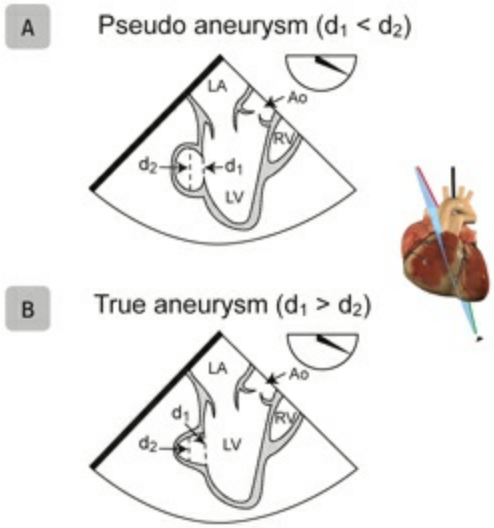

Fig. 6.17 Pseudo-aneurysm and true aneurysm. The differences between a pseudo-aneurysm and a true aneurysm are illustrated. (A) In a pseudo-aneurysm, the diameter of the orifice (d1) is smaller than the diameter of the aneurysm (d2). (B) The opposite is found in a true aneurysm. Ao, aorta; LA, left atrium; LV, left ventricle; RV, right ventricle. (Reproduced with permission from Denault *et al.*[2])

Ventricular Septal Defect

A ventricular septal defect (VSD) complicating an anterior or inferior wall infarction occurs in 1-2% of patients in the first week following infarction. On TEE, VSD often presents as a single perforation but can be irregular and serpiginous in shape. A VSD resulting from an anterior wall infarction is usually located near the apex and associated with anterior akinesis (**Figure 6.18**). A VSD resulting from an inferior wall infarction usually spares the apex and is located in the basal septum with extensive inferior wall dyskinesis (**Figure 6.19**). Pulsed-wave (PW) and color flow Doppler can identify the site of the defect site using a mosaic color pattern from the turbulent flow (**Figure 6.19**). Thorough assessment of RV function is crucial because it is a major predictor of outcome.

Myocardial Rupture

Rupture of the LV free wall is usually a sudden event that accounts for 8–17% of all in-hospital deaths in the post-infarction period. It equally affects the anterior, inferior, and lateral walls. Transesophageal echocardiography demonstrates a pericardial effusion and pericardial thrombus. [27]

Right Ventricular Infarction

Inferior myocardial infarction may extend into the RV free wall and compromise RV function. Transesophageal echocardiography findings will include RV regional wall motion hypokinesis, akinesis, or global RV dysfunction (**Figure 6.20**). [28] The LV inferior wall is usually also affected.

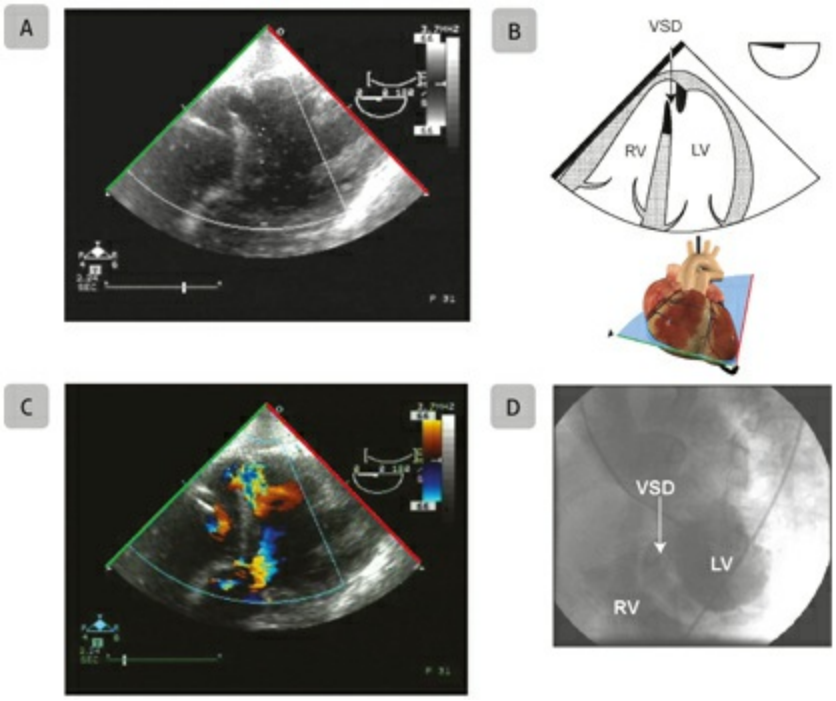

Fig. 6.18 Apical ischemic ventricular septal defect (VSD). (A—C) Deep transgastric long-axis views without and with color Doppler (Nyquist 66 cm/s) show an ischemic VSD involving the left ventricle (LV) apex in a 60-year-old male with anterior myocardial infarction. (D) Left ventriculography demonstrates passage of contrast media from the LV to the right ventricle (RV) through the serpiginous VSD. Photo D courtesy of Dr Philippe L L'Allier. (Reproduced with permission from Denault *et al.*[2])

C: https://youtu.be/B9CpaMd9GAA D: https://youtu.be/4nHc_nDM7MU

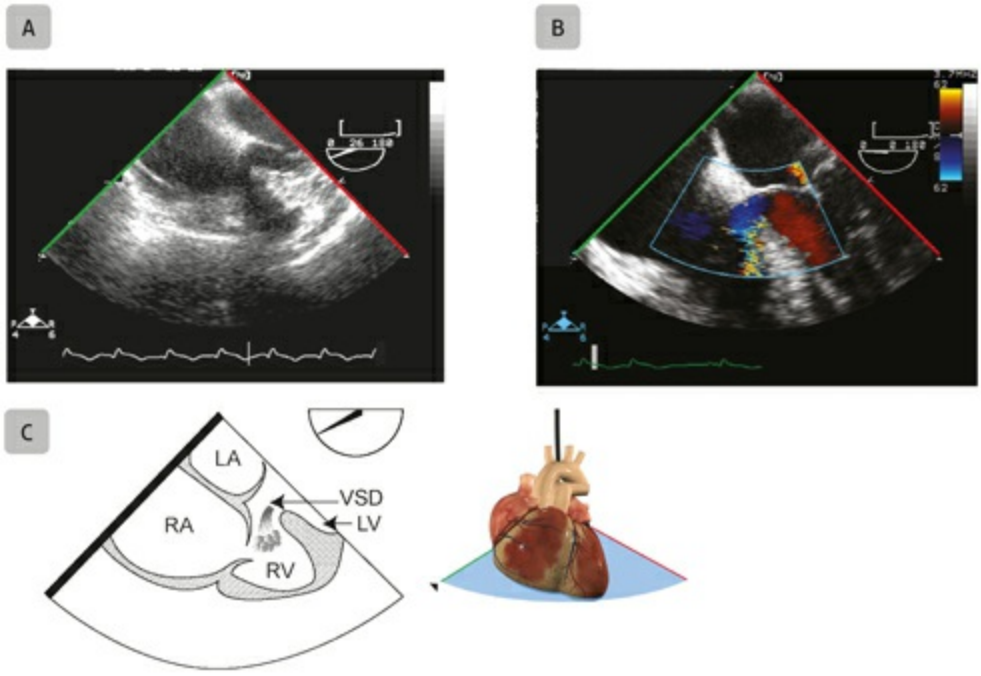

Fig. 6.19 Ischemic ventricular septal defect (VSD). (A—C) Mid-esophageal four-chamber views with and without color Doppler (Nyquist 62 cm/s) show an acquired VSD in the basal septum in a 71-year-old male after inferior myocardial infarction. LA, left atrium; LV, left ventricle; RA, right atrium; RV, right ventricle. (Reproduced with permission from Denault *et al.*[2])

B: https://youtu.be/2A-dsVfjR2A

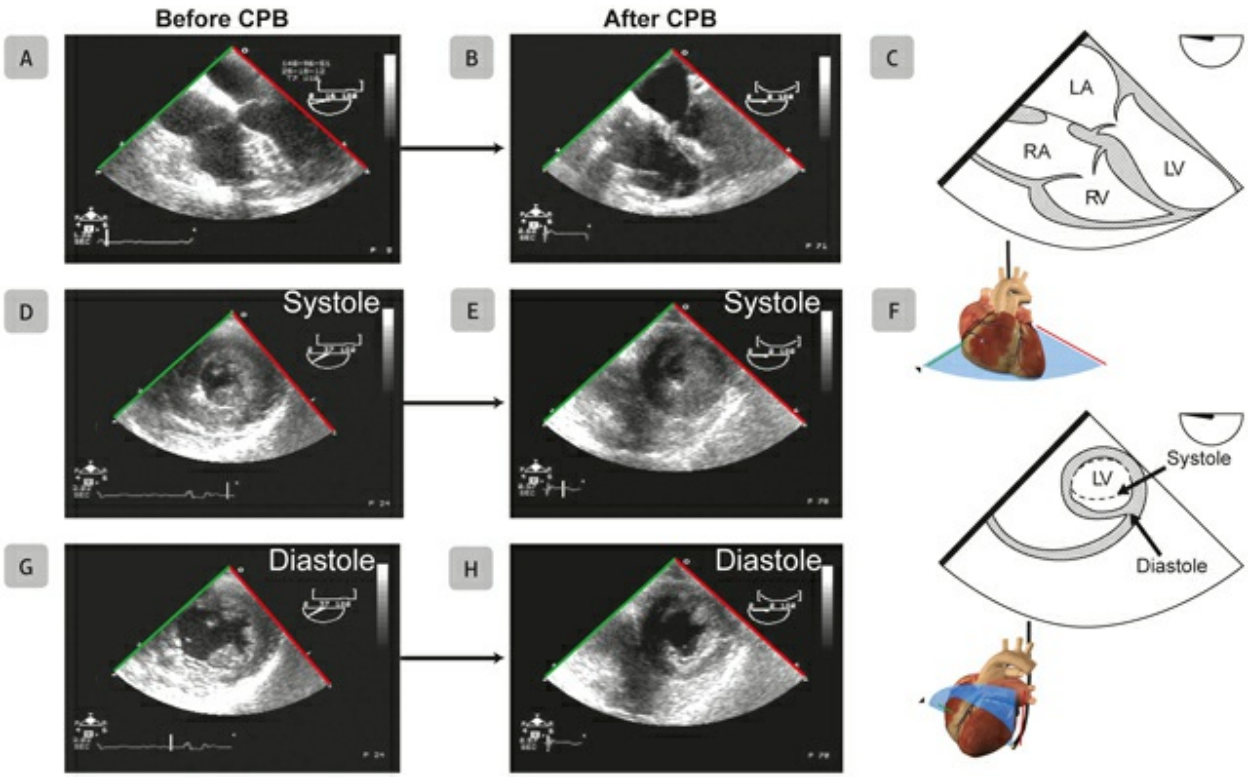

Fig. 6.20 Right ventricle (RV) ischemia. Severe acute right ventricular ischemic dysfunction is seen in a 71-year-old female after cardiopulmonary bypass (CPB). (A—C) The mid-esophageal four-chamber views demonstrate the new appearance of acute RV dilatation. (D-H) Left ventricle (LV) inferior wall akinesis is indicated by the dotted line on the transgastric mid short-axis views. LA, left atrium; RA, right atrium. (Reproduced with permission from Denault et al.[2])

https://youtu.be/b6TD6pve2Pk

CONCLUSION

Transesophageal echocardiography is a powerful perioperative diagnostic tool for the clinician not only to detect, identify, and quantify segmental myocardial ischemia, but also its many mechanical complications.

REFERENCES

1. CerqueiraM.D., WeissmanN.J., DilsizianV., JacobsA.K., KaulS., LaskeyW.K., et al. Standardized

myocardial segmentation and nomenclature for tomographic imaging of the heart. A statement for healthcare professionals from the Cardiac Imaging Committee of the Council on Clinical Cardiology of the American Heart Association. *Int J Cardiovasc Imaging*. 2002;*18*:539–42.

2. DenaultA.Y., CoutureP., VegasA., BuithieuJ., TardifJ.C.. *Transesophageal Echocardiography Multimedia Manual, Second Edition: A Perioperative Transdisciplinary Approach*. New York, NY: Informa Healthcare; 2011.
3. ReevesS.T., FinleyA.C., SkubasN.J., SwaminathanM., WhitleyW.S., GlasK.E., et al. Special article: Basic perioperative transesophageal echocardiography examination: a consensus statement of the American Society of Echocardiography and the Society of Cardiovascular Anesthesiologists. *Anesth Analg*. 2013;*117*:543–58.
4. VoelkelN.F., QuaifeR.A., LeinwandL.A., BarstR.J., McGoonM.D., MeldrumD.R., et al. Right ventricular function and failure: report of a National Heart, Lung, and Blood Institute working group on cellular and molecular mechanisms of right heart failure. *Circulation*. 2006;*114*:1883–91.
5. SmithJ.S., CahalanM.K., BenefielD.J., ByrdB.F., LurzF.W., ShapiroW.A., et al. Intraoperative detection of myocardial ischemia in high-risk patients: electrocardiography versus twodimensional transesophageal echocardiography. *Circulation*. 1985;*72*:1015–21.
6. LeungJ.M., O'KellyB., BrownerW.S., TubauJ., HollenbergM., MangnanoD.T.. Prognostic importance of postbypass regional wall-motion abnormalities in patients undergoing coronary artery bypass graft surgery. *SPI Research Group. Anesthesiology*. 1989;*71*:16–25.
7. van DaeleM.E., SutherlandG.R., MitchellM.M., FraserA.G., PrakashO., RulfE.N., et al. Do changes in pulmonary capillary wedge pressure adequately reflect myocardial ischemia during anesthesia? A correlative preoperative hemodynamic, electrocardiographic, and transesophageal echocardiographic study. *Circulation*. 1990;*81*:865–71.
8. GallagherK.P., KumadaT., KoziolJ.A., McKownM.D., KemperW.S., RossJ.Jr. Significance of regional wall thickening abnormalities relative to transmural myocardial perfusion in anesthetized dogs. *Circulation*. 1980;*62*:1266–74.
9. LangR.M., BierigM., DevereuxR.B., FlachskampfF.A., FosterE., PellikkaP.A., et al. Recommendations for chamber quantification: a report from the American Society of Echocardiography's Guidelines and Standards Committee and the Chamber Quantification Writing Group, developed in conjunction with the European Association of Echocardiography, a branch of the European Society of Cardiology. *J Am Soc Echocardiogr*. 2005;*18*:1440–63.
10. BerningJ., Steensgaard-HansenF.. Early estimation of risk by echocardiographic determination of wall motion index in an unselected population with acute myocardial infarction. *Am J Cardiol*. 1990;*65*:567–76.
11. InnocentiF., CerabonaP., DonniniC., ContiA., ZanobettiM., PiniR.. Long-term prognostic value of stress echocardiography in patients presenting to the ED with spontaneous chest pain. *Am J Emerg Med*2014; *32*: 731–6.
12. KanG., VisserC.A., KoolenJ.J., DunningA.J.. Short and long term predictive value of admission wall motion score in acute myocardial infarction. A cross sectional echocardiographic study of 345 patients. *Br Heart J*. 1986;*56*:422–7.
13. SwaminathanM., MorrisR.W., De MeytsD.D., PodgoreanuM.V., JollisJ.G., GrocottH.P., et al. Deterioration of regional wall motion immediately after coronary artery bypass graft surgery is associated with long-term major adverse cardiac events. *Anesthesiology*. 2007;*107*:739–45.
14. ShapiroE., MarierD.L., St John SuttonM.G., GibsonD.G.. Regional non-uniformity of wall dynamics in normal left ventricle. *Br Heart J*. 1981;*45*:264–70.
15. CoutureP., BolducL., DemeyN., DeschampsA., PellerinM., DenaultA., et al. Real-time compared to off-line evaluation of segmental wall motion abnormalities with transesophageal

echocardiography using dobutamine stress testing. *J Cardiothorac Vasc Anesth*. 2012;*26*:191–6.
16. LondonM.J., TubauJ.F., WongM.G., LayugE., HollenbergM., KrupskiW.C., et al. The “natural history” of segmental wall motion abnormalities in patients undergoing noncardiac surgery. *SPI Research Group. Anesthesiology*. 1990;*73*:64455.
17. MaclarenG., KlugerR., PriorD., RoyseA., RoyseC.. Tissue Doppler, strain, and strain rate echocardiography: principles and potential perioperative applications. *J Cardiothorac Vasc Anesth*. 2006;*20*:583–93.
18. BachD.S., ArmstrongW.F., DonovanC.L., MullerD.W.. Quantitative Doppler tissue imaging for assessment of regional myocardial velocities during transient ischemia and reperfusion. *Am Heart J*. 1996;*132*:721–5.
19. DerumeauxG., OvizeM., LoufouaJ., Andre-FouetX., MinaireY., CribierA., et al. Doppler tissue imaging quantitates regional wall motion during myocardial ischemia and reperfusion. *Circulation*. 1998;*97*:1970–7.
20. EdvardsenT., AakhusS., EndresenK., BjomerheimR., SmisethO.A., IhlenH.. Acute regional myocardial ischemia identified by 2-dimensional multiregion tissue Doppler imaging technique. *J Am Soc Echocardiogr*. 2000;*13*:986–94.
21. AmundsenB.H., Helle-ValleT., EdvardsenT., TorpH., CrosbyJ., LyseggenE., et al. Noninvasive myocardial strain measurement by speckle tracking echocardiography: validation against sonomicrometry and tagged magnetic resonance imaging. *J Am Coll Cardiol*. 2006;*47*:789–93.
22. LangR.M., BadanoL.P., Mor-AviV., AfilaloJ., ArmstrongA., ErnandeL., et al. Recommendations for cardiac chamber quantification by echocardiography in adults: an update from the American Society of Echocardiography and the European Association of Cardiovascular Imaging. *J Am Soc Echocardiogr*. 2015;*28*:1–39.
23. SunJ.P., PopovicZ.B., GreenbergN.L., XuX.F., AsherC.R., StewartW.J., et al. Noninvasive quantification of regional myocardial function using Doppler-derived velocity, displacement, strain rate, and strain in healthy volunteers: effects of aging. *J Am Soc Echocardiogr*. 2004;*17*:132–8.
24. JenkinsC., BricknellK., ChanJ., HanekomL., MarwickT.H.. Comparison of two- and three-dimensional echocardiography with sequential magnetic resonance imaging for evaluating left ventricular volume and ejection fraction over time in patients with healed myocardial infarction. *Am J Cardiol*. 2007;*99*:300–6.
25. CorsiC., CoonP., GoonewardenaS., WeinertL., SugengL., PolonskyT.S., et al. Quantification of regional left ventricular wall motion from real-time 3-dimensional echocardiography in patients with poor acoustic windows: effects of contrast enhancement tested against cardiac magnetic resonance. *J Am Soc Echocardiogr*. 2006;*19*:886–93.
26. ChenC., KoschykD., HammC., SieversB., KupperW., BleifeldW.. Usefulness of transesophageal echocardiography in identifying small left ventricular apical thrombus. *J Am Coll Cardiol*. 1993;*21*:208–15.
27. Lopez-SendonJ., GonzalezA., de LopezS.E., Coma-CanellaI., RoldanI., DominguezF., et al. Diagnosis of subacute ventricular wall rupture after acute myocardial infarction: sensitivity and specificity of clinical, hemodynamic and echocardiographic criteria. *J Am Coll Cardiol*. 1992;*19*:1145–53.
28. HaddadF., CoutureP., TousignantC., DenaultA.Y.. The right ventricle in cardiac surgery, a perioperative perspective: I. Anatomy, physiology, and assessment. *Anesth Analg*. 2009;*108*:407–21.

Chapter 7

Basic Valve Diseases

Mustapha Belaidi and Antoine G Rochon

INTRODUCTION

The incidence of valvular diseases in the general population is about 1–2%. [1] These cardiac lesions have important hemodynamic repercussions because they modify preload, afterload, systolic, and diastolic ventricular function. Over time there is adaptive ventricular remodelling but gradually the disease exceeds the compensatory capacity of the heart. This chapter will focus on the echocardiographic assessment of valvular diseases for the novice echocardiographer. Modalities useful to identify valvular anomalies and evaluate their severity are presented.

AORTIC VALVE

The aortic valve is a complex three-dimensional structure that is part of the aortic root, which is a key central component of the heart. The aortic root complex is comprised of the (1) aortic valve (AoV), (2) sinuses of Valsalva, and (3) interleaflet triangles. The AoV is composed of three similarly sized semilunar cusps. The right and left coronary cusps are associated with the origin of the coronary artery that bears the same name. The posterior located non-coronary cusp is not associated with a coronary ostium and is near the interatrial septum. Each cusp body is attached to the aortic wall at hinge points that extend to the sinotubular junction (STJ) to form commissures between adjacent cusps (**Figures 7.1 and** 7.2). This creates a crown-shaped fibrous ring that defines the physiologic aorto-ventricular junction.

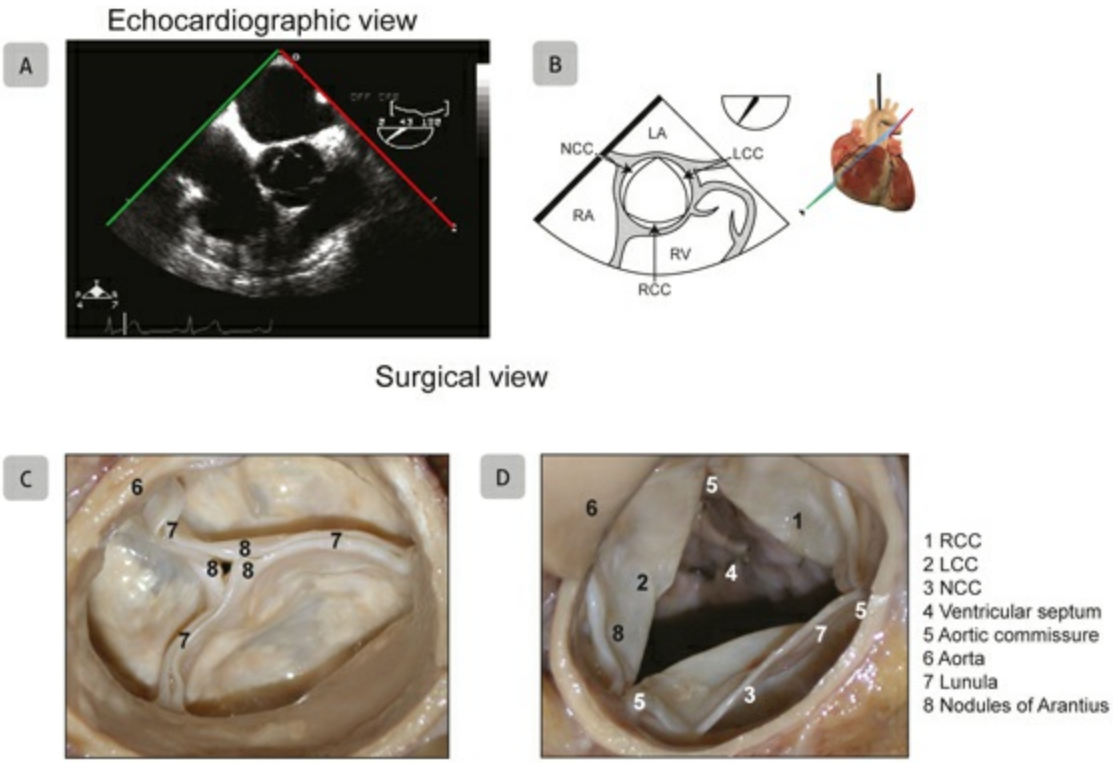

Fig. 7.1 Aortic valve (AoV) anatomy. (A, B) Mid-esophageal AoV short-axis view shows the AoV in systole compared with the anatomic specimens (C) in diastole and (D) in systole. LA, left atrium; LCC, left coronary cusp; NCC, noncoronary cusp; RA, right atrium; RCC, right coronary cusp; RV, right ventricle. Source: Photos C and D courtesy of Nicolas Dürrleman. (Reproduced with permission from Denault *et al.* [2])

A: https://youtu.be/QgrTjKLNyCI

A: https://youtu.be/wuJjCZswFnk

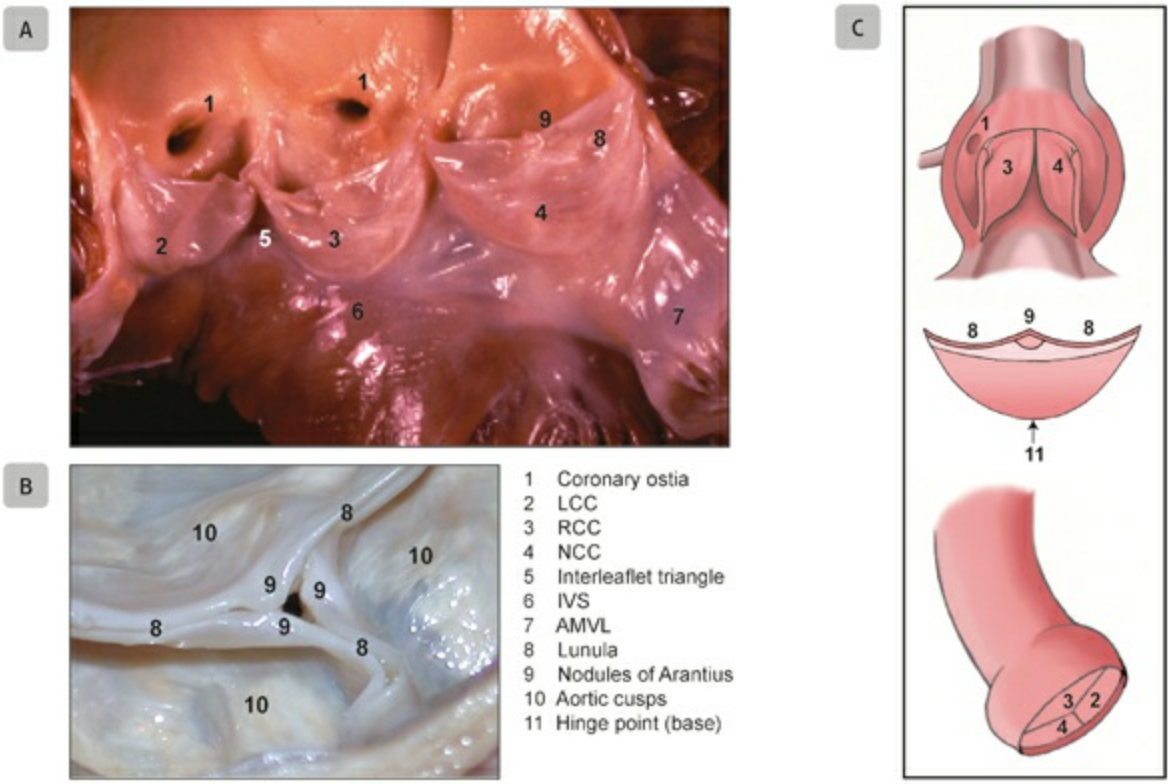

Fig. 7.2 Aortic valve (AoV) anatomy. (A) View of an open aortic root specimen shows the aortic-mitral curtain which represents the fibrous continuity (intervalvular fibrosa) between the aortic root and the anterior mitral valve leaflet (AMVL). (B) Anatomic specimen of the AoV shows the curvilinear coaptation of each aortic cusp, the lunula, and the location of the nodules of Arantius near the middle portion of each cusp edge. (C) Schematic representation of the AoV anatomy is shown. IVS, interventricular septum; LCC, left coronary cusp; NCC, noncoronary cusp; RCC, right coronary cusp. Source: Photo B courtesy of Nicolas Durrleman and illustration C with permission, copyright Gian-Marco Busato. (Reproduced with permission from Denault *et al.* [2]*).*

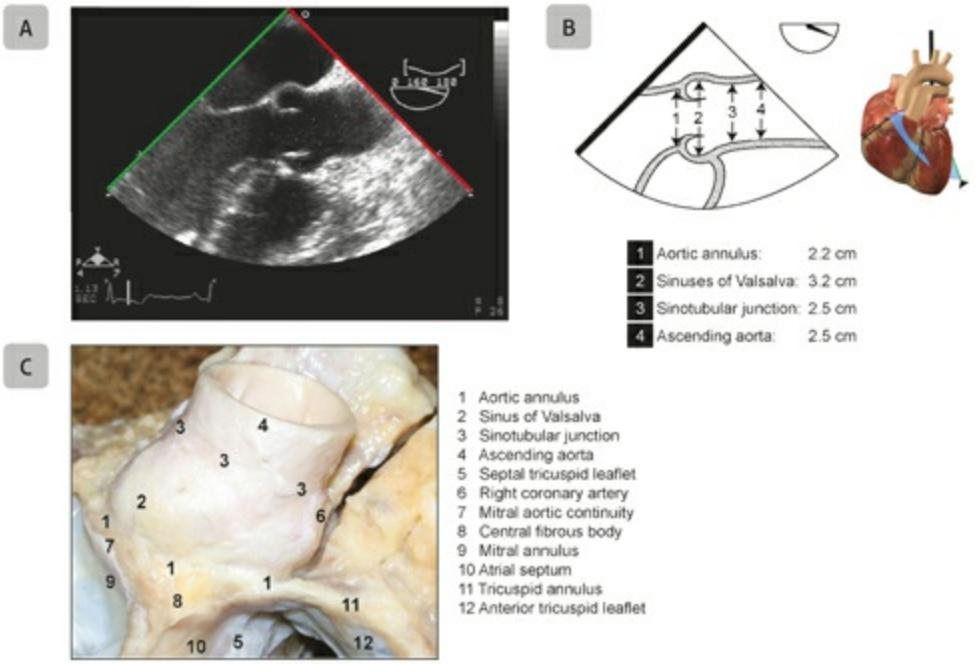

Fig. 7.3 Aortic root anatomy. (A, B) Mid-esophageal aortic valve long-axis view of the aortic root with a range of normal measurements obtained during systole compared with (C) the anatomic specimen. Source: Photo C courtesy of Nicolas Dürrleman. (Reproduced with permission from Denault *et al*.2)

https://youtu.be/I1TO3P0vwb0

The AoV is positioned above the mitral valve (MV). It is oriented so that the non-coronary cusp is posterior and the right coronary cusp is anterior. The nodule of Arantius is located at the center of the free edge, at the point of coaptation (**Figure 7.1**). Lambl's excrescences are benign, thin, mobile filamentous strands that can sometimes be found on the ventricular side of the AoV cusps. During systole, the normal open aortic valve area is 3–4 cm^2. The aortic cusps open parallel to blood flow during ejection, the flow remains laminar (velocity 1.0–1.5 m/s) and the transvalvular peak pressure gradient (PG) is <10 mmHg. The normal aortic root dimensions are represented in **Figure 7.3**.

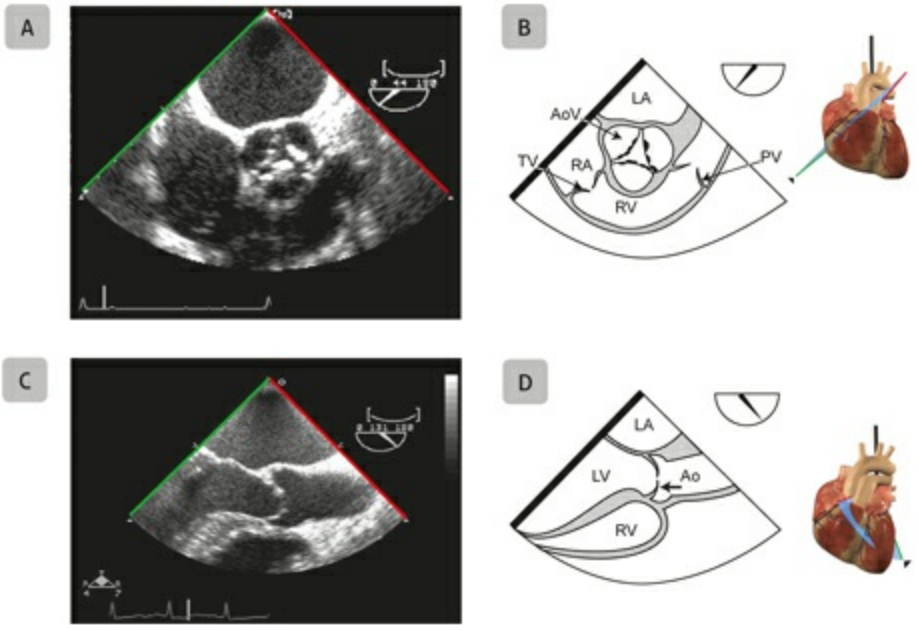

Fig. 7.4 Aortic stenosis. (A, B) Mid-esophageal (ME) aortic valve (AoV) short-axis view at 44° shows severe calcific non-rheumatic aortic stenosis with absence of commissural fusion of the AoV. (C, D) ME AoV long-axis view at 131° shows AoV systolic doming (arrow) and commissural fusion characteristic of rheumatic heart disease. Ao, aorta; LA, left atrium; LV, left ventricle; PV, pulmonic valve; RA, right atrium; RV, right ventricle; TV, tricuspid valve. (Reproduced with permission from Denault *et al.* [2])

A&C: https://youtu.be/O-u-k_6WeBo

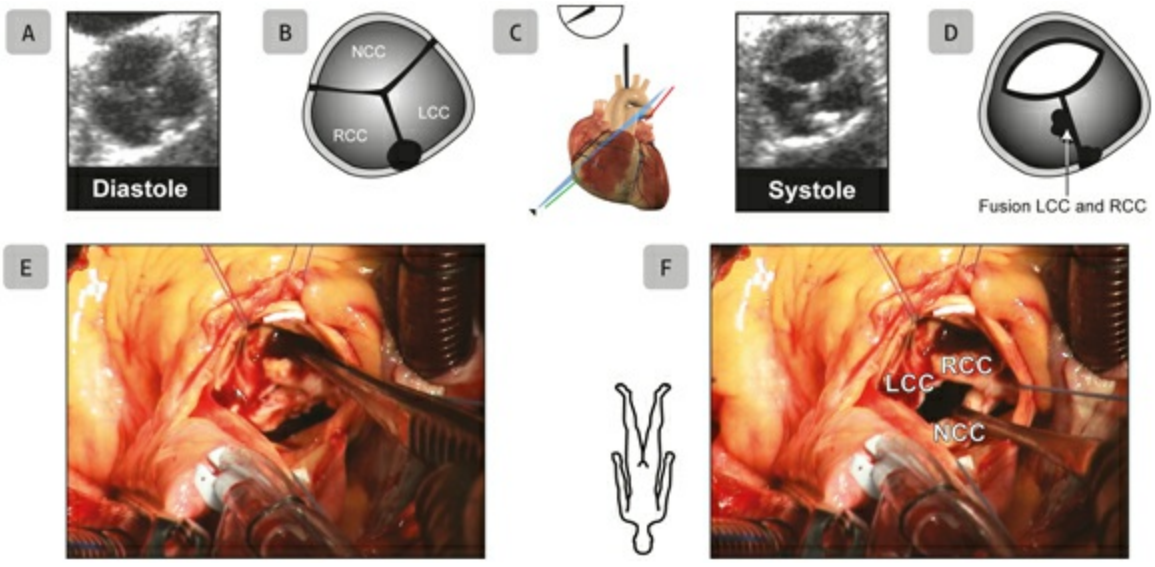

Fig. 7.5 Bicuspid aortic valve (AoV). (A—D) Zoom of mid-esophageal AoV short-axis views of a bicuspid bicommissural AoV with a raphe between the left coronary cusp (LCC) and right coronary cusp (RCC). Note that in diastole (A, B) the raphe gives the impression that the AoV has three normal cusps. (E, F) In the surgical aortotomy view, the non-coronary cusp (NCC) is located posteriorly in the lower part, as opposed to the transesophageal echocardiographic view where it is seen on the upper part of the screen. Source: Photos E and F courtesy of Dr Denis Bouchard. (Reproduced with permission from Denault *et al.* [2] *)*

A: https://youtu.be/UQughw6zNC0

E: https://youtu.be/YOKO6QwYCII

Aortic Stenosis

Etiology

1. Calcification.

   The most common etiology of aortic stenosis is calcific degeneration encountered in patients over 65 years of age. Calcified deposits in the body of the cusps create nodular growths without commissural fusion that fix the valve in a semi-closed position often creating an irregularshaped orifice. Conversely, rheumatic involvement is characterized by a thickening of the cusp edges from fibro-calcification, restricted mobility, and commissural fusion that creates a triangular systolic orifice (**Figure 7.4**). Aortic sclerosis is an irregular cusp thickening that does not restrict cusp opening nor increases the PG and is common in persons over 65 years of age.
2. Congenital anomalies of the aortic valve.

   Congenital anomalies of the AoV include bicuspid, unicuspid, quadricuspid, and even pentacuspid valves. [3] Bicuspid AoV is the

most common congenital anomaly with an incidence of 1–2% in the general population. [4] Usually, a bicuspid valve will have one small cusp and a larger one with a raphe from the failed separation of two cusps. In approximately 80% of cases, the raphe is between the right and left coronary cusps, resulting in a smaller posterior and larger anterior cusp (**Figure 7.5**). In a long-axis (LAX) view, a bicuspid AoV has an asymmetric closure line and systolic doming from incomplete opening of the AoV. Though the latter is most commonly associated with bicuspid AoVs, it may also appear with commissural fusion in rheumatic heart disease. A bicuspid AoV is bicommissural when the patient has three cusps, but two are fused with a raphe. When two equal cusps are seen without a raphe, the bicuspid valve is described as unicommissural (**Figure 7.6**).

3. Supra- and subaortic stenosis.

   While supra-aortic stenosis is uncommon, subaortic stenosis (**Figure 7.7**) may origiJnate from dynamic obstruction or fixed structural anomalies, such as a subaortic membrane. The AoV itself is often hypoplasic and functionally insufficient.

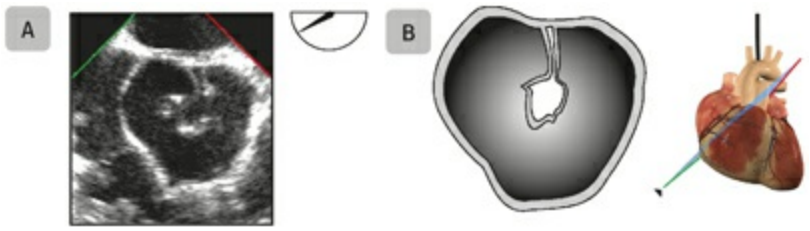

Fig. 7.6 Unicuspid unicommissural aortic valve (AoV). (A, B) In the mid-esophageal AoV short-axis view, the unicuspid AoV appearance has been likened to a shirt collar, toilet seat, or tear drop. (Reproduced with permission from Denault *et al.* [2])

A: https://youtu.be/mGGtyWBci34

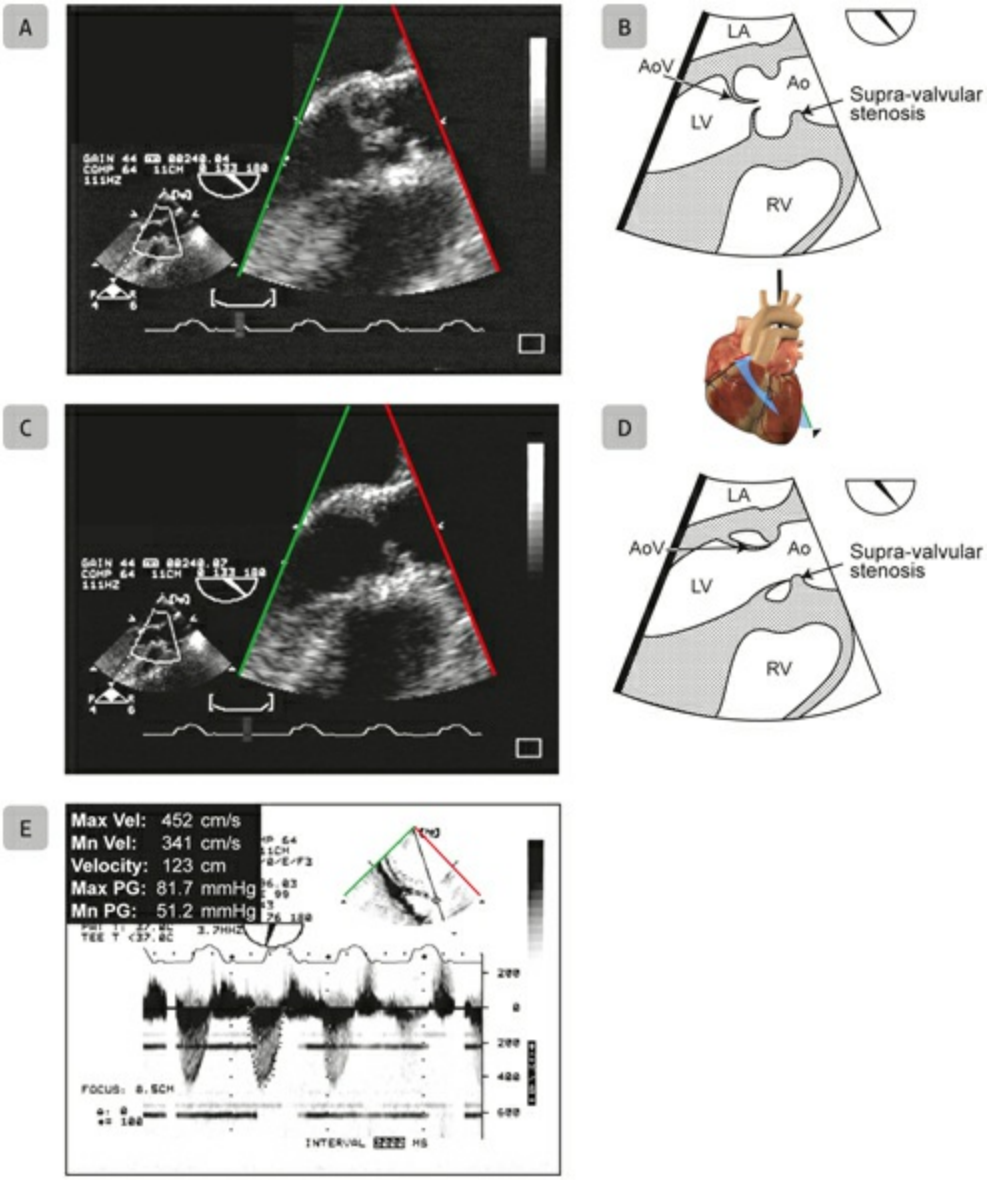

Fig. 7.7 Supravalvular aortic membrane. A 25-year-old female is operated on for aortic stenosis. (A-D) Mid-esophageal aortic valve (AoV) long-axis view in diastole and systole shows normal aortic cusp opening but a fibrous membrane is present 9 mm above the level of the AoV. (E) Continuous wave Doppler is used to measure maximal (81.7 mmHg) and mean (51.2 mmHg) pressure gradients (PG) across the stenosing membrane. Ao, aorta; LA, left atrium; LV, left ventricle; Max, maximal; Mn, mean; RV, right ventricle; Vel, velocity. (Reproduced with permission from Denault *et al.* [2])

C: https://youtu.be/qflrWiW-5CE

Two-Dimensional Imaging

The AoV can be analyzed using five transesophageal echocardiographic (TEE) views, mid-esophageal (ME) AoV short-axis (SAX), and LAX, ME five-chamber, transgastric (TG) LAX (**Figure 7.8**) and deep TG views (**Figure 7.10**). The morphology of the AoV in aortic stenosis aids diagnosis of the etiology. Degenerative calcifications can appear in the cusp body and may gradually spread to other structures, including the aortic annulus, the base of the anterior MV leaflet, or the aortic root. With a bicuspid AoV, calcifications predominate at the raphe and commissures. In rheumatic disease, the cusp body is less dense, while the free edges are thickened and partially fused at the commissures. However, this differentiation is not so easily made, especially in tight calcified stenosis where structures are difficult to distinguish. Two-dimensional imaging can also show morphological changes induced by the increased afterload, such as concentric left ventricular (LV) hypertrophy, in which the LV wall thickens (>1.2 cm) and LV cavity size shrinks. Systolic function is generally preserved, but LV thickening is associated with diastolic dysfunction. Left atrial (LA) dilation (diameter >5 cm), in the absence of mitral regurgitation, is pathognomonic of diastolic dysfunction. In severe cases, a restrictive LV filling pattern appears.

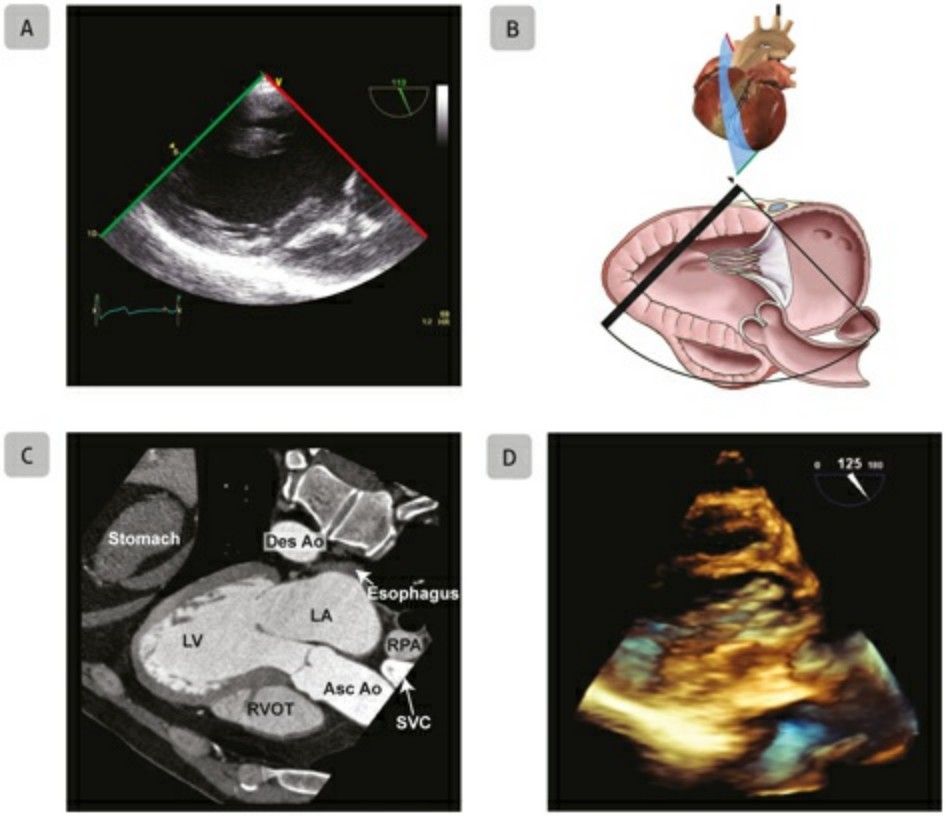

Fig. 7.8 Transgastric long- axis (LAX). Transgastric LAX viewsviews obtained with (A, B) two-dimensional echocardiography (113°), (C) ECG-gated computed tomography, and (D) threedimensional echocardiography are shown. Ao, aorta; Asc, ascending; Des, descending; ECG, electrocardiographic; LA, left atrium; LV, left ventricle; RPA, right pulmonary artery; RVOT, right ventricular outflow tract; SVC, superior vena cava. Source: Illustration B courtesy of Gian-Marco Busato. (Reproduced with permission from Denault *etal.* [2])

A: https://youtu.be/CWKvwTD_lI8

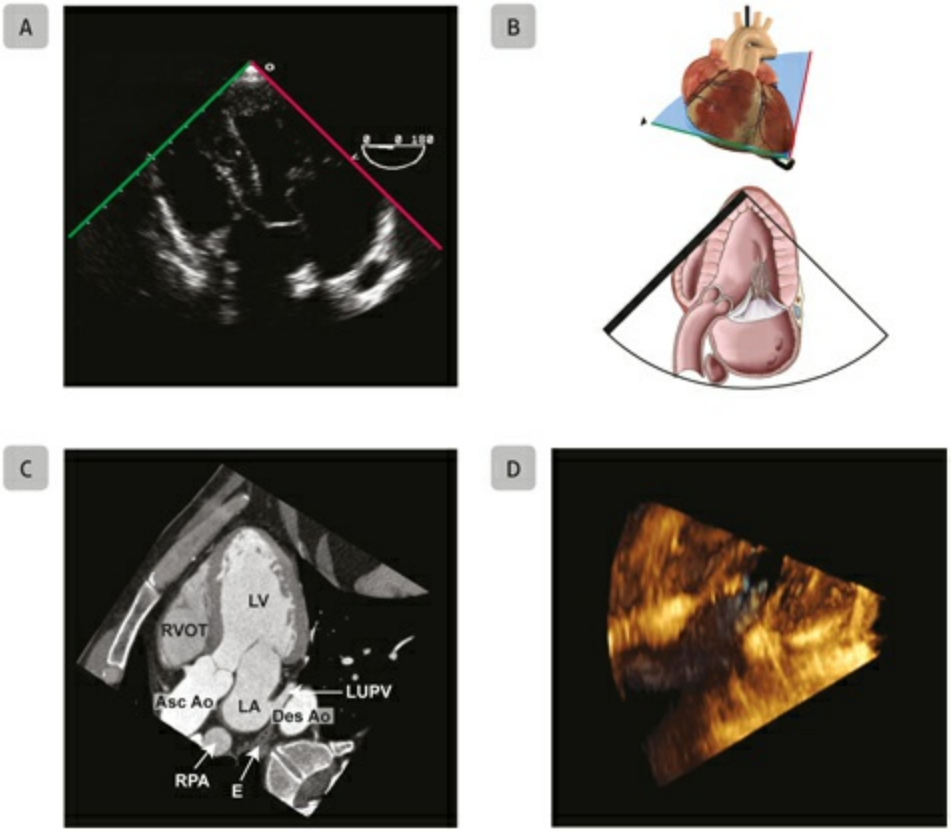

Fig. 7.9 Deep transgastric (TG) views. Deep TG long-axis views of the aortic root obtained with (A, B) two-dimensional echocardiography (0°), (C) electrocardiographic-gated computed tomography, and (D) three-dimensional echocardiography are shown. Asc Ao, ascending aorta; Des Ao, descending aorta; E, esophagus; LA, left atrium; LUPV, left upper pulmonary vein; LV, left ventricle; RPA, right pulmonary artery; RVOT, right ventricular outflow tract. (Reproduced with permission from Denault *et al.* [2])

A: https://youtu.be/H968D4_heHI

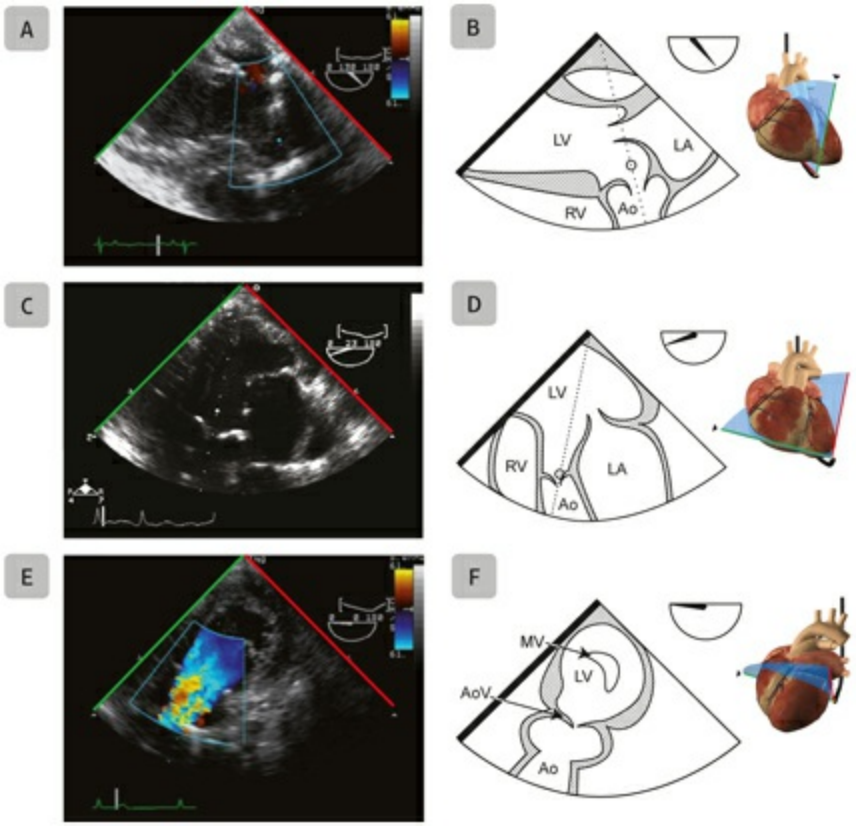

Fig. 7.10 Transgastric (TG) views of aortic valve (AoV). (A, B) TG long-axis view at 130°, (C, D) deep TG view at 23°, and (E, F) basal TG view of the aortic valve (AoV) at 0° with color Doppler (Nyquist 61 cm/s) obtained by anteflexing the probe are shown. In all of these views, the aortic flow is well aligned with the spectral Doppler ultrasound beam. Ao, aorta; LA, left atrium; LV, left ventricle; MV, mitral valve; RV, right ventricle. (Reproduced with permission from Denault *et al.* [2])

A: https://youtu.be/fdTXuglNYKk

E: https://youtu.be/ZPIG5NvfUhg

Doppler Flow

Color Doppler shows acceleration of flow through the stenosis and turbulence of flow downstream from the valve. In a SAX view, this can help

identify the small opening of the AoV. In addition, mitral regurgitation (MR) is present in 75% of cases and may have several etiologies, [5] such as functional MR related to an increased LV afterload. Finally mitral and aortic valves will often share degeneration and calcific disease.

The spectral Doppler ultrasound cursor can be aligned parallel to the aortic flow in the TG views at 0° and 120°. Optimal Doppler alignment can be aided by using color Doppler (**Figure 7.10**). The flow velocities in the left ventricular outflow tract (LVOT) and through the AoV are simultaneously recorded using continuous wave (CW) Doppler interrogation. These are represented as two distinct but superimposed Doppler signals, called a "double envelope". [6] , [7] The low velocity represents flow in the LVOT, and the higher velocity signal (>4 m/s) is flow through the AoV (**Figure 7.11**). The ratio between these velocities is the flow velocity ratio (FVR), also known as the dimensionless index defined as follows:

$$FVR = V_{LVOT} V_{AoV}$$

(normal is 0.8)

where V_{LVOT} is the flow velocity proximal to the stenosis in the LVOT and V_{AoV} is the maximal flow velocity at the AoV. This index is less affected by variations in stroke volume and cardiac output. Consequently, the FVR may prove useful in the setting of low cardiac output, low gradient aortic stenosis or in patients with low ejection fraction.

Quantitative Assessment of Aortic Stenosis

Guidelines [8] recommend the following parameters for the echocardiographic evaluation of aortic stenosis: (1) jet velocity, (2) mean transaortic PG, and (3) aortic valve area. Ultrasound criteria for severe aortic stenosis are summarized

in **Table 7.1**.

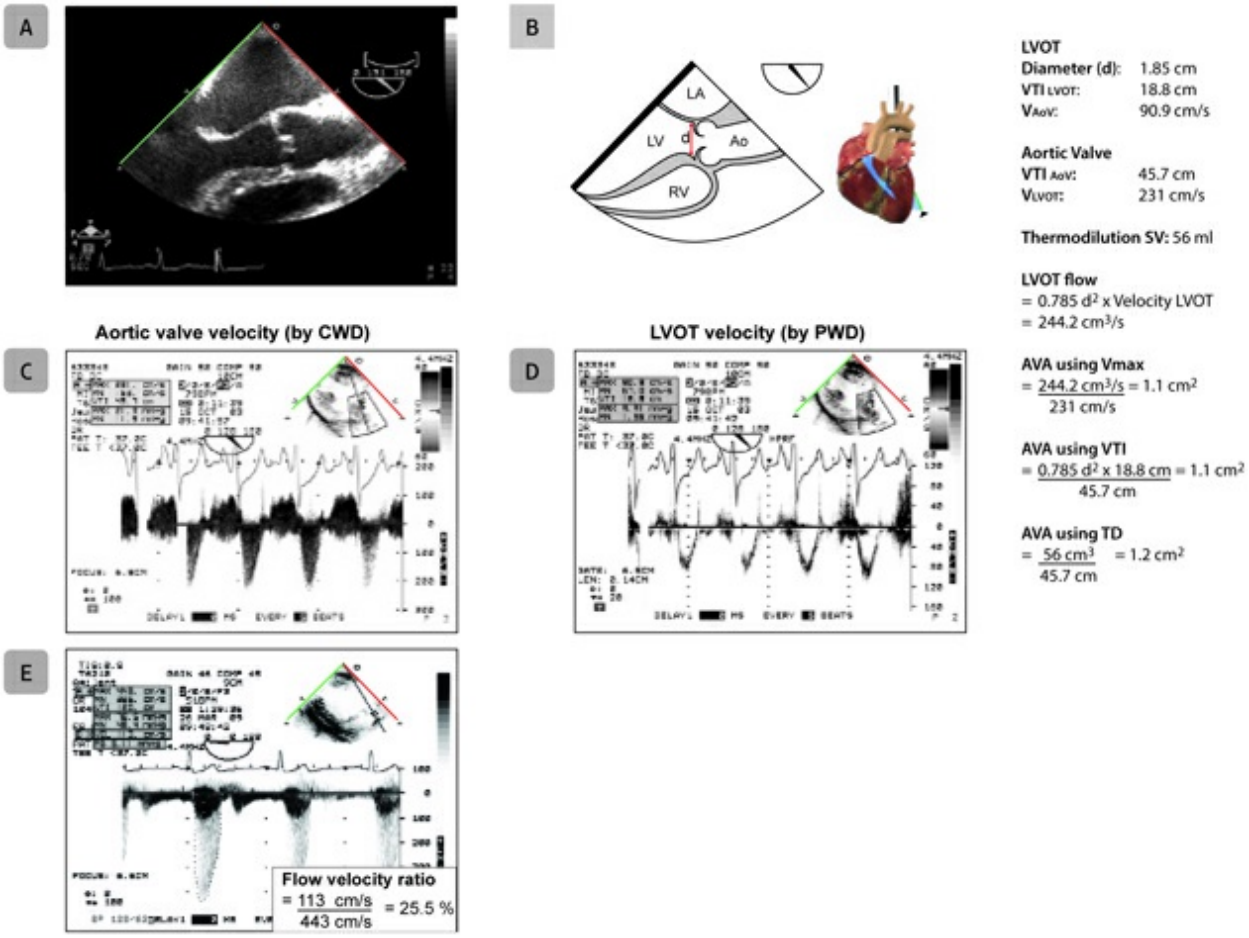

Fig. 7.11 Aortic valve area (AVA) calculation. (A, B) Mid-esophageal aortic valve (AoV) long-axis view of the left ventricular outflow tract (LVOT) in a 71-year-old female with aortic stenosis is shown. (C) Maximal velocity (Vmax) across the AoV is obtained by continuous wave Doppler (CWD) and (D) the LVOT velocity (V) is obtained by pulsed wave Doppler (PWD). On the right, the AVA is calculated using either the LVOT flow velocity, velocity time integral (VTI) or the stroke volume (SV) derived from thermodilution (TD). (E) Example of CWD double envelope technique: the darker lower-velocity envelope is used for LVOT and the fainter higher-velocity envelo pe is used for AoV velocity. The flow velocity (dimensionless) ratio is 25.5%, consistent with severe aortic stenosis (AS). Ao, aorta; d, diameter; LA, left atrium; LV, left ventricle; RV, right ventricle. (Reproduced with permission from Denault *et al.* [2] *)*

Table 7.1 Valve Evaluation.

2D imaging	Color Doppler flow	Spectral Doppler flow
Aortic stenosis		
Calcification, poor cusp motion LV hypertrophy	Accelerated flow in LVOT	VAo >4 m/s FVR <0.25 Mean PG >40 mmHg AVA <1 cm^2 (continuity)
Aortic regurgitation		
Dilation and spherification of LV	Scope of diastolic jet (severe AR: until mid-LV) Vena contracta ≥0.6 cm Ratio diameter jet/LVOT ≥60%	AR PHT (severe AR: <250 ms)
Mitral stenosis		
LA enlargement (±spontaneous contrast) and small LV	PISA >1 cm (at 21 cm/s Nyquist limit)	Accelerated diastolic flow (≥2.0 m/s) and turbulent Mean PG ≥12 mmHg PHT >220 ms MVA <1 cm^2 (0.6 cm^2/m^2)
Mitral regurgitation		
LA dilation (diameter >40 mm) LV hypertrophic dilation (end diastolic diameter >4.0 cm/m^2)	MR jet color area >40% LA area PISA radius >0.9 cm Vena contracta >0.7 cm	Dense, high, truncated, triangular regurgitant jet Systolic flow reversal in PV (may be absent)
Tricuspid stenosis		
RA enlargement Dilated IVC		Mean PG >5 mmHg PHT >190 ms
Tricuspid regurgitation		
No leaflet coaptation LA and RV dilation, septal bulge in the LA Dilation and pulsatility of the SVC, IVC, and hepatic veins	Jet area central >30% of RA area PISA radius >0.5 cm Vena contracta width >7 mm	Jet density and contour dense, triangular with early peaking Hepatic vein systolic reversal
Pulmonary stenosis		
Thickened cusps PA dilated	Turbulent flow	Mean PG >60 mmHg Peak velocity >4 m/s
Pulmonary regurgitation		
Abnormal valve	Small jet	PRI <0.75 is a sign of regurgitant fraction >25%

AR, aortic regurgitation; AVA, aortic valve area; FVR, flow velocity ratio; IVC, inferior vena cava; LA, left atrium; LV, left ventricle; LVOT, left

ventricular outflow tract; MVA, mitral valve area; MR, mitral regurgitation; PA, pulmonary artery; PG, pressure gradient; PHT, pressure half time; PISA, proximal isovelocity surface area; PRI, pulmonary regurgitation index; PV, pulmonary vein; RA, right atrium; RV, right ventricular; SVC, superior vena cava; VAo, aortic valve velocity

1. Maximum jet velocity (Vmax) is measured across the narrowed AoV orifice using CW Doppler aligned in the TG views. Peak velocity through the normal AoV is 1.0–1.5 m/s and Vmax >4 m/s represents severe AS.
2. Blood flow velocity across cardiac valves can be converted to a peak PG according to the Bernoulli equation:

   $$\Delta P = 4 \times (V A o V 2 - V L V O T 2)$$

   where V_{AoV} is the maximal velocity and V_{LVOT} is the LVOT velocity. In most cases, the square value of the V_{LVOT} is insignificant compared with V_{AoV}, and the Bernoulli equation is simplified to:

   $$\Delta P = 4 \times V A o V 2$$

   This represents the instantaneous peak PG across the AoV which is often higher than the “peak to peak” PG measured at cardiac catheterization.

   The mean transaortic PG is obtained by tracing the Doppler flow velocity curve which averages the instantaneous PG over the ejection time. The mean PG is more accurate than the peak PG in quantifying aortic stenosis severity. Normal physiological mean transaortic PG is <7 mmHg and with aortic stenosis, the PG increases in a linear manner to a value >40 mmHg in severe aortic stenosis.
3. The anatomic aortic valve area (AVA) is measured by tracing the

contour of the AoV opening (planimetry) in the ME AoV SAX view during systole. [9] It is important to advance and withdraw the TEE probe to identify the level with the smallest AoV opening. This measurement is not always easy because of acoustic shadowing from valvular calcification. [10] , [11] Thereby, estimation of the physiologic AVA using the continuity equation is recommended (**Figure 7.11**). This is based on the principle of conservation of mass so that flow (velocity time integral (VTI) multiplied by the area) across the LVOT must equal the flow across the AoV, as described by the formula:

$$\text{Flow LVOT} = \text{Flow AoV}$$

$$\mathrm{Area\,LVOT} \times \mathrm{VLVOT} = \mathrm{Area\,AoV} \times \mathrm{VAoV}$$

$$\mathrm{AVA} = \mathrm{Area\,LVOT} \times \mathrm{VLVOT} \,/\, \mathrm{VAoV}$$

$$= \pi r2 \times \mathrm{VLVOT} \,/\, \mathrm{VAoV}$$

$$= \pi \left(\mathrm{dLVOT}2 / 4 \right) \times \mathrm{VLVOT} \,/\, \mathrm{VAoV}$$

$$\mathrm{AVA} = 0.785\,\mathrm{dLVOT}2 \times \mathrm{VLVOT} \,/\, \mathrm{VAoV}$$

Aortic Regurgitation

Etiology

Aortic regurgitation (AR) may be caused by (1) intrinsic cusp pathology (myxoid degeneration, cusp prolapse, bicuspid morphology, rheumatic disease, endocarditis, and drug toxicity); (2) loss of commissural support

(trauma, aortic dissection, supracristal ventricular septal defect); or (3) dilatation of the aortic root (annuloaortic ectasia, Marfan aneurysm, aortitis). A functional classification of AR has been proposed: [12] Type I is characterized by normal cusps, dilatation of the aortic annulus, and a central jet. Type II is associated with excess tissue and movement of one or more cusps, prolapse, or eccentric jet. Finally, type III consists of restricted movement of cusps, calcification, and a variable jet.

Two-Dimensional Imaging

Volume overload related to increased diastolic aortic pressure causes severe eccentric LV dilation (LV end diastolic volume >200 mL) and a spherical LV. Two-dimensional imaging of AR is characterized by the following elements: central malcoaptation (SAX triangular orifice) (**Figure 7.12)**, cusp(s) tearing or excessive opening, and diastolic fluttering of the anterior MV leaflet.

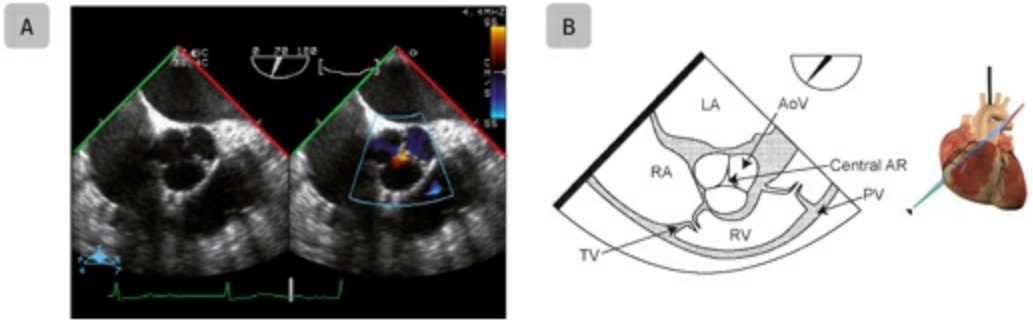

Fig. 7.12 Effective regurgitant orifice (ERO) area. (A, B) Mid-esophageal aortic valve (AoV) short-axis view at 70° shows the anatomic ERO area in the two-dimensional imaging (left split screen) and with color flow Doppler (right split screen) of a jet of aortic regurgitation (AR). Tracing the smallest orifice will measure the anatomic ERO area. LA, left atrium; PV, pulmonic valve; RA, right atrium; RV, right ventricle; TV, tricuspid valve. (Reproduced with permission from Denault *et al.* [2] *)*

A: https://youtu.be/UEaHhHjYPfo

Doppler Flow

The characteristic image is the presence of a turbulent jet in the LVOT in diastole with color flow Doppler (CFD) (**Figure 7.13**). Using color Doppler

and measuring the SAX area of the regurgitant jet from the parasternal SAX view at the level of the high LVOT relative to the SAX area of the LVOT at the same location, the so-called Perry index is a common method to evaluate severity. [13] The ratio is 0.3–0.5 in moderate AR and >0.6 in severe AR. The diameter of the vena contracta, which is the narrowest portion of the regurgitant jet, at its origin just distal to the valve, is also a good way to quantify the AR. This measurement does not appear to vary with afterload changes. [14] Aortic vena contracta measures between 0.3–0.6 cm in moderate AR and is >0.6 cm in severe AR.

The AR flow obtained by CW Doppler in the TG views shows a distinctive spectral pattern: the maximal velocity is 3–4 m/s, and the density of the trace represents AR severity. During the progressive flow deceleration of diastole, the slope is directly dependent on the speed with which the pressures equalize between the aorta and LV. If the regurgitant orifice is small, the PG between the aorta and the LV decreases slowly in diastole and the slope is gradual (mild AR). With a large regurgitant orifice, the PG decreases faster as the LV fills rapidly and the slope is very steep (severe AR). The deceleration slope of AR enables calculation of the pressure half-time (PHT), which is the time required for the PG to decrease by 50% or velocity to decrease to 70% of Vmax. [15] A PHT > 500 ms represents mild AR and PHT <250 ms is severe AR (**Figure 7.14**).

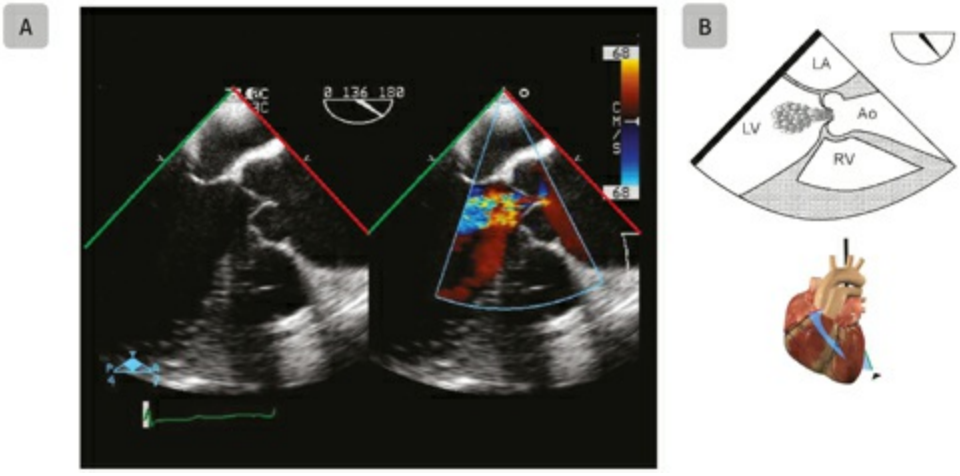

Fig. 7.13 Aortic regurgitation. (A, B) Mid-esophageal aortic valve long-axis view with color Doppler (Nyquist 68 cm/s) shows a central AR jet. The color Doppler sample box should be widened to show the extent of the AR jet into the left ventricle (LV) cavity. Ao, aorta; LA, left atrium; RV, right ventricle.

A: https://youtu.be/HNX068Blh-U

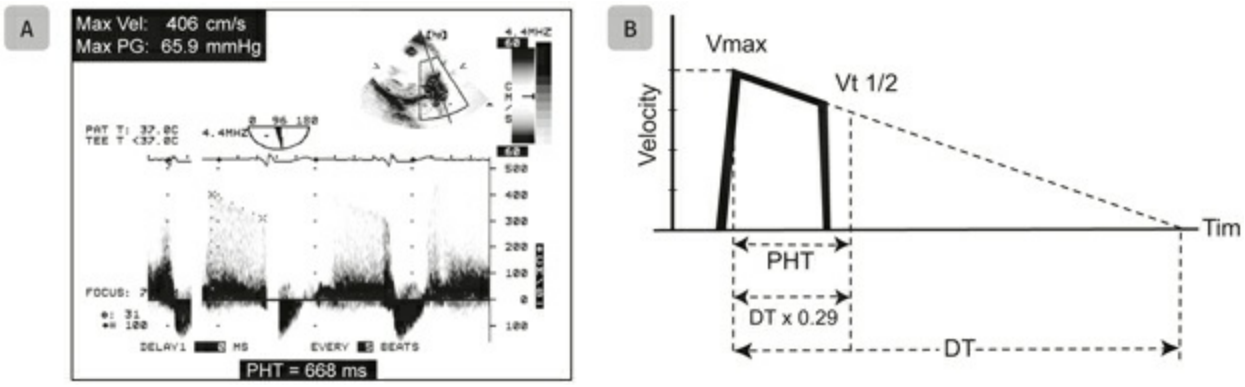

Fig. 7.14 Pressure half-time (PHT). (A) Continuous wave Doppler interrogation across the regurgitant aortic valve (AoV) from a transgastric window. The regurgitant PHT is measured at 668 ms, consistent with mild aortic regurgitation. (B) The relationship between the PHT and blood flow velocity across the AoV in diastole is illustrated. DT, deceleration time; Max, maximal; PG, pressure gradient; Vel, velocity; Vmax, maximal velocity; Vt 1/2, velocity at the PHT point. (Reproduced with permission from Denault *et al.* [2]

Several factors impact the interpretation of the quantitative measurement of AR. For example, in chronic AR, the LV will dilate and be compliant, accommodating a greater volume of regurgitant blood. Therefore, for the same regurgitant volume, acute AR will have a steeper AR slope and a shorter PHT compared with chronic AR (**Figure 7.15**). The quantification of AR is defined in **Table 7.1**.

MITRAL VALVE

The MV apparatus is a complex structure which consists of three elements: leaflets, annulus, and subvalvular apparatus. There are two mitral leaflets: a larger anterior mitral leaflet and a smaller posterior mitral leaflet. The latter has several notches, dividing the leaflet into three anatomical scallops: P1, P2, and P3. By analogy, the anterior leaflet is segmented into corresponding A1, A2, and A3. Both leaflets are joined at the two commissures (**Figure 7.16**). The mitral annulus is an incomplete fibrous ring shaped like a horse saddle to which both mitral leaflets attach. The posterior portion of the ring is

thinned and expands to cause annular dilatation. The subvalvular apparatus consists of two pillars (antero-lateral and postero-medial papillary muscles) and first-order chordae that insert at the leaflet free edge and the second-order chordae into the underside of the leaflets. Normal MV area in diastole is 4–6 cm^2 .

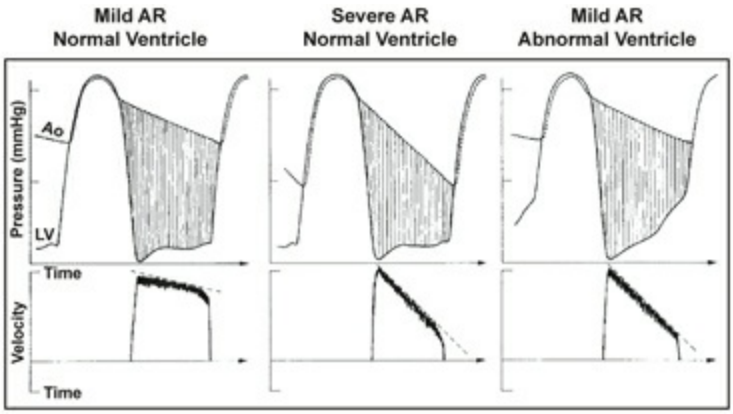

Fig. 7.15 Pressure half-time (PHT). Determinants of the PHT in aortic regurgitation (AR) are shown. Upper panels show invasive pressure tracings obtained in the aorta (Ao) and the left ventricle (LV). Lower panels show continuous wave Doppler tracings across the aortic valve (AoV) obtained during diastole. The slope of the blood flow velocity corresponds to the fall in the measured pressure gradient between the Ao and LV. The calculation of PHT with Doppler echocardiography is derived from the rate of decrease in blood flow velocity across the AoV in patients with AR. (Reproduced with permission from Denault *et al.* [2] *)*

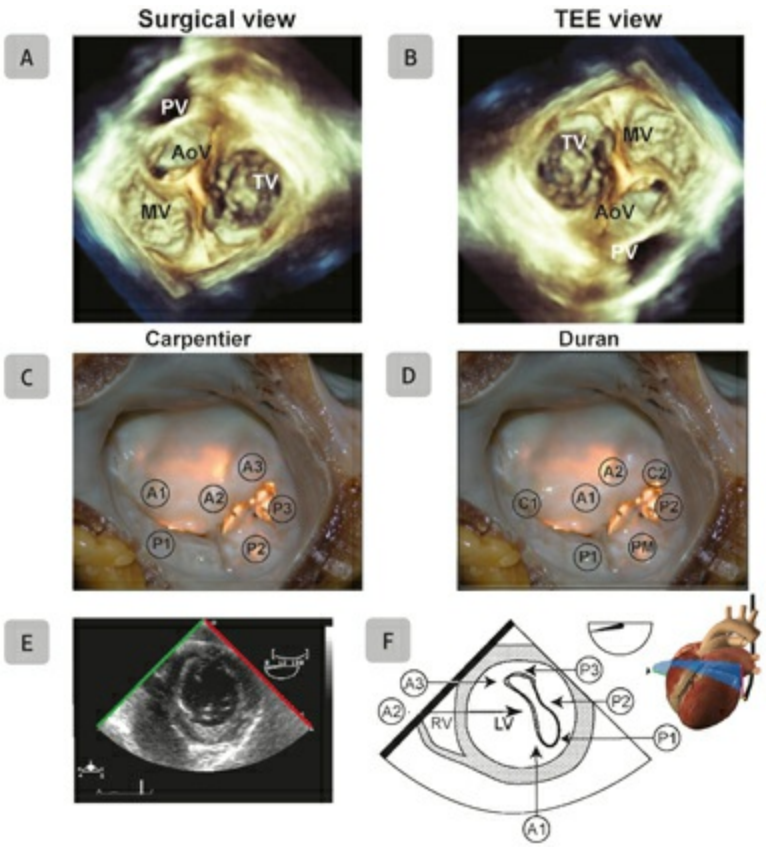

Fig. 7.16 Mitral valve (MV) anatomy. (A, B) Threedimensional transesophageal echocardiography (TEE) views in (A) the surgical and (B) traditional TEE orientations of the MV are shown. (C) The Carpentier nomenclature divides both the anterior and posterior mitral leaflets each into three parts. In the surgeon's orientation, the anterior leaflet is seen above while the posterior leaflet is visible inferiorly with the lateral part of the valve (A1 and P1) oriented towards the left. (D) The Duran nomenclature, names the three scallops of the posterior leaflet as P1, P2, and PM (middle). The anterior leaflet is divided in two segments, A1 and A2, and the commissural areas are named C1 and C2. (E, F) In a transgastric basal short-axis view, the leaflets appear upside down, with the P3 segment at the top right of the screen, and the P1 segment at the bottom. AoV, aortic valve; LV, left ventricle; PV, pulmonic valve; RV, right ventricle; TV, tricuspid valve. Source: Photo B courtesy of Dr Nicolas Durrleman. (Reproduced with permission from Denault *et al.* [2])

E: https://youtu.be/W5fat2-M0Fg

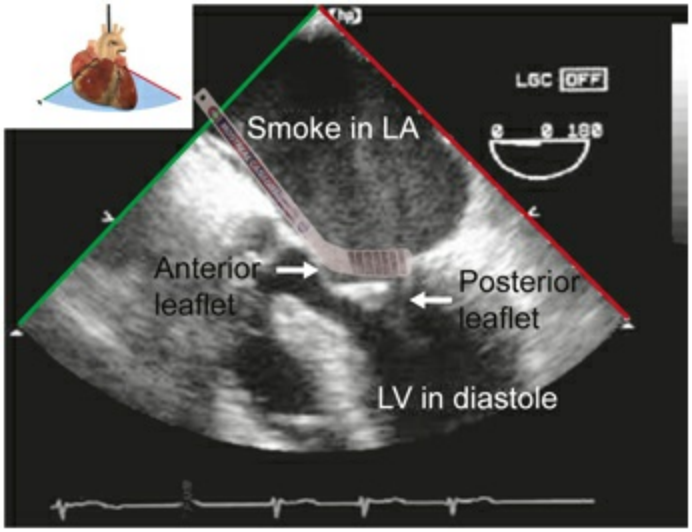

Fig. 7.17 Mitral stenosis. Mid-esophageal four- chamber view shows the “hockey-stick” deformation of the mitral valve apparatus during diastole with spontaneous contrast or smoke in the left atrium (LA). LV, left ventricle.

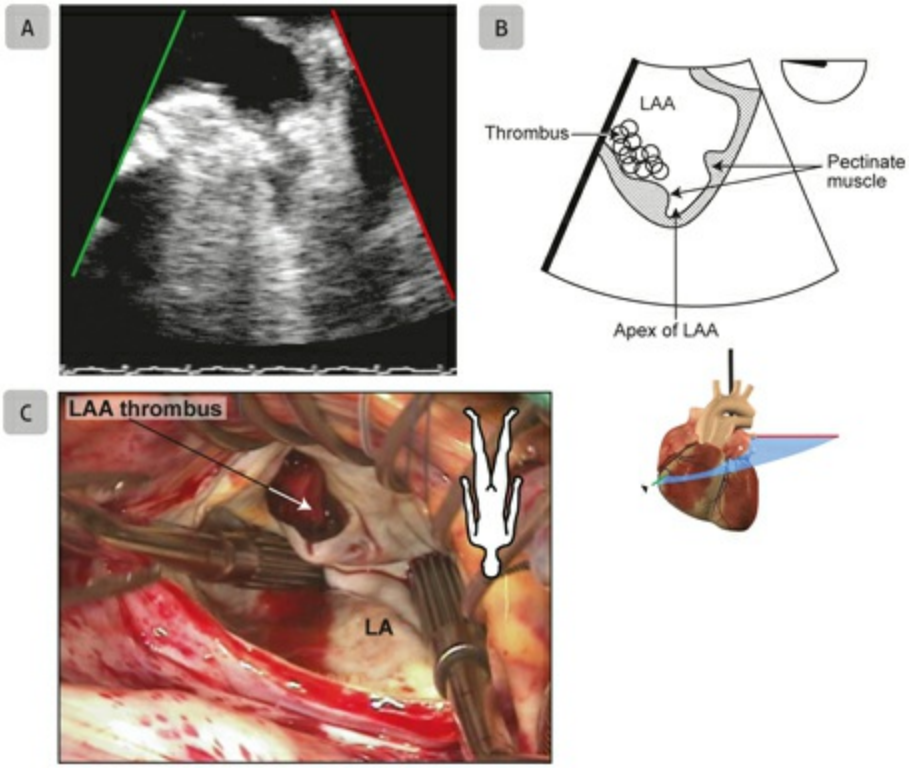

Fig. 7.18 Left atrial appendage (LAA) thrombus. (A, B) A thrombus fills the LAA at the level of two prominent pectinate muscles in this zoomed view of the LAA. (C) Intraoperative view of a LAA thrombus is shown. LA, left atrium. Source: Photo C courtesy of Dr Michel Pellerin. (Reproduced with permission from Denault *et al.* [2] *)*

A: https://youtu.be/kJRMpqAk43Q

C: https://youtu.be/BdyhqU4kzXY

Mitral Stenosis

The most common etiology of mitral stenosis (MS) is rheumatic heart disease. Other etiologies include non-rheumatic calcification or infiltration of the mitral annulus and leaflets, congenital lesions (parachute, supravalvular ring), and several miscellaneous lesions (vegetation, tumor).

Two-Dimensional Imaging

The typical 2D echocardiographic features of the rheumatic MV [16] include thickening and calcification of the mitral leaflets with commissural fusion, calcification, and shortening of the subvalvular apparatus, "hockey-stick" deformation of the anterior leaflet in diastole, decreased mobility of the posterior leaflet, and LA enlargement (**Figure 7.17).** The LV is small in size from reduced LV filling and in some patients a thrombus in the left atrial appendage (LAA) may be present (**Figure 7.18**).

Doppler Flow

During atrial contraction, blood flow accelerates towards the MV. In MS, hemispheric concentric zones are seen above the MV, while flow through the stenosis is turbulent with a high velocity (1.5–2.5 m/s). Color Doppler flow highlights the concentric flow acceleration zone called "PISA" (proximal isovelocity surface area) on the atrial side. The PISA dimension is proportional to the degree of MS, with a PISA radius >10 mm associated with severe MS (**Figure 7.19**). The severity of MS is graded on the magnitude of the transvalvular diastolic PG and the mitral valve area (MVA). The diastolic maximal and mean PG across the MV are measured using CW Doppler from the mitral inflow velocity according to the modified Bernoulli

equation. Mitral stenosis flow is distinctive (**Figure 7.20**) with a high Vmax (1.5–2.5 m/s) and very slow deceleration slope flow (E wave). The slow deceleration of mitral flow is due to the slight pressure drop in the LA in diastole because of the small mitral orifice size. The mean PG is >12 mmHg in severe MS. Thrombus is common in the LAA, particularly in patients with atrial fibrillation. Pulsed- wave (PW) Doppler interrogation of LAA contractility is assessed (**Figure 7.21**). [17] When velocities are <25 cm/s, the risk of thrombosis is increased but if the velocity is >55 cm/s, the risk of thrombosis is negligible. [18]

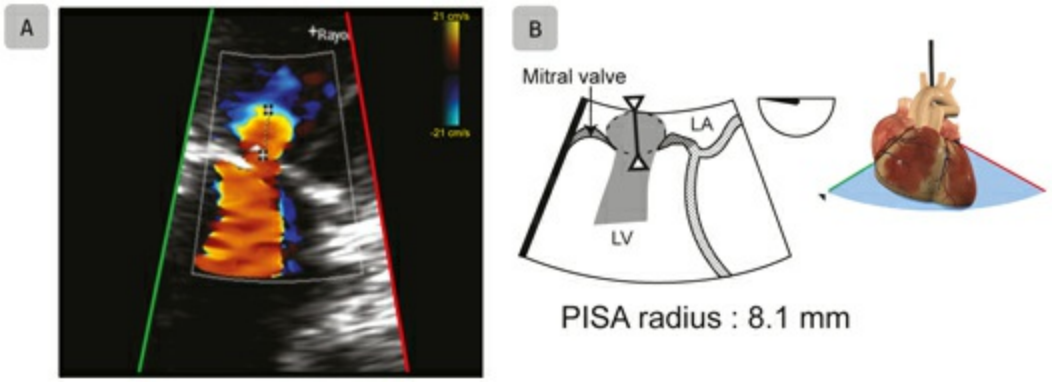

Fig. 7.19 . Mitral stenosis. (A) Color Doppler (Nyquist 21 cm/s) shows a proximal isovelocity surface area (PISA) on the auricular side of the mitral valve. The PISA radius is 8.1 mm, which can be used to calculate the mitral valve area (B). LA, left atrium; LV, left ventricle. (Reproduced with permission from Denault *et al.* [2] *)*

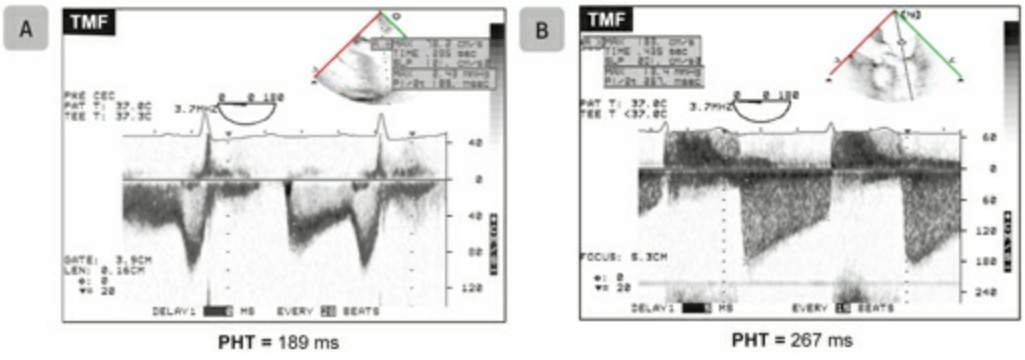

Fig. 7.20 Pressure halftime (PHT) in mitral stenosis (MS). Spectral continuous wave Doppler tracings of transmitral flow (TMF) in (A) moderate MS with a PHT of 189 ms and (B) severe MS with a PHT of 267 ms. (Reproduced with permission from Denault *et al.* [2] *)*

Mitral valve area can be (already defined) measured by direct planimetry of the orifice in a TG SAX view or calculated using the PHT, and the continuity equation. The PHT is defined as the time interval in milliseconds

(ms) when the PG has decreased to half the initial value. The PHT is measured on the same CW Doppler signal previously obtained for the maximal and mean PG (**Figure 7.22**). The relationship between PHT and MVA was determined empirically and can be evaluated by the following equation: [19] MVA = PHT/220, where MVA is in cm ^{2} and PHT is in ms. Several hemodynamic factors can affect PHT which should be borne in mind when using it to estimate MVA (**Table 7.2**). The continuity equation states that during hemodynamic stability in the absence of valvular regurgitation and atrial or ventricular septal defect, the stroke volume (SV) across the MV must equal that of other valves or subvalvular regions, such as LVOT, at the same time.

Qmitral = Qaortic

$MVA = 0.785\ d^2_{LVOT} \times VTI_{LVOT}/VTI_{mitral}$

The VTI_{LVOT} is measured using PW Doppler examination in the deep TG view close to the aortic annulus (**Figure 7.9**) at the same position as the LVOT diameter. The VTI_{mitral} is measured by CW Doppler across the native or prosthetic MV from the ME four-chamber or LAX views. The continuity equation cannot be used to calculate MVA in the presence of atrial fibrillation, AR, or significant MR. The quantification of mitral stenosis is summarized in **Table 7.1**.

Mitral Regurgitation

It is easy to diagnose MR with TEE, though quantification and identification of the mechanism are more complex (**Figure 7.23**) and may require an expert opinion. Carpentier's functional classification [20] (**Figure 7.24**) of MR is based on the opening and closing motion of the mitral leaflets.

Two-Dimensional Imaging

Chronic severe MR is characterized by a series of injuries to and remodelling of the left cardiac cavities. It may result from malcoaptation of the mitral leaflets, mitral annulus dilation, or redundant leaflets with chordae bulging into the LA and LA dilatation. The inter-atrial septum bows towards the RA in systole and the LV shows hypertrophic dilation (diameter in diastole >4.0 cm/m ^{2}). Although left ventricular ejection fraction (LVEF) is usually preserved (≥50%), it does not correspond to real LV function. The decrease in effective afterload artificially improves systolic LV performance and over-

estimates true LVEF. In fact, the regurgitant volume returns to the LV during diastole. This increases preload and allows the LV to be optimally positioned on the Starling curve. Finally in chronic MR, the LV becomes more spherical and geometric approximations used for calculation of LVEF are no longer applicable. The systolic LV dimension (end-systolic diameter <2.5 cm/m [2]) correlates better with LV performance than the LVEF. [22]

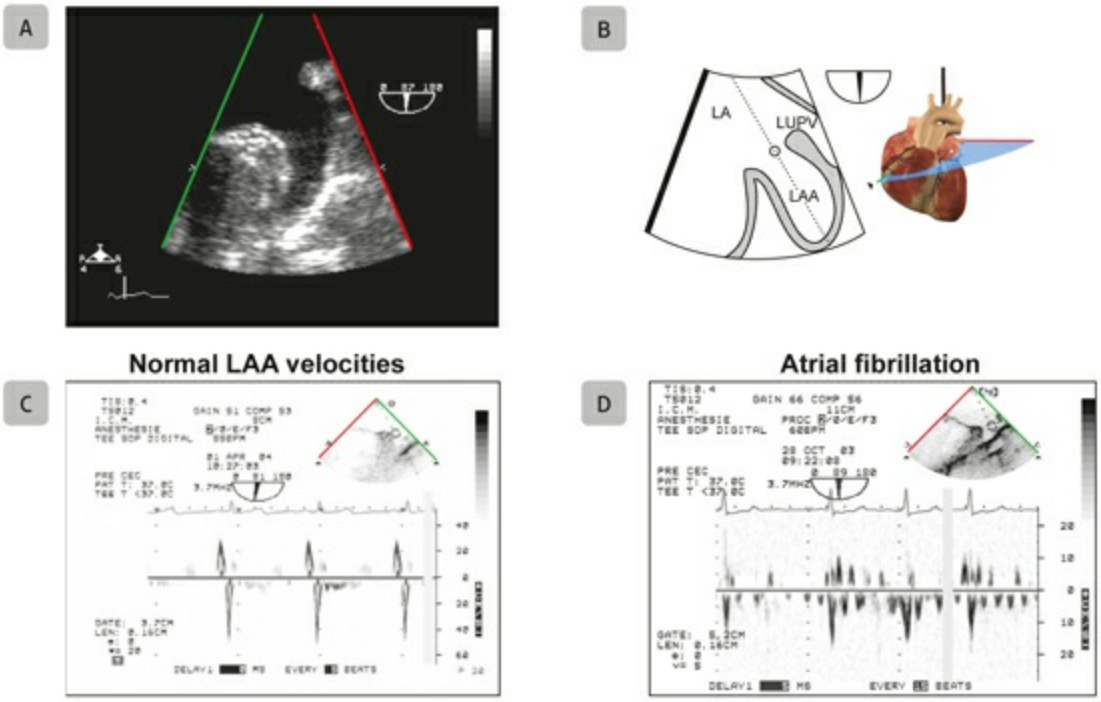

Fig. 7.21 Left atrial appendage (LAA) velocities. (A, B) A 71-year-old male undergoing aortic valve replacement. Midesophageal LAA view with positioning of the pulsed wave Doppler (PWD) sample volume at the ostium. (C) Normal PWD spectral tracing of the LAA shows a main atrial contraction (positive) and relaxation (negative) waves, followed by much smaller secondary waves. (D) In a 52-year-old female with mitral stenosis, the LAA spectral Doppler tracing shows the chaotic multiple waves of variable and lower velocities (<50 cm/s) typical of atrial fibrillation. LA, left atrium; LUPV, left upper pulmonary vein. (Reproduced with permission from Denault *et al.* [2])

A: https://youtu.be/589g9Vzcx1A

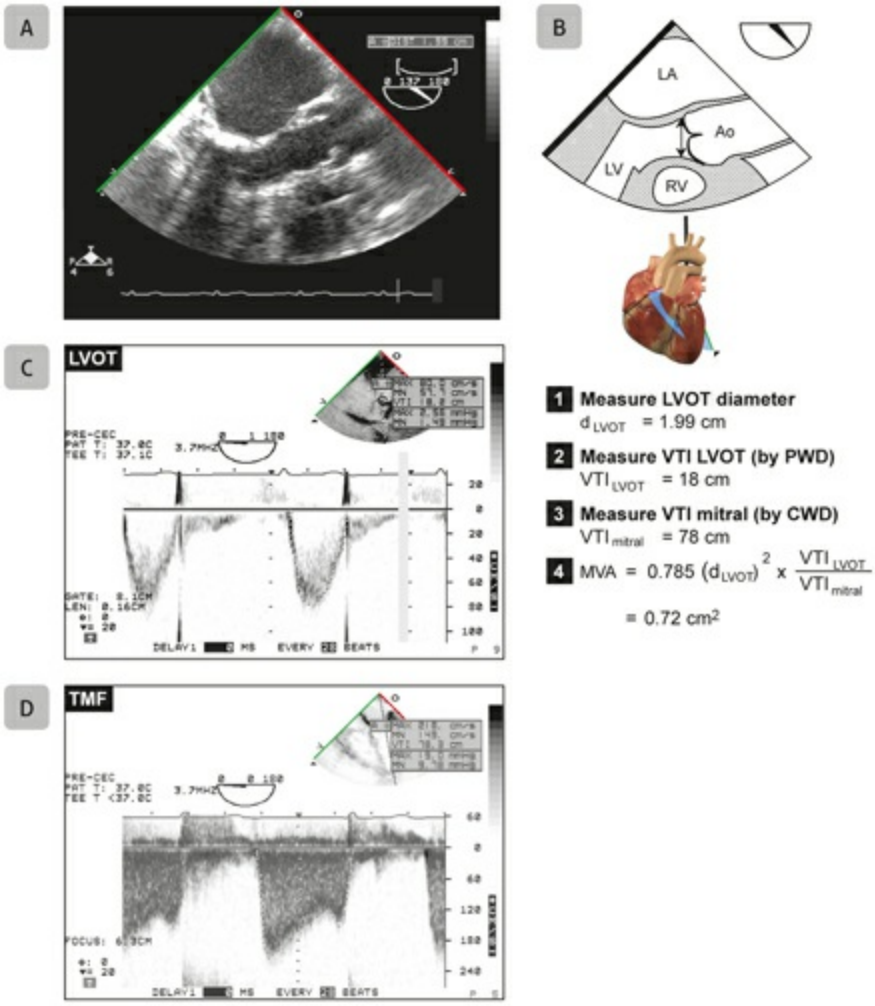

Fig. 7.22 Mitral valve area (MVA) by continuity equation. (A, B) The left ventricular outflow tract (LVOT) diameter (d) is measured from the mid-esophageal aortic valve long- axis view at 135°. (C) To complete the calculation of the stroke volume (SV), the LVOT velocity-time integral (VTI_{LVOT}) is obtained by pulsed wave Doppler (PWD) of a deep transgastric (TG) view at 0° (or alternatively from a TG long-axis view at 110°). The SV_{LVOT} is calculated from the product of 0.785 x (LVOT diameter) [2] and the VTI_{LVOT}. (D) The VTI_{mitral} is given by continuous wave Doppler (CWD) of transmitral flow (TMF) from a mid-esophageal view. The MVA is calculated by dividing the SV_{LVOT} by the VTI_{mitral}. Ao, aorta; LA, left atrium; LV, left ventricle; RV, right ventricle. (Reproduced with permission from Denault *et al.* [2])

Table 7.2 Factors Affecting Pressure Half-Time (PHT)

↓ PHT	↑ PHT
Larger MVA by PHT Underestimate MS severity	**Smaller MVA by PHT Overestimate MS severity**
↓ Ventricular compliance, aging	Hypovolemia
Moderate-to-severe aortic regurgitation	Large left atrium
↑ Cardiac output	Eccentric aortic regurgitant jet impinging on the anterior mitral leaflet opening (Austin Flint)

MS, mitral stenosis; MVA, mitral valve area. Reproduced with permission from Denault *et al.* [2].

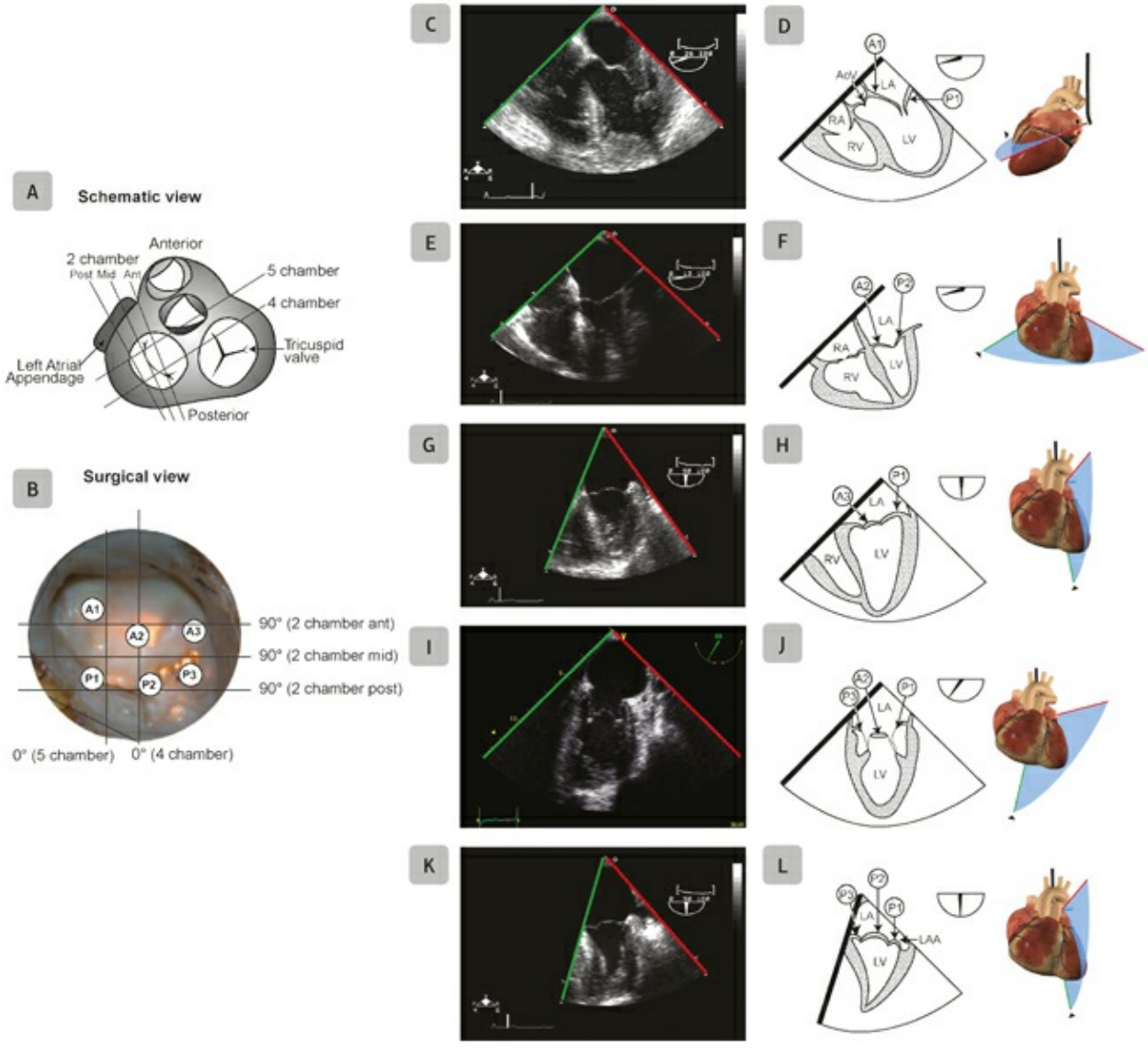

Fig. 7.23 Transesophageal echocardiography (TEE) assessment of mitral valve (MV). (A) Schematic

anatomic drawing of the heart through the base of the atrioventricular valves depicts the different planes used during a systematic TEE examination using the mid-esophageal (ME) views. (B) Corresponding surgical view of the MV from the left atrium (LA) with the corresponding TEE imaging planes. (C, D) ME five-chamber view of the MV at approximately 0° with slight anteflexion of the probe is shown. (E, F) ME four-chamber view of the MV near 0° is easily obtained by either inserting the TEE probe slightly deeper and/or releasing anteflexion from the five-chamber view. (G, H) ME two-chamber anterior view at 90° is obtained with slight anterior clockwise rotation of the TEE probe shaft toward the right. Part of the right ventricle (RV) may become visible as the field of view is progressively aimed toward the right. (I, J) ME two-chamber mid-commissural view at 70° with the tip of the anterior leaflet (A2) visible in the center of the mitral annulus and the posteromedial (P3) and anterolateral (P1) scallops of the posterior leaflet attached to their respective left ventricle (LV) wall. (K, L) ME two-chamber posterior view is obtained at 90° with slight counterclockwise posterior rotation of the TEE probe shaft toward the left. Ant, anterior; AoV, aortic valve; LA, left atrium; LAA, left atrial appendage; Mid, middle; Post, posterior; RA, right atrium. Source:Adapted with permission from Bruce and Connolly. [21] Photo B courtesy of Dr Nicolas Durrleman. (Reproduced with permission from Denault *et al.* [2] *)*

C: https://youtu.be/-jqpQuzUMCQ

E: https://youtu.be/kSmAXBlqnVc

G: https://youtu.be/AY1ucYVUav8

I: https://youtu.be/YXFmMOnAixI

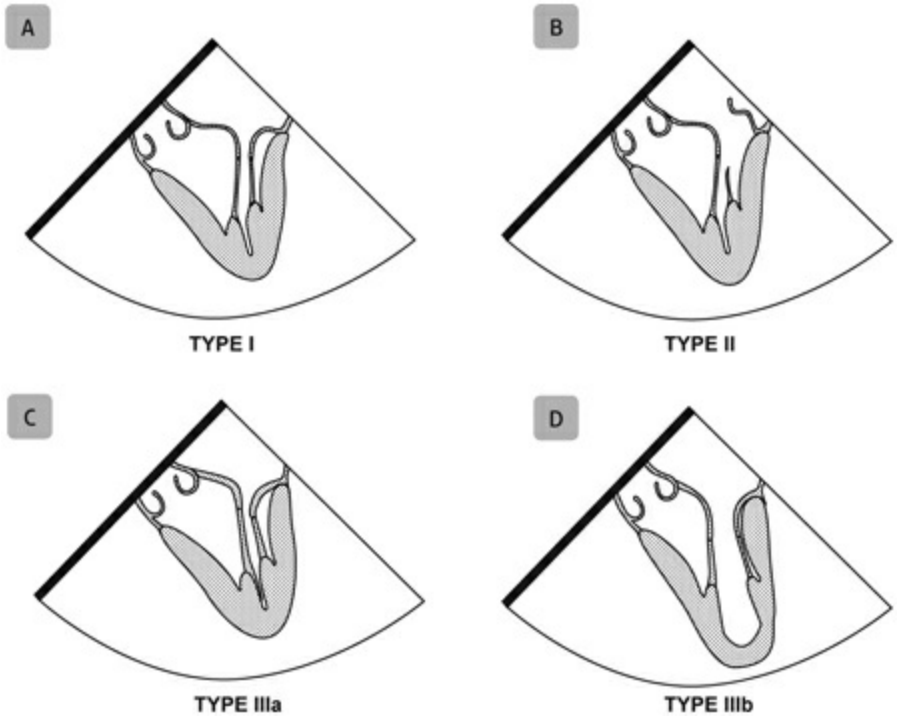

Fig. 7.24 Carpentier's classification of mitral regurgitation (MR). This functional classification is based on the opening and closing motions of the mitral leaflets. (A) Type 1 has normal leaflet motion and MR is on the basis of leaflet perforation or annular dilatation. (B) In type II dysfunction (increased leaflet motion), the leaflet free edge travels above the plane of the mitral annulus during systole due to chordal elongation or rupture. (C) Type IIIa dysfunction implies restricted opening leaflet motion during systole and diastole due to rheumatic changes. (D) Type IIIb dysfunction correlates to restricted leaflet motion during systole secondary to papillary muscle displacement and ventricular remodeling typically due to ischemia. (Reproduced with permission from Denault *et al.* [2] *)*

Doppler Flow

Doppler analysis of MR must always be interpreted under normal hemodynamic conditions. The direction of regurgitant flow into the LA can give an indication as to the mechanism of MR. It is central from bileaflet pathology and eccentric from leaflet restriction or prolapse. It should be noted that the regurgitant color flow is velocity mapping and not a measurement of blood volume. The extent and intensity depends on the instantaneous gradient between the LV and LA in systole, which is determined by four elements: (1) ventricular systolic pressure, which increases if systolic artery pressure increases; (2) maximal MR velocity across the orifice decreases if the LV systolic function is abnormal; (3) LA pressure; and (4) regurgitant orifice size: the greater the regurgitant orifice size, the faster MR Vmax will decrease. For example, in acute MR with papillary muscle rupture, the

regurgitant orifice is so large and cardiogenic shock so profound that the regurgitant flow can appear unimportant. Nevertheless, the size of the color jet area in the LA is an easy way to intuitively assess the importance of MR. A color jet area >20% of the LA area is considered moderate, whereas a color jet area >40% is considered severe. [25] The vena contracta uses the width of the regurgitant jet at its narrowest portion close to its origin to evaluate MR severity. This is best performed by obtaining high-resolution, zoomed images of the MV with color Doppler in either the ME four-chamber or LAX views. [24] A vena contracta <3 mm usually denotes mild MR, whereas the cut-off value for severe MR ranges between 6.0 and 8.0 mm (**Figure 7.25**). [23]

The maximal velocity of the regurgitant flow itself does not provide useful information about the severity of MR. However, the density of the CW Doppler signal is proportional to the number of red blood cells reflected in the ultrasound beam and is used as a qualitative index of MR severity. The contour of the MR velocity profile may also provide information about MR severity; for example, a truncated, triangular jet suggests an elevated LA pressure. Mitral antegrade Vmax flow is higher than 1.2 cm/s because of the increased diastolic blood volume from the regurgitant volume during the previous systole. With increasing MR severity, there is systolic blunting and a progressive diminution of systolic velocity in the pulmonary vein flow. [26] Severe MR results in systolic flow reversal in the pulmonary veins (**Figure 7.25**). Interrogation of all four pulmonary veins should be performed as an eccentric jet may be preferentially directed towards a single vein where systolic flow reversal will be found. The quantification of MR is summarized in **Table 7.1**.

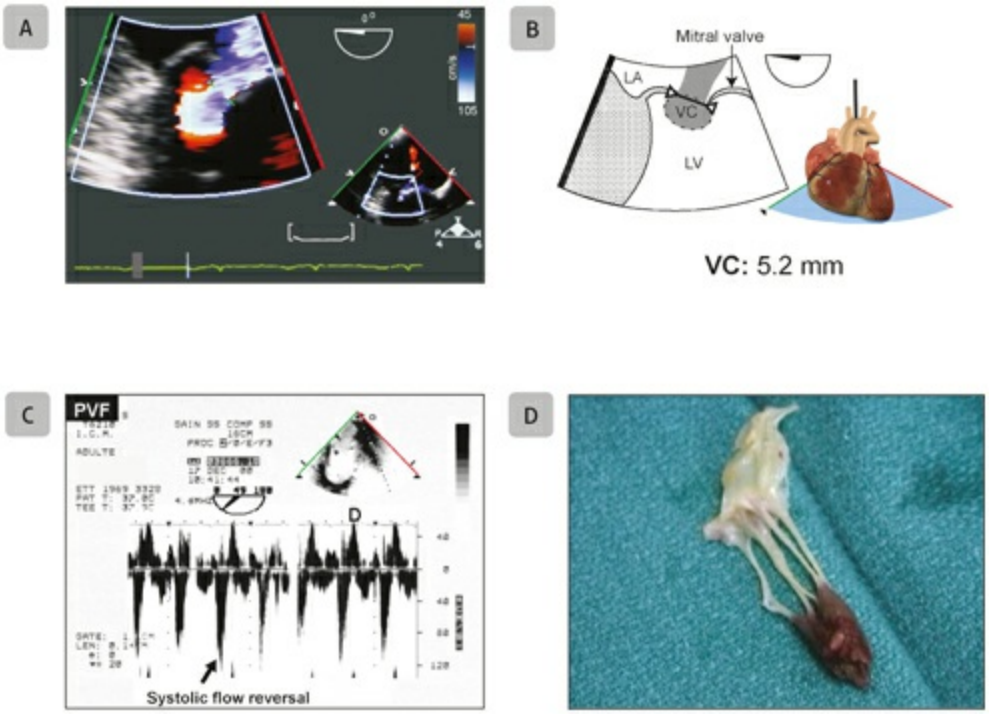

Fig. 7.25 Vena contracta and pulmonary venous flow (PVF). (A) Zoom of color Doppler mid-esophageal five-chamber view demonstrates moderate mitral regurgitation (MR) with (B) a vena contracta (VC) measured at 5.2 mm. (C) Pulsed wave Doppler spectral trace of the PVF shows significant systolic flow reversal (the equivalent of a "v" wave), consistent with severe MR. (D) Excised pathology specimen from a 61-year-old male with acute MR due to rupture of the posteromedial papillary muscle. D, diastolic PVF velocity; LA, left atrium; LV, left ventricle. (Reproduced with permission from Denault *et al.* [2] *)*

Acute Mr

Characteristic LV remodelling is absent in acute MR due to papillary muscle rupture, endocarditis, or extensive ischemia. Besides tachycardia and cardiogenic shock, acute MR has special echocardiographic characteristics, [25] which include a normal LV size, papillary muscle rupture, leaflet prolapse, and leaflet perforation. In addition, the extent of regurgitant color flow and the velocity of MR are reduced because of LV dysfunction and the increase in LA pressure. The width of the vena contracta is still valid and systolic flow reversal in pulmonary veins will be observed because of low LA compliance.

TRICUSPID VALVE

The tricuspid valve (TV) constitutes three asymmetric leaflets: septal,

anterior, and posterior. It has a large orifice area between 7 and 9 cm^2 and annular circumference of 12–14 cm. Guidelines for the measurement of the tricuspid annulus have previously been published (see **Figure 5.3**). An annular diameter above 4 cm is considered abnormal. [27] The usual views to analyze the TV are the ME four-chamber and the right ventricular (RV) inflow outflow tract (see **Figure 5.3**).

Tricuspid Stenosis

Etiology

Tricuspid stenosis (TS) is rarely an isolated lesion and is often associated with rheumatic mitral stenosis. It can also be congenital or occur with carcinoid syndrome and endomyofibrosis. [28]

Two-Dimensional Imaging

Anatomic assessment by 2D imaging shows TV leaflet thickening, calcification, and restricted mobility with diastolic leaflet doming and right atrial enlargement. The leaflet may be completely immobile, as occurs with carcinoid syndrome. The subvalvular apparatus is shortened and thickened (**Figure 7.26**). The right atrium (RA) is dilated (diameter >5 cm), as are the inferior vena cava and hepatic veins.

Doppler Flow

Color Doppler imaging shows a narrow turbulent diastolic inflow often with associated tricuspid regurgitation (**Figure 7.26**). The characteristic feature of the spectral Doppler trace is an increased peak transvalvular tricuspid inflow velocity of >1 m/s with a significant mean PG >5 mmHg (normal <2 mmHg). [29] A mean PG of >7 mmHg corresponds to severe tricuspid stenosis (area <1 cm^2). The tricuspid valve area (TVA) can be estimated using the PHT, as was the case for the MVA, but uses a constant of 190 ms (corresponding to a TVA of 1 cm^2), thus:

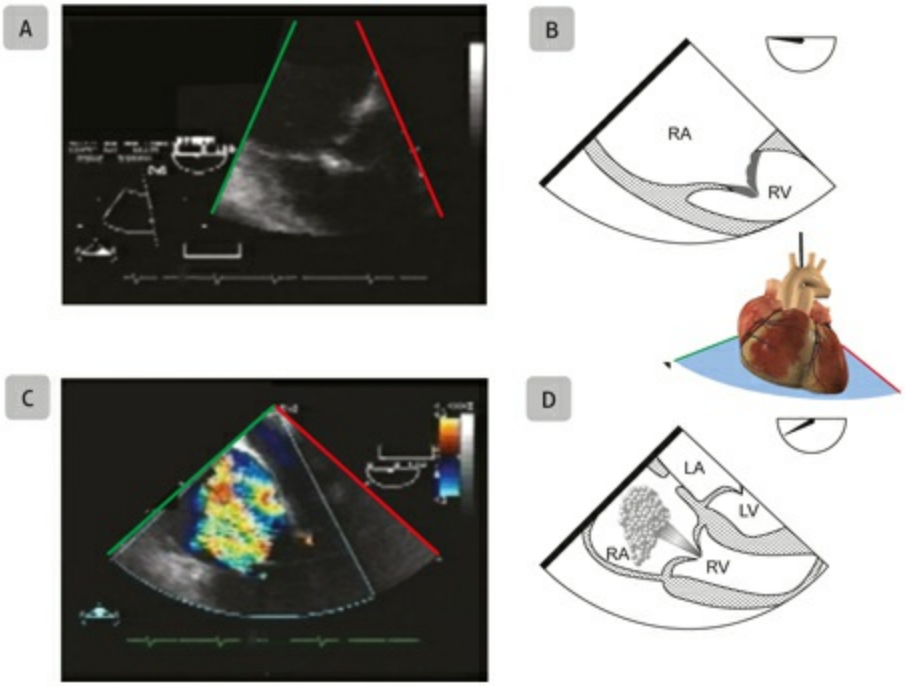

Fig. 7.26 Rheumatic tricuspid valve (TV). (A, B) Zoomed mid-esophageal four-chamber view of the TV shows restricted motion from chordal shortening and fusion. (C, D) Color Doppler (Nyquist 43 cm/s) shows severe tricuspid regurgitation. LA, left atrium; LV, left ventricle; RA, right atrium; RV, right ventricle. (Reproduced with permission from Denault *et al.* [2])

A: https://youtu.be/30TTDpIG_eM

C: https://youtu.be/TLeIbRVE7OI

TVA = 190/PHT

The quantification of TV stenosis is summarized in **Table 7.1**.

Tricuspid Regurgitation

Tricuspid regurgitation (TR) is a frequent echocardiograph- ic finding in 70% of the general population, and to some degree it is considered a normal finding in all individuals. [30] Indeed, the right heart cavities are in a low

pressure system and therefore do not need to be completely sealed.

Etiology

Functional TR results from TV annulus dilatation due to RV dilation that occurs with left heart valvular diseases, pulmonary hypertension, and RV dysfunction. Valvular anomalies are rare but can be seen with Ebstein's anomaly, rheumatism, myxoid degeneration, carcinoid syndrome, endocarditis, trauma, toxicity, and shock. [21] , [31] , [32]

Two-Dimensional Imaging

Tricuspid regurgitation is associated with several findings, although none is discriminative alone. Chronic severe TR is generally associated with RA dilation (diameter ≥5 cm, volume >35 mL/m ^{2}); RV dilation (ME four-chamber diastolic diameter cavity >4 cm); tricuspid annular dilation ≥3.5 cm; systolic bowing of the inter-atrial septum into the LA; no central coaptation of the leaflets, and plethoric inferior vena cava (diameter >2.0 cm in systole). [23] , [29] , [33]

Doppler Flow

The TR jet typically is a mosaic pattern with CFD that is directed toward the inter-atrial septum (**Figure 7.27**). This is because TV annulus dilation occurs principally in its non-fibrotic postero-lateral portion, thus avoiding the anterior and posterior leaflets (**Figure 7.28**). In addition, the TV septal leaflet is shorter and more restrictive with less motion than the others. Color Doppler imaging has become the primary method used to grade TR severity. Loading conditions, which depend on RV systolic function, pulmonary resistance and venous central pressure, may limit the ability of regurgitant jet color flow area to grade TR (jet area >9 cm ^{2} is significant, while a jet area <4 cm ^{2} is mild). Severe TR is best correlated with the width of color regurgitant jet or vena contracta (>0.7 cm) and to the presence of a large zone of proximal convergence (PISA radius >0.9 cm). The spectral Doppler axis is generally properly aligned with the TR jet in the mid-esophageal views. Severe TR is characterized by a high density triangular jet that is early peaking from rapid pressure equalization between the RV and RA (**Figure 7.29**). The TR maximal velocity depends on the PG in systole and varies from 1.5 to 4 m/s. It is low when the regurgitant orifice is large. With severe

TR, an accelerated antegrade flow: E Vmax >1 m/s and hepatic vein systolic reversal will be observed (**Figure 7.30)**. The latter may be absent if the RA is significantly dilated. In some patients, severe TR is associated with RV failure and abnormal pulsatile portal and splenic venous flows (see **Figure 4.39**). The presence of TR allows calculation of the PG across the TV between the RA and RV, and can estimate pulmonary artery systolic pressure (**Figure 7.30**). Quantification of TR is summarized in **Table 7.1**.

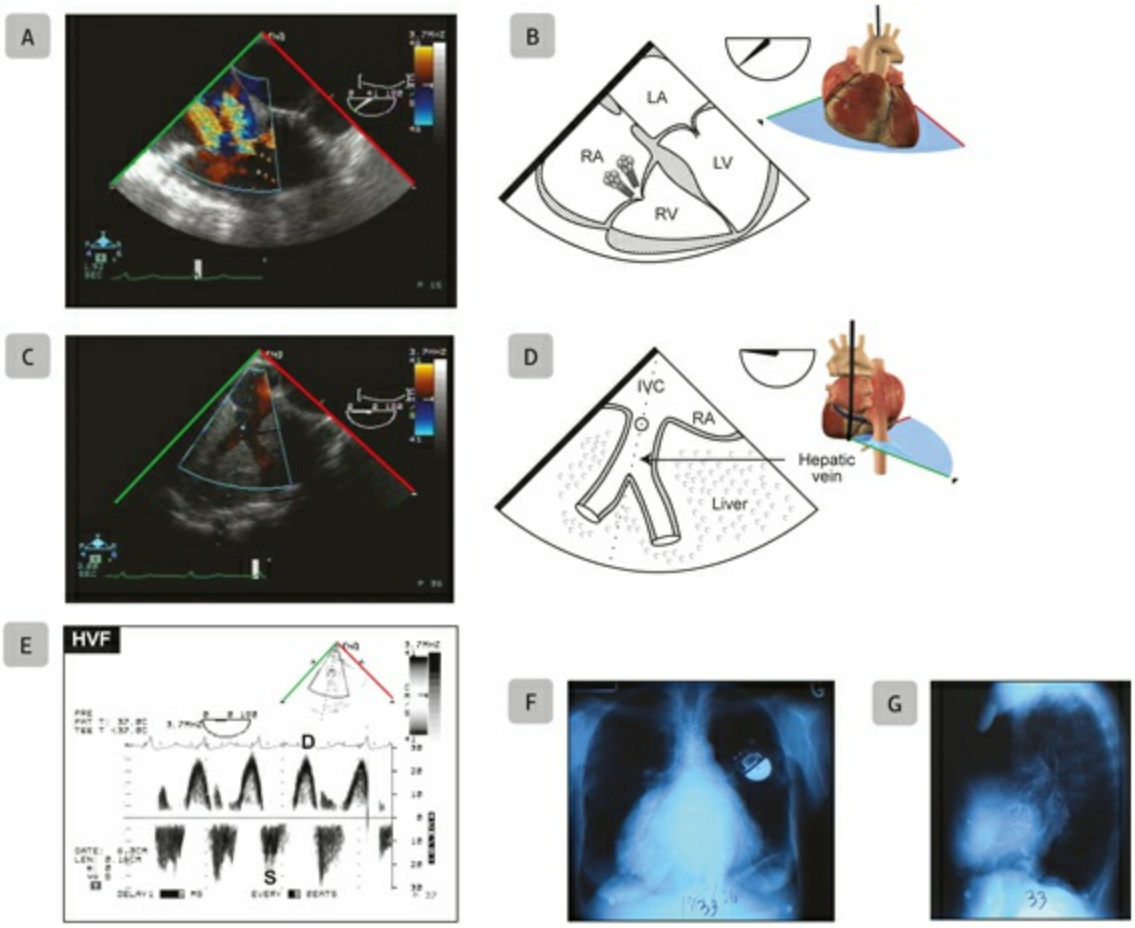

Fig. 7.27 Tricuspid regurgitation (TR). (A, B) Color Doppler midesophageal four-chamber view shows severe TR in a 77-year- old female before tricuspid annuloplasty. (C, D) Transgastric inferior vena cava (IVC) long-axis view indicates dilated hepatic veins. (E) Pulsed wave Doppler of hepatic venous flow (HVF) shows systolic flow reversal. (F, G) Chest radiography confirms the abnormal right heart border consistent with dilated rightsided structures. D, diastolic HVF velocity; LA, left atrium; LV, left ventricle; RA, right atrium; RV, right ventricle; S, systolic HVF velocity. (Reproduced with permission from Denault *et al.* [2] *)*

A: https://youtu.be/uI_dNOXFtn8

PULMONARY VALVE

The pulmonary valve is a delicate anterior positioned structure that is poorly echogenic, making it difficult to assess with TEE. It can be evaluated in the ME right ventricular outflow tract (RVOT) and upper esophageal aortic SAX views (**Figure 7.31**. This latter view is also useful to monitor cardiac output using Doppler. In adults, serious pathologies located at the RV outflow tract and pulmonary valve are extremely rare, most often associated with congenital heart diseases.

Pulmonary Stenosis

Pulmonary stenosis is rare in adults and usually results from congenital (commissural fusion, unicuspid or bicuspid valve) or carcinoid syndrome. It is defined as valve opening of <2 cm^2/m^2. The valve may appear thickened, calcified with extremely immobile leaflets, or systolic bulging leaflets. The RV is severely hypertrophied and sometimes failing. The pulmonary artery trunk is expanded (>20 mm) beyond the stenosis (**Figure 7.32**). The same applies to the left pulmonary artery, which is usually anatomically aligned with the axis of RV flow ejection. [34] Color Doppler shows systolic flow acceleration through the valve (**Figure 7.32**). Using Doppler spectral flow, the stenosis shows an accelerated flow in early systole [21] (normal maximal flow velocity 0.5–1 m/s) and an increased PG. The quantification of pulmonary stenosis is summarized in **Table 7.1**.

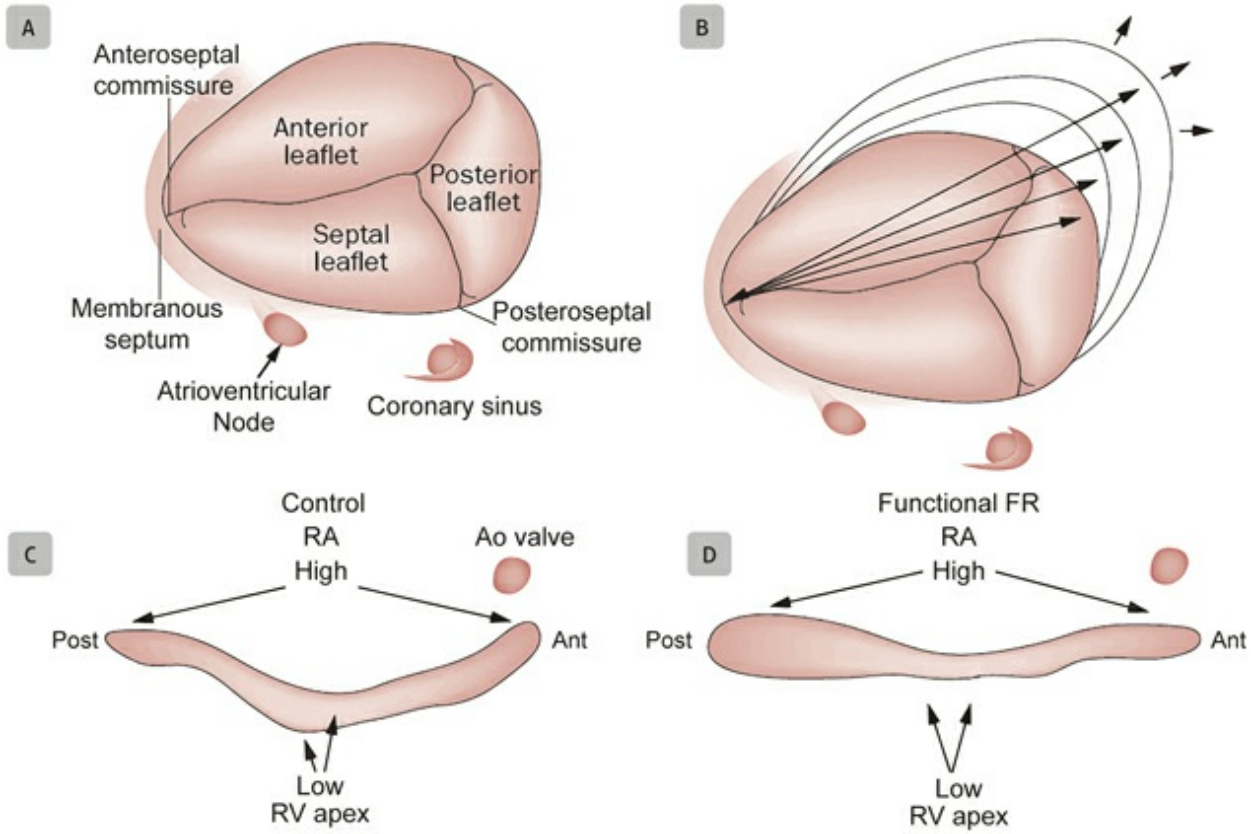

Fig. 7.28 Tricuspid valve (TV) annular dilatation. (A) Schematic of a normal TV is shown with important surrounding structures. (B) Tricuspid annular dilatation from left-sided heart valve disease occurs predominantly in the septal-lateral direction. (C) Profile of the tricuspid annulus in a patient with a normal TV (C) has two high points located anteroposteriorly, compared to a patient with functional tricuspid regurgitation (TR) (D, where the annulus becomes flatter with no distinct high point. Ant, anterior; Ao, aortic; Post, posterior; RA, right atrium; RV, right ventricle. (Reproduced with permission from Macmillan Publishers [35] and adapted from Dreyfus *et al.* [36] and Ton-Nu *et al.* [37] *)*

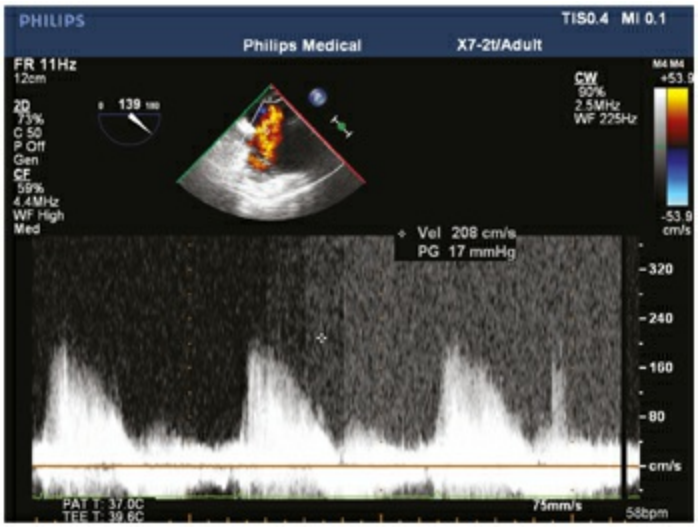

Fig. 7.29 Tricuspid regurgitation. Mid-esophageal long-axis view with right-sided rotation along the right ventricular inflow allows good alignment for spectral Doppler interrogation of tricuspid regurgitation jets. The maximum pressure gradient (PG) is 17 mmHg. Vel, velocity.

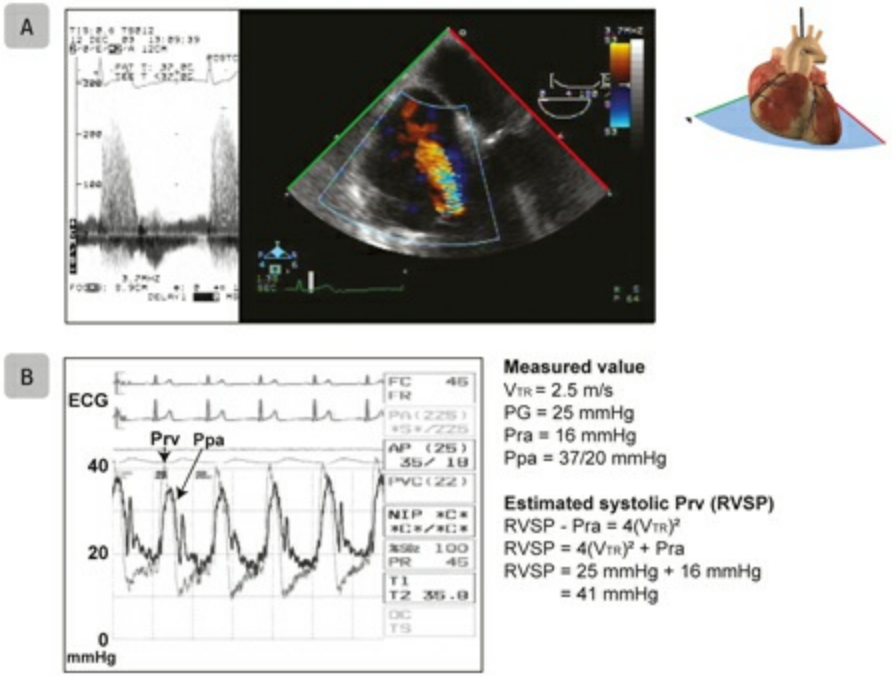

Fig. 7.30 Right ventricular systolic pressure (RVSP). (A) Estimation of RVSP using the pressure gradient (PG) obtained from tricuspid regurgitation (TR) and right atrial pressure (Pra). (B) Note that the RVSP is higher than the systolic pulmonary artery pressure (Ppa) due to a small gradient across the pulmonic valve. ECG, electrocardiogram; Prv, right ventricular systolic pressure; V_{TR}, peak tricuspid regurgitant velocity. (Reproduced with permission from Denault *et al.* [2])

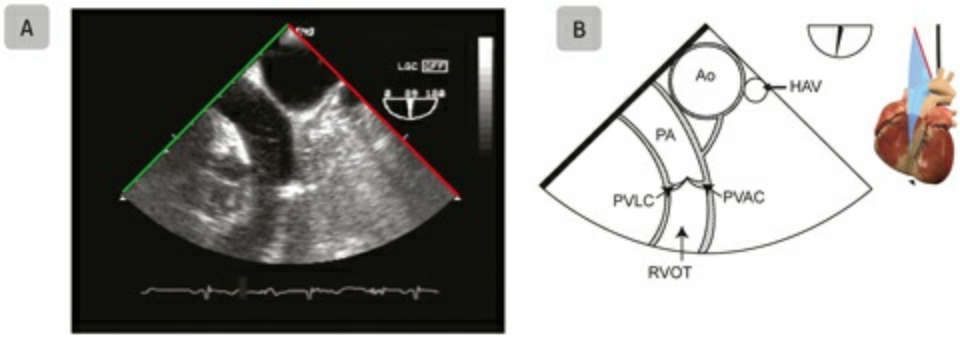

Fig. 7.31 Pulmonic valve (PV). (A, B) Upper esophageal view of the PV shows a sagittal view of the right ventricular outflow tract (RVOT) and PV with good alignment for Doppler evaluation. Ao, aorta; HAV, hemiazygos vein; PA, pulmonary artery; PVAC, pulmonic valve anterior cusp; PVLC, pulmonic valve left cusp. (Reproduced with permission from Denault *et al.* [2])

A: https://youtu.be/OE-2qlRILmg  A: https://youtu.be/JXDTfifnC94

Pulmonary Regurgitation

The prevalence of physiological pulmonary regurgitation (PR) is 30–75% in the general population. [25] , [30] It is common for PR to be secondary to annulus or RV outflow tract dilatation. Pulmonary valve lesions are rare outside congenital or acquired diseases (endocarditis, carcinoid syndrome). Mild PR represents a small color jet (<1.0 cm in length) from a commissure or central malcoaptation of the valve directed into the axis of the RVOT and varies with respiration (**Figure 7.33**). In severe PR, the pulmonary artery (PA), RVOT, and RV are dilated. Pressure equalization between the PA and RV is so fast that the jet does not last throughout diastole. With spectral display, the deceleration slope of the PR flow is steep and does not last throughout diastole. The maximal velocity of PR flow is often low (color flow without turbulence) because the opening is wide. Arrhythmias are common. The pulmonary regurgitation index (PRI) is the ratio between the duration of PR and the duration of diastole. When PR is moderate, the deceleration slope is more gradual and present throughout diastole. A PRI <0.75 is a sign of regurgitant fraction >25%. [38] Severe PR is an indication for surgical valve replacement. [24]

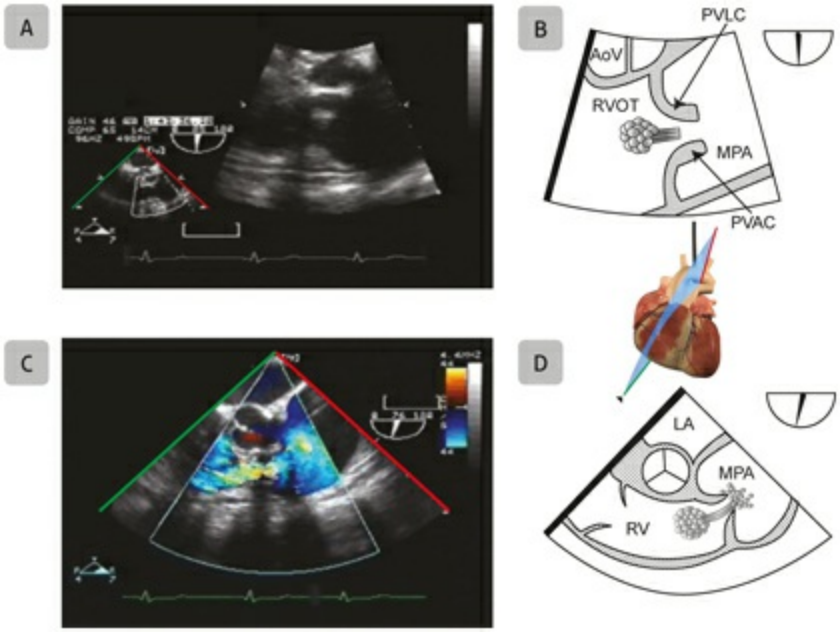

Fig. 7.32 Pulmonary artery post-stenotic aneurysm. (A, B) Zoom of modified midesophageal right ventricular inflow/ outflow view shows thickened pulmonic valve (PV) cusps with systolic doming. (C, D) Color Doppler (Nyquist 44 cm/s) in a mid-esophageal right ventricular inflow/outflow view shows a dilated main pulmonary artery (MPA) with mild pulmonary regurgitation. The gradient across the PV was measured at 19 mmHg by continuous wave Doppler (not shown). AoV, aortic valve; LA, left atrium; PVAC, PV anterior cusp; PVLC, PV left cusp; RV, right ventricle; RVOT, right ventricular outflow tract. (Reproduced with permission from Denault *et al.* [2] *)*

A: https://youtu.be/qZKPaOnw4WI

C: https://youtu.be/0kBtGCaFv8U

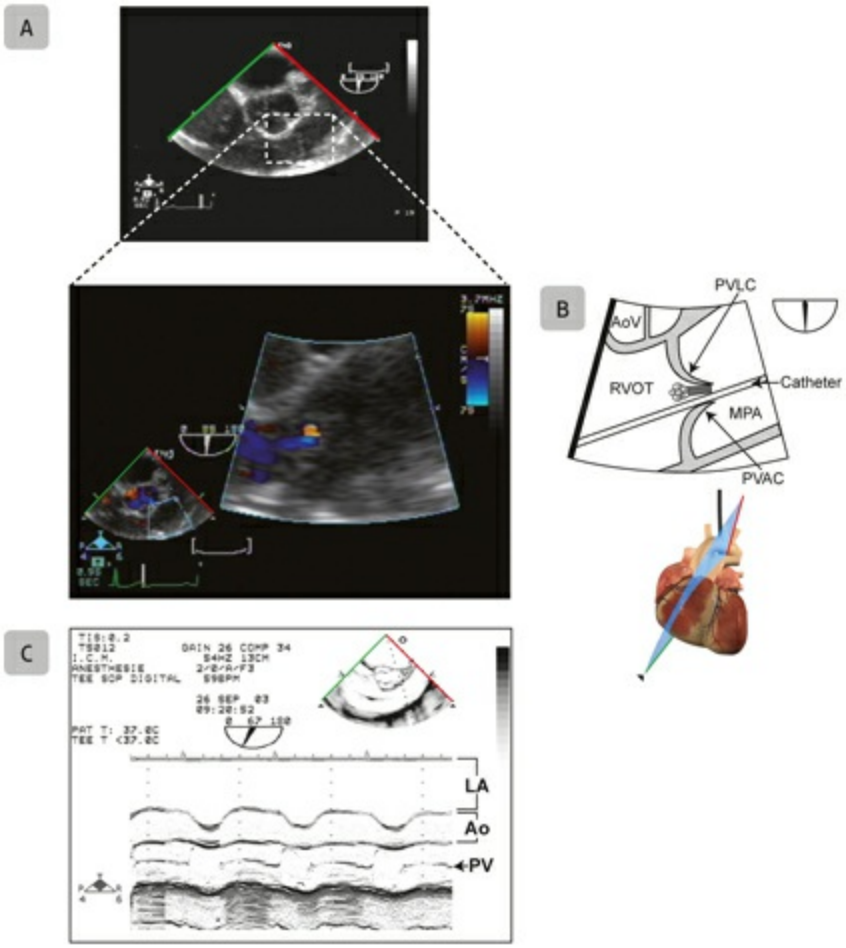

Fig. 7.33 Normal pulmonic valve (PV). (A, B) Mid-esophageal right ventricular inflow/outflow views at 85° and (C) M-mode show the normal PV in a 23-year-old male undergoing mitral valve replacement. A small jet of pulmonary regurgitation is present around the pulmonary artery catheter. Ao, aorta; AoV, aortic valve; LA, left atrium; MPA, main pulmonary artery; PVAC, PV anterior cusp; PVLC, PV left cusp; RVOT, right ventricular outflow tract. (Reproduced with permission from Denault *et al.* [2])

A: https://youtu.be/e01Evu6g3Vo

PROSTHETIC VALVES

Prosthetic valves are classified according to the material (biological or mechanical) and occluder design.

Mechanical Valves

Mechanical valves are distinguished by the design of their main occluder. “Ball cage valves” consists of a metal cage holding a mobile silicone spherical ball with a Teflon sewing ring (**Figure 7.34 A**). “Tilting disc valves” consist of a single circular disc suspended within a metal valve-housing with a central hole (**Figure 7.34 B**). The maximum tilting angle varies between 55° and 70°; consequently, in the open position, these valves have one large and one small orifice. “Bileaflet valves” (**Figure 7.34 C**) have two semi-circular discs centrally mounted on hinges that pivot open by 70–80° creating two equal semi-circular (major) and one central slit-like (minor) orifices. As for tilting disc valves in the closed position, these prostheses have converging transvalvular flow as well as diverging regurgitant jets, at the periphery between the hemidisc and the sewing two hemidiscs. The transvalvular PG is measured across the two lateral orifices and not centrally, where it is higher. Globally, bileaflet valves are the most commonly implanted prosthetic valves because of their better dynamic profile.

Biological Prostheses

Biological prostheses are classified according to the presence (stented) or absence (stentless) of a structural support and according to the tissue origin, with homografts (human) versus heterografts (porcine or bovine) (**Figure 7.35**).

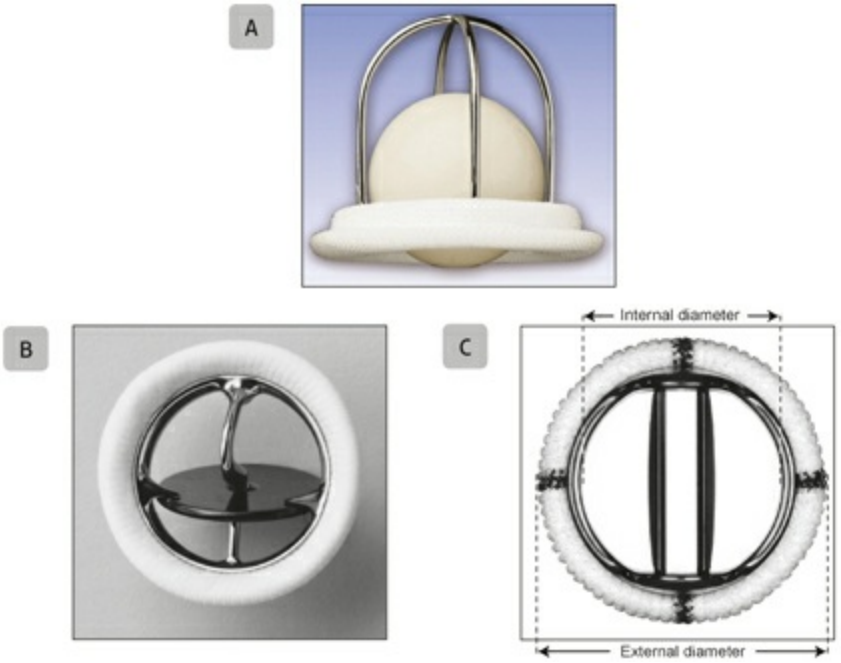

Fig. 7.34 Mechanical heart valves. Models of mechanical valve prostheses are shown: (A) Starr-Edwards (Edwards Lifesciences, Irvine, CA, USA), (B) Medtronic Hall (©Medtronic, Minneapolis, MN, USA), (C) St Jude Medical (©St Jude Medical, St Paul, MN, USA). (Reproduced with permission from Denault *etal.* [2] *)*

A: https://youtu.be/xEuLWF3V6Hc

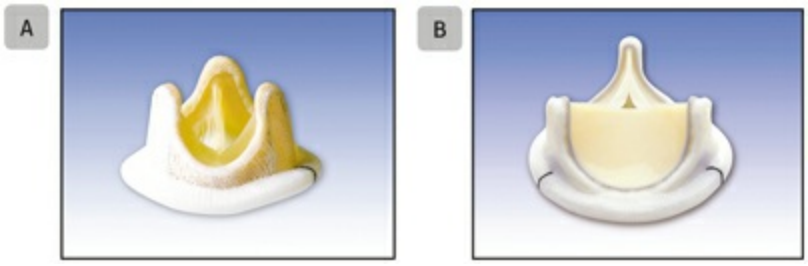

Fig. 7.35 Bioprosthetic valves. (A) Carpentier-Edwards porcine, (B) Carpentier-Edwards Perimount™ pericardial tissue mitral valve bioprostheses are shown. Source: Courtesy of Edwards Lifesciences. (Reproduced with permission from Denault *et al.* [2] *)*

Two-Dimensional Imaging

The prosthetic material causes many artifacts. The presence of foreign

material creates shadows and causes many reverberations. In the SAX view, biological prostheses appear round when open and as three-point stars when closed. In the LAX view, they appear as two pins parallel to the transvalvular flow axis with the coaptation point downstream of the prosthetic valve annulus (**Figure 7.36**). Throughout the cardiac cycle, a normal prosthetic valve should move simultaneously with the base of the ventricle to which it is sutured. A rocking motion is always abnormal, and caused by a dehiscence of the sewing ring. Thrombus, vegetation, abnormal tissue growth (pannus), interfering residual subvalvular apparatus, and intrinsic prosthetic valve feature could all be responsible for an abnormal asymmetric leaflet movement, which can cause incomplete valve closure and result in regurgitation (**Figure 7.37**). A peri-annulus cavity without echo suggests an abscess or fistula. [39]

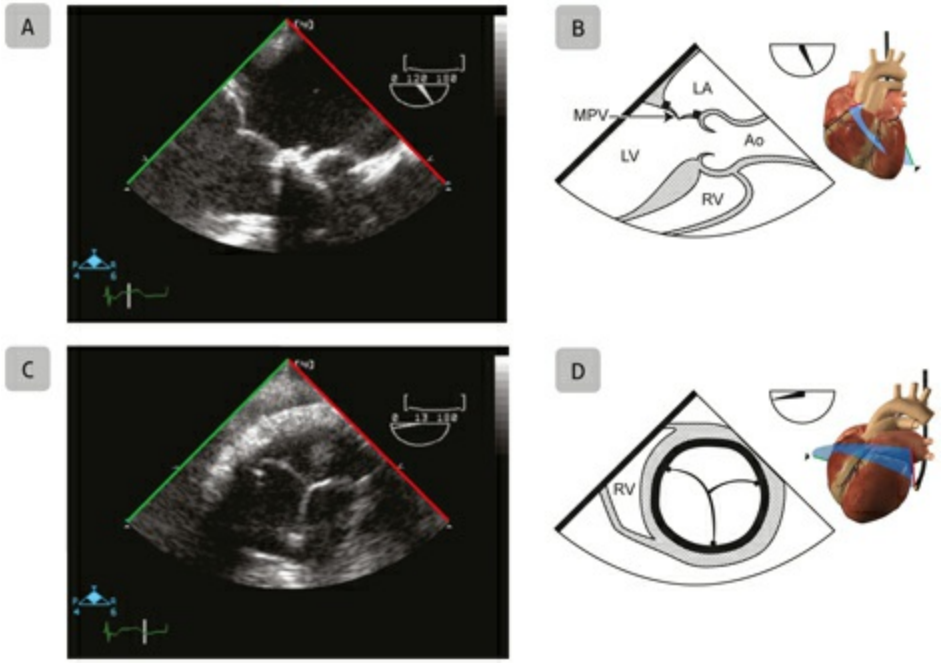

Fig. 7.36 Mitral valve (MV) bioprostheses. (A, B) Midesophageal long-axis view shows the thickness and motion of normal MV bioprosthesis leaflets. (C, D) Transgastric view shows the three struts and three leaflets “en face” of the mitral prosthetic valve (PMV). Ao, aorta; LA, left atrium; LV, left ventricle; RV, right ventricle. (Reproduced with permission from Denault *et al.* [2])

A&C: https://youtu.be/_CAKFA9okD4

A&C: https://youtu.be/5qz-IuXWOFc

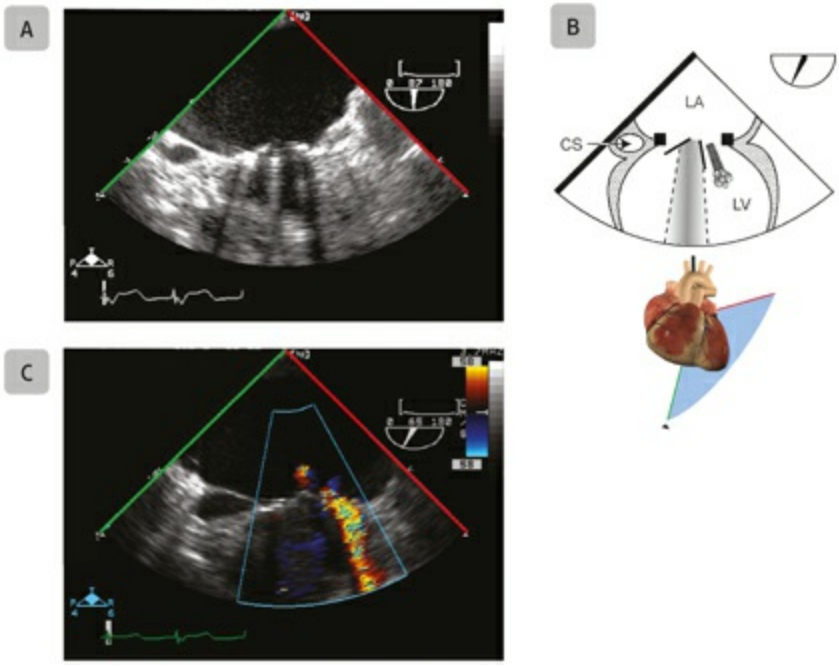

Fig. 7.37 Mechanical bileaflet dysfunction. (A, B) Mid-esophageal two-chamber view of a mechanical bi-leaflet prosthetic mitral valve (PMV) shows immobility of the left hemi-disc compared with normal mobility of the right hemi-disc immediately after cardiopulmonary bypass. (C) Color Doppler (Nyquist 58 cm/s) flow was present through only one major orifice, while no flow is associated with the immobile hemi-disc. CS, coronary sinus; LA, left atrium; LV, left ventricle. (Reproduced with permission from Denault *et al.* [2])

A: https://youtu.be/rgLQMch6ooo

C: https://youtu.be/NmEMMiK9sjw

Color Doppler Imaging

Normal prosthetic valves may present with a mild degree of intraprosthetic functional regurgitation characteristic of the specific valve design. Biological prosthetic valves generally have central leaks, but they can sometimes be seen at the commissures. Tilting valves and bi-leaflet valves have a small quantity (5–15 mL/beat) intrinsic intra-prosthetic regurgitation, which does not represent prosthetic dysfunction. Moreover, these normal intrinsic regurgitant jets have a functional antithrombotic effect, “washing out” the prosthesis occluder edges with each systole. In bi-leaflet valves, the jet forms a converging pattern in the plane parallel to the central slit orifice and a diverging pattern in the plane perpendicular to it (**Figure 7.38**). Paravalvular leaks are located between the prosthesis and anatomical ring and are always pathological.

Pressure gradients

All valvular prostheses are restrictive compared with native valves. For prostheses of the same size, the PG increases as follows: autografts < homograft < non-mounted bioprosthesis (stentless) < mechanical valves and mounted bioprosthesis. **Table 7.3** offers reference values[24,25,40] of PG and maximal velocities in a simplified manner to identify prosthetic valve dysfunction. Indeed, higher values can be considered pathological and warrant an expert opinion.

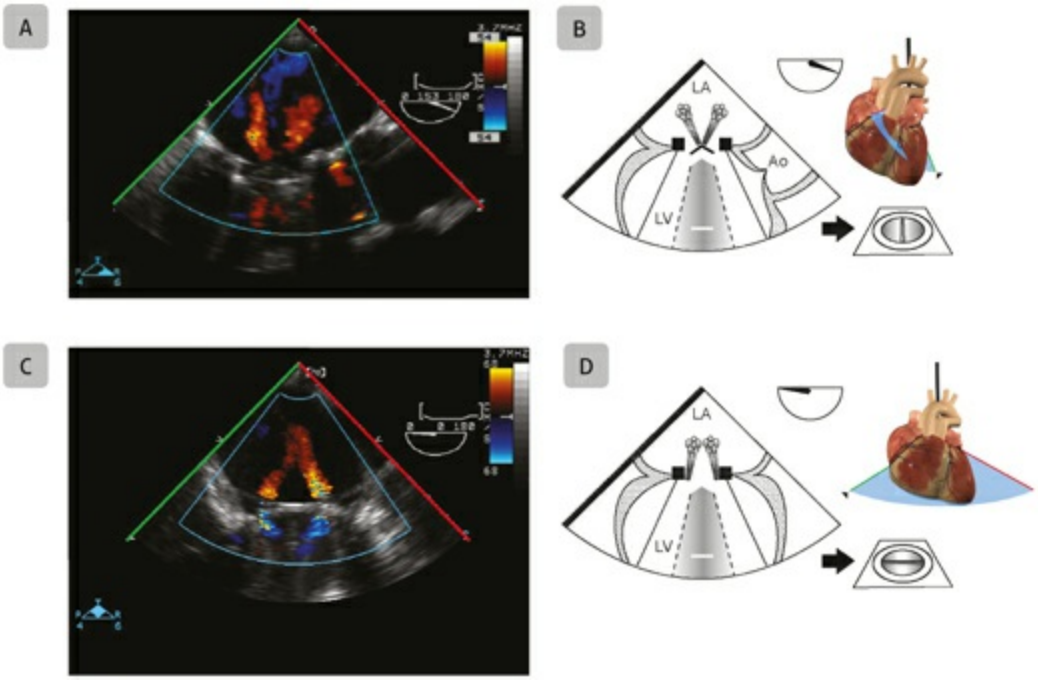

Fig. 7.38 Washing jets. Color Doppler mid-esophageal long- axis and four-chamber views showing the normal signature of (A, B) the diverging and (C, D) converging regurgitant washing jets of a mechanical bi-leaflet St Jude prosthetic mitral valve. The diverging jets are seen when the view is perpendicular to the axis of the central slit orifice. Ao, aorta; LA, left atrium; LV, left ventricle. (Reproduced with permission from Denault *etal.* [2])

A: https://youtu.be/e9eUUGyrRB0

Table 7.3 Prosthetic Valves

Aortic	Stentless bioprosthesis	Mechanical valve	Bioprosthesis
Mean gradient	4–8 mmHg	6–15 mmHg	8–20 mmHg
Vmax	1.5–1.8 m/s	2–2.5 m/s	2.5–3 m/s

Mitral		Bi-leaflet mechanical valve	Bioprosthesis
Mean gradient		3–5 mmHg	6 mmHg
Vmax		1.2–1.6 m/s	1.5–1.8 m/s

Vmax, maximum velocity.

SUMMARY

Transesophageal echocardiography assessment of valvuar diseases is a complex process, requiring both precise measurements and clinical experience. This chapter presents some tools easily applicable in the non-cardiac operating room or the intensive care unit, allowing the novice echocardiographer to recognize a valvular anomally, appreciate the severity and, when warranted, request a more expert opinion.

REFERENCES

1. NkomoV.T., GardinJ.M., SkeltonT.N., GottdienerJ.S., ScottC.G., Enriquez-SaranoM.. Burden of valvular heart diseases: a population-based study. *Lancet*. 2006;*368*:1005–11.
2. DenaultA.Y., CoutureP., VegasA., BuithieuJ., TardifJ.C.. *Transesophageal Echocardiography Multimedia Manual, A Perioperative Transdisciplinary Approach*. New York, NY: Informa Healthcare; 2011.
3. CemriM., CengelA., TimurkaynakT.. Pentacuspid aortic valve diagnosed by transoesophageal echocardiography. *Heart*. 2000;*84*:E9.
4. TzemosN., TherrienJ., YipJ., ThanassoulisG., TremblayS., JamorskiM.T., et al. Outcomes in adults with bicuspid aortic valves. *JAMA*. 2008;*300*:1317–25.
5. MoazamiN., DiodatoM.D., MoonM.R., LawtonJ.S., PasqueM.K., HerrenR.L., et al. Does functional mitral regurgitation improve with isolated aortic valve replacement?*J Card Surg*. 2004;*19*:444–8.
6. MaslowA.D., HaeringJ.M., HeindelS., MashikianJ., LevineR., DouglasP.. An evaluation of prosthetic aortic valves using transesophageal echocardiography: the double-envelope technique. *Anesth Analg*. 2000;*91*:509–16.
7. MaslowA.D., MashikianJ., HaeringJ.M., HeindelS., DouglasP., LevineR.. Transesophageal echocardiographic evaluation of native aortic valve area: utility of the double-envelope technique. *J Cardiothorac Vasc Anesth*. 2001;*15*:293–9.
8. BaumgartnerH., HungJ., BermejoJ., ChambersJ.B., EvangelistaA., GriffinB.P., et al. Echocardiographic assessment of valve stenosis: EAE/ASE recommendations for clinical practice. *J Am Soc Echocardiogr*. 2009;*22*:1–23.
9. CormierB., lungB., PorteJ.M., BarbantS., VahanianA.. Value of multiplane transesophageal echocardiography in determining aortic valve area in aortic stenosis. *Am J Cardiol*1996; *77*:882–5.
10. HoffmannR., FlachskampfF.A., HanrathP.. Planimetry of orifice area in aortic stenosis using multiplane transesophageal echocardiography. *J Am Coll Cardiol*. 1993;*22*:529–34.
11. TardifJ.C., RodriguesA.G., HardyJ.F., LeclercY., PetitclercR., MongrainR., et al. Simultaneous determination of aortic valve area by the Gorlin formula and by transesophageal echocardiography under different transvalvular flow conditions. Evidence that anatomic aortic valve area does not change with variations in flow in aortic stenosis. *J Am Coll Cardiol*. 1997;*29*:1296–302.
12. BoodhwaniM., de KL, Glineur D, Poncelet A, Rubay J, Astarci P, et al. Repair-oriented classification of aortic insufficiency: impact on surgical techniques and clinical outcomes. *J Thorac Cardiovasc Surg*. 2009;*137*:286–94.
13. PerryG.J., HelmckeF., NandaN.C., ByardC., SotoB.. Evaluation of aortic insufficiency by Doppler

color flow mapping. *J Am Coll Cardiol*. 1987;*9*:952–9.
14. WillettD.L., HallS.A., JessenM.E., WaitM.A., GrayburnP.A.. Assessment of aortic regurgitation by transesophageal color Doppler imaging of the vena contracta: validation against an intraoperative aortic flow probe. *J Am Coll Cardiol*. 2001;*37*:1450–5.
15. GrayburnP.A., HandshoeR., SmithM.D., HarrisonM.R., DeMariaA.N.. Quantitative assessment of the hemodynamic consequences of aortic regurgitation by means of continuous wave Doppler recordings. *J Am Coll Cardiol*. 1987;*10*:135–41.
16. YauT.M., El-GhoneimiY.A., ArmstrongS., IvanovJ., DavidT.E.. Mitral valve repair and replacement for rheumatic disease. *J Thorac Cardiovasc Surg*. 2000;*119*:53–60.
17. MuggeA., KuhnH., NikuttaP., GroteJ., LopezJ.A., DanielW.G.. Assessment of left atrial appendage function by biplane transesophageal echocardiography in patients with nonrheumatic atrial fibrillation: identification of a subgroup of patients at increased embolic risk. *J Am Coll Cardiol*. 1994;*23*:599–607.
18. HandkeM., HarloffA., HetzelA., OlschewskiM., BodeC., GeibelA.. Left atrial appendage flow velocity as a quantitative surrogate parameter for thromboembolic risk: determinants and relationship to spontaneous echocontrast and thrombus formation - a transesophageal echocardiographic study in 500 patients with cerebral ischemia. *J Am Soc Echocardiogr*. 2005;*18*:1366–72.
19. HatleL., AngelsenB., TromsdalA.. Noninvasive assessment of atrioventricular pressure half-time by Doppler ultrasound. *Circulation*. 1979;*60*:1096–104.
20. CarpentierA.F., LessanaA., RellandJ.Y., BelliE., MihaileanuS., BerrebiA.J., et al. The “physio-ring”: an advanced concept in mitral valve annuloplasty. *Ann Thorac Surg*. 1995;*60*:1177–85.
21. BruceC.J., ConnollyH.M.. Right-sided valve disease deserves a little more respect. *Circulation*. 2009;*119*:2726–34.
22. MatsumuraT., OhtakiE., TanakaK., MisuK., TobaruT., AsanoR., et al. Echocardiographic prediction of left ventricular dysfunction after mitral valve repair for mitral regurgitation as an indicator to decide the optimal timing of repair. *J Am Coll Cardiol*. 2003;*42*:458–63.
23. ZoghbiW.A., Enriquez-SaranoM., FosterE., GrayburnP.A., KraftC.D., LevineR.A., et al. Recommendations for evaluation of the severity of native valvular regurgitation with twodimensional and Doppler echocardiography. *J Am Soc Echocardiogr*. 2003;*16*:777–802.
24. NishimuraR.A., OttoC.M., BonowR.O., CarabelloB.A., ErwinJ.P., lll, Guyton RA, et al. AHA/ACC Guideline for the Management of Patients With Valvular Heart Disease: Executive Summary: A Report of the American College of Cardiology/American Heart Association Task Force on Practice Guidelines. *J Am Coll Cardiol*. 2014;*2014*(63):2438–88.
25. ZoghbiW.A., ChambersJ.B., DumesnilJ.G., FosterE., GottdienerJ.S., GrayburnP.A., et al. Recommendations for evaluation of prosthetic valves with echocardiography and doppler ultrasound: a report From the American Society of Echocardiography’s Guidelines and Standards Committee and the Task Force on Prosthetic Valves, developed in conjunction with the American College of Cardiology Cardiovascular Imaging Committee, Cardiac Imaging Committee of the American Heart Association, the European Association of Echocardiography, a registered branch of the European Society of Cardiology, the Japanese Society of Echocardiography and the Canadian Society of Echocardiography, endorsed by the American College of Cardiology Foundation, American Heart Association, European Association of Echocardiography, a registered branch of the European Society of Cardiology, the Japanese Society of Echocardiography, and Canadian Society of Echocardiography. *J Am Soc Echocardiogr*. 2009;*22*:975–1014.
26. PuM., GriffinB.P., VandervoortP.M., StewartW.J., FanX., CosgroveD.M., et al. The value of assessing pulmonary venous flow velocity for predicting severity of mitral regurgitation: A quantitative assessment integrating left ventricular function. *J Am Soc Echocardiogr*.

1999;*12*:736–43.
27. TanC.O., HarleyI.. Perioperative transesophageal echocardiographic assessment of the right heart and associated structures: a comprehensive update and technical report. *J Cardiothorac Vasc Anesth*. 2014;*28*:1100–23.
28. BallJ.D., WilliamsA.W., DaviesJ.N.. Endomyocardial fibrosis. *Lancet*. 1954;*266*:1049–54.
29. VahanianA., BaumgartnerH., BaxJ., ButchartE., DionR., FilippatosG., et al. Guidelines on the management of valvular heart disease: The Task Force on the Management of Valvular Heart Disease of the European Society of Cardiology. *Eur Heart J*. 2007;*28*:230–68.
30. KleinA.L., BurstowD.J., TajikA.J., ZachariahP.K., TaliercioC.P., TaylorC.L., et al. Age-related prevalence of valvular regurgitation in normal subjects: a comprehensive color flow examination of 118 volunteers. *J Am Soc Echocardiogr*. 1990;*3*:54–63.
31. KimJ.B., SpevackD.M., TunickP.A., BullingaJ.R., KronzonI., ChinitzL.A., et al. The effect of transvenous pacemaker and implantable cardioverter defibrillator lead placement on tricuspid valve function: an observational study. *J Am Soc Echocardiogr*. 2008;*21*:284–7.
32. RogersJ.H., BollingS.F.. The tricuspid valve: current perspective and evolving management of tricuspid regurgitation. *Circulation*. 2009;*119*:2718–25.
33. TribouilloyC., RusinaruD., SzymanskiC., MezghaniS., FournierA., LevyF., et al. Predicting left ventricular dysfunction after valve repair for mitral regurgitation due to leaflet prolapse: additive value of left ventricular end-systolic dimension to ejection fraction. *Eur J Echocardiogr*. 2011;*12*:702–10.
34. FernandesV., KaluzaG.L., ZymekP.T., DeFeliceC.A., HustR., RaiznerA.E.. Successful balloon valvuloplasty in an adult patient with severe pulmonic stenosis and aneurysmal poststenotic dilatation. *Catheter Cardiovasc Interv*. 2002;*55*:376–80.
35. ShinnS.H., SchaffH.V.. Evidence-based surgical management of acquired tricuspid valve disease. *Nat Rev Cardiol*. 2013;*10*:190–203.
36. DreyfusG.D., CorbiP.J., ChanK.M., BahramiT.. Secondary tricuspid regurgitation or dilatation: which should be the criteria for surgical repair?*Ann Thorac Surg*. 2005;*79*:127–32.
37. Ton-NuT.T., LevineR.A., HandschumacherM.D., DorerD.J., YosefyC., FanD., et al. Geometric determinants of functional tricuspid regurgitation: insights from 3-dimensional echocardiography. *Circulation*. 2006;*114*:143–9.
38. LiW., DavlourosP.A., KilnerP.J., PennellD.J., GibsonD., HeneinM.Y., et al. Doppler-echocardiographic assessment of pulmonary regurgitation in adults with repaired tetralogy of Fallot: comparison with cardiovascular magnetic resonance imaging. *Am Heart J*. 2004;*147*:165–72.
39. KarchmerA.W., LongworthD.L.. Infections of intracardiac devices. *Infect Dis Clin North Am*. 2002;*16*:477–505, xii.
40. PibarotP., DumesnilJ.G.. Prosthetic heart valves: selection of the optimal prosthesis and long-term management. *Circulation*. 2009;*119*:1034–48.

Chapter 8

Intra-Cavitary Contents

Yiorgos Alexandros Cavayas and Yoan Lamarche

INTRODUCTION

A wide variety of entities may appear inside the cardiac chambers, ranging from normal structures to life-threatening conditions. Intra-cardiac masses can present clinically as asymptomatic incidental findings or patients may experience severe symptoms, such as heart failure or systemic embolization. Both transthoracic (TTE) and transesophageal echocardiography (TEE) are essential tools in the evaluation of intra-cardiac masses as they allow simultaneous characterization of the mass location, attachment, morphology, size, and mobility, along with the hemodynamic impact. These features reveal important clues to help identify the etiology of the mass, which can have significant implications on the acute management of patients. Non-neoplastic masses, such as thrombi and vegetations, must be differentiated from normal anatomic variants. This chapter will review the principal causes of Intra-cavitary content with a focus on the key echocardiographic and contextual features that allow etiologic differentiation.

NORMAL ANATOMIC VARIANTS

Left Atrium

Pectinate muscles in the left atrial appendage (LAA) (Figure 8.1) represent muscle fibers running along the atrial wall in parallel ridges resembling the teeth of a comb, which can be mistaken for a thrombus. Moreover, an inverted LAA after cardiac surgery can be confused with an atrial mass. A

dilated coronary sinus can mimic a cystic mass in the TTE parasternal long-axis (LAX) view. Persistent left superior vena cava (SVC) is the most common cause of coronary sinus dilation and can be demonstrated by the administration of agitated saline through the left arm (Figure 8.2). Interatrial septal aneurysm may also appear as a cystic mass bulging into either atrial cavity (Figure 8.3). Atrial cords originating at the interatrial septum and inserting into the atrial surface of the mitral leaflets have also been described.

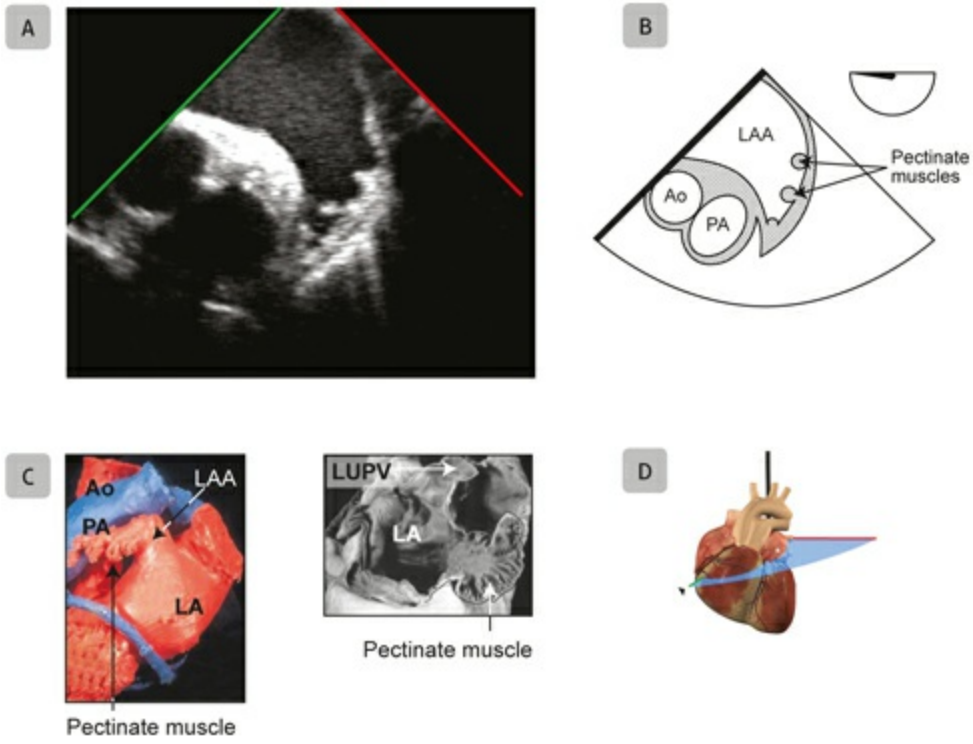

Fig. 8.1 Pectinate muscles. (A, B) Pectinate muscles in the left atrial appendage (LAA) are seen in this mid-esophageal view compared with an (C) anatomic luminal cast and (D) view of a LAA. Ao, aorta; LA, left atrium; LUPV, left upper pulmonary vein; PA, pulmonary artery. (Reproduced with permission from Denault *et al.* [1]).

Right Atrium

Pectinate muscle can also be present in the right atrial appendage (RAA) (Figure 8.4). Multiple embryologic remnants can be seen in the right atrium (RA). The crista terminalis is a dense vertical muscle ridge running just lateral to the caval orifices. The Eustachian valve is a crescentic fold of endocardium of variable length and thickness arising from the anterior rim of the inferior vena cava (IVC) orifice (Figure 8.5a). In the embryologic circulation, it directs the oxygenated blood from the IVC through the foramen

ovalis and away from the right ventricle (RV). Another remnant is the Chiari network, a web-like structure composed of fibers of variable caliber attached to the floor of the RA between the crista terminalis and the Eustachian valve (Figure 8.5). A characteristic whip-like motion helps to differentiate it from thrombi. Again, pectinate muscles may also be seen in the RA appendage and can extend to the RA free wall. Finally, lipomatous hypetrophy of the interatrial septum may mimic a mass (Figure 8.6). However, the thickness is usually easily distinguished because it spares the fossa ovalis, resulting in a characteristic dumbbell appearance. When doubt persists, magnetic resonance imaging (MRI) may help determine the fatty nature of the mass.

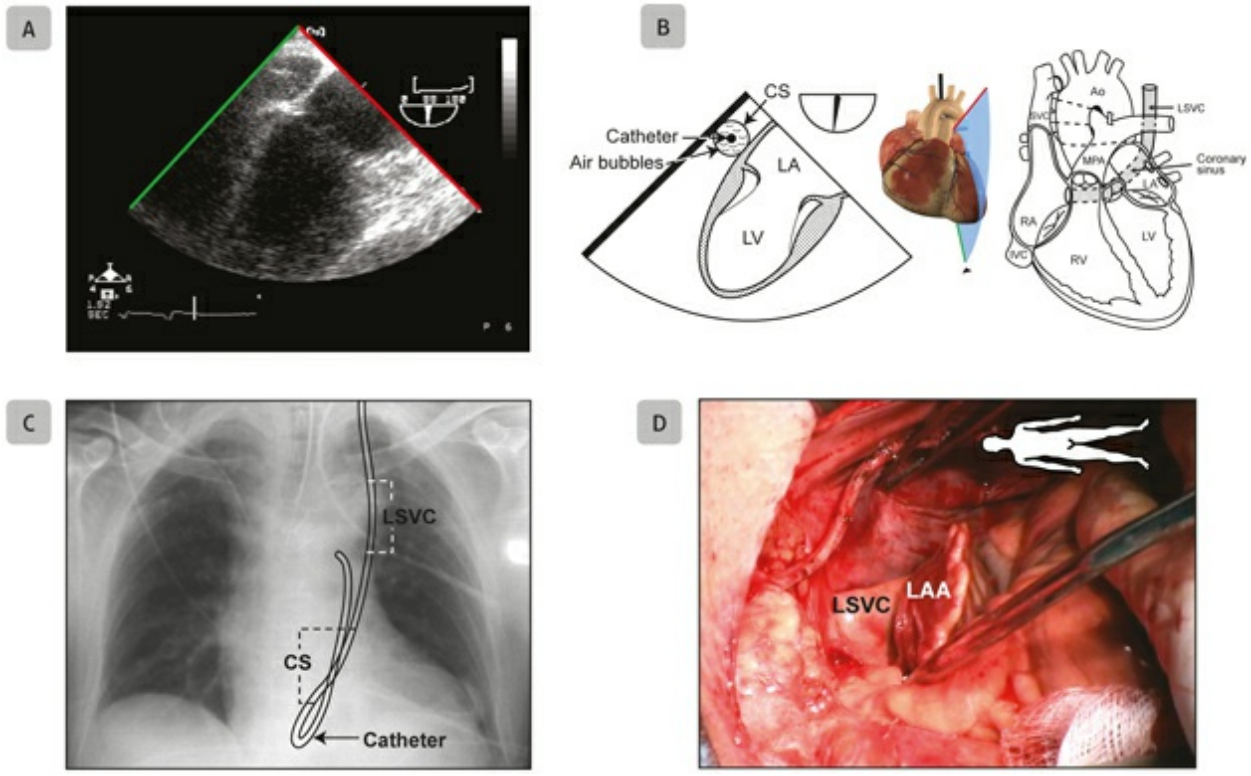

Fig. 8.2 Persistent left-sided superior vena cava (LSVC). (A, B) Mid-esophageal two-chamber view shows a dilated coronary sinus (CS) in which a pulmonary artery catheter (PAC) and bubbles are visible. (C) Postoperative chest X-ray demonstrates the PAC inadvertently coursing through the LSVC and the CS, then normally into the right atrium (RA), right ventricle (RV), and pulmonary artery. (D) Intraoperative view demonstrates the LSVC adjacent to the left atrial appendage (LAA). Ao, aorta; IVC, inferior vena cava; LA, left atrium; LV, left ventricle; MPA, main pulmonary artery; PA, pulmonary artery; SVC, superior vena cava. (Reproduced with permission from Denault *etal.* [1]) **(video symbol missing globally)**

A: https://youtu.be/kLfxKxw3ejE

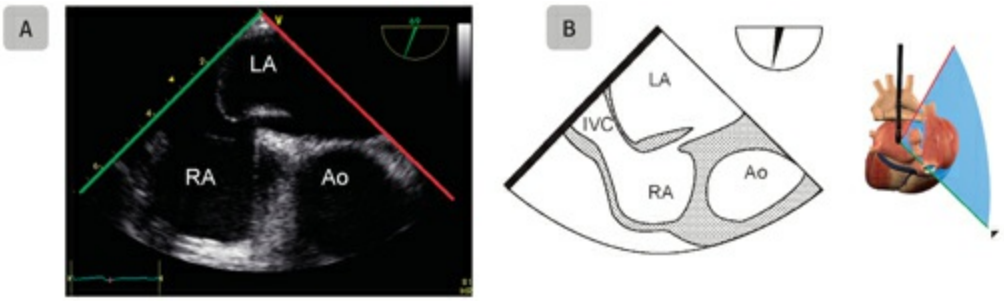

Fig. 8.3 Atrial vena cava; septal aneurysm. Modified midesophageal view (69°) shows an inter-atrial septal aneurysm which can be associated with interatrial septal defects. Ao, aorta; IVC, inferior LA, left atrium; RA, right atrium.

A: https://youtu.be/FcVi_DvSKC4

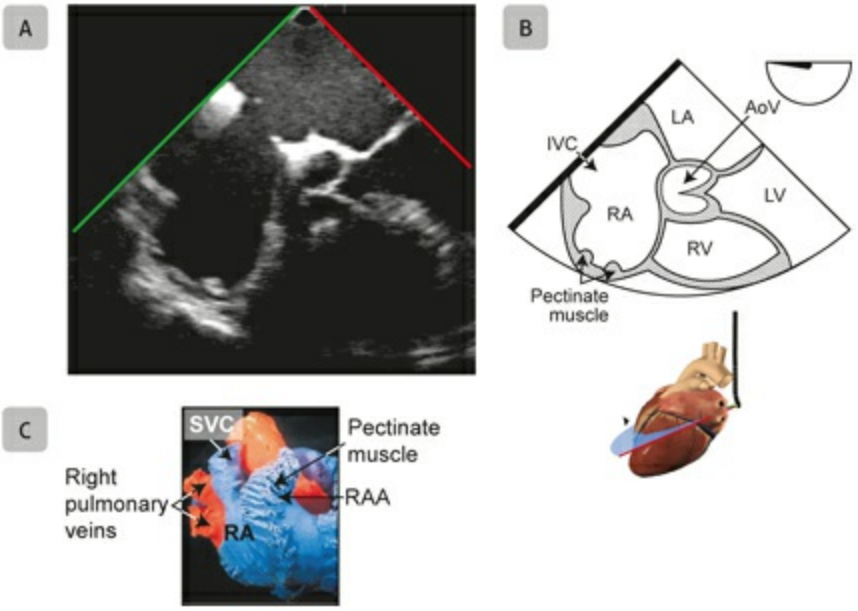

Fig. 8.4 Pectinate muscles. (A, B) Pectinate muscles in the right atrium (RA) are seen in this mid-esophageal five-chamber view compared with (C) anatomic luminal cast, and view of a right atrial appendage (RAA). AoV, aortic valve; IVC, inferior vena cava; LA, left atrium; LV, left ventricle; RA,

right atrium; RV, right ventricle; SVC, superior vena cava. (Reproduced with permission from Denault *et al.* [1]).

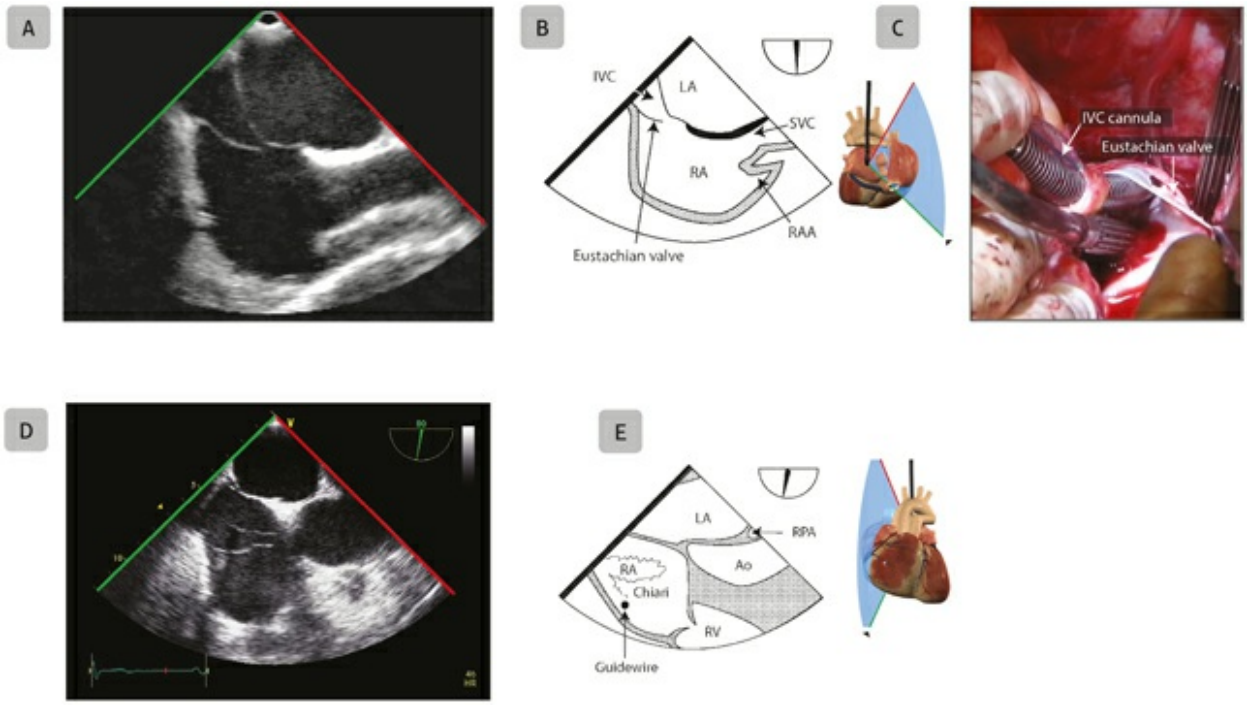

Fig. 8.5 Eustachian valve and Chiari network. (A, B) Mid-esophageal bicaval view shows a prominent Eustachian valve. This embryologic remnant is inserted on the anterior aspect of the orifice of the inferior vena cava (IVC) and is used in fetal life to direct flow from the IVC towards the foramen ovale. (C, D) Mid-esophageal view at 80° shows a Chiari network undulating in the right atrium (RA). Ao, aorta; LA, left atrium; RAA, right atrial appendage; RPA, right pulmonary artery; RV, right ventricle; SVC, superior vena cava. (Reproduced with permission from Denault *et al.* [1]).

A: https://youtu.be/f_amPsWo-kc

C: https://youtu.be/dsetGBks6JY

D: https://youtu.be/yTYtgtxiI04

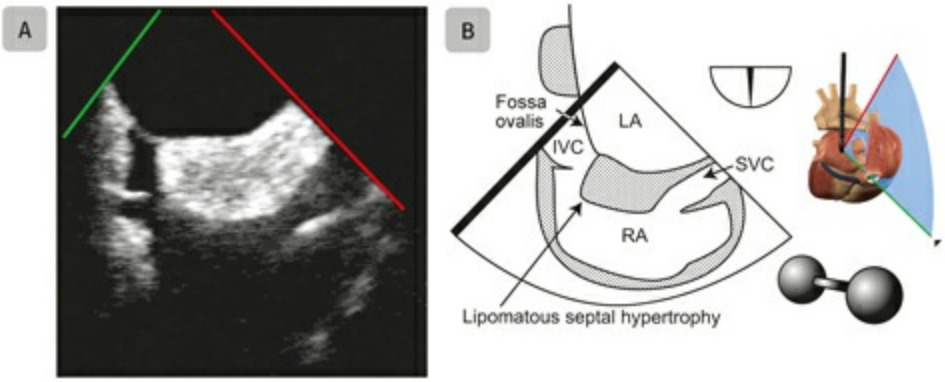

Fig. 8.6 Lipomatous hypertrophy. (A, B) Mid-esophageal bicaval view shows lipomatous hypertrophy of the interatrial septum (IAS) in a 74-year-old female. The IAS reaches 25 mm in thickness. The sparing of the fossa ovalis results in a typical dumbbell appearance of the IAS. IVC, inferior vena cava; LA, left atrium; RA, right atrium; SVC, superior vena cava. (Reproduced with permission from Denault *et al.* [1]).

A: https://youtu.be/c0nRYX9BlBc

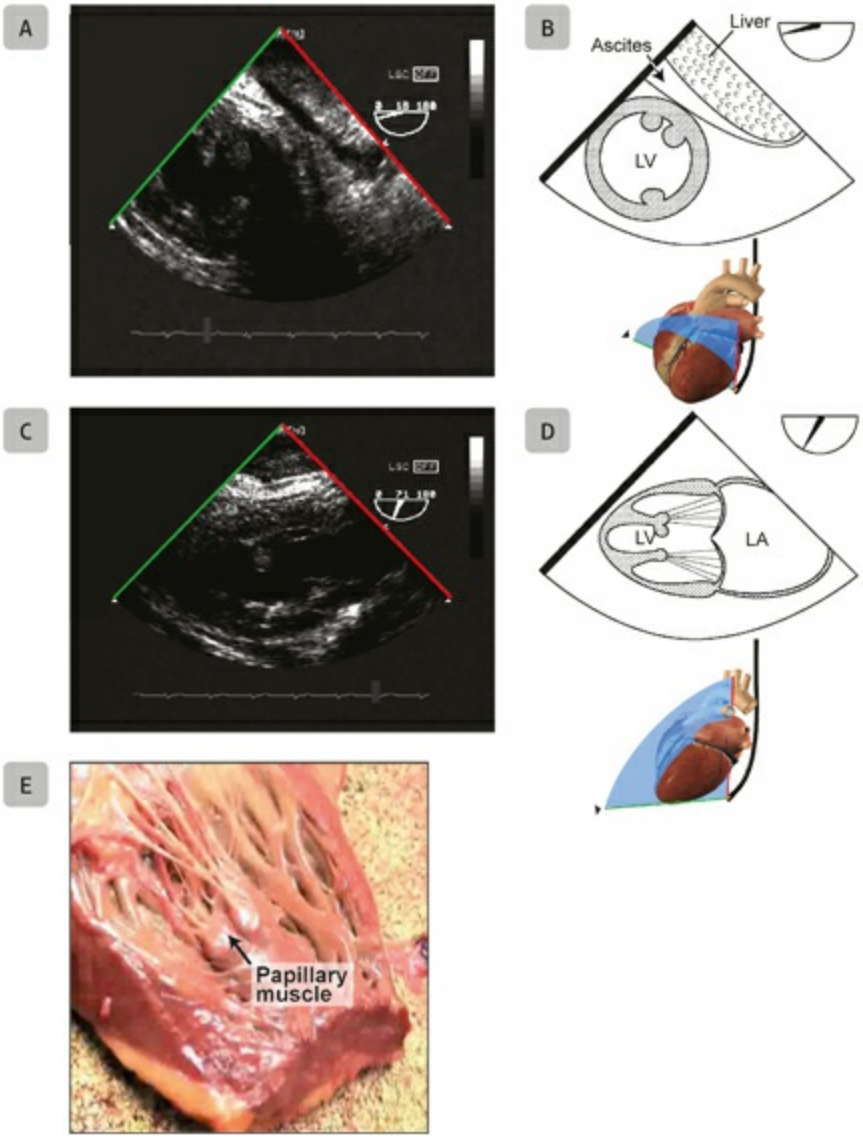

Fig. 8.7 Papillary muscle as a pseudo-mass. A 36-year-old male presents with end-stage Crohn's disease complicated by respiratory insufficiency, renal failure, and sepsis. (A, B) The transgastric mid short-axis and (C, D) 71° views show a mobile mass in the left ventricle (LV) close to the posterior-medial papillary muscle. (E) The patient died from multi-organ failure and an autopsy confirmed a double-headed papillary muscle. LA, left atrium. (Reproduced with permission from Denault *et al.* [1]).

A&C: https://youtu.be/krzykyR-UAI

E: https://youtu.be/rFyiLtfMco0

Left Ventricle

In the left ventricle (LV), prominent calcified papillary muscles can be confused with a mass (Figure 8.7), especially when ruptured or cut after mitral valve replacement. Webs, false tendons (Figure 8.8), aberrant chordae, and prominent trabeculations can also mimic apical pathologies. Administration of contrast could help establish if the echodensity seen is a thrombus.

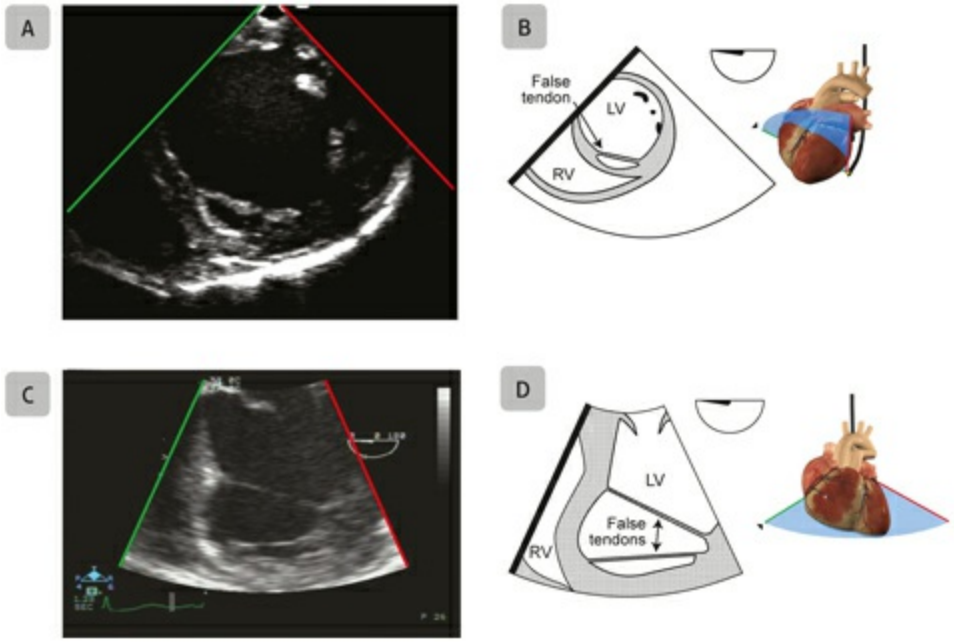

Fig. 8.8 False tendon. (A, B) Transgastric mid short-axis view of the left ventricle (LV) demonstrates a false tendon extending from the ventricular septum to the anterior wall. (C, D) Mid-esophageal four-chamber view shows two false tendons at the LV apex. RV, right ventricle. (Reproduced with permission from Denault *et al.* [1]).

C: https://youtu.be/nX6NzAT2pO0

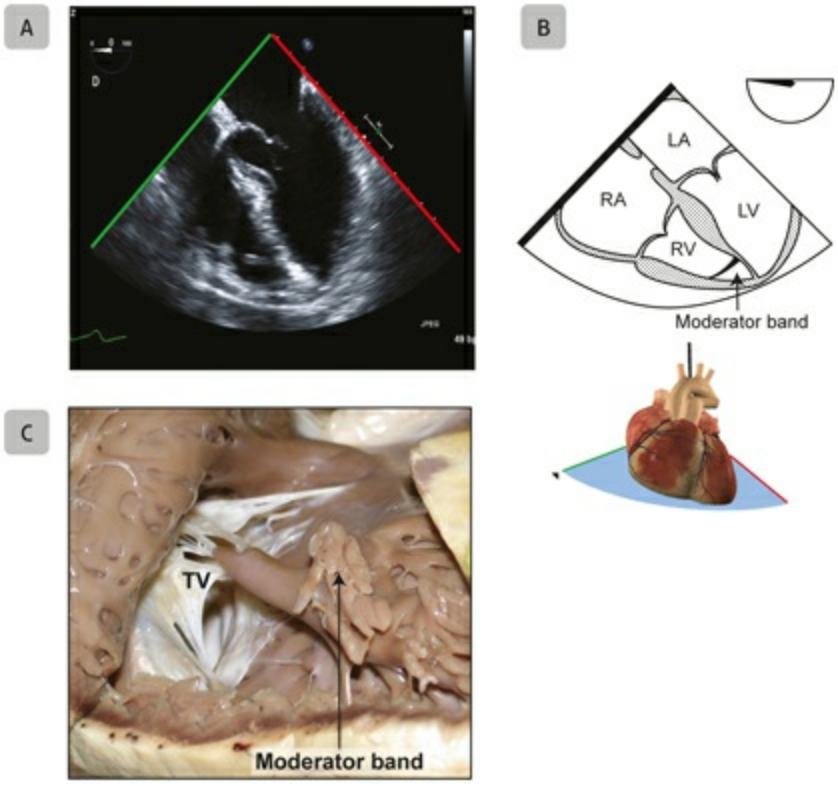

Fig. 8.9 Moderator band. (A, B) Dilatation of the right ventricle (RV) facilitates visualization of the moderator band and the densely trabeculated RV apex in this mid-esophageal four-chamber view. (C) Anatomic specimen shows the moderator band. LA, left atrium; LV, left ventricle; RA, right atrium; TV, tricuspid valve. Source: Photo C courtesy of Dr Nicolas Durrleman. (Reproduced with permission from Denault *et al.* [1]).

A: https://youtu.be/dcdBMCV33-8

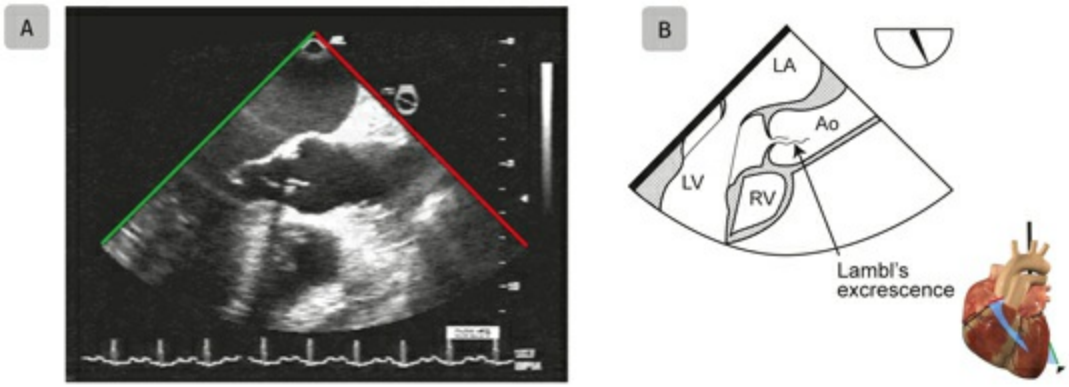

Fig. 8.10 Lambl's excrescence. (A, B) Mid-esophageal long-axis view shows Lambl's excrescence on the aortic valve. Ao, aorta; LA, left atrium; LV, left ventricle; RV, right ventricle. (Reproduced with permission from Denault *et al.* [1]).

A: https://youtu.be/eJpiRHw6fdk

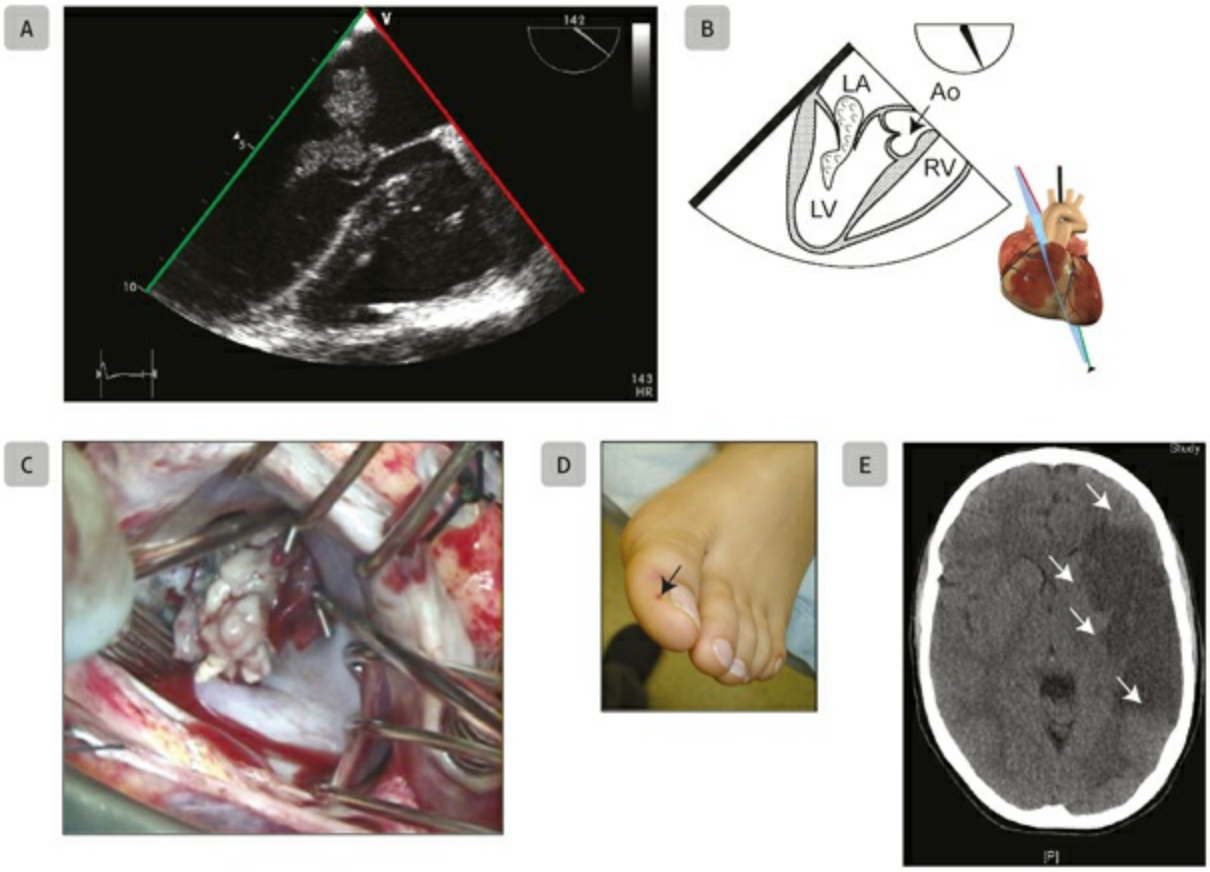

Fig. 8.11 Endocarditis. (A, B) Mid-esophageal long-axis view in a 30-year-old female with acute bacterial endocarditis of the mitral valve shows a large complex vegetation with (C) corresponding intraoperative findings. Additional findings included (D) peripheral embolic lesions on the big toe and (E) large hemispheric temporal stroke on brain computed tomography. Ao, aorta; LA, left atrium; LV, left ventricle; RV, right ventricle. (Reproduced with permission from Denault *et al.* [1]).

A: https://youtu.be/Ttb5wiE16cQ

C: https://youtu.be/-AxH9dv_lms

C: https://youtu.be/iBnN8_4hASg

Right Ventricle

The most common normal Intra-cavitary findings in the RV are moderator bands (Figure 8.9), trabeculations, and papillary muscles. Indwelling catheter and pacemaker leads should be inspected closely as they can create reverbation artifacts, but can also harbor thrombi.

Valves

Nodules of Arantius (see Figure 7.1) and Lambl's excrescences (Figure 8.10) can sometimes arise from the aortic valve of older individuals and thus mimic vegetations. Redundant mitral chordae and leaflet tissue may be difficult to distinguish from vegetations solely based on the echocardiographic features; however, in some cases the aspect is obvious (Figure 8.11). Clinical information is of prime importance when such questions arise.

THROMBUS

Echocardiography is indicated to assess the presence of an Intra-cavitary thrombus, especially in the setting of stroke, systemic embolization or before cardioversion. The ACC/ AHA guidelines recommend echocardiography as a class I indication for patients requiring cardioversion for atrial fibrillation or flutter for whom extended precardioversion anticoagulation is undesirable. Echocardiography is appropriately indicated and a class IIa recommendation with known underlying heart disease [1] , [2] and class IIb recommendation without heart disease in all patients presenting with atrial fibrillation of less

than 48 hours duration. Echocardiography is also indicated in all patients presenting atrial fibrillation of less than 48 hours duration with or without known underlying heart disease. [2] – [4] In the setting of stroke, echocardiography is recommended in patients without evidence of cerebrovascular disease or other obvious cause, and in all patients less than 45 years old. [5] Transesophageal echocardiography (TEE) is the method of choice to exclude atrial thrombus. Thrombus can result from a primary cardiac, hematologic, or immunologic pathology. Multiple factors can predispose to thrombus formation. Thrombi usually develop in an area of blood stasis, most often in the left atrial appendage (LAA) (Figure 8.12) or in the setting of LV apical akinesia or aneurysm (Figure 8.13). Stasis of blood can be suspected in the presence of spontaneous echo-contrast, which typically appears as dynamic smoke-like echoes with a characteristic swirling pattern (Figure 8.14). Foreign objects, such as indwelling catheters and systemic hyper-coagulable states, can also predispose to the formation of thrombi. Finally, some thrombi may have extra-cardiac origin, but can be seen in transit in the heart chambers.

Left Atrial Body and Appendage

Factors that predispose to the formation of a LA thrombus include LA enlargement, atrial fibrillation, mitral stenosis, prosthetic mitral valve, or the performance of a maze procedure (Figure 8.12). On the other hand, mitral regurgitation seems to exert a protective effect. A thrombus can form in the LA body, where it usually appears as a well-circumscribed acoustic density that has asynchronous motion with the underlying myocardium. However, the most likely site of thrombus formation is the LAA where it appears as an ill-defined sludge-like echogenic mass with a broad-based attachment. When thrombus is suspected (see Figure 7.18), blood flow in LAA is measured, with low flow (<20 cm/s) significantly increasing the embolic risk (see Figure 7.21). Again, contrast-enhanced harmonic imaging can be a useful adjunct if doubt persists (see Figure 15.7). The differential diagnosis includes artifacts, myxomas (usually attached to the fossa ovalis), fibroelastomas, or other tumors. Transesophageal echocardiography has a high sensitivity (95–100%), specificity, and negative predictive value for LA thrombus. [6]

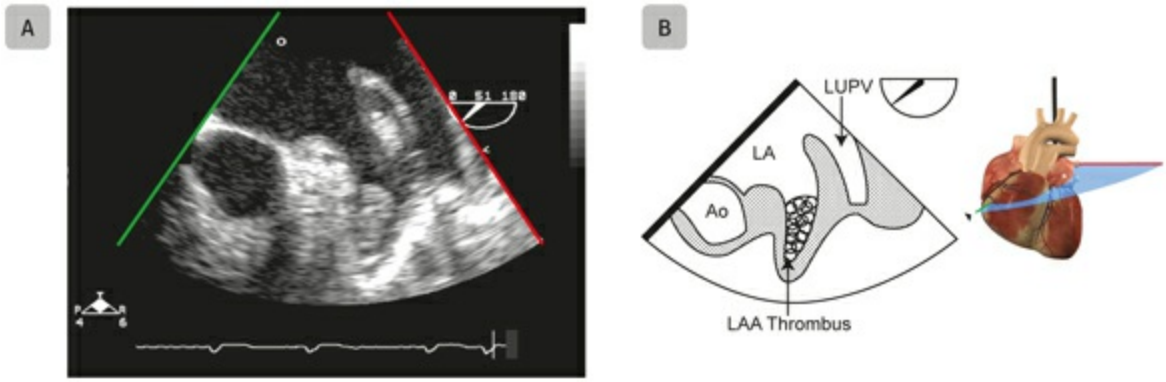

Fig. 8.12 Left atrial appendage (LAA) thrombus. (A, B) Mid-esophageal LAA view at 51° of a patient in atrial fibrillation with dilated cardiomyopathy shows a thrombus in the LAA. Ao, aorta; LA, left atrium; LUPV, left upper pulmonary vein. (Reproduced with permission from Denault *et al.* [1]).

Right Atrium

When seen in the RA, thrombi are often in transit (see Figure 9.15) appearing as “casts” of large deep veins. They may be seen entangled in the tricuspid valve apparatus, giving a classic “popcorn” appearance. Their migrating nature can be demonstrated by the documentation of additional thrombi in the IVC, RV, main pulmonary trunk, or crossing a patent foramen ovale (Figure 8.15). *In situ* thrombus formation can also occur, most often in the setting of significant stasis, enlarged RA, atrial arrhythmias, or cardiomyopathies (Figure 8.16). Foreign material, such as indwelling catheters or pacemaker leads, can also serve as a nidus for the formation of thrombus. The differential diagnosis of RA thrombus includes the Chiari network, the Eustachian valve, tumors, or vegetations.

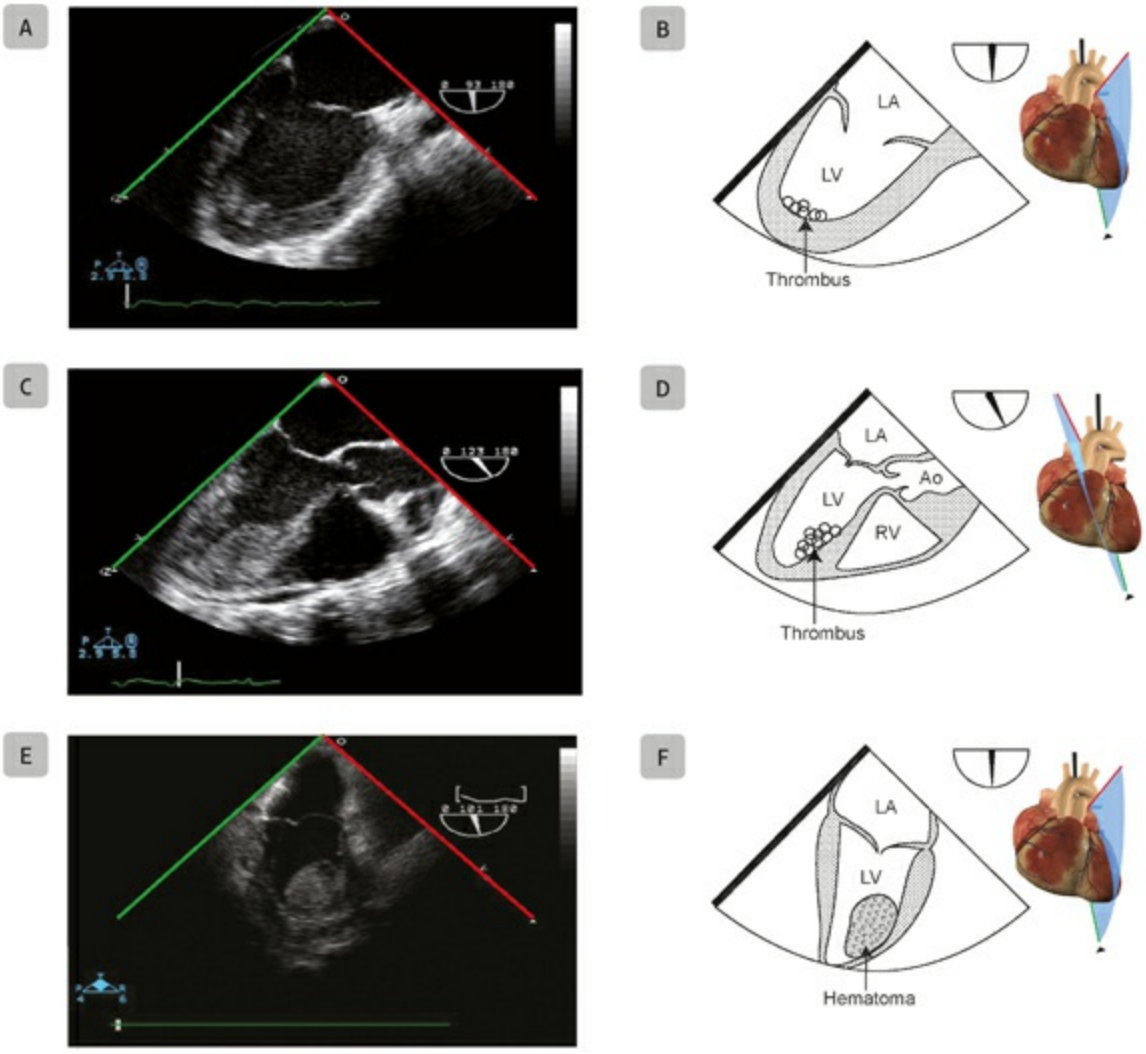

Fig. 8.13 Left ventricle (LV) thrombus and hematoma. (A, B) Mid-esophageal (ME) two-chamber view shows a thickened LV apex suggestive of thrombus in a patient after a large anteroseptal myocardial infarction. (C, D) ME long-axis view shows a concomitant thrombus of the anteroseptal wall. (E, F) ME two-chamber view in a different patient after cardiopulmonary bypass for aortic valve replacement shows a new apical mass/ wall hematoma from the decompression cannula positioned through the mitral valve toward the LV apex. Ao, aorta; LA, left atrium; RV, right ventricle. (Reproduced with permission from Denault *et al.* [1]).

E: https://youtu.be/TQYXfEbvbxY

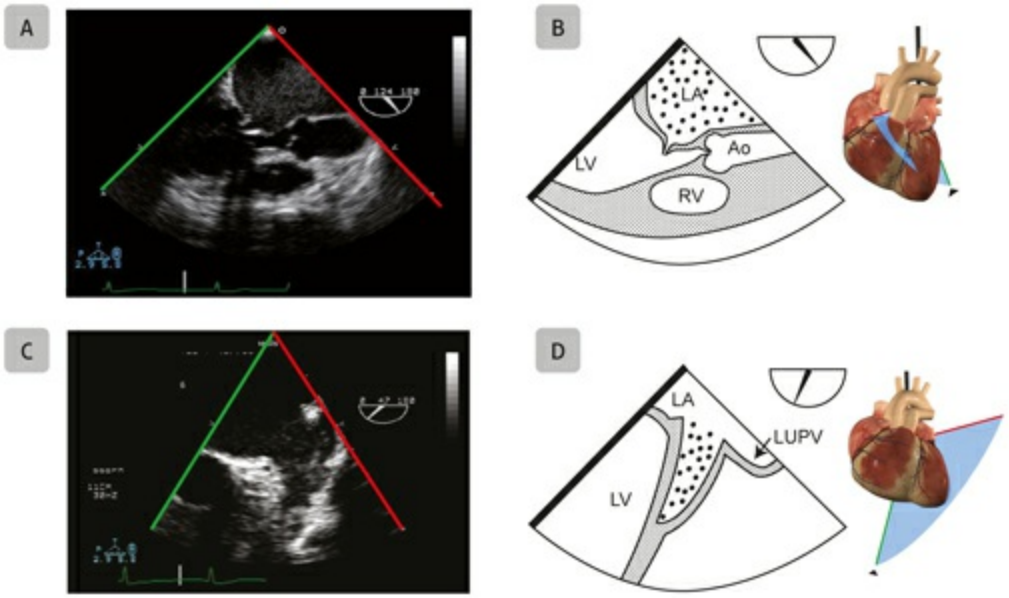

Fig. 8.14 Spontaneous echo contrast. (A, B) Mid-esophageal aortic valve long-axis view shows significant spontaneous echo contrast (SEC) in a dilated left atrium (LA) in a patient with mitral stenosis and junctional rhythm. (C, D) The SEC is also present in the left atrial appendage at 60°. Ao, aorta; LUPV, left upper pulmonary vein; LV, left ventricle; RV, right ventricle. (Reproduced with permission from Denault *et al.* [1]).

A: https://youtu.be/6GKcqFNV9FY

C: https://youtu.be/WP97-F10V84

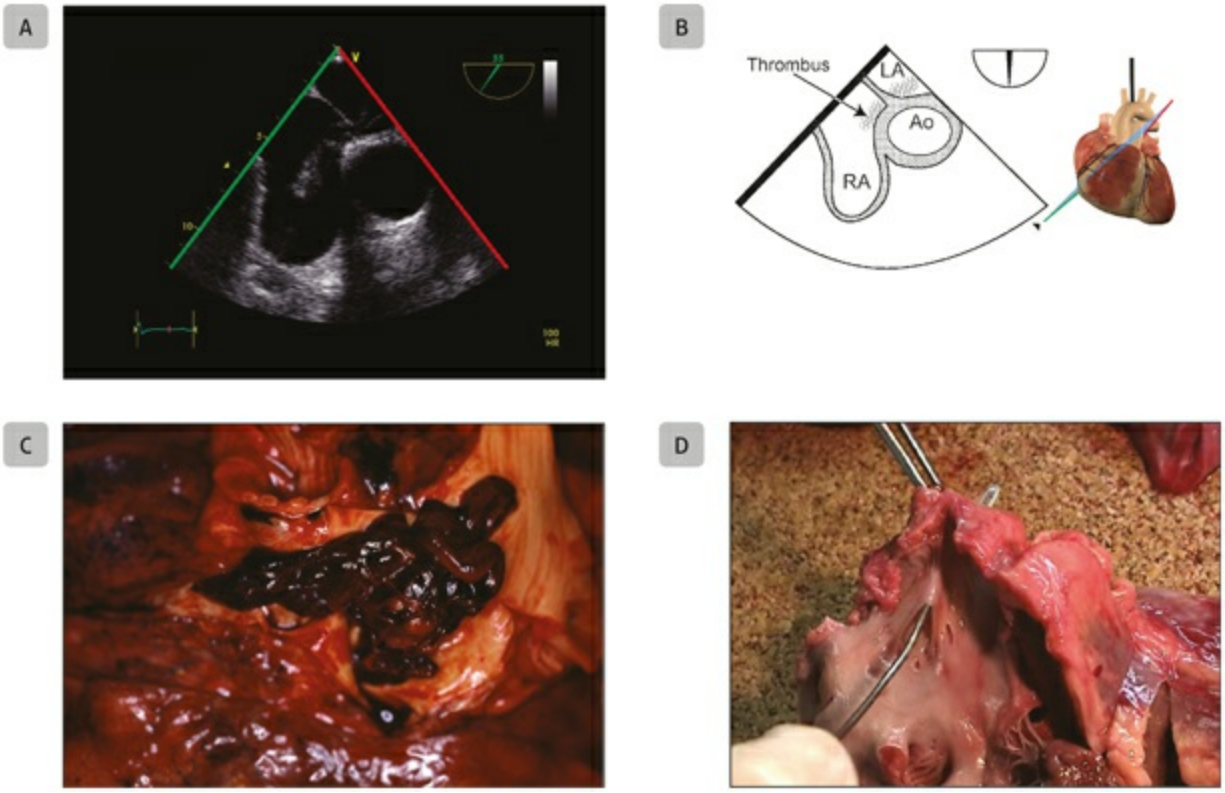

Fig. 8.15 Paradoxical embolism. (A, B) Modified mid-esophageal aorta (Ao) short-axis view at 55° shows a thrombus crossing a patent foramen ovale (PFO). (C) Corresponding intraoperative findings of other thrombi in the pulmonary arteries is shown. (D) Autopsy finding of a PFO from another patient who died of refractory hypoxia. LA, left atrium; RA, right atrium. (Reproduced with permission from Denault *et al.* [1]).

A: https://youtu.be/T828DxgA2Ug

D: https://youtu.be/MRcb5T4EyDA

Left Ventricle

Left ventricle thrombus typically appears as an amorphous echogenic mass of variable shape and size apposed to endocardium (Figure 8.17). Thrombus

formation usually necessitates some degree of stasis and wall motion abnormality as occurs with severe LV systolic dysfunction, dilated cardiomyopathy, myocardial infarction, or LV aneurysm (see Figure 6.14). It is classically located at an akinetic or dyskinetic LV apex. Features that increase the risk of embolization include: large, mobile, protruding thrombus, a hypoechoic center suggesting a fresh thrombus, and a hyperkinetic segment adjacent to the thrombus. Masses seen in the setting of normal wall motion should point towards another etiology. The differential diagnosis includes artifacts, tumors, prominent papillary muscles, trabeculations, or false tendons. Apical filling caused by hypereosinophilic syndrome, apical hypertrophic cardiomyopathy, primary lymphoma, or metastatic malignancy can sometimes be difficult to differentiate from a thrombus. The use of contrast can sometimes be helpful to further delineate the borders of the endocardium and the potential mass (see Figure 15.7). Transthoracic echocardiography is the modality of choice to diagnose LV thrombus with a sensitivity of up to 95%. Nervertheless, an improper ultrasonographic plane can cut the muscle tangentially at the apex, mimicking an apical thrombus.

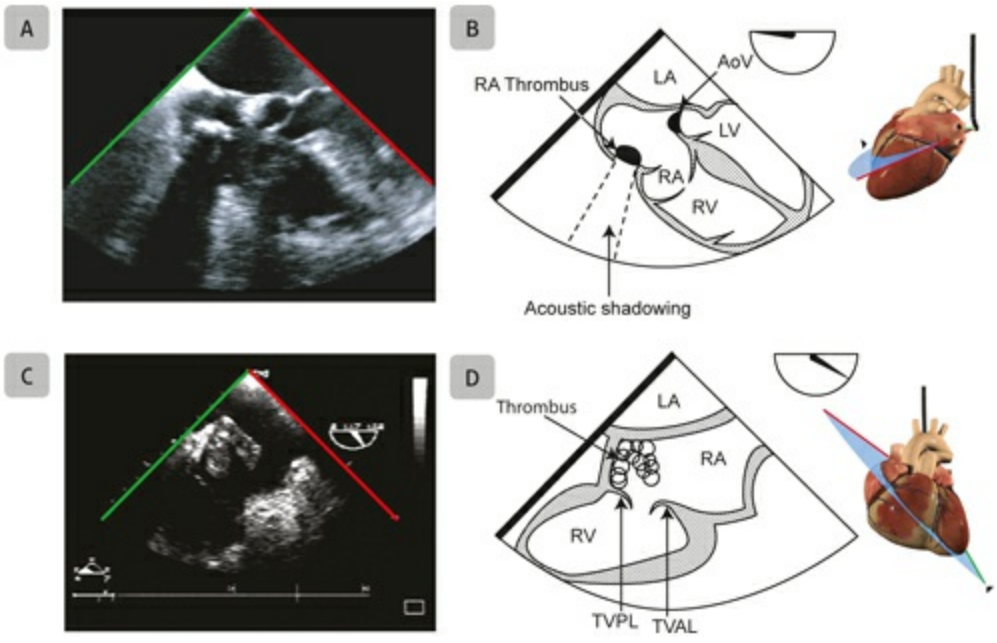

Fig. 8.16 Right atrium (RA) thrombus. (A, B) Midesophageal (ME) five- chamber view displays a calcified thrombus in the RA with secondary acoustic shadowing that extends from the thrombus surface to the far field. (C, D) ME right ventricular view at 117° shows a “popcornlike” thrombus in transit in the RA in a different patient. AoV, aortic valve; LA, left atrium; LV, left ventricle; RV, right ventricle; TVAL, tricuspid valve anterior leaflet; TVPL, tricuspid valve posterior leaflet. (Reproduced with permission from Denault *et al.* [1]).

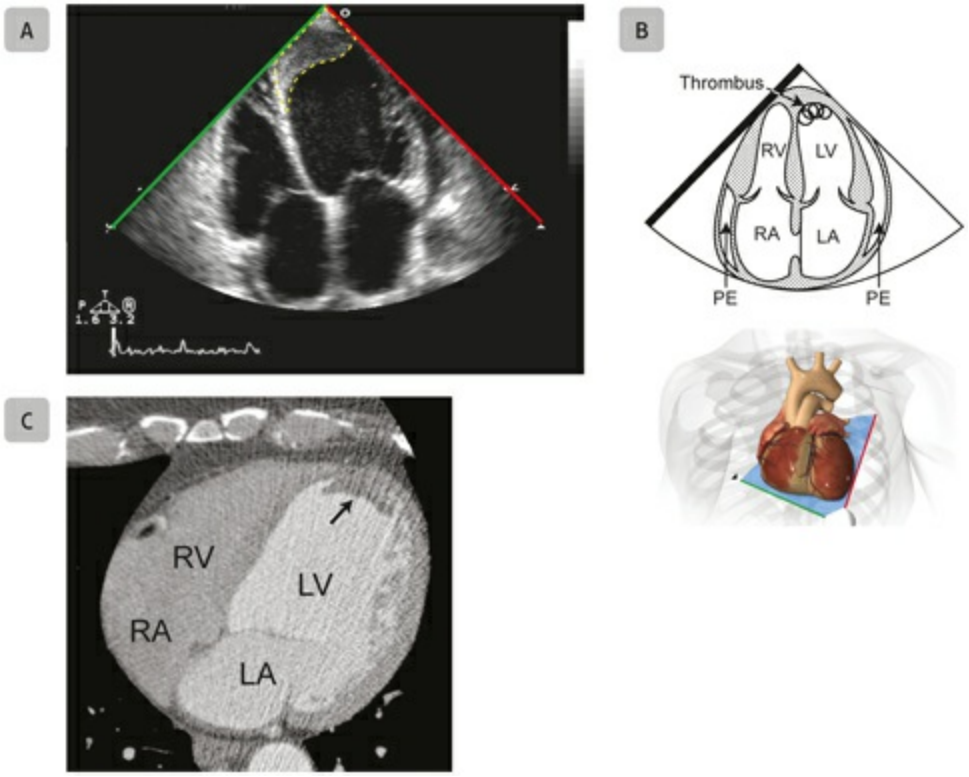

Fig. 8.17 Apical thrombus. (A, B) Transthoracic apical four-chamber view in a patient with dilated cardiomyopathy shows a laminated apical thrombus in the left ventricle (LV). (C) Axial 16-DCT image in a 63-year-old male showing LV dilatation with apical thinning and a small curvilinear non- calcified thrombus at the LV apex. LA, left atrium; PE, pericardial effusion; RA, right atrium; RV, right ventricle. (Reproduced with permission from Denault *et al.* [1]).

Right Ventricle and Biventricular

Right ventricular thrombi are rare and usually associated with conditions with decreased blood flow, such as RV infarction or failure, cor pulmonale, severe cardiomyopathies, or hypercoagulable states (Figure 8.18). Thrombi can sometimes conceal an underlying endomyocardial fibroelastoma. Biventricular thrombi are extremely rare, but can be seen in the setting of dilated cardiomyopathies, severe systolic dysfunction or a hypercoagulable state (Figure 8.18).

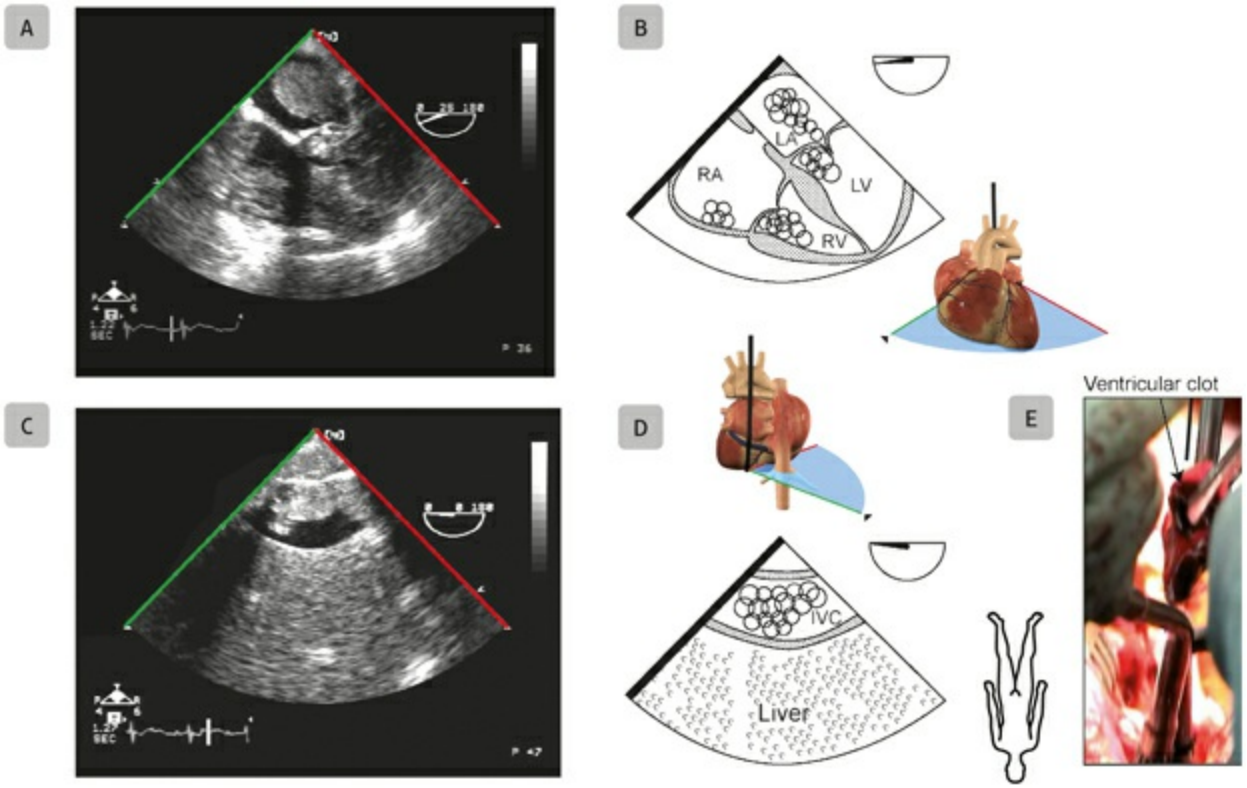

Fig. 8.18 Intra-cardiac thrombus. A 73-year-old male is re-operated on for an aortic pseudo aneurysm and develops an acute hypercoagulable state after cardiac surgery. (A, B) Mid-esophageal four-chamber view shows clots in all of the cardiac chambers and (C, D) the inferior vena cava (IVC) in this transgastric view. (E) Intraoperative findings during re-exploration as the clots are removed. LA, left atrium; LV, left ventricle; RA, right atrium; RV, right ventricle. (Reproduced with permission from Denault *et al.* [1]).

A: https://youtu.be/Bvx5uYJfwFk

E: https://youtu.be/yCJl8vUYR8w

PULMONARY EMBOLUS

Echocardiography cannot exclude pulmonary embolism (PE) as findings may

be normal in up to 50% of cases. [7] , [8] However, it can reveal direct and indirect signs that provide important information regarding the hemodynamic impact of large emboli, which are key components of the treatment algorithm in submassive and massive PEs. Transesophageal echocardiography has a higher sensitivity (80–97%) and specificity (up to 97%), especially for massive PE [7] , [9] when detecting an embolus (see Figure 9.15). Transesophageal echocardiography provides better visualization of the main and right pulmonary arteries, but poor visualization of the left pulmonary artery (PA) and distal vasculature because of the left pulmonary bronchus shadow. Transesophageal echocardiography should be considered for the unstable intubated patient as it can simultaneously diagnose hemodynamically significant PE and exclude other causes of hemodynamic instability, without the need to mobilize the patient. However, most authors agree that a normal TEE is insufficient to exclude the diagnosis of PE. Chest contrast enhanced computed tomography remains the examination of choice (see Figure 10.14).

As previously alluded to, characteristic worm-like thrombi can be directly visualized in the IVC, RA, RV, right ventricular outflow tract (RVOT), or PA in about 4% of individuals with PE (Figure 8.19). The abrupt increase in pulmonary resistance causes RV pressure overload. This manifests as RV dilatation and hypokinesis along with flattening, leftward displacement, or paradoxical motion of the interventricular septum. The McConnell sign consists of moderate to severe free wall hypokinesis with normal or hyperdynamic wall motion of the RV apex. It has a specificity 94% [10] for PE. Right ventricle overload can also be accompanied by increased filling pressures resulting in dilation of the RA (see Figure 15.12) with interatrial septum bowing to the left, as well as IVC dilatation with diminished respiratory variation. Increased pulmonary artery systolic pressure (PASP) can be documented by measuring an increased peak tricuspid regurgitation velocity (>2.7 m/s) (see Figure 15.12). However, this is not a consistent finding as the RV may not be able to generate increased systolic pressures when facing an acute increase in afterload.

VEGETATIONS

Vegetations are discrete mobile masses attached to normal heart structures or

foreign material. They are most often caused by infective endocarditis, which can be bacterial or fungal. The differential diagnosis also includes Libman-Sachs endocarditis in the setting of systemic lupus erythematosus, marantic endocarditis, granulomatous diseases, and systemic sclerosis. All patients with suspected endocarditis should undergo formal echocardiographic assessment. The diagnosis of infective endocarditis is based on the modified Duke criteria. [11]

Typical acute bacterial endocarditic vegetations appear as circumscribed pedunculated soft tissue density echo with an irregular shape arising from a valvular leaflet tip (Figure 8.11). These masses are usually mobile with a swinging motion independent of underlying cardiac structure. The morphologic features of vegetations vary depending on the etiology of endocarditis, the underlying characteristics of the valve itself, and the disease activity. Vegetations can present as discrete sessile masses closely adherent to the valves, pedunculated, friable clumps that prolapse freely, or elongated fibrous thickened strands (Figure 8.11). Vegetations usually lie on the low pressure side of a regurgitant jet. For example, a mitral regurgitation jet would predispose to the formation of vegetations predominantly on the LA side of the mitral valve leaflets. Vegetations also form more easily on structurally abnormal valves. Transesophageal echocardiography is the modality of choice for the diagnosis of endocarditis, when combined with clinical and microbiological clues. Indeed, the sensitivity of TEE for the detection of vegetations is close to 100% on native valve and 86-94% on prosthetic valve, with a specificity of 88-100%. [12] However, a single TEE study is insufficient to exclude infective endocarditis and should be repeated within 7–10 days if the clinical findings strongly suggest the diagnosis of endocarditis. False-negative examination can be a result of embolization of infected material, inadequate visualization from acoustic shadowing or very small vegetation size. When both TTE and TEE are performed, the negative predictive value is 95%. [12]

Native Valves

The mitral valve (MV) is the most common site of vegetations, which usually lie on the atrial side of one or both leaflets. Involvement of the chordae tendinae of the anterior mitral leaflet is generally secondary to seeding from aortic valve (AoV) endocarditis. The clinical setting will help differentiate vegetations from other causes of MV anomalies, such as myxomatous

degeneration, fibroelastoma, and myxoma (Figure 8.20). The AoV is often involved in combination with the MV. An underlying structural anomaly with deformity of valve cusps, bicuspid, or degeneration and calcification predisposes to vegetations. Destruction of valvular leaflet can result in acute aortic regurgitation. A rare, but potentially catastrophic complication of AoV endocarditis is the development of a pseudo-aneurysm of the intervalvular fibrosa, which can lead to coronary compression or fistulous tract formation (see Figure 9.20). Pulmonary valve endocarditis is quite rare. When it occurs, it is usually in the setting of congenital heart disease. Tricuspid valve (TV) vegetations are most commonly caused by *Staphylococcus aureus*. These generally occur in the setting of acute rather than subacute endocarditis. Predisposing factors include intravenous drug abuse, infected catheters, and virulent soft tissue infection (Figure 8.21). In contrast to the other sites, these may form on a structurally normal valve. Tricuspid valve vegetations typically appear as large echo-dense masses that disrupt the usual smooth leaflet contour on the atrial surface, leaflet margins, or ventricular surface. Staphylococcal endocarditis can be quite destructive and result in chordal rupture.

Prosthetic Valves

Prosthetic valve endocarditis can be more challenging to detect because of the acoustic shadows created by the dense prosthetic material. The infectious process usually begins in the perivalvular area at the ring margin and can eventually lead to valve dehiscence (Figure 8.22). It can also extend along the struts where it may cause valve dysfunction by interfering with the normal motion of the occluder. With bioprostheses, the infection may spread to the leaflets. The differential diagnosis includes the formation of a pannus, an abnormal layer of fibrovascular tissue or granulation, typically more echo-dense than thrombus.

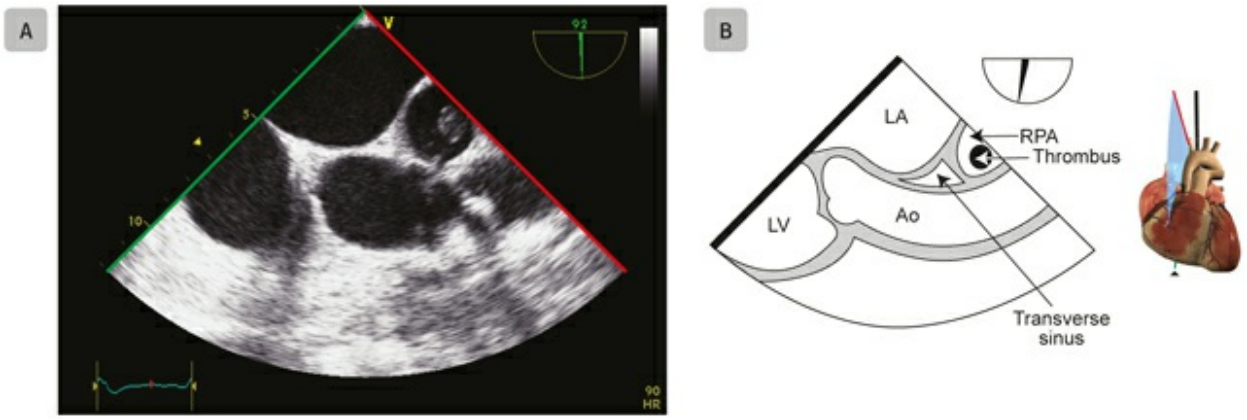

Fig. 8.19 Chronic pulmonary embolism. (A, B) Mid-esophageal ascending aorta (Ao) long-axis view in a 65-year-old female with chronic pulmonary embolism shows the mobile clot adherent to the wall of the right pulmonary artery (RPA). LA, left atrium; LV, left ventricle. (Reproduced with permission from Denault *et al.* [1]).

A: https://youtu.be/fneS35t8ujU

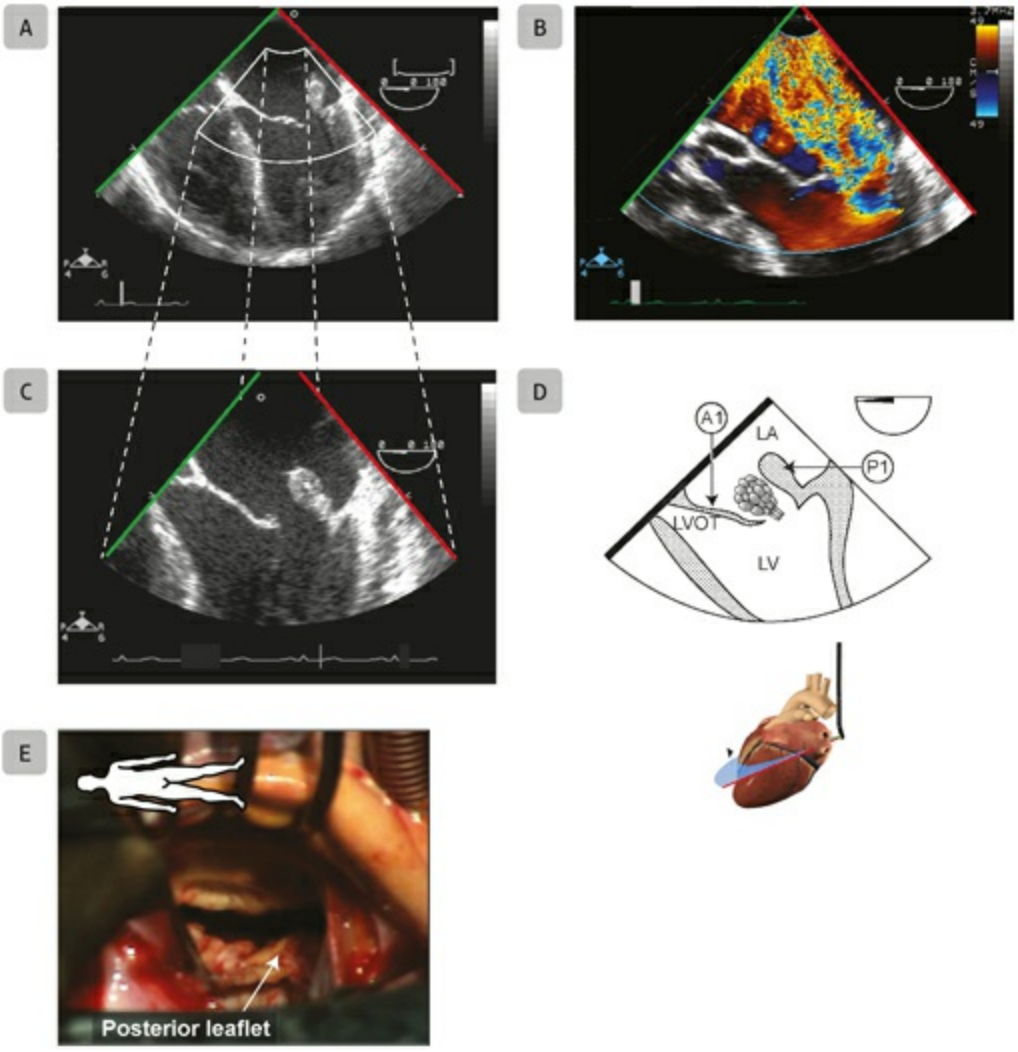

Fig. 8.20 Endocarditis. Mid-esophageal (A, B) four-chamber and (C, D) five- chamber views at 0° of a 57-year-old male with endocarditis and large flail of the posterior leaflet (P1) scallop associated with severe mitral regurgitation. (E) Intraoperative findings confirm flail of the entire posterior leaflet. The patient underwent mitral valve replacement. A1, anterior leaflet; LA, left atrium; LV, left ventricle; LVOT, left ventricular outflow tract. Source: Photo E courtesy of Dr Michel Carrier. (Reproduced with permission from Denault *et al.* [1]).

A: https://youtu.be/Ug4jbOkgD2k

B: https://youtu.be/tM0RTxErOlA

E: https://youtu.be/It0NVc2pM8A

Complicatons of Infective Endocarditis

Endocarditis can lead to obstruction or incompetence of the valve and eventually heart failure. Vegetations may also embolize and this occurs more often with the MV than AoV. In addition, a periannular abscess can form, consisting of a pus cavity that may involve the annulus, myocardium, or interventricluar fibrosa (see Figure 9.20). It can appear as a hypo- or hyper-echoic area in tissue adjacent to a valve. By definition, the abscess cavity does not communicate with a cardiac chamber or vessel, is non-pulsatile, and does not have color Doppler flow. A fistula can result from rupture of an abscess or pseudo-aneurysm. It is defined as an abnormal communication between cardiac chambers in which flow can be demonstrated. A pseudo-aneurysm of intervalvular fibrosa is seen as a pulsatile echo-free area between the aortic annulus and base of the anterior mitral leaflet. An early systolic flow from the LVOT along with an early diastolic emptying can be seen. Finally, endocarditis can cause dehiscence of a prosthetic valve. This occurs when more than 40% of the sewing ring is involved in the infectious process. A gap between tissue and the sewing ring can be seen, along with an abnormal rocking motion independent of surrounding structures. This can result in significant paravalvular regurgitation on color Doppler assessment.

NEOPLASIA

Ninety percent of cardiac neoplasms are found incidentally. Most cardiac tumors are metastases from primary extracardiac malignancies (Figure 8.23). Primary cardiac tumors are much less common. Benign tumors account for 75% of all primary cardiac tumors, myxoma being the most common. Sarcomas constitute the vast majority of malignant primary cardiac tumors. Atrial tumors are mostly Intra-cavitary, while ventricular tumors are mostly intramural.

BENIGN PRIMARY CARDIAC NEOPLASM

Myxomas

Myxomas constitute 50% of benign tumors and 30% of all primary cardiac tumors. In younger patients, these are familial, with multiple tumors that tend to recur as part of Carney complex. These tumors are typically gelatinous, globular, polypoid, pedunculated masses. While some are friable, others are round with a smooth surface (Figure 8.24). Myxomas are typically non-homogenous with areas of hemorrhage, necrosis, and calcification and are thus at risk of embolization. The echocardiographic appearance of myxoma can be quite variable. Myxomas may be irregularly shaped or filamentous, or appear like a “cluster of grapes”. The average size is 4–8 cm, but may reach up to 15 cm, thus causing significant mitral inflow obstruction. Masses with a long pedicle may even be seen intermittently popping in and out of the mitral orifice during the cardiac cycle. Classic left atrial myxomas (75% of cases) are found in the LA body, anchored to the interatrial septum by a stalk-like pedicle in the region of the fossa ovalis (Figure 8.24). Non-classic left atrial myxomas (10% of cases), arise from other sites. RA myxomas (10% of all myxomas) tend to have a broader base. The remainder of these benign tumors is ventricular and may originate from the septum with a variable appearance. Multifocal myxomas (5%) are mostly biatrial.

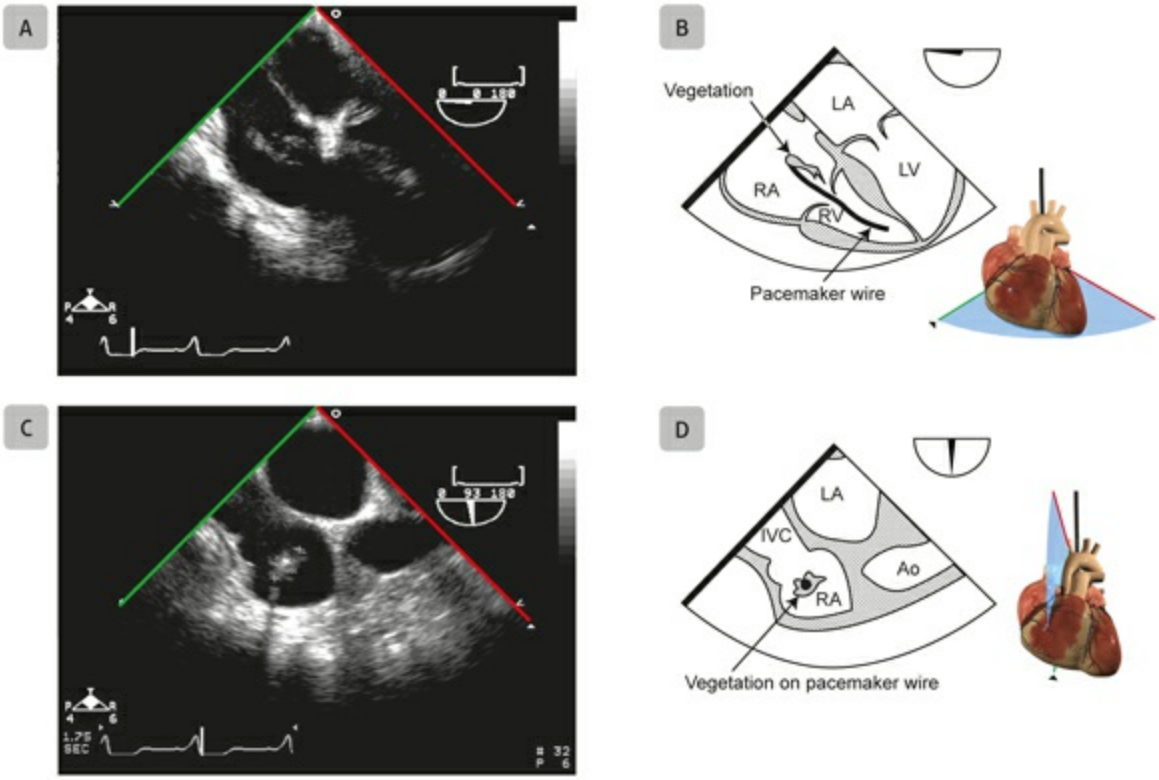

Fig. 8.21 Tricuspid valve endocarditis. Echogenic material attached to a pacemaker wire is seen in midesophageal (A, B) four-chamber and (C, D) 90° views. Ao, aorta; IVC, inferior vena cava; LA, left atrium; LV, left ventricle; RA, right atrium; RV, right ventricle. (Reproduced with permission from Denault *etal.* [1]).

A: https://youtu.be/vw8cVxmu8Pk

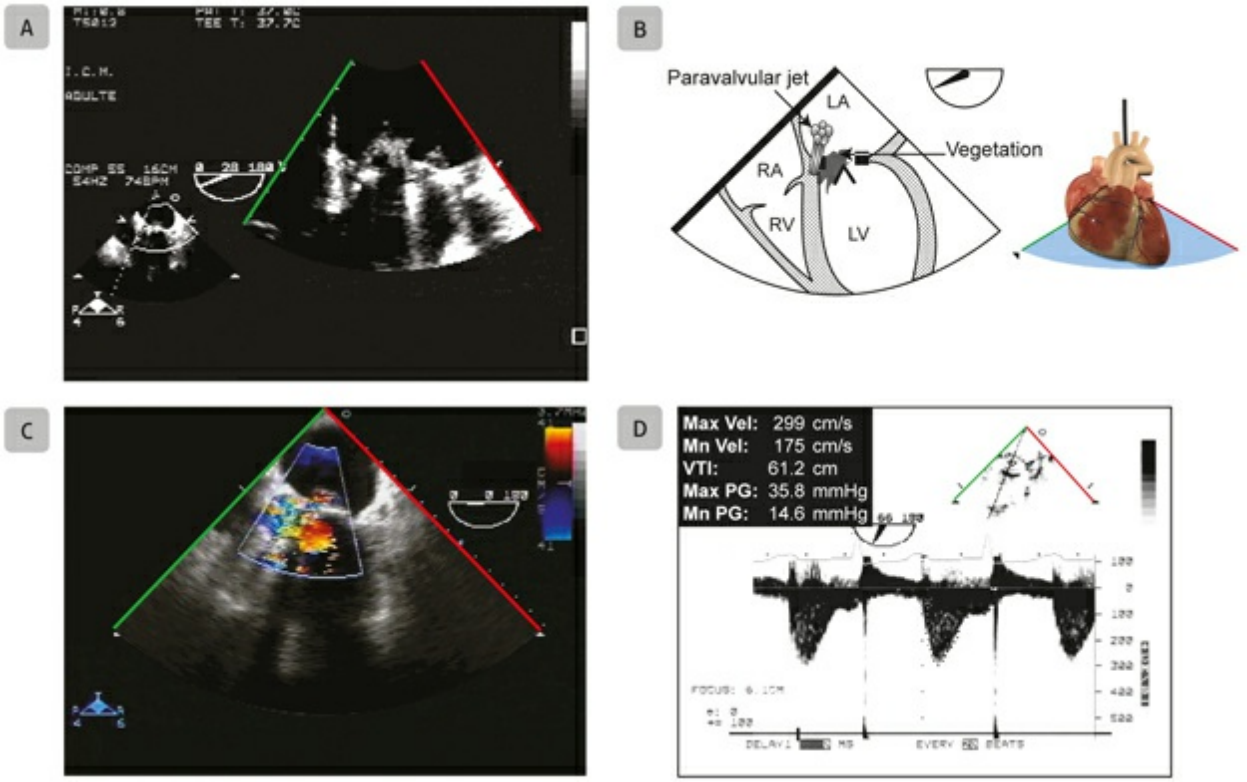

Fig. 8.22 Endocarditis. (A, B) Mid-esophageal (ME) 28° view shows two vegetations, a very large medial and a smaller lateral one, protruding through the orifices of a mechanical bi-leaflet prosthetic mitral valve (PMV) during both diastole and systole. (C) In the color Doppler (Nyquist 41 cm/s) ME four-chamber view, an associated color jet directed from the left ventricle (LV) to the left atrium (LA) during systole is consistent with a ruptured abscess and perivalvular fistula from an infectious process. (D) Continuous wave Doppler across the PMV demonstrates an increased transprosthetic pressure gradient (PG) due to the large obstructive vegetation. Max, maximal; Mn, mean; RA, right atrium; RV, right ventricle; Vel, velocity; VTI, velocity-time integral. (Reproduced with permission from Denault et al. [1]).

A: https://youtu.be/qlTD8ZeCiMs

C: https://youtu.be/kOBkQTmdX9Y

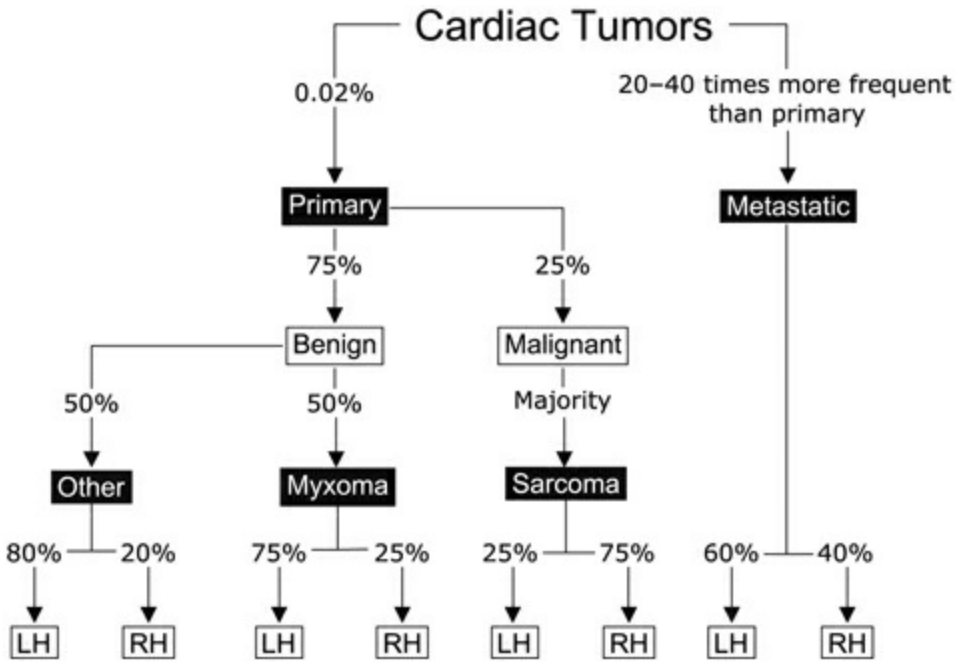

Fig. 8.23 Cardiac tumors. A classification and incidence for cardiac tumors is presented. LH, left heart; RH, right heart. (Reproduced with permission from Denault *et al.* [1]).

Papillary Fibroelastomas

Papillary fibroelastomas are the most common primary valve tumor and represent 8% of all primary cardiac neoplasms. These tumors can present in any age group, but occur more often in patients over 60 years of age. The tumor is composed of dense connective tissue and poses a high risk for embolization. On echocardiography, the tumor appears as small (0.5–2.0 cm) mobile pedunculated masses with variable shapes, such as filamentous, frondlike, or oval (Figure 8.25). These tumors arise in areas of endocardial damage, such as in the setting of valvular sclerosis, rheumatic heart disease, or post-cardiac surgery. Papillary fibroelastomas primarily involve the valves, most often the AoV, MV, and less often the mitral chordae, papillary muscles, and left atrial appendage. The tumors attach to the atrial surface of the atrioventricular valves and either side of the semilunar valve cusps. Fibroelastomas can sometimes be confused with vegetations, in which case the clinical setting is of prime importance in order to differentiate both types of valvular masses.

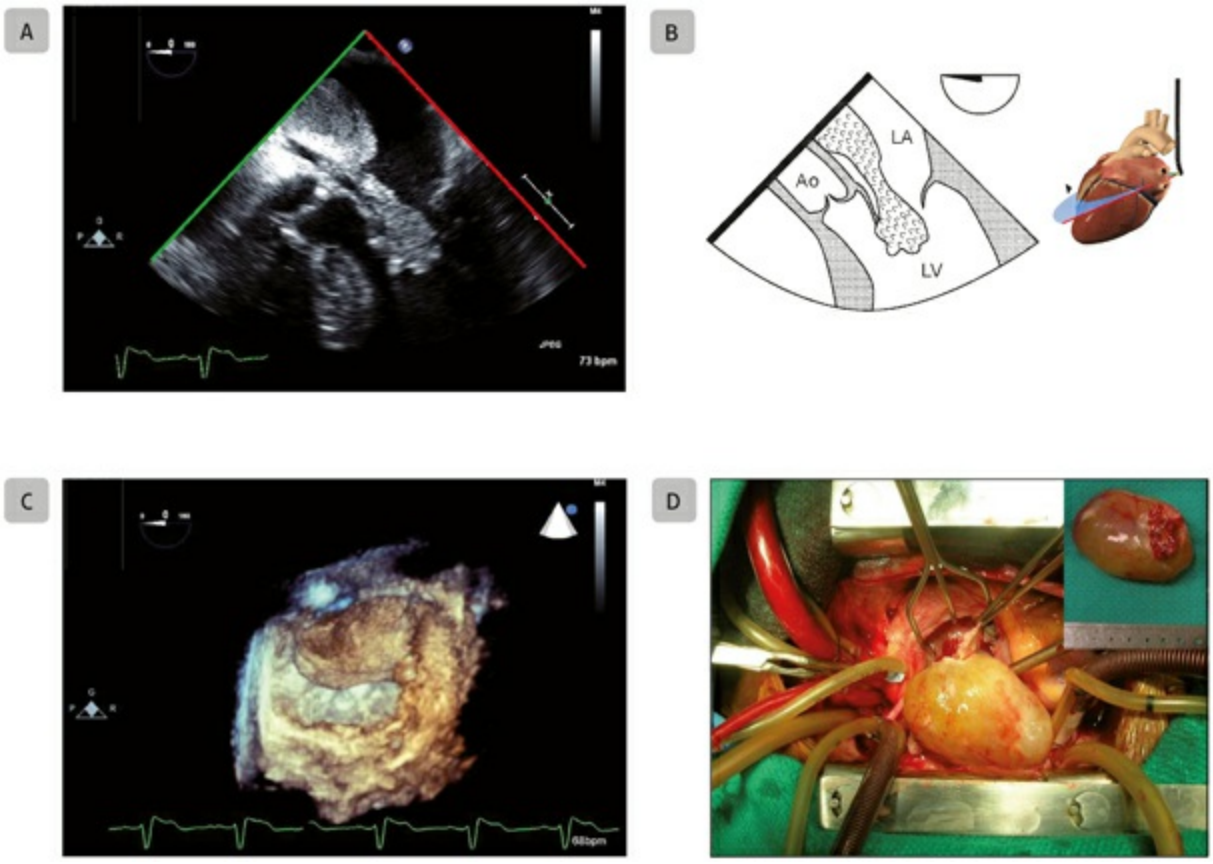

Fig. 8.24 Left atrial (LA) myxoma. (A, B) Mid-esophageal four-chamber view shows a LA myxoma prolapsing through the mitral valve and partially obstructing flow. (C) The mass is shown from the LA in the surgeon's orientation using 3D transesophageal echocardiography and (D) confirmed with the intraoperative findings. Ao, aorta; LV, left ventricle. (Reproduced with permission from Denault *et al.* [1]).

A: https://youtu.be/NNhM2G4sp6o

C: https://youtu.be/_w7LPV2C8ik

Lipomas

Lipomas represent 10% of all primary cardiac tumors and can affect all age

groups, without a particular gender predominance. Lipomas can occur anywhere in the heart, but are most often located in the LV or RA. These tumors may be sessile or pedunculated and 25% are completely intramyocardial. On echocardiography, these masses can usually be differentiated from myxomas by their more fixed hyperechoic appearance and sparing of the fossa ovalis. Other differential diagnoses include fibromas, papillary fibroelastomas, and thrombi. Magnetic resonance imaging may be a useful adjunct to demonstrate the fat content of the mass.

Rhabdomyomas

Rhabdomyomas are the most common benign cardiac tumors in the pediatric population and are strongly associated with tuberous sclerosis. Rare after adolescence, these tumors only account for 6% of primary cardiac tumors in the adult population. Most rhabdomyomas regress spontaneously. These masses are usually seen as multiple intramural or Intra-cavitary tumors involving both ventricles with equal frequency and uncommonly involve the atria.

Fibromas

Fibromas are the second most common primary cardiac tumors in the pediatric population, occurring frequently in children <1 year old, but can affect all ages and both sexes equally. In the adult population, these are one of the least common primary cardiac tumors (3%). Fibromas are benign, low-grade, connective tissue tumors. These masses are classically solitary and involve the ventricular myocardium, most often at the level of the septum (Figure 8.26). Their clinical importance results from potential impediment to LV filling along with damage to the conduction system,resulting in bundle branch blocks or pro-arrhythmic effect. Fibromas are usually large and well demarcated from the surrounding structures by multiple calcifications. When located at the apex, a fibroma can also mimic apical hypertrophic cardiomyopathy.

Hemangiomas

Hemangiomas are rare, benign proliferations of endothelial cells, accounting for only 2% of primary cardiac tumors. These tumors often present as an incidental finding on chest X-ray. Hemangiomas classically appear as

solitary, intramural, or intra-cavitary sessile masses with echolucent areas (Figure 8.27). There may be an accompanying pericardial effusion from tumor rupture. These tumors arise anywhere in the heart or pericardium, but are more commonly found in the right chambers. Potential complications include chamber compression, ventricular outflow tract obstruction, compression of the coronaries, and arrhythmias.

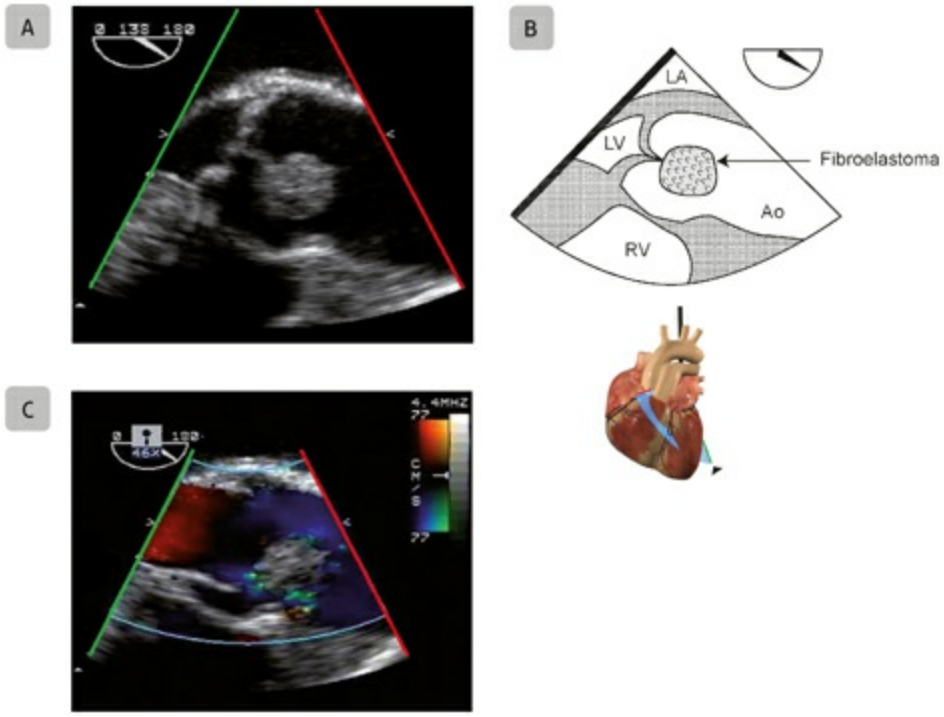

Fig. 8.25 Fibroelastoma. (A, B) An asymptomatic 45-year-old female presenting with a "pom-pom"-like mass attached to the aortic valve (AoV) is shown in the mid-esophageal AoV long-axis view. (C) Color Doppler (Nyquist 77 cm/s) imaging shows no obstruction to flow through the AoV. Pathology demonstrated a fibroelastoma. Ao, aorta; LA, left atrium; LV, left ventricle; RV, right ventricle. (Reproduced with permission from Denault *et al.* [1]).

D: https://youtu.be/na29Br9650c

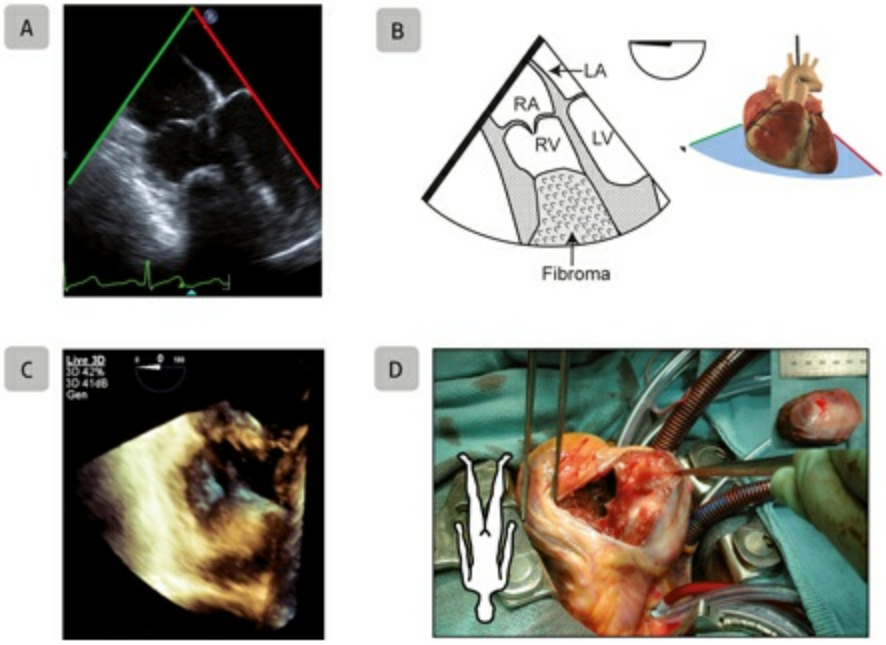

Fig. 8.26 Fibroma. A patient presents with a tumor of the right ventricle (RV) for complete resection and reconstruction with pericardial patch. The mass is seen in the mid-esophageal four-chamber view (A, B) and 3D transesophageal echocardiographic view (C), and is confirmed with the intraoperative findings (D). Pathology demonstrated a fibroma. LA, left atrium; LV, left ventricle; RA, right atrium. (Reproduced with permission from Denault *etal.* [1]).

A: https://youtu.be/FRj3W7_28KQ

C: https://youtu.be/XBlEMqMWK40

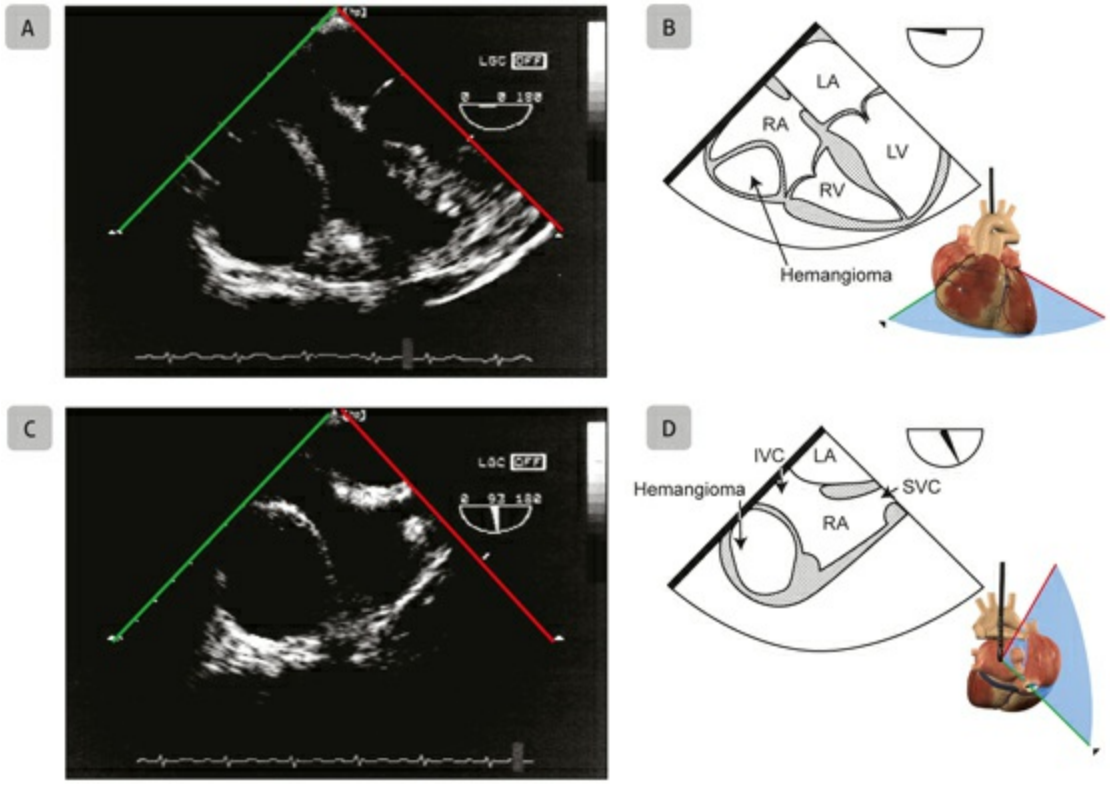

Fig. 8.27 Cardiac hemangioma. (A, B) Mid-esophageal four-chamber and (C, D) two-chamber views show a large echolucent cystic mass causing partial compression of the right atrium (RA). A vague, curvilinear echodensity is seen within the mass, possibly representing trabeculum within the hemangioma. IVC, inferior vena cava; LA, left atrium; LV, left ventricle; RV, right ventricle; SVC, superior vena cava. (Reproduced with permission from Denault *et al.* [1]).

Pericardial Cysts

Pericardial cysts are benign, fluid-filled tumors of the parietal epicardium, most commonly found on the cardiophrenic border (Figure 8.28).

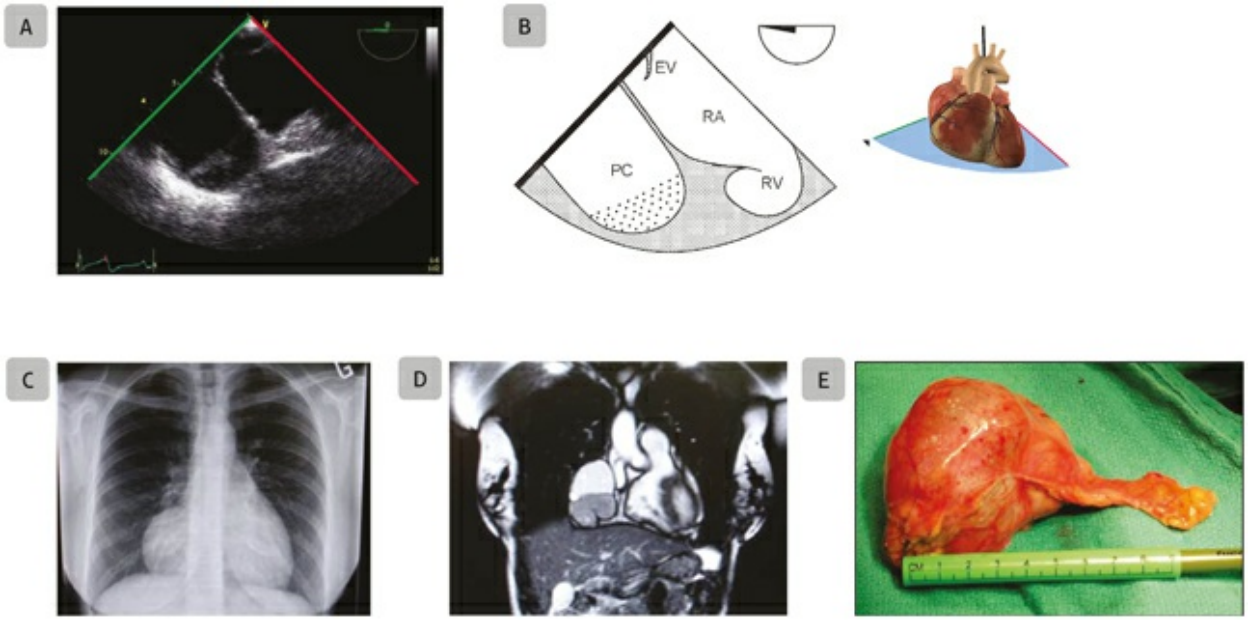

Fig. 8.28 Pericardial cyst. (A, B) Mid-esophageal view at 0° with right-sided rotation of the probe shows an echolucent cavity consistent with a pericardial cyst adjacent to the right atrium (RA) and left atrium. Compare with (C) chest X-ray, (D) magnetic resonance imaging coronal view, and (E) pathologic specimen. EV, Eustachian valve; PC, pericardial cyst; RV, right ventricle. Source: Photo E courtesy of Dr Michel Pellerin. (Reproduced with permission from Denault *et al.* [1]).

A: https://youtu.be/EQsbwMzLR0A

D: https://youtu.be/X9anFW9oCaQ

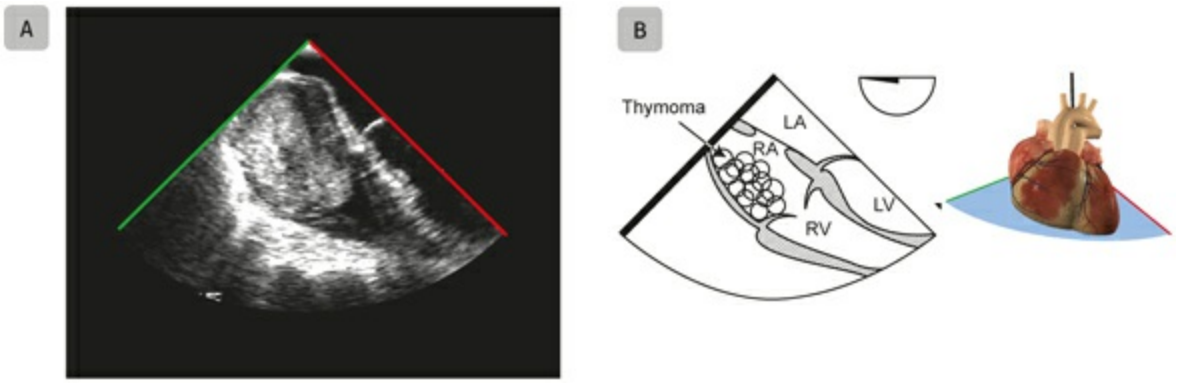

Fig. 8.29 Thymoma. (A, B) Mid-esophageal four-chamber view in a 40-year-old male shows a mass in the right atrium (RA) consistent with recurrent thymoma. He presented a few months earlier with a large mediastinal mass and the diagnosis of a thymoma was made at the time. LA, left atrium; LV, left ventricle; RV, right ventricle. (Reproduced with permission from Denault *et al.* [1]).

MALIGNANT PRIMARY CARDIAC TUMORS

Thymomas and Lymphosarcoma

Thymomas primarily involve the anterior mediastinum. These tumors can present as extracardiac masses causing compression of a cardiac chamber. The pericardium can sometimes also be the primary site of origin (Figure 8.29). Lymphosarcomas are rare primary lymphomas of the heart and pericardium (2% of primary cardiac tumors) that can present at all ages. Immunosuppression (for example, AIDS, post-transplant) predisposes to the development of these tumors. These tumors have a characteristic myocardial infiltration, which can be diffuse or with multiple intra-cavitary nodules. Right chambers are more frequently involved, followed by the pericardium, LA, and LV. The mass can sometimes fill the LV apex and be confused with a thrombus or hypertrophic cardiomyopathy.

Angiosarcomas and Rhabdomyosarcomas

Angiosarcomas are the most common primary cardiac malignancy (8% of primary cardiac tumors) and afflict mostly men. The vast majority originate as large masses in the RA that can invade surrounding structures, including the TV, SVC, IVC, and the aorta (Figure 8.30). Pericardium can also be quite extensively involved leading to constriction or hemopericardium. Angiosarcomas may be difficult to differentiate from other sarcomas. Rhabdomyosarcomas are the second most common primary sarcoma (5% of primary cardiac tumors) with 25% of cases in patients less than 20 years of age. This tumor arises as an intra-mural mass that grows into adjacent cardiac chambers, pericardium, or valves. These may be multiple and affect any cardiac chamber.

CARDIAC METASTASES

Cardiac metastases are between 20 and 40 times more common than primary

cardiac tumors. Almost any type of cancer, with the exception of brain, can metastasize to the heart. Malignancies with a high propensity to metastasize to the heart include melanoma (65% cardiac metastases) and lymphomas (45% cardiac metastases). However, because of their higher incidence, other cancers are more commonly responsible for cardiac metastases (Figure 8.31). These include bronchogenic carcinoma, by direct extension from the pulmonary veins, breast carcinoma by hematogenous or lymphatic spread, as well as colorectal, gastric, and hepatocellular cancers. Moreover, renal cell carcinoma may progress to the right heart by vascular invasion (Figure 8.32). Finally, carcinoid tumors may cause tricuspid and pulmonary valve thickening and also involve the liver (Figure 8.33).

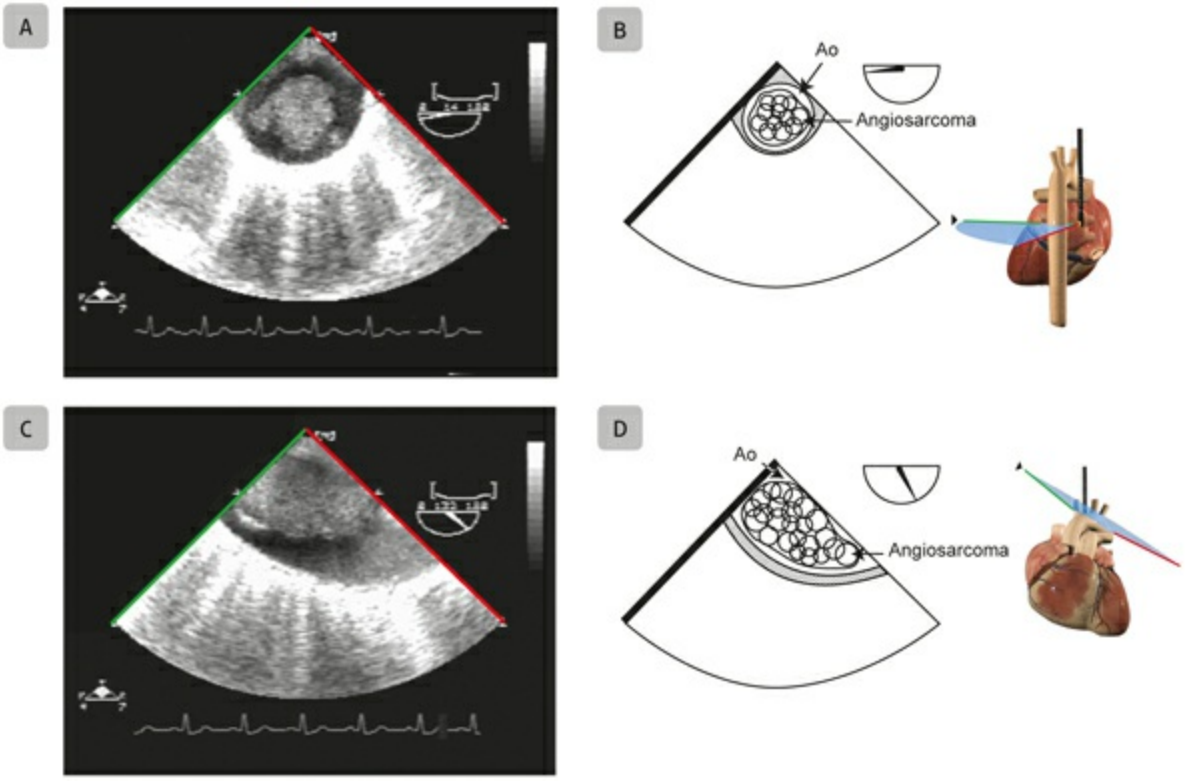

Fig. 8.30 Aortic angiosarcoma. A 55-year-old female was referred to the echocardiography laboratory for investigation of recurrent transient ischemic attacks. (A, B) Mid-esophageal descending aorta (Ao) short-axis and (C, D) upper esophageal aortic arch long-axis views demonstrate a large intraluminal mass. Surgical removal was complicated with multiple emboli to the lower limbs. Biopsy revealed an angiosarcoma. (Reproduced with permission from Denault *et al.* [1]).

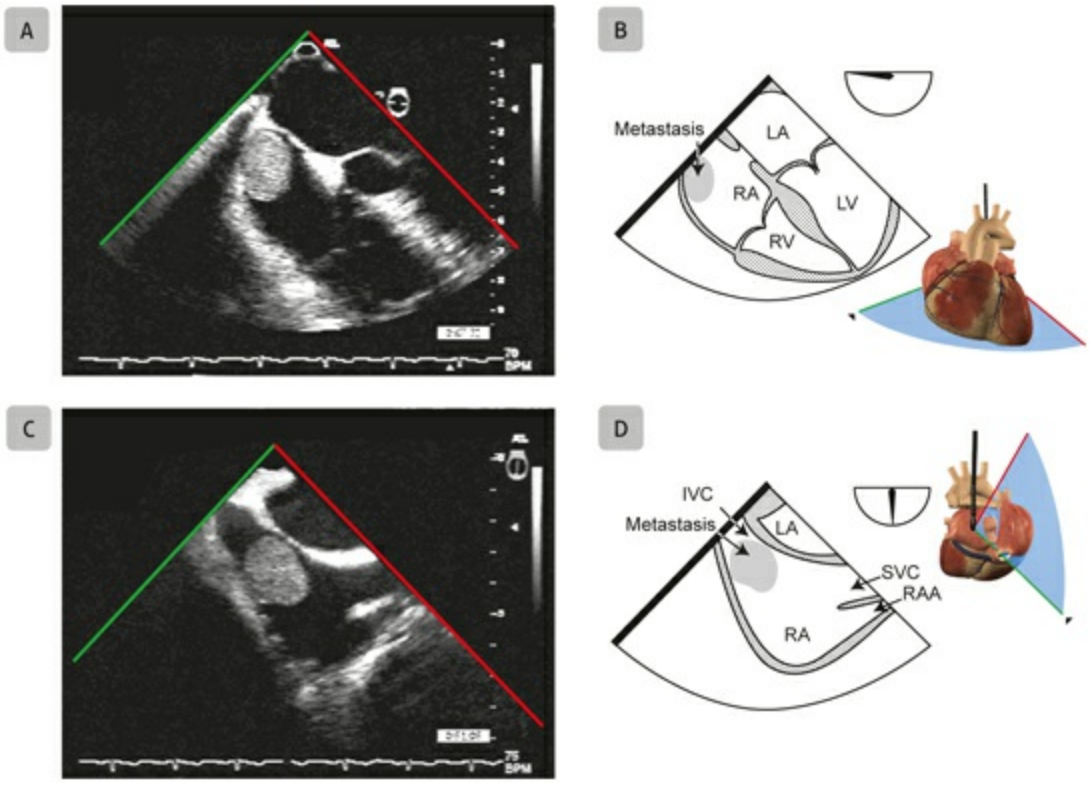

Fig. 8.31 Breast cancer. (A, B) Mid-esophageal four-chamber and (C, D) bicaval views in a 60-year-old female with a history of metastatic breast cancer, increasing dyspnea, and right heart failure. A large mass was seen in the right atrium (RA) consistent with tumor metastasis. IVC, inferior vena cava; LA, left atrium; LV, left ventricle; RAA, right atrial appendage; RV, right ventricle; SVC, superior vena cava. (Reproduced with permission from Denault *et al.* [1]).

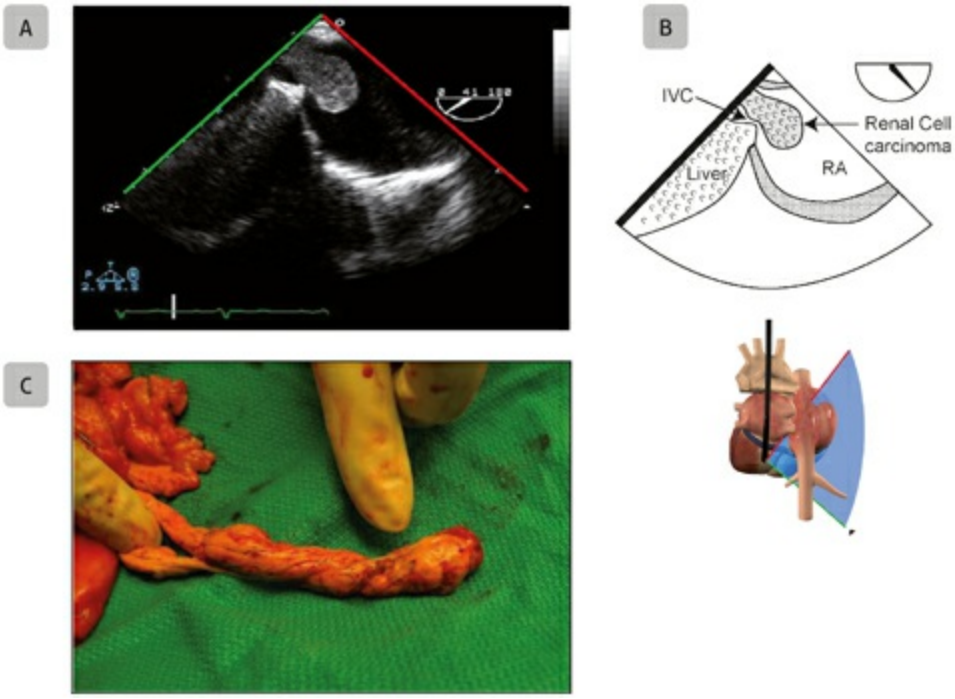

Fig. 8.32 Renal cell cancer. An 80-year-old female presents with a history of palpitations and a left renal cell carcinoma extending into her inferior vena cava (IVC). (A, B) Lower esophageal view at 41° at the junction of the IVC and right atrium (RA) shows the mass partially obstructing the IVC. (C) Excised specimen showing the tumor portion in the IVC. (Reproduced with permission from Denault *et al.* [1]).

A: https://youtu.be/sVq9e__8YWs

IATROGENIC

Intra-cavitary Air

Intra-cavitary air appears as a hyperintense signal with dispersion of ultrasound creating artifacts beyond the bubbles. The significance and potential consequences of air vary greatly with the clinical setting and anatomical location. Left-sided air is usually more worrisome as it can cause systemic embolization. It might be seen with venous introduction of air in a patient with a right-to-left shunt or with intra-cardiac introduction of air during open heart surgery or surgery in prone position (see Figure 12.24).

CATHETERS

Venous Catheters and Wires

Echocardiography can be used to assess the position and integrity of indwelling catheters in the heart and great vessels and exclude thrombus formation or infection. Correct placement of jugular and subclavian central lines, ideally 2 cm above the SVC-RA junction, can be confirmed (see Figure 18.12). The PA catheters can be placed under ultrasonographic guidance in difficult cases. The inflated balloon may be seen as it advances through the RA, RV, and RVOT. A characteristic pulsatile to-and-fro movement of the catheter called “shuttle movement” should be seen provided the balloon is not wedged. Upon wedging, the “shuttle movement” stops and this is called the “anchoring sign”. [13] When the shuttle movement stops while still reading RA, RV, or PA pressure curves, this usually means that the catheter has wedged in the RV apex, in a narrow RVOT or that it has coiled somewhere. Echocardiography can help elucidate the cause of pacemaker malfunction, such as lead migration or fracture.

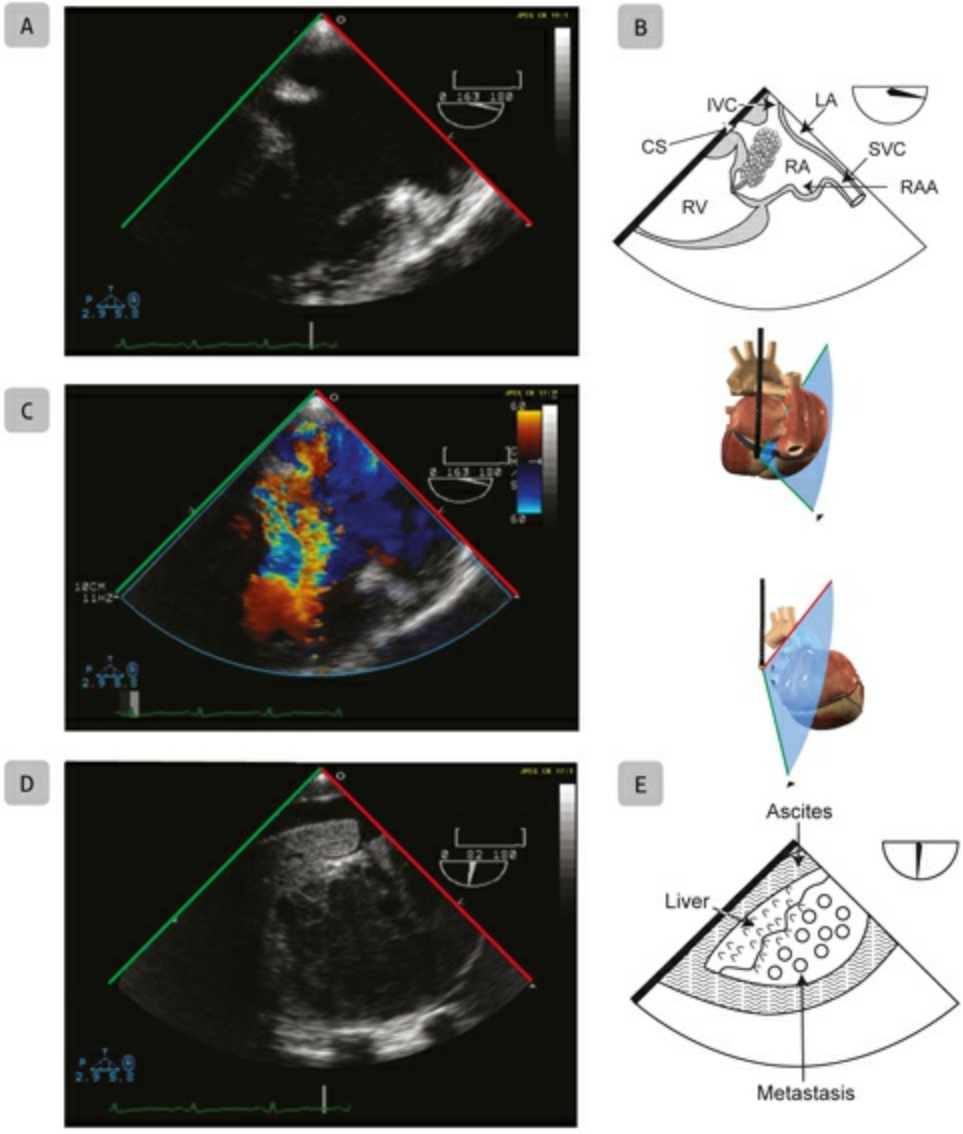

Fig. 8.33 Carcinoid heart disease. (A—C) Mid-esophageal views with rightward rotation shows severe tricuspid regurgitation with a huge regurgitant orifice due to thickened tricuspid valve leaflets retracted in the open position. (D, E) Transgastric view at 82° of the liver in the same patient shows liver metastasis from the large carcinoid tumor. CS, coronary sinus; IVC, inferior vena cava; LA, left atrium; RA, right atrium; RAA, right atrial appendage; RV, right ventricle; SVC, superior vena cava. (Reproduced with permission from Denault *et al.* [1]).

A: https://youtu.be/9YN3XX7fcfI

C: https://youtu.be/bhjbiUIkAOY

D: https://youtu.be/hqAbGmUNvYk

Intra-aortic Balloon Pump

Transesophageal echocardiography can assist during intra-aortic ballon pump (IABP) catheter placement in the absence of fluoroscopy (Figure 8.34). A preplacement examination can exclude contraindications to IABP placement, such as aortic regurgitation (more than mild) and dynamic left ventricular outflow tract (see Figure 9.13). The aortic arch and descending aorta are carefully examined for significant atherosclerosis, aneurysms and dissection as these are relative contraindications. During placement, a descending aorta LAX view (Figure 8.34) confirms visualization of the guidewire in the descending aorta before dilating the femoral vessel. When this is done, the IABP catheter can be advanced over the wire, which is removed when the catheter has reached the thoracic aorta.

The IABP catheter is then further advanced to a position 1–2 cm distal to the left subclavian artery, at the inferior border of the aortic arch. Once the pump is started, the aorta should be re-examined for signs of new pathology and for the presence of a large volume of air bubbles that would mandate immediate removal of the IABP because of suspected balloon rupture. [14]

ECMO Cannulas

Peripheral extracorporeal membrane oxygenation (ECMO) cannulation is performed using a Seldinger technique. Echocardiography can guide the correct placement of cannulas during the insertion process. The ideal cannula position varies according to the mode of ECMO and the type of cannula. The guidewire and cannula can be directly visualized in the ME bicaval view (see Figure 3.13). The position of the ports is assessed with the injection of microbubbles through the cannula or simply with color Doppler during

ECMO (Figure 8.35). Position of the cannula below or outside the azygos vein (see Figure 4.16) is important in order not to impede cerebral venous drainage (Figure 8.35). Echocardiography may also be used to reassess cannula position intermittently afterwards as they can migrate. Improper placement can lead to local complications, such as ventricular perforation and tamponade. With veno-venous ECMO, incorrect cannula placement frequently leads to recirculation of blood, with a significantly detrimental effect on oxygenation. This can be quantified using ultrasonographic techniques that are beyond the scope of this chapter. [15]

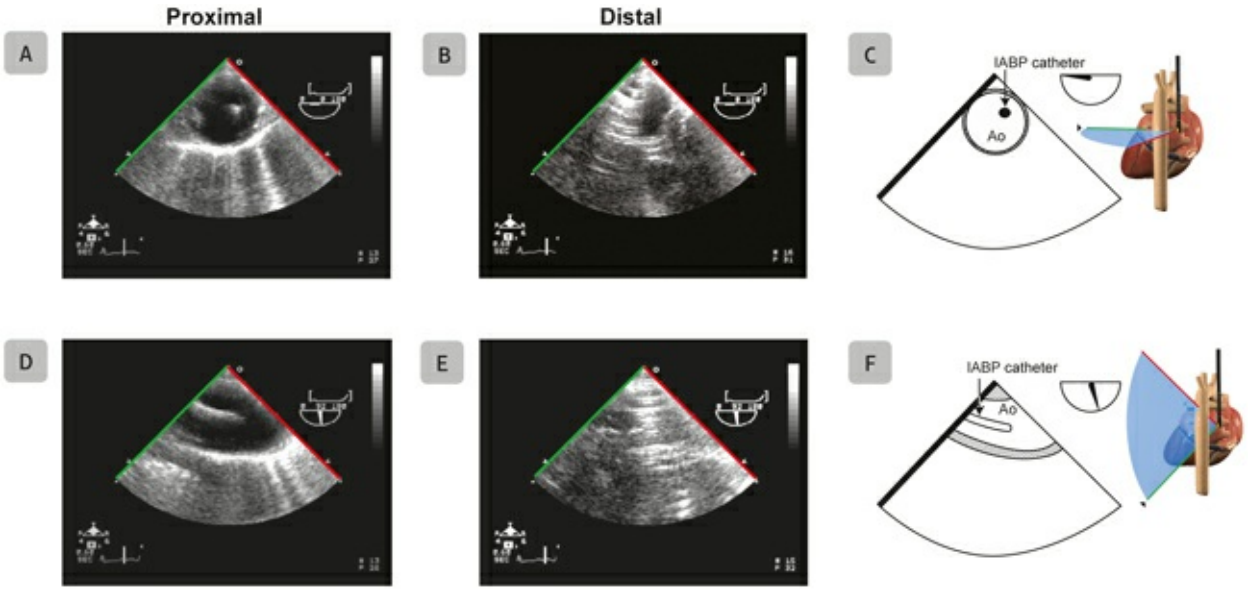

Fig. 8.34 Intra-aortic balloon pump (IABP) catheter. An IABP catheter is positioned in the aorta (Ao) of a 75-year-old male before coronary revascularization. The descending Ao (A—C) short-axis and (D-F) long- axis views are shown. The tip of the catheter should ideally be located 5-10 cm below the origin of the left subclavian artery. Note that during inflation, air in the catheter prevents visualization of the aortic wall. (Reproduced with permission from Denault *et al.* [1]).

A-D: https://youtu.be/YCQSWERxAEI

In summary, TEE is unsurpassed in its ability to identify Intra-cavitary content, catheter positions and diagnose hemodynamic instability or acute neurological events resulting from a cardiogenic source.

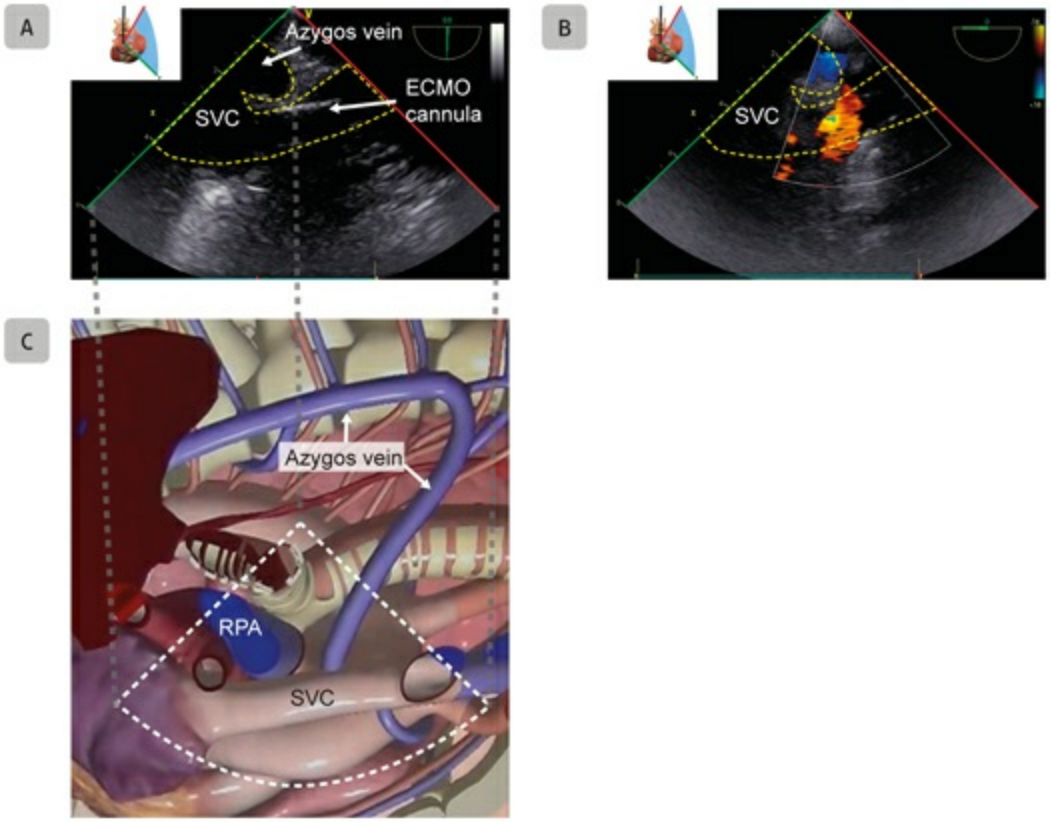

Fig. 8.35 Extracorporeal membrane oxygenation (ECMO) cannula. (A) Modified upper esophageal bicaval view just above the right pulmonary artery (RPA) showing the ECMO cannula in the superior vena cava (SVC) beyond the azygos vein. Malposition of the ECMO cannula in the azygos vein could impair cerebral venous drainage and result in a SVC syndrome. (B) Color Doppler is used to identify the low flow of the azygos vein. (C) Anatomic representation using the Vimedix simulator.

A: https://youtu.be/rJvGaj0LcuY

B: https://youtu.be/_BnAYTl1b0Q

C: https://youtu.be/0EY0rygNVOY

REFERENCES

1. DenaultA.Y., CoutureP., VegasA., BuithieuJ., TardifJ.C.. *Transesophageal Echocardiography Multimedia Manual, Second Edition: A Perioperative Transdisciplinary Approach*. New York: Informa Healthcare, 2011.
2. CheitlinM.D., AlpertJ.S., ArmstrongW.F., AurigemmaG.P., BellerG.A., BiermanF.Z.*et al*. ACC/AHA Guidelines for the Clinical Application of Echocardiography. A report of the American College of Cardiology/American Heart Association Task Force on Practice Guidelines (Committee on Clinical Application of Echocardiography). Developed in collaboration with the American Society of Echocardiography. *Circulation*. 1997;*95*:1686–744.
3. DouglasP.S., GarciaM.J., HainesD.E., LaiW.W., ManningW.J., PatelA.R., et al. ACCF/ASE/AHA/ASNC/HFSA/HRS/SCAI/SCCM/SCCT/ SCMR 2011 Appropriate Use Criteria for Echocardiography. A Report of the American College of Cardiology Foundation Appropriate Use Criteria Task Force, American Society of Echocardiography, American Heart Association, American Society of Nuclear Cardiology, Heart Failure Society of America, Heart Rhythm Society, Society for Cardiovascular Angiography and Interventions, Society of Critical Care Medicine, Society of Cardiovascular Computed Tomography, Society for Cardiovascular Magnetic Resonance American College of Chest Physicians. *J Am Soc Echocardiogr*. 2011;*24*:229–67.
4. JanuaryC.T., WannL.S., AlpertJ.S., CalkinsH., CigarroaJ.E., ClevelandJ.C.Jr, *et al*. 2014 AHA/ACC/HRS guideline for the management of patients with atrial fibrillation: executive summary: a report of the American College of Cardiology/ American Heart Association Task Force on practice guidelines and the Heart Rhythm Society. *Circulation*. 2014;*130*:2071–104.
5. CheitlinM.D., ArmstrongW.F., AurigemmaG.P., BellerG.A., BiermanF.Z., DavisJ.L.*et al*.. ACC/AHA/ASE 2003 guideline update for the clinical application of echocardiography. Summary article: a report of the American College of Cardiology/American Heart Association Task Force on Practice Guidelines (ACC/AHA/ASE Committee to Update the 1997 Guidelines for the Clinical Application of Echocardiography). *Circulation*. 2003;*108*:1146–62.
6. ManningW.J., WeintraubR.M., WaksmonskiC.A., HaeringJ.M., RooneyP.S., MaslowA.D., *et al*. Accuracy of transesophageal echocardiography for identifying left atrial thrombi. A prospective, intraoperative study. *Ann Intern Med*. 1995;*123*:817–22.
7. LeibowitzD.. Role of echocardiography in the diagnosis and treatment of acute pulmonary thromboembolism. *J Am Soc Echocardiogr*. 2001;*14*:921–6.
8. MiniatiM., MontiS., PrataliL., DiR.G., MariniC., FormichiB., *et al*. Value of transthoracic echocardiography in the diagnosis of pulmonary embolism: results of a prospective study in unselected patients. *Am J Med*. 2001;*110*:528–35.
9. PruszczykP., TorbickiA., Kuch-WocialA., SzulcM., PachoR.. Diagnostic value of transoesophageal echocardiography in suspected haemodynamically significant pulmonary embolism. *Heart*. 2001;*85*:628–34.
10. McConnellM.V., SolomonS.D., RayanM.E., ComeP.C., GoldhaberS.Z., LeeR.T.. Regional right ventricular dysfunction detected by echocardiography in acute pulmonary embolism. *Am J Cardiol*. 1996;*78*:469–73.
11. LiJ.S., SextonD.J., MickN., NettlesR., FowlerV.G.Jr, RyanT.*et al*. Proposed modifications to the Duke criteria for the diagnosis of infective endocarditis. *Clin Infect Dis*. 2000;*30*:633–8.
12. RyanE.W., BolgerA.F.. Transesophageal echocardiography (TEE) in the evaluation of infective

endocarditis. *Cardiol Clin*. 2000;*18*:773–87.
13. OrihashiK., NakashimaY., SuedaT., YamanoueT., YugeO., MatsuuraY.. Usefulness of transesophageal echocardiography for guiding pulmonary artery catheter placement in the operating room. *Heart Vessels*. 1994;*9*:315–21.
14. KlopmanM.A., ChenE.P., SniecinskiR.M.. Positioning an intraaortic balloon pump using intraoperative transesophageal echocardiogram guidance. *Anesth Analg*. 2011;*113*:40–3.
15. JavidfarJ., WangD., ZwischenbergerJ.B., CostaJ., MongeroL., SonettJ.*et al*. Insertion of bicaval dual lumen extracorporeal membrane oxygenation catheter with image guidance. *ASAIO J*. 2011;*57*:203–5.

Chapter 9

Basic Hemodynamic Assessment

Andre Y Denault, Jennifer Cogan and Annette Vegas

INTRODUCTION

Hemodynamic instability leading to shock is defined as a situation where oxygen transport is inadequate to meet oxygen requirements. An understanding of the mechanism(s) of reduced cardiac output (CO), a determinant of oxygen transport, is crucial in order to initiate appropriate therapy to manage shock. The concepts of venous return and the pressure-volume relationship, popularized by Guyton *et al.*, [1] combined with bedside ultrasound (US) appears to be the most comprehensive way to understand the state of shock. [2] , [3] If the patient in shock is unresponsive to general resuscitation measures, bedside US examination of the heart, lung, and abdomen, using either a transthoracic or a transesophageal approach, is performed. Ultrasound can be useful to: (1) determine the mechanism(s) of shock, (2) establish the etiology, and (3) evaluate the response to therapy. This chapter provides a diagnostic approach to shock based on the integration of non-echocardiographic and echocardiographic variables.

CONCEPT OF VENOUS RETURN

Combining the concepts of venous return and the ventricular pressure-volume relationship provide a useful method to appreciate the complex circulatory physiology of shock. A detailed description of the venous return concept is beyond the scope of this chapter, but interested readers are referred to two excellent reviews by Jacobsohn and Funk. [4] , [5] In simple terms, venous return is determined by a pressure gradientVR

Pms — Pra Rvr

and, in steady state, is equal to CO. The pressure gradient corresponds to the difference between the mean systemic venous pressure (Pms) in the periphery and the right atrial pressure (Pra). Venous return (VR) is inversely proportional to the resistance to venous return (Rvr).

Venous return and, consequently, CO will be reduced if: (1) Pms is low, (2) Pra is elevated, and/or (3) Rvr is increased.

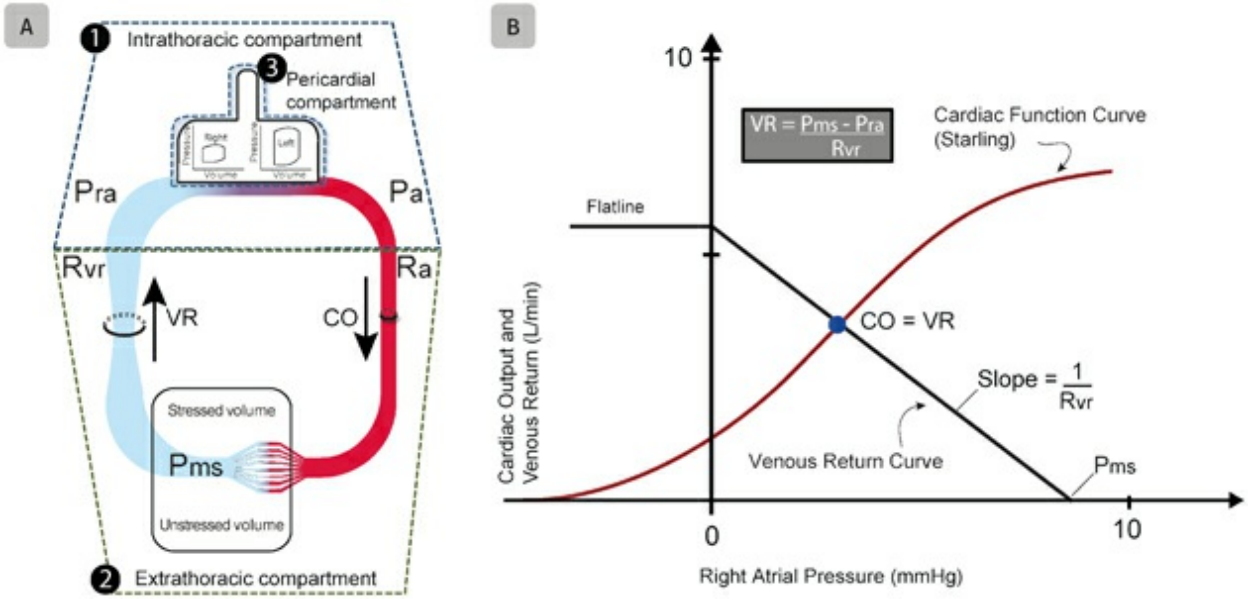

Fig. 9.1 . Function curves. (A) The closed circuit circulatory system contains venous and arterial components, and is divided into three compartments, (1) thoracic, (2) abdominal (extrathoracic) and (3) pericardial, which includes the heart. (B) In this closed system, venous return (VR) equals cardiac output (CO) and can be described by using function (or pressure-flow) curves. The cardiac function curve (or Starling curve) depicts the relationship of CO (dependent variable) and right atrial pressure (Pra) (independent variable). The venous return curve shows the association of VR (dependent variable) and Pra (independent variable). Both curves intersect at the normal resting state for the cardiovascular system where VR equals CO, thus giving specific values for CO and Pra. Pa, arterial pressure; Pms, mean systemic venous pressure; Ra, arterial resistance; Rvr, resistance to venous return. (Adapted with permission from Denault *et al.* [2] *)*

FUNCTION CURVES

The circulatory system is a closed circuit consisting of arterial and venous components, with 70% of the blood volume in the venous system. There are three compartments: (1) thoracic, (2) abdominal, and (3) pericardial, which includes the heart. The Pms is determined by the distribution of total blood

volume between the veins and arteries and by the venous compliance. The Pms consists mainly of the stressed volume (about 30 mL/kg), which is only a portion of the venous reservoir. In this closed system, VR must equal CO and can be described with function (or pressure-flow) curves (**Figure 9.1**). The cardiac function curve (or Starling curve) depicts the relationship of CO (dependent variable) and Pra (independent variable). As Pra increases, CO will increase proportionally until a plateau is reached when the heart becomes over-distended. The venous return curve shows the association of VR (dependent variable) and Pra (independent variable) but as an inverse relationship; an increase in Pra produces a decrease in VR. The x-intercept is the Pms, which is the pressure in the system when CO and VR is zero or the heart is stopped. The slope of the curve is a function of the right ventricle (RV). At negative Pra values, such as during inspiration, the abdominal veins collapse impeding VR causing a flat line in the curve. Both curves intersect at the normal resting state for the cardiovascular system where VR equals CO, thus giving specific values for CO and Pra. Any change in curve position, as in diseased states, creates a new steady state with different CO and Pra. **Figure 9.2** illustrates how similar reductions in VR and consequently CO from three different mechanisms will alter this relationship.

MECHANISMS OF SHOCK

Mean systemic venous pressure is determined by the volume status and the compliance of the venous reservoir. Thus, hemorrhagic shock and distributive shock can both reduce Pms and alter the VR curve (**Figure 9.3 A**). In hemorrhagic shock, the stressed blood volume decreases reducing Pms which shifts the VR curve left. At the new steady state, CO and Pra are both decreased (**Figure 9.3 A, from point A to point B**). An increase in blood volume raises the stressed volume, increasing Pms and shifts the VR curve right (**Figure 9.3 A**, **from point B back to point A**). At the new steady state with more volume, the CO and Pra are both increased (**Figure 9.3 A, from point A to point C**).

In cardiogenic shock, the cardiac function curve shifts downwards as CO is decreased, and Pra is increased, from less blood ejection with each beat (**Figure 9.3 B**, **from point A to point B**). As compensation the Pms increases, shifting the VR curve right, without changing its slope. A positive

inotropic effect shifts the cardiac function curve upwards as CO is increased, and Pra is decreased from more blood ejection with each heartbeat (**Figure 9.3 B**, **from point A to point C**). Cardiogenic shock can be due to left ventricular (LV) and right ventricular (RV) systolic dysfunction, diastolic failure, LV and RV outflow tract obstruction (LVOTO and RVOTO), [6] , [7] acute valvular insufficiency and pulmonary embolism. Hypoxemia and hypercapnia, if acute and uncorrected, will cause pulmonary hypertension leading to increased Pra and, in susceptible patients, if left untreated can lead to RV failure.

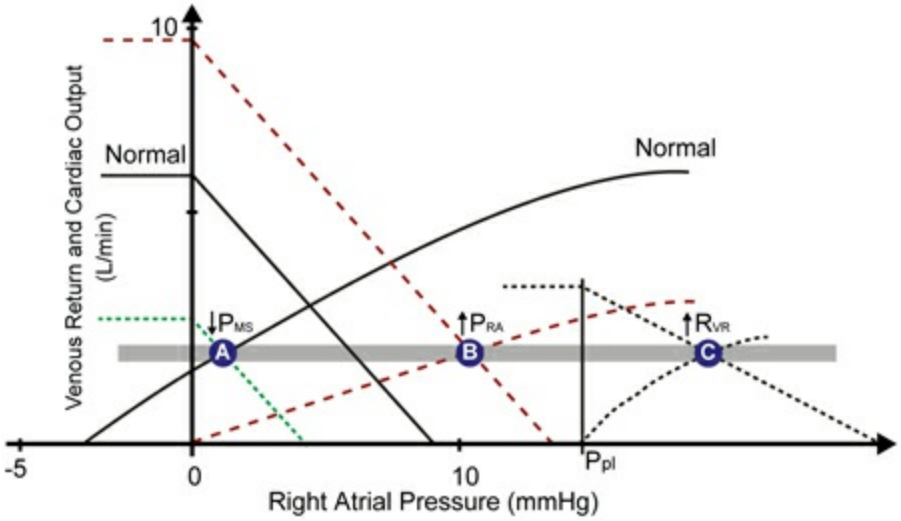

Fig. 9.2 . Mechanism of reduction in venous return. Identical level of reduction in venous return and cardiac output (grey bar) from three different mechanisms are shown in graphic form. (Point A) Hemorrhagic shock (dotted green line) has a decline in mean systemic venous pressure (Pms) and right atrial pressure (Pra), but without a change in resistance to venous return (Rvr). (Point B) Cardiogenic shock (red dotted line) results in an increased Pra, compensatory increase in Pms, but no change in Rvr. (Point C) Shock associated with increased resistance to venous return (black dotted line) as in a pneumothorax, increases Rvr, with a compensatory increase in Pms and an increase in Pra directly from the raised pleural pressure (Ppl). (Adapted with permission from Denault *et al.* [2] *)*

The effect of changing afterload or total peripheral resistance (TPR) on VR and CO is shown in **Figure 9.3 C**. The Pra changes with TPR are balanced. This results in a change in angle of the VR relationship. VR curve. A decrease in TPR (afterload) also decreases arterial pressure, which increases CO (upward shift cardiac function curve) and VR (clockwise change in angle of the VR relationship) (**Figure 9.3 C, point A to point C**). An increased TPR (afterload) also increases arterial pressure which reduces CO (downward shift of cardiac function curve) and returns less blood to the heart

(counterclockwise change in angle of the VR relationship) (**Figure 9.3 C, point A to point B**).

Shock as a result of compression of the inferior vena cava (IVC) in a pregnant patient is the best example of an acute increase in Rvr. Other examples include tamponade, pneumothorax, severe hyperinflation with intrinsic positive end-expiratory pressure (PEEP), and acute abdominal compartment syndrome. The VR curve for an increased Rvr is specific (**Figure 9.2 , point C**) and shows a modified VR slope from reduced VR, reduced CO (reduced Starling slope) and a compensatory increase in Pms. The increased pleural pressure, from a pneumothorax for instance, becomes the limiting factor to VR (**Figure 9.3 D, point A to point B**). A patient may develop shock in the presence of normal blood volume and cardiac function when an increase in Rvr prevents blood from reaching the heart. Relief of the pneumothorax will significantly increase CO, as the increased difference between Pms and Pra will favour greater VR. As a consequence, some patients may develop acute RV failure and pulmonary edema secondary to acute exacerbation of LV diastolic dysfunction following treatment of a tension pneumothorax or tamponade. [8] This mechanism explains the phenomenon called “re-expansion pulmonary edema”.

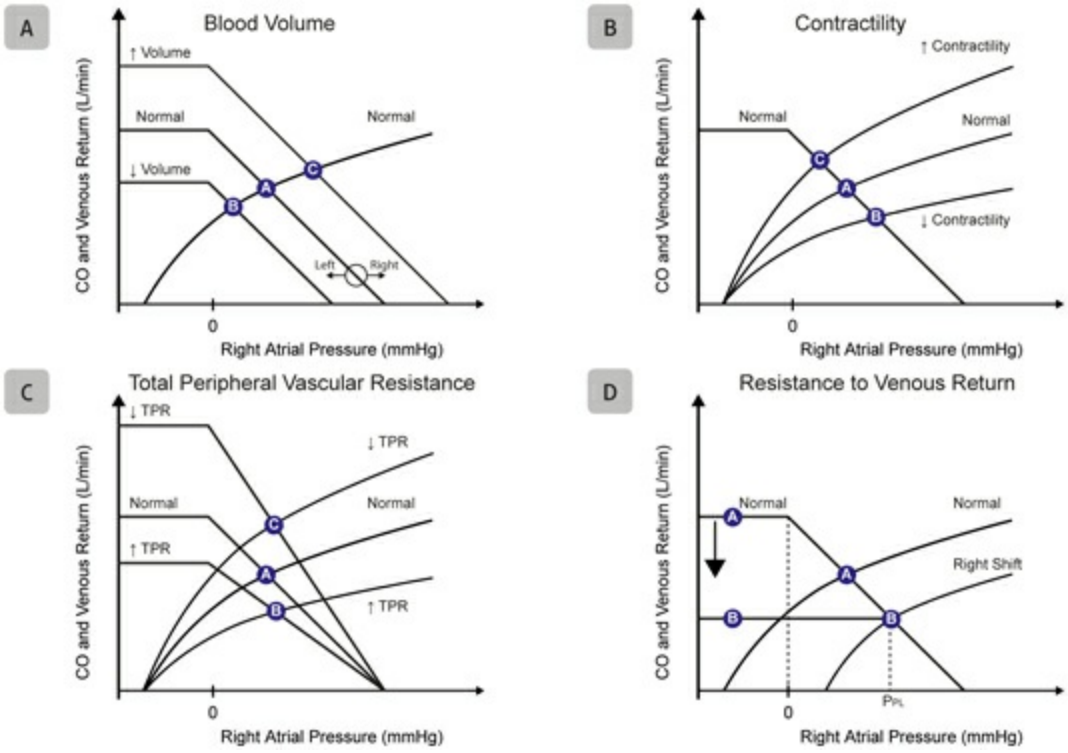

Fig. 9.3 . Determinants of venous return (VR). (A) Changes in blood volume or venous compliance alter the VR curve. The VR curve in hemorrhagic shock shows less VR (left shift with unchanged slope), reduced cardiac output (CO) (unchanged Starling slope), and reduced right atrial pressure (Pra). (B) Changes in inotropy affect the cardiac function curve, but not the VR curve. The cardiac function curve with systolic dysfunction shows reduced contractility and increased Pra, which reduces VR and results in a compensatory increase in mean systemic venous pressure (Pms). Increasing contractility by using inotropes will increase VR. (C) Changes in total peripheral resistance (TPR) or afterload alters systemic arterial pressure and VR to the heart, thus affecting both curves. This results in a rotation of the VR curve, clockwise with low TPR and counterclockwise for increased TPR. (D) In the presence of increased resistance to venous return (Rvr), VR is determined by the difference in Pms and the increased external pressure (pleural, pericardial, or abdominal) not the Pra (point B). The VR curve is also altered so the inflection of the plateau point is shifted downwards. The cardiac function curve is shifted to the right as cardiac function is impaired. To maintain VR, the Pms must increase significantly (not shown). Ppl, pleural pressure. (Adapted with permission from Denault *et al.* [2] *)*

There are situations, however, where more than one component of the VR curve is modified. For instance, inotropic agents will not only change contractility but will reduce Rvr through peripheral vasodilatation and, if the patient is hypovolemic, a reduction in Pms can also occur. [4] In addition, pulmonary conditions such as pneumothorax can also compress the heart creating a tamponade, and the associated hypoxemia can lead to pulmonary hypertension and an increased Pra. **Table 9.1** summarizes the most common causes of shock using the concept of VR.

Table 9.1 The Classification of Shock Using the Concept of Venous Return

Reduced mean systemic venous pressure (Pms)	Increased right atrial pressure (Pra)	Increased resistance to venous return (Rvr)
1. Hemorrhagic/hypovolemic shock	1. Systolic and diastolic dysfunction (ischemic or other)	1. Extrinsic
External bleeding	2. Acute valvular insufficiency	Supra-diaphragmatic:
Internal bleeding: thorax, abdominal	3. Outflow tract obstruction	tamponade
Distributive shock:	4. Pulmonary embolism	pneumothorax
2. Septic	5. Hypoxemia and hypercapnia	mediastinal tamponade
Non-septic:		severe hyperinflation (auto-PEEP)
anaphylactic		Infra-diaphragmatic:
endocrine: ↓ adrenal and thyroid function		abdominal compartment syndrome (intraluminal, extraluminal and parietal)
liver failure		2. Intrinsic
neurogenic and neuroaxial blockade		Vena cava obstruction from sutures, tumors, devices
pharmacological and toxic		
post CPR and CPB		
inflammatory: burns, pancreatitis, multiple trauma, SIRS		

Notes: CPB, cardiopulmonary bypass; CPR, cardiopulmonary resuscitation; PEEP, positive-end-expiratory pressure; SIRS, systemic inflammatory response syndrome. (Adapted with permission from Denault *et al.* [2] *)*

PRESSURE-VOLUME RELATIONSHIP

The relationship between ventricular function and hemodynamics is best described using pressure-volume (PV) loops (**Figure 9.4**). These curves present a graphic description of ventricular function by displaying the volume of a single cardiac cycle against pressure over time and include seven time-related events. Though the PV loop can be obtained through continuous pressure and volume measurement, this is rarely done in clinical practice. Individual determinants of the PV loop may be obtained by using: (1) echocardiography to assess the volume of cardiac chambers, (2) pulmonary artery catheter to estimate pulmonary artery pressures, and (3) an arterial pressure (Pa) catheter to measure systemic pressures. Estimates of LV end-systolic pressure (LVESP) from systolic arterial pressure (SAP) and the LV end-diastolic pressure (LVEDP) can be obtained from the pulmonary artery-derived “wedge” pressure at end asdiastole. The LV end-systolic volume (LVESV) from the end-systolic area and LV end-diastolic volume (LVEDV) can be estimated from the end-diastolic area using echocardiography. The stroke volume (SV), which is the difference between the LVEDV and the LVESV, can be calculated from the ratio of the CO obtained by Doppler or thermodilution divided by the heart rate (HR).

BEDSIDE ULTRASOUND

The use of bedside US can rapidly identify the mechanism of shock and thus determine the underlying etiology. If using transesophageal echocardiography (TEE), a mid-esophageal (ME) four-chamber view is the most efficient view. If using transthoracic or abdominal US, examination of the IVC is best (see **Figure 16.15**). [3] The stratification regarding the mechanism of reduced stroke volume can occur by examining the ME views, IVC size, PV loop estimation, and the concept of VR (**Figure 9.5**). In patients with low Pms, the ME four-chamber view will show a normal or small heart (A), small IVC (F) with respiratory variation in a spontaneously breathing

patient and reduced ventricular pressure and volume (J) in the PV loop, with medial shift of the VR curve (O).

In the presence of increased Rvr, the ME four-chamber view will show a normal or small heart (A) and variable sized IVC (G and H). In the setting of IVC obstruction near the right atrium, the distended IVC does not vary with ventilation (G); however, the PV loop (J) and the VR curve (O) will behave as if the patient has reduced Pms. These patients are typically unresponsive to fluid administration. If fluid is given, splanchnic venous congestion may occur causing elevated liver enzymes and lactate, and deterioration in renal function. In the setting of abdominal compartment syndrome, the IVC diameter is significantly reduced, also without respiratory variation (H). The elevated intra-abdominal pressure is transmitted to the pleural pressure; the PV loop has a normal or reduced stroke volume, but increased ventricular pressure (K). This is similar to diastolic dysfunction except that no major intrinsic myocardial dysfunction is present. Tamponade and pneumothorax usually distends the IVC and the increased external pressure displaces the PV loop upward (normal or reduced stroke volume) and reduces the VR curve slope (K).

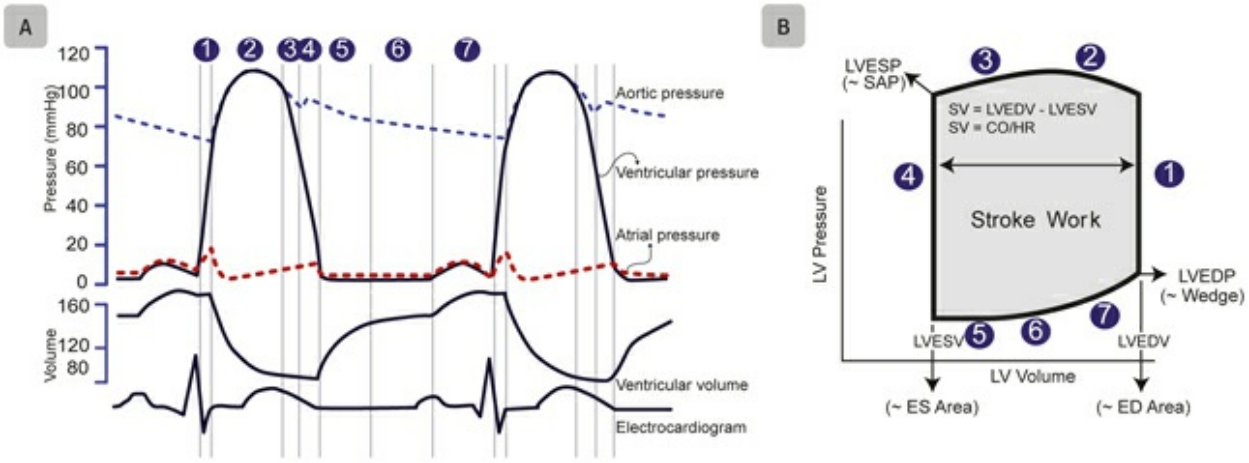

Fig. 9.4 . Pressure and volume during a cardiac cycle. (A) Left ventricular (LV) pressure and volume over time during a cardiac cycle is characterized by seven time-related events. Isovolumic contraction (1) is followed by early (2) and late (3) ejection. Diastole starts with isovolumic relaxation (4) followed by the early filling phase after the opening of the mitral valve (5), diastasis (6), and atrial contraction (7). (B) Individual determinants of the pressure-volume (PV) loop may be obtained by using (1) echocardiography to assess the volume of cardiac chambers, (2) pulmonary artery catheter to estimate pulmonary artery pressures, and (3) an arterial pressure catheter to measure systemic pressures. The LV stroke work corresponds to the area of the LV PV diagram (gray area). Changes in LV compliance can explain why the filling pressure does not always correlate with ventricular size. CO, cardiac output; ED, end diastolic; ES, end systolic; HR, heart rate; LVEDP, left ventricular end-diastolic pressure;

LVEDV, left ventricular end-diastolic volume; LVESP, left ventricular end-systolic pressure; LVESV, left ventricular end-systolic volume; SAP, systolic arterial pressure; SV, stroke volume. (Reproduced with permission from Denault *et al.* [9] *)*

In both forms of increased Rvr, the VR will be reduced and shifted to the right (P). An increase in Pra distends the IVC (I) without any respiration variation. The PV loop will depend on the mechanism of cardiogenic shock. In diastolic dysfunction (L), a medial shift of the PV loop is seen with increased LV pressure, but with normal or reduced volume. Systolic dysfunction shows a lateral shift (M) as the major characteristic of LV or RV systolic dysfunction is chamber dilatation. If either LVOTO or RVOTO is present, LV and RV volume is reduced, but the intraventricular pressure is increased (N). Both these findings are also associated with non-ischemic mitral and tricuspid valve regurgitation, although here, the VR curve is displaced medially.

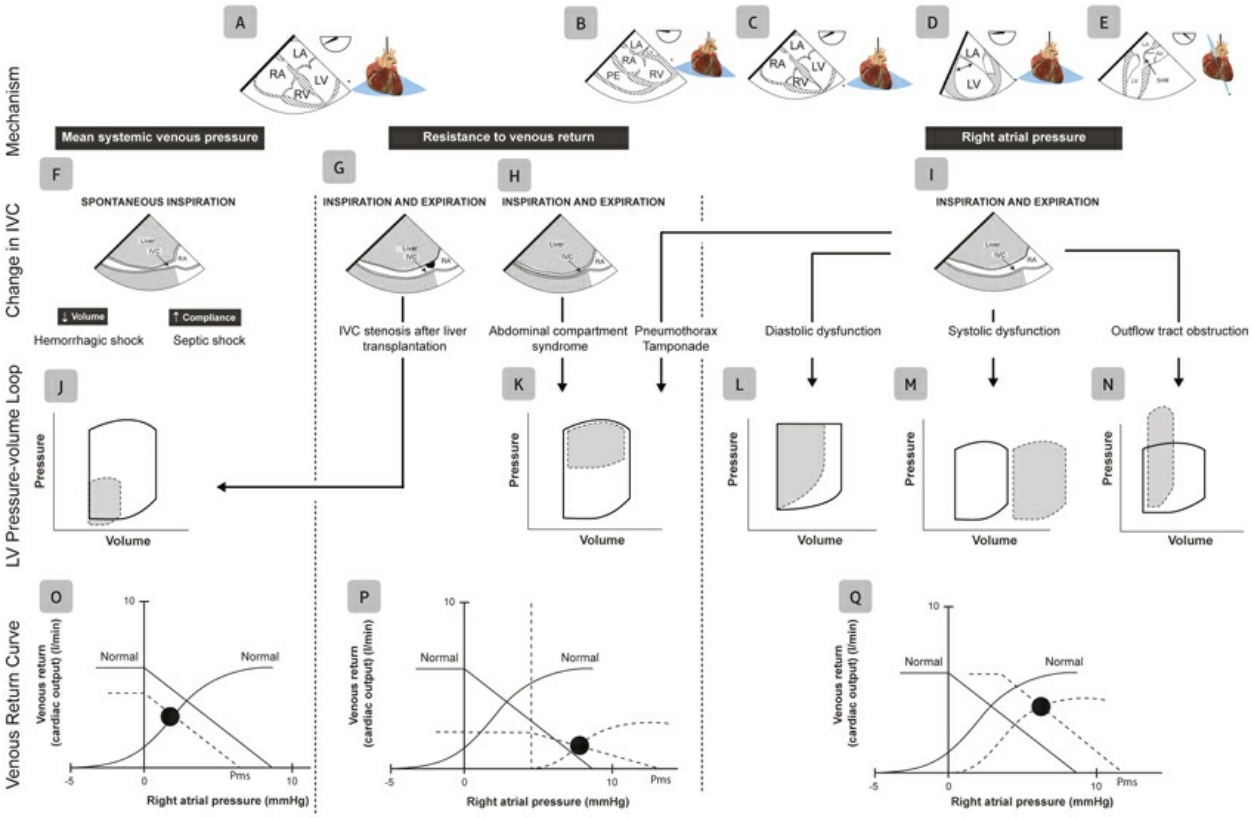

Fig. 9.5 . Mechanism of hemodynamic instability. Stratification of shock by integrating the transesophageal echocardiography examination of the inferior vena cava (IVC), with the pressure-volume (PV) loop and the concept of venous return is shown. See text for details. LA, left atrium; LV, left ventricular; PE, pericardial effusion; Pms, mean systemic venous pressure; RA, right atrium; RV, right ventricle. (Adapted from Denault *et al.* [2] , [9] *)*

INITIAL EVALUATION OF THE PATIENT IN SHOCK

When a patient is in shock, the mechanism and etiology are often determined through simple steps (**Figure 9.6**), such as obtaining a history, performing a physical examination, observation of the monitors, simple key laboratory values, and an electrocardiogram (ECG). For instance, patients in shock with a history of intracranial hemorrhage may have acute systolic and diastolic cardiac dysfunction from brain- heart syndrome (**Figure 9.7**). [10] In patients with septic shock vasodilatation, biventricular myocardial dysfunction[11, 12] and abdominal hypertension [13] can co-exist. Rapid physical examination should include documentation of the clinical signs of shock, evaluation of neurological and cardiopulmonary status, as well as assessment of abdominal compliance and an inspection of the extremities. Clinical observation of unequal pupils, skin rashes, stigmata of cirrhosis, localized bruising of the flanks (Grey Turner's sign) (see **Figure 16.24**), or leg edema can help narrow the diagnosis.

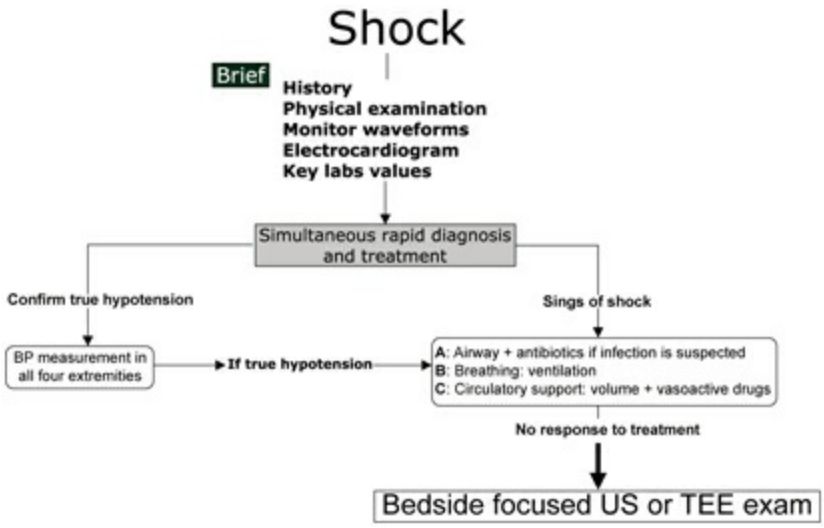

Fig. 9.6 . General approach to shock. In the presence of shock, a brief focused history and examination of the patient and the monitors is performed. In addition, key laboratory values and an electrocardiogram are obtained. Once hypotension is confirmed and the signs of shock are present, an ABC approach is proposed as described in the text. If these initial steps do not work, bedside focused ultrasound (US) or transesophageal echocardiography (TEE) focused echographic examination of the unstable patient should be considered. BP, blood pressure. (Adapted with permission from Denault *et al.* [2] *)*

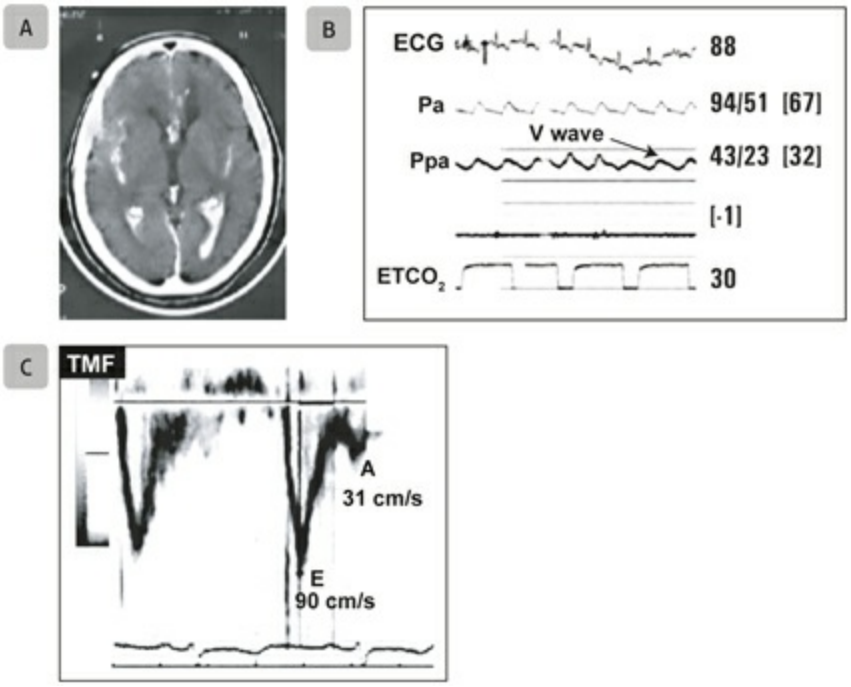

Fig. 9.7 . Brain–heart syndrome. Left ventricular diastolic dysfunction occurred in a hemodynamically unstable 37-yearold female with subarachnoid hemorrhage. (A) Brain computed tomography scan demonstrates an intraventricular bleed. (B) Hemodynamic data shows a heart rate of 88 beats/min, arterial pressures (Pa), pulmonary artery pressures (Ppa) with a prominent "V" wave on the wedged tracing. However, no significant mitral regurgitation was seen on color Doppler imaging (not shown). (C) Pulsed wave Doppler of transmitral flow (TMF) reveals a high E/A ratio suggesting diastolic dysfunction. A, late diastolic TMF velocity; E, early diastolic TMF velocity; ECG, electrocardiogram; ETCO2, end-tidal carbon dioxide. (Adapted with permission from Denault *et al*.9)

A: https://youtu.be/yt2LWrBhsB4

B: https://youtu.be/hr_wqrqHifA

C: https://youtu.be/bob66OJEgsE

Observation of monitors can also orient the clinician toward a specific mechanism. Attention is given to the ECG looking for arrhythmias, signs of ischemia, and some specific ECG abnormalities (**Figure 9.8**). The aspect of the arterial pressure waveform (**Figure 9.9**), respiratory waveform (**Figure 9.10**) and the presence of a "V" wave on the right atrial or pulmonary artery catheter waveforms (**Figures 9.7 and** 9.11) may offer important clues. Laboratory tests, such as a complete blood count, electrolytes, glucose, troponin, and blood gases, also provide valuable information, however, these results are rarely immediately available unless point-of-care laboratory testing is used.

Once all of the above elements have been obtained, it is still important to verify if the arterial pressure is truly reduced. Blood pressure should be measured in all four extremities because patients can have severe vascular disease and the brachial artery values may be underestimated. Any pressure discrepancy that goes unrecognized can lead to the inappropriate use of vasoactive agents. In addition, for unclear reasons, the use of vasoactive agents can cause significant radial to femoral arterial pressure gradients. [14] , [15] Measurement of the pressure gradient across the mitral valve, when mitral regurgitation is present, can be used in some patients to identify non-invasively this commonly unrecognized problem (**Figure 9.12**).

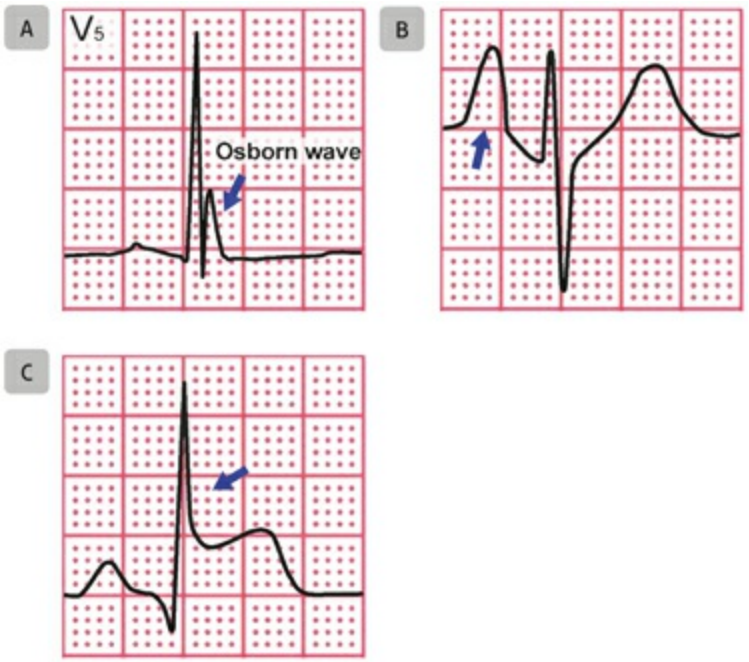

Fig. 9.8 . Electrocardiographic changes. (A) Osborn wave is a positive deflection at the junction

between the QRS complex and the ST segment. It may be present in hypothermia (<32°C), hypercalcemia, and brain injury. (B) Pulmonale P wave is a peaked P wave (>2.5 mm tall) that indicates atrial enlargement often seen with cor pulmonale. (C) An elevated ST and T wave may be present with acute myocardial ischemia and heart-brain syndrome. (Adapted with permission from Denault *et al.* [2])

B: https://youtu.be/QNnnQ3I-_qw

INITIAL MANAGEMENT OF THE PATIENT IN SHOCK

Once true hypotension is confirmed and signs of shock are present, airway (A) management, ventilation or breathing support (B), and circulatory (C) support are undertaken (**Figure 9.6**). In the "A" category (airway management), one should also include antibiotics as this is the only efficacious treatment for septic shock. This is important because the mortality in septic shock is 6-7% per hour [16] compared to 1% per hour in aortic dissection, despite the fact that both conditions can cause severe hypotension. [17] Blood cultures should be drawn before the expeditious administration of broad-spectrum antibiotics. The "B" stands for "breathing" or ventilatory support. Inadequate ventilation, if acute and uncorrected, may lead to hypercapnia, pulmonary hypertension, increased Pra and RV failure in susceptible patients. Supportive ventilation should be adjusted for the underlying condition. Many acute hemodynamically unstable conditions have reduced Pms, therefore fluid administration should always be considered as an initial step to support the "C" circulation in certain conditions (such as LV and RV systolic and diastolic failure) and in fluid overload with splanchnic congestion (see **Figure 4.39**). The selection of the type of fluid is controversial and remains a subject of debate, but usually crystalloid solutions are used. Finally, concomitantly, vasopressors are introduced with noradrenaline used as an agent of first-choice unless the patient has symptomatic bradycardia or severe LV dysfunction. [18] If these initial steps lead to a successful restoration of the arterial pressure and the mechanism of shock is clearly apparent, then the patient is closely followed. If however, this

approach fails and increasing vasoactive support is required, then bedside US examination should be performed at this time. [19]

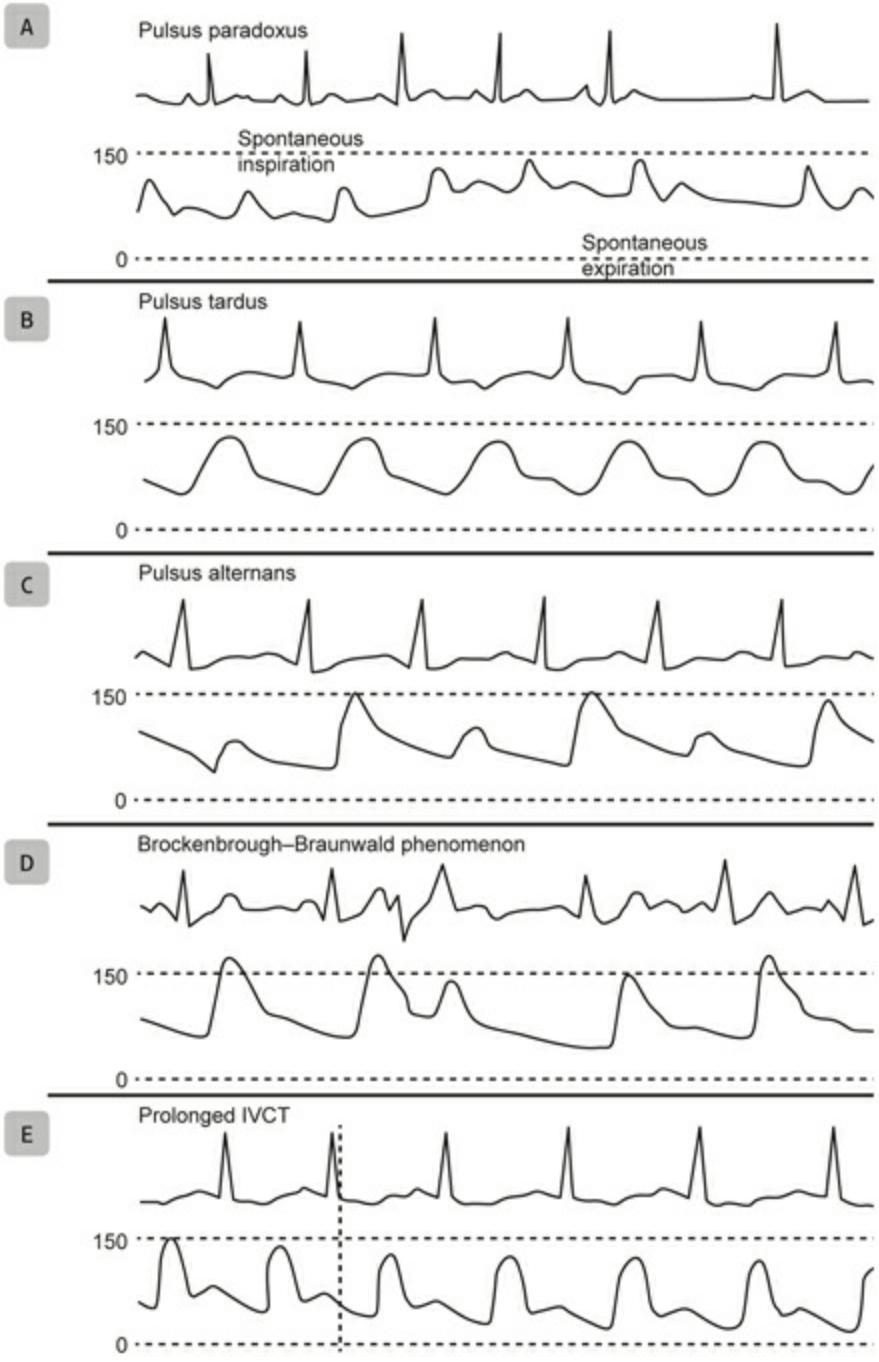

Fig. 9.9 . Arterial pressure waveforms. (A) Pulsus paradoxus is the respiratory variation of the pressure waveform which can be present with all three mechanisms of shock: (1) reduced mean systemic venous pressure from hypovolemia; (2) increased right atrial pressure from severe right heart failure with an under-filled left ventricle (LV); and (3) increased resistance to venous return from severe bronchospasm. (B) Pulsus tardus is a slow rising pulse with an anacrotic notch that is typically

associated with aortic stenosis but can be present in severe LV failure. (C) Pulsus alternans is alternating weak and strong arterial waveforms that are often associated with severe LV failure. (D) Brockenbrough–Braunwald phenomenon is the decrease in arterial pressure associated with the first systole after a premature ventricular contraction, which is pathognomonic of left ventricular outflow tract obstruction. (E) Prolonged isovolumic contraction time (IVCT) causes a delay between the QRS and the beginning of the arterial pressure waveform that can be seen in LV failure. (Reproduced with permission from Denault *et al*.2)

A: https://youtu.be/EdINIHyqa3M

C: https://youtu.be/qnogNOjvm0Y

E: https://youtu.be/n1bQEQsN_VI

B: https://youtu.be/zAOfBtNcR94

D: https://youtu.be/dTstrLYBn0Q

E: https://youtu.be/637ITIH1-H8

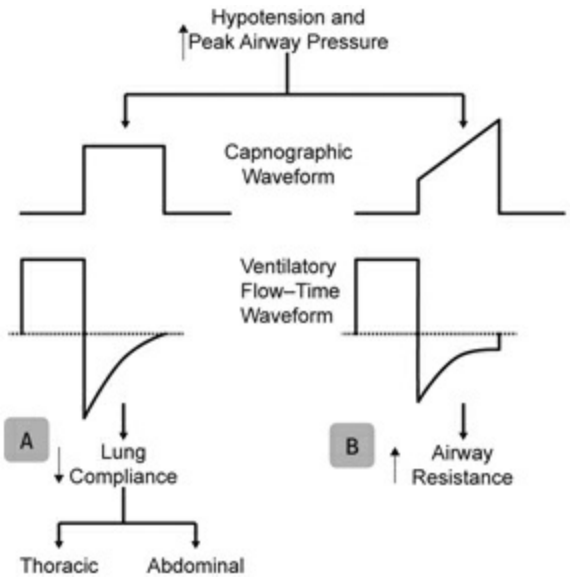

Fig. 9.10 . Capnography and ventilator flow-time waveforms. High airway pressure increases resistance to venous return, resulting in hypotension, the cause of which can be differentiated by inspection of both the capnography and ventilator flow-time waveforms. (A) With reduced lung compliance from either thoracic or abdominal causes, the capnograph waveform is normal with a horizontal expiratory phase and the ventilator flow-time waveform is normal or with shortened expiration. (B) With increased airway resistance, the capnograph waveform shows a typical prolonged expiratory phase or oblique slope which is also reflected in the prolonged ventilator flow-time waveform. In this situation, a rapid respiratory rate may cause intrinsic positive-end expiratory pressure (PEEP) or auto-PEEP to develop. Disconnecting the endotracheal tube from the ventilator or prolonging the expiratory time can correct the hypotension if the mechanism is auto-PEEP. (Reproduced with permission from Denault *et al.* [2] *)*

B: https://youtu.be/byalEMEfOso

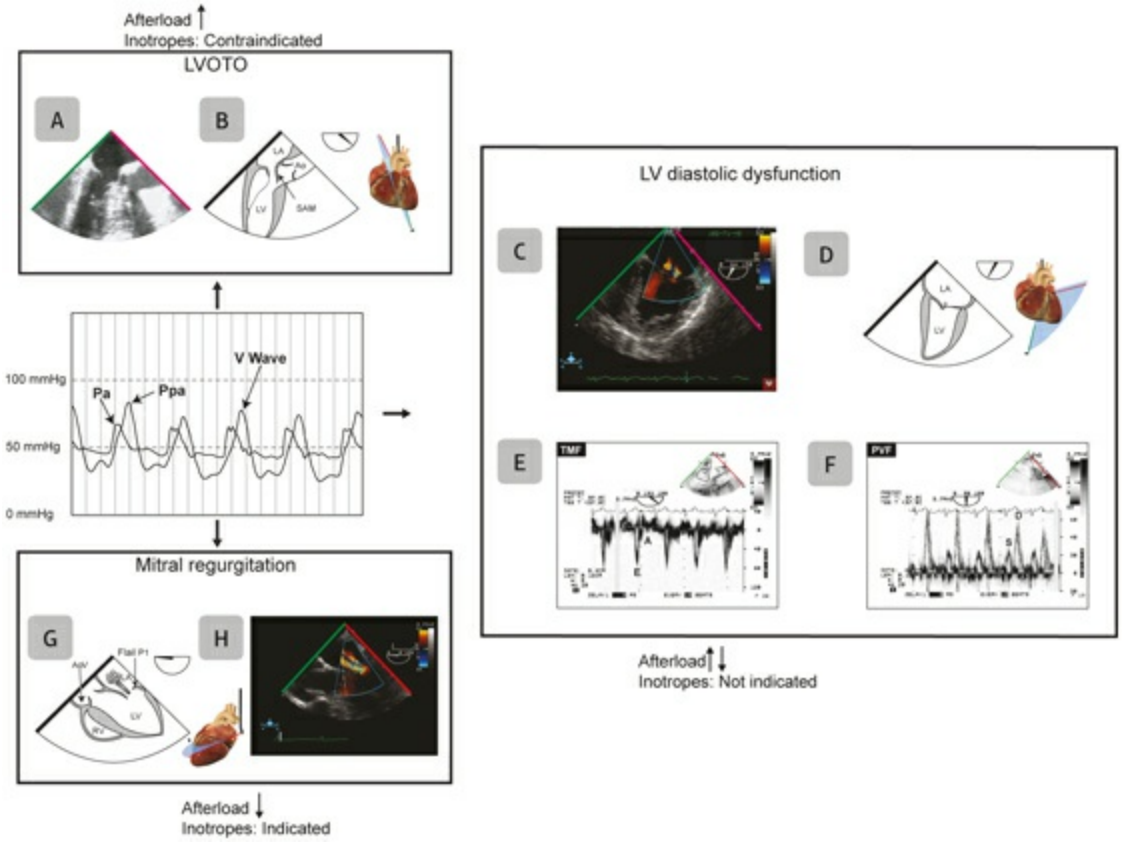

Fig. 9.11 . V wave. A "V" wave on the pulmonary artery pressure (Ppa) can result from mitral regurgitation (MR) and/or severe left ventricular (LV) diastolic dysfunction. (A,B) When MR is from left ventricular outflow tract obstruction (LVOTO), the treatment consists of increasing afterload and reducing heart rate. In this situation, inotropes are contraindicated. (C-F) With severe LV diastolic dysfunction and preserved ejection fraction, inotropes are rarely useful. (G, H) However, in the presence of significant MR unrelated to LVOTO, inotropes, afterload reduction, and higher heart rate may be considered. Ao, aorta; AoV, aortic valve; LA, left atrium; P1, posterior leaflet; Pa, arterial pressure; PVF, pulmonary venous flow; RV, right ventricle; SAM, systolic anterior motion; TMF, transmitral flow. (Adapted with permission from Denault *et al.* [9])

A: https://youtu.be/q40kWSg4Was

A: https://youtu.be/rOZb8zTkQIc

C: https://youtu.be/pb3yy3htg3I

H: https://youtu.be/Ia-ilYWeRsA

H: https://youtu.be/L1-mfjG-4eY

ULTRASOUND-GUIDED RESUSCITATION

There have been several proposed approaches for the use of bedside US in patients with shock. These include the FOCUSED, [20] FATE, [21] FAST, [22] RUSH, [23] and HEARTscan [24] protocols (**Table 9.2**). Common to all these protocols is the use of point-of-care US, [25] which emphasizes the following three points: (1) the examination is performed at the bedside by the clinician managing the patient; (2) the dynamic images are correlated with the clinical picture; and (3) the examination can be repeated as often as needed to monitor progress. We suggest an approach that combines examination of the thorax, heart, abdomen, and vasculature. With the concept of VR and this integrated approach, the clinician will be able to classify the mechanism of shock into one of the three fundamental mechanisms discussed earlier. [2] Both transthoracic echocardiography (TTE) and TEE can be used at the bedside. In non-intubated patients, TTE is always used first with TEE reserved for those who are intubated and in whom the information cannot be obtained from TTE. [26] There are three steps to follow when using US to manage a patient with shock: (1) determine which one of the three mechanisms (reduced Pms, increase Pra, and Rvr) alone or in combination are operating; (2) establish the etiology; and (3) evaluate response to therapy.

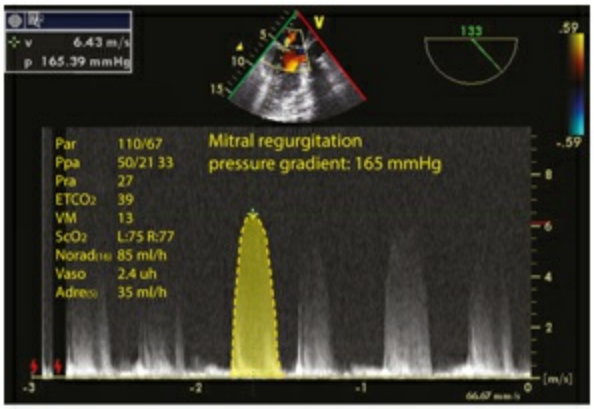

Fig. 9.12 . Systolic blood pressure. Hemodynamic instability occurred in a 54-year-old male following aortic valve repair from an aortic root abscess. Upon arrival in the intensive care unit, his systolic radial artery pressure (Par) was 110 mmHg and he was on adrenaline (Adre), noradrenaline (Norad), vasopressin (Vaso), and amiodarone for atrial fibrillation. His brain saturation (ScO_2) was normal. A transesophageal echocardiographic examination was performed that showed mitral regurgitation with a peak pressure gradient of 165 mmHg. Femoral artery pressure measurement confirmed the higher central aortic pressure. Adrenaline was stopped. $ETCO_2$, end-tidal carbon dioxide; Pra, right atrial pressure; Ppa, pulmonary artery pressure; VM, minute ventilation.

https://youtu.be/aF19ZwIC4-c

Table 9.2 Common Bedside Ultrasound Protocols

Protocol		Ultrasound location	Assessment
FOCUSED	Focused Cardiac Ultrasound[20]	TTE	Cardiac, hemodynamics
FATE	Focused Assessed Transthoracic Echo[21]	TTE + pleural	Cardiac, lung
FAST	Focused Assessment with Sonography in Trauma[22]	TTE, pleural, abdominal	Cardiac, lung, abdomen
RUSH	Rapid Ultrasound for Shock and Hypotension[23]	TTE, pleural, abdomen	Cardiac, lung, abdomen
HEARTscan	Hemodynamic Echocardiography Assessment in Real Time[24]	TTE views	Cardiac, hemodynamics

Notes: TTE, transthoracic echocardiography. Adapted with permission from Vegas *et al.* [3]

DETERMINING THE MECHANISM

The first step when dealing with the hemodynamically unstable patient who is unresponsive to standard care is to identify the underlying mechanism of shock. This can be determined rapidly with the use of echocardiography (TEE or TTE) by differentiating cardiogenic (increased Pra) from a non-cardiogenic cause (reduced Pms or increased Rvr). The ME four-chamber, inflow/outflow, and long-axis (LAX) views permit the rapid diagnosis of LV and RV dysfunction, LVOTO (**Figure 9.13**), RVOTO (**Figure 9.14**), pulmonary embolism (**Figure 9.15**), and acute valvular insufficiency. Acute LV or RV diastolic dysfunction is often present in hemodynamically unstable patients with elevated filling pressures [27] and can be associated with both normal and abnormal systolic ventricular function. Both left and right atrial dimensions are often increased. The ME views are also used to exclude thoracic causes of increased Rvr, such as regional or global tamponade (**Figure 9.16**), tension pneumothorax (**Figure 9.17**), unilateral lung over-inflation (**Figure 9.18**), and IVC occlusion (**Figure 9.19**) (see also **Figures 12.19 and 12.22**). Causes of abdominal compartment syndrome are better evaluated with abdominal ultrasound (see Chapter 15, Critical Care Examination of the Cardiovascular System).

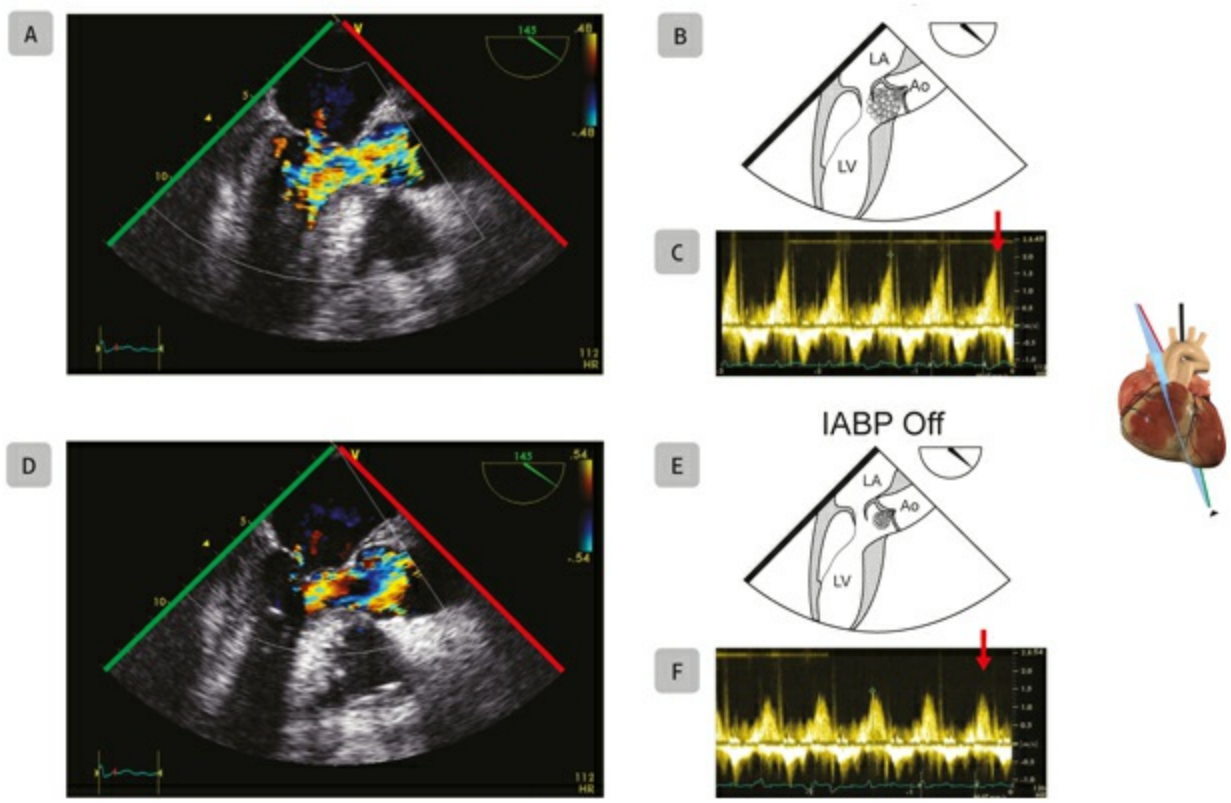

Fig. 9.13 . Left ventricular outflow tract (LVOT) obstruction. Persistent hemodynamic instability developed in a 64-year-old male with tamponade in whom an intra-aortic balloon pump (IABP) catheter was inserted. (A,B) The color Doppler mid-esophageal long-axis views show turbulent flow in the LVOT and (C) a late peak systolic pressure gradient with continuous wave Doppler. (D, E) When the IABP is turned off, the turbulent flow and (F) LVOT gradient are reduced. Ao, aorta; LA, left atrium; LV, left ventricle. (Reproduced with permission from Denault *et al.* [9] *)*

A: https://youtu.be/9fSsiYceugs D: https://youtu.be/wfp8d4lQdoA

In the presence of reduced Pms, reduced bi-ventricular dimension will be observed and in some patients, this can lead to LVOTO (see **Figure 12.21**) and RVOTO. [6] , [28] If the suspected cause of Pms reduction is increased compliance, TEE will be useful in the identification of causes of septic shock such as endocarditis (**Figure 9.20**) (see **Figures 8.18 – 8.20**), pneumonia and empyema (**Figure 9.21**) (see also **Figures 4.7 and 4.11**). Ultrasound is also helpful in identifying a reduction in Pms due to blood loss in the thorax (see **Figures 4.8 and 4.9**). However, abdominal sources of septic shock, such as peritonitis, cholecystitis, pyelonephritis, colitis, and blood loss in the abdomen (**Figure 9.22**) from upper gastrointestinal bleeding and retroperitoneal hematoma, are better assessed with US of the abdomen by using TEE (see Chapter 4, Extra-Cardiac Transesophageal Ultrasonography), surface US (see Chapter 15, Critical Care Examination of the Cardiovascular System), or computed tomography.

Another method of determining the mechanism of shock using echocardiography is through examination of the IVC and the application of Doppler interrogation of the hepatic venous flow (HVF) velocities (**Figure 9.23**). In the presence of reduced Pms, the IVC will be small with associated respiratory variations and the HVF velocities will be normal or increased. In the presence of increased Pra, the IVC will be distended and present abnormal HVF velocities. However, when increased Rvr is present, the IVC can be small if an intra-abdominal compartment syndrome is present, dilated if a distal IVC occlusion is present (see **Figure 12.22)** or if an intrathoracic cause such as acute tamponade or pneumothorax are present. However, in these situations, because VR cannot reach the heart, cardiac function will be

normal or hyperdynamic, but the HVF velocities will be significantly reduced or absent. This will be associated with normal or elevated pulmonary venous flow velocities because the left heart has no problem in receiving blood. [29]

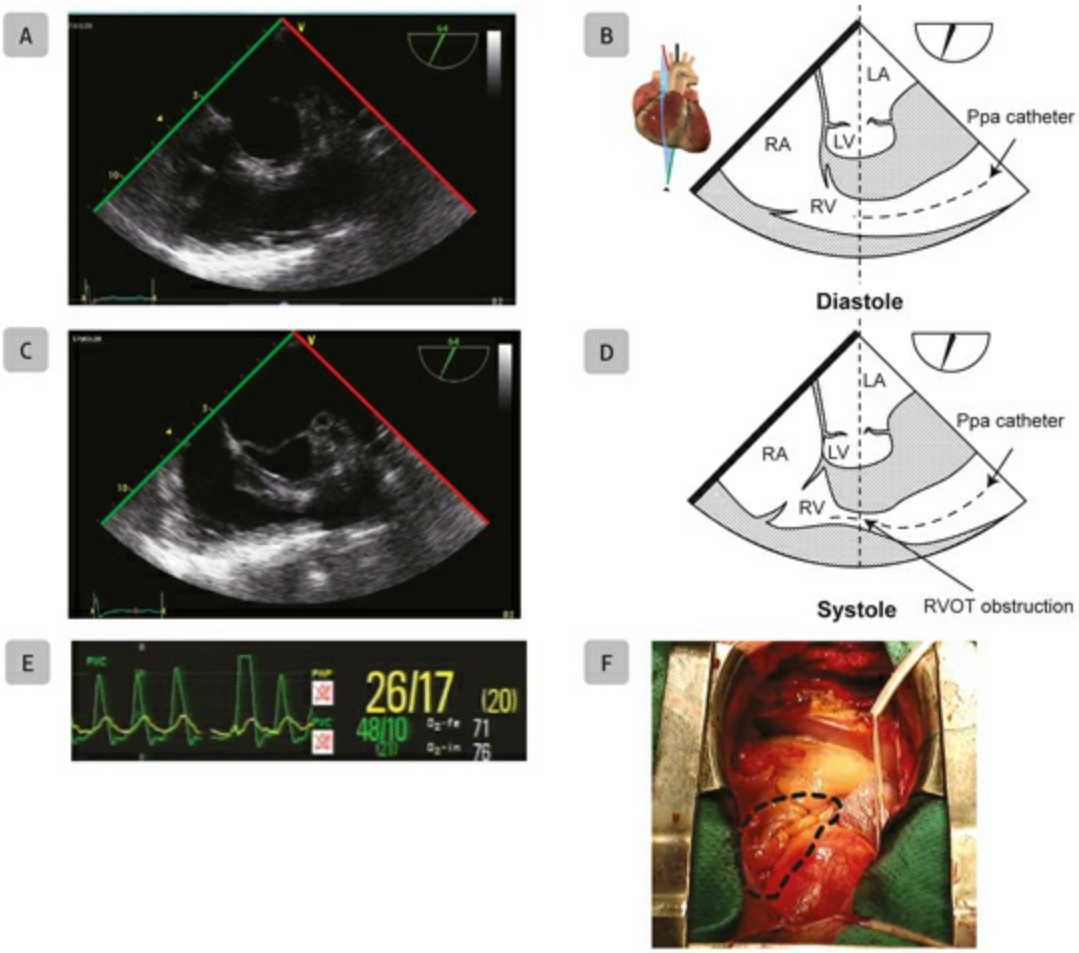

Fig. 9.14 . Right ventricular outflow tract (RVOT) obstruction. Mid-esophageal inflow-outflow views in (A,B) diastole and (C,D) systole show significant collapse of the RVOT during systole. (E) A 22 mmHg pressure gradient is present using combined right ventricular and pulmonary artery pressure (Ppa) waveforms. (F) The intraoperative aspect of the right ventricle (RV) shows a dimpling on the RVOT. LA, left atrium; LV, left ventricle; RA, right atrium. (Reproduced with permission from Denault *et al.* [28] *)*

A: https://youtu.be/MIc5MqQTfBQ

E: https://youtu.be/q3BnYBNi1uE

F: https://youtu.be/p-pGFf9BQtY

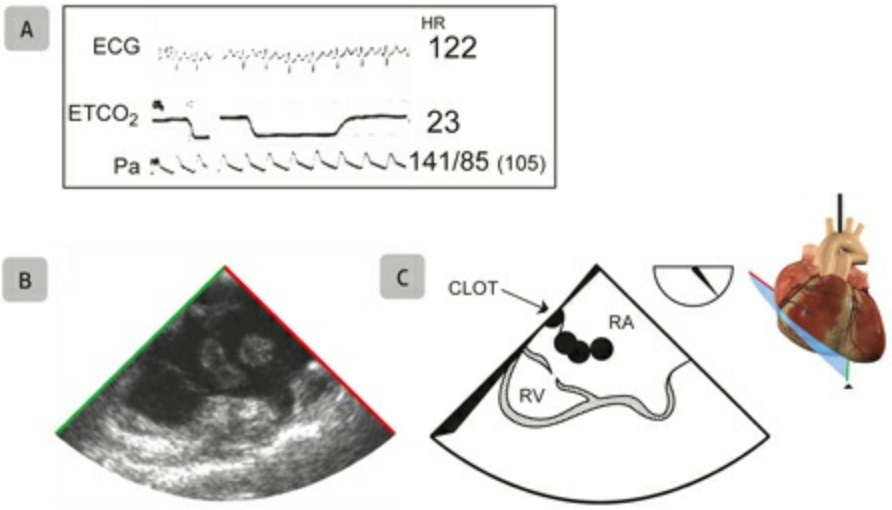

Fig. 9.15 . Acute pulmonary emboli. A 68-year-old female presents with dyspnea and hypotension 4 weeks after removal of a brain meningioma. (A) Hemodynamic data are shown with the patient on noradrenaline at 10 μg/ min. Note the peaked P-waves on the electrocardiogram (ECG) waveform suggesting dilatation of the right atrium (RA). (B, C) Mid-esophageal modified bicaval view at 120° shows highly mobile clots floating in the RA. $ETCO_2$, end-tidal carbon dioxide; HR, heart rate; Pa, arterial pressure; RV, right ventricle. (Reproduced with permission from Denault *et al.* [9])

A: https://youtu.be/hjKnlNG_eXM

B: https://youtu.be/IP8-CClsxQM

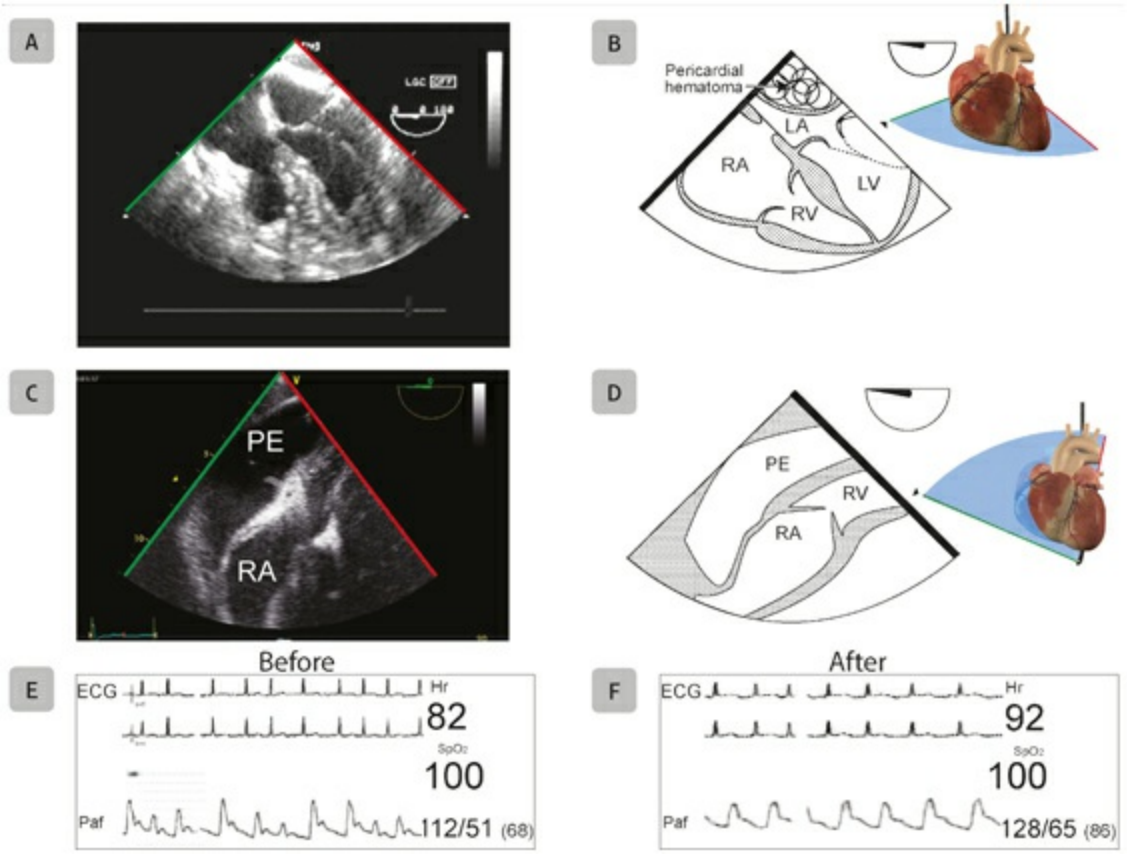

Fig. 9.16 . Cardiac tamponade. (A,B) Modified mid-esophageal four-chamber view shows left atrial (LA) compression, which was missed by transthoracic echocardiography. (C,D) Deep transgastric view shows right ventricular (RV) compression from a large pericardial effusion (PE). (E) Corresponding pulsus paradoxus is seen on the femoral arterial pressure (Paf) waveform with resolution (F) after drainage. ECG, electrocardiogram; Hr, heart rate; LV, left ventricle; RA, right atrium; SpO_2, oxygen saturation with pulse oximetry. (Adapted with permission from Denault *et al.* [9] *)*

A: https://youtu.be/ML6Nx9Ovfw4

C: https://youtu.be/7d6SW5sMy-c

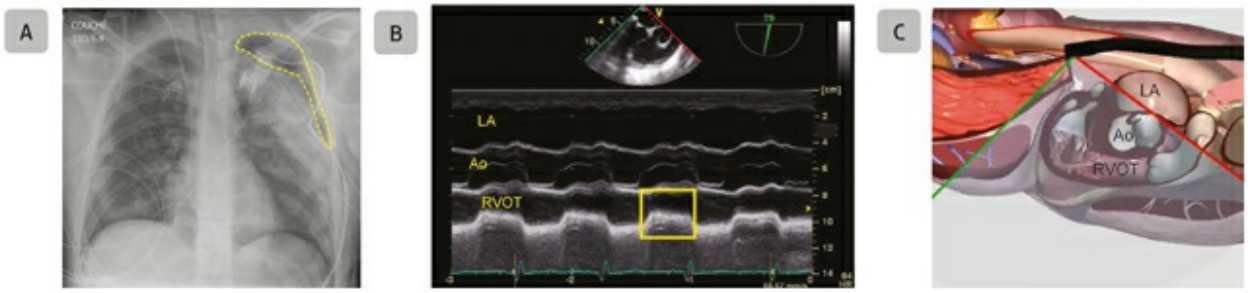

Fig. 9.17 . Left-sided pneumothorax. (A) Chest radiograph shows a left pneumothorax (dotted area) in a 19-year-old hemodynamically unstable male with a chest contusion admitted for organ donation. (B) Using transesophageal echocardiography, a mid-esophageal view of the right ventricular outflow tract (RVOT) shows diastolic obstruction of the RVOT with M-mode. This obstruction was from the anterior portion of the left pneumothorax compressing the RVOT. (C) The anatomic position of the ultrasound beam shows how the lingula portion of the left lung lies anterior to the RVOT using the Vimedix simulator. Ao, aorta; LA, left atrium. (Reproduced with permission from Vegas *et al.* [3])

B: https://youtu.be/MBat-Exgdyo

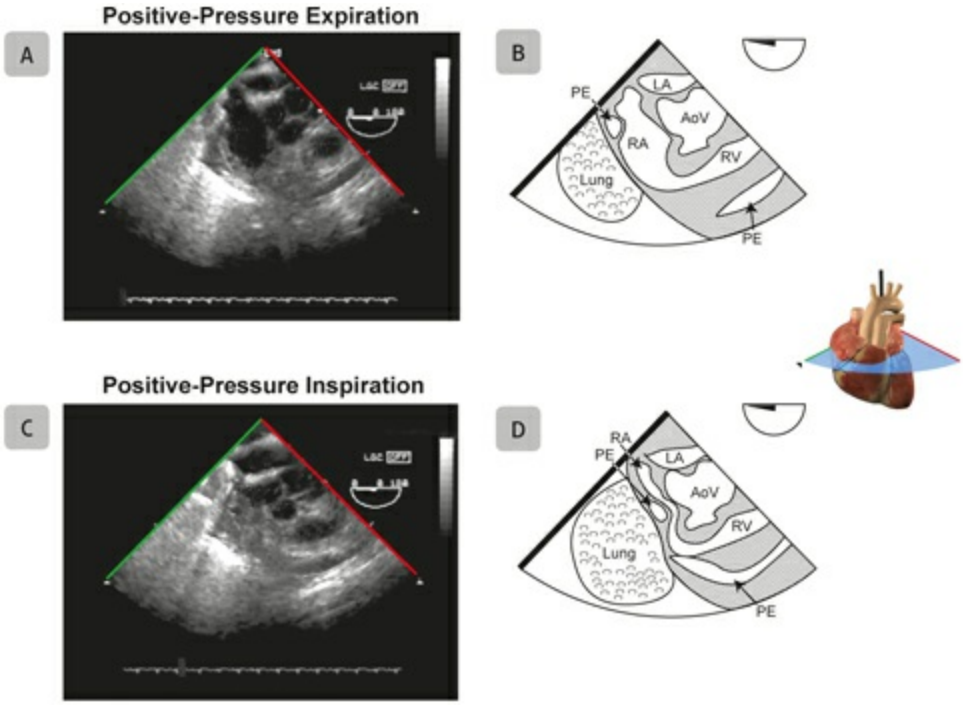

Fig. 9.18 . Compression of the right atrium (RA). Modified mid-esophageal four-chamber views during positive-pressure ventilation in (A,B) expiration and (C,D) inspiration shows extrinsic collapse of the

RA from over-inflation of the right lung. AoV, aortic valve; LA, left atrium; PE, pericardial effusion; RV, right ventricle. (Adapted with permission from Denault *et al.* [9])

A: https://youtu.be/J8a87ntvKTU

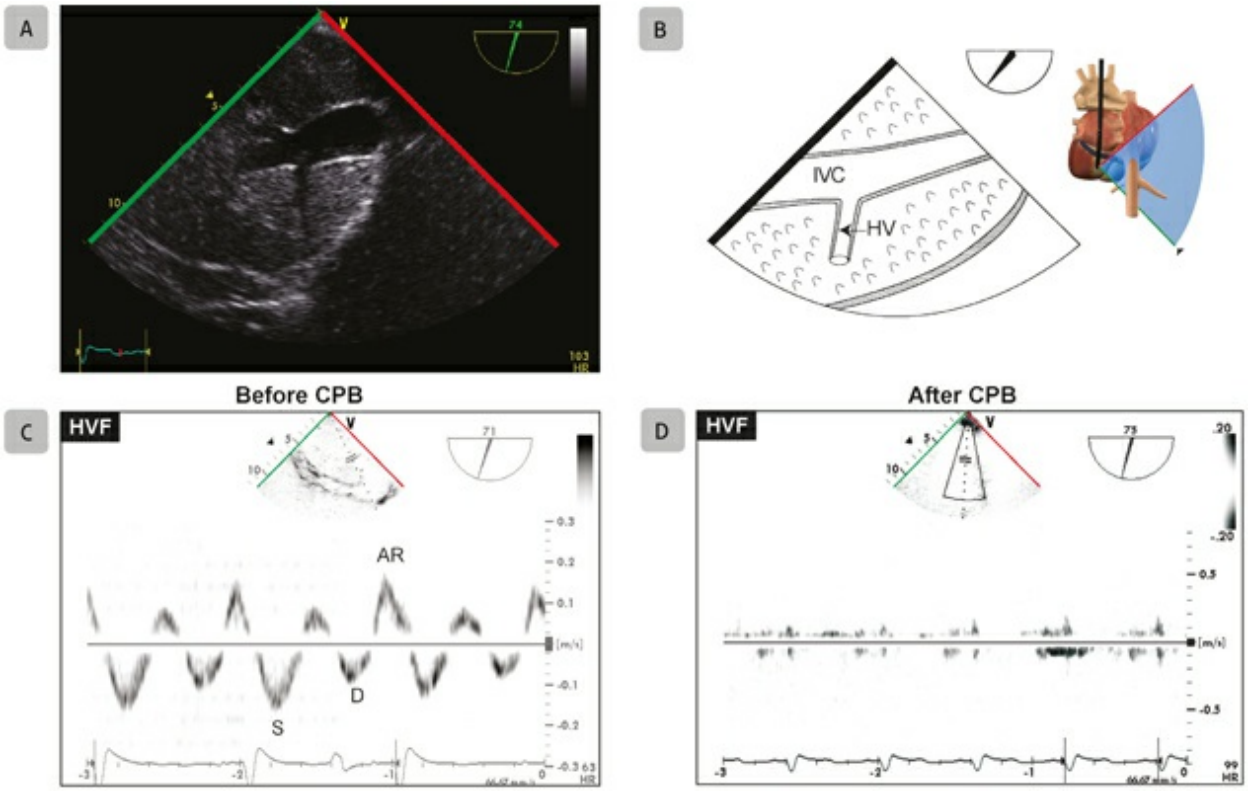

Fig. 9.19 . Inferior vena cava (IVC) occlusion during Fontan procedure. (A,B) Transgastric IVC long-axis view shows a dilated IVC following a Fontan procedure due to a partial occlusion at the level of the graft anastomosis to the IVC. (C,D) Hepatic venous flow (HVF) is present (C) before and is almost absent (D) after cardiopulmonary bypass (CPB). AR, atrial reversal HVF velocity; D, diastolic HVF velocity; HR, heart rate; HV, hepatic vein; S, systolic HVF velocity. (Reproduced with permission from Denault *et al.* [9])

A: https://youtu.be/k-ZvpvYRXNw

LIMITATIONS

Despite its multiple advantages there are limitations to the use of US in determining the causes of shock (**Table 9.3**). For example, in the case of a patient with bilateral auto-PEEP, measured values will be inaccurate. Fluid responsiveness can be evaluated with TEE by looking at the respiratory variation of the superior vena cava (see **Figure 15.14**). However, there are other methods in determining fluid responsiveness such as the effect of leg raising on capnography. [30 – 33]

Finally, although bedside US can estimate CO, it does not provide information on the adequacy of oxygen transport. This can only be ascertained using arterial and venous blood gas for mixed venous oxygen tension and the difference in veno-arterial carbon dioxide, [34] lactate levels, and non-invasive cerebral or somatic oxygen spectroscopy [35 – 37] However, the latter does not inform the clinician of the mechanism of reduced oxygen transport. Therefore, both oxygen transport variables and bedside US are essential when dealing with a patient in shock.

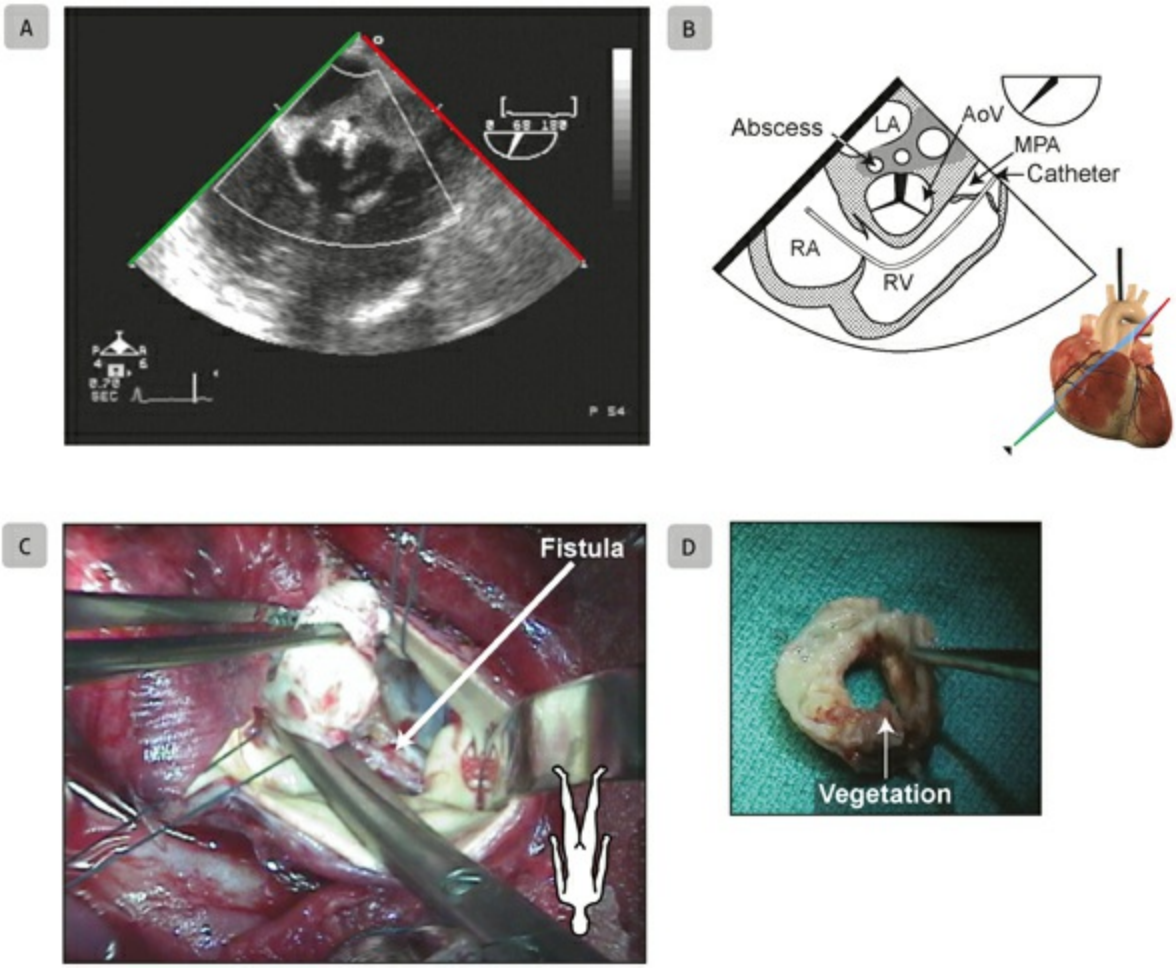

Fig. 9.20 . Endocarditis with aortic root abscess. A 46-year-old female with a bicuspid aortic valve (AoV) is diagnosed with endocarditis. A posterior abscess with a fistula was diagnosed from this mid-esophageal AoV short-axis view (A,B) and confirmed intraoperatively (C,D). LA, left atrium; MPA, main pulmonary artery; RA, right atrium; RV, right ventricle. (Reproduced with permission from Denault *et al.* [9])

A: https://youtu.be/01CdSgXH7qE

A: https://youtu.be/jHCAQJveZFM

C: https://youtu.be/qgIFNPR7YXc

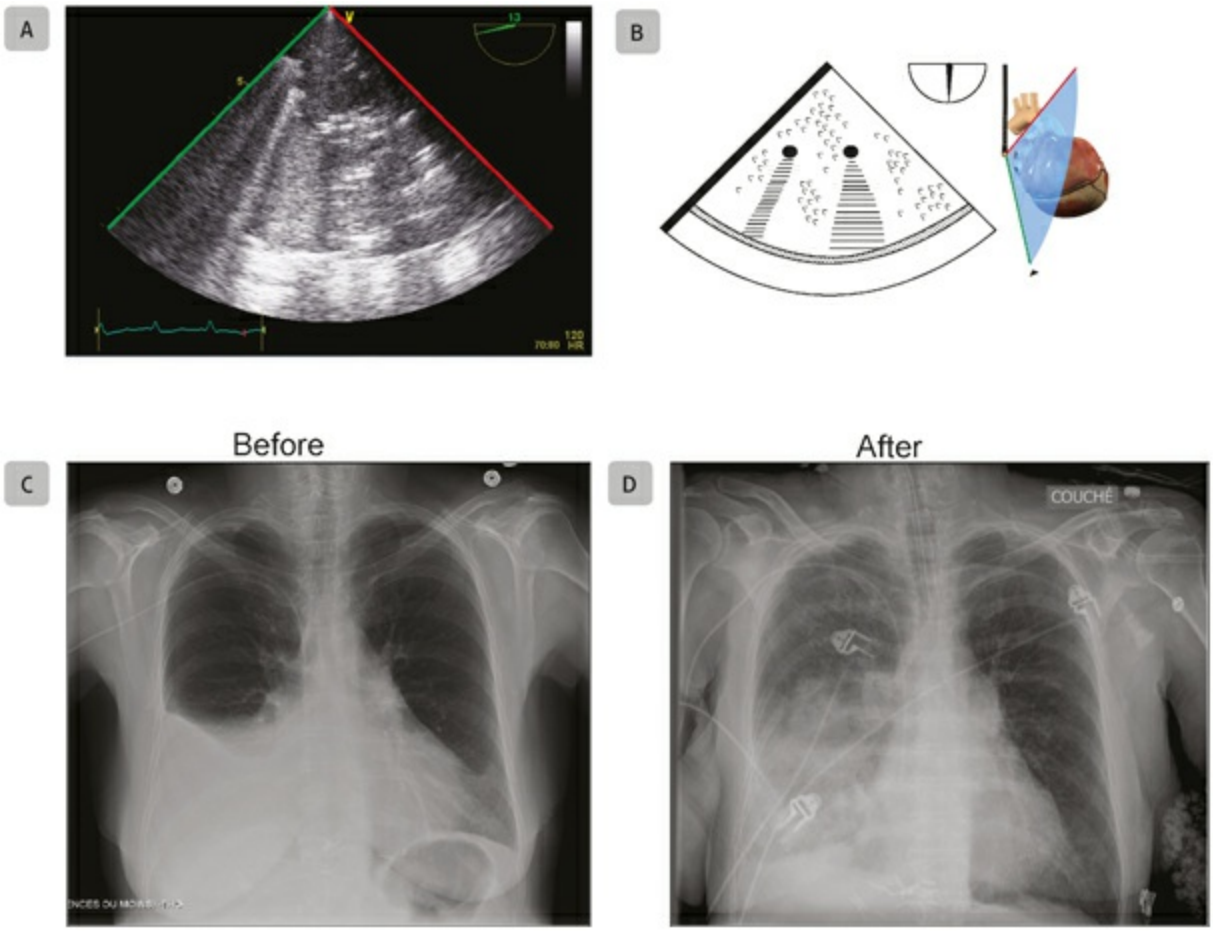

Fig. 9.21 . Pneumonia. A 58-year-old female is hemodynamically unstable after liver transplantation. (A,B) Transesophageal echocardiography images of the chest reveal significant consolidation of the lung parenchyma. Chest radiographs (C) before intensive care unit admission and (D) during hemodynamic instability show a new right-sided lung infiltrate. (Reproduced with permission from Denault *et al*.9)

A: https://youtu.be/7MXK8Eh9QqM

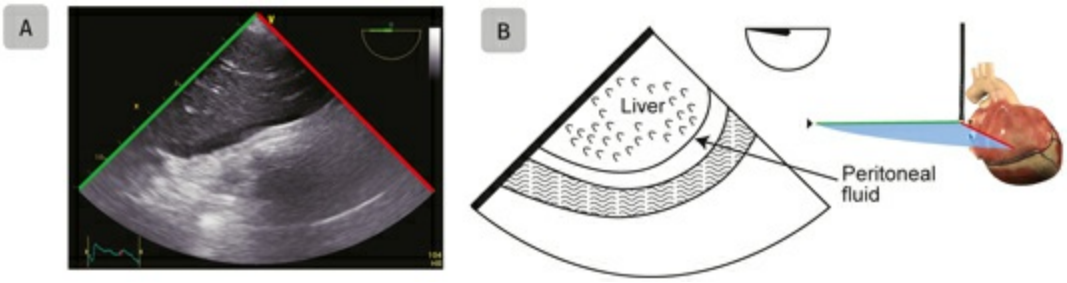

Fig. 9.22 . Peritoneal bleed. (A,B) Transgastric view shows a new echo-free space (blood) around the liver consistent with a new peritoneal bleeding from arterial dissection during the insertion of a femoral arterial cannula. (Reproduced with permission from Denault *et al.* [9])

A: https://youtu.be/3yu3P2AUzRg

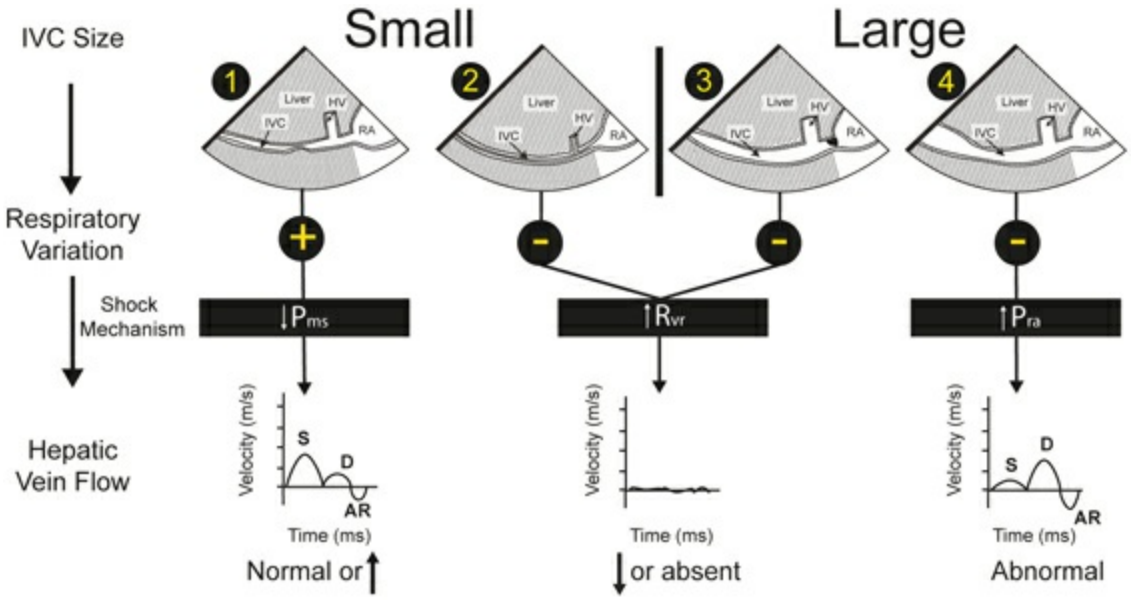

Fig. 9.23 . Shock mechanism. Algorithm to determine the mechanism of shock by evaluating the inferior vena cava (IVC) size, respiratory variation during spontaneous ventilation, and hepatic venous flow (HVF) is shown. In patients with reduced mean systemic venous pressure (Pms), the IVC is small with respiratory variation (1) and the HVF is typically normal or increased due to the reduced dimension of the hepatic vein (HV). In patients with increased resistance to venous return (Rvr), the IVC can be collapsed from an abdominal compartment syndrome (2) or distended due to a mechanical obstruction at the right atrial-IVC junction (3). In both situations, the HVF signal is significantly reduced, monophasic or absent. In a situation where the right atrial pressure (Pra) is increased, the IVC is dilated without respiratory variation (4) and the HFV will be abnormal with reduced systolic to diastolic velocity ratio. AR, atrial reversal velocity of the HVF; D, diastolic HVF velocity; RA, right atrium; S, systolic HVF velocity (Reproduced with permission from Vegas *et al.* [3])

Table 9.3 Limitations Using the IVC to Estimate Filling Pressure

Mechanical obstruction
Prominent Eustachian valve
Web, tissue, tumor, thrombus, aortic aneurysm
Foreign body, such as filters present in the IVC
narrowing of the IVC-right atrial junction
Athletic training
Large body surface area
Mechanical ventilation

Notes: IVC, inferior vena cava. Adapted with permission from Beigel *et al.* [38]

CONCLUSION

In summary, bedside US with TEE or TTE can be used to rapidly evaluate the mechanism, diagnose the etiology, and assess the response to therapy at the bedside. The relevance of echocardiography is further increased when combined with clinical information and other monitoring and diagnostic modalities.

REFERENCES

1. Guyton, A. C., A. W.Lindsey, B.Bernathy, and T.Richardson. 1957. "Venous return at various right atrial pressures and the normal venous return curve." *Am J Physiol 189*: 609–15.
2. Denault, A. Y., A.Vegas, and C.Royse. 2014. "A bedside clinical and ultrasound-based approaches to the management of hemodynamic instability - Part I: focus on the clinical approach: continuing professional development." *Can J Anesth 61*: 843–64.
3. Vegas, A., A. Y.Denault, and C.Royse. 2014. "A bedside clinical and ultrasound-based approach to hemodynamic instability - Part II: bedside ultrasound in hemodynamic shock: continuing professional development." *Can J Anesth 61*: 1008–27.
4. Jacobsohn, E., R.Chorn, and M.O'Connor. 1997. "The role of the vasculature in regulating venous return and cardiac output: historical and graphical approach." *Can J Anesth 44*: 849–67.
5. Funk, D. J., E.Jacobsohn, and A.Kumar. 2013. "The role of venous return in critical illness and shock - Part I: Physiology." *Crit Care Med 41*: 255–62.
6. Denault, A. Y., M.Chaput, P.Couture, Y.Hebert, F.Haddad, and J. C.Tardif. 2006. "Dynamic right ventricular outflow tract obstruction in cardiac surgery." *J Thorac Cardiovasc Surg 132*: 43–9.
7. Rochon, A. G., P. L.L'Allier, and A. Y.Denault. 2009. "Always consider left ventricular outflow tract obstruction in hemodynamically unstable patients." *Can J Anesth 56*: 962–8.

8. Tan, H. C., K. H.Mak, A.Johan, Y. T.Wang, and S. C.Poh. 2002. “Cardiac output increases prior to development of pulmonary edema after reexpansion of spontaneous pneumothorax.” *RespirMed 96*: 461–5.
9. Denault, A. Y., P.Couture, A.Vegas, J.Buithieu, and J. C.Tardif. 2011. *Transesophageal Echocardiography Multimedia Manual, Second Edition: A Perioperative Transdisciplinary Approach*. New York, NY: Informa Healthcare.
10. McLaughlin, N., M. W.Bojanowski, and A.Denault. 2005. “Early myocardial dysfunction following subarachnoid haemorrhage.” *Br J Neurosurg 19*: 141–7.
11. Jafri, S. M., S.Lavine, B. E.Field, M. T.Bahorozian, and R. W.Carlson. 1990. “Left ventricular diastolic function in sepsis.” *Crit Care Med 18*: 709–14.
12. Mitsuo, T., S.Shimazaki, and H.Matsuda. 1992. “Right ventricular dysfunction in septic patients.” *Crit Care Med 20*: 630–4.
13. Regueira, T., A.Bruhn, P.Hasbun, M.Aguirre, C.Romero, O.Llanos, et al. 2008. “Intra-abdominal hypertension: incidence and association with organ dysfunction during early septic shock.” *J Crit Care 23*: 461–7.
14. Denault, A., and A.Deschamps. 2009. “Abnormal aortic-to-radial arterial pressure gradients resulting in misdiagnosis of hemodynamic instability.” *Can J Anesth 56*: 534–6.
15. Dorman, T., M. J.Breslow, P. A.Lipsett, J. M.Rosenberg, J. R.Balser, Y.Almog, et al. 1998. “Radial artery pressure monitoring underestimates central arterial pressure during vasopressor therapy in critically ill surgical patients.” *Crit Care Med 26*: 1646–9.
16. Kumar, A., D.Roberts, K. E.Wood, B.Light, J. E.Parrillo, S.Sharma, et al. 2006. “Duration of hypotension before initiation of effective antimicrobial therapy is the critical determinant of survival in human septic shock.” *Crit Care Med 34*: 1589–96.
17. Meszaros, I., J.Morocz, J.Szlavi, J.Schmidt, L.Tornoci, L.Nagy, et al. 2000. “Epidemiology and clinicopathology of aortic dissection.” *Chest 117*: 1271–8.
18. De Backer, D., P.Biston, J.Devriendt, C.Madl, D.Chochrad, C.Aldecoa, et al. 2010. “Comparison of dopamine and norepinephrine in the treatment of shock.” *N Engl J Med 362*: 779–89.
19. Vincent, J. L., and D.De Backer. 2013. “Circulatory shock.” *N Engl J Med 369*: 1726–34.
20. Spencer, K. T., B. J.Kimura, C. E.Korcarz, P. A.Pellikka, P. S.Rahko, and R. J.Siegel. 2013. “Focused cardiac ultrasound: recommendations from the American Society of Echocardiography.” *J Am Soc Echocardiogr 26*: 567–81.
21. Holm, J. H., C. A.Frederiksen, P.Juhl-Olsen, and E.Sloth. 2012. “Perioperative use of focus assessed transthoracic echocardiography (FATE).” *Anesth Analg 115*: 1029–32.
22. Scalea, T. M., A.Rodriguez, W. C.Chiu, F. D.Brenneman, W. F.FallonJr, K.Kato, et al. 1999. “Focused Assessment with Sonography for Trauma (FAST): results from an international consensus conference.” *J Trauma 46*: 466–72.
23. PereraP., MailhotT., RileyD., MandaviaD.The RUSH exam: Rapid Ultrasound in SHock in the evaluation of the critically lll. *Emerg Med Clin North Am*2010; *28*: 29–56, vii.
24. Faris, J. G., M. G.Veltman, and C. F.Royse. 2009. “Limited transthoracic echocardiography assessment in anaesthesia and critical care.” *Best Pract Res Clin Anaesthesiol 23*: 285–98.
25. Moore, C. L., and J. A.Copel. 2011. “Point-of-care ultrasonography.” *N Engl J Med 364*: 749–57.
26. Hahn, R. T., T.Abraham, M. S.Adams, C. J.Bruce, K. E.Glas, R. M.Lang, et al. 2013. “Guidelines for performing a comprehensive transesophageal echocardiographic examination: recommendations from the American Society of Echocardiography and the Society of Cardiovascular Anesthesiologists.” *J Am Soc Echocardiogr 26*: 921–64.
27. Costachescu, T., A. Y.Denault, J. G.Guimond, P.Couture, S.Carignan, P.Sheridan, et al. 2002. “The hemodynamically unstable patient in the intensive care unit: hemodynamic vs. transesophageal echocardiographic monitoring.” *Crit Care Med 30*: 1214–23.

28. Denault, A. Y., Y.Lamarche, A.Rochon, and A.Deschamps. 2014. “Innovative approach in the perioperative care of the cardiac surgical patient in the operating room and the intensive care unit.” *Can J Cardiol 30* (12 Suppl.): S459–11.
29. Hulin, J., P.Aslanian, G.Desjardins, M.Belaïdi, and A. Y.Denault. 2016. “Critical importance of hepatic venous bloodflow Doppler assessment in patients in shock.” *Anesth & Analg Case Reports 6*: 114–20.
30. Maizel, J., N.Airapetian, E.Lorne, C.Tribouilloy, Z.Massy, and M.Slama. 2001. “Diagnosis of central hypovolemia by using passive leg raising.” *Intensive Care Med 33*: 1133–8.
31. Monnet, X., A.Bataille, E.Magalhaes, J.Barrois, C. M.Le, C.Gosset, et al. 2013. “End-tidal carbon dioxide is better than arterial pressure for predicting volume responsiveness by the passive leg raising test.” *Intensive Care Med 39*: 93–100.
32. Monnet, X., and J. L.Teboul. 2008. “Passive leg raising.” *Intensive Care Med 34*: 659–63.
33. Toupin, F., A.Denault, Y.Lamarche, and A.Deschamps. 2013. “Hemodynamic instability and fluid responsiveness.” *Can J Anesth 60*: 1240–1.
34. Johnson, B. A., and M. H.Weil. 1991. “Redefining ischemia due to circulatory failure as dual defects of oxygen deficits and of carbon dioxide excesses.” *Crit Care Med 19*: 1432–8.
35. Denault, A., A.Deschamps, and J. M.Murkin. 2001. “A proposed algorithm for the intraoperative use of cerebral near-infrared spectroscopy.” *Semin Cardiothorac Vasc Anesth 11*: 214–81.
36. Ghosh, A., C.Elwell, and M.Smith. 2012. “Review article: Cerebral near-infrared spectroscopy in adults: a work in progress.” *Anesth Analg 115*: 1313–83.
37. Harel, F., A.Denault, Q.Ngo, J.Dupuis, and P.Khairy. 2008. “Near-infrared spectroscopy to monitor peripheral blood flow perfusion.” *J Clin Monit Comput 22*: 31–43.
38. Beigel, R., B.Cercek, H.Luo, and R. J.Siegel. 2013. “Noninvasive evaluation of right atrial pressure.” *J Am Soc Echocardiogr 26*: 1033–42.

Chapter 10

Related Diagnostic Imaging Modalities

Kim-Nhien Vu, Anne S Chin and Carl Chartrand-Lefebvre

INTRODUCTION

Along with echocardiography, many other non-invasive imaging techniques can be used to assess cardiac pathology. From the routine chest X-ray (CXR) to multi-detector computed tomography (CT) and magnetic resonance imaging (MRI), each modality yields complementary information that can be used to more accurately diagnose heart disease and assess the repercussions on adjacent vasculature and lung. This chapter will present some imaging modalities that are alternatives or can complement ultrasonography.

CHEST RADIOGRAPHY

Despite the availability of advanced cross-sectional techniques for imaging the heart, the plain CXR, with its low cost, minimal radiation, and high accessibility, still remains the first imaging examination prescribed when cardiac pathology is suspected. Modifications of the cardiac silhouette on CXR can be the initial clue to cardiac disease. In addition, hemodynamic effects on pulmonary transparency and vasculature can also help determine disease severity. In this section, a basic review of cardiac anatomy seen on the plain CXR will be detailed, followed by a discussion of various pathological radiographic findings.

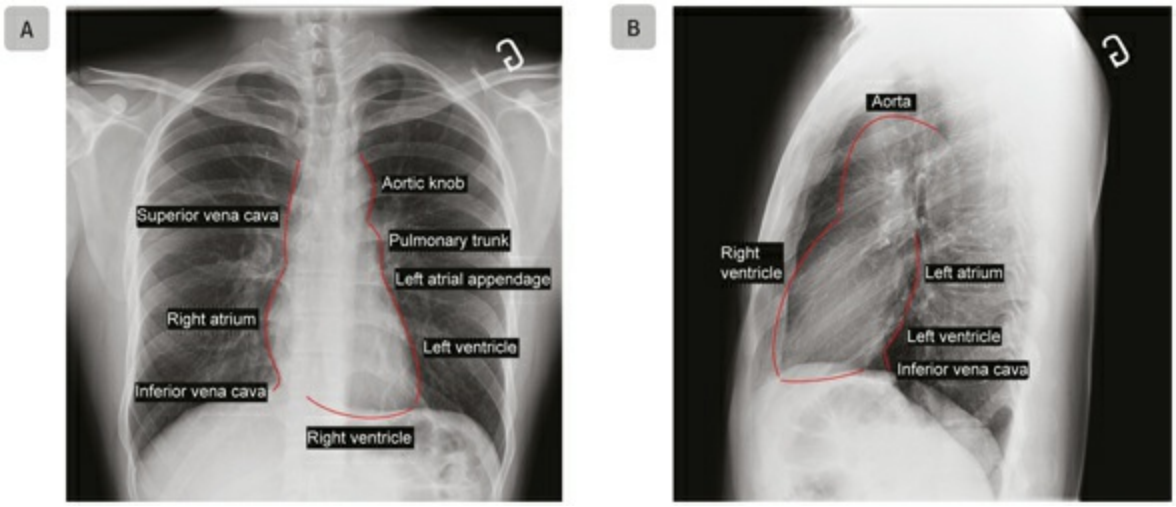

Fig. 10.1 . Heart borders on chest radiographs. A normal chest radiograph demonstrates the different heart borders on (A) frontal and (B) lateral views. The curvature of the left atrial appendage is not visible, unless the left appendage and/or the left atrium are dilated.

BASIC ANATOMY

Heart Borders

A CXR is a static two-dimensional projection of the three-dimensional heart. Understanding the anatomy behind each heart border on both frontal and lateral films is crucial for proper evaluation of normal and pathologic cardiac processes (**Figure 10.1**). In frontal views, the left ventricle (LV) forms the left heart border and the right atrium (RA) forms the right heart border; the lower border of the right ventricle (RV) is in contact with the diaphragm. Most of the normal left atrium (LA) is not seen on frontal films. In the lateral radiograph, the RV forms the anterior heart border with the LA and LV the upper and lower portions of the posterior heart border, respectively.

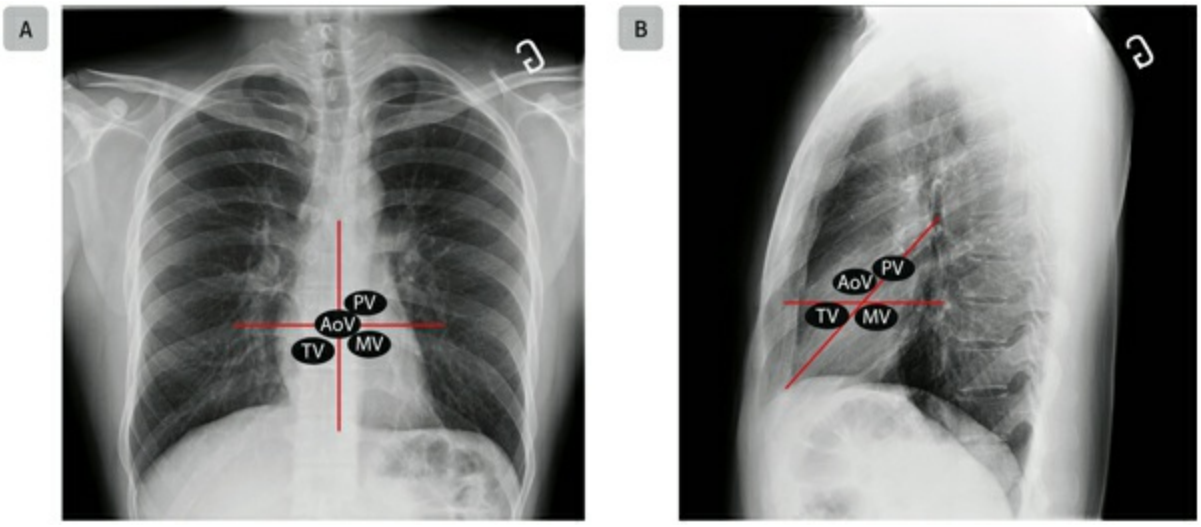

Fig. 10.2 . Valve location on chest radiographs. (A) A frontal film with imaginary lines (red lines) drawn vertically at the sternum and perpendicularly through the midpoint of the heart shows the estimated location of each valve. (B) A lateral film with an imaginary line (red line) drawn from the cardiac apex to the carina and a second line (red line) perpendicular to the sternum through the midpoint of the heart shows the estimated location of each valve. AoV, aortic valve; MV, mitral valve; PV, pulmonic valve; TV, tricuspid valve.

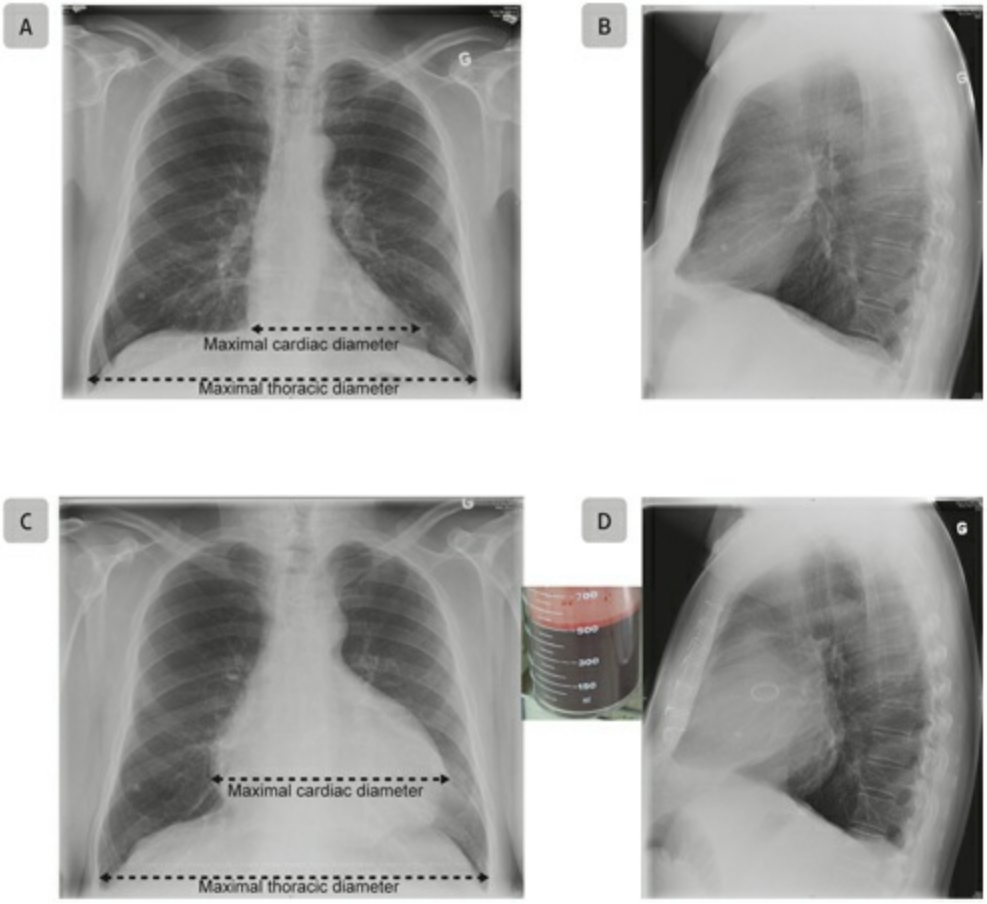

Fig. 10.3 . Cardiothoracic ratio. (A,B) Frontal and lateral chest radiographs of a 66-year-old male before aortic valve replacement depict a normal cardiothoracic ratio of less than 0.5, as calculated by taking the ratio of the maximal cardiac diameter (top black line) to the maximal thoracic diameter (bottom black line). (C,D) Postoperative tamponade is present with an increased cardiothoracic ratio in both the frontal and lateral chest radiographs. A total of 500 mL of pericardial fluid was removed.

Valve Location

Valve calcification and replaced valve(s) are often seen on CXRs. Exact identification of these valves can be made on both frontal and lateral views using anatomic landmarks (**Figure 10.2**). On the frontal film, a vertical line is drawn at the sternum and a second perpendicular line bisects the heart at the level of the aortic valve. The pulmonic valve appears in the upper left quadrant, the mitral valve in the lower left quadrant, and the tricuspid valve in the lower right quadrant, whereas the aortic valve can be seen lying within the intersection of both imaginary lines. On the lateral film, lines are drawn from the cardiac apex to the carina and perpendicular to the sternum to bisect the heart. The aortic valve appears in the upper anterior quadrant, the pulmonic valve near the upper posterior quadrant, the mitral valve in the lower posterior quadrant, and the tricuspid valve in the lower anterior quadrant.

PATHOLOGICAL FINDINGS

Heart Size

Frontal CXRs have been used to screen for cardiomegaly since 1919 when Danzer [1] initially described the cardiothoracic ratio. This is the ratio of the cardiac diameter (maximal horizontal distance from the right to left border of the cardiac silhouette) to the thoracic diameter (widest horizontal distance between the inner margins of the ribs). Classically, a normal cardiothoracic ratio in adults is less than 0.5, [1] with an enlarged heart suspected above this ratio (**Figure 10.3**). The cardiothoracic ratio can predict cardiomegaly with 70% accuracy. [2] Chest radiographs can also give clues to specific cardiac chamber enlargement.

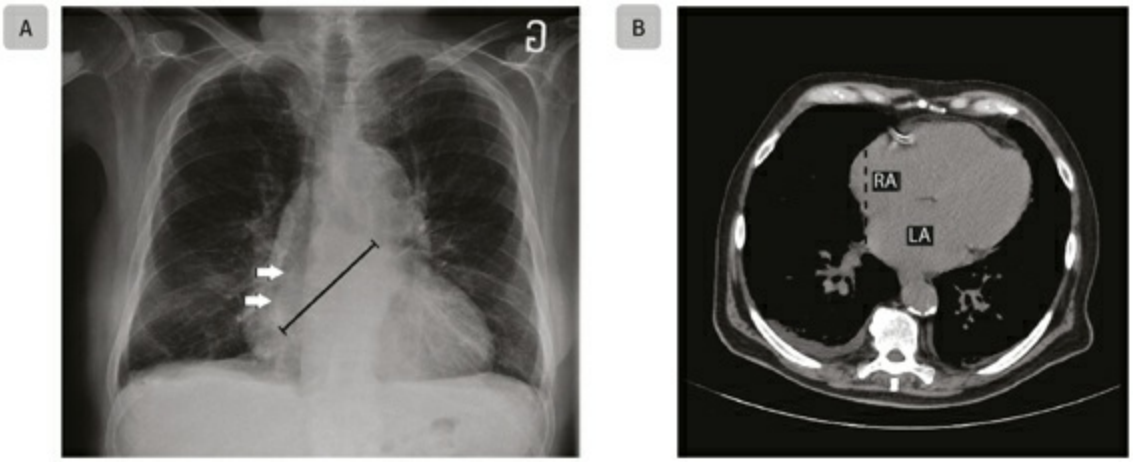

Fig. 10.4 . Heart chamber enlargements. (A) Frontal view of an 80-year-old male with left atrium (LA) enlargement depicts the double density sign, where the right border of an enlarged LA (arrows) can be seen near the normal right heart border. A measurement taken from the right lateral border of the LA to the inferior border of the left main bronchus (black line) is greater than 7 cm, suggesting enlargement of the LA. (B) Unenhanced axial computed tomography image of the same patient shows the right border of the enlarged LA displaced towards the right and creating a second density (dashed black lines) behind the right atrium (RA)

An enlarged LV is suspected when the left heart border is displaced inferiorly, posteriorly, or toward the left. A double density sign is seen on frontal films when the right lateral border of an enlarged LA is superimposed near or even beyond the normal right heart border. [3] , [4] A measurement taken from the right lateral border of the LA to the inferior border of the left main bronchus exceeding 7 cm predicts LA enlargement in 90% of pathological cases (**Figure 10.4**). [4] In severe cases, the right lateral border of the LA can extend to the right thoracic wall, causing splaying of the carina. This giant left atrium sign is pathognomonic for rheumatic disease, most commonly mitral regurgitation. The curvature of the left atrial appendage is usually not visible on the frontal CXR, unless it and/or the LA are dilated. Right atrial enlargement can be suspected when the right heart border is displaced toward the right of the spine on the frontal film. Finally, when the RV contacts more than one-fourth of the length of the distal sternum on the lateral film, or fills more than one-third of retrosternal clear space, enlargement is likely. When RV enlargement is severe, it can even be seen forming the right heart border on the frontal view (see **Figure 7.27**). [3] When the RV is externally compressed, indirect signs such as medial displacement of a pulmonary artery catheter can suggest the presence of a regional tamponade (see **Figure 5.19**).

Myocardium and Pericardium

Myocardial calcification can arise from previous infarction in association with a LV aneurysm. Pericardial calcifications, on the other hand, signal the sequelae of prior pericarditis. Such calcifications appear around the periphery of the heart silhouette, whereas myocardial calcification is located within the cardiac silhouette (**Figure 10.5**).

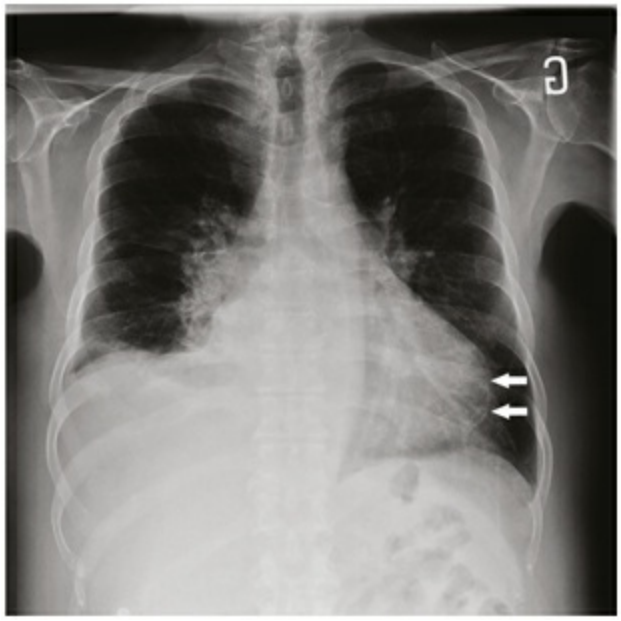

Fig. 10.5 . Myocardial calcifications. A frontal chest radiograph of a 76-year-old male with previous infarction demonstrates myocardial calcifications of the left ventricle (arrows) located within the heart silhouette. Small right pleural effusion can also be seen.

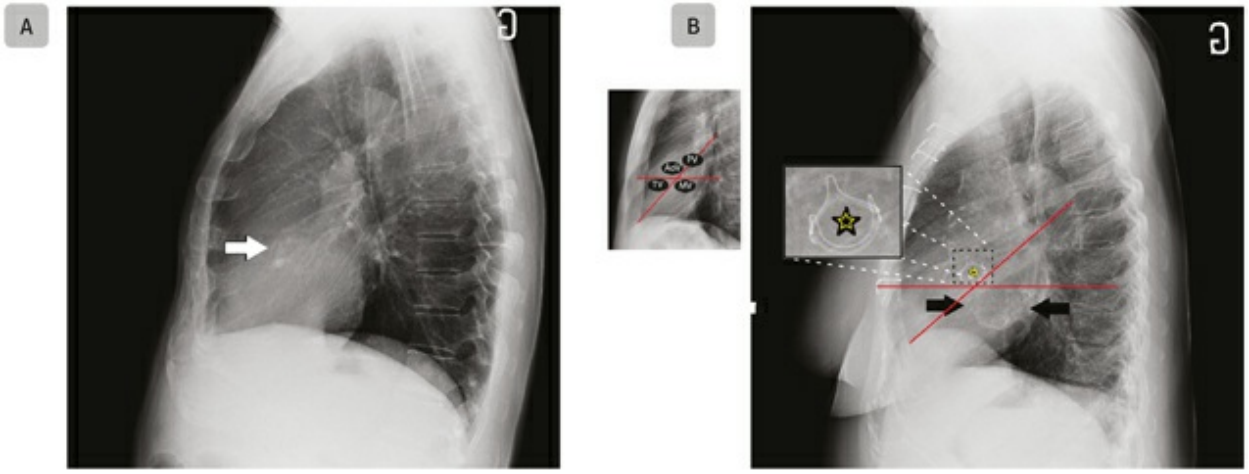

Fig. 10.6 . Valve calcifications. (A) A lateral chest radiograph of a 55-year-old male with severe aortic stenosis depicts important aortic calcifications (arrow) requiring valve replacement surgery. (B) A

lateral chest radiograph of a 74-year-old female with previous aortic valve (A) replacement (star) shows mitral annulus calcifications (black arrows). AoV, aortic valve; MV, mitral valve; PV, pulmonic valve; TV, triscupid valve.

Valves

Chest radiographs can also identify direct and indirect signs of valvulopathy. For example, dystrophic nodular calcifications of the aortic valve (AoV) in patients over the age of 35 years with premature or accelerated calcification are suggestive of bicuspid AoV stenosis (**Figure 10.6**). A significant amount of AoV calcification is predictive of severe stenosis needing valve replacement. The presence of both AoV and mitral valve (MV) calcifications suggests previous rheumatic heart disease or infective endocarditis is the likely aetiology. Mitral valve calcifications are usually a sign of chronic rheumatic disease, whereas mitral annulus calcification is related to degenerative changes (**Figure 10.6**). Although valvular and even coronary calcifications may be visible on CXRs, CT is more sensitive and accurate for the detection and localization of cardiac calcifications. Indirect signs of valvulopathy, such as aortic root dilatation and an enlarged LV from aortic regurgitation, may be present. Pulmonic valve stenosis can dilate the pulmonary trunk and left pulmonary artery.

Pulmonary Parenchymal Disease

The CXR also has the advantage of simultaneously informing on both cardiac and pulmonary disease. A common indication for ordering a CXR is the assessment for pulmonary edema, which can be the first clue to underlying cardiac dysfunction. An initial radiographic sign of pulmonary edema is cephalization of pulmonary vasculature, where visible vessels increase in number and in size in the upper lobes. In a normal upright CXR, the gravitational effect on pulmonary veins increases their prominence in lower lung lobes compared with the upper zones. With interstitial edema, thickening of interlobular septa (Kerley B-lines) appear as thin linear opacities extending a few centimeters perpendicular to the lung periphery. When seen transversely, thickened interstitium appears as bronchial cuffing in the perihilar regions. As pulmonary edema progresses, the perihilar alveolar opacities form a butterfly pattern. Finally, pleural effusions are an indication of more severe edema (**Table 10.1** and **Figure 10.7**). This is typically associated with B-lines using lung ultrasound (see **Figure 14.16**).

Table 10.1 Classification of Radiographic Signs of Pulmonary Edema

Grade	Left atrial pressure	Radiographic signs
I: Vascular redistribution	12–19 mmHg	Cephalization of pulmonary vasculature
II: Interstitial edema	20–25 mmHg	Kerley B-lines Peribronchial cuffing
III: Alveolar edema	>25 mmHg	Perihilar hazing Pleural effusion

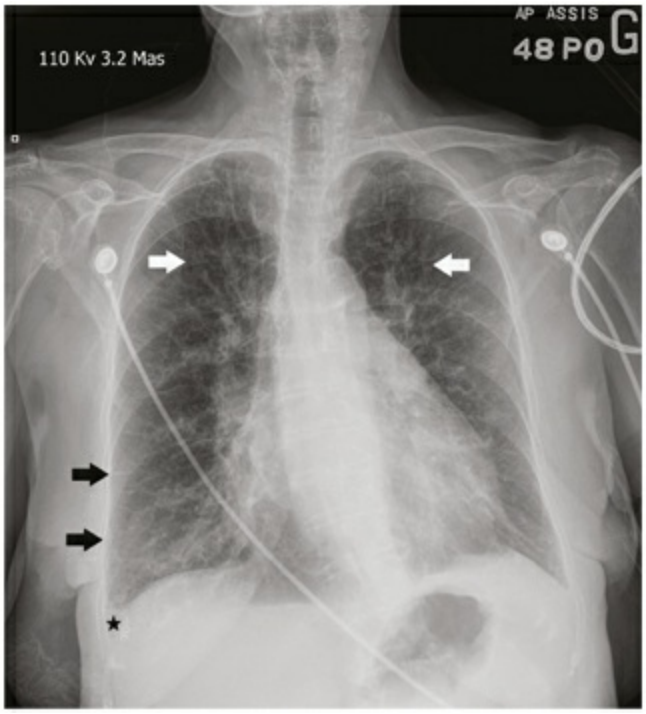

Fig. 10.7 . Frontal chest radiograph of an 81-year-old female with cardiomegaly depicts apical redistribution of pulmonary vasculature (white arrows), thickened interlobular septa (black arrows), and a small right pleural effusion (black star), all signs indicating pulmonary edema.

Conditions such as pneumonia, pneumothorax, atelectasis, acute respiratory distress syndrome, pleural effusion, and interstitial lung disease are commonly seen in the intensive care setting. A detailed description of all these conditions is beyond the scope of this chapter and references are suggested for interested readers. If the nature of the pleural or parenchymal pathology is unclear, lung ultrasound (see Chapter 4, Extra-Cardiac Transesophageal Ultrasonography and Chapter 14, Critical Care Examination of the Respiratory System) or CT should be considered.

COMPUTED TOMOGRAPHY

Chest radiography is a useful and readily available tool for the initial evaluation of cardiac and pulmonary pathology. However, its two-dimensional nature and resultant superposition of pertinent anatomy can make CXRs difficult to interpret. Cross-sectional imaging, such as cardiac CT, is a more precise technique for detailed cardiac evaluation and image resolution; however, echography has a superior temporal resolution, is less expensive and more readily available at the bedside.

ANATOMY AND TECHNIQUE

As opposed to routine helical CT for evaluating the lungs, CT imaging of the heart is technically more challenging due to requirements for both higher spatial resolution and temporal resolution, particularly for valvular or coronary artery imaging. Technological advances, including faster acquisition time and electrocardiographic (ECG)-gated acquisition, have overcome these challenges. Two types of ECG-gating are used. First, retrospective ECG-gating with continuous helical scanning acquires images throughout the entire cardiac cycle. Subsequent reconstructions during specific phases of the cardiac cycle [5] allow dynamic evaluation of heart function. [6] , [7] Second, prospective ECG-gating (step-and- shoot scanning) significantly reduces radiation exposure by only acquiring images during end-diastole, when there is minimal movement of the heart. [8] A typical cardiac CT includes the region from the carina to the cardiac apex. The imaging field can be extended to the origins of the internal mammary and subclavian arteries for evaluation before or after a coronary bypass procedure. [9]

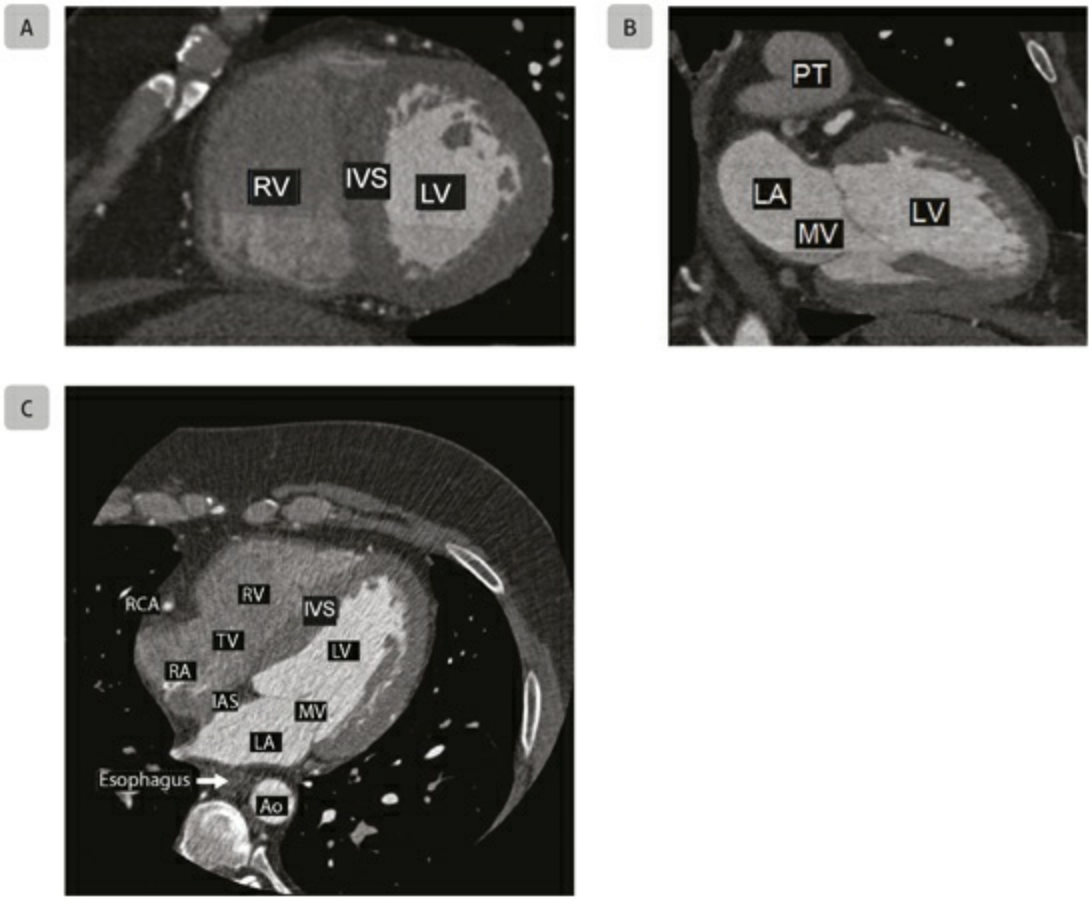

Fig. 10.8 . Normal anatomy on cardiac computed tomography (CT). (A) Short-axis view on cardiac CT shows the interventricular septum (IVS), left ventricle (LV), right ventricle (RV), and allows evaluation of myocardial thickness. (B) Long-axis or two-chamber view on cardiac CT depicts the left atrium (LA) and LV. (C) Long-axis four-chamber view on cardiac CT allows the general evaluation of cardiac valves and all four cardiac chambers. Ao, aorta; IAS, interatrial septum; MV, mitral valve; PT, pulmonary trunk; RA, right atrium; RCA, right coronary artery; TV, tricuspid valve.

A great advantage of CT imaging is that it provides an isometric dataset enabling more complex postprocessing and 3D reformations. Indeed, a single CT acquisition can generate various multi-planar and curved reformations, including all the traditional echocardiographic cardiac planes (**Figure 10.8**). The correlation between the basic transesophageal echocardiographic views proposed by Reeves *et al.* [10] are shown in Appendix 1.

PATHOLOGICAL FINDINGS

Calcium Score

Computed tomography calcium score is calculated using a low-dose, unenhanced acquisition that detects the total coronary calcium burden. Although this score does not include uncalcified coronary plaques and only accounts for a portion of the total plaque burden, it remains a proven predictive factor for myocardial infarction and death. [9] Indeed, a high calcium score correlates with high plaque burden and high relative risk for cardiac events. [11] The presence of a positive score alone increases cardiovascular event risk by four times in 3–5 years. [12]

Coronary Computed Tomography Angiography

Coronary computed tomography angiography (CCTA) is a faster non-invasive method of evaluating coronary vessel patency as compared to conventional intra-arterial catheter angiography. Intra-arterial catheter angiography evaluates the coronary lumen providing a lumenogram, which underestimates disease extent particularly when positive remodelling is present. Coronary computed tomography angiography circumvents this pitfall by simultaneously evaluating the coronary lumen and wall to determine lumen stenosis (**Figure 10.9**). [13] Visualization of the coronary wall allows better quantification of plaque burden and characterization of plaque composition, such as calcified, fibrous, or fatty content. The newer 64-multi-detector CT angiography enables accurate assessment of distal coronary segments, [14] compared to the suboptimal imaging afforded by previous cardiac CT systems. [15] Using such new scans, sensitivity and specificity for detecting significant coronary stenosis of more than 50% can be as high as 100% and 94%, respectively. [16] Computed tomography angiography also allows the general evaluation of coronary anatomy, the presence of aberrant vessels, and availability of collaterals. This coronary mapping permits non-invasive planning of a proper treatment approach before percutaneous intervention, bypass surgery, or defibrillator implantation. However, at the present time, very few cardiologists or cardiac surgeons would plan coronary operations based on a CT angiogram. However, in young patients, it can help rule out coronary artery disease and therefore avoid an invasive coronary angiogram.

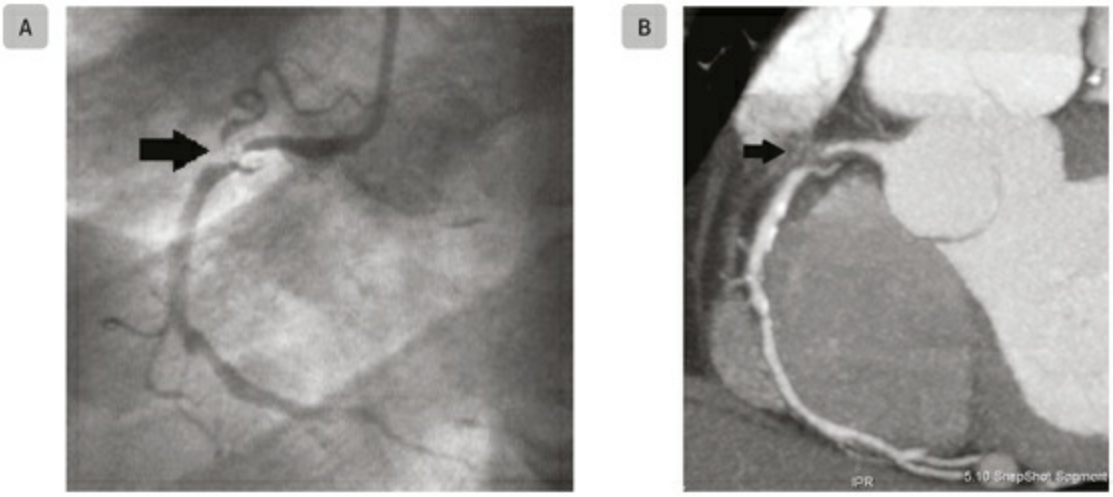

Fig. 10.9 . Coronary computed tomography angiography (CCTA). (A) Conventional catheter angiography of a 64-year-old male with coronary disease showing severe stenosis of the proximal right coronary artery (black arrow). (B) CCTA of the same patient allows assessment of coronary walls and lumen, which shows extensive atheromatous disease causing severe stenosis of the proximal right coronary (black arrow). (Reproduced with permission from Bordeleau *et al.* [13] *)*

Cardiac Function

Ventricular volumes and ejection fraction can be calculated over the entire cardiac cycle using a retrospective ECG-gated acquisition. However, the limited temporal resolution with cardiac CT underestimates LV ejection fraction as end-systolic volumes are overestimated and end-diastolic volumes underestimated. [17] Despite recent studies showing accurate measurements of ejection fraction with newer 64-multidetector and dual source CT [18] , echocardiography and MRI remain the more widely used methods for estimating ventricular volume and stress imaging, without added radiation or contrast administration. Cardiac CT can also detect abnormal hypokinetic or dyskinetic wall motion seen with myocardial infarction.

Valves

Echocardiography remains the primary method of investigating valve pathologies, although cardiac CT is a useful complementary tool when echocardiographic images are suboptimal or cardiac MRI contraindicated. The better spatial resolution of retrospective ECG-gated CT evaluates valvular anatomy, mobility, and function with finer anatomic detail. [19] Opening valve areas and coaptation defects can be measured in stenotic and regurgitant valves, respectively, with an accuracy comparable to

echocardiography and MRI, [19] but at the cost of radiation exposure and intravenous contrast administration. Computed tomography angiography is the most sensitive technique in the assessment of valve calcification. The literature shows good correlation between calcification quantification and the severity of aortic stenosis, need for valve replacement, and prognosis. [19] , [20] In patients with endocarditis, cardiac CT is superior to echocardiography for detection of complications such as perivalvular abscess (see **Figure 9.20**), pseudo-aneurysm formation, and myocardial/pericardial involvement (**Figure 10.10**). [21] , [22] In cases when excessive valvular calcifications cause acoustic shadowing precluding accurate echocardiographic evaluation, cardiac CT can depict the valve anatomy (number of leaflets, valve thickening/calcification, and presence of vegetations). [19] , [21] , [22] Computed tomography also provides assessment of metallic prosthetic valves with fewer artifacts. [19] , [23] When surgical treatment is indicated, CCTA can be used non-invasively to exclude concomitant coronary disease in low-risk patients. [19] , [21] , [22] Coronary computed tomography angiography is now key in the evaluation of aortic annulus for transapical valve implantation. [24]

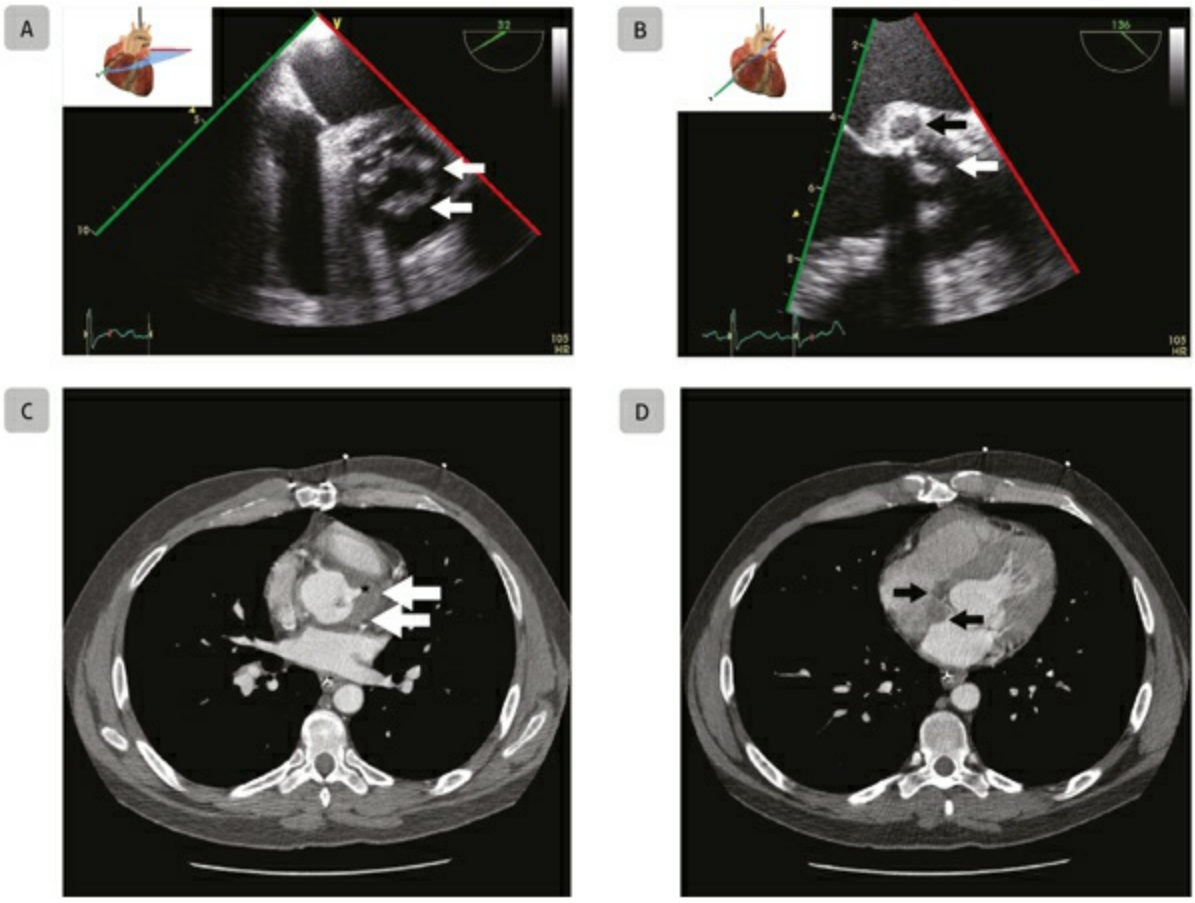

Fig. 10.10 . Endocarditis. (A) Transesophageal echocardiography (TEE) of a 44-year-old male with a previous aortic valve replacement (bioprosthesis) shows thickened and irregular valve cusps (white arrows) in the mid-esophageal (ME) aortic valve (AoV) short-axis view, indicating aortic valve endocarditis. (B) A TEE ME AoV long-axis view shows thickening in the posterior aortic root with a less dense central area (black arrow) suggesting an abscess. (C) Cardiac computed tomography images of the same patient allow detection of the anterior portion of the perivalvular abscess (white arrows) seen as an adjacent hypodense collection. A blunt tract (black star, C), that has not yet fistulized, can also be seen. (D) There is also involvement of the interatrial septum (black arrows).

Myocardium and Pericardium

Myocardial thickness can be accurately assessed on cardiac CT by measuring the LV wall thickness at end diastole, with a normal thickness ranging from 0.6 to 1.0 cm and hypertrophy when thickness exceeds 1.1 cm. [25] Focal myocardial anomalies, such as myocardial thinning, aneurysmal bulging, fatty infiltration, and ventricular calcifications are easily detected and may indicate prior myocardial infarct. [6] , [25] Intravenous contrast administration also can detect a myocardial perfusion deficit after an acute coronary syndrome, which appears as areas of delayed or absent myocardial enhancement. [6] , [7] Cardiac tumors, such as metastases, myxomas (**Figure 10.11**), and papillary fibroelastoma, [26] are pathologic entities that can be evaluated with CT, including regional extension to adjacent mediastinal structures and lung parenchyma.

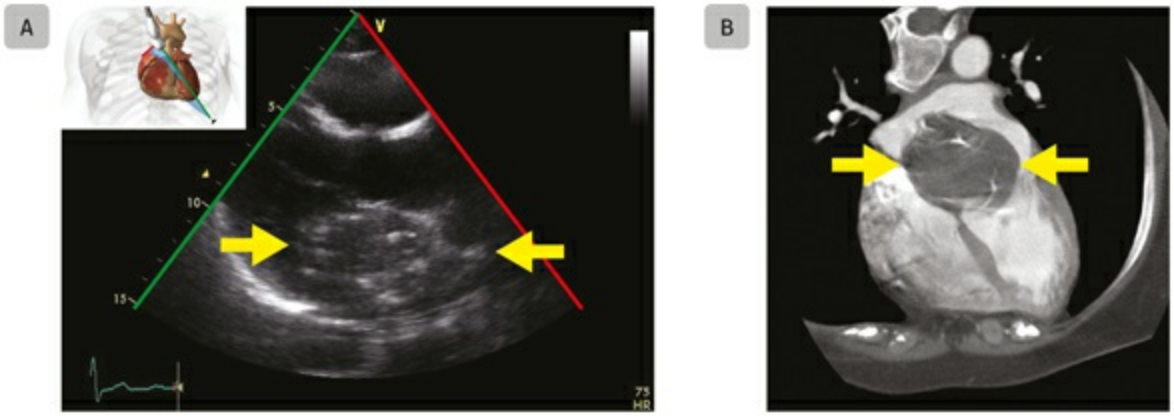

Fig. 10.11 . Myxoma. (A) Transthoracic echocardiography of a 62-year-old female shows a hyperechoic mass (yellow arrows) with punctuate calcifications in the left atrium. (B) Cardiac computed tomography of the same patient depicts the homogenously hypodense mass (yellow arrows) with calcifications. This was diagnosed as a left atrial myxoma. Note the close contact of the mass with the atrial septum, which is an imaging sign highly specific for myxoma. Most atrial myxomas are attached to this septum.

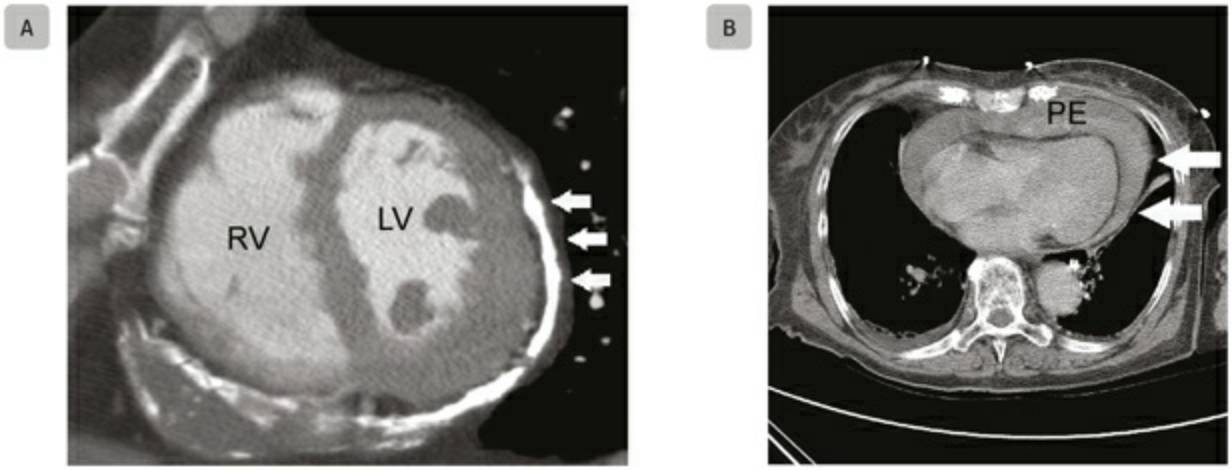

Fig. 10.12 . Pericardial effusion. (A) Axial contrast-enhanced computed tomography (CT) shows thickened and calcified pericardium (white arrows) in a patient with constrictive pericarditis. (B) Axial contrast-enhanced CT of a 90-year-old female presenting with chest pain depicts moderate pericardial effusion (PE) of high attenuation (white arrows), indicating hemorrhagic effusion. LV, left ventricle; RV, right ventricle.

Cardiac CT allows qualitative and quantitative evaluation of pericardial effusions. Presence of septations, gas, blood, nodules, and calcifications can be identified, which can better orientate towards the underlying cause of the effusion (**Figure 10.12**). Cardiac tamponade is suspected when a large effusion straightens the interventricular septum, compromising ventricle expansion, and contrast refluxes into the venae cavae. [27]

Extra-Cardiac Structures

Cardiac CT provides a comprehensive evaluation of the extra-cardiac structures such as the lungs, mediastinum, great vessels, thoracic cage, and upper abdominal structures. In patients presenting with chest pain, CT allows evaluation of coronary arteries for myocardial infarction, the aorta for dissection and aneurysm (**Figure 10.13**), pneumothorax (see **Figure 14.14**), pulmonary venous infarction (see **Figure 14.22**) and pulmonary arteries for pulmonary embolism (**Figure 10.14**). Benign causes of chest pain can also be detected, such as pneumonia. Computed tomography provides a more accurate and complete evaluation of the lung parenchyma (**Figure 10.15**) compared with the limited sensitivity of a CXR (see **Figure 14.18**). As with CXRs, pulmonary and hemodynamic repercussions of heart diseases, such as aortic or pulmonary trunk dilatation, can be assessed on cardiac CT.

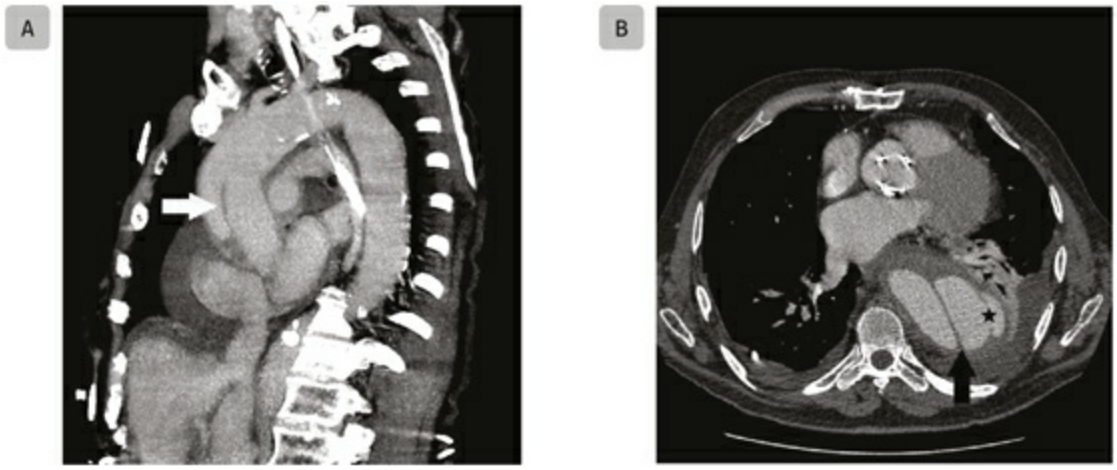

Fig. 10.13 . Aortic dissection. (A) Cardiac computed tomography images of a 78-year-old male with acute chest pain depict thoracic aortic dissection (white arrow in a sagittal image), (B) (black arrow in the axial image) that is shown to be ruptured (black star) with associated pericardial effusion.

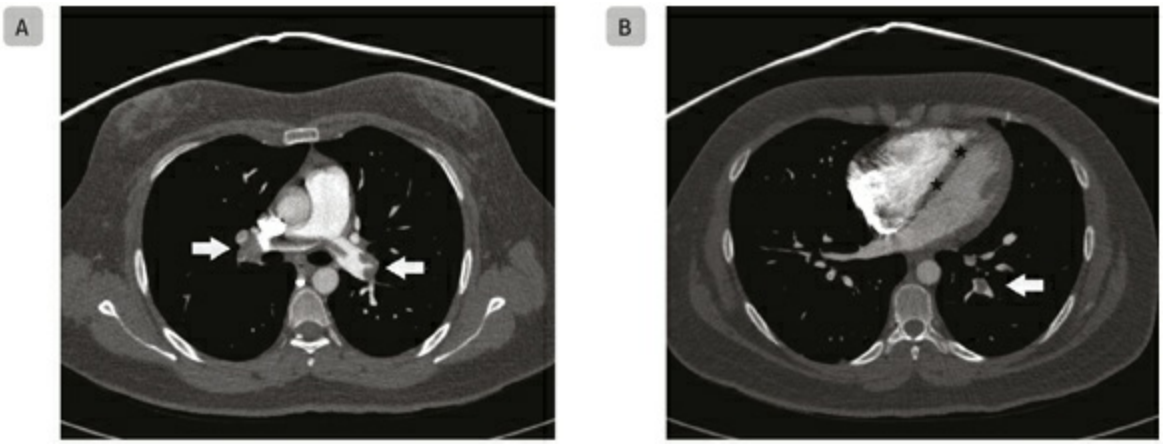

Fig. 10.14 . Pulmonary embolism. (A) Cardiac computed tomography axial images of a 30-year-old female presenting with acute chest pain demonstrate central pulmonary embolism in the main pulmonary arteries (white arrows). (B) A straightened interventricular septum (black stars) indicates right ventricular dysfunction.

MAGNETIC RESONANCE IMAGING

Cardiovascular magnetic resonance (CMR) is a novel and versatile tool for the evaluation of patients with cardiovascular disease.

Technique and Indications

Cardiovascular magnetic resonance techniques are based on imaging within a

magnetic field which has the potential for movement of ferromagnetic objects and dysfunction or damage of electronic circuits. Proper screening of patients before CMR is essential. This should be in the form of a MRI safety questionnaire that is completed and signed by the patient under physician supervision. Cardiovascular magnetic resonance of patients with devices containing conducting materials can be potentially harmful by inducing electrical currents. [28] In addition to general restrictions regarding MRI, such as intracranial clips and cochlear implants, special considerations are required when considering CMR in cardiac patients. Sternal wires, retained epicardial pacing wires, all heart valve prostheses, and annuloplasty rings following cardiac surgery are considered MRI safe, although localized artifacts may interfere with image analysis. [29] , [30] Patients with correctly deployed coronary stents are considered to be safe to undergo CMR any time after implantation. [31] Non-coronary intravascular stents, such as aortic stent grafts, as well as coils and filters, can be imaged at any time after implantation if they are non-ferromagnetic. The issue of CMR in patients with pacemakers is highly controversial and currently under re-evaluation. Most institutions consider pacemakers a strong relative contraindication to CMR due to the potential risk of inappropriate pacing during gradient switching, temporary/permanent malfunction, and localized heating causing myocardial damage. [32] Implantable cardioverter defibrillators are even more problematic and should be considered a contraindication until more information is available. [33]

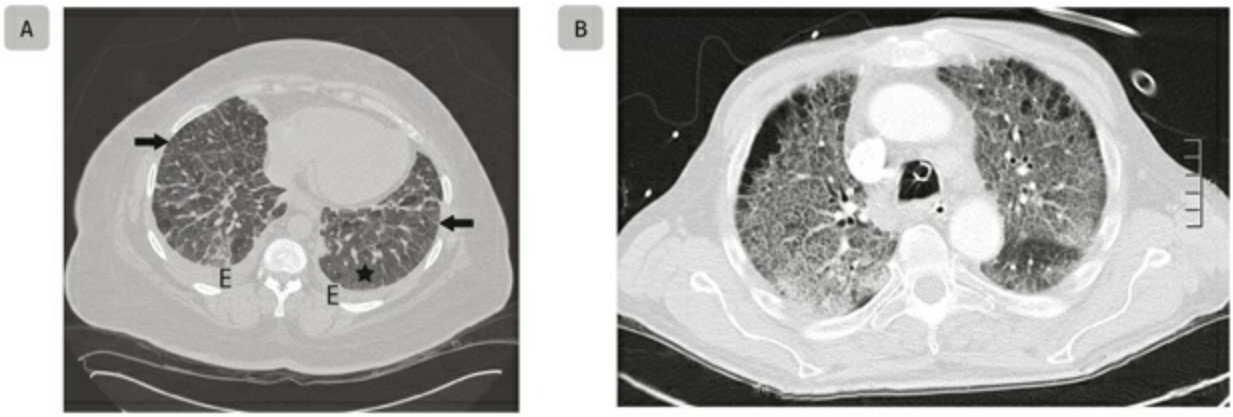

Fig. 10.15 . Lung parenchyma. (A) Cardiac computed tomography (CT) axial images of a 49-year-old female with acute dyspnea show thickened interlobular septa (black arrows), ground-glass opacities (black star), and bilateral pleural effusions (E), indicating pulmonary edema. (B) CT findings of pulmonary fibrosis in a 63-year-old male. Note the absence of any pleural effusion.

Cardiovascular magnetic resonance evaluation requires a stable and cooperative patient, and therefore is not generally appropriate for critically ill or unstable patients. The patient must tolerate a 30– to 45–minute examination in the supine position, perform repeated 10–20 seconds of breath-holds, and ideally not have significant cardiac arrhythmia which can significantly degrade the diagnostic quality of the examination. Acutely ill patients may benefit from CMR evaluation, particularly if more readily accessible imaging techniques, such as echocardiography and/or cardiac CT, have not yielded a definitive diagnosis. With proper precautions, these patients can safely undergo CMR. All equipment used in the CMR scanner room must be fully MRI-compatible (i.e. specialized non-ferromagnetic oxygen cylinder, intravenous pumps, anesthetic equipment), or else must remain in the control room and connected to the patient with long lines. The American College of Cardiology and numerous other cardiovascular societies have published guidelines regarding clinical practice of CMR, including appropriateness criteria, which are a useful reference. [34]

PATHOLOGICAL FINDINGS

Cardiac Volumes and Function

Cardiovascular magnetic resonance is the gold standard for measuring ventricular volumes and mass. [18] The high accuracy and reproducibility of ventricular volumes allows for normalization of measurements to body surface area and gender. In particular, CMR provides accurate assessment of RV morphology, volume, and function which are often sub-optimally evaluated. [35]

Cardiomyopathy

Cardiovascular magnetic resonance provides a comprehensive evaluation in the clinical setting of acute cardiomyopathy and often provides a definitive diagnosis. In addition to morphologic cardiac assessment, functional evaluation including wall motion abnormalities, and ventricular volume/mass quantification, CMR has unique tissue characterization abilities. Delayed enhanced CMR (DE-CMR) performed 10 minutes after contrast administration can detect areas of acute/chronic myocardial infarction,

fibrosis, and infiltration. [36] The pattern of late-gadolinium-enhancement (LGE), when characteristic, results in quick and definitive differentiation between an ischemic and non-ischemic etiology for new onset heart failure. [37]

Myocardial Infarction

With new onset of heart failure and an enlarged heart, a diagnosis of non-ischemic dilated cardiomyopathy must be differentiated from sequelae of acute or chronic coronary artery disease - ischemic dilated cardiomyopathy. Angiography is often performed to make this distinction; however, it is limited in its ability to detect downstream infarction versus bystander coronary stenosis. Delayed enhanced CMR is highly sensitive for detection of acute and chronic myocardial infarction. [38] Additionally, the extent of LGE on DE-CMR is predictive of functional recovery after revascularization. Cardiovascular magnetic resonance accurately predicts which patients have viable myocardium despite decreased function, and would benefit from revascularization over optimized medical therapy. Specifically, with greater than 50% transmural infarction, seen as greater than 50% LGE, there is a 90% chance of no functional recovery after revascularization (**Figure 10.16**). Conversely, with less than 50% transmural LGE, there is an 80% chance of functional recovery after surgery or stenting. [38]

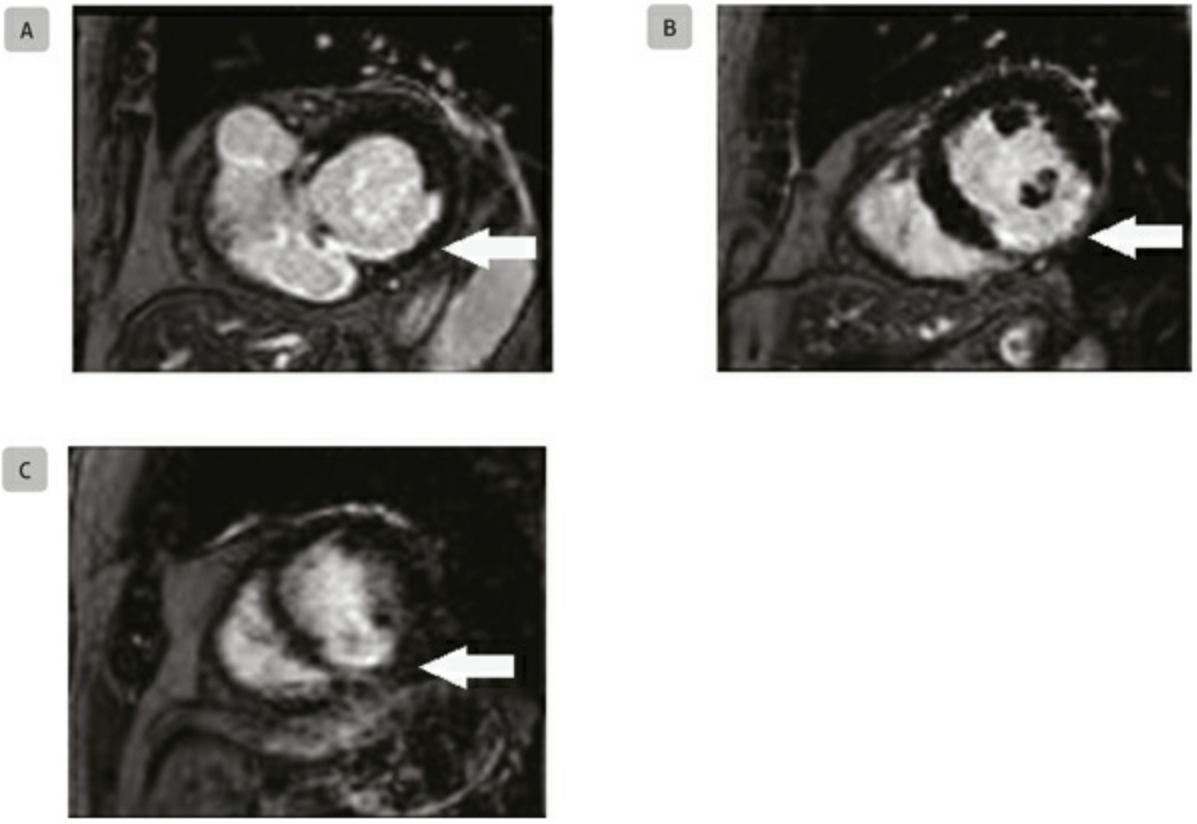

Fig. 10.16 . Myocardial infarction. A 50-year-old male presents with severe three-vessel coronary artery disease, moderately decreased left ventricular function, and ejection fraction quantified at 30% on cardiovascular magnetic resonance (CMR) (not shown). (A—C) Short-axis delayed enhanced CMR performed at the (A) base, (B) mid-cavity, and (C) apical segments shows late-gadolinium-enhancement (LGE) (white arrow) of greater than 50% transmurality involving the inferior wall indicating non-viable segments that will unlikely benefit from revascularization. Importantly, there is no LGE of the other myocardial segments indicating viability of the septum, anterior, and lateral walls. If the left anterior descending and circumflex arteries are suitable targets for revascularization, these walls will likely recover in function.

Myocarditis

A significant percentage of patients presenting with acute chest pain and elevated troponins may be shown to have an alternative diagnosis by CMR, most commonly myocarditis (**Figure 10.17**). In the appropriate clinical setting of a patient without risk factors for coronary occlusion, angiography may be obviated if CMR findings are compatible with acute myocarditis. In the equivocal clinical setting where coronary occlusion is not ruled out, a characteristic non-ischemic LGE pattern of myocarditis can confirm the non-ischemic etiology for acute chest pain and elevated troponin levels. Myocardial edema imaging can confirm the acuity of myocardial injury. [39] , [40]

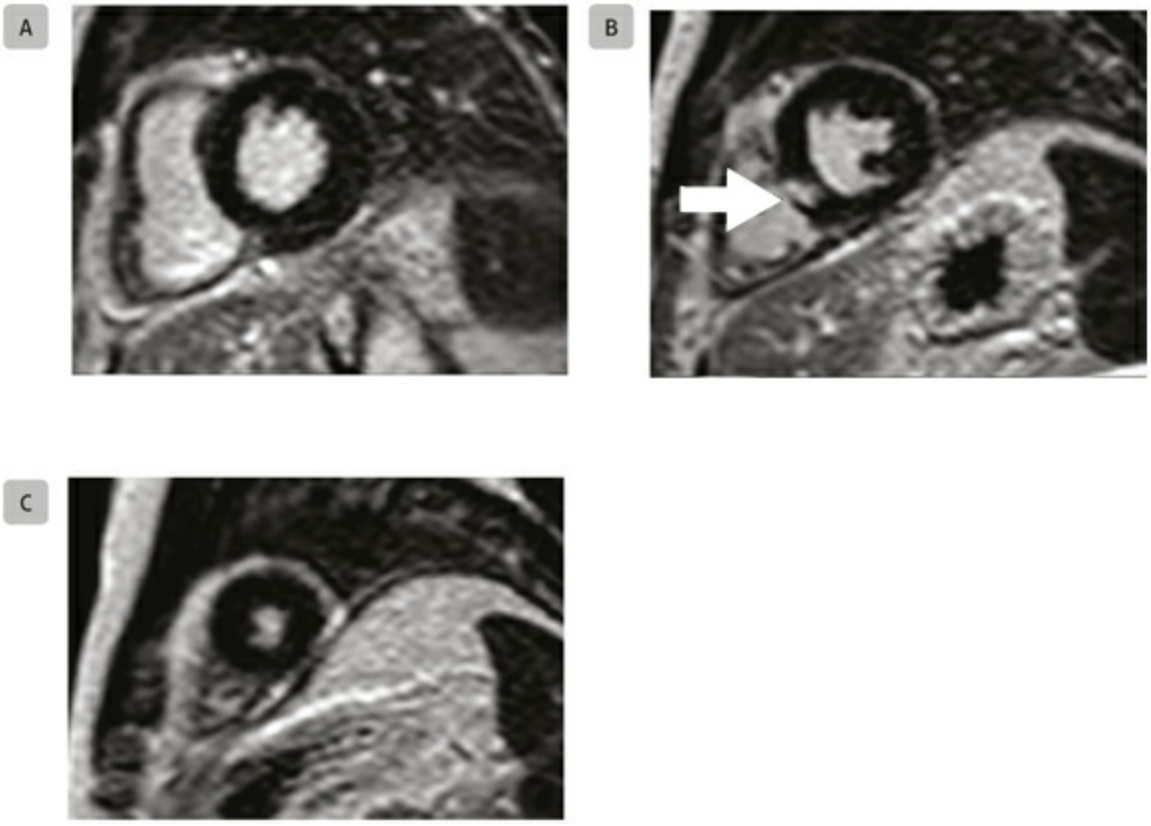

Fig. 10.17 . Acute myocarditis. A 30-year-old male presents with retrosternal chest pain and elevated troponins. (A—C) Delayed enhanced cardiovascular magnetic resonance short-axis images of the (A) base, (B) mid-cavity, and (C) apex show focal late-gadolinium-enhancement (LGE) (white arrow) in the mid-cavity of the interventricular septum. The endocardium is normal, appearing black. Thus, the focus of LGE is non-ischemic in etiology. The classic epicardial/myocardial pattern of LGE is demonstrated. Further questioning revealed a history of recent viral illness.

Other Cardiomyopathies

Comprehensive bi-ventricular coverage afforded by CMR may demonstrate distinctive findings of other cardiomyopathies leading to new heart failure and/or sudden cardiac death. Possible CMR findings that suggest a definitive etiology include the following: asymmetric myocardial hypertrophy of hypertrophic cardiomyopathy, marked trabeculation of persistent spongy myocardium of LV non-compaction, abnormal RV morphology and fibrosis of arrhythmogenic RV dysplasia, apical ballooning of stress-induced or Takotsubo cardiomyopathy. [41] CMR can also provide a comprehensive evaluation in the clinical setting of aborted sudden cardiac death. [39] , [41]

In summary, there are multiple modalities used in the diagnosis of cardiopulmonary conditions in the critically ill patients and those requiring

cardiac or non-cardiac surgery. Their specific role, indication, advantages, and comparison are summarized in **Table 10.2**.

Table 10.2 Comparison of Diagnostic Modalities

	TEE	CXR	CT	MRI
General	Real-time acquisition High temporal resolution Low spatial resolution High accessibility Transportable Low cost No radiation Operator dependant Window dependant	Difficult to interpret Short acquisition time High accessibility Transportable Low cost Low radiation	Short scanning time Low temporal resolution High spatial resolution High cost High radiation Multiplanar reformations Contraindications (renal insufficiency, iodine contrast allergy)	Long scanning time High temporal resolution Low spatial resolution Tissue characterization Low accessibility High cost No radiation Multiplanar reformations No detection of calcium Contraindications (hemodynamic instability, cardiac implantable electronic devices, renal insufficiency)
Functional studies	Most commonly used Accurate Stress imaging	Poor (except acute edema)	Fairly accurate	Accurate Reproducible Stress imaging
Valves	Anatomy Mobility	Severe calcifications Indirect signs of valve pathology	Finer anatomic detail Mobility Best tool for calcification Good evaluation of prosthetic and heavily calcified valves	Finer anatomic detail Mobility
Endocarditis	Most commonly used Small vegetations (<4 mm) Perforation	–	Perivalvular extent	–
Coronary arteries	–	Very severe calcifications	Non-invasive Accurate Aberrant vessels Occlusive disease CT calcium score Plaque composition Blooming artifacts with heavily calcified coronaries	Non-invasive Aberrant vessels Occlusive disease Origin and proximal coronaries only Plaque composition Good evaluation of heavily calcified coronaries

Myocardium	Thickness Mobility	Ventricular and atrial enlargement Severe calcifications	Thickness Mobility Enhancement	Thickness Mobility Precise evaluation of transmural extent Delayed enhancement Edema
Pericardium	Quantification of pericardial effusion Repercussions on cardiac contractility	Severe calcifications	Calcifications Quantification and qualification of pericardial effusion Repercussions on cardiac contractility	Quantification and qualification of pericardial effusion Repercussions on cardiac contractility
Tumors	Limited tumor extension	–	Detailed tumor extension	Detailed tumor extension
Extra-cardiac structures	Limited evaluation	Extra-cardiac repercussions of cardiac diseases (pulmonary edema)	Extra-cardiac repercussions of cardiac diseases (pulmonary edema) Alternative diagnosis (aortic dissection or rupture, pulmonary embolism)	Limited evaluation

Notes: CT, computed tomography; CXR, chest radiography; MRI, magnetic resonance imaging; TEE, transesophageal echocardiography.

REFERENCES

1. Danzer, C. S.1919. “The Cardiothoracic Ratio: An index of cardiac enlargement.” *Am J Med Sci 157*.
2. Glover, L., W. A.Baxley, and H. T.Dodge. 1973. “A quantitative evaluation of heart size measurements from chest roentgenograms.” *Circulation 47*: 1289–96.
3. Dinsmore, R. E., D. J.Goodman, and C. A.Sanders. 1966. “Some pitfalls in the valuation of cardiac chamber enlargement on chest roentgenograms.” *Radiology 87*: 267–73.
4. Higgins, C. B., R. T.Reinke, N. E.Jones, and T.Broderick. 1978. “Left atrial dimension on the frontal thoracic radiograph: a method for assessing left atrial enlargement.” *AJR Am J Roentgenol 130*: 251–5.
5. Chartrand-Lefebvre, C., A.Cadrin-Chenevert, E.Bordeleau, P.Ugolini, R.Ouellet, J. L.Sablayrolles, et al. 2007. “Coronary computed tomography angiography: overview of technical aspects, current concepts, and perspectives.” *Can Assoc Radiol J 58*: 92–108.
6. Geyer, L. L., J. R.Silverman, A. W.Krazinski, P.Suranyi, J. G.Ravenel, S.Wirth, et al. 2014. “Integrated cardiothoracic imaging with computed tomography.” *Semin Respir Crit Care Med 35*: 50–63.
7. Hoffmann, U., A. J.Pena, R. C.Cury, S.Abbara, M.Ferencik, F.Moselewski, et al. 2006. “Cardiac CT in emergency department patients with acute chest pain.” *Radiographics 26*: 963–78.
8. Earls, J. P., and J.Leipsic. 2010. “Cardiac computed tomography technology and dose-reduction strategies.” *Radiol Clin North Am 48*: 657–74.

9. Sundaram, B., S.Patel, N.Bogot, and E. A.Kazerooni. 2009. “Anatomy and terminology for the interpretation and reporting of cardiac MDCT: Part 1, Structured report, coronary calcium screening, and coronary artery anatomy.” *AJR Am J Roentgenol 192*: 574–83.
10. Reeves, S. T., A. C.Finley, N. J.Skubas, M.Swaminathan, W. S.Whitley, K. E.Glas, et al. 2013. “Basic perioperative transesophageal echocardiography examination: a consensus statement of the American Society of Echocardiography and the Society of Cardiovascular Anesthesiologists.” *J Am Soc Echocardiogr 26*: 443–56.
11. Keelan, P. C., L. F.Bielak, K.Ashai, L. S.Jamjoum, A. E.Denktas, J. A.Rumberger, et al. 2001. “Long-term prognostic value of coronary calcification detected by electron-beam computed tomography in patients undergoing coronary angiography.” *Circulation 104*: 412–7.
12. Greenland, P., R. O.Bonow, B. H.Brundage, M. J.Budoff, M. J.Eisenberg, S. M.Grundy, et al. 2007. “ACCF/AHA 2007 clinical expert consensus document on coronary artery calcium scoring by computed tomography in global cardiovascular risk assessment and in evaluation of patients with chest pain: a report of the American College of Cardiology Foundation Clinical Expert Consensus Task Force (ACCF/AHA Writing Committee to Update the 2000 Expert Consensus Document on Electron Beam Computed Tomography) developed in collaboration with the Society of Atherosclerosis Imaging and Prevention and the Society of Cardiovascular Computed Tomography.” *J Am Coll Cardiol 49*: 378–402.
13. Bordeleau, E., A.Lamonde, J.Prenovault, A.Belblidia, G.Cote, J.Lesperance, et al. 2007. “Accuracy and rate of coronary artery segment visualization with CT angiography for the noninvasive detection of coronary artery stenoses.” *Int J Cardiovasc Imaging 23*: 771–80.
14. Sun, Z., C.Lin, R.Davidson, C.Dong, and Y.Liao. 2008. “Diagnostic value of 64-slice CT angiography in coronary artery disease: a systematic review.” *Eur J Radiol 67*: 78–84.
15. Mollet, N. R., F.Cademartiri, K.Nieman, F.Saia, P. A.Lemos, E. P.McFadden, et al. 2005. “Noninvasive assessment of coronary plaque burden using multislice computed tomography.” *Am J Cardiol 95*: 1165–9.
16. Stein, P. D., A.Beemath, F.Kayali, E.Skaf, J.Sanchez, and R. E.Olson. 2006. “Multidetector computed tomography for the diagnosis of coronary artery disease: a systematic review.” *Am J Med 119*: 203–16.
17. Abbara, S., B. J.Chow, A. J.Pena, R. C.Cury, U.Hoffmann, K.Nieman, et al. 2008. “Assessment of left ventricular function with 16- and 64-slice multi-detector computed tomography.” *Eur J Radiol 67*: 481–6.
18. Asferg, C., L.Usinger, T. S.Kristensen, and J.Abdulla. 2012. “Accuracy of multi-slice computed tomography for measurement of left ventricular ejection fraction compared with cardiac magnetic resonance imaging and two-dimensional transthoracic echocardiography: a systematic review and meta-analysis.” *Eur J Radiol 81*: e757–62.
19. Chen, J. J., M. A.Manning, A. A.Frazier, J.Jeudy, and C. S.White. 2009. “CT angiography of the cardiac valves: normal, diseased, and postoperative appearances.” *Radiographics 29*: 1393412.
20. Koos, R., H. P.Kuhl, G.Muhlenbruch, J. E.Wildberger, R. W.Gunther, and A. H.Mahnken. 2006. “Prevalence and clinical importance of aortic valve calcification detected incidentally on CT scans: comparison with echocardiography.” *Radiology 241*: 76–82.
21. Bruun, N. E., G.Habib, F.Thuny, and P.Sogaard. 2014. “Cardiac imaging in infectious endocarditis.” *Eur Heart J 35*: 624–32.
22. FeuchtnerG.Imaging of cardiac valves by computed tomography. *Scientifica (Cairo)*2013; *2013*: Article ID 270579, 13 pages.
23. Chheda, S. V., M. B.Srichai, R.Donnino, D. C.Kim, R. P.Lim, and J. E.Jacobs. 2010. “Evaluation of the mitral and aortic valves with cardiac CT angiography.” *J Thorac Imaging 25*: 76–85.

24. Jilaihawi, H., N.Doctor, M.Kashif, T.Chakravarty, A.Rafique, M.Makar, et al. 2013. “Aortic annular sizing for transcatheter aortic valve replacement using cross-sectional 3-dimensional transesophageal echocardiography.” *J Am Coll Cardiol 61*: 908–16.
25. Sundaram, B., S.Patel, P.Agarwal, and E. A.Kazerooni. 2009. “Anatomy and terminology for the interpretation and reporting of cardiac MDCT: part 2, CT angiography, cardiac function assessment, and noncoronary and extracardiac findings.” *AJR Am J Roentgenol 192*: 584–98.
26. Tremblay-Paquet, S., M.Chandonnet, P.Romeo, D.Bouchard, and C.Chartrand-Lefebvre. 2012. “Case of the month #174: papillary fibroelastoma of the aortic valve.” *Can Assoc Radiol J 63*: 69–72.
27. Restrepo, C. S., D. F.Lemos, J. A.Lemos, E.Velasquez, L.Diethelm, T. A.Ovella, et al. 2007. “Imaging findings in cardiac tamponade with emphasis on CT.” *Radiographics 27*: 1595–610.
28. Kanal, E., J. P.Borgstede, A. J.Barkovich, C.Bell, W. G.Bradley, S.Etheridge, et al. 2004. “American College of Radiology White Paper on MR Safety: 2004 update and revisions.” *AJR Am J Roentgenol 182*: 1111–4.
29. Edwards, M. B., K. M.Taylor, and F. G.Shellock. 2000. “Prosthetic heart valves: evaluation of magnetic field interactions, heating, and artifacts at 1.5 T.” *J Magn Reson Imaging 12*: 363–9.
30. Shellock, F. G.2002. *Reference Manual for Magnetic Resonance Safety*. 2nd ed. Salt Lake City, UT: Amirsys.
31. Strohm, O., D.Kivelitz, W.Gross, J.Schulz-Menger, X.Liu, B.Hamm, et al. 1999. “Safety of implantable coronary stents during 1H-magnetic resonance imaging at 1.0 and 1.5 T.” *J Cardiovasc Magn Reson 1*: 239–45.
32. Martin, E. T., J. A.Coman, F. G.Shellock, C. C.Pulling, R.Fair, and K.Jenkins. 2004. “Magnetic resonance imaging and cardiac pacemaker safety at 1.5-Tesla.” *J Am Coll Cardiol 43*: 1315–24.
33. Shinbane, J. S., P. M.Colletti, and F. G.Shellock. 2007. “MR in patients with pacemakers and ICDs: Defining the issues.” *J Cardiovasc Magn Reson 9*: 5–13.
34. Taylor, A. J., M.Cerqueira, J. M.Hodgson, D.Mark, J.Min, P.O’Gara, et al. 2010. “ACCF/SCCT/ACR/AHA/ASE/ASNC/NASCI/SCAI/SCMR 2010 Appropriate Use Criteria for Cardiac Computed Tomography. A Report of the American College of Cardiology Foundation Appropriate Use Criteria Task Force, the Society of Cardiovascular Computed Tomography, the American College of Radiology, the American Heart Association, the American Society of Echocardiography, the American Society of Nuclear Cardiology, the North American Society for Cardiovascular Imaging, the Society for Cardiovascular Angiography and Interventions, and the Society for Cardiovascular Magnetic Resonance.” *J Cardiovasc Comput Tomogr 4* (407): e1–33.
35. Maceira, A. M., S. K.Prasad, M.Khan, and D. J.Pennell. 2006. “Reference right ventricular systolic and diastolic function normalized to age, gender and body surface area from steady-state free precession cardiovascular magnetic resonance.” *Eur Heart J 27*: 2879–88.
36. Mahrholdt, H., A.Wagner, R. M.Judd, U.Sechtem, and R. J.Kim. 2005. “Delayed enhancement cardiovascular magnetic resonance assessment of non-ischaemic cardiomyopathies.” *Eur Heart J 26*: 1461–74.
37. Jackson, E., N.Bellenger, M.Seddon, S.Harden, and C.Peebles. 2007. “Ischaemic and non-ischaemic cardiomyopathies - cardiac MRI appearances with delayed enhancement.” *Clin Radiol 62*: 395–403.
38. WeinsaftJ.W., KlemI., JuddR.M.MRI for the assessment of myocardial viability. *Magn Reson Imaging Clin N Am*2007; *15*: 505–25, v-vi.
39. Cocker, M., and M. G.Friedrich. 2010. “Cardiovascular magnetic resonance of myocarditis.” *Curr Cardiol Rep 12*: 82–9.
40. Giri, S., Y. C.Chung, A.Merchant, G.Mihai, S.Rajagopalan, S. V.Raman, et al. 2009. “T2 quantification for improved detection of myocardial edema.” *J Cardiovasc Magn Reson 11*: 56.

41. O’Donnell, D. H., S.Abbara, V.Chaithiraphan, K.Yared, R. P.Killeen, R.Martos, et al. 2012. “Cardiac MR imaging of nonischemic cardiomyopathies: imaging protocols and spectra of appearances.” *Radiology 262*: 403–22.

Chapter 11

Simple Congenital Heart Disease in Adults

Wilfredo Puentes and Annette Vegas

INTRODUCTION

Congenital heart disease (CHD) in adults comprises a broad spectrum of pathologies which may have normal or abnormal relationships of chambers, valves, and vessels, resulting in abnormal flow. The complex nature of the cardiac lesions in adult CHD typically requires thorough interrogation by ultrasound using advanced cognitive and technical transesophageal echocardiographic (TEE) skills. [1] However, identification of simple shunts related to the presence of defects in the interatrial septum (IAS) and interventricular septum (IVS) does form part of a basic TEE examination. This may identify a potential mechanism of unexplained hypoxia or hemodynamic instability in a patient. Atrial septal defects (ASD) account for 25–33% of all adult congenital heart disease. Ventricular septal defects (VSD) are the most common infant cardiac anomalies and account for approximately 10% of adult congenital cases. A high incidence of spontaneous closure reduces the prevalence between the adult and pediatric population. This chapter will review the embryology, anatomy, defects, and TEE views for assessment of patent foramen ovale (PFO), ASD, and VSD.

EMBRYOLOGY INTERATRIAL SEPTUM

Division of the primitive atrium occurs during the 5th and 7 th weeks of life. Formation of the IAS involves the development and resorption of two

membranes: the septum primum (SP) and septum secundum (SS) as described in **Figure 11.1**. Failure of this process is the basis for the occurrence of defects in the IAS.

Anatomy of the Right Atrium

A clear understanding of right atrial anatomy is important to avoid misidentifying normal structures as pathology with TEE. The right atrium (RA) has a smooth wall, the sinus venarium, into which the great veins open and has a rough trabeculated wall derived from the primitive atrium. The crista terminales (internal) and sulcus terminales (external) separate the smooth and rough portions. The posteromedial wall of the RA is the IAS. The thin fossa ovalis is in the center of the IAS and represents the remnant of the foramen ovale covered by the septum primum. The remainder of the IAS is formed from the septum secundum, the free margin of which forms the limbus fossa ovalis. Following birth the two septa, primum and secundum, fuse at the limbus.

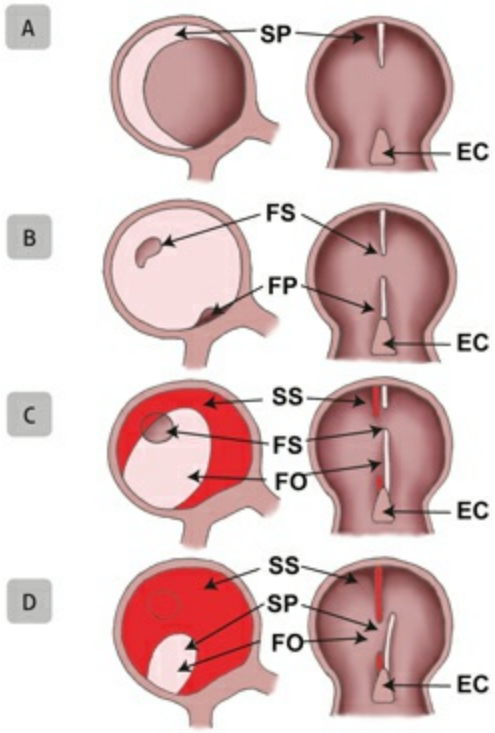

Fig. 11.1 . Embryology of the interatrial septum. (A) A thin crescent-shaped membrane, the septum primum (SP), grows from the dorso-cranial wall of the primitive atrium towards the endocardial cushions (EC). (B) As the SP grows, a large opening, the foramen primum (FP), remains above the EC. Before the FP is obliterated, perforations in the upper SP coalesce to form the foramen secundum (FS).

The free edge of the SP fuses with the EC obliterating the FP. (C) Another membrane, the septum secundum (SS), grows from the ventrocranial wall of the atrium on the right side of the SP. The SS covers the FS and FP, but leaves an oval opening called the foramen ovale (FO). (D) The upper part of the SP disappears; with the remaining part covering the FO and can function as a valve. (Reproduced with permission from Denault *et al.* [2] *)*

Patent Foramen Ovale

A PFO is an interatrial communication without deficiency in septal tissue that arises from a failure of the septum primum to adhere to the limbus of the septum secundum (**Figure 11.2)**. Thus flow may occur between the floor of the fossa ovalis and upper margin of the limbus. This is a common lesion found at autopsy in 25% of patients and in nearly 50% of patients presenting with a stroke. Patients with a PFO are asymptomatic, although they have an increased risk of stroke or migraines.

Atrial Septal Defects

Absence of atrial septal tissue defines ASDs, which are classified into four types according to their location (**Figure 11.3)**: ostium secundum (75%), ostium primum (15%), sinus venosus (5%), and coronary sinus (rare) defects. Each type of ASD may be associated with other cardiac anomalies. [3]

1. Ostium secundum has a variable amount of tissue missing usually in the center of the IAS and is bounded on all sides by atrial septal tissue. It may be part of other complex congenital heart lesions and may have associated mitral valve prolapse (30%). Atrial septal defects from an ostium secundum may result from: (a) abnormal resorption of the septum primum during formation of the foramen secundum; (b) resorption in abnormal locations of the septum primum; (c) an abnormally large FO resulting from defective development of the septum secundum (a normal septum primum will not close the FO); and (d) large ASDs may result from a combination of excessive resorption of the septum primum and large FO.
2. Ostium primum is a defect involving the inferior IAS near the atrioventricular valves and is a variant of atrioventricular septal defects or endocardial cushion (EC) defects. The septum primum does not fuse with the EC leaving a patent foramen primum. The tricuspid valve (TV) and mitral valve (MV) insert at the same level

into the IVS. There may be a “cleft” or commissure in the anterior MV leaflet causing mitral regurgitation and chordal attachments to the IVS.

3. Sinus venosus defects are located near the superior vena cava (SVC) or SVC type. They can also be close to the inferior vena cava (IVC) or IVC type. These lesions may result from incomplete resorption of the sinus venosus into the RA and/or failure of abnormal development of the septum secundum. This type of ASD is commonly associated with partial anomalous pulmonary venous drainage of right upper pulmonary vein from unroofing of the wall that separates the pulmonary veins from the left atrium (LA).
4. Coronary sinus defect is a rare interatrial communication between the LA and coronary sinus. The fossa ovalis may be intact, or there may be an ostium secundum defect. There is often associated anomalous drainage of a left-sided superior vena cava (LSVC) into the coronary sinus. A persistent LSVC is seen as a wedge-shaped, echo-free space between the left upper pulmonary vein (LUPV) and left atrial appendage in the mid-esophageal (ME) mitral commissural view (60°). Contrast echo with injection of agitated saline into the left Arm or left neck vein opacifies the LSVC and coronary sinus (see **Figure 8.2**).

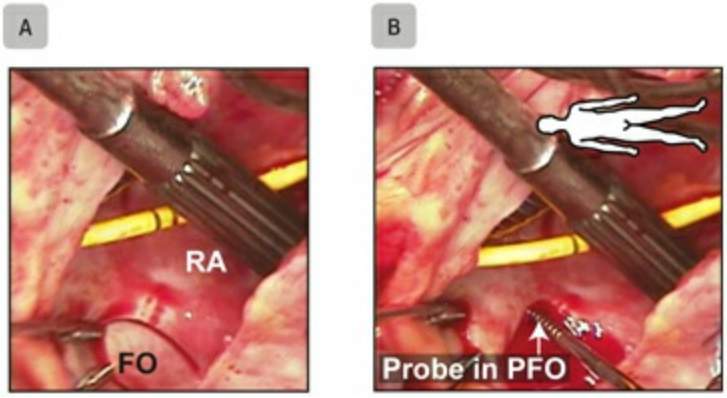

Fig. 11.2 . Patent foramen ovale (PFO). Intraoperative views through a right atriotomy of a PFO diagnosed and closed intraoperatively in a 67-year-old male undergoing tricuspid annuloplasty. (A) At baseline, the fossa ovalis (FO) is visible at the lower part of the image. A suction device and a Swan-Ganz catheter are also visible in the right atrium (RA). (B) Upon mild pressure on the FO with a surgical probe, blood appears in the RA, coming from the left atrium through the PFO. (Source: Courtesy of Dr Michel Pellerin; with permission from Denault *etal.* [2] *)*

A&B: https://youtu.be/GO9BfFH05TU

Physiology Atrial Septal Defects

Any ASD results in variable shunting of blood between the LA and RA. The defect size, ventricular compliances, and pulmonary artery pressures determine the magnitude of the shunt. Large defects with significant left-to-right (L-to-R) atrial level shunting enlarge the right ventricle (RV) and RA because of the increased volume. In older patients, the degree of L-to-R shunting may decrease as RV dysfunction and tricuspid regurgitation (TR) develop. In other patients, due to systemic hypertension and reduced left ventricular (LV) compliance, the L-to-R shunt increases. In an untreated ASD, pulmonary vascular disease may develop reversing it to a right-to-left (R-to-L) shunt and causing hypoxia that may be intermittent and severe depending on RV function.

Closure of an ASD is indicated if the pulmonary to systemic shunt ratio is greater than 1.5:1 and the calculated pulmonary vascular resistance (PVR) is less than 6–8 Wood units/m^2. Most adolescents are asymptomatic, but adults in their 30s and 40s commonly develop atrial fibrillation or reduced exercise tolerance, and eventually heart failure. It is preferable to close the defect when the diagnosis is made, prior to the development of significant symptoms.

TEE EVALUATION OF THE INTERATRIAL SEPTUM

2D Imaging

Transesophageal echocardiography provides excellent interrogation of the IAS with a sensitivity exceeding that of transthoracic echocardiography for the detection of ASDs. Multiple TEE planes ME bicaval, ME four-chamber (4C), ME RV inflow-outflow) are used to image the IAS and can identify an ASD (**Figure 11.4**). The ME bicaval view best interrogates the IAS as the imaging plane is perpendicular to tissue and spectral Doppler alignment is

parallel to flow. In the ME 4C view, the TEE plane is parallel to the IAS so tissue may appear absent from ultrasound dropout. Ideally, tissue defects should be confirmed in more than one view and by using color Doppler. Measurement of the ASD size uses the minor axis obtained from a ME RV inflow-outflow or ME 4C views and the major axis obtained from a ME bicaval view (**Figure 11.4**).

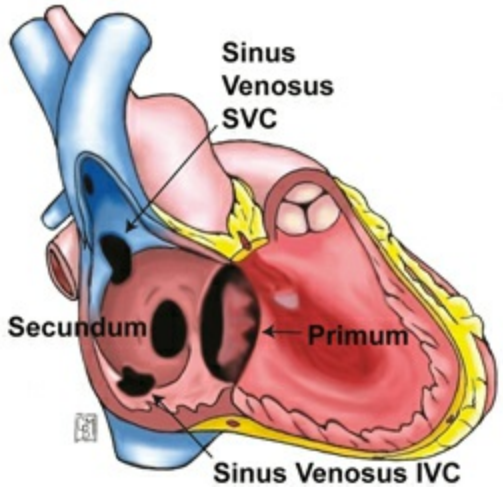

Fig. 11.3 . Atrial septal defect types. An atrial septal defect (ASD) is a deficiency in the wall of the interatrial septum that is classified according to location as shown: sinus venosus superior vena cava (SVC) type, sinus venosus inferior vena cava (IVC) type, ostium secundum ASD, ostium primum ASD, and coronary sinus ASD which is not shown. (Illustration courtesy of M. Busato; with permission from Denault *et al.* [2] *)*

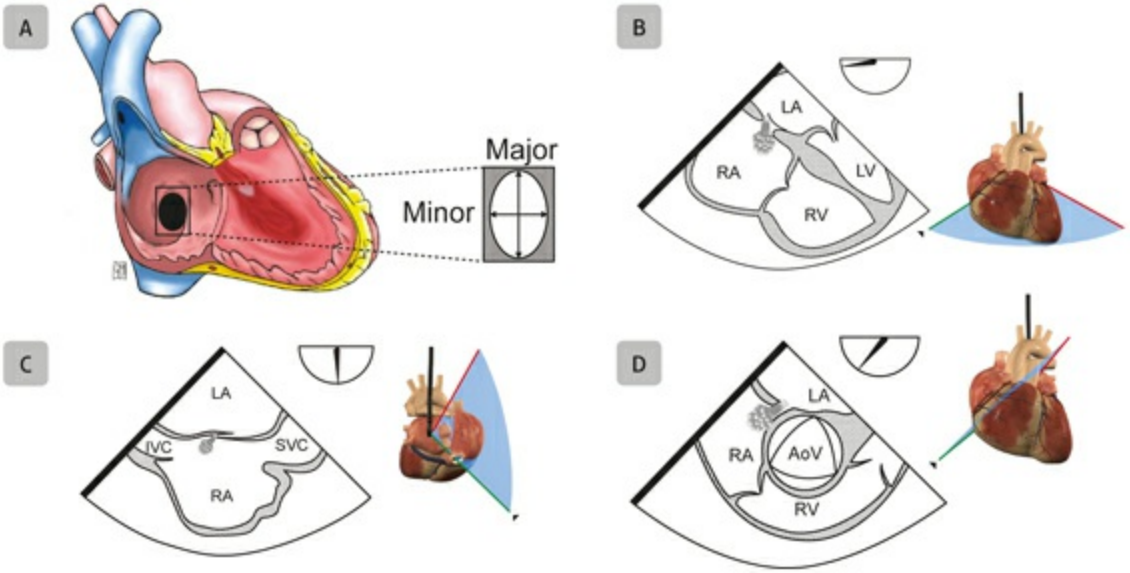

Fig. 11.4 . Transesophageal echocardiography (TEE) views to image the interatrial septum (IAS). (A)

Multiple TEE views are used to assess the IAS and determine the presence of an atrial septal defect (ASD) or patent foramen ovale (PFO). (B-D) These midesophageal (ME) TEE views are the (B) ME four-chamber, (C) ME bicaval, and (D) ME RV inflow-outflow. A secundum ASD is often oval-shaped with a major (ME bicaval view) and minor axis (ME RV inflow-outflow or ME four-chamber views). AoV, aortic valve; IVC, inferior vena cava; LA, left atrium; LV, left ventricle; RA, right atrium; RV, right ventricle; SVC, superior vena cava. (Illustration courtesy of M. Busato, with permission from Denault *et al.* [2])

Color and Spectral Doppler

The diagnostic evaluation of ASDs is assisted by the use of spectral pulsed-wave (PW) and color Doppler, which demonstrates abnormal flow across the IAS (**Figure 11.5**). Left-to-right shunting is usually the case for an isolated ASD. At a Nyquist of 50 cm/s, laminar flow is typical with a large ASD, whereas turbulent flow suggests a small gap with restriction to flow. Spectral PW Doppler reveals low velocity (<1 m/s) continuous triphasic flow, with predominantly diastolic flow. Early systolic flow reversal (R-to-L shunt) may worsen with positive pressure ventilation. The peak velocity across the defect is inversely proportional to defect size, a larger defect having lower velocity laminar flow. The right ventricular systolic pressure (RVSP), an estimate of the pulmonary artery systolic pressure (PASP), can be determined from the peak velocity of the TR jet if present and right atrial pressure (RAP) as previously discussed (see **Figure 7.30**).

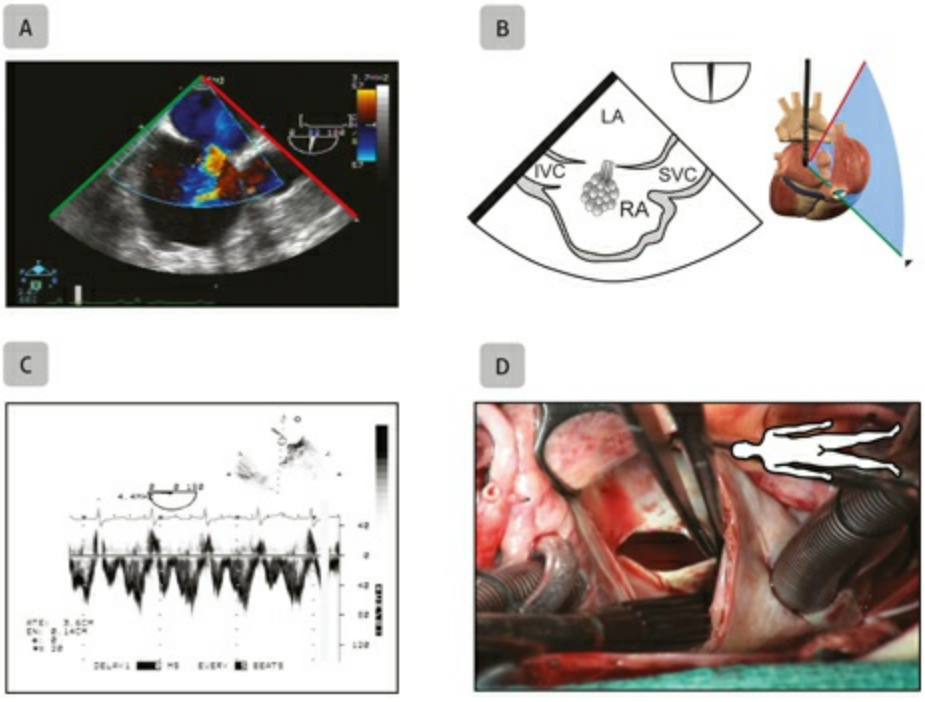

Fig. 11.5 . Atrial septal defect (ASD) secundum. Ostium secundum ASD in the midportion of the atrial septum is diagnosed in a 50-year-old male undergoing coronary revascularization. (A,B) Color Doppler (Nyquist 67 cm/s) mid-esophageal bicaval view at 86° shows the left-to-right shunt from the left atrium (LA) to the right atrium (RA). (C) Pulsed wave Doppler of an ASD demonstrates both systolic and diastolic flow. (D) Intraoperative aspect of an ASD is shown. IVC, inferior vena cava; SVC, superior vena cava. (Source: Photo C courtesy of Dr Michel Carrier; with permission from Denault *et al.* [2] *)*

A: https://youtu.be/YtY1KJa0qZk

D: https://youtu.be/B5r4h1Ngr84

The shunt fraction or ratio of pulmonary to systemic flow can be determined by comparing the stroke volume at two intracardiac sites. The stroke volume is calculated from the cross-sectional area (CSA) multiplied by the velocity time integral (VTI) obtained from tracing the spectral Doppler waveform (see **Figure 15.8**). For an ASD, this would be systemic flow (Qs) through the aortic valve (AoV) or left ventricular outflow tract (LVOT), and the pulmonary flow (Qp) through the pulmonary artery (PA).

Shunt fraction = Q p Q s = SV Pulmonary SV systemic = CSA × VTI PA CSA × VTI LVOT or AoV

Contrast Echocardiography

Saline contrast is the most sensitive method to detect interatrial shunting, being more reliable than angiography or oximetry. To perform a contrast study, 3-10 mL of saline is agitated with <1 mL of air and injected rapidly into a central or arm vein. Microbubbles form in the bloodstream where they act as strong ultrasound reflectors, opacifying the right cardiac chambers. The microbubbles are fully absorbed in the lungs.

The use of saline contrast for the identification of a PFO and ASDs depends on the small degree of R-to-L shunting that occurs when RAP exceeds left atrial pressure (LAP) at the onset of ventricular systole or during

a cough or Valsal-va maneuver. A ventilated patient, sustaining an inspiratory pressure of 25 mmHg for approximately 10 seconds, can simulate a Valsalva maneuver. A negative study represents no flow of bubbles across the IAS. A positive study indicates R-to-L shunting (RAP > LAP) with microbubbles present in the LA within five heartbeats. A false-positive study with bubbles appearing in the LA may occur from a pulmonary arteriovenous malformation. Additionally, the presence of negative contrast from non-contrasted blood appearing in the contrast-filled RA may be helpful in identifying L-to-R shunting.

Patent Foramen Ovale

A PFO may be difficult to detect using 2D TEE imaging alone, but should be suspected in the presence of an oblique gap between the septum primum and limbus of the fossa ovalis. Color Doppler at a lower Nyquist limit (30 cm/s) may help identify a small amount of flow if present. The direction of color flow will depend on the relationship of the TEE probe and the PFO. Typically, turbulent flow may be present indicating a small restrictive defect. Laminar blue color flow often represents flow away from the transducer (L-to-R shunt), although if RAP is elevated, color flow may appear red in color indicating a R-to-L shunt. The use of saline contrast increases PFO detection both at rest and with raised RAP as during a Valsalva maneuver (**Figure 11.6**). Transcranial Doppler can also be used to evaluate shunt severity (see **Figure 13.25**).

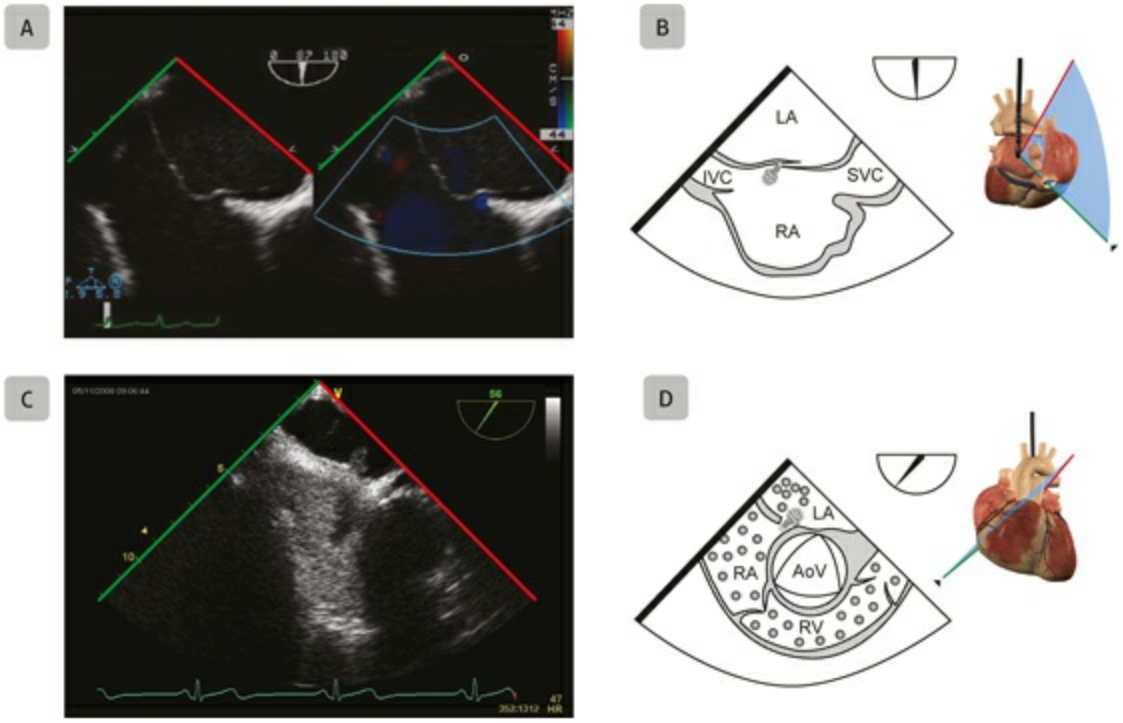

Fig. 11.6 . Patent foramen ovale (PFO). (A,B) A PFO is demonstrated by color Doppler (Nyquist 44 cm/s) in a midesophageal (ME) bicaval view. (C,D) ME right ventricular inflow/outflow view shows opacification of the right-sided cardiac chambers during intravenous injection of agitated normal saline. At the release phase of a Valsalva maneuver, microbubbles are seen crossing from the right atrium (RA) to the left atrium (LA) through a PFO. AoV, aortic valve; IVC, inferior vena cava; RV, right ventricle; SVC, superior vena cava. (Reproduced with permission from Denault *et al.* [2] *)*

C: https://youtu.be/eNdHRUrSMHY

Ostium Secundum Atrial Septal Defect

Identification of a centrally located ostium secundum ASD in the region of the fossa ovalis is best imaged from ME bicaval or ME RV inflow-outflow views. These defects are bound on all sides by atrial septal tissue and may be single or of the multiple fenestrated type. Evaluation of an ASD includes confirmation of the defect location, size, assessment of shunt flow, chamber and vessel enlargement, and an estimation of pulmonary artery pressures.

Other Echocardiographic Findings

Transesophageal echocardiography examination for the other types of ASDs is beyond the scope of basic TEE practice. However, the presence of a dilated RA, RV, and PA suggests the presence of volume overload from LA to RA shunting of blood and may prompt a search for the etiology, such as an ASD. Right atrial and RV enlargement with diastolic flattening and paradoxical motion of the IVS septum are evidence of RV volume overload and a significant L-to-R shunt (see **Figure 5.12**).

Interatrial Septal Anomalies

Transesophageal echocardiography can identify the presence of other anomalies of the IAS. Normally, the IAS is relatively fixed in position and moves passively with the movement of the entire heart. Occasionally, the septum is hypermobile, which is linked to the presence of an aneurysm of the IAS, defined as a 15 mm bulge into either atria or as total excursion. In this setting, the septum is thin and may be fenestrated, resulting in variable degrees of interatrial flow. A PFO is more common in patients with an IAS aneurysm or a Chiari network in the RA.

Device Closure

Transesophageal echocardiography also plays an important role in the cardiac catheterization laboratory during transcatheter closure of ASDs by providing real-time observation and confirmation of appropriate device placement and effectiveness of occlusion. Transesophageal echocardiography provides confirmation of the diagnosis, and assists in sizing of the defect, determination of optimal occluder dimensions, imaging of atrial septal rims, and evaluation of pulmonary venous return. It also allows for recognition of potential problems, such as unusual device arm positions, distortion of systemic or pulmonary venous inflows, and atrioventricular valves. Following successful deployment of an ASD device, there is still some residual flow through the device until endothelialization occurs after 3 months. Despite the presence of an ASD occluding device in up to 10% of patients, significant residual shunting may be present that requires additional treatment.

INTERVENTRICULAR SEPTAL ANATOMY

Morphologically, the ventricular septum is composed mostly of muscle (95%) with a small membranous portion, and it is divided into four components: (1) membranous, (2) inlet, (3) trabecular, and (4) outlet septa. The IVS is obliquely placed, facing forward and to the right, bulging into the RV. The small membranous septum is bordered superiorly by fibrous tissue in the base of the heart directly below the aortic valve (right and non-coronary cusps) and immediately antero-inferior to the TV septal leaflet. It is surrounded by the three regions of muscular septum identified as: the inlet septum (posterior to the membranous septum), outlet or infundibular septum (anterior to the membranous septum), and the larger trabecular septum. The membranous septum forms the superior border of the LVOT and is intimately related with the atrioventricular conduction system.

Ventricular Septal Defects

Ventricular septal defects are categorized into four anatomic types (**Figure 11.7**) according to their location, although there is frequent crossover between the different VSD types. For example, those in the muscular septum may extend into the membranous septum.

1. Membranous VSD (70%) results from failure of the membranous septum to develop from the endocardial cushions and fuse with the muscular IVS. These VSDs are rarely limited to the membranous septum, but more often extend into the muscular region hence the term “perimembranous”. The *perimembranous* type represents the majority of VSDs presenting later in life. This defect is located beneath the TV septal leaflet between the divisions of the septal band. It is in close proximity to the non-coronary or right coronary AoV cusps and may cause aortic regurgitation from cusp prolapse through the VSD. The presence of an interventricular septal aneurysm has been associated with a high incidence of spontaneous defect closure.
2. Muscular VSD (20%) probably results from excessive resorption of myocardial tissue during formation of the muscular portion of the septum (**Figure 11.8**). These defects may appear anywhere in the muscular septum and may be single or multiple. Congenital VSDs often close in the first year of life and are thus unlikely to be present in adulthood. Acquired muscular VSD may occur as a complication

of myocardial infarction. The apical septal location (anterior myocardial infarction, left anterior descending artery) is involved more often than the inferior septal location (inferior myocardial infarction, right coronary, or circumflex arteries) (see **Figures 6.18 and 6.19**).

3. Subarterial VSD (5%) is located in the supracristal area and lies directly beneath the pulmonic valve. The right coronary cusp of the aortic valve and sometimes the non-coronary cusp may prolapse into the defect. An outlet VSD when they abut both semilunar valves, are sometimes referred to as supracristal or doubly committed subarterial defects.
4. Inlet VSD is located in the inlet of the RV adjacent to the central fibrous body, tricuspid and mitral valves. These lesions are part of the spectrum of EC defects or atrioventricular septal defects which form from abnormal cardiac septation. This results in defects that typically involve deficiencies on the atrial, atrioventricular, and inlet ventricular septae.

Physiology of Ventricular Septal Defect

Small restrictive VSDs may allow survival to adulthood without surgical treatment. Such defects are likely to result from partial spontaneous closure or from residual patch leaks following earlier surgical closure. Use of the term *restrictive* implies a pressure gradient between the ventricles. Surgical correction is indicated in the presence of Qp/Qs shunt >1.8:1, PVR <6 Woods units/m^2, paradoxical embolus, enlarging RV, and arrhythmias.

In patients with large VSDs there is unrestricted flow, shunting is significant, and the RV enlarges. The pressures within the right heart will become “systemic” and identical to those in the left. Long-standing high flow into the lungs may cause severe pulmonary vascular disease to develop. These patients ultimately will become cyanotic as a result of R-to-L shunting and will eventually die of complications of Eisenmenger’s syndrome if they are not operated upon. Unfortunately, closure of the defect would produce suprasystemic RV pressures and the only surgical options available are either heart-lung transplantation or lung transplantation with repair of the VSD.

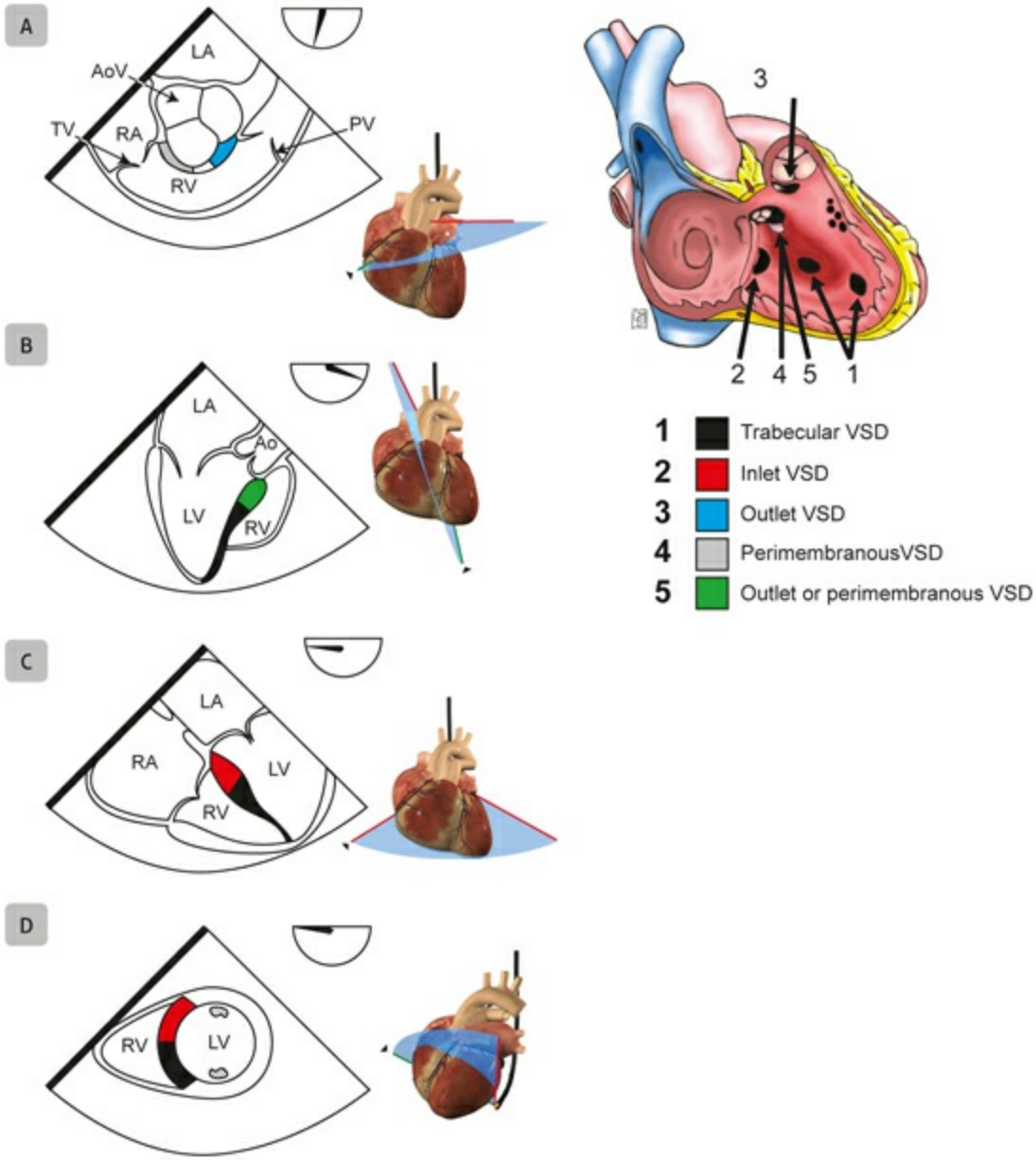

Fig. 11.7 . Ventricular septal defect (VSD). Classification of VSDs according to locations and as imaged by transesophageal echocardiography include the (A) mid-esophageal (ME) right ventricular inflow/outflow, (B) ME long-axis, (C) ME four-chamber, and (D) transgastric (TG) mid short-axis views. Ao, aorta; AoV, aortic valve; LA, left atrium; LV, left ventricle; PV, pulmonic valve; RA, right atrium; RV, right ventricle; TV, tricuspid valve. (Illustration courtesy of M. Busato; with permission from Denault *et al.* [2] *)*

ECHOCARDIOGRAPHIC EVALUATION OF THE INTERVENTRICULAR SEPTUM

The IVS is curved and does not lie in one plane, thus requiring multiple TEE views for adequate interrogation. The echocardiographic examination should consider the region of the septum involved in each view. The sensitivity of echo for diagnosing VSD depends on the location. Sensitivity is highest for inlet and outlet defects, slightly less for perimembranous and least for trabecular defects. The combination of 2D echocardiography, spectral, and color Doppler modalities is needed for adequate evaluation. Using 2D imaging, each type of VSD can be identified including the location, size, and number of defects, chamber sizes, and ventricular function.

Color and Spectral Doppler

Color Doppler (Nyquist 30–60 cm/s) over the IVS in all relevant TEE views can aid in defining the location of even a small defect. Many acquired VSDs are muscular with restrictive flow that is seen as turbulent flow only by using color Doppler. In addition, color Doppler provides optimal alignment of the spectral Doppler beam, assisting in the estimation of interventricular pressure gradients.

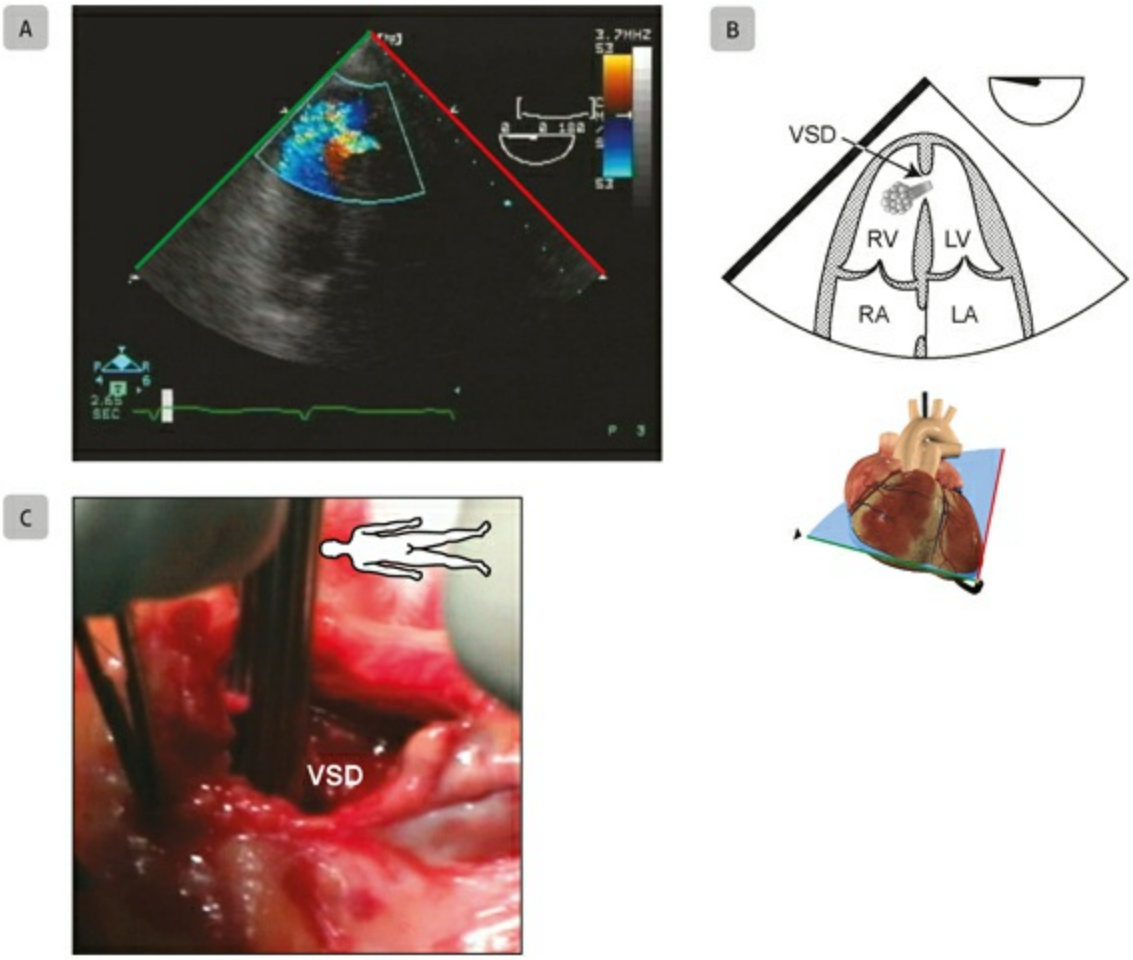

Fig. 11.8 . Muscular ventricular septal defect (VSD). (A,B) Color Doppler deep transgastric long-axis view shows a trabecular muscular VSD with left-to-right shunt that is confirmed by (C) the intraoperative findings. LA, left atrium; LV, left ventricle; RA, right atrium; RV, right ventricle. (Reproduced with permission from Denault *et al.* [2] *)*

A: https://youtu.be/8eWPqkn3TTE

C: https://youtu.be/xIZX2qVG2T0

Spectral Doppler shows continuous flow with systolic predominance as LV

pressure exceeds RV pressure throughout the cardiac cycle. A smaller, restrictive defect has a larger pressure difference between the ventricles. A large VSD has a small pressure gradient with unrestricted shunt flow that enlarges the RV. Eisenmenger's syndrome may occur in an unrestricted VSD with elevated PA pressure causing shunt reversal (R-to-L). Estimation of RVSP or PASP can be obtained from the TR jet, as previously described, or from the VSD jet where

RVSP = LV systolic Pressure - 4 V vsd peak 2

Similar to an ASD, and as previously described, the shunt fraction (Qp/Qs) can be determined by comparing the stoke volume (SV) at two intracardiac sites, where SV = CSA x VTI. For a VSD this would be Qs only through the aortic valve or LVOT and Qp only through the PA or right ventricular outflow tract.

Saline Contrast

Contrast injection is less helpful, as in most cases RV pressure is lower than LV pressure, requiring identification of a VSD by negative "wash-out" of uncontrasted blood in the contrast-filled RV. When RV pressure exceeds LV pressure resulting in R-to-L shunting, contrast echocardiography is exquisitely sensitive to identifying small VSDs, as only a few microbubbles in the LV confirm the diagnosis. This is a particularly useful technique for suspected defects that cannot be imaged by standard approaches and for small muscular defects in association with pulmonary hypertension.

Perimembranous and Muscular VSDs

The most common defect, the perimembranous type, is located near the TV just beneath the AoV. These defects are best seen in the ME RV inflow-outflow (60°), ME five-chamber (5C) view (0°) and ME AoV long-axis (LAX) view (0–120°). A gap in the IVS may be apparent, although confirmation with color and spectral Doppler is usually required. There may be associated TV abnormalities, AoV cusp herniation with aortic regurgitation, and subaortic stenosis.

Muscular (trabecular) VSD is bound entirely by muscular septum and occurs in the central or apical region. Muscular defects may be multiple and, depending on their size, may be quite difficult to see with 2D imaging. The

use of color Doppler in different TEE views (ME 4C, ME LAX, and TG) can help identify small, serpiginous and multiple ("Swiss cheese") defects. Identification of inlet and outlet VSDs are beyond the scope of basic TEE examination.

SUMMARY

A basic TEE examination using 2D imaging, color Doppler, and contrast can screen for defects in the IAS and IVS. Common lesions include a PFO, ostium secundum ASD, perimembranous VSD, and muscular VSD. It may be important to exclude the presence of a shunt, particularly a PFO in a patient with unexplained hypoxemia or a muscular VSD in a hemodynamically unstable patient. Detailed assessment of ASDs and VSDs requires the skills of an advanced TEE echocardiographer. More resources on the use of TEE for congenital heart disease can be found on the Internet. [4]

REFERENCES

1 Lai, W. W., T.Geva, G. S.Shirali, P. C.Frommelt, R. A.Humes, M. M.Brook, et al. 2006. "Guidelines and standards for performance of a pediatric echocardiogram: a report from the Task Force of the Pediatric Council of the American Society of Echocardiography." *J Am Soc Echocardiogr 19*: 1413–30.

2 Denault, A. Y., P.Couture, A.Vegas, J.Buithieu, and J. C.Tardif. 2001. *Transesophageal Echocardiography Multimedia Manual, Second Edition: A Perioperative Transdisciplinary Approach*. New York, NY: Informa Healthcare.

3 Burch, T. M., K. A.Mizuguchi, and J. A.DiNardo. 2012. "Echocardiographic assessment of atrial septal defects." *Anesth Analg 115*: 772–5.

4 Russell, I. A., K.Rouine-Rapp, G.Stratmann, and W. C.Miller-Hance. 2006. "Congenital heart disease in the adult: a review with internet-accessible transesophageal echocardiographic images." *Anesth Analg 102*: 694–723.

Chapter 12

Echocardiography in Non-Cardiac Procedures and Trauma

Andrew Roscoe, Ashraf Fayad, François M Carrier and André Y Denault

INTRODUCTION

The practice guidelines for transesophageal echocardiography (TEE) monitoring during non-cardiac surgery recommend that “it may be used when the nature of the planned surgery or the patient’s known or suspected cardiovascular pathology might result in severe hemodynamic, pulmonary, or neurologic compromise.” In addition, “when equipment and expertise are locally available, TEE should be used when unexplained life-threatening circulatory instability persists despite corrective measure.” [1] , [2] Assessment of unexplained hemodynamic instability is warranted in any patient undergoing any surgical procedure. Some non-cardiac surgical procedures are complex and hemodynamic instability is a common occurrence. In addition, TEE can provide specific information to guide the surgical procedure. In this chapter, the role of TEE during non-cardiac surgical procedures, such as thoracic surgery, lung transplantation, aortic and vascular surgery, liver and renal transplantation, and trauma is explored. These procedures can alter cardiac function, but also affect pulmonary, hepatic, and renal function.

PERIOPERATIVE ECHOCARDIOGRAPHY EXAMINATION

Performance of the perioperative echocardiography examination as a baseline assessment during non-cardiac surgery follows the same steps as the comprehensive intraoperative TEE examination recommended by the American Society of Echocardiography (ASE) and the Society of Cardiovascular Anesthesiologists (SCA) task force. However, in hemodynamically unstable patients, echocardiography should focus primarily on examining ventricular function and preload conditions. [4] The following seven questions need to be answered:

1. What is the volume stauts? Is the heart full or empty?
2. Is there significant left ventricular (LV) and right ventricular (RV) systolic dysfunction?
3. Are there regional wall motion abnormalities (RWMA)?
4. Is there a significant valvular lesion?
5. Is there significant pericardial effusion?
6. Is there a significant hemothorax/pneumothorax?
7. Is there free fluid in the abdomen?

A focused examination to assess the hemodynamics may be achieved with only a limited number of TEE views (see **Figure** 3**.1**) or transthoracic echocardiography (TTE) views (see **Figure** 1**5.2**). Once the patient is stabilized, a full comprehensive echocardiographic examination can be performed. The echocardiographer should be familiar with the nomenclature and terminology used during the echocardiography exam. An echocardiography report should be produced for all studies. A summary of the case and hemodynamic management may be added to the report with the supporting images.

THORACIC SURGERY

Although there is no evidence for the routine use of TEE during lung resection surgery, its clinical utility as a hemodynamic monitor is becoming more attractive. The advantages of TEE over a pulmonary artery catheter (PAC) as a hemodynamic monitor are well recognized. [5] Intraoperative TEE can be used to accurately evaluate LV preload in major thoracic surgeries, such as extrapleural pneumonectomy or Pancoast tumor resection with vertebral body involvement, where major blood loss is encountered. In elderly patients with concomitant cardiac disease, the LV can be assessed for

signs of ischemia and reduced contractility (see **Figure** 5**.24**). Transesophageal echocardiography also plays a key role in the early detection of RV dysfunction, allowing for prompt treatment (**Figure 12.1**). Impending RV failure presents with RV dilatation and reduced contractility, as assessed by fractional area change (FAC) (**Figure 12.2**), tricuspid annular plane systolic excursion (TAPSE) (see **Figure** 5**.13**) and tissue Doppler imaging (TDI) (**Figure 12.3**) of tricuspid annulus. [6]

Transesophageal echocardiography may play a useful role in delineating the size of mediastinal masses and the extent of any invasion into surrounding structures, such as the atria, pulmonary veins, pulmonary artery (PA), or superior vena cava (**Figure 12.4**) (see also **Figures 4.12–4.15**). It may also guide surgery to determine if complete tumor resection has been achieved (**Figure 12.5**). [7] , [8] Transesophageal echocardiography is also invaluable in establishing the size of any associated pericardial effusion and its hemodynamic effects (**Figure 12.1**). Pulmonary thromboendarterectomy is the treatment of choice for patients who develop chronic thromboembolic pulmonary hypertension. It is a cardiac surgical procedure and done under cardiopulmonary bypass. Patients may have supra- systemic PA pressures and evaluation with appropriate management of RV function is paramount. [9] Transesophageal echocardiography is essential to exclude interatrial septal defects with intracardiac shunting (see **Figure** 11**.6**), assess biventricular function, and detect any residual thrombus within the PA (**Figure 12.6**).

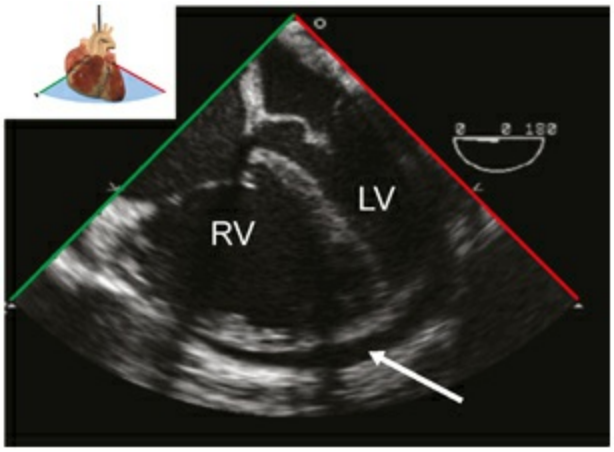

Fig. 12.1 Right ventricular (RV) dilatation. Mid-esophageal four-chamber view shows severe RV dilatation, leftward shift of the interventricular septum, and a small pericardial effusion (arrow). LV, left ventricle.

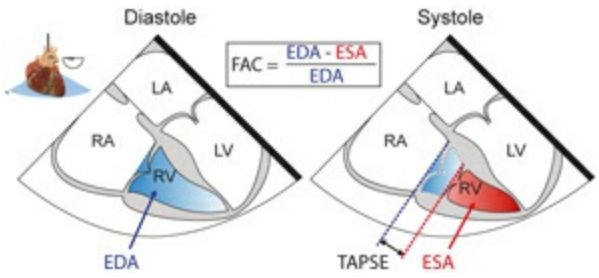

Fig. 12.2 Right ventricular (RV) assessment. The RV fractional area change (FAC) corresponds to the difference of the RV end-diastolic area (EDA) minus the RV end-systolic area (ESA) divided by the RV EDA. Tricuspid annular plane systolic excursion (TAPSE) represents the systolic excursion of the lateral tricuspid annulus. TAPSE can be measured from the change in the distance (arrow) in diastole between the apex and the lateral tricuspid annulus. Normal TAPSE should be >17 mm. [5] LA, left atrium; LV, left ventricle; RA, right atrium. (Adapted from Denault *et al.* [3])

C: https://youtu.be/2F6UIX6ZXzA

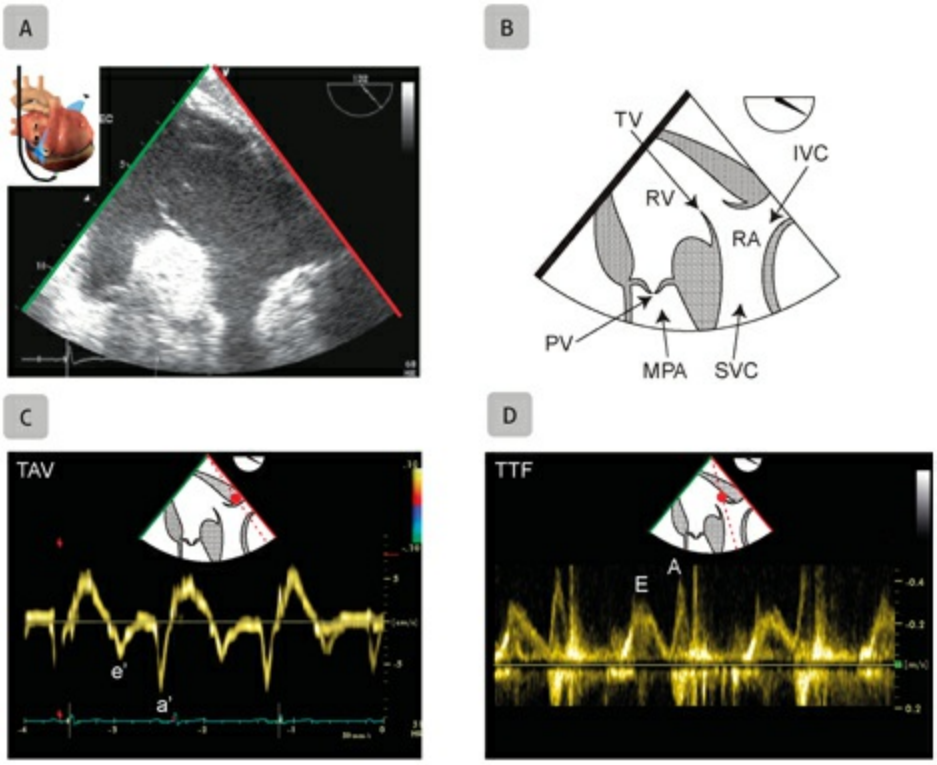

E

Parameter	Mean ± SD	Abnormality threshold
E wave deceleration time (msec)	180 ± 31	< 119 or > 242
E/A	1.4 ± 0.3	< 0.80 or > 2.0
e'/a'	1.18 ± 0.33	< 0.52
e'	14.0 ± 3.1	< 7.8
E/e'	4.0 ± 1.0	< 6.0

Fig. 12.3 Tissue Doppler imaging (TDI) for right ventricular (RV) function. (A,B) Transesophageal echocardiographic transgastric RV inflow/outflow long- axis view can evaluate both the pulsed-wave Doppler interrogation of the tricuspid valve (TV) and TDI of the tricuspid annulus along the dotted line. (C) The tissue Doppler signal is obtained at the base of the tricuspid annulus and shows e' and a' waves. (D) Transtricuspid flow (TTF) can be assessed using pulsed- wave Doppler from this transgastric view to show early diastolic TTF velocity (E) and peak late diastolic TTF velocity (A) waves. a', peak late diastolic tricuspid annular velocity (TAV); e', peak early diastolic TAV; IVC, inferior vena cava; MPA, main pulmonary artery; PV, pulmonic valve; RA, right atrium; SD, standard deviation; SVC, superior vena cava. (Reproduced with permission from Denault *et al.* [3] *)*

LUNG TRANSPLANTATION

The intraoperative use of TEE during lung transplantation was originally classified as a IIb indication by the ASE [10] for the evaluation of vascular anastomotic sites. However, the 2010 updated report by the SCA recommended that TEE should be used during lung transplantation. [1] **Table**

12.1 summarizes the role of TEE as an intraoperative monitor in lung transplantation.

Before Lung Transplantation

In addition to performing a full standard TEE examination, special consideration is given to the detection of an intracardiac shunt, assessment of RV function and visualization of pulmonary venous drainage. [11] The interatrial septum is interrogated in its entirety, from 0° (mid-esophageal (ME) 4-chamber view) through to 100° (ME bicaval view), using color flow Doppler (CFD), to exclude any defects. A saline contrast study is performed if the use of CFD is inconclusive. The presence of a small patent foramen ovale (PFO) (see **Figure** 11**.6**) may not warrant surgical closure, but the use of high levels of positive-end expiratory pressure in the postoperative period may cause significant right-to-left shunting through the PFO. [12] Signs of RV overload include flattening of the interventricular septum, resulting in a D-shaped LV and compromised LV filling (see **Figure** 5**.12**). Initial poor RV function may predict more hemodynamic instability during surgery [11] and its communication to the surgical team may lead to the use of cardiopulmonary bypass for the procedure. All four pulmonary veins should be seen with CFD, [13] to allow for post-transplantation comparison. In addition, TEE can help in cannula placement in order to establish cardiopulmonary bypass in selected patients.

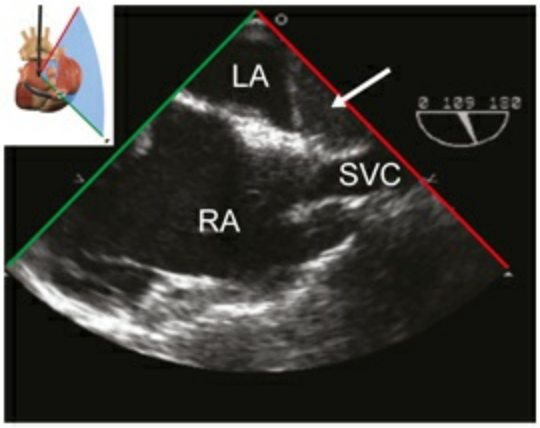

Fig. 12.4 Mediastinal tumor. Mid-esophageal modified bicaval view, shows a mediastinal tumor (arrow) compressing the left atrium (LA). RA, right atrium; SVC, superior vena cava.

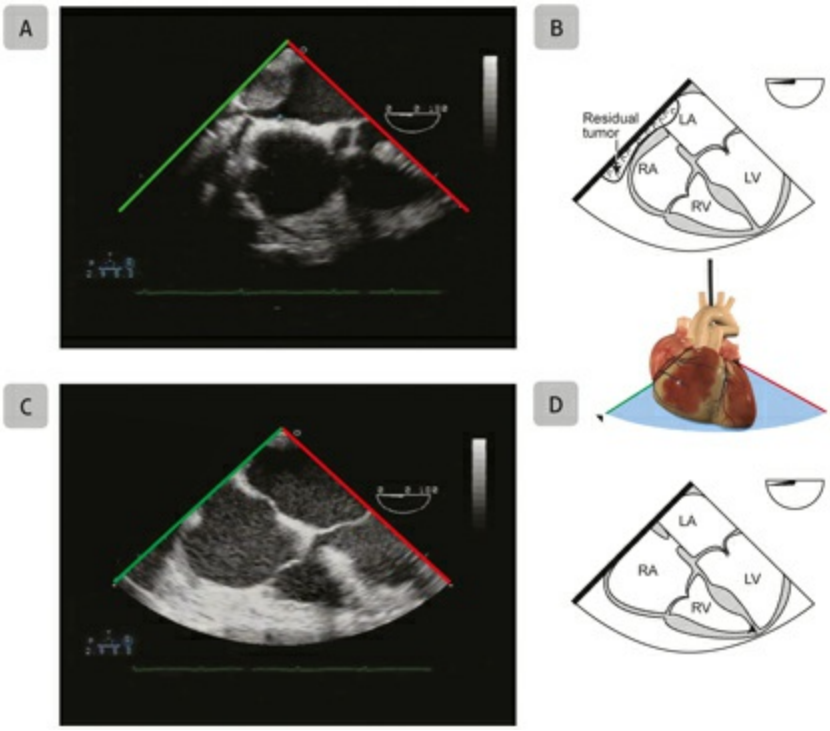

Fig. 12.5 Mediastinal tumor. Prior to chest closure, a repeat transesophageal echocardiography examination after resection of a posterior mediastinal neurogenic tumor demonstrated residual tumor. (A,B) Mid-esophageal four-chamber view revealed significant residual tumor in the left atrium (LA) which was (C,D) further completely resected. LV, left ventricle; RA, right atrium; RV, right ventricle. (Reproduced with permission from Denault *et al.* [3])

During Lung Transplantation

Throughout the surgical procedure, periods of cardiovascular instability can be rapidly diagnosed by TEE, expediting appropriate treatment. Systemic hypotension may be due to hypovolemia or vasodilatation, necessitating fluid boluses or vasopressors, or from LV systolic dysfunction, requiring inotropic support. Cross-clamping of the PA may induce RV failure. Removal of the left atrial clamp and reperfusion of the implanted lung can cause air embolization into the left heart (**Figure 12.7**).

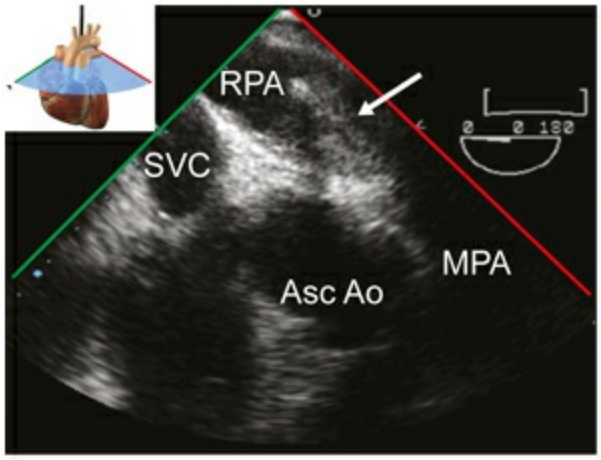

Fig. 12.6 Thrombus. Mid-esophageal ascending aorta (Asc Ao) short-axis view shows thrombus (arrow) within the right pulmonary artery (RPA). MPA, main pulmonary artery; SVC, superior vena cava.

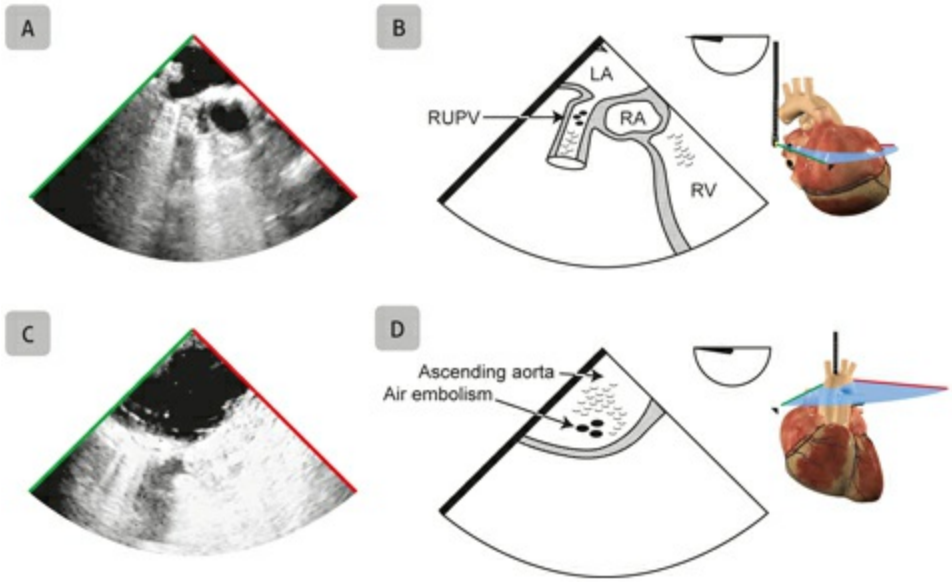

Fig. 12.7 Air emboli. (A,B) Mid-esophageal view with right-sided rotation shows air bubbles coming from the right upper pulmonary vein (RUPV) at the completion of the vascular anastomosis during lung transplantation. (C,D) Upper esophageal aortic arch longaxis view also shows air bubbles in the aorta. LA, left atrium; RA, right atrium; RV, right ventricle. (Reproduced with permission from Denault *et al*.[3])

A: https://youtu.be/UoQC5TfCaXg

Table 12.1 Transesophageal Echocardiography for Lung Transplantation.

Stage	Echo Exam
Pre-implantation	Intracardiac shunt Baseline RV function Baseline pulmonary venous drainage
During implantation	PA clamping: RV dysfunction PA unclamping: air in left heart
Post-implantation	Pulmonary vein anastomosis PA anastomosis

PA, pulmonary artery; RV, right ventricle.

After Lung Transplantation

After organ implantation, it is essential to evaluate the pulmonary vein anastomoses to exclude significant stenosis (**Figure 12.8**). A pulmonary vein diameter <5 mm and a peak systolic velocity >1 m/s are suggestive of significant anastomotic stenosis. [14] However, TEE may overestimate left lower pulmonary vein velocities and caution must be exercised when making management decisions regarding surgical re-intervention. [15] Venous obstruction can lead to lung venous thrombosis and congestion (see **Figure** 14**.22**). Pulmonary artery anastomoses are more difficult to view with TEE, as typically only the right pulmonary artery anastomosis is visualized. In patients who develop severe primary graft dysfunction, veno-venous extracorporeal membrane oxygenation (ECMO) is occasionally employed to "rest" the implanted lungs. Transesophageal echocardiography is useful in positioning of the ECMO cannulae (see **Figure** 8**.35**).

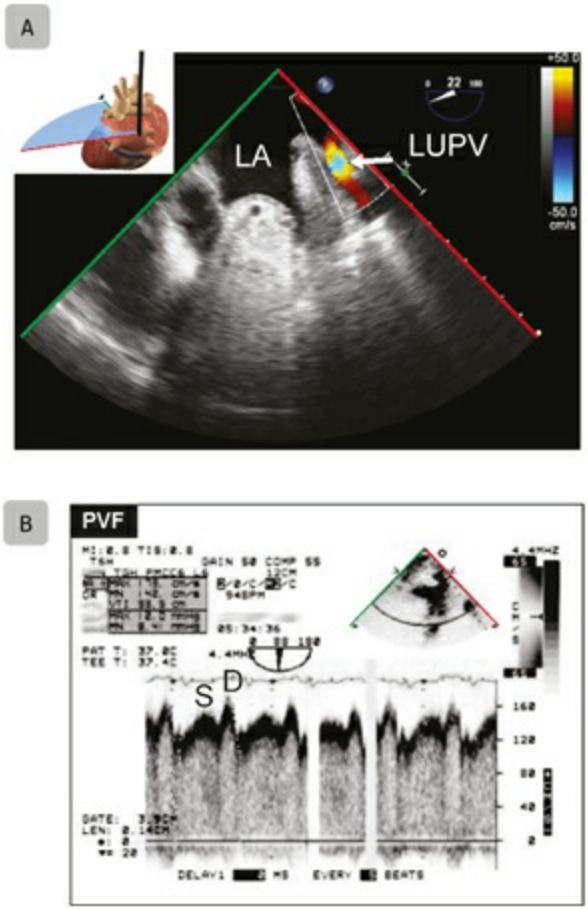

Fig. 12.8 Left upper pulmonary vein (LUPV) stenosis. (A) Color Doppler (Nyquist 50 cm/s) mid-esophageal view at 22° shows turbulence at the anastomosis of the LUPV after lung transplantation. (B) Pulsed-wave Doppler of the pulmonary venous flow (PVF) demonstrates elevated systolic (S) and diastolic (D) velocities with spectral broadening and abnormal diastolic flow predominance (S < D), consistent with increased pressure gradient across the anastomosis, in a different patient. LA, left atrium.(Adapted with permission from Denault *et al.* [3])

A: https://youtu.be/9gMcVSuPyzY

VASCULAR SURGERY

Patients undergoing major vascular surgery are at increased risk for perioperative cardiac complications. [16] There is a poor correlation between the traditional monitors and hemodynamics during vascular surgical

procedures. [17 – 19] There is a relatively weak correlation between pulmonary capillary wedge pressure and left ventricular end-diastolic pressure (LVEDP) using intraoperative TEE during abdominal aortic aneurysm (AAA) repair. Furthermore, the strength of the correlation worsened during surgery, particularly after aortic unclamping. [19] This led to the conclusion that TEE may be a valuable adjunct in guiding volume resuscitation of patients undergoing AAA repair [19] and thoracoabdominal aortic aneurysm (TAAA) repair. [18]

Transesophageal echocardiography is a sensitive diagnostic tool that allows direct visualization and characterization of the aortic plaques (**Figure 12.9**), [20] ulcerations, dissections, aneurysms, leaks, and endoleaks. [21 – 23] Unlike an angiogram, TEE has the unique advantage of portability and can obtain high-resolution images of the normal and abnormal anatomy of all three aortic wall layers and the aortic lumen. [24] Transesophageal echocardiography is also a highly sensitive and specific method of detecting injury to the thoracic aorta (Ao) (**Figure 12.10**). [25] In addition, TEE provides additional and critical information in thoracic endovascular aortic repair (TEVAR) that impacts early and late outcomes. [26 – 29]

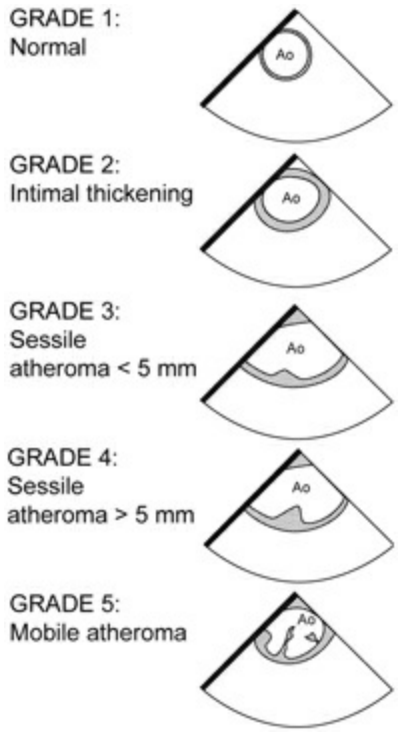

Fig. 12.9 Classification of aortic atheroma. Grades of atheromatous disease of the aorta (Ao) are represented in this illustration. (Reproduced with permission from Denault *et al.* [3])

Transesophageal Echocardiography Examination of the Thoracic Aorta

All parts of the Ao should be examined and assessed using the recommended TEE views (see **Figure** 3**.1**): ME ascending Ao long-axis (LAX) (120–150°) (see **Figure** 3**.9**) and short- axis (SAX) (0–10°) (see **Figure 3.10**), ME descending Ao LAX (90–110°) and SAX (0°) (see **Figure 3.15**), and upper esophageal aortic arch LAX (0°) and SAX (90°) (**Figure 12.11**). Transesophageal echocardiography examination is unable to image the mid- and distal ascending Ao (42% of the length) and the proximal aortic arch in any detail. [30] Mahajan *et al.* [31] suggested the proximal transgastric (TG) view for the ascending and aortic arch using a newer TEE probe (**Figure 12.12**).

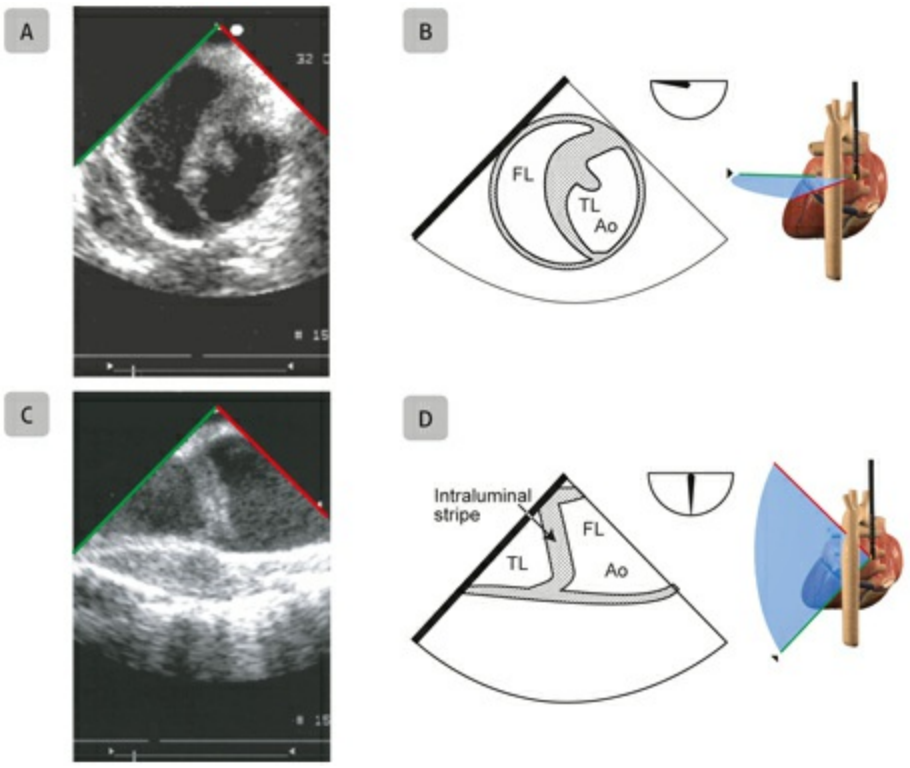

Fig. 12.10 Aortic trauma. Intraluminal stripe due to intimal and medial laceration is seen in the descending aorta (A,B) short-axis and (C,D) long-axis views in a 32-year-old male with traumatic aortic injury. Ao, aorta; FL, false lumen; TL, true lumen. (Reproduced with permission from Denault *et al.* [3] *)*

Open Surgical Repair for Thoracoabdominal Aortic Aneurysm

Hemodynamic instability associated with TAAA repair warrants the use of intraoperative TEE. [32] Surgical TAAA repair can be performed by clamping the proximal Ao and suturing expeditiously. This approach relies on surgical speed to limit ischemia. Aortic cross-clamping is associated with a sudden increase in afterload, distal ischemia, with a significantly increased LV end systolic dimension [33] and changes in cardiac output as measured by PAC. Most TAAA surgery is now performed on left heart bypass or cardiopulmonary bypass (CPB). An alternative approach in some centers is for a conduit to be inserted between the proximal and distal Ao, which shunts blood in an attempt to maintain spinal cord, renal, and lower extremity perfusion. Following aortic cross-clamp, blood is circulated to the lower body via femoral-femoral bypass or left atrio-femoral bypass (LAFB). This popular approach utilizes extracorporeal circulation and results in fewer perioperative complications. [34] , [35] Transesophageal echocardiography confirms the correct position of the left atrial (LA) cannula (**Figure 12.13**). [18] The LAFB flow rate determines the amount of blood diverted and the LA pressure does not reflect the LVEDP. Transesophageal echocardiography currently is the only monitor capable of monitoring LV dimension in this situation. Acute diastolic dysfunction occurs during aortic cross-clamping and may result in postoperative myocardial ischemia. [36]

Open Surgical Repair for Abdominal Aortic Aneurysm

During open surgical repair of AAA hemodynamic instability from systolic and diastolic dysfunction is common during aortic clamping and unclamping [37] , [38] and may increase postoperative morbidity and mortality. There is a poor correlation between PAC parameters and the intravascular volume in patients undergoing AAA repair. [32]

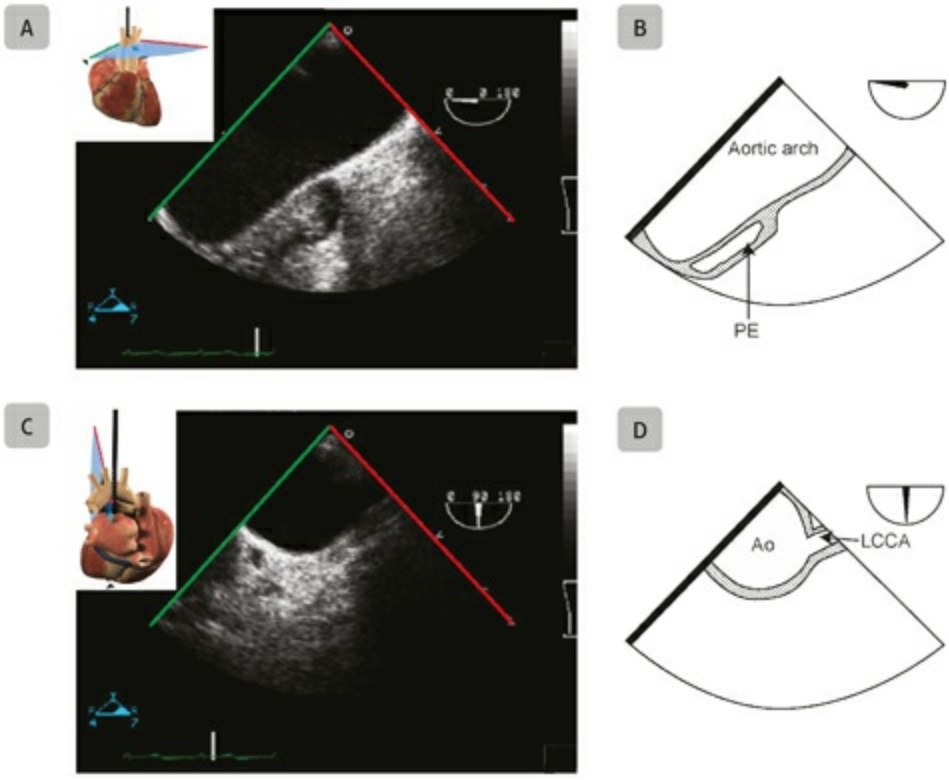

Fig. 12.11 Transverse aorta. Normal upper esophageal aortic arch (A,B) long-axis and (C,D) short-axis views are shown. Ao, aorta; LCCA, left common carotid artery; PE, pericardial effusion. (Reproduced with permission from Denault *et al.* [3])

A&C: https://youtu.be/G0D2zV5uZWA

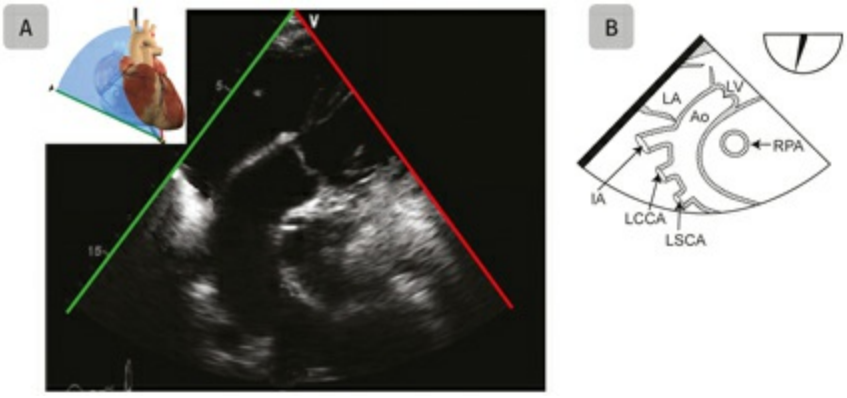

Fig. 12.12 Transgastric (TG) view of the aorta. (A,B) Deep TG view at 80° with right-sided rotation shows the ascending and transverse aorta (Ao) and the branch vessels. IA, innominate artery; LA, left

atrium; LCCA, left common carotid artery; LSCA, left subclavian artery; LV, left ventricle; RPA, right pulmonary artery. (Reproduced with permission from Denault *et al*. [3])

Endovascular Repair of Aortic Aneurysm

Endovascular repair of aortic aneurysm (EVAR) is a relatively new alternative with lower mortality and morbidity then traditional open surgical techniques. [39] Imaging guidance during implantation is not yet well defined. Vascular surgeons and radiologists rely mainly on intraoperative fluoroscopy or angiography to deploy the endovascular stent graft in any portion of the Ao. However, encouraging reports are emerging that demonstrate the superiority of TEE over intraoperative fluoroscopy in imaging thoracic and upper abdominal aneurysms. [26 – 28], [40], [41] Currently, TEE is the only imaging modality that can simultaneously assess cardiac function and provide reliable images for the thoracic Ao. Often EVAR for AAA and peripheral arteries require other imaging modalities.

TEE Exam during Thoracic Endovascular Aortic Repair

Patients presenting for EVAR of the thoracic aorta or TEVAR undergo preoperative imaging tests to identify the aortic pathology and create a general road map for stent graft placement. After induction of anesthesia, the preliminary intraoperative TEE examination confirms the aortic pathology, identifies the proximal and distal landing zones, side branches (intercostals), and major vessels, such as the celiac trunk (see **Figure** 4.35), and documents aortic dissection if present. Aortic thrombus may easily form within the aortic aneurysm and must be excluded from the landing zones. Intraoperative TEE is superior to angiography to visualize thrombus (**Figure 12.14**). [42] The presence of intraluminal “smoke” and CFD imaging are used to identify flow patterns through the aortic aneurysm. All the standard cardiac images are obtained to complete the examination. Intraoperative fluoroscopy and TEE provide guidance for precise positioning of the device across an aortic lesion. The TEE probe may significantly interfere with fluoroscopic imaging and may need to be withdrawn during predeployment fluoroscopic examinations. Following femoral artery cannulation, TEE confirms the proper location of the guidewire proximal to the aortic pathology both in SAX and LAX views. In dissecting aneurysms, the guidewire should be in the true lumen and not the false lumen (**Figure 12.15**). [26], [43] **Table 12.2** summarizes an approach in the use of TEE in TEVAR procedures.

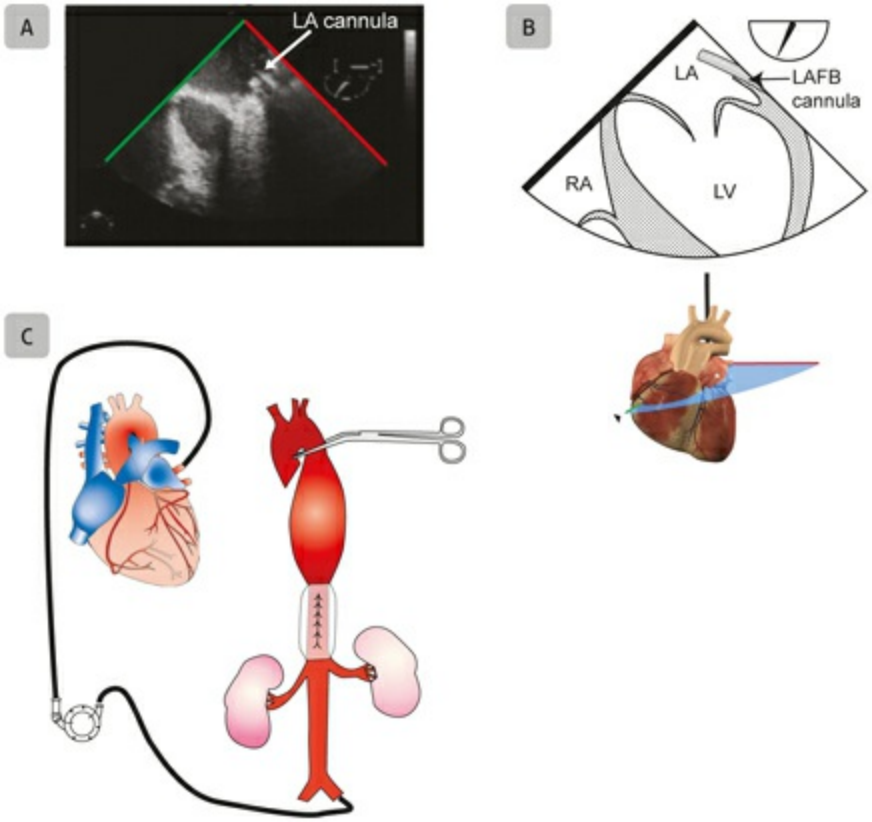

Fig. 12.13 Left atrio-femoral bypass (LAFB). Cannula positioning for LAFB during thoracoabdominal aneurysm repair is shown. (A,B) Midesophageal view at 50° shows the left atrial (LA) cannula correctly positioned in the left upper pulmonary vein. (C) Diagram of the LAFB circuit is presented. LV, left ventricle; RA, right atrium. (Reproduced with permission from Denault *et al.* [3] *)*

A: https://youtu.be/4Lp0jDLu3oY

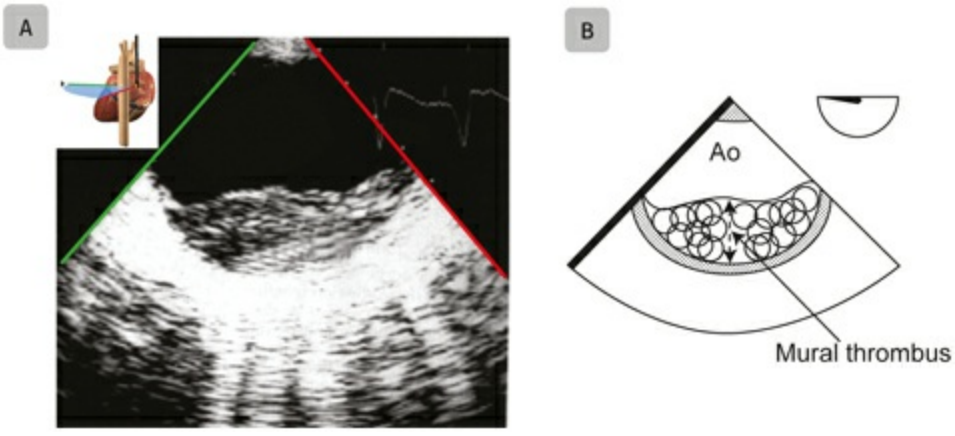

Fig. 12.14 Aortic thrombus. Mid-esophageal descending aorta (Ao) short-axis view demonstrates ectasia of the Ao and mural thrombus formation. (Reproduced with permission from Denault *et al.* [3])

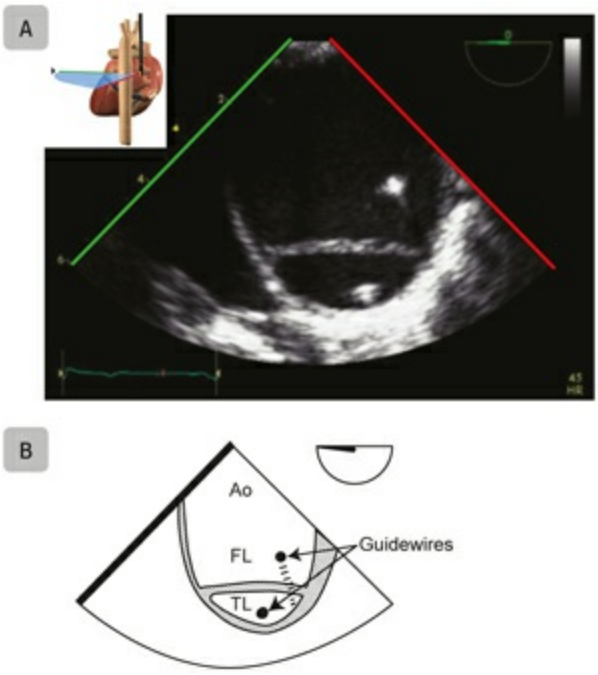

Fig. 12.15 Guidewire position. (A,B) Descending aorta (Ao) short-axis view in a patient with an aortic dissection shows different guidewires in both the true lumen (TL) and false lumen (FL). (Reproduced with permission from Denault *et al.* [3])

A: https://youtu.be/dlG7fr55U58

Proximal Landing Zone

The proximal landing zone is examined for aortic plaque, mural thrombus, or calcification, to avoid stent deployment in unfavourable aortic segments. The aortic diameter at the landing zone is measured in both SAX and LAX to confirm the stent graft size, which usually is oversized by 15–20% of this landing zone diameter. Once the stent graft is deployed, it remains fixed in position. To avoid graft migration, the landing zones should be at least 2 cm long and multiple stent grafts (when deployed) should generously overlap to prevent late disconnection. [44] If the proximal landing zone is before the left subclavian artery (LSCA), flow in the left common carotid artery is assessed

with a transthoracic probe and CFD (**Figure 12.16**). When there is <15 mm of normal Ao between the lesion and LSCA, the stent graft may cover the origin of the LSCA. A left carotid-subclavian artery bypass may be created beforehand, although many have reported coverage of the LSCA ostium without symptoms. [45]

Table 12.2 Transesophageal Echocardiography in Thoracic Endovascular Aneurysm Repair

Before deployment of stent graft
Aortic pathology and dissection (length of aneurysm)
Aortic plaques in short- and long-axis views
Aortic angulation and tortuosity
Aortic thrombus and periaortic hematoma
Aortic branch arteries
Measure landing zones (proximal and distal necks)
Aortic neck should be >15 mm
Confirm the proper graft size of which is 15–20% bigger than the aortic diameter. (For instance, a diameter of 40 mm will require a stent of 44 mm)
Perform standard echocardiography examination
Assess the systolic and diastolic ventricular function
During stent graft deployment
Confirm correct position of the guidewire
Confirm correct position of the device delivery system at the proximal landing zone
Aid in stent graft positioning
Confirming stent deployment and expansion
If more than one stent is used, the TEE probe is advanced to the distal end of the stent graft and is a landmark to confirm the correct position of the next graft
Post deployment of the stent graft
Detecting the flow in the aorta by CFD
Examine for endoleaks using CFD in short and long axis
Aliasing velocity for CFD may need to be reduced to 20–30 cm/s to detect low flow endoleaks
Ballooning at endoleak site should be confirmed with the TEE and re-examined for the endoleaks

CFD, color flow Doppler; CT, computed tomography; MRI, magnetic resonance imaging; TEE, transesophageal echocardiography.

Distal Landing Zone

The distal device diameter is oversized by 15–20% in a manner similar to the proximal device diameter. If the difference between the proximal and distal diameters is >5 mm, the patient may require a special graft device or may not be considered for EVAR. The distal end of the stent is examined for endoleaks or retrograde flow.

Length of Aortic Coverage

Transesophageal echocardiography is used to confirm the full coverage of the aneurysm with the stent graft. In general, if the amount of coverage is ≤12 cm, a single graft can be used. Multiple stents may be required to cover the entire length of the aneurysm particularly if the Ao is tortuous. Reports have documented malalignment and endoleak in a tortuous Ao. [28] In the case of the multiple stents, TEE imaging should ensure there is sufficient overlapping of the stents.

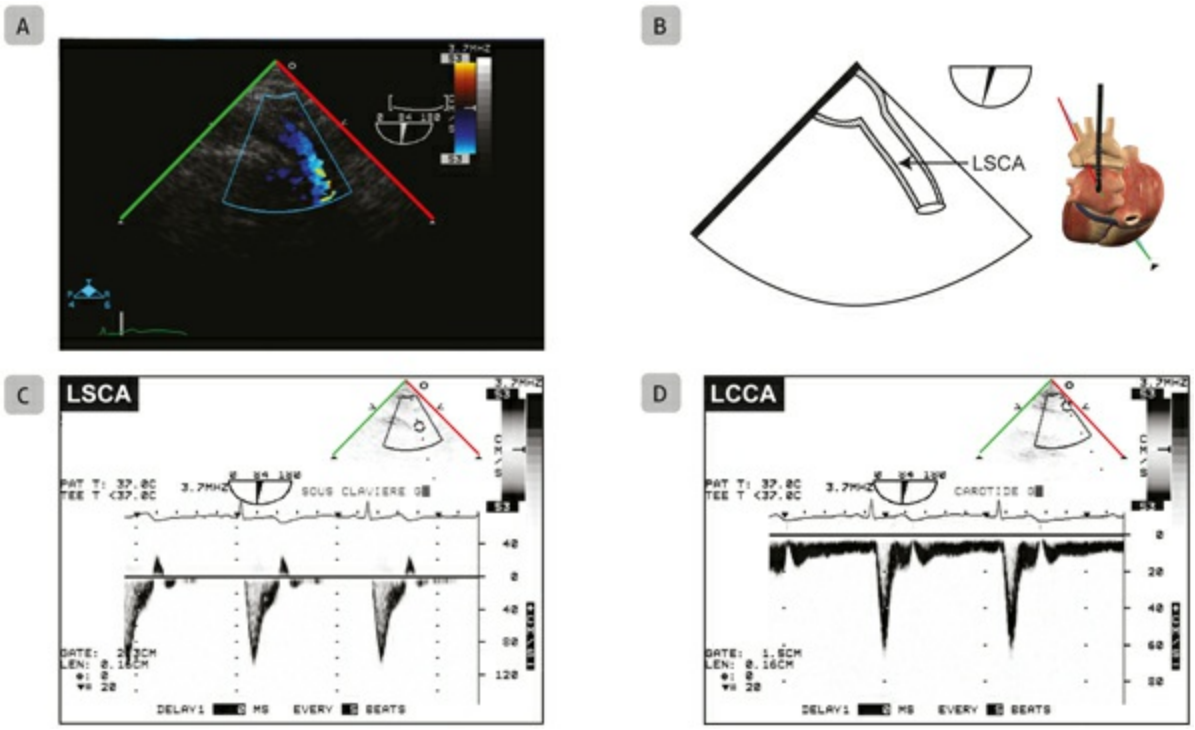

Fig. 12.16 Aortic arch vessels. (A,B) Color Doppler upper esophageal aortic arch short-axis view at 84° shows the left subclavian artery (LSCA). (C) Pulsed wave Doppler of the LSCA shows a typical triphasic pattern due to high vascular resistance of the downstream normal muscular vascular bed at rest. Note the absence of a diastolic flow. (D) Pulsed wave Doppler of the left common carotid artery (LCCA) has a diastolic flow component that originates from the low vascular resistance in the downstream normal cerebral vascular bed. (Reproduced with permission from Denault *et al.* [3])

A: https://youtu.be/4O1MTyoz4Lw

Endoleaks

An endoleak is defined as a persistence of blood flow outside the stent graft (perigraft zone) after stent deployment. Transesophageal echocardiography is valuable in detecting endoleaks (**Figure 12.17**). [40] , [46] Endoleaks are classified into four types (**Table 12.3**). [47] Type I is an attachment site leak that may result from incomplete graft adhesion to the aortic wall at the proximal or distal ends. These are usually large leaks that may require balloon inflation to better mold the stent graft onto the aortic wall. Type II is the branch leak, which could be simple to and fro flow in one or more branches. Type III is the dislocation or junction leaks between grafts or a mid-graft hole. Type IV is from graft wall porosity. Endoleaks can be classified on the basis of the time of first detection as: perioperative, within 24 hours; early, 1–90 days; and late, after 90 days. Primary endoleaks are present from the time of EVAR; secondary endoleaks appear after not being present initially and delays occur after prior negative computed tomographic (CT) scan results. Secondary endoleaks can appear several weeks, months, or years after stent insertion and are the main cause of late treatment failure in endovascular approach. [48 – 50] These are probably related to stent dislodgment, structural changes of the aortic wall, or simply misdiagnosed endoleaks at the time of the insertion.

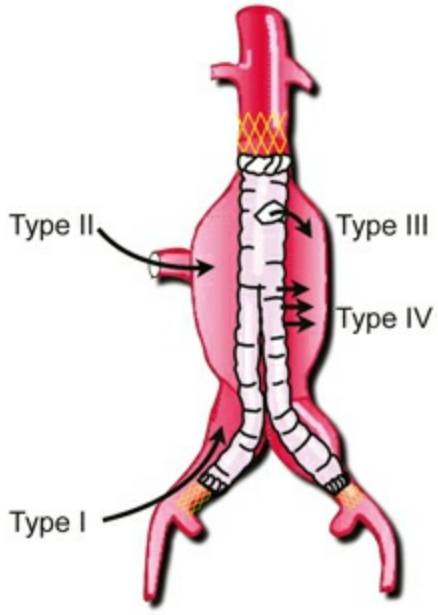

Fig. 12.17 Endoleaks. Classification of endoleaks as described in Table 12.3 are presented. (Reproduced with permission from Denault *et al.* [3])

Table 12.3 Classification of Endoleaks.

1. Attachment site leaks
A. Proximal end of endograft B. Distal end of endograft C. Iliac occluder (plug)
2. Branch leaks (without attachment site connection)
A. Simple or to-and-fro (from only 1 patent branch) B. Complex or flow-through (with 2 or more patent branches)
3. Graft defect
A. Junctional leak or modular disconnect B. Fabric disruption (mid-graft hole) Minor (<2 mm, e.g. suture holes) Major (≥2 mm)
4. Graft wall (fabric) porosity (<30 days after graft placement)

Adapted from Veith *et al.*[47] and Denault *et al.*[3]

LIVER TRANSPLANTATION

Liver transplantation (LT) is now a widespread procedure for the management of end-stage liver disease (ESLD). [51] The successful survival of LT recipients has broadened the recipient pool to include older patients with more comorbidities, especially of the cardio-pulmonary system. [52] Preoperative evaluation and optimization of these comorbidities before a high-risk procedure, such as a LT, is important and echocardiography is part of this. [53] Hemodynamic changes occur during every stage of LT surgery with maintenance of tissue perfusion a constant challenge. [54] This section presents the cardiopulmonary comorbidities found in ESLD patients, main stages of LT surgery and the role of TEE as a hemodynamic monitor and diagnostic tool.

Cardiopulmonary Comorbidities In End-Stage Liver Disease

Many cardiac and pulmonary diseases may exist in ESLD patients (**Table 12.4**). Some share a common etiology with the underlying liver disease and others are caused by liver failure. Up to 25% of patients undergoing a LT may have a coronary artery disease (CAD). [55] Risk factors are the same as in the general population: age, familial history of CAD, smoking, diabetes, hypercholesterolemia, and hypertension. Age over 50–60 years, diabetes, and non-alcoholic steatohepatitis seem to be particularly associated with perioperative events. [56] Severe untreated CAD is an absolute contraindication to LT, but treated CAD does not preclude LT as there is no increase in the perioperative risk. [57] There is no clear consensus on the appropriate investigation algorithm for CAD in these patients. Both nuclear medicine imaging and stress echocardiogram have low predictive value in this population and significant CAD might be missed by noninvasive testing. [58] In recent guidelines, coronary angiogram has been recommended in patients with more than one risk factor for CAD. [59] Therefore, perioperative physicians might have to deal with treated CAD, latent CAD, or even an acute coronary syndrome, even though the occurrence seems to be low. [60] Transesophageal echocardiography is a very sensitive monitoring tool for myocardial ischemia and might be useful for this purpose in higher risk patients. [61]

Table 12.4 Cardiopulmonary Abnormalities in End-Stage Liver Disease

1. Comorbidities affecting the perioperative management
Coronary artery disease and ischemic cardiomyopathy Chronic obstructive pulmonary disease
2. Comorbidities that share a common etiology
Alcoholic cardiomyopathy Hemochromatosis cardiomyopathy
3. Comorbidities caused by liver disease
Cirrhotic cardiomyopathy Portopulmonary hypertension Hepatopulmonary syndrome Pericardial and pleural effusions

Specific etiologies of ESLD might impact the cardiopulmonary status of patients and preoperative screening should have identified these patients. Heavy alcohol consumption can induce a dilated cardiomyopathy with eccentric hypertrophy, wall thinning, systolic and diastolic dysfunction, and postcapillary pulmonary hypertension (see **Figure 5.24**). [62] Hemochromatosis, a disease caused by iron overload, may also be associated with dilated cardiomyopathy and arrhythmias. [63]

End-stage liver disease creates a hyperdynamic circulation, characterized by a high cardiac output, a low blood pressure and low systemic vascular resistance. [64] “Global” hemodynamic values give a false perception of the underlying tissue perfusion and myocardial reserve. However, regional hemodynamics is very different between organs. Most of the vascular networks are constricted and have low blood flow. [65] The splanchnic vascular network is fully dilated, congestive, and contributes to the global low vascular resistance and afterload. The high output state gives the impression that these patients have good heart function, but many of them suffer from cirrhotic cardiomyopathy (**Table 12.5**). This cardiomyopathy, chronically masked by low afterload, might be unmasked when the systolic demand or the vascular resistances become higher, such as during a dobutamine-stress echocardiogram, during LT, or with the vascular tone changes occurring with calcineurin-inhibitor based immunosuppressive regimens. [66] Clinical consequences are postoperative congestive heart failure or low-output state associated with tissue hypoperfusion. The presence of diastolic dysfunction has also been associated with a higher rate of postreperfusion syndromes and hemodynamic instability in the neohepatic phase of the procedure. [67]

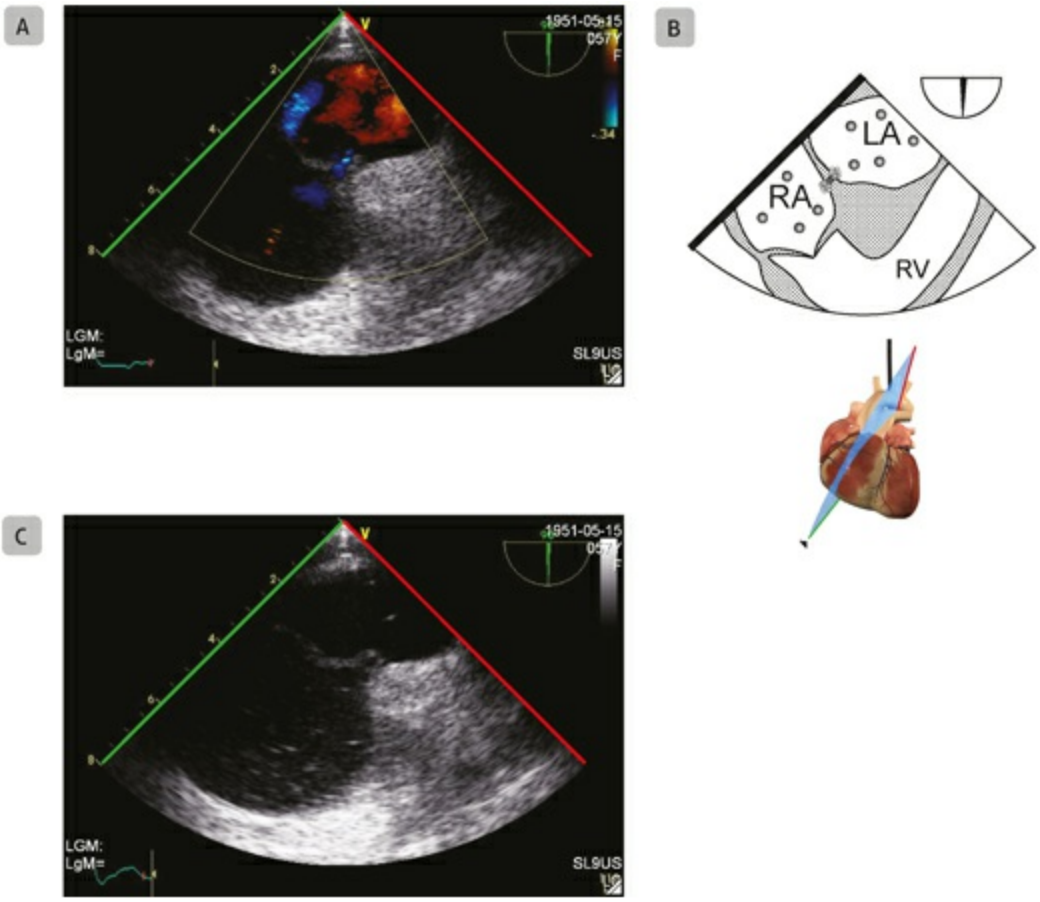

Fig. 12.18 Patent foramen ovale (PFO). (A,B) Mid-esophageal right ventricular inflow/outflow view with color Doppler interrogation of the interatrial septum in a severely hypoxic patient after liver transplantation is shown. (C) Right cardiac chamber opacification with agitated saline demonstrates right-to-left shunting through a PFO appearing within three cardiac cycles. LA, left atrium; RA, right atrium; RV, right ventricle. (Reproduced with permission from Denault *et al.* [3])

Table 12.5 Cirrhotic Cardiomyopathy

1. Dilated left atrium
2. Diastolic dysfunction
3. Low or no systolic contractile reserve
4. Autonomic dysfunction (chronotropic incompetence)
5. Relative hypovolemia

Portopulmonary hypertension is a well-described pathology of pulmonary

hypertension associated with portal hypertension, that affects 5% of patients with ESLD. [68] Guidelines suggest that LT should be contraindicated in patients with mean PA pressure >50 mmHg or between 35 and 50 mmHg with pulmonary vascular resistance >240 dynes sec/cm [5] measured by a PAC. [59] , [69] If TEE shows severe RV dysfunction associated with a high PA pressure at the beginning of the procedure, the transplant should probably be aborted. Even mild RV dysfunction and mild tricuspid regurgitation are associated with increased postoperative morbidity. Perioperative right heart function should therefore be carefully monitored. [70]

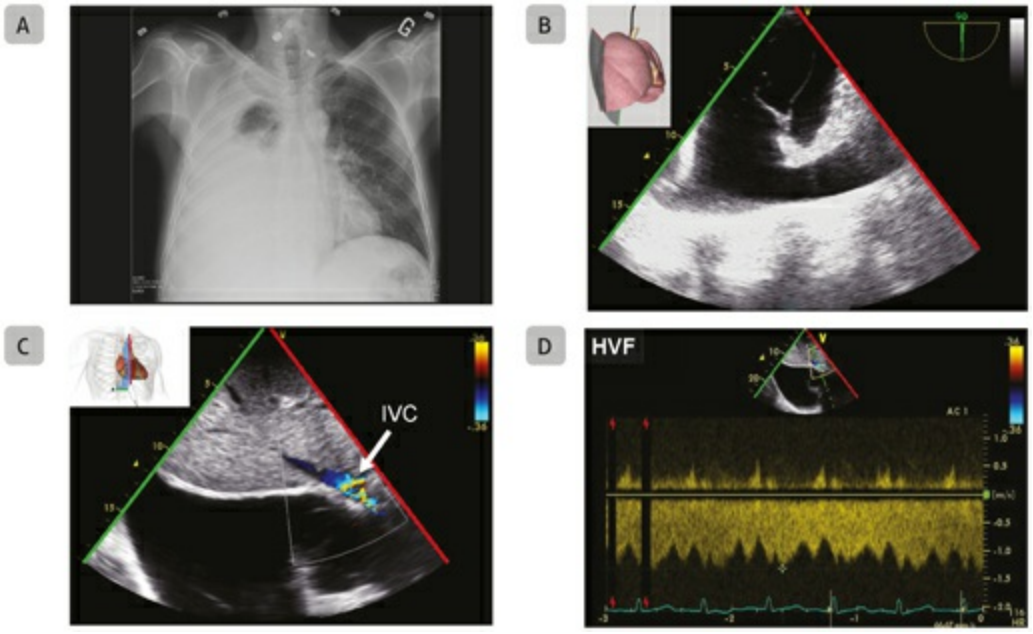

Fig. 12.19 Pleural effusion. (A) Chest radiograph and (B) right basal coronal view with lung ultrasound shows a right-sided pleural effusion in a hemodynamically unstable patient following liver transplantation. (C) Transthoracic subcostal view of the inferior vena cava (IVC) with color Doppler (Nyquist 36 cm/s) shows flow acceleration at the entrance of the IVC (arrow). (D) Pulsed-wave Doppler demonstrates abnormal hepatic venous flow (HVF). Once the right-sided pleural was drained, the hemodynamic condition of the patient improved and the HVF normalized.

B: https://youtu.be/OespD9MxCM4

C: https://youtu.be/WvdC6lfblK4

Hepatopulmonary syndrome is a cause of hypoxemia. Echocardiography helps define this pathology by suggesting the presence of intrapulmonary shunts when a “bubble test”, with bubbles being present in the LA three to five beats after being seen in the right atrium (RA), is positive. If bubbles are present earlier, then a PFO might be the etiology of the hypoxemia (**Figure 12.18**). [71] Pleural and pericardial effusions are common in ESLD and may have hemodynamic consequences (**Figure 12.19**). [72]

TEE During Liver Transplantation

The most recent American Society of Anesthesiologists (ASA) and American Heart Association (AHA) guidelines could not agree on a formal recommendation for the use of TEE during LT, mainly because of a lack of supporting evidence. However, other authors concluded the opposite from a thorough literature review. [73] Since the ASA recommends the use of TEE for unexplained hemodynamic instability, it seems clinically relevant to use TEE as a monitoring tool during a LT procedure, filled with many periods of hemodynamic instability. In a survey, TEE was used as an intraoperative hemodynamic monitor in 40% of LT centers in the United States. [74] However its role, as the sole hemodynamic monitoring tool during LT, has to be better defined. Intraoperative TEE might be particularly useful as a screening tool for cardiac comorbidities, especially if the recipient has been listed for a long time without recent investigations. The risk-benefit ratio of TEE in this population must also be evaluated, particularly if esophageal or gastric varices are present (see **Figure** 4.**34**). Since oesophageal varices are always in the distal third of the esophagus, the risk of contact between the probe and the varices is minimal if the probe is in the mid-oesophageal position. Even though the insertion of a gastric tube has never been associated with an increased risk of variceal bleeding, TEE during LT should probably be limited to mid-oesophageal views when possible.

Table 12.6 Role of TEE at Different Phases of the Procedure

Phases Objectives of TEE Evaluation
1. Dissection phase
Starting conditions Volemia Systolic and diastolic functions Valvular competency Pericardial or pleural effusions Patent foramen ovale Pulmonary artery pressure Ongoing evaluation of volemia Detection of myocardial ischemia
2. Anhepatic phase
Impacts of caval clamping on venous return Impacts of metabolic changes on heart function and volemia
3. Neohepatic phase
Causes of hemodynamic instability Hypovolemia Right ventricular failure Left ventricular failure LVOT and RVOT dynamic obstruction Recognition of specific rare events Intracardiac clot Caval anastomosis stenosis Patent foramen ovale and paradoxal embolus

LVOT, left ventricular outflow tract; RVOT, right ventricular outflow tract; TEE, transesophageal echocardiography.

Hemodynamic and Echocardiographic Changes during Phases of Liver Transplantation

The LT surgical procedure is divided into three stages, each with different hemodynamic considerations and management goals (**Table 12.6**).

Stage 1. Dissection phase

The initial phase consists of a basic laparotomy to dissect the liver free from surrounding structures and isolate the key vascular components. The stage ends with a trial of clamping of the major inflow (portal vein) and outflow (suprahepatic and infrahepatic inferior vena cava [IVC]) to the liver, after which the patient becomes “anhepatic”. The main hemodynamic concerns during this phase are bleeding and hypovolemia from drainage of ascites causing an LV end-systolic cavity obliteration (see **Figure 5.5**). Bleeding

might be increased by portal hypertension, and sometimes a complex coagulopathy. [75] Some centers use phlebotomy, which can reduce splanchnic congestion and minimize blood loss during this phase. [76] , [77] Of course, this strategy creates a state of “controlled hypovolemia” that has to be managed accordingly. One of the role of TEE during this phase is to first identify any pre-existing cardiac conditions that either precludes the procedure or requires specific management. Preload optimization remains the main objective during this phase. Dynamic fluid responsiveness tests are more specific than end-diastolic area measurements for this purpose.

Stage 2. Anhepatic phase

Two strategies exist to manage the IVC clamping; either total cross-clamping with transection of the IVC or partial clamping, in which the donor IVC is attached to the recipient’s IVC using a piggyback technique. The first is technically easier, but the second is associated with less hemodynamic instability and renal failure. Cross-clamping of the IVC will impact venous return and may reduce cardiac output by up to 40%. [78] The role of TEE is to monitor preload and cardiac function. Options to optimize preload in this phase are limited, since venous return depends mostly on collateral flow (porto-systemic shunts). Therefore, a careful amount of fluid must be used to prevent overloading of the cardiovascular system and hypervolemia after unclamping.

Stage 3. Neohepatic phaseE

This phase is the most challenging. After completion of the caval and portal vascular anastomosis, graft inflow and outflow are unclamped and the graft is reperfused. Thereafter, surgical hemostasis is completed, hepatic artery and biliary anastomosis are performed and the abdomen is closed. Abdominal TEE could be used to evaluate venous and arterial anastomosis (see **Figures 4.29–4.31**). Graft reperfusion is associated with the release of cold, acidotic, and hyperkalemia fluid containing vasoactive substances that create hemodynamic perturbations through systemic vasodilatation, pulmonary vasoconstriction, and cardiac dysfunction. [79] This is called the “postreperfusion syndrome” and is defined as a blood pressure drop of 30% under baseline value for more than 1 minute, within 5 minutes after unclamping. [80] , [81] This syndrome worsens patient outcomes. [80] Even though

it is mostly caused by severe vasodilatation, there may be decreased myocardial contractility. [82] Fortunately, it is often mild and short-lived, but may persist for more than 30 minutes. The risk is increased by a long cold ischemia time, poor graft quality, absence of a porto-caval anastomosis during the anhepatic phase, and the presence of diastolic dysfunction. [67] , [80] , [81] Bleeding is also common at this stage and is caused by surgical leaks, hyperfibrinolysis, hypofibrinoginemia, thrombocytopenia, dilutional coagulopathy, and the release of heparin-like substances. This mix of vasoplegia and hypovolemia often mimics septic shock. Vasopressors, fluid replacement, and transfusion of blood products, in conjunction with treatment of coagulopathy, are therefore part of the management.

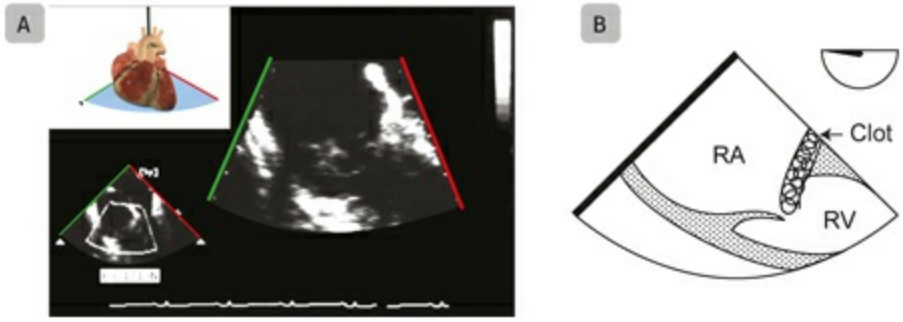

Fig. 12.20 Thromboembolism. (A,B) Within 5 minutes after reperfusion of the transplanted liver, the mid-esophageal four- chamber view shows a large thrombus in the right atrium (RA) attached to the tricuspid valve. RV, right ventricle. (Reproduced with permission from Denault *et al.* [3])

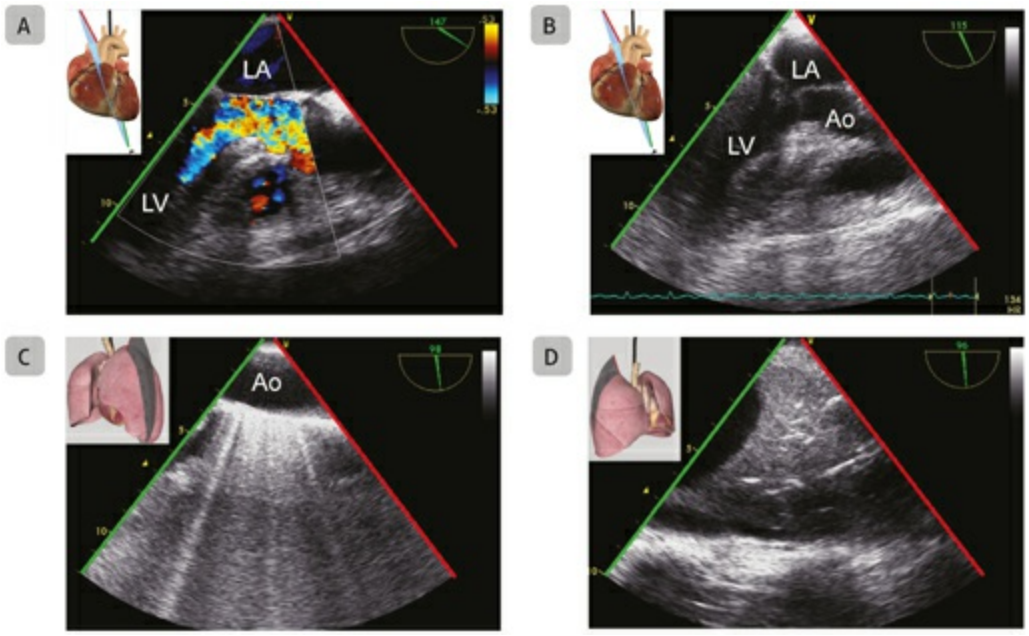

Fig. 12.21 Left ventricular outflow tract obstruction (LVOTO) and hypoxemia. (A,B) Mid-esophageal long-axis views with and without color Doppler in a hemodynamically unstable patient 3 days after liver transplantation are presented. The patient suddenly became unstable and hypoxemic from LVOTO. This was associated with (C) pulmonary edema and (D) right-sided atelectasis as shown in these left and right pulmonary ultrasound views obtained with transesophageal echocardiography. Ao, aorta; LA, left atrium; LV, left ventricle.

A: https://youtu.be/m_V2SGex4E0

C: https://youtu.be/JC0ftpqXAUI

D: https://youtu.be/1_NER_Q9pQM

Preload optimization is again an important part of the hemodynamic management. However, other causes of hemodynamic instability may be identified by TEE (**Figure 12.20**). Acute left ventricular outflow tract obstruction (LVOTO), as well as LV and RV dysfunction may occur and contribute to a low cardiac output state (**Figure 12.21**). [83] , [84]

The postreperfusion syndrome associated with a lack of inotropic reserve caused by the cirrhotic cardiomyopathy are presumed to be the cause of some heart dysfunction. [85] An acute increase of pulmonary resistance may also contribute to acute RV dysfunction. With the more liberal use of TEE during LT, intracardiac thrombi are increasingly reported as a potential cause for acute right heart failure (**Figure 12.20**). [86] , [87] The incidence might be as high as 4% and risk factors are not well defined. As expected, its associated outcome is often catastrophic. [88] , [89] Abnormal venous return caused by massive pleural effusions (**Figure 12.19**) [90] or IVC stenosis (**Figure 12.22**) may also contribute to hemodynamic instability. Inferior vena cava stenosis may be diagnosed with the bicaval view or the inferior vena cava and hepatic view

KIDNEY TRANSPLANTATION

Kidney transplantation is a procedure that is most often free of any significant hemodynamic instability. [91] However, patients with end-stage renal diseases (ESRD) often have an associated heart conditions, such as CAD (40–60%), systolic or diastolic heart failure (20%), valvular calcifications, pulmonary hypertension, and pericardial effusions. [58] An echocardiogram is often part of the preoperative evaluation of ESRD patients; some echocardiographic findings are even associated with postoperative outcomes. [92] Of course, reversible conditions and significant CAD should be addressed preoperatively. [58] American Heart Association/ASA guidelines do not include kidney transplantation in the procedures for which intraoperative TEE is recommended. [1] Transesophageal echocardiography should only be used with an unexplained life-threatening circulatory instability. Some cardiac conditions may only manifest themselves intraoperatively and a certain index of suspicion must be maintained during surgery. When used, TEE is oriented to the most probable etiologies of hemodynamic instability based on the cardiac conditions these patients might have: myocardial ischemia, acute ventricular dysfunction, pulmonary hypertension with RV failure, unrecognized valvular disease, or tamponade.

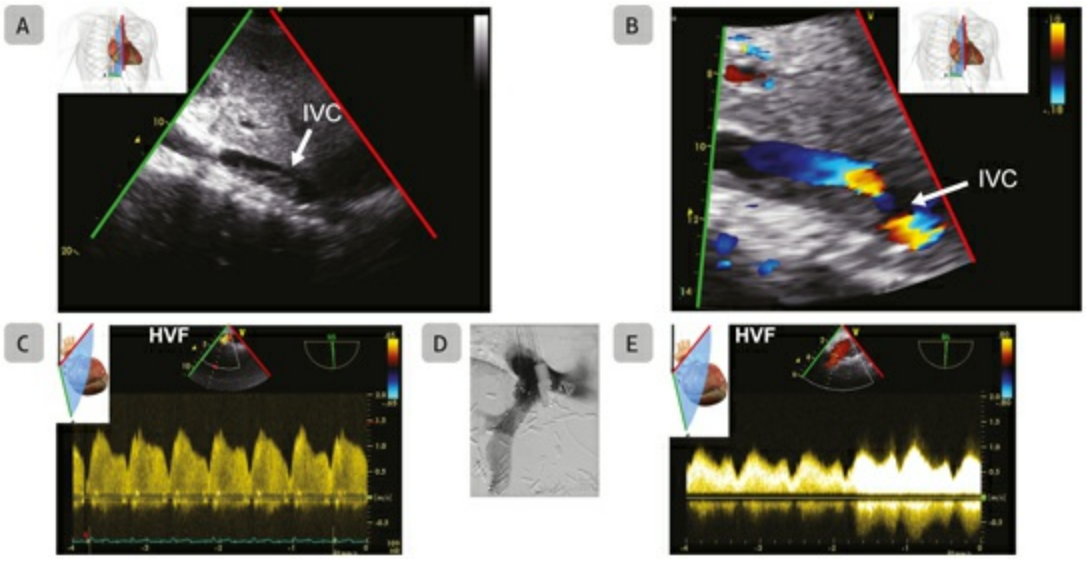

Fig. 12.22 Inferior vena cava (IVC) stenosis. Sudden hemodynamic instability in the previous patient after liver transplantation was from new onset IVC stenosis. (A) Transthoracic subcostal view of the IVC (arrow) shows a laminar thrombus causing stenosis and (B) color flow acceleration (arrow). (C) Hepatic venous flow (HVF) before and (D, E) after shows the reduction in velocity after the IVC was

stented.

A: https://youtu.be/xxHoyvAwpFo

B: https://youtu.be/K0QY6LJzuYw

C: https://youtu.be/xbSXm4zp2_Y

E: https://youtu.be/B8TwFbzFIGk

TRAUMA

Echocardiography is a valuable diagnostic or monitoring tool to guide the management of trauma patients with blunt or penetrating trauma. [93] , [94] Focus TTE examination may be considered at an early stage of trauma assessment to exclude life-threatening major cardiovascular emergen-cies. In trauma patients who require emergency surgery, TEE would be the appropriate imaging modality. Either TTE or TEE is indicated in trauma patients with unexplained hemodynamic instability or hypoxia. Contraindications for TEE in trauma patients would involve those with signs of gastrointestinal bleed and other conditions, as discussed in Chapter 2, Patient Safety and Imaging Artifacts.

The availability of affordable high quality portable ultrasound machines and the rapid diagnostic ability allowed point of care ultrasonography (or Focused Assessment with Sonography in Trauma (FAST)) to become an

integral part of management of trauma patients. Many trauma centers have developed different protocols including the Rapid Ultrasound for Shock and Hypotension (RUSH) and Abdominal Cardiac Evaluation with Sonography in Shock (ACES) to improve diagnostic certainty and guide patient management. Initial ultrasound scanning can exclude life-threatening conditions, such as pneumothorax, hemothorax, pericardial effusion, cardiac tamponade, aortic dissection, hypovolemia, myocardial contusion, valvular regurgitation, and intra-abdominal hemorrhage. Although TTE may provide early and quick diagnosis, TEE is more sensitive in the diagnosis of thoracic aortic dissection and the extent of cardiac trauma lesions.

Pneumothorax

Ultrasound assessment of the lungs for pneumothorax becomes part of the extended FAST. Extended FAST enables the clinician to exclude a pneumothorax with high sensitivity (90.9%) and specificity (98.2%) compared with chest radiography (CXR) sensitivity (50.2%) and specificity (99.4%). However, a major limitation of the ultrasound imaging to detect pneumothorax is the presence of subcutaneous emphysema (see **Figure 14.14**). As described in Chapter 14, Critical Care Examination of the Respiratory System, the presence of lung sliding, lung pulse, or B-line ("comet tails") indicates that the visceral and parietal pleura are normally adjoined, thus safely excluding a pneumothorax in this lung region. In M-mode, lung sliding is absent, the image is made of multiples horizontal lines, referred to as the "barcode sign" (see **Figure** 14**.27**). Trauma patients with pleural adhesion, pulmonary contusion, lung fibrosis, pulmonary bullous diseases, and acute respiratory distress syndrome may not show the lung sliding signs. A pneumothorax cannot be diagnosed with TEE; however the cardiac consequence of a left or right pneumothorax can be detected with TEE (see **Figures 9.17 and 9.18**).

Hemothorax

Ultrasound is a sensitive and specific diagnostic modality in detecting hemothorax (see **Figure** 4**.8**). The fluid/blood level is easily detected as an echogenic (black) area with ultrasound techniques. Compared to CXR, ultrasonography detects volumes of ≥20 mL versus 200 mL on CXR. Once diagnosed, a clinical decision is made as to whether chest tube insertion is

required, or observation and follow-up. Ultrasonography is used to assist safe insertion of a pigtail or a chest tube away from any solid organ or lungs and ensure its correct position (see **Figure** 17**.10**). If the patient is to undergo emergency surgery, TEE can be used to observe the hemothorax for any expansion and guide intraoperative management. As described in Chapter 14, Critical Care Examination of the Respiratory System, hemothorax is diagnosed as the presence of a black area above the diaphragm in a longitudinal plane in the mid-axillary line at the level of the xyphoid. If TEE is utilized, the hemothorax is visualized as an echo free-space posterior to the descending thoracic Ao as opposed to pericardial fluid, which is anterior to the thoracic Ao (see **Figures 5.20, 15.6, and 17.3**).

Pericardial Effusion and Cardiac Tamponade

Pericardial effusion is seen as an echo-free space in the pericardial sac with echocardiography. Early recognition of this life-threatening condition (circumferential or regional tamponade) with TTE at the initial contact in a hypotensive trauma patient facilitates proper intervention (see **Figure 5.19**). Transthoracic echocardiography enables the clinician to perform pericardiocentesis under ultrasound guidance to temporize the situation as a preparation for the definitive surgical treatment in the operating room (OR) (see **Figure** 17**.5**). The volume of pericardial fluid can be estimated based on the width of the pericardial sac (see **Table** 5**.2**). [95] In a patient with chest trauma, cardiac tamponade is a clinical diagnosis suspected with persistent hypotension, tachycardia, pulsus paradoxus, and distended jugular veins. The sonographic features of cardiac tamponade were discussed in Chapter 5, Assessment of Global Ventricular Function, Pericardium, and Cardiomyopathy. Pericardial effusion is best viewed using TTE in the subxyphoid (see **Figure** 15**.15**), parasternal LAX, and apical four-chamber views using a low frequency phased array transducer. If TEE is used, mid-esophageal and TG views are obtained (see **Figures 5.18–5.20**).

Traumatic Aortic Injury

Blunt chest trauma is a common cause of aortic injury in previously healthy subjects particularly if the patient complains of back pain. Aortic dissection is a life threatening condition that requires rapid diagnosis and treatment. Depending on patient factors, operator skill, and the location of injury,

traumatic aortic dissections may be visualized by TTE using the suprasternal approach. However, the sensitivity of TEE or CT scan to diagnose thoracic aortic dissection approaches 100%. Diagnosis of aortic dissection is based on the identification of the intimal flap that creates false and true lumens (**Figure 12.23**). Transesophageal echocardiography examination with CFD is used to identify the entry and exit site between the two lumens, aortic insufficiency and any involvement of the coronary artery ostia.

Volume Status

The amount of intravenous fluid administered in trauma patients may present a challenge as both hypovolemia and excessive fluid therapy result in higher morbidity. There is developing evidence for the benefits of goal-directed fluid therapy to improve outcome. Echocardiography represents an accurate and practical tool to guide goal-directed fluid therapy by estimating LV volume from changes in LV size in the TG mid-SAX view. Obliteration of the LV cavity during systole indicates severe hypovolemia (see **Figure 5.5)**. In addition, respiratory variation of the IVC diameter measured in the TG view is another indicator of volume status (see **Figure 5.6**). The correlation between IVC diameter and the estimated central venous pressure (CVP) is shown in **Table** 5**.2**. The superior vena cava diameter during respiratory variation is also useful in assessing preload (see **Figures 5.7 and 15.14**).

Ventricular Function

Reduction in ventricular function is common in trauma patients and may be a result of myocardial contusion, metabolic acidosis, myocardial hypoperfusion, or other pathology. Echocardiography is a real-time monitor for both RV and LV function. Ventricular dysfunction may present in the form of acute systolic or diastolic dysfunction [36] or both. A quick “eye ball method” by a trained echocardiographer can rapidly determine the LV systolic function and estimate LV ejection fraction. If LV systolic dysfunction is diagnosed, titration of inotropes can be started and ventricular response can be closely monitored by echocardiography. [96] An increase in afterload from administering vasopressors to restore blood pressure can significantly reduce LV contractility and unmask LV dysfunction. When trauma patients become hemodynamically unstable with a normal preload and normal contractility, diastolic dysfunction may be considered (see **Figure**

5.16). Acute diastolic dysfunction of the LV during aortic cross-clamping has been reported and resulted in hemodynamic instability. Pulmonary embolism, pneumothorax, hemothorax, pericardial effusion, hypoxia, and acidosis may result in acute RV failure. Echocardio-graphic signs of RV failure have been discussed previously.

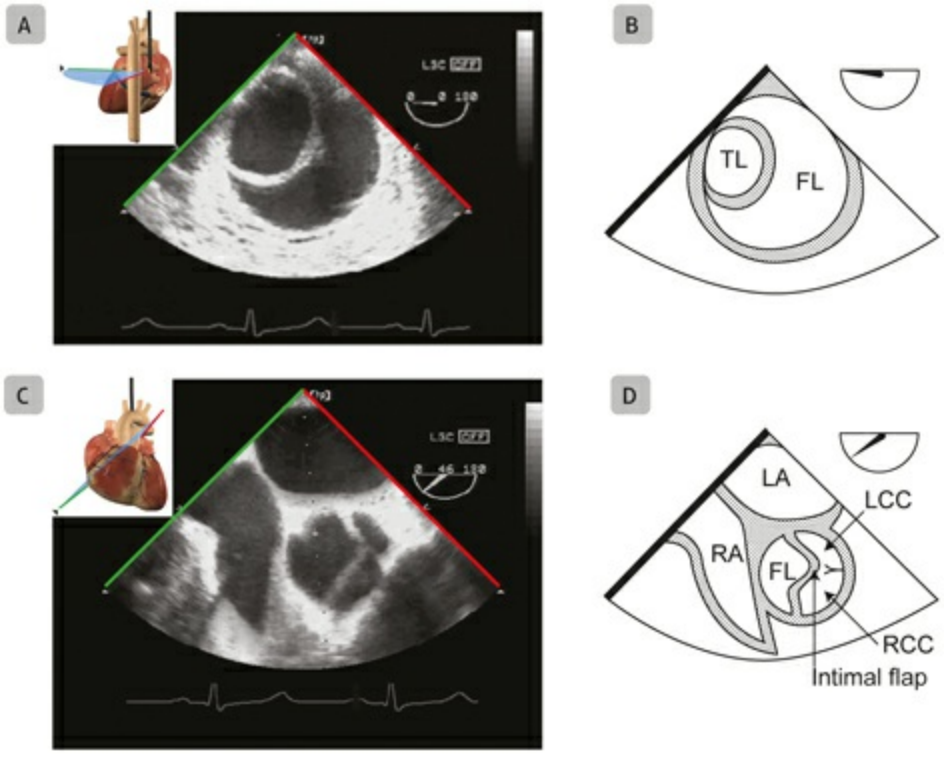

Fig. 12.23 Aortic dissection Stanford type A. (A,B) Midesophageal descending aorta short-axis view shows the true lumen (TL) is smaller and more pulsatile as compared with the false lumen (FL). (C,D) Mid-esophageal aortic valve (AoV) short-axis view reveals proximal extension of the intimal flap to the level of the sinuses of Valsalva above the AoV. LA, left atrium; LCC, left coronary cusp; RA, right atrium; RCC, right coronary cusp. (Reproduced with permission from Denault *et al.* [3])

A: https://youtu.be/nVSxPs45mfQ

C: https://youtu.be/UZXjAERzzZA

Myocardial Ischemia

Patients who sustain major trauma may be at risk of myocardial ischemia and infarction. Echocardiography is a well-recognized sensitive monitor for detection of perioperative myocardial ischemia. Analysis of LV segmental function is based on assessment of wall motion and thickening during systole. The TG mid-papillary SAX view of the LV can detect RWMAs of each major coronary artery territory (see **Figure** 6**.3**). With evolving technology, speckle-tracking echocardiography may more accurately quantify wall movement and assess LV global and regional function (see **Figures 6.11 and 6.12**). If a RWMA is persistent and unresponsive to treatment, it may indicate myocardial infarction. New-onset mitral regurgitation (MR) or an increase in severity of pre-existing MR may represent early echocardiographic features of myocardial ischemia.

Valvular Lesions

Acute hemodynamic instability caused by severe regurgitation of the mitral and aortic valves has been reported with direct chest trauma. [97] In this case, TEE is focused in identifying the pathology, monitoring hemodynamics, and the measures taken to minimize the regurgitant volume and maximize cardiac output (see Chapter 7, Basic Valve Diseases). New development of severe MR in the perioperative period may occur due to myocardial ischemia or infarction and result in cardiogenic shock.

Intracardiac and Intrapulmonary Shunting

Shunting from chest trauma has been reported. Trauma patients with an existing shunt may also present for an urgent surgical procedure. The presence of an atrial septal defect or PFO may increase the risk of paradoxical embolization (see **Figure** 8**.15**) as persistent hypotension, hypoxia, hypoventilation, and acidosis precipitate right-to-left shunts that may cause hemodynamic instability or refractory hypoxemia. Color flow Doppler and agitated saline contrast are used for both diagnosis and monitoring of any measures taken to minimize the shunt fraction (see Chapter 11, Simple Congenital Heart Disease in Adults). Right-to-left shunting may also occur in the presence of pulmonary arteriovenous fistulas.

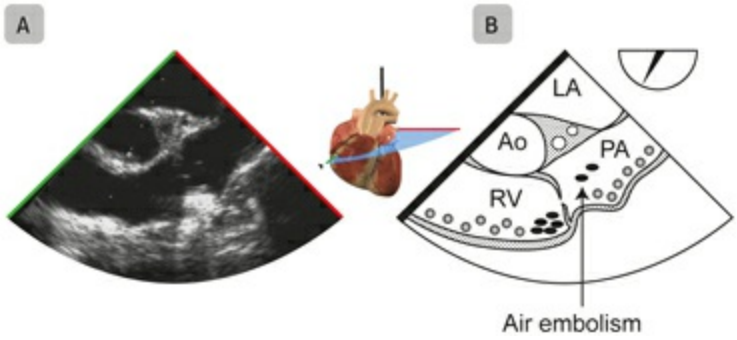

Fig. 12.24 Air embolism. A 46-year-old female became hemodynamically unstable during spinal surgery in the prone position. She was returned back to a supine position. (A,B) Mid-esophageal right ventricular outflow view disclosed the presence of residual air bubbles in the most anterior aspect of the right ventricle (RV), pulmonary artery (PA), and on both sides of the pulmonic valve. Ao, aorta; LA, left atrium. (Reproduced with permission from Denault *et al.* [3]).

A: https://youtu.be/szVsH-iIHYI

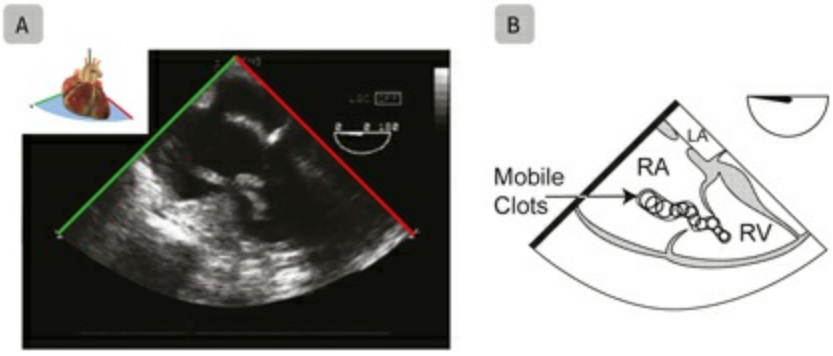

Fig. 12.25 Embolus. An elderly female with metastatic cancer underwent orthopedic surgery for a femoral fracture. During the procedure, she became hemodynamically unstable. (A,B) Mid-esophageal, four- chamber view reveals several mobile clots in the right-sided chambers. LA, left atrium; RA, right atrium; RV, right ventricle. Courtesy of Dr Daniel Boudreault. (Reproduced with permission from Denault *et al.* [3])

A: https://youtu.be/Z_T4PbneIVU

Pulmonary Emboli, Air, and Fat Emboli

Trauma patients are at risk of developing coagulopathy and thromboembolic events that may result in pulmonary embolism (PE) and hemodynamic instability. Echocardiography is a reliable tool to detect right side changes related to acute RV pressure overload in acute PE. Clinical findings and end-tidal carbon dioxide can support the diagnosis of PE (see **Figure** 9**.15**). Rarely, TEE may permit direct visualization of PE in transit. Intraoperative TEE has demonstrated the ability to monitor air and fat embolism in both neurosurgery and orthopedic surgery (**Figures 12.24 and** 12.25). [98]

In summary, both TEE and TTE are becoming an important tool in the monitoring and management of patients undergoing non-cardiac surgery. It is useful since it can identify pre-existing cardiac conditions and causes of hemodynamic instability. In those patients in whom a TTE is indicated but cannot be performed, it is appropriate to perform TEE. [99] In the future, it will be important to have equipment and adequately trained clinicians to provide this service.

REFERENCES

1. Practice guidelines for perioperative transesophageal echocardiography. An updated report by the American Society of Anesthesiologists and the Society of Cardiovascular Anesthesiologists Task Force on Transesophageal Echocardiography. *Anesthesiology*2010;*112*:1084–96.
2. HahnR.T., AbrahamT., AdamsM.S., BruceC.J., GlasK.E., LangR.M.*et al*. Guidelines for performing a comprehensive transesophageal echocardiographic examination: recommendations from the American Society of Echocardiography and the Society of Cardiovascular Anesthesiologists. *J Am Soc Echocardiogr*2013;*26*:921–64.
3. DenaultA.Y., CoutureP., VegasA., BuithieuJ., TardifJ.C.. *Transesophageal Echocardiography Multimedia Manual, Second Edition: A Perioperative Transdisciplinary Approach*. New York, NY: Informa Healthcare; 2011.
4. ReevesS.T., FinleyA.C., SkubasN.J., SwaminathanM., WhitleyW.S., GlasK.E.*et al*. Basic perioperative transesophageal echocardiography examination: a consensus statement of the American Society of Echocardiography and the Society of Cardiovascular Anesthesiologists. *J Am Soc Echocardiogr*2013;*26*:443–56.
5. DellaR.G., BrondaniA., CostaM.G.. Intraoperative hemodynamic monitoring during organ transplantation: what is new?*Curr Opin Organ Transplant*2009;*14*:291–6.
6. RudskiL.G., LaiW.W., AfilaloJ., HuaL., HandschumacherM.D., ChandrasekaranK.*et al*. Guidelines for the Echocardiographic Assessment of the Right Heart in Adults: A Report from the American Society of Echocardiography Endorsed by the European Association of Echocardiography, a registered branch of the European Society of Cardiology, and the Canadian Society of Echocardiography. *J Am Soc Echocardiogr*2010;*23*:685–713.
7. RedfordD.T., KimA.S., BarberB.J., CopelandJ.G.. Transesophageal echocardiography for the

intraoperative evaluation of a large anterior mediastinal mass. *Anesth Analg*2006;*103*:578–9.
8. YangY.L., LuH.I., HuangH.W., TsengC.C.. Mediastinal tumor resection under the guidance of transoesophageal echocardiography. *Anaesth Intensive Care*2007;*35*:312.
9. KatherineC., OrozcoD., AbelloM., OsorioJ., SarquisT., BarreroD.*et al*. Utility of intraoperative transesophageal echocardiography in pulmonary thromboendarterectomy. *Open J Anesthesiol*2014;*4*:63–7.
10. CheitlinM.D., ArmstrongW.F., AurigemmaG.P., BellerG.A., BiermanF.Z., DavisJ.L.*et al*. ACC/AHA/ASE 2003 guideline update for the clinical application of echocardiography: summary article: a report of the American College of Cardiology/American Heart Association Task Force on Practice Guidelines (ACC/AHA/ASE Committee to Update the 1997 Guidelines for the Clinical Application of Echocardiography). *Circulation*2003;*108*:1146–62.
11. EvansA., DwarakanathS., HogueC., BradyM., PoppersJ., MillerS.*et al*. Intraoperative echocardiography for patients undergoing lung transplantation. *Anesth Analg*2014;*118*:725–30.
12. SukernikM.R., MetsB., Bennett-GuerreroE.. Patent foramen ovale and its significance in the perioperative period. *Anesth Analg*2001;*93*:1137–46.
13. CartwrightB.L., JacksonA., CooperJ.. Intraoperative pulmonary vein examination by transesophageal echocardiography: an anatomic update and review of utility. *J Cardiothorac Vasc Anesth*2013;*27*:111–20.
14. Gonzalez-FernandezC., Gonzalez-CastroA., Rodriguez-BorreganJ.C., Lopez-SanchezM., SuberviolaB., FranciscoN.J.*et al*. Pulmonary venous obstruction after lung transplantation. Diagnostic advantages of transesophageal echocardiography. *Clin Transplant*2009;*23*:975–80.
15. FeltenM.L., Michel-CherquiM., SageE., FischlerM.. Transesophageal and contact ultrasound echographic assessments of pulmonary vessels in bilateral lung transplantation. *Ann Thorac Surg*2012;*93*:1094–100.
16. PoldermansD., BoersmaE., BaxJ.J., ThomsonI.R., van de VenL.L., BlankensteijnJ.D.*et al*. The effect of bisoprolol on perioperative mortality and myocardial infarction in high-risk patients undergoing vascular surgery. Dutch Echocardiographic Cardiac Risk Evaluation Applying Stress Echocardiography Study Group. *N Engl J Med*1999;*341*:1789–94.
17. D'AngeloA.J., KlineR.G., ChenM.H., HalpernV.J., CohenJ.R.. Utility of transesophageal echocardiography and pulmonary artery catheterization during laparoscopic assisted abdominal aortic aneurysm repair. *Surg Endosc*1997;*11*:1099–101.
18. FayadA., SawchukC., YangH., CinaC.. Transesophageal echocardiography in the management of left atrio-femoral bypass during thoracoabdominal aortic aneurysm repair: a case report. *Can J Anesth*2002;*49*:1081–3.
19. GillespieD.L., ConnellyG.P., ArkoffH.M., DempseyA.L., HilkertR.J., MenzoianJ.O.. Left ventricular dysfunction during infrarenal abdominal aortic aneurysm repair. *Am J Surg*1994;*168*:1447.
20. KronzonI., CzinerD.G., KatzE.S., GargiuloA., TunickP.A., FreedbergR.S.*et al*. Buckling of the tip of the transesophageal echocardiography probe: a potentially dangerous technical malfunction. *J Am Soc Echocardiogr*1992;*5*:176–7.
21. FreemanW.K., SewardJ.B., KhandheriaB.K., TajikA.J.. *Transesophageal Echocardiography*. Boston, MA: Little Brown; 1994.
22. KyoS., TakamotoS., OmotoR., MatsumuraM., KimuraS., NeyaK.*et al*. Intraoperative echocardiography for diagnosis and treatment of aortic dissection. Utility of color flow mapping for surgical decision making in acute stage. *Herz*1992;*17*:377–89.
23. RizzoR.J., ArankiS.F., AklogL., CouperG.S., AdamsD.H., CollinsJ.J.Jr*et al* .Rapid noninvasive diagnosis and surgical repair of acute ascending aortic dissection. Improved survival with less angiography. *J Thorac Cardiovasc Surg*1994;*108*: 567–74.

24. WillensH.J., KesslerK.M.. Transesophageal echocardiography in the diagnosis of diseases of the thoracic aorta: Part 1. Aortic dissection, aortic intramural hematoma, and penetrating atherosclerotic ulcer of the aorta. *Chest*1999;*116*:1772–9.
25. SmithD.C., BansalR.C.. Transesophageal echocardiography in the diagnosis of traumatic rupture of the aorta. *N Engl J Med*1995;*333*:457–8.
26. FayadA.. A misplaced guide wire in the false lumen during endovascular repair of a type B aortic dissection. *Can J Anesth*2007;*54*:947–8.
27. FayadA.. Images in anesthesia. Transesophageal echocardiographic diagnosis of a failed balloon catheter during endovascular stenting of a descending thoracic aneurysm. *Can J Anesth*2007;*54*:848–9.
28. FayadA.. Echocardiography images of endovascular mal- aligned stent grafts. *Can J Anesth*2008;*55*:306–7.
29. SawchukC., FayadA.. Confirmation of internal jugular guide wire position utilizing transesophageal echocardiography. *Can J Anesth*2001;*48*:688–90.
30. KonstadtS.N., ReichD.L., QuintanaC., LevyM.. The ascending aorta: how much does transesophageal echocardiography see?*Anesth Analg*1994;*78*:240–4.
31. MahajanA., CrowleyR., HoJ.K., SanchezE., TrivediP., NattersonB.*et al*. Imaging the ascending aorta and aortic arch using transesophageal echocardiography: the expanded aortic view. *Echocardiography*2008;*25*:408–13.
32. lafratiM.D., GordonG., StaplesM.H., MackeyW.C., BelkinM., DiehlJ.et al.Transesophageal echocardiography for hemodynamic management of thoracoabdominal aneurysm repair. *Am J Surg 1993*;*166*:179–85.
33. EideT.O., AaslandJ., RomundstadP., StensethR., SaetherO.D., AadahlP.*et al*. Changes in hemodynamics and acid-base balance during cross-clamping of the descending thoracic aorta. A study in patients operated on for thoracic and thoracoabdominal aortic aneurysm. *Eur Surg Res*2005;*37*:330–4.
34. CoselliJ.S.. Thoracoabdominal aortic aneurysms: experience with 372 patients. *J Card Surg*1994;*9*:638–47.
35. FehrenbacherJ.W., McCreadyR.A., HormuthD.A., BeckmanD.J., HalbrookH.G., HerodG.T.*et al*. One-stage segmental resection of extensive thoracoabdominal aneurysms with left-sided heart bypass. *J Vasc Surg*1993;*18*:366–70.
36. FayadA., YangH., NathanH., BrysonG.L., CinaC.S.. Acute diastolic dysfunction in thoracoabdominal aortic aneurysm surgery. *Can J Anesth*2006;*53*:168–73.
37. GoodingJ.M., ArchieJ.P.Jr, McDowellH.. Hemodynamic response to infrarenal aortic cross-clamping in patients with and without coronary artery disease. *Crit Care Med*1980;*8*:382–5.
38. MahmoodF., MatyalR., SubramaniamB., MitchellJ., PomposelliF., LernerA.B.*et al*. Transmitral flow propagation velocity and assessment of diastolic function during abdominal aortic aneurysm repair. *J Cardiothorac Vasc Anesth*2007;*21*:486–91.
39. DakeM.D., MillerD.C., SembaC.P., MitchellR.S., WalkerP.J., LiddellR.P.. Transluminal placement of endovascular stent-grafts for the treatment of descending thoracic aortic aneurysms. *N Engl J Med*1994;*331*:1729–34.
40. FattoriR., CaldareraI., RapezziC., RocchiG., NapoliG., ParlapianoM.*et al*. Primary endoleakage in endovascular treatment of the thoracic aorta: importance of intraoperative transesophageal echocardiography. *J Thorac Cardiovasc Surg*2000;*120*:490–5.
41. KoschykD.H., NienaberC.A., KnapM., HofmannT., KodolitschY.V., SkriabinaV.*et al*. How to guide stent-graft implantation in type B aortic dissection? Comparison of angiography, transesophageal echocardiography, and intravascular ultrasound. *Circulation*2005;*112*(9 Suppl.):I260–I264.

42. CriadoE., WallP., LucasP., GasparisA., ProffitT., RicottaJ.. Transesophageal echo-guided endovascular exclusion of thoracic aortic mobile thrombi. *J Vasc Surg*2004;*39*:238–42.
43. DobsonG., PetrasekP., AlvarezN.. Images in anesthesia: transesophageal echocardiography enhances endovascular stent placement in traumatic trans-section of the thoracic aorta. *Can J Anesth*2004;*51*:931.
44. CzermakB.V., WaldenbergerP., PerkmannR., RiegerM., SteingruberI.E., MallouhiA.*et al*. Placement of endovascular stent-grafts for emergency treatment of acute disease of the descending thoracic aorta. *Am J Roentgenol*2002;*179*:337–45.
45. FattoriR., NapoliG., LovatoL., RussoV., PaciniD., PierangeliA.*et al*. Indications for, timing of, and results of catheter-based treatment of traumatic injury to the aorta. *Am J Roentgenol*2002;*179*:603–9.
46. MoskowitzD.M., KahnR.A., KonstadtS.N., MittyH., HollierL.H., MarinM.L.. Intraoperative transoesophageal echocardiography as an adjuvant to fluoroscopy during endovascular thoracic aortic repair. *Eur J Vasc Endovasc Surg*1999;*17*:22–7.
47. VeithF.J., BaumR.A., OhkiT., AmorM., AdiseshiahM., BlankensteijnJ.D.*et al*. Nature and significance of endoleaks and endotension: summary of opinions expressed at an international conference. *J Vasc Surg*2002;*35*:1029–35.
48. GolzarianJ., StruyvenJ., AbadaH.T., WeryD., DussaussoisL., MadaniA.*et al*. Endovascular aortic stent-grafts: transcatheter embolization of persistent perigraft leaks. *Radiology*1997;*202*:731–4.
49. MitchellR.S., MillerD.C., DakeM.D., SembaC.P., MooreK.A., SakaiT.. Thoracic aortic aneurysm repair with an endovascular stent graft: the “first generation”. *Ann Thorac Surg*1999;*67*:1971–4.
50. WhiteG.H., YuW., MayJ., ChaufourX., StephenM.S.. Endoleak as a complication of endoluminal grafting of abdominal aortic aneurysms: classification, incidence, diagnosis, and management. *J Endovasc Surg*1997;*4*:152–68.
51. MartinP., DiMartiniA., FengS., BrownR.Jr, FallonM.. Evaluation for liver transplantation in adults: 2013 practice guideline by the American Association for the Study of Liver Diseases and the American Society of Transplantation. *Hepatology*2014;*59*:1144–65.
52. CareyW.D., DumotJ.A., PimentelR.R., BarnesD.S., HobbsR.E., HendersonJ.M.*et al*. The prevalence of coronary artery disease in liver transplant candidates over age 50. *Transplantation*1995;*59*:859–64.
53. GargA., ArmstrongW.F.. Echocardiography in liver transplant candidates. *JACC Cardiovasc Imaging*2013;*6*:105–19.
54. OzierY., KlinckJ.R.. Anesthetic management of hepatic transplantation. *Curr Opin Anaesthesiol*2008;*21*:391–400.
55. PatelS., KieferT.L., AhmedA., AliZ.A., TremmelJ.A., LeeD.P.*et al*. Comparison of the frequency of coronary artery disease in alcohol-related versus non-alcohol-related endstage liver disease. *Am J Cardiol*2011;*108*:1552–5.
56. VanwagnerL.B., BhaveM., TeH.S., FeinglassJ., AlvarezL., RinellaM.E.. Patients transplanted for nonalcoholic steatohepatitis are at increased risk for postoperative cardiovascular events. *Hepatology*2012;*56*:1741–50.
57. WrayC., ScovottiJ.C., TobisJ., NiemannC.U., PlaninsicR., WaliaA.*et al*. Liver transplantation outcome in patients with angiographically proven coronary artery disease: a multiinstitutional study. *Am J Transplant*2013;*13*:184–91.
58. LentineK.L., CostaS.P., WeirM.R., RobbJ.F., FleisherL.A., KasiskeB.L.*et al*. Cardiac disease evaluation and management among kidney and liver transplantation candidates: a scientific statement from the American Heart Association and the American College of Cardiology Foundation. *J Am Coll Cardiol*2012;*60*:434–80.
59. RavalZ., HarinsteinM.E., SkaroA.I., ErdoganA., DeWolfA.M., ShahS.J.*et al*. Cardiovascular risk

assessment of the liver transplant candidate. *J Am Coll Cardiol*2011;*58*:223–31.
60. BradleyS.M., SoineL.A., CaldwellJ.H., GoldbergS.L.. Screening stress myocardial perfusion imaging and eligibility for liver transplantation. *Am J Cardiol*2010;*105*:1010–13.
61. SmithJ.S., CahalanM.K., BenefielD.J., ByrdB.F., LurzF.W., ShapiroW.A.*et al*. Intraoperative detection of myocardial ischemia in high-risk patients: electrocardiography versus twodimensional transesophageal echocardiography. *Circulation*1985;*72*:1015–21.
62. PianoM.R.. Alcoholic cardiomyopathy: incidence, clinical characteristics, and pathophysiology. *Chest*2002;*121*:163850.
63. BoyerT.D.. *Zakim and Boyer's Hepatology: A Textbook of Liver Disease*. Philadelphia, PA: Saunders/Elsevier; 2006.
64. CostaM.G., ChiarandiniP., DellaR.G.. Hemodynamics during liver transplantation. *Transplant Proc*2007;*39*:1871–3.
65. BernardiM., TrevisaniF.. Systemic and regional hemodynamics in pre-ascitic cirrhosis. *J Hepatol*1997;*27*:588–91.
66. ZardiE.M., AbbateA., ZardiD.M., DobrinaA., MargiottaD., Van TassellB.W.*et al*. Cirrhotic cardiomyopathy. *J Am Coll Cardiol*2010;*56*:539–49.
67. XuZ.D., XuH.T., YuanH.B., ZhangH., JiR.H., ZouZ.*et al*. Postreperfusion syndrome during orthotopic liver transplantation: a single-center experience. *Hepatobiliary Pancreat Dis Int*2012;*11*:34–9.
68. KuoP.C., PlotkinJ.S., GaineS., SchroederR.A., RustgiV.K., RubinL.J.*et al*. Portopulmonary hypertension and the liver transplant candidate. *Transplantation*1999;*67*:1087–93.
69. KrowkaM.J., PlevakD.J., FindlayJ.Y., RosenC.B., WiesnerR.H., KromR.A.. Pulmonary hemodynamics and perioperative cardiopulmonary-related mortality in patients with portopulmonary hypertension undergoing liver transplantation. *Liver Transpl*2000;*6*:443–50.
70. KiaL., ShahS.J., WangE., SharmaD., SelvarajS., MedinaC.*et al*. Role of pretransplant echocardiographic evaluation in predicting outcomes following liver transplantation. *Am J Transplant*2013;*13*:2395–401.
71. Rodriguez-RoisinR., KrowkaM.J., HerveP., FallonM.B.. Pulmonary-hepatic vascular disorders (PHD). *Eur Respir J*2004;*24*:861–80.
72. DogrulM.I., AkcayS., SavasB.S., ErD.B., OnerE.F., MorayG.*et al*. Pleural effusion in patients with end-stage liver disease who are candidates for transplant. *Exp Clin Transplant*2014;*12*(Suppl. 1):149–52.
73. BurtenshawA.J., IsaacJ.L.. The role of trans-oesophageal echocardiography for perioperative cardiovascular monitoring during orthotopic liver transplantation. *Liver Transpl*2006;*12*:1577–83.
74. SchumannR., MandellM.S., MercaldoN., MichaelsD., RobertsonA., BanerjeeA.*et al*. Anesthesia for liver transplantation in United States academic centers: intraoperative practice. *J Clin Anesth*2013;*25*:542–50.
75. TripodiA., MannucciP.M.. The coagulopathy of chronic liver disease. *N Engl J Med*2011;*365*:147–56.
76. MassicotteL., DenaultA.Y., BeaulieuD., ThibeaultL., HevesiZ., NozzaA.*et al*. Transfusion rate for 500 consecutive liver transplantations: experience of one liver transplantation center. *Transplantation*2012 May 21.
77. MassicotteL., PerraultM.A., DenaultA.Y., KlinckJ.R., BeaulieuD., RoyJ.D.*et al*. Effects of phlebotomy and phenylephrine infusion on portal venous pressure and systemic hemodynamics during liver transplantation. *Transplantation*2010;*89*:920–7.
78. BelghitiJ., NounR., ZanteE., BalletT., SauvanetA.. Portal triad clamping or hepatic vascular exclusion for major liver resection. *A controlled study. Ann Surg*1996;*224*:155–61.
79. RamsayM.. The reperfusion syndrome: have we made any progress?*Liver Transpl*2008;*14*:412–

14.
80. HilmiI., HortonC.N., PlaninsicR.M., SakaiT., Nicolau-RaducuR., DamianD.*et al*. The impact of postreperfusion syndrome on short-term patient and liver allograft outcome in patients undergoing orthotopic liver transplantation. *Liver Transpl*2008;*14*:504–8.
81. Paugam-BurtzC., KavafyanJ., MerckxP., DahmaniS., SommacaleD., RamsayM.*et al*. Postreperfusion syndrome during liver transplantation for cirrhosis: outcome and predictors. *Liver Transpl*2009;*15*:522–9.
82. KrennC.G., HodaR., NikolicA., GreherM., PlochlW., ChevtchikO.O.*et al*. Assessment of ventricular contractile function during orthotopic liver transplantation. *Transpl Int*2004;*17*:101–4.
83. AniskevichS., ShineT.S., FeinglassN.G., StapelfeldtW.H.. Dynamic left ventricular outflow tract obstruction during liver transplantation: the role of transesophageal echocardiography. *J Cardiothorac Vasc Anesth*2007;*21*:577–80.
84. RipollC., CatalinaM.V., YottiR., OlmedillaL., Perez-PenaJ., LoI.O.*et al*. Cardiac dysfunction during liver transplantation: incidence and preoperative predictors. *Transplantation*2008;*85*:1766–72.
85. EscobarB., TauraP., Martinez-PalliG., FondevilaC., BalustJ., BeltranJ.*et al*. Stroke volume response to liver graft reperfusion stress in cirrhotic patients. *World J Surg*2014;*38*:927–35.
86. HudcovaJ., SchumannR.. Fatal right ventricular failure with intracardiac thrombus formation during liver transplantation not apparent on postmortem examination. *Anesth Analg*2006;*103*:506.
87. SibuleskyL., PeirisP., TanerC.B., KramerD.J., CanabalJ.M., NguyenJ.H.. Intraoperative intracardiac thrombosis in a liver transplant patient. *World J Hepatol*2010;*2*:198–200.
88. SakaiT., MatsusakiT., DaiF., TanakaK.A., DonaldsonJ.B., HilmiI.A.*et al*. Pulmonary thromboembolism during adult liver transplantation: incidence, clinical presentation, outcome, risk factors, and diagnostic predictors. *Br J Anaesth*2012;*108*:469–77.
89. XiaV.W., HoJ.K., NourmandH., WrayC., BusuttilR.W., SteadmanR.H.. Incidental intracardiac thromboemboli during liver transplantation: incidence, risk factors, and management. *Liver Transpl*2010;*16*:1421–7.
90. BrouwersM.A., de JongK.P., PeetersP.M., BijleveldC.M., KlompmakerI.J., SlooffM.J.. Inferior vena cava obstruction after orthotopic liver transplantation. *Clin Transplant*1994;*8*:19–22.
91. RicaurteL., VargasJ., LozanoE., DiazL.. Anesthesia and kidney transplantation. *Transplant Proc*2013;*45*:1386–91.
92. GuH., AkhtarM., ShahA., MallickA., OstermannM., ChambersJ.. Echocardiography predicts major adverse cardiovascular events after renal transplantation. *Nephron Clin Pract*2014;*126*:75–80.
93. BoulangerB.R., BrennemanF.D., McLellanB.A., RizoliS.B., CulhaneJ., HamiltonP.. A prospective study of emergent abdominal sonography after blunt trauma. *J Trauma*1995;*39*:325–30.
94. CampbellN.C., ThomsonS.R., MuckartD.J., MeumannC.M., VanM., BothaJ.B.. Review of 1198 cases of penetrating cardiac trauma. *Br J Surg*1997;*84*:1737–40.
95. MeurinP., TabetJ.Y., ThabutG., CristofiniP., FarrokhiT., FischbachM.*et al*. Nonsteroidal anti-inflammatory drug treatment for postoperative pericardial effusion: a multicenter randomized, double-blind trial. *Ann Intern Med*2010;*152*:137–43.
96. FontesM.L., BellowsW., NgoL., MangnoD.T.. Assessment of ventricular function in critically ill patients: limitations of pulmonary artery catheterization. Institutions of the McSPI Research Group. *J Cardiothorac Vasc Anesth*1999;*13*:521–7.
97. JametB., ChabertJ.P., MetzD., ElaertsJ.. Acute aortic insufficiency. *Ann Cardiol Angeiol (Paris)*2000;*49*:183–6.
98. BulgerE.M., SmithD.G., MaierR.V., JurkovichG.J.. Fat embolism syndrome. A 10-year review. *Arch Surg*1997;*132*:435–9.

99. DouglasP.S., GarciaM.J., HainesD.E., LaiW.W., ManningW.J., PatelA.R.*et al*. ACCF/ASE/AHA/ASNC/HFSA/HRS/SCAI/SCCM/SCCT/ SCMR 2011 Appropriate Use Criteria for Echocardiography. A Report of the American College of Cardiology Foundation Appropriate Use Criteria Task Force, American Society of Echocardiography, American Heart Association, American Society of Nuclear Cardiology, Heart Failure Society of America, Heart Rhythm Society, Society for Cardiovascular Angiography and Interventions, Society of Critical Care Medicine, Society of Cardiovascular Computed Tomography, Society for Cardiovascular Magnetic Resonance American College of Chest Physicians. *J Am Soc Echocardiogr*2011;*24*:229–67.

PART II

Chapter 13

Critical Care Ultrasound Examination of the Nervous System

Andrea Rigamonti, Robert Chen, Ramamani Mariappan and Céline Odier

INTRODUCTION

Monitoring cardiovascular and respiratory function is an important aspect of patient management in the intensive care unit (ICU) and operating room. Cardiovascular and pulmonary functions are continuously monitored during anesthesia and in critical care, but the monitoring of cerebrovascular function is not routinely performed. With the availability of non-invasive monitors like transcranial Doppler (TCD), quantitative electroencephalographic monitoring and near-infrared spectroscopy, continuous monitoring of cerebrovascular function is possible. Patient care can be enhanced when the information collected from these monitors are used to guide patient management. In this chapter, the role of ultrasound (US) in examining the central nervous system, including TCD, US of the optic nerve, and direct visualization of the brain using 2D echography will be presented.

TRANSCRANIAL DOPPLER ULTRASOUND

Transcranial Doppler US is a simple, non-invasive, relatively cheap bedside tool that can provide real-time dynamic information regarding cerebral blood flow velocity in the basal cerebral blood vessels. Since the first clinical application in 1982, [1] the use of TCD has expanded rapidly over the past two decades. The portability and non-invasive nature of TCD allows both

monitoring during emergencies and serial monitoring in the ICU. The clinical applications of TCD are summarized in **Table 13.1**. Transcranial Doppler is currently used in neuro-critical care units, acute stroke units, operating rooms, emergency departments, and even in outpatient settings to assess the hemodynamic changes associated with stenosis of large cerebral arteries or to determine patients at risk of stroke with sickle cell disease. For the experienced vascular neurologist, neuro-intensivist, and neuro-anesthesiologist, the small portable TCD device serves as a "stethoscope for the brain". [2]

Table 13.1 Applications of Transcranial Doppler

Setting	Role
Neuro-critical care	Cerebral vasospasm monitoring to assess progression and the treatment effect (angioplasty or medical treatment) after subarachnoid hemorrhage
	Monitoring intracranial pressure (ICP) and combining it with ocular ultrasound in traumatic head injury or other conditions associated with elevated ICP
	Assessment of the degree of hyperemia after arteriovenous malformation resection, carotid endarterectomy (CEA), carotid angioplasty and stenting (CAS) and in patients with malignant hypertension and fulminant hepatic failure
	Diagnosis of cerebral circulatory arrest and ancillary brain death confirmation
Stroke unit	Diagnosis of acute ischemic stroke
	To enhance clot resolution in acute ischemic stroke and to assess the arterial patency after thrombolytic treatment
	Diagnosis of hyperemia after conversion of acute ischemic to hemorrhagic stroke
Operating room	For emboli detection during CEA, CAS, and during cardiac and major vascular surgeries
	To assess the collateral circulation after great vessels clamping or shunting (e.g. innominate artery, common and internal carotid)
Various	Assessment of cerebral auto-regulation and cerebrovascular carbon dioxide reactivity
	Diagnosis of intracranial carotid or basilar arteries stenosis
	For guiding the chronic red cell transfusion therapy in patients with sickle cell disease who are at risk of developing stroke
	Detection of patent foramen ovale

BASIC PRINCIPLES OF TRANSCRANIAL DOPPLER

The TCD probe works only using Doppler signals and does not acquire 2D imaging.

It emits a range gated, pulsed-wave Doppler US beam at a low (2 MHz) frequency. The US beam penetrates the skull at areas called "acoustic windows" and is scattered in the tissue. Some of the US wave are reflected

back at an altered frequency by the moving red blood cells. The difference in frequency between the transmitted and received sound waves is called the “Doppler frequency shift” (Fd) or “Doppler effect”. The reflected waves are received by the Doppler probe and transformed into an electrical signal. The computer performs a fast Fourier analysis to transform this electric signal into a moving graphic display with the time on the x-axis and the blood flow velocity on the y-axis (see Chapter 2, Patient Safety and Imaging Artifacts). Apart from insonation angle, other factors such as the vessel diameter, hematocrit, arterial carbon dioxide tension ($PaCO_2$), blood pressure, body temperature, and the presence of collateral flow can also affect the cerebral blood flow velocity (CBFV). Some epidemiologic and physiologic factors such as age, gender, pregnancy, and sleep-awake pattern can also affect the CBFV. These should all be kept in mind while interpreting the CBFV in various clinical situations. [3]

Fig. 13.1 Transcranial Doppler devices. Specialized transcranial Doppler monitoring devices are shown: (A) ST3 (Spencer Technology, Seattle WA) and (B) Sonara (Natus Medical, San Carlos, CA, USA)

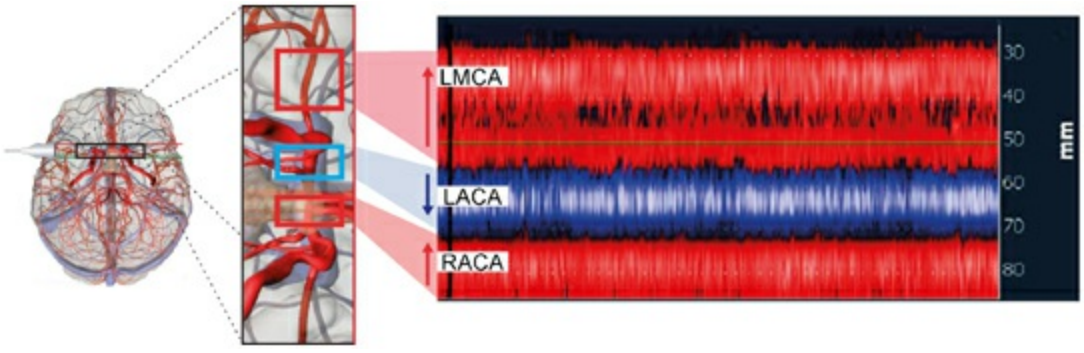

Fig. 13.2 Power motion (M)-mode Doppler. Diagram shows interrogation of cerebral vessels with power M-mode or combined color Doppler and M-mode transcranial Doppler (TCD). The ultrasound

probe is positioned over the left temporal region. The TCD display shows an upper portion in red, which corresponds to flow in the ipsilateral left middle cerebral artery (LMCA). The middle blue portion is associated with the ipsilateral left anterior cerebral artery (LACA) Doppler signal moving away from the transducer. The lower red portion corresponds to flow in the contralateral right anterior cerebral artery (RACA)

DEVELOPMENTS IN TRANSCRANIAL DOPPLER TECHNOLOGY

There are several measurements in TCD using either specialized equipment (**Figure 13.1)** or the basic transthoracic probe. These modalities include:

- Continuous and pulsed wave technique, which are described in Chapter 1, Ultrasound Imaging: Acquisition and Optimization.
- Power motion-mode Doppler (PMD/TCD): Moehring and Spencer [4] introduced this mode of Doppler technique in 2002. This modality displays all available flow signals and direction over a range of 6 cm of intracranial space simultaneously in a single spectral display (**Figure 13.2**). Time spent for TCD examination is reduced compared to a single channel spectral TCD. This mode simplifies the TCD examination for the inexperienced operator.
- Transcranial color-coded duplex sonography (TCCS): This mode combines pulsed-wave Doppler with two-dimensional, real-time B-mode imaging (**Figure 13.3**). Transcranial color-coded duplex sonography allows the visualization of all basal cerebral arteries through the intact skull and allows precise placement of the Doppler sample volume in the vessel. Transcranial color-coded duplex sonography is more reliable and accurate in the detection of pathological hemodynamic changes than conventional TCD for intracranial arteries, other than middle cerebral artery (MCA) or in the setting of anatomical distortions from tumor, hematoma, and edema displacing normal structures. [4] – [6]

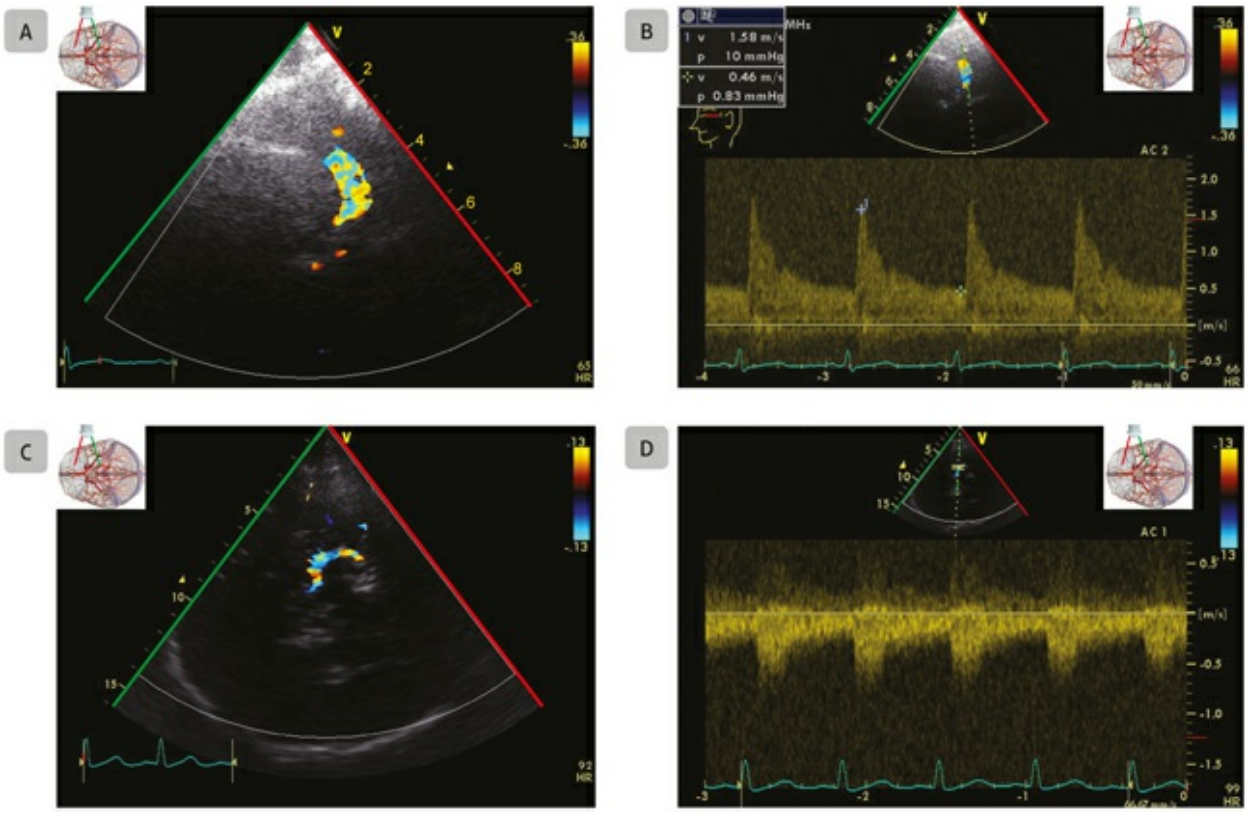

Fig. 13.3 Transcranial Doppler color-coded duplex sonography (TCCS). The middle cerebral artery (MCA) is interrogated using a transthoracic probe positioned over the right temporal region. (A) A 2D image of cerebral artery structure and color Doppler (Nyquist 36 cm/s) flow interrogation is obtained. (B) Sample volume positioning in the vessel allows precise determination of the MCA velocity spectral Doppler profile. (C) In this patient, half of the Circle of Willis is imaged using TCCS. (D) Spectral Doppler profile of the anterior cerebral artery shows the velocity direction is away from the transducer. HR, heart rate

A: https://youtu.be/ds-aGdinxuM

B: https://youtu.be/NVEFR6aPY4w

ACOUSTIC WINDOWS

In order to interrogate the brain, it is essential to obtain an acoustic window through the skull. Normally, the US waves undergo gradual loss of intensity as they move through different body structures. The degree of attenuation is directly proportional to the attenuation coefficient of the medium and to the US frequency. Since bone has a relatively high attenuation coefficient, it is difficult to measure CBFV using a conventional 5–10 MHz Doppler probe. The use of a lower frequency (1–2 MHz) probe is required. Transcranial Doppler examinations are commonly performed through four “acoustic windows” where the bone is relatively thin or absent. The orientation of the ultrasound probe in each acoustic window is shown in **Figure 13.4**. The depth, direction of blood flow, and the CBFV of the vessels insonated in each window are shown in **Table 13.2**. **Table 13.3** summarizes how to perform TCD .

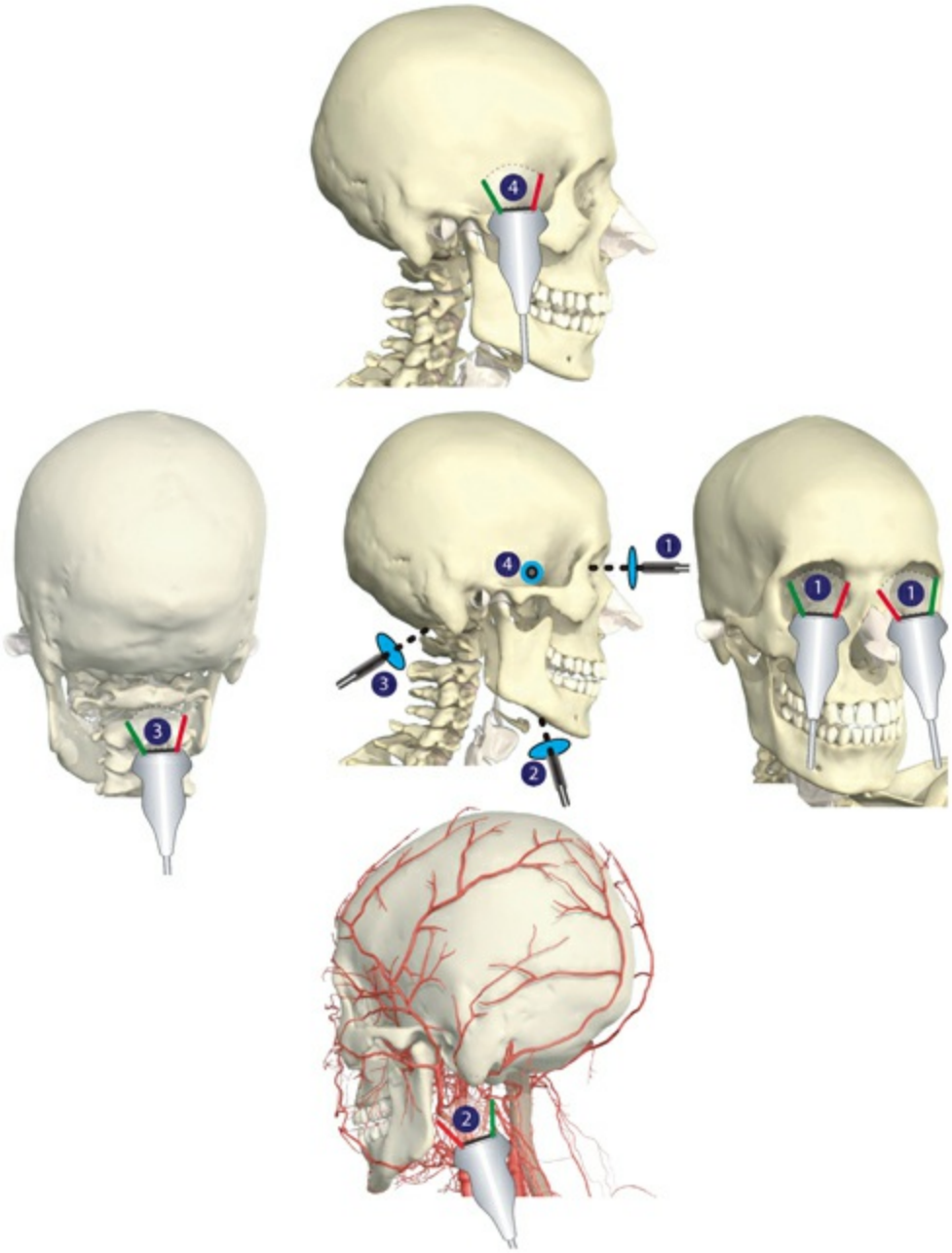

Fig. 13.4 Acoustic windows and ultrasound probe position. Lateral skull diagram showing probe positions used to obtain acoustic windows for transcranial Doppler: (1) trans-orbital, (2) submandibular, (3) suboccipital or transforaminal, and (4) transtemporal. (Anatomical images with permission of Primal Pictures, Wolters Kluwer Health.)

Table 13.2 Normal Doppler Values

Vessel	Depth (mm)	Direction	Velocity (cm/s)			PI	RI
			Peak	Mean	ED		
Transtemporal							
MCA	30–67	Toward	90–110	62 ± 12	35–55	0.81–0.97	0.54–0.62
ACA (A1)	60–80	Away	80–90	50 ± 11	30–40	0.76–0.92	0.53–0.59
PCA (P1)	55–80	Toward	66–81	39 ± 10	26–33	0.78–0.97	0.53–0.60
PCA (P2)	60–70	Away	68–71	42–53	26–32	0.77–0.97	0.53–0.60
TICA (C7)	60–67	Bidirectional	39 ± 9				
Transorbital							
Ophthalmic	40–60	Toward	21 ± 5	High			
Carotid siphon (C2–4)	60–80	Bidirectional	47 ± 14				
Suboccipital							
Vertebral	40–85	Away	54–74	38 ± 10	23–34	0.77–0.95	0.51–0.60
Basilar	>80	Away	52–66	41 ± 10	22–31	0.78–0.94	0.53–0.59
Submandibular							
ICA (C1)	35–70	Away	37 ± 9				

ACA, anterior cerebral artery; C, carotid segments (C1, cervical or submandibular segment; C2,petrous segment; C3, lacerum segment; A1, ACA first horizontal segment; C4, cavernous segment; C5, clinoid segment; C6, ophthalmic segment; C7, communicating or terminal (t) segment); ED, end-diastolic; ICA, internal carotid artery; MCA, middle cerebral artery; P1, PCA first horizontal segment; P2, PCA second horizontal segment; PCA, posterior cerebral artery; PI, pulsatility index; RI, resistance index; TICA, terminal internal carotid artery or C7. (Adapted from Rigamonti *et al.* [7])

Table 13.3 General Procedural Steps in Echo-Guided Transcranial Doppler

1.	Proper site: start with temporal, orbital, submandibular and occipital windows
2.	Probe selection: select a low frequency probe (1–2 MHz) and the transcranial profile
3.	Position the patient: supine for temporal and orbital, lateral decubitus for submandibular and occipital
4.	Position the echo machine so that the ultrasound images and the chosen site for vascular access will be in the same visual field
5.	Position of the operator: head of the bed while stabilizing the hand using a pillow
6.	Preparation: adjust gain, depth (14–16 cm), color scale and M-mode. Use initially a 10–15 mm sample volume then adjust
7.	Trans-temporal window: identify with 2D the petrous ridge posteriorly, carotid canal (C2–C3), foramen lacerum, cerebral falx, sphenoid wing anteriorly, cerebral peduncle and the contralateral cranial bone (**Figure 13.7**). Use color Doppler (scale 25 cm/s) to identify the vessels in the following order (**Figure 13.7**): bidirectional "butterfly" TICA signal (C7) in the foramen lacerum, MCA, ACA, ACoA, then move back to TICA and find the PCoA then the PCA, proximal (P1) and distal (P2) portion around the cerebral peduncle
8.	Transorbital window: select a high-frequency probe (7.5–10 MHz), reduce power setting (SPTA 17mW/cm^2 and MI 0.28) with minimal pressure on the closed eyelid. On 2D, identify the optic nerve then with color Doppler the ophthalmic artery, then the carotid artery genu (C6) "butterfly" signal. Aim the probe upward to identify the supraclinoid segment (C7) and then inferiorly to identify the cavernous or parasellar segment (C7)
9.	Suboccipital window: lateral decubitus position with slight neck flexion, aim the probe at the nose ridge. Identify the foramen magnum and the 2 vertebral and the distal basilar artery
10.	Submandibular window: position the probe at the angle of the mandible and direct it medially and cephalad towards the carotid canal
11.	Report velocities values and refer to normal values adjusted by age

ACA, anterior cerebral artery; ACoA, anterior communication artery; C, carotid segments (C1, cervical or submandibular segment; C2, petrous segment; C3, lacerum segment; C4, cavernous segment; C5, clinoid segment; C6, ophthalmic segment; C7, communicating or terminal (t) segment); MCA, middle cerebral artery; MI, mechanical index; P1, PCA first horizontal segment; P2, PCA second horizontal segment; PCA, posterior cerebral artery; PCoA, posterior communicating artery; SPTA, spatial peak temporal average; TICA, terminal internal carotid artery.Trans-temporal window: The probe is placed over an area just above the zygomatic arch represented by a line joining the tragus to the lateral canthus of the eye. There are four locations within the trans-temporal window: anterior, middle, posterior, and frontal (**Figure 5**). The MCA, anterior cerebral artery (ACA), posterior cerebral artery (PCA), and internal carotid artery (ICA) can be interrogated (**Figure 6**). Reference points using 2D imaging, are the petrous bone, foramen lacerum, sphenoid wing, and the opposite cranial wall (**Figure 7**). In order to see the latter, the depth has to be adjusted to at least twice the distance from the midline cerebral falx which is typically at 8 cm.

1. Trans-temporal window: The probe is placed over an area just above the zygomatic arch represented by a line joining the tragus to the lateral canthus of the eye. There are four locations within the trans-temporal window: anterior, middle, posterior, and frontal

(**Figure 13.5**). The MCA, anterior cerebral artery (ACA), posterior cerebral artery (PCA), and internal carotid artery (ICA) can be interrogated (**Figure 13.6**). Reference points using 2D imaging, are the petrous bone, foramen lacerum, sphenoid wing, and the opposite cranial wall (**Figure 13.7**). In order to see the latter, the depth has to be adjusted to at least twice the distance from the midline cerebral falx which is typically at 8 cm.

2. Transorbital window: The probe is placed over the upper eyelid to insonate the ophthalmic artery (OA) and portions of ICA (cavernous, genu, and supraclinoid), across the carotid siphon. While measuring the CBFV through this window, the ultrasound power has to bedecreased to the minimum (10%) to avoid thermal injury to the retina (**Figure 13.8**).
3. Suboccipital or transforaminal window: In this window the terminal portion of the vertebral arteries (VA) and the basilar artery (BA) are insonated. The probe is initially placed in the midline over the upper part of posterior neck (2.5 cm below the skull edge), while the patient is sitting or lying in the lateral position. This approach facilitates insonation of the BA, while moving the probe 2.5 cm lateral from the midline on each side identifies the VA (**Figure 13.9**).
4. Sub-mandibular window: The probe lies below the angle of the mandible to insonate the extra-cranial portion of ICA. Anatomic features of the patient may make the differentiation of the ICA from the external carotid artery (ECA) challenging. However, typically the diastolic component of the ICA is more apparent than the ECA because of increased resistance of the musculararterritories irrigated by the ECA (**Figure 13.10**).

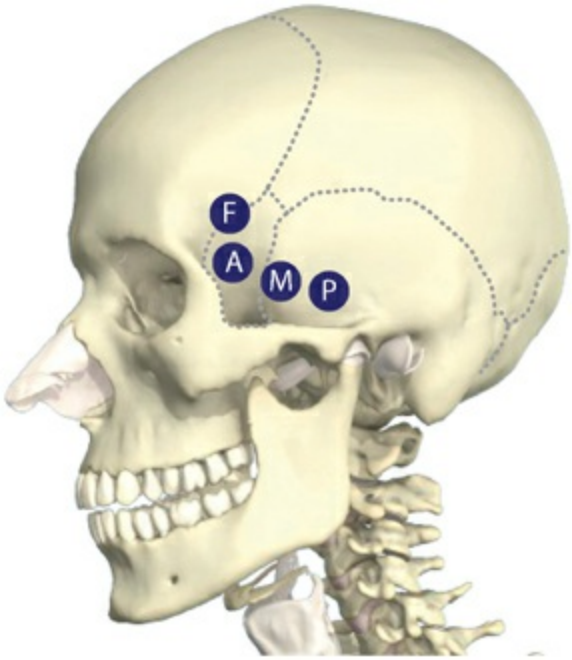

Fig. 13.5 Temporal windows. The four locations for probe position within the transtemporal window for the (A) middle cerebral artery (MCA); (B) bifurcation of the MCA and anterior cerebral artery (ACA); (C) ACA; (D) terminal internal carotid artery (TICA); (E) pre-communicating posterior cerebral artery (PCA); and (F) post-communicating PCA. (Anatomical images with permission of Primal Pictures, Wolters Kluwer Health.)

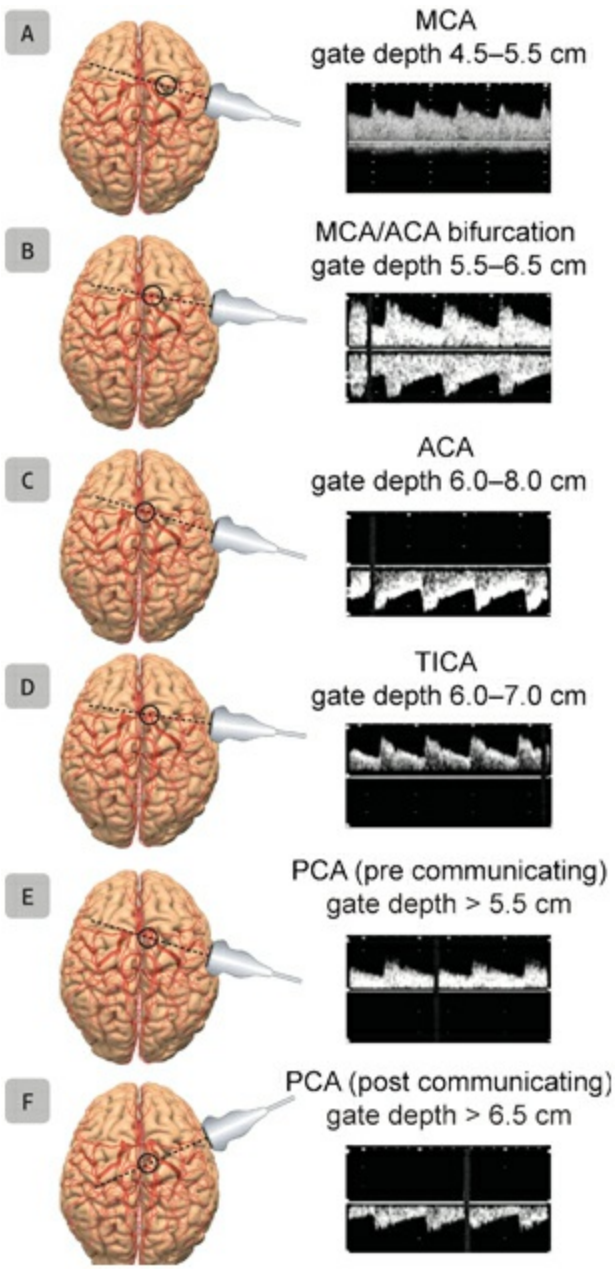

Fig. 13.6 Transcranial Doppler signals. Probe position in the temporal window and normal transcranial Doppler signals are shown for the (A) middle cerebral artery (MCA); (B) bifurcation of the MCA and anterior cerebral artery (ACA); (C) ACA; (D) terminal internal carotid artery (TICA); (E) pre-communicating posterior cerebral artery (PCA); and (F) post-communicating PCA. (Anatomical images with permission of Primal Pictures, Wolters Kluwer Health.)

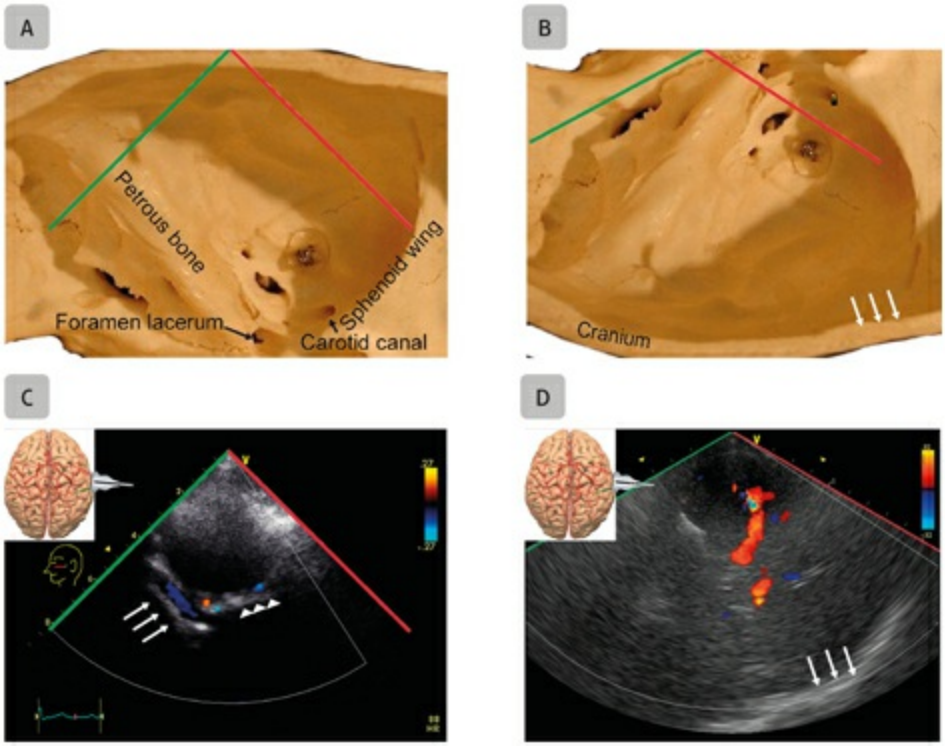

Fig. 13.7 Temporal windows. (A,B) Using 2D imaging, anatomic reference points shown with these cut portions of the skull are the petrous bone, foramen lacerum, sphenoid wing, and the opposite cranial wall (arrows). (C) Color Doppler (Nyquist 27 cm/s) showing blood flow in the petrous bone (arrows). The sphenoid wing is shown (triangles). (D) The display depth is initially adjusted in order to see the opposite skull (arrows). (Anatomical images with permission of Primal Pictures, Wolters Kluwer Health.)

D: https://youtu.be/tCUYNUnxoDw

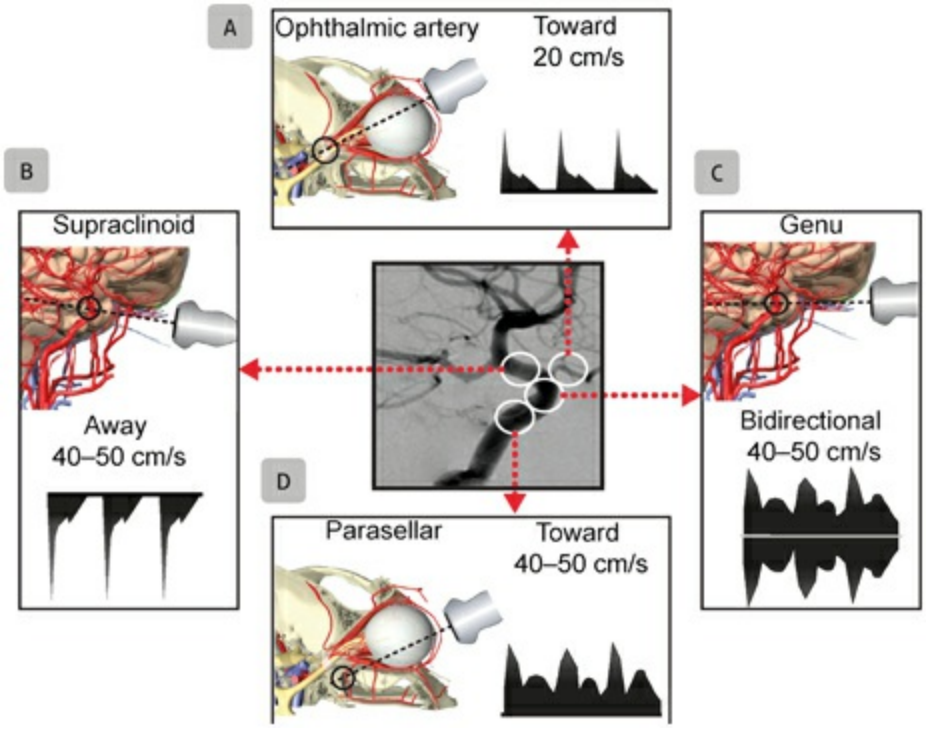

Fig. 13.8 Orbital window. Probe positions in the orbital window and transcranial Doppler signals are shown for different segments of the internal carotid artery (ICA). The most distal portion is the (A) ophthalmic artery that originates from the ophthalmic segment. From distal to proximal the segments of the ICA are the (B) supraclinoid segment, (C) petrous segment that includes the bend or genu, and (D) parasellar segment or cavernous carotid siphon. (Anatomical images with permission of Primal Pictures, Wolters Kluwer Health.)

B: https://youtu.be/SgM4wEEyFdQ

Transcranial Doppler Indices

The peak systolic flow velocity s(FVs) and the end-diastolic flow velocity (FVd) are measured directly by analyzing the waveform. The mean flow velocity (FVm), pulsatility index (PI) and resistance index (RI) are estimated from these measured values using the following formulas. Ultrasound machines with automatic or manual spectral waveform tracing calculate FVm as the area under the traced curve.

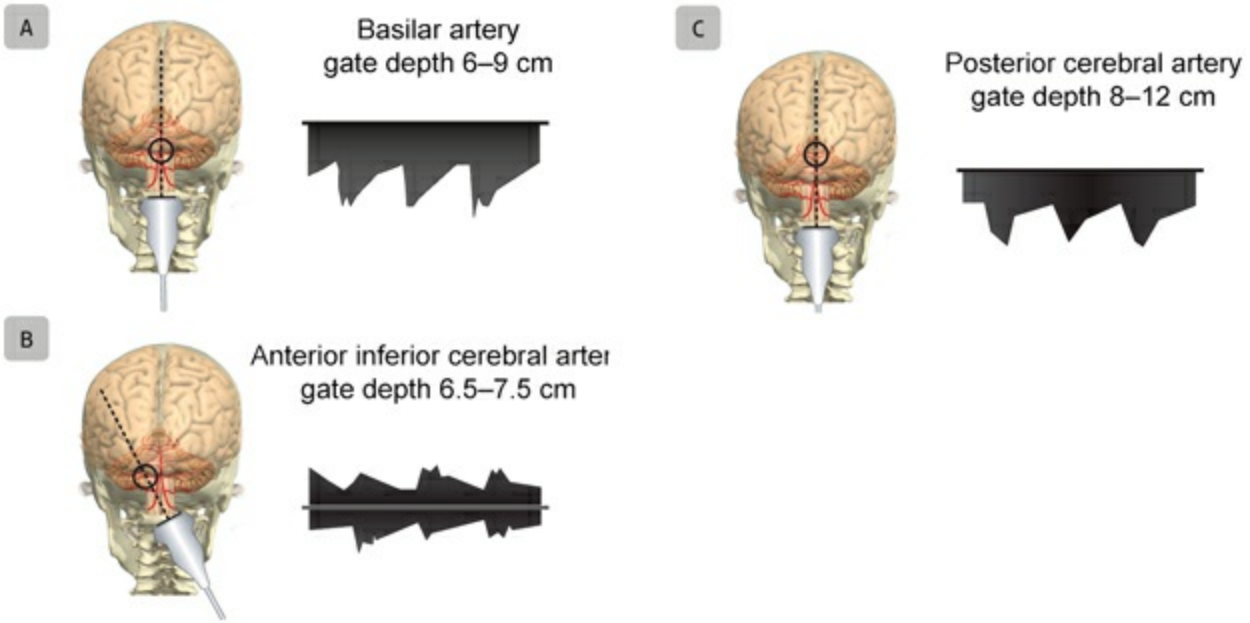

Fig. 13.9 Occipital window. Probe positions in the occipital window and transcranial Doppler signals are shown for the (A) basilar artery, (B) anterior inferior cerebralartery, and (C) posterior cerebral artery. (Anatomical images with permission of Primal Pictures, Wolters Kluwer Health.)

https://youtu.be/k_dsZ-Lkf8g

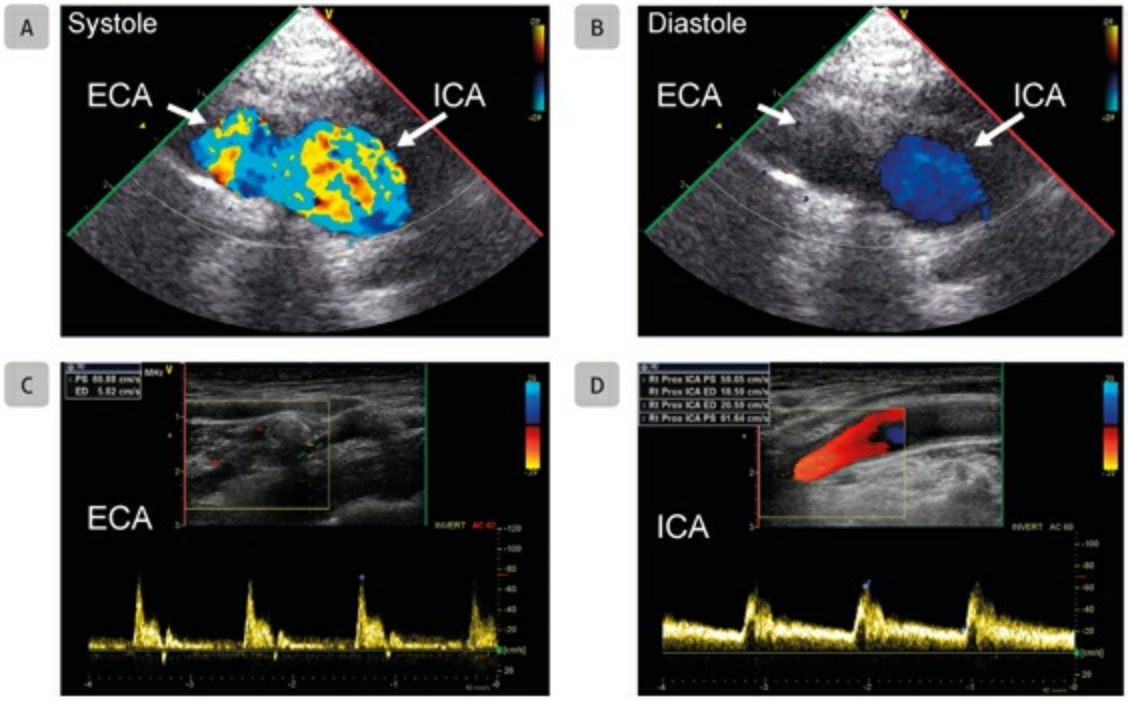

Fig. 13.10 Submandibular window. (A) 2D image with color Doppler (Nyquist 9 cm/s) shows systolic flow in both the external carotid artery (ECA) and internal carotid artery (ICA). (B) 2D image with color Doppler (Nyquist 9 cm/s) shows more prominent diastolic flow in the ICA, helping to distinguish the ICA and ECA. (C,D) Spectral Doppler trace confirms systolic flow in the ECA and continuous flow with systolic predominance in the ICA

A&B: https://youtu.be/3hfEcxh6dII

C&D: https://youtu.be/safqsNGVVqc

Mean flow velocity FVm = FVs + 2 x FVd /3 or = FVs - FVd /3 + FVd

Pulsatility index (PI) = (FVs - FVd)/FVm

Resistance index (RI) = (FVs - FVd)/FVs

Table 13.2 shows the normal mean velocities, PI, RI, and the diameter of basal cerebral vessels. Arterial velocity normally follows this order of magnitude: MCA > ACA ≥ Siphon ≥ PCA ≥ BA > VA > OA. A simple rule

for mean velocity (in cm/s) is MCA 60, ACA, and TICA 50, PCA 40, BA 30, and VA 20. The The difference among the MCA, ACA, and PCA velocities should velocities should be <30%. In a normal MCA, the FVm should not exceed 170 cm/s in children and 80 cm/s in adults. With normal breathing, the normal end-diastolic velocity should be 25–50% of the peak systolic velocities and the PI should be low (0.6–1.1), except for the OA (PI >1.2).

Limitations of Transcranial Doppler

1. Transcranial Doppler is highly operator dependent and requires detailed 3D knowledge of cerebrovascular anatomy and good knowledge of confounding factors affecting CBFV.
2. Transcranial Doppler is impossible or very difficult in 8–10% of patients because of inadequate temporal windows. Poor to absent temporal window is more common in those of African descent, Asians, and elderly female patients. This is related to thickness and porosity of the temporal bone attenuating ultrasound energy transmission.
3. The direction of blood flow can vary; altering the interpretation of TCD. It has been found that in more than 50% of healthy brains and in more than 80% of dysfunctional brains, the Circle of Willis contains at least one artery that is absent or underdeveloped. [8] , [9] Anatomical variants are described in up to 52%. [10]

Applications of Transcranial Doppler

Aneurysmal Subarachnoid Hemorrhage

Cerebral vasospasm leading to delayed cerebral ischemia (DCI) and infarction is the most common and devastating complication following an aneurysmal subarachnoid hemorrhage (aSAH). Vasospasm can affect either the stem of major intracerebral vessels, distal vessels, or both. Cerebral vasospasm usually peaks at 3–7 days following aSAH and can last for 10–14 days. Following aSAH, 14–46% of patients develop DCI, of which 64% will develop infarction due to severe narrowing (<1 mm) of intracranial arteries. [2] For the past two decades, there has been a significant reduction in mortality following aSAH, due to improved vasospasm surveillance technologies. Digital subtraction angiography, computed tomography angiogram (CTA),

and computed tomography perfusion (CTP) are very useful tools for the diagnosis of vasospasm. These techniques give snap-shot pictures rather than a continuous assessment and expose the patient to radiation and contrast. Transcranial Doppler is a simple, non-invasive, continuous, bedside tool for monitoring vasospasm without exposing the patient to radiation or contrast. According to the 2008 guidelines of the American Academy of Neurology, TCD is accepted as a tool for diagnosing and monitoring cerebral vasospasm (Recommendation A/I to II). A recent meta-analysis, [11] comparing TCD with angiography showed that TCD reliably predicted MCA vasospasm in 97% of SAH with a specificity of 99% and a sensitivity of 67%. However, there is poor sensitivity and specificity in evaluating vasospasm in the ACA and PCA territory. As mentioned previously, several factors such as mean arterial pressure (MAP), $PaCO_2$, hematocrit, collateral flow pattern, response to therapeutic intervention, intracranial pressure, age, and technical error can all affect the TCD velocities. While interpreting the results, all those factors have to be considered before making a definitive conclusion.

The mean blood flow velocity increases when vasospasm involves a proximal vessel (**Figure 13.11**). Whereas when vasospasm involves the distal part of the intracranial arteries, the mean blood flow velocity does not increase, but blood flow creates focal pulsatility, that increases the PI to >1.2. Studies have shown that an increase in MCA mean velocity by >25 to 40 cm/s per day or by 50% from the baseline in 24 hours is an indicator of vasospasm. In order to follow these criteria, the baseline MCA velocity at admission should be measured for comparison. MCA vasospasm can be graded as mild, moderate, and severe according to the MCA blood flow velocity (**Table 13.3**). Studies have shown a correlation between TCD grading and angiographic vasospasm.

The Lindegaard Index (LI) are a set of given criteria used to differentiate the increase in flow velocity caused by hyperemia from vasospasm by comparing intra- to extra-cranial blood flow velocities (**Figure 13.12**).

LI = FVm in MCA/FVm in extracranial portion of ipsilateral ICA.

When increased flow velocity is due to hyperemia, it affects both intracranial arteries and the extracranial portion of the ICA, therefore the ratio will be low (typically <3). When vasospasm is the cause of high flow velocity, the extracranial portion of the ICA is unaffected; therefore the Lindegaard index will be elevated. Transcranial Doppler is very specific for for diagnosing vasospasm in the posterior circulation. [12] A modified LI is

used to differentiate hyperemia from vasospasm in the posterior circulation with a value >2 indicating vasospasm. [13]

Modified LI = FVm (BA)/FVm (VA)

Several authors have combined different TCD indices to increase the sensitivity and specificity. Gonzalez *et al.* [14] combined the TCD velocity and with ipsilateral hemispheric blood flow using Xenon and created a vasospasm index, where a value of >3.5 indicates vasospasm.

Vasospasm Index = TCD velocity/hemispheric blood flow Nakae *et al.* [15] combined the ipsilateral and contralateral mean blood flow velocity using TCD. A ratio between both of >1.5 predicted delayed cerebral ischemia more accurately than absolute blood flow velocity alone. Finally, if there is a carotid artery stenosis, velocities will also be increased proportional to the degree of the stenosis (**Table 13.4**).

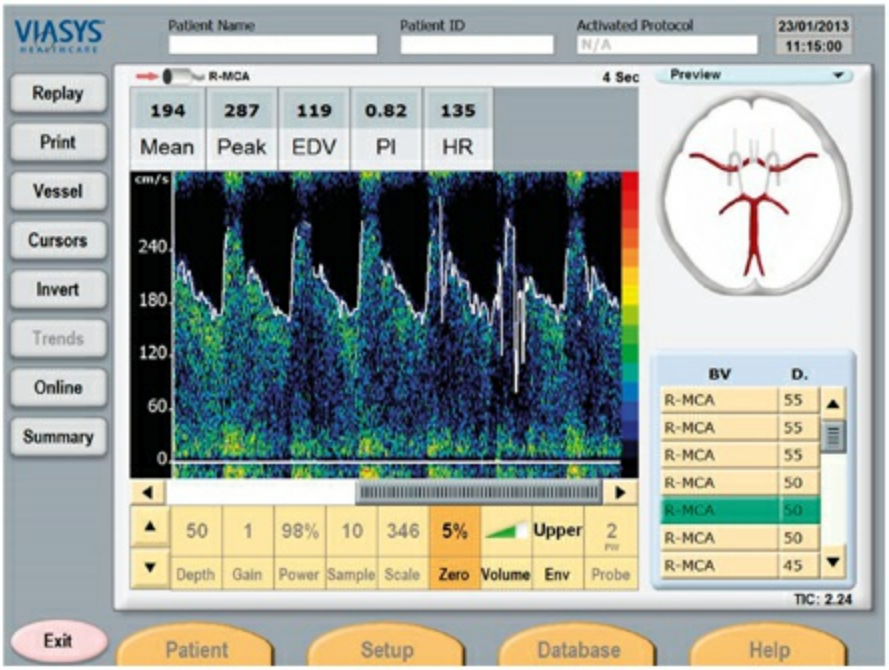

Fig. 13.11 Vasospasm. Increased right middle cerebral artery (R-MCA) velocities are shown with transcranial Doppler in a patient with cerebral vasospasm following aneurysmal subarachnoid hemorrhage. Both normal peak (80–120 cm/s) and mean (62 ± 12 cm/s) velocities are exceeded. EDV, end-diastolic velocity; HR, heart rate; PI, pulsatility index

A: https://youtu.be/K00LkmjSyB4

C: https://youtu.be/tl6FgBc-Gc0

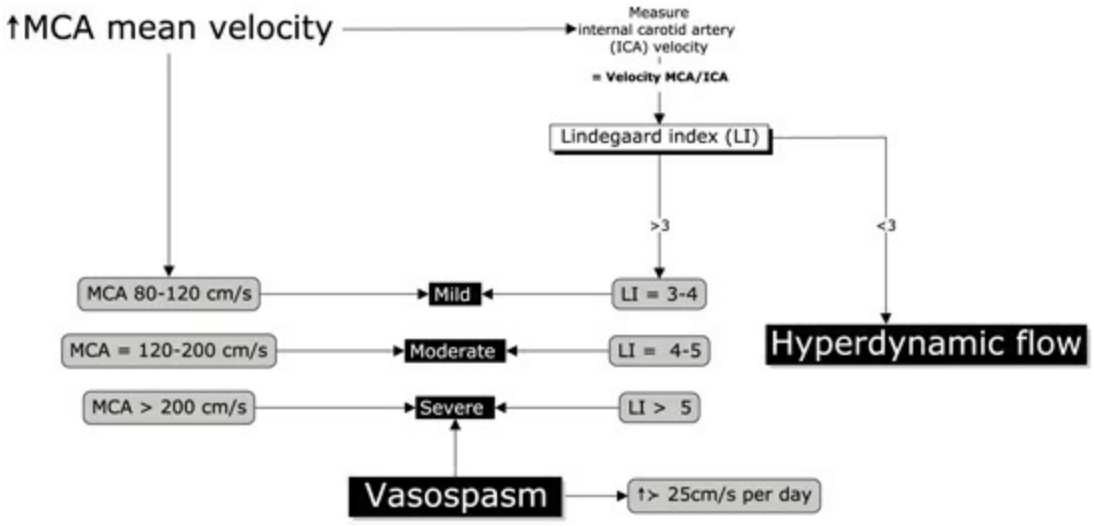

Fig. 13.12 Vasospasm algorithm. An algorithm for the differentiation of cerebral vasospasm versus hyperdynamic flow using mean middle cerebral artery (MCA) velocities and the Lindegaard Index is presented. For basilar artery vasospasm, the criteria are: basilar artery velocity > 85 cm/s + LI (basilar artery/MCA) > 2-3

Brain Death

Brain death is defined as “an irreversible loss of brain function including the brainstem”. The American Academy of Neurology has published diagnostic requirements for confirming brain death by clinical criteria. In certain clinical situations where brain death determination cannot be reliably performed by clinical criteria, confirmatory tests are mandatory. These situations include severe facial trauma, pre-existing pupillary abnormalities, toxic levels of sedative drugs, aminoglycosides, tricyclic antidepressants, anticholinergics, antiepileptics, chemotherapeutic agents or neuromuscular blocking agents, metabolic disturbances, hypothermia, conditions like severe sleep apnea or severe cardiorespiratory disease, or the inability to correctly perform an apnea test. Absence of cerebral blood flow demonstrated by four-vessel digital angiography is considered the gold standard for diagnosing brain death. Other ancillary radiological tests, such as CTA, CTP and magnetic

resonance angiography are also used to confirm brain death. These tests are invasive, expensive, require transport of critically ill patients, and, for iodinated contrast studies, have additional contrast-induced complications.

Transcranial Doppler has been used for the diagnosis of cerebral circulatory arrest (CCA) since 1987 [16] , [17] with a high sensitivity (91–100%) and specificity (100%). There have been several reports of positive CBF on TCD, in patients who are clinically brain dead. In these cases, the brain insult or damage was limited to the cerebellum or brainstem leaving blood flow in the anterior cerebral circulation relatively intact. For this reason, it is important to obtain bilateral MCA and BA flow patterns on two occasions at an interval of 30 minutes before diagnosing CCA by TCD. Infants (open fontanelle) and patients who underwent decompressive craniotomy with an intraventricular drainage catheter, will still have detectable CBF even in the presence of clinical brain death (false negative). Following transient hypotension and cardiac arrest, TCD findings can be similar to CCA findings (false positive). Caution is needed before interpreting the TCD results in this situation.

Table 13.4 Doppler Spectral Criteria to Evaluate Carotid Stenosis

Diameter stenosis (%)	Peak systolic velocity (cm/s)	End diastolic velocity (cm/s)	ICA/CCA systolic velocity ratio	ICA/CCA diastolic velocity ratio
0–40	<110 >25	<40	<1.5	<2.6
41–59	>120	<40	>1.8	<2.6
60–79	>130	>40	>1.8	>2.6
80–99	>250 <25	>80–135	>3.7	>5.5

In the presence of ICA occlusion: unilateral dampened flow will be observed in the CCA. In addition, absent or reversed diastolic flow proximal to ICA occlusion will be present. CCA, common carotid artery; ICA, internal carotid artery. (Adapted from Carroll *et al.* [12] *)*

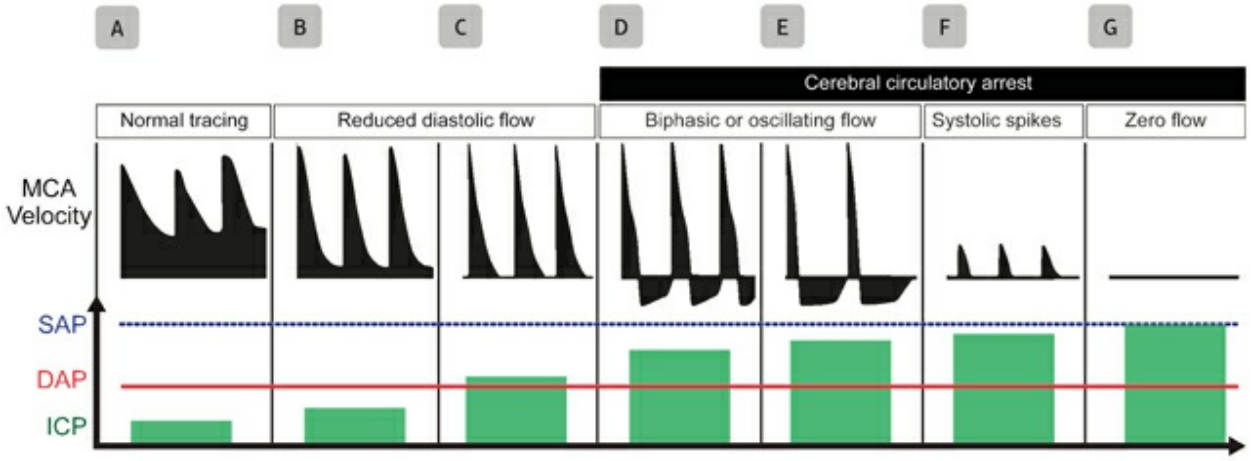

Fig. 13.13 Intracranial hypertension and circulatory arrest. Transcranial Doppler changes in middle cerebral artery (MCA) mean flow with progressive increase in intracranial pressure (ICP) are shown compared with (A) normal MCA flow trace and normal ICP. (B, C) The initial stage has a typical pattern of systolic peaks with progressive reduction in diastolic velocities. (D—G) The three patterns that correspond to intracranial circulatory arrest are shown: biphasic oscillating flow, systolic spike flow, and zero flow. DAP, diastolic arterial pressure; SAP, systolic arterial pressure. (Adapted from Hassler *et al.* [18] and Conti *et al.* [19] *)*

Flow Patterns with Increased Intracranial Pressure Leading to Cerebral Circulatory Arrest

Three types of flow patterns are noted in the Doppler spectral wave form in cerebral circulatory arrest (**Figure 13.13**). First, the oscillating or reverberant flow pattern represents systolic flow towards the brain and a diastolic flow away from the brain - so-called ‘bidirectional’ or ‘reverberant’ flow (**Figure 13.13 D,E**). Oscillating flow is defined by signals with forward and reverse flow component in one cardiac cycle. The area under the curve of both the antegrade and retrograde flow pattern (to-and-fro movement) should be identical. In this situation, extensive ischemia, intracranial bleeding, or brain swelling can severely increase intracranial pressure (ICP). When ICP reaches the level at which it obstructs the microcirculation, forward flow during systole expands the arterial tree, but due to the very high distal resistance, little or no flow occurs through the microcirculation. The second pattern is the systolic spike pattern that occurs when the ICP reaches the diastolic pressure (**Figure 13.13 C)**. The peak intensity of the systolic spike should be <50 cm/s and the duration <200 ms without a flow signal during the remaining cardiac cycle. Finally, the third pattern corresponds to the “no flow pattern” (**Figure 13.13 F,G**). When ICP reaches MAP, there will be no flow

in the major intracranial arteries. Since there is an absent acoustic window in 10% of patients, there should have been an initial documented flow pattern before interpreting this pattern of CCA. This can be associated with disappearance of diastolic flow in the extra-cranial segment of the ICA and tendency to evolve toward the oscillating flow. Note that the TCD changes observed with a progressive increase in ICP are almost identical to those described with circulatory arrest. The aspect of the TCD signals will also be influenced by the underlying cardiac pathologies and devices such as intra-aortic balloon pump (**Figure 13.14**).

Hyper-Intensity Thromboembolic Signals

Cerebral embolism is common during carotid endarterectomy (CEA), coronary artery bypass graft (CABG) surgery, cardiac valve surgeries, and aortic surgery. This embolism produces characteristic hyper-intensity thromboembolic signal (HITS) on TCD examination. The duration and relative increase in intensity of the HITS from the background signal correlates with the size of emboli (**Figure 13.15**).

For demonstration of HITS, all of the following criteria are required: (1) random occurrence; (2) brief duration (0.01–0.1 s); (3) high intensity (3 dB above the background intensity); (4) primarily unidirectional quality within the Doppler spectrum; (5) causing a spike in the power/intensity trace; and (6) accompanied by an audible “chirp” or “pop.” Hyper-intensity thromboembolic signals can be easily differentiated from artifacts created by probe movement, patient movement, and electrical interference by its low frequency, non-harmonic quality. The high-risk periods for embolic stroke in patients undergoing CEA include shunt insertion, carotid cross-clamp application and release, wound closure, and during the initial 12-hour, post-operative period. A finding of >10 HITS during any phase of surgery, >5 during any 15-minute period in the recovery room, or >50 HITS per hour during the postoperative phase is predictive for the development of cerebral infarction following CEA.

Postoperative neurological complications significantly alters recovery after cardiac surgery. [20] The incidence of clinically apparent periprocedural strokes are estimated to occur in 1.6–6.1% of patients undergoing cardiac surgery. [21] – [23] Several factors increase this risk, including the presence of extracranial ICA stenosis, a history of previous stroke, and a prolonged bypass pump time. Hyper-intensity thromboembolic signal are common at the aortic cross-

clamp application and removal during CABG. The number of HITS is even higher during cardiac valve surgeries. Hyper-intensity thromboembolic signal occurring in patients with prosthetic valves often have intensities exceeding 24 dB with durations >50 ms. With the availability of ambulatory TCD (similar to the Holter monitoring system), continuous TCD monitoring is possible for up to 8 hours. This can assess the true embolic load and predict the stroke risk, especially for asymptomatic carotid stenosis of >50%.

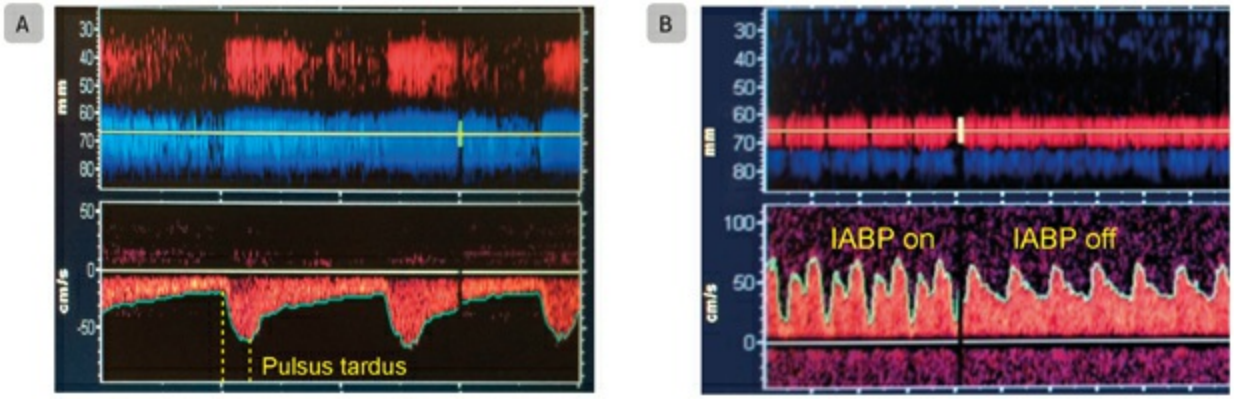

Fig. 13.14 Transcranial Doppler (TCD) display. (A) Anterior cerebral artery velocity in an elderly patient with severe aortic stenosis. Note the delayed upstroke or pulsus tardus (dotted line) that was bilateral. When unilateral, carotid stenosis should be suspected. (B) Right middle cerebral artery TCD signal with an intra-aortic balloon pump (IABP) turned on and off are shown

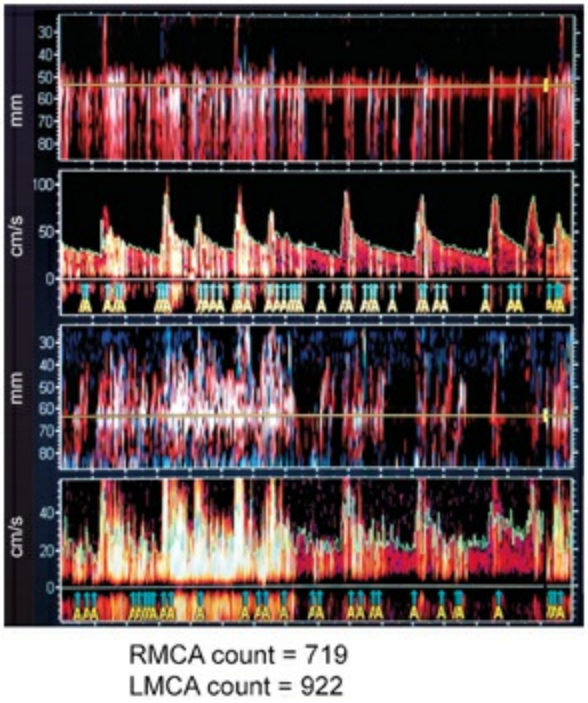

Fig. 13.15 Hyper-intensity thromboembolic signal (HITS). Note the significant number of HITS in both the M-mode and Doppler signals (arrows) demonstrated with TCD during a percutaneous aortic valve procedure. The HITS appeared during guidewire positioning across the ascending aorta. The total number of HITS was 719 on the right middle cerebral artery (RMCA) and 922 on the left middle cerebral artery (LMCA)

Transcranial Doppler can help assess the risk of stroke in asymptomatic carotid stenosis, [24] the adequacy of anticoagulation in patients with acute embolic stroke in the proximal cerebral arteries and in patients with prosthetic cardiac valves. There are, however, several limitations in using TCD as a monitor of embolic stroke. First, it is very difficult to differentiate between embolic materials containing air, atheromatous plaques, lipid or platelet aggregates. In order to distinguish gaseous emboli from solid emboli during carotid surgery, inspiring 100% oxygen reduces the HITS rate by >90%, indicating that most of the embolic signals are from gaseous origin. These embolic signals produce a low frequency sound and have high reflectivity, the signal goes beyond the waveform of the Doppler spectrum, while solid emboli signals are contained within the waveform of Doppler spectrum.

RAISED INTRACRANIAL PRESSURE IN PATIENTS WITH SEVERE HEAD INJURY

Cerebral perfusion pressure (CPP)-guided management with ICP monitoring is the standard of care in patients with severe head injury. Intraventricular ICP monitoring is considered the gold standard for measuring ICP, although with the potential risks of infection, hemorrhage, malposition, and malfunction. In certain clinical situations, the use of invasive ICP monitoring (both intraventricular and intraparenchymal) is not feasible either because of non-availability of personnel and/ or instruments or it is too risky to perform (coagulopathy or very small or compressed ventricles). In order to circumvent these limitations, two alternative techniques can be used, optic nerve sheath diameter (ONSD) and TCD monitoring.

Optic Nerve Sheath Diameter

It has been said by Biblical scholars and poets that “the eye is the window of the soul.” Certainly, with the advent of fundoscopy, the eye became a

window to the brain. The association between papilledema and raised ICP is well known (**Figure 13.16**). As cerebrospinal fluid (CSF) pressure increases, so does the pressure in the optic nerve and its sheath. The resultant edema is the bulging noted as the nerve inserts into the retina. Logically, the optic nerve diameter may change with the edema caused by increased CSF pressure. The use of portable ocular ultrasound has the potential value of detecting increased ICP by measuring the ONSD. The optic nerve sheath is a continuation of dura mater around the optic nerve. The perineural space of the intraorbital portion of the optic nerve, which is the space between the optic nerve sheath and optic nerve, is in direct communication with the subarachnoid space of the brain. This portion of the optic nerve is directly affected by changes in ICP When ICP rises above 20 mmHg, CSF is displaced into the perineural space of the optic nerve, increasing the nerve sheath diameter. Several clinical studies have proven that millimetric increase in ONSD directly correlates with increasing ICP values. The receiver operating characteristics of an ONSD >5 mm as a cut-off to detect an ICP above 20 cm H_2O is 0.93. [25]

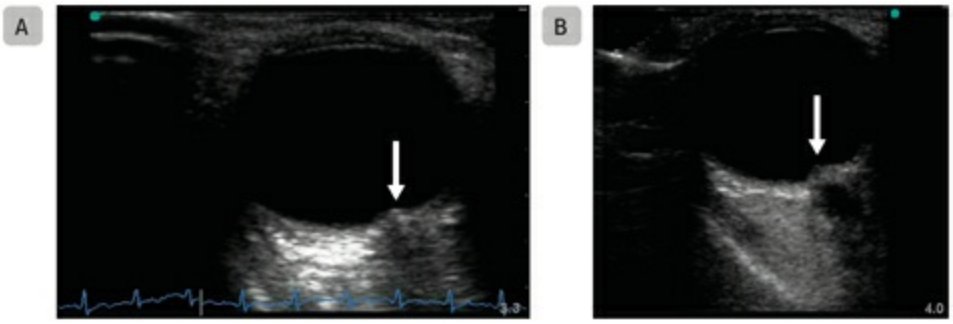

Fig. 13.16 Papilledema. (A,B) Ultrasound of the eye orbit showing 2D images of papilledema (arrow) in two brain dead patients for organ donation

A: https://youtu.be/w_U283Pr_NQ

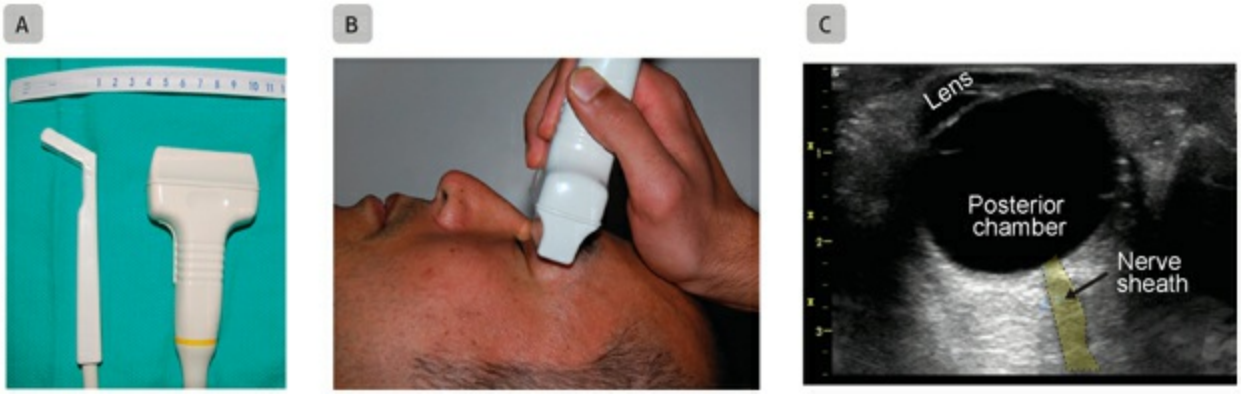

Fig. 13.17 Optic nerve examination. (A) Photo of high frequency ultrasound probes that can be (B) gently positioned over the eyelid of a closed eye. (C) A 2D image easily displays the ocular structures, including the lens, posterior chamber, and optic nerve sheath

C: https://youtu.be/5UhFLyB6UBU

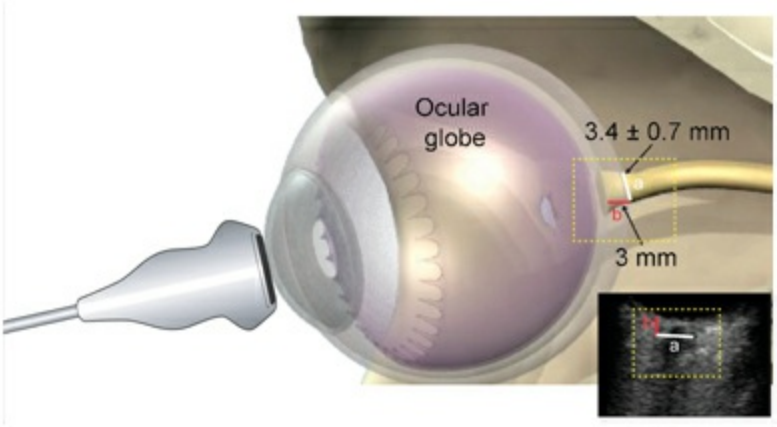

Fig. 13.18 Optic nerve sheath measurement. The site for measuring the diameter of the optic nerve sheath is shown. A 3 mm perpendicular line is drawn from the middle of the optic nerve, at which point the transverse measurement of the optic sheath is performed. Note that the measurement includes the sheath and stops at the transition contrast between the optic nerve and surrounding tissue. Inset shows the optic nerve sheath measurement in a comatose patient

Measurement Technique for Optic Nerve Sheath Diameter

The examination is performed through the eyelid, which protects the ocular

globe from abrasion. The liquid-filled globe is an excellent conductor of US much as a full bladder is for a pelvic US. A 7.5-10 MHz probe is placed without pressure over the closed upper eyelid after applying an adequate amount of US gel. The transmitted US power is reduced to 50%. The Bromage grip (**Figure 13.17**) is used; the examiner's hand or wrist rests on the patient's cheek or forehead supporting the weight of the probe allowing for more delicate probe manipulation. The frequency chosen should be the highest that will allow visualization of the optic nerve and sheath. The nerve and nerve sheath have a distinctive US texture that is different from the rest of the posterior globe. It is imaged as a hypoechoic structure extending from the retina posteriorly. The optic nerve sheath is subtly more echogenic and surrounds the nerve (**Figure 13.17**). As with all US examinations, the region of interest is placed in the middle of the US display with the focus. Given the average globe size of 2.5 cm, an ONSD examination rarely requires more than 4–5 cm of total depth. Authors have described scanning the ONSD in both an axial and saggital plane. [26] The differences measured are in the submillimeter range. Our local standard is to scan only in the axial plane.

The ONSD is measured 3 mm deep to the retina (**Figure 13.18**). Measurements should be taken in each eye and averaged to obtain the binocular ONSD. In case of unilateral eye injury, only one eye measurement can be taken. We advocate saving a still image and measuring off-line. Such a practice prevents distracted scanning of the orbit and possible application of undue pressure as well as reducing the difficulty of measuring a moving target. If available, a "sweep" through the orbit could be saved as a cine loop on the US machine allowing the user to freeze the image where the largest ONSD is noted. Care must be taken to avoid the measurement of artifacts. [27] Studies have shown that an ONSD measurement of >5 mm is considered abnormal with a sensitivity of 100% and specificity of 65%. In pediatric, head-injured patients, a reported cut-off value of >4.5 mm in children older than 1 year was considered to be abnormal. The use of color Doppler to identify retinal vessels can improve the accuracy. [28] In addition, retinal vessel velocity has been shown to correlate with systolic blood pressure and can be used to determine the presence of flow and confirm the patency of the Circle of Willis (**Figure 13.19**). [29] The major advantages of OSND technique are its simplicity, portability, non-invasiveness, and low cost, which allow repeated measurements without the risk of transportation. It is important to note that the CT findings will be normal during the early stages of head injury. Serial

US examination can reveal ICP changes in these patients and can guide further management before the secondary insult occurs. Combining both OSND and TCD gives more insight into brain pathophysiology (**Figure 13.20**).

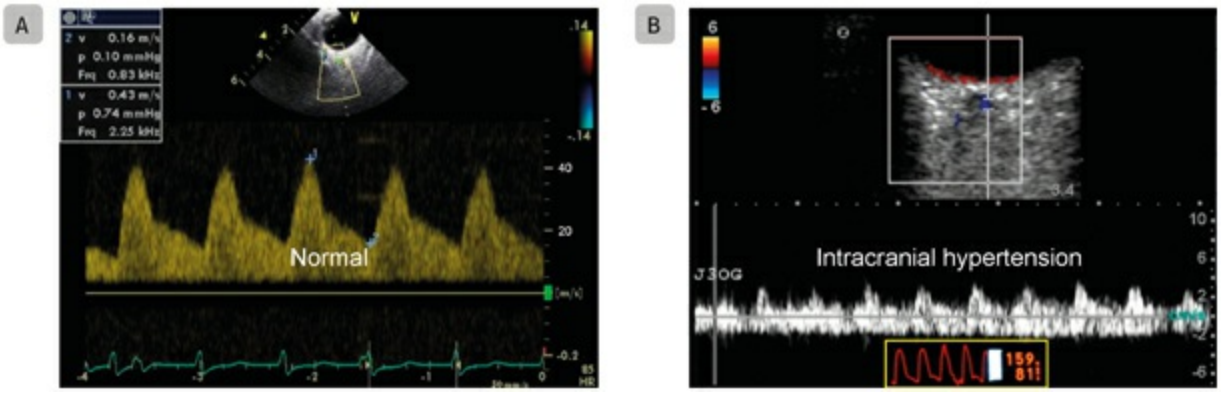

Fig. 13.19 Retinal artery Doppler. Transcranial Doppler traces of the retinal artery in (A) a normal patient and (B) a patient with intracranial hypertension are shown. Note the reduced velocity despite adequate blood pressure in the patient with raised intracranial pressure

There are some limitations to this technique: First, 10% of patients with severe head injury have associated facial fractures involving the orbit precluding ocular examination. Second, as with any US technique, clinicians need to be well trained in ocular sonography in order to avoid erroneous results. Finally in patients with optic neuritis, anterior orbital mass, cavernous sinus pathology, optic nerve injury will have increased ONSD without elevation in ICP making it difficult to diagnose elevated ICP in these patients. [26]

MIDLINE SHIFT

With the availability of TCCS, imaging of intracranial arteries, veins, and parenchymal structures is easier (**Figure 13.21**). It can be repeated at frequent intervals in patients with head injury, stroke, and intracerebral hemorrhage to assess the midline shift (MLS) by measuring the displacement of the third or lateral ventricles (**Figure 13.22**). A comparison of transcranial echography with CT scan in patients who had decompressive craniotomy showed a correlation between the two and concluded that it is a valid tool to assess the progression of edema following the primary insult. [30] Rapid progression of

MLS from edema (poststroke or hemorrhage) has been found to correlate closely with a poorer outcome. The transtemporal window is used to assess MLS in a patient with an intact skull. An outcome predictor score for death caused by cerebral herniation in patients with a space-occupying stroke predicts that specificity and positive predictive values of MLS >2.5, 3.5, 4.0, and 5.0 mm after 16, 24, 32, and 40 hours were 1.0. [31]

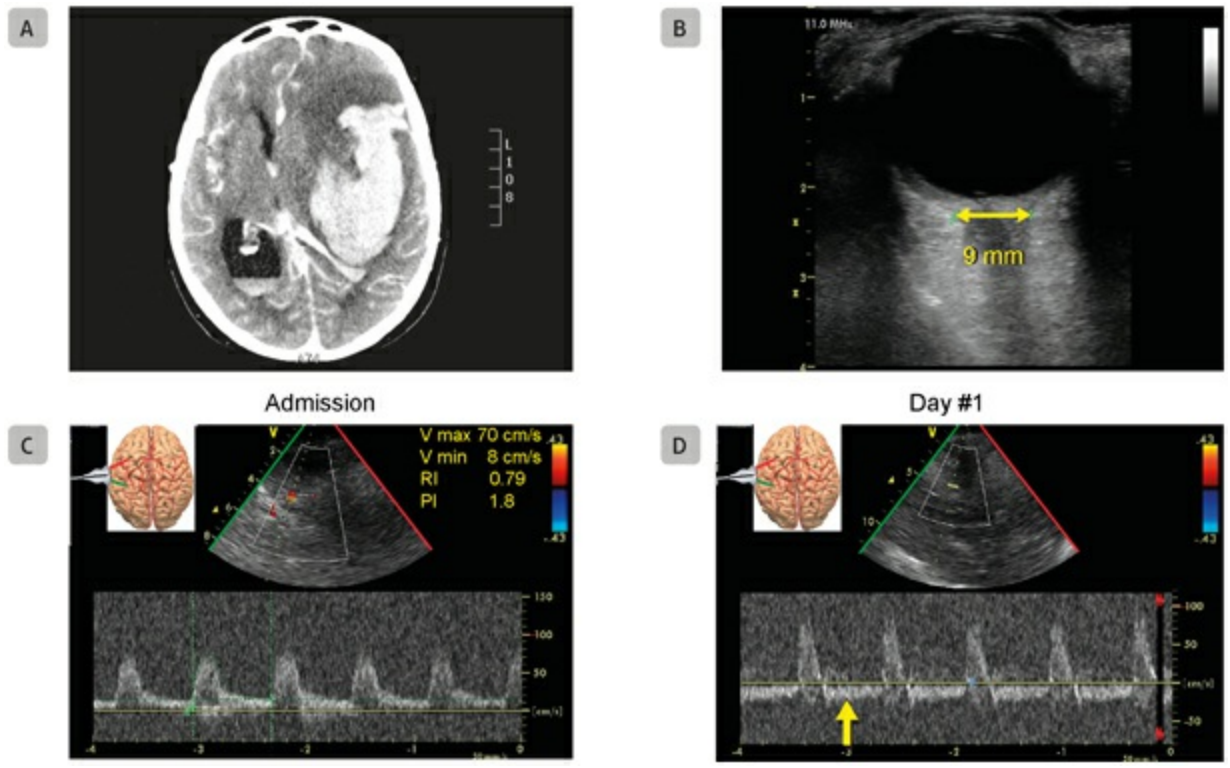

Fig. 13.20 Cerebral hematoma. (A) Computed tomography of a 56-year-old female with left hemispheric cerebral hematoma is shown. (B) Ultrasound of the eye showed the optic nerve sheath measured 9 mm. (C) Upon admission transcranial Doppler examination of the right middle cerebral artery revealed a resistance index (RI) of 0.79 and a pulsatility index (PI) of 1.8. (D) The following day, however, there was diastolic reversal (arrow) in the right middle cerebral artery that was associated with brain death. V, velocity. (Courtesy of Dr Catalina Sokoloff.)

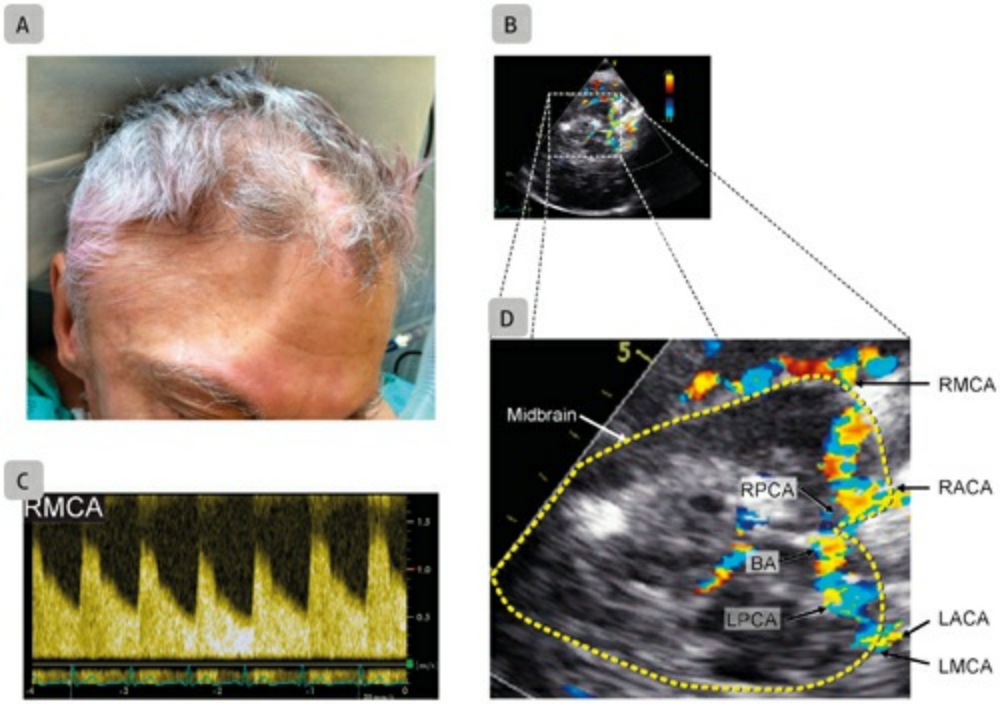

Fig. 13.21 Postcraniotomy. (A) Photo of a patient after right-sided craniotomy for cerebral edema is shown. (B) Cerebral ultrasound 2D image with color Doppler (Nyquist 13 cm/s) shows part of the Circle of Willis. (C) Transcranial Doppler of the right middle cerebral artery (RMCA) velocity is interrogated. The velocities are elevated. BA, basilar artery; LACA, left anterior cerebral artery; LMCA, left middle cerebral artery; LPCA, left posterior cerebral artery; RACA, right anterior cerebral artery; RPCA, right posterior cerebralartery. (Courtesy of Michel W. Bojanowski.)

B: https://youtu.be/MfTPt7bLL4c

Technique to Assess the Midline Shift by Transcranial Color-Coded Duplex Sonography

After insonating the MCA and ICA vessels, the third ventricle is displayed at a depth of 6 to 8 cm by tilting the US probe 10° upward. This structure is easily identified by its hyperechogenic margins, the surrounding hypoechogenic thalamus, and the hyperechogenic pineal gland. The distance between the TCCS probe and the center of the third ventricle was measured in a line perpendicular to the walls of the third ventricle from both the ipsilateral (**Figure 13.23 A**) and contralateral (**Figure 13.23 B**) sides, and the

deviation from the presumed midline was calculated by the equation MLS = (A - B)/2. Assessing the MLS will help estimate the outcome at 16 hours following stroke, and help identify patients who need early decompressive craniectomy.

CEREBROVASCULAR REACTIVITY AND AUTOREGULATION

Carbon dioxide (CO_2) is a powerful vasoactive stimulus for the brain. Change in cerebral blood flow (CBF) in response to changes in arterial CO_2 ($PaCO_2$) is termed cerebrovascular reactivity (CVR). CBF changes linearly with $PaCO_2$ between 20 and 60 mmHg. [32] The measurement of CVR helps to assess the reserve capacity of the cerebrovascular system and to diagnose, treat, and prognosticate patients with cerebrovascular disease. Studies have shown that patients with impaired CVR are at risk of developing stroke. [33] , [34] CBF is directly proportional to cerebral blood flow velocity (CBFV), provided the diameter of the larger blood vessels remains constant. Change in $PaCO_2$ does not affect the major cerebral blood vessels significantly, but modifies CVR in the cerebral arterioles and small distal vessels, which in turn alters the CBFV. Hence, the change in CBFV as measured by TCD directly correlates with the change in CBF. The diameter of the proximal MCA does not dilate more than 4% during variations in $PaCO_2$ or MAP, nor does it change appreciably with systemic administration of nitroprusside or phenyleph- rine. [35] Other studies have shown that the change in CBFV measured by TCD correlated well with the changes in blood flow measured by single photon emission computed tomography (SPECT scan). [36] Several other authors have used TCD to assess the effect of different anesthetics on CVR and have shown that it is a very reliable tool for assessing CVR. [37] – [39]

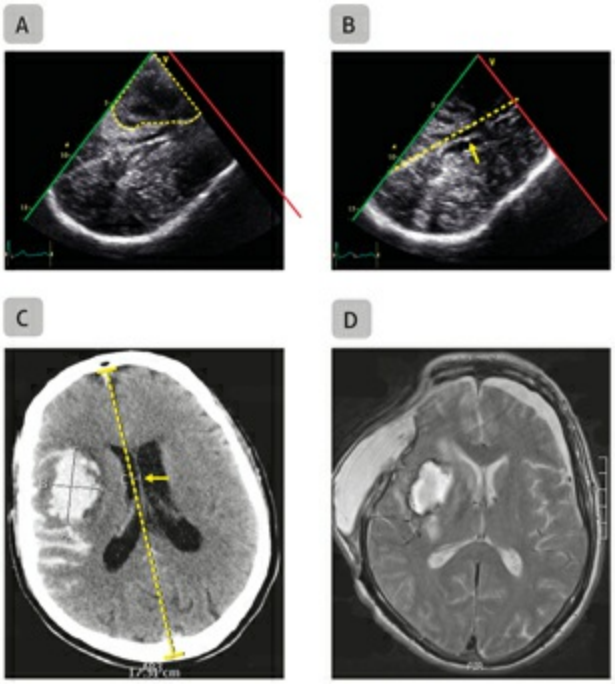

Fig. 13.22 Cerebral hematoma. (A) Transcranial 2D image ofan intraparenchymal hematoma (dotted line) shows a (B) right midline shift (arrow). (C) Initial computed tomography upon presentation with midline shift (arrow) and (D) magnetic resonance imaging views following craniotomy taken at different levels are presented for comparison

A: https://youtu.be/njqTXjP_Bw8

B: https://youtu.be/KAZnirNbgtM

CVR is expressed in terms of absolute reactivity or relative reactivity. Absolute reactivity is defined as change in CBFV in cm/s per mmHg change in $PaCO_2$ tension. Relative reactivity is defined as percentage change from the baseline. The following formulas are used to calculate the CO_2 reactivity using TCD:

Absolute CO_2 reactivity = $\Delta CBFV/\Delta PaCO_2$.

The normal value is 2–5 cm/s per mmHg change in $PaCO_2$)

100 x absolute CO_2 reactivity

Relative CO_2 reactivity =

baseline CBFV

The normal range is 2.5–6% change from baseline.

ΔCBFV = the difference in CBFV between the baseline andhyper- or hypocapnia.

$\Delta PaCO_2$ = the difference in $PaCO_2$ between the baseline and hyper-or hypocapnia. [32] , [35] , [40] , [41]

The breath-holding index (BHI) technique is a simple method to evaluate carbon dioxide reactivity. The patient holds his breath for 30 seconds and the MCA velocity is measured beforehand and afterwards (**Figure 13.24**). [43]

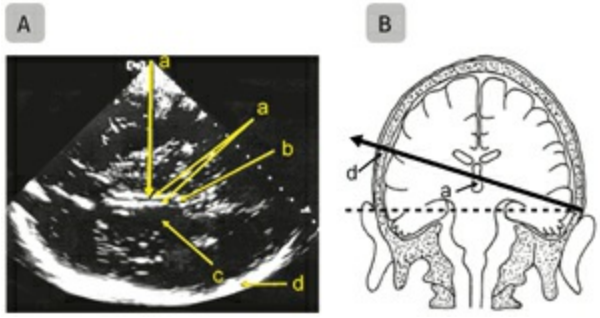

Fig. 13.23 Brain ultrasound. (A,B) Axial trans-temporal transcranial ultrasound 2D examination of the brain showing the (a) 3rd ventricle as a double reflex, (b) pineal region, (c) hypoechogenic thalamus, and (d) contralateral skull. (Adapted with permission from Stolz *et al.* [42] *)*

BHI = [(MCA velocity end - inspiration - MCA velocity rest x 100)]/30 seconds MCA velocity rest

Normal values for BHI in the MCA and the BA are 1.5 ± 0.5 and 1.5 ± 0.6% per second. [44] Values below 0.69 are predictive of risk of stroke in patients with carotid vascular disease.

Cerebral autoregulation is defined as the ability of cerebral blood vessels to maintain a constant CBF during variations in CPP by altering the CVR. The CBF is constant over 50–150 mmHg of MAP and 50–100 of CPP There are two components of cerebral autoregulation: static and dynamic, both are derived parameters. While measuring cerebral autoregulation, confounding factors such as PaO_2, $PaCO_2$, $CMRO_2$, temperature, and sympathetic tone should be kept constant. Impaired autoregulation is associated with adverse clinical outcome.

Static autoregulation is defined as the magnitude of change in CBF in

response to change in CPP during the steady state. Normal value is 0.5–4% change in CBF per mmHg change in CPP. Static autoregulation can be measured alternatively using the formula of Index of Autoregulation (IOA): a value of 1 indicates intact autoregulation; a value of<0.4 indicates abolished or impaired autoregulation. Since TCD can assess CBFV, an indirect measure of CBF, static autoregulation is easily measured.

Dynamic autoregulation is defined as the rate at which the CBF is restored to normal in response to change in CPP. The normal rate of dynamic autoregulation response is 20% per second. If autoregulation is intact, by approximately 5 seconds, the CBF will be restored to normal for a change in CPP.

SICKLE CELL DISEASE

Sickle cell disease (SCD), a common inherited hemoglobin disorder, has been associated with a high risk of stroke. This vaso-occlusive crisis is common (11%) in children between 2–20 years of age leading to neurological disability. TCD is effective in screening children with SCD who are at risk of developing stroke. [45] The stroke prevention trial in sickle cell anemia (STOP I trial) demonstrated a 90% reduction in primary stroke with chronic transfusion therapy in children who had abnormal results with TCD screening. [46] TCD results were classified according to the mean flow velocity (MFV) in the internal carotid or MCA into normal (MFV <170 cm/s), conditional (MFV, 170–199 cm/s), abnormal (MFV, >200 cm/s), or inadequate (TCD, not interpretable). Children whose time-averaged mean velocity (TAMV) >200 cm/s measured in the distal ICA or MCA have approximately a 10–20-fold higher stroke risk than those with normal TCD velocities (TAMV, <170 cm/s). The STOP II trial demonstrated that halted transfusion after 30 months of chronic transfusion therapy causes reversing of normal TCD results to abnormal and increases the risk of silent brain infarction. [47]

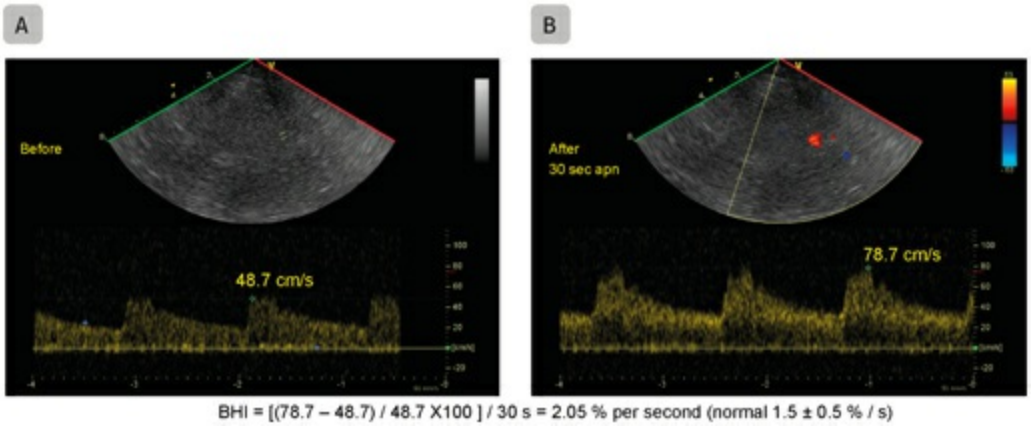

Fig. 13.24 Breath-holding index (BHI). (A,B) Transcranial Doppler images of the middle cerebral artery (A) before and (B) after 30 seconds of apnea. Note the middle cerebral artery velocity increases from 48 to 78 cm/s after apnea. The BHI is normal at 2.05% per second

PATENT FORAMEN OVALE

Patent foramen ovale (PFO) is present in 20% of the adult population. [48]a PFO has a normal amount of tissue as the septum primum is complete but does not fuse with the septum secundum to obliterate the foramen ovale. A right-to-left shunt can be elicited with a Valsalva maneuver and shown using transthoracic or more accurately by transesophageal echocardiography (TEE). It usually has no consequences unless it is responsible for a stroke through paradoxical emboli. The use of TCD for the diagnosis of

right-to-left shunt, most often due to PFO, has a very high specificity (96%), good concordance with TEE but is much less invasive. [49] Accordingly, TCD can be recommended as a simple, non-invasive, and reliable technique, when the use of TEE is restricted inselected patients in whom TEE is not feasible or closure not considered. Shunt severity can be assessed using a scale of 1 to 5 according to the TCD pattern (**Figure 13.25**). Cardiac right-to-left shunt can also be distinguished from pulmonary according to the timing of detection of HITS from the infusion of intravenous bubbles.

SUMMARY

In summary, several non-invasive modalities are available to evaluate neurological functions including TCD, 2D ultrasound of the optic nerve and

the brain if an acoustic window is available, and finally the combination of 2D and Doppler modalities or Duplex. These diagnostic and monitoring modalities when added to vascular, cardiac, pulmonary, and abdominal ultrasound can allow a full comprehensive assessment of the critically ill and surgical patient.

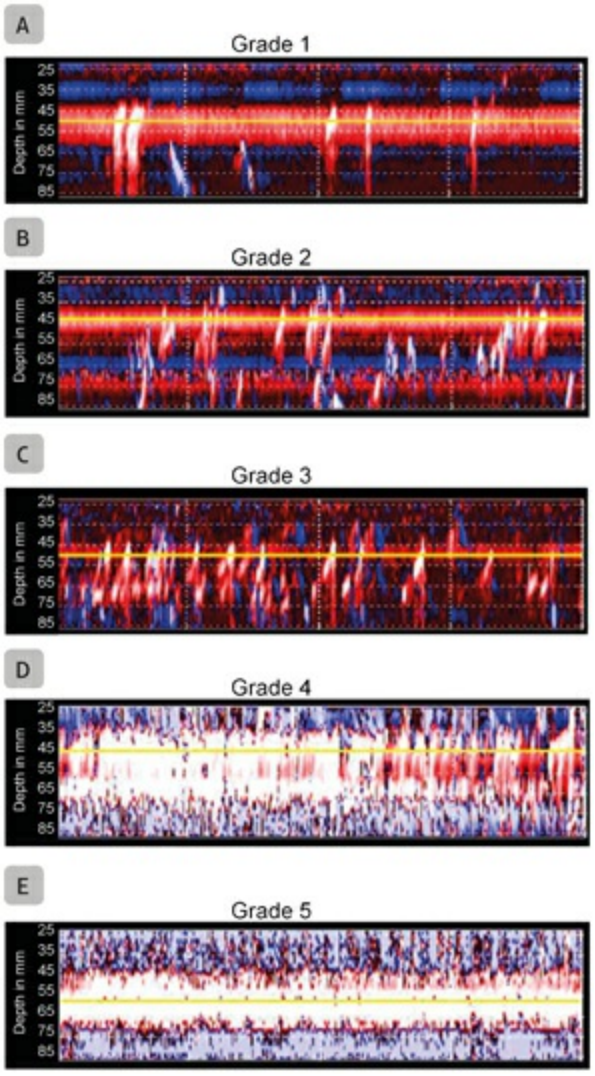

Fig. 13.25 Shunts and emboli. (A–E) Intracardiac shunt severity can be graded using transcranial Doppler imaging. (Courtesy of Nick Raible, Spencer Technology.)

https://youtu.be/_3-CZTU1Ml

REFERENCES

1. AaslidR., MarkwalderT.M., NornesH.. Noninvasive transcranial Doppler ultrasound recording of flow velocity in basal cerebral arteries. *J Neurosurg*1982;*57*:769–74.
2. TsivgoulisG., AlexandrovA.V., SloanM.A.. Advances in transcranial Doppler ultrasonography. *Curr Neurol Neurosci Rep*2009;*9*:46–54.
3. RingelsteinE.B., KahlscheuerB., NiggemeyerE., OtisS.M.. Transcranial Doppler sonography: anatomical landmarks and normal velocity values. *Ultrasound Med Biol*1990;*16*:745–61.
4. MoehringM.A., SpencerM.P.. Power M-mode Doppler (PMD) for observing cerebral blood flow and tracking emboli. *Ultrasound Med Biol*2002;*28*:49–57.
5. BartelsE., FlugelK.A.. [Transcranial color-coded Doppler ultrasound - a new procedure for routine diagnosis of cerebrovascular diseases?] *Vasa Suppl*1992;*35*:16–20.
6. GoertlerM., KrossR., BaeumerM., JostS., GroteR., WeberS., et al. Diagnostic impact and prognostic relevance of early contrast- enhanced transcranial color-coded duplex sonography in acute stroke. *Stroke*1998;*29*:955–62.
7. RigamontiA., AckeryA., BakerA.J.. Transcranial Doppler monitoring in subarachnoid hemorrhage: a critical tool in critical care. *Can J Anesth*2008;*55*:112–23.
8. DevaultK., GremaudP.A., NovakV., OlufsenM.S., VernieresG., ZhaoP.. Blood flow in the Circle of Willis: modeling and calibration. *Multiscale Model Simul*2008;*7*:888–909.
9. RiggsH.E., RuppC.. Variation in form of circle of Willis. The relation of the variations to collateral circulation: anatomic analysis. *Arch Neurol*1963;*8*:8–14.
10. IqbalS.. A comprehensive study of the anatomical variations of the circle of willis in adult human brains. *J Clin Diagn Res*2013;*7*:2423–7.
11. LysakowskiC., WalderB., CostanzaM.C., TramerM.R.. Transcranial Doppler versus angiography in patients with vasospasm due to a ruptured cerebral aneurysm: A systematic review. *Stroke*2001;*32*:2292–8.
12. SloanM.A., BurchC.M., WozniakM.A., RothmanM.I., RigamontiD., PermuttT., et al. Transcranial Doppler detection of vertebrobasilar vasospasm following subarachnoid hemorrhage. *Stroke*. 1994;*25*:2187–97.
13. SoustielJ.F., ShikV., ShreiberR., TavorY., GoldsherD.. Basilar vasospasm diagnosis: investigation of a modified “Lindegaard Index” based on imaging studies and blood velocity measurements of the basilar artery. *Stroke*2002;*33*:72–7.
14. GonzalesN.R., BoscardinW.J., GlennT., MartinN.A.. Vasospasm probability index: a combination of transcranial doppler velocities, cerebral blood flow, and clinical risk factors to predict cerebral vasospasm after aneurysmal subarachnoid hemorrhage. *J Neurosurg*2007;*107*:1101–12.
15. NakaeR., YokotaH., YoshidaD., TeramotoA.. Transcranial Doppler ultrasonography for diagnosis of cerebral vasospasm after aneurysmal subarachnoid hemorrhage: mean blood flow velocity ratio of the ipsilateral and contralateral middle cerebral arteries. *Neurosurgery*2011;*69*:876–83.
16. DucrocqX., BraunM., DebouverieM., JungesC., HummerM., VespignaniH.. Brain death and transcranial Doppler: experience in 130 cases of brain dead patients. *J Neurol Sci*1998;*160*:41–6.
17. DucrocqX., HasslerW., MoritakeK., NewellD.W., von ReuternG.M., ShiogaiT., et al. Consensus opinion on diagnosis of cerebral circulatory arrest using Doppler-sonography: Task Force Group on Cerebral Death of the Neurosonology Research Group of the World Federation of Neurology. *J Neurol Sci*1998;*159*:145–50.
18. HasslerW., SteinmetzH., PirschelJ.. Transcranial Doppler study of intracranial circulatory arrest. *J Neurosurg*1989;*71*(195–201):19.
19. ContiA., lacopinoD.G., SpadaA., CardaliS.M., GiusaM., LaT.D.*et al*.Transcranial Doppler

ultrasonography in the assessment of cerebral circulation arrest: improving sensitivity by transcervical and transorbital carotid insonation and serial examinations. *Neurocrit Care*2009; *10*: 326–35.

20. ArrowsmithJ.E., GrocottH.P., RevesJ.G., NewmanM.F.. Central nervous system complications of cardiac surgery. *Br J Anaesth*2000;*84*:378–93.
21. AhlgrenE., ArenC.. Cerebral complications after coronary artery bypass and heart valve surgery: risk factors and onset of symptoms. *J Cardiothorac Vasc Anesth*1998;*12*:270–3.
22. RoachG.W., KanchugerM., MangañoC.M., NewmanM., NussmeierN., WolmanR., et al. Adverse cerebral outcomes after coronary bypass surgery. Multicenter Study of Perioperative Ischemia Research Group and the Ischemia Research and Education Foundation Investigators. *N Engl J Med*1996;*335*:1857–63.
23. HogueC.W., GottesmanR.F., StearnsJ.. Mechanisms of cerebral injury from cardiac surgery. *Crit Care Clin*2008; *24*: 83–ix.
24. KingA., MarcusH.S.. Doppler embolic signals incerebrovascular disease and prediction of stroke risk: a systematic review and meta-analysis. *Stroke*2009;*40*:3711–7.
25. KimberlyH.H., ShahS., MarillK., NobleV.. Correlation of optic nerve sheath diameter with direct measurement of intracranial pressure. *Acad Emerg Med*2008;*15*:201–4.
26. GirisginA.S., KalkanE., KocakS., CanderB., GulM., SemizM.. The role of optic nerve ultrasonography in the diagnosis of elevated intracranial pressure. *Emerg Med J*2007;*24*:251–4.
27. RajajeeV., VanamanM., FletcherJ.J., JacobsT.L.. Optic nerve ultrasound for the detection of raised intracranial pressure. *Neurocrit Care*2011;*15*:506–15.
28. CopettiR., CattarossiL.. Optic nerve ultrasound: artifacts and real images. *Intensive Care Med*2009;*35*:1488–9.
29. OrihashiK., MatsuuraY., SuedaT., ShikataH., MoritaS., HiraiS., et al. Flow velocity of central retinal artery and retrobulbar vessels during cardiovascular operations. *J Thorac Cardiovasc Surg*1997;*114*:1081–7.
30. CaricatoA., PitoniS., MontiniL., BocciM.G., AnnettaP., AntonelliM.. Echography in brain imaging in intensive care unit: State of the art. *World J Radiol*2014;*6*:636–42.
31. GerrietsT., StolzE., KonigS., BabacanS., FissI., JaussM., et al. Sonographic monitoring of midline shift in space–occupying stroke: an early outcome predictor. *Stroke*2001;*32*:442–7.
32. ItoH., KannoI., IbarakiM., HatazawaJ., MiuraS.. Changes in human cerebral blood flow and cerebral blood volume during hypercapnia and hypocapnia measured by positron emission tomography. *J Cereb Blood Flow Metab*2003;*23*:665–70.
33. KleiserB., WidderB.. Course of carotid artery occlusions with impaired cerebrovascular reactivity. *Stroke*1992;*23*:171–4.
34. MarkusH., CullinaneM.. Severely impaired cerebrovascular reactivity predicts stroke and TIA risk in patients with carotid artery stenosis and occlusion. *Brain*2001;*124*:457–67.
35. GillerC.A., BowmanG., DyerH., MootzL., KrippnerW.. Cerebral arterial diameters during changes in blood pressure and carbon dioxide during craniotomy. *Neurosurgery*1993;*32*:737–41.
36. DahlA., RussellD., Nyberg-HansenR., RootweltK., BakkeS.J.. Cerebral vasoreactivity in unilateral carotid artery disease. A comparison of blood flow velocity and regional cerebral blood flow measurements. *Stroke*1994;*25*:621–6.
37. ChoS., FujigakiT., UchiyamaY., FukusakiM., ShibataO., SumikawaK.. Effects of sevoflurane with and without nitrous oxide on human cerebral circulation. *Transcranial Doppler study Anesthesiology*1996;*85*:755–6033.
38. NishiyamaT., MatsukawaT., YokoyamaT., HanaokaK.. Cerebrovascular carbon dioxide reactivity during general anesthesia: a comparison between sevoflurane and isoflurane. *Anesth Analg*1999;*89*:1437–41.

39. StrebelS., KaufmannM., GuardiolaP.M., SchaeferH.G.. Cerebral vasomotor responsiveness to carbon dioxide is preserved during propofol and midazolam anesthesia in humans. *Anesth Analg*1994;*78*:884–8.
40. KadoiY., SaitoS., TakahashiK.. The comparative effects of sevoflurane vs. isoflurane on cerebrovascular carbon dioxide reactivity in patients with hypertension. *Acta Anaesthesiol Scand*2007;*51*:1382–7.
41. KadoiY., TakahashiK., SaitoS., GotoF.. The comparative effects of sevoflurane versus isoflurane on cerebrovascular carbon dioxide reactivity in patients with diabetes mellitus. *Anesth Analg*2006;*103*:168–72.
42. StolzE., GerrietsT., FissI., BabacanS.S., SeidelG., KapsM.. Comparison of transcranial color-coded duplex sonography and cranial CT measurements for determining third ventricle midline shift in space-occupying stroke. *AJNR Am J Neuroradiol*1999;*20*:1567–71.
43. MarkusH.S., HarrisonM.J.. Estimation of cerebrovascular reactivity using transcranial Doppler, including the use of breath-holding as the vasodilatory stimulus. *Stroke*1992;*23*:668–73.
44. Jimenez-CaballeroP.E., SeguraT.. [Normal values of cerebral vasomotor reactivity using the Breath-Holding Test] *Rev Neurol*2006;*43*:598–602.
45. AdamsR.J.. TCD in sickle cell disease: an important and useful test. *Pediatr Radiol*2005;*35*:229–34.
46. AdamsR.J., McKieV.C., HsuL., FilesB., VichinskyE., PegelowC., et al. Prevention of a first stroke by transfusions in children with sickle cell anemia and abnormal results on transcranial Doppler ultrasonography. *N Engl J Med*1998;*339*:5–11.
47. AbboudM.R., YimE., MusallamK.M., AdamsR.J.. Discontinuing prophylactic transfusions increases the risk of silent brain infarction in children with sickle cell disease: data from STOP II. *Blood*2011;*118*:894–8.
48. SukernikM.R., Bennett-GuerreroE.. The incidental finding of a patent foramen ovale during cardiac surgery: should it always be repaired?*A core review Anesth Analg*2007;*105*:602–10.
49. ZitoC., DattiloG., OretoG., Di BellaG., LamariA., IudicelloR., et al. Patent foramen ovale: comparison among diagnostic strategies in cryptogenic stroke and migraine. *Echocardiography*2009;*26*:495–503.

Chapter 14

Critical Care Examination of the Respiratory System

Eric Piette and Martin Girard

INTRODUCTION

Ultrasound (US) is considered an extension of a clinician's physical examination and may even replace the common stethoscope. [1] Point-of-care ultrasound (POCUS) is being used in many medical specialties, with published guidelines for POCUS training. [2] – [6] Many residency programs have also made POCUS training mandatory in their curriculum. [7] , [8]

Physic principles dictate that air is an enemy to any US examination. Indeed, air acts as a mirror to completely reflect US beams. It seems logical to think the lung would not be the right candidate for POCUS. However, lungs are not only made of air, but from various combinations of lung parenchyma and physiologic or pathologic fluids. The passage of US beams through normal or pathologic lung creates artifacts. Lung US relies on the interpretation of these artifacts in combination with the clinical setting to make a diagnosis. By following a simple algorithm, it is easy to diagnose the most common thoracic and lung pathologies such as pleural effusion, pulmonary edema, acute respiratory distress syndrome (ARDS), pneumonia, and pneumothorax. Lung US is also useful to exclude esophageal and mainstem bronchial intubation. It can also diagnose diaphragmatic paralysis.

ULTRASOUND EXAMINATION OF THE RESPIRATORY SYSTEM

All US machines can be used to perform a lung US examination with any of the three most commonly used transducers (microconvex, abdominal, and high-frequency linear probe). [9] As each of the above provides a slightly different US image, the probe choice relies mostly on physician preference. It is even possible to use a transesophageal probe in cases where the chest is not accessible, such as during cardio- thoracic surgery (see Chapter 4, Extra-Cardiac Transesophageal Ultrasonography). To optimize image quality, the harmonics function should not be used, nor any software that dampens artifacts. Artifacts are needed in lung US.

The lung US examination can be done in a sitting or supine position, but since most critical care patients are supine, this approach will be discussed here. For a patient examined in the supine position, the thorax is separated into eight (**Figure 14.1**) or 12 zones. [10] – [13] All zones must be scanned in order to obtain a complete lung examination. These zones are related to specific anatomical lung lobes (**Figures 14.2 and 14.3**), although the goal of the examination as in Chapter 4, is not to identify lobes but artifacts. It is also important to scan low enough on the chest to see the costo-diaphragmatic junction to avoid missing a small pleural effusion and, when pertinent, evaluate diaphragmatic motion.

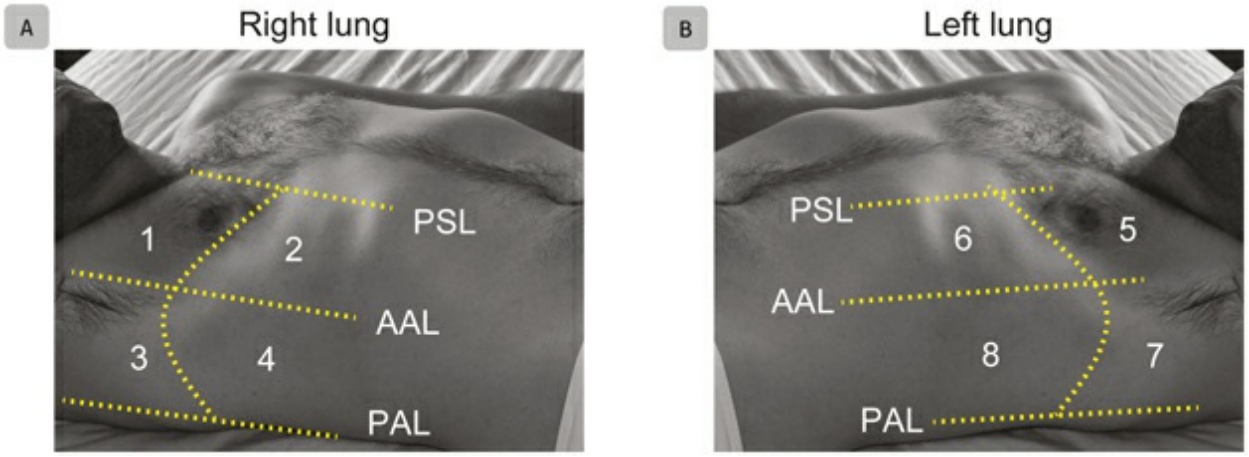

Fig. 14.1 Surface anatomy. According to Volpicelli, each hemithorax is separated into four zones bounded by the parasternal line (PSL), anterior axillary line (AAL), posterior axillary line (PAL), and fifth intercostal space (curved line). (Adapted from Piette *et al.* [14])

A combination of coronal and sagittal views is used in lung US. Most of the examination is performed in the two-dimensional (2D) mode, but motion mode (M-mode), as well as color Doppler can be used, depending on the

expected pathology. Each thoracic zone is scanned perpendicularly to the short axis of the thorax in order to cut the ribs in a transverse fashion. A typical image contains subcutaneous tissue, two or more ribs, the pleural interface, and the underlying lung parenchyma (**Figure 14.4**). The ribs are easily identified by the anechoic shadow they cast on the US screen. The pleural interface is composed of the parietal and visceral pleura. It is represented by the hyperechoic linear structure beneath the subcutaneous tissue between the ribs. The lung parenchyma is located under the pleural interface. Scanning in a parallel axis to the ribs allows better visualization of the pleura, but has a steeper learning curve. This can be useful in search of pneumothorax, as will be discussed later.

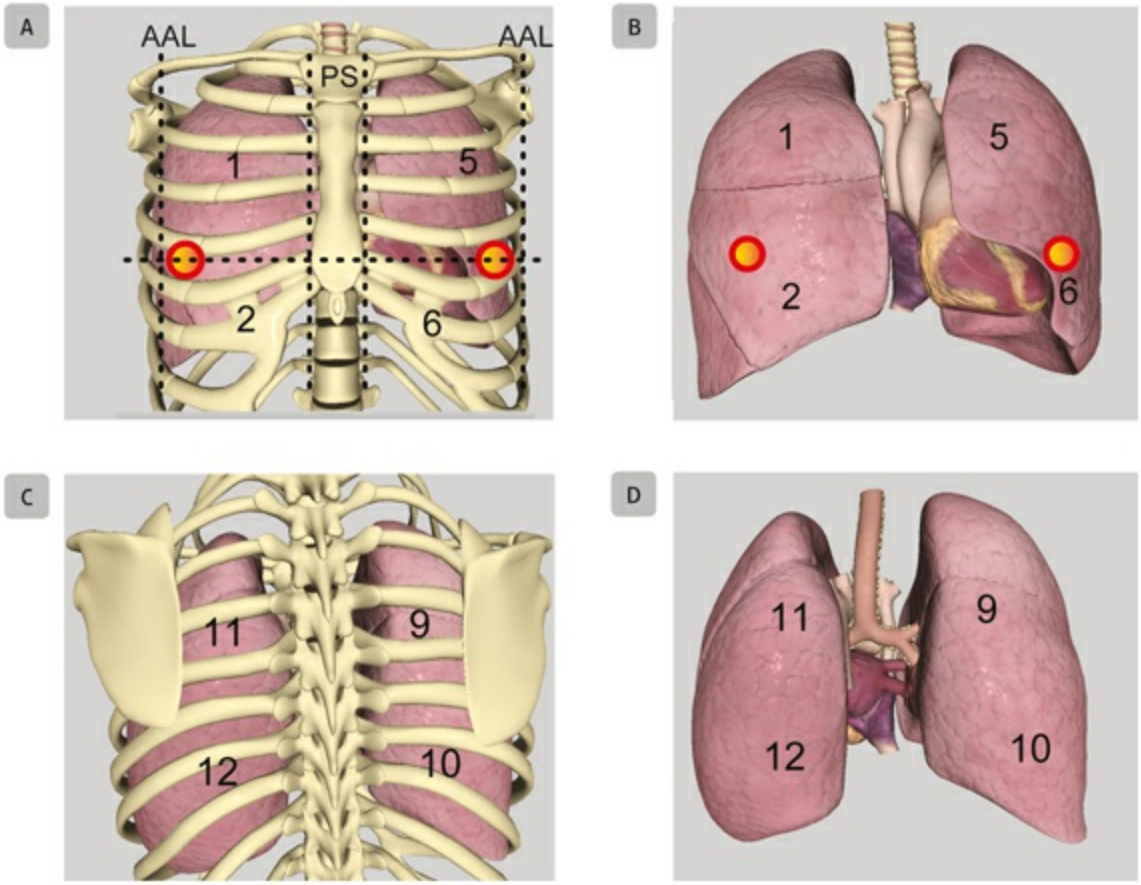

Fig. 14.2 Anatomic correlation. The correlation between the surface anatomy and the lung lobes is shown using the Vimedix simulator. The red dot corresponds to the nipple. (A,B) In this anterior view of the thorax, the following anatomical correlates occur: zone 1 (right upper lobe), zone 2 (right middle lobe), zone 5 (left upper lobe) and zone 6 (left lingula). (C,D) This posterior view of the thorax shows zone 9 (apical and posterior segments of the right upper lobe and superior segment of the right lower lobe), zone 10 (posterobasal and laterobasal segments of the right lower lobe), zone 11 (apical and posterior segments of the left upper lobe and superior segment of the left lower lobe), and zone 12

(posterobasal and laterobasal segments of the left lower lobe). AAL, PS, parasternal.

A: https://youtu.be/E_lUoC17fEc

A: https://youtu.be/gCiZewmFRcs

B: https://youtu.be/2lmfsL3SVaw

C: https://youtu.be/K0bucw3BtDU

C: https://youtu.be/sfgX9sbHfeU

LUNG ULTRASOUND ARTIFACTS

It is often said that lung US makes facts out of artifacts (**Table 14.1**). As mentioned earlier, lung US relies on the interpretation of artifacts generated by the lung parenchyma. The main artifacts relevant to lung US examination are lung sliding, lung pulse, A-lines, B-lines, E-lines, and Z-lines.

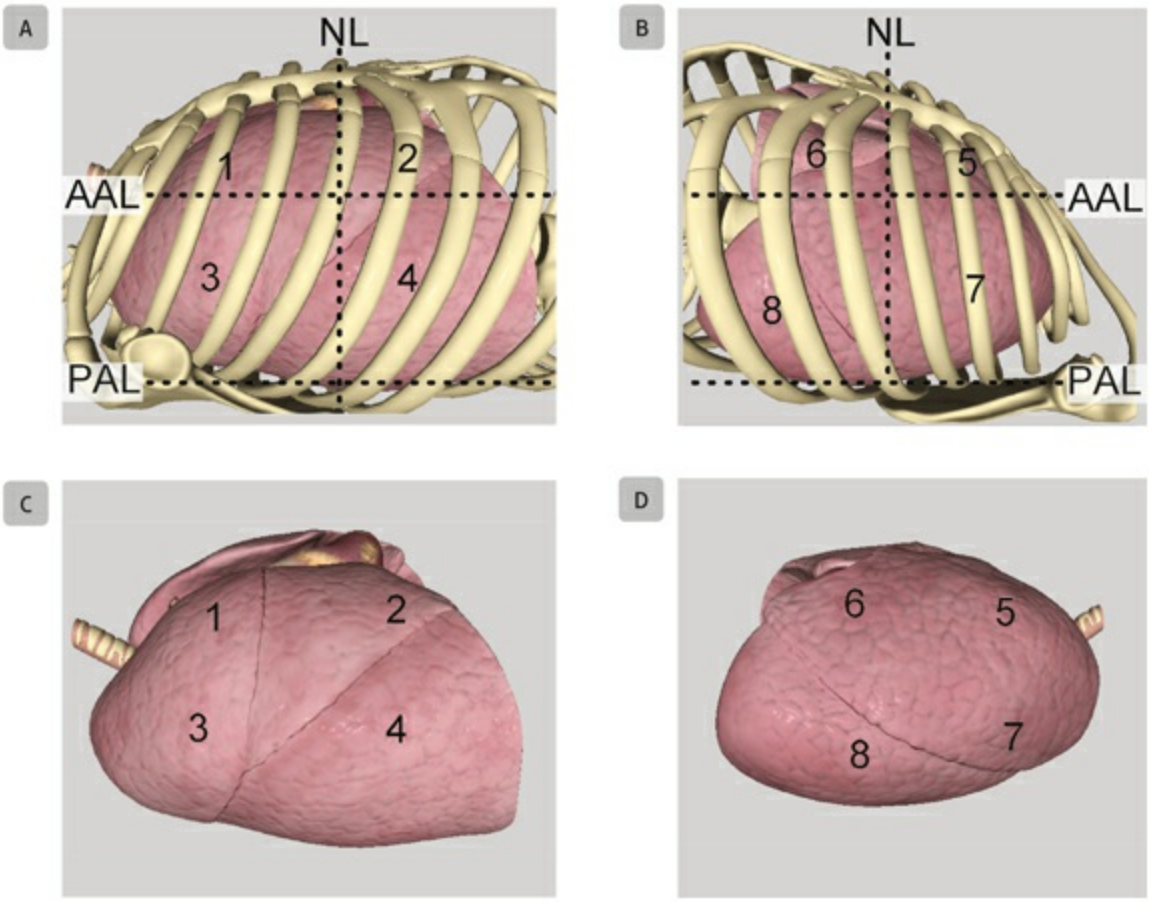

Fig. 14.3 Anatomic correlation. The correlation between the surface anatomy of the Volpicelli zones and the lung lobes is shown using the Vimedix simulator. (A,B) In this axillary view of the right lung anatomical correlates include zone 3 (right upper lobe) and zone 4 (right lower lobe). (C,D) Similarly this axillary view of the left lung shows zone 7 (left upper lobe) and zone 8 (left lower lobe). AAL, anterior axillary line; NL, nipple line; PAL, posterior axillary line.

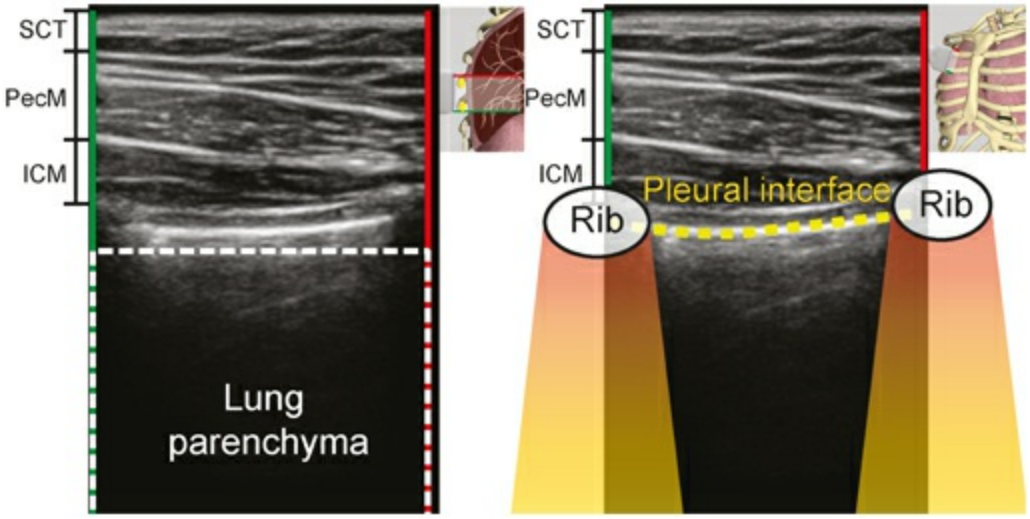

Fig. 14.4 Lung ultrasound image. A typical lung ultrasound two-dimensional image obtained using a linear probe from an intercostal space shows the subcutaneous tissue (SCT) chest wall soft tissue, pectoralis muscle (PecM), intercostal muscle (ICM), two or more ribs (acoustic shadows), pleural interface (yellow dotted line), and underlying lung parenchyma.

Lung Sliding and Lung Pulse

Lung sliding consists of the movement of the visceral on the parietal pleura one on another during the respiratory cycle with spontaneous or mechanical ventilation (**Figure 14.5**). Lung sliding was initially used to describe the diagnosis of pneumothorax in horses. [15] Lung sliding is of greater amplitude and easier to see near the diaphragm, and more subtle near the lung apices. At the lung apex, it is also possible to see a stretching movement of the pleura where the pleural interface simultaneously moves to the left on the left part of the screen, and to the right on the right part of the screen.

Table 14.1 Lung Ultrasound Findings

	Mode	Normal	Pathology
Lung sliding	2D	Yes	If absent
Lung pulse	2D, M-mode	Yes	If absent
A-Line	2D	Yes	Pneumothorax
B-Line	2D	Yes, if single	Consolidation (multiple) Alveoli-interstitial Pneumothorax (ruled-out)
Z-Line	2D	Yes	Differentiate from B-lines
E-Line	2D	No	Subcutaneous emphysema Metal
Lung point	2D, M-mode	No	Pneumothorax
Seashore	M-mode	Yes	
Barcode	M-mode	No	Pneumothorax

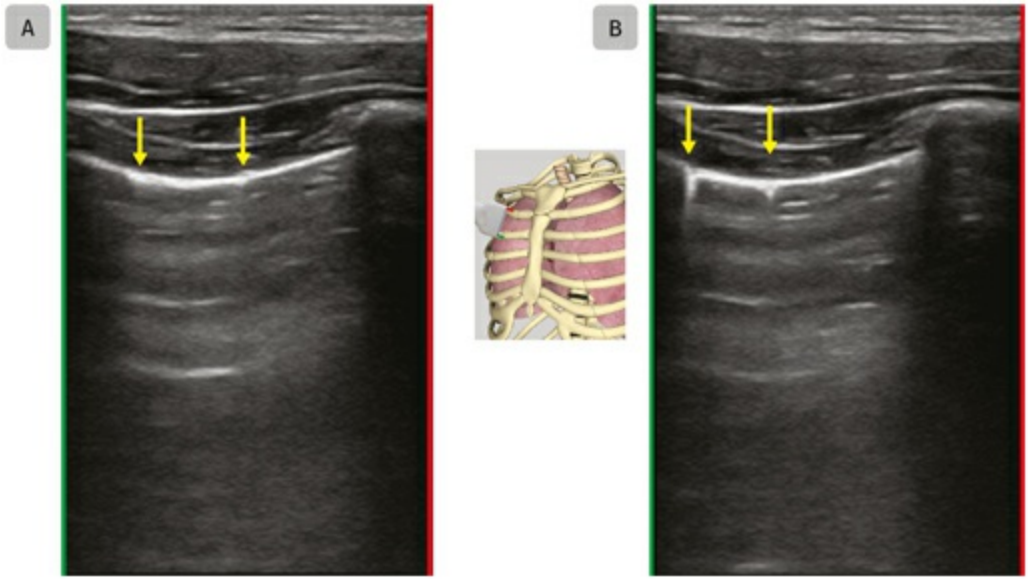

Fig. 14.5 Normal lung sliding. (A,B) Normal lung sliding can be seen in a 2D image at the pleural interface, with changes in position of the small hyperechoic signals (arrows) along the pleural line during respiration.

A&B: https://youtu.be/5xiZVlDoIRU

The lung pulse artifact appears as the smaller, faster rhythmic movements of the pleural interface synchronous with a patient's heartbeat. This artifact is induced by transmitted heart movements from pulsatile blood-flow through the pulmonary vessels. [16] It can be seen with 2D, M-mode and color M-mode (**Figure 14.6**). Lung pulse is best seen when the usually superimposed lung sliding is absent, such as during periods of apnea. Both these artifacts are of the uttermost importance in lung US, particularly in excluding pneumothorax or confirming endotracheal intubation. Both pleural movements can be better visualized by using color Doppler. [17] Remember that both these artifacts are present in a normal lung US examination.

A-Lines

Once emitted by the probe, the US beam is reflected in part by each successive layer of subcutaneous tissue. Each returning echo is received and analyzed by the probe to yield an anatomically correct image on the screen.

At the pleural interface, the residual beam is completely reflected back towards the probe because of the strong acoustic impedance difference between the air contained in the normally aerated lung and the subcutaneous tissue. However, while part of this returning US beam will be received and analyzed by the probe, part is also reflected back by the probe-patient interface towards the patient, yielding a new, weaker, beam that is reflected once more by the pleural interface. Given that the time delay between the original US beam emission and its reception is responsible for determining a structure's depth, this reflected beam travelling back to the US probe is falsely interpreted by the machine's software as a deeper structure. An A-line is this phantom image of the pleural interface (**Figure 14.7**). This back and forth movement of the US beam can generate a number of A-lines until the beam becomes too weak. Given their genesis, A-lines are necessarily equally spaced by a distance equal to the thickness of the subcutaneous tissue between the US probe and the pleural interface. They are typically more intense near the region of the pleural interface that is exactly parallel to the probe surface. A-lines can be seen in normal lung, as well as in the presence of a pneumothorax.

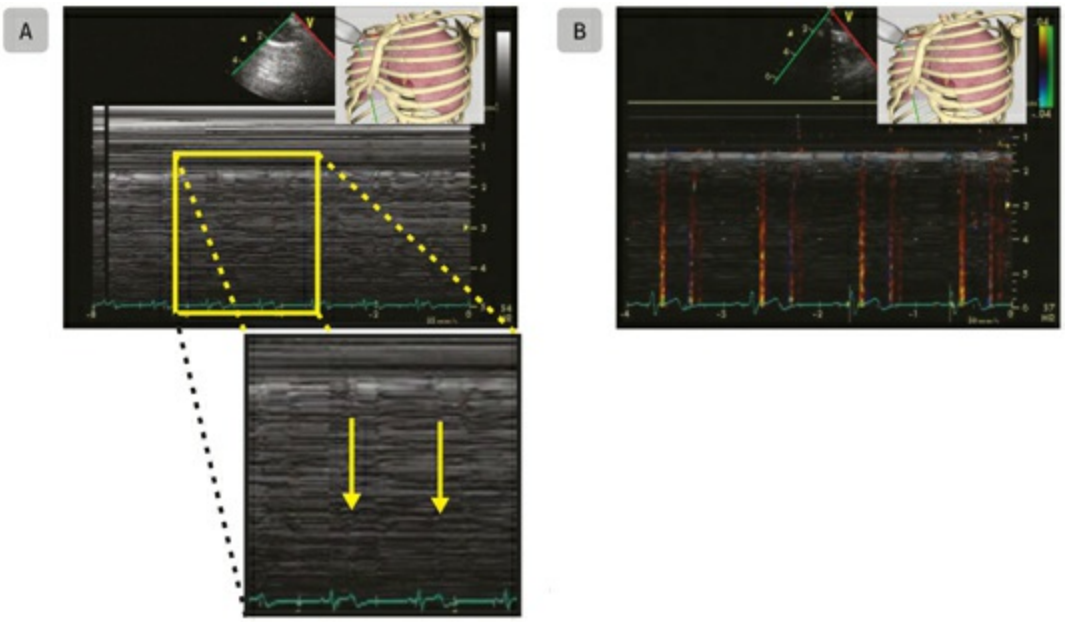

Fig. 14.6 Lung pulse. The lung pulse artifact is created by small fast rhythmic movements of the pleural interface synchronized with the heartbeat. This can be seen with 2D images, but is better recognized using M-mode. (A) In M-mode, the lung pulse corresponds to the regular linear artifact (arrows) synchronized with the electrocardiogram. (B) In color M-mode, these lung pulse artifacts are more

easily identified. (Adapted from Piette *et al.* [14])

A: https://youtu.be/Y8mH43nyx6M

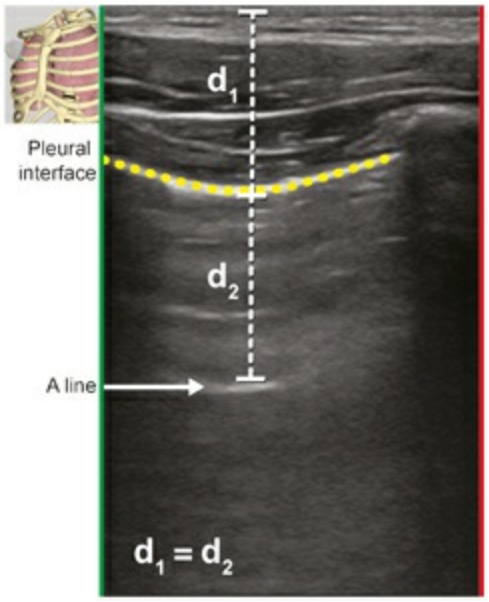

Fig. 14.7 A-line. Reflection of the pleural interface (yellow dotted line) within the lung parenchyma creates the A-line artifact in 2D imaging of the lung. The A-line is separated from the pleural interface by a distance (d) equal to the thickness of the subcutaneous tissue overlying the pleural interface.

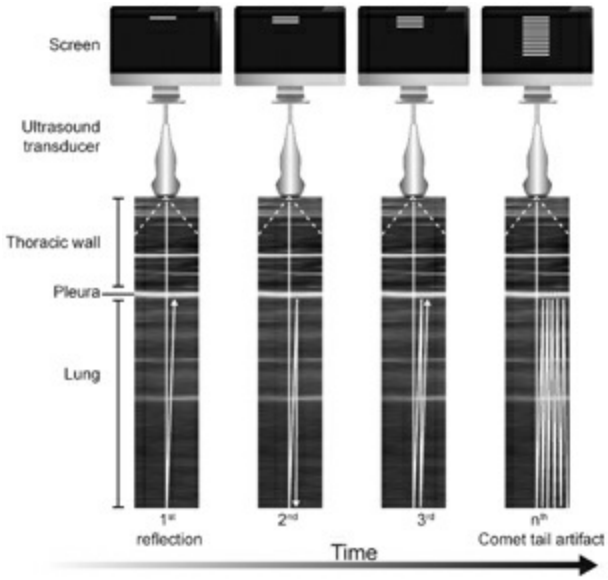

Fig. 14.8 B-line. The returning ultrasound beam is successively reflected multiple times inside the lung to create a comet-tail artifact. This is seen on the ultrasound display as an hyperechoic vertical line called a B-line in the lung parenchyma. (Adapted from Lichtenstein *et al.* [21])

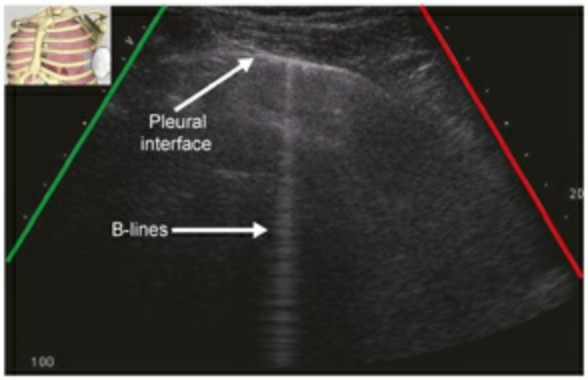

Fig. 14.9 Single B-line. The B-line is a vertical laser-like hyperechoic line originating from the pleural interface, erasing all other structures in its path and reaching the extremity of the ultrasound field. An isolated B-line in 2D imaging of the lung may be an ultrasound finding in normal lung.

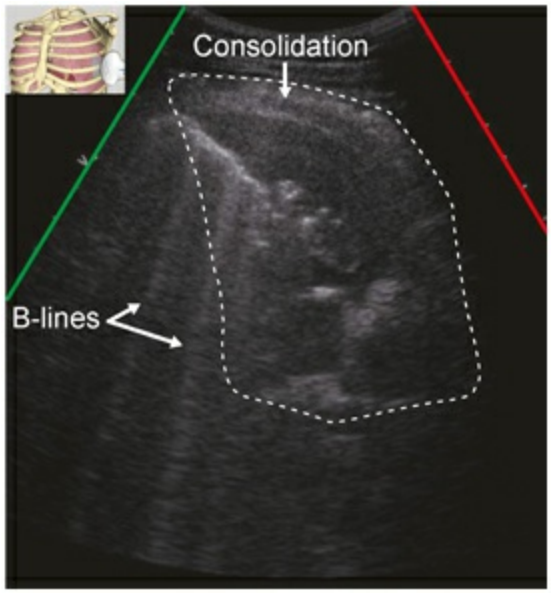

Fig. 14.10 Multiple B-lines. Lung ultrasound image using a convex probe shows the presence of multiple B-lines (>3) in this left lung (zone 6) ultrasound view that suggests overlying lung pathology, in this case lung consolidation (white dotted line).

B-Lines

B-lines are also referred to “comet tails” or “lung rockets”. Lung parenchyma may contain air, tissue, and fluid in various concentrations depending on the physiological or pathological state of the patient. The density of lung

parenchyma can increase because of either a decrease in aeration (e.g. atelectasis), [18] , [19] or an excess of tissue or fluid (e.g. pulmonary edema, pulmonary fibrosis, pneumonia). [20] The focal absence of air allows the beam to penetrate the lung past the visceral pleura. This will result in diffuse reflection of the beam: part of the beam will return to the probe, and the remainder will self-perpetuate inside the lung, returning US signals back to the probe with each reflection (**Figure 14.8**). These multiple successive reflections inside the lung parenchyma create artifacts visible as hyperechoic laser-like vertical lines originating from the visceral pleura, and extending all the way down the US field (**Figure 14.9**). When the correct lung parenchymal density is present, B-lines can also originate from the underside border of a region of consolidated lung (**Figure 14.10**). B-lines erase all other images in the US field. They also always reach the end of the US field, no matter the depth. These two features are important in differentiating them from Z-lines (discussed later). Some experts advocate increasing the depth of the US field to 16 cm when using a convex probe in order to help differentiating B-lines from Z-lines.

B-lines are useful to identify the presence of an alveo-lo-interstitial syndrome, as well as to exclude the presence of a pneumothorax (discussed later). Isolated B-lines can be seen in a normal lung. B-lines are considered pathologic if there are more than three seen in an intercostal space with a microconvex probe, [21] more than six on the whole scan when seen by a linear probe, [22] and more than three on the whole scan if separated by less than 7 mm when examined with an abdominal or cardiac phased array probe (**Figure 14.11**). [23] , [24] They can be seen in non-cardiogenic pathologies such as pulmonary fibrosis, ARDS, alveolo-interstitial syndromes, pneumonia, atelectasis and lung contusion (**Figure 14.12** and **Table 14.2**).

Z-Lines

Z-lines are artifacts that originate from the visceral pleura and are visible as hyperechoic vertical lines. They can resemble B-lines but, most importantly, do not erase other artifacts and images on the US screen. Also differentiating them from B-lines is their inhomogeneous appearance: B-lines are almost solid white, while Z-lines are hatched. Finally, Z-lines tend to fade gradually and do not reach the edge of the screen when set deep enough. Their origin is not completely understood, and they have no real utility in lung POCUS.

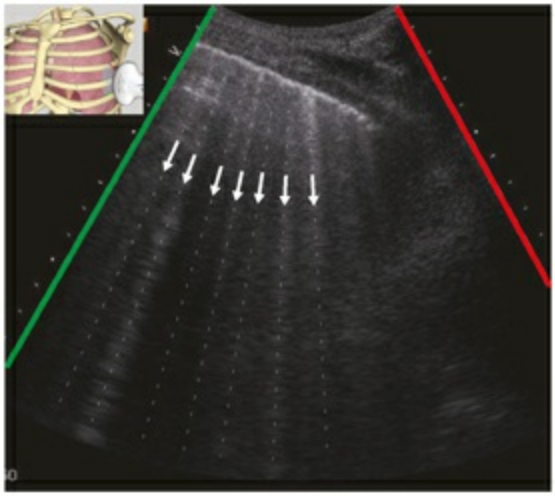

Fig. 14.11 Multiple B-lines. In a patient with congestive heart failure multiple B-lines (arrows) are seen in this left lung (zone 6) ultrasound 2D image.

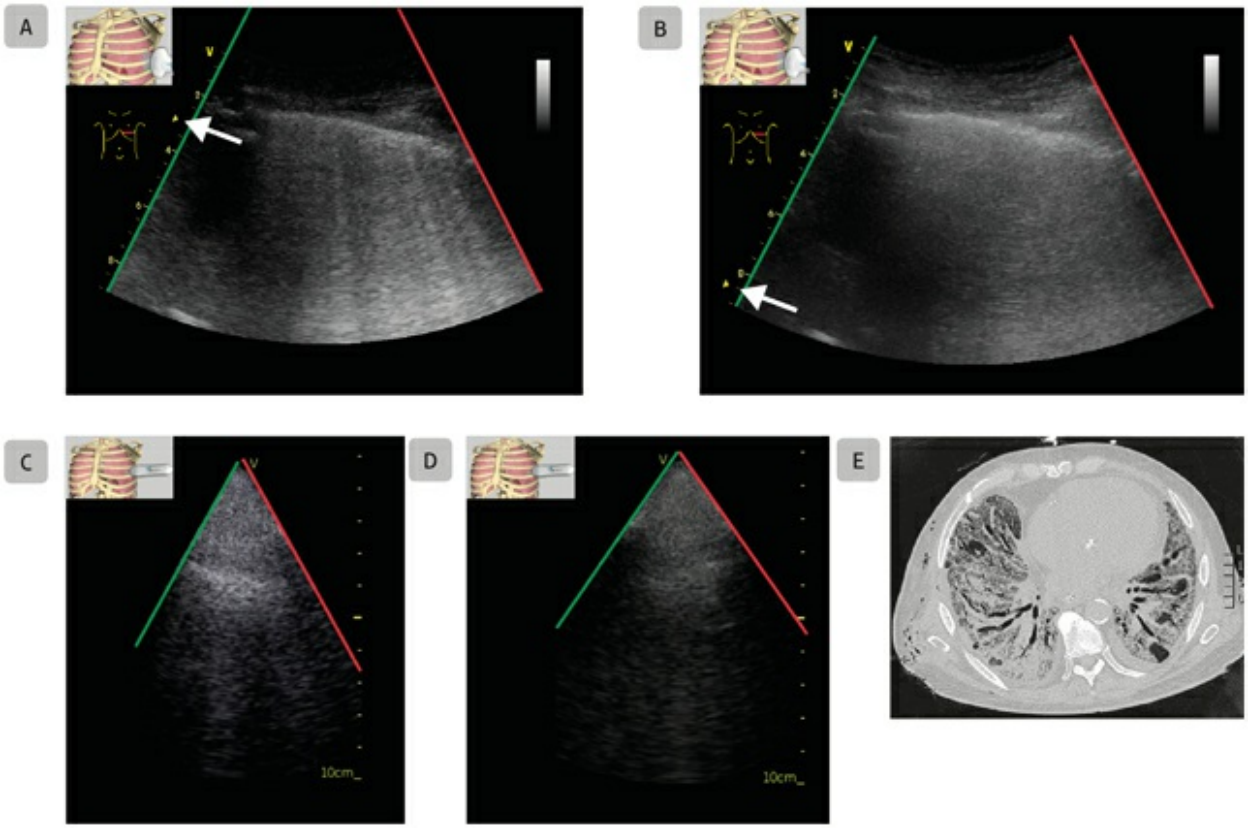

Fig. 14.12 Ultrasound settings and B-lines. Lung scanning in a 70-year-old male with pulmonary fibrosis showing thickening of the pleural line. The number of B-lines will be reduced if the focus point (arrow) is changed from (A) the optimal of 3 cm to (B) 9 cm, or if imaging is performed using a (C) cardiac or (D) abdominal preset. (E) Computed tomographic of the lung showing severe pulmonary fibrosis of both lungs.

A: https://youtu.be/5bYfiRoXYl8

C: https://youtu.be/3aj6WUmliQI

B: https://youtu.be/SC5IFJquA6A

D: https://youtu.be/xluowZi9KHs

Table 14.2 Lung Ultrasound Findings in Lung Pathology

Pathology	Lung ultrasound findings
Alveolo-interstitial	Multiple B-lines, white lung
Pulmonary edema	Bilateral B-lines increasing in number in a gravity-dependent manner, no skip areas
ARDS	Patchy areas of B-lines, irregular pleural line, small consolidation, reduced lung sliding
Pulmonary fibrosis	Bilateral B-lines, irregular pleural thickening, reduced lung sliding
Consolidation	Lung hepatization
Atelectasis	Lung hepatization, mechanism for atelectasis (e.g. big pleural effusion), no dynamic air bronchogram
Pneumonia	Possibly darker lung tissue, dynamic air bronchogram
Pulmonary embolism	Small triangular or rounded well-demarcated consolidations without any blood flow on color Doppler
Pneumothorax	Absence of lung sliding, presence of lung point, Barcode sign
Pleural fluid	Homogeneously black, particles, echotexture and/or swirling
Diaphragmatic paralysis	Absence of thickening and movement

ARDS, acute respiratory distress syndrome.

E-Lines

E-lines are artifacts created by subcutaneous emphysema or a foreign metallic body. These were first described in a patient who suffered a gunshot wound. [25] E-lines resemble B-lines as they appear as hyperechoic vertical white lines erasing other artifacts and images on the US screen, and reach the end of the display (**Figure 14.13**). They differ from B-lines as their point of origin is different, from the skin or subcutaneous tissue rather than from the visceral pleura or underside of lung consolidation. Subcutaneous emphysema severely impedes lung US, and other diagnostic means should be considered. In the majority of times no image can be seen and important pulmonary pathologies can be missed (**Figure 14.14**).

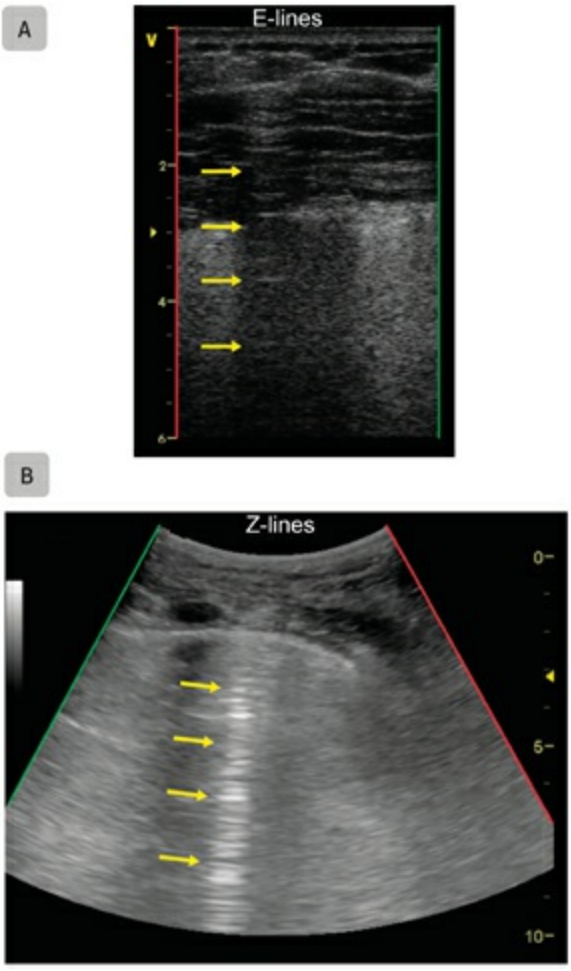

Fig. 14.13 E- and Z-lines. (A) Lung ultrasound 2D image showing hyperechoic vertical E-lines (yellow arrows) that originate from subcutaneous tissue. (B) Lung ultrasound 2D image showing hyperechoic vertical Z-lines which originate from the visceral pleura. It is important to differentiate both E- and Z-lines from B-lines in lung ultrasound.

A: https://youtu.be/AbsoVozRcbc

B: https://youtu.be/XYu13pXZbwo

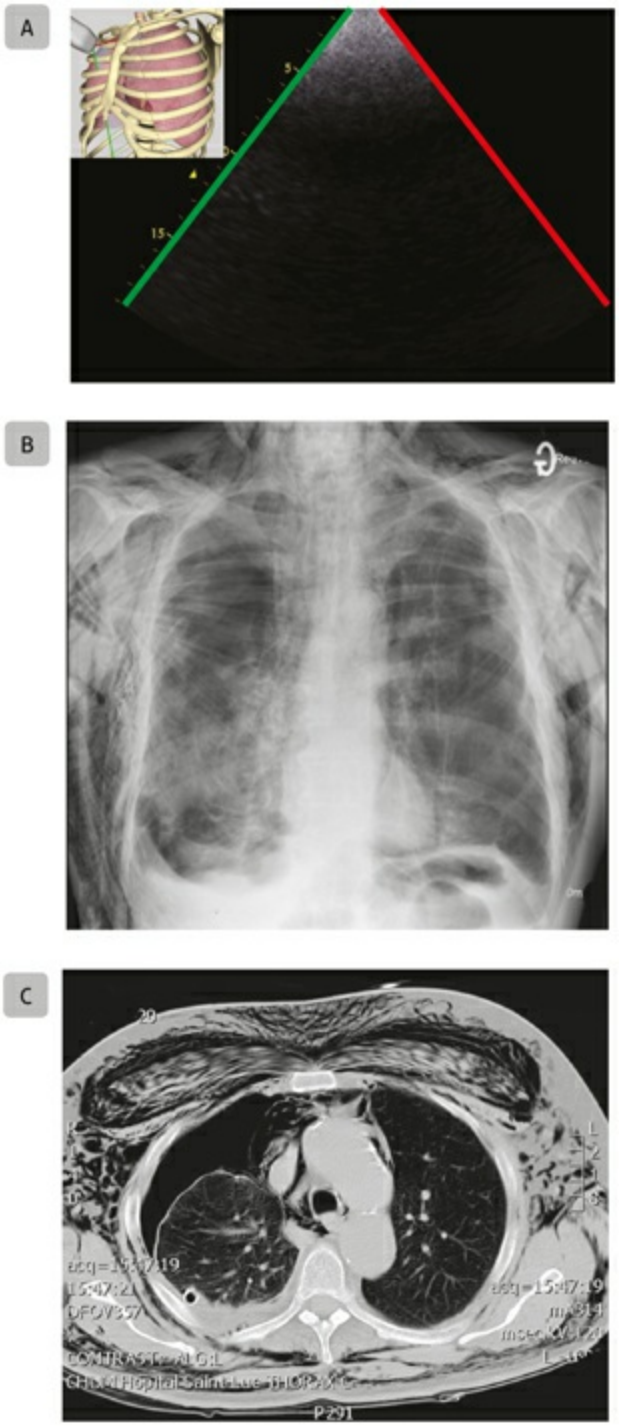

Fig. 14.14 Subcutaneous emphysema. In the majority of patients with subcutaneous emphysema, lung scanning with (A) ultrasound (zone 1) will show a total anechoic region as compared with (B) the chest radiograph. (C) Note that the right anterior pneumothorax on the computed tomographic scan will be completely missed with lung ultrasound.

A: https://youtu.be/qiLQwVTk31Q

NORMAL LUNG EXAMINATION

A normal lung examination is characterized by the presence of A-lines, Z-lines, lung sliding, lung pulse, and sparse isolated B-lines. Lastly, three or more B-lines in the lowest intercostal space can be imaged in the laterobasal zones (and posterobasal zones if using a 12-zone model) in up to 25% of individuals with a normal chest radiography (CXR). [21] – [24]

PATHOLOGICAL FINDINGS

Lung US has an 96% sensitivity and specificity to diagnose pathology occult to CXR if one of these US finding is present: absence of pleural sliding, presence of diffuse or localized B-lines, peripheral alveolar consolidation, and pleural thickening or irregularity, with or without localized effusion (**Table 14.2**). [26] , [27] Scanning each thoracic zone is important to visualize one of these signs and diagnose lung pathology. In experienced hands, lung US could replace CXR in many clinical situations. [28] While specific diagnostic algorithms have been suggested to evaluate dyspneic patients, [14] , [29] interpreting lung US findings must be done in conjunction with the clinical picture. The ultrasound appearance of various pathologies will be described below.

Alveolo-Interstitial Syndrome

Alveolo-interstitial syndrome comprises all pathologies with increasing density of lung parenchyma while retaining a significant amount of air. As discussed above, the presence of multiple B-lines is the hallmark. Visualizing three or more B-lines separated by less than 7 mm has a sensitivity of 92.5% in diagnosing underlying lung pathology. [30] The more severe the alveolo-interstitial syndrome, the more B-lines will be seen. In severe disease, B-lines coalesce, yielding an image called white lung (**Figure 14.15**). [31] Because of

the uniformity of the image, care should be taken not to falsely conclude it is normal. The key in differentiating normal lung from white lung is the loss of A-lines, and the loss of differentiation between the hyperechoic-pleural interface and the normally gray-black lung parenchyma.

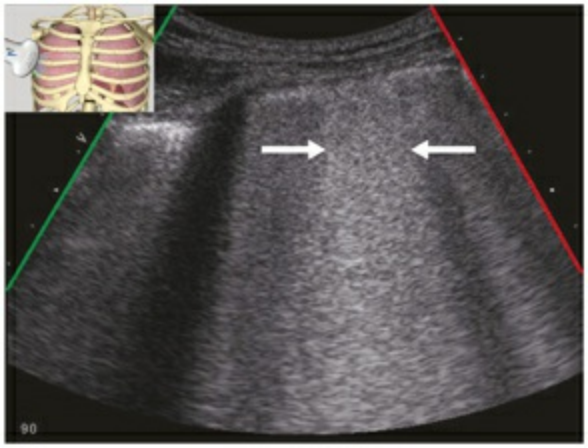

Fig. 14.15 White lung. Severe alveolo-interstitial syndrome yields multiple coalescent B-lines creating the image of a white lung (between white arrows) with lung ultrasound. Note the absence of an A-line in the lung parenchyma

There is a characteristic distribution of B-lines exhibited for each pathology. Widespread bilateral B-lines are present in pathologies affecting both lungs diffusely: pulmonary edema (cardiogenic or non-cardiogenic), ARDS, interstitial pneumonia and pulmonary fibrosis. Pulmonary contusions, lobar pneumonia and atelectasis are usually unilateral, but could also be bilateral. In most descriptions, coalescing B-lines or B-lines separated by less than 3 mm correspond to an alveolar pathology, compared to B-lines separated by 3–7 mm, which indicate an interstitial process. [11] However, some experts dispute this claim. [32]

The most frequent cause of bilateral B-lines is pulmonary edema (**Figure 14.16**). Studies have shown a significant regression of bilateral B-lines in hypervolemic patients during dialysis. [33] , [34] Since the patients were not in clinical respiratory distress, these studies show the high sensitivity of lung US in detecting extravascular lung water even in asymptomatic patients. As extravascular lung water rises, more B-lines will be detected. Lung US was shown to be very useful in the monitoring of acute decompensated heart failure. [31] It also allows to easily differentiate between cardiac and pulmonary causes of respiratory distress. Patients suffering from an exacerbation of their chronic obstructive pulmonary disease (COPD) will exhibit none or only few

B-lines compared to patients with acute pulmonary edema. [29] , [35]

As with pulmonary edema, pulmonary fibrosis exhibits an increasing number of bilateral B-lines with increasing severity. [36] However, severe pulmonary fibrosis also features bilateral irregular thickening of the pleural line and reduced lung sliding, allowing it to be distinguished from pulmonary edema (**Figures 14.17 and** 14.18). [37] Acute respiratory distress syndrome will also exhibit diffuse bilateral B-lines. However, in contrast to pulmonary edema, ARDS features areas devoid of B-lines (spared areas), irregularity or thickening of the pleural line, small subpleural or frank consolidations, and impaired lung sliding. [38]

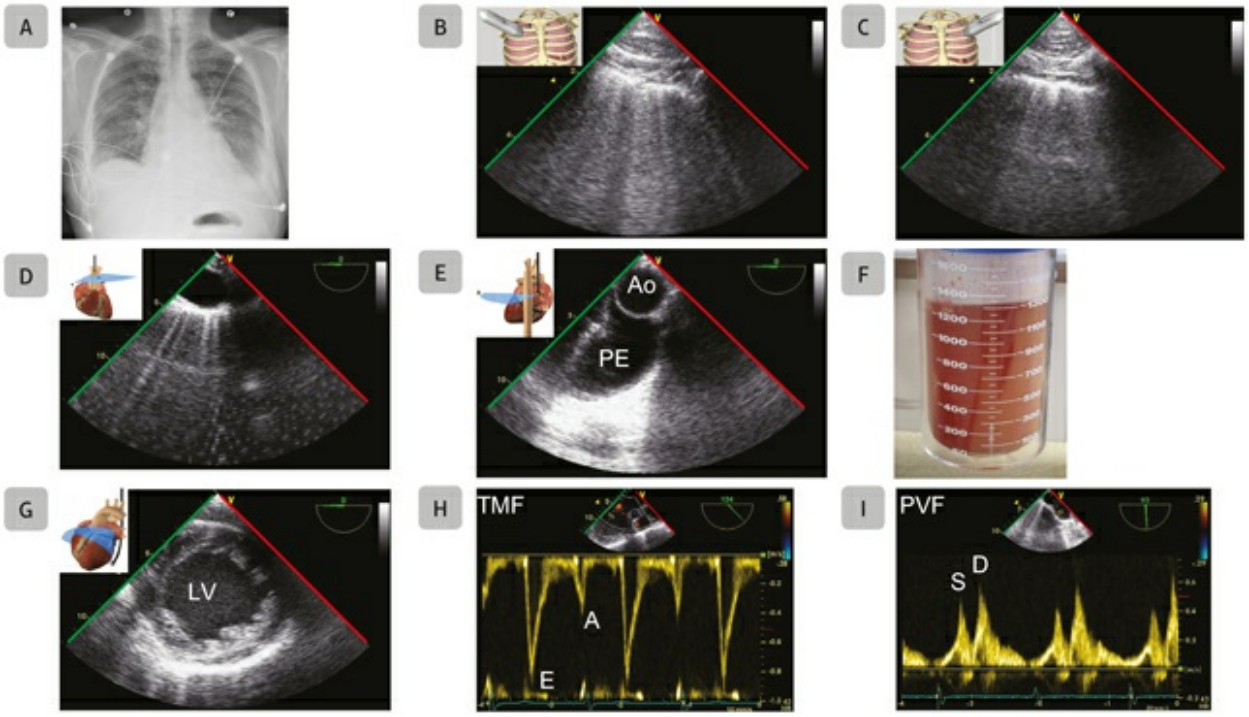

Fig. 14.16 Congestive heart failure. (A) Chest radiograph of an 86-year-old male and lung ultrasound images (B, C) show diffuse B-lines in zones 1 and 5. Using transesophageal echocardiography, (D) B-lines are also present in the lung below the aortic arch, and (E, F) there is a left pleural effusion (PE) of 1300 ml around the descending aorta (Ao). (G) Transgastric mid-papillary view of the left ventricle (LV) showing severe systolic (S) and diastolic (D) dysfunction using the (H) transmitral flow (TMF) early (or E) and late or atrial (or A) and (I) pulmonary venous flow (PVF). A, late diastolic TMF velocity; D, diastolic PVF; E, early diastolic TMF velocity; PE, pleural effusion; S, systolic PVF.

B: https://youtu.be/v516Z7oNmi0

E: https://youtu.be/VCV6tFvbxXk

C: https://youtu.be/otcDT7xGew0

G: https://youtu.be/dgvMIyBQShI

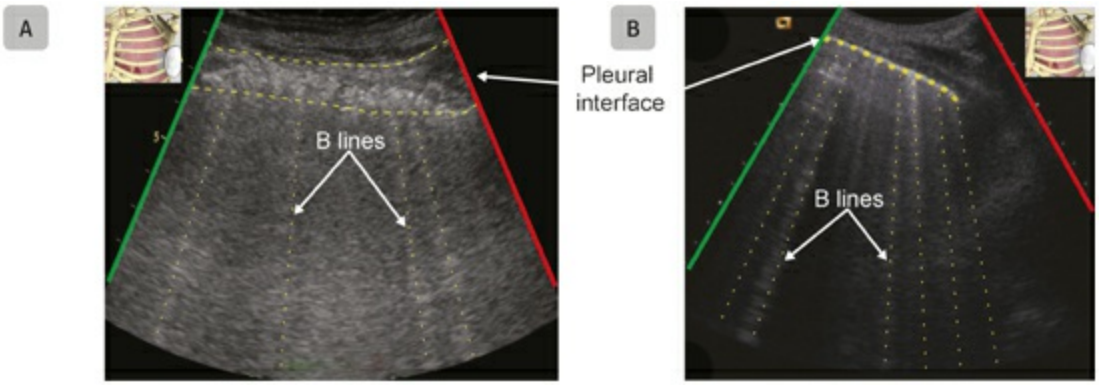

Fig. 14.17 Pulmonary fibrosis. (A) Lung ultrasound (zone 7) in a patient with pulmonary fibrosis on the left compared with (B) a patient with pulmonary edema on the right side. Both pathologies exhibit multiple B-lines, but pulmonary fibrosis also has irregular pleural thickening.

Consolidation

The complete de-aeration of lung tissue from either complete air removal (e.g. atelectasis) or complete air replacement (e.g. pneumonia) will result in lung consolidation. Consolidated lung parenchyma has the same ultrasound appearance as hepatic tissue. This is commonly referred to as lung hepatization (**Figure 14.19** and see **Figure 9.21**). Consolidation may be of various etiologies: atelectasis (passive or obstructive), pneumonia, lung contusion, pulmonary embolism, and also tumor. When compared to thoracic

computed tomography (CT), lung US has been shown to accurately identify the presence of lung consolidation. [39] , [40]

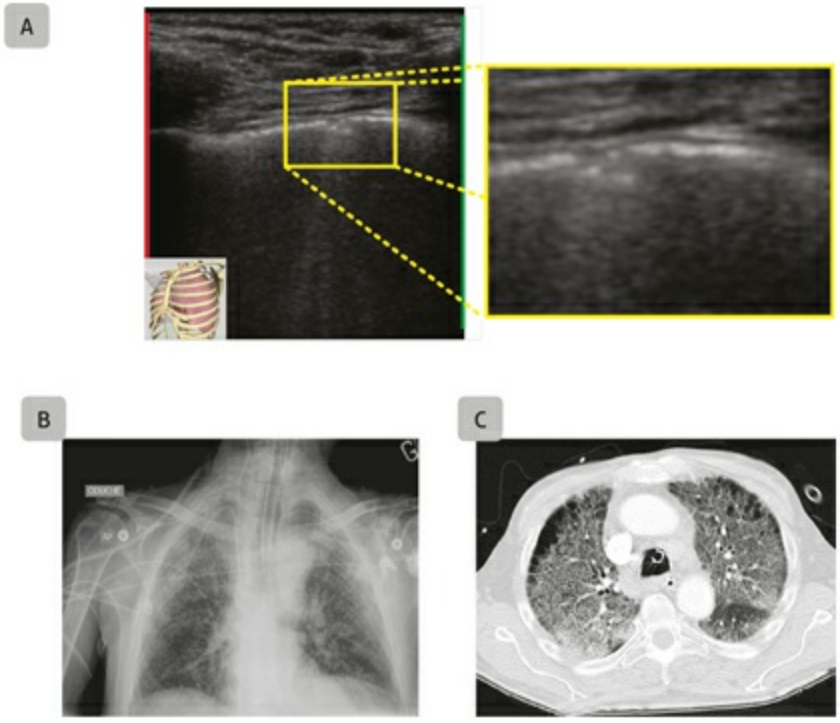

Fig. 14.18 Pulmonary fibrosis. (A) Note the focal thickening on the pleural line with lung ultrasound, (B) corresponding chest radiograph, and (C) computed tomographic scan in a patient with pulmonary fibrosis.

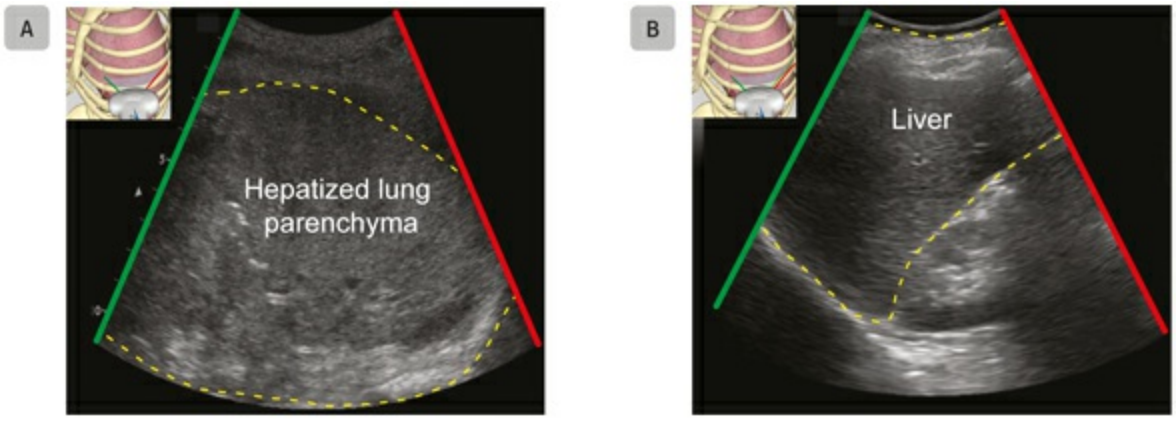

Fig. 14.19 Hepatization of lung parenchyma. (A) A lung ultrasound 2D image obtained with a convex probe of the left lower lobe (zone 8) shows lung parenchyma that has the same appearance as (B) normal hepatic parenchyma.

The absence of any significant air inside a lung consolidation allows the imaging of its anatomical constituents: bronchi and pulmonary blood vessels.

Bronchi are typically thicker walled structures compared to pulmonary blood vessels. When imaged in the correct plane, their tubular or branching nature can be observed but, most often, they are imaged in their cross-section. Residual air inside a bronchus may be present, and is represented as collections of tiny white dots called static air bronchograms (**Figure 14.20**). When a bronchus becomes filled with a mixture of secretions and air bubbles, a to-and-fro movement of the same white dots can occur with the respiratory cycle. This is called a dynamic air bronchogram and excludes the possibility of a proximal bronchial obstruction (**Figure 14.20**). When only fluid is present in a bronchus, it can masquerade as a blood vessel and color Doppler is the definitive way to separate the two (**Figure 14.20**). These so-called fluid bronchograms can be associated with a proximal obstruction. A consolidation displaying only fluid bronchograms is an indication for bronchoscopy to investigate a possible obstruction.

Atelectasis will usually result in the presence of a lung consolidation with B-lines present at the border where the lung becomes partially aerated. In the case of an acute proximal bronchial obstruction, newly atelectatic lung will not appear consolidated, but will rather be characterized by localized B-lines and absent lung sliding with preserved lung pulse. [16] , [18] , [41] While any supine mechanically ventilated patient will have some degree of atelectasis, the cause of significant atelectasis is usually self-evident: significant pleural effusion, cranially displaced diaphragms from increased abdominal pressure, diaphragmatic paralysis (discussed later), proximal bronchial obstruction, etc. The correct position of the endotracheal tube in intubated patients must be verified, as well as aspiration of possible secretions.

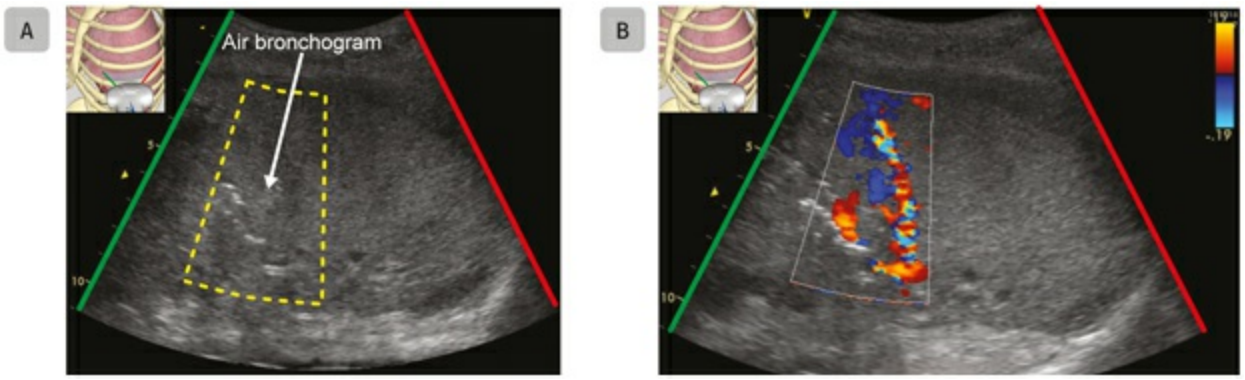

Fig. 14.20 Air bronchogram. (A) In this lung ultrasound 2D image (zone 6) of pneumonia, residual air bubbles in bronchi are seen as tiny irregular white dots, creating a bronchogram. The associated video shows a mix of air bubbles and secretions moving to and fro in a bronchus, creating a dynamic air

bronchogram. (B) Adding color Doppler (Nyquist 19 cm/s) to the previous 2D image enables visualization of the blood vessels and confirms that the movement of air and secretions is located in a bronchus. This is most useful if there is only liquid in the bronchus, which could be mistaken for a blood vessel.

B: https://youtu.be/9CNgL3fm-fc

Pneumonia is another disease process causing lung consolidation that commonly features irregular serrated margins. In its early exudative form, it characteristically sports a darker shade of gray (higher water content) than a similar consolidation from atelectasis. Because of pleural inflammation, decreased/abolished lung sliding and small pleural effusions can be noted. Another hallmark of pneumonia is the presence of dynamic air bronchograms which have been found to be very specific but moderately sensitive. [42] Early pneumonia, viral pneumonia, [43] or central pneumonia may manifest as localized irregular or confluent B-lines without any lung consolidation (**Figure 14.21**). Lung US has been found to be very accurate in diagnosing pneumonia in patients presenting to the emergency department, with high sensitivities and specificities of over 90%. [44] Serial follow-up of improving patients usually demonstrates shrinking consolidation. [45] Considering the high rates of pre-existing atelectasis in mechanically ventilated patients and their pathogenesis, ventilator-associated pneumonias usually result in less prominent consolidations, less dynamic air bronchograms, and are more difficult to diagnose (see **Figure 4.10**). [46]

In patients with suspected pulmonary embolism, a recent meta-analysis showed lung US is sensitive (87%) and specific (82%) in making the diagnosis. [47] However, multiple methodological drawbacks were present in the original studies, thus limiting conclusions. Lung US will only reveal the presence of pulmonary infarcts, which, at best, are present on 32–36% of pulmonary CT angiograms in patients with confirmed pulmonary embolisms. [48] , [49] Significant proximal pulmonary embolisms usually do not result in pulmonary infarction, thus leading to a falsely reassuring lung US. When present, pulmonary infarction typically appears as small triangular or rounded well-demarcated consolidations (Westermark sign), without any blood flow on color Doppler. Because of predominant blood flow to the lung bases,

approximately 70% of lesions will be found in these regions. [50] To increase the utility of POCUS, it is important to look for deep venous thrombosis (see **Figure 18.24**) as well as right ventricular function and strain when evaluating patients with suspected pulmonary embolism (see **Figure 9.15**). Pulmonary venous thrombosis that can occur in lung transplant recipients may be similar to a consolidated area; it is however typically more anechoic (**Figure 14.22**).

The lower regions of the thorax can be source of artifacts. Normal reflection of the US beam by healthy lung may create a mirror image of the liver and spleen. This should not be considered a pathological consolidation when hepatized tissue is seen. The absence of B-lines, the presence of the diaphragm between these two images, and the disappearance of the mirror image with respiration are good clues to the presence of this normal mirror artifact (**Figure 14.23**). This stresses the importance of considering the whole clinical picture, and not only relying on information provided by POCUS.

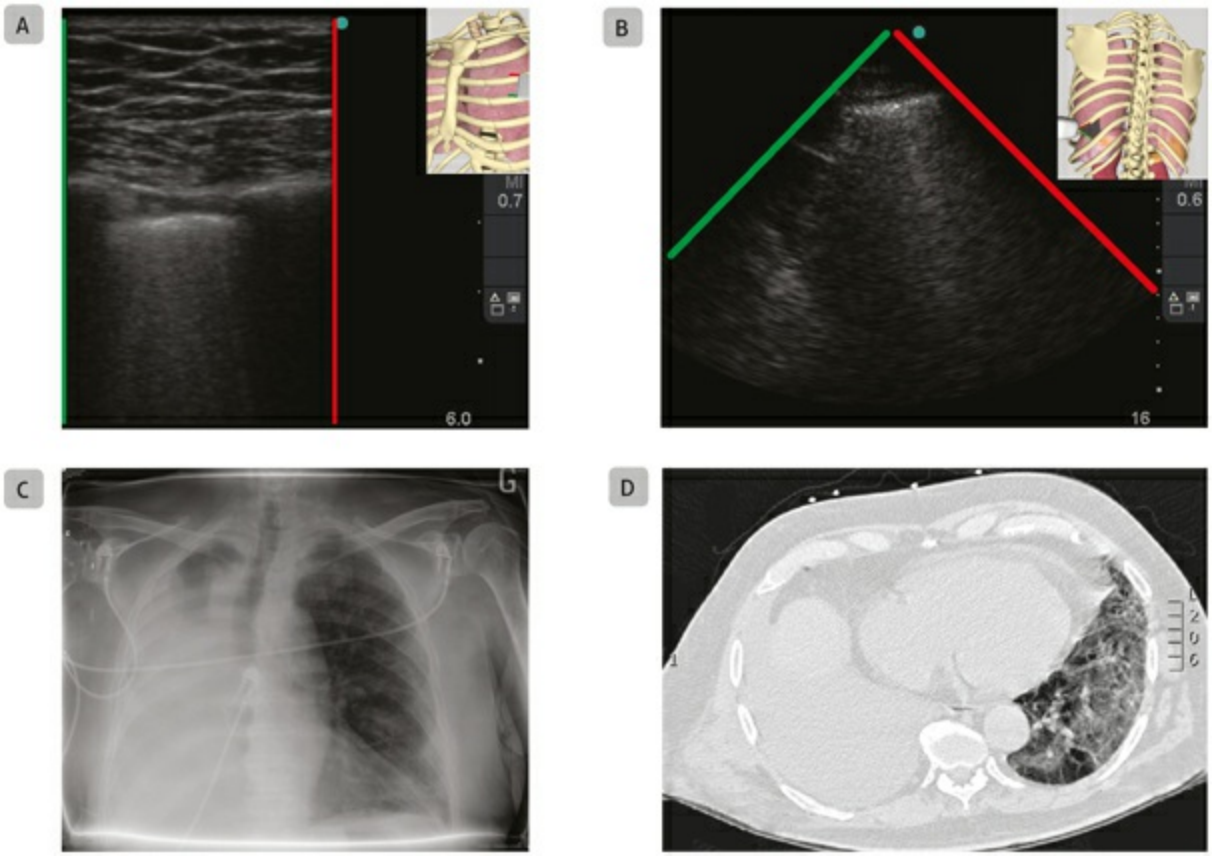

Fig. 14.21 Viral pneumonia. Lung ultrasound in a patient with a previous right lobectomy using (A) a linear probe in zone 5 of the left upper lobe and (B) a phased-array probe in zone 8 of the left lower lobe demonstrates B-lines, compared with the corresponding (C) chest radiograph and (D) computed

tomographic scan.

A: https://youtu.be/4g3rpvJJ8_k

B: https://youtu.be/X03qg_Qrhrs

Pneumothorax

The presence of a pneumothorax can be deadly, particularly in an intubated patient. Conventional supine CXR lacks sensitivity to diagnose pneumothorax. [51] , [52] A recent systematic review compared conventional CXR (sensitivity 28–75%, specificity 100%) to lung US (sensitivity 92–100%, specificity 100%) for the diagnosis of pneumothorax, with CT scan as the gold standard. [53] Other studies done in interventional radiology suites, intensive care units, and trauma bays, also demonstrated a greater sensitivity with lung US. [30] , [54] – [57]

A pneumothorax, traumatic or not, is the infiltration of air between the visceral and parietal pleura. The diagnosis or exclusion of pneumothorax by US relies on artifacts proving the integrity of the pleural interface. Air from a pneumothorax usually sets in the highest point of the thorax. In a supine patient this appears in the anterior thorax under the nipples, as compared to the apices in the sitting patient. In a supine CXR, the deep sulcus sign refers to an occult pneumothorax located in the antero-inferior pleural sulcus **(Figure** 14.24 **).** [58] The ultrasonographic deep sulcus sign refers to a small pneumothorax that is located in this same region, and that could easily be missed if the US does not cover this region. [59] Examining each zone of the thorax systematically, starting with the low anterior portions, safely excludes a pneumothorax. When diagnosing a pneumothorax, the US examination focuses on the pleural interface. The presence of lung sliding or even lung pulse indicates that the visceral and parietal pleura are normally adjoined, thus safely excluding a pneumothorax in this lung region. [16] , [55] In the absence of pleural sliding or lung pulse, the presence of even one B-line demonstrates

the integrity of the pleural interface, and safely excludes the presence of a pneumothorax in this region. [21] , [30] , [57] If a pneumothorax was present, the air inside the pleural cavity would hinder the passage of the US beam and not permit the genesis of B-lines. Subcutaneous emphysema is often associated with a pneumothorax. A common error is to wrongly identify E-lines (**Figure 14.14**), which originate from the air in the subcutaneous tissue, as being B-lines.

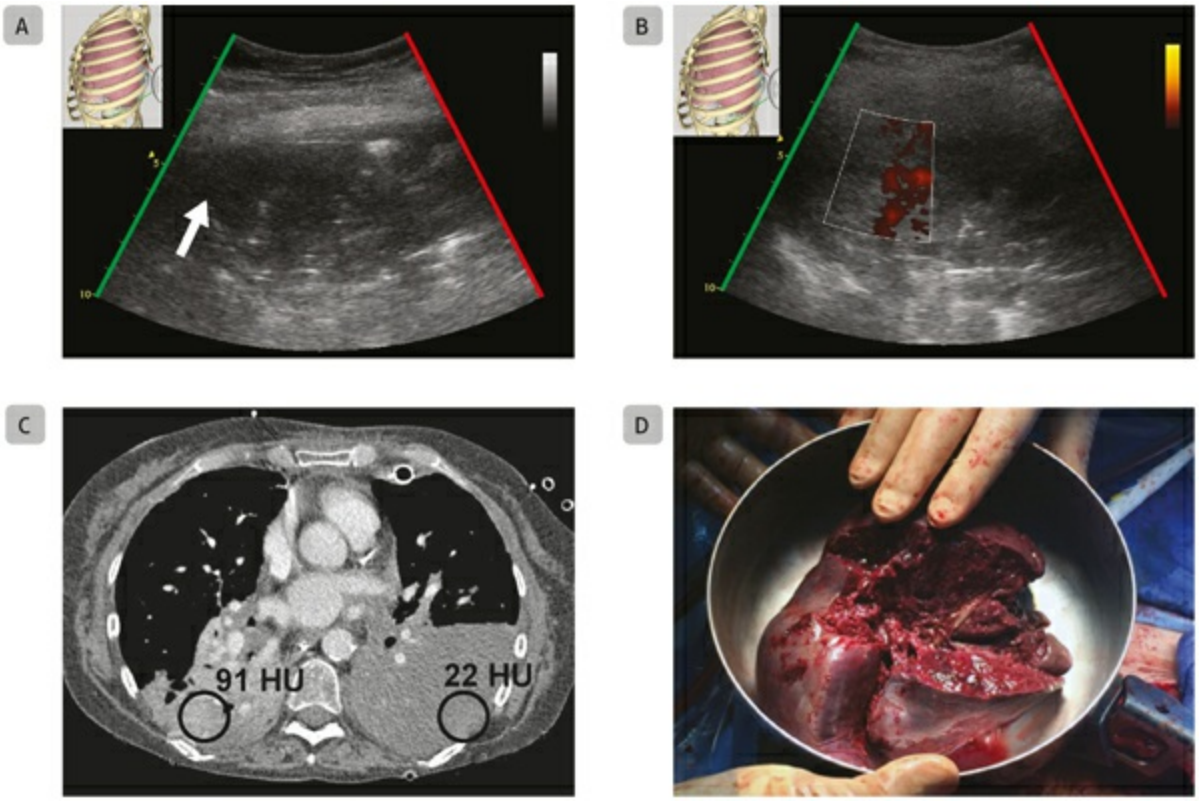

Fig. 14.22 Pulmonary venous thrombosis. Ultrasound scanning of the left lower lung (zone 12) following bilateral lung transplantation demonstrates venous thrombosis. (A) Note the dark appearance of the peripheral pulmonary tissue from venous congestion (arrow). (B) Using power Doppler imaging, only pulsatile flow can be seen. (C) Computed tomographic scan shows reduced radiodensity as measured by the Hounsfield unit (HU) of the left parenchyma compared to the right. Further examination revealed the absence of a pulmonary vein compared to the right. (D) The patient went to the operating room and the thrombosed lung was removed.

A: https://youtu.be/QmHT6e4GsxY

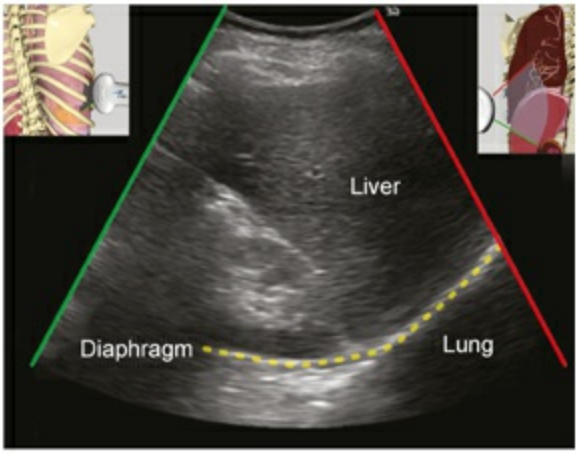

Fig. 14.23 Mirror artifact. Air contained in a normal lung will reflect the ultrasound beam and create a mirror image of the proximal structure in the right lower lobe (zone 4). In this image, the lung is healthy and not consolidated. The image seen is the reflection of liver parenchyma by the normal lung

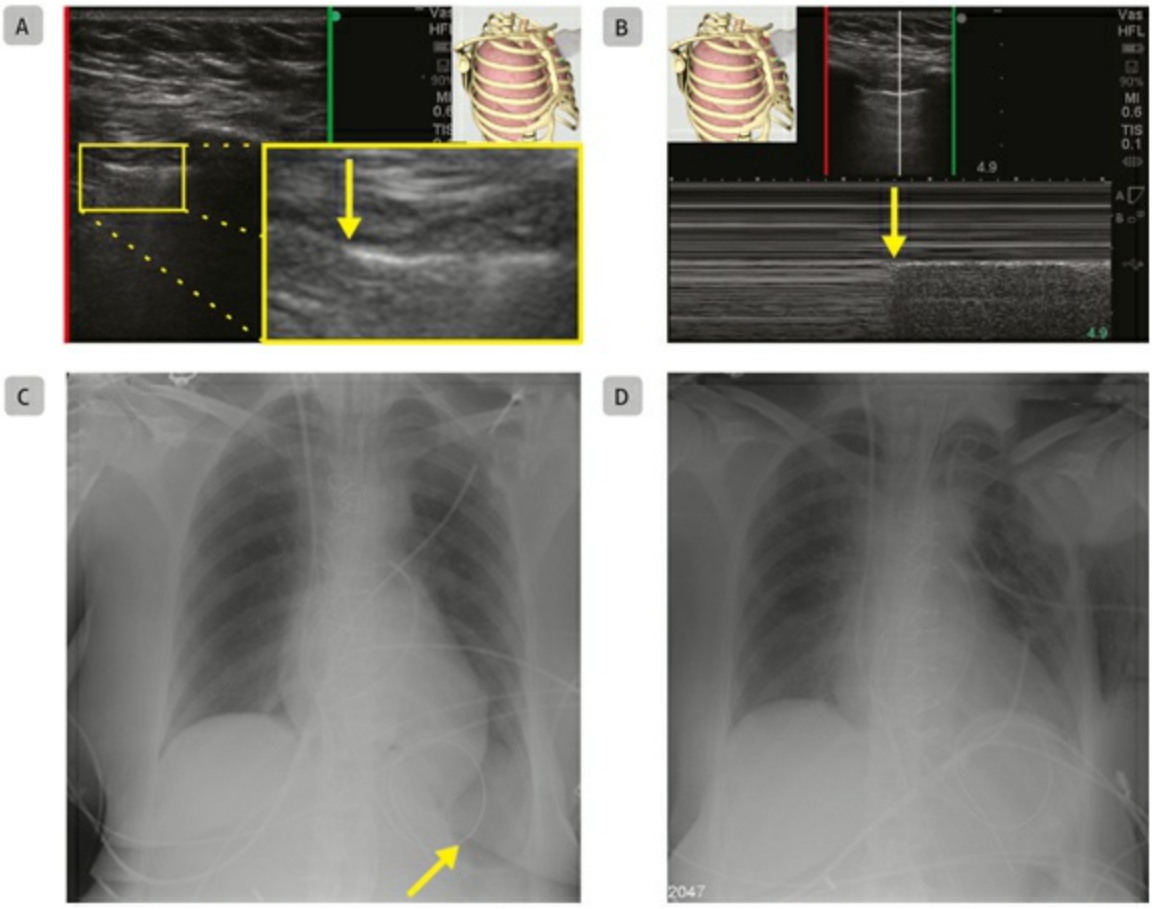

Fig. 14.24 Pneumothorax. Lung ultrasound examination of zone 5 of the upper left lung shows a lung point using (A) 2D and (B) M-mode scanning. The lung point is the transition point between a normal pleural interface and the separation of the visceral and parietal pleura by air from a pneumothorax. It can be identified when the normal pleural interface and underlying B-lines seem to disappear. Supine

chest radiographs show (C) a deep sulcus sign (arrow) which (D) disappears after drainage of the pneumothorax.

A: https://youtu.be/r9KOgiWfFf0

Once a pneumothorax is suspected, a lung point should be sought as it is 100% specific in the diagnosis of pneumothorax. [60] The lung point is the position on the US image where there is transition between the presence and absence of lung sliding. This corresponds to the point where the parietal and visceral pleura start to separate, and accurately delineates the margin of the pneumothorax (**Figures 14.24 and** 14.25). [61] , [62] Holding the probe parallel to the ribs while scanning the pleural interface can facilitate the identification of the lung point. M-mode can also help diagnose a pneumothorax by lung US. [60] When lung sliding is present, the M-mode image resembles a beach with water, commonly referred to as the seashore sign (**Figure 14.26**). When lung sliding is absent, no movement is present, and the M-mode image comprises multiple horizontal lines, referred to as the barcode sign (**Figure 14.27**). The lung point can also be identified on the M-mode, and corresponds to the point where the image transitions from the seashore sign to a barcode sign image (**Figures 14.24 and** 14.28).

Incorrectly diagnosing a pneumothorax is possible in certain situations. If the lung is not ventilated, no lung sliding will be present. When no B-lines are visible, a lung pulse should be sought. If not present and if a lung point cannot be identified, other diagnostic means should be used to confirm pneumothorax. Large emphysema bubbles may also mimic pneumothorax. Lung point can be falsely identified in the lowest regions of the thorax when the normal cephalad movement of the diaphragm during expiration moves the lung out of view. The same phenomenon may occur with the heart. These signs are called abdominal point and heart point.

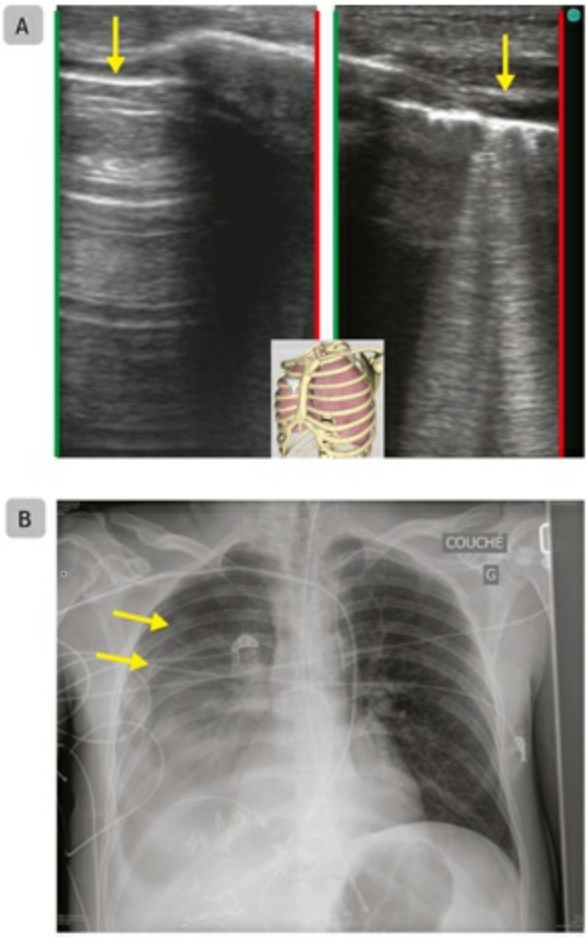

Fig. 14.25 Pneumothorax. (A) Lung ultrasound 2D image of zone 1 showing A-lines (yellow arrow) on the left and B-lines (yellow arrow) on the right. The transition between the two (coincidentally) corresponds to the lung point in ultrasound and the border of pneumothorax (double arrow) as shown in (B)

A: https://youtu.be/DbGR96LnIPI

Pleural Fluid

Pleural effusion is the accumulation of free fluid in the pleural space. On a standard upright CXR, approximately 200 cc of fluid is necessary for an effusion to be seen. In a lateral upright CXR, 50 cc may be detected in the posterior costo-diaphragmatic junction. Lung US can identify as little as 20 cc of fluid [63] , [64] and is more reliable in supine patients. [65] The interest in lung

US lies in its ability to estimate the quantity of pleural fluid present, and to determine its nature. Using a low frequency probe, scanning should begin in both upper abdominal quadrants on the middle and posterior axillary lines to identify the diaphragms and liver or spleen. In normal lung, a mirror artifact will be present, giving off an image of the liver or spleen over the diaphragm in the chest. When fluid is present, this mirror image is lost and fluid can be seen.

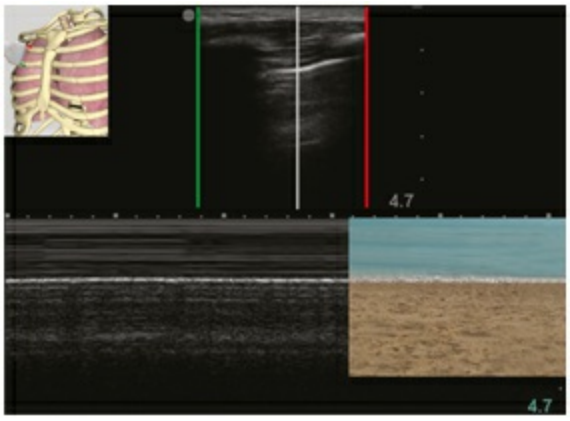

Fig. 14.26 Seashore sign. Normal lung parenchyma scanned with a linear probe in zone 1 showing the ultrasound 2D image and, with M-mode, exhibits the appearance of a seashore.

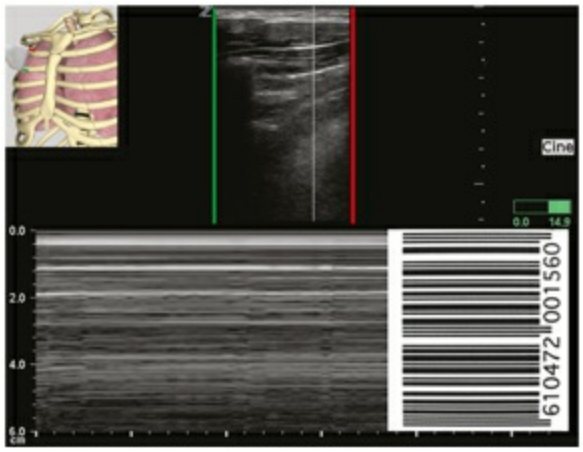

Fig. 14.27 Barcode sign. Lung ultrasound of a pneumothorax using a linear probe in zone 1 shows this 2D image. In M-mode, the fixed subcutaneous tissue is mirrored by the air in the pneumothorax, giving the appearance of fixed horizontal lines, the same as a barcode, hence the name “Barcode sign”.

https://youtu.be/ggT6jvIYU-g

While the size of a massive effusion will be rapidly appreciated, the size of a small or moderate effusion is trickier to estimate. Many different formulas have been devised in order to estimate the quantity of pleural fluid. [66] A simple pleural effusion will be homogeneously black (**Figure 14.29**). The presence of any particles, echotexture and/or swirling indicates an exudate (**Figure 14.30**). In the case of a clotted hemothorax, the effusion will be heterogeneous and may even seem gelatinous. An empyema will be heterogeneous in nature and will feature more or less prominent septations (**Figure 14.31**). Finally, it is important not to misidentify free peritoneal fluid as pleural fluid. Peritoneal free fluid will lie over the liver and spleen, but under the diaphragm.

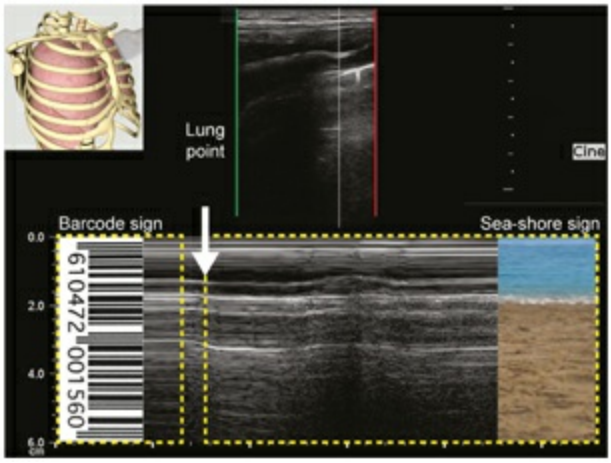

Fig. 14.28 Lung point in M-mode. Lung ultrasound of a pneumothorax using a linear probe in zone 5 shows the lung point on the 2D image. In M-mode, the lung point can be identified as the transition point between a “Barcode sign” and a “Seashore sign”.

https://youtu.be/PfcsAEE5NQg

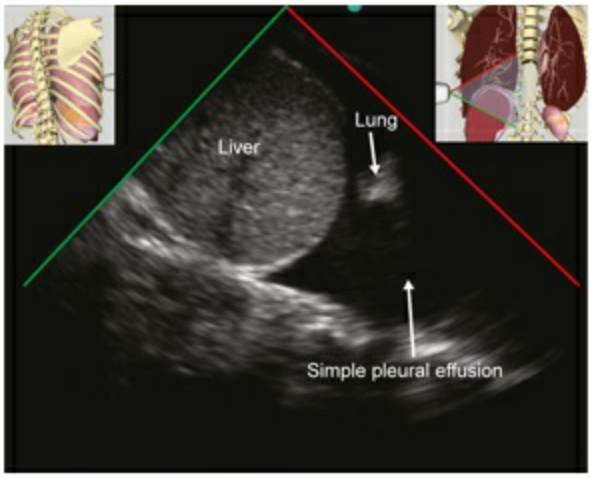

Fig. 14.29 Pleural effusion. Lung ultrasound 2D image using a phased array probe in zone 4 shows a simple pleural effusion that appears homogeneously black.

https://youtu.be/EnF1kvZiV9A

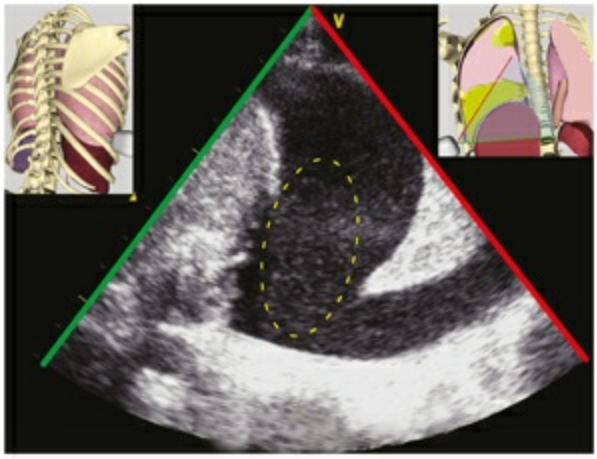

Fig. 14.30 Exudate. Lung ultrasound 2D image using a phased array probe in zone 4 shows a complex pleural effusion containing particles and swirling artifacts giving an appearance of echotexture (yellow dotted line) suggestive of an exudate.

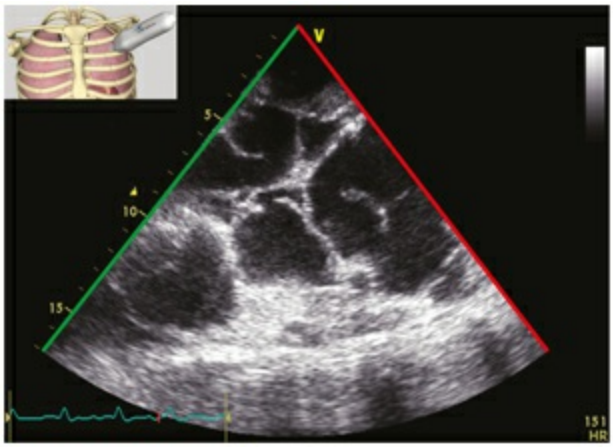

Fig. 14.31 Empyema. Lung ultrasound 2D image using a phased-array probe probe in zone 5 shows a heterogeneous pleural effusion with multiple septations, suggesting an empyema.

https://youtu.be/nIoB8fK0SUc

Diaphragmatic Paralysis

The diaphragm can be imaged with a high frequency probe over the lower chest, where it is between the rib cage and the abdominal content. It is easily recognized by its tri-layered structure: a heterogeneous poorly echogenic muscular layer (diaphragm proper) bordered by two echogenic layers, the peritoneum, and the parietal pleura. Like any muscle, the diaphragm will shorten and thicken with each active contraction. While visible with 2D imaging, this thickening can be better appreciated with M-mode (**Figures 14.32 and** 14.33). With maximal effort, a thickening fraction of less than 20% is diagnostic of diaphragmatic paralysis. [67] Previously only available in a research setting, preliminary data also indicate that the thickening ratio is a reliable measure of a patient's work of breathing. [68] Actual diaphragmatic excursion can be better appreciated when a low frequency probe is placed immediately below the costal margin at the mid-clavicular or anterior axillary line, and the beam is directed medially, cephalad and dorsally. With the US beam intersecting perpendicularly the dome of the corresponding hemi-diaphragm, diaphragmatic motion is easily assessed. Precise cutoff values to diagnose diaphragmatic paralysis have yet to be described. A complete

description is beyond the scope of this chapter, and interested readers are directed to this excellent review. [69]

Other Practical Applications of Lung Ultrasound

Lung US can also be used to confirm endotracheal tube (ETT) intubation. Earlier studies used ultrasound in neonates to ascertain the distance between the ETT tip and the aortic arch or sternal manubrium. [70] , [71] Visualization of diaphragmatic movement is shown to be accurate in paralysed patients. [72] Visualization of the ETT in the trachea (**Figure 14.34**) or esophagus in adult and pediatric populations was also described with sensitivity and specificity up to 100%. [73] – [78] Visualization of lung sliding is another technique that has been validated in a cadaveric model, in elective surgery patients, and in pre-hospital care settings to confirm ETT intubation. [79] – [82] Adequate positioning of a double lumen ETT has also been done using lung US. [83] , [84]

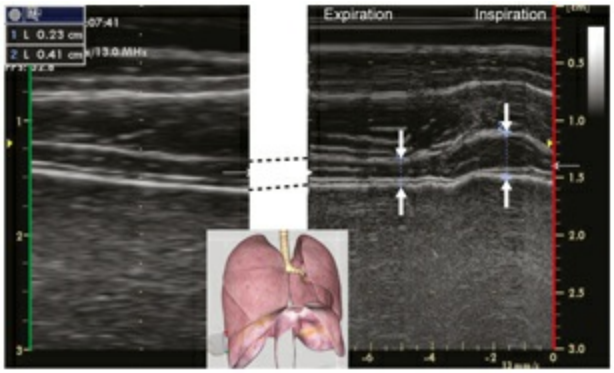

Fig. 14.32 Normal diaphragm thickening. Lung ultrasound 2D and M-mode images obtained using a linear probe in zone 4 shows normal thickening of the diaphragm during respiration.

Limitations of Lung Ultrasound

Air creates significant impedance to US beams, making it impossible to use US in patients with subcutaneous emphysema. Bone will also impede the propagation of the US beam. For example, the lung regions behind the scapula are inaccessible to lung US. Furthermore, except for consolidated lung, only superficial parts of the lung are evaluated by lung US, with deeper pathology not being visualized properly. Central pneumonia and proximal pulmonary embolism are examples of pathologies that likely will not be adequately visualized by lung US. Obese patients or women with large breasts may also have suboptimal lung US examinations because the

thickness of their subcutaneous tissues requires a deeper US field. Like most diagnostic modalities, lung US remains operator dependent. To ensure proper use and high accuracy, adhering to a structured curriculum, such as the one proposed by the American College of Chest Physician, is recommended. [85] Finally, as mentioned many times already, lung US and POCUS are powerful tools only if interpreted in conjunction with a patient's clinical context.

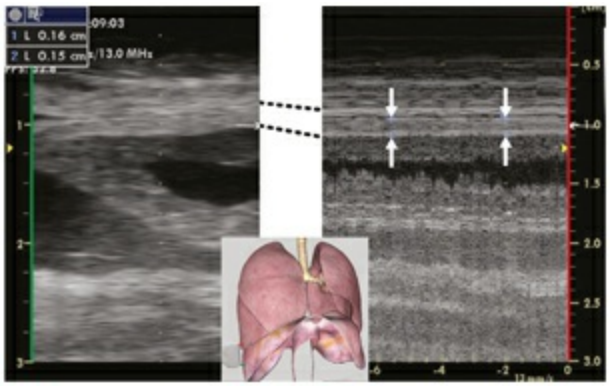

Fig. 14.33 Paralyzed diaphragm. Lung ultrasound 2D and M-mode images obtained using a linear probe in zone 4 showing diaphragm thickening of less than 20%, compatible with diaphragmatic paralysis.

SUMMARY

Multiple diagnostic algorithms using lung US have been described. The best known of these is the Blue Protocol, which correctly diagnosed dyspneic patients in 90.5% of cases. [29] A more recent study also demonstrated that most CXR could be avoided when using lung US. [28] **Figure 14.35** represents an algorithm that depicts and incorporates the basic notions described in this chapter. [14] As clinicians become more experienced with POCUS, adding other modalities such as advanced cardiac ultrasound and lower extremity compression ultrasonography can help in making a more global and complete assessment of critical care patients.

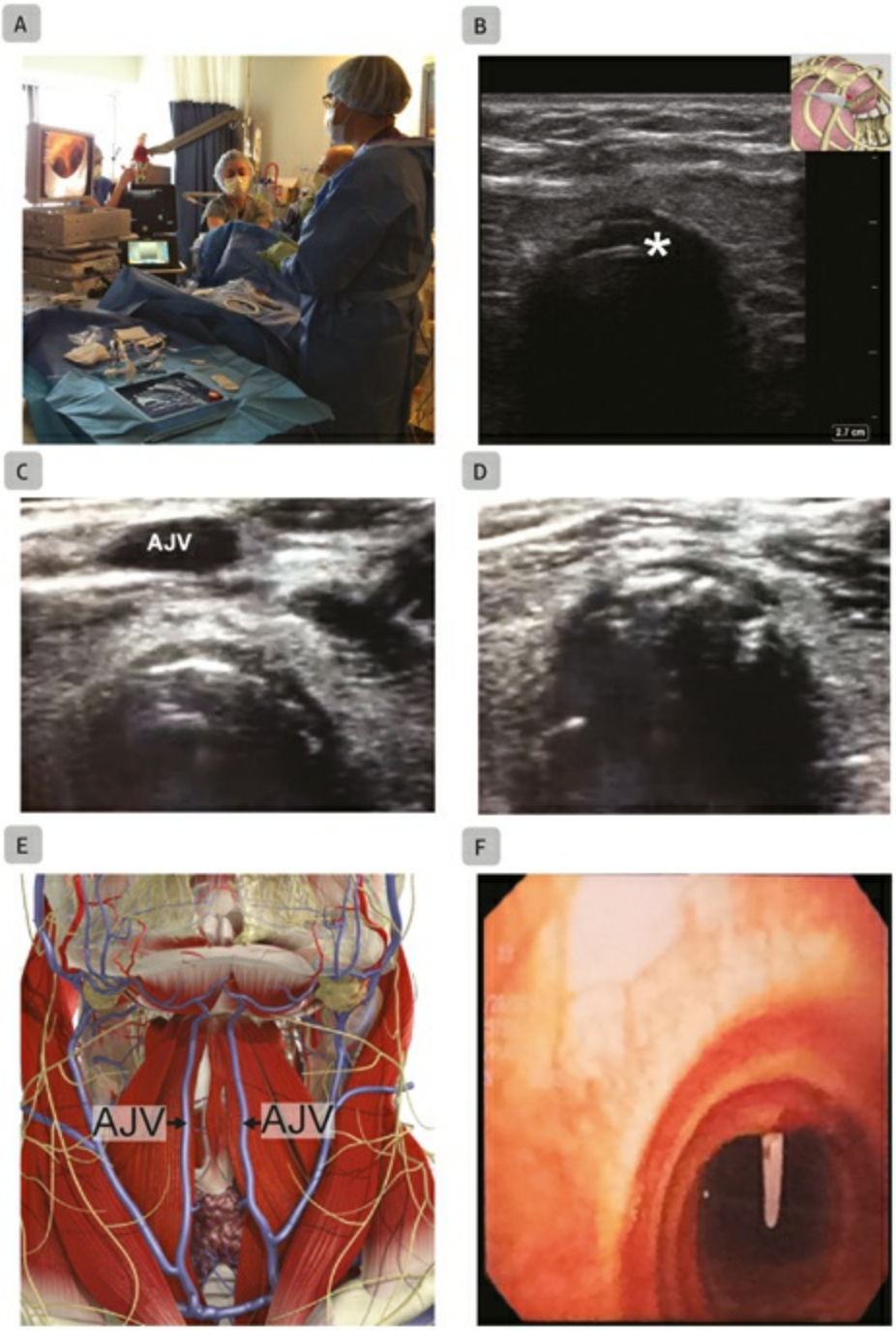

Fig. 14.34 Percutaneous tracheostomy. (A) During percutaneous tracheostomy in an intubated patient, (B) ultrasound can be used to position the tracheostomy centrally. Ultrasound is used to examine the anterior cervical region and avoid vascular structures and the thyroid isthmus. The endotracheal tube artifact is seen (*) just below the thyroid isthmus. (C) In some patients, an anterior jugular vein (AJV) can be positioned anterior to the trachea which will occlude (D) and disappear upon pressure. (E) Diagram of the normal position of the AJV is shown. (F) Video bronchoscopy will confirm the central position of the tracheostomy. (Anatomical images with permission of Primal Pictures, Wolters Kluwer Health.)

C: https://youtu.be/7Znp88CxkNU

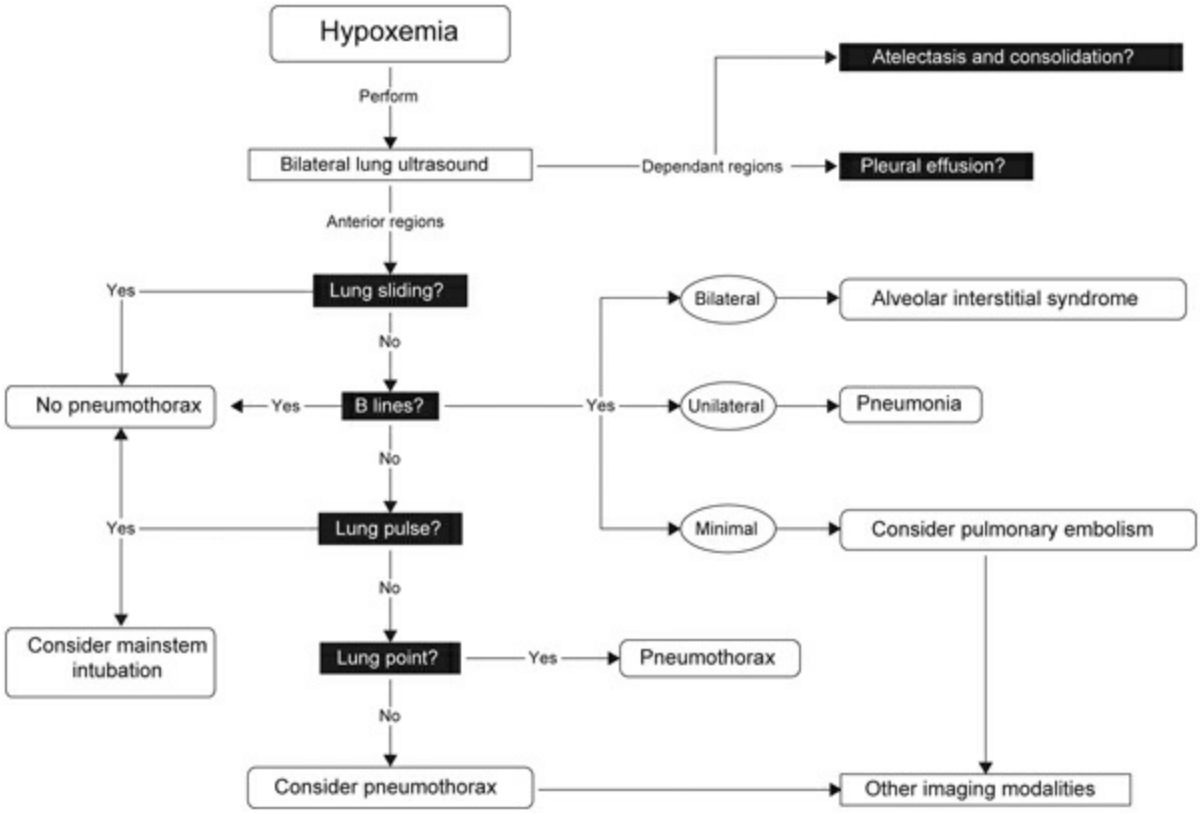

Fig. 14.35 Lung ultrasound algorithm. Simple algorithm incorporating the notions presented in this chapter to assess the lung with ultrasound. (Adapted from Piette *et al.* [14])

REFERENCES

1. SolomonS.D., SaldanaF.. Point-of-care ultrasound in medical education - stop listening and look. *N Engl J Med*2014; *370*: 1083–5.
2. American College of Emergency Physicians. Emergency ultrasound guidelines. *Ann Emerg Med*2009; *53*: 550–70.
3. International expert statement on training standards for critical care ultrasonography. *Intensive Care Med*2011; *37*: 1077–83.
4. RuppS.M., ApfelbaumJ.L., BlittC., CaplanR.A., ConnisR.T., DominoK.B., et al. Practice guidelines for central venous access: a report by the American Society of Anesthesiologists Task Force on Central Venous Access. *Anesthesiology*2012; *116*: 539–73.
5. ThomasH.A., BeesonM.S., BinderL.S., BrunettP.H., CarterM.A., ChisholmC.D., et al. The 2005 Model of the Clinical Practice of Emergency Medicine: the 2007 update. *Acad Emerg Med*2008; *15*: 776–9.

6. TroianosC.A., HartmanG.S., GlasK.E., SkubasN.J., EberhardtR.T., WalkerJ.D., et al. Guidelines for performing ultrasound guided vascular cannulation: recommendations of the American Society of Echocardiography and the Society of Cardiovascular Anesthesiologists. *J Am Soc Echocardiogr*2011; *24*: 1291–318.
7. *Objectives of Training in Emergency Medicine. Royal College of Physicians and Surgeons of Canada*. 2011.
8. HellerM.B., MandaviaD., TayalV.S., CardenasE.E., LambertM.J., MateerJ., et al. Residency training in emergency ultrasound: fulfilling the mandate. *Acad Emerg Med*2002; *9*: 835–9.
9. VolpicelliG., ElbarbaryM., BlaivasM., LichtensteinD.A., MathisG., KirkpatrickA.W., et al. International evidence-based recommendations for point-of-care lung ultrasound. *Intensive Care Med*2012; *38*: 577–91.
10. BouhemadB., ZhangM., LuQ., RoubyJ.J.. Clinical review: Bedside lung ultrasound in critical care practice. *Crit Care*2007; *11*: 205.
11. LichtensteinD., GoldsteinI., MourgeonE., CluzelP., GrenierP., RoubyJ.J.. Comparative diagnostic performances of auscultation, chest radiography, and lung ultrasonography in acute respiratory distress syndrome. *Anesthesiology*2004; *100*: 9–15.
12. VolpicelliG., MussaA., GarofaloG., CardinaleL., CasoliG., PerottoF., et al. Bedside lung ultrasound in the assessment of alveolar-interstitial syndrome. *Am J Emerg Med*2006; *24*: 689–96.
13. ZieleskiewiczL., ArbelotC., HammadE., BrunC., Textoris JMartin C, et al. [Lung ultrasound: clinical applications and perspectives in intensive care unit]. *Ann Fr Anesth Reanim*2012; *31*: 793–801.
14. PietteE., DaoustR., DenaultA.. Basic concepts in the use of thoracic and lung ultrasound. *Curr Opin Anaesthesiol*2013; *26*: 20–30.
15. RantanenN.W.. Diseases of the thorax. *Vet Clin North Am Equine Pract*1986; *2*: 49–66.
16. LichtensteinD.A., LascolsN., PrinS., MeziereG.. The, “lung pulse”: an early ultrasound sign of complete atelectasis. *Intensive Care Med*2003; *29*: 2187–92.
17. CunninghamJ., KirkpatrickA.W., NicolaouS., LiuD., HamiltonD.R., LawlessB., et al. Enhanced recognition of “lung sliding” with power color Doppler imaging in the diagnosis of pneumothorax. *J Trauma*2002; *52*: 769–71.
18. AcostaC.M., MaidanaG.A., JacovittiD., BelaunzaranA., CerecedaS., RaeE., et al. Accuracy of transthoracic lung ultrasound for diagnosing anesthesia-induced atelectasis in children. *Anesthesiology*2014; *120*: 1370–9.
19. SoldatiG., InchingoloR., SmargiassiA., SherS., NennaR., InchingoloC.D., et al. *Ex vivo* lung sonography: morphologic- ultrasound relationship. *Ultrasound Med Biol*2012; *38*: 1169–79.
20. SoldatiG., GiuntaV., SherS., MelosiF., DiniC.. “Synthetic” comets: a new look at lung sonography. *Ultrasound Med Biol*2011; *37*: 1762–70.
21. LichtensteinD., MeziereG., BidermanP., GepnerA., BarreO.. The comet-tail artifact. An ultrasound sign of alveolar-interstitial syndrome. *Am J Respir Crit Care Med*1997; *156*: 1640–6.
22. ReissigA., KroegelC.. Transthoracic sonography of diffuse parenchymal lung disease: the role of comet tail artifacts. *J Ultrasound Med*2003; *22*: 173–80.
23. AgricolaE., BoveT., OppizziM., MarinoG., ZangrilloA., MargonatoA., et al. ‘Ultrasound comet-tail images’: a marker of pulmonary edema: a comparative study with wedge pressure and extravascular lung water. *Chest*2005; *127*: 1690–5.
24. VolpicelliG., CaramelloV., CardinaleL., MussaA., BarF., FrasciscoM.F.. Detection of sonographic B-lines in patients with normal lung or radiographic alveolar consolidation. *Med Sci Monit*2008; *14*: CR122–8.
25. ZiskinM.C., ThickmanD.I., GoldenbergN.J., LapayowkerM.S., BeckerJ.M.. The comet tail artifact. *J Ultrasound Med*1982; *1*: 1–7.

26. VolpicelliG., CaramelloV., CardinaleL., CravinoM.. Diagnosis of radio-occult pulmonary conditions by real-time chest ultrasonography in patients with pleuritic pain. *Ultrasound Med Biol*2008; *34*: 1717–23.
27. VolpicelliG., CaramelloL., BerchiallaP., MussaA., BarF., FrasciscoM.F.. A comparison of different diagnostic tests in the bedside evaluation of pleuritic pain in the ED. *Am J Emerg Med*2012; *30*: 317–24.
28. ZanobettiM., PoggioniC., PiniR.. Can chest ultrasonography replace standard chest radiography for evaluation of acute dyspnea in the ED?*Chest*2011; *139*: 1140–7.
29. LichtensteinD.A., MeziereG.A.. Relevance of lung ultrasound in the diagnosis of acute respiratory failure: the BLUE protocol. *Chest*2008; *134*: 117–25.
30. LichtensteinD., MeziereG., BidermanP., GepnerA.. The comettail artifact: an ultrasound sign ruling out pneumothorax. *Intensive Care Med*1999; *25*: 383–8.
31. VolpicelliG., CaramelloV., CardinaleL., MussaA., BarF., FrasciscoM.F.. Bedside ultrasound of the lung for the monitoring of acute decompensated heart failure. *Am J Emerg Med*2008; *26*: 585–91.
32. SoldatiG., CopettiR., SherS.. Sonographic interstitial syndrome: the sound of lung water. *J Ultrasound Med*2009; *28*: 163–74.
33. TrezziM., TorzilloD., CerianiE., CostantinoG., CarusoS., DamavandiP.T., et al. Lung ultrasonography for the assessment of rapid extravascular water variation: evidence from hemodialysis patients. *Intern Emerg Med*2013; *8*: 409–15.
34. VitturiN., DugoM., SoattinM., SimoniF., MarescaL., ZagattiR., et al. Lung ultrasound during hemodialysis: the role in the assessment of volume status. *Int Urol Nephrol*2014; *46*: 169–74.
35. CardinaleL., VolpicelliG., BinelloF., GarofaloG., PriolaS.M., VeltriA., et al. Clinical application of lung ultrasound in patients with acute dyspnea: differential diagnosis between cardiogenic and pulmonary causes. *Radiol Med*2009; *114*: 1053–64.
36. MohammadiA., OshnoeiS., Ghasemi-radM.. Comparison of a new, modified lung ultrasonography technique with high-resolution CT in the diagnosis of the alveolo-interstitial syndrome of systemic scleroderma. *Med Ultrason*2014; *16*: 27–31.
37. SperandeoM., VarrialeA., SperandeoG., FilabozziP., PiattelliM.L., CarnevaleV., et al. Transthoracic ultrasound in the evaluation of pulmonary fibrosis: our experience. *Ultrasound Med Biol*2009; *35*: 723–9.
38. CopettiR., SoldatiG., CopettiP.. Chest sonography: a useful tool to differentiate acute cardiogenic pulmonary edema from acute respiratory distress syndrome. *Cardiovasc Ultrasound*2008; *6*: 16.
39. LichtensteinD.A., LascolsN., MeziereG., GepnerA.. Ultrasound diagnosis of alveolar consolidation in the critically ill. *Intensive Care Med*2004; *30*: 276–81.
40. SoldatiG., TestaA., SilvaF.R., CarboneL., PortaleG., SilveriN.G.. Chest ultrasonography in lung contusion. *Chest*2006; *130*: 533–8.
41. BlaivasM., TsungJ.W.. Point-of-care sonographic detection of left endobronchial main stem intubation and obstruction versus endotracheal intubation. *J Ultrasound Med*2008; *27*: 785–9.
42. LichtensteinD., MeziereG., SeitzJ.. The dynamic air bronchogram. A lung ultrasound sign of alveolar consolidation ruling out atelectasis. *Chest*2009; *135*: 1421–5.
43. TestaA., SoldatiG., CopettiR., GiannuzziR., PortaleG., Gentiloni-SilveriN.. Early recognition of the 2009 pandemic influenza A (H1N1) pneumonia by chest ultrasound. *Crit Care*2012; *16*:R30.
44. ReissigA., CopettiR., MathisG., MempelC., SchulerA., ZechnerP., et al. Lung ultrasound in the diagnosis and follow-up of community-acquired pneumonia: a prospective, multicenter, diagnostic accuracy study. *Chest*2012; *142*: 965–72.
45. ReissigA., KroegelC.. Sonographic diagnosis and follow-up of pneumonia: a prospective study. *Respiration*2007; *74*: 537–47.

46. BouhemadB., LiuZ.H., ArbelotC., ZhangM., FerarriF., Le-GuenM., et al. Ultrasound assessment of antibiotic-induced pulmonary reaeration in ventilator-associated pneumonia. *Crit Care Med*2010; *38*: 84–92.
47. SquizzatoA., RancanE., DentaliF., BonziniM., GuastiL., SteidlL., et al. Diagnostic accuracy of lung ultrasound for pulmonary embolism: a systematic review and meta-analysis. *J Thromb Haemost*2013; *11*: 1269–78.
48. HeyerC.M., LemburgS.P., KnoopH., Holland-LetzT., NicolasV., RoggenlandD.. Multidetector-CT angiography in pulmonary embolism - can image parameters predict clinical outcome?*Eur Radiol*2011; *21*: 1928–37.
49. JohnsonP.T., WechslerR.J., SalazarA.M., FisherA.M., NazarianL.N., SteinerR.M.. Spiral CT of acute pulmonary thromboembolism: evaluation of pleuroparenchymal abnormalities. *J Comput Assist Tomogr*1999; *23*: 369–73.
50. ComertS.S., CaglayanB., AkturkU., FidanA., KiralN., ParmaksizE., et al. The role of thoracic ultrasonography in the diagnosis of pulmonary embolism. *Ann Thorac Med*2013; *8*: 99–104.
51. BallC.G., KirkpatrickA.W., FelicianoD.V.. The occult pneumothorax: what have we learned?*Can J Surg*2009; *52*:E173–9.
52. WolfmanN.T., GilpinJ.W., BechtoldR.E., MeredithJ.W., DitesheimJ.A.. Occult pneumothorax in patients with abdominal trauma: CT studies. *J Comput Assist Tomogr*1993; *17*: 56–9.
53. WilkersonR.G., StoneM.B.. Sensitivity of bedside ultrasound and supine anteroposterior chest radiographs for the identification of pneumothorax after blunt trauma. *Acad Emerg Med*2010; *17*: 11–7.
54. DulchavskyS.A., HamiltonD.R., DiebelL.N., SargsyanA.E., BillicaR.D.. Williams Dr Thoracic ultrasound diagnosis of pneumothorax. *J Trauma*1999; *47*: 970–1.
55. LichtensteinD.A., MenuY.. A bedside ultrasound sign ruling out pneumothorax in the critically ill. *Lung sliding. Chest*1995; *108*: 1345–8.
56. TarghettaR., BourgeoisJ.M., ChavagneuxR., BalmesP.. Diagnosis of pneumothorax by ultrasound immediately after ultrasonically guided aspiration biopsy. *Chest*1992; *101*: 855–6.
57. TarghettaR., BourgeoisJ.M., ChavagneuxR., CosteE., AmyD., BalmesP., et al. Ultrasonic signs of pneumothorax: preliminary work. *J Clin Ultrasound*1993; *21*: 245–50.
58. GordonR.. The deep sulcus sign. *Radiology*1980; *136*: 25–7.
59. SoldatiG., TestaA., PignataroG., PortaleG., BiasucciD.G., LeoneA., et al. The ultrasonographic deep sulcus sign in traumatic pneumothorax. *Ultrasound Med Biol*2006; *32*: 1157–63.
60. LichtensteinD., MeziereG., BidermanP., GepnerA.. The, “lung point”: an ultrasound sign specific to pneumothorax. *Intensive Care Med*2000; *26*: 1434–40.
61. SoldatiG., TestaA., SherS., PignataroG., La SalaM., SilveriN.G.. Occult traumatic pneumothorax: diagnostic accuracy of lung ultrasonography in the emergency department. *Chest*2008; *133*: 204–11.
62. ZhangM., LiuZ.H., YangJ.X., GanJ.X., XuS.W., YouX.D., et al. Rapid detection of pneumothorax by ultrasonography in patients with multiple trauma. *Crit Care*2006; *10*:R112.
63. FroudarakisM.E.. Diagnostic work-up of pleural effusions. *Respiration*2008; *75*: 4–13.
64. RothlinM.A., NafR., AmgwerdM., CandinasD., FrickT., TrentzO.. Ultrasound in blunt abdominal and thoracic trauma. *J Trauma*1993; *34*: 488–95.
65. XirouchakiN., MagkanasE., VaporidiK., KondiliE., PlatakiM., PatrianakosA., et al. Lung ultrasound in critically ill patients: comparison with bedside chest radiography. *Intensive Care Med*2011; *37*: 1488–93.
66. RemerandF., DellamonicaJ., MaoZ., FerrariF., BouhemadB., JianxinY., et al. Multiplane ultrasound approach to quantify pleural effusion at the bedside. *Intensive Care Med*2010; *36*: 656–64.

67. GottesmanE., McCoolF.D.. Ultrasound evaluation of the paralyzed diaphragm. *Am J Respir Crit Care Med*1997; *155*: 1570–4.
68. VivierE., Mekontso DessapA., DimassiS., VargasF., LyazidiA., ThilleA.W., et al. Diaphragm ultrasonography to estimate the work of breathing during non-invasive ventilation. *Intensive Care Med*2012; *38*: 796–803.
69. MatamisD., SoilemeziE., TsagouriasM., AkoumianakiE., DimassiS., BoroliF., et al. Sonographic evaluation of the diaphragm in critically ill patients. Technique and clinical applications. *Intensive Care Med*2013; *39*: 801–10.
70. LingleP.A.. Sonographic verification of endotracheal tube position in neonates: a modified technique. *J Clin Ultrasound*1988; *16*: 605–9.
71. SlovisT.L., PolandR.L.. Endotracheal tubes in neonates: sonographic positioning. *Radiology*1986; *160*: 262–3.
72. KerreyB.T., GeisG.L., QuinnA.M., HornungR.W., RuddyR.M.. A prospective comparison of diaphragmatic ultrasound and chest radiography to determine endotracheal tube position in a pediatric emergency department. *Pediatrics*2009; *123*: e1039–44.
73. DrescherM.J., ConardF.U., SchambanN.E.. Identification and description of esophageal intubation using ultrasound. *Acad Emerg Med*2000; *7*: 722–5.
74. GalicinaoJ., BushA.J., GodambeS.A.. Use of bedside ultrasonography for endotracheal tube placement in pediatric patients: a feasibility study. *Pediatrics*2007; *120*: 1297–303.
75. HsiehK.S., LeeC.L., LinC.C., HuangT.C., WengK.P., LuW.H.. Secondary confirmation of endotracheal tube position by ultrasound image. *Crit Care Med*2004; *32*(9 Suppl.):S374–7.
76. MaG., DavisD.P., SchmittJ., VilkeG.M., ChanT.C., HaydenS.R.. The sensitivity and specificity of transcricothyroid ultrasonography to confirm endotracheal tube placement in a cadaver model. *J Emerg Med*2007; *32*: 405–7.
77. MillingT.J., JonesM., KhanT., Tad-yD., MelnikerL.A., BoveJ., et al. Transtracheal 2-d ultrasound for identification of esophageal intubation. *J Emerg Med*2007; *32*: 409–14.
78. WernerS.L., SmithC.E., GoldsteinJ.R., JonesR.A., CydulkaR.K.. Pilot study to evaluate the accuracy of ultrasonography in confirming endotracheal tube placement. *Ann Emerg Med*2007; *49*: 75–80.
79. ChunR., KirkpatrickA.W., SiroisM., SargasynA.E., MeltonS., HamiltonD.R., et al. Where's the tube? Evaluation of handheld ultrasound in confirming endotracheal tube placement. *Prehosp Disaster Med*2004; *19*: 366–9.
80. LyonM., WaltonP., BhallaV., ShiverS.A.. Ultrasound detection of the sliding lung sign by prehospital critical care providers. *Am J Emerg Med*2012; *30*: 485–8.
81. ParkS.C., RyuJ.H., YeomS.R., JeongJ.W., ChoS.J.. Confirmation of endotracheal intubation by combined ultrasonographic methods in the Emergency Department. *Emerg Med Australas*2009; *21*: 293–7.
82. WeaverB., LyonM., BlaivasM.. Confirmation of endotracheal tube placement after intubation using the ultrasound sliding lung sign. *Acad Emerg Med*2006; *13*: 239–44.
83. SusticA.. Role of ultrasound in the airway management of critically ill patients. *Crit Care. Med*2007; *35*(5 Suppl.):S173–7.
84. SusticA., ProticA., CicvaricT., ZupanZ.. The addition of a brief ultrasound examination to clinical assessment increases the ability to confirm placement of double-lumen endotracheal tubes. *J Clin Anesth*2010; *22*: 246–9.
85. MayoP.H., BeaulieuY., DoelkenP., Feller-KopmanD., HarrodC., KaplanA., et al. American College of Chest Physicians/La Societe de Reanimation de Langue Frangaise statement on competence in critical care ultrasonography. *Chest*2009; *135*: 1050–60.

Chapter 15

Critical Care Examination of the Cardiovascular System

Ying Tung Sia, Karim Serri and Jean-Claude Tardif

INTRODUCTION

Although echocardiography was introduced to North America in the early 1950s, it was not until a decade later that Harvey Feigenbaum brought cardiac ultrasound into clinical practice. In collaboration with Harold Dodge, he applied the M-mode technique to measure left ventricular (LV) wall thickness and dimensions, LV stroke volume, and ejection fraction in patients with cardiac disease. [1] With technological advances including real-time 2D imaging, pulsed-wave and continuous wave spectral Doppler, color Doppler, transesophageal echogradiography (TEE), and 3D imaging, its use has extended beyond cardiology and has entered into other clinical theaters, such as the operating room, emergency room, and intensive care unit (ICU).

Interest in using bedside echocardiography to manage critically ill patients has been continually growing in the last two decades. Since 1990, more than 100 articles related to its use in the ICU and the training of non-cardiology physicians have been published each year. Bedside transthoracic echocardiography (TTE) allows intensivists to obtain information regarding ventricular function, valvular function, and volume status in critically ill patients, thus helping to determine the causes of shock. [2] – [4] It is a portable, non-invasive, and radiation-free technique. Given the absence of risk for the patient and its accessibility, point-of-care TTE has become a first-line diagnostic modality widely used by the intensivist to manage patients with an unstable hemodynamic status. [5] Such point-of-care echocardiographic examinations are usually “directed” or “focused” toward a specific clinical

question and are of significantly shorter duration than a comprehensive echocardiographic examination. [3] , [6] Kimura *et al.* [7] found that directed TTE to rule out pericardial effusion identified significant incidental findings in 45% of cases. Therefore, intensivists must remain vigilant and be able to recognize these significant incidental findings while performing a focused TTE study. A complete TTE examination should be requested if such findings are identified. This chapter will discuss the basic principles of ultrasound in the setting of focused TTE assessment of ventricular function, valvular function, pericardial effusion, and volume status.

GENERAL APPROACH TO TRANSTHORACIC EXAMINATION

Echocardiography is a highly operator-dependent technique. Accurate diagnosis relies on obtaining high quality images and adequate Doppler tracings. Artifacts (see Chapter 1, Ultrasound Imaging: Acquisition and Optimization), inappropriate system settings, and poor patient positioning provide poor images that could lead to misdiagnosis. Moreover, TTE imaging of ICU patients is often limited because of difficult patient positioning, presence of chest tubes, dressings, and lung hyperinflation from mechanical ventilation. Where TTE is non-diagnostic, other diagnostic imaging modalities, such as focused TEE, [8] could represent an alternative (see Chapter 3, Normal Cardiac Anatomy and TEE Imaging Planes).

A focused TTE examination can be performed with most small portable ultrasound systems and hand-held devices (**Figure 15.1**). All available systems possess variable characteristics (abdominal, vascular, and cardiac presets) adapted to the situation. Irrespective of the system used, one has to determine the indication and main questions to be answered by bedside TTE before performing the exam. **Table 15.1** details the most common indications for TTE in critical care settings. [3] , [9]

In order to successfully perform a TTE examination, several points need to be taken into account:

1. The patient needs to be optimally positioned for the area being studied. The left lateral decubitus position brings the heart closer to the chest wall and left arm abduction widens the intercostal space improving the acoustic window between the ribs.

2. A dark environment improves image visualization. This might not always be possible in the acute care setting or during cardiac arrest.
3. All images are gated to the electrocardiogram to differentiate systole and diastole.
4. Adequate probe selection is important, as a higher frequency probe eanhances spatial resolution and a lower frequency probe allows greater penetration, but at the expense of resolution (see **Figure 18.2**). The typical cardiac probe for TTE is a phased-array probe that emits and receives ultrasound in a range of 3.5–5 MHz. The linear probe is infrequently used for adult cardiac evaluation. The use of the abdominal probe with lower frame rate is not recommended for evaluation of cardiac function.
5. Minimize sector width and depth to obtain the maximal frame rate. The higher the frame rate, the better the spatial resolution.
6. Image recording: the images are stored in digital format to allow subsequent review of images and quality control.

Optimize image quality (or spatial resolution) by using appropriate gain, compression, and adjusting the focus. Minimize the gain to avoid artifact and to enhance image resolution. Attenuate more distant structures by using time gain compensation. Automatic time-gain compensation adjustments are available on several point-of-care ultrasound systems. Higher compression provides a softer image, whereas reduced compression produces a more contrasted image. Position the focus point on the area of interest to obtain better lateral resolution.

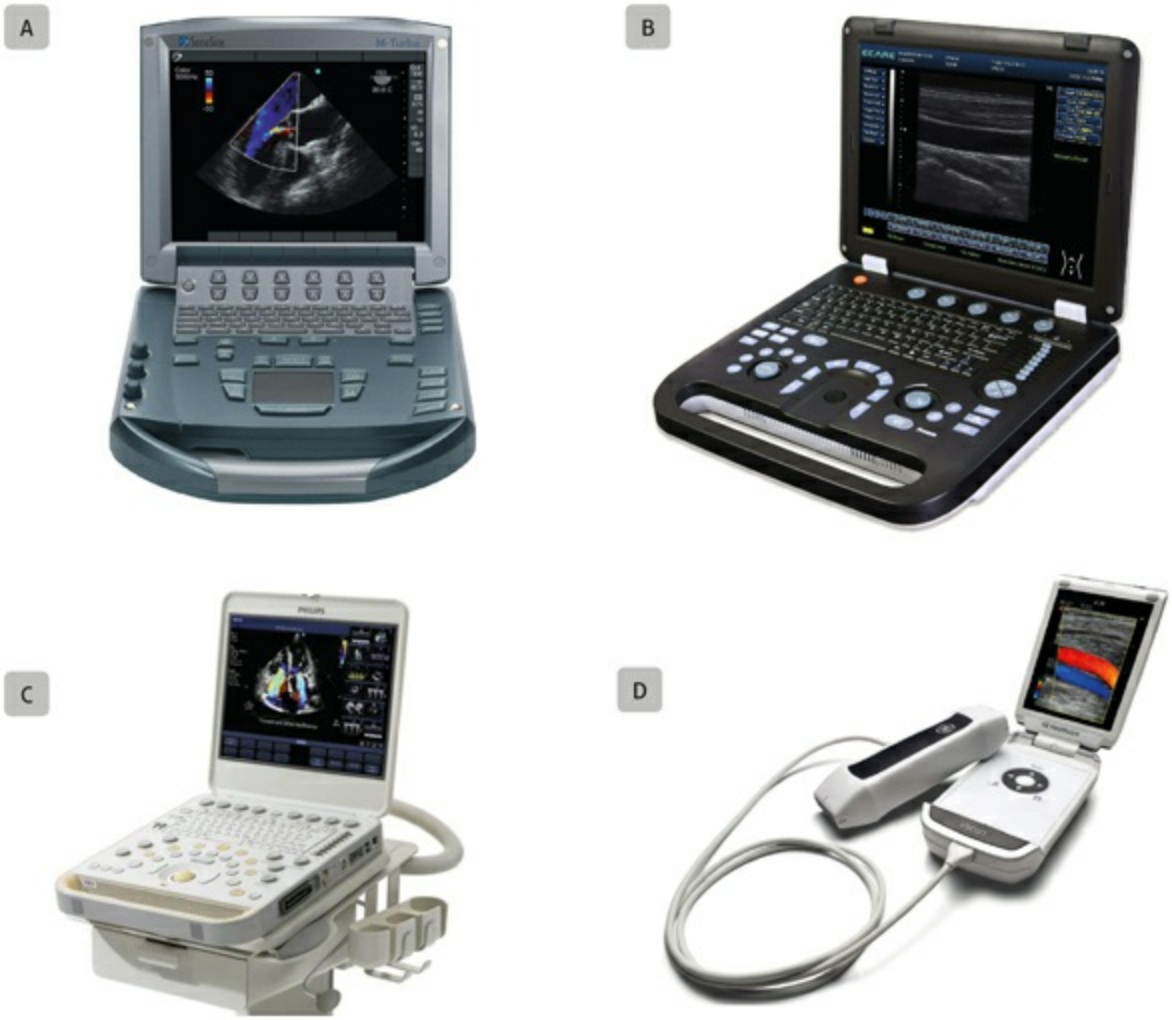

Fig. 15.1 . Portable ultrasound systems. Different ultraound machines are shown including the (A) Sonosite M Turbo; (B) General Electric Vivid I; (C) Philips CX 50; (D) General Electric handheld Vscan 3rd generation.

Table 15.1 Indication of Focused Transthoracic Echocardiography in Acute Care Setting.

Cardiac failure	Respiratory failure
Tamponade	Cardiogenic
LV dysfunction	Non cardiogenic
Valvulopathies	Ventilator weaning issue
Pulmonary embolism	
Volume status assessment	**Thoracic trauma**
Hemodynamic assessment	
Post cardiac arrest	

Note: LV, left ventricular.

General TTE Views

Transthoracic echocardiography scanning is performed from three main areas: parasternal, apical, and sub-costal (**Figure 15.2**). The suprasternal area is rarely used in critically ill patients, but it should not be omitted when aortic dissection, coarctation, or patent ductus arteriosus are suspected. This view can be also used as a non-invasive estimate of cardiac output or for fluid responsiveness during passive leg raising. Multiple views are generated from these areas when performing a systematic TTE examination (**Figure 15.3** and **Table 15.2**). In an outpatient setting, these views are easily obtained in 85–90% of patients. When one view is challenging, sufficient information can often be obtained by another view. The sequence of scanning can be modified according to the clinical circumstances. For instance, during resuscitation, the subcostal view is sometimes the only view used in order to facilitate chest compression and intubation. However, the physician needs to adopt a standardized sequence of scanning in order not to omit any view.

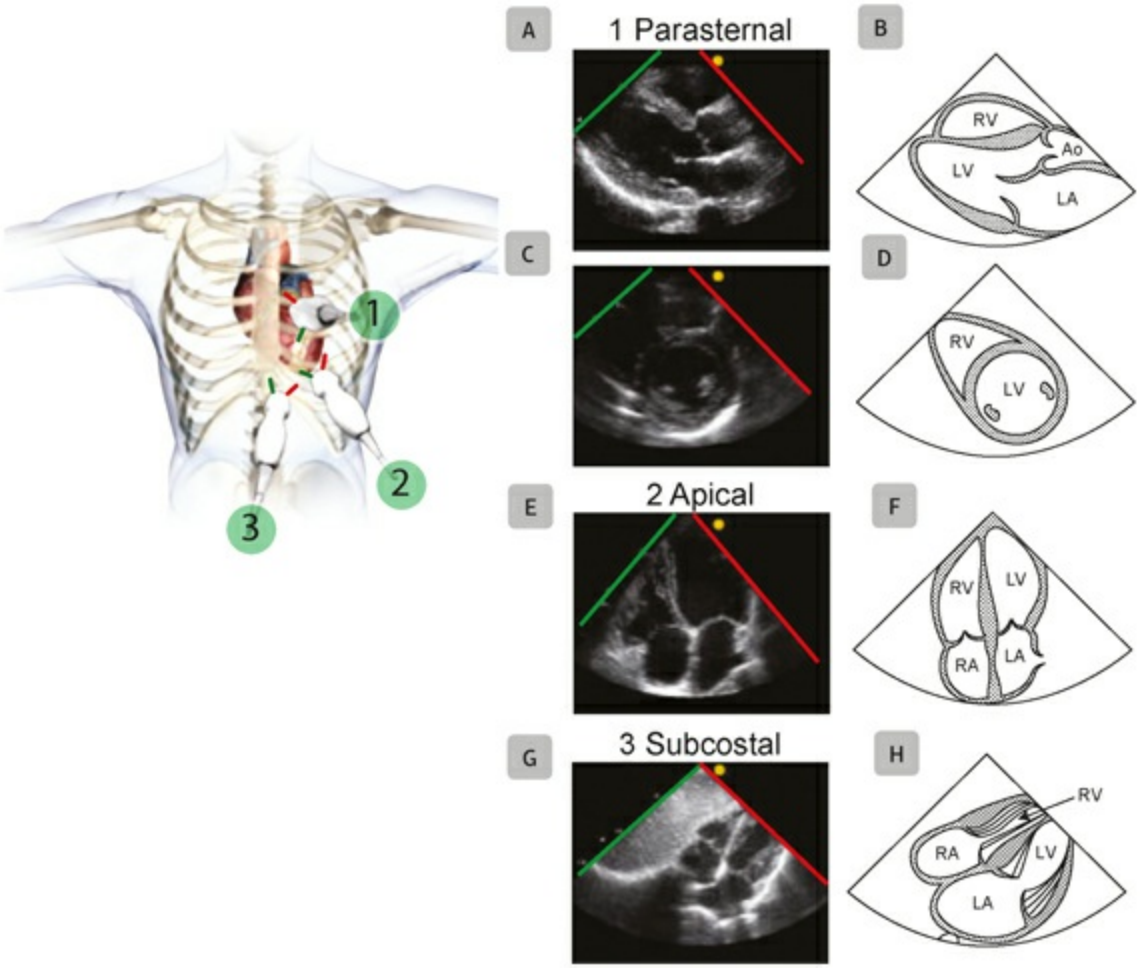

Fig. 15.2 Focused cardiac ultrasound study (FOCUS) examination. The FOCUS examination includes these important transthoracic echocardiographic views. Scanning should be performed in a systematic, clockwise fashion, from three main areas: (1) parasternal, (2) apical, and (3) subcostal. Ao, aorta; LA, left atrium; LV, left ventricle; RA, right atrium; RV, right ventricle. Source: Adapted from the FOCUS pocket guide, with permission from ICCU Imaging Inc (Reproduced with permission from Denault *etal.* [9] *)*

A: https://youtu.be/zsLAupoKJVA

C: https://youtu.be/joOi3OQHrZo

E: https://youtu.be/H3QbJmmgUEk

G: https://youtu.be/04mBUADcyxk

ADDITIONAL TTE VIEWS

Many other views can be used when standard views are suboptimal. This is beyond the scope of the basic TTE examination; however, some views are particularly useful for the intensivist. The right parasternal view provides an echographic window to image the ascending aorta beyond the sino-tubular junction and to assess aortic valve stenosis (**Figure 15.4)**. This view can also be used to evaluate right ventricular (RV) function (**Figure 15.5**). When there is a significant left pleural effusion, a left paraspinal view (**Figure 15.6**) can be used to scan the LV, left atrium, mitral valve, aortic valve, ascending aorta, and thoracic descending aorta. It should be noted that the images obtained from left paraspinal view are inverted as compared to left parasternal long axis (LAX) given the fact that the ultrasound beam is directed from the spine to the sternum.

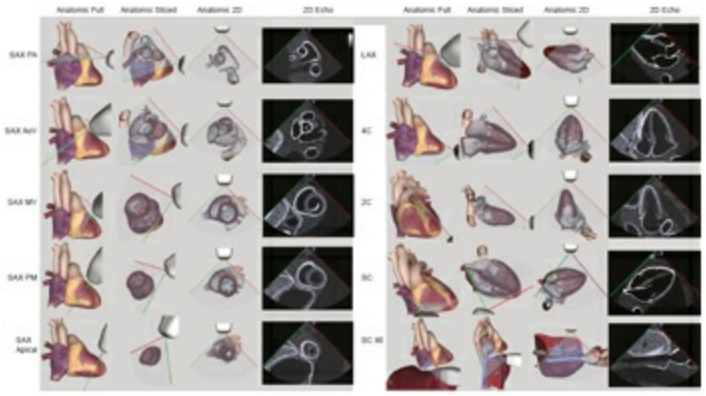

Fig. 15.3 . Transthoracic echocardiographic views. Transthoracic echocardiographic views are demonstrated using the Vimedix simulator. A focused cardiac ultrasound study comprises a subset of these views: LAX, 4C, 2C, SAX PM, SC, and SC 90. AoV, aortic valve; LAX, long- axis; MV, mitral

valve; PA, pulmonary artery; PM, papillary muscle; SAX, short-axis; SC, subcostal; 2C, two-chamber; 4C, four-chamber.

Table 15.2 Transthoracic Echocardiographic Views.

Parasternal	Apical
Long axis	4-Chamber
Short axis (base, MV, mid, apical)	3-Chamber
RV inflow	2-Chamber
Pulmonic valve	5-Chamber
Subcostal	**Suprasternal**
4-Chamber	
Short axis (basal, mid)	
Inferior vena cava/abdominal aorta	

Note: MV, mitral valve; RV, right ventricular.

LEFT VENTRICULAR FUNCTION ASSESSMENT

Evaluation of systolic LV function and dimension is an essential part of TTE study. All views mentioned above are used to assess LV function and size. Left ventricular size is either measured by M-mode or by 2D at the tip of the mitral leaflets in the left parasternal LAX view. The American Society of Echocardiography (ASE) guidelines detail several methods of LV size and mass measurements and suggest cut-offs to classify LV dilatation and LV hypertrophy (See Chapter 5, Assessment of Global Ventricular Function, Pericardium, and Cardiomyopathy). [10] , [11] A simple approximation for LV dilatation is 40/55 mm for systolic and diastolic dimensions. Pocket cards can provide trainees with rapid access to the ASE guidelines on chamber quantification (see **Figure 5.1**). The ASE also provides free web-based guidelines (http:// asecho.org/clinical-information/guidelines-standards/).

Evaluation of LV systolic function is a difficult task. There is a high inter-observer's variability among echocardiographers in the assessment of LV ejection fraction when only a visual "eye ball" method is being used. [12] To reduce the variability, many echo laboratories routinely employ a

combination of different methods (Simpson's, wall motion score, etc.) to quantify LV function (see **Figure 5.8**). However, these methods are time-consuming and are not suitable in an acute ICU setting. To simplify the task, some authors suggest the qualitative assessment of global LV ejection fraction (LVEF), which is categorized into three groups: normal LV function (LVEF >55%), mildly to moderately reduced LV function (LVEF 30–55%), and severely reduced LV function (LVEF <30%). By using this nomenclature, Randazzo *et al.* [13] showed that there is a good correlation in reporting LV function between non-echocardiographers and echocardiographers. Estimation of global LV function is often used to guide therapy in a hemodynamically unstable patient, such as using inotropic agents or mechanical intervention. If LV function is normal or hyperdynamic, another cause of hemodynamic instability will be sought such as sepsis, bleeding, or pneumothorax depending on the clinical situation (see Chapter 9, Basic Hemodynamic Assessment). A comprehensive TTE study should be requested if new wall abnormalities are detected as detailed characterization of the LV wall motion abnormalities is beyond the goal of focused TTE (see Chapter 6, Basic Regional Ventricular Systolic Function).

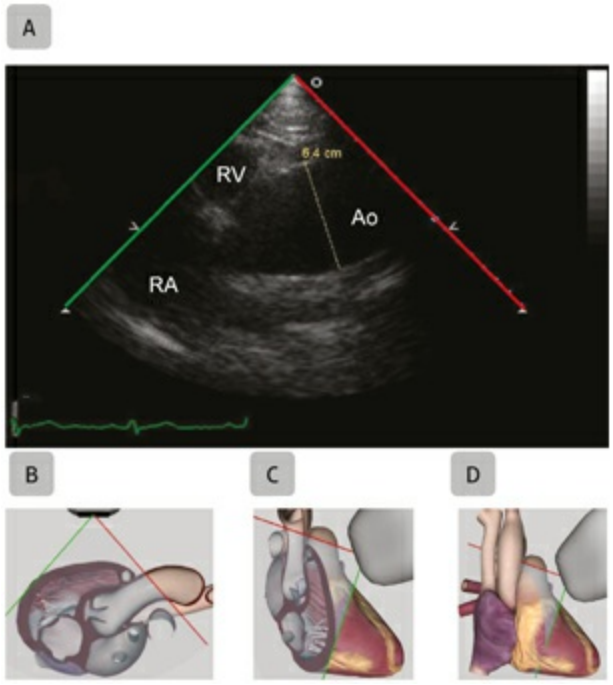

Fig. 15.4 . Ascending aorta (Ao) aneurysm. (A) An ascending aortic aneurysm is diagnosed using a right parasternal long-axis view with (B-D) Vimedix probe position and correspondence to the (B) anatomic 2D, (C) anatomic sliced, and (D) anatomic full heart model. RA, right atrium; RV, right

ventricle.

A: https://youtu.be/2Fsvdkb9yAw

B: https://youtu.be/uL1mCLpmmdo

C: https://youtu.be/9CE388fJwKs

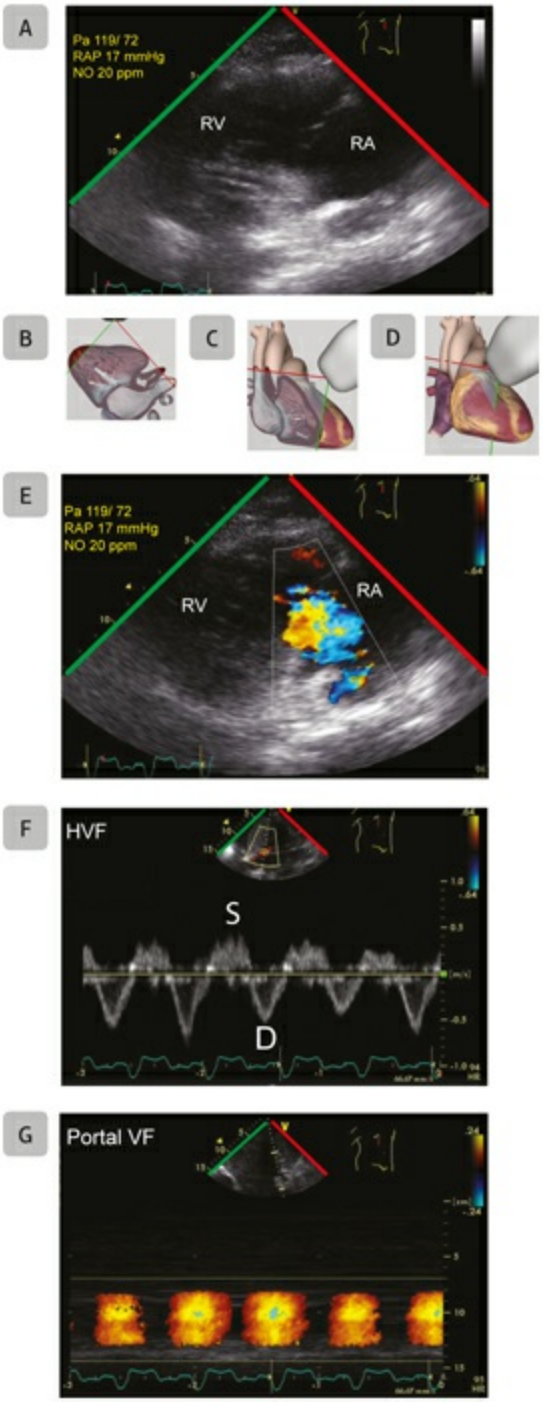

Fig. 15.5 . Right ventricular (RV) dysfunction. (A-D) Right parasternal view in a 24-year- old patient with RV dysfunction associated with (E) severe tricuspid regurgitation (TR) by color Doppler (Nyquist 64 cm/s). (F, G) The TR was associated with (F) systolic (S) hepatic venous flow (HVF) velocity reversal and (G) pulsatile portal venous flow (VF) shown by color M-mode. D, diastolic HVF; NO, nitric oxide; Pa, arterial pressure; RA, right atrium; RAP, right atrial pressure.

A: https://youtu.be/EUHBssJXNgo

E: https://youtu.be/Gyq8C_dySbU

G: https://youtu.be/DwjoxcKTdVU

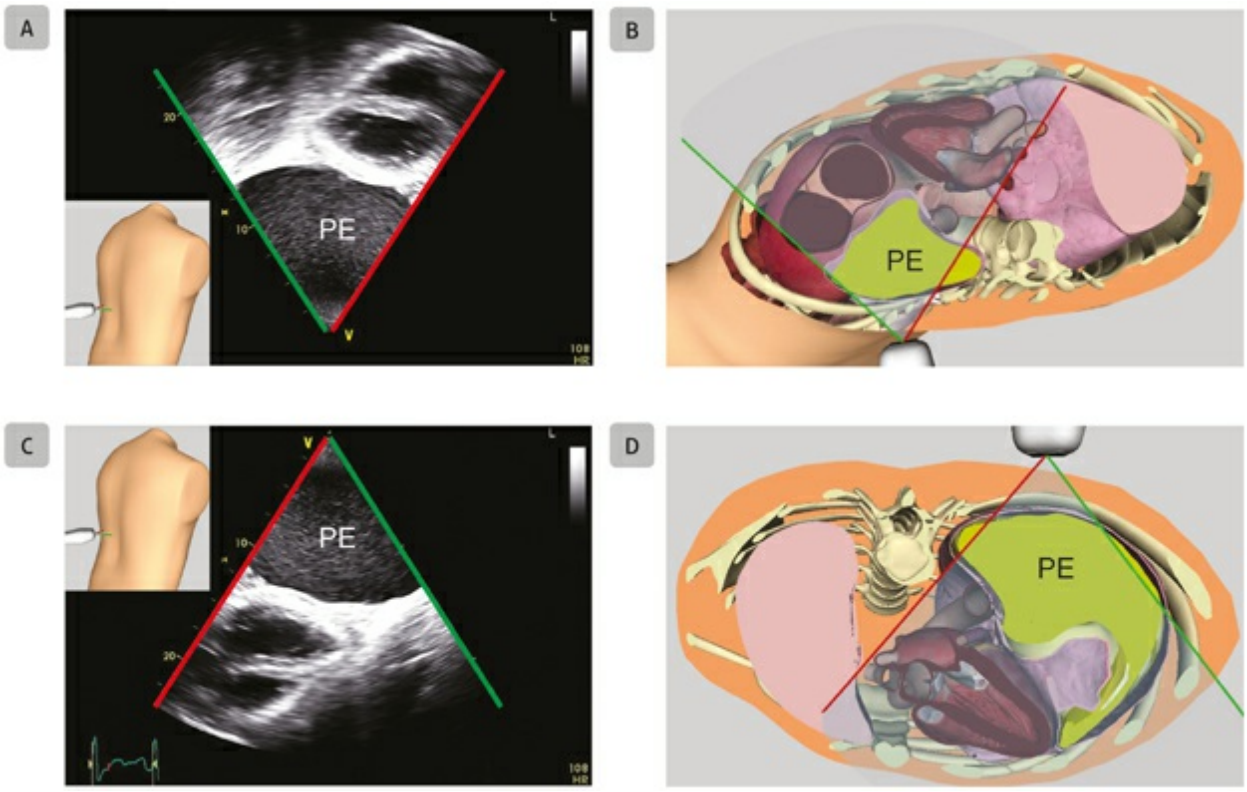

Fig. 15.6 . Pleural effusion (PE). Paraspinal views of the heart in a patient with a left-sided PE are shown using the Vimedix simulator. (A,B) Left paraspinal long-axis view using the PE as an acoustic window. (C,D) Same view, but with a 180° flip of the image. Note that the image quality is adequate for interpretation.

A: https://youtu.be/auxgMut8hS4

C: https://youtu.be/QkFJzys9ieo

As mentioned earlier, imaging of ICU patients is more challenging because of the multiple factors listed above. If image quality is inadequate, intravenous echo contrast (Definity®, Lantheus Medical Imaging, N Billerica, MA, USA) can be used for LV opacification, thus facilitating the visualization of LV wall motion and ruling in/out apical thrombus (**Figure 15.7**). If not available, TEE might be considered. Contrast is typically reserved for cardiologists with formal and more extensive echo training.

DOPPLER ECHOCARDIOGRAPHIC ASSESSMENT

Doppler assessment is an integral part of TTE examination. Application of Doppler echocardiography is the preferred method for hemodynamic assessment. **Table 15.3** lists the most useful Doppler-derived hemodynamic data. Determination of Doppler-derived filling pressures is beyond the scope of the focused examination and other resources should be consulted. [9]

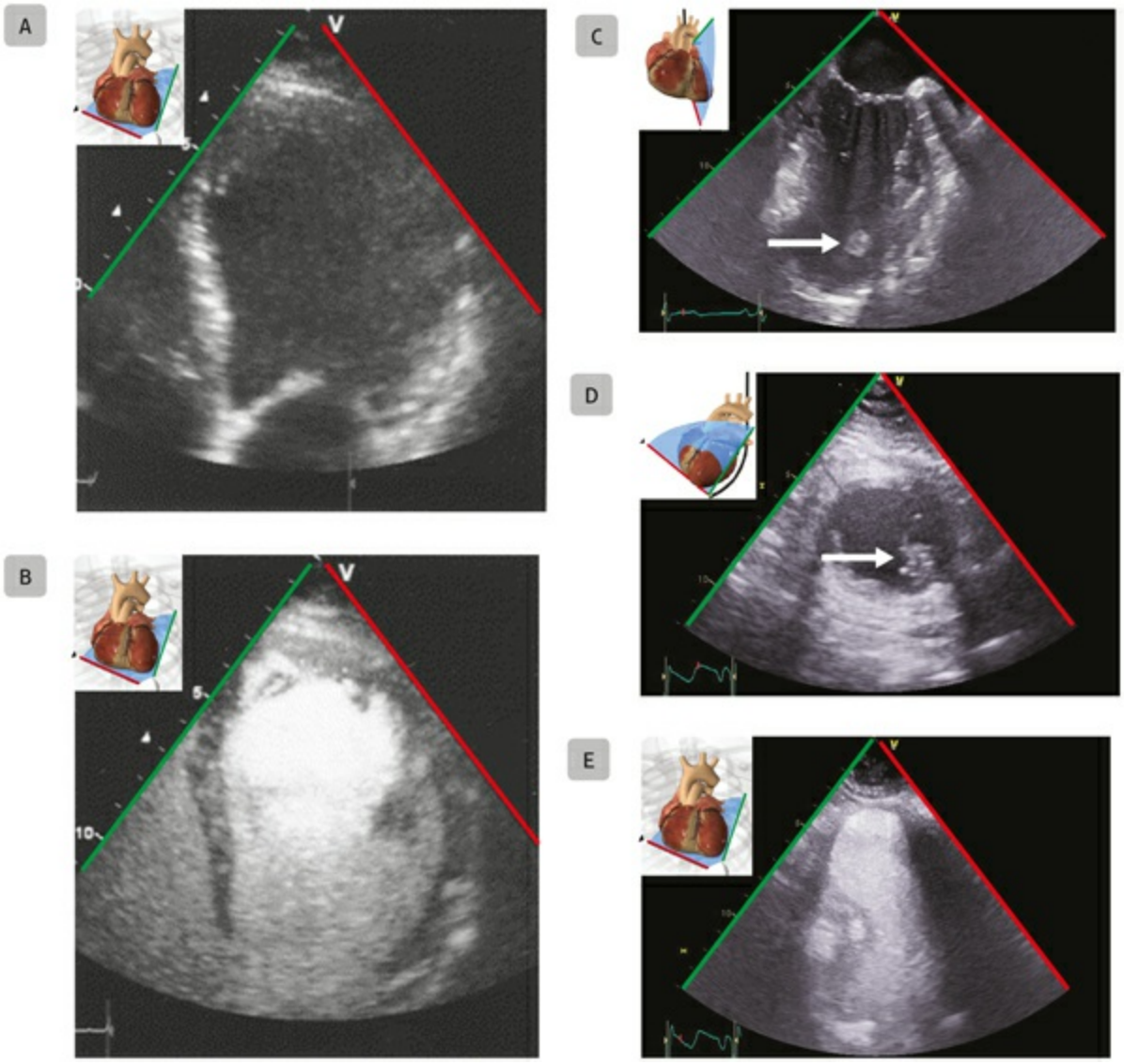

Fig. 15.7 . Echo contrast. (A,B) Apical four-chamber views with zoom of the left ventricle (LV) before (A) and after (B) intravenous injection of echocontrast (Definity™). Note the absence of an apical thrombus when using contrast. (C)(text missing)

Table 15.3 Doppler-Derived Hemodynamic Data.

Cardiac output =	π (LVOT)^2/4 x LVOT VTI X heart rate
Right ventricular systolic pressure =	4 (peak tricuspid regurgitation velocity)^2
Pulmonary artery systolic pressure =	RVSP + right atrial pressure (in the absence of pulmonic stenosis)
Pulmonary artery end-diastolic pressure =	4(PREDV)^2 + right atrial pressure
Left atrial pressure =	SBP – 4 (Vmv)^2
Left ventricular end-diastolic pressure =	DBP – 4 (aortic regurgitation EDV)^2

Note: DBP, diastolic blood pressure; EDV, end-diastolic velocity; LVOT, left ventricular outflow tract; PREDV, pulmonary regurgitation end- diastolic velocity; RVSP, right ventricular systolic pressure; SBP, brachial systolic blood pressure measured with sphygmomanometry; Vmv, mitral valve regurgitant velocity; VTI, velocity time integral.

Cardiac Output

Determination of cardiac output (CO) is of great importance in the management of an unstable ICU patient. It is one of the main parameters that intensivists follow to manage patients in shock. It is described by the following equations (see **Figure 5.10**). [9]

$$\text{Cardiac index (L/min/m}^2\text{)} = \text{CO/Body surface area}$$

$$\text{Cardiac output (L/min)} = \text{Stroke volume x Heart rate}$$

In the absence of significant aortic regurgitation, stroke volume can be calculated by the product of LV outflow tract (LVOT) area [= 0.785 (LVOT diameter)^2] and the velocity time integral (VTI) across this area.

$$\text{Stroke volume (mL)} = \text{LVOT area x VTI}$$

Left ventricular outflow tract is measured in the parasternal long-axis view zoomed on the aortic valve (**Figure 15.8 A**). The LVOT VTI is measured with pulsed-wave (PW) Doppler in the apical five-chamber view by placing the sample volume in the middle of LVOT, 1 cm below the aortic valve. The Doppler beam needs to be aligned with the LVOT and the Doppler envelope is then traced to measure the VTI (**Figure 15.8c**).

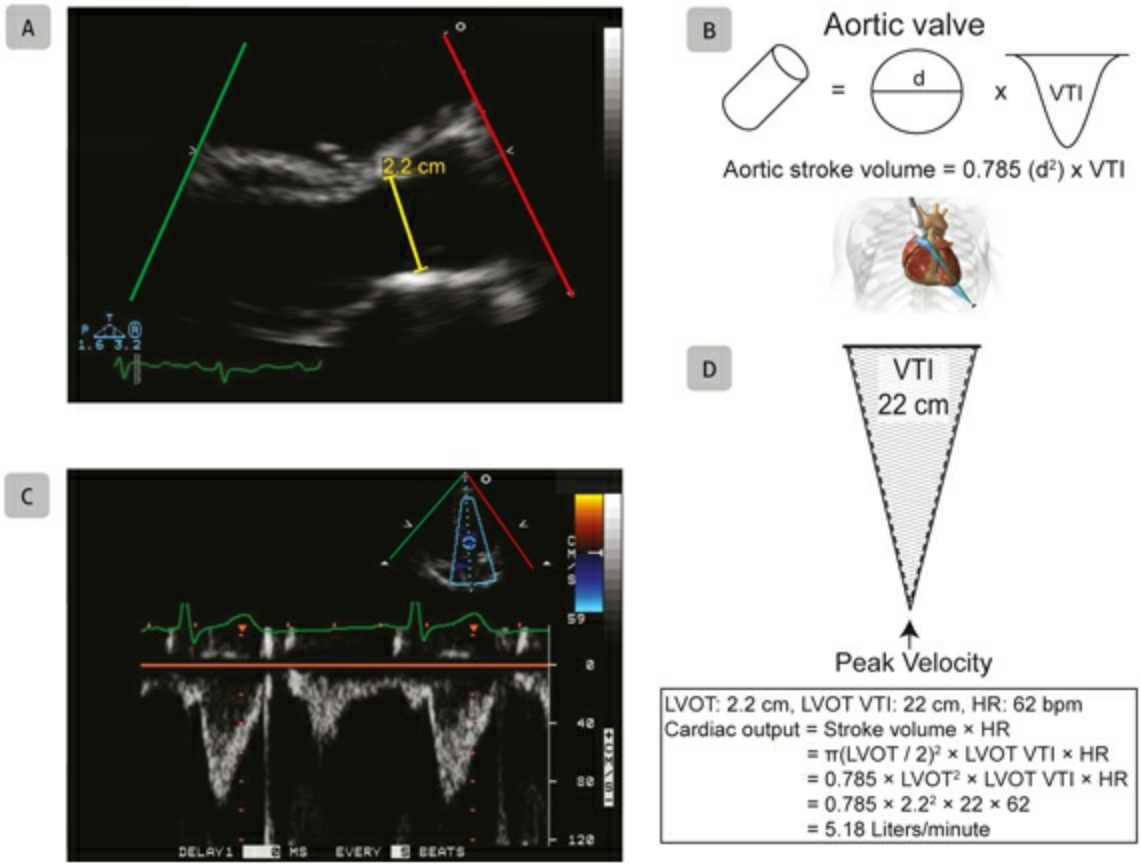

Fig. 15.8 . Cardiac output (CO). Calculation of CO involves (A) measurement of the aortic annulus diameter (d) in a zoom of the left ventricular outflow tract (LVOT) from the parasternal long-axis view. (B) Formula to calculate CO is shown. (C,D) The velocity of the LVOT is obtained from the apical five-chamber view. (D) Tracing the outline of the velocity trace gives the time integral (VTI) of the LVOT. HR, heart rate. (Adapted with permission of Denault *et al.* [9] *)*

Some pitfalls of Doppler-derived cardiac index calculation need to be considered. First, it is important to have a good image with the true long axis of the LVOT and to use the zoom of LVOT to minimize measurement errors. Any error in the measurement of LVOT diameter is magnified as this number is squared, thus causing significant variability. Second, it is possible that the LVOT area may be elliptical instead of circular, which is best determined by 3D imaging. Third, the ultrasound beam to measure LVOT VTI needs to be completely aligned with LVOT, otherwise the cardiac index will be underestimated. Lastly, if the patient has arrhythmias, the LVOT VTI will vary during each beat. It is important to average at least 5–10 measurements for such patients.

Tricuspid Regurgitation and Right Ventricular Systolic

Pressure

Doppler echocardiography can assess right ventricular systolic pressure (RVSP) and pulmonary artery systolic pressure (PASP) (see **Figure 7.30**) using the right atrial pressure (RAP) by applying the Bernoulli equation:

$$RASP = PASP = 4(V_{TR})^2 + RAP$$

The peak tricuspid regurgitation (TR) velocity (V_{TR}) can be obtained with continuous wave (CW) Doppler across the tricuspid valve guided by color Doppler in multiple views (RV inflow view, parasternal short-axis (SAX) view at the base, and apical four-chamber view). [9] The RAP is estimated from respiratory variations in the inferior vena cava (IVC) diameter (further discussed under Volume Status Assessment). In the absence of pulmonic stenosis or right ventricular outflow tract (RVOT) obstruction, RVSP equals PASP. The TR envelope needs to be complete to accurately assess the RVSP If the TR signal is suboptimal, then injection of intravenous saline bubbles may enhance the signal. Again, if the ultrasound beam is not completely aligned with the TR color Doppler signal, the RVSP will be underestimated.

Systemic Arterial Pressure

Transthoracic echocardiography can be used also to estimate systemic arterial pressure [9] in situations where arterial blood pressure is difficult to obtain clinically or discordant with the patient's clinical condition (see **Figure 9.12**). By using CW Doppler interrogation across a regurgitant mitral valve, a pressure gradient can be obtained. This pressure gradient represents the difference of systolic pressure between the left atrium (LA) and LV. The sum of the pressure gradient and the LA pressure gives the LV end systolic pressure (LVESP). Without LVOT obstruction or aortic valve stenosis, the LVESP corresponds to systemic arterial blood pressure.

RIGHT VENTRICULAR FUNCTION ASSESSMENT

The RV is about two-thirds of the LV size and is divided into three parts: inlet, apical trabecular, and outlet. [14] Because of its non-ellipsoid anatomy, the geometric assumptions used for LV mass and volume measurement are

not applicable to the RV. Functional assessment of the RV is of utmost importance in patients with cardiac disease. Right ventricular dysfunction carries the worst prognosis in patients with LV dysfunction, [15] massive pulmonary embolism, [16] and acute respiratory distress syndrome (ARDS). [17] Imaging the RV is quite challenging because of its crescentic shape, wrapping around the LV, irregular endocardial surface, and complex contraction pattern. The RV is assessed in the left parasternal LAX and SAX, RV inflow, apical four-chamber and subcostal LAX and SAX views. [18] All views are complementary and should be obtained in order to fully evaluate RV function and size.

A qualitative assessment of RV size and function is commonly performed during TTE examination. A visual comparison of RV and LV size can be made in an apical four-chamber view. Right ventricular dilatation is defined as moderate when the ratio between RV and LV end-diastolic areas is >0.6 and as severe for ratio >1 (**Figure 15.9**). [3] , [18] However, RV size can be artificially increased if the probe is not positioned at the apex as may occur in the apical four-chamber view. In general, RV dilatation is confirmed when at least two different views show increased RV size (**Figure 15.10**).

Right ventricular function is often overlooked during TTE examination. Determination of RV systolic function is similar to LV, but more challenging. A qualitative assessment mostly relies on the thickening and endocardial excursion of the free wall and interventricular septum (IVS).

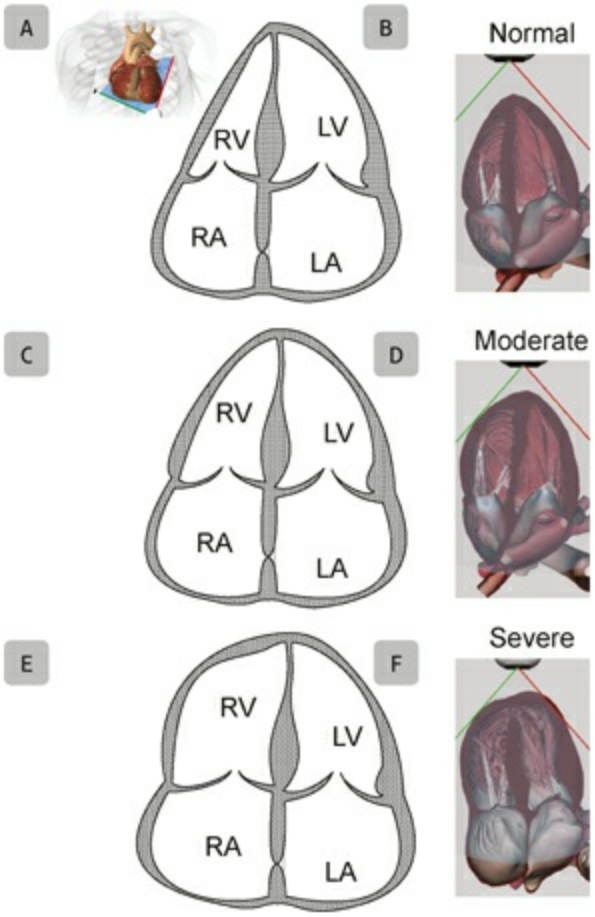

Fig. 15.9 . Right ventricular assessment. Apical four-chamber views and corresponding views from the Vimedix simulator are shown for (A,B) a normal patient, (C,D) a patient with moderate dilatation of the right ventricle (RV) from pulmonary hypertension, and (E,F) severe RV dilatation from a ventricular septal defect. LA, left atrium; LV, left ventricle; RA, right atrium. (Adapted from Rudski *et al.* [18] *)*

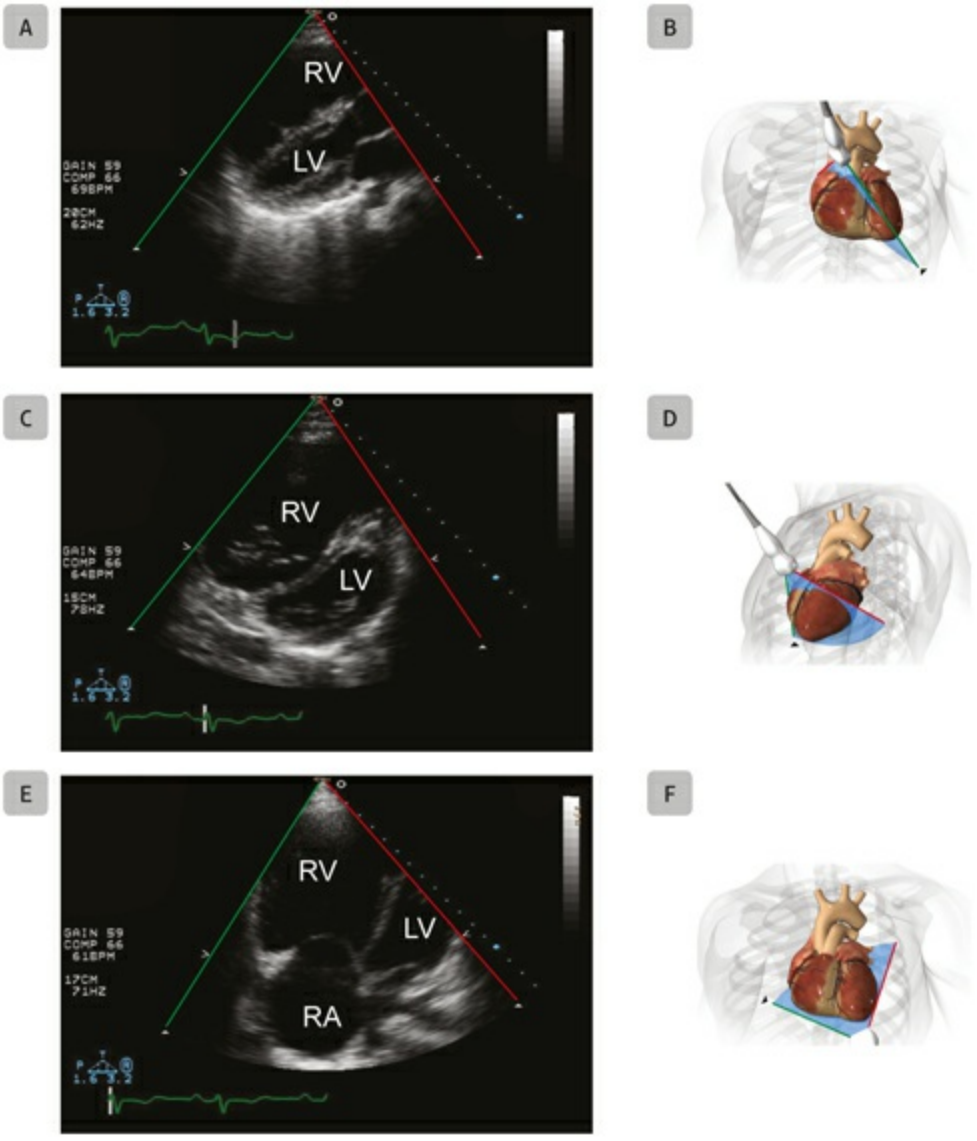

Fig. 15.10 . Right ventricular dysfunction. A 67-year-old male presented to the emergency room with hemodynamic instability and underwent a transthoracic echocardi-ography examination. (A,B) The parasternal long-axis view revealed acute dilatation of the right atrium (RA) and the right ventricle (RV). (C,D) The left ventricle (LV) was compressed by the RV as shown in the parasternal mid-papillary short-axis view. (D,E) The apical four-chamber view confirmed RV and RA dilatation. Ancillary testing revealed the presence of pulmonary artery emboli.

A: https://youtu.be/xeCqovPFuQQ

C: https://youtu.be/G_bVaa7Jp-Q

E: https://youtu.be/X_FOoWw_7C4

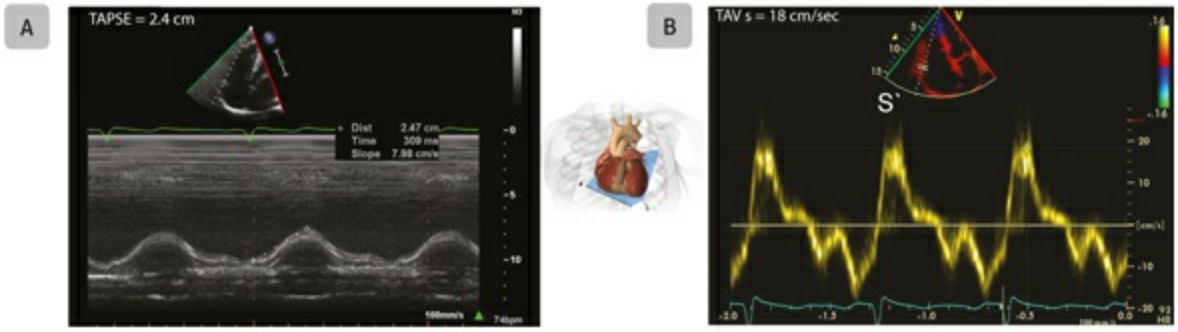

Fig. 15.11 . Right ventricular function indices. (A) Tricuspid annular plane systolic excursion (TAPSE) of >1.7 cm is obtained from an apical four-chamber view. (B) Normal tricuspid annular velocities (TAV) by tissue Doppler, the systolic (S') component of >10 cm/s is obtained from the lateral triscupid annulus in an apical four-chamber view. (Reproduced with permission from Denault *et al.* [9] *)*

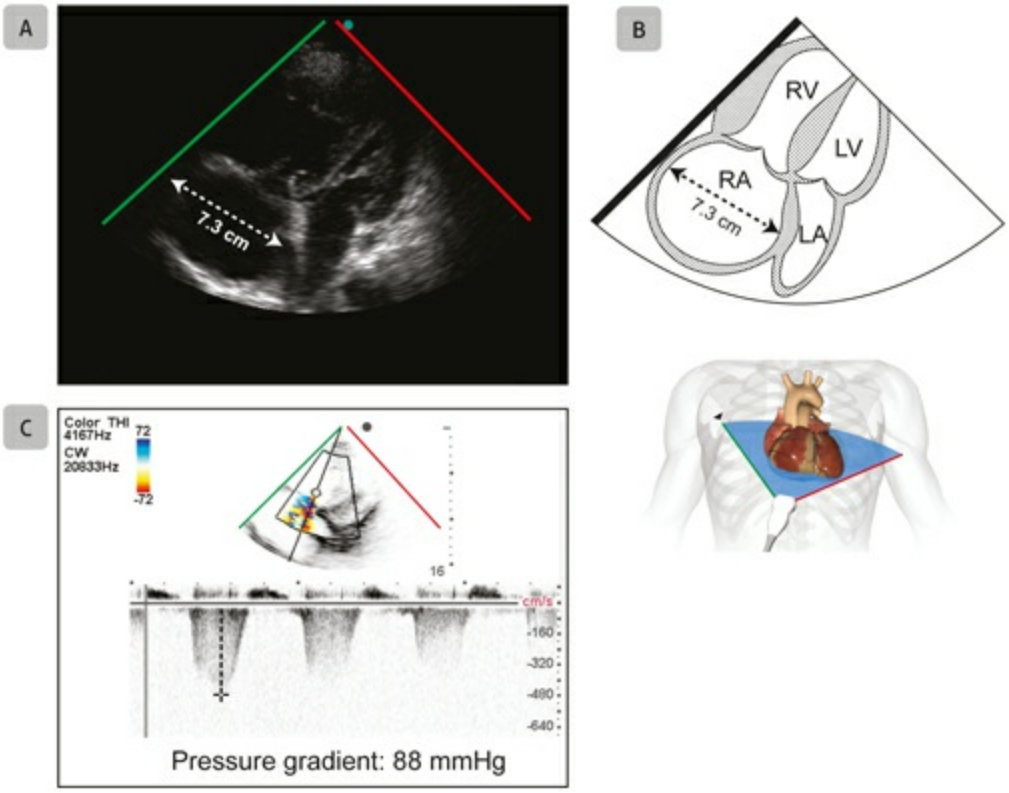

Fig. 15.12 . Right ventricular dysfunction and pulmonary hypertension. A 67-year-old male presented with hemodynamic instability to the emergency room. (A,B) Subcostal view examination revealed dilatation of the right atrium (RA) and the right ventricle (RV). The left ventricle (LV) was compressed by the RV. (C) Using continuous wave Doppler, a transtricuspid valve gradient of 88 mmHg was present. Ancillary testing revealed the presence of pulmonary artery emboli. LA, left atrium. (Reproduced with permission from Denault *et al*. [9])

A: https://youtu.be/Kjx7j8uZLNo

Regional wall motion can be assessed quantitatively by using tricuspid annular plane systolic excursion (TAPSE) and systolic tricuspid annular velocity (TAV) measured using tissue Doppler mode. Both measurements are obtained in the apical four-chamber view and have been validated with radionuclide angiography. A Doppler volume sample or M-mode cursor is placed at the lateral tricuspid annulus and the measurement is made at the peak of longitudinal velocity of the tricuspid annulus during systole. Tricuspid annular plane systolic excursion less than 17 mm [10] , [19] and systolic

TAV less than 10 cm/s denote RV systolic dysfunction (**Figure 15.11**). [20] There is, however, a paucity of data regarding these measurements and outcomes in critically ill patients.

Inter-ventricular septal movement abnormalities provide important information regarding RV loading. In a normal heart, the round shape of the LV is maintained during the entire cardiac cycle given the higher pressure within the LV cavity. When RV pressure is increased, the IVS shifts towards the LV, with the shift proportional to the pressure in the RV cavity. The higher the RV pressure, the greater is the shift towards the LV. The LV appears as D-shaped and is better identified in parasternal SAX view. In the presence of RV pressure overload, the D-shape is maintained in both systole and diastole. In contrast, RV volume overload only leads to D-shape during diastole (see **Figure 5.12**). Occasionally, focused TTE can identify RV dilatation, D-shape in both systole and diastole, and a free floating echo dense mass, all features that strongly suggest massive pulmonary embolism. However, in the absence of thrombus or mobile mass in the right side of heart, TTE is not the diagnostic imaging modality to exclude pulmonary embolism. [3] , [21] Other conditions, such as tension pneumothorax, RV infarct, lung atelectasis, ARDS, pre-existent pulmonary hypertension, TR, pulmonic stenosis, mitral stenosis, and left-right shunt, can also induce RV dilatation, dysfunction, and right atrial (RA) dilatation from volume or pressure overload (**Figure 15.12**). In such conditions, the broad differential warrants a complete TTE examination.

VOLUME STATUS ASSESSMENT

The assessment of volume status is of great importance in the management of critically ill patients and remains a difficult task. Despite extensive research, the accurate diagnostic test for hypovolemia remains to be identified. Central venous pressure (CVP) is commonly used to estimate the intravascular volume status. A low CVP suggests low intravascular volume in patients without mechanical ventilation support. The Surviving Sepsis Campaign emphasizes the pivotal role of early aggressive fluid resuscitation in septic shock and suggests that fluid administration should achieve CVP >8–12 mmHg. [22] However, this concept is being challenged, [23] as the consequences of fluid overload are increasingly recognized. [24] , [25]

Right atrial pressure correlates with CVP and can be estimated by the inspiratory collapse in IVC diameter. [26] Spontaneous inspiration induces negative intrathoracic pressure that decreases RA pressure despite an increase in venous return. This is transmitted back to the IVC and with normal intravascular volume causes the IVC diameter to decrease. This phenomenon is exaggerated with low intravascular volume. In contrast, in patients with high intravascular volume, an increased RA pressure results in IVC dilatation and reduced inspiratory IVC collapse. The subcostal view is the most useful view to scan the IVC in its long axis below the diaphragm. Its diameter is measured at 0.5–3 cm proximal to the junction of RA in end expiration (**Figure 15.13**). The IVC collapse is measured when the patient is asked to sniff. Its collapsibility is measured as the ratio of the sniff IVC diameter over expiratory IVC diameter. A ratio greater than 50% combined with a diameter less than 21 mm suggests normal RA pressure (range, 0–5 mmHg). [26] The cut-off values have recently been published in the ASE guidelines; although these parameters perform well in estimating low or high RA pressure, they are less accurate in intermediate values. Also, these parameters have only been validated in patients without mechanical ventilation support. In some patients, the presence of chest tubes or dressings may prevent access to the subcostal view. Fortunately, since the distal portion of the IVC is intrahepatic and the liver is large, imaging through the liver from any lower right intercostal position provides an acoustic window to the IVC (see **Figure 16.15**).

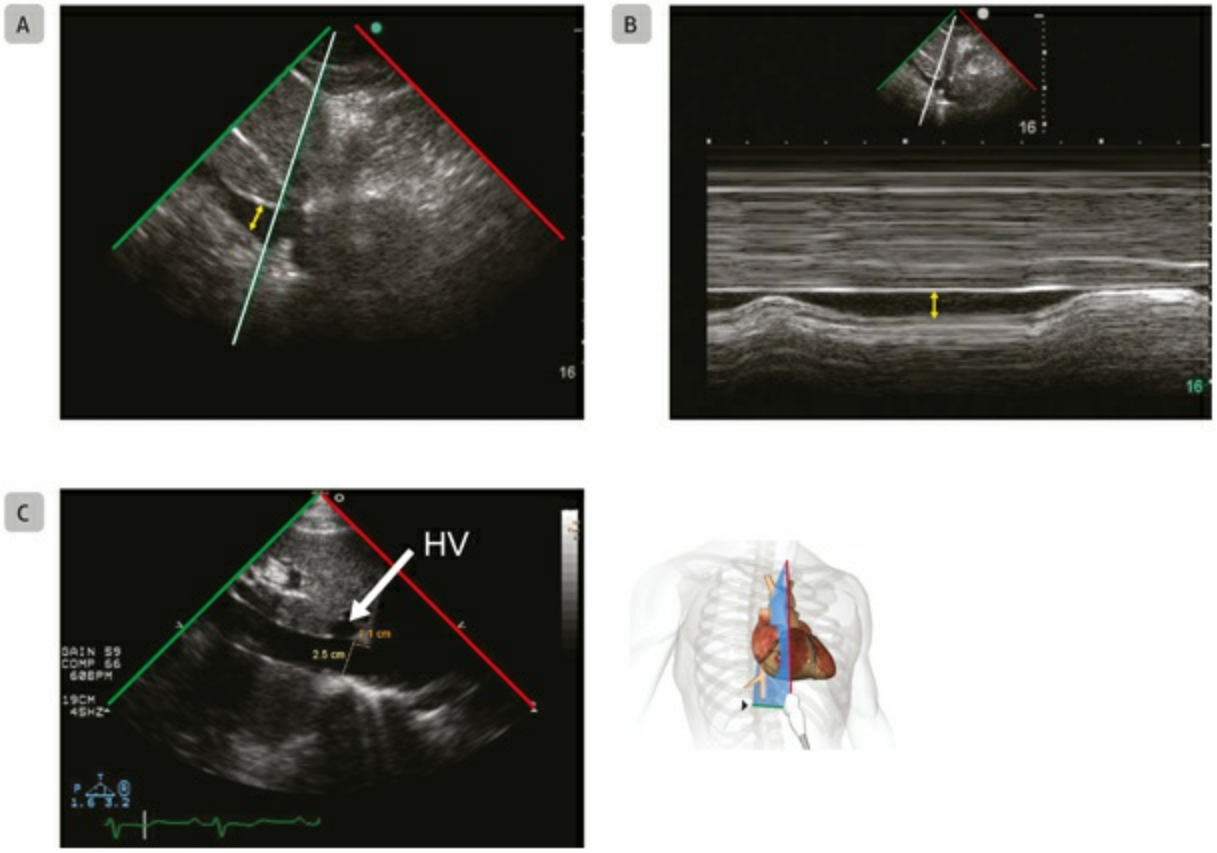

Fig. 15.13 . Inferior vena cava (IVC) diameter. Subcostal longitudinal views of the IVC with respiratory variation are shown with (A) 2D and (B) M-mode. (C) The IVC diameter is measured within 1.5 cm of the IVC-right atrial junction just before the hepatic vein (HV). (Reproduced with permission from Denault *et al.*[9])

A: https://youtu.be/5dub12TmYFs

B: https://youtu.be/pyhYN_I7rHc

The ability to image the IVC in the vast majority of patients justifies our choice of the IVC, rather than the heart, for this initial portion of the ultrasound examination in a patient in shock (see Chapter 9, Basic Hemodynamic Assessment).[2],[4] There are, however, limitations for using the

IVC to estimate mean systemic venous pressure (see **Table 9.3**). In contrast to a spontaneously breathing patient, mechanical ventilation causes reversed changes in the IVC during the respiratory cycle. A normal patient receiving positive pressure ventilation has an increase in IVC size during inspiration (from increased intrathoracic pressure) and decrease in size during expiration. Thus, any changes in IVC diameter can still be used to assess fluid responsiveness, albeit as a function of IVC distensibility. [27]

In patients with mechanical ventilation support, other echocardiographic/Doppler markers such as respiratory variation of peak LVOT velocity [28] or superior vena cava (SVC) size variation (assessed by TEE) have been described as good predictors for volume responsiveness in patients with septic shock. [29] In practice, we use PW Doppler variation of the SVC with a linear probe to obtain the same information (**Figure 15.14**). Volume responsiveness is defined as a 15% increase in cardiac index 30 minutes after volume expansion. A variation of peak velocity >12% allows identification of volume responders with a sensitivity of 100% and specificity of 89%. A number of caveats exist when using these markers for volume responsiveness: first, patients must be mechaanically ventilated with 8–10 mL/kg of tidal volume and application of these dynamic markers is questionable in patients with ARDS treated with lung protective ventilation (tidal volume less than 8 mL/kg); second, patients must be deeply sedated; third, patients must have preserved LV and RV function and must be in sinus rhythm; finally, in most studies change of in CO after volume expansion was measured only with 2D and Doppler method and has not systematically been validated with thermodilution. Mayer *et al.* [30] showed only a moderate correlation between changes in CO with thermodilution and TTE. The accuracy of TTE to measure the change in CO induced by volume expansion has not clearly been demonstrated. Finally, in vasodilated patients with adequate blood pressure, volume responsiveness might not always warrant volume but vasopressors. In those patients excessive fluid will lead to increased extracellular fluid and edema which can complicate their evolution. [24]

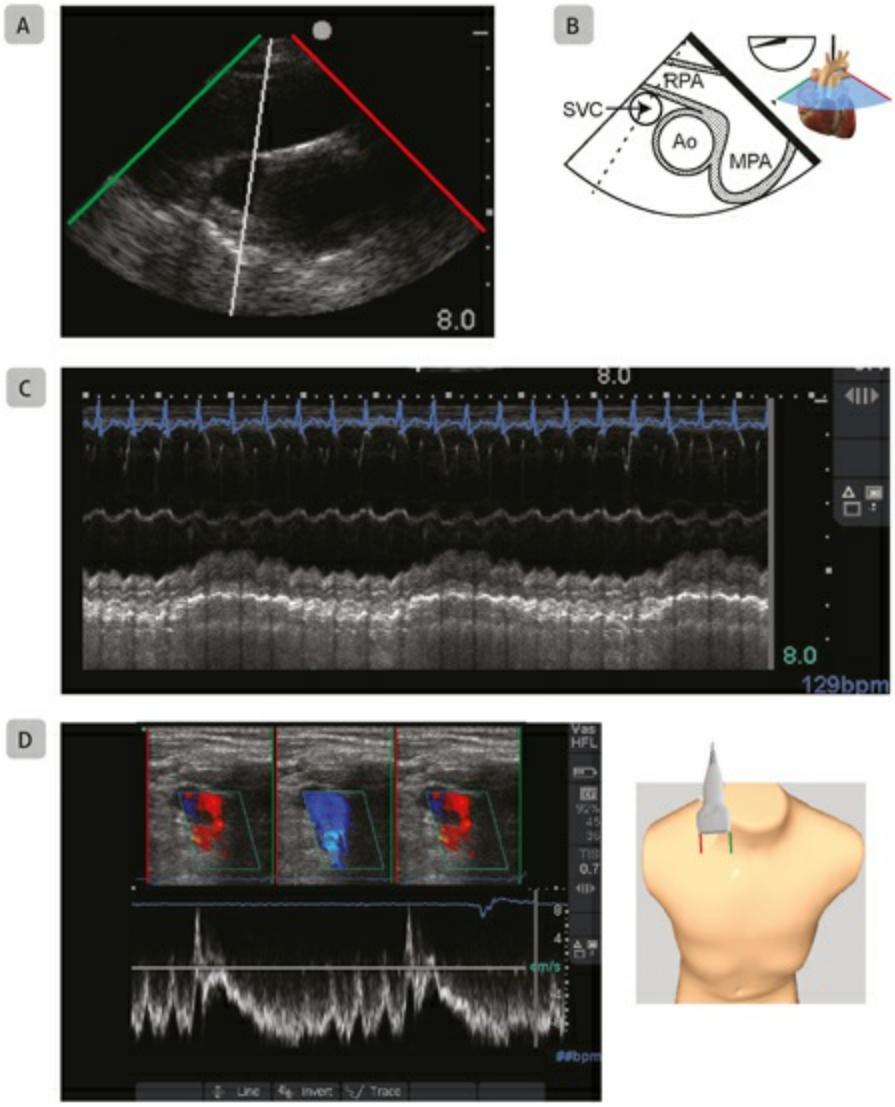

Fig. 15.14 . Respiratory variation of the superior vena cava (SVC). A 76-year-old male in the intensive care unit is dialyzed for 1.8 liters fluid removal. (A,B) The transesophageal, mid-esophageal ascending aorta (Ao) short-axis view with (C) M-mode of the SVC shows significant respiratory variation of the SVC diameter. (D) With a linear probe positioned in the right cervical region over the distal internal jugular, the phasic respiratory changes in Doppler signals can be appreciated. MPA, main pulmonary artery; RPA, right pulmonary artery. (Reproduced with permission from Denault *et al.* [9])

A: https://youtu.be/OBQtrfBCWHk

D: https://youtu.be/uYn7120L5-E

PERICARDIAL EFFUSION

Identification of pericardial effusion is easily achieved with focused TTE. The subcostal view is commonly used for this purpose in patients with unstable hemodynamics. Other views (parasternal and apical) can assess the extent of pericardial effusion and determine its hemodynamic impact. Studies show that there is a substantial agreement between non-cardiology residents, intensivists, and cardiologists for identification of moderate to large pericardial effusion. [31] , [32] However, agreement for pericardial effusion with significant hemodynamic compromise or diagnosis of tamponade remains to be established. Some TTE studies comparing intensivists and cardiologists include only RV diastolic compression as a sign of tamponade [33] as it has high sensitivity (92%) and specificity (100%). [34] However, tamponade is a continuous process with progressive hemodynamic compromise, with RV diastolic collapse appearing late in the continuum. Relying on this single sign could cause delay in diagnosis and potential complications.

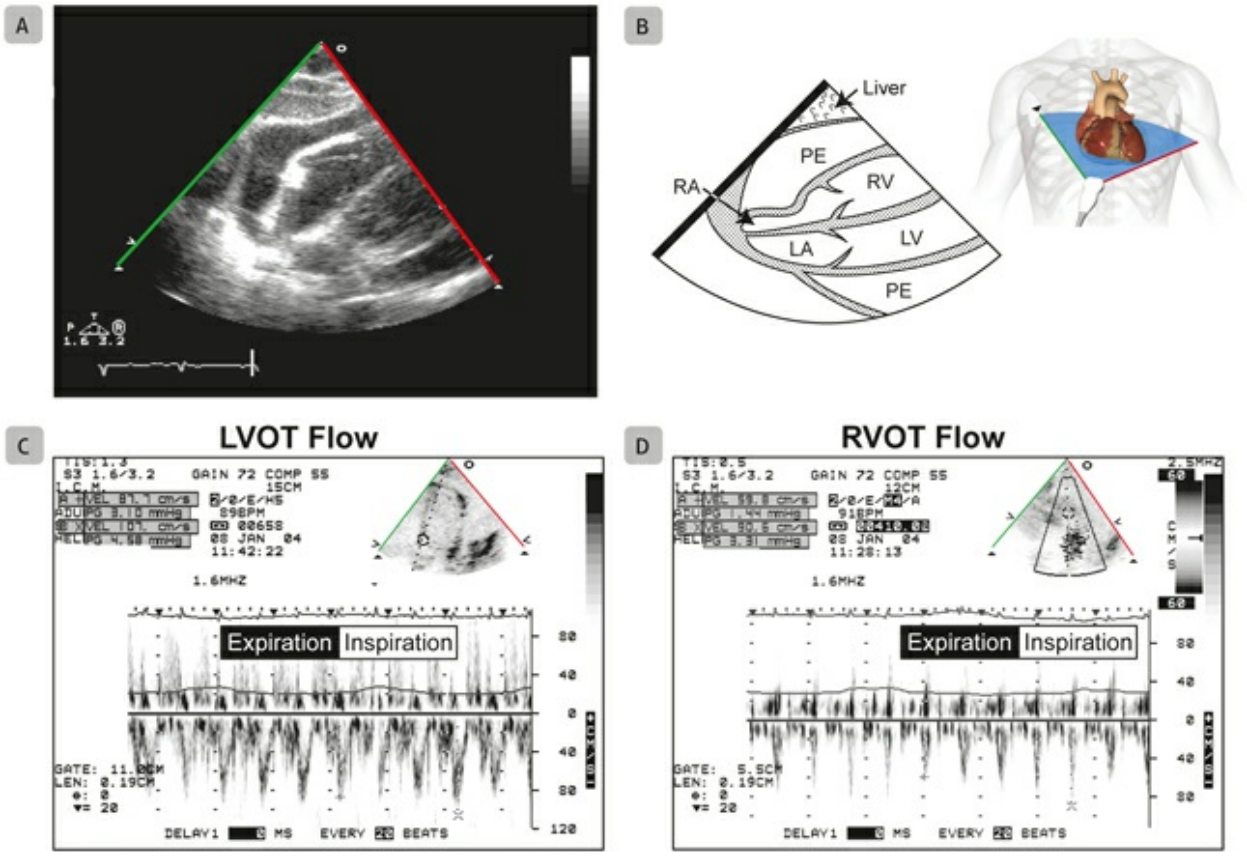

Fig. 15.15 . Cardiac tamponade. Cardiac tamponade occurs in a 53-year-old female treated for pericarditis. (A,B) Transthoracic subcostal view shows right atrial (RA) collapse. (C,D) Pulsed-wave Doppler examination demonstrates that the right ventricular outflow tract (RVOT) velocities increase with spontaneous inspiration with opposite respiratory changes in the left ventricular outflow tract (LVOT) velocities. LA, left atrium; LV, left ventricle; PE, pericardial effusion; RV, right ventricle. (Reproduced with permission from Denault *et al.* [9] *)*

A: https://youUbe/GuA5j7XfLAE

Identification of tamponade physiology is complex and includes various TTE Doppler and 2D markers such as compression of right- and left-sided cavities, dilated IVC without respiratory collapse, respiratory variation of tricuspid and mitral E velocities, and respiratory variation of peak LVOT velocity (**Figure 15.15**). Pericardial effusion should be differentiated from left pleural effusion. In pericardial effusion, fluid is present between the LA and the aorta. In pleural effusion, the fluid is anterior to the aorta (**Figure**

15.1 6A, and see **Figure 17.3**). Pericardial fluid should also be differentiated from ascites. In ascites, fluid will also be found in the dependent regions and the aspect of the liver in some patients will point toward a diagnosis of cirrhosis (**Figure 15.16 C**). Some of these markers are not applicable to all patients, in particular those who are mechanically ventilated, have mechanical prostheses, postcardiotomy patients with loculated clots and patients with atrial fibrillation, who may need a comprehensive TTE or TEE. More detail on pericardiocentesis can be found in Chapter 17, Ultrasound for Critical Care Procedure.

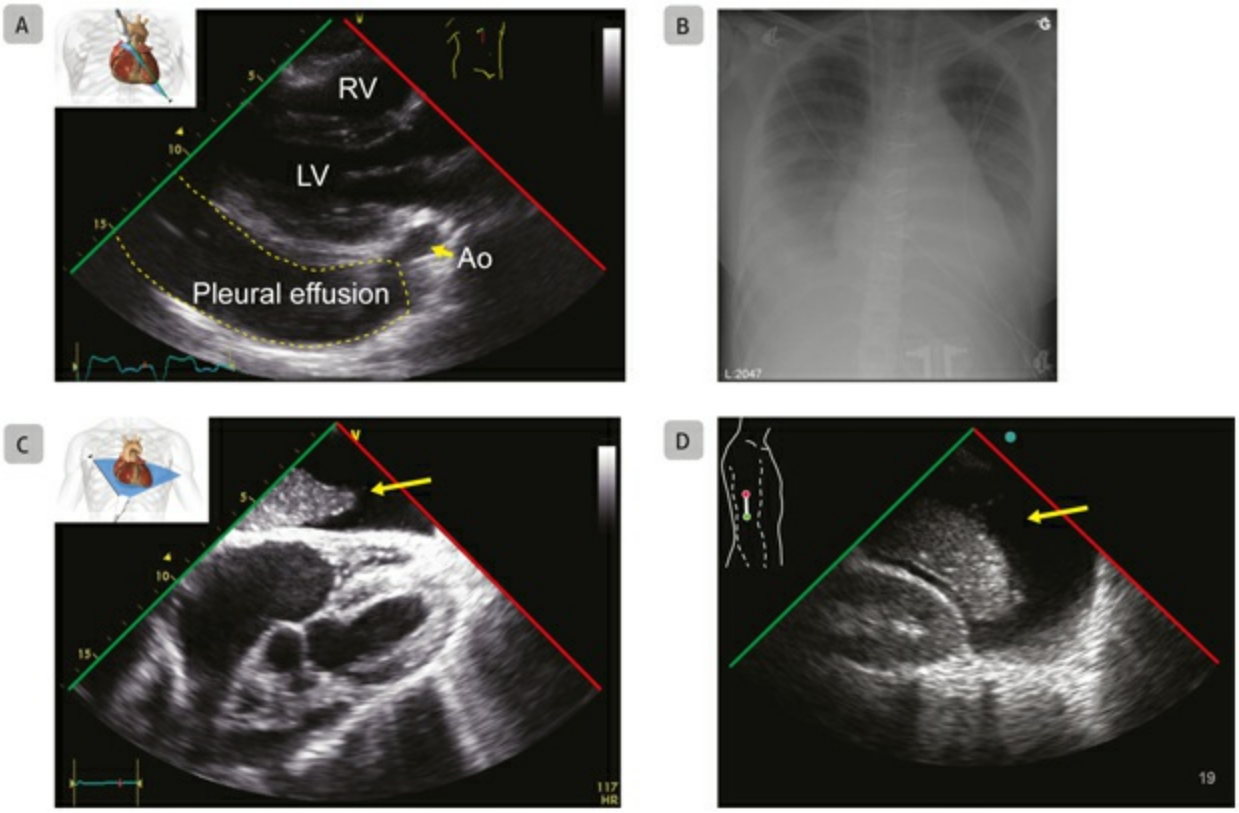

Fig. 15.16 . Pleural effusion. (A) Parasternal long-axis view of a patient with a left-sided pleural effusion and (B) corresponding chest radiograph. Note the absence of fluid between the left atrium and the aorta (Ao) which would indicate a pericardial effusion. (C) Subcostal view of a patient with peritoneal fluid (arrow) secondary to cirrhosis. (D) Left coronal midaxillary view demonstrates ascites (arrow) and a cirrhotic liver. LV, left ventricle; RV, right ventricle.

A: https://youtu.be/7eZ8XUI1m98

C: https://youtu.be/MjAJeO7sXzU

D: https://youtu.be/6n08oF1ESsA

CARDIAC ARREST

The use of focused TTE during cardiac arrest of unknown origin is increasing in the emergency department and ICU. Its role is two-fold: first, focused TTE can rapidly identify reversible causes of cardiac arrest (tamponade, massive pulmonary embolism, hypovolemic shock, fine ventricular fibrillation) and second, it can provide prognostic information during resuscitation. In the prehospital setting, patients presenting with asystole as the initial rhythm and no ventricular contraction on TTE despite aggressive resuscitative efforts have a dismal survival rate. [35] Bedside TTE can help differentiate true pulseless electrical activity (PEA) defined as absence of ventricular contraction despite the presence of electrical activity from pseudo-PEA defined as the presence of ventricular activity. Patients with true PEA have a poorer prognosis, with minimal likelihood of return of spontaneous circulation (ROSC), if there is persistence of absence of ventricular motion on TTE after initial resuscitation. [36] However, TTE findings should not be used as the sole basis for the decision to interrupt cardiopulmonary resuscitation (CPR) maneuvers. A meta-analysis undertaken by Blyth *et al.* [31] demonstrated that as a predictor of ROSC during cardiac arrest, TTE had a pooled sensitivity of 91.6% but a specificity of 80%. Therefore, absence of cardiac activity at any stage of resuscitation harbors only a significant lower probability of ROSC. The last international guidelines on advanced life support (ACLS) do not recommend the routine use of focused echo to guide resuscitation because of lack of data clearly demonstrating a benefit on survival outcome. [38] However, in the 2011 ACLS provider manual, it is

mentioned “that cardiac tamponade, tension pneumothorax, and massive pulmonary embolism cannot be treated unless recognized. Bedside ultrasound, when performed by a skilled provider, may aid in rapid identification in these conditions.” The guidelines also raised the concern that focused TTE could lead to early interruption of CPR. Therefore, additional data are needed to better elucidate this issue. An approach to hemodynamic instability applicable to both TTE and TEE is proposed in **Figure 9.23** .

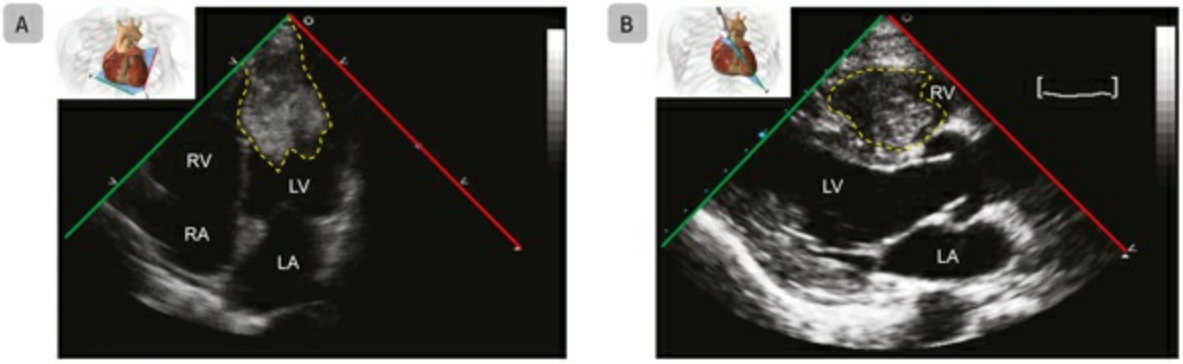

Fig. 15.17 . Thrombus. (A) Apical four-chamber view shows a large left ventricular thrombus post myocardial infarction. (B) Parasternal long-axis view shows a right ventricular outflow tract thrombus. LA, left atrium; LV, left ventricle; RA, right atrium; RV, right ventricle.

A: https://youtu.be/PioqeXTN8zc

B: https://youtu.be/rRLKUvfZOoQ

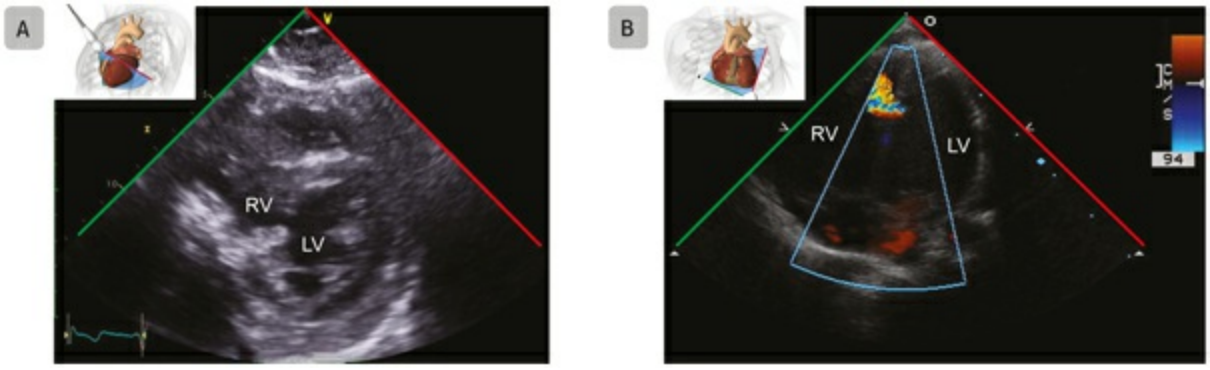

Fig. 15.18 . Ventricular septal defect (VSD). (A) Parasternal short-axis view of a VSD complicating an occlusion of the right coronary artery is shown. (B) Apical four-chamber view with color Doppler shows a muscular VSD with flow across the interventricular septum. LV, left ventricle; RV, right ventricle.

A: https://youtu.be/gMkOxqRxIjc

B: https://youtu.be/RjsvGi9qfV0

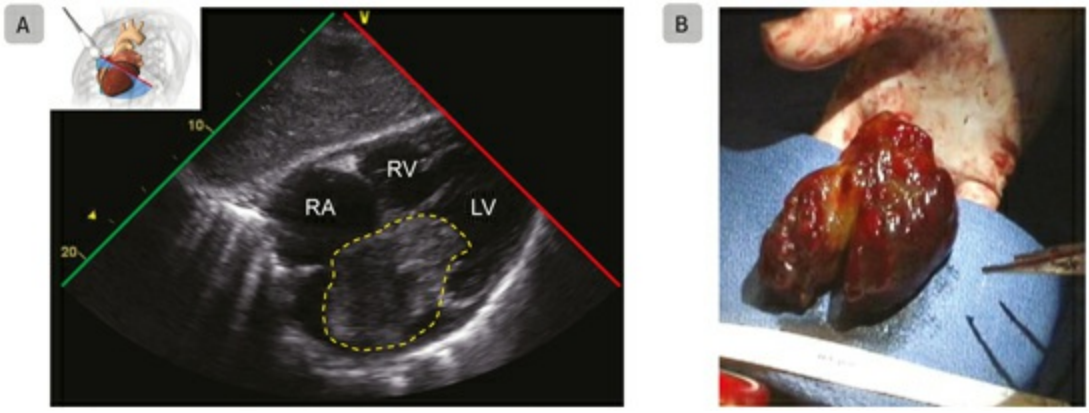

Fig. 15.19 . Myxoma. (A) Subcostal view of a 26-year-old female with a left atrial myxoma and (B) pathologic intraoperative specimen is shown. LV, left ventricle; RA, right atrium; RV, right ventricle. (Adapted from St-Pierre *et al.* [39])

A: https://youtu.be/8WMNXazhm1A

B: https://youtu.be/7R9GJTDJOIA

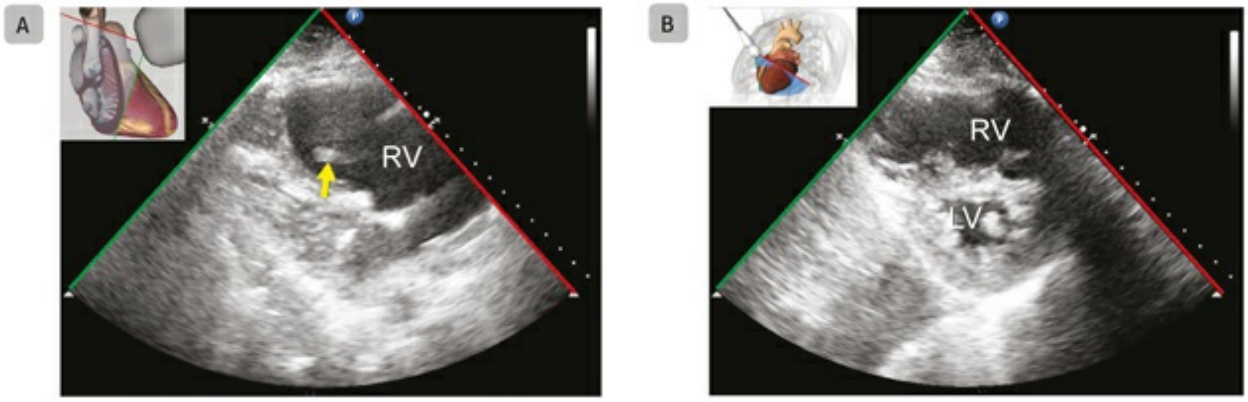

Fig. 15.20 . Pulmonary embolism. (A) Right parasternal long-axis view of the right ventricle (RV) shows a mobile clot in a patient with pulmonary embolism. (B) Parasternal short-axis view confirms the presence of RV dilatation with a D-shaped left ventricle (LV).

A: https://youtu.be/tkhclBBlkJI

B: https://youtu.be/KOIhylvn5rk

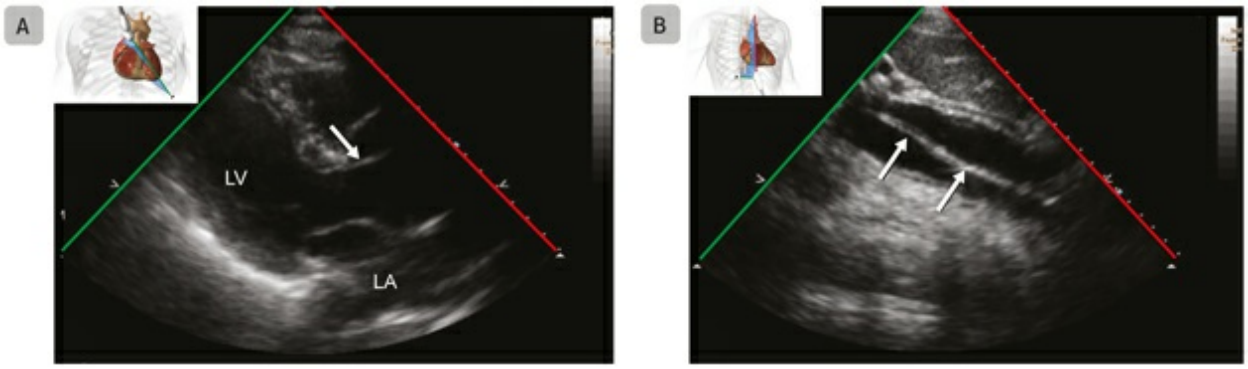

Fig. 15.21 . Aortic dissection. (A) Left parasternal long-axis view of a patient showing the origin of an aortic dissection (arrow) present in the ascending aorta. (B) Subcostal view of the descending aorta shows the true and false lumens in the abdominal aorta. The arrows are pointing to the dissecting membrane. LA, left atrium; LV, left ventricle.

A: https://youtu.be/MC10ox2Rx4w

B: https://youtu.be/qvfhFGB56fg

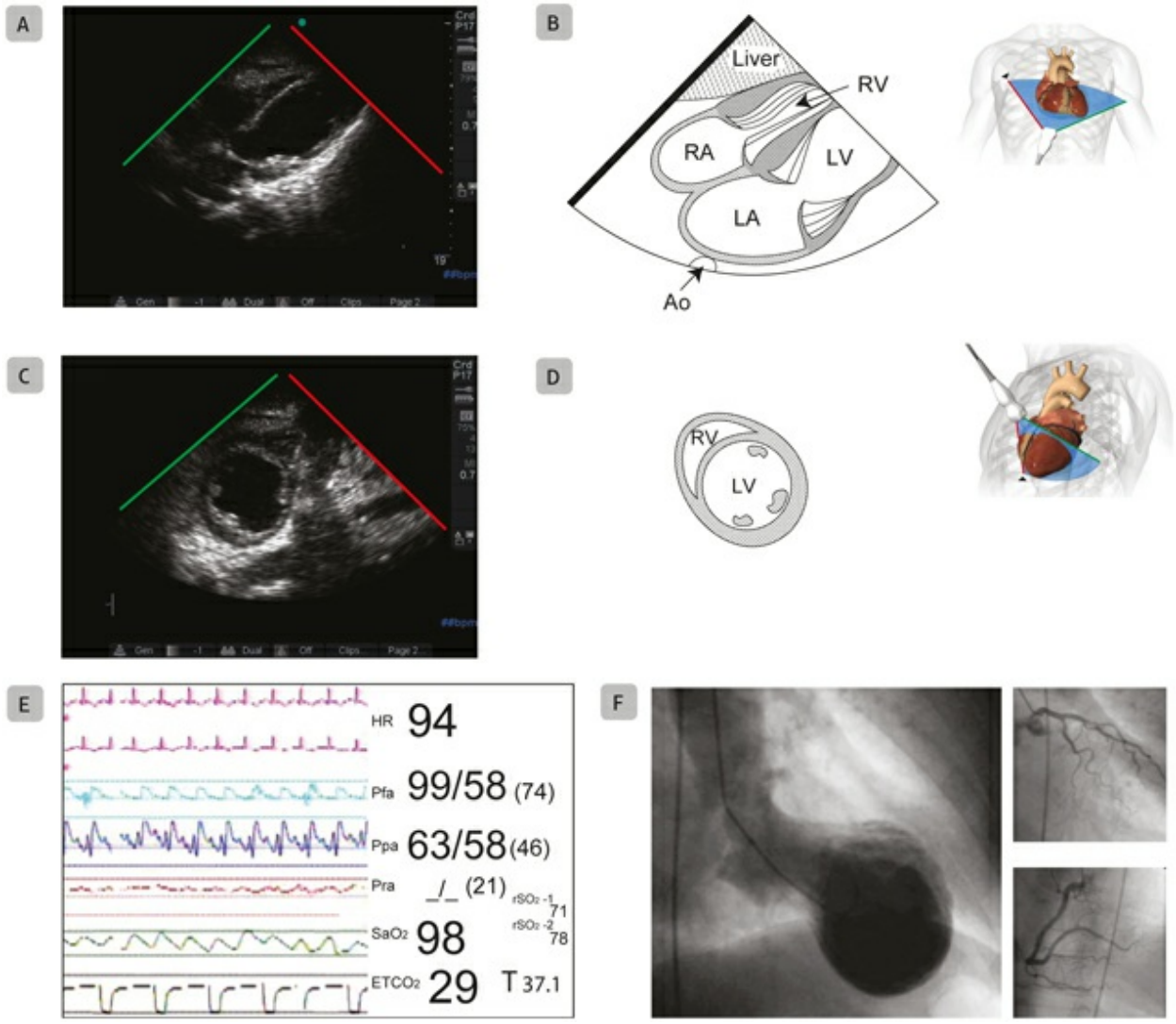

Fig. 15.22 . Takotsubo syndrome. Acute hemodynamic instability in a 73-year-old female after duodenal perforation required investigation. (A,B) A Focused Cardiac Ultrasound Study (FOCUS) using a subcostal view revealed the presence of severe left ventricular (LV) dysfunction with basal sparing typical of Takotsubo syndrome. (C,D) A parasternal short-axis view confirms abnormal LV function. The patient recovered completely the following week. (E) Hemodynamic conditions of the patient showed severe pulmonary hypertension. (F) Left ventriculography in a patient with stress-induced cardiomyopathy shows apical dilatation with normal left and right coronary arteries. Ao, aorta; $ETCO_2$, end-tidal carbon dioxide; HR, heart rate; LA, left atrium; Pfa, femoral artery pressure; Ppa, pulmonary artery pressure; Pra, right atrial pressure; Prv, right ventricular pressure; RA, right atrium; RV, right ventricle; rSO_2, regional cerebral oxygen saturation; SaO_2, oxygen saturation. (Reproduced with permission from Denault *et al.* [9])

A: https://youtu.be/s94AfseZixs

C: https://youtu.be/OjLU3CqWDJk

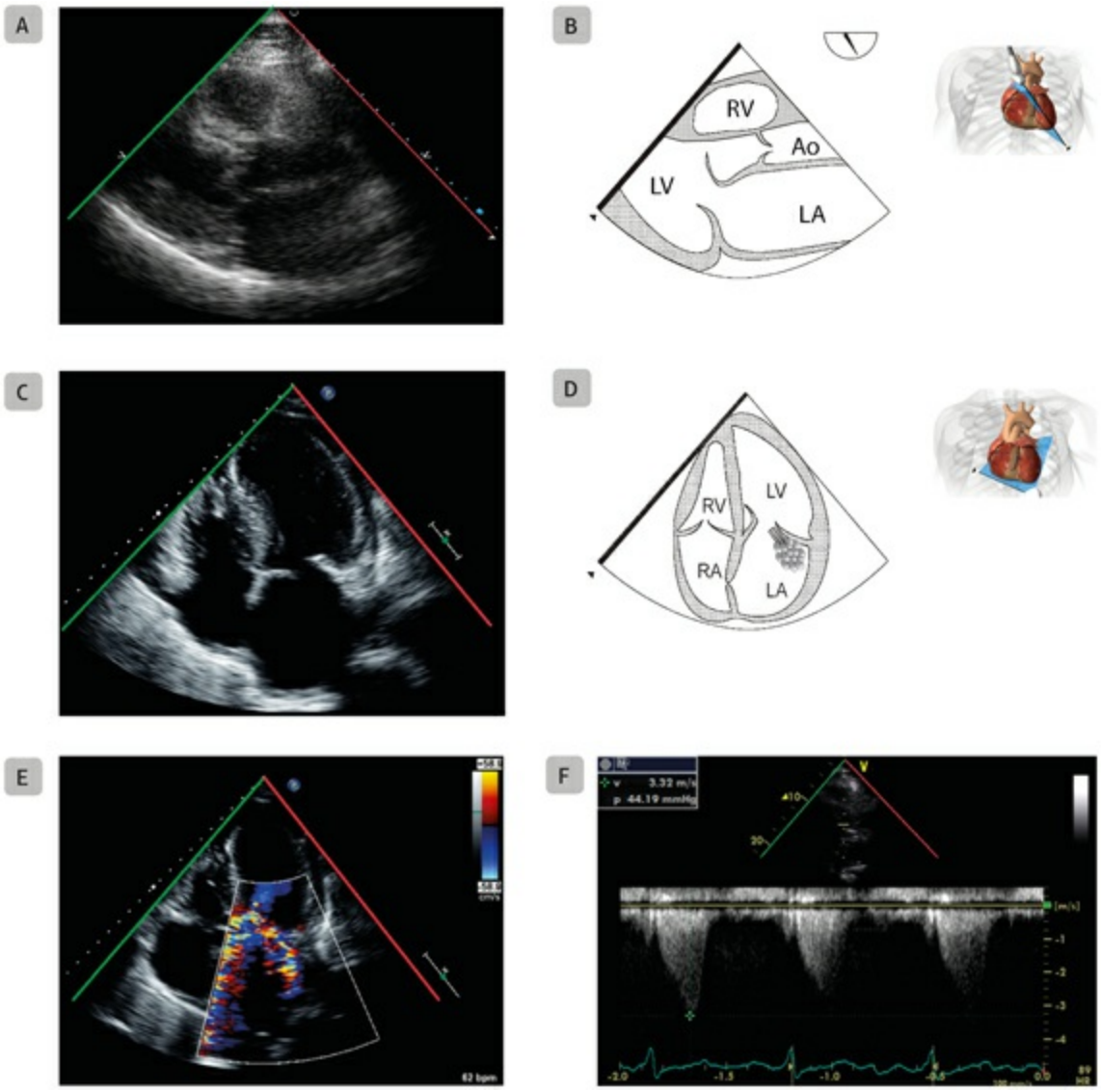

Fig. 15.23 . Outflow tract obstruction. (A,B) Parasternal long-axis view of a patient shows dynamic left ventricular outflow tract (LVOT) obstruction from systolic anterior motion of the anterior mitral valve leaflet. (C—E) Apical four-chamber view has displacement of the anterior mitral valve leaflet against the interventricular septum. This was associated with eccentric mitral regurgitation. (F) Dagger-shaped acceleration through the LVOT with 44 mmHg pressure gradient using continuous wave Doppler. Ao, aorta; LA, left atrium, LV, left ventricle; RA, right atrium; RV, right ventricle. (Adapted from Rochon

et al; [43] courtesy of Dr Gordon Finlayson).

A: https://youtu.be/gb7Cz-nbhGI

C: https://youtu.be/DibUsXr8PpE

E: https://youtu.be/JBiBwf2QQjA

CRITICAL TTE FINDINGS

Finally, several conditions should be recognized when evaluating cardiac function and unstable patients. Some of these, such as valvular pathologies, are beyond the scope of the focused examination and expertise should be sought. These conditions include complications of myocardial infarction, such as severe valvular insufficiency (see **Figure 7.13**), intracardiac thrombus (**Figure 15.17**), ventricular septal defects (**Figure 15.18**), and regional wall motion abnormalities. Abnormal intracardiac content such as tumors (**Figure 15.19**), vegetations, and right-sided thrombus (**Figure 15.20**) in pulmonary embolism can be easily identified, as well as aortic dissection (**Figure 15.21**) in patients with new onset acute chest pain. In hemodynamically unstable patients, Ta- kotsubo syndrome or brain-heart syndrome (**Figure 15.22**), [40] septic myocardial depression, [41] and right or LVOT obstruction (**Figure 15.23**) [42] , [43] should be evaluated when deciding to use inotropic agents or not. This is important as some patients may develop cardiac complications such as LVOT obstruction secondary to milrinone often used to treat vasospasm in subarachnoid hemorrhage (**Figure 15.24**). Treatment of the underlying cardiac disorder will lead to improvement in systemic cerebral blood flow hemodynamics. Finally, if cardiac function is

normal in an unstable patient, the clinician should extend the examination to the thorax (see Chapter 14, Critical Care Examination of the Respiratory System), the abdomen (see Chapter 16, Critical Care Examination of the Abdomen), and the vascular tree (see Chapter 18, Ultrasound-Guided Vascular Access and Examination).

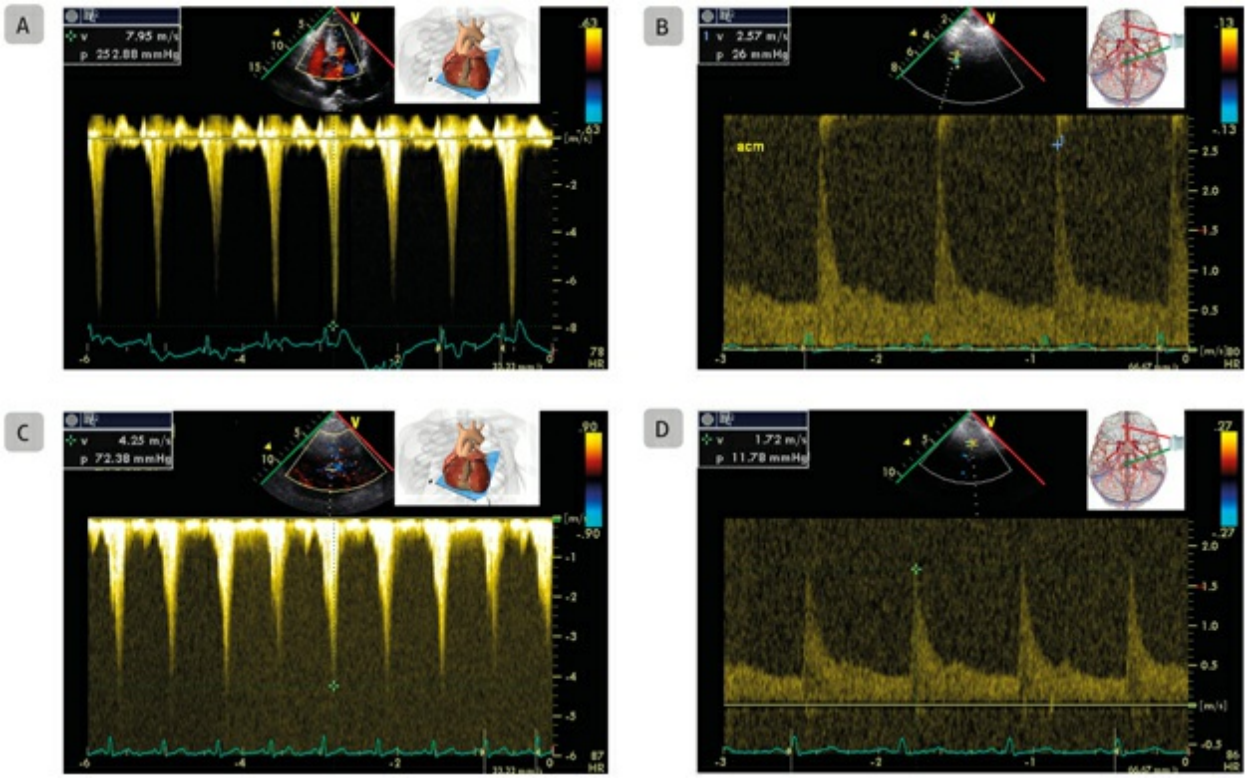

Fig. 15.24 . Left ventricular outflow tract (LVOT) obstruction. A 31-year-old male with subarachnoid hemorrhage receiving intravenous milrinone develops LVOT obstruction. (A) Note the significant pressure gradient (252 mmHg) and velocities (7.9 m/s) across the LVOT obtained using an apical five-chamber view. (B) The associated transcranial Doppler velocities of the right middle cerebral artery (MCA) was 2.57 m/s. Following a bolus of 500 mL of crystalloid and milrinone withdrawal, (C) the LVOT gradient drops to 72 mmHg, and (D) the right MCA velocity decreases to 1.72 m/s.

A: https://youtu.be/_Jmz9DsnYMU

A: https://youtu.be/kkSQMQUJgmc

CONCLUSION

Focused TTE has become an essential skill for critical care physicians to manage critically ill patients with unstable hemodynamics. It can identify various cardiac abnormalities, assess volume responsiveness and provide prognosis during resuscitation. However, focused TTE has its limits and could be misleading in some situations. For instance, a normal focused TTE in patients with shock does not exclude acute papillary muscle rupture or acute aortic dissection nor other mechanisms, such as septic shock or abdominal compartment syndrome. An approach to shock using both TTE and TEE is described in Chapter 9, Basic Hemodynamic Assessment. If echo findings do not explain the clinical condition of the patient, other diagnostic modalities are indicated. The most important thing to remember when performing focused TTE is to appreciate the operator's level of training in bedside ultrasound and not hesitate to ask for advanced expertise if necessary.

REFERENCES

1. FeigenbaumH.. Evolution of echocardiography. *Circulation*1996; *93*: 1321–7.
2. DenaultA., VegasA., RoyseC.. Bedside clinical and ultrasound- based approaches to the management of hemodynamic instability-part I: focus on the clinical approach: continuing professional development. *Can J Anesth*2014; *61*: 843–64.
3. LabovitzA.J., NobleV.E., BierigM., GoldsteinS.A., JonesR., KortS., *et al*. Focused cardiac ultrasound in the emergent setting: a consensus statement of the American Society of Echocardiography and American College of Emergency Physicians. *J Am Soc Echocardiogr*2010; *23*: 1225–30.
4. VegasA., DenaultA., RoyseC.. A bedside clinical and ultrasound- based approach to hemodynamic instability - Part II: bedside ultrasound in hemodynamic shock: continuing professional development. *Can J Anesth*2014; *61*: 1008–27.
5. MayoP.H., BeaulieuY., DoelkenP., Feller-KopmanD., HarrodC., KaplanA., *et al*. American College of Chest Physicians/La Societe de Reanimation de Langue Frangaise statement on competence in critical care ultrasonography. *Chest*2009; *135*: 1050–60.
6. MooreC.L., CopelJ.A.. Point-of-care ultrasonography. *N Engl J Med*2011; *364*: 749–57.
7. KimuraB.J., PezeshkiB., FrackS.A., DeMariaA.N.. Feasibility of "limited" echo imaging: characterization of incidental findings. *J Am Soc Echocardiogr*1998; *11*: 746–50.
8. ReevesS.T., FinleyA.C., SkubasN.J., SwaminathanM., WhitleyW.S., GlasK.E., *et al*. Basic perioperative transesophageal echocardiography examination: a consensus statement of the American Society of Echocardiography and the Society of Cardiovascular Anesthesiologists. *J Am*

*Soc Echocardiogr*2013; *26*: 443–56.
9. DenaultA.Y., CoutureP., VegasA., BuithieuJ., TardifJ.C.. *Transesophageal Echocardiography Multimedia Manual, Second Edition: A Perioperative Transdisciplinary Approach*. New York: Informa Healthcare, 2011.
10. LangR.M., BadanoL.P., Mor-AviV., AfilaloJ., ArmstrongA., ErnandeL., *et al*. Recommendations for cardiac chamber quantification by echocardiography in adults: an update from the American Society of Echocardiography and the European Association of Cardiovascular Imaging. *J Am Soc Echocardiogr*2015; *28*: 1–39. e14.
11. LangR.M., BierigM., DevereuxR.B., FlachskampfF.A., FosterE., PellikkaP.A., *et al*. Recommendations for chamber quantification: a report from the American Society of Echocardiography's Guidelines and Standards Committee and the Chamber Quantification Writing Group, developed in conjunction with the European Association of Echocardiography, a branch of the European Society of Cardiology. *J Am Soc Echocardiogr*2005; *18*: 1440–63.
12. McGowanJ.H., ClelandJ.G.. Reliability of reporting left ventricular systolic function by echocardiography: a systematic review of 3 methods. *Am Heart J*2003; *146*: 388–97.
13. RandazzoM.R., SnoeyE.R., LevittM.A., BinderK.. Accuracy of emergency physician assessment of left ventricular ejection fraction and central venous pressure using echocardiography. *Acad Emerg Med*2003; *10*: 973–7.
14. HoS.Y., NihoyannopoulosP.. Anatomy, echocardiography, and normal right ventricular dimensions. *Heart*2006; *92*Suppl 1: i2–13.
15. GhioS., GavazziA., CampanaC., InserraC., KlersyC., SebastianiR., et al. Independent and additive prognostic value of right ventricular systolic function and pulmonary artery pressure in patients with chronic heart failure. *J Am Coll Cardiol*2001; *37*: 183–8.
16. RibeiroA., LindmarkerP., Juhlin-DannfeltA., JohnssonH., JorfeldtL.. Echocardiography Doppler in pulmonary embolism: right ventricular dysfunction as a predictor of mortality rate. *Am Heart J*1997; *134*: 479–87.
17. Vieillard-BaronA., JardinF.. Why protect the right ventricle in patients with acute respiratory distress syndrome?*Curr Opin Crit Care*2003; *9*: 15–21.
18. RudskiL.G., LaiW.W., AfilaloJ., HuaL., HandschumacherM.D., ChandrasekaranK., *et al*. Guidelines for the echocardiographic assessment of the right heart in adults: a report from the American Society of Echocardiography endorsed by the European Association of Echocardiography, a registered branch of the European Society of Cardiology, and the Canadian Society of Echocardiography. *J Am Soc Echocardiogr*2010; *23*: 685–713.
19. MillerD., FarahM.G., LinerA., FoxK., SchluchterM., HoitB.D.. The relation between quantitative right ventricular ejection fraction and indices of tricuspid annular motion and myocardial performance. *J Am Soc Echocardiogr*2004; *17*: 443–7.
20. LindqvistP., WaldenstromA., HeneinM., MornerS., KazzamE.. Regional and global right ventricular function in healthy individuals aged 20–90 years: a pulsed Doppler tissue imaging study: Umea General Population Heart Study. *Echocardiography*2005; *22*: 305–14.
21. ArntfieldR.T., MillingtonS.J.. Point of care cardiac ultrasound applications in the emergency department and intensive care unit - a review. *Curr Cardiol Rev*2012; *8*: 98–108.
22. DellingerR.P., LevyM.M., RhodesA., AnnaneD., GerlachH., OpalS.M., *et al*. Surviving sepsis campaign: international guidelines for management of severe sepsis and septic shock: 2012. *Crit Care Med*2013; *41*: 580–637.
23. InvestigatorsA., Group ACT, PeakeS.L., DelaneyA., BaileyM., BellomoR., *et al* .Goal-directed resuscitation for patients with early septic shock. *N Engl J Med*2014; *371*: 1496–506.
24. MarikP.E., LemsonJ.. Fluid responsiveness: an evolution of our understanding. *Br JAnaesth*2014; *112*: 617–20.

25. ProwleJ.R., EcheverriJ.E., LigaboE.V., RoncoC., BellomoR.. Fluid balance and acute kidney injury. *Nat Rev Nephrol*2010; *6*: 107–15.
26. BeigelR., CercekB., LuoH., SiegelR.J.. Noninvasive evaluation of right atrial pressure. *J Am Soc Echocardiogr*2013; *26*: 1033–42.
27. ToupinF., DenaultA., LamarcheY., DeschampsA.. Hemodynamic instability and fluid responsiveness. *Can J Anesth*2013; *60*: 1240–7.
28. FeisselM., MichardF., ManginI., RuyerO., FallerJ.P., TeboulJ.L.. Respiratory changes in aortic blood velocity as an indicator of fluid responsiveness in ventilated patients with septic shock. *Chest*2001; *119*: 867–73.
29. Vieillard-BaronA., CherguiK., RabillerA., PeyrousetO., PageB., BeauchetA., *et al*. Superior vena caval collapsibility as a gauge of volume status in ventilated septic patients. *Intensive Care Med*2004; *30*: 1734–9.
30. MayerS.A., ShermanD., FinkM.E., HommaS., SolomonR.A., LennihanL., et al. Noninvasive monitoring of cardiac output by Doppler echocardiography in patients treated with volume expansion after subarachnoid hemorrhage. *Crit Care Med*1995; *23*: 1470–4.
31. BeraudA.S., RizkN.W., PearlR.G., LiangD.H., PattersonA.J.. Focused transthoracic echocardiography during critical care medicine training: curriculum implementation and evaluation of proficiency. *Crit Care Med*2013; *41*: e179–81.
32. VignonP., MuckeF., BellecF., MarinB., CroceJ., BrouquiT., *et al*. Basic critical care echocardiography: validation of a curriculum dedicated to noncardiologist residents. *Crit Care Med*2011; *39*: 636–42.
33. CaroniaJ., KutnickR., SarzynskiA., PanagopoulosG., MahdaviR., MinaB.. Focused transthoracic echocardiography performed and interpreted by medical residents in the critically ill. *ICU Director*2013; *4*: 177–82.
34. SinghS., WannL.S., SchuchardG.H., KlopfensteinH.S., LeimgruberP.P., KeelanM.H.Jr, *et al*. Right ventricular and right atrial collapse in patients with cardiac tamponade - a combined echocardiographic and hemodynamic study. *Circulation*1984; *70*: 966–71.
35. AichingerG., ZechnerP.M., PrauseG., SachererF., WildnerG., AndersonC.L., *et al*. Cardiac movement identified on prehospital echocardiography predicts outcome in cardiac arrest patients. *Prehosp Emerg Care*2012; *16*: 251–5.
36. SalenP., MelnikerL., ChooljianC., RoseJ.S., AlteveerJ., ReedJ., *et al*. Does the presence or absence of sonographically identified cardiac activity predict resuscitation outcomes of cardiac arrest patients?*Am J Emerg Med*2005; *23*: 459–62.
37. BlythL., AtkinsonP., GaddK., LangE.. Bedside focused echocardiography as predictor of survival in cardiac arrest patients: a systematic review. *Acad Emerg Med*2012; *19*: 1119–26.
38. MorrisonL.J., DeakinC.D., MorleyP.T., CallawayC.W., KerberR.E., KronickS.L., *et al*. Part 8: Advanced life support: 2010 International Consensus on Cardiopulmonary Resuscitation and Emergency Cardiovascular Care Science With Treatment Recommendations. *Circulation*2010; *122*: S345–421.
39. St-PierreP., DeschampsA., CartierR., BasmadjianA., DenaultA.Y.. Inhaled milrinone and epoprostenol in a patient with severe pulmonary hypertension, right ventricular failure and reduced baseline brain saturation value from a left atrial myxoma. *J Cardiothorac Vasc Anesth*2014; *28*: 723–9.
40. LatulippeS., GirardM., DenaultA.. Diagnosing hemodynamic instability in the comatose patient. *Can J Anesth*2010; *57*: 167–71.
41. LapointeV., JocovD., DenaultA.. Hemodynamic instability in septic shock. *Can J Anesth*2009; *56*: 864–7.
42. DenaultA.Y., ChaputM., CoutureP., HebertY., HaddadF., TardifJ.C.. Dynamic right ventricular

outflow tract obstruction in cardiac surgery. *J Thorac Cardiovasc Surg*2006; *132*: 43–9.
43. RochonA.G., L'AllierP.L., DenaultA.Y.. Always consider left ventricular outflow tract obstruction in hemodynamically unstable patients. *Can J Anesth*2009; *56*: 962–8.

Chapter 16

Critical Care Examination of the Abdomen

INTRODUCTION

Hemodynamic instability can result from an acute intra-abdominal process such as bleeding, infection, and abdominal compartment syndrome. The rapid identification of the underlying mechanism helps in stratifying the cause and consequently the best treatment. In addition, abnormal findings are common in the intensive care unit (ICU). In a study of400 critically ill patients who underwent abdominal ultrasound (US), new pathological findings were observed in 31%, of which 10% required an intervention, and in 6% other therapeutic interventions were performed. [1]

Focused US examination of the abdomen has the advantage of being performed at the bedside by the clinician in charge of the patient, with knowledge of all the associated conditions. It can also be repeated as often as needed. However some diagnoses are simple and others are more complex. In addition, in some situations, information from US cannot be obtained or may be unnecessary when, for instance, signs of perforation are evident on a simple plain abdominal film. Therefore it is important that the clinician is aware of the limitations of abdominal US, and seeks expertise when the answer is unclear. In this chapter, the most common pathologies with implications in critical care will be discussed, except for a detailed evaluation of the biliary tract and the pancreas.

Table 16.1 Technical (Image Acquisition) and Cognitive (Image Interpretation) Elements Required for Competence in Abdominal Ultrasonography.

Assessment for intraperitoneal fluid
Identification of a relatively echo-free space surrounded by typical anatomic boundaries: abdominal wall, diaphragm, liver, gallbladder, spleen, kidney, bladder, bowel, uterus, spinal column, aorta, inferior vena cava
Identification of abdominal wall, diaphragm, liver, gallbladder, spleen, kidney, bladder, bowel, uterus, spinal column, aorta, inferior vena cava
Identification of characteristic dynamic findings of intraperitoneal fluid, such as diaphragmatic motion, floating bowel, bowel peristalsis, dynamic fluid motion, and respire-phasic shape change, compressibility
Characterization of fluid: anechoic; echogenicity (using liver/spleen as reference); homogeneous or heterogeneous; presence of strands/debris/septations
Qualitative assessment of intraperitoneal fluid volume
Recognition of specific limitations of ultrasonography to identify intraperitoneal fluid, such as inadequate image quality due to technical limitations, hemoperitoneum, echo-dense purulent fluid
Assessment of the urinary tract
Bladder: identification of bladder, identification of urinary catheter, identification of abnormal bladder contents
Differentiation of distended bladder from ascites
Qualitative assessment of intravesicular volume, identification of overdistention
Kidneys: identification of both kidneys, identification of presence or absence of hydronephrosis, measurement of kidney in longitudinal axis
Assessment of the aorta
Identification of abdominal aorta
Identification of abdominal aortic aneurysm

Note: Adapted from Mayo *et al.* [2]

Table 16.2 Abdominal Organ Dimensions.

Structure	Normal		Abnormal
Liver	Cranio-caudal	<140 mm	
	Antero-posterior	<120 mm	
Gallbladder	Length	<120 mm	Dilated if >90 mm longitudinal and 50 mm transverse[3]
	Width	<40 mm	
	Wall thickness	<4 mm	
Bile Duct	Diameter	<6 mm	Dilated if >7 mm or same size as portal vein
	(<9 mm post cholecystectomy)		
Spleen	Cranio-caudal	<110 mm	Perpendicular line product >20 sq.cm [4]
	Antero-posterior	<40 mm	
Kidney	Cranio-caudal	<120 mm	
	Antero-posterior	<50–70 mm	
	Cortex thickness	<13–25 mm	
Inferior vena cava	Transverse diameter	<20 mm	
Intestine	Wall thickness	<4 mm	Dilatation >3 cm
	Cross-sectional area	<12 mm^2	
Aorta	Transverse diameter upper abdominal	<25 mm	Aneurysm >3 cm
	Transverse diameter lower abdominal	<20 mm	
Portal vein	Transverse diameter	<13 mm	
Pancreas	Head	<30 mm	
	Body and tail	<25 mm	
	Wirsung	<2 mm	
Prostate	Longitudinal diameter	<45 mm	
	Transverse diameter and height	<35 mm	
	Volume	<25 ml	

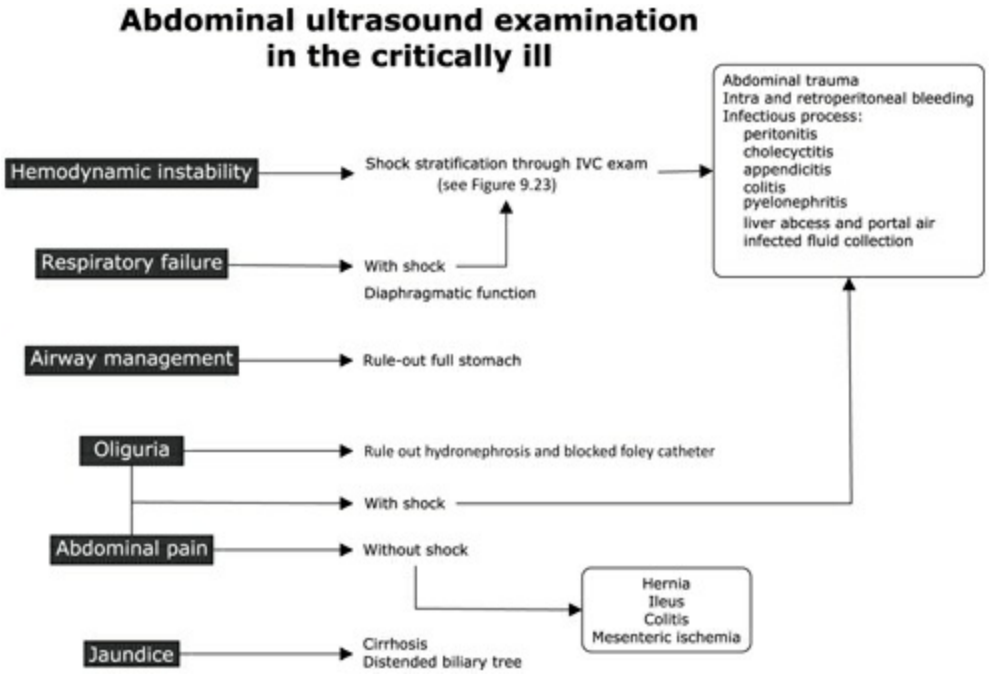

Fig. 16.1 Abdominal ultrasound. An algorithm integrating the role of the abdominal ultrasound examination in the assessment of the critically ill patient is presented. IVC, inferior vena cava.

OBJECTIVES OF ABDOMINAL ULTRASOUND EXAMINATION

In 2009, Mayo *et al* in collaboration with the American College of Chest Physicians and the Societe de Reanimation de Langue Frangaise published a statement on competence in critical care ultrasonography. [2] In 2014, Canadian guidelines were also published through the Canadian Critical Care Society. [5] In the critically ill patient, abdominal US examination is most often considered during assessment of hemodynamic and respiratory instability, renal failure, abdominal pain, abdominal trauma, jaundice, and to guide paracentesis (**Table 16.1**). An approach to the abdominal examination in the critically ill is summarized in **Figure 16.1**. The reported dimensions of abdominal organs can be found in **Table 16.2**. The following sections will first describe the normal anatomy, and then address some pathologies, with the main focus being the presence of intraperitoneal fluid.

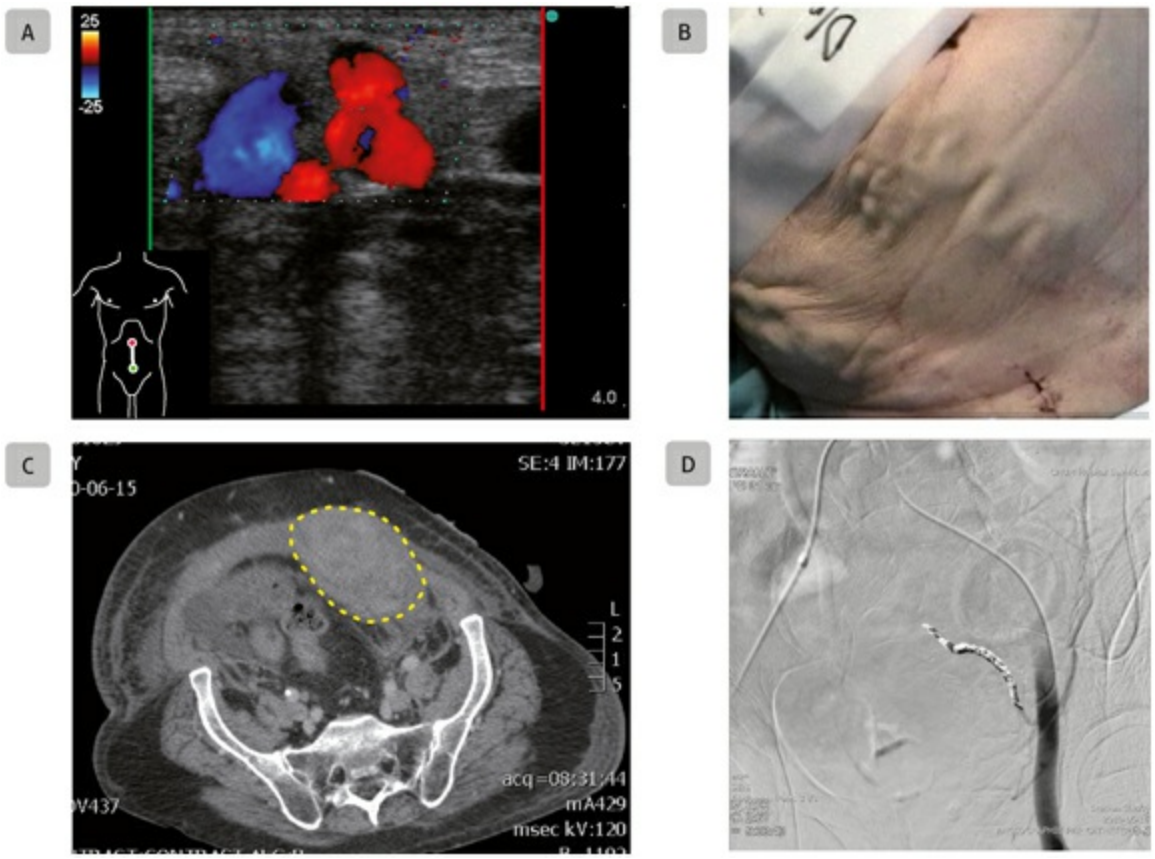

Fig. 16.2 Abdominal wall varices. (A) Mid-abdominal transverse ultrasound view of the abdomen with a linear probe in a patient with subcutaneous varices or caput medusa. (B) Abdominal wall varices in

another patient are seen on physical inspection. (C) Accidental epigastric artery puncture with hematoma formation (dotted line) in a patient, following drainage of ascites using the landmark technique, is shown by computed tomography. (D) Treatment of this complication required arterial embolization that further led to acute tubular necrosis from shock and contrast administration.

A: https://youtu.be/ragrzTVCI-8

B: https://youtu.be/umZcRxQ0L7U

PROBE TYPE AND POSITIONING

Low frequency US probes are used to scan the abdomen (see **Figure** 1.**6**). Typically the large curvilinear abdominal US probe is used because there is sufficient penetration to allow the collection of a large amount of information, and to measure organ dimensions. A microconvex or a cardiac phased-array US probe is useful to examine between the ribs and evaluate cardiac function at the same time as the abdomen. The frame rate of the abdominal US probe makes it inadequate for cardiac evaluation in patients with a rapid heart rate. The possibility of switching from one probe to the next can be considered; however, in a focused examination where key information is sought, this may prolong the patient's evaluation. In the ICU and in the operating room, the majority of intensivists only use a phased-array cardiac probe with both cardiac and abdominal presets. In the emergency room (ER) and radiology suite, the abdominal probe is favored. Finally there is little role for the high frequency linear probe, except for the evaluation of more superficial intra-abdominal structures, soft tissue, vascular structure, and during the insertion of vascular access. For instance in patients with cirrhosis undergoing paracentesis, localizing superficial varices might be relevant in order to avoid iatrogenic hematomas (**Figure 16.2**).

The orientation of the probe in relation to the anatomic structure is different in the abdomen compared to the heart. The radiological as opposed

to the cardiology convention is favoured when scanning the abdomen (**Figure 16.3**). In the radiological convention, in a longitudinal, sagittal and coronal plane, the right-side of the screen corresponds to the lower portion of the body, as opposed to the upper portion in the cardiology convention. In both radiology and cardiology conventions in the transverse plane, the right-side of the screen corresponds to the left side of the patient (**Figure 16.4**). As the evaluation of unstable patients will not be limited to the abdomen, it might be awkward to switch from one convention to the other as the probe is moved from the chest to the abdomen. Therefore, there has been support for an "anatomical" convention in which the US image corresponds to the anatomic position of the organs from the point of view of the clinician who is examining the patient. For instance, when the clinician stands to the right of the patient examining the liver in a posterior axillary coronal view, the radiology convention corresponds to the anatomical perspective. The debate regarding this issue is beyond the scope of this chapter, but it is important that the clinician performing bedside US understand the orientation of the plane of cut in relation to the true anatomy. The transverse, coronal and longitudinal (or sagittal), oblique, intercostal and flank views can be used to scan the abdomen (**Figure 16.5**)

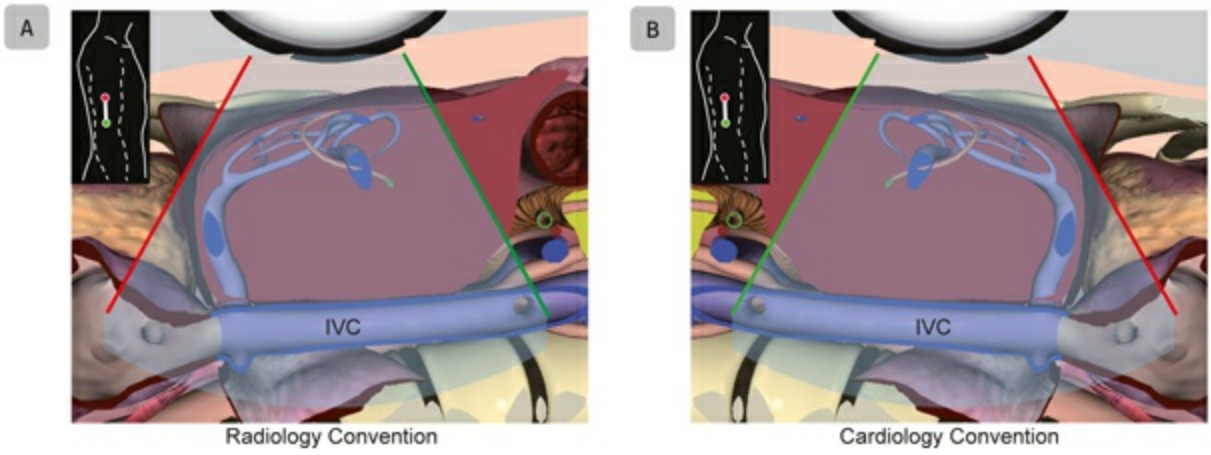

Fig. 16.3 Imaging conventions. Right posterior axillary line upper abdominal coronal view of the liver and the inferior vena cava (IVC) is shown using a Vimedix simulator. (A) In the radiology convention, the head is to the left and the feet to the right. From an anatomic point of view, this indicates that the operator is looking at the anatomy from the perspective of being to the right of the patient. This corresponds to the anatomic location of these structures. (B) In the cardiology convention, it is the opposite. The same rules apply for the coronal view. From an anatomic point of view, this indicates that the operator is looking at the anatomy from the perspective of being to the left of the patient.

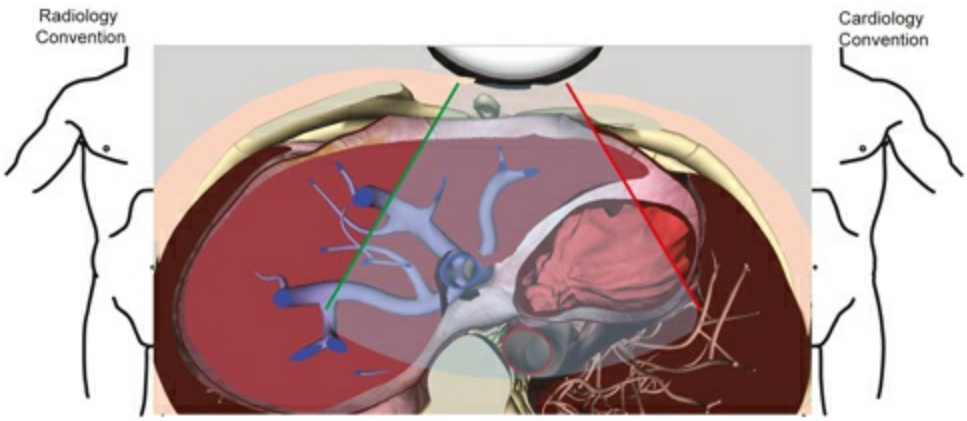

Fig. 16.4 Imaging conventions. Mid-upper abdominal transverse view across the left lobe of the liver is shown using the Vimedix simulator. In both the radiology convention and the cardiology convention, the image displayed on the right side represents the left side of the patient. Images displayed on the left side correspond to the right side of the screen. From an anatomic point of view, this indicates that the operator is looking at the anatomy from the perspective of being at the feet of the patient.

NORMAL RELEVANT ANATOMY

Liver

The liver is the largest solid organ in the abdomen, occupying most of the right upper quadrant. It has a homogeneous appearance with a smooth border, and contains both vascular and biliary structures. The Couinaud classification describes liver segmentation (**Figure 16.6** and **Table 16.3**).

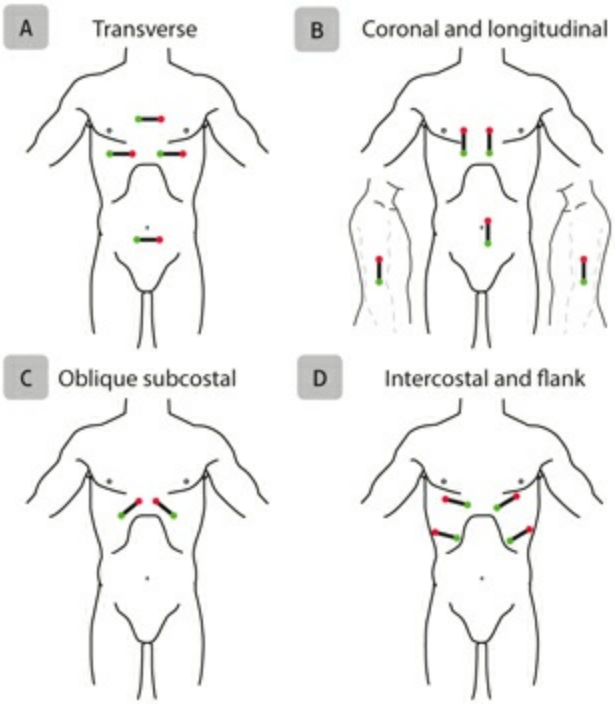

Fig. 16.5 Abdominal views. Diagrams for the ultrasound probe position and orientation that are used to obtain abdominal ultrasound views are shown. These include the (A) upper, lower, right and left transverse views; (B) upper, lower, right longitudinal with right and left coronal; (C) right and left oblique subcostal; and (D) left and right upper intercostal and flank views.

Table 16.3 Hepatic Anatomy.

Couinaud	Traditional
Segment 1	Caudate lobe
Segment 2	Lateral segment left lobe (superior)
Segment 3	Lateral segment left lobe (inferior)
Segment 4	Medial segment left lobe
Segment 5	Anterior segment right lobe (inferior)
Segment 6	Posterior segment right lobe (inferior)
Segment 7	Posterior segment right lobe (superior)
Segment 8	Anterior segment right lobe (superior)

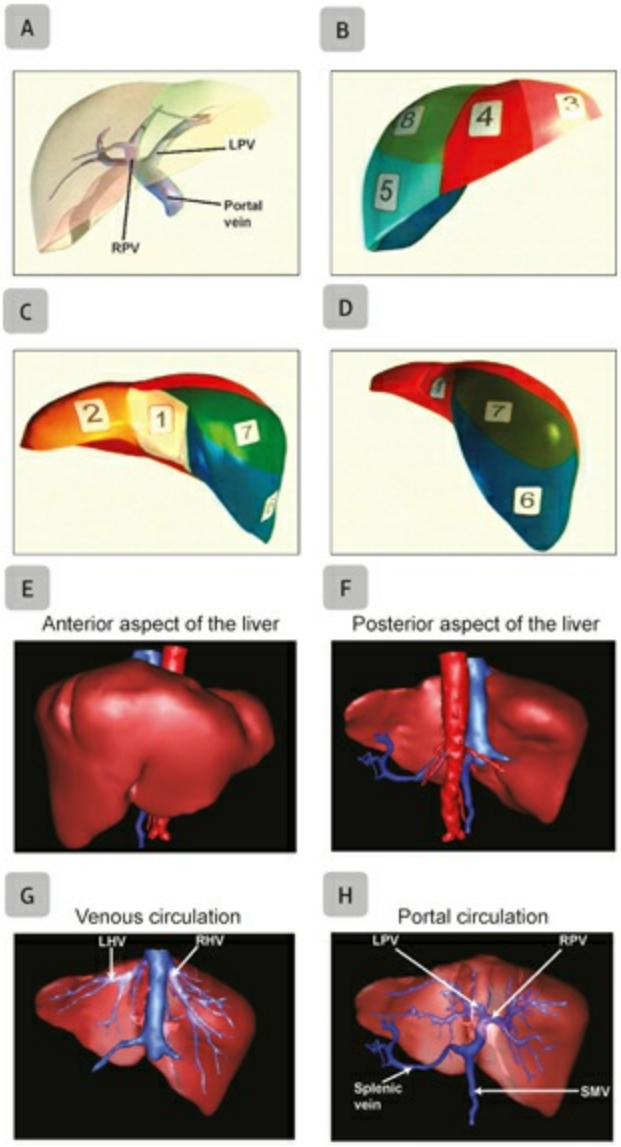

Fig. 16.6 Normal liver anatomy. (A–D) The Couinaud classification divides the liver into eight independent segments, each of which has its own vascular inflow, outflow, and biliary drainage. Anterior (A,B) and posterior (C,D) views of the liver are shown compared with a 3D reconstruction of the hepatic circulation as orientated from the anterior (E) and posterior (F–H) perspectives. LHV, left hepatic vein; LPV, left portal vein; SMV, superior mesenteric vein; RHV, right hepatic vein; RPV, right portal vein. Source: Courtesy of Sanofi Aventis and l'Institut de Recherche Contre les Cancers de l'Appareil Digestif, Strasbourg, France. (Reproduced with permission from Denault et al.6).

https://youtu.be/3u6-41PBLsk

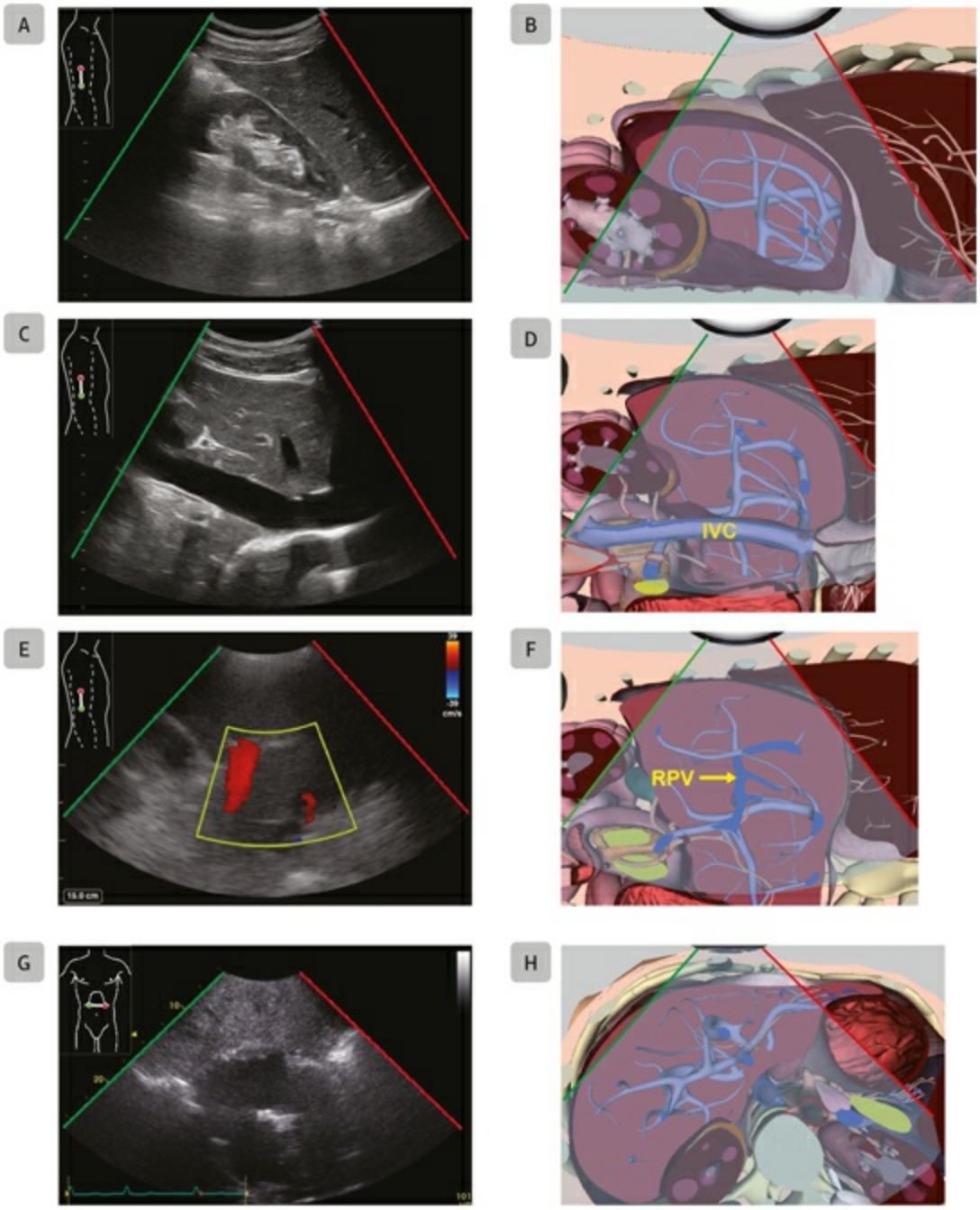

Fig. 16.7 Right posterior axillary coronal upper and mid-abdominal ultrasound views. Tilting the abdominal ultrasound probe from the top to bottom, and using the liver as an acoustic window, different variations of this view are obtained using the Vimedix simulator. These views are particularly useful in the evaluation of (A,B) the liver parenchyma and posterior hepato-renal space; (C,D) the inferior vena cava (IVC); (E,F) the right portal vein (RPV) just above the IVC; and (G, H) an anterior portion of the gallbladder.

B, D, F: https://youtu.be/ho8tMed-Y30

H: https://youtu.be/e0ujg64qlik

Several views can be used to scan the right lobe, the right upper quadrant, intercostal, mid-axillary line coronal, and the subcostal views. The right posterior axillary line coronal view is commonly used to scan the right lobe and the associated vascular structures (**Figure 16.7**). The left lobe of the liver is best examined using the subxyphoid view, the same view as for cardiac examination.

Gallbladder and Biliary Tract

The gallbladder (GB) sits in the fossa created by the right and left main liver lobes. It is a pear-shaped organ. Ultrasound images normally show the GB as an empty anechoic structure surrounded by an echogenic membrane (**Figure 16.8**). The normal thickness of the GB wall is less than 3 mm. It should be non-tender when applying pressure with the US probe.

Kidney

The renal cortex is slightly less echogenic than the normal liver. The renal medulla contains the pyramids that are less echogenic than the cortex, and each have a triangular shape pointing toward the renal pelvis. The renal pelvis is the echogenic central collecting system of the kidney. Both kidneys are surrounded by a hyperechoic stripe (Gerota's fascia) (**Figure 16.9**). The normal kidney size is 9-12 cm. Both right and left kidneys can be examined using a right or left posterior axillary coronal view.

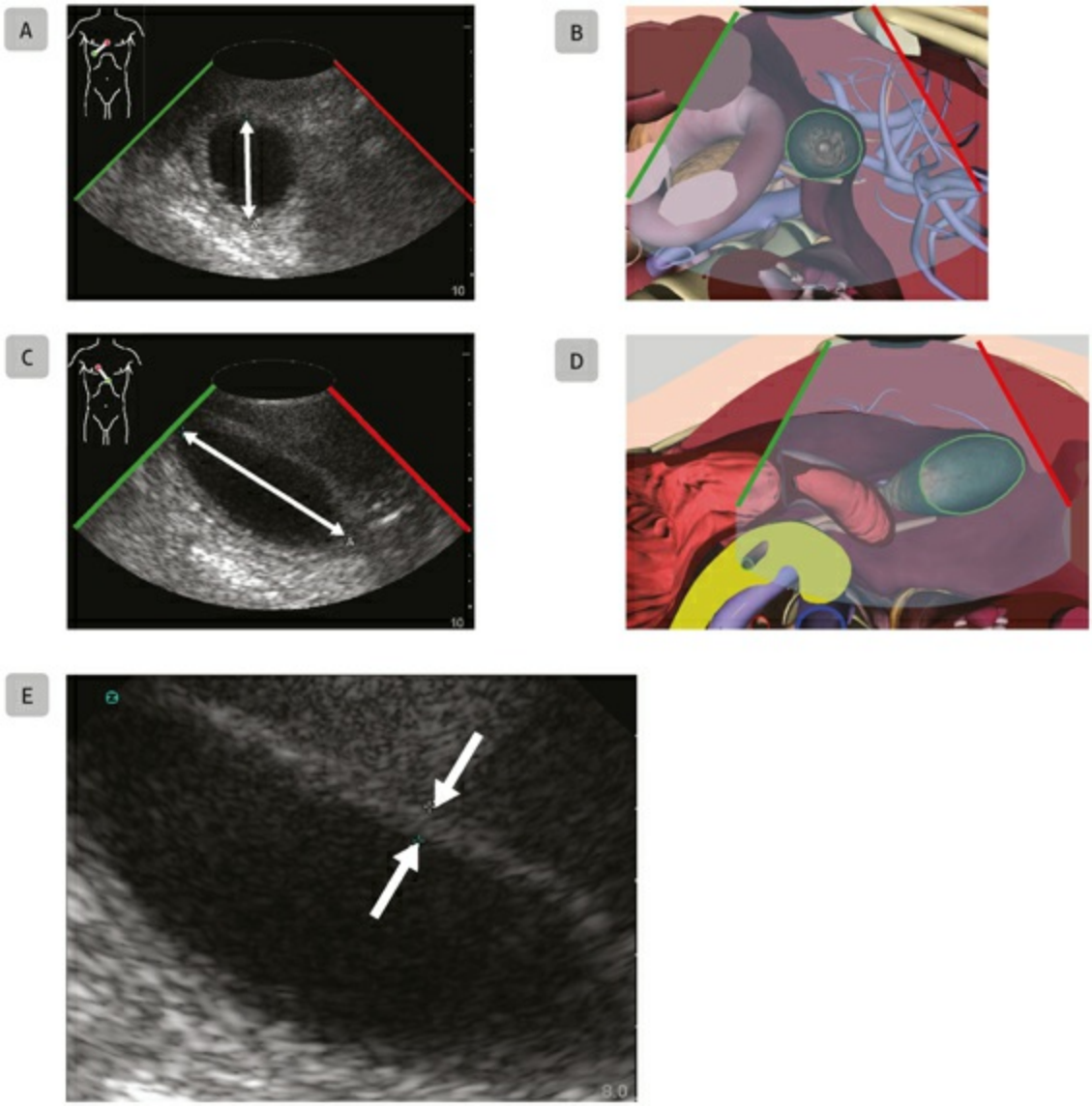

Fig. 16.8 Gallbladder. (A,B) Upper transverse and (C,D) longitudinal abdominal ultrasound images obtained with a convex probe show a normal gallbladder with the Vimedix simulator diagrams. (E) The normal gallbladder wall thickness should be less than 3 mm.

B: https://youtu.be/EPK6wzplGXQ

C: https://youtu.be/7JxaumPXWBM

D: https://youtu.be/ttfzBZSqF40

Spleen

The spleen occupies the superior, posterior, and lateral aspects of the left upper quadrant. It is very homogeneous but more echogenic than the liver, with a smooth border. The spleen is smaller than the liver with no visible intraparenchymal vessels. The spleen is typically less than 13 cm using a coronal view. The spleen is imaged using a coronal view along the left posterior axillary line (**Figure 16.10**).

Diaphragm

Diaphragmatic motion can be quantified using two-dimensional US and with anatomical M-mode (**Figure 16.11**), although the diaphragm often disappears as the lung moves. Comparing both sides is essential. Both left and right diaphragm can be identified as a bright echogenic line that is a few millimeters thick (see **Figure** 14**.32**). Normal diaphragmatic motion goes downward with inspiration and upward in expiration. The left and right posterior axillary line at the level of the subxyphoid process can be used to image diaphragmatic motion.

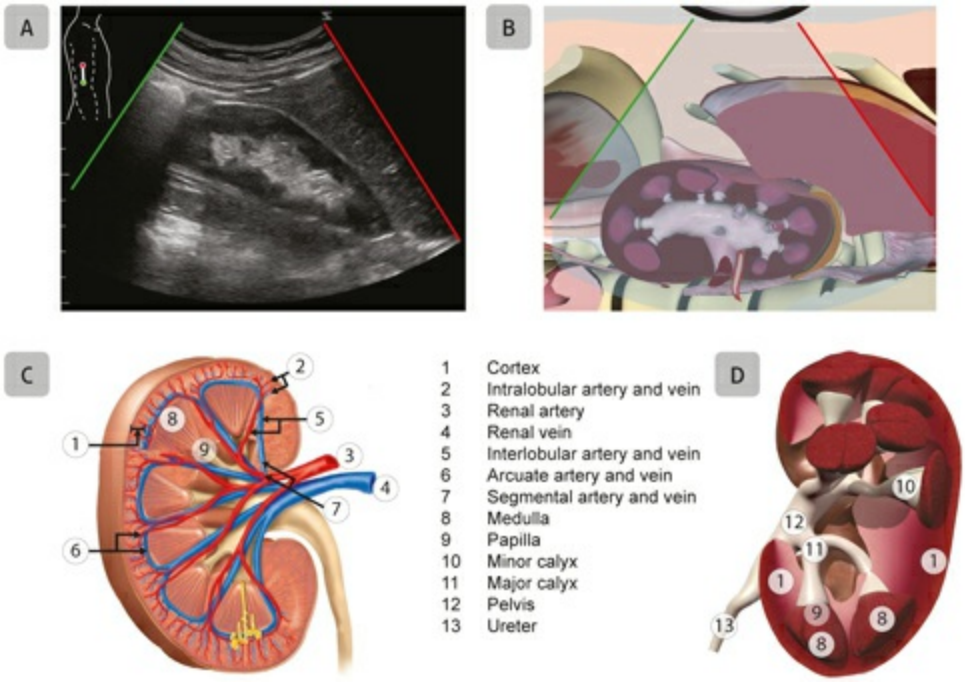

Fig. 16.9 Kidney. (A,B) Normal kidney is seen in this image from a right posterior axillary coronal view, using abdominal ultrasound image obtained with a convex probe and shown with the Vimedix simulator diagram. (C,D) Illustrations of normal kidney vasculature and anatomy are shown. (Anatomical images with permission of Primal Pictures, Wolters Kluwer Health.).

A: https://youtu.be/S8SlCk4250U

B: https://youtu.be/oVt1A9N79ac

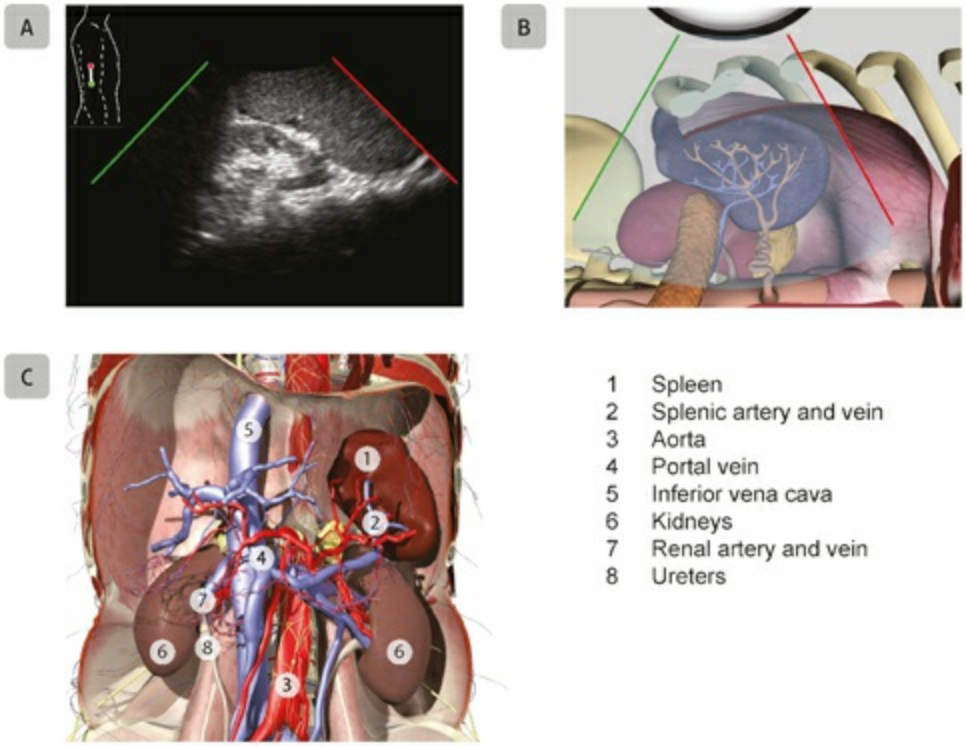

Fig. 16.10 Spleen. (A,B) Normal spleen is seen in this left posterior axillary coronal abdominal ultrasound image obtained with a convex probe and shown with the Vimedix simulator diagram. (C) The vasculature to the spleen and adjacent organs are shown. Note that the splenic vein drains into the portal vein. (Anatomical images with permission of Primal Pictures, Wolters Kluwer Health.).

A: https://youtu.be/XCmYn15J2oc

B: https://youtu.be/s3ygPk30Vbw

B: https://youtu.be/inbL0P1u0DA

Abdominal Aorta

The abdominal aorta appears as a circular structure in the short-axis view, and tubular in the long-axis view. The echogenic walls are pulsatile with anechoic content that is not compressible. It lies on top of the vertebral body (**Figure 16.12**). The abdominal aorta dimension exhibits a proximal-to-distal tapering in size after giving off the big branches such as the celiac axis, superior mesenteric artery (SMA), and renal arteries. The normal dimension above the celiac artery is <3.5 cm, and should be <3 cm below this reference point. The common iliac artery is typically <1.5 cm. Measurement of the greatest diameter of the aorta should be performed from outer wall to outer wall. Both transverse and longitudinal views should be obtained in order not to underestimate its maximal diameter (**Figure 16.13**). The aorta is to the left of the inferior vena cava (IVC). Close examination of the aorta can allow identification of the celiac trunk, SMA, renal artery, and iliac bifurcation at the umbilical level (**Figure 16.14**). In order to obtain a transverse view of the aorta, start with a subxyphoid transverse view with sufficient depth, look at the heart, and then slowly follow the entire aorta down to the iliac arteries. For the longitudinal view of the aorta, switch to a subxyphoid longitudinal view. If gas is present, maintain firm pressure for 30 seconds and milk away the gas or turn the patient into a lateral decubitus position. In some patients, the aorta can also be visualized through the spleen and the liver in a posterior coronal view.

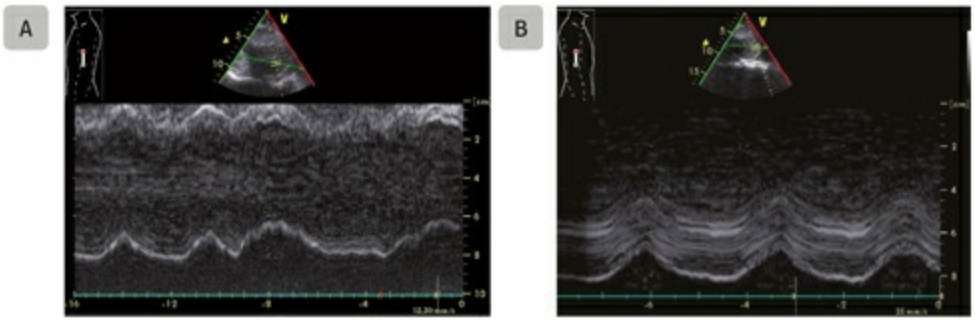

Fig. 16.11 Diaphragmatic motion. (A,B) Posterioraxillary upper coronal abdominal ultrasound images in anatomic M-mode of (A) the right diaphragm, and (B) the left diaphragm show symmetric but reduced motion in a patient after cardiac surgery.

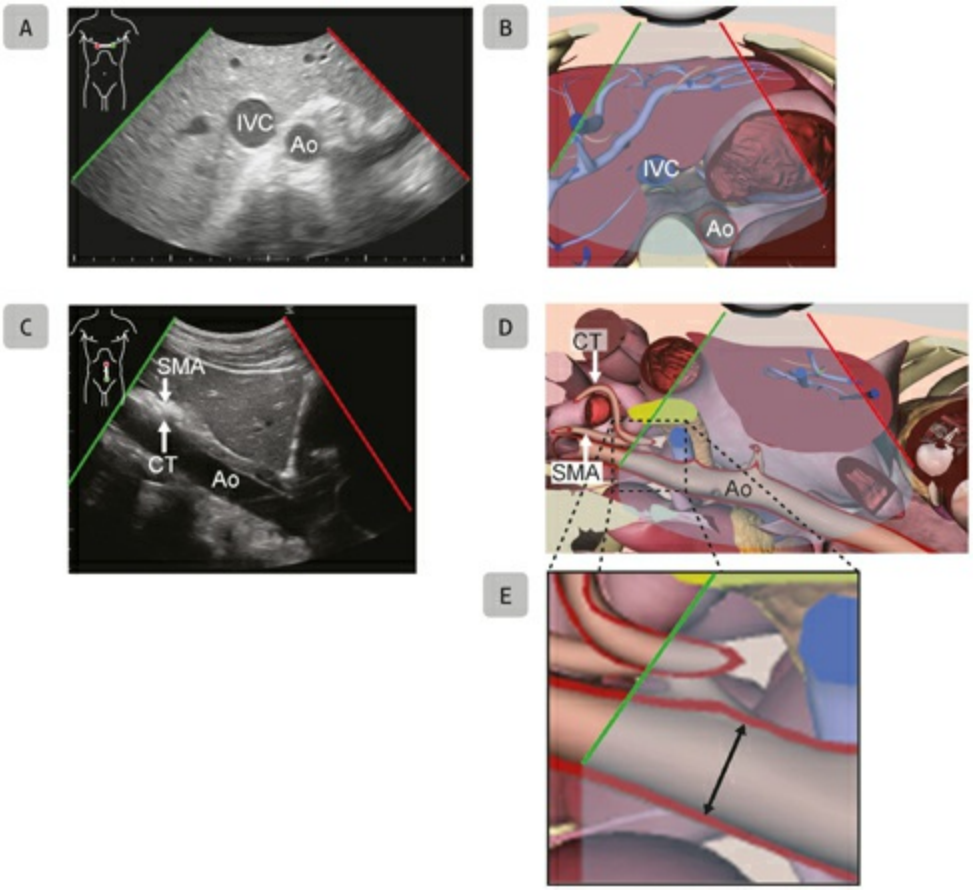

Fig. 16.12 Abdominal aorta (Ao). (A,B) Upper transverse abdominal ultrasound image of the Ao and the inferior vena cava (IVC) shown both in short-axis with the Vimedix simulator diagram. (C,D) Mid-transverse abdominal ultrasound image shows a long-axis view of the Ao with the corresponding Vimedix diagram. (E) Zoomed portion of the Ao diagram shows the normal measurement of the maximal diameter in a longitudinal view. CT, celiac trunk; SMA, superior mesenteric artery.

B: https://youtu.be/tXynMnhNDI4

C: https://youtu.be/LDK0jxBWce0

D: https://youtu.be/Rqrydold9QY

Inferior Vena Cava

The IVC is also a tubular structure with a thinner wall compared to the aorta that ends in the right atrium.

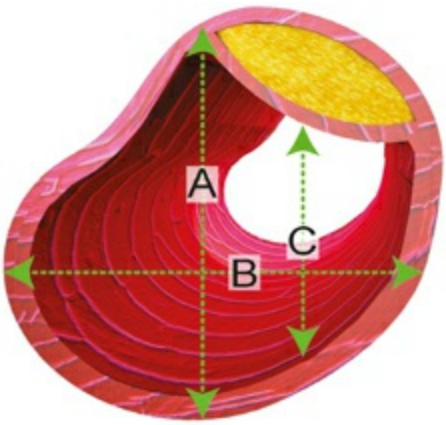

Fig. 16.13 Abdominal aorta measurements. In a presence of a tortuous aorta, the maximal longitudinal (A) and transverse (B) diameters should be used. The presence of atheromatous plaques could underestimate (C) the true diameter.

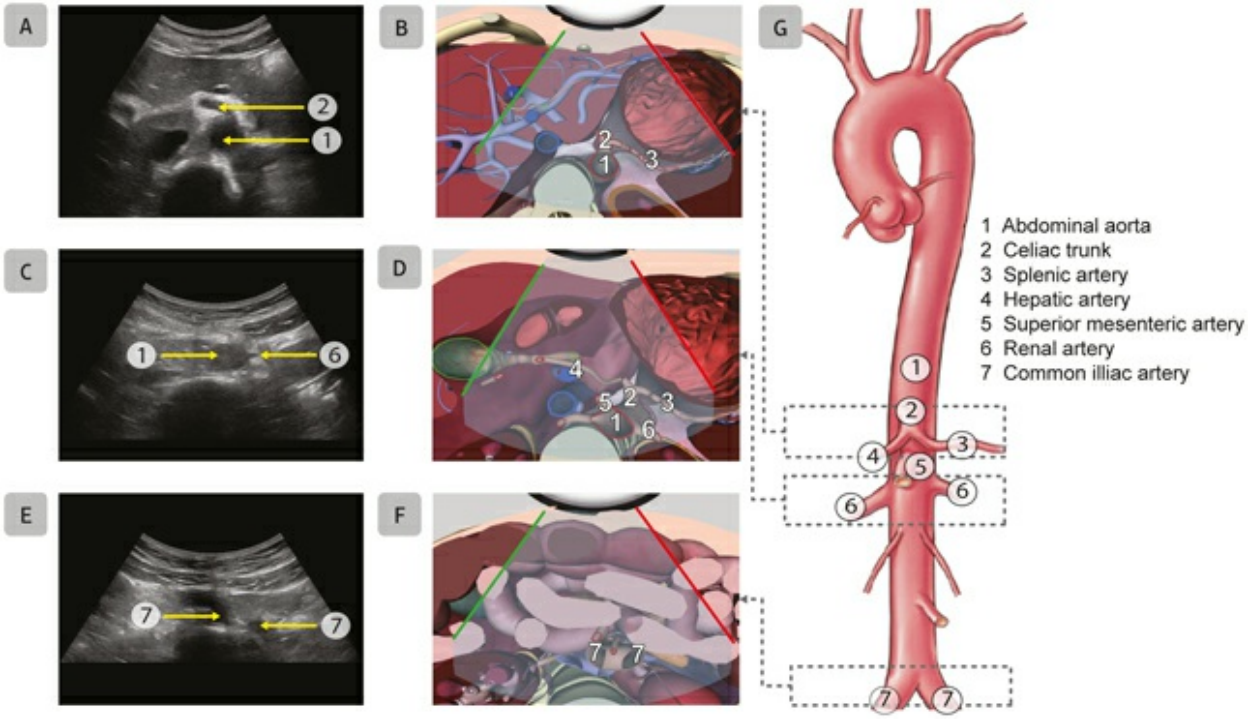

Fig. 16.14 Abdominal aorta branches. Mid-transverse abdominal ultrasound views and corresponding Vimedix simulator diagrams are shown at different levels: (A,B) celiac bifurcation, (C,D) renal and

mesenteric arteries, and (E,F) iliac artery bifurcation close to the umbilicus. (G) Graphic view of the aorta is presented.

A, C, E: https://youtu.be/8LfJYdSu2eg

B, D, F: https://youtu.be/0k_yXno_t0g

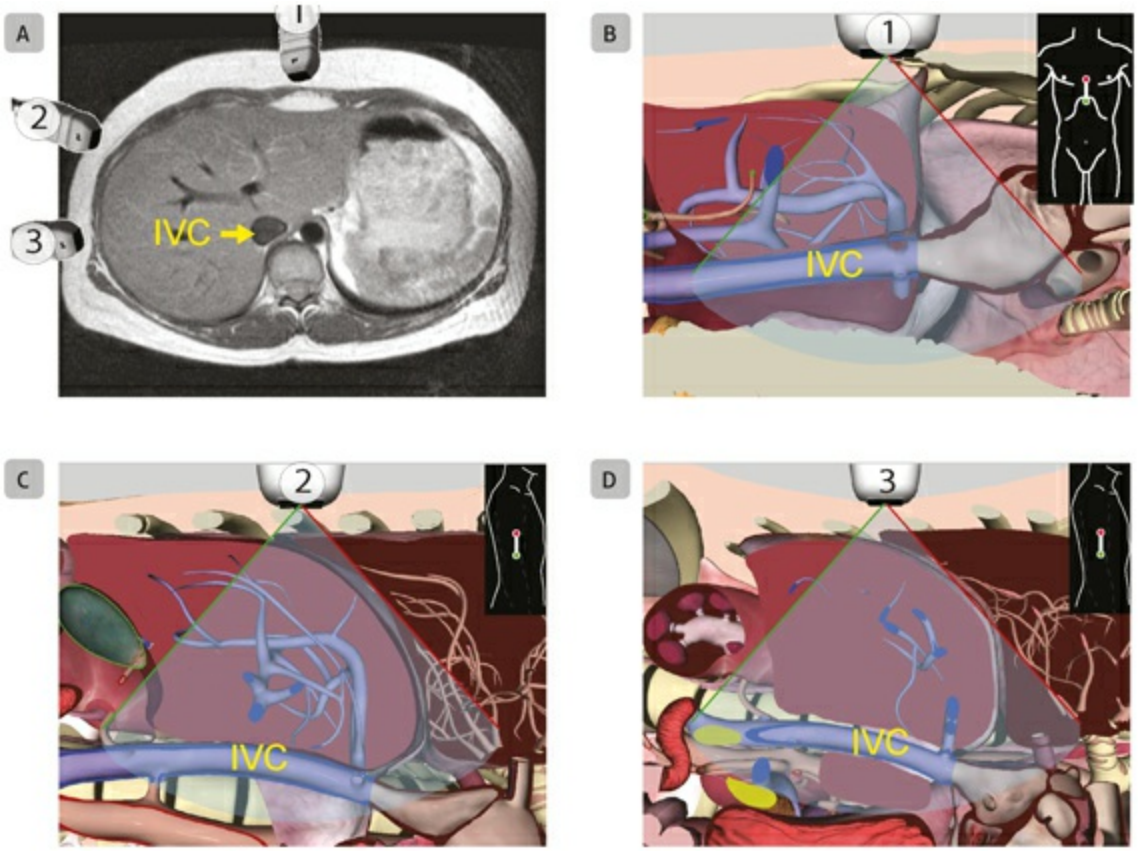

Fig. 16.15 Inferior vena cava (IVC). (A) Axial T1 weighted magnetic resonance image of the liver scan of the liver showing different positions of the ultrasound probe that can be used to obtain a longitudinal view of the IVC. (B-D) The subxyphoid (1), anterior axillary line (2) and posterior axillary line (3) positions using the Vimedix simulator are shown. The subxyphoid view is obtained in the supine patient by positioning the probe in the subcostal region with the probe marker placed towards the head at 12 o'clock. The ultrasound plane is directed towards the liver to show a longitudinal view of the IVC. The IVC can be distinguished from the pulsatile aorta by identifying the following criteria: (1) the

IVC drains into the right atrium; (2) liver surrounds the IVC; (3) lack of pulsatility of the IVC (unless severe tricuspid regurgitation is present); and (4) hepatic veins draining into the IVC. (Adapted with permission from Vegas et al.7).

B: https://youtu.be/O6scbRIw64o

C: https://youtu.be/p1JeFzII2Sg

D: https://youtu.be/KzGaVPveQ5I

Normally the IVC is not pulsatile, easily compressible, and located to the patient's right compared to the aorta (**Figure 16.1**2). The IVC is one of the easiest anatomic structures to identify because a portion is located in the liver. Therefore multiple views through the liver, which has favorable acoustic properties, can be used to analyze it (**Figure 16.15**). Hepatic veins drain into the IVC. The hepatic vein walls are thin with triphasic flow away from the transducer (**Figure 16.16**). The portal vein walls are thicker from the association with hepatic artery and biliary ducts (**Figure 16.17**), with monophasic flow toward the transducer. Rapid evaluation of the IVC can be used to stratify the mechanism of shock (see **Figure** 9**.23**).

Bladder

The bladder is a black membrane-bound structure in the pelvis whose dimension will vary in relation to the amount of urine. It is positioned cephalad to the pubic bone. Bladder volume can be calculated using a transverse and a longitudinal view (**Figure 16.18**). [8]

Uterus

The uterus is a solid organ with a texture that resembles splenic and hepatic tissue in a non-gravid state. It is rarely centrally located but usually more to the right or to the left of midline. The fundus of the uterus can be anteverted or retroverted. The vagina and the cervix will always be juxtaposed to the bladder. In order to image the uterus, place the probe above the pubic symphysis in transverse view, or turn to a longitudinal view. The normal uterus has the shape of a pear, and the endometrial stripe appears as a linear echogenic zone centrally (**Figure 16.19**). It is easily evaluated with endovaginal US.

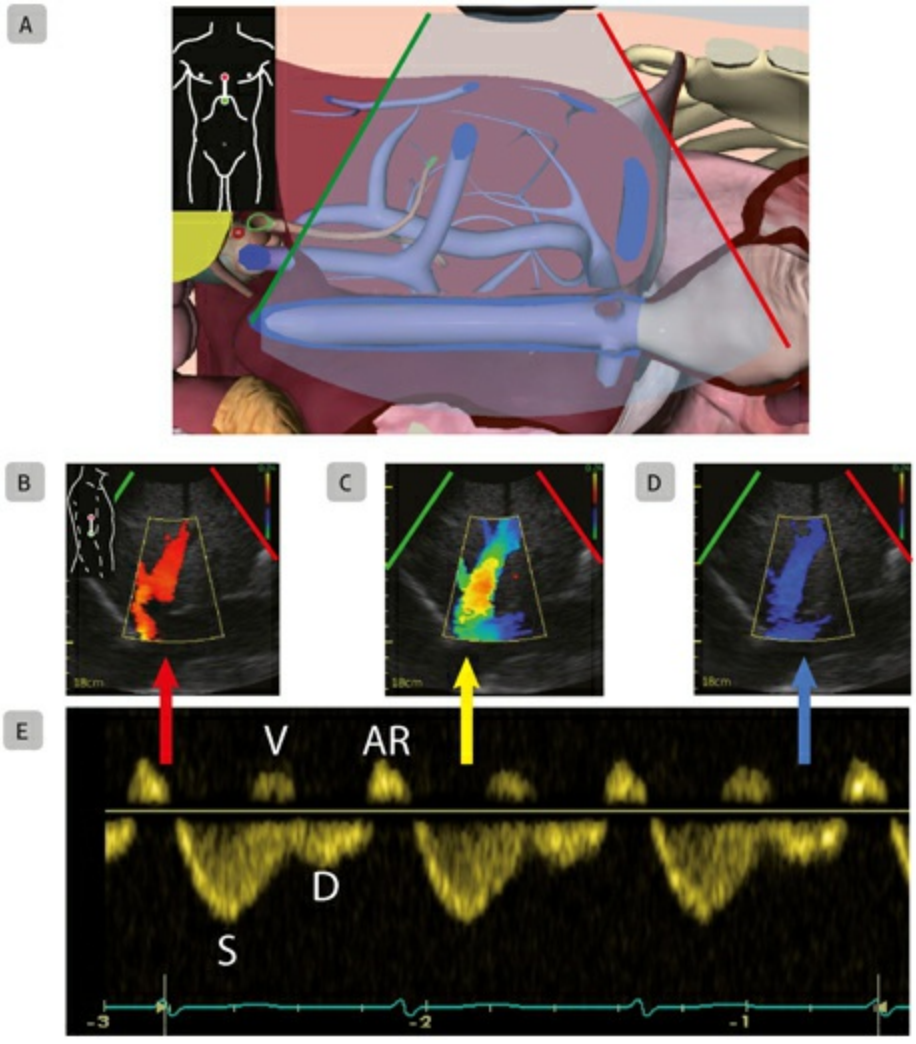

Fig. 16.16 Hepatic venous flow. (A) The normal triphasic Doppler hepatic venous flow obtained from a subxyphoid abdominal ultrasound image using the Vimedix simulator with color Doppler has (B) an atrial reversal (AR) velocity, (C) a systolic (or S) velocity which can be followed by a V wave, and (D) a diastolic (or D) velocity. (E) Corresponding pulsedwave Doppler velocities show that normal S and D velocities are away from the transducer, as opposed to the AR and V wave that are toward the

transducer.

A: https://youtu.be/UAMjQwnwwak

B, C, D: https://youtu.be/CnGFtTRPXc4

Gastrointestinal Tract

Imaging of the stomach, small bowel, and large bowel is only done when conditions such as full stomach, ileus, or colitis are considered. The aspect of the stomach will depend on its content (**Figure 16.20**). The stomach can be found by using the spleen as an acoustic window and just tilting anteriorly. The estimation of gastric volume can be performed with US. [9] The antrum cross-sectional area (CSA), using a longitudinal upper abdominal view in a lateral position, seems the best predictor of gastric volume. [9 – 11] A CSA >15 cm^2 is typically associated with gastric volume of 200 mL or more.

COMMON ABDOMINAL PATHOLOGIES

Intra-Abdominal Free Fluid

One of the most important roles of the clinician evaluating an unstable patient is to determine the presence of free abdominal fluid. Two types of fluid collections can be identified: simple, which is anechoic; or complex, when material such as fibrin is present. Free fluid will have an irregular shape: it "fills the space" without a wall, and will typically be positioned against an organ. No motion or peristalsis is seen. The fluid typically is located in the most dependent region of the peritoneum, which varies depending on the patient's position, and thus can move with position. The most common locations to look for free fluid are:

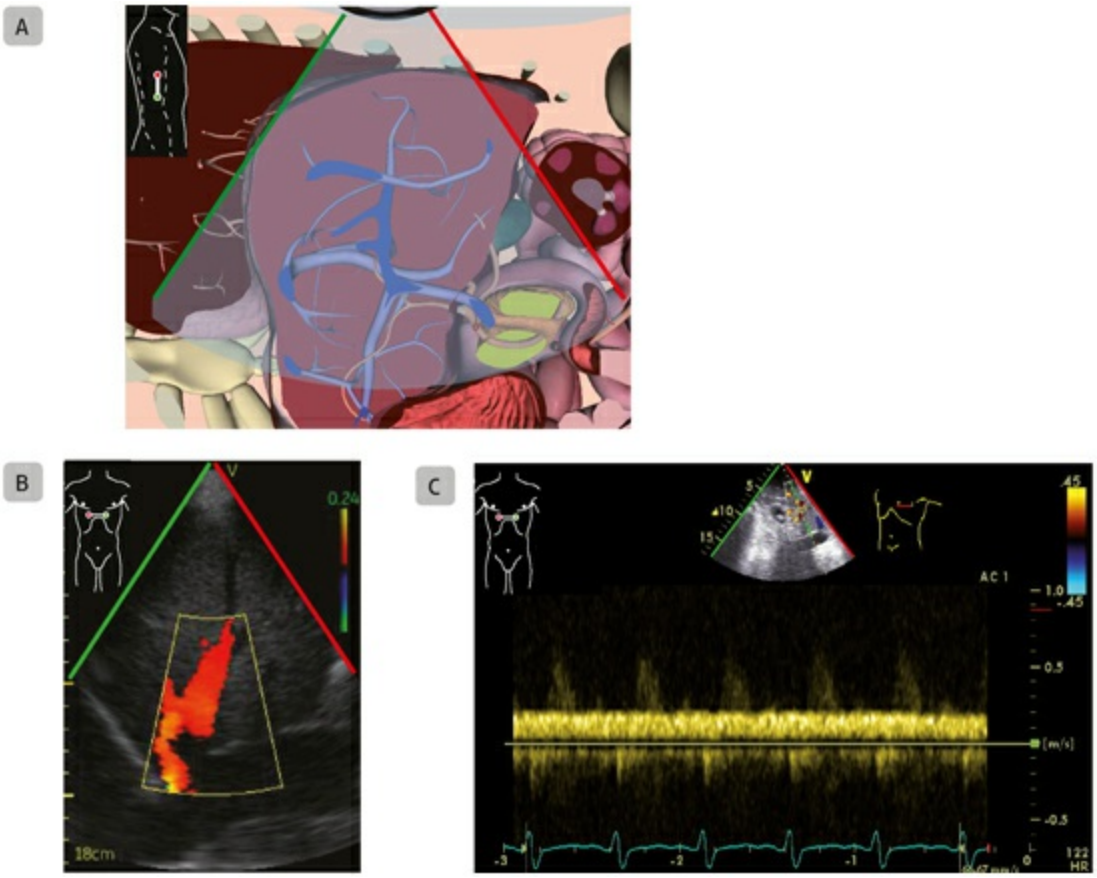

Fig. 16.17 Portal venous flow. (A) Using the Vimedix simulator, normal portal venous flow obtained from a posterior axillary line coronal view with (B) color Doppler and (C) pulsed-wave Doppler, has a monophasic signal indicating that blood is directed toward the transducer. Note the background pulsatile higher velocity of the hepatic artery, which is in the same direction. B:

https://youtu.be/N_m0tyL6avo

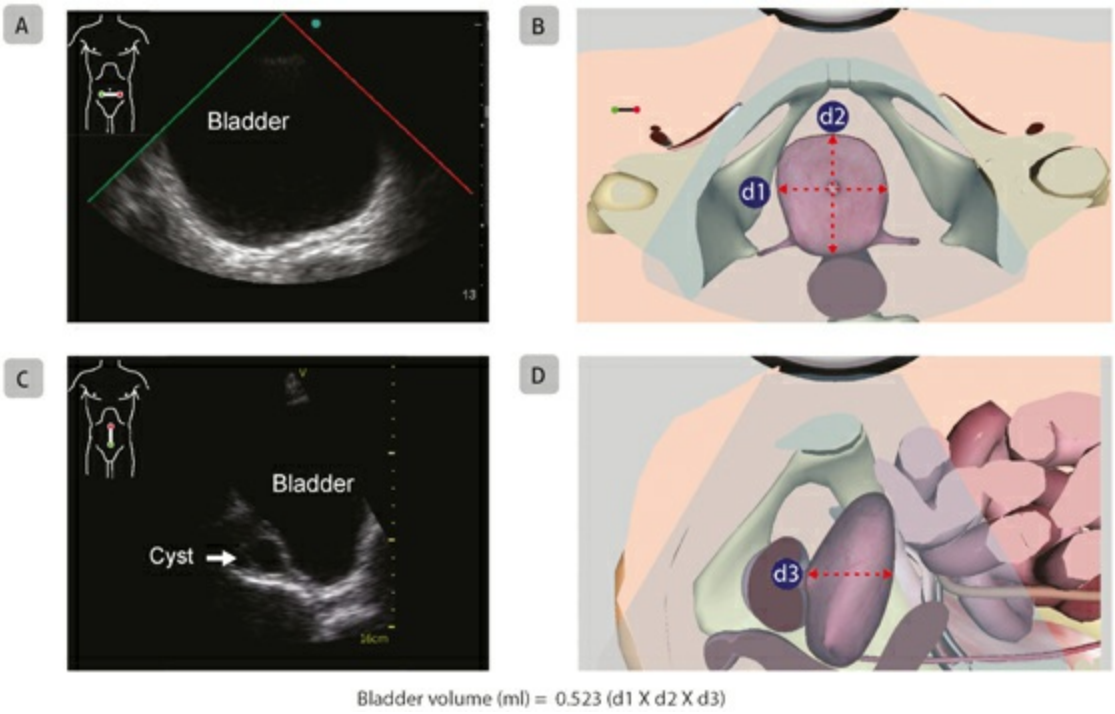

Fig. 16.18 Bladder. (A,B) Transverse and (C,D) longitudinal abdominal ultrasound images of the bladder are shown with the corresponding Vimedix simulator diagrams. The bladder volume can be estimated using the 3 diameters (d1, d2, d3) obtained from these two views.

A: https://youtu.be/3uLixMIf3GY

- Right upper quadrant. In order to exclude fluid, it is important to sweep the hepatorenal space (Morison's pouch) completely, and visualize the caudal tip of the liver (**Figure 16.21**). Conditions such as peritonitis associated with a complex effusion or cirrhosis can be easily diagnosed (**Figure 16.22**).
- Left upper quadrant. In this area, free fluid can accumulate all around the spleen. Sweep the splenorenal space and the diaphragm completely, by beginning anterior and then posterior, until it disappears. In order not to miss any fluid, the diaphragm should be seen from the most lateral to posterior position. Finally, sweep the caudal tip of the spleen.
- Pelvis: In females, the vesico-uterine space is interrogated using a

longitudinal view. In addition, the cephalad portion of the uterine fundus will be scanned (“bowel-uterus space”) followed by the recto-uterine portion (Douglas space) (**Figure 16.23**). In males, the cephalad portion of the bladder will be identified (“bowel-vesical space”), then the recto-vesical portion will be analyzed.

- Retroperitoneal hemorrhage. Retroperitoneal hemorrhage can be imaged in some patients as an anechoic or isoechoic structure that can extend into the peritoneal cavity. There is an association with Grey’s Turner sign, which appears later in the process (**Figure 16.24**).

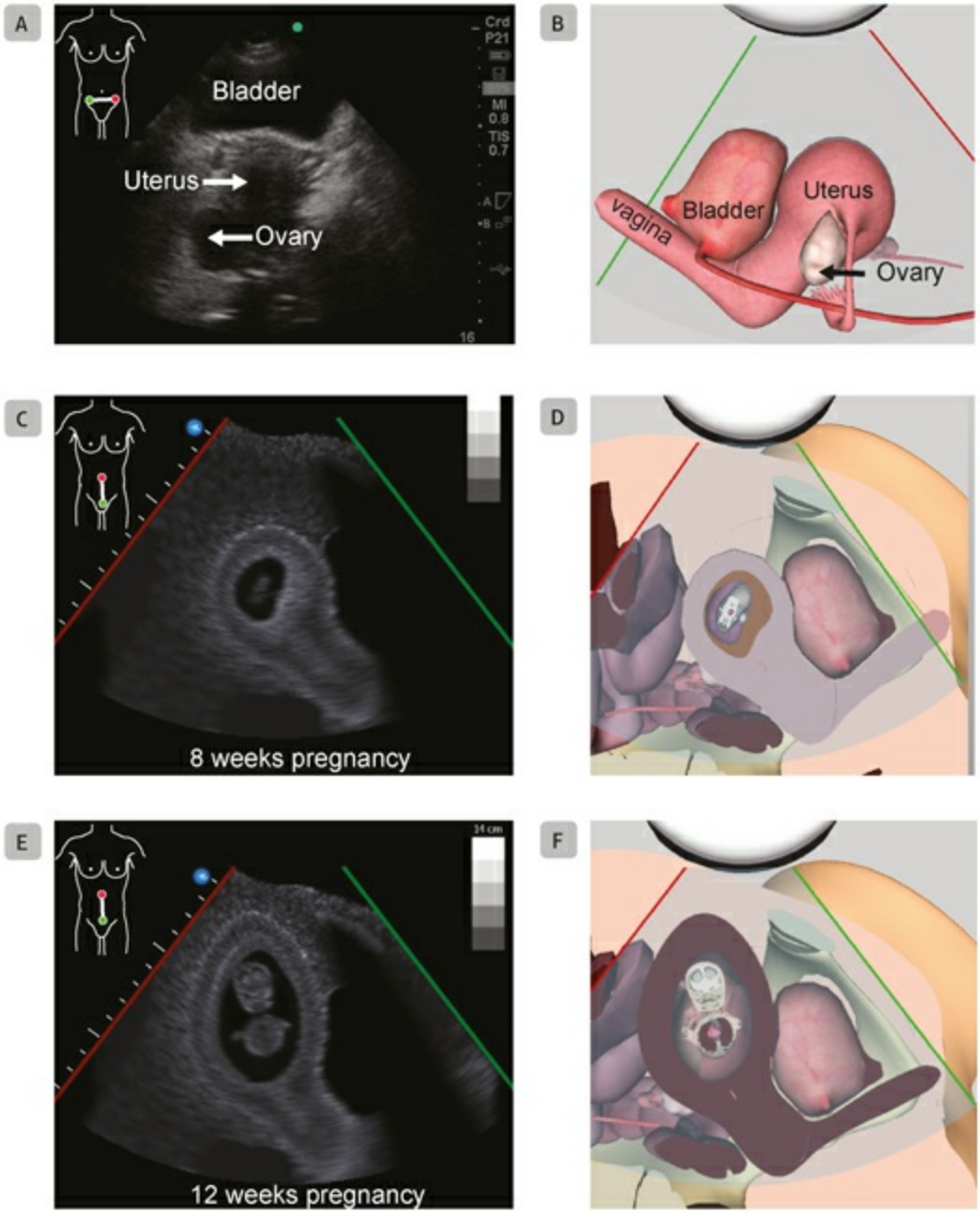

Fig. 16.19 Uterus. (A,B) Normal aspect of the uterus using abdominal ultrasound is shown. (C–F) Lower longitudinal abdominal ultrasound images of a pregnancy at (C,D) 8 weeks and (E,F) 12 weeks are shown with the corresponding Vimedix simulator diagrams.

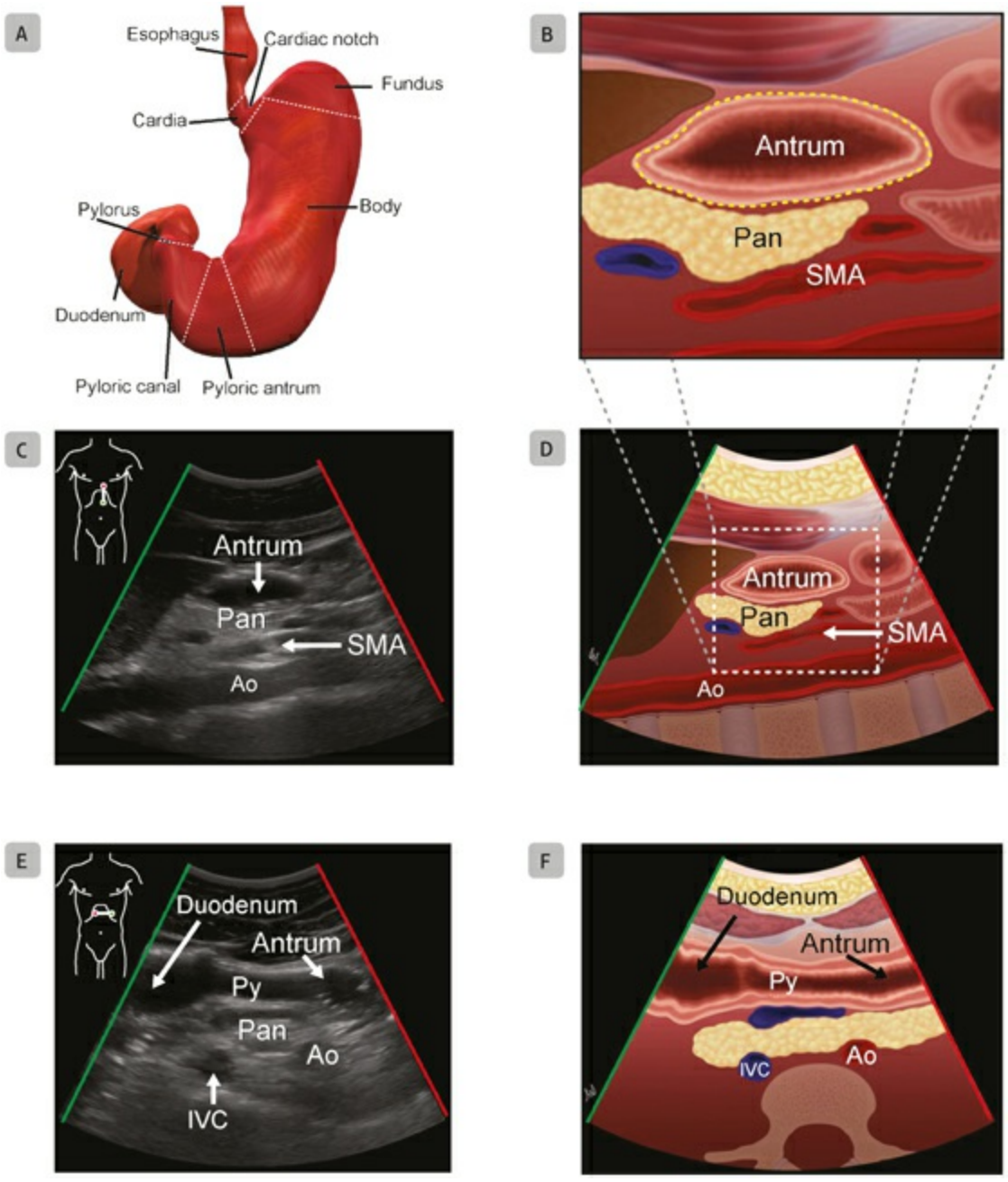

Fig. 16.20 Stomach. (A) The diagram shows the specific anatomic regions of the stomach. (B–D) Longitudinal view of the antrum of the stomach by abdominal ultrasound can be used to estimate gastric volume. (E,F) Transverse view of the antrum of the stomach by abdominal ultrasound is shown. Ao, aorta; IVC, inferior vena cava; Pan, pancreas; Py, pylorus; SMA, superior mesenteric artery. (With permission from Cubillos et al.10)

https://youtu.be/QVQewxu7mr8

https://youtu.be/6ZX9u-4cHEI

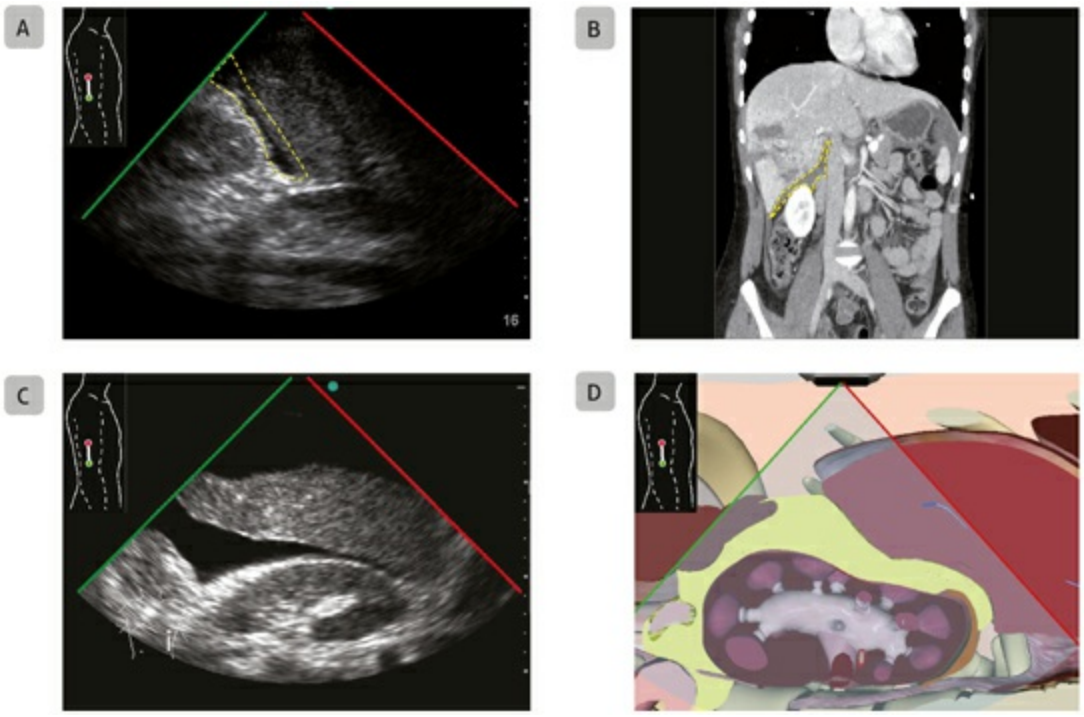

Fig. 16.21 Free fluid. Right middle axillary coronal abdominal ultrasound image in a 48-year-old patient with a liver laceration after a car accident is shown. (A) Free fluid (yellow dotted line) is seen in the hepatorenal space as compared with (B) the corresponding coronal computed tomography scan. (C) Free fluid in a patient with ascites and (D) the corresponding Vimedix simulator image is shown.

A: https://youtu.be/1gux_O5idp4

C: https://youtu.be/FfUZiDsicQE

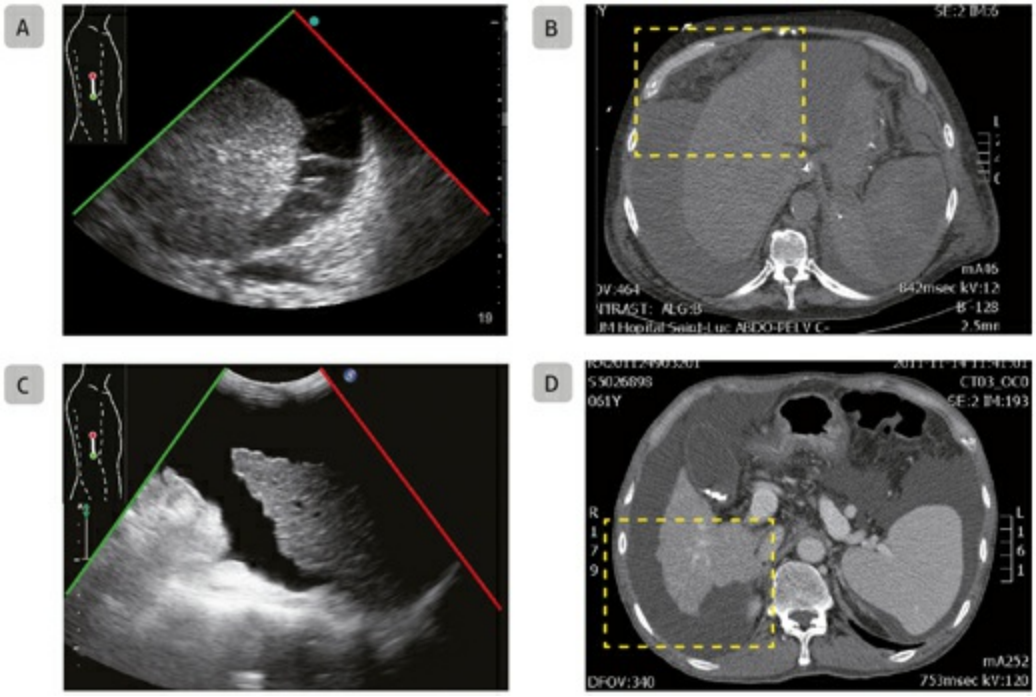

Fig. 16.22 Subdiaphragmatic abscess. A patient with cirrhosis presents in shock. (A,B) Right posterior axillary coronal abdominal ultrasound image demonstrates a complex abdominal effusion compared with the corresponding computed tomography (CT). Note that ultrasound better characterizes the simple or complex nature of free abdominal fluid. (C,D) Typical aspect of a liver with cirrhosis and an irregular border as shown with (C) abdominal ultrasound and (D) corresponding CT.

A: https://youtu.be/nU6aJzLyebk

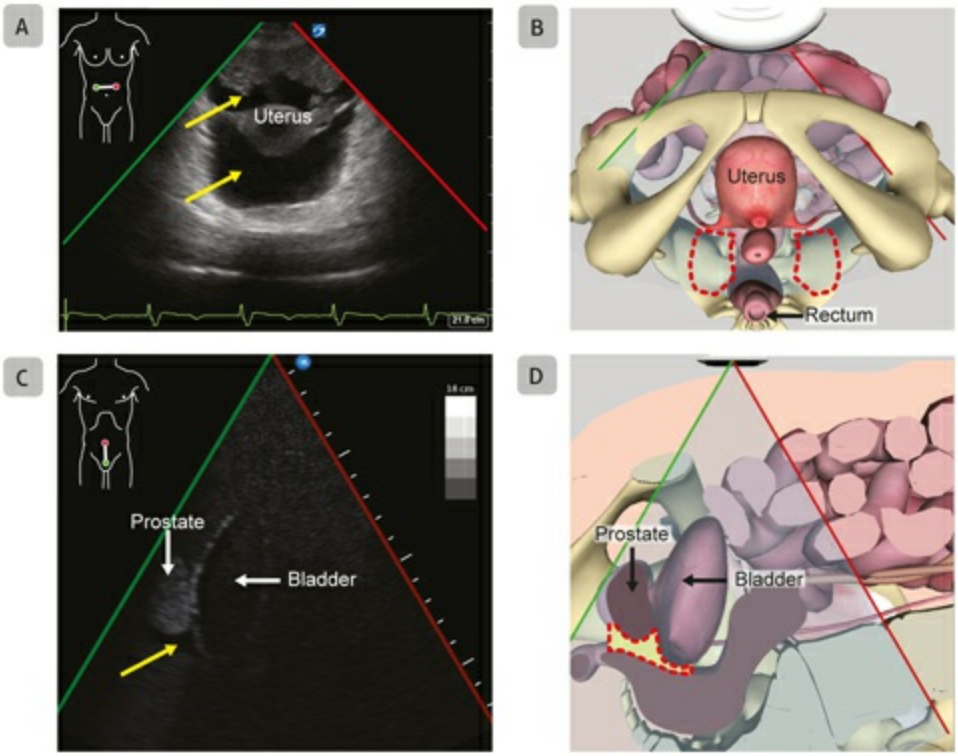

Fig. 16.23 Rectosigmoid free fluid. (A) Lower transverse abdominal ultrasound image of free fluid (yellow arrow) behind the uterus in a female with ascites is shown, with (B) the corresponding Vimedix image. The red dotted line corresponds to the rectosigmoid region. (C,D) Lower longitudinal abdominal ultrasound image of a small amount of free fluid (yellow arrow) in the rectosigmoid region under the prostate in a male with (D) the corresponding Vimedix image.

A: https://youtu.be/fyCG2GnyOYk

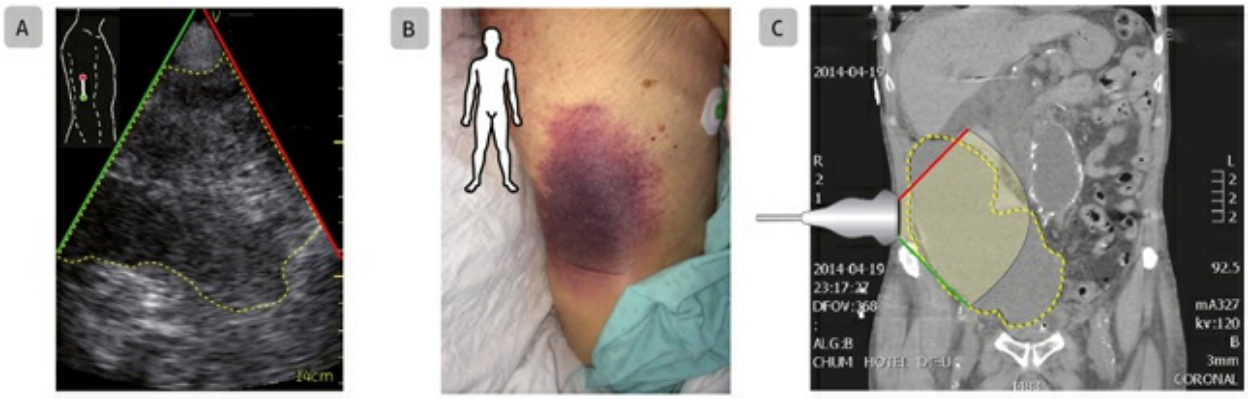

Fig. 16.24 Retroperitoneal hemorrhage. (A) Anterior axillary coronal abdominal ultrasound image shows a retroperitoneal hemorrhage following a coronary angiogram. (B) Photo of Grey's Turner sign that appeared the next day. (C) The corresponding computed tomography shows the extent of the hemorrhage.

A: https://youtu.be/QhqMrjLubbE

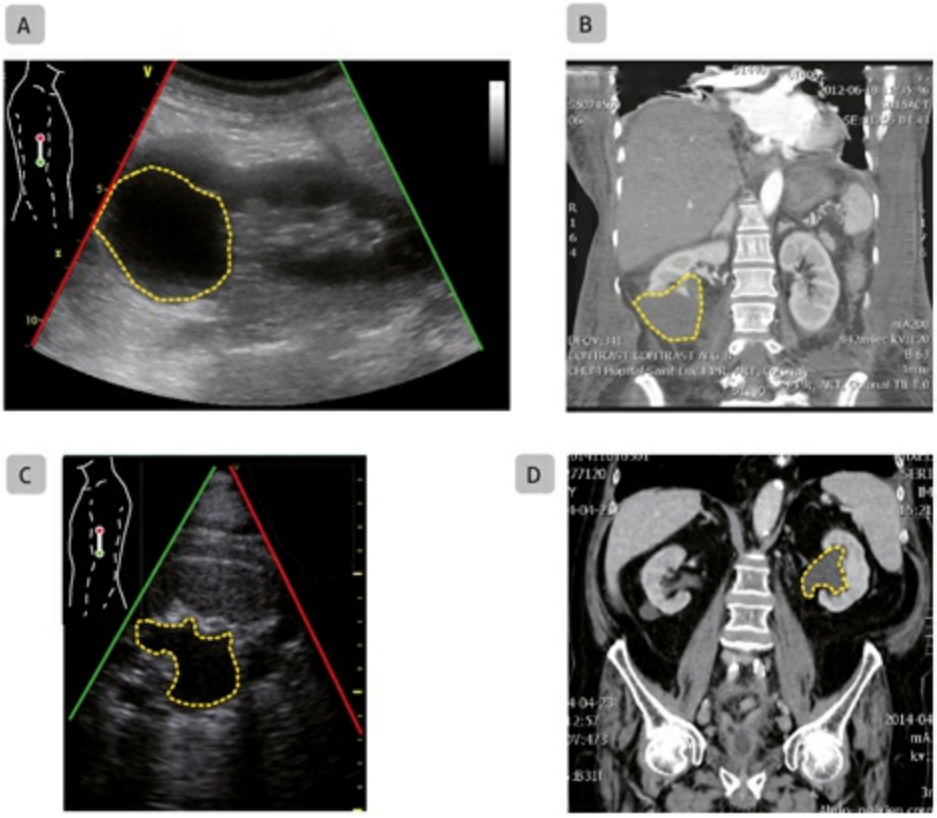

Fig. 16.25 Abnormal kidneys. (A,B) Right posterior axillary coronal abdominal ultrasound image shows a renal cyst (yellow dotted line) at the lower pole of the right kidney, with the corresponding computed tomography (CT). (C,D) Left posterior axillary line coronal abdominal ultrasound image of the left kidney shows hydronephrosis compared with the corresponding CT.

C: https://youtu.be/NUb305Q4L5E

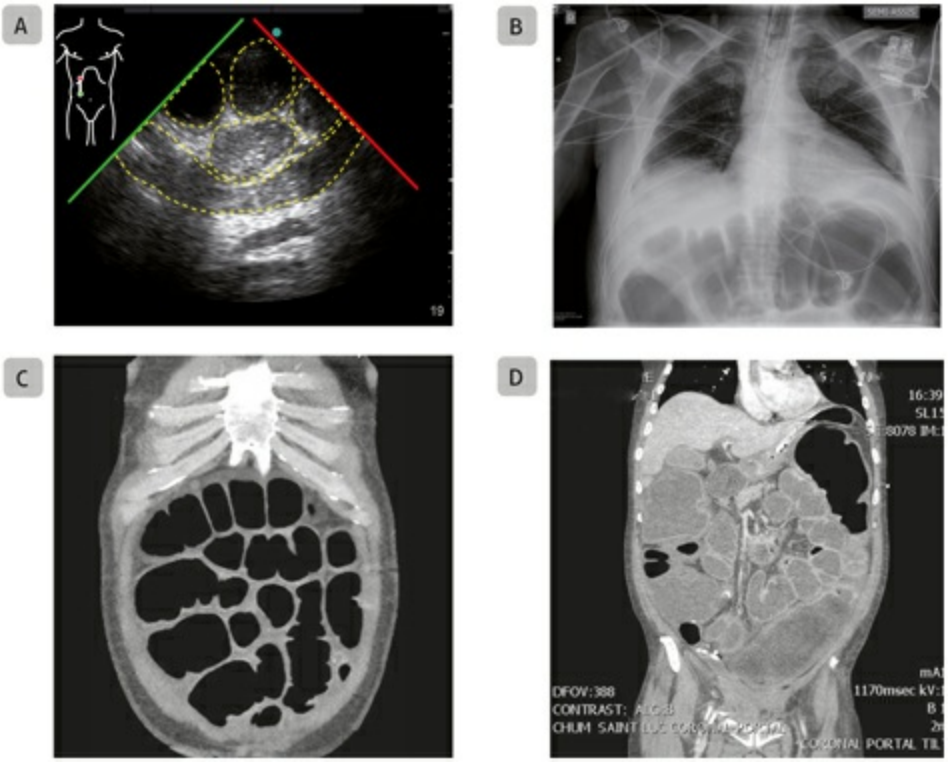

Fig. 16.26 Ileus. (A) Upper longitudinal abdominal ultrasound image of multiple distended loops of bowel compared with (B) corresponding abdominal film and (C,D) computed tomography images.

A: https://youtu.be/_y3oaufVFg8

False Positives (Imitators of Free Fluid)

A normal distended GB can appear as an anechoic structure, but it has a hyperechoic membrane and is a pouch. Therefore the fundus and neck can be identified (**Figure 16.8**). Cystic structure like kidney cyst will also display a hyperechoic membrane (**Figure 16.25 A**). If an irregular anechoic structure is present in the renal hilum, hydronephrosis or parapyelic cysts should be considered (**Figure 16.25** C). Intraluminal bowel fluids should not be mistaken for free fluid. The presence of peristalsis and the echogenic bowel wall can help differentiate (**Figures 16.26 and** 16.27). Fertile females can have a small amount of physiologic fluid, and the seminal vesicles in males

can be mistaken for a small fluid collection.

False Negatives for Free Fluid

There are several situations or limitations where free fluid can be present, but are ill-defined or difficult to detect.

1. The US appearance of peritoneal fluid depends on the fluid content. In the ICU and ER, bedside US is often used to search for signs of hemoperitoneum. This is a frequently encountered condition in these settings, as patients are commonly admitted for trauma or postsurgery care. The appearance of hemoperitoneum on US images can sometimes be misleading. In the acute phase, massive hemoperitoneum can appear as a hyperechoic mass that does not freely distributes in the peritoneal cavity as simple fluid would. The echo texture can also mimic solid organs and bowel content. With time, blood in the peritoneal cavity will appear as a mixture of hypoechoic fluid with solid or semi-solid components, which represent blood clots layering in the more posterior portion of the peritoneal cavity. [12 – 15] Therefore the sonographer has to keep in mind that a negative examination for free fluid does not rule out hemoperitoneum, organ laceration, or postsurgery bleed. If there is high clinical suspicion of a major abdominal bleed, and the search for free fluid is inconclusive, patients should be evaluated by computed tomography (CT) scan if hemodynamically stable in order to detect organ injuries not associated with free fluid. [16] Patients with acute or chronic peritonitis can also present with peritoneal fluid on US.
2. The US appearance of fluid will depend on the cellular and protein content (transudate or exudate). For example, chronic bacterial peritonitis and peritoneal carcinomatosis present with fluid as echoic as solid organs. Pus can also be hyperechoic, and this has to be kept in mind in the setting of postsurgery care. Inflammatory and infectious processes involving the peritoneum often show fluid, with internal septa and low-level echoes that can organize into loculated fluid collections (**Figure 16.22**) and even abscesses. These generally are present with irregular and measurable borders, mass effects, and content that does not freely move in the peritoneal

space. Inter-loop complex fluid can also be trapped in the more central abdominal cavity. [17] The sonographer has to keep in mind that such fluid will not necessarily always accumulate in the paracolic gutters, Morison's space, and pelvis as normal free fluid would.

3. Adhesions from prior surgeries will lead to free fluid accumulation in different and unknown locations in the abdomen.
4. When there is little free peritoneal fluid located in the pelvis, an empty bladder can affect the quality of the examination. A full bladder is generally used as an acoustic window to be able to evaluate the Douglas pouch for free fluid. [18]
5. If the amount of free air in the abdomen (pneumoperitoneum) is significant, artifacts can limit the evaluation of free fluid as it accumulates in the deeper portions of the peritoneal cavity, where image quality is deteriorated by shadowing. However the presence of air in the non-dependant region is an important sign that can point toward bowel perforation (see section on Pneumoperitoneum and **Figure 16.28** A). [19] In addition, air in the bowel wall or organ such as the liver can be associated with perforation, or indicate infection with a gas-forming organism (**Figure 16.28** C).
6. For the same reason as pneumoperitoneum, subcutaneous emphysema is another important pitfall when looking for free fluid. [20]

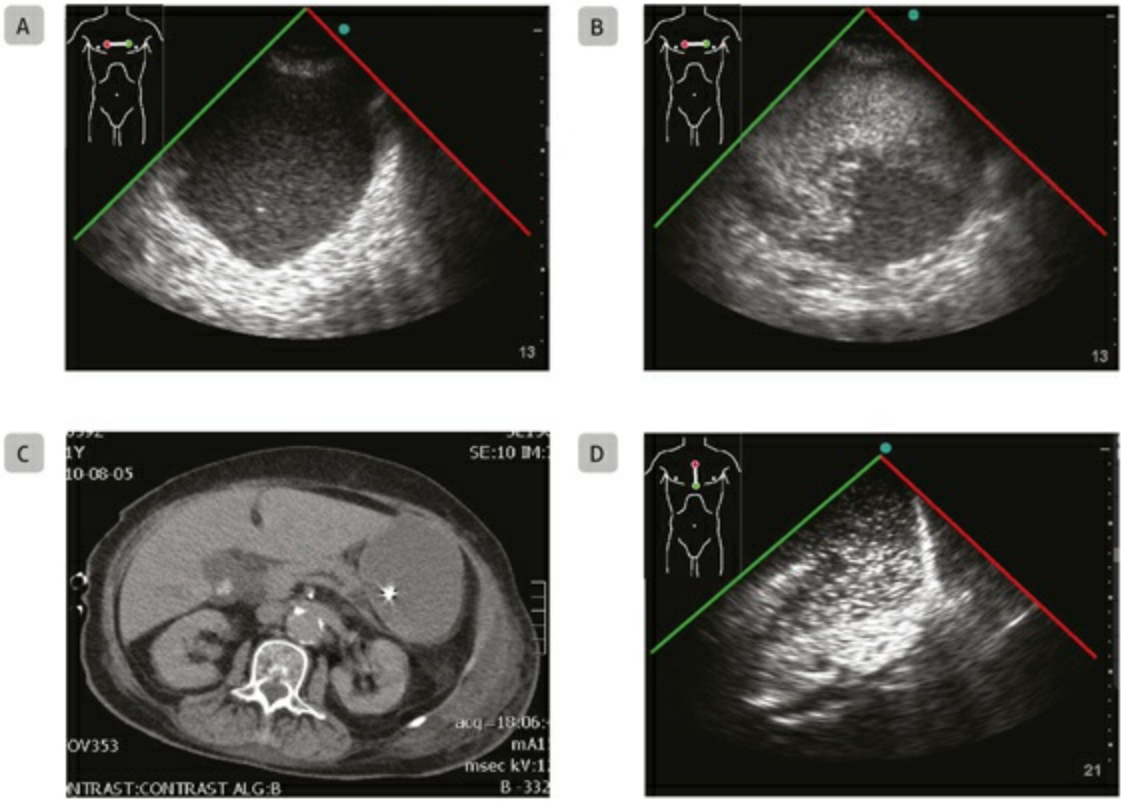

Fig. 16.27 Full stomach. (A) A left upper transverse abdominal ultrasound image obtained in a hemodynamically unstable patient shows a stomach distended with liquid. (B) Injecting 60 ml of air through the nasogastric tube confirms the diagnosis. (C) Corresponding computed tomography of this patient with a full stomach is shown. Note the white dot in the stomach corresponding to the nasogastric tube. (D) Active upper gastro-intestinal bleeding shows more hyperechogenic stomach in this upper longitudinal abdominal ultrasound image.

A: https://youtu.be/ulrn_XefVUg

B: https://youtu.be/n2alkRcvK74

D: https://youtu.be/Tw6NEzDeHGM

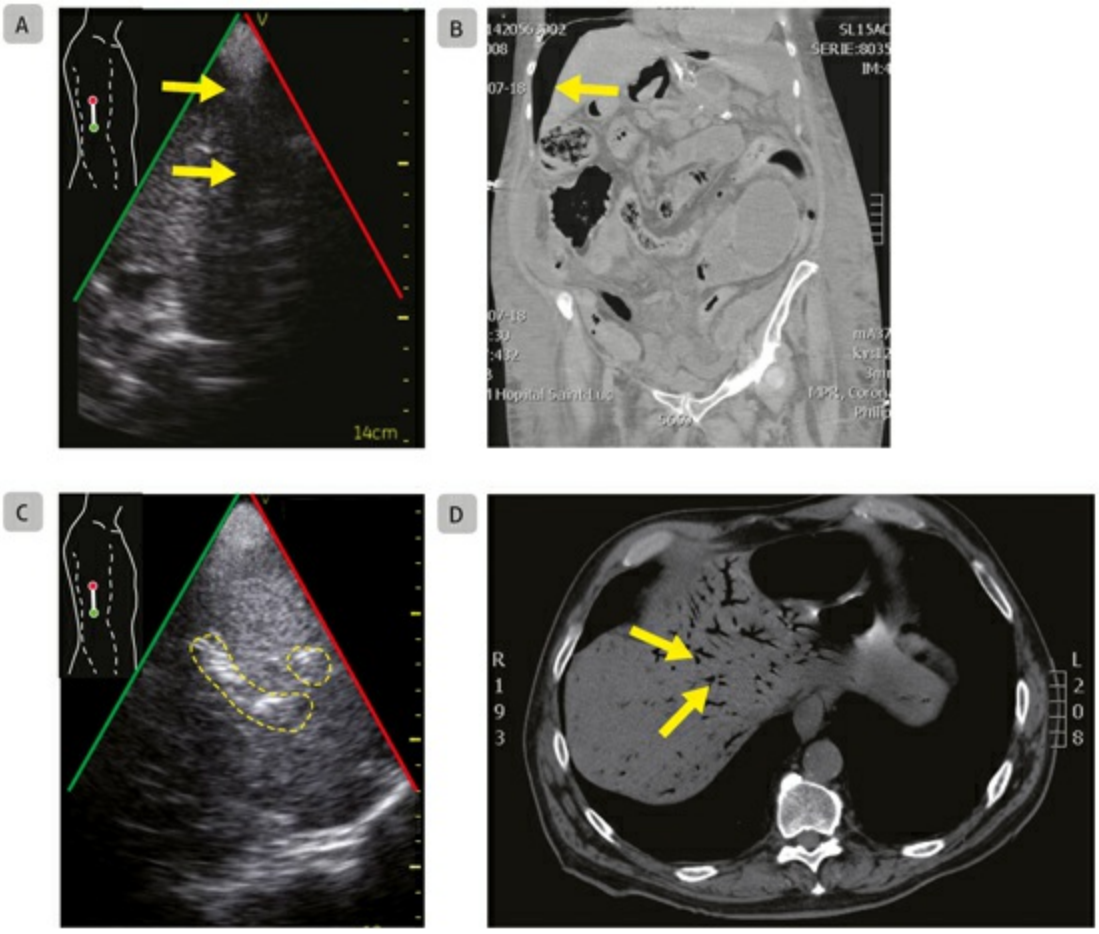

Fig. 16.28 Air in the liver. (A,B) Transient appearance of air (yellow arrows) with shadowing from a bowel perforation is seen in the liver during inspiration in this right coronal abdominal ultrasound image, and in the corresponding computed tomography (CT). (C,D) Hyperechogenic signals in the liver (dotted lines) of a patient with acute abdominal pain appear in this right coronal abdominal ultrasound image. The axial CT scan demonstrated air in the liver from mesenteric ischemia.

A: https://youtu.be/qXE6Pg9RK7c

C: https://youtu.be/FF0QGxoEBMY

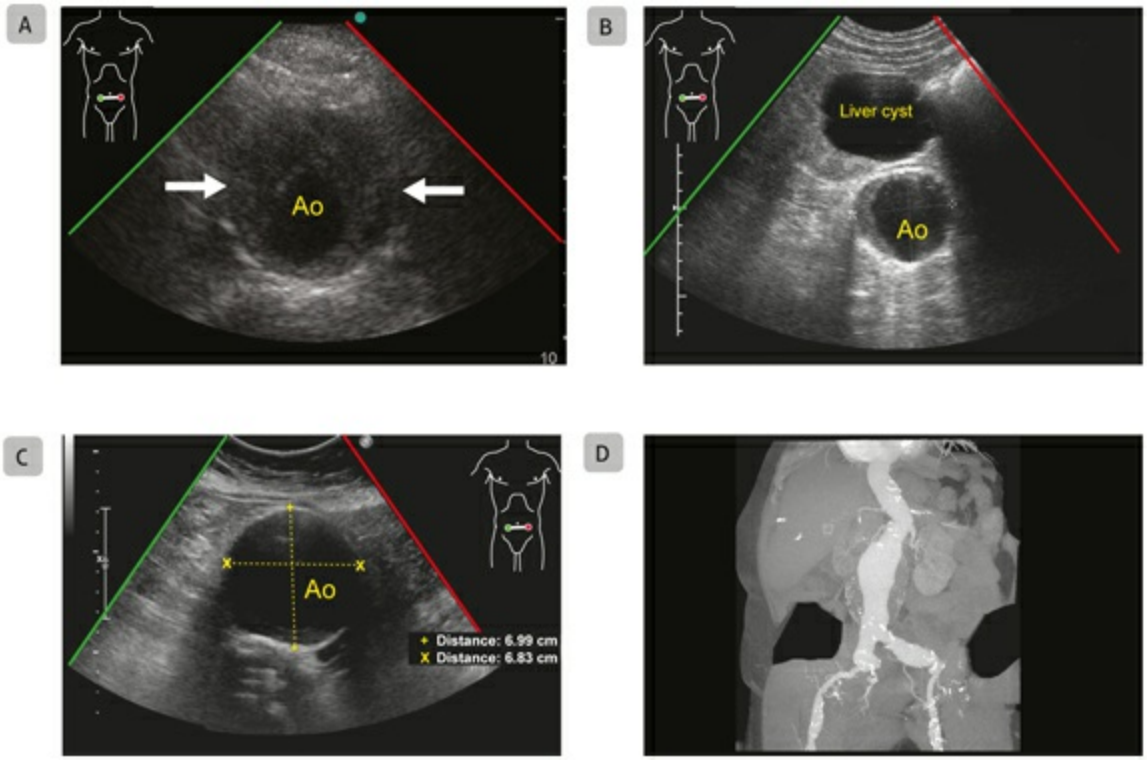

Fig. 16.29 Abdominal aortic aneurysm. (A) The reduced aortic lumen from severe atheromatous infiltration (white arrows) of an abdominal aortic aneurysm (AAA) is present in this mid-transverse abdominal ultrasound image. (B) A liver cyst is present just above the AAA. (C) Measurement of the dilated AAA diameters from a mid-transverse abdominal ultrasound image is shown. (D) The corresponding computed angiogram shows a significantly tortuous abdominal aorta (Ao).

A: https://youtu.be/XibgQnmDApI

D: https://youtu.be/_z-MPPEjtSc

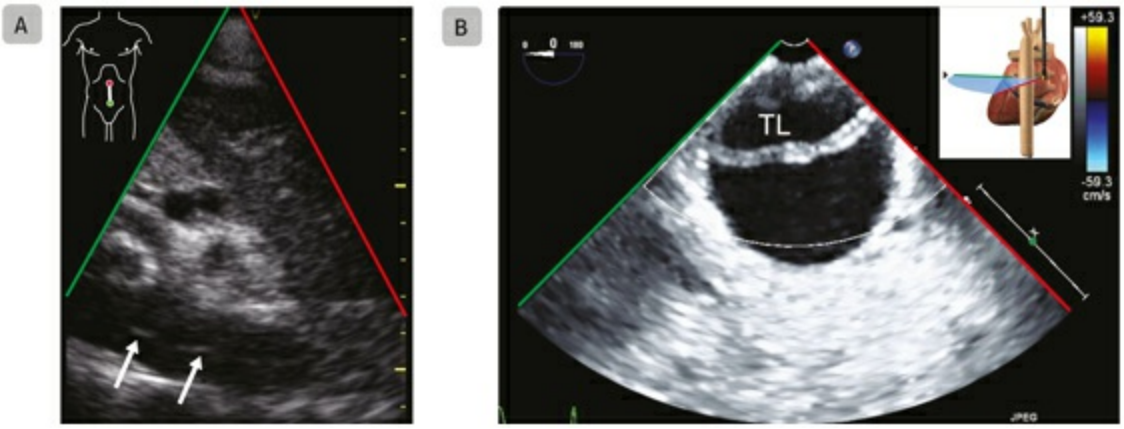

Fig. 16.30 Aortic dissection. (A) Mid-upper longitudinal view obtained using abdominal ultrasound shows dissection (arrows) of the descending aorta in a 47-year-old male presenting with acute chest pain. (B) Corresponding transesophageal echocardiographic short-axis view of the thoracic aorta demonstrates the true lumen (TL) and the lower false lumen. (Courtesy of Dr Alain Deschamps.).

A: https://youtu.be/Yf7XIC56KxQ

B: https://youtu.be/DQrXG_rMdtk

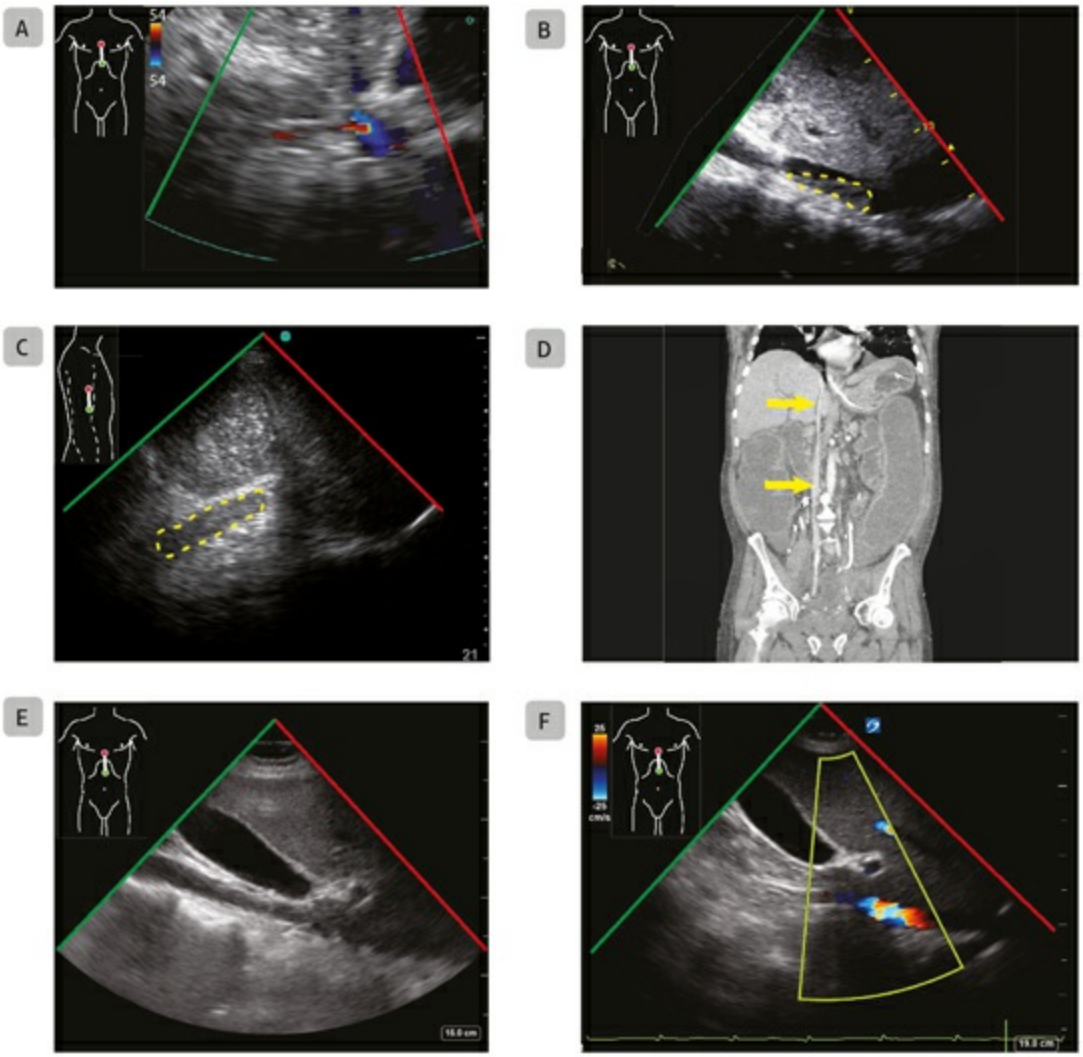

Fig. 16.31 Abnormal inferior vena cava (IVC). (A) An upper longitudinal abdominal ultrasound image shows a small IVC in a patient with hemorrhagic shock. Color Doppler acceleration is present at the junction between the hepatic vein and the IVC. (B) An upper longitudinal abdominal ultrasound image shows IVC stenosis from a laminar thrombus (yellow dotted line) in a liver transplant patient. (C,D) A distended duodenum gives the appearance of a pseudo IVC (yellow dotted line) in this right coronal abdominal ultrasound image of a patient with abdominal compartment syndrome from an ileus. The corresponding computed tomography showed dilated bowel. Note the reduced dimension of the IVC (yellow arrows) typical of abdominal compartment syndrome. (E,F) A vertically positioned gallbladder can be mistaken for the IVC in this upper longitudinal abdominal ultrasound image. The absence of flow by color Doppler confirms that this is not a vascular structure.

A: https://youtu.be/77S5kJ7NKRU

B: https://youtu.be/moLBEYNIsQY

C: https://youtu.be/4cnEUG4kDQI

C: https://youtu.be/RCU4VHazStA

E: https://youtu.be/fh2wCM8DcCw

F: https://youtu.be/EwGqkTlHeSk

AORTIC AND VENA CAVA PATHOLOGY

Bedside US can be used to diagnosis abdominal aortic aneurysm and dissection. The majority of aortic aneurysms are infrarenal (95%) compared to suprarenal (5%) (**Figure 16.29**). Aortic dissection is characterized by a flap that separates a true from a false lumen (**Figure 16.30**). The IVC can be difficult to see in hypovolemic patients, or those with abdominal compartment syndrome, because the dimension will be significantly reduced. In those situations, color Doppler may help to identify the IVC (**Figure 16.31 A**). Thrombus in the IVC can be seen easily (**Figure 16.31** B). It is important not to confuse duodenal dilatation or a vertical GB with the IVC (**Figure 16.31 C-F**). Color Doppler is also very useful in those patients with distended

IVC in order to identify pulsatile portal venous flow, which is commonly seen in patients with right ventricular failure, severe tricuspid regurgitation, and fluid overload or hypervolemia (**Figure 16.32** and see **Figure 4.39**).

Cholecystitis

Acute cholecystitis can be associated with the presence of gallstones in the GB (**Figure 16.33 A**). When tract obstruction is encountered leading to biliary tract dilatation a “double barrel” sign can be observed (**Figure 16.33** C). Detailed examination of the biliary tract is beyond the scope of a focused examination. Signs suggestive of cholecystitis include pain with pressure on the GB (Positive Murphy sign), wall thickening (>3 mm) measured at the narrowest point of the anterior wall in a short-axis view (**Figure 16.34**), pericholecystic fluid, GB distension (greater than 10 x 5 cm), and biliary sludge. One of the most sensitive findings in acute cholecystitis is the presence of cholelithiasis in combination with the sonographic Murphy sign. Thickening of the GB wall alone is common in the edematous and hypoalbuminemic ICU patient and, when isolated, is insufficient to diagnose cholecystitis.

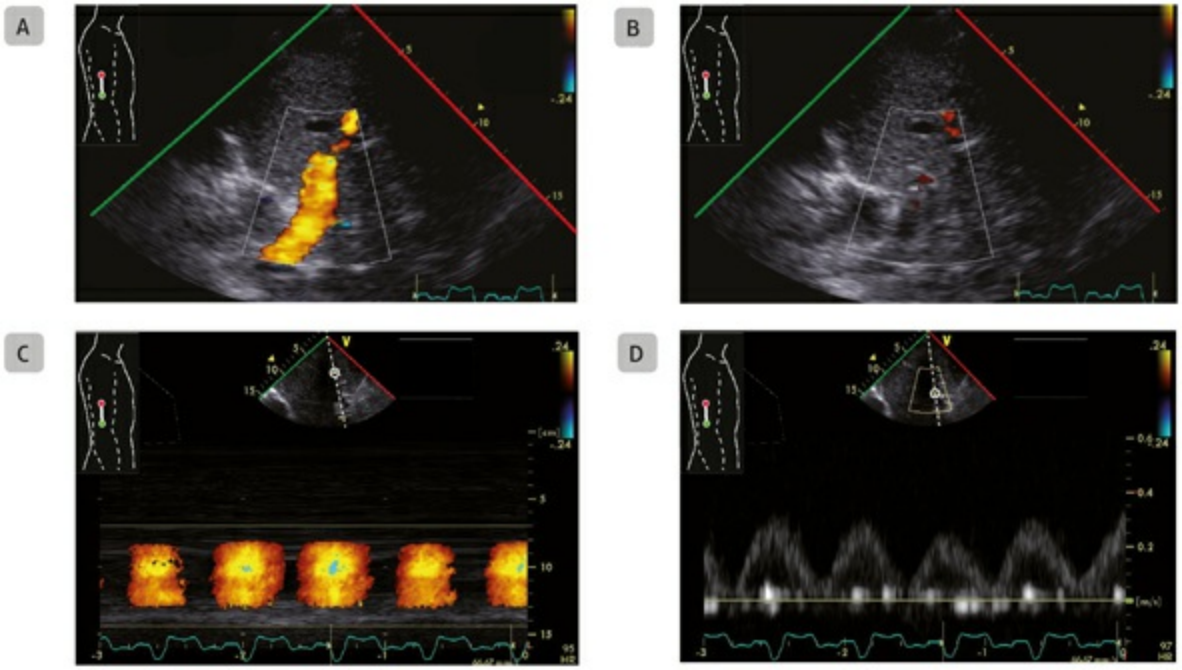

Fig. 16.32 Abnormal portal vein velocity. A 23-year-old female with right ventricular failure and fluid overload after a Ross procedure is imaged with abdominal ultrasound. (A–D) Right posterior-axillary coronal view with color Doppler of the right portal vein in (A) systole and (B) diastole and the

corresponding (C) color M-mode and (D) pulsed-wave Doppler are shown. The increased pulsatility was associated with renal dysfunction and increased liver enzymes, which resolved with aggressive diuresis.

A: https://youtu.be/3AZqkSkoQeU

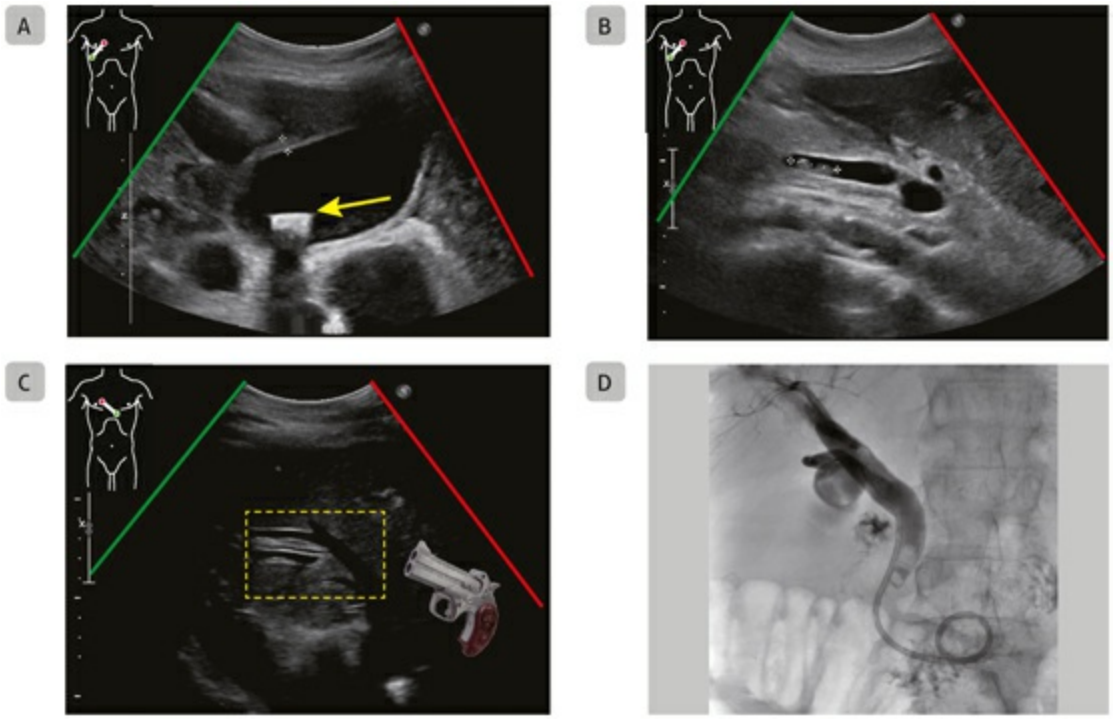

Fig. 16.33 Gallstone complications. (A,B) Right oblique subcostal views obtained using abdominal ultrasound shows (A) a gallbladder with a gallstone (arrow) but also (B) dilatation of the biliary tree with stones. (C) Using a right intercostal view, the "double-barrel" sign is seen. This sign represents the dilated right biliary tree whose dimension is similar to the corresponding right portal vein. (D) Percutaneous drainage of the gallbladder was performed under fluoroscopic guidance.

A: https://youtu.be/NEdebgN70EE

Hydronephrosis

In the presence of an obstruction to urine flow, the renal pelvis and calyces dilate first. A black (anechoic) area distending the normal bright white (hyperechoic) central area of the kidney will be seen (**Figure 16.35**). As obstruction continues, the renal parenchyma becomes compressed, and thinning of the pyramids will appear. It is important to always scan both kidneys for comparison, and correlate the US findings with the patient's status and clinical presentation. Remember that mild hydronephrosis can be a normal finding in healthy patients with a full bladder or in pregnant women, typically on the right side. Hilar vessels can sometimes be mistaken for mild hydroureter: color Doppler can differentiate between both.

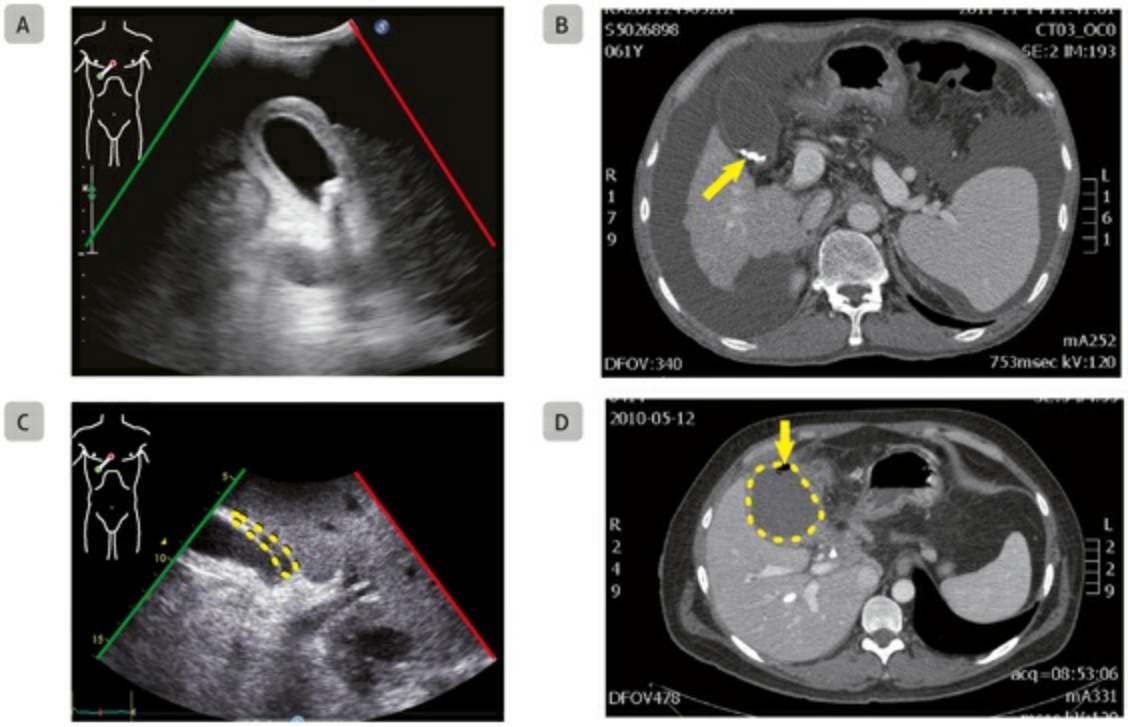

Fig. 16.34 Abnormal gallbladder. (A,B) Right oblique subcostal abdominal ultrasound image shows an edematous gallbladder wall and gallstone (acoustic shadow) in a patient with cirrhosis. The corresponding computed tomography (CT) scan shows cirrhosis and the gallstone (arrow). (C) Acute cholecystitis in a patient with a positive sonographic Murphy sign. Note the edematous gallbladder wall (yellow dotted line). (D) Typical CT scan shows the gallbladder (yellow dotted line) with air in the gallbladder wall (arrow).

C: https://youtu.be/GzLOXnmTy00

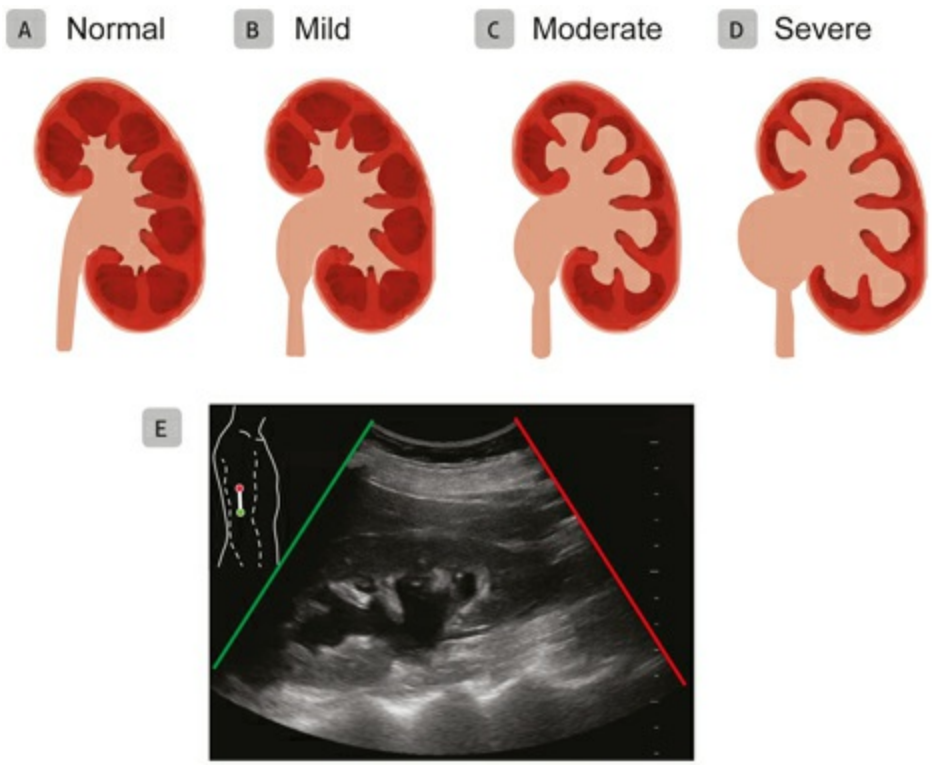

Fig. 16.35 Hydronephosis. (A–D) Diagrams illustrate the progression of hydronephrosis from normal to severe are presented. (E) Right coronal abdominal ultrasound image of a patient with moderate hydronephrosis in the right kidney is shown.

E: https://youtu.be/HAfEOOOaB50

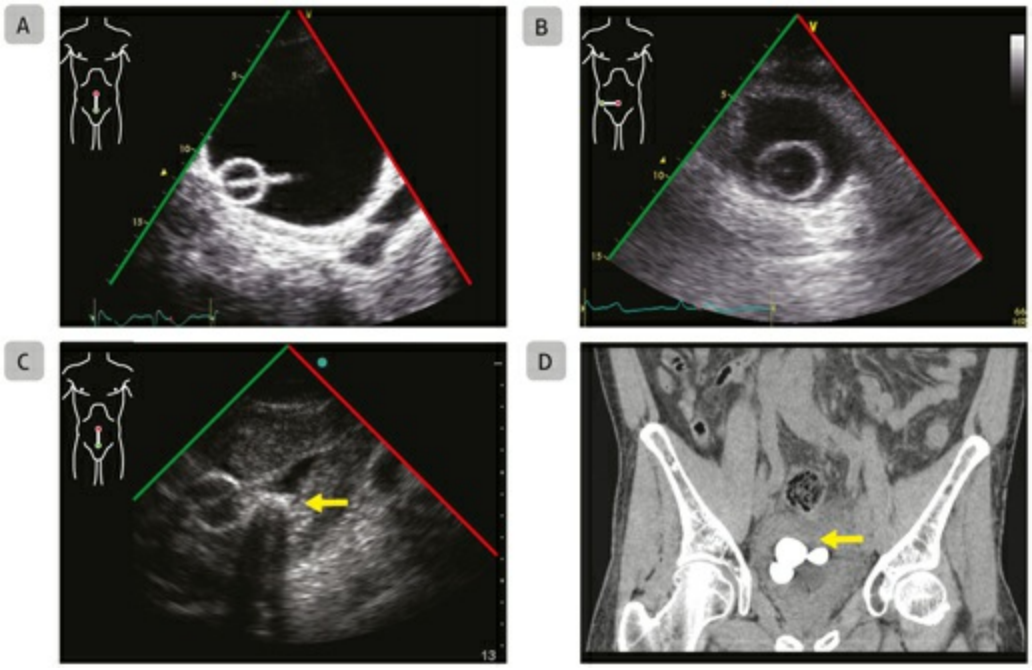

Fig. 16.36 Foley catheter. A 25-year-old female unconscious in the intensive care unit developed reduced urine output and an abdominal ultrasound was performed. (A) The middle lower abdominal transverse view shows the tip of the urinary catheter in a distended bladder from an occluded Foley catheter. Once the catheter was unblocked, 600 mL of urine were drained. Note the free fluid in the rectosigmoid region. (B) Compare this middle lower longitudinal abdominal ultrasound view of a well-drained bladder. (C,D) Bladder stones (arrow) with shadowing are seen with an abdominal ultrasound image and with the corresponding computed tomography.

A: https://youtu.be/PBlUL_Odqhc

B: https://youtu.be/Dr-eSiV-Kgk

C: https://youtu.be/MNyiyxbCLWg

Bladder Pathologies

Obstruction of a Foley catheter is common in the ICU, and should always be excluded in any patient presenting with anuria or reduced urine output. If the Foley catheter tip is not seen, injection of sterile water under US guidance can help in locating it. Bladder clots can cause obstruction, and continuous irrigation may be required with close US monitoring. Clots should not be confounded with polyps, tumors, or stones (**Figure 16.36**).

Pneumoperitoneum

Bedside US can help evaluate acute abdominal pain in the ICU and emergency room. In this setting, patients can suffer from conditions such as acute appendicitis, diverticulitis, ulcer perforation, colitis, and intestinal ischemia. If untreated, these conditions can result in air in the peritoneal cavity (pneumoperitoneum) (**Figure 16.28**), or retroperitoneal space (retropneumoperitoneum). Thus, air distribution depends on the perforation site. When the patient is examined in the supine position, pneumoperitoneum accumulates in the anterior portion of the peritoneal cavity. It can be seen first in the epigastrium or right upper quadrant. Free air is known to shift with patient positioning. For example, it will shift from the anterior part of the liver if the patient is in the supine position, to the lateral aspect of the liver, in the left lateral decubitus position. [21] Air in the peritoneal cavity is seen as echogenic lines, or spots with ring-down also called “comet-tail” artifacts.

Diaphragmatic Paralysis

Diaphragmatic function can be altered after cardiac surgery, liver transplantation, and non-cardiac surgery. [22] In addition, in the shock state with reduced oxygen transport, the diaphragm motion can become paradoxical. This is a sign of impending cardio-respiratory arrest (see **Figure 14.33**).

GASTRIC DISTENSION

In the hemodynamically unstable or hypoxemic patient, gastric atonia is often present (**Figure 16.27**). The risk of aspiration can be reduced by inserting a nasogastric tube before airway management. As mentioned previously,

gastric volume can be estimated with US (**Figure 16.20**). To ensure the stomach is being imaged and not a fluid collection in that area, inject air in the nasogastric tube, and look for the appearance of swirling echogenic bubbles. If positive, then it is the stomach; if absent, another fluid collection should be suspected (**Figure 16.27** B).

Bowel Pathologies

Peristalsis will be absent if ileus is present. Lumen distension of >3 cm and bowel wall thickness >4 mm is abnormal (**Figure 16.37**). Bowel ischemia can be suspected in the presence of acute abdominal pain, free fluid in the wall, and air in the liver (**Figure 16.28**). Colitis with the "thumb-printing sign" can also be seen in some patients (**Figure 16.37**).

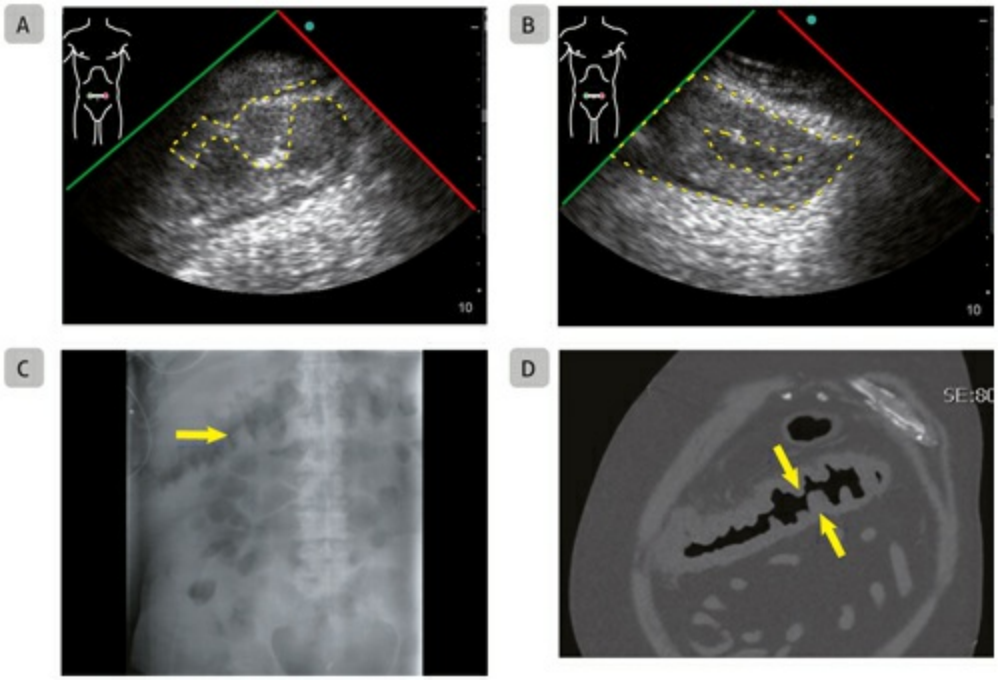

Fig. 16.37 Acute colitis. A patient with Clostridium difficile colitis undergoes abdominal imaging. Thumbprinting and significant edema (yellow arrows) of the transverse colon is shown with (A,B) transverse midabdominal view obtained using abdominal ultrasound, (C) abdominal films, and (D) computed tomography.

A: https://youtu.be/DjyqYDORNUI

B: https://youtu.be/-2tWY2915Gk

LIVER AND SPLEEN PATHOLOGIES

Numerous conditions can produce heterogeneity in the liver including steatosis, hematomas, hemangiomas, abscess, and cancer (**Figure 16.38**). Other modalities and even biopsies may be necessary to clarify the diagnosis. Splenic pathologies include splenomegaly, hilar varices, hematomas, and an accessory spleen (**Figure 16.39**).

GENERAL PITFALLS

When using bedside US evaluation in the ICU unit or resuscitation area of the ER, several pitfalls can limit diagnostic performance. It is well recognized by sonographers that patient morphology is one of the most important factors in achieving technically sound examinations. Soft tissues and subcutaneous fat create important US wave attenuation that render even the search of free peritoneal fluid difficult. [23] Patient positioning can also be a limiting factor. Patients can sometimes be kept in lateral decubitus after surgery, making evaluation of free fluid difficult. [24] Furthermore, ICU and trauma patients are often partially covered with dressings, leaving only a small acoustic window for the sonographer. Collaboration with the nursing team is essential in order to remove bandages in a timely manner, so that it minimizes the risk of hospital-acquired infections.

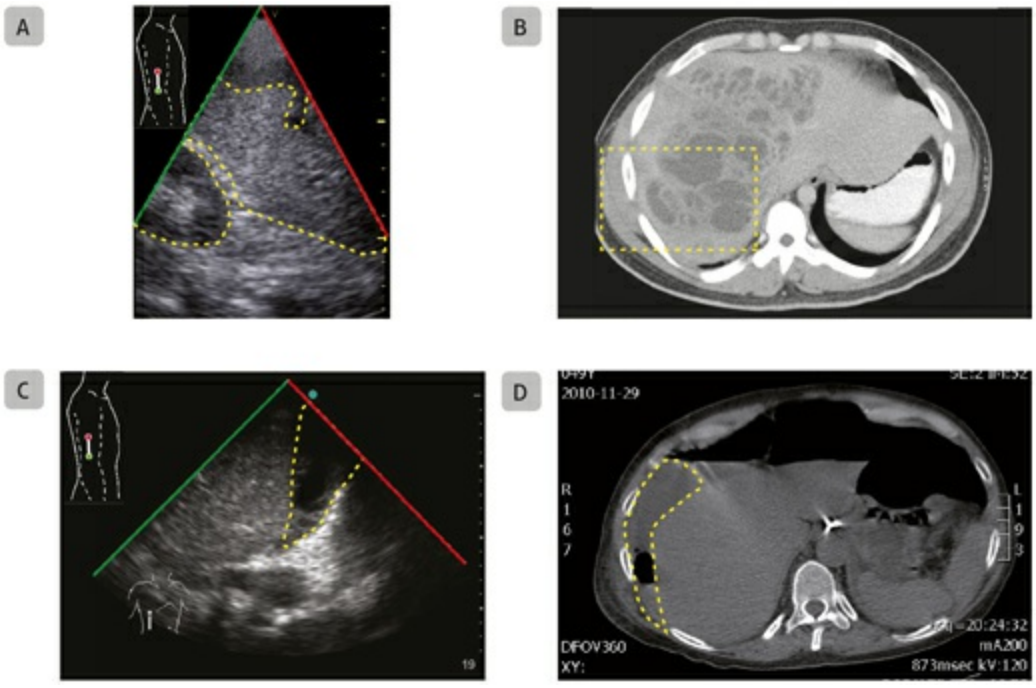

Fig. 16.38 Abnormal liver. (A) Right posterior axillary coronal view obtained using abdominal ultrasound shows steatosis in an obese patient. Note the striking hyperechogenicity (yellow dotted line) of the liver compared to the cortical portion of the kidney. (B) Liver mass with anechoic and isoechoic components is shown with computed tomography (CT). (C) Liver abscess in a patient with fever shows as an anechoic region below the diaphragm (dotted line) in this right coronal abdominal ultrasound image. (D) The corresponding CT scan shows a localized air collection (dotted line).

C: https://youtu.be/au7wKEacxqI

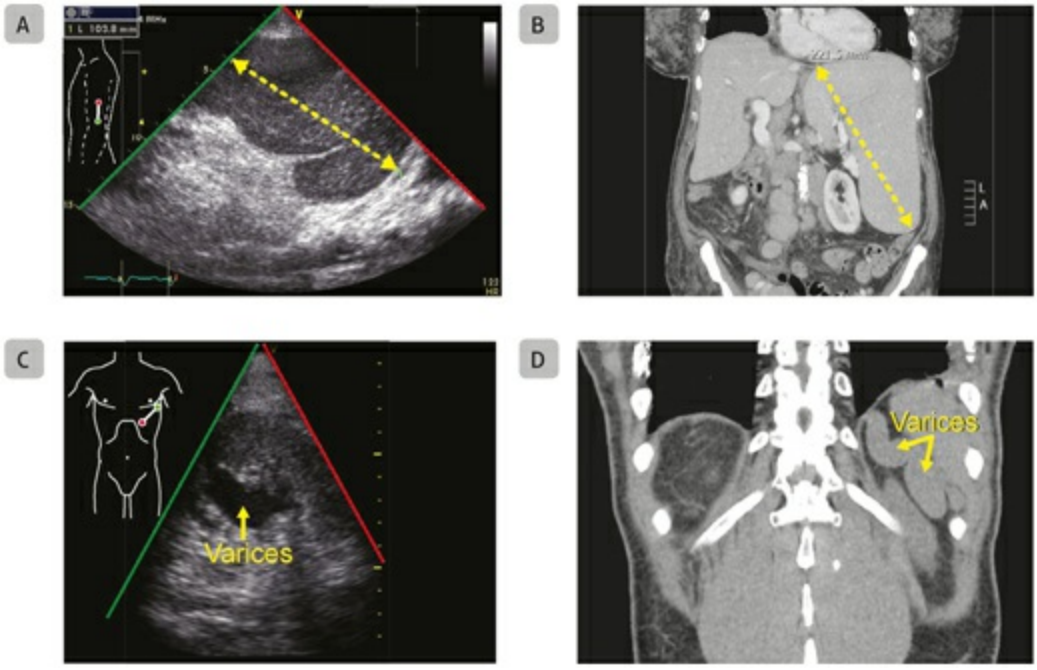

Fig. 16.39 Abnormal spleen. (A,B) A patient with chronic lymphocytic leukemia presents with an enlarged spleen. Splenomegaly is seen with this (A) left coronal abdominal ultrasound image and (B) corresponding coronal computed tomography (CT) scan. Note that the spleen is larger than the liver. (C,D) A patient with cirrhosis has varices. (C) The varices (yellow arrow) are seen as an anechoic region under the spleen in this right oblique subcostal abdominal ultrasound image compared with (D) the corresponding CT.

A: https://youtu.be/k5byzlxAGF4

C: https://youtu.be/ou4od2xQRbE

REFERENCES

1. SchachererD., KleblF., GoetzD., BuettnerR., ZierhutS., SchoelmerichJ., et al. Abdominal ultrasound in the intensive care unit: a 3-year survey on 400 patients. *Intensive Care Med*. 2007;*33*:841–4.
2. MayoP.H., BeaulieuY., DoelkenP., Feller-KopmanD., HarrodC., KaplanA., et al. American College of Chest Physicians/La Societe de Reanimation de Langue Frangaise statement on

competence in critical care ultrasonography. *Chest*. 2009;*135*:1050–60.
3. MirvisS.E., VainrightJ.R., NelsonA.W., JohnstonG.S., ShorrR., RodriguezA., et al. The diagnosis of acute acalculous cholecystitis: a comparison of sonography, scintigraphy, and CT. *AJR Am J Roentgenol*. 1986;*147*:1171–5.
4. WangH.P., ChenS.C.. Upper abdominal ultrasound in the critically ill. *Crit Care Med*. 2007;*35*(5 Suppl.):S208–15.
5. ArntfieldR., MillingtonS., AinsworthC., AroraR., BoydJ., FinlaysonG., et al. Canadian recommendations for critical care ultrasound training and competency. *Can Respir J*. 2014;*21*:341–5.
6. DenaultA.Y., CoutureP., VegasA., BuithieuJ., TardifJ.C.. *Transesophageal Echocardiography Multimedia Manual, Second Edition: A Perioperative Transdisciplinary Approach* New York, NY: Informa Healthcare, 2011.
7. VegasA., DenaultA.Y., RoyseC.. A bedside clinical and ultrasound- based approach to hemodynamic instability - Part II: bedside ultrasound in hemodynamic shock: continuing professional development *Can. J Anesth*. 2014;*61*:1008–27.
8. RiccabonaM., NelsonT.R., PretoriusD.H., DavidsonT.E.. *In vivo* three-dimensional sonographic measurement of organ volume: validation in the urinary bladder. *J Ultrasound Med*. 1996;*15*:627–32.
9. BouvetL., MazoitJ.X., ChassardD., AllaouchicheB., BoselliE., BenhamouD.. Clinical assessment of the ultrasonographic measurement of antral area for estimating preoperative gastric content and volume. *Anesthesiology*. 2011;*114*:108692.
10. CubillosJ., TseC., ChanV.W., PerlasA.. Bedside ultrasound assessment of gastric content: an observational study. *Can J Anesth*. 2012;*59*:416–23.
11. PerlasA., ChanV.W., LupuC.M., MitsakakisN., HanbidgeA.. Ultrasound assessment of gastric content and volume. *Anesthesiology*. 2009;*111*:82–9.
12. ChiuW.C., CushingB.M., RodriguezA., HoS.M., MirvisS.E., ShanmuganathanK., et al. Abdominal injuries without hemoperitoneum: a potential limitation of focused abdominal sonography for trauma (FAST). *J Trauma*. 1997;*42*:617–23.
13. KimuraA., OtsukaT.. Emergency center ultrasonography in the evaluation of hemoperitoneum: a prospective study. *J Trauma*. 1991;*31*:20–3.
14. RozyckiG.S., OchsnerM.G., SchmidtJ.A., FrankelH.L., DavisT.P., WangD., et al. A prospective study of surgeon-performed ultrasound as the primary adjuvant modality for injured patient assessment. *J Trauma*. 1995;*39*:492–8.
15. WherrettL.J., BoulangerB.R., McLellanB.A., BrennemanF.D., RizoliS.B., CulhaneJ., et al. Hypotension after blunt abdominal trauma: the role of emergent abdominal sonography in surgical triage. *J Trauma*. 1996;*41*:815–20.
16. PolettiP.A., KinkelK., VermeulenB., IrmayF., UngerP.F., TerrierF.. Blunt abdominal trauma: should US be used to detect both free fluid and organ injuries?*Radiology*. 2003;*227*:95–103.
17. EdellS.L., GefterW.B.. Ultrasonic differentiation of types of ascitic fluid. *AJR Am J Roentgenol*. 1979;*133*:111–4.
18. McGahanJ.P., RoseJ., CoatesT.L., WisnerD.H., NewberryP.. Use of ultrasonography in the patient with acute abdominal trauma. *J Ultrasound Med*. 1997;*16*:653–62.
19. HoffmannB., NurnbergD., WestergaardM.C.. Focus on abnormal air: diagnostic ultrasonography for the acute abdomen. *Eur J Emerg Med*. 2012;*19*:284–91.
20. GrassiR., DiM.R., PintoA., CioffiA., RomanoL.. Rotondo A. [Sixty- one consecutive patients with gastrointestinal perforation: comparison of conventional radiology, ultrasonography, and computerized tomography, in terms of the timing of the study] *Radiol Med*. 1996;*91*:747–55.
21. LeeD.H., LimJ.H., KoY.T., YoonY.. Sonographic detection of pneumoperitoneum in patients with

acute abdomen. *AJR Am J Roentgenol*. 1990;*154*:107–9.
22. KimS.H., NaS., ChoiJ.S., NaS.H., ShinS., KohS.O.. An evaluation of diaphragmatic movement by M-mode sonography as a predictor of pulmonary dysfunction after upper abdominal surgery. *Anesth Analg*. 2010;*110*:1349–54.
23. MachannJ., HorstmannA., BornM., HesseS., HirschF.W.. Diagnostic imaging in obesity. *Best Pract Res Clin Endocrinol Metab*. 2013;*27*:261–77.
24. BranneyS.W., WolfeR.E., MooreE.E., AlbertN.P., HeinigM., MestekM., et al. Quantitative sensitivity of ultrasound in detecting free intraperitoneal fluid. *J Trauma*. 1995;*39*:375–80.

Chapter 17

Ultrasound for Critical Care Procedures

Martin Albert

INTRODUCTION

Numerous procedures are being performed in the intensive care unit (ICU) setting. An increasing number of techniques incorporating ultrasound (US) have been published. Ultrasound can be used to provide guidance and anatomical support during these procedures over traditional landmark guidance. [1 – 4] Ultrasound also has the capacity to improve both precision and completion rate, and significantly reduce side affects. This chapter will review the most currently used techniques in the ICU, which are pericardiocentesis, pleurocentesis, pneumothorax US-guided drainage, and paracentesis. Vascular access related techniques are discussed in Chapter 18, Ultrasound-Guided Vascular Access and Examination.

PERICARDIOCENTESIS

Pericardiocentesis is a commonly performed procedure in the ICU. [1 , 5] Numerous pathologies are associated with an increase in the quantity of pericardial fluid: hemorrhage secondary to coagulation disorders, thoracic trauma or cardiac surgery, malignant effusion, pericarditis, autoimmune and inflammatory processes among others. [6] In some of these situations, pericardiocentesis is needed to confirm the etiology of the fluid accumulation. The quantity of fluid accumulated, the rapidity of fluid accumulation and the type of fluid determines the clinical impact. Cardiac

tamponade is the consequence of an intrapericardial pressure increase to a level affecting right ventricular filling. [7] This complication represents a medical emergency and the initial management step is usually to perform a pericardiocentesis. Historically, these procedures have been achieved using anatomic landmarks through a subxyphoid approach. In the last decades, fluoroscopy has been used to help the clinicians to guide their puncture to the pericardial space. [8] Presently, US-guided pericardiocentesis is rapidly becoming a standard of care in this situation given its ability to assure a high completion rate while maintaining a low rate of complications. [1, 3, 5, 9, 10]

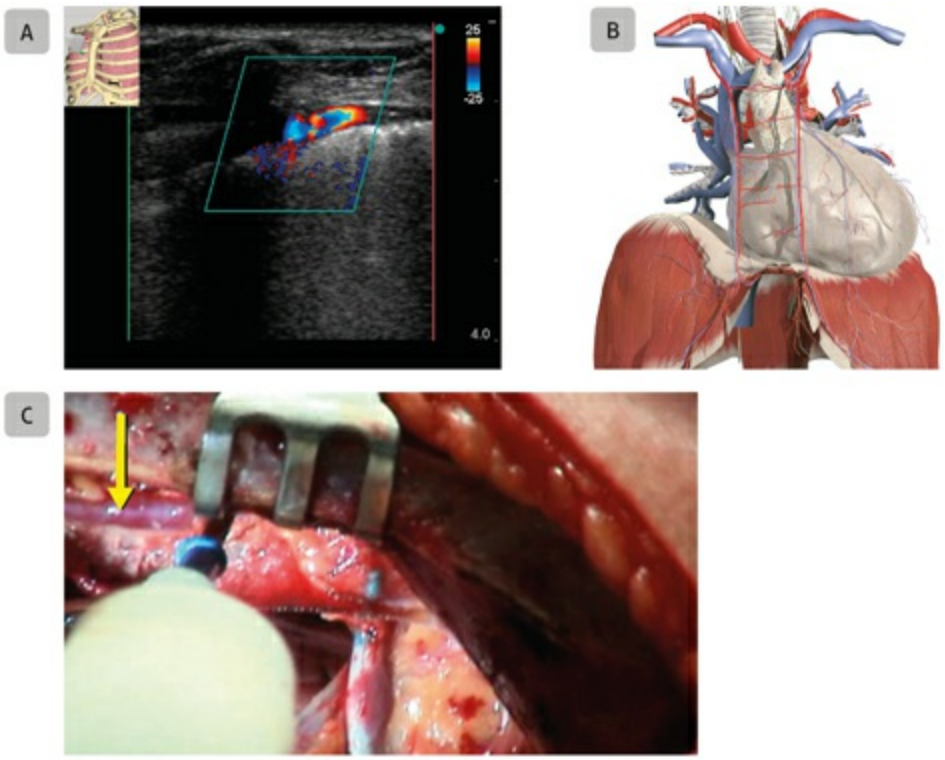

Fig. 17.1 Internal mammary artery. (A) Color Doppler interrogation of the right mammary artery from a sagittal para-sternal view. (B) Both right and left internal mammary arteries (IMA) originate from the subclavian artery and move caudal, lateral to the sternum, where they reach the epigastric arteries. (C) The IMA can easily be seen during cardiac surgery (arrow). (Anatomical images with permission of Primal Pictures, Wolters Kluwer Health.)

A: https://youtu.be/Bq89-f7TMBA

C: https://youtu.be/jtQFRskKyYQ

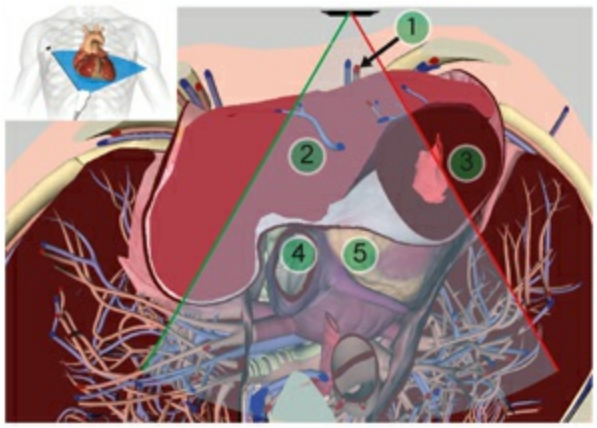

1 Mammary artery
2 Liver and hepatic vessels
3 Stomach
4 Right atrium
5 Right ventricle

Fig. 17.2 Anatomy for pericardiocentesis. Anatomic structures that are at risk of being injured using a subxyphoid approach for pericardiocentesis are shown using the Vimedix simulator

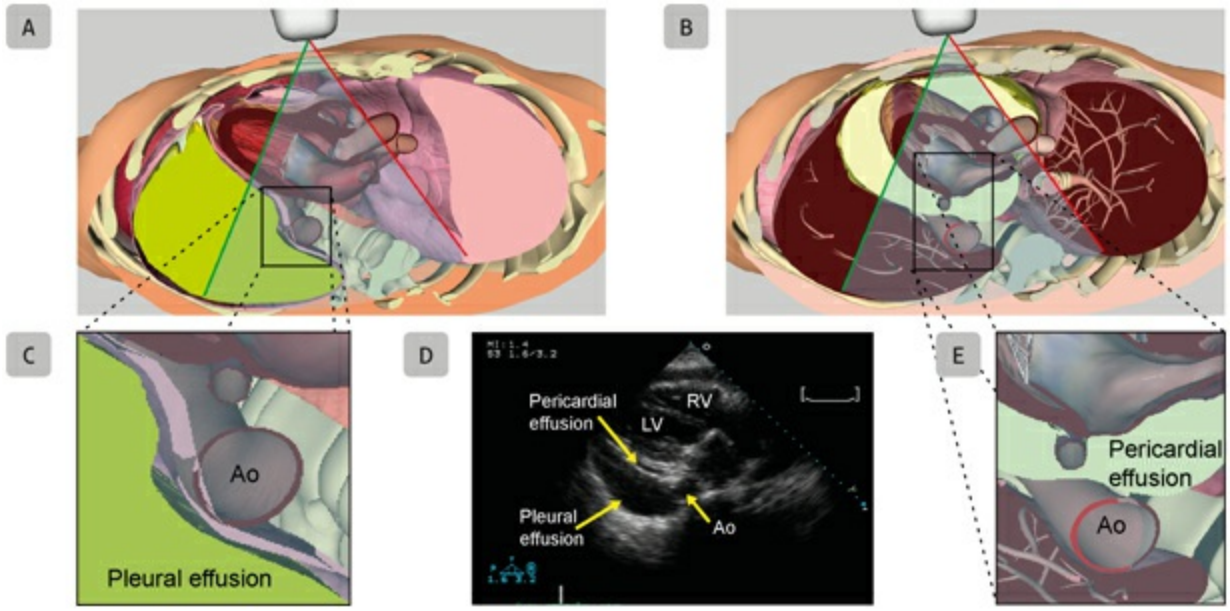

Fig. 17.3 Effusions. The difference in location between (A, C) a pleural and (B, E) a pericardial effusion is shown in these diagrams from the Vimidex simulator. (D) A paraternal long-axis transthoracic image with both types of effusions is shown. Ao, aorta; LV, left ventricle; RV, right ventricle.

D: https://youtu.be/5OotD3iX7qA

Anatomy

The heart is protected by the parietal and the visceral pericardium with a minimal amount (<50 mL) of serous pericardial fluid separating these two layers. The pericardium closely delineates the heart and great vessels (see **Figure 5.17**). Within the pericardium, the anterior heart surface is dominated by the right side chambers especially the right ventricle, making it more vulnerable to unintentional puncture during pericardiocentesis. The right coronary and left anterior descending coronary arteries are unprotected as they traverse the anterior heart surface. Important vessels course along the thoracic cage: an intercostal vessel in their neurovascular bundles at the inferior rib margin and the left internal mammary artery is 1-2 cm parallel to the sternal margin which is easily identified with US (**Figure 17.1**). A significant number of organs (liver, diaphragm, bowel, lungs, and the heart) are in the route to the pericardium through the subxyphoid approach, further exposing the patient to potential complications (**Figure 17.2**). It is important to differentiate a pericardial from a pleural effusion using the thoracic aorta in a long-axis view. Fluid in a pericardial effusion will accumulate between the cardiac structure and the aorta, however this space will be free of fluid with a pleural effusion (**Figure 17.3**).

Procedure

In most situations, the patient is supine with the head of the bed at 20-30° to bring the heart closer to the chest and avoid exacerbating any respiratory distress in dyspneic patients. Assessment of the apical, subxyphoid, and parasternal views are performed using a phase array transducer (1-5 MHz) or a curvilinear probe (2-5 MHz). The phased array probe is easier to use given the limited intercostal space available for the technique. The heart, the pericardium, and adjacent structures are identified. The best approach is personalized on the basis of the distance from the skin to the pericardium, the quantity of fluid at this level, and the presence of adjacent structures. In most patients, the apical approach is simpler to perform given the minimal distance

from the skin to the pericardium and the absence of anatomic structures in between. [1] , [3] However, a suitable apical view may sometimes be difficult to obtain in patients that are obese or have chronic obstructive pulmonary disease, and in female patients with large breasts. In these situations, the other views are preferred.

When the appropriate view has been chosen, antiseptic skin cleaning is performed, sterile drapes applied on the patient, and the US probe covered with a sterile protection (**Figure 17.4**). Lidocaine 1% or 2% is injected at the puncture site. A pericardiocentesis needle (6-10 cm and usually 18 gauge) is slowly advanced under real-time echographic guidance and directed to the pericardial space. Aspiration using a 20-50 ml syringe attached to the needle generates mild negative pressure. The needle tip is then observed slowly entering the pericardial space. Using the syringe, fluid can be promptly removed to relieve the physiologic consequences of tamponade. If uncertainty remains about the final destination of the needle tip, a bubble test is performed to confirm the location of the catheter tip inside the pericardium (**Figure 17.5**). [11] , [12] In an emergency situation, however, confirmation of the guidewire in the pericardial space might be sufficient (**Figure 17.6**). We have encountered situations where part of the guidewire was in the pericardium and also in the right ventricle, thus requiring surgical intervention (**Figure 17.6 C**). In most cases, a drainage catheter should be placed. To perform this, a J-guidewire is inserted and advanced into the needle, the needle is withdrawn and a suitable catheter, such as a simple multilumen central venous catheter, is inserted over the guidewire. Many commercial pericardial drainage kits are available which are the same as those used for thoracentesis (**Figure 17.7**). Finally, connecting the catheter to a drainage system and interposing a three-way valve allows the pericardium to drain safely.

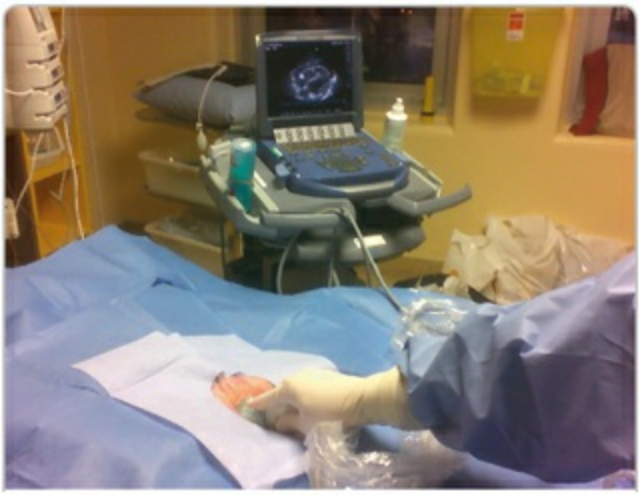

Fig. 17.4 Pericardiocentesis. The technique for ultrasound (US)-guided pericardial drainage involves the use of sterile draping of the patient, gown and gloves by the operator, and a sterile sheath for the US probe.

Fig. 17.5 Pericardiocentesis. A bubble test can be used to confirm the position of the drainage catheter. (A) Subcostal four-chamber view shows a pericardial effusion (arrow) around the right ventricle prior to drainage. (B) Three-way stopcocks with two syringes of saline and a small amount of air allows agitation of the with the production of a contrast media. (C) Subcostal four- chamber view after injection shows contrast (arrow) surrounding the cardiac silhouette. (Courtesy of CAE-Healthcare.)

A: https://youtu.be/3t1Zoa2BV-8

B: https://youtu.be/HdBzbAcj2dA

C: https://youtu.be/cuWFVyEtyHk

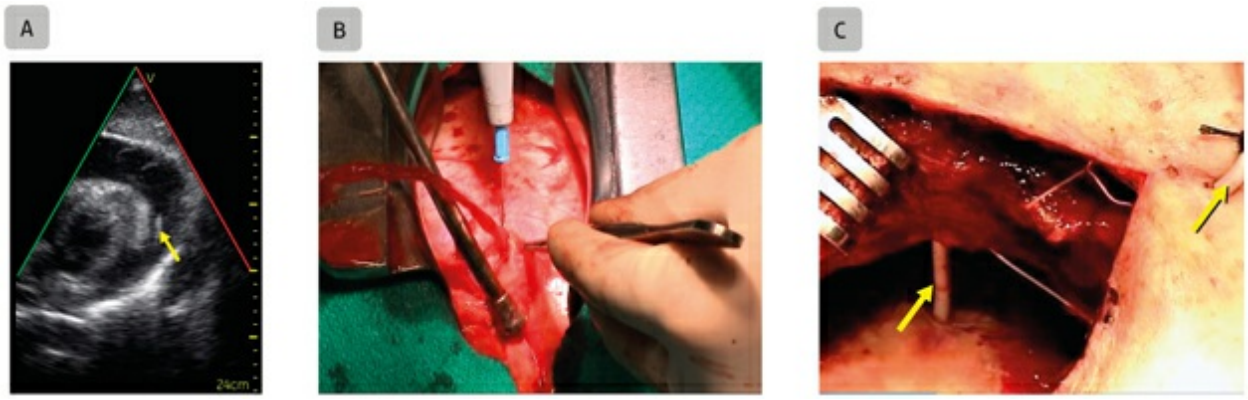

Fig. 17.6 Pericardiocentesis. (A) Subcostal four-chamber view shows a guidewire positioned in the pericardial space in a patient with a pericardial effusion. (B) Surgical pericardial drainage may be necessary in some patients. (C) Surgical removal of a pericardial drainage catheter (arrow) accidentally positioned in the right ventricle (arrow) in a patient with a pericardial effusion.

A: https://youtu.be/pE1YELsTfVc

B: https://youtu.be/9-1WfEGaVog

C: https://youtu.be/kX7VoAzSYe0

C: https://youtu.be/35cgYXctwZ4

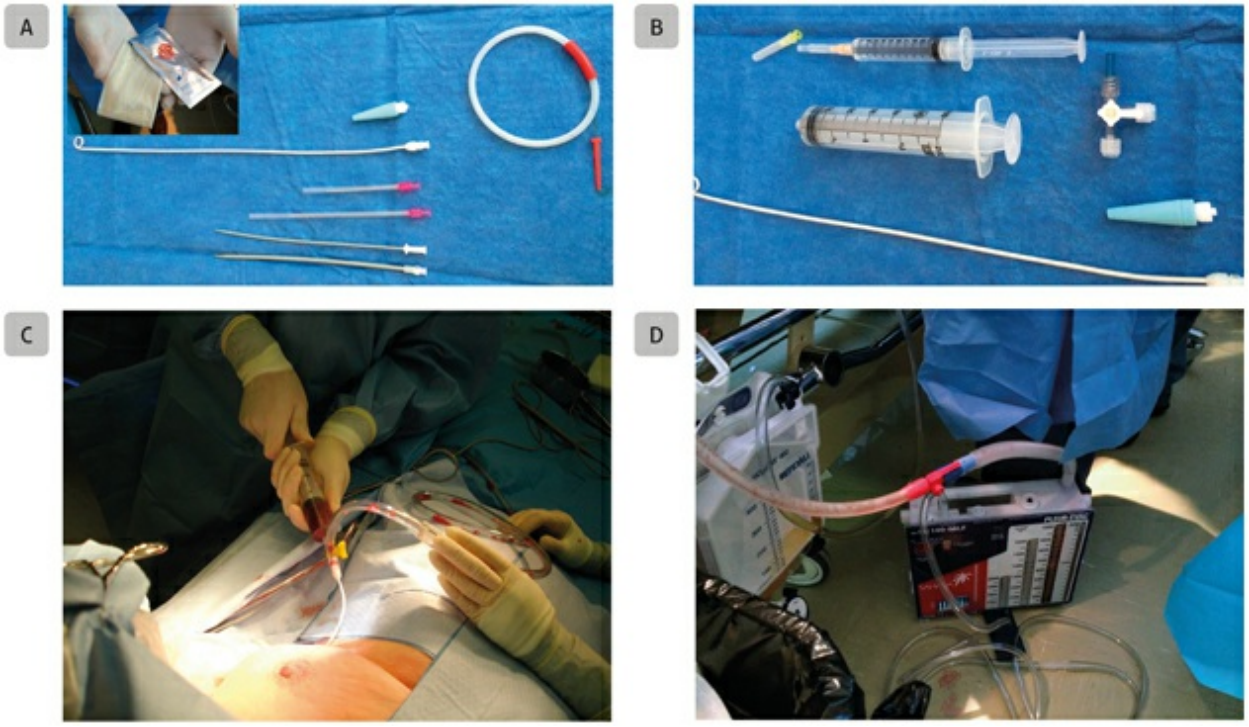

Fig. 17.7 Drainage kits. (A, B) Pericardiocentesis and pleurocentesis kits with needles and dilators are shown. The inset shows a sterile sheath and ultrasound (US) gel that is used to cover the US probe. The fluid can be drained through (C) aspiration by a syringe or (D) connected to a drainage collection system.

Precautions

Coagulation abnormalities that increase the risk of bleeding should be corrected if possible before performing pericardiocentesis. However, numerous reports have described an uneventful procedure in patients despite pre-existing uncorrected coagulopathy, so this should not delay emergent pericardiocentesis. [3] A blinded subxyphoid approach has been associated with significant complications including mortality (0-3%), ventricular puncture (0-12%), and liver puncture (0-5%). [13] Most of these complications are easily avoided using an US-guided approach. [1] , [3] The most serious and immediate mechanical complications of pericardiocentesis are myocardial puncture or laceration, vascular injury (coronary, intercostal, internal mammary, or intra-abdominal), pneumothorax, and arrhythmia. Observational studies of echocardiography-guided pericardiocentesis suggest a major complication rate below 2%. [5] In patients with large clots or with localized tamponade, a surgical drainage might be preferable. Finally, in patients with aortic dissection, percutaneous pericardial drainage is contraindicated. Removal of

pericardial fluid can lead to progression of dissection with immediate death. In these situations, emergency transfer to a cardiac operating room is indicated. **Figure 17.8** summarizes an approach to pericardial effusion and tamponade. [14]

PLEUROCENTESIS

Historically, the diagnosis of pleural effusion has been based on the interpretation of chest radiography and clinical examination. Increasingly, pleurocentesis has been performed in the ICU to confirm the etiology of the effusion, place a drainage system, or improve respiratory system compliance. Although a single case report described the use of US during thoracentesis in 1977, it has taken many years for the broad dissemination of this technique. [15] In the last decade, use of US has been established to be a very important tool to detect pleural effusion, assess its importance, and evaluate an alternative diagnosis. [16]

Anatomy

Both lungs are surrounded by pleura. This thin membrane covers both the outer surface of the lung (visceral pleura) and the inner surface of the thoracic cavity (parietal pleura). Physiologically, a minimal amount of pleural fluid is present in the pleural cavity to ensure lubrication and free sliding of both surfaces. The pleural fluid is normally reabsorbed through the lymphatic system. When the production exceeds the reabsorption capacity, pleural fluid accumulates in the pleural cavity, causing a pleural effusion (see **Figure 14.29**). Causes of pleural effusion are multiple given that an imbalance in hydrostatic pressure, change in oncotic pressure or increase in pleural permeability can all trigger the excess amount of fluid.

Procedure

The presence of a significant amount of pleural fluid usually offers an excellent acoustic window that allows easy assessment of the pleural space and surrounding organs. Assessment of the pleural space is best performed using a curvilinear probe (2-5 MHz) but a phased array transducer (1-5 MHz) can also be utilized. If the thoracic wall is thin, a high frequency linear probe can also be used. It has the advantage of localizing small anatomical

structures such as intercostal arteries. The curvilinear probe has the advantage of a larger footprint but the phase array probe is often easier to fit between the ribs. Pleural fluid is hypoechoic when compared with the liver (isoechoic reference). The surrounding air-filled lung is hyperechoic except in areas of atelectasis, edema or consolidation where the echographic heterogeneity is easily observed, especially with the presence of pleural effusion. During inspiration, the sliding movement of the lung identifies the position of the pleura. [16] Some ultrasonographic characteristics of the fluid can be exploited to differentiate exudative effusions and empyema (see Chapter 14, Critical Care Examination of the Respiratory System). The presence of internal acoustic densities within the pleural fluid suggest an exudative effusion. [17] The surrounding anatomy including the diaphragm, liver, spleen, heart, pericardium, and adjacent thoracic structures are identified. As for the pericardiocentesis, the best approach to pleurocentesis is chosen following multiple scans to detect the area where the distance between the skin and the pleural space is minimal, the amount of liquid is sufficient to tap safely, and the area is free of surrounding organs.

When the appropriate view has been chosen, the pleural fluid collection is located and marked. An antiseptic skin cleaning is done, sterile drapes applied on the patient, and the US probe covered with a sterile protection (**Figure 17.9**). Lidocaine 1% or 2% is injected at the puncture site intradermally, subcutaneously up to the rib, and subsequently into the parietal pleura. The lower part of the intercostal space is accessed since the intercostal nerve and vessels run just below the ribs. A similar technique to the pericardial drainage can be used, or for diagnostic purposes a 14-gauge plastic catheter needle system is used to enter the pleural space. Once the pleural space is entered, the needle is withdrawn and fluid is removed through the catheter. [16] Continuous US observation of needle entry into the fluid collection is recommended if the amount of fluid is small, an important organ is close to the entry site, or the patient has a coagulopathy. When a pigtail catheter is used to drain a large amount of fluid the patients can be lying on their back, or often we will have them sitting on the side of the bed and lying on a pillowed table (**Figure 17.9**). Once blood is withdrawn from the needle (**Figure 17.10**), the position of the guidewire above the diaphragm is confirmed with US (**Figure 17.11**).

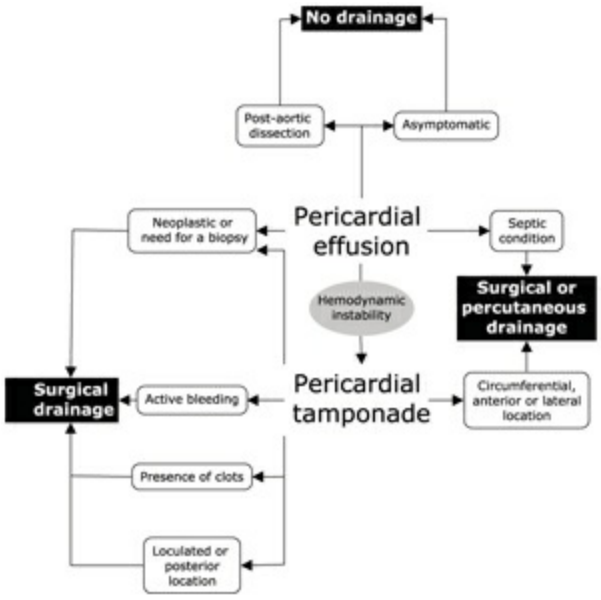

Fig. 17.8 Pericardial effusion. A proposed approach to patient management in the presence of pericardial effusion and cardiac tamponade is presented. (Adapted from Durand *et al.* [14] *)*

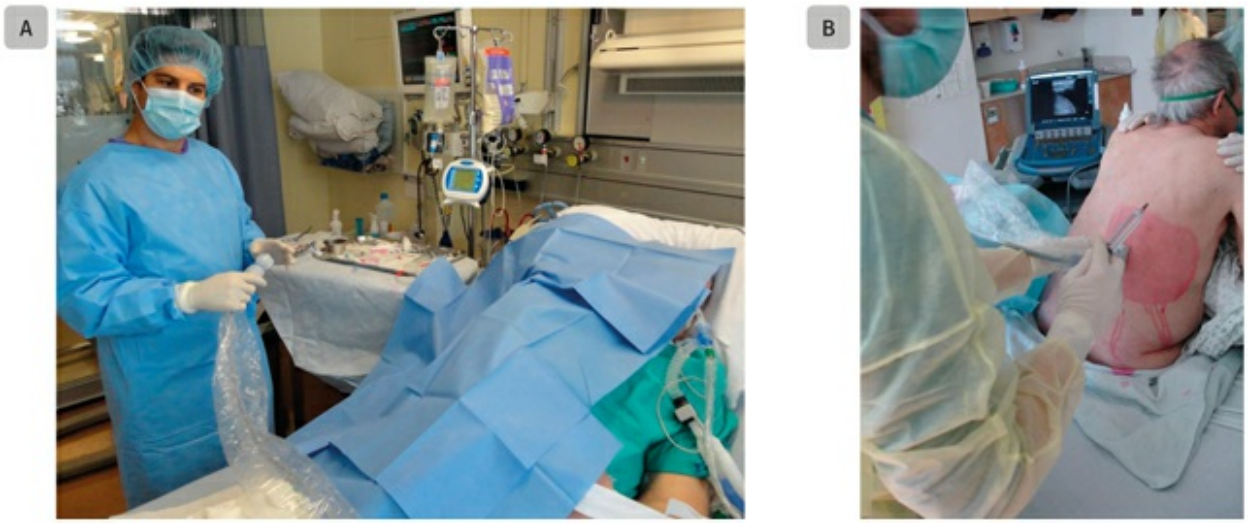

Fig. 17.9 Pleurocentesis. The patient can be positioned in either the (A) supine or (C) sitting position for pleurocentesis using a sterile technique.

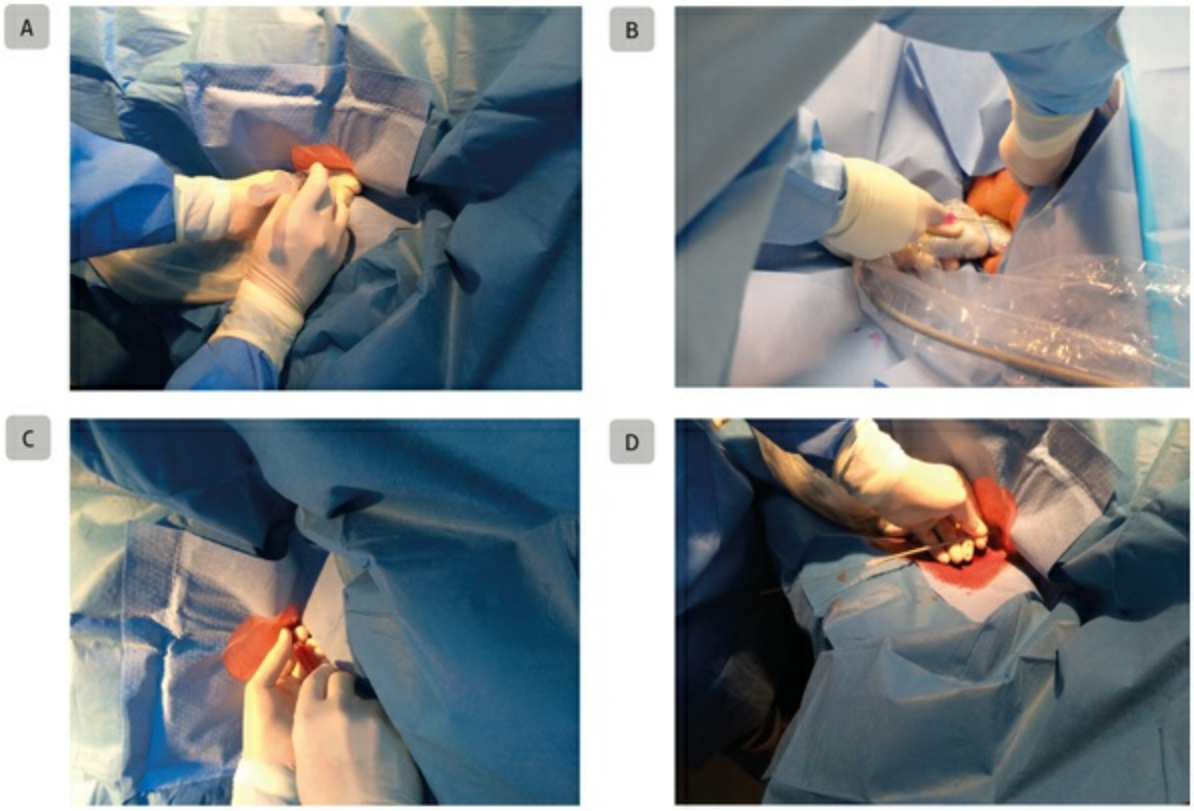

Fig. 17.10 Pleurocentesis. The steps during pleurocentesis are (A) injection of local anesthesia; (B) ultrasound- guided needle insertion; (C) fluid aspiration; and (D) dilatation and guidewire insertion.

https://youtu.be/rvYF2dNuy_o

Precautions

Significant potential complications of pleurocentesis include pneumothorax, bleeding, pleural space and soft tissue infection, spleen or liver puncture. Prospective observational studies indicate that pneumothorax occurs in up to 30% of blind pleurocentesis, although most studies found rates <12%. [18] Pleurocentesis performed under US-guidance in non-ventilated patients has been associated with <2% occurrence of pneumothorax. [19] Experienced operators performing US-guided pleurocentesis also have a remarkably low level of infectious complications. Liver and spleen punctures tend to occur

more commonly in supine patients because diaphragmatic movement in such patients is associated with a more cephalic movement of the abdominal organ. Acknowledging known risk factors for complications can reduce complication rates for pleurocentesis. These risk factors are related to patient variables (small effusions, obesity, multiple loculations, supine patient, coagulopathy, mechanical ventilation, and intrapleural adhesions), technical factors (operator inexperience, absence of US-guidance, and large volume drainage), and systems features (lack of coordination and non-standardized system). [16]

ECHO-GUIDED PNEUMOTHORAX DRAINAGE

As seen in Chapter 14, Critical Care Examination of the Respiratory System, pneumothorax can be diagnosed and ruled-out with US. Once a pneumothorax is confirmed, it can be drained using an US-based technique. The preparation and material is the same as for a pleurocentesis, except that the position of the needle will be in a more anterior position because pneumothoraces are typically anterior and can be present even with chest tubes (**Figure 17.12**). The area selected for drainage is typically mid-clavicular with no sliding lung. Identifications of the lung points are important in order to define the depth and lateral extension of the pneumothorax. With this information in mind, a 14-gauge plastic catheter needle attached to a syringe system is used to enter the pleural space above the rib in an area free of vessels. The syringe can be filled with fluid allowing early detection of pleural air (**Figure 17.13**). Once the pleural space is entered, the needle is withdrawn, the catheter advanced, or the guidewire inserted through the needle. Because air does not transmit US there is no way to confirm the guidewire position. The skin is dilated and the pigtail catheter advanced. A three-way stopcock is connected to a 60 ml syringe and the drainage system (**Figure 17.14**) with aspiration of air to determine the volume of the pneumothorax. A chest X-ray and lung US is performed to confirm the return of lung sliding. After 24 hours the pigtail catheter is clamped. A repeat lung US for lung sliding and chest X-ray is performed six hours later (**Figure 17.15**) and if negative, the pigtail catheter is removed. The patient is then monitored with sliding lung for 24 hours.

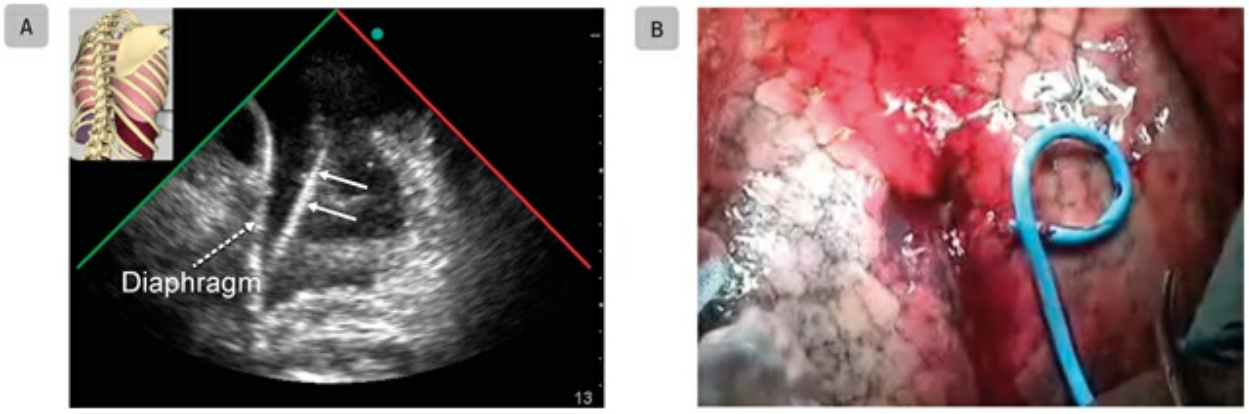

Fig. 17.11 Pleurocentesis. (A) Lung ultrasound confirms the guidewire position in the pleural space (double arrows). The hyperechoic diaphragm (dotted arrow) confirms the intrapleural and not intra-abdominal position of the guidewire. (Courtesy of Dr Philippe Rolla.) (B) Lung perforation following pigtail insertion despite echo guidance following elective insertion of a drainage catheter with a trocar.

A: https://youtu.be/qppWWBuBcPY

B: https://youtu.be/2HPaGlstAXU

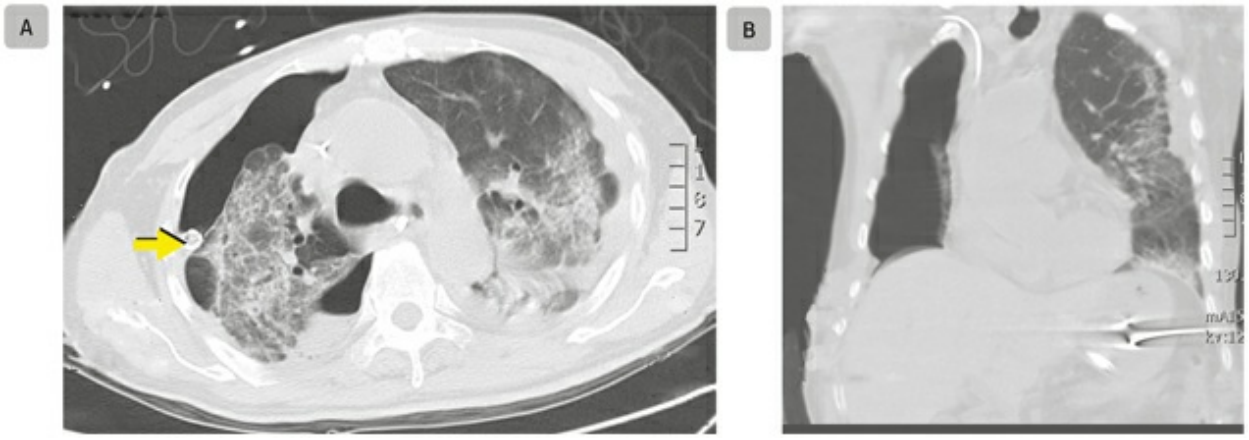

Fig. 17.12 Pneumothorax. A large anterior right pneumothorax is shown by computed tomography in (A) axial and (B) coronal views. Note the presence of a chest tube (arrow) in the right pleural cavity.

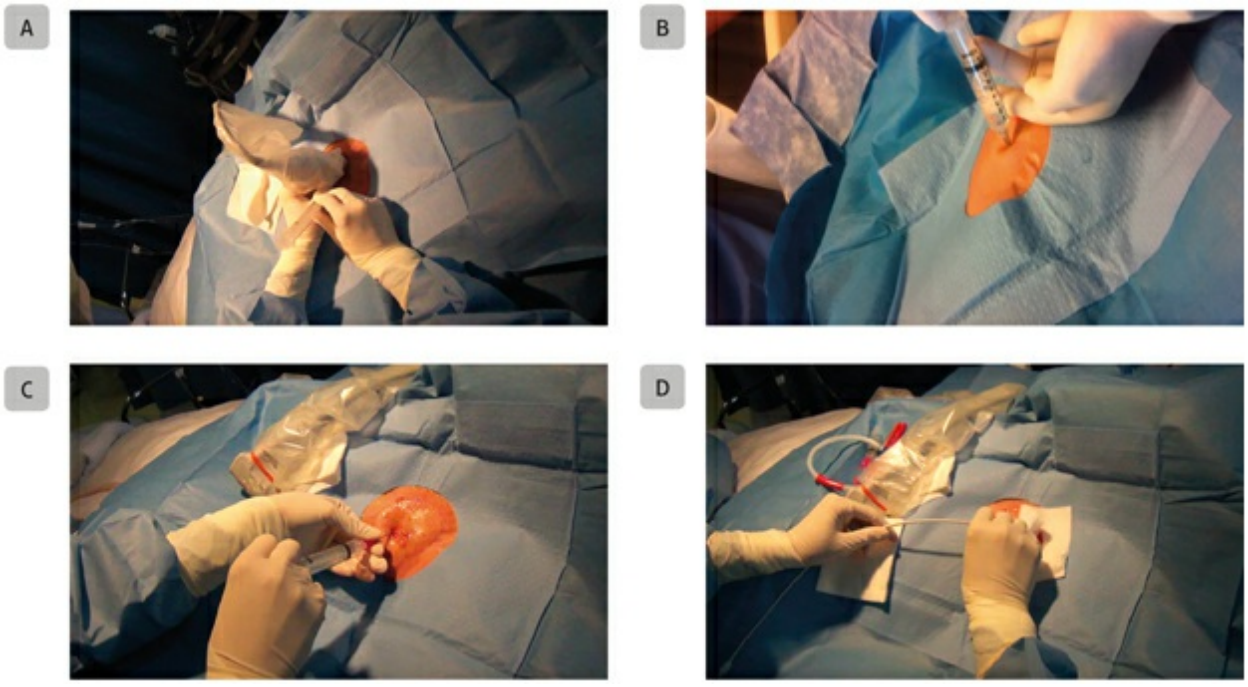

Fig. 17.13 Pneumothorax. The steps in ultrasound-guided pneumothorax drainage are shown. (A) Once the position of the pneumothorax is confirmed with 2D ultrasound; (B) local anesthesia is injected; and (C) needle aspiration in the mid-clavicular line is performed. Sterile saline can be used in order to rapidly identify the pleural air. (D) Once air is present in the syringe, a guidewire is inserted, the tract is dilated, and pigtail catheter insertion is performed.

A: https://youtu.be/uEP8HVMLzm4

C: https://youtu.be/rYtQPG4TQag

C: https://youtu.be/g-TTRbxwq0c

B: https://youtu.be/DJeszhCH_b8

D: https://youtu.be/g6tRgvg5-DI

D: https://youtu.be/6ZzvPrhnZ_8

PARACENTESIS

Accumulation of fluid within the peritoneal cavity results in ascites. In North America, ascites is due to portal hypertension resulting from cirrhosis in up to 80% of the cases. Other common causes include malignant and infectious peritonitis, heart failure, and hypoalbuminemia. Successful treatment of ascites depends upon a precise diagnosis of the cause. There are many well-established indications for paracentesis: assessment of new onset ascites, examination of ascitic fluid in a patient with pre-existing ascites, or clinical deterioration and management of tense or diuretic-resistant ascites.

Anatomy

In the midline, close to the umbilicus, abdominal wall collateral vessels may be present, so those regions should be avoided (see **Figure 16.2**). The inferior epigastric artery is present just lateral from the pubic tubercle (approximately 2-3 cm lateral to the symphysis pubis), cephalad within the rectus sheath. Thus, this site should also be specifically avoided.

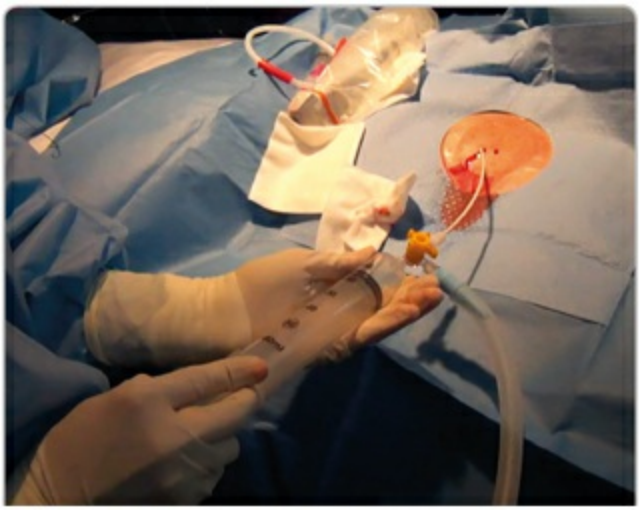

Fig. 17.14 Pneumothorax. Air is removed using a three-way stopcock in order to quantify and completely remove the pneumothorax.

https://youtu.be/80B8Wvf-Kz8

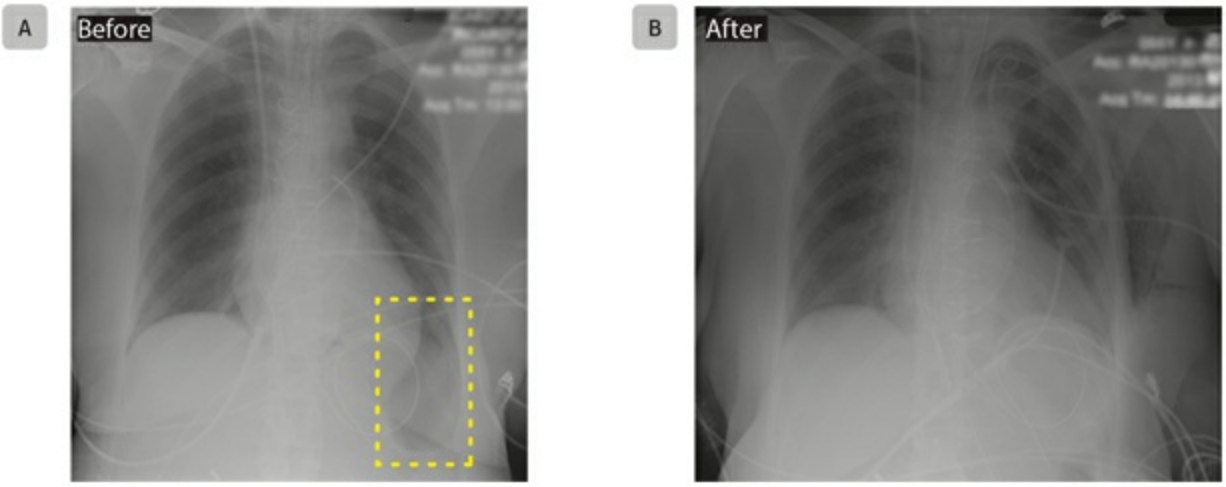

Fig. 17.15 Pneumothorax. Confirmation of drainage of the pneumothorax is performed by using ultrasound to demonstrate return of sliding lung and also by chest radiograph. In this patient, the chest radiographs demonstrate (A) the location of the left pneumothorax (outlined region) with (B) disappearance of the deep sulcus sign after evacuation of air.

Procedure

Ultrasonography has been used for many years to assist during paracentesis because of the relatively ease of use and high success rate[3], [20] A study comparing US-guided with blinded paracentesis demonstrated that 95% of the US group had a safe and successful aspiration, whereas only 61% of those in the blinded group were successful. [3] Therefore, US is commonly used especially in the ICU where patients often present a more technical challenge and have a coagulopathy. Paracentesis is performed with the patient in a supine position with the head of the bed slightly elevated. The patient may be rolled slightly to the side to permit pooling of fluid in the area of interest. [20] Assessment of the ascites is best performed using a curvilinear probe (2-5 MHz): with the larger footprint, however, a phase array transducer (1-5 MHz) and linear probe for thin abdominal walls can also be utilized. Blinded paracentesis was typically performed through the left lower quadrant. With the help of the US, the best approach is chosen after a complete abdominal scan. It is important to identify a safe area of at least 10 mm distance or more to perform paracentesis. Complex ascites (peritonitis) and bowel walls have to be identified. The intraluminal aspect of the large bowel with haustrations must not be confounded for free peritoneal fluid (**Figure 17.16**). Once an appropriate site for paracentesis is identified with the US, the skin is marked. Depending on the amount of fluid visualized, the puncture is subsequently performed only using the skin mark or under US guidance.

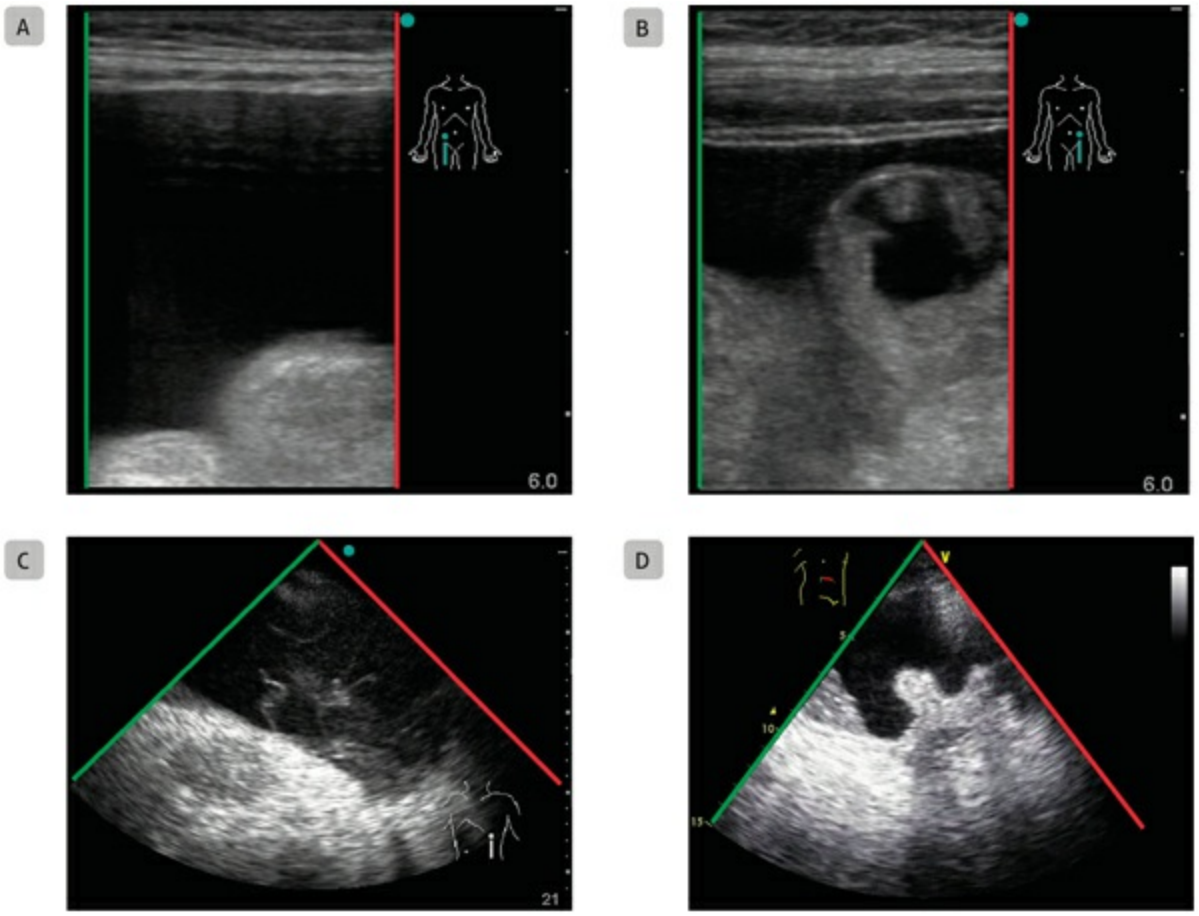

Fig. 17.16 Paracentesis. (A) An adequate ultrasound image for assessment of ascites is shown; (B) however, a slight angulation of the probe reveals the presence of a bowel loop. (C,D) Complex ascites should not be confused with the content of the large bowel. In the latter, haustra and thumb printing can be seen and in some patients peristalsis will be present.

A: https://youtu.be/84-s_Huwlis

B: https://youtu.be/hAmeNhbLk08

C: https://youtu.be/DPepdrrEppo

An antiseptic skin cleaning is done, sterile drapes applied on the patient, and the US probe covered with sterile protection (**Figure 17.17**). The paracentesis can also be safely executed under direct US guidance using only a sterile technique with adhesive dressing. The skin can then be anesthetized by approaching the chosen entry site tangentially with the needle and raising a wheal with a small amount of lidocaine. The needle is then withdrawn and placed at the entry site perpendicular to the curve of the abdominal wall. Using a Z-track technique, lidocaine is injected through a #16 G catheter to anesthetize the entire soft tissue tract. The Z-track creates a non-linear pathway between the skin and the ascitic fluid, thereby helping to minimize the chance of an ascitic fluid leak. The depth of needle entry must be stabilized so that it does not pull out of the peritoneal cavity. The catheter is left in situ for slow drainage.

Precautions

Coagulation abnormalities are frequently encountered in patients with ascites. However, an increased international normalized ratio or thrombocytopenia is not a contraindication to paracentesis. For most patients, blood product transfusion in this context is unnecessary since this is not supported by existing literature and exposes the patient to transfusion risk with little benefits. [18] , [21] However, patients with clinically apparent disseminated intravascular coagulation or hyperfibrinolysis have an increased risk of bleeding and may require treatment to decrease the risk of bleeding before the procedure. To avoid any complication to proximity organs, special attention is given to the liver and the spleen if the puncture is performed on the upper abdomen, or for a patient with massive organomegaly. Massive ileus with bowel distension also carries an increased risk. In a patient with portal hypertension, varicose veins of the abdominal wall can be visualized and must be avoided during the procedure (see **Figure 16.2**). Surgical scars and visible veins should also be avoided. Surgical scars may be associated with bowel that is tethered to the abdominal wall by adhesions, thus putting the patient at risk for bowel injury if the paracentesis is performed near a scar. Infection related to the US-guided paracentesis remains extremely rare. [22]

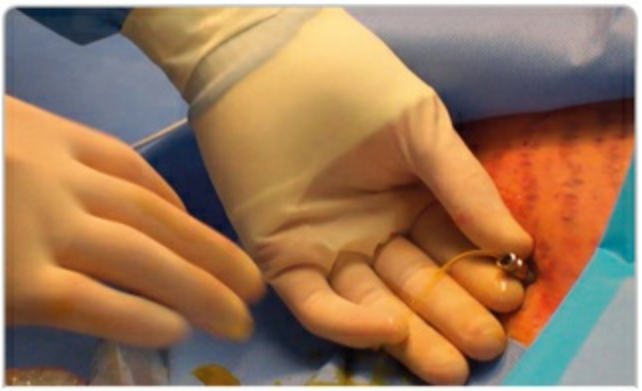

Fig. 17.17 Paracentesis. Free drainage of ascitic fluid following insertion of a needle is shown in a patient with elevated abdominal pressure.

https://youtu.be/gBWj55L8DC8

In summary, ICU-related procedures are commonly performed. Adequate understanding of the underlying anatomy and appreciation of potential complications with careful and controlled manipulation of the needle are essential in providing these techniques safely to ICU patients.

Acknowledgments

Dr Albert would like to dedicate this chapter to his wife Maryse and his son Leo for their support.

REFERENCES

1. AndruszkiewiczP., SobczykD.. Ultrasound in critical care. *Anaesthesiol Intensive Ther*. 2013;*45*:177–81.
2. Feller-KopmanD.. Ultrasound-guided thoracentesis. *Chest*. 2006;*129*:1709–14.
3. HatchN., WuT.S., BarrL., RoqueP.J.. Advanced ultrasound procedures. *Crit Care Clin*. 2014;*30*:305–29.,vi.
4. NicolaouS., TalskyA., KhashoggiK., VenuV.. Ultrasound-guided interventional radiology in critical care. *Crit Care Med*. 2007;*35*(5 Suppl.):S186–97.
5. BastianA., MeissnerA., LinsM., SiegelE.G., MollerF., SimonR.. Pericardiocentesis: differential aspects of a common procedure. *Intensive Care Med*. 2000;*26*:572–6.
6. CookV.J., FitzGeraldJ.M.. Case 22-2004: a 30-year-old woman with a pericardial effusion. *N Engl*

J Med. 2004;*351*:1804–5.
7. ReedR.M., RamaniG.V., HashmiS.. Unraveling the paradox of cardiac tamponade: case presentation and discussion of physiology. *BMJ Case Rep*. 2012 Apr;*23*:2012.
8. McLearyR.D., AlexanderD.K., BrownR.K.. B-scan ultrasound directed pericardiocentesis. *A safer approach. Radiology*. 1982;*144*:923.
9. GarthA.P., HwangJ.Q., SchuurJ.D., RosboroughS.. Ultrasound guided pericardiocentesis of cardiac tamponade. *Acad Emerg Med*. 2009;*16*:811.
10. GoodmanA., PereraP., MailhotT., MandaviaD.. The role of bedside ultrasound in the diagnosis of pericardial effusion and cardiac tamponade. *J Emerg Trauma Shock*. 2012;*5*:72–5.
11. O'SullivanJ., HeadsA., HunterS.. Microbubble image enhancement and pericardiocentesis. *Int J Cardiol*. 1993;*42*:95–6.
12. WatzingerN., BrusseeH., FruhwaldF.M., SchumacherM., ZweikerR., StoschitzkyK., et al. Pericardiocentesis guided by contrast echocardiography. *Echocardiography*. 1998;*15*:635–40.
13. WongB., MurphyJ., ChangC.J., HasseneinK., DunnM.. The risk of pericardiocentesis. *Am J Cardiol*. 1979;*44*:1110–4.
14. DurandM., LamarcheY., DenaultA.. Pericardial tamponade. *Can. J Anesth*. 2009;*56*:443–8.
15. FreimanisA.S.. Ultrasound and thoracentesis. *JAMA*. 1977;*238*:1631.
16. SachdevaA., ShepherdR.W., LeeH.J.. Thoracentesis and thoracic ultrasound: state of the art in 2013. *Clin Chest Med*. 2013;*34*:1–9.
17. KomatsudaT., IshidaH., KonnoK., HamashimaY., NaganumaH., SatoM., et al. Differentiation of exudate from transudate ascites by Doppler sonography. *Abdom Imaging*. 2003;*28*:609–13.
18. MercaldiC.J., LanesS.F.. Ultrasound guidance decreases complications and improves the cost of care among patients undergoing thoracentesis and paracentesis. *Chest*. 2013;*143*:532–8.
19. PerazzoA., GattoP., BarlasciniC., Ferrari-BravoM., NicoliniA.. Can ultrasound guidance reduce the risk of pneumothorax following thoracentesis?*J Bras Pneumol*. 2014;*40*:6–12.
20. TrovatoG.M., SperandeoM., CatalanoD.. Thoracic ultrasound guidance for access to pleural, peritoneal, and pericardial space. *Chest*. 2013;*144*:1735–6.
21. WieseS.S., MortensenC., BendtsenF.. Few complications after paracentesis in patients with cirrhosis and refractory ascites. *Dan Med Bull*. 2011;*58*:A4212.
22. CerviniP., HesleyG.K., ThompsonR.L., SampathkumarP., KnudsenJ.M.. Incidence of infectious complications after an ultrasound-guided intervention. *AJR Am J Roentgenol*. 2010;*195*:846–50.

Chapter 18

Ultrasound-Guided Vascular Access and Examination

Christian Ayoub, Serge McNicoll, Blandine Mondesert, Massimiliano Meineri, Manoj M Lalu and Andre Y Denault

INTRODUCTION

This chapter will present currently used techniques for ultrasound (US)-guided central venous and arterial access. In addition, common pathologies encountered during the vascular examination will be described. A general approach to teaching US-guided venous catheterization is suggested. Finally, the use of a US-guided technique for peripherally inserted central catheter (PICC) insertion is reviewed as it is becoming more popular particularly for patients who are moving out of the intensive care unit (ICU).

CENTRAL VENOUS CANNULATION

More than 5 million central venous catheters (CVC) are implanted each year in the United States alone. [1] When taking into account all intravascular catheters, it is likely that this number exceeds 100 million. [2] Since Seldinger developed the technique in 1953 to safely cannulate vessels, many different vascular access points have been routinely used. [3] The main indications for CVC in the operating room (OR) or ICU include central venous pressure monitoring, insertion of a pulmonary artery catheter, and administration of fluids and drugs, such as vasopressors, inotropes, and chemotherapeutic agents. These catheters are also used to administer parenteral nutritional support, facilitate the placement of temporary or permanent pacemakers, and

are needed for procedures such as hemodialysis, hemofiltration, and plasmapheresis.

Initially, the only available option for central venous catheterization involved percutaneous puncture based on various anatomical surface landmarks (i.e. the “landmark [LM] technique”). Without access to US, the success of this technique was highly dependent on physician experience and knowledge of anatomy. As early as 1978, US-guided central venous catheterization was described as an effective technique to reduce the rate of mechanical complications. [1] , [4] Subsequent studies have led several health agencies, such as the British National Institute for Health and Care Excellence (NICE) and the Agency for Healthcare Research and Quality Evidence to publish guidelines strongly supporting the use of US for vascular access. These recommendations were based on studies that show a significant decrease in the rate of failed punctures (86%), reduced complications (57%), and a shorter performance time (1.1 min versus 2.6 min). [5] – [7] Although there is a great deal of evidence that US-guided vascular access can be beneficial, there is still significant resistance from experienced practitioners, although this is slowly changing. In order to address these perceived barriers, this chapter will summarize the general techniques, evidence, and potential benefits of US-guided cannulation.

Table 18 1 General Procedural Steps in Echo-Guided Vascular Access Performed at the Montreal Heart Institute

Rule of P: Proper site, Probe selection, Position the patient, Preparation of the operator and the machine and Precaution, Perform and Precaution	
1.	**Proper site:** decide location of the vascular access: upper or lower body, central or peripheral
2.	**Probe selection:** choose the probe type based on the site and distance from the skin to the vessel target (**Figure 18.4**)
3.	**Position the patient:** patient neck position, bed height, close to the operator (**Figure 18.8**) or elevation of the groin if femoral (**Figure 18.40**). If the patient is awake, elevate head 30^0 (or 45^0 if patient is dyspneic). Wait before moving the patient to a supine or Trendelenburg position until you are ready to proceed with the puncture. **Position** the echo machine so that the ultrasound images and the chosen site for vascular access will be in the same visual field (**Figure 18.8D**)

4.	**Preparation**: material is prepared on a separate sterile table (**Figure 18.3**) **Preparation**: complete sterile technique using gown, mask and gloves **Preparation**: clean all the potential sites for vascular access, both internal jugular and subclavian if upper body access and both femoral sites if lower body access (**Figure 18.8C**) **Preparation**: drape the patient and leave the target area accessible (**Figure 18.8C**) **Preparation**: cover the ultrasound probe with a long sterile sheath (**Figure 18.8D**) **Preparation**: localize the target vessel and adjust the gain, the depth, image orientation in transverse and longitudinal
5.	**Precaution**: verify the presence of a sliding lung before and after the procedure for upper body cannulation (see **Figure 14.5**) **Precaution**: differentiate the vein from the artery using compression, color and pulsed-wave Doppler (**Figure 18.5**)
6.	**Perform**: start in a transverse fashion and identify the needle tip. Use local anesthesia if patient awake. Both hands have to move in the transverse approach. Advance both the probe and the needle until 2-3 mm of the vessel is at 12:00 with a 45° to 60° perpendicular axis. Reposition the needle if the position is not at 12:00 o'clock. In some patients, the angulation between the probe and the needle is reduced as the needle is advanced. Never advance the needle if the tip is not seen. Tremble the tip and find it with the ultrasound beam **Perform needle penetration**: once in the optimal transverse position, turn the probe to 90° and identify the largest diameter of the target vessel. Lower the needle to less than 30° or as low as possible. In the longitudinal view, only one hand moves, the one holding the needle. Insert the needle slowly in order to always see its full length. Then perforate the anterior wall. The two distal echodense artifacts will be seen in the lumen (**Figure 18.11**). Aspiration may be unnecessary as blood will come up in the needle **Perform**: hold the needle in place and advance the guidewire (**Figure 18.12**). The most common etiology of a guidewire blockade is because the needle tip is against the posterior wall. If it occurs, turn the needle 90°, pull back slightly and try again. Instead of pushing the guidewire, roll it as it moves in
7.	**Precaution**: once the guidewire is inside the vessel, confirm the intravascular position before dilating the vein and fixing the catheter (**Figure 18.12**). If transesophageal echocardiography is already in use, confirm superior vena cava position. If septic shock is suspected, draw blood cultures **Precaution**: once the catheter is in place, confirm the presence of a sliding lung for upper body vascular access (see **Figure 14.5**)

GENERAL CONSIDERATIONS: ULTRASOUND-GUIDED CATHETERIZATION TECHNIQUES

The key points in performing echo-guided vascular access are summarized in **Table 18.1** and **Figure 18.1**.

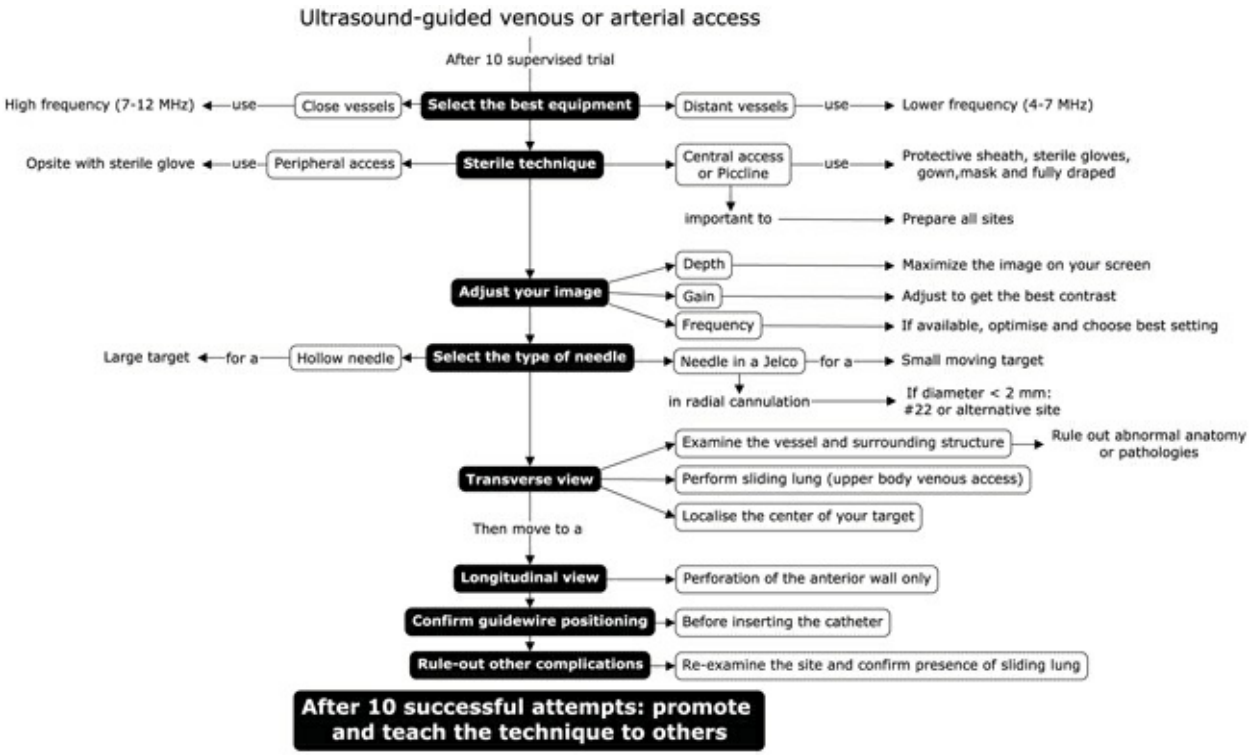

Fig. 18.1 Vascular access. Montreal Heart Institute approach for ultrasound-guided venous or arterial access is presented.

Choice of Probe

Before performing US-guided vascular access, it is important to select an appropriate US probe. Two types of US probes are currently available; high-frequency (8-12 MHz) and low-frequency (1-4 MHz). The choice of probe depends on the image quality that is desired and the depth of the targeted structure. Resolution refers to the ability to distinguish two adjacent anatomic structures. A high frequency probe has a shorter wavelength and better spatial resolution, but with only a limited imaging depth (**Figure 18.2**). In general, high-frequency probes are used for superficial structures, such as the internal jugular vein. However, for deeper structures such as femoral access in obese patients, a low frequency probe may be required. Doppler is rarely used unless there is ambiguity in differentiating a venous from an arterial vascular structure as occurs with the axillary vessels (see below).

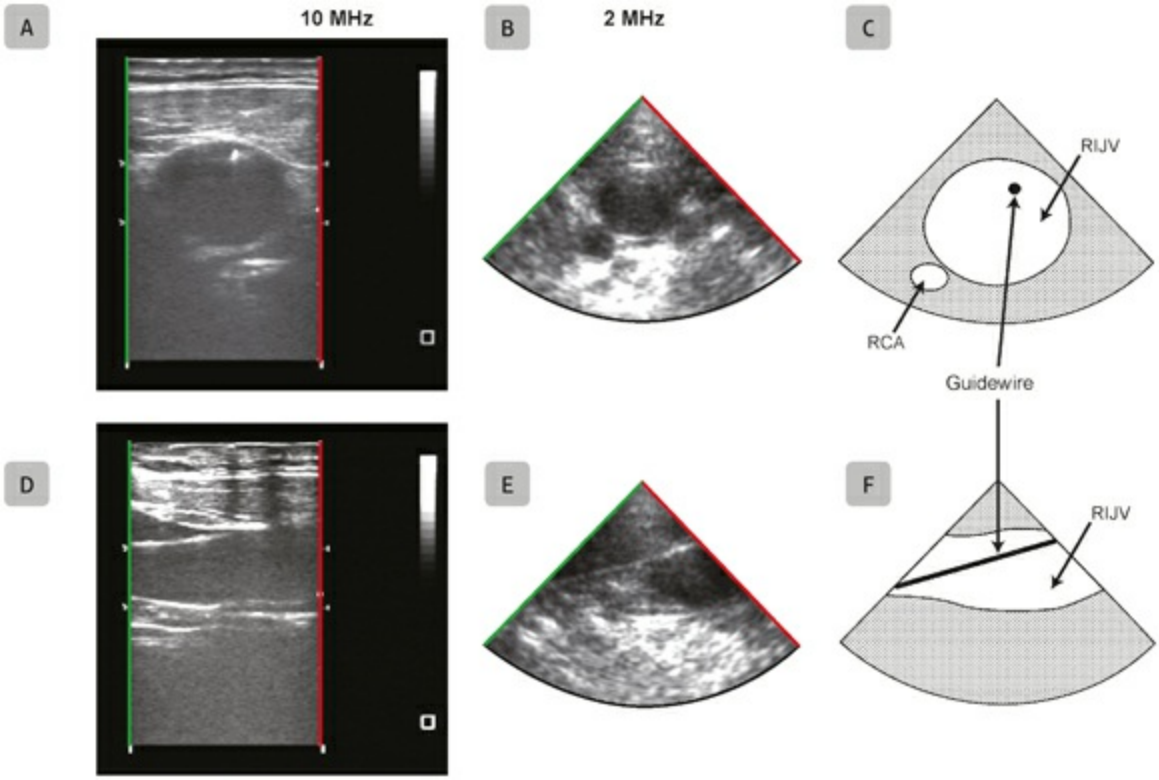

Fig. 18.2 Ultrasound probe frequency. The right internal jugular vein (RIJV) and right carotid artery (RCA) are imaged in (A—C) a transverse plane and (D-F) a longitudinal plane using two different ultrasound probes. The images obtained with (A) the higher frequency 10 MHz transducer provide more anatomic details, but the deeper positioned RCA is not clearly seen as with (B) the 2 MHz probe, that allows more depth penetration. (With permission from Denault *et al.* [8])

Preparation for Cannulation

The equipment needed to perform US catheterization includes an US device, an appropriate US probe, a sterile sheath to isolate the probe from the patient, and the catheterization kit. The material is typically prepared on a separate table (**Figure 18.3**). The presence of an assistant (wearing a mask and scrub cap) is also useful. The US probe is coated with sterile US gel and placed in a long sterile sheath to cover the entire probe connector. Note, some US probe sheaths do not require gel as they have an adhesive strip that interfaces directly with the probe. The gel serves as an interface and increases the transmission of US waves. If the sheath is perforated, gel will escape on the patient's skin making the area no longer sterile. The use of a saline solution on the skin is preferred over gel for sheath-skin interface. Holding the US probe with the non-dominant hand and the catheter/needle assembly with the dominant hand (i.e. the single-operator technique) allows the practitioner to

make fine adjustments to the spatial relationship between the US probe (image plane) and the catheter direction.

Cannulation Technique

There are two possible approaches when using US: static and dynamic. The static approach involves a preliminary visualization of the anatomical structures exclusively for anatomical identification. Although this has limited benefit, it is superior to the LM technique allowing visualization of the vein and any contraindications to cannulation. Next, the location of the vein is drawn on the skin with a sterile pencil. The rest of this technique is performed in a “blind” manner based on the surface LMs previously identified. The dynamic approach, which is also called the “real-time” US location is the preferred approach. It includes anatomical identification of the vascular structure, follows the tip of the needle progression and confirms the intravascular position of the guidewire and cannula within the vein.

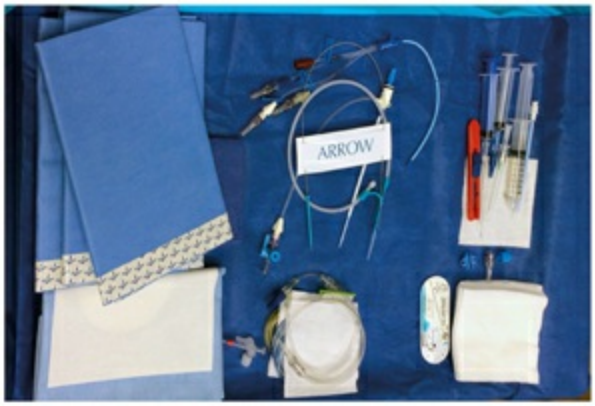

Fig. 18.3 Central line kit. Equipment for **trerBW/** central line insertion is prepared and displayed on a sterile table.

https://youtu.be/_LbifUcuE9U

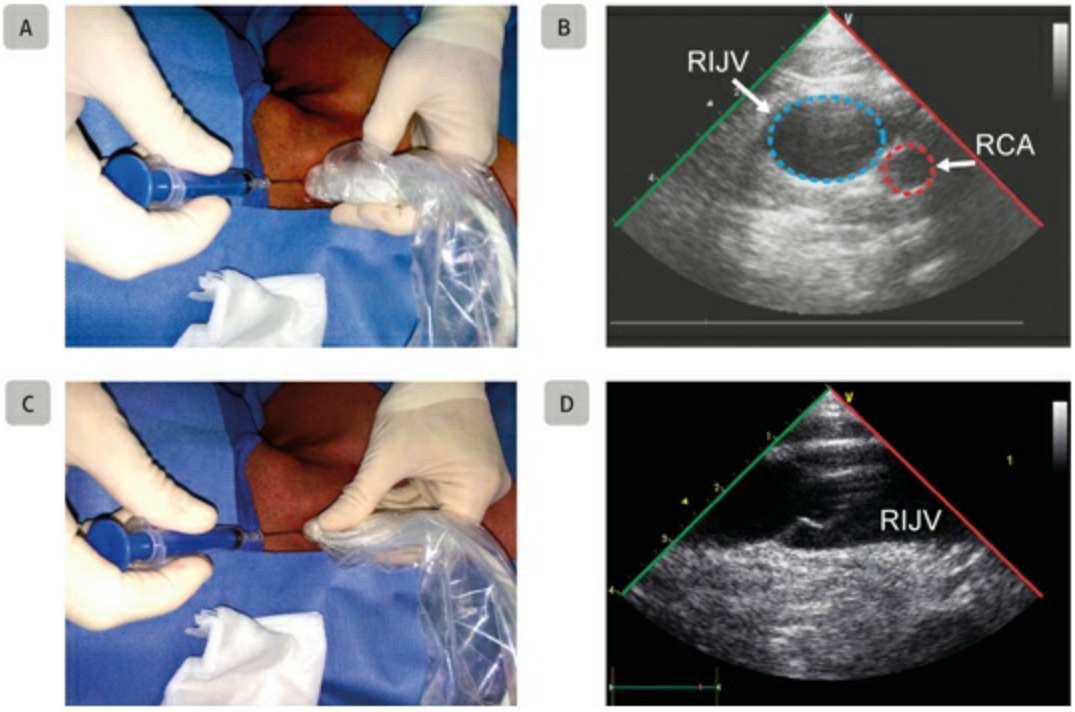

Fig. 18.4 Internal jugular vein. (A,B) Transverse and (C,D) longitudinal position of the ultrasound probe during imaging of the right internal jugular vein (RIJV) and the right carotid artery (RCA). Note the gel-filled, sterile, sheathed ultrasound probe is manipulated by the non-dominant hand. The operator is standing at the head of the patient.

https://youtu.be/jyy6Qn8aTZ0

Identification of the vein is made with the probe placed perpendicular to the neck in order to obtain a transverse view of the vessels (**Figures 18.4**). At this point, the gain, frequency, and depth are adjusted. To distinguish a vein from the artery, the US probe should be held in a stable position, allowing for small adjustments in the applied pressure. Veins will be compressed first, and as the applied pressure increases and eventually exceeds the diastolic arterial pressure, arterial pulsations will be enhanced and the artery clearly identified in most cases. The arterial wall is also thicker compared with a peripheral vein and may have atherosclerotic changes including visible calcified plaques. Color Doppler can further help distinguish a vein from an artery as the arterial lumen will be displayed in red or blue depending on the probe

angle relative to the blood flow. Aliasing or bright, turbulent appearing flow may be seen in the higher velocity artery compared with a more laminar venous flow pattern. With proper probe positioning (angled slightly toward the periphery), the pulsed-wave Doppler signal derived from arterial blood flow will be directed away from the probe and peaking during systole compared with biphasic flow toward the probe at a lower velocity seen with venous blood flow (**Figure 18.5**). Gain control should be adjusted so that fine anatomic details can be differentiated in order, for instance, to see atherosclerotic plaques in the arterial wall.

Using a dynamic approach, two main imaging techniques can be used, the transverse and the longitudinal technique. The transverse approach images the vessel in short axis with the needle plane perpendicular to the US plane (**Figure 18.4 A,B**). The main advantage of the short axis approach is that the artery and vein can be visualized simultaneously side by side during cannulation. The disadvantage of this approach is that the needle tip is not always visualized, and it can be difficult to follow the needle tip as it approaches the target structure. The US imaging plane and the needle plane can be viewed as the two sides of a triangle that should meet/ intersect at the depth for which cannulation is attempted. The experienced operator will change the angle between the two planes (US and needle) and the distance (needle insertion site versus imaging plane) depending on the depth of the vascular structure. Additionally, to follow the needle tip in the transverse approach, the US plane must be adjusted to follow the needle tip from entry through the skin to the perforation of the vessel. Additional helpful signs are an indentation of the vessel wall as the needle tip encounters the anterior aspect of the vessel. The most important aspect of imaging a needle out of plane is avoiding the mistake of visualizing the needle shaft rather than the needle tip. This happens frequently, especially early in a clinician’s experience. If not recognized, the needle tip can inadvertently exit the posterior aspect of the vessel in view and enter deeper structures.

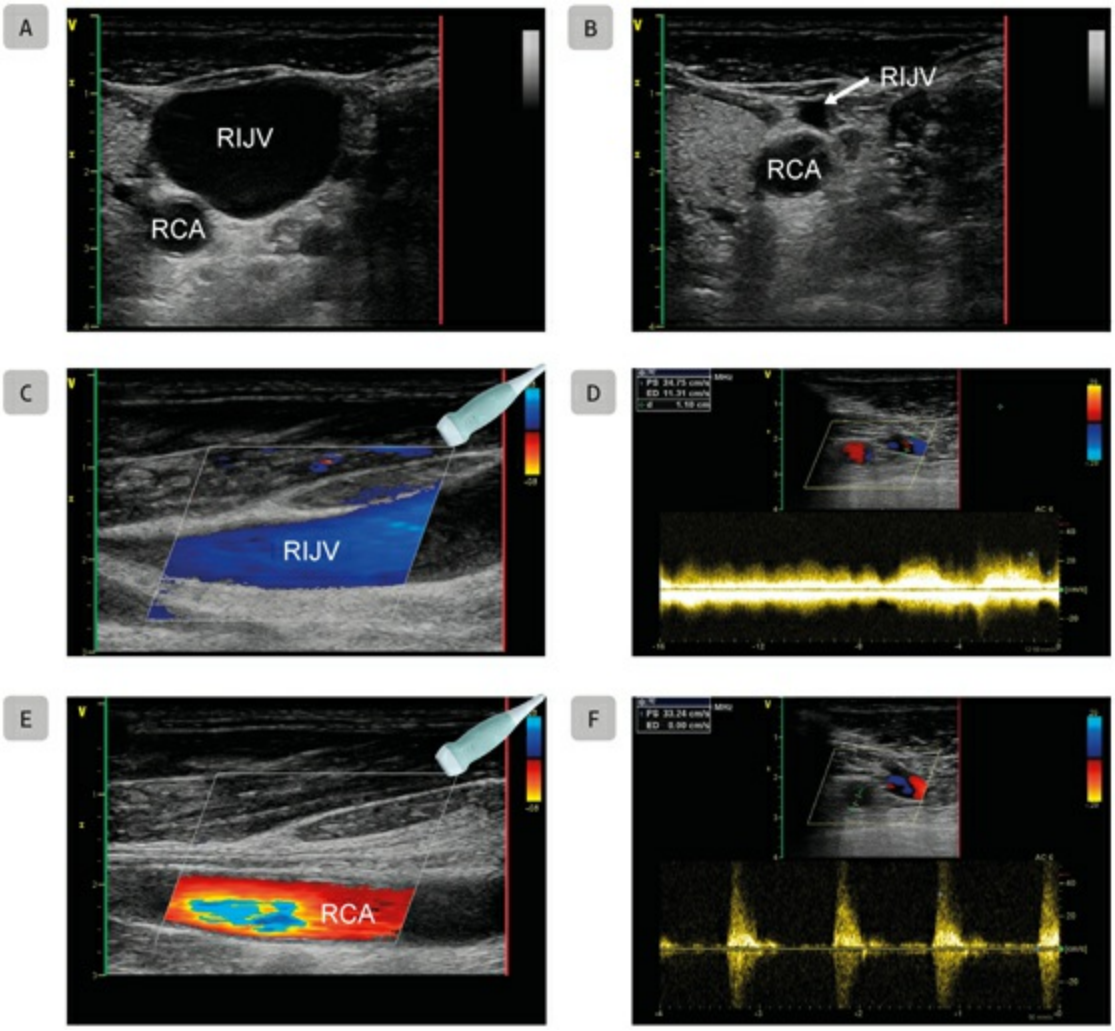

Fig. 18.5 Vein versus artery. (A,B) Right internal jugular vein (RIJV) before (A) and after (B) compression with the ultrasound probe. Note the reduced RIJV dimension compared to the right carotid artery (RCA). (C,D) Longitudinal view of the RIJV with (C) color and (D) pulsed-wave Doppler shows continuous flow toward the transducer. Note the continuous low velocity signal that changes with respiration typical of a venous flow. (E,F) Longitudinal view of the RCA with (E) color and (F) pulsed-wave Doppler demonstrates pulsatile flow in the opposite direction, away from the transducer.

The longitudinal approach shows the vessel and needle/ catheter in the long axis (**Figure 18.4 C,D**). This better visualizes the true needle tip throughout insertion and vessel penetration; however, the simultaneous display of relevant structures and their relationship to each other is lost. Another limitation is that the US beam is very narrow, so it requires great precision in lining up the probe with the needle and the probe must be oriented directly parallel with the needle at all times.

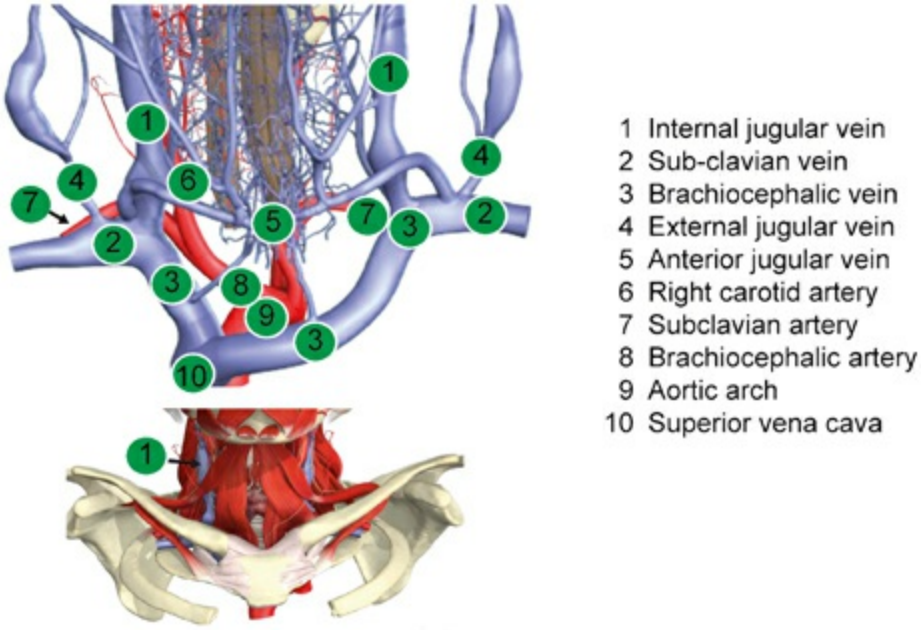

Fig. 18.6 Cervical vascular anatomy. An anatomic diagram of the major vessels in the neck is presented. (Anatomic images with permission of Primal Pictures, Wolters Kluwer Health.)

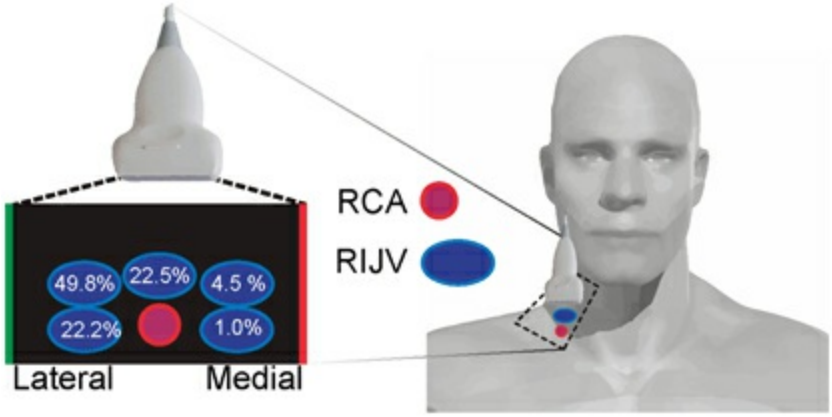

Fig. 18.7 Internal jugular vein. There is variable overlap between the internal jugular vein and carotid artery as shown in this diagram. The right internal jugular vein (RIJV) is expected to be anterolateral to the right carotid artery (RCA). In over half of patients, approximately 50% of the jugular vein surface area is anterior to the carotid. [2] (Adapted from Ayoub *et al.* [11] and Troianos *et al.* [7] *)*

When the longitudinal and transverse approach were compared with each other in simulator studies, the transverse technique was faster to learn and had a higher rate of success compared with the longitudinal technique, [9] whereas needle visualization was better with the longitudinal approach. [10]

CENTRAL VENOUS SITES

The most accepted sites for central venous access have remained the same over time, i.e. internal jugular, subclavian, axillary, and femoral veins. The choice of cannulation site is based on convenience, ease of access, and patient comfort.

Internal Jugular Vein

Local Anatomic Considerations

The anatomy of the internal jugular vein and surrounding structures is shown in **Figure 18.6**. Generally, the internal jugular vein is anterior and lateral to the carotid artery. However, this theoretical position is variably confirmed by US (9-92% of cases). [2] , [12] In over half of patients, approximately 50% of the vein's surface is located over the artery. Consequently, it is quite possible to puncture the artery by going through the posterior wall of the internal jugular vein. The degree of overlap of the vein and artery depends on the location of the puncture site in the neck (**Figure 18.7**), as well as rotation of the head. [13] In addition, in 1-5% of the internal jugular vein is medial to the carotid and in 3-18% it is thrombosed or absent. [14] The right internal jugular mean diameter is 11.5 mm, but it can be <5 mm in 13-18% of cases. [15] Thus, it is not surprising to have only partial success when puncturing lateral to the artery using a blind technique.

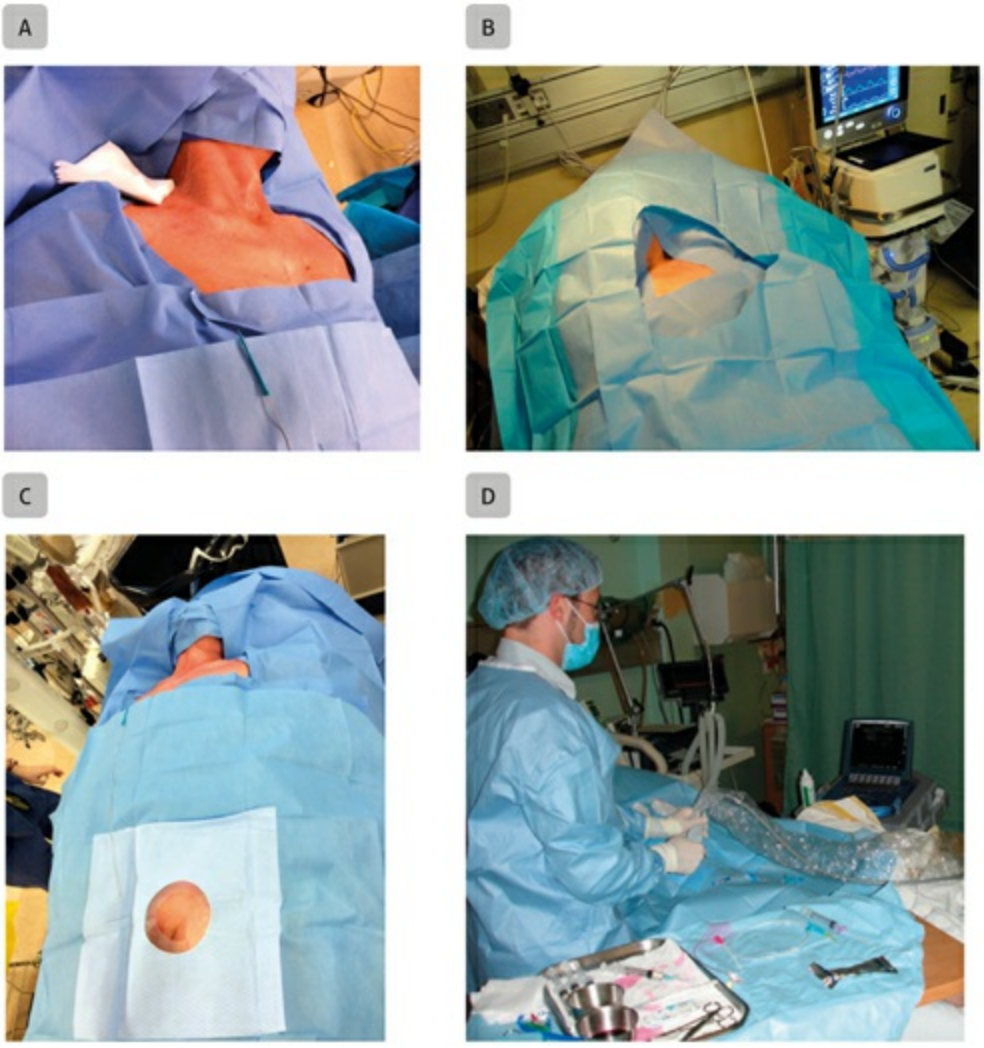

Fig. 18.8 Sterile draping and ultrasound machine position. (A-C) Full body sterile drapes for central venous access are widely positioned to allow access to (A,B) both internal jugular and axillary vessels as well as (C) the femoral vessels if indicated. (D) Optimal ultrasound machine screen position is in front of the operator and within the visual field of the vascular access.

Positioning

The patient is placed in a supine position, with or without the Trendelenburg depending on the clinical situation and volume status and with a slight head rotation of <30° towards the opposite direction. Exaggerated cervical rotation can cause a greater overlap of the internal jugular vein with the carotid artery and therefore increase the likelihood of arterial puncture. [13] The patient's skin is disinfected at all possible catheterization sites, including both jugular and subclavian vein sites (**Figure 18.8**). The operator position and US machine should be such that the US display can be easily visualized during needle

advancement, usually on the other side of target (**Figure 18.8 D**).

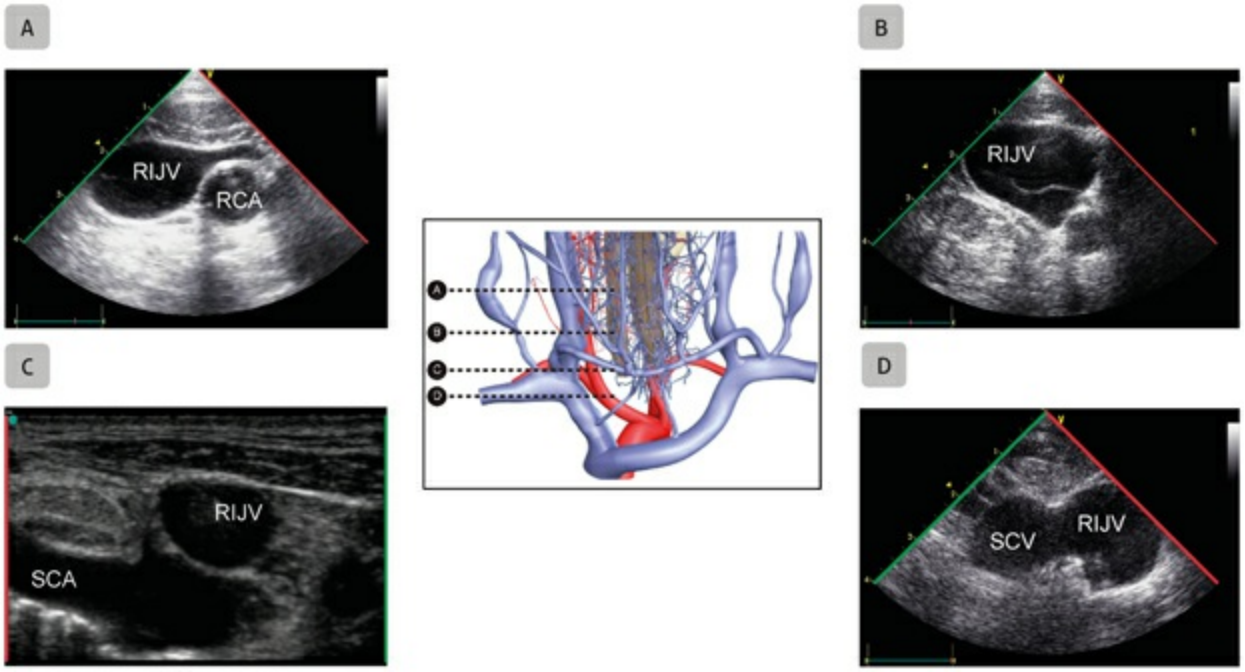

Fig. 18.9 Internal jugular vein. Ultrasound examination of the right internal jugular vein (RIJV) from (A) cephalad, (B) mid and (C,D) distal positions are displayed and described in the text. RCA, right carotid artery; SCA, subclavian artery; SCV, subclavian vein. (Anatomic images with permission of Primal Pictures, Wolters Kluwer Health.)

A: https://youtu.be/uMvovZyzXHE

B: https://youtu.be/g1eiIWlCoOA

B: https://youtu.be/F-KLsRX-qs4

C: https://youtu.be/5uEfYhgCdjU

D: https://youtu.be/-ME9zPBtqOY

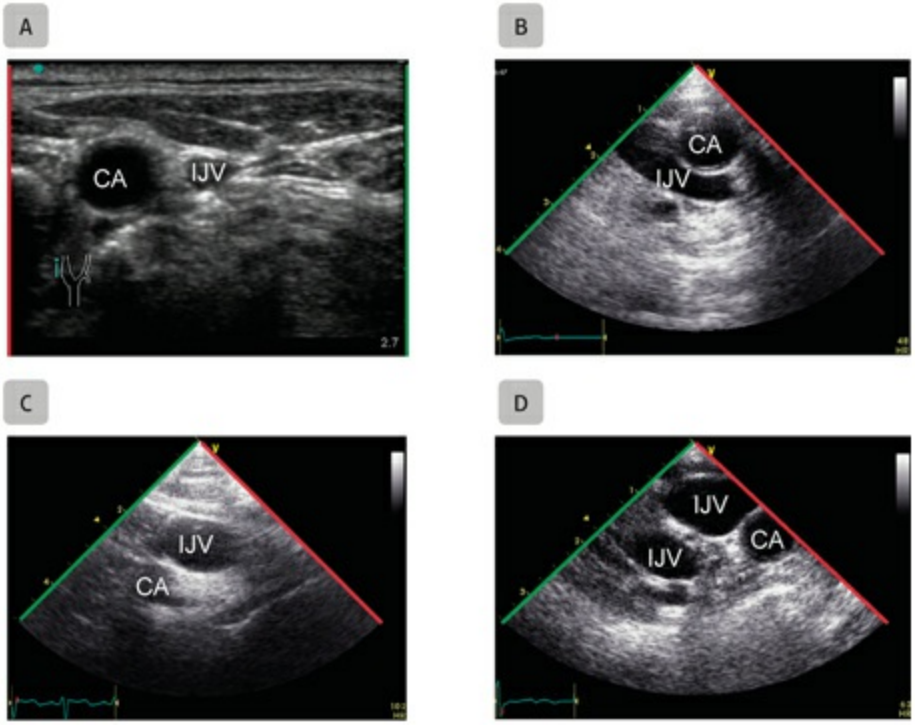

Fig. 18.10 Internal jugular vein (IJV). Examples of anatomic variations of the IJV are shown that include (A) atrophy, (B) posterior, and (C) medial positions in relation to the carotid artery (CA) and (D) a double IJV.

A: https://youtu.be/PirgJEuWyVk

B: https://youtu.be/g47ek_gTwK0

C: https://youtu.be/OhLdMeTjK1E

D: https://youtu.be/JTl-AruXkcQ

Ultrasound Examination of the Internal Jugular Vein

Before proceeding to cannulation, it is important to examine the internal jugular vein (**Figure 18.9**). Both the jugular vein and carotid artery are easily identified in the more cepha- lad portion (**Figure 18.9 A**). As the probe moves towards the clavicle, jugular valves (**Figure 18.9 B**), superposition of the jugular vein over the subclavian artery (**Figure 18.9 C**), and the junction of the internal jugular and the subclavian vein (**Figure 18.9 D**) can be seen in some patients. Anatomical variants, such as an atrophic jugular vein, aberrant position such as posterior or medial to the carotid and duplicated vein can be identified (**Figure 18.10**).

Once the site of insertion is determined, the US depth, gain, and frequency are adjusted. The probe is oriented so that the displayed image moves in the same direction as the probe, which is left to right and from the bottom up. Regular needle or intravenous catheter (Jelco type) can be used. The catheter is preferred if the target is small and the dimension of the vein is changing with respiration as in an awake patient. This allows rapid positioning of a catheter in the vein between two respirations. Using a transverse approach, the needle tip is located and positioned at the 12 o'clock position relative to the vessel. Then, a longitudinal view of the vessel is obtained by rotating the probe 90°; this will allow precise perforation of only the anterior vessel wall. The tip of needle will be seen in the target vessel as a double echo (**Figure 18.11**). Once blood is present in the needle, the guidewire is advanced. It is also essential to see the guidewire in the target vessel before dilatation and catheter insertion (**Figure 18.12**). If transesophageal echocardiography is already available, guidewire position in the superior vena cava (SVC) can be

confirmed (**Figure 18.12 D**). Carefully examine the carotid artery to confirm the absence or presence of the guidewire (**Figure 18.13 A**) [10] before dilating the vessels. If resistance to guidewire motion is encountered, use the US to follow the guidewire. The most common cause is the needle abutting against the posterior venous wall. In that situation, turning the needle 90° or pulling the needle back a few millimeters will resolve the issue. If there is more distal resistance, there could be mechanical obstruction, such as thrombosis, small venous branches or external obstruction (**Figure 18.13 C,D**). If there is any doubt, it is recommended to either measure venous pressure or measure oxygen partial pressure in a blood sample before dilating the vessel. When performing dilatation, it is important to dilate only the skin and not the vein, therefore, a small skin incision is generally sufficient. Pushing the dilator too far can result in SVC or right atrial perforation, tamponade, and hemothorax.

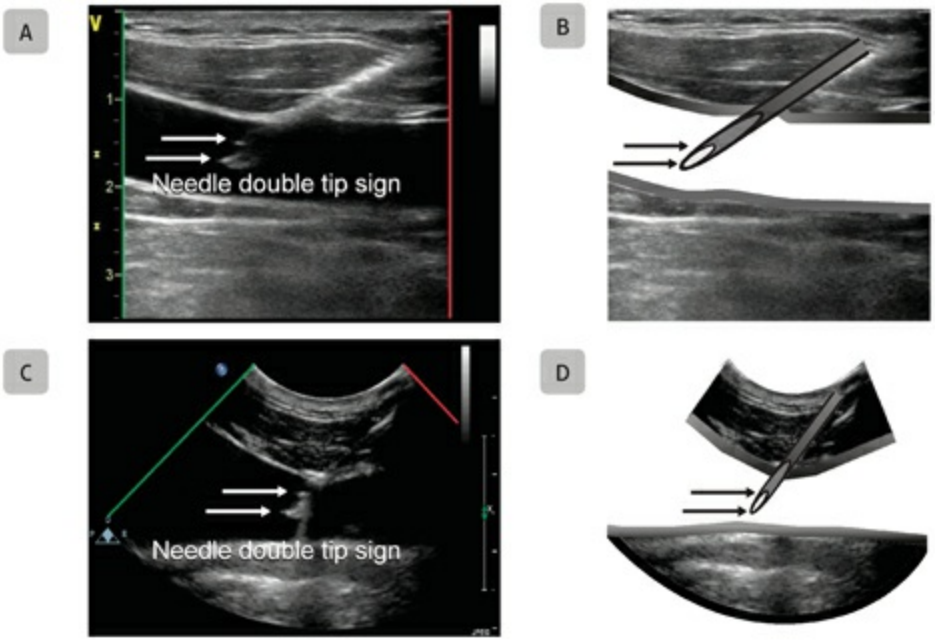

Fig. 18.11 Double tip sign. Ultrasound images of the needle in a long-axis view with the double tip sign are shown using (A,B) linear and (C,D) curvilinear microconvex probes.

A: https://youtu.be/dJuvZ_vA2wQ

A: https://youtu.be/VGwzMUg-vHM

B: https://youtu.be/peuegayfZtU

For both internal jugular and subclavian venous cannulation, consider performing lung US before and after the procedure to identify the presence and persistence of a sliding lung (see **Figure 14.5**). More details on the technical aspect of internal vein cannulation can be found in the article by Ayoub *et al.* [11] and Troianos *et al.* [7]

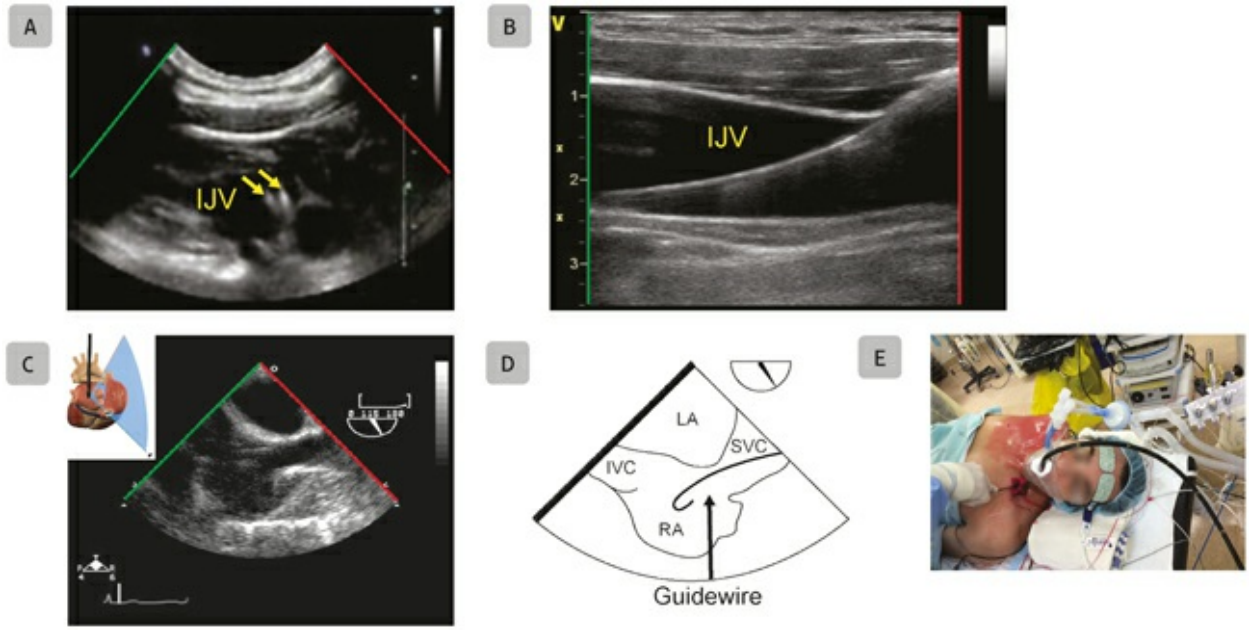

Fig. 18.12 Guidewire position. Two guidewires (arrows) are seen in (A) a transverse view and one guidewire in (B) a long-axis view of the right internal jugular vein (IJV). (C,D) A J-shaped guidewire is seen originating from the superior vena cava (SVC) in this transesophageal echocardiography (TEE) mid-esophageal bicaval view at 115°. (E) Intraoperative view of the TEE probe position is shown. IVC, inferior vena cava; LA, left atrium; RA, right atrium. (With permission from Ayoub *et al.* [11] and Denault *et al.* [8])

A: https://youtu.be/HoMLCXnNBI4

C: https://youtu.be/HEa88h7rb94

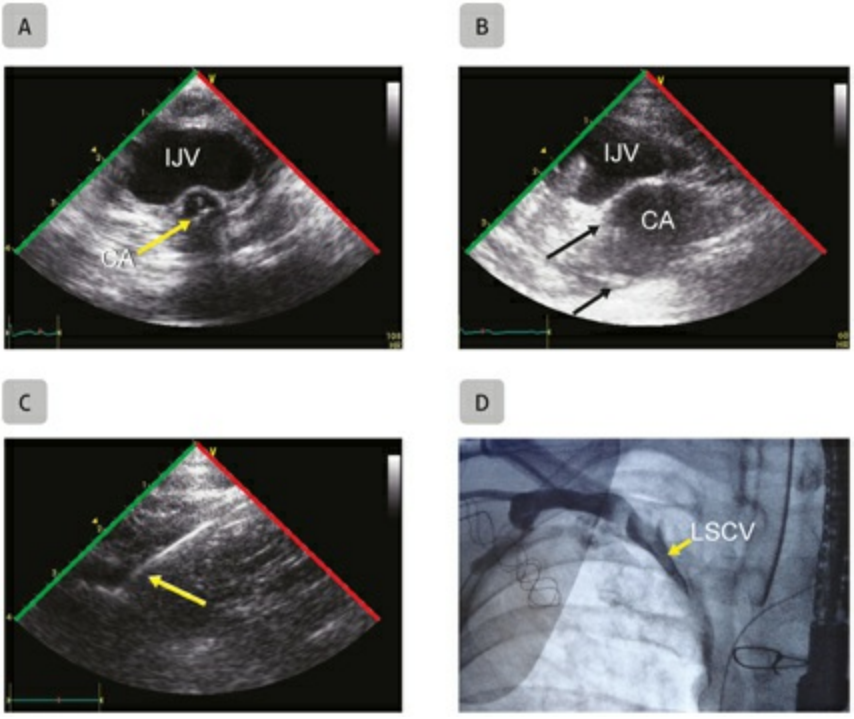

Fig. 18.13 Guidewire malpositions. (A) Ultrasound image shows a guidewire in the carotid artery (CA) (arrow). (B) Two guidewires (arrows) appear in the CA. However, these are mirror images originating from the internal jugular vein (IJV) because the carotid/jugular wall acts as a reflector. (C) Longitudinal ultrasound view of a guidewire blocked by a venous obstruction of the distal IJV (arrow) from a thrombus in a patient with a pacemaker. (D) Note the distal tapering and distal occlusion of the left subclavian vein (LSCV) on fluoroscopy.

B: https://youtu.be/qXWmo9Zd6cI

C: https://youtu.be/QpxyLZ0_2nc

Subclavian and Axillary Vein

Local Anatomic Considerations

At the thoracic level, the subclavian approach is routinely used to insert a central line, a pulmonary artery catheter (Swan-Ganz), or a permanent pacemaker in order to get fast, easy, and safe access to the SVC and right heart. The subclavian vein and artery are situated at the junction of the intrathoracic cavity and the extrathoracic zone (**Figure 18.14)**. The majority of significant complications that occur with the subclavian approach are intrathoracic, including pneumothorax, hemothorax, or chylothorax. The capacity to puncture the axillary vein when it is still extrathoracic before it becomes the subclavian vein and penetrates into the thoracic cavity prevents these complications. From an anatomic point of view, the axillary vein starts in the axillary region, just after the junction of the brachial and the basilic veins, and becomes the subclavian vein after passing above the first rib and under the subclavius muscle and the clavicle. Generally, it is situated caudal to the axillary artery, under the pectoral muscle. It is, as mentioned earlier, extrathoracic and is easily locatable and identifiable by US. It is normally situated 1-4 cm deep below the skin, depending on the patient's size, adipose tissue, and muscle structure.

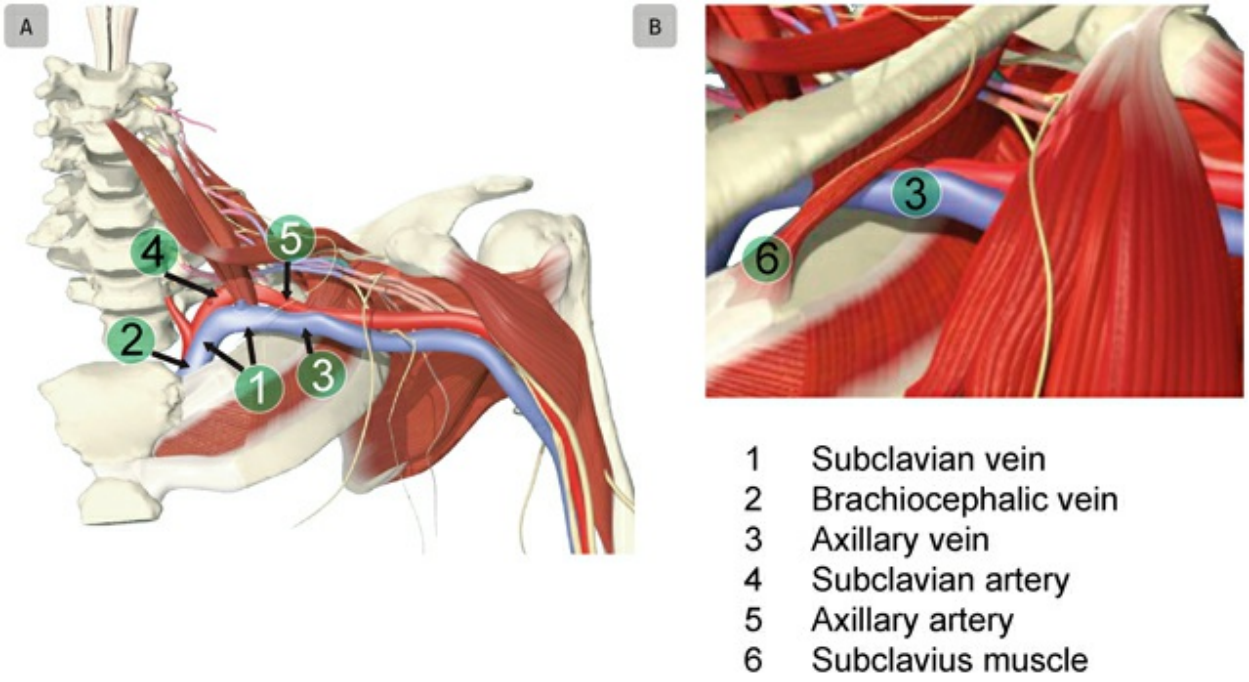

Fig. 18.14 Subclavian and axillary vein anatomy. (A) Anatomical correlations. (B) The axillary vein becomes the subclavian vein under the subclavius muscle and the clavicle as shown in these diagrams. (Anatomic images with permission of Primal Pictures, Wolters Kluwer Health.)

Ultrasound Examination of the Subclavian and Axillary Vein

The supine patient is placed in Trendelenburg (5-10°), to promote venous drainage towards the upper thorax and increasing the axillary vein diameter to facilitate imaging. The probe is oriented so that the displayed image moves in the same direction as the probe, which is left to right and from the bottom up. Begin imaging close to the clavicle, where the vessels are the biggest and closer to the skin, in short axis to display the vessels transversely and side by side (**Figure 18.15**). The vein normally can be found in the median position relative to the artery and superficial to the artery. [16] There are many anatomical variations such that the vein can be seen below or caudal to the artery. The artery pulsates, whereas the vein can collapse due to the probe's pressure or during deep inhalation. If there is any doubt, color or pulsed-wave Doppler (**Figure 18.5**) can be used in short axis, but is more convincing in long axis which is obtained by rotating the probe 90° clockwise (**Figure 18.16**) to place the vein's proximal side on the right side of the screen. The puncturing needle will penetrate from right to left as seen on the screen, following the venous flow's direction. Positioning of the needle and probe in

this configuration will make the process more intuitive, with the interventionist's hand movements matching those displayed on the image.

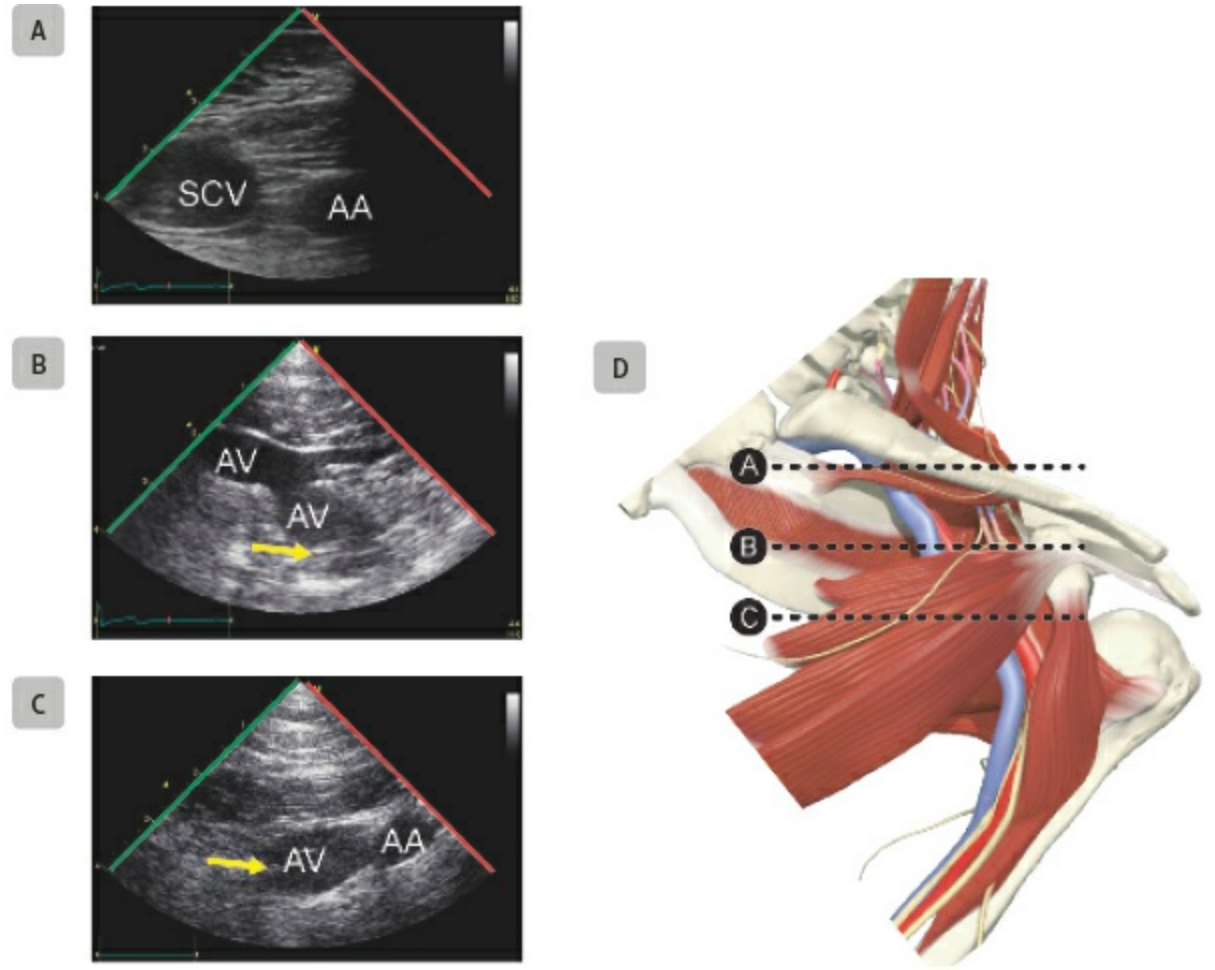

Fig. 18.15 Ultrasound of axillary vasculature. (A-C) Ultrasound examination in a transverse plane of the subclavian vein (SCV), axillary vein (AV), and axillary artery (AA) from (A) under the clavicle, (B) mid-clavicular, and (C) distal positions. Air bubbles (arrow) are often seen in patients with an ipsilateral peripheral venous catheter. (D) Anatomical correlations. (Anatomic images with permission of Primal Pictures, Wolters Kluwer Health.)

B: https://youtu.be/OVUK6VOgN-k

C: https://youtu.be/IIFbEwhCoqw

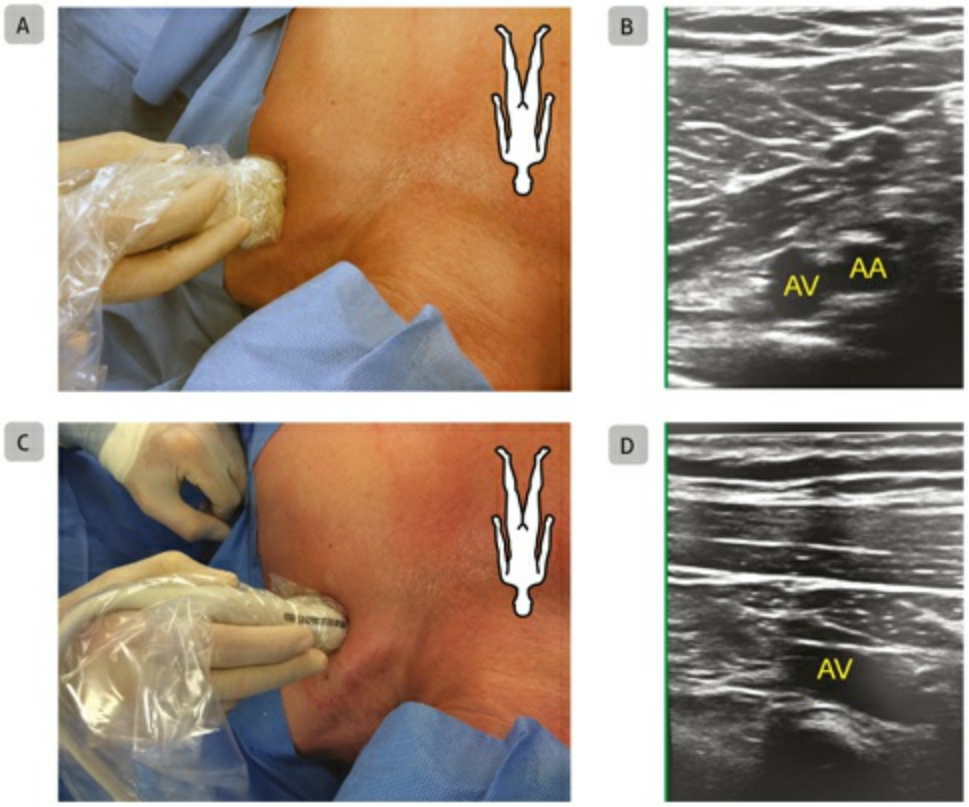

Fig. 18.16 Axillary vein. (A,B) Transverse and (C,D) longitudinal position of the ultrasound probe with imaging of the left axillary vein (AV) and the left axillary artery (AA).

A: https://youtu.be/6zL1aCKMd-k

B: https://youtu.be/g8T_KQgpx0Q

In short axis, the probe is moved obliquely a few centimeters towards the axilla, following the vessels side by side until the optimal place is found where the vein distances itself from the artery. The vein must maintain an acceptable diameter and be not too deep or too close to the axilla, while

staying at a certain distance from the clavicle in such a way that the puncturing needle never ends up underneath this bone, at the subclavian level. This avoids puncturing the vessel in the intrathoracic area and exposing the patient to possible complications. At this point, it is recommended to image the vessels longitudinally with color Doppler if necessary to identify the vessels and surrounding tissues and space.

Generally, aim to locate the perfect spot to puncture the axillary vein, which is approximately located at a third of the distance between the clavicle and axilla. If using a linear probe, one with a smaller footprint may allow for optimal image without having the clavicle obscure or interfere with imaging of the vein. When the probe is well positioned, the axillary vein is imaged in a short axis in the center of the screen with the point of venous puncture directly underneath the probe. In an awake patient, local anesthesia is administered on the skin and subcutaneous tissue by inclining the needle 45° towards the probe's center. The same path is used to puncture the axillary vein with a 7 cm 18-G needle ("Echo tip" type) with a distal tip that is a slightly more luminescent alongside an US (**Figure 18.17**). Careful synchronization of the hands and the eyes is necessary so that the needle tip reaches its goal, the axillary vein. Once the needle has penetrated a few centimeters of subcutaneous tissue, delicately tilt the probe to the patient's head to find either the luminescent tip, or the needle's rod, which will produce the double echo signs as previously described (**Figure 18.11**).

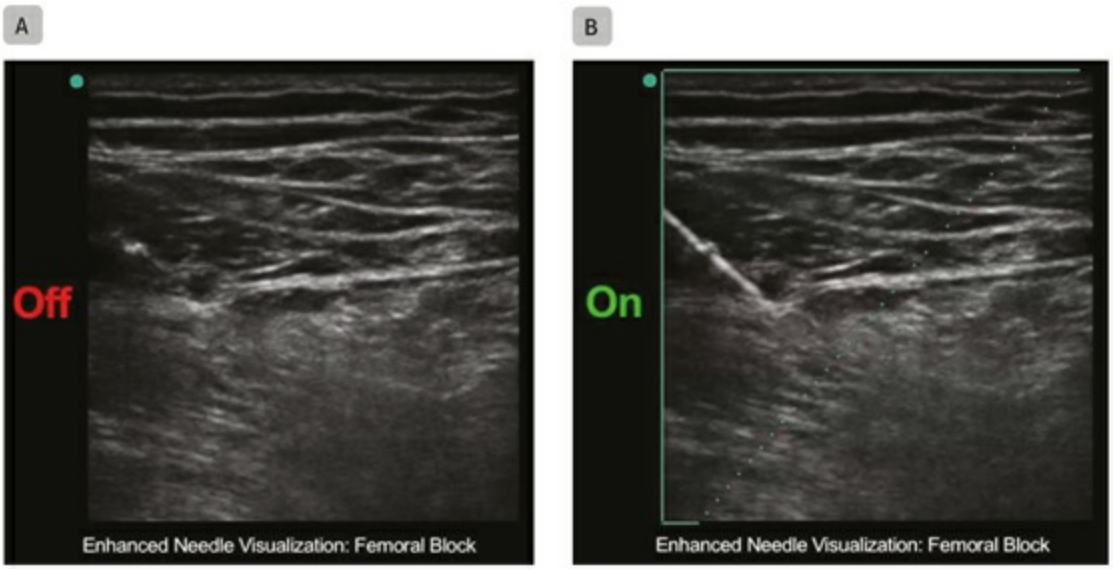

Fig. 18.17 Enhanced needle. Enhanced needle visualization (A) off and (B) on is shown.

A: https://youtu.be/smWTVUIG1iY

When the needle's tip reaches the vein's superior wall, turn the probe 90° clockwise to see the vein longitudinally. This confirms that the needle in long axis is angled close to 45° away from the artery that is situated just beneath it. If it is not so, it is necessary to return to short axis and realign the needle towards the center of the vein. Once this configuration has been achieved, continue introducing the needle (with continuous aspiration applied to the syringe), until the needle is seen penetrating the vein and blood enters the syringe. Either the puncture will immediately be successful by piercing the superior wall, or it will be necessary to transfix both vein walls before seeing a venous return when delicately withdrawing the needle, once both walls are separated. With the axillary vein punctured, put aside the US probe and insert the guidewire into the vessel prior to withdrawing the needle. Guidewire confirmation for the axillary vessel can be done as for the internal jugular vein (**Figure 18.18**). When the axillary vessel is too deep and the guidewire not well seen, examine the adjacent internal jugular vein to exclude an aberrant position of the guidewire in the internal jugular vein. In addition, as the US beam is moved downwards to the clavicle, the guidewire can often be seen in the ipsilateral innominate vein (**Figure 18.18**).

Femoral Vein

The femoral site has numerous advantages both with elective vascular access and in critically ill patients. The common femoral vein is often used for central venous access during emergency situations, [17] because of its relative safe accessible location with predictable anatomic LMs, relatively short access times, and fewer complications. Femoral venous access is used routinely for hemodynamic and electrophysiologic studies to insert catheters into the heart. Femoral access avoids the risks of hemothorax and pneumothorax, which is particularly important in patients with severe coagulopathy, anticoagulation medication (especially for invasive cardiologic procedures), or if non-intubated with significant respiratory compromise. In addition, the femoral site permits cannulation attempts without interruption of cardiopulmonary resuscitation during cardiac arrest. Ultrasound can visualize

the vascular anatomy without relying on an arterial pulsation, when traditional LM and palpation techniques for arterial cannulation are almost impossible [17] , [18] as in patients with non-pulsatile ventricular assist device. Both LM-based and US-guided techniques are challenging in patients with difficult vascular access due to obesity, edema, hematoma from previous attempts, and weak or missing arterial pulsations. Femoral access should be avoided in patients with grossly contaminated inguinal regions because of high risk of catheter-related infections. If a CVC is needed for resuscitation from shock, the catheter can be replaced subsequently at the most appropriate site for the patient, with good aseptic conditions.

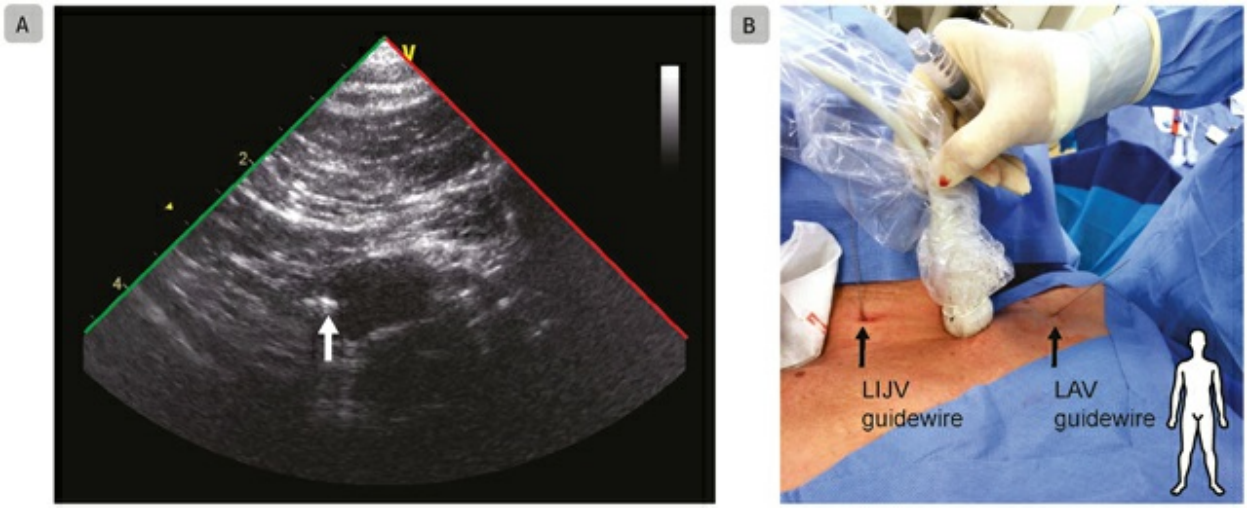

Fig. 18.18 Axilary vein guidewire. (A) Guidewire coming from the left axillary vein (LAV) (arrow) is shown. (B) In order to see the guidewire, the ultrasound probe can be positioned above the LAV or along the left internal jugular vein (LIJV) just above the left clavicle.

Local Anatomic Considerations

A detailed understanding of the regional anatomy is important for performing femoral venous cannulation using a LM-guided technique (**Figure 18.19**). The use of US for vascular access has provided practitioners with more precise data regarding the anatomic relationship of vascular structures. [19] The common femoral artery and vein lie within the femoral triangle in the inguinal-femoral region (**Figure 18.19**), which is bordered by the inguinal ligament (superior), adductor longus muscle (medial), and sartorius muscle (lateral). Another important LM is the femoral arterial pulse that lies at the midpoint of the inguinal ligament connecting the anterior superior iliac spine to the pubic tubercle. The common femoral vein typically lies medial to the

common femoral artery within the femoral sheath, although significant vessel overlap may occur, particularly in children. [20] – [22] It is essential to appreciate that the relationship between the inguinal crease and the inguinal ligament is highly variable, so the inguinal crease is not always a useful surface LM. [23]

Ultrasound Examination of the Femoral Vein

The modified Seldinger technique is the most common method used to access the common femoral vein, [3] using the traditional LM and palpation techniques. The major disadvantage is the overlap of the femoral vein by the femoral artery which increases from 5% to 60% moving distal to the inguinal ligament, particularly in children. There is a one in five chance of failure to locate the femoral vein by the landmark technique. [24] There is also no evidence to suggest that the right or left femoral vein should be favored for attempts to CVC; however, it has been reported that practitioners will choose the right nearly two-thirds of the time. [25]

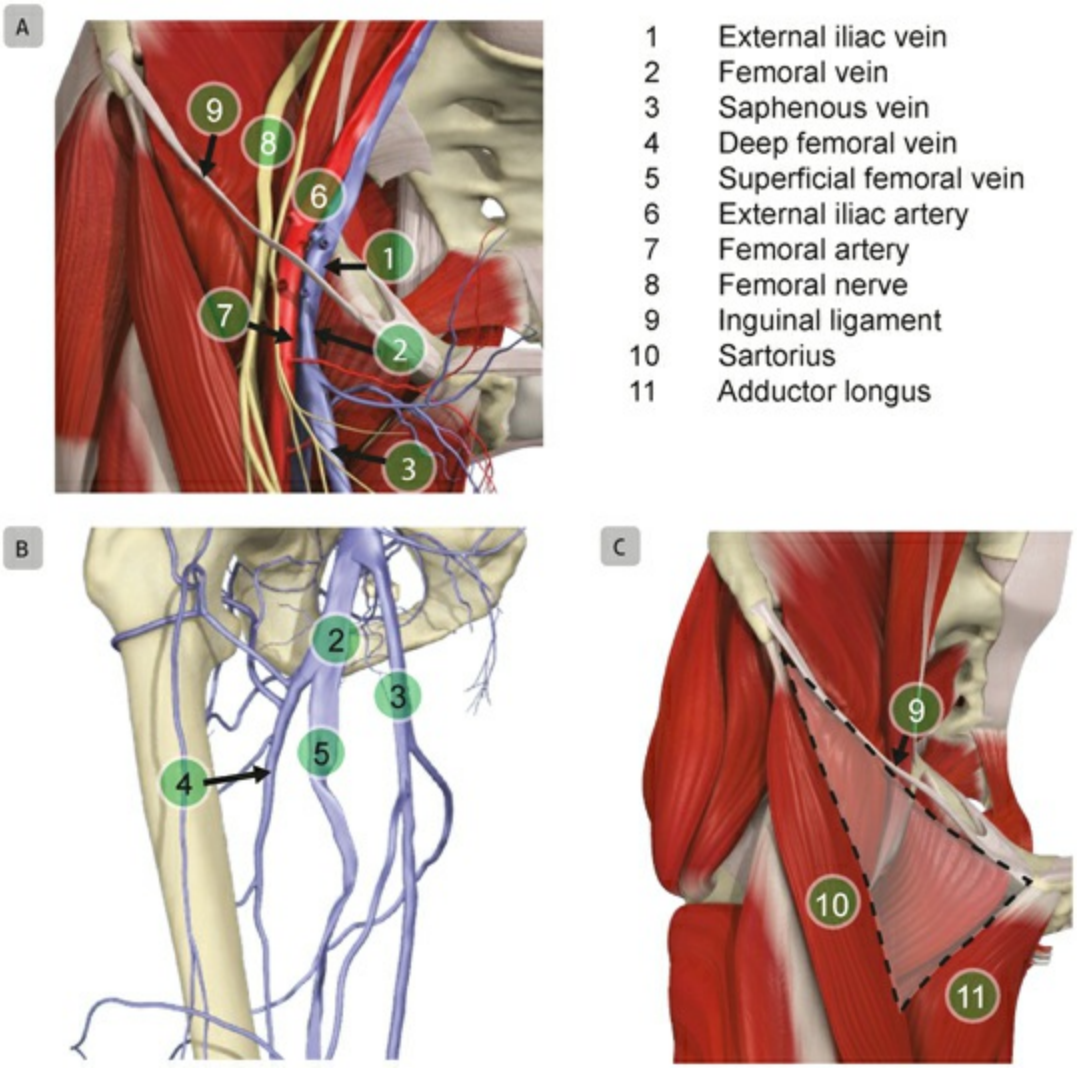

Fig. 18.19 Femoral vessels. Diagrams are presented of the (A) iliac anatomy, (B) femoral venous anatomy, and (C) femoral triangle landmarks. (Anatomic images with permission of Primal Pictures, Wolters Kluwer Health.)

When using the US-based technique, [26] the proper probe orientation must be confirmed so the lateral aspect on the displayed image matches the correct anatomic orientation before needle insertion. The US depth is adjusted so the target femoral vein and artery and their relationship are clearly visualized and identified. Differentiation between the vein and artery is performed as discussed previously.

Examination of the femoral vein is important before performing cannulation. Close to the inguinal ligament, both the femoral vein and artery will be seen (**Figure 18.20 A**). The long saphenous vein will be identified in this region which is a common site for deep venous thrombosis (DVT). As

the probe moves in a caudal direction, the femoral artery bifurcation will be seen (**Figure 18.20 B**). The deep femoral vein will often pass between the superficial and the deep femoral artery (**Figure 18.20 C**). Anatomical variations can occur as in other anatomic regions. Vascular access will follow the same approach as for the internal jugular and axillary vein. In the end, the correct intravascular position of the guidewire should be confirmed using real-time US. A randomized controlled trial reported a higher first-attempt success rate and fewer needle passes with real-time US-guided puncture of the femoral vein compared with the anatomic LM approach in pediatric patients. [27]

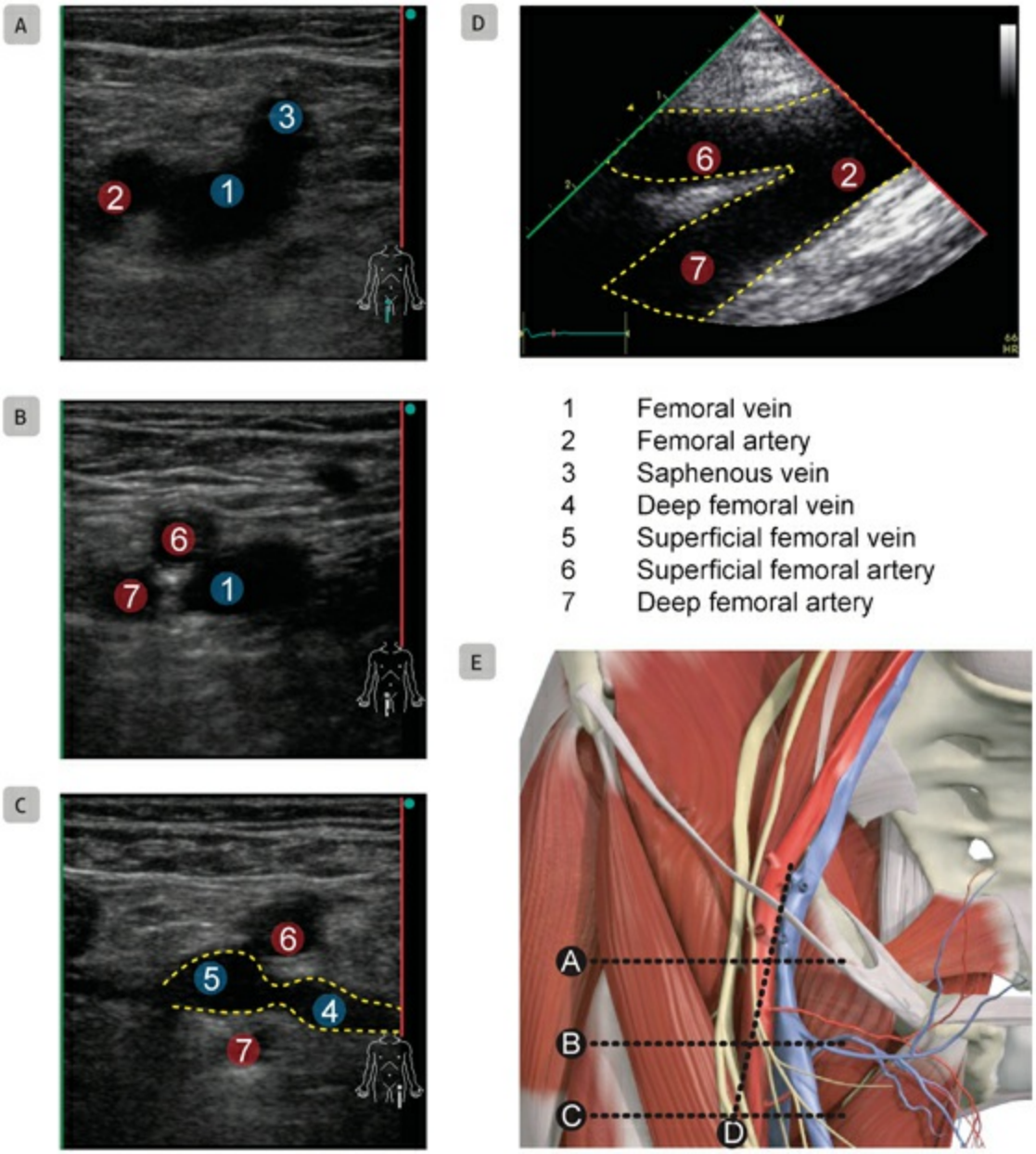

Fig. 18.20 Femoral vessel examination. The origins of the (A) saphenous vein, (B) femoral arterial and venous bifurcation are the required key elements to identify during ultrasound examination of the femoral vessels. (C) The deep femoral vein will often pass between the superficial and the deep femoral artery. (D) Longitudinal aspect of the femoral arterial bifurcation is shown. (E) Anatomical correlation. (Anatomic images with permission of Primal Pictures, Wolters Kluwer Health.)

A: https://youtu.be/RJ-Ta55V71c

C: https://youtu.be/9pwdYrHOYLs

D: https://youtu.be/9P0DHM5XGGs

Complications of Central Venous Catheters

Ultrasound guidance has been shown to reduce the number of attempts, total number of needle sticks, arterial punctures, and failed access. [1] However complications still occur for all sites of venous access (**Table 18.2**). Complications for US-guided internal jugular vein access are infrequent, although hematomas and arterio-venous fistula can occur particularly with inexperienced users (**Figure 18.21 A,B**). Spontaneous venous contrast can be seen in patients with elevated right-sided pressure; however, this is not a contraindication for jugular venous access (**Figure 18.21 C**). An extravascular structure such as the thyroid, if enlarged, can distort the internal jugular vein making it unsuitable for CVC (**Figure 18.21 D**). In a study involving 171 high-risk patients requiring a dialysis catheter, the success rate using US was 100%, with 1.8% incidence of inadvertent arterial puncture and no hemothorax or pneumothorax requiring intervention. [28] A large trial involving 900 patients also showed the superiority of US-guided over LM techniques for axillary venous access. [29]

Table 18.2 Frequency of Mechanical Complications According to the Route of Catheterization

Complication	Frequency (%)		
	Internal jugular	Subclavian	Femoral
Arterial puncture	6.3–9.4	3.1–4.9	9.0–15.0
Hematoma	<0.1–2.2	1.2–2.1	3.8–4.4
Hemothorax	NA	0.4–0.6	NA
Pneumothorax	<0.1–0.2	1.5–3.1	NA
Total	6.3–11.8	6.2–10.7	12.8–19.4

From McGee and Gould. [1]

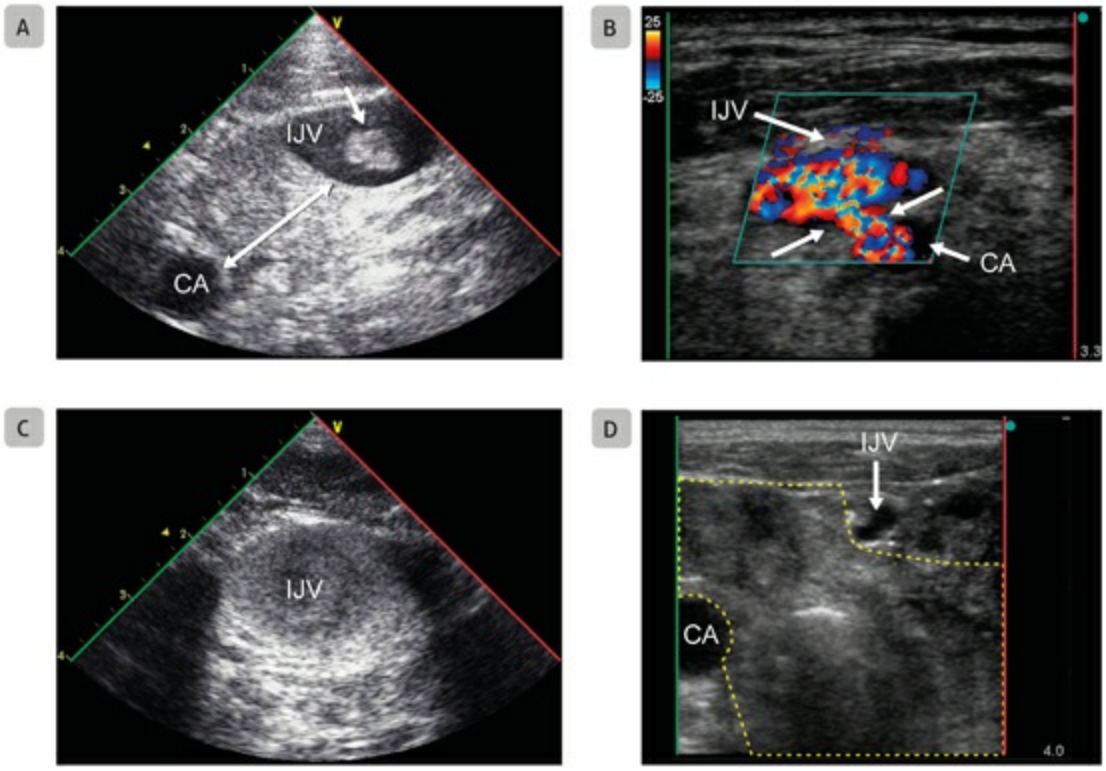

Fig. 18.21 Complications. (A) Ultrasound image shows floating spontaneous thrombus (arrow) in the internal jugular vein (IJV) following accidental puncture of the carotid artery (CA). Note the increased distance between the IJV and CA (double-head arrow). (B) Arteriovenous fistula (arrows) is created between the IJV and CA as shown with color Doppler. (C) Spontaneous contrast is seen in the lumen of the left IJV. (D) A large goiter (dotted line) increases the distance between the IJV and CA.

A: https://youtu.be/GLI27a4SWsw

C: https://youtu.be/lGj2GgbXa44

B: https://youtu.be/hkfurWcyWRo

B: https://youtu.be/HLtouOv9z_M

In a study comparing US-guided subclavian vein access in 401 patients, [30] the US group achieved significantly more ($p < 0.05$) successful cannulation (100%) compared with the LM group (87.5%). Average access time and number of attempts were significantly reduced in the US group compared with the LM group ($p < 0.05$). Complications were higher in the LM group, artery puncture and hematoma (5.4%), hemothorax (4.4%), pneumothorax (4.9%), brachial plexus injury (2.9%), phrenic nerve injury (1.5%), and cardiac tamponade (0.5%). The only complication in the US group was inadvertent arterial puncture and hematoma (0.5%). Hematoma and thrombus can occur in the subclavian vessels (**Figure 18.22**). A subsequent meta-analysis of US use for subclavian vein cannulation demonstrated that overall complication rates were reduced with US use compared to the LM group, with reduced inadvertent arterial puncture, pneumothorax, and hematoma formation. [31] Dynamic US also demonstrated a significant decrease in failed catheterization compared to the LM technique.

Spontaneous contrast in the axillary vein has the same significance as in the internal jugular vein. Perforation of the posterior wall of the subclavian venous wall can also occur using the LM technique and be only recognized upon removal of the catheter (**Figure 18.23 A**). Finally, in both internal jugular and subclavian venous access, hemothorax can occur especially if the

dilator is pushed too far in the vessel (**Figure 18.23**).

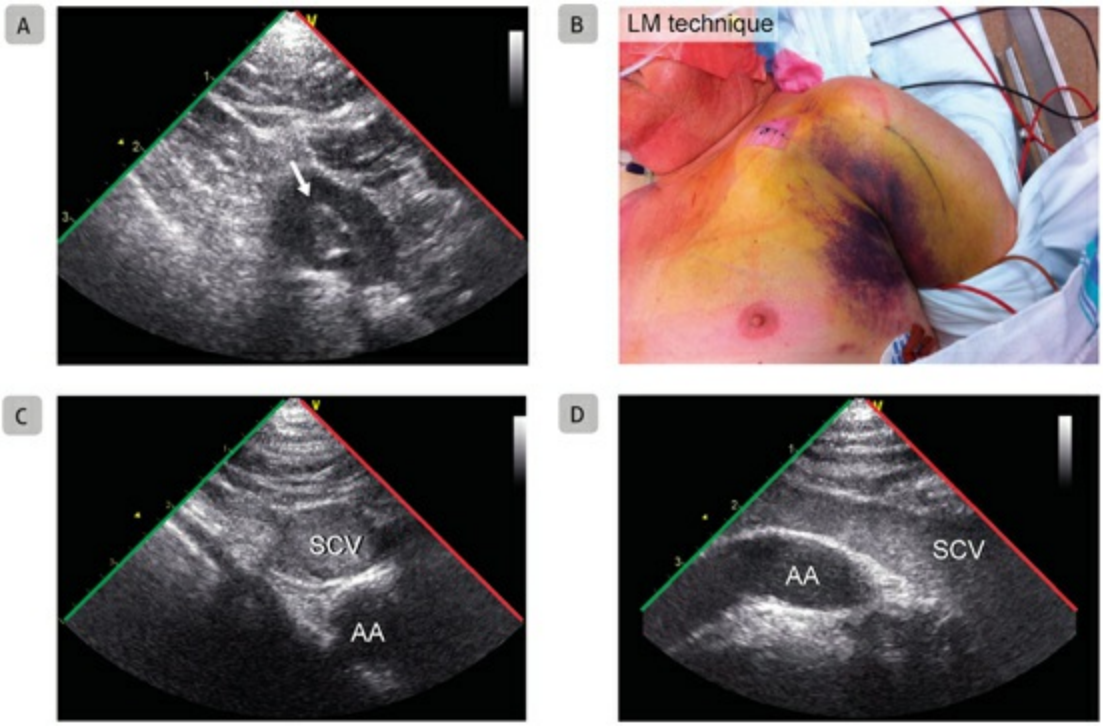

Fig. 18.22 Complications. (A) An ultrasound image shows a left peripherally inserted central catheter. (B) Extensive hematoma in the axillary region was associated with use of the landmark (LM) technique for pacemaker insertion in this patient. (C,D) Spontaneous contrast in the left subclavian vein (SCV) is shown in (C) short-axis and (D) long-axis views in a 72-year-old male with coronary artery disease. AA, axillary artery.

A: https://youtu.be/d25HsaCD5fA

C: https://youtu.be/oQss8z2IZkk

D: https://youtu.be/5Rp9SRuKwhs

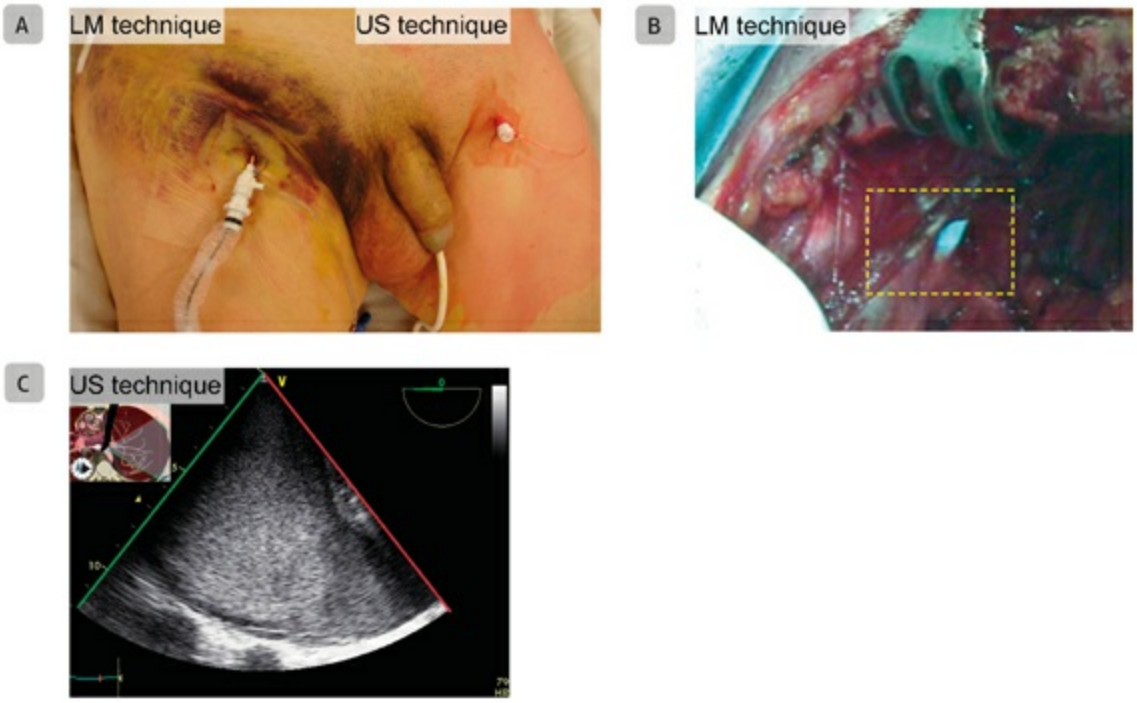

Fig. 18.23 Complications. (A) Right femoral vein hematoma occurred using a landmark (LM) technique compared with the left femoral artery cannulation performed using an ultrasound (US)-guided technique. (B) Photo of a subclavian vein posterior wall perforation using the LM technique. Bleeding from the vein is prevented by the catheter, which occluded the hole in the posterior wall. Hemothorax can occur upon withdrawal. (C) Right-sided hemothorax imaged with transesophageal echocardiography from a superior vena cava perforation that was due to a vessel dilator being advanced too far.

B: https://youtu.be/OjoGeFOSSj8

C: https://youtu.be/AQh6W8LqWs4

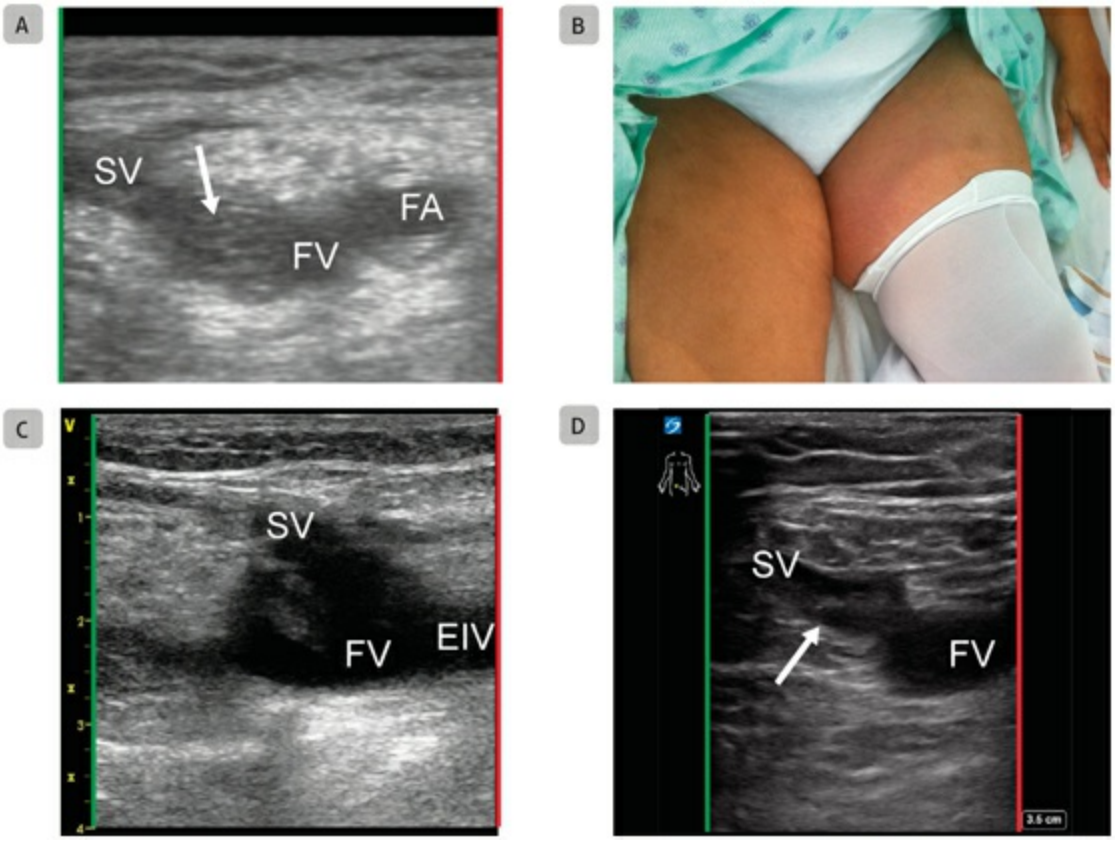

Fig. 18.24 Complications. (A) Ultrasound short-axis view of a femoral vein (FV) thrombus (arrow) in a female with (B) a swollen left leg is shown. (C,D) The FV thrombus (arrow) is often close to the bifurcation with the saphenous vein (SV) as seen in short- axis and (D) long-axis views by ultrasound. EIV, external iliac vein; FA, femoral artery.

A: https://youtu.be/LVG6wMtZHjU

C: https://youtu.be/U8F6tFQGQvA

D: https://youtu.be/HpG4pa-mCS4

Complications during femoral vein cannulation in adults are less severe than those that occur with subclavian and internal jugular vein cannulation. Static US guidance is recommended only for identifying vessel overlap and patency. [7] However, a meta-analysis showed that real-time US guidance for hemodialysis catheter placement decreased incidence of arterial punctures, risk of placement failure, and risk of failed first-time access. [32] The LM approach to the femoral vein is associated with complications, including bleeding, vascular injury, and neurological complications, resulting in significant morbidity and mortality (**Figure 18.23 B**). Infection remains one of the most common problems with femoral catheters (19.8%). [33] Thrombus may develop within the femoral vein or iliac vein in up to 21.5% of patients because of the presence of the catheter or during compression upon removal (**Figure 18.24**). [33] Ultrasound-guided femoral arterial and venous cannulation most likely reduces the incidence of complications because the anatomy is better defined. [27] , [34]

Finally, when US guidance is used, the operator can be distracted by searching for the needle on the monitor. This combined with a false sense of security and the technical limitations of not always visualizing the needle tip especially during the transverse approach, can lead to inadvertent artery puncture. There are few if any disadvantages or complications associated with using US for cannulation compared with a blind palpation technique. Potential disadvantages include the loss of skill and confidence with the palpation technique, which becomes critical when US equipment is not readily available; delays waiting for US equipment; expense of the equipment; and a theoretical increased risk of infection.

PERIPHERAL INTRAVENOUS CENTRAL CANNULATION

Peripherally inserted central catheter cannulation has gained popularity in the critical care setting in recent years. [35] , [36] These catheters can provide central venous access at the cost of a peripheral venipuncture, avoiding the well-known complications of central venous cannulation. [1] The advent of modern tip tracking technology allows precise tip positioning at the bedside without the need for fluoroscopy. The availability of multiple lumen catheters that allow high infusion rates have made PICC lines the preferable venous access

in many ICUs in North America. Their ease and safety of insertion has led to the successful creation of nurse-lead PICC insertion teams. [37] The main determinant to make PICC insertion available at the bedside has been the availability of portable US machines and training in US-guided venous cannulation.

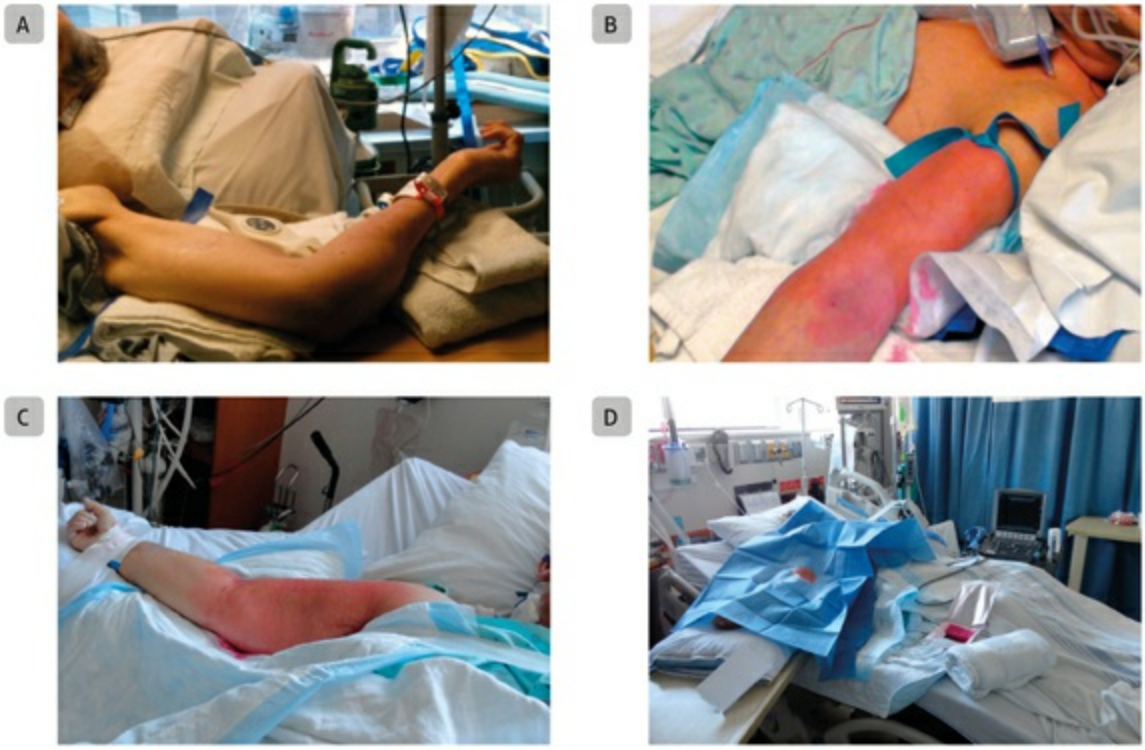

Fig. 18.25 Peripherally inserted central catheter (PICC) line. (A—D) Different positions of the arm and ultrasound equipment are shown for insertion of left- and right-sided PICC.

Peripherally inserted central catheter lines were initially introduced for long-term venous access in oncology patients. More recently, they have been considered far better than central lines for long-term venous access in the ICU set- ting. [35] However, recent meta-analyses have raised concerns about the advantage of PICC versus central line access. [38] There is a comparable incidence of central line-associated blood stream infections (5.2%) [39] and a higher incidence of catheter-related deep venous thrombosis at the site of PICC insertion (13.9%). [40] Simple measures and awareness of these and other limitations, can minimize the incidence of these complications. [41]

Bedside PICC line insertion begins with patient assessment. First, it is important to confirm the indication for PICC insertion such as difficult/impossible central or peripheral venous access and the need for long-

term venous access. Relative contraindications are coagulopathy, complex congenital cardiac disease, on-going renal replacement therapy, and potential need for arterio-venous fistulas. Absolute contraindications are lack of patient consent and no suitable vessels. In reviewing past medical history, special attention should be paid to a history of DVT, congenital cardiac disease, previous PICC lines and venous stenosis. Physical examination should identify the presence of other lines and scars in the subclavian area (pacemakers/previ- ous permanent venous catheters) and examination of the upper extremities for unilateral edema.

Preparation

Patient preparation includes sedation and positioning. Most cooperative patients tolerate PICC insertion under local anesthesia alone. A consistent subset of ICU patients may require optimization of sedation and analgesia during line insertion. It is recommended to aspirate secretions in intubated or tracheotomized patients prior to positioning to minimize coughing and movement during line insertion. Optimal positioning requires supination and extension of the selected arm to 90°. A folded towel under the arm will increase patient comfort and allow better positioning with a side table to support the elbow and forearm (**Figure 18.25**). The head can be elevated up to 45° to improve patient comfort.

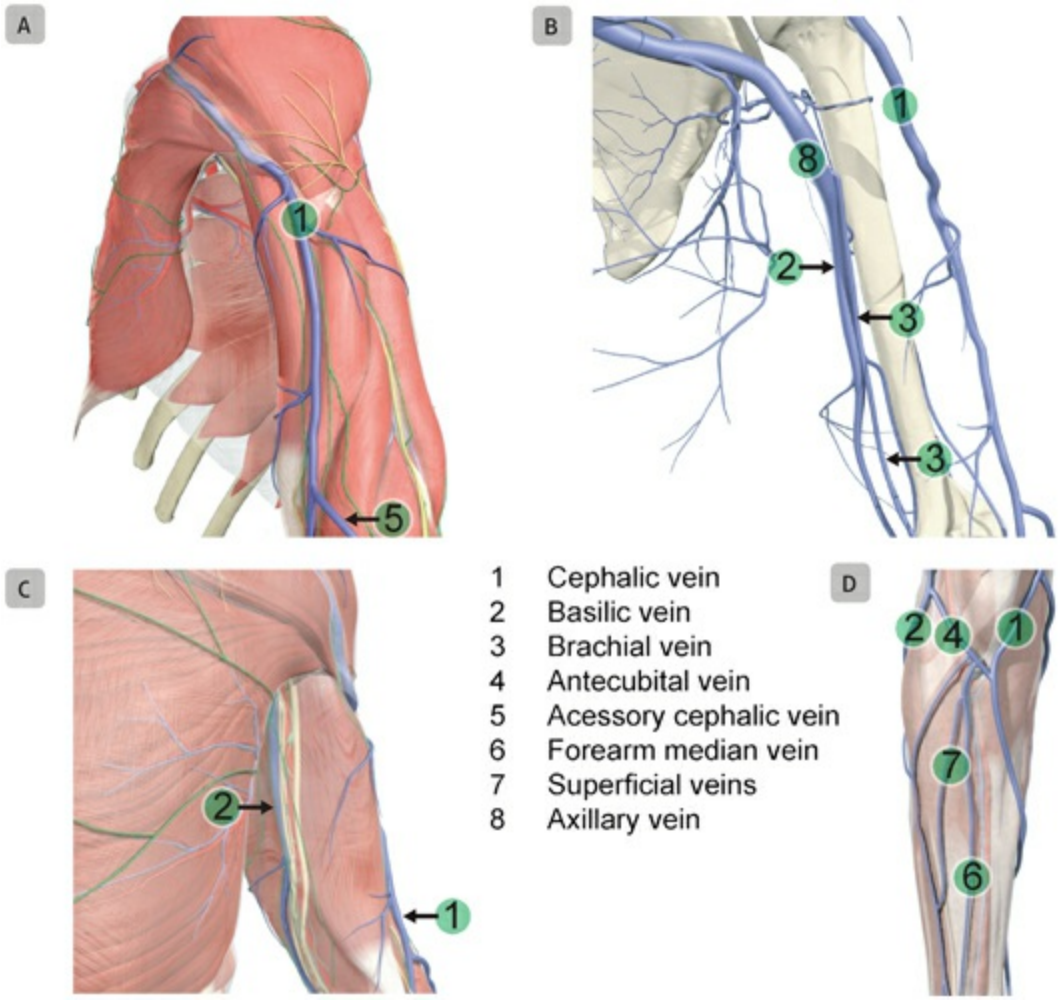

Fig. 18.26 Upper extremity venous anatomy. Diagrams are presented of the venous anatomy of the (A) cephalic vein, (B,C) basilic vein, and (D) antecubital vein. (Anatomic images with permission of Primal Pictures, Wolters Kluwer Health.)

Local Anatomic Considerations

In most patients, the upper arm venous system drains into the subclavian vein and is constituted by three major vessels: basilic vein (most medial), brachial vein (adjacent to the brachial artery), and cephalic vein (most lateral) (**Figure 18.26**). Anatomical variability is well known among patients.

Ultrasound Examination of the Upper Extremity

Ultrasound scanning is performed using a high frequency linear array probe (5-12 MHz). The screen is positioned in front of the operator and the radiology convention is usually chosen (**Figure 18.27**). The probe marker is

oriented towards the operator's left side to match the screen. The optimal puncture site is as high as possible in the proximal right arm [42] whenever possible. Scanning of the arm is initially performed without a tourniquet and is aimed at identifying the most suitable vessel. Skin compression with the US probe will completely occlude (collapse) patent veins and demonstrate visible pulsatility of arteries. A complete scan of the arm from the antecubital fossa to the subclavian system is recommended to confirm patency. In order to minimize the risk of thrombosis, the largest vessel is cho- sen. [41] There is no consensus on the best vessel for insertion however; the brachial vein is usually the last choice to minimize the risk for arterial puncture. The most commonly cannulated vessel is the basilic vein.

Catheter Selection

A wide choice of PICC kits have become commercially available and include single, double, and triple lumen; trimmable and adjustable length (**Figure 18.28**); regular (3 mL/s) and rapid injection (up to 5 mL/s) flow rates. The number of lumens required should be carefully assessed as it is directly related to complications. [42] The rule of thumb is to choose the largest possible vein and use the smallest catheter. [43]

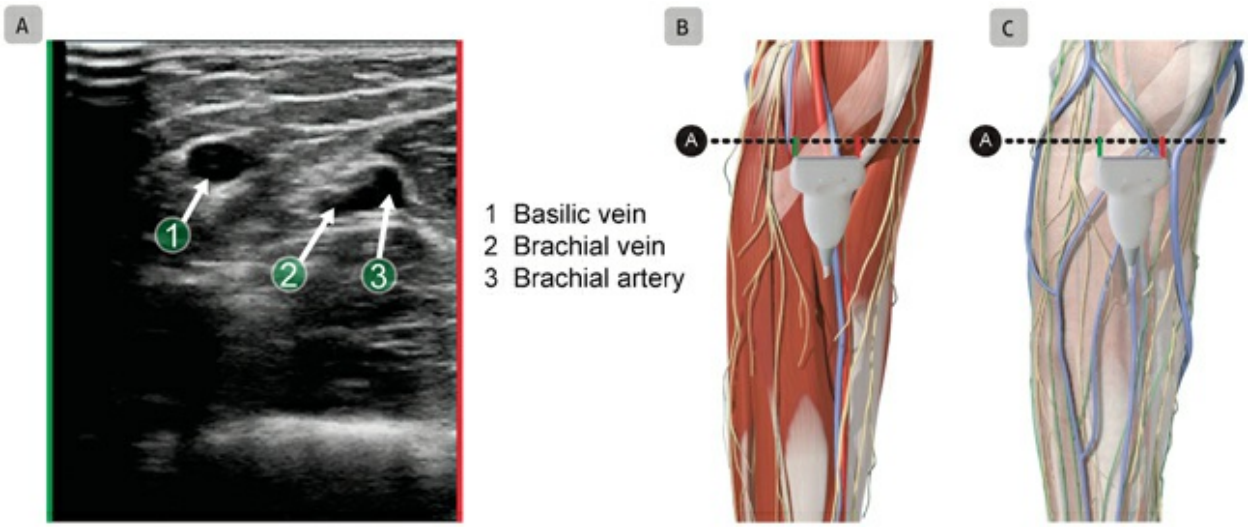

Fig. 18.27 Ultrasound-guided examination of the upper extremity. (A) The upper arm is imaged using a linear ultrasound probe with the marker pointed to the left to match the display. (B,C) Vessels that are shown include the basilic vein, brachial vein, and brachial artery. (Anatomic images with permission of Primal Pictures, Wolters Kluwer Health.)

https://youtu.be/R60Ue0uNWS4

Insertion Technique

Once the best vessel has been identified, the approximate line length is calculated by measuring in stages the distance from the insertion site to the mid portion of the clavicle, from there to the sternal notch and finally to the second intercostal space in the parasternal line (**Figure 18.29**). A tourniquet is placed and the skin prepped in sterile fashion. Maximum sterile barrier and full body draping is used as for any central venous catheterization. The target vein is identified with US and local anesthesia infiltration is performed at the puncture site (**Figure 18.29**). Once the target vein depth has been established a free hand technique or an appropriate wedge needle guide can be used. The Seldinger technique with a soft tip small wire is used to cannulate the vein with a catheter introducer. Once the introducer is in place, the wire is removed and the dilator capped to stop back-bleeding.

Catheter Tip Positioning

Blind insertion is still practiced in many centers as it does not require any specific equipment. The following three maneuvers will minimize the risk of cephalad migration: ipsilateral head rotation, arm extension above the shoulder, and ipsilateral shoulder elevation with a pillow/wedge. The use of US will help confirm the correct tip positioning with agitated saline injection (1 mL air/9 mL of normal saline). Using a linear probe, a second operator can exclude the presence of air bubbles in the unilateral internal jugular vein and visualize opacification of the right atrium or ventricle in the transthoracic subcostal four-chamber view with a phased array probe (**Figure 18.30**).

Different technologies have become available at the bedside to guide catheter advancement and confirm final positioning. They include the use of electromagnetic fields, endovascular Doppler, and electrocardiogram (ECG). Intravascular ECG relies on P-wave analysis (**Figures 18.31 and** 18.32). P-wave increases in amplitude moving closer to the SVC-right atrial (RA) junction and decreases in amplitude to become biphasic as the catheter moves into the RA. This technology is very precise and has eliminated the use of

post positioning routine chest X-rays in many centers. Its main limitation is the requirement of a sinus rhythm. Electromagnetic tracking requires a detector to be placed on the patient's chest (**Figure 18.31**). A special wire is loaded into the catheter and the wire tip will be tracked in three-dimensional space. The wire tip also records intravascular ECG to allow precise catheter positioning. This technology is proprietary and can be integrated into a dedicated US system (BARD Salt Lake City, UT, USA). Intravascular Doppler uses a microcatheter that is loaded into any PICC catheter at the tip (**Figure 18.33**) and will also detect intravascular ECG. When connected, the monitor (Telflex Medical, Triangle Park, NC, USA) will display as a positive deflection flow moving away from the catheter (green arrow) and as a negative deflection flow (red arrow) moving towards the catheter. Advancing the catheter in the direction of the flow will guide correct positioning in the SVC. P-wave analysis will allow precise tip positioning (blue bull's eye) (**Figure 18.33**).

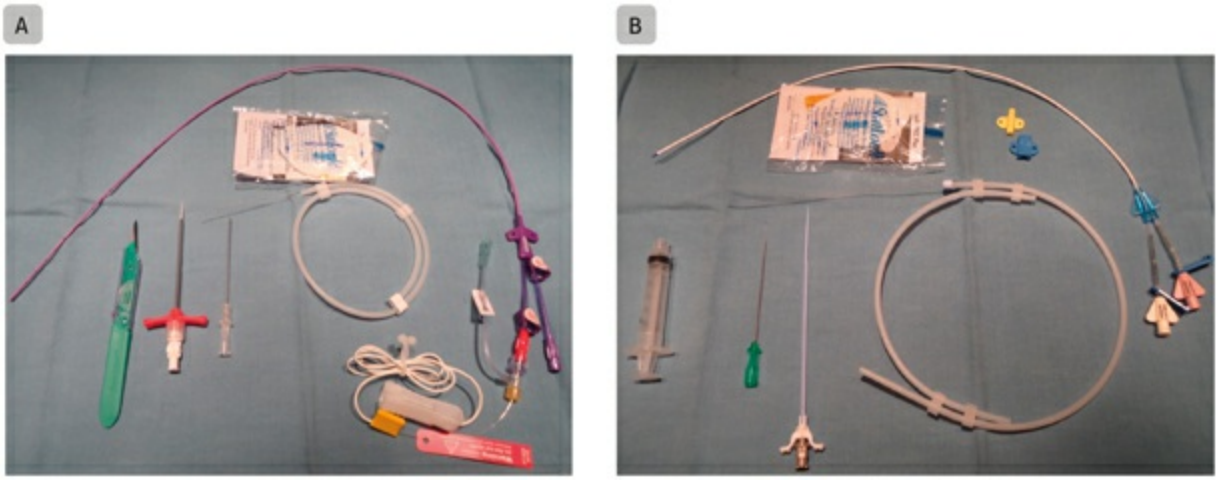

Fig. 18.28 Peripherally inserted central catheter (PICC) kits. (A) Double lumen PICC line kit includes a trimmable catheter (original length 60 cm), needle, microwire, scalpel, introducer, loaded tip tracking wire, and adhesive securing system. (B) Double lumen PICC line kit includes a non-trimmable catheter (50 cm), needle, microwire, introducer, loaded tip tracking wire, and adhesive securing system.

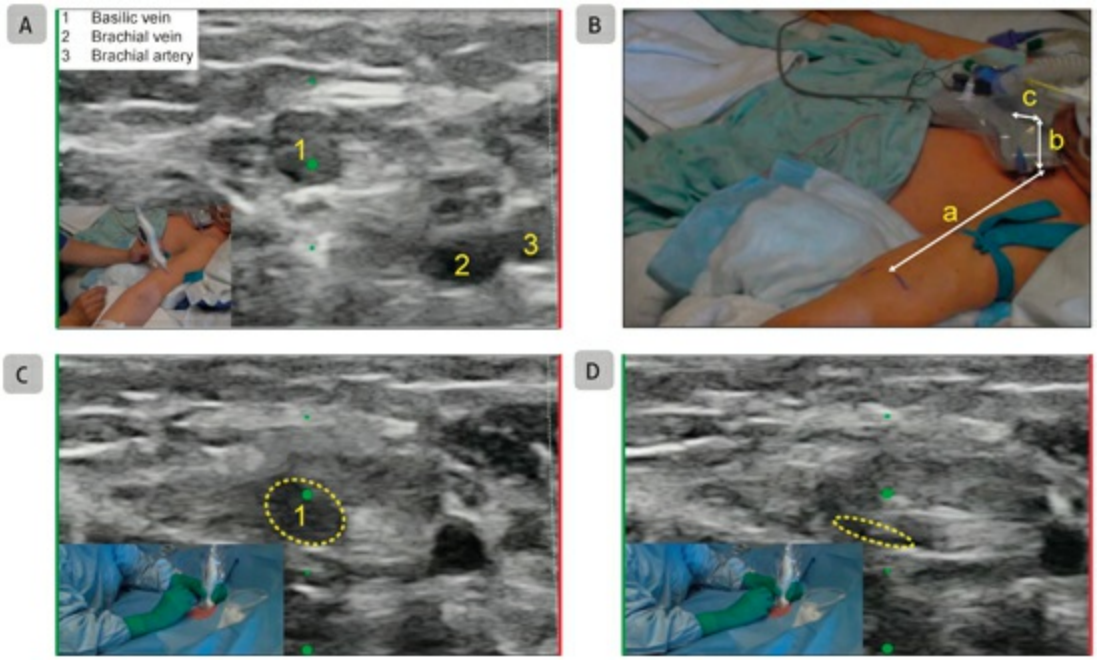

Fig. 18.29 Peripherally inserted central catheter insertion. (A) The upper arm is scanned and the vasculature is identified. (B) The length of catheter insertion is determined by estimating the distance from (a) arm to mid-clavicle, (b) mid-clavicle to sternal notch, and (c) sternal notch to second intercostal space. (C,D) The basilic vein is identified and compressed by the ultrasound probe.

A: https://youtu.be/HieV3TzmRes

D: https://youtu.be/fCEsvHOjzTc

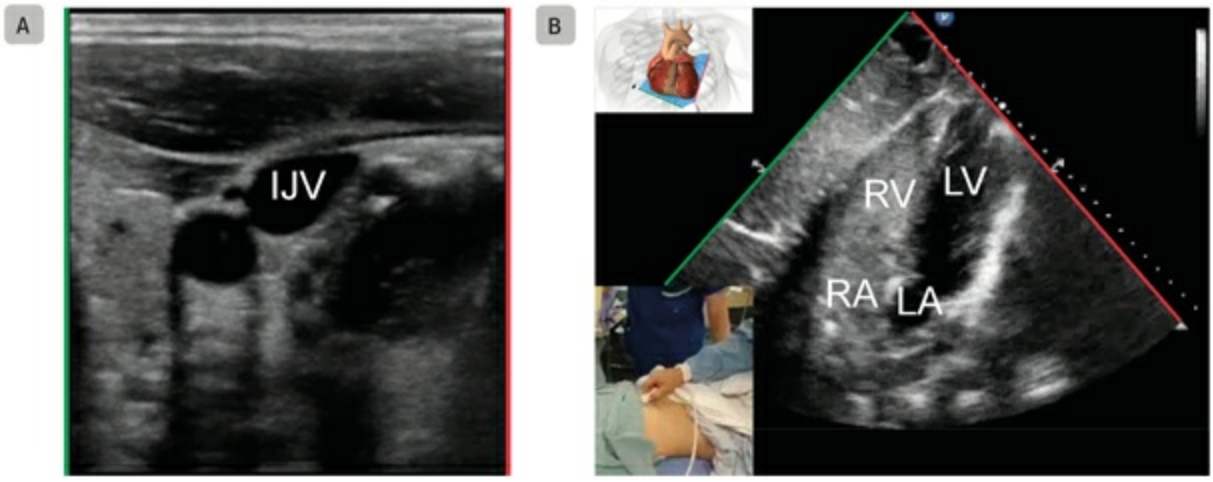

Fig. 18.30 Peripherally inserted central catheter (PICC) position. (A) The internal jugular vein (IJV) is examined by ultrasound to exclude aberrant positioning of the PICC line. (B) Contrast study using a subcostal four-chamber view shows the appearance of contrast in the right atrium (RA) and right ventricle (RV). LA, left atrium; LV, left ventricle.

A: https://youtu.be/_C3s3laEGZY

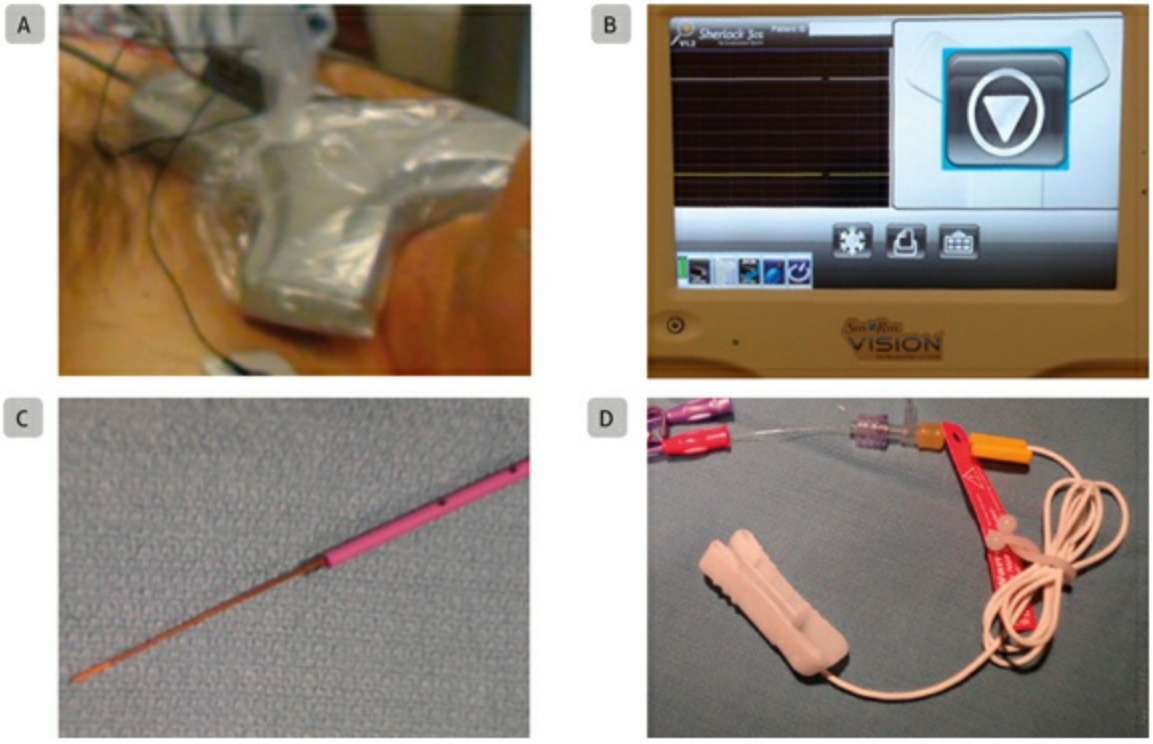

Fig. 18.31 Electromagnetic tip tracking system. The (A) shown for this system.

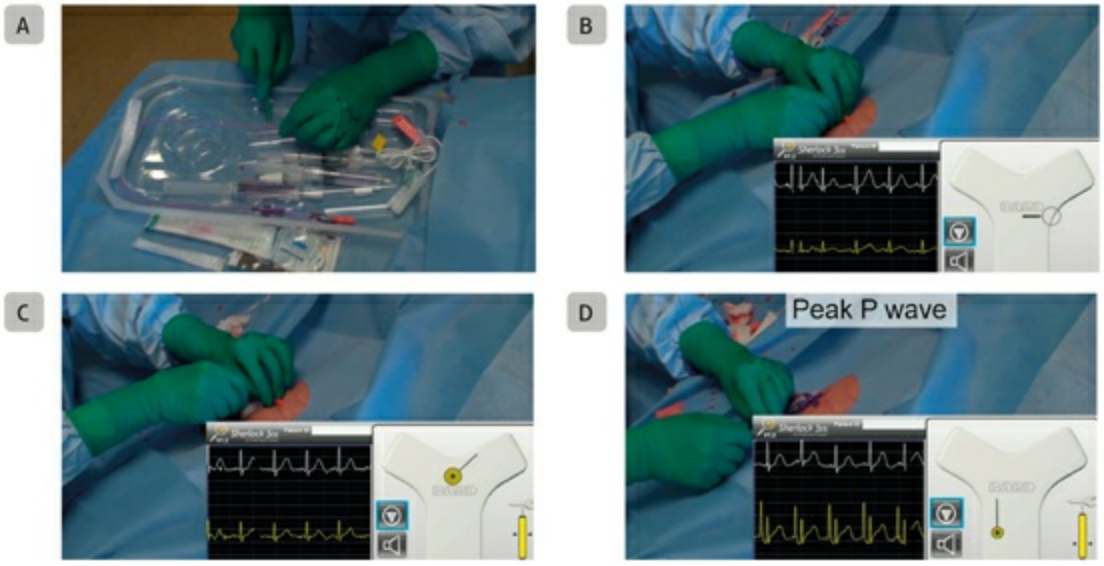

Fig. 18.32 Peripherally inserted central catheter (PICC) insertion. (A—D) Steps in advancing the PICC line catheter using the electromagnetic system are shown. Note that localization of the distal catheter tip is indicated by a change in the P-wave configuration of the electrocardiogram (see text for details).

https://youtu.be/xfTOdbz8brE

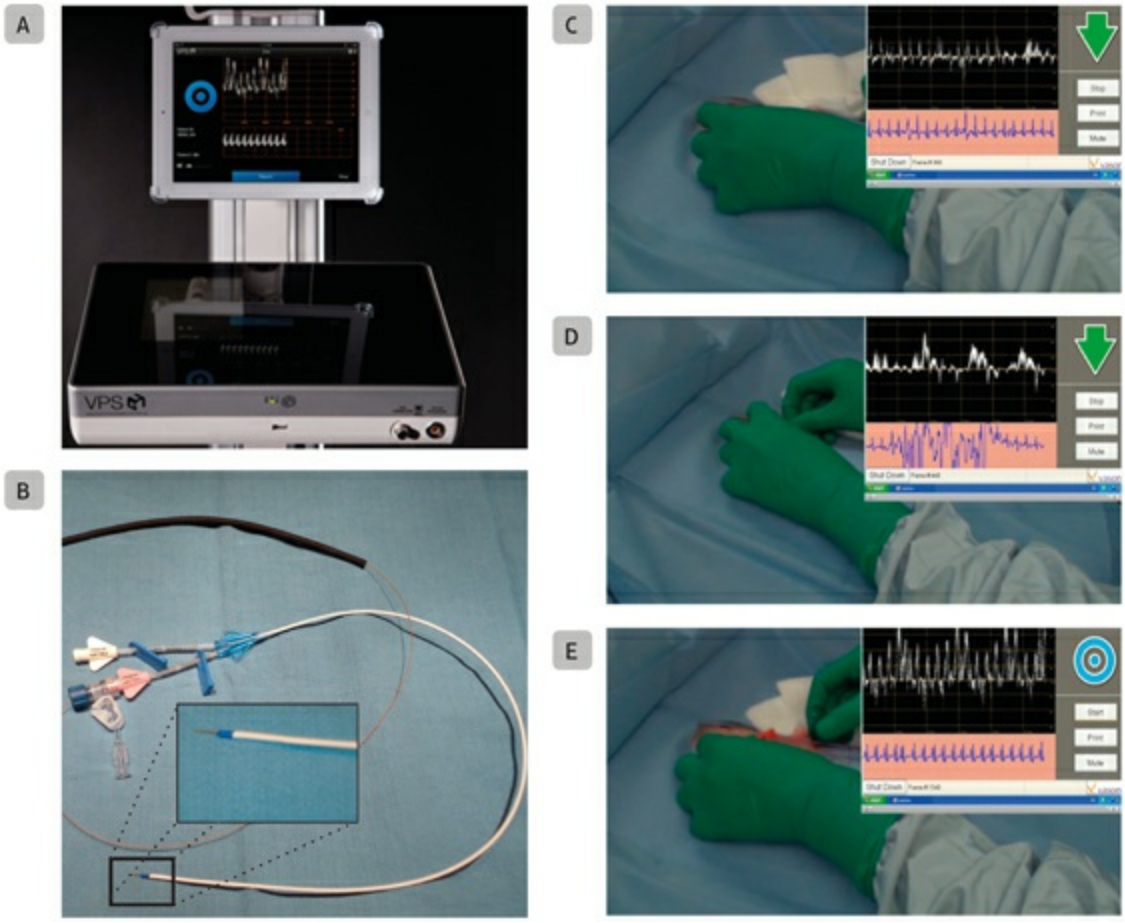

Fig. 18.33 Intravascular Doppler tip tracking system. The (A) monitor and (B) wire tip for the intravascular Doppler tracking Doppler are shown. Note that localization of the distal catheter tip is indicated by an increase in the velocity signal and a target sign (see text for details).

https://youtu.be/UgRpntssVeg

Confirmation of Catheter Tip Position

Optimal PICC tip positioning is considered within 3 cm from the SVC-RA junction. This location has been associated with fewer complication and thrombosis. Chest X-ray remains the gold standard to confirm tip positioning despite its obvious limitations, especially in the ICU setting. The LM for PICC tip positioning is the right RA-SVC angle (**Figure 18.34**). Peripherally inserted central catheter malposition can be due to suboptimal insertion

technique (>50% of blind insertions) or anatomical variance. Common malpositions include (**Figure 18.35**): contralateral subclavian vein, unilateral subclavian vein, unilateral internal jugular vein, azygos vein, and vascular abnormalities, such as left persistent SVC. PICC malposition may result in vessel perforation or early thrombosis and should prompt line removal or repositioning under fluoroscopy.

ARTERIAL VASCULAR ACCESS

Arterial vascular access can be facilitated by US. The technique is similar to venous access with the difference that a transverse view is often sufficient as blood will emerge spontaneously from the needle. The three most common sites for arterial vascular access are the radial, brachial, and femoral arteries.

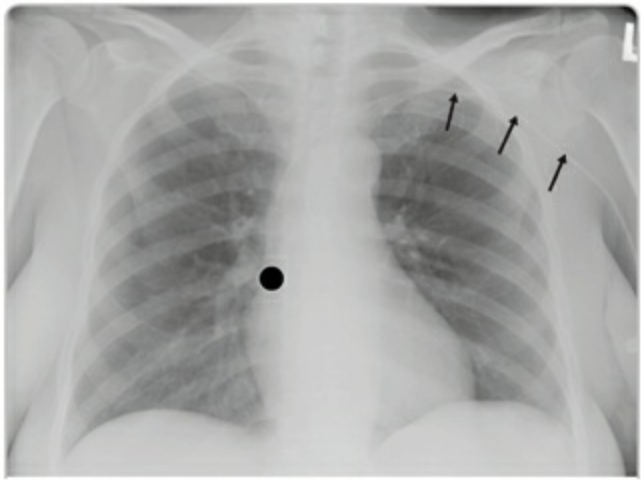

Fig. 18.34 Peripherally inserted central catheter (PICC) position. Left-sided, PICC (black arrows) with tip in distal superior vena cava is shown on chest X-ray. The black dot indicates the ideal PICC tip position.

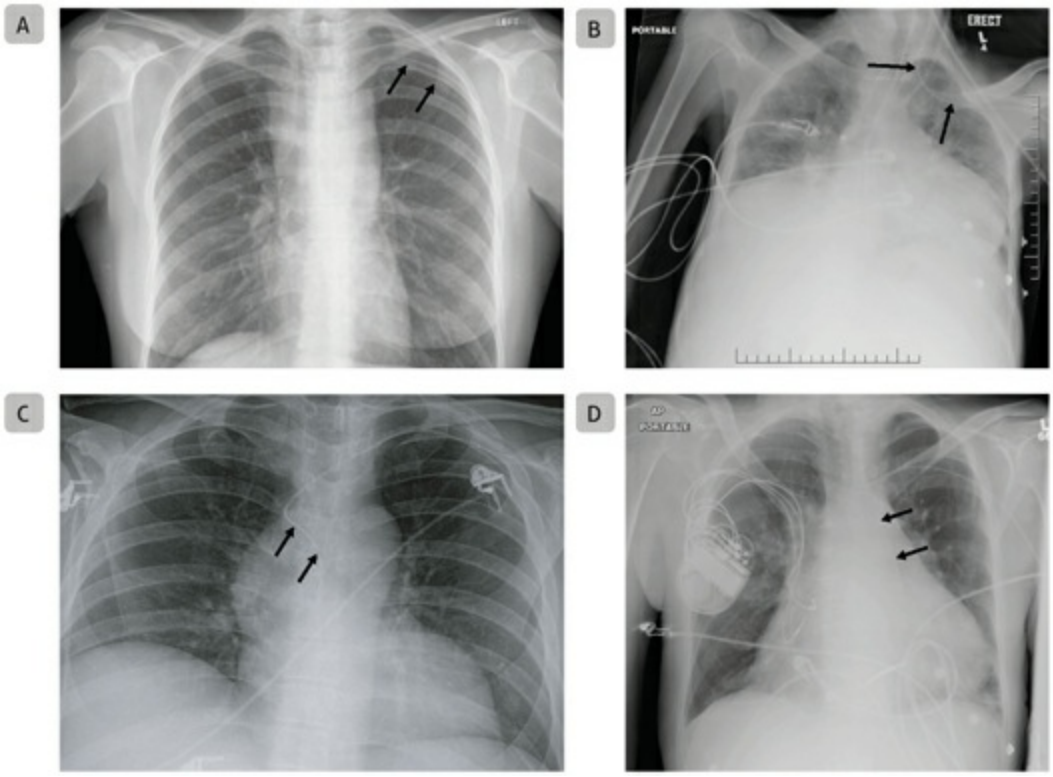

Fig. 18.35 Peripherally inserted central catheter (PICC) malposition. Left sided PICC tip is shown malpositioned on chest X-rays in the (A) left subclavian vein (arrow), (B) left internal jugular vein (arrow), (C) azygos vein with an unusually tortuous S-shaped vessel (arrow), and (D) persistent left superior vena cava (arrow).

Anatomic Considerations

The radial artery originates from the brachial artery medial to the biceps tendon (**Figure 18.36**). It travels in the forearm before it comes to lie anterior to the distal radius where the radial pulse is readily felt. The distal radial artery is positioned lateral to the flexor carpi radialis tendon. It gives branches to the hand and is connected to the median and ulnar arteries.

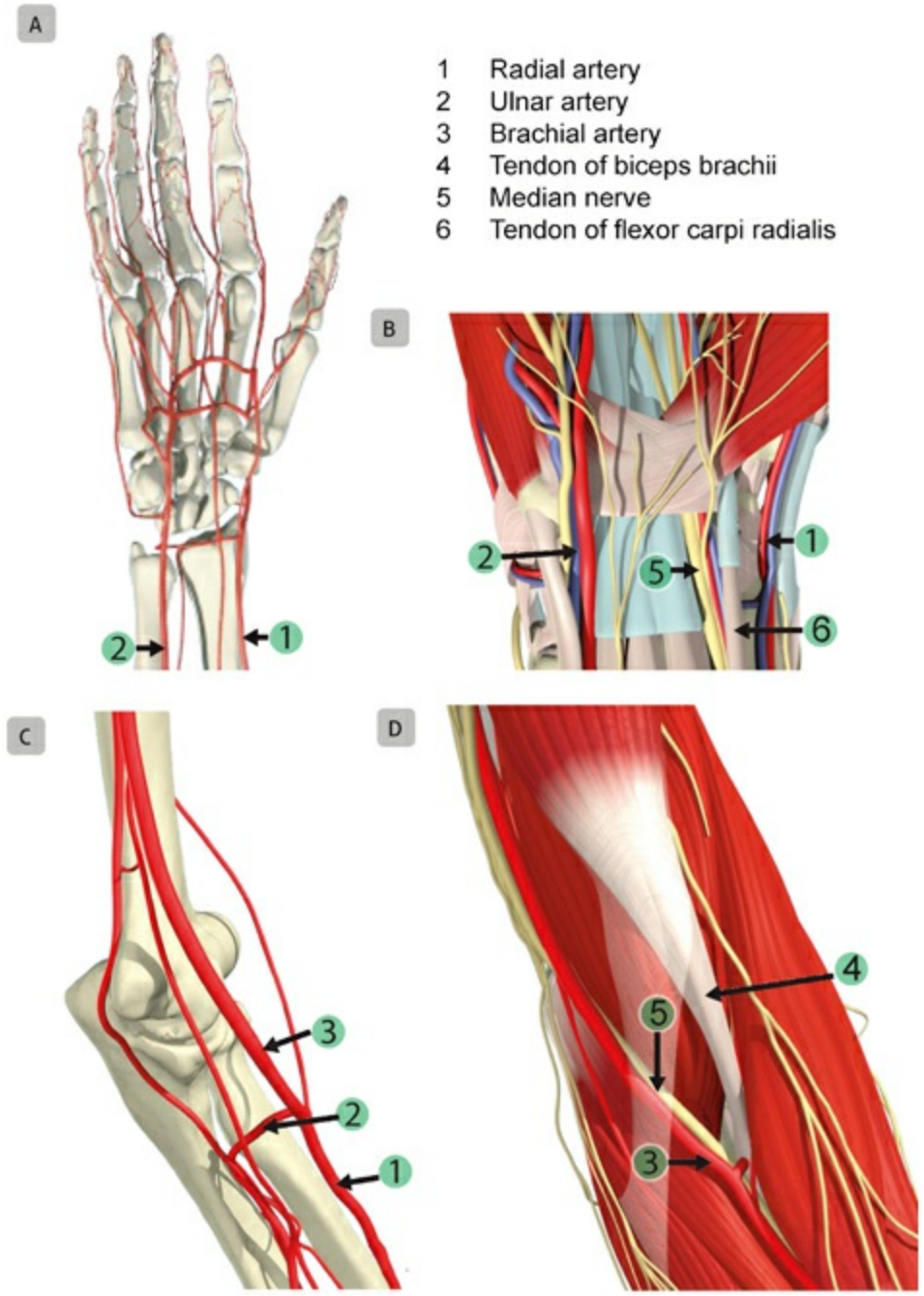

Fig. 18.36 Upper extremity arterial anatomy. Diagrams are presented of the arterial anatomy of the (A,B) radial artery and (C,D) brachial artery. (Anatomic images with permission of Primal Pictures, Wolters Kluwer Health.)

Ultrasound Examination of the Radial Artery

After positioning the wrist with 30-45° extension (**Figure 18.37**) under sterile technique, the radial artery is first examined to determinse dimension and

pulsatility. The imaging depth is reduced to <2 cm and zoomed if necessary. The dimension of the radial artery is a key factor in determining success in vascular access. It is typically 2.2 ± 0.4 mm and smaller in women. [44] When the dimension is <1.5 mm, another site should be considered because the reduced diameter is associated with arterial pressure under-estimation. [45] In an artery of adequate dimension, the catheter is positioned at a 12 o'clock just over the artery. Then, the angulation between the skin and artery is reduced in order to facilitate the insertion of the catheter into the artery. A Seldinger technique can also be used with small guidewires. The approach for the brachial artery is the same, however, it is easier because the diameter is typically larger than the radial artery. Monitoring of upper extremity perfusion is recommended in all patients with radial and brachial arterial access.

Femoral Artery

Anatomical Considerations

Femoral artery anatomy is described in the section on femoral vessels. The common femoral artery is formed by the deep femoral artery and the superficial femoral artery close to the take-off of the great saphenous vein. Once it courses under the inguinal ligament, it becomes the external iliac artery (**Figure 18.38**).

Ultrasound Technique

The use of US for femoral access has been shown to reduce the number of unnecessary attempts [46] particularly in obese patients. [47] In a supine patient both femoral sites are prepared. The femoral artery is first examined with US to determine pulsatility, vascular patency, and the absence of significant plaques or dissection (**Figure 18.39**). If significant anomalies occur, the contralateral site is examined. The US examination may exclude any venous branches anterior to the femoral artery and help identify the bifurcation of the common femoral artery into the deep and superficial arteries. The site of puncture should be just above the point which will be under the inguinal ligament. The technique is the same as for the other arterial vascular access. Monitoring of lower extremity perfusion is recommended in all patients with arterial femoral access. In very obese patients, for both arterial and venous access, abdominal pannus can be retracted by tape or an assistant to expose

the groin or a covered bed pan under the buttocks may elevate the femoral region (**Figure 18.40 A**). In the operating room, a transient supine jackknife position can be helpful (**Figure 18.40 B**).

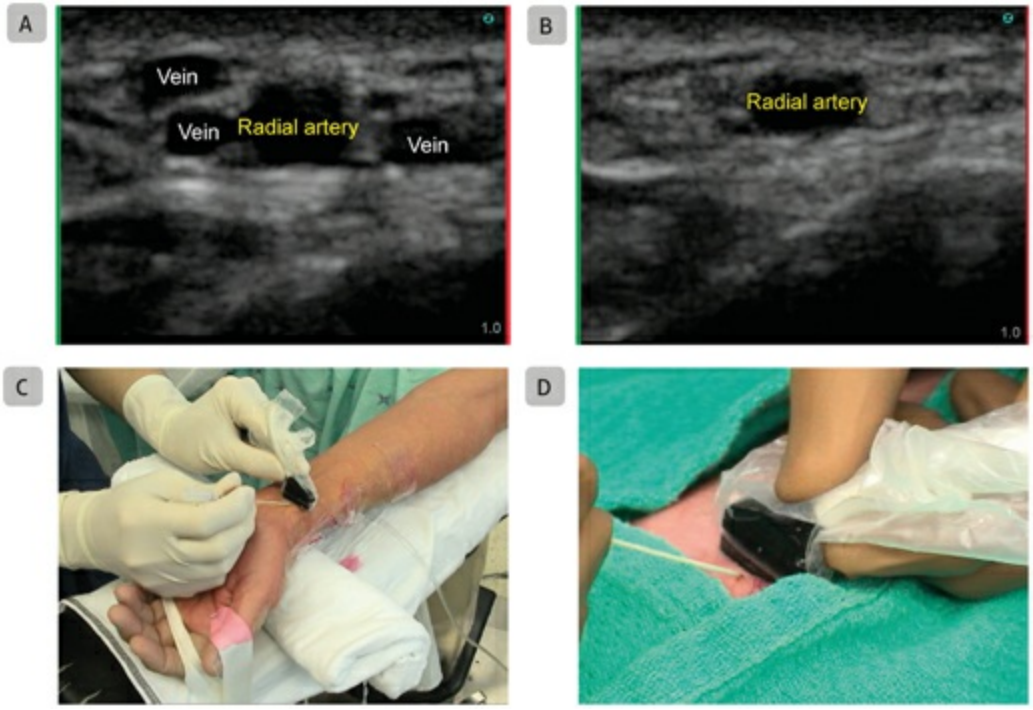

Fig. 18.37 Radial artery. (A,B) Ultrasoundguided examination of the radial artery demonstrates three veins around the radial artery that disappear upon compression. (C,D) Photos show the correct hand position during arterial cannulation with a zoomed view.

A: https://youtu.be/KvaTMKdWExc

D: https://youtu.be/K7fUypbGmtI

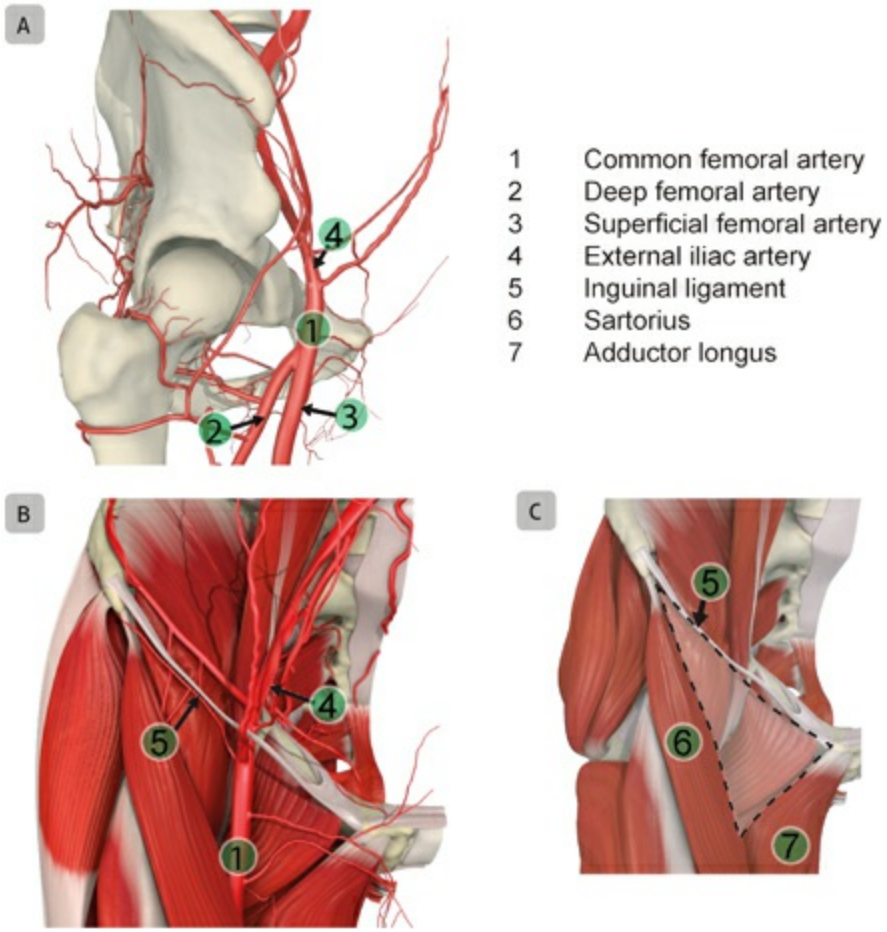

Fig. 18.38 Femoral arterial vascular anatomy. Diagrams are presented of the groin region showing the (A) common femoral artery and (B) relationship to the inguinal ligament, and (C) boundaries of the femoral triangle. (Anatomic images with permission of Primal Pictures, Wolters Kluwer Health.)

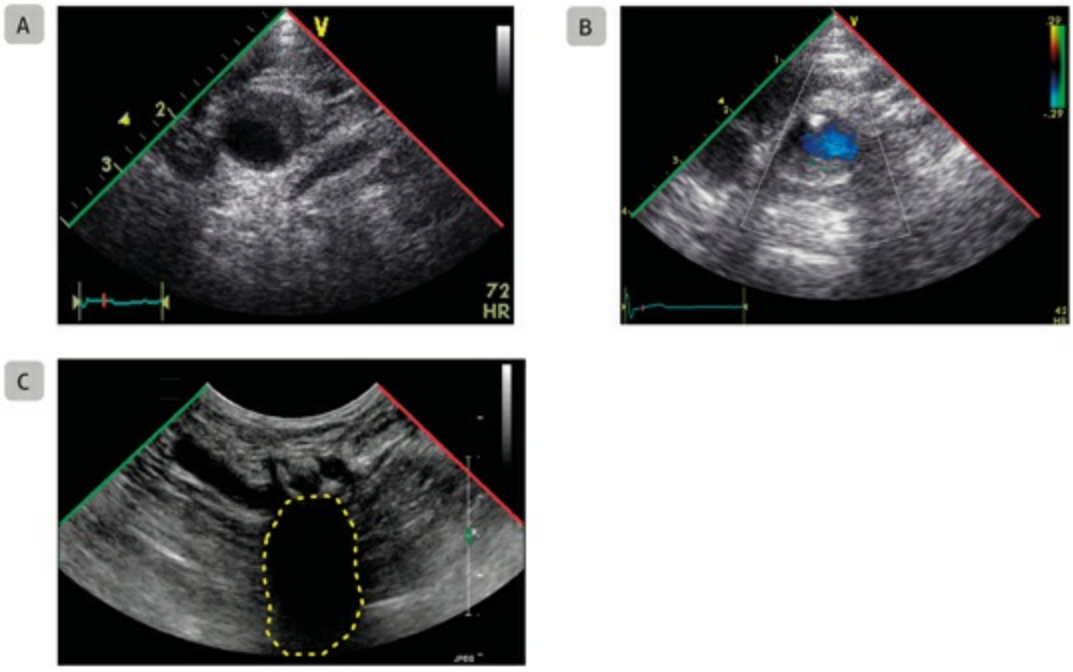

Fig. 18.39 Arterial vascular pathologies. Arterial pathologies are shown including (A) arterial carotid dissection, (B) carotid artery partial occlusion, and (C) severe plaque in the femoral artery. Note the significant acoustic shadowing produced by the calcified femoral vessel (dotted area).

A: https://youtu.be/Am5NN24Jx50

B: https://youtu.be/5OMPF7o85RQ

C: https://youtu.be/NW7y5rvxR9w

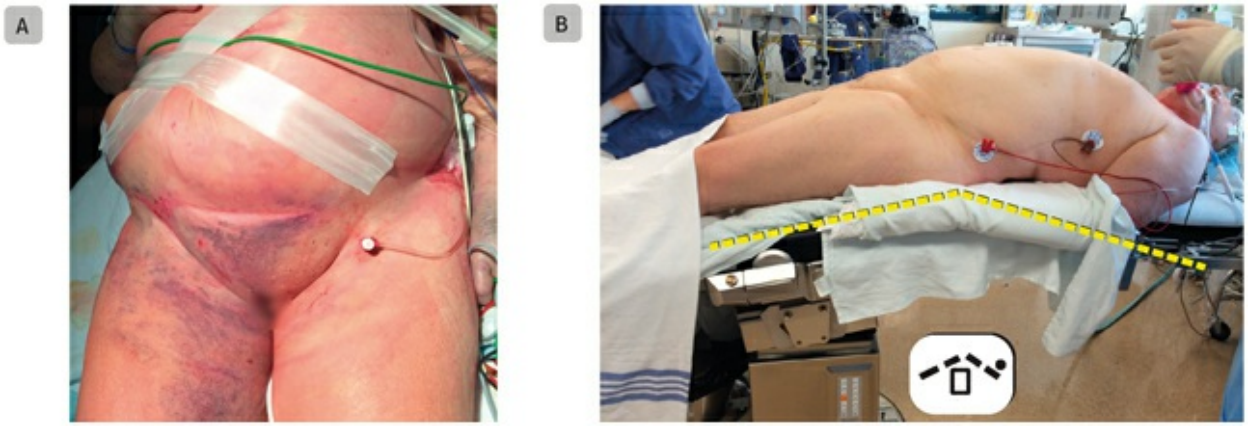

Fig. 18.40 Femoral access. (A) Photo shows the patient position for femoral access in obese patients. (B) Jacknife or flex position in the operating room which facilitate femoral vascular access.

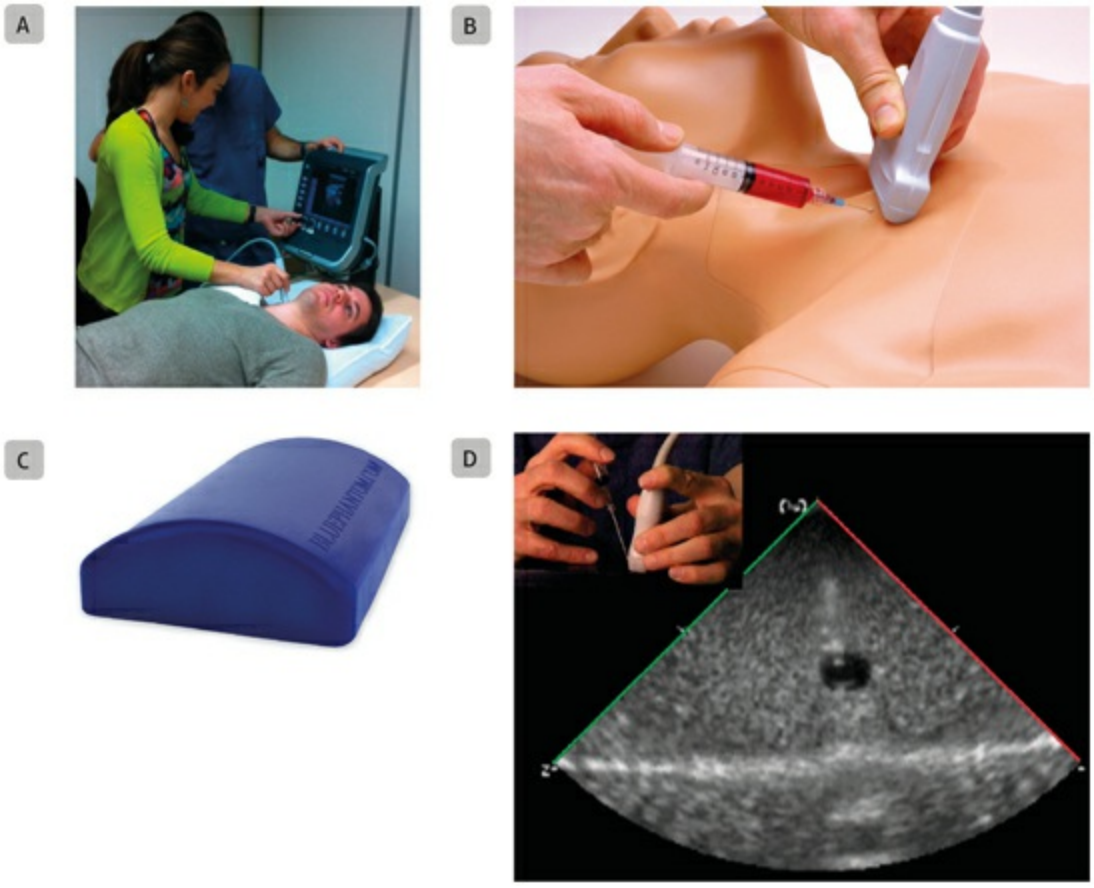

Fig. 18.41 Ultrasound training. Training techniques in teaching ultrasound-guided vascular access include practice with (A) volunteers, peers, or (B) ultrasound phantoms for internal jugular and subclavian venous access and (C,D) basic vascular access.

D: https://youtu.be/etY80wigVjY

D: https://youtu.be/ZOY-9UNZKs8

TEACHING AND TRAINING IN ECHO-GUIDED VASCULAR ACCESS

Several of the authors for this chapter are currently involved in teaching US-guided vascular access and have developed an online course: the ICCU e-learning CAE-Healthcare at the Universite de Montreal (see Chapter 19, Training Guidelines and Simulation). The online course is followed by a half-day practical session where residents and fellows learn anatomy by practicing on themselves and on simulators (**Figure 18.41**). A recent study from the Universite de Montreal has shown that this approach was superior to the traditional learning technique of learning vascular access. [48]

VASCULAR ACCESS RECOMMENDATIONS

After reviewing available scientific evidence from 1990 to 2011, the American Society of Echocardiography and the Society of Cardiovascular Anesthesiologists' guidelines recommended the use of US for the placement of all CVC as a gold standard to improve patient care, especially femoral vein cannulation in children. [7] The scientific evidence for real-time US-guided CVC for the internal jugular vein is category A, level 1; subclavian or axillary vein is category A, level 3; and femoral vein is category C, level 2. For real-time US-guided arterial vascular access, it is category A, level 1 in order to improve first-pass success and for real-time US-Guided peripheral vein cannulation, it is category B, level 2. [7] The American Society of Anesthesiologists has also published detailed practice guidelines [49] for all aspects of vascular access. We recommend their implementation.

REFERENCES

1. McGeeD.C., GouldM.K.. Preventing complications of central venous catheterization. *N Engl J Med*2003; *348*: 1123–33.
2. MaeckenT., GrauT.. Ultrasound imaging in vascular access. *Crit Care Med*2007; *35* (5 Suppl.): S178–85.
3. SeldingerS.I.. Catheter replacement of the needle in percutaneous arteriography; a new technique. *Acta Radiol*1953; *39*: 368–76.
4. UllmanJ.I., StoeltingR.K.. Internal jugular vein location with the ultrasound Doppler blood flow detector. *Anesth Analg*1978; *57*: 118.
5. American College of Emergency Physicians. Use of ultrasound imaging by emergency physicians. *Ann Emerg Med*2001; *38*: 469–70.
6. RothschildJ.M.. Ultrasound guidance of central vein catheterization. Making health care safer: A critical analysis of patient safety practices: Agency for Healthcare Research and Quality, 2010. Available from: http://www.ahrq.gov/clinic/ptsafety/chap21.htm.
7. TroianosC.A., HartmanG.S., GlasK.E., SkubasN.J., EberhardtR.T., WalkerJ.D.*et al*. Guidelines for performing ultrasound guided vascular cannulation: recommendations of the American Society of Echocardiography and the Society of Cardiovascular Anesthesiologists. *J Am Soc Echocardiogr*2011; *24*: 1291–318.
8. DenaultA.Y., CoutureP., VegasA., BuithieuJ., TardifJ.C.. *Transesophageal echocardiography multimedia manual, second edition: A perioperative transdisciplinary approach*. New York: Informa Healthcare, 2011.
9. BlaivasM., BrannamL., FernandezE.. Short-axis versus long- axis approaches for teaching ultrasound-guided vascular access on a new inanimate model. *Acad Emerg Med*2003; *10*: 1307–11.
10. StoneM.B., MoonC., SutijonoD., BlaivasM.. Needle tip visualization during ultrasound-guided vascular access: Short-axis vs long-axis approach. *Am J Emerg Med*2010; *28*: 343–7.
11. AyoubC., LavalleeC., DenaultA.. Ultrasound guidance for internal jugular vein cannulation: Continuing Professional Development. *Can J Anesth*2010; *57*: 500–14.
12. GordonA.C., SalikenJ.C., JohnsD., OwenR., GrayR.R.. US-guided puncture of the internal jugular vein: complications and anatomic considerations. *J Vasc Interv Radiol*. 1998; *9*: 333–8.
13. SulekC.A., GravensteinN., BlackshearR.H., WeissL.. Head rotation during internal jugular vein cannulation and the risk of carotid artery puncture. *Anesth Analg*1996; *82*: 125–8.
14. LichtensteinD., SaifiR., AugardeR., PrinS., SchmittJ.M., PageB.*et al*. The internal jugular veins are asymmetric. Usefulness of ultrasound before catheterization. *Intensive Care Med*2001; *27*: 301–5.
15. Samy ModeliarS., SevestreM.A., de CagnyB., SlamaM.. Ultrasound evaluation of central veins in the intensive care unit: Effects of dynamic manoeuvres. *Intensive Care Med*2008; *34*: 333–8.
16. NetterF.H.. *Atlas of human anatomy Summit*, N.J.: CIBA-GEIGY Corp., 1989.
17. DaileyR.H.. Femoral vein cannulation: A review. *J Emerg Med*1985; *2*: 367–72.
18. HiltyW.M., HudsonP.A., LevittM.A., HallJ.B.. Real-time ultrasound- guided femoral vein catheterization during cardiopulmonary resuscitation. *Ann Emerg Med*1997; *29*: 331–6.
19. DenysB.G., UretskyB.F.. Anatomical variations of internal jugular vein location: Impact on central venous access. *Crit Care Med*1991; *19*: 1516–9.
20. HopkinsJ.W., WarkentineF., GracelyE., KimI.K.. The anatomic relationship between the common femoral artery and common femoral vein in frog leg position versus straight leg position in pediatric patients. *Acad Emerg Med*2009; *16*: 579–84.

21. HughesP., ScottC., BodenhamA.. Ultrasonography of the femoral vessels in the groin: Implications for vascular access. *Anaesthesia*2000; *55*: 1198–202.
22. WarkentineF.H., Clyde PierceM., LorenzD., KimI.K.. The anatomic relationship of femoral vein to femoral artery in euvolemic pediatric patients by ultrasonography: Implications for pediatric femoral central venous access. *Acad Emerg Med*2008; *15*: 426–30.
23. LechnerG., JantschH., WaneckR., KretschmerG.. The relationship between the common femoral artery, the inguinal crease, and the inguinal ligament: A guide to accurate angiographic puncture. *Cardiovasc Intervent Radiol*1988; *11*: 165–9.
24. BhatiaN., SivaprakasamJ., AllfordM., GuruswamyV.. The relative position of femoral artery and vein in children under general anesthesia - an ultrasound-guided observational study. *PaediatrAnaesth*2014; *24*: 1164–8.
25. RileyW., FitzgeraldD., CohnL.. Single, percutaneous, femoral venous cannulation for cardiopulmonary bypass. *Perfusion*2007; *22*: 211–5.
26. WeinerM.M., GeldardP., MittnachtA.J.. Ultrasound-guided vascular access: A comprehensive review. *J Cardiothorac Vasc Anesth*2013; *27*: 345–60.
27. AouadM.T., KanaziG.E., AbdallahF.W., MoukaddemF.H., TurbayM.J., ObeidM.Y.*et al*. Femoral vein cannulation performed by residents: A comparison between ultrasound-guided and landmark technique in infants and children undergoing cardiac surgery. *Anesth Analg*2010; *111*: 724–8.
28. OguzkurtL., TercanF., KaraG., TorunD., KizilkilicO., YildirimT.. US-guided placement of temporary internal jugular vein catheters: Immediate technical success and complications in normal and high-risk patients. *EurJ Radiol*2005; *55*: 125–9.
29. KarakitsosD., LabropoulosN., De GrootE., PatrianakosA.P., KouraklisG., PoularasJ., et al. Real-time ultrasound-guided catheterisation of the internal jugular vein: A prospective comparison with the landmark technique in critical care patients. *Crit Care*2006; *10*: R162.
30. FragouM., GravvanisA., DimitriouV., PapaloisA., KouraklisG., KarabinisA.*et al*. Real-time ultrasound-guided subclavian vein cannulation versus the landmark method in critical care patients: A prospective randomized study. *Crit Care Med*2011; *39*: 1607–12.
31. LaluM.M., FayadA., AhmedO., BrysonG.L., FergussonD.A., BarronC.C.*et al*. Ultrasound-guided subclavian vein catheterization: A systematic review and meta-analysis. *Crit Care Med*2015; *43*: 1498–507.
32. RabindranathK.S., KumarE., ShailR., VauxE.. Use of real-time ultrasound guidance for the placement of hemodialysis catheters: A systematic review and meta-analysis of randomized controlled trials. *Am J Kidney Dis*2011; *58*: 96470.
33. AltinR.S., FlickerS., NaidechH.J.. Pseudoaneurysm and arteriovenous fistula after femoral artery catheterization: Association with low femoral punctures. *AJR Am J Roentgenol*1989; *152*: 629–31.
34. KolluriR., FowlerB., NandishS.. Vascular access complications: Diagnosis and management. *Curr Treat Options Cardiovasc Med*2013; *15*: 173–87.
35. Moraza-DulantoM.I., Garate-EcheniqueL., Miranda-SerranoE., Armenteros-YeguasV., Tomas-LopezM.A., Benitez-DelgadoB.. [Ultrasound-guided peripherally inserted central catheters (PICC) in cancer patients: Success of the insertion, survival and complications] *Enferm Clin*2012; *22*: 135–43.
36. TejedorS.C., TongD., SteinJ., PayneC., DresslerD., XueW.*et al*. Temporary central venous catheter utilization patterns in a large tertiary care center: Tracking the “idle central venous catheter”. *Infect Control Hosp Epidemiol*2012; *33*: 50–7.
37. AlexandrouE., SpencerT.R., FrostS.A., MifflinN., DavidsonP.M., HillmanK.M.. Central venous catheter placement by advanced practice nurses demonstrates low procedural complication and infection rates - and infection rates–a report from 13 years of service*. *Crit Care Med*2014; *42*: 536–43.

38. PrandoniP.. Peripherally inserted catheters: All that glitters is not gold. *Lancet*2013; *382*: 288–90.
39. MermelL.A., AllonM., BouzaE., CravenD.E., FlynnP., O'GradyN.P.*et al*. Clinical practice guidelines for the diagnosis and management of intravascular catheter-related infection: 2009 update by the Infectious Diseases Society of America. *Clin Infect Dis*2009; *49*: 1–45.
40. ChopraV., AnandS., HicknerA., BuistM., RogersM.A., SaintS.*et al*. Risk of venous thromboembolism associated with peripherally inserted central catheters: A systematic review and meta-analysis. *Lancet*2013; *382*: 311–25.
41. EvansR.S., SharpJ.H., LinfordL.H., LloydJ.F., WollerS.C., StevensS.M.*et al*. Reduction of peripherally inserted central catheter- associated DVT. *Chest*2013; *143*: 627–33.
42. O'BrienJ., PaquetF., LindsayR., ValentiD.. Insertion of PICCs with minimum number of lumens reduces complications and costs. *J Am Coll Radiol*2013; *10*: 864–8.
43. NifongT.P., McDevittT.J.. The effect of catheter to vein ratio on blood flow rates in a simulated model of peripherally inserted central venous catheters. *Chest*2011; *140*: 48–53.
44. AshrafT., PanhwarZ., HabibS., MemonM.A., ShamsiF., ArifJ.. Size of radial and ulnar artery in local population. *J Pak Med Assoc*2010; *60*: 817–9.
45. DenaultA., DeschampsA.. Abnormal aortic-to-radial arterial pressure gradients resulting in misdiagnosis of hemodynamic instability. *Can J Anesth*2009; *56*: 534–6.
46. GedikogluM., OguzkurtL., GurS., AndicC., SariturkC., OzkanU.. Comparison of ultrasound guidance with the traditional palpation and fluoroscopy method for the common femoral artery puncture. *Catheter Cardiovasc Interv*2013; *82*: 118792.
47. ZaremskiL., QuesadaR., KovacsM., SchernthanerM., UthoffH.. Prospective comparison of palpation versus ultrasound- guided radial access for cardiac catheterization. *J Invasive Cardiol*2013; *25*: 538–42.
48. BeaulieuY., LapriseR., DroletP., ThiviergeR.L., SerriK., AlbertM., et al. Bedside ultrasound training using web-based e-learning and simulation early in the curriculum of residents. *Crit Ultrasound J*2015; *7*: 1.
49. RuppS.M., ApfelbaumJ.L., BlittC., CaplanR.A., ConnisR.T., DominoK.B.*et al*. Practice guidelines for central venous access: A report by the American Society of Anesthesiologists Task Force on Central Venous Access. *Anesthesiology*2012; *116*: 539–73.

Chapter 19

Training Guidelines and Simulation

Han Kim and Feroze Mahmood

INTRODUCTION

A number of medical societies have produced guidelines for the training of perioperative echocardiography over recent years, with revisions to accommodate current clinical and educational practice. Transthoracic echocardiography (TTE) was the subject of initial practice guidelines, but this was soon followed by transesophageal echocardiography (TEE) practice guidelines published in 1996 by the American Society of Anesthesiologists and the Society of Cardiovascular Anesthesiologists (ASA/SCA), [1] then further revised in 2010 [2] and 2013. [3] Canadian guidelines for perioperative echocardiography training, published in 2005 by the Canadian Cardiovascular Society (CCS) and the Canadian Society of Echocardiography (CSE), described a training path for TEE that required an advanced level of TTE proficiency before permitting independent TEE practice. [4] While applicable to cardiology trainees, this was deemed to be impractical for anesthesiologists performing intraoperative TEE. This led to the development in 2006 of Canadian guidelines by the Cardiovascular Section of the Canadian Anesthesiologists' Society and the CSE that were specific to intraoperative TEE practice. [5] Revised CCS/CSE guidelines, published in 2010, reflect the increased use of echocardiography as a powerful tool in a growing number of specialties. [6] This chapter reviews current guidelines for training in echocardiography and the educational options to acquire the necessary knowledge and technical skills.

TEE TRAINING GUIDELINES

Guidelines for the practice of perioperative TEE provide a national consensus for the training in adult perioperative TEE. This ensures safety and quality standards are upheld, crossing country-wide, regional and specialty-based practice variations.

The Canadian guidelines for perioperative TEE exhibit some key differences compared to those published by the ASA/SCA. First of all, the number of studies required differs for the levels of TEE proficiency; for the basic level it is 100 studies (50 by the ASE/SCA) and for the advanced level 200 studies (150 by the ASE/SCA) (**Table 19.1**). There is also a greater emphasis on perioperative imaging in the

Canadian guidelines, with the required number of TEE studies performed extended to include those completed outside the operating room. Furthermore, additional views describing the identification of pulmonary veins and both atrial appendages are outlined in the Canadian guidelines to supplement the 20 standard views advocated in the ASE/ SCA comprehensive TEE examination. [7] Those views (a total of 28) are now part of the updated ASE/SCA guidelines. [3] The basic level in the ASE/SCA guidelines limits the physician to monitoring, while the more rigorous standards of the Canadian guidelines also allow a basic echocardiographer a limited diagnostic role.

The Canadian guidelines outline three levels of proficiency, labeled as basic, advanced, or director level of expertise. Each level is associated with a minimum number of examinations performed, duration of training, continuing medical education (CME) hours, and success at a particular National Board of Echocardiography (NBE) examination that is linked to the desired level of proficiency (**Table 19.1**).

Basic Level

This level describes a trainee who has the ability to use perioperative TEE, with a minimum of 11 ASE/SCA views, [8] as a monitoring tool with limited diagnosis of hemodynamic derangements. These diagnoses may relate to changes in preload, systolic or diastolic dysfunction, ischemia, or simple valvular dysfunction. They may also assist in the echocardiographic guidance of common device placements, such as coronary sinus catheters or intra-aortic balloon pumps. There is the understanding that the basic echocardiographer possesses the ability to recognize when more advanced

consultation is required, particularly where it may affect surgical decision-making, such as in the evaluation of advanced valvular lesions. The time commitment for the basic level involves a 3-month fellowship in perioperative TEE with a minimum of 150 complete examinations, of which at least 100 are personally performed. Transthoracic echocardiography examinations may count towards those exams personally performed. Another 50 hours of CME credits related to perioperative TEE must also be obtained, of which 25 must be accredited. These requirements for time and number of examinations must be completed within 1 year.

Advanced Level

Advanced level expertise allows diagnosis in advanced pathology, especially when it may involve changes in surgical decision-making. The full adult TEE examination has been mastered, and these represent consultants in the perioperative use of TEE for all indications. This level also allows training of other physicians who wish to also achieve advanced proficiency. The advanced level requires 6 months in a cardiac anesthesia or echocardiography fellowship, and a testimonial letter from the perioperative TEE service director attesting to the acquisition of the appropriate technical skills. The minimum number of examinations includes 300 complete examinations in a variety of cases, of which 200 must be comprehensive TEE exams personally performed and interpreted with supervision. As for the basic level, 50 CME credits relevant to the practice of perioperative TEE must be acquired. If these requirements are completed in conjunction with clinical practice, they may be completed within 2 years.

Director Level

This level comprises the total expertise required to lead a perioperative echocardiography service. Not only does the technical and clinical knowledge need to be advanced in all echocardiography topics, the individual would additionally require a thorough knowledge of the administrative aspects of running a perioperative TEE service. This involves management of resources such as personnel, equipment, and facilities, as well as ensuring quality control of all clinical activity performed. Adding to the expertise gained at the advanced level, a director level candidate must train for a further 3 months in perioperative TEE in a maximum period of 2 years.

Reflecting this increased length of time, 450 examinations must have been interpreted, with 300 being personally performed, interpreted, and reported. At this level, 100 hours of CME credits must be accumulated over 4 years, of which 50 are accredited.

Table 19.1 Canadian Guidelines for Training in Perioperative TEE (2006)

	Basic	Advanced[a]	Director[b]
Minimum No. of examinations[c]	150	300	450
Minimum No. of TEE[d]	100	200	300
Duration of training (months)	3	6	9
PTE examination	Yes	Yes	Yes
CME hours (accredited CME hours)[e]	50 (25)	50 (25)	100 (50)
MOC: CME hours (accredited CME hours)[f]	50 (25)	50 (25)	100 (50)
MOC: minimum No. of TEE per year	50	50	75

Notes:

a Total for basic training may be counted toward advanced training.

b Program director qualification includes an advanced level of training in perioperative echocardiography and an additional 150 complete echocardiographic examination including at least 100 comprehensive perioperative TEE examinations. The trainee should also have completed a total of 100 hours of CME including 50 hours of accredited CME.

c Complete echocardiographic examinations interpreted by the trainee under appropriate s upervision. May include transthoracic studies recorded by qualified individuals other than the trainee.

d Comprehensive perioperative TEE examinations personally performed, interpreted, and reported by the trainee under appropriate supervision.

e CME hours to achieve either a basic or an advanced level should be completed within a 2-year period. The CME hours required for a director level should be completed within a 4-year period.

f CME hours for MOC at the basic, advanced, or director level should be completed within a 4-year period.

CME, continuous medical education; MOC, maintenance of competence; PTE, perioperative transesophageal echocardiography; TEE, transesophageal echocardiography.

(Reproduced with permission from Denault *et a/.* [9])

Maintenance of Certification

A certain number of examinations per year are expected to maintain the skill and expertise gained by achieving each level. The Canadian guidelines

propose 50 comprehensive examinations performed, interpreted, and reported each year for both basic and advanced levels to maintain competency. At the director level, 75 must be reviewed with 50 of these being personally performed. To keep abreast of new indications and modalities, a minimum of 50 hours of CME (including 25 accredited) are required for basic and advanced with 75 hours (37.5 accredited) for director level (**Table 19.1**).

EXAMINATION FOR PERIOPERATIVE TEE

All three levels of expertise described by the Canadian guidelines require successful completion of the level-appropriate perioperative TEE examination (PTEeXAM) offered by the NBE. This is in contrast to the ASE/SCA guidelines that do not require this step. Eligibility requirements for both examinations include a valid medical license or good standing in an ACGME-accredited program with a confirmatory notarized letter from the program director. The exams are computer based and administered at local designated test centers in North America. Both exams include blocks of multiple-choice questions followed by a block of case-oriented questions based on echocardiography videos. Each block is independent, allowing review of all questions in the given block within the allotted time, but it is not permitted to return to the questions in the previous block once it is completed.

Table 19.2 Basic and Advanced PTEeXAM Content Outline

Basic	Advanced
Patient safety considerations	Principles of ultrasound
Echocardiographic imaging: Acquisition and optimization	Transducers
Normal cardiac anatomy and imaging plane correlation	Imaging
Global ventricular function	Principles of Doppler ultrasound
Regional ventricular systolic function and recognition of pathology	Doppler flow profiles for normal and abnormal physiology
Basic recognition of cardiac valve abnormalities	Quantitative echocardiography
Identification of intracardiac masses in non-cardiac surgery	Artifacts and pitfalls of imaging
Basic perioperative hemodynamic assessment	Equipment, infection control, and safety
Related diagnostic modalities	Normal anatomy and flow during the complete examination
Basic recognition of congenital heart disease in the adult	Myocardial ischemia and segmental ventricular function
Surface ultrasound for vascular access	Ventricular function and hemodynamics
	Recognizing intracavitary contents
	Echocardiographic manifestations of congenital heart disease in adult patients
	Hypertrophic obstructive cardiomyopathy
	Dilated and restricted cardiomyopathies
	Echocardiography for the pericardium and extracardiac anatomy
	Echocardiography during cardiac surgery
	Assessing heart valves during the perioperative period
	Indications for transesophageal echocardiography
	Non-TEE imaging and other diagnostic modalities

Notes: TEE, transesophageal echocardiography.

The scope of the basic PTEeXAM describes a perioperative TEE examination limited to non-diagnostic monitoring in the regular clinical practice of anesthesia. Any study that may require diagnostic skill or surgical intervention must be confirmed with an advanced examiner or by an alternative imaging modality. The advanced PTEeXAM expects the applicant to have the capability to fully diagnose cardiac pathology and provide guidance in situations where surgical management may be altered by echocardiographic findings. The content guideline for the basic and advanced PTEeXAM is listed in **Table 19.2**. Testamur status is granted once either exam is passed and implies a special competence in the basic or advanced PTEeXAM and allows further application for certification.

CERTIFICATION FOR PERIOPERATIVE TEE

Although the guidelines outline the expected standards of care for each level

of echocardiograpic expertise, it does not imply either credentialing or certification. Perioperative TEE and TTE certification for anesthesiologists in North America is a process governed by the NBE. Another form of certification for critical care physicians interested primarily in focused surface echocardiography is a 2-day course offered by the American College of Chest Physicians (ACCP). However, whether these certifications are absolutely required for the practice of clinical echocardiography by a given practitioner is variable and hospital-based.

NBE Certification

Certification at the basic and advanced levels are offered by the NBE contingent on PTEeXAM completion, as well as specific requirements for Training length and number of examinations at each level. [10] There are three pathways to reach certification: the supervised training pathway, practice experience pathway, and extended CME pathway. While the supervised training pathway is the common route for those training straight out of their residency programs into fellowship, the practice experience pathway is meant for those who have been grandfathered into the system from before the advent of the certification process. The pathway for each level requires different numbers of examinations reviewed, performed, and reported independently. A log of these examinations must be kept to verify the number, but also to demonstrate a broad range of indications and pathology through the course of training. The details for basic and advanced PTE board certification are presented in **Table 19.3**.

Table 19.3 NBE Certification Guidelines

	Basic	Advanced
Supervised training pathway	150 examinations reviewed under supervision 50 personally performed and supervised ACGME-accredited program Completed in 4 years	300 examinations reviewed under supervision 150 personally performed ACGME training program or Canadian program of 1-year duration after 5-year residency Completed in 2 years or less
Practice experience pathway	150 examinations performed and interpreted in 4 years No less than 25 in any year At least 40 CME hours Not offered to those finishing anesthesiology residency after 30 June 2016	300 examinations performed and interpreted in 4 years No less than 50 in any year At least 50 CME hours Not offered to those finishing fellowship training after June 30, 2009
Extended CME pathway	50 examinations performed and interpreted in two of the three preceding years Successful completion of the ASA/SCA Basic Perioperative TEE Education Program within 2 years of application[a]	Not available

Notes: ACGME, Accreditation Council for Graduate Medical Education; ASA, American Society of Anesthesiologists; CME, continuous medical education; NBE, National Board of Echocardiography; SCA, Society of Cardiovascular Anesthesiologists.

[a] https://education.asahq.org/tee. (Adapted from http://www.echoboards.org.)

ACCP Certification

For acute-care specialties such as critical care, emergency medicine, and trauma, the use of focused TTE and bedside ultrasound (US) for non-cardiac, life-threatening conditions, particularly lung applications, has grown exponen- tially. [11] – [16] This has created a great demand for training of these highly useful skills in trainees and established practitioners. However, there is currently no standard for training of this modality by the Royal College of Canada. Guidelines from the Canadian Critical Care Society have been published in 2014 regarding recommendations for critical care US training and competency. [17] They are based on four steps: initial training, portfolio building, competency assessment, and quality assurance and maintenance of competence (**Table 19.4**). The core critical US examination includes basic critical care echocardiography (five views), lung and pleural US, US guidance of vascular access and identification of free abdominal fluid. The optional portion includes examination of the kidney for hydronephrosis, abdominal aorta to exclude aneurysm, and the diagnosis of deep vein

thrombosis. These guidelines were inspired from the ACCP who has been offering certification for critical care ultrasonography since 2011. Through their Certificate of Completion Program, advanced expertise in the topic of critical care ultrasonography is offered by completion of a series of requirements to gain expertise. This is accomplished by a series of four learning modules and courses that include the following:

1. Completion of the CAE online learning module for pulmonary and critical care ultrasonography. These are e-learning tutorials designed to review the essentials of critical care US.
2. Attend the ultrasonography Essentials in Critical Care workshop to practice image acquisition on human models and review normal and pathologic images.
3. Attend the Focused Thoracic and Vascular US workshop, reviewing the use of thoracic and vascular ultrasonography in applications specific to critical care patients.
4. Attend the Critical Care Echocardiography workshop, which further integrates echocardiography with critical care applications.

Following these four learning modules, an online portfolio must be created for review by ACCP faculty. Feedback and evaluation will occur through 102 video clips uploaded to the portfolio as outlined below, as well as beginning a candidate's teaching file. The 102 images fall into a number of categories encompassing cardiac, lung/pleural, abdominal, and vascular (**Table 19.5**). After these components have been completed, the final requirement is to pass a comprehensive assessment examination at the CHEST annual meeting.

Table 19.4 Canadian Critical Care Society Critical Care Ultrasound Training and Competency Guidelines

1. Introductory Training
Didactic and hands on training (*suggested 10 hours for each CCE and GCCUS*)
Curriculum based on ACCP consensus document
2. Portfolio Completion
Supervised studies in core exam types with feedback
Suggested number of studies (will vary by individual) Basic critical care echo 30 studies Lung and pleura 20 studies Guidance of vascular access 10 studies Abdominal free fluid 10 studies
3. Competency Assessment
Synchronous with portfolio completion
Local expert may administer final competency evaluation
4. Quality Assurance (QA) and Maintenance of Competence
Locally driven QA mechanisms
Continuing medical education

Notes: ACCP, American College of Chest Physicians; CCE, critical care echocardiography; GCCUS, general critical care ultrasound.

(Adapted from Arntfield *et al*.[17])

ONLINE ECHOCARDIOGRAPHY LEARNING MODULES

The advancement of web-based technology and the ease of access of online resources have led to a growth in teaching resources available on the internet. These range from didactic video lectures to complex interactive learning modules. The ability to review these resources in their own time before exposure to a time-limited proctored learning experience allows trainees the most efficient use of resource-intensive training sessions with real patients or with experienced staff.

Toronto General Hospital Virtual TTE and TEE Modules

Much of the difficulty associated with the learning curve in trainees of echocardiography is the ability to mentally recreate a 3D structure from a series of 2D images. A high fidelity echocardiography simulator provides the optimal way to master this mental manipulation. An inexpensive alternative is to virtually manipulate cardiac models through an online module. In a

learning module created by the Department of Anesthesia and Pain Management at the Toronto General Hospital in Toronto, Ontario, Canada, this type of interface is offered online or through an iPad application. These TTE (pie.med.utoronto.ca/TTE) and TEE (pie.med.utoronto.ca/TEE) modules are based on a static digital 3D heart model built on cardiac computerized tomographic (CT) images, allowing rotation around a horizontal or vertical axis. The heart model is displayed with the corresponding real echocardiography video image and a flow chart linking the 20 standard views together in a logical workflow (**Figure 19.1**). This freely available resource on the internet was shown in a brief study to improve trainees' knowledge of navigation between the 20 standard TEE views. [18]a further refinement has been the development of an online TEE simulator (pie.med.utoronto.ca/) that allows the manipulation of the TEE probe to show infinite TEE images of a static heart. Various slider bars allow changes in depth, rotation, and angle, as well as including a dropdown menu to go to each of the 20 standard TEE views.

Table 19.5 Views Required for ACCP Certification

Study	View
Cardiac study (10 studies per view)	Parasternal long-axis view
	Parasternal short-axis view
	Apical four-chamber view
	Subcostal long-axis view
	Inferior vena cava longitudinal view
Lung/pleural study (4 studies per view)	Pleural effusion (any size)
	Sliding lung
	Consolidation
Abdominal study (4 studies per view)	Left kidney longitudinal view with splenorenal space
	Right kidney longitudinal view with hepatorenal recess
	Abdominal aorta longitudinal view
	Bladder transverse view
Vascular diagnostic DVT study (3 studies per view, include both legs, with compression)	Right common femoral vein
	Left common femoral vein
	Right common femoral vein at saphenous intake
	Left common femoral vein at saphenous intake
	Right superficial femoral vein
	Left superficial femoral vein
	Right popliteal vein
	Left popliteal vein

Notes: ACCP, American College of Chest Physicians; DVT, deep vein thrombosis.

http://www.chestnet.org/Education/Advanced-Clinical-Training/Certificate-of-Completion-Program/Critical-Care-Ultrasonography

CT2TEE

Initially started as a scientific project in 2009, CT2TEE (http://www.ct2tee.agh.edu.pl) has grown in popularity as an interactive method to teach echocardiography through an online module. Developed by Aleksander Kempny, MD (University Hospital of Munster, Munster, Germany) and Adam Piorkowki, PhD (AGH University of Science and

Technology, Krakow, Poland), it provides a series of CT images which can be manipulated in a virtual 3D space to create the representative TEE views (**Figure 19.2**). Various slider bars allow changes in depth, rotation, and angle, as well as including a drop-down menu to go to one of the 20 standard TEE views. Although the images displayed are actual CT planes, they are comparable to the associated echocardiography images in any given plane. It is freely accessible online, and the developers have expressed interest in further expanding their software to include 3D representations, cardiac motion from functional CTs, and pathology. There are plans to develop a virtual model with a physical mannequin and TEE probe, but the online version will continue as a free resource.

CAE Healthcare Innovative Critical Care Ultrasound

This web-based interactive multimedia curriculum spans the essential topics of bedside US and TEE in the form of e-learning tutorials, using 3D animations and video lectures (https:// http://www.caeiccu.com/lms). These topics range from acquisition of the basic views, use of advanced modalities such as Doppler, M-mode, and harmonic, to the diagnosis of pathology (**Figure 19.3**). There are also lectures on vascular access, as well as lung US for critical care physicians, which are part of the ACCP mandatory courses. While free trials are available, these lectures come with a cost, although group rates can be acquired for institutions. The course is CME accredited, and provides an organized way to progress through the curriculum. Each module offers a pre- and post-test to assess knowledge gained, as well as a global test at the end of each category of topics. This ensures systematic progress through the essential components, and helps identify areas where more guidance may be required. In a larger curriculum, it also allows supervisor administrative features at a higher level to monitor progress through modules and test scores obtained by each trainee to help guide progress.

Ultrasound Education Group: HeartWeb

In Australia, the University of Melbourne has developed a series of online courses and workshops on bedside US at both basic and advanced levels (http://www.heartweb.com.au/). These courses can lead to a Graduate Certificate, Diploma or Master in clinical US (**Figure 19.4**). Courses are also

available as professional development programs through the Society of Cardiovascular Anesthesiologists as the On-CUE program, and the Basic Perioperative TEE CME program through the ASA and SCA. A sample package of the level 1 course can be downloaded from http://www.heartweb.com/samples.

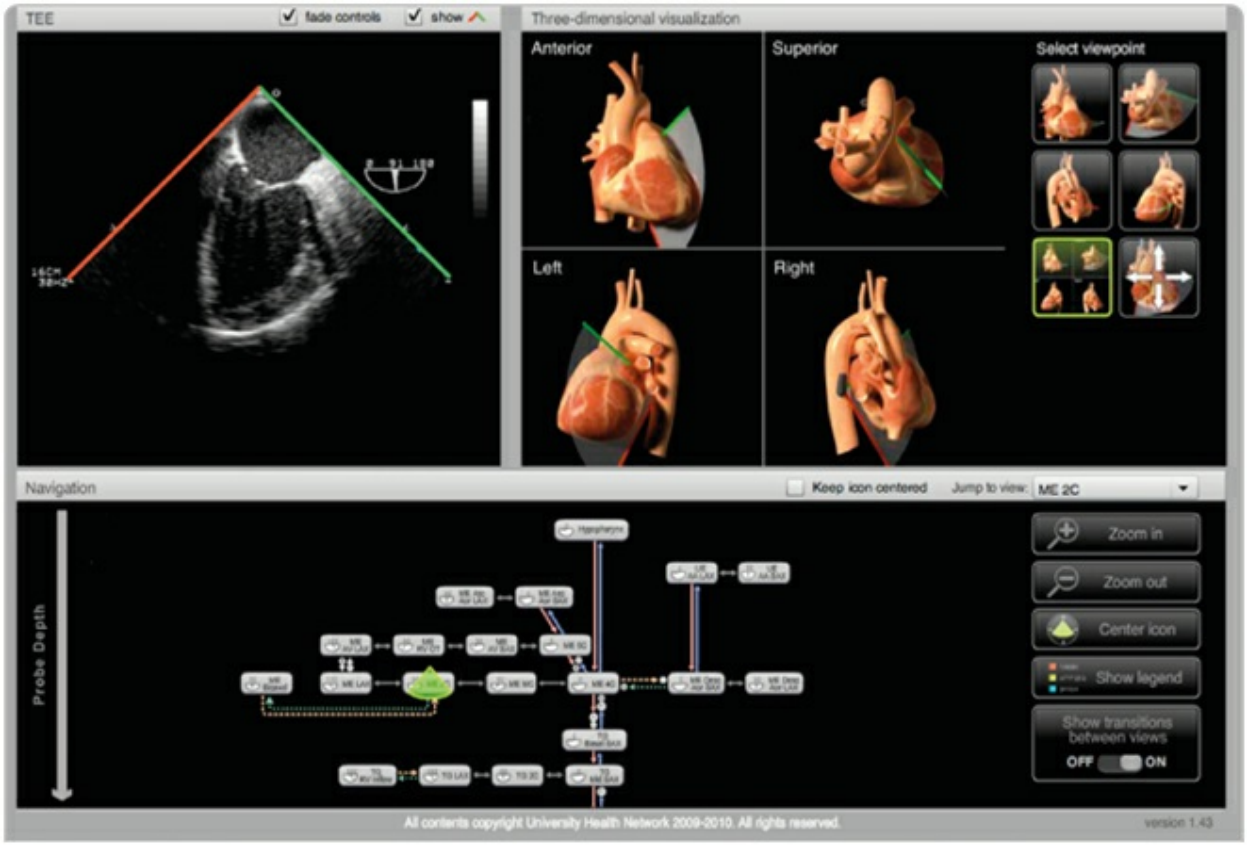

Fig. 19.1 Visual Interactive Resource for Teaching, Understanding And Learning (VIRTUAL) transesophageal echocardiography (TEE) online simulator created by Toronto General Hospital, showing the ultrasound image, a static 3D heart model, and a flowchart of the relationship between the standard TEE views (pie.med.utoronto.ca/TEE/TEE_content/TEE_virtualTEE.html).

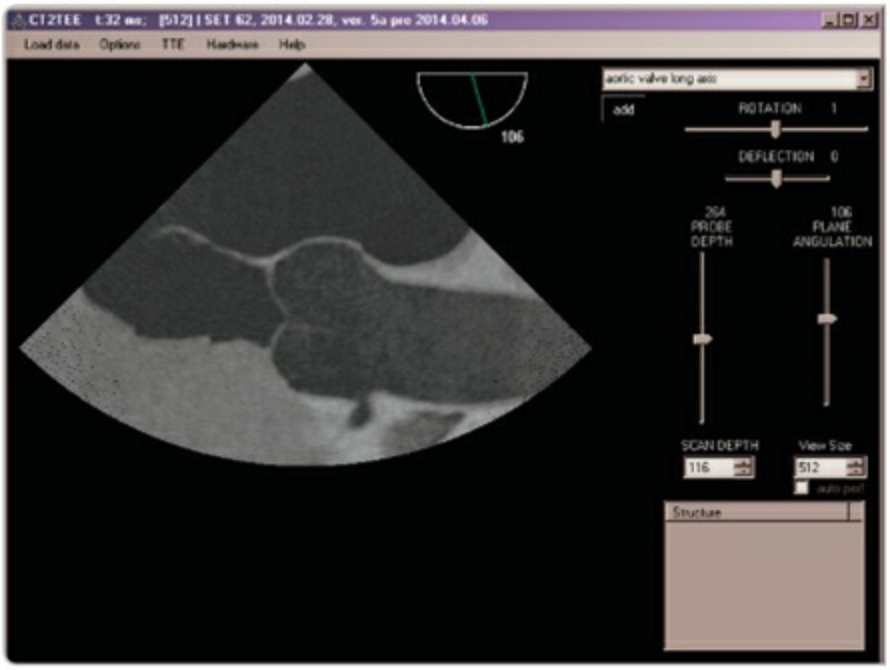

Fig. 19.2 CT2TEE module. This is an online module (http://www.ct2tee.agh. edu.pl) created from computed tomographic (CT) images with the ability to manipulate a transesophageal echocardiography (TEE) probe. All movements of a TEE probe can be simulated with changes in the CT representation of the ultrasound image portrayed on the left.

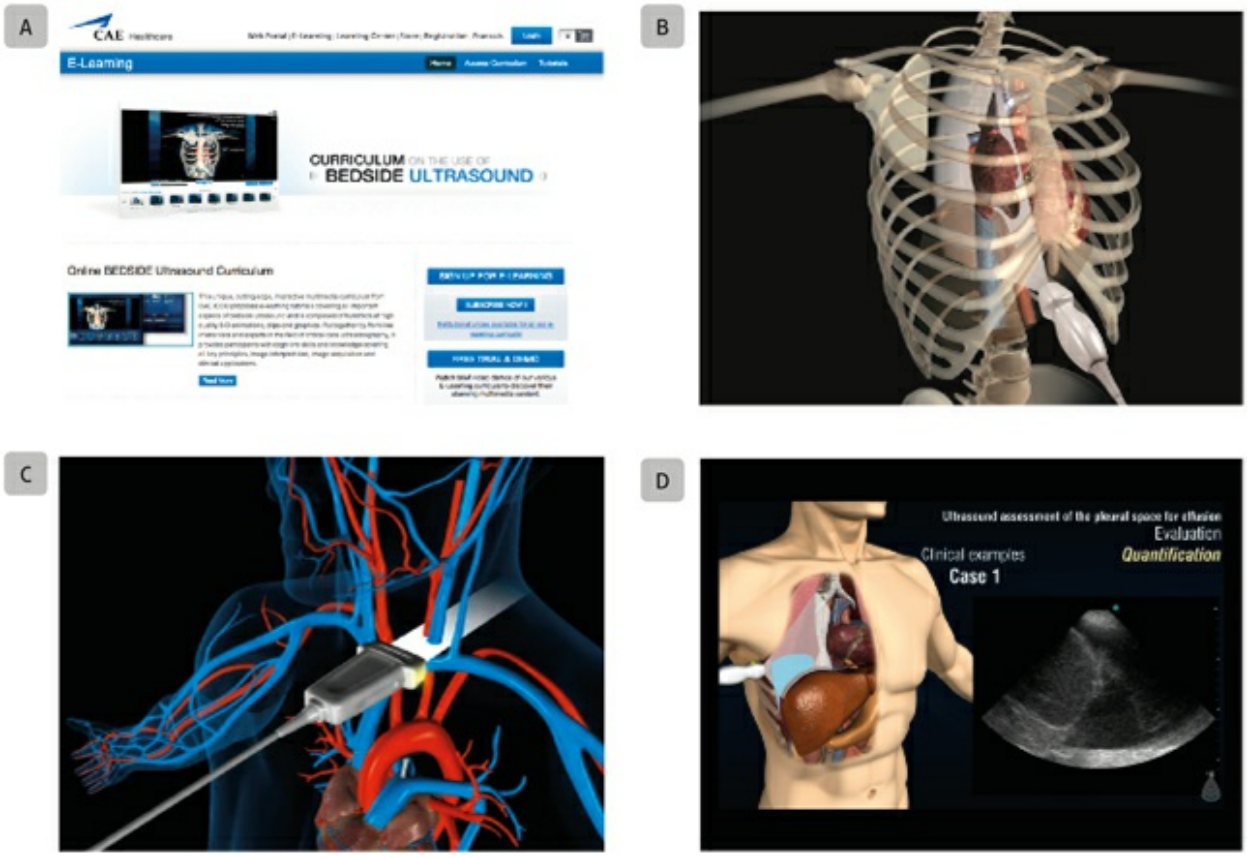

Fig. 19.3 CAE ICCU E-Learning. (A) This website provides a number of online learning curricula, each with its own set of interactive modules. (B) Focused cardiac transthoracic echocardiography (TTE), transesophageal echocardiography (TEE), (C) central and peripheral vascular access, and (D) lung ultrasound are the curricula offered from this portal. (Courtesy of CAE Healthcare, Montreal, Canada). CAE, Canadian Aviation Electronics; ICCU, Imaging Curriculum in Critical Care Ultrasound.

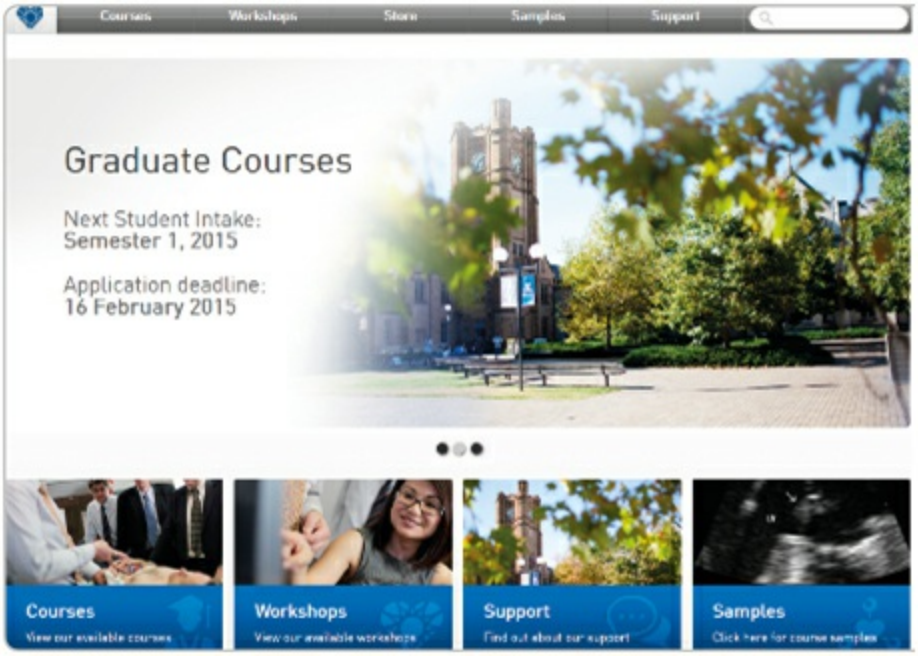

Fig. 19.4 HeartWeb. This website (http://www.heartweb.com.au/) aims to provide an educational package for practitioners that includes the detailed knowledge required to become competent at clinical ultrasound and echocardiography.

ECHOCARDIOGRAPHY SIMULATORS

Effective training in TEE requires two components: background knowledge of cardiac anatomy, physiology, and pathology, as well as proficiency in technical skills for image acquisition. These dual requirements challenge the efficient teaching of TEE. Much of the limitation comes from acquiring the technical skills, as traditionally this component has been learned on real patients. However, learning in this environment is often time-limited by the small number of patients examined, the need to rapidly gain clinically useful information before the cardiopulmonary bypass period, and interference by cautery from the surgery. This model of training also requires the supervision of an expert in TEE, who may be few in number and also limited in time, as they are often also in charge of administrating the anesthetic. With these brief exposures to TEE and with the added pressures of clinical decision-making, there may be a lengthy learning period to develop efficacy in image acquisition.

Simulation has long been used for the acquisition of technical skills. Technological advancements have developed high-fidelity echocardiography

simulators that accurately portray the mental and manual manipulations required for image acquisition in TTE and TEE. This allows a student to intuitively link the change in the US plane based on movements of the probe. As no patient is involved, these complex skills can be learned without the pressure of time or risk to the patient, and with the reduced need for an experienced instructor. Many recent studies have shown the validity of simulation as an effective tool to teach echocardiography. [19] – [23] There are a number of echocardiography simulators available with different specificities and limitations as described below.

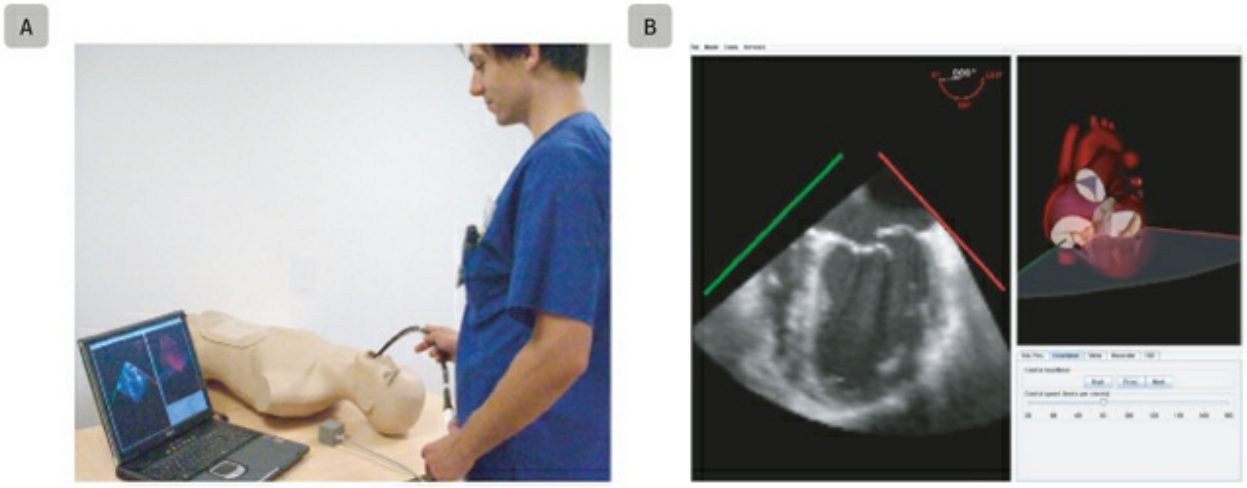

Fig. 19.5 EchoComTEE simulator. (A) This transesophageal echocardiography (TEE) simulator consists of a mannequin, TEE probe with sensor on the tip, a computer running software to display the computer tomography (CT) created images and a heart model. (B) An augmented view on the left of the screen is created from apical rotational views with 3D reconstruction. The panel in the bottom right allows manipulation of the heart rate, and settings related to the views, such as superimposed views of the cardiac structures outside the image plane.

EchoCom

EchoComTEE deserves mention as it was the first augmented reality simulator used for the training of TEE. [24] Created in Germany, it was started as the prototype of a research project and was never made commercially available. Subsequently, a TTE model was also developed using the same principle, as well as a neonatal model for TTE. This simulator consists of a mannequin placed within an electromagnetic field (**Figure 19.5**). Placement of the replica TEE probe with the same mechanical movements as a regular TEE probe transmits signals to a standard computer via a digital tracking system placed at the probe tip. Echocardiographic datasets previously

captured from 3D reconstruction software by apical rotational scans can be manipulated through augmented reality by movement of the probe. Probe movements are transferred to the computer where the image plane is calculated and the appropriate plane from the data set displayed (**Figure 19.5**). One limitation of this simulator is that as the images were created from apical rotational views, upper esophageal views or the descending aorta cannot be seen. Also, no adult pathology is included. Interestingly, congenital defects can be portrayed in the neonatal TTE model.

HeartWorks

Created by Inventive Medical (London, UK), the HeartWorks echocardiography simulator uses a dynamic 3D augmented reality model of an anatomically correct heart that can be manipulated by both TTE and TEE probes on a mannequin. The workstation consists of either a desktop computer or a laptop, showing the augmented reality US plane beside the actual 3D heart model (**Figure 19.6**). The heart model can also be manipulated separately from the probe by use of a mouse and keyboard. Pathologies have been released, including hypovolemia, global left ventricular impairment, anterior hypokinesis, aortic stenosis, mitral stenosis, and mitral regurgitation. Color Doppler is also offered as a feature. Inventive Medical have also recently released an online CME program, endorsed by the American Society of Echocardiography (ASE), consisting of videos, images, diagrams, and self-tests within each topic. Currently, a metrics system to track kinematic movement does not exist, but is in the preliminary stages of development. This simulator has been validated in recent studies to improve the training of TEE to novice learners. [20] , [25]

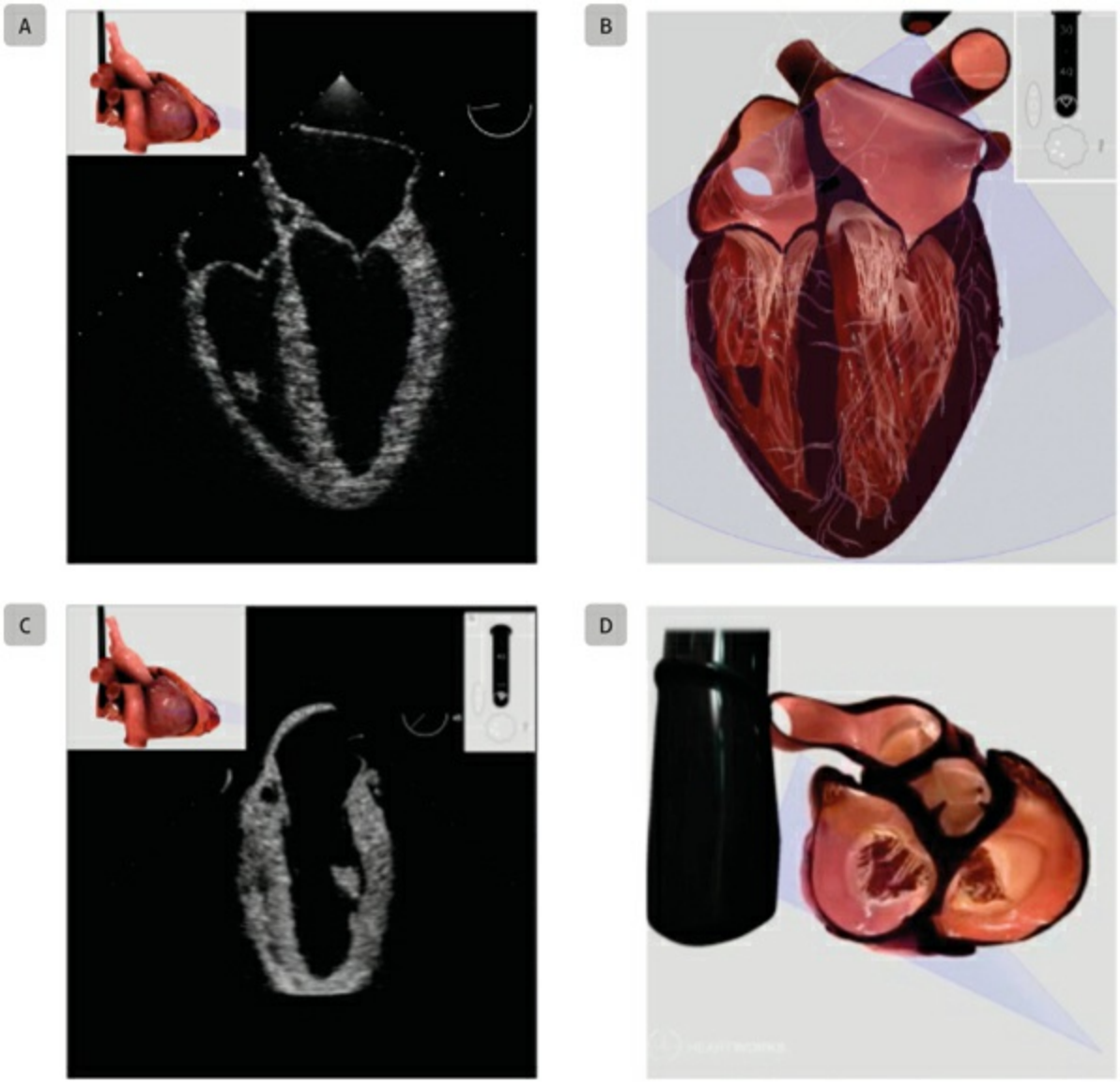

Fig. 19.6 HeartWorks simulator. This high fidelity ultrasound simulator uses an accurate dynamic 3D heart model with a superimposed ultrasound plane. Both the augmented reality on the right of the screen and the computer-generated transesophageal echocardiography (TEE) image are synchronized to respond to real-time probe motion. The heart model may also be manipulated with a keyboard and mouse. (A,B) Mid-esophageal four-chamber and (C,D) two-chamber views are shown. (Courtesy of HeartWorks by Inventive Medical Ltd, UK.)

CAE Vimedix

The Vimedix simulation system manufactured by CAE Healthcare, Montreal, Canada, is based on a rendered augmented reality heart (**Figure 19.7**). Replicas of TEE, TTE, and Focused Assessment with Sonography in Trauma (FAST) probes have all the functions of a real probe as these interface with

the mannequin. As of 2014, a lung and obstetrical simulator has been released. The virtual US image produced is displayed beside the 3D anatomic heart model to provide guidance **(Figure** 19.8). In addition to cardiac structures, lung and intra-abdominal structures are present in the virtual model as well. More than 80 pathologic states for cardiac, as well as pleural and gastrointestinal organs can be selected for virtual diagnosis, some associated with case-based presentations of symptoms and investigations. The US model also contains M-mode and color Doppler to be used with all normal and some pathological cases, as well as the ability to measure dimensions of structures. Software upgrades are offered with a service contract renewed on an annual basis for the addition of new features, as well as upgrades to pathology and accuracy of the imaging of the augmented reality and heart model. This simulator also possesses the unique ability to measure metrics of the operator by tracking the user-controlled probe through time and space. [22] Quantification of image acquisition is created by measuring time and distance traveled to achieve the target cut plane, to assess the technical proficiency of the user. A snapshot of the final view is acquired to assess the accuracy of the image achieved. Recently, this simulator has been validated in a number of research studies as being effective in the training of TTE and TEE learners. [21] , [22] , [26 – 29]

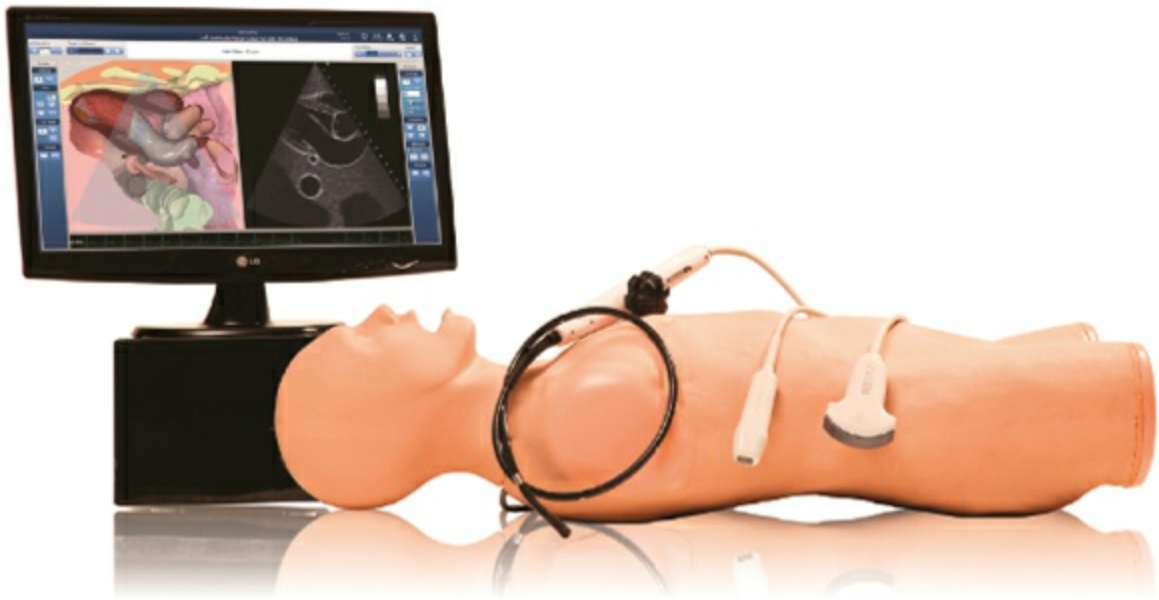

Fig. 19.7 CAE Vimedix simulator. This high fidelity ultrasound simulator can use different ultrasound probes to perform transesophageal echocardiography (TEE), transthoracic echocardiography (TTE), and Focused Assessment with Sonography in Trauma (FAST) examinations. The mannequin is paired

with a dedicated computer for creation of the augmented reality models for cardiac, intrathoracic, and intra-abdominal structures. (Courtesy of CAE Healthcare, Montreal, Canada.)

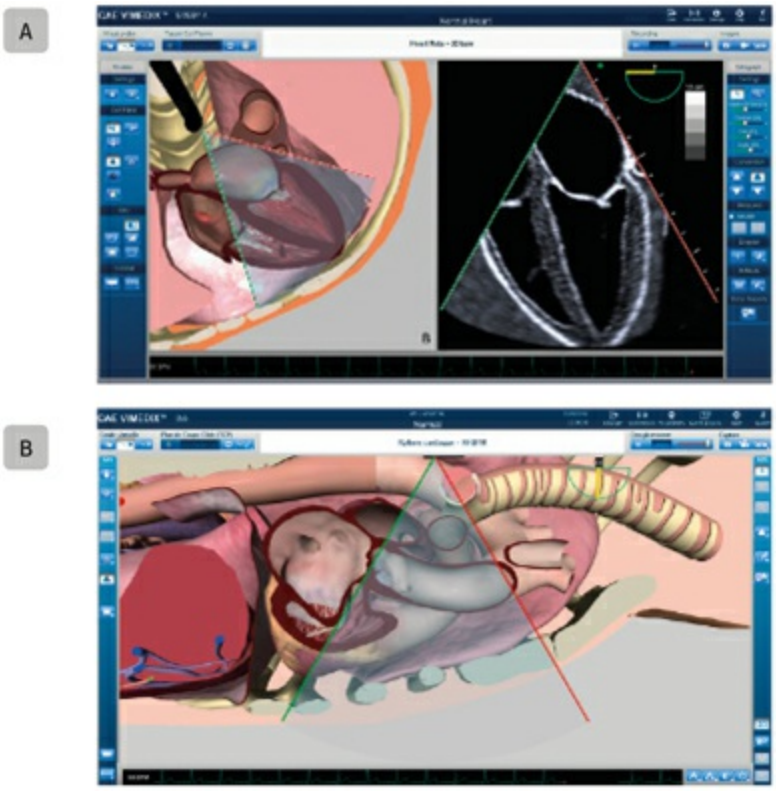

Fig. 19.8 CAE Vimedix simulator display. (A) The augmented reality display of the CAE Vimedix simulator shows a transesophageal echocardiography (TEE) mid-esophageal, four- chamber view. (B) The augmented reality image on the left may be displayed alone or hidden from view so that only the echocardiographic image is displayed depending on the educational need. Color Doppler, M-mode, and measurements may be made on normal and pathologic representations. (Courtesy of CAE Healthcare, Montreal, Canada.)

The U/S Mentor Simulation Platform

The U/S Mentor is a multidisciplinary simulator that is manufactured by 3D Systems - Simbionix and offers hands-on training for diverse ultrasound examinations and interventions (**Figure 19.9**). The U/S Mentor features a highly realistic simulation within a comprehensive educational environment, supporting both independent and instructed hands-on training.

The simulator is designed to provide an optimal educational environment to achieve and demonstrate competency levels. The system includes unique step-by-step tasks for self-learning of multiple protocols. Various educational aids such as anatomy labels, corresponding external visualization, standard views helpers and more are available to accelerate the learning curve and

support independent training. As in real life assessments, different anatomical regions for various scanning protocols as well as probes and scan approach (trans-thoracic/trans-esophageal, trans-ab- dominal/trans-vaginal) can be alternated within a continuous training workflow. Dynamic and anatomically accurate external visualization of the anatomy (3D Map) provides additional guidance and understanding. The 3D Map is controlled via a multi-touch screen and can be operated either linked or separated from the probe.

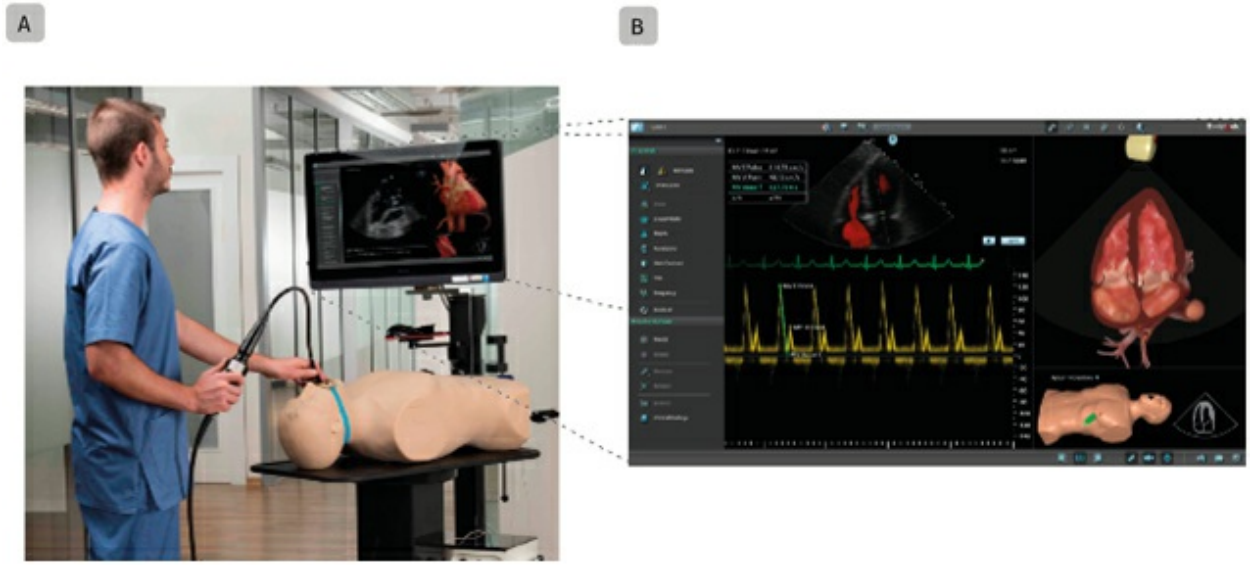

Fig. 19.9 The U/S Mentor is shown for (A) transesophageal echocardiography training. (B) Detailed screen showing combined simultaneous electrocardiographic, Doppler and anatomic visualization. (Courtesy of Amy Natsis, Symbionix.)

The simulation incorporates image enhancement tools, advanced measurements for structural, physiological and hemodynamic assessment, basic and advanced Doppler modes, cine-loop recording, standard view assessment, and clinical findings reporting. These features support training to the full extent of the actual procedure while providing accurate and immediate feedback on the quality of the examination. The performance assessment generated covers both the technical skills of scan performance and documentation, and the diagnostic capacity of image interpretation and derived clinical diagnosis.

Blue Phantom

The Blue Phantom training model created by CAE Healthcare is another type

of TEE and TTE simulator.This system contains an echogenic static heart inside a mannequin. The benefit compared to other high fidelity simulators is the ability to introduce any TEE or TTE US system for practice. This allows practice with knobology and analysis on a platform on which the trainee will become familiar, particularly with modalities not offered on virtual simulators, such as 3D TEE. In addition to imaging and analysis, it also allows echo-guided pericardiocentesis procedures with the ability to introduce fluid around the heart, central and peripheral vascular access (**Figure 19.10**).

TRANSCRANIAL DOPPLER SIMULATOR

Dr Rune Aaslid has developed a transcranial Doppler simulator that is freely accessible to learn basic functions (www. hemodynamic.com/). The simulator allows manual position of the US probe for Doppler interrogation of all the intracranial arteries through all four windows. An advanced module is available for the recognition of various neuropathologies (**Figure 19.11**).

REMOTE ULTRASOUND EDUCATION USING THE INTERNET

New, innovative telemedicine software solutions like the REACTS™ platform (Remote Education, Augmented Communication, Training and Supervision) allow secure streaming of multiple video feeds, including US, over the internet. This allows for an instructor to remotely supervise a user performing a bedside US study or procedure in another center (**Figure 19.12**). Being able to provide remote education and assessment brings a new dimension to training in bedside US. The instructor and student can discuss cases, review videos, interact during live scanning, and exchange videos, pictures, and documents (**Figure 19.13**). REACTS also integrates augmented reality and real-time image overlay bringing remote interaction to another level: it brings “hyperpresence” (additional info at http://www.iitreacts.com) (**Figure 19.14**).

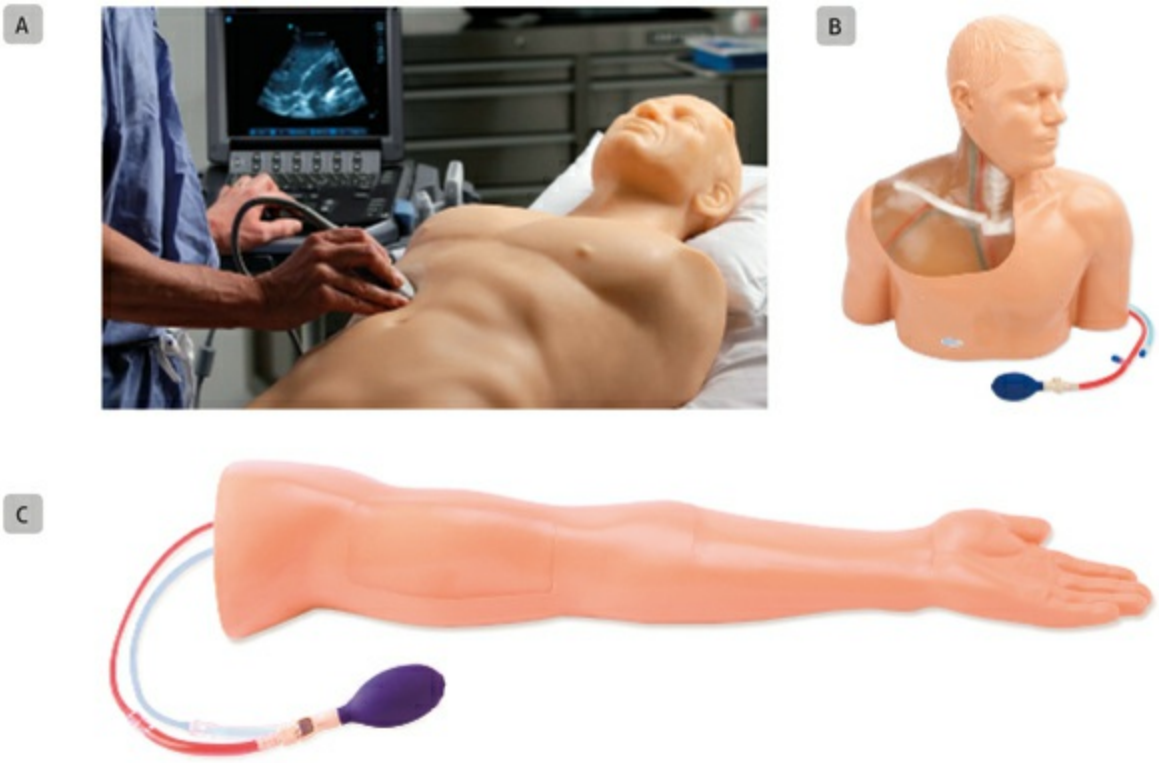

Fig. 19.10 Blue Phantom simulator. (A) The CAE Healthcare Blue Phantom Echocardiography raining Model allows the use of any ultrasound platform and transthoracic probe for imaging of a static heart model. This mannequin also allows practice of ultrasound guided (A) pericardiocentesis, (B) central, and (C) peripheral vascular access using a separate arm model. (Courtesy of CAE Healthcare, Montreal, Canada.)

SUMMARY

The development of strict training guidelines and certification requirements herald the era of TEE as a specialized skill to be upheld to acceptable standards of clinical expertise. With these goals of proficiency combined with technological advancement, effective learning tools are now available to level out the steep learning curve of gaining proficiency in TEE. A variety of interactive online web-based resources are available to learn not only the background knowledge relevant to echocardiography, but also enable learning of the complex mental manipulation required to create 3D cardiac structures from a series of 2D US planes. Online renderings allow each view to be understood in its relation to cardiac anatomy. Advancing this learning concept further, echocardiography simulators permit the opportunity to develop this skill in a fully interactive and realistic hands-on way. In this

fashion, both bedside US and TEE skills may be gained without the pressures of learning on real patients in a high-pressure clinical environment. Finally telemedicine allow distant supervision. These learning pathways provide a much more intuitive introduction to bedside US and TEE, and may expedite the transition from novice to expert.

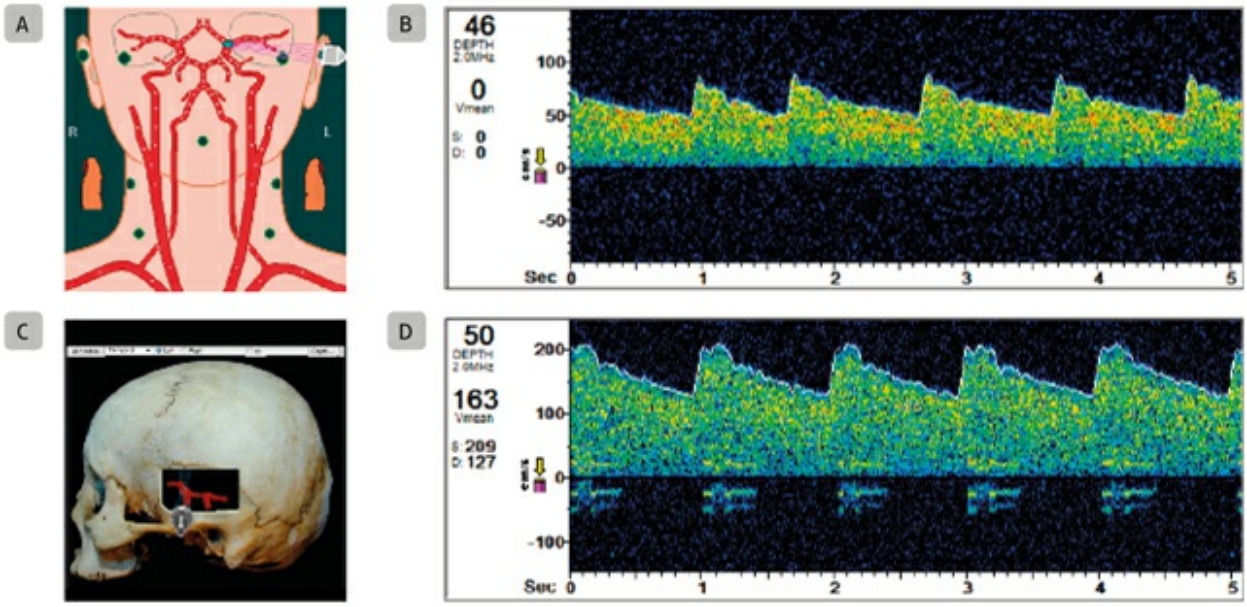

Fig. 19.11 Transcranial Doppler simulator. This simulator shows (A) brain vascularization, (B) normal right middle cerebral artery (RMCA) velocity, (C) temporal window, and (D) RMCA vasospasm in a patient with subarachnoid hemorrhage. (Reproduced with permission from http://www.hemodynamic.com.)

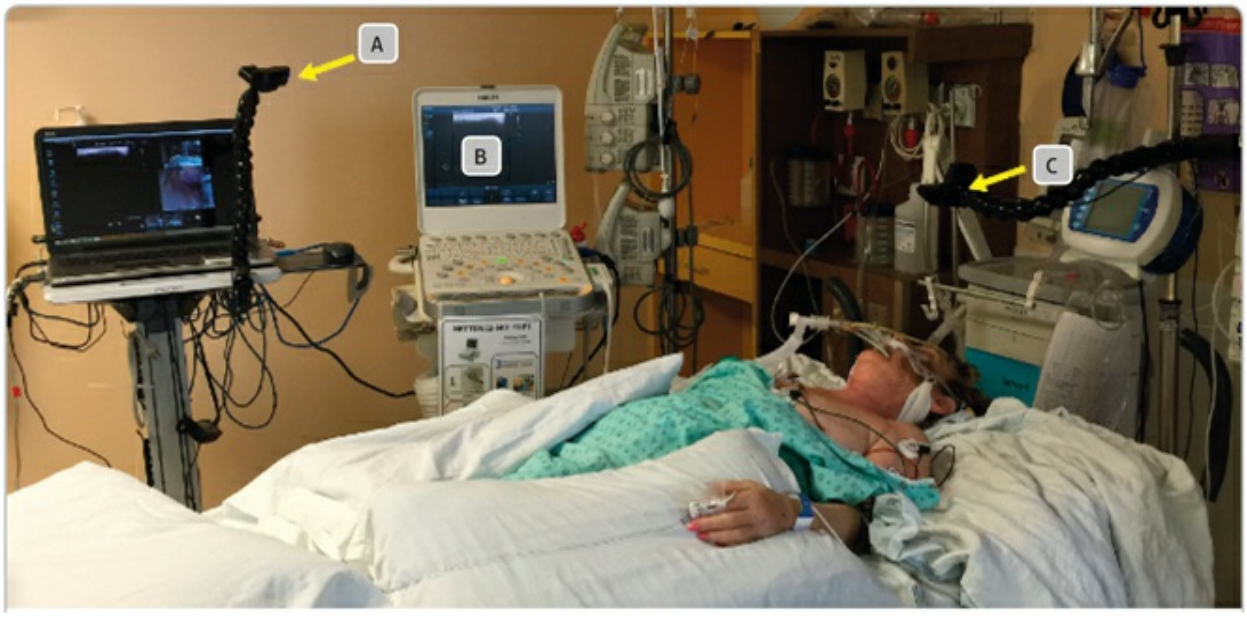

Fig. 19.12 REACTS bedside set up. The REACTS software is installed on a standard laptop connected to the internet. An external webcam (A) connected to the laptop (USB port) gives an overall view of the patient. The ultrasound machine (B) is connected to a video converter that connects to the laptop via USB. (C) A second external webcam also connected to the laptop computer by USB is positioned just above the left subclavian area where a central venous catheter will be inserted by the "on-site" physician. All three video feeds will be streamed via REACTS to the remote expert who will be supervising the procedure. REACTS, Remote Education, Augmented Communication, Training and Supervision. (Courtesy of Dr Yanick Beaulieu.)

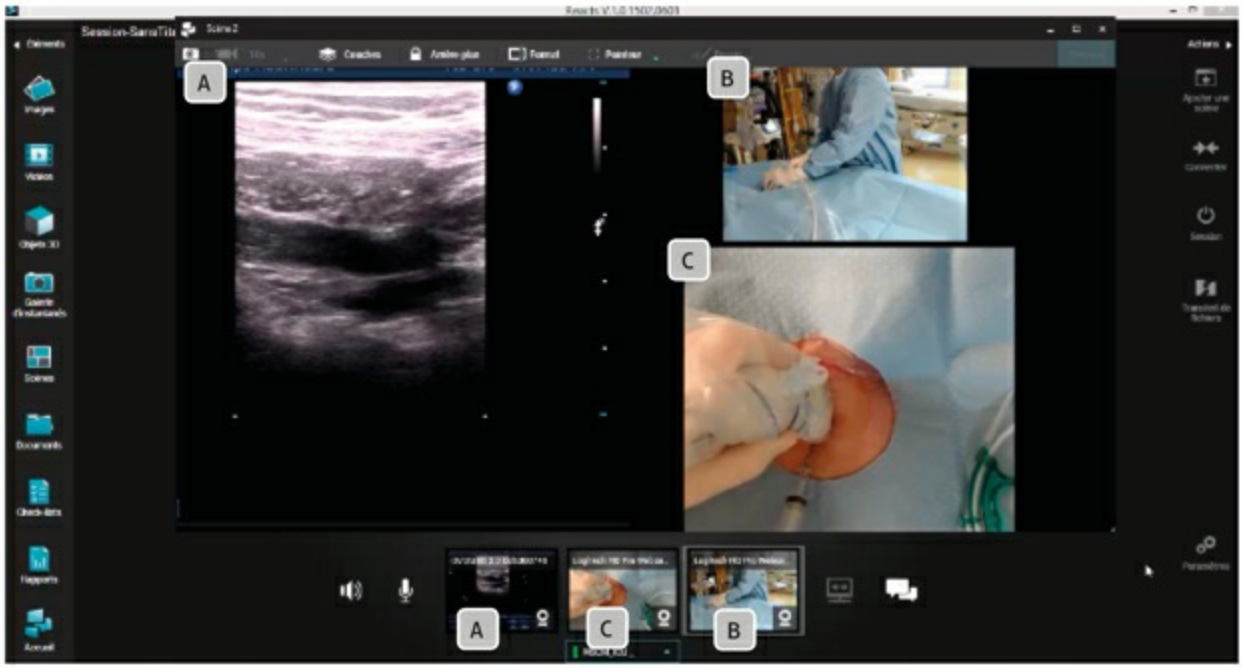

Fig. 19.13 REACTS platform. Video feeds from the webcam show (A) screenshot during the ultrasound procedure, (B) an overall view of the patient, and (C) the left subclavian area. The video feeds are streamed live to the remote supervisor. REACTS, Remote Education, Augmented Communication, Training and Supervision. (Courtesy of Dr Yanick Beaulieu.)

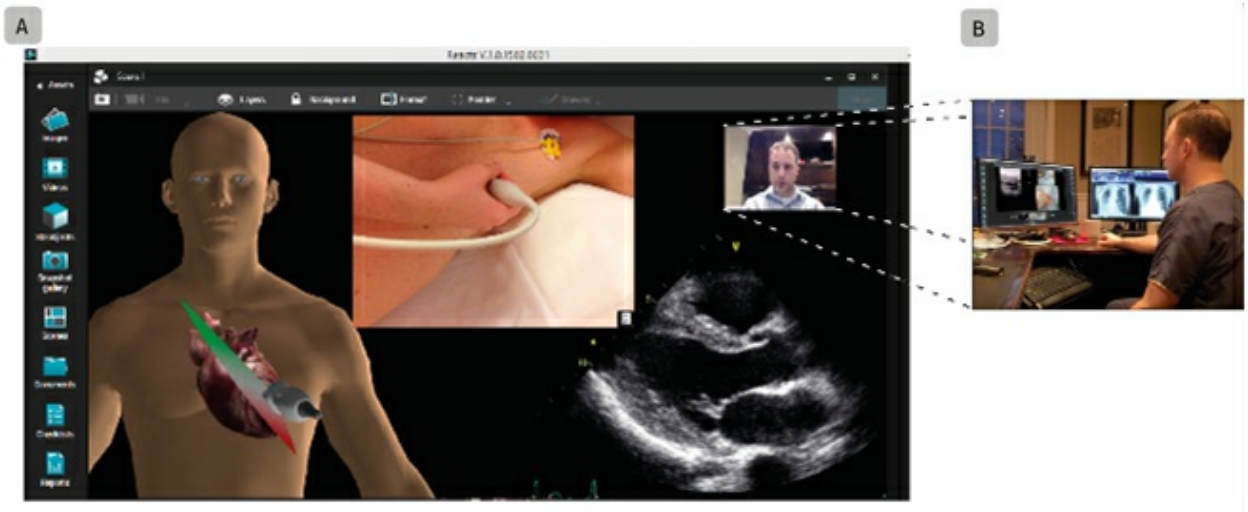

Fig. 19.14 REACTS platform. (A) Remote ultrasound education using digital collaboration (screenshot of a REACTS session), incorporation of 3D objects, image overlay, videos, augmented reality, and other interactive features to remote ultrasound training creates unique digital collaborative sessions. (B) The instructor can remotely supervise the ultrasound-guided procedure from home through the REACTS platform. As shown here, he can also review radiographic studies of the patient through the platform by a simple "share application" function. REACTS, Remote Education, Augmented Communication, Training and Supervision. (Courtesy of Dr Yanick Beaulieu.)

REFERENCES

1 Practice guidelines for perioperative transesophageal echocardiography. 1996. "A report by the American Society of Anesthesiologists and the Society of Cardiovascular Anesthesiologists Task Force on Transesophageal Echocardiography." *Anesthesiology 84*: 986–1006.

2 Practice guidelines for perioperative transesophageal echocardiography. 2010. "An updated report by the American Society of Anesthesiologists and the Society of Cardiovascular Anesthesiologists Task Force on Transesophageal Echocardiography." *Anesthesiology 112*: 1084–96.

3 Hahn, R. T., T.Abraham, M. S.Adams, C. J.Bruce, K. E.Glas, R. M.Lang, et al. 2013. "Guidelines for performing a comprehensive transesophageal echocardiographic examination: recommendations from the American Society of Echocardiography and the Society of Cardiovascular Anesthesiologists." *J Am Soc Echocardiogr 26*: 921–64.

4 Finegan, B. A.2006. "Progress through cooperation: securing a sound training pathway for perioperative transesophageal echocardiography." *Can J Anesth 53*: 969–72.

5 Beique, F., M.Ali, M.Hynes, S.Mackenzie, A.Denault, A.Martineau, et al. 2006. "Canadian guidelines for training in adult perioperative transesophageal echocardiography. Recommendations of the Cardiovascular Section of the Canadian Anesthesiologists' Society and the Canadian Society of Echocardiography. *Can*." *J Anesth 53*: 1044–60.

6 Burwash, I. G., A.Basmadjian, D.Bewick, J. B.Choy, B.Cujec, D. S.Jassal, et al. 2011. "2010 Canadian Cardiovascular Society/Canadian Society of Echocardiography Guidelines for Training and Maintenance of Competency in Adult Echocardiography." *Can J Cardiol 27*: 862–4.

7 Shanewise, J. S., A. T.Cheung, S.Aronson, W. J.Stewart, R. L.Weiss, J. B.Mark, et al. 1999. "ASE/SCA guidelines for performing a comprehensive intraoperative multiplane transesophageal echocardiography examination: recommendations of the American Society of Echocardiography Council for Intraoperative Echocardiography and the Society of Cardiovascular Anesthesiologists Task Force for Certification in Perioperative Transesophageal Echocardiography." *Anesth Analg 89*: 870–84.

8 Reeves, S. T., A. C.Finley, N. J.Skubas, M.Swaminathan, W. S.Whitley, K. E.Glas, et al. 2013. "Basic perioperative transesophageal echocardiography examination: a consensus statement of the American Society of Echocardiography and the Society of Cardiovascular Anesthesiologists." *J Am Soc Echocardiogr 26*: 443–56.

9 Denault, A. Y., P.Couture, A.Vegas, J.Buithieu, and J. C.Tardif. 2011. *Transesophageal Echocardiography Multimedia Manual, Second Edition: A Perioperative Transdiciplinary Approach*. New York, NY: Informa Healthcare.

10 National Board of Echocardiography. (Updated 2014). Available from http://www.echoboards.org.

11 Andrus, P., and A.Dean. 2013. "Focused cardiac ultrasound. *Global*." *Heart 8*: 299–303.

12 Beaulieu, Y.2007. "Bedside echocardiography in the assessment of the critically ill." *Crit Care Med 35* (5 Suppl.): S235–S249.

13 Hew, M., and S.Heinze. 2012. “Chest ultrasound in practice: a review of utility in the clinical setting.” *Intern Med J 42*: 856–65.
14 Labovitz, A. J., V. E.Noble, M.Bierig, S. A.Goldstein, R.Jones, S.Kort, et al. 2010. “Focused cardiac ultrasound in the emergent setting: a consensus statement of the American Society of Echocardiography and American College of Emergency Physicians.” *J Am Soc Echocardiogr 23*: 1225–30.
15 Piette, E., R.Daoust, and A.Denault. 2013. “Basic concepts in the use of thoracic and lung ultrasound.” *Curr Opin Anaesthesiol 26*: 20–30.
16 Schmidt, G. A.2009. “ICU ultrasound. The coming boom.” *Chest 135*: 1407–8.
17 Arntfield, R., S.Millington, C.Ainsworth, R.Arora, J.Boyd, G.Finlayson, et al. 2014. “Canadian recommendations for critical care ultrasound training and competency.” *Can Respir J 21*: 341–5.
18 Vegas, A., M.Meineri, A.Jerath, M.Corrin, C.Silversides, and G.Tait. 2013. “Impact of online transesophageal echocardiographic simulation on learning to navigate the 20 standard views.” *J Cardiothorac Vasc Anesth 27*: 531–5.
19 Damp, J., R.Anthony, M. A.Davidson, and L.Mendes. 2013. “Effects of transesophageal echocardiography simulator training on learning and performance in cardiovascular medicine fellows.” *J Am Soc Echocardiogr 26* (1450–6): e2.
20 Ferrero, N. A., A. V.Bortsov, H.Arora, S. M.Martinelli, L. M.Kolarczyk, E. C.Teeter, et al. 2014. “Simulator training enhances resident performance in transesophageal echocardiography.” *Anesthesiology 120*: 149–59.
21 Jelacic, S., A.Bowdle, K.Togashi, and P.VonHomeyer. 2013. “The use of TEE simulation in teaching basic echocardiography skills to senior anesthesiology residents.” *J Cardiothorac Vasc Anesth 27*: 670–5.
22 Matyal, R., J. D.Mitchell, P. E.Hess, B.Chaudary, R.Bose, J. S.Jainandunsing, et al. 2014. “Simulator-based transesophageal echocardiographic training with motion analysis: a curriculum-based approach.” *Anesthesiology 121*: 389–99.
23 Tanzola, R. C., S.Walsh, W. M.Hopman, D.Sydor, R.Arellano, and R. V.Allard. 2013. “Brief report: Focused transthoracic echocardiography training in a cohort of Canadian anesthesiology residents: a pilot study.” *Can J Anesth 60*: 32–7.
24 Weidenbach, M., H.Drachsler, F.Wild, S.Kreutter, V.Razek, G.Grunst, et al. 2007. “Echocomtee - a simulator for transoesophageal echocardiography.” *Anaesthesia 62*: 347–53.
25 Bick, J. S., S.DemariaJr, J. D.Kennedy, A. D.Schwartz, M. M.Weiner, A. I.Levine, et al. 2013. “Comparison of expert and novice performance of a simulated transesophageal echocardiography examination.” *Simul Healthcare 8*: 329–34.
26 Beraud, A. S., N. W.Rizk, R. G.Pearl, D. H.Liang, and A. J.Patterson. 2013. “Focused transthoracic echocardiography during critical care medicine training: curriculum implementation and evaluation of proficiency.” *Crit Care Med 41*: e179–81.
27 Cawthorn, T. R., C.Nickel, M.O’Reilly, H.Kafka, J. W.Tam, L. C.Jackson, et al. 2014. “Development and evaluation of methodologies for teaching focused cardiac ultrasound skills to medical students.” *J Am Soc Echocardiogr 27*: 302–9.
28 Platts, D. G., J.Humphries, D. J.Burstow, B.Anderson, T.Forshaw, and G. M.Scalia. 2012. “The use of computerised simulators for training of transthoracic and transoesophageal echocardiography. The future of echocardiographic training?” *Heart Lung Circ 21*: 267–74.
29 Sohmer, B., C.Hudson, J.Hudson, G. D.Posner, and V.Naik. 2014. “Transesophageal echocardiography simulation is an effective tool in teaching psychomotor skills to novice echocardiographers.” *Can J Anesth 61*: 235–41.

Appendix

Recommended Views in Transesophageal Echocardiography

Carl Chartrand-Lefebvre, André Y Denault and Annette Vegas

CT Correlation. antero posterior view, transverse plane view and sagittal plane view from computed tomographic images

https://youtu.be/T9U9pl-GKeE

https://youtu.be/va-HEt3M48g

https://youtu.be/ARaty0Ww-pQ

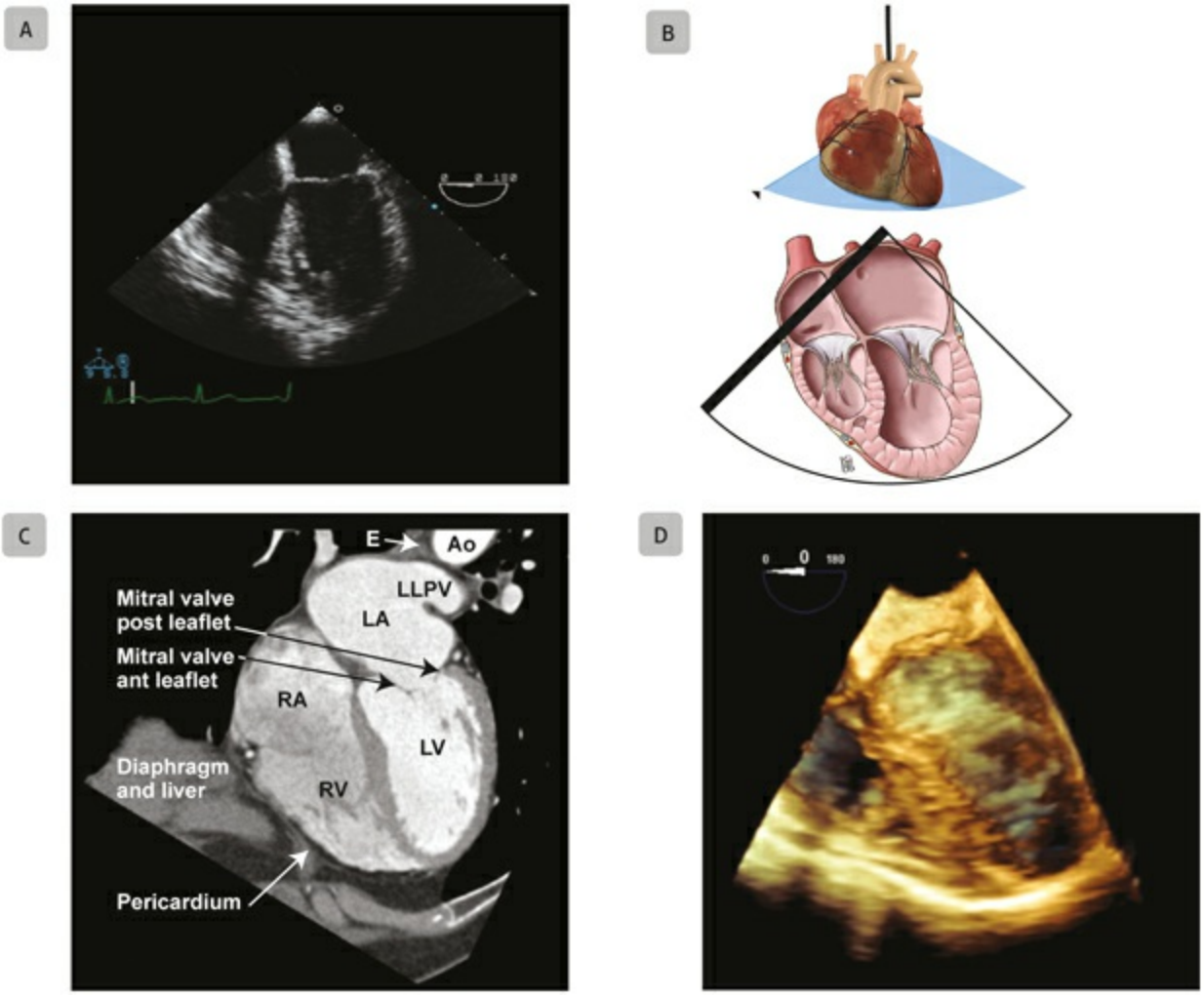

A1 Mid-Esophageal Four-Chamber. Mid-esophageal four-chamber views obtained with two-dimensional echocardiography (**A**,**B**), ECG-gated computed tomography (**C**), and three-dimensional echocardiography (**D**). *Abbreviations:* Ao, aorta; E, esophagus; ECG, electrocardiogram; LA, left atrium; LLPV, left lower pulmonary vein; LV, left ventricle; RA, right atrium; RV, right ventricle. *Source:* Illustration B courtesy of Gian-Marco Busato.

https://youtu.be/Ebj0jNtM2h8

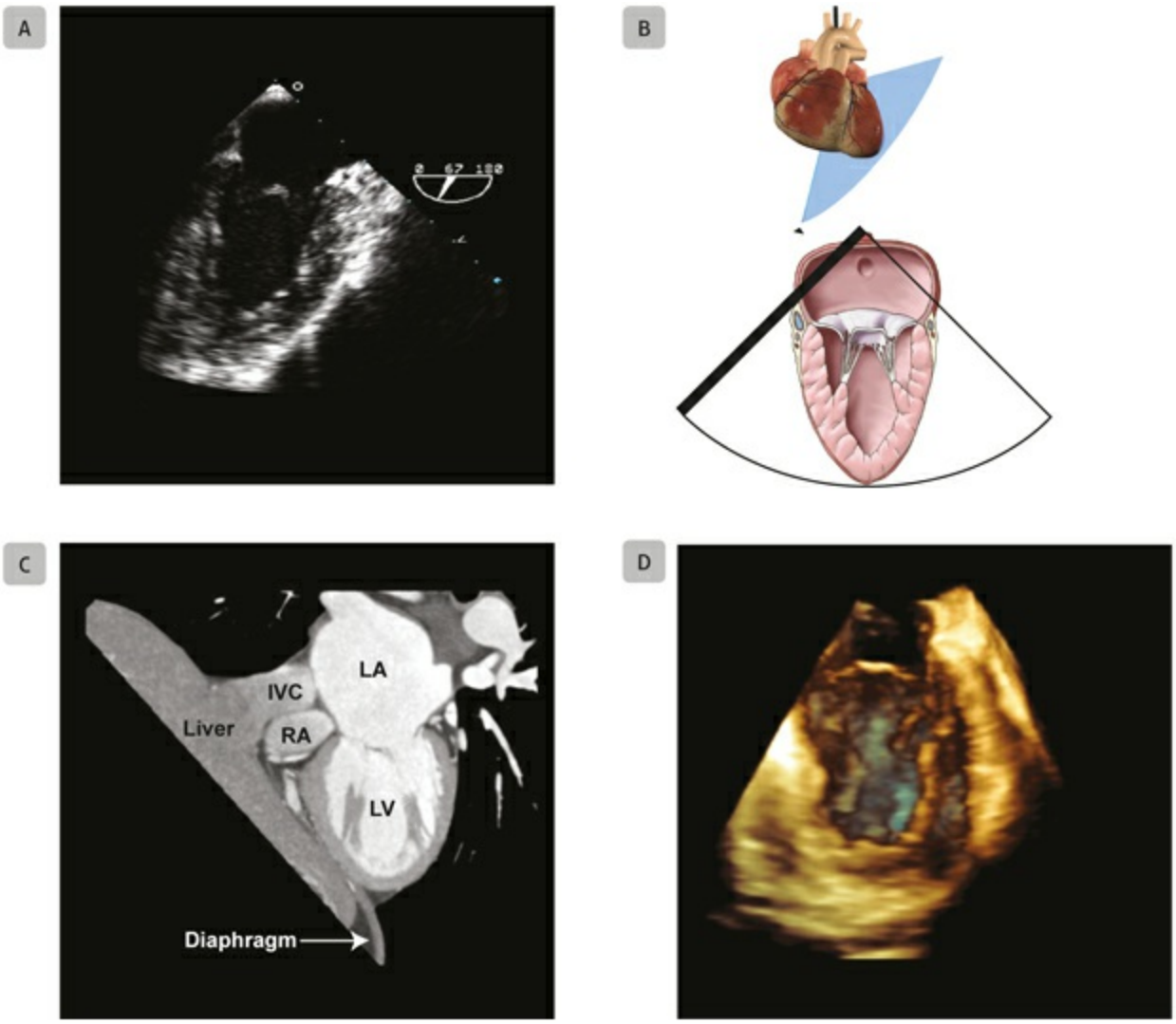

A2 Mid-Esophageal Two-Chamber Mitral Commissural. Mid-esophageal two-chamber mitral commissural views obtained with two-dimensional echocardiography (**A**,**B**), ECG-gated computed tomography (**C**), and three-dimensional echocardiography (**D**). *Abbreviations:* ECG, electrocardiogram; IVC, inferior vena cava; LA, left atrium; LV, left ventricle; RA, right atrium. *Source:* Illustration B courtesy of Gian-Marco Busato.

https://youtu.be/j2X-EC7Jkys

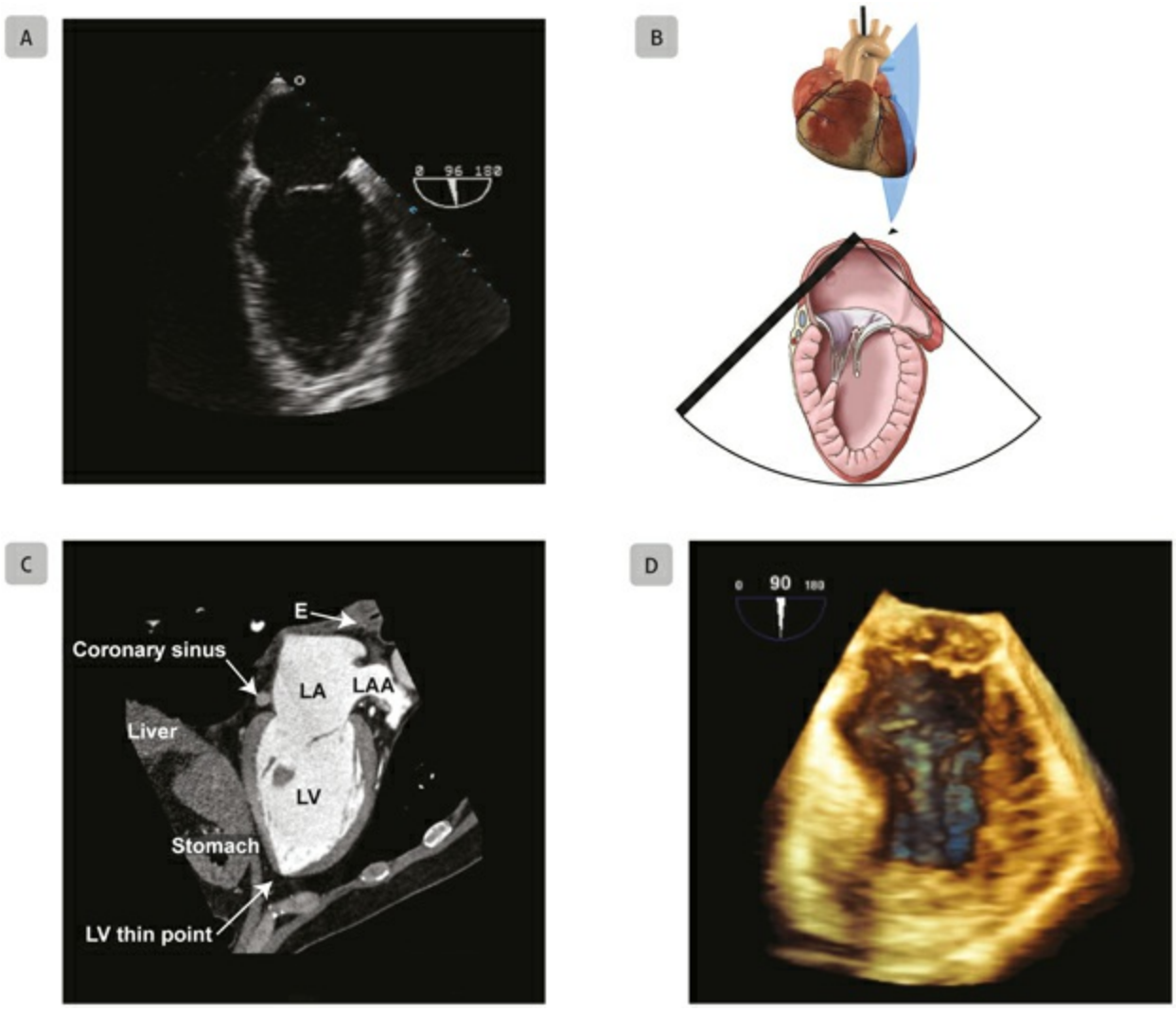

A3 Mid-Esophageal Two-Chamber. Mid-esophageal two-chamber views obtained with two-dimensional echocardiography (**A**,**B**), ECG-gated computed tomography (**C**), and three-dimensional echocardiography (**D**). *Abbreviations:* E, esophagus; ECG, electrocardiogram; LA, left atrium; LAA, left atrial appendage; LV, left ventricle. *Source:* Illustration B courtesy of Gian-Marco Busato.

https://youtu.be/bYotE-CB0TU

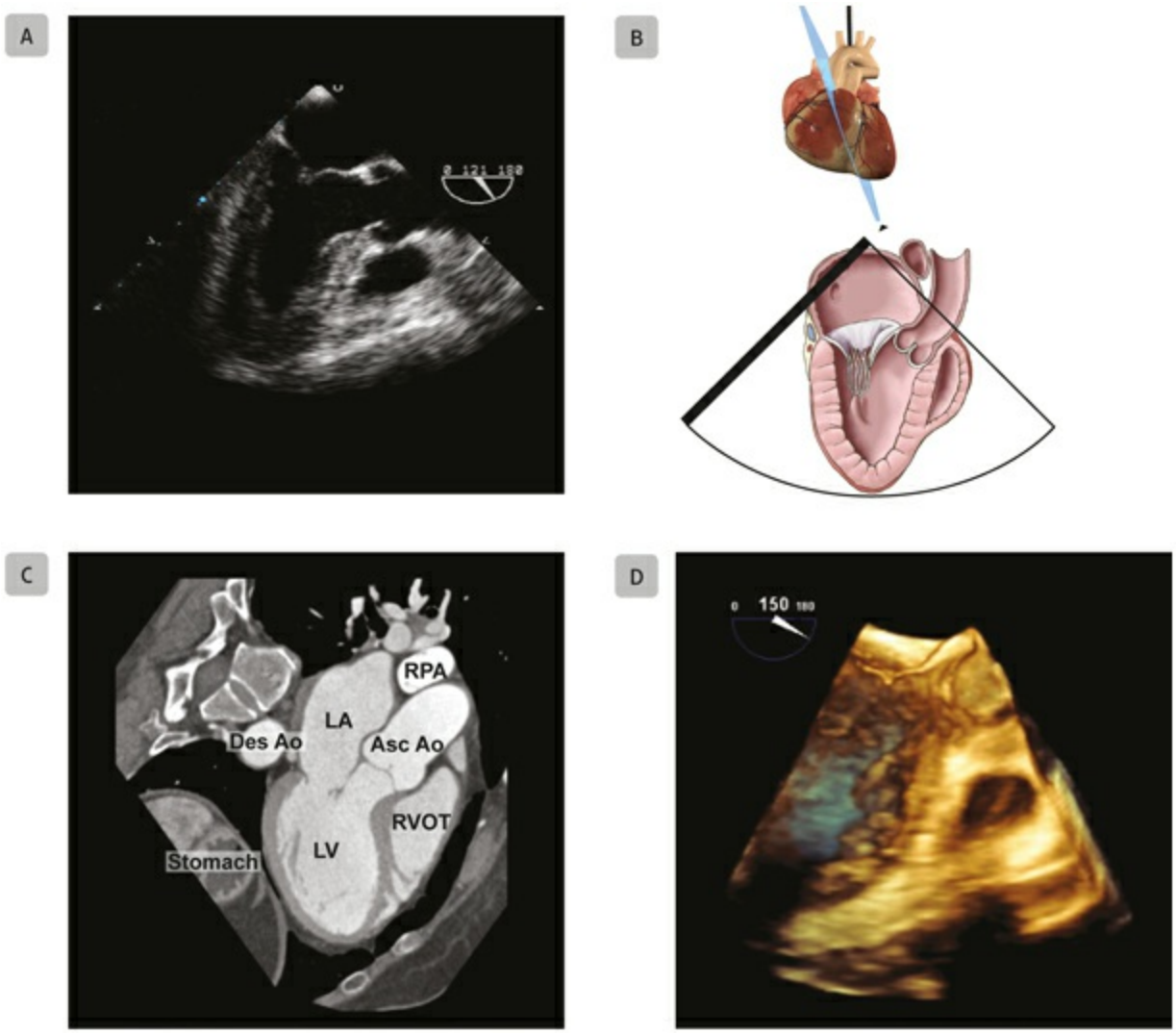

A4 Mid-Esophageal Long-Axis. Mid-esophageal long-axis views obtained with two-dimensional echocardiography (**A**,**B**), ECG-gated computed tomography (**C**), and three-dimensional echocardiography (**D**). *Abbreviations:* Ao, aorta; Asc, ascending; Des, descending; ECG, electrocardiogram; LA, left atrium; LV, left ventricle; RPA, right pulmonary artery; RVOT, right ventricular outflow tract. *Source:* Illustration B courtesy of Gian-Marco Busato.

https://youtu.be/EyvQmFyaSzY

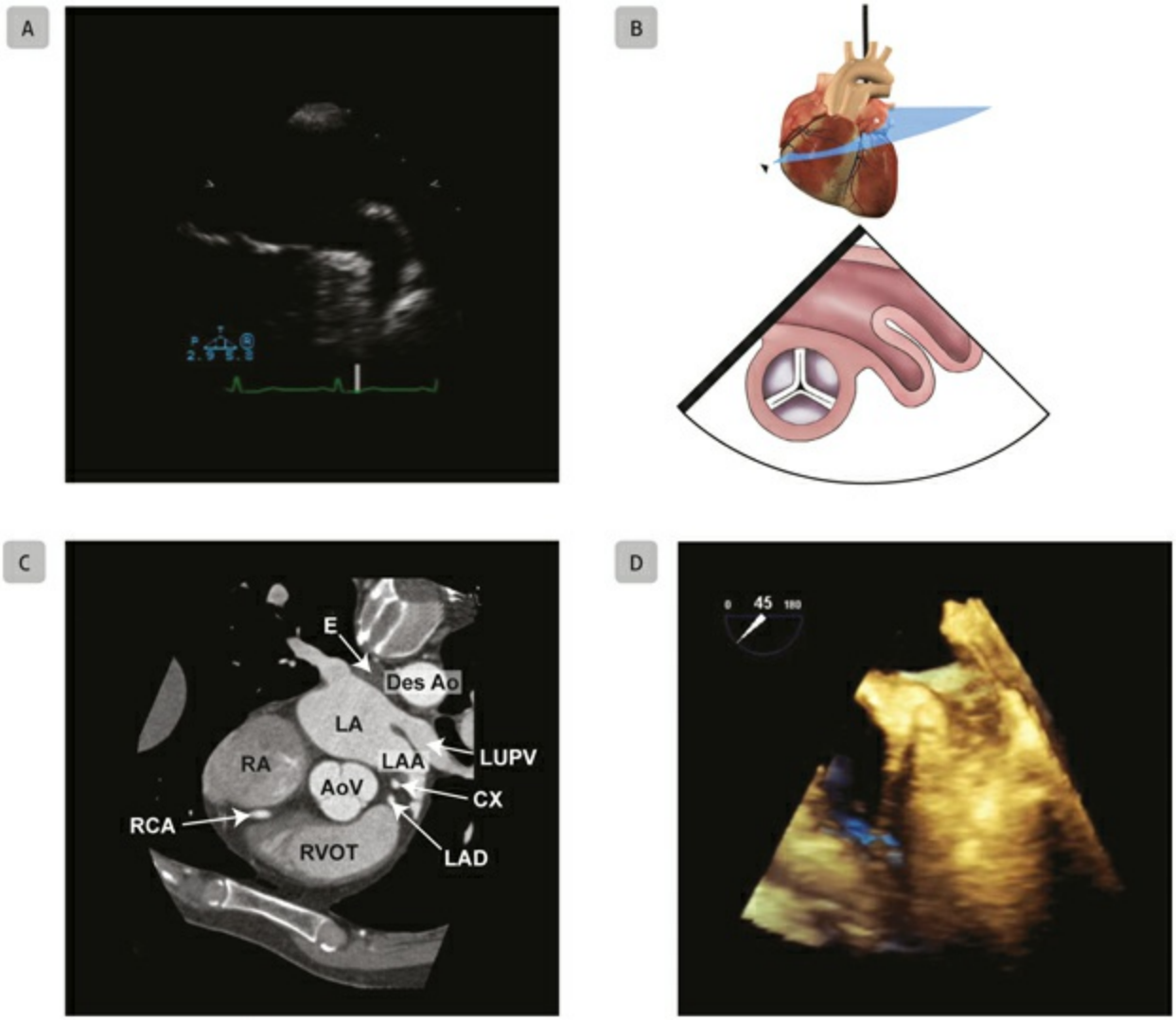

A5 Mid-Esophageal Left Atrial Appendage. Mid-esophageal left atrial appendage views obtained with two-dimensional echocardiography (**A**,**B**), ECG-gated computed tomography (**C**), and three-dimensional echocardiography (**D**). *Abbreviations:* Ao, aorta; AoV, aortic valve; CX, circumflex artery; Des, descending; E, esophagus; ECG, electrocardiogram; LA, left atrium; LAA, left atrial appandage; LAD, left anterior decending artery; LUPV, left upper pulmonary vein; RA, right atrium; RCA, right coronary artery; RVOT, right ventricular outflow tract. *Source:* Illustration B courtesy of Gian-Marco Busato.

A: https://youtu.be/Nt-EPvyiH6k

D: https://youtu.be/yQoGlkZA3Gc

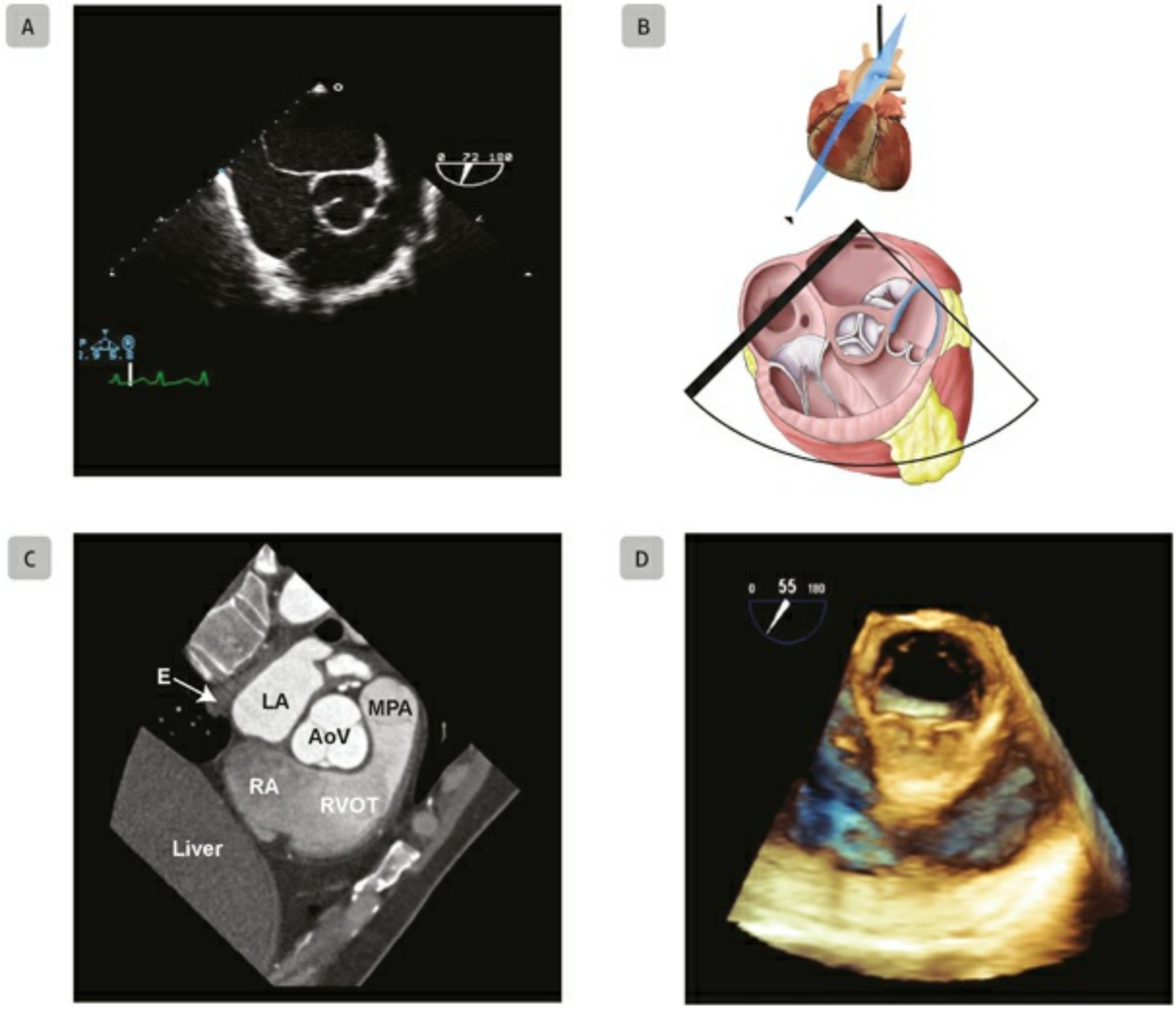

A6 Mid-Esophageal Right Ventricular Outflow Tract. Mid-esophageal right ventricular outflow tract views obtained with two-dimensional echocardiography (**A**,**B**), ECG-gated computed tomography (**C**), and three-dimensional echocardiography (**D**). *Abbreviations:* AoV, aortic valve; E, esophagus; ECG, electrocardiogram; LA, left atrium; MPA, main pulmonary artery; RA, right atrium; RVOT, right ventricular outflow tract. *Source:* Illustration B courtesy of Gian-Marco Busato.

A: https://youtu.be/x0fKqo71Aa8

D: https://youtu.be/nFXS_CHGOzM

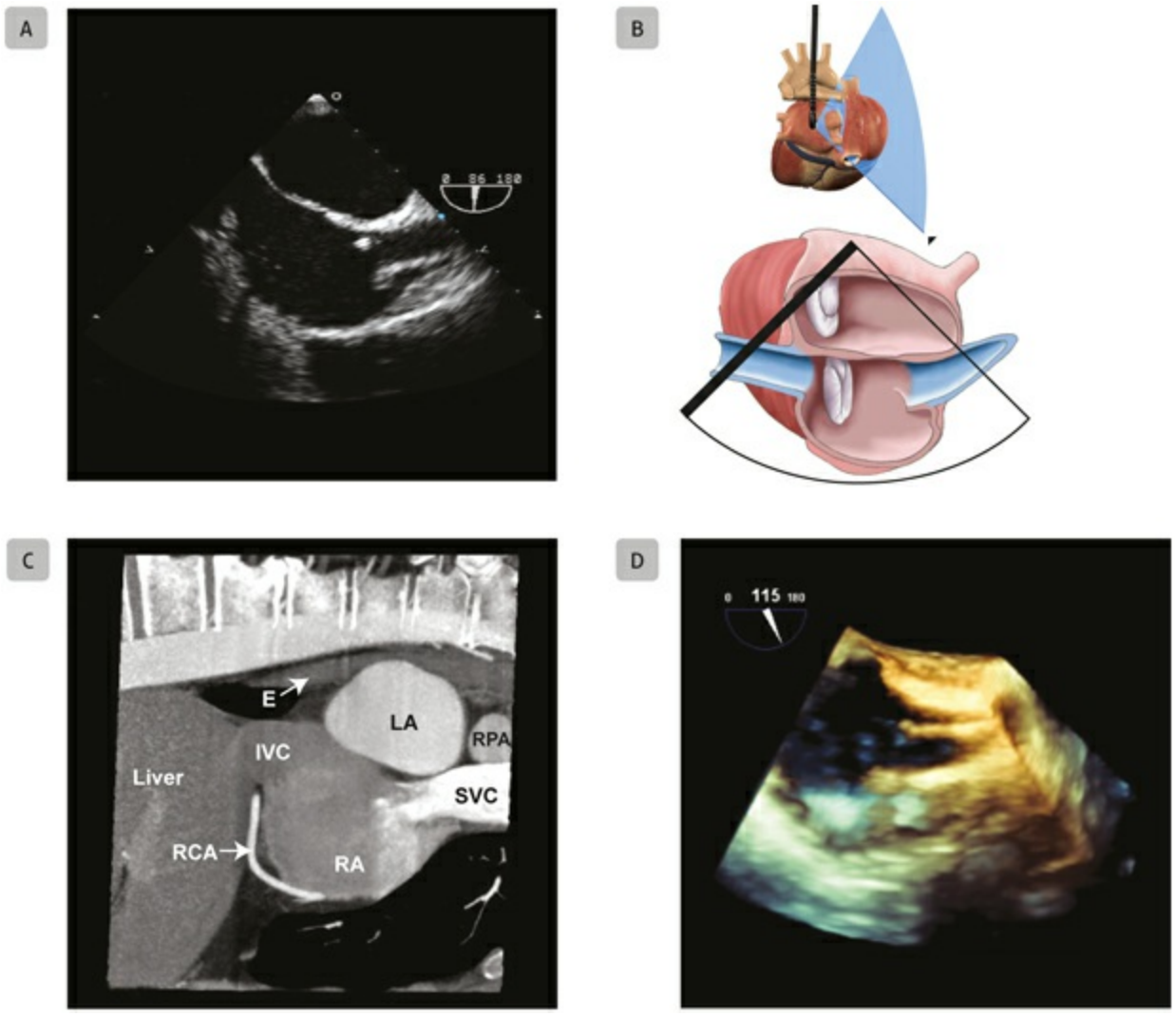

A7 Mid-Esophageal Bicaval. Mid-esophageal bicaval views obtained with two-dimensional echocardiography (**A**,**B**), ECG-gated computed tomography (**C**), and three-dimensional echocardiography (**D**). *Abbreviations:* E, esophagus; ECG, electrocardiogram; IVC, inferior vena cava; LA, left atrium; RA, right atrium; RCA, right coronary artery; RPA, right pulmonary artery; SVC superior vena cava. *Source:* Illustration B courtesy of Gian-Marco Busato.

https://youtu.be/qhywHNLzMG4

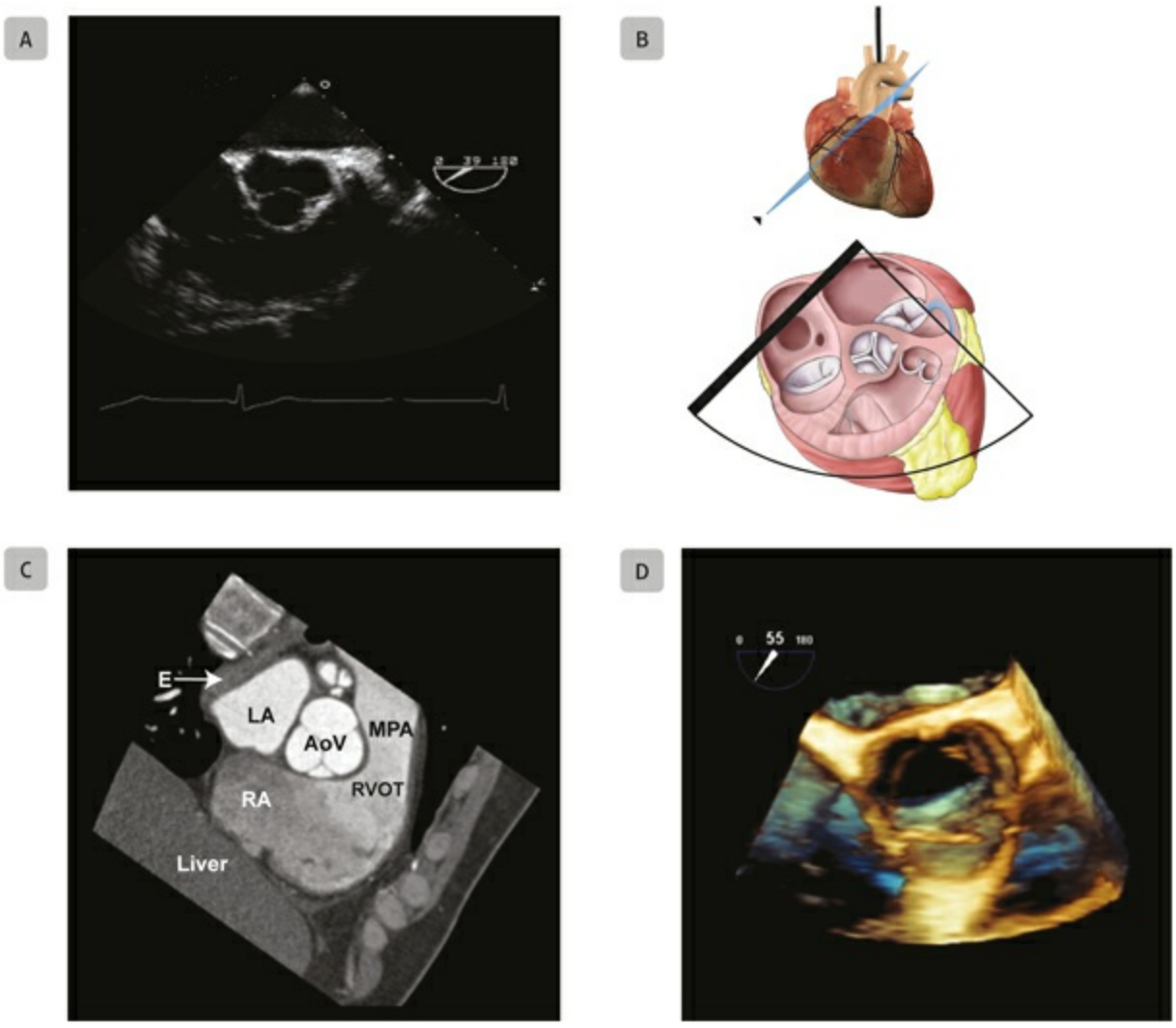

A8 Mid-Esophageal Aortic Valve Short-Axis. Mid-esophageal aortic valve short-axis views obtained with two-dimensional echocardiography (**A**,**B**), ECG-gated computed tomography (**C**), and three-dimensional echocardiography (**D**). *Abbreviations:* AoV, aortic valve; E, esophagus; ECG, electrocardiogram; LA, left atrium; MPA, main pulmonary artery; RA, right atrium; RVOT, right ventricular outflow tract. *Source:* Illustration B courtesy of Gian-Marco Busato.

A: https://youtu.be/_2R1RpJLAO8

D: https://https://youtu.be/5uwulKFdk_s

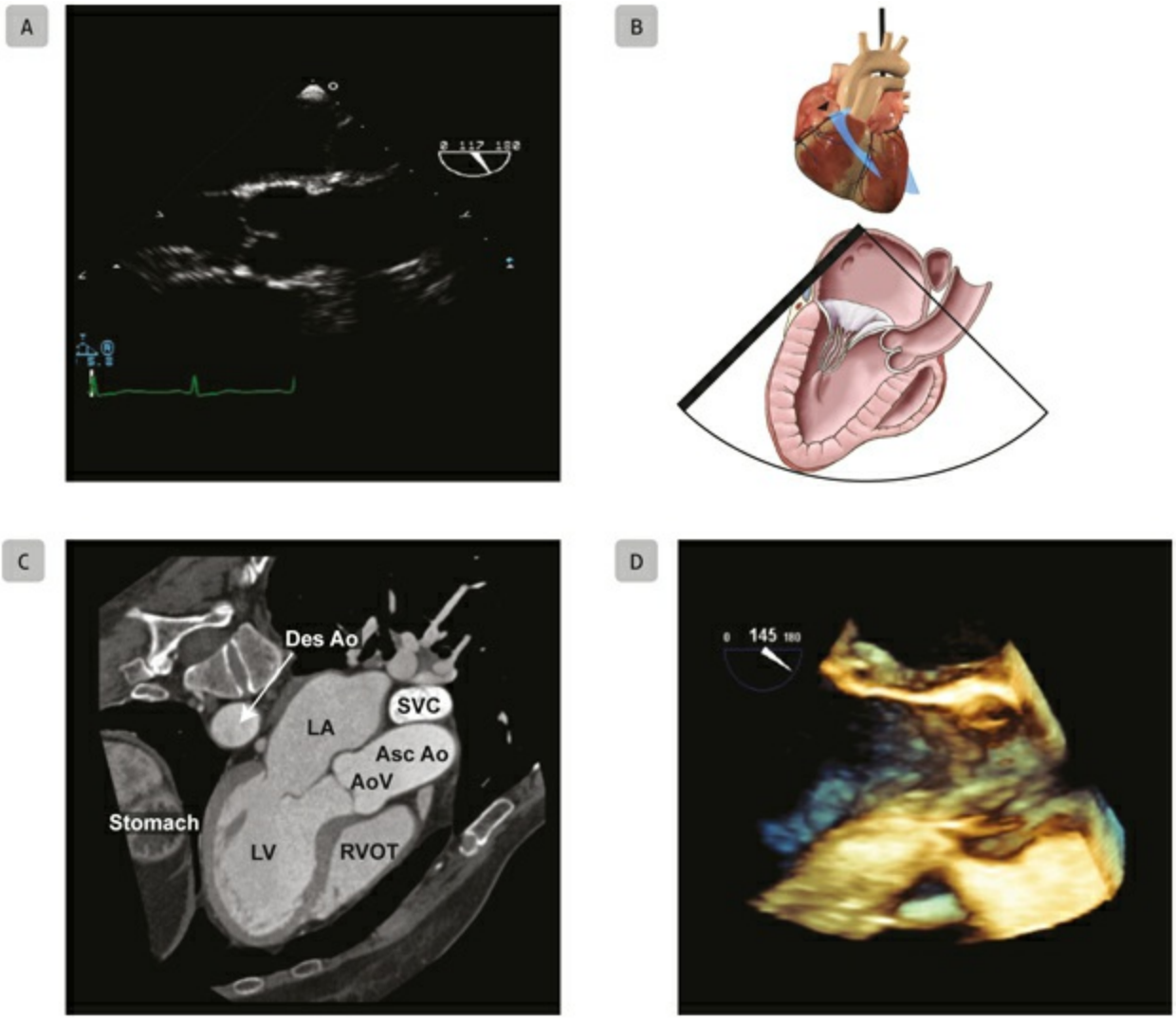

A9 Mid-Esophageal Aortic Valve Long-Axis. Mid-esophageal aortic valve long-axis views obtained with two-dimensional echocardiography (**A**,**B**), ECG-gated computed tomography (**C**), and three-dimensional echocardiography (**D**). *Abbreviations:* Ao, aorta; AoV, aortic valve; Asc, ascending; Des, descending; ECG, electrocardiogram; LA, left atrium; LV, left ventricle; RVOT, right ventricular outflow tract; SVC, superior vena cava. *Source:* Illustration B courtesy of Gian-Marco Busato.

https://youtu.be/E67fo08LR4I

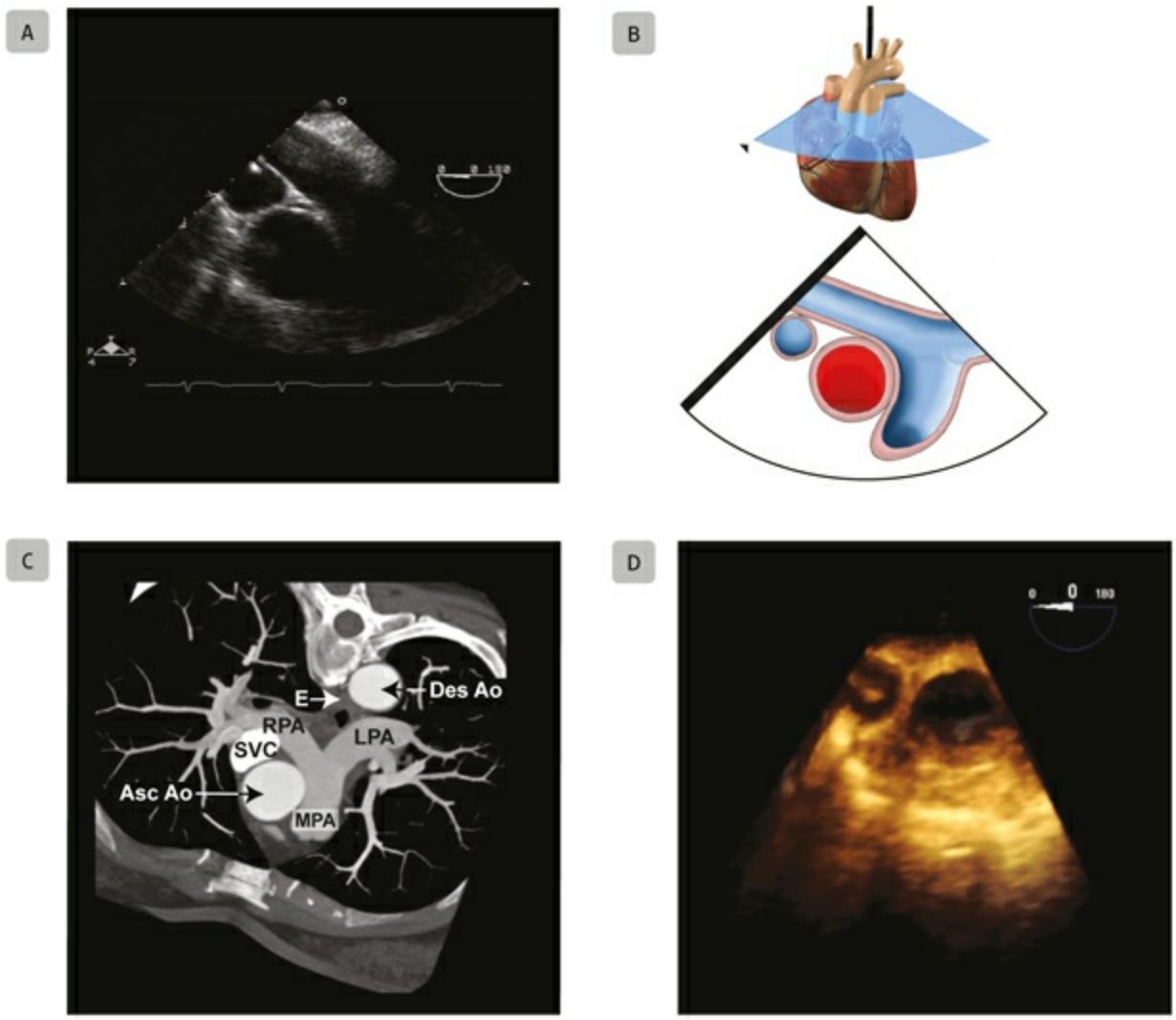

A10 Mid-Esophageal Ascending Aortic Short-Axis. Mid-esophageal ascending aortic short-axis views obtained with two-dimensional echocardiography (**A**,**B**), ECG-gated computed tomography (**C**), and threedimensional echocardiography (**D**). *Abbreviations:* Ao, aorta; Asc, ascending; Des, descending; E, esophagus; ECG, electrocardiogram; LPA, left pulmonary artery; MPA, main pulmonary artery; RPA, right pulmonary artery; SVC, superior vena cava. *Source:* Illustration B courtesy of Gian-Marco Busato.

https://youtu.be/n5AaSB9FwIw

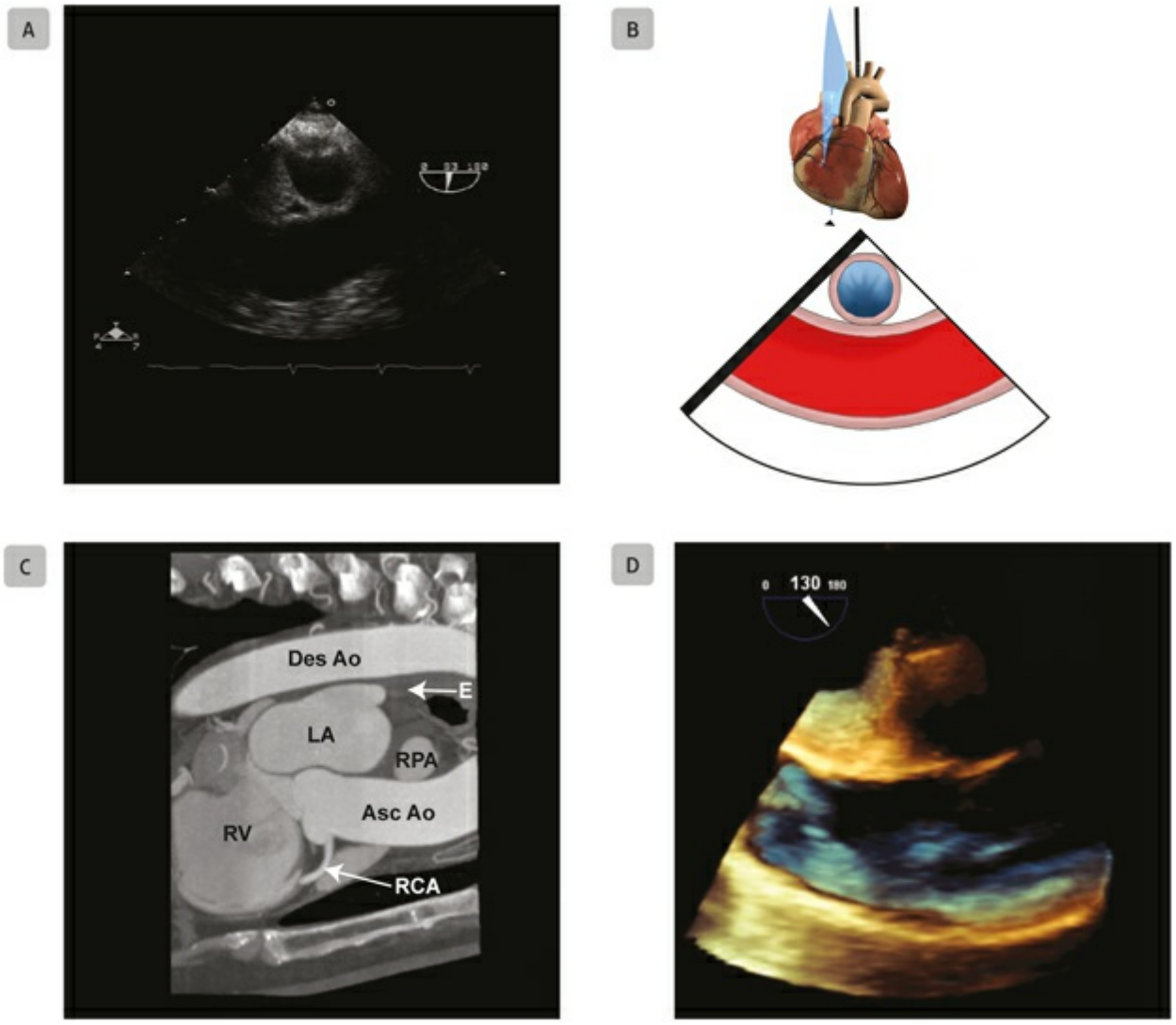

A11 Mid-Esophageal Ascending Aortic Long-Axis. Mid-esophageal ascending aortic long-axis views obtained with two-dimensional echocardiography (**A**,**B**), ECG-gated computed tomography (**C**), and three-dimensional echocardiography (**D**). *Abbreviations:* Ao, aorta; Asc, ascending; Des, descending; E, esophagus; ECG, electrocardiogram; LA, left atrium; RCA, right coronary artery; RPA, right pulmonary artery; RV, right ventricle. *Source:* Illustration B courtesy of Gian-Marco Busato.

https://youtu.be/lbZp5ubQzL8

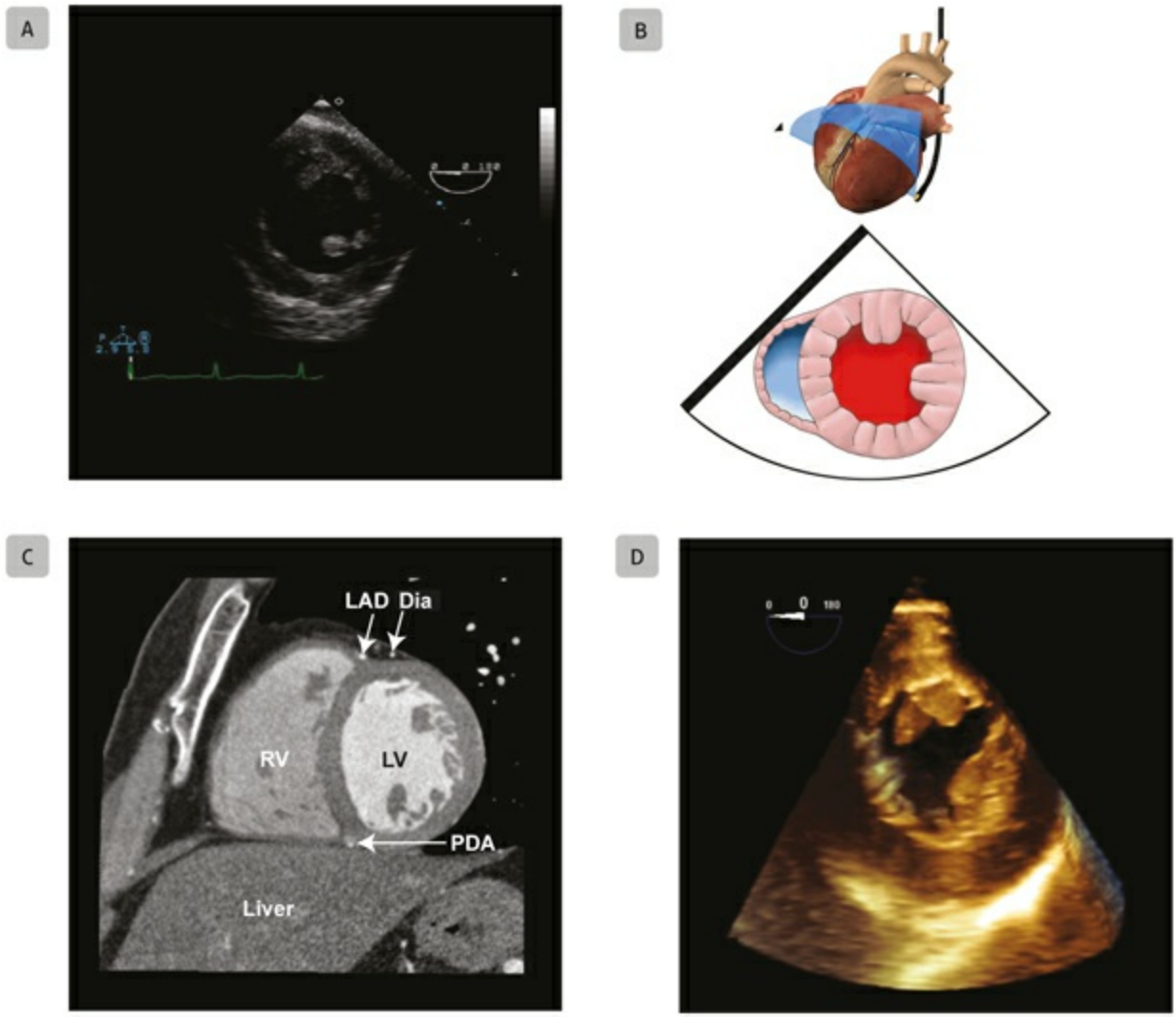

B1 Transgastric Mid-Papillary Short-Axis. Transgastric mid-papillary short-axis views obtained with two-dimensional echocardiography (**A**,**B**), ECG-gated computed tomography (**C**), and three-dimensional echocardiography (**D**). *Abbreviations:* Dia, diagonal artery; ECG, electrocardiogram; LAD, left anterior descending artery; LV, left ventricle; PDA, posterior descending artery; RV, right ventricle. *Source:* Illustration B courtesy of Gian-Marco Busato.

https://youtu.be/oFjoRxrmvdw

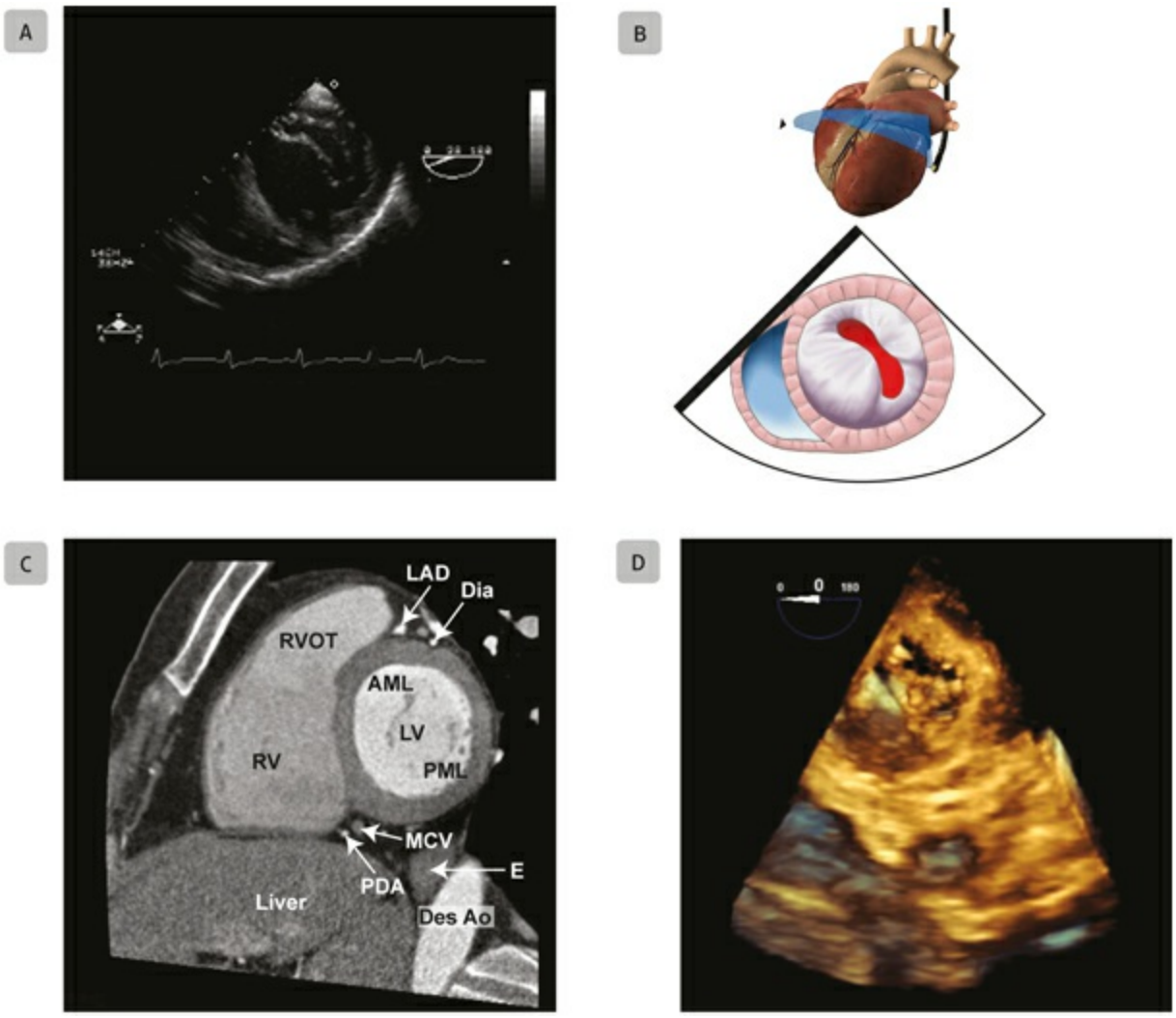

B2 Transgastric Basal Short-Axis. Transgastric basal short-axis views obtained with two-dimensional echocardiography (**A**,**B**), ECG-gated computed tomography (**C**), and three-dimensional echocardiography (**D**). *Abbreviations:* AML, anterior mitral leaflet; Ao, aorta; Des, descending; Dia, diagonal artery; E, esophagus; ECG, electrocardiogram; LAD, left anterior descending artery; LV, left ventricle; MCV, middle cardiac vein; PDA, posterior descending artery; PML, posterior mitral leaflet; RV, right ventricle; RVOT, right ventricular outflow tract. *Source:* Illustration B courtesy of Gian-Marco Busato.

A: https://youtu.be/f9639tOFibk

D: https://youtu.be/RTQLmQkhM3M

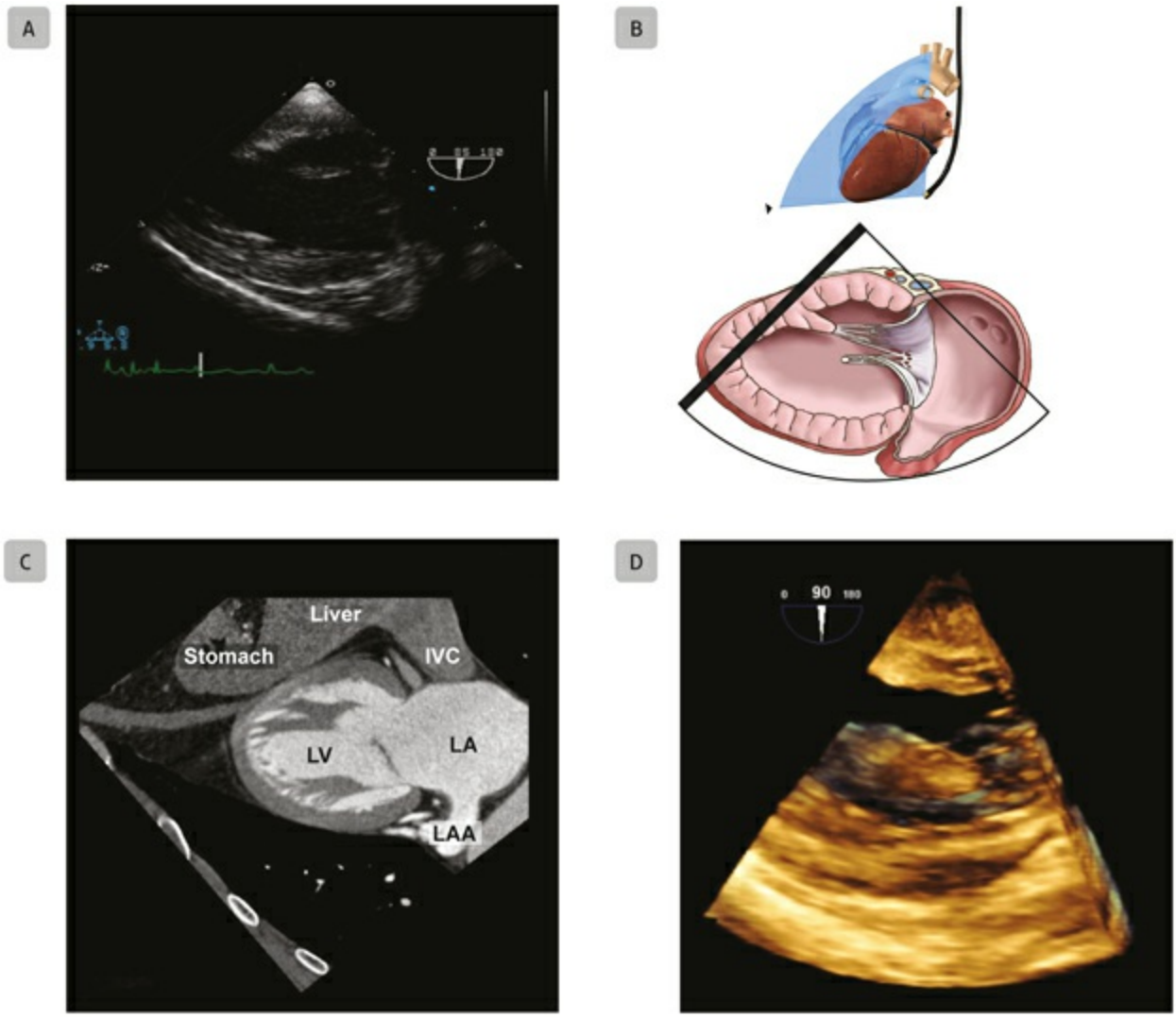

B3 Transgastric Two-Chamber. Transgastric two-chamber views obtained with two-dimensional echocardiography (**A**,**B**), ECG-gated computed tomography (**C**), and three-dimensional echocardiography (**D**). *Abbreviations:* ECG, electrocardiogram; IVC, inferior vena cava; LA, left atrium; LAA, left atrial appendage; LV, left ventricle. *Source:* Illustration B courtesy of Gian-Marco Busato.

https://youtu.be/-LX8T8v3ntA

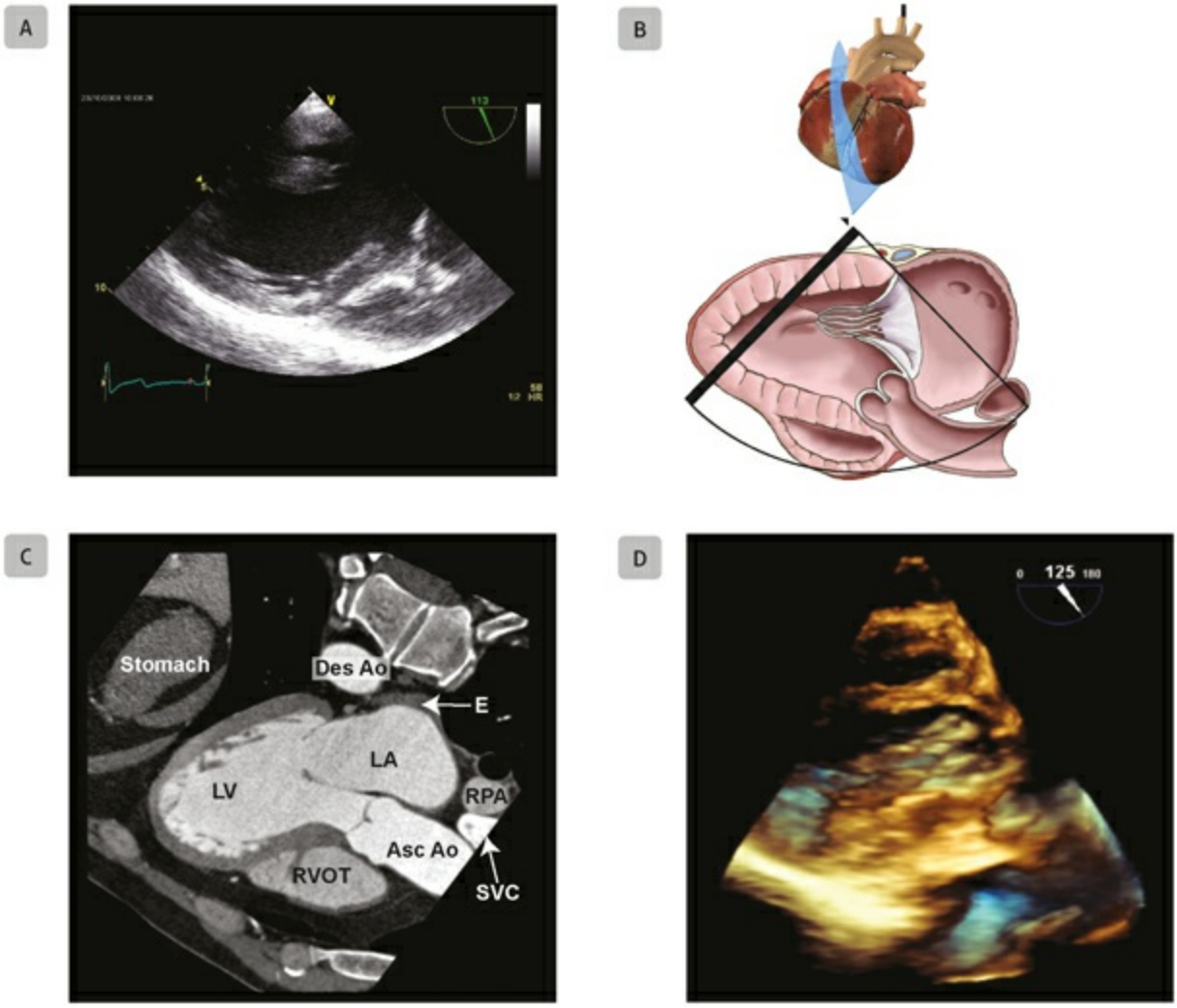

B4 Transgastric Long-Axis. Transgastric long-axis views obtained with two-dimensional echocardiography (**A**,**B**), ECG-gated computed tomography (**C**), and three-dimensional echocardiography (**D**). *Abbreviations:* Ao, aorta; Asc, ascending; Des, descending; E, esophagus; ECG, electrocardiogram; LA, left atrium; LV, left ventricle; RPA, right pulmonary artery; RVOT, right ventricular outflow tract; SVC, superior vena cava. *Source:* Illustration B courtesy of Gian-Marco Busato.

https://youtu.be/9T-tHMBr7lI

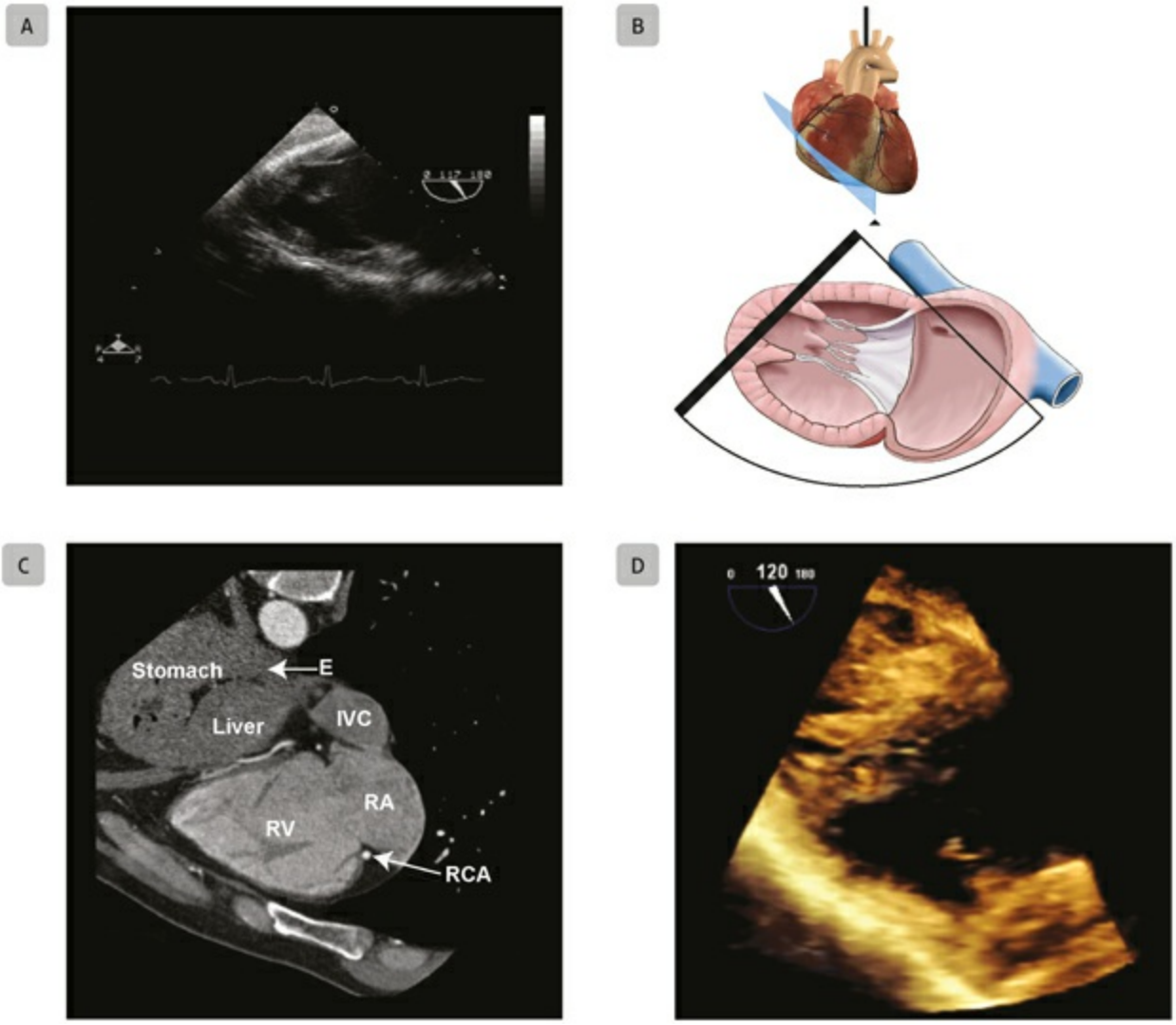

B5 Transgastric Right Ventricle. Transgastric right ventricular views obtained with two-dimensional echocardiography (**A**,**B**), ECG-gated computed tomography (**C**), and three-dimensional echocardiography (**D**). *Abbreviations:* E, esophagus; ECG, electrocardiogram; IVC, inferior vena cava; RA, right atrium; RCA, right coronary artery; RV, right ventricle. *Source:* Illustration B courtesy of Gian-Marco Busato.

https://youtu.be/NoFVXYzQ-yY

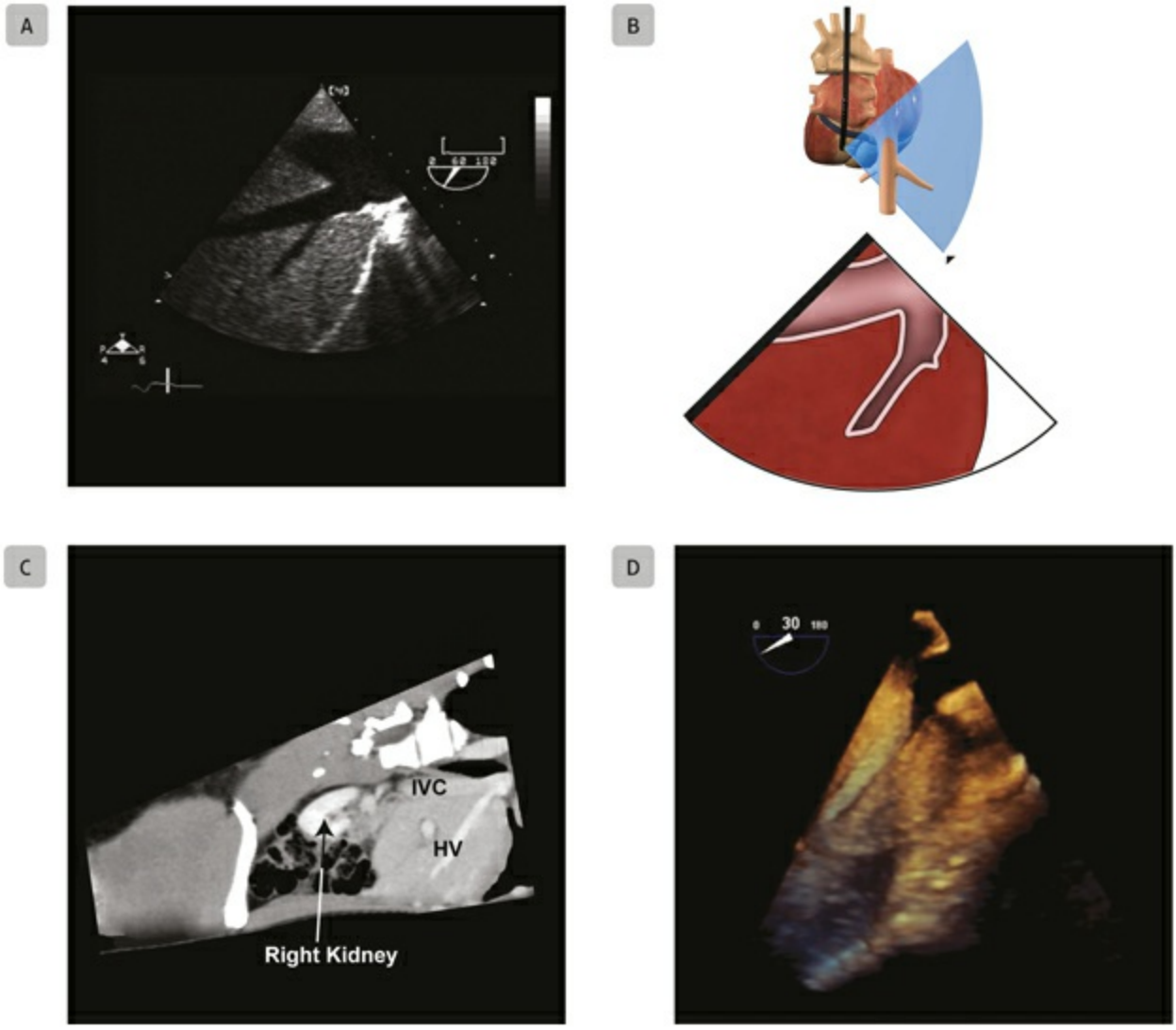

B6 Transgastric Inferior Vena Cava Long-Axis. Transgastric inferior vena cava long-axis views obtained with two-dimensional echocardiography (**A**,**B**), ECG-gated computed tomography (**C**), and three-dimensional echocardiography (**D**). *Abbreviations:* ECG, electrocardiogram; HV, hepatic vein; IVC, inferior vena cava. *Source:* Illustration B courtesy of Gian-Marco Busato.

A: https://youtu.be/27RgV33uHAU

D: https://youtu.be/Pq5xiiwf2Uc

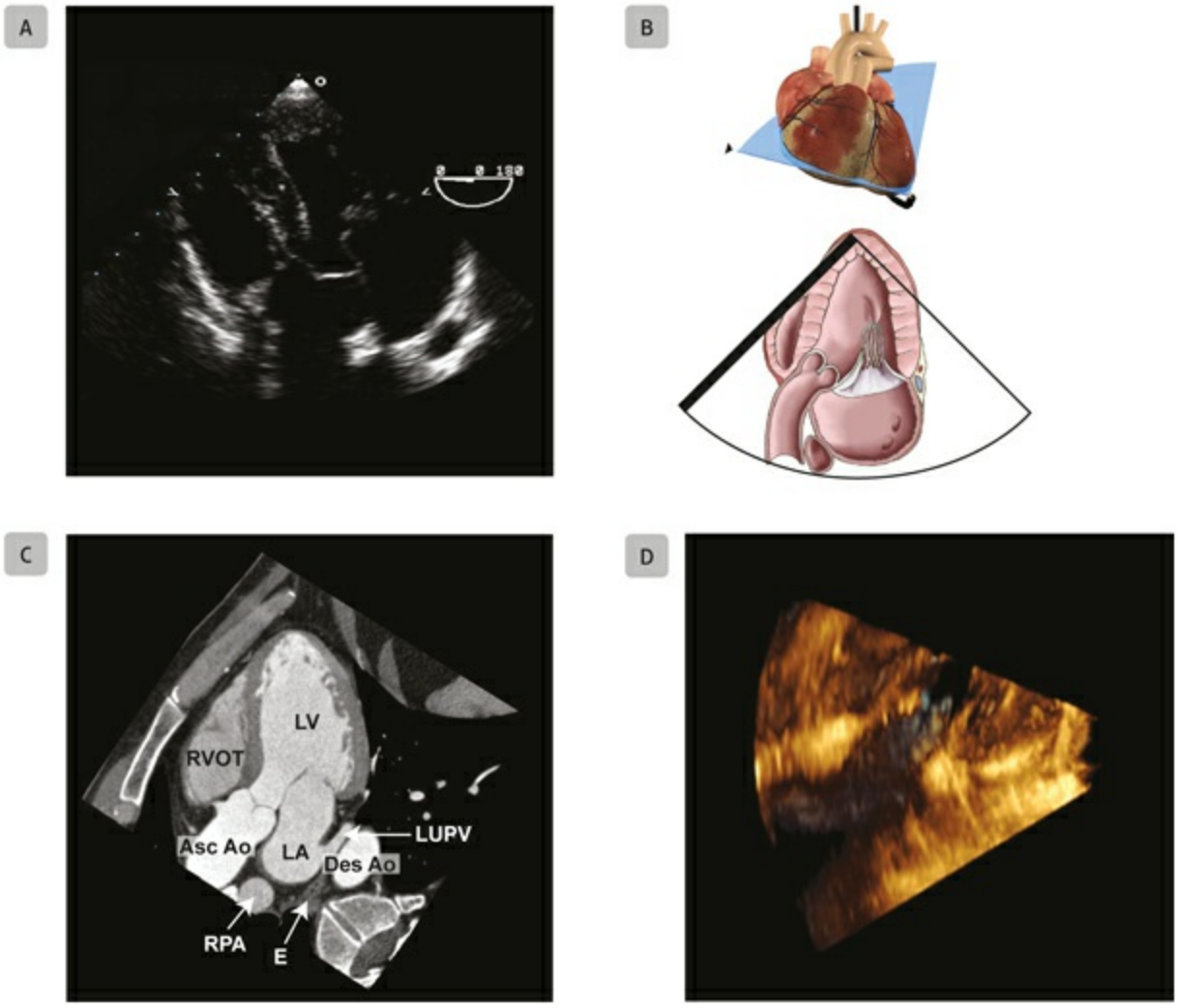

C1 Deep Transgastric. Deep transgastric views obtained with two-dimensional echocardiography (**A**,**B**), ECG-gated computed tomography (**C**), and three-dimensional echocardiography (**D**). *Abbreviations:* Ao, aorta; Asc, ascending; Des, descending; E, esophagus; ECG, electrocardiogram; LA, left atrium; LUPV, left upper pulmonary vein; LV, left ventricle; RPA, right pulmonary artery; RVOT, right ventricular outflow tract. *Source:* Illustration B courtesy of Gian-Marco Busato.

https://youtu.be/mFa7ge_RGME

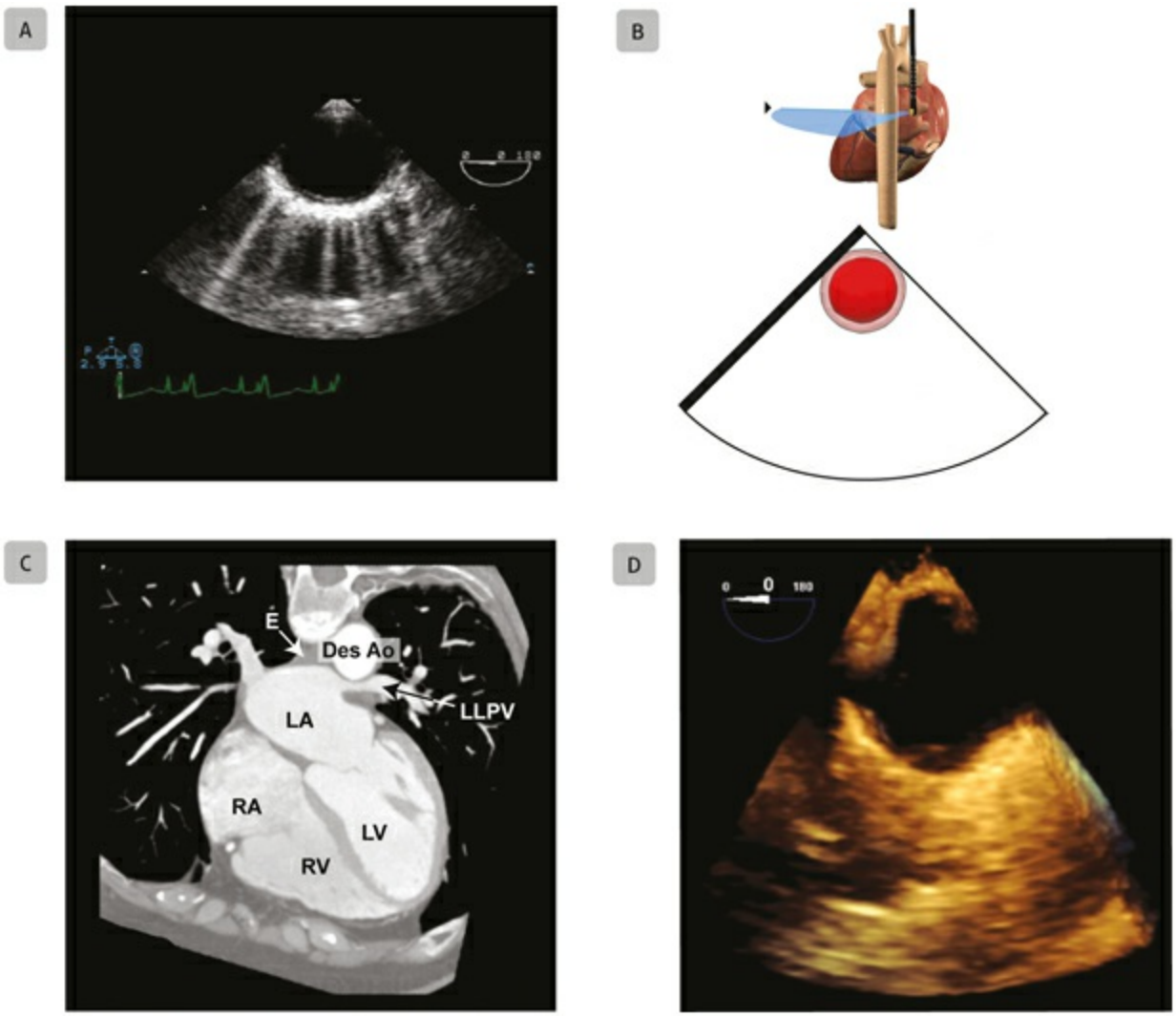

D1 Descending Aortic Short-Axis. Descending aortic short-axis views obtained with two-dimensional echocardiography (**A**,**B**), ECG-gated computed tomography (**C**), and three-dimensional echocardiography (**D**). *Abbreviations:* Ao, aorta; Des, descending; E, esophagus; ECG, electrocardiogram; LA, left atrium; LLPV, left lower pulmonary vein; LV, left ventricle; RA, right atrium; RV, right ventricle. *Source:* Illustration B courtesy of Gian-Marco Busato.

https://youtu.be/VsXCHHIFaIU

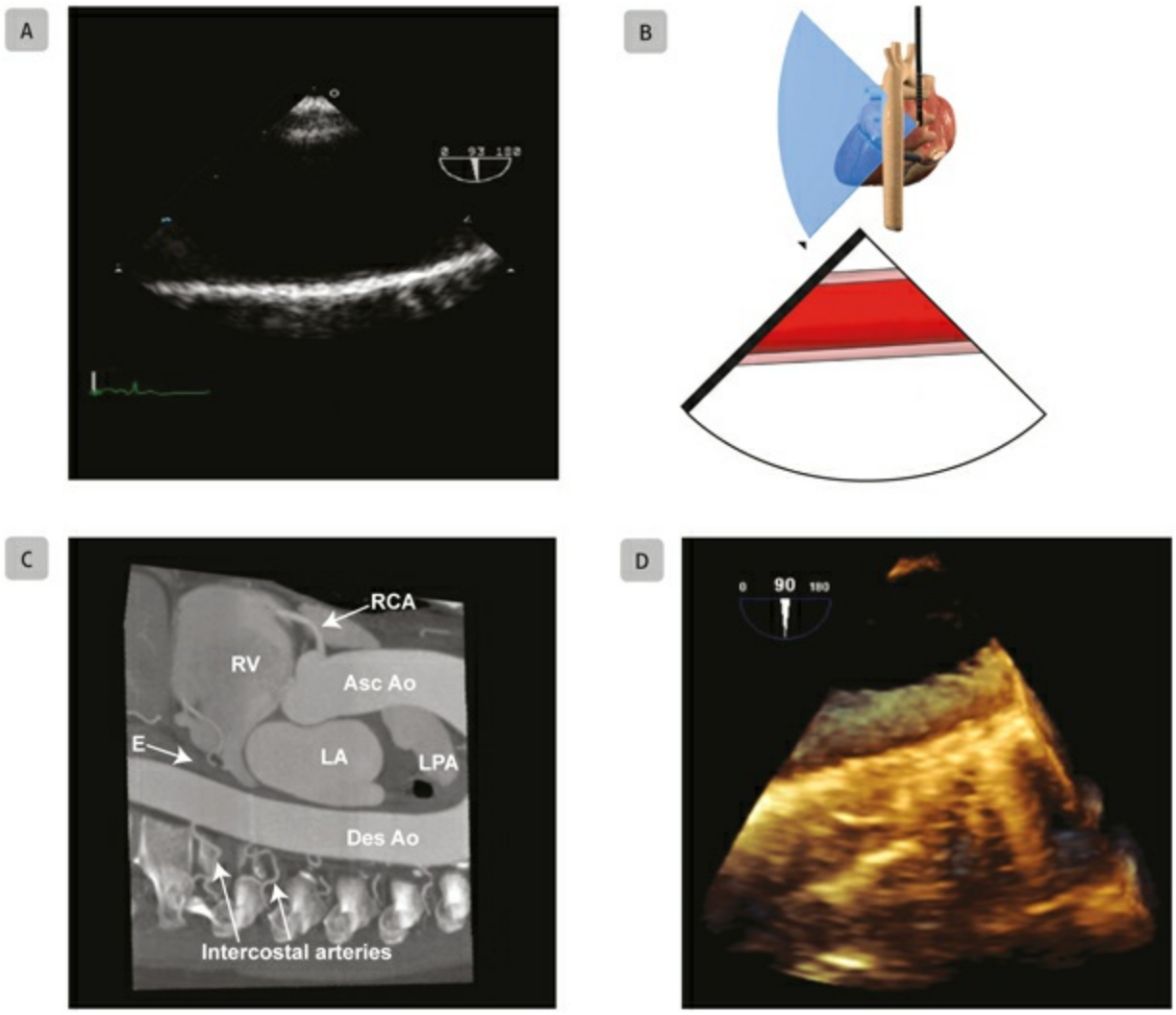

D2 Descending Aortic Long-Axis. Descending aortic long-axis views obtained with two-dimensional echocardiography (**A**,**B**), ECG-gated computed tomography (**C**), and three-dimensional echocardiography (**D**). *Abbreviations:* Ao, aorta; Asc, ascending; Des, descending; E, esophagus; ECG, electrocardiogram; LA, left atrium; LPA, left pulmonary artery; RCA, right coronary artery; RV, right ventricle. *Source:* Illustration B courtesy of Gian-Marco Busato.

https://youtu.be/BkXGYPGEzN4

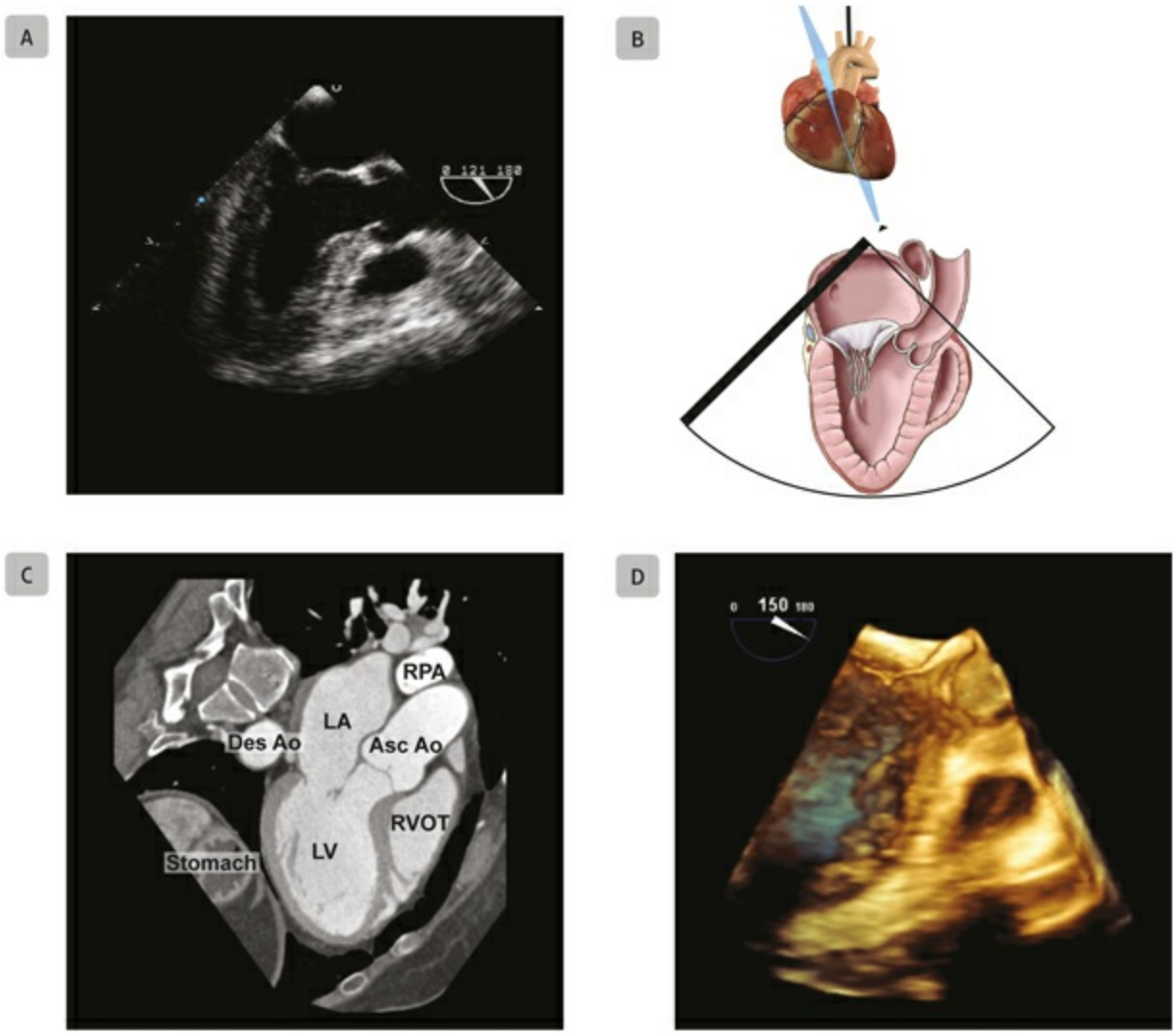

E1 Upper Esophageal Aortic Long-Axis. Upper esophageal aortic long-axis views of the aortic arch obtained with two-dimensional echocardiography (**A**,**B**), ECG-gated computed tomography (**C**), and three-dimensional echocardiography (**D**). *Abbreviations:* ECG, electrocardiogram; SVC, superior vena cava. *Source:* Illustration B courtesy of Gian-Marco Busato.

https://youtu.be/XatVn727JTs

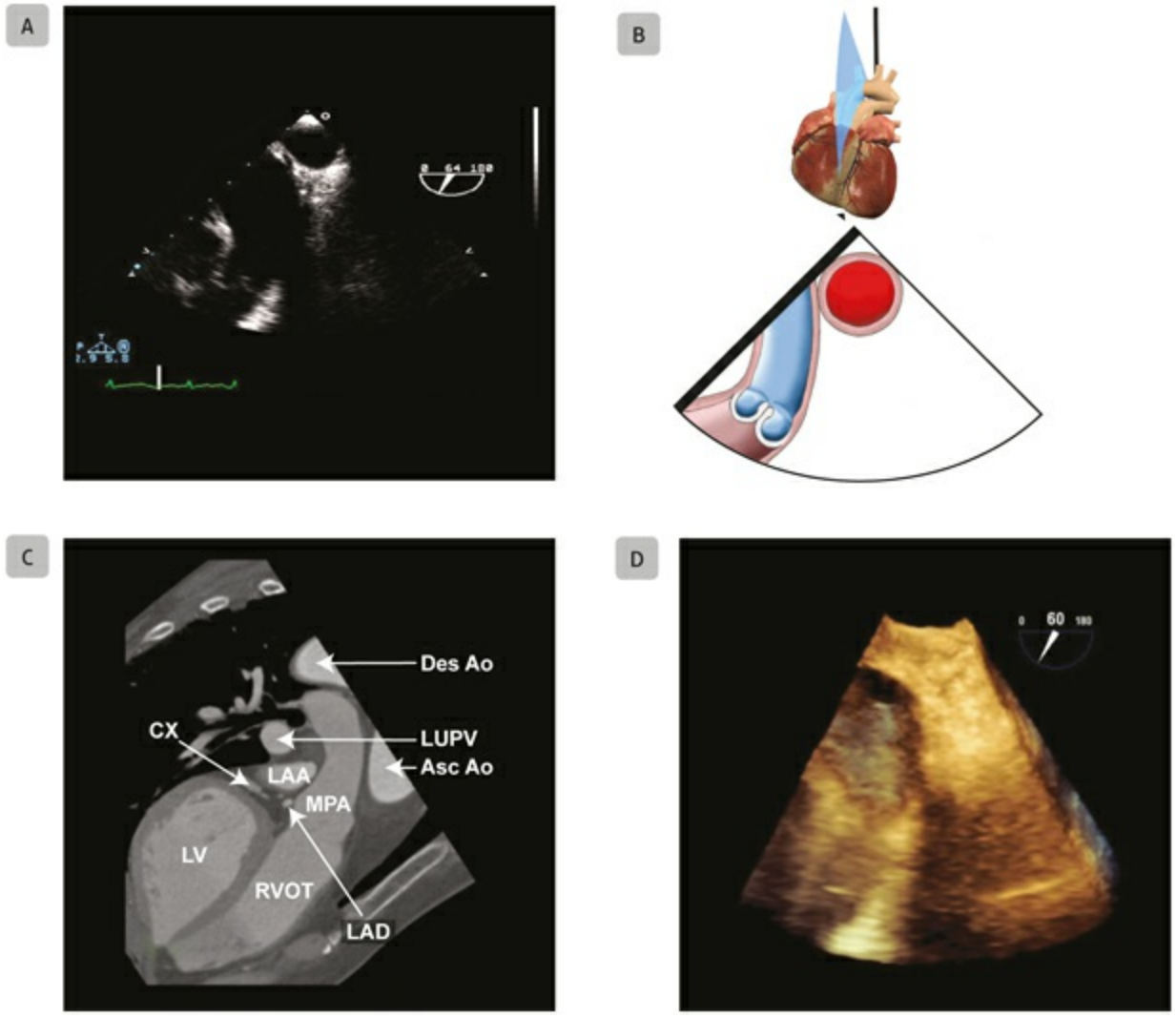

E2 Upper Esophageal Aortic Short-Axis. Upper esophageal aortic short-axis views of the ascending aorta obtained with two-dimensional echocardiography (**A**,**B**), ECG-gated computed tomography (**C**), and three-dimensional echocardiography (**D**). *Abbreviations:* Ao, aorta; Asc, ascending; CX, circumflex artery; Des, descending; ECG, electrocardiogram; LAA, left atrial appendage; LAD, left anterior descending artery; LUPV, left upper pulmonary vein; LV, left ventricle; MPA, main pulmonary artery; RVOT, right ventricular outflow tract. *Source:* Illustration B courtesy of Gian-Marco Busato.

https://youtu.be/z7FkN-bbNYg

INDEX

Note: Page numbers underscored or in italic refer to figures and tables respectively,

B

C

D

E

G

N

O

P

R

S

T

V

W

Z